

A11100 987985

NAT'L INST OF STANDARDS & TECH R.I.C.



A11100987985

Materials Research S/Characterization of  
QC100 .U57 V561:V1:1979 C.1 NBS-PUB-C 19























National Bureau of Standards  
Library, E-01 Admin. Bldg.

OCT 1 1981

191080

QC

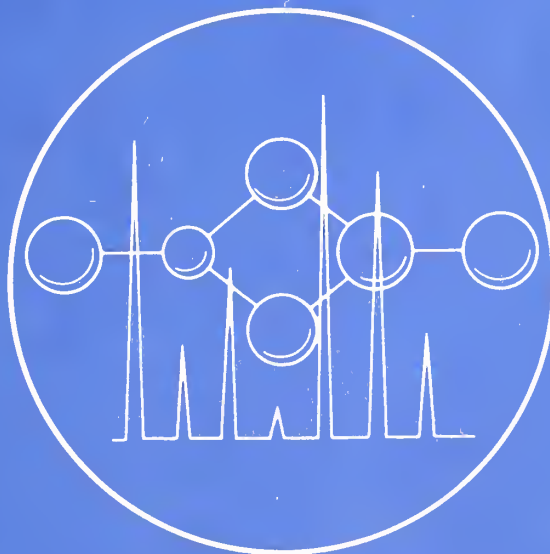
100

.457

# **10<sup>th</sup> MATERIALS RESEARCH SYMPOSIUM**

## **on CHARACTERIZATION OF HIGH TEMPERATURE VAPORS AND GASES**

**NBS SPECIAL PUBLICATION 561  
Volume 1**



QC  
100  
U57  
NO. 561  
V. 1  
1979  
C.2

**U.S. DEPARTMENT OF COMMERCE / National Bureau of Standards**



## NATIONAL BUREAU OF STANDARDS

The National Bureau of Standards<sup>1</sup> was established by an act of Congress on March 3, 1901. The Bureau's overall goal is to strengthen and advance the Nation's science and technology and facilitate their effective application for public benefit. To this end, the Bureau conducts research and provides: (1) a basis for the Nation's physical measurement system, (2) scientific and technological services for industry and government, (3) a technical basis for equity in trade, and (4) technical services to promote public safety. The Bureau's technical work is performed by the National Measurement Laboratory, the National Engineering Laboratory, and the Institute for Computer Sciences and Technology.

**THE NATIONAL MEASUREMENT LABORATORY** provides the national system of physical and chemical and materials measurement; coordinates the system with measurement systems of other nations and furnishes essential services leading to accurate and uniform physical and chemical measurement throughout the Nation's scientific community, industry, and commerce; conducts materials research leading to improved methods of measurement, standards, and data on the properties of materials needed by industry, commerce, educational institutions, and Government; provides advisory and research services to other Government agencies; develops, produces, and distributes Standard Reference Materials; and provides calibration services. The Laboratory consists of the following centers:

Absolute Physical Quantities<sup>2</sup> — Radiation Research — Thermodynamics and Molecular Science — Analytical Chemistry — Materials Science.

**THE NATIONAL ENGINEERING LABORATORY** provides technology and technical services to the public and private sectors to address national needs and to solve national problems; conducts research in engineering and applied science in support of these efforts; builds and maintains competence in the necessary disciplines required to carry out this research and technical service; develops engineering data and measurement capabilities; provides engineering measurement traceability services; develops test methods and proposes engineering standards and code changes; develops and proposes new engineering practices; and develops and improves mechanisms to transfer results of its research to the ultimate user. The Laboratory consists of the following centers:

Applied Mathematics — Electronics and Electrical Engineering<sup>2</sup> — Mechanical Engineering and Process Technology<sup>2</sup> — Building Technology — Fire Research — Consumer Product Technology — Field Methods.

**THE INSTITUTE FOR COMPUTER SCIENCES AND TECHNOLOGY** conducts research and provides scientific and technical services to aid Federal agencies in the selection, acquisition, application, and use of computer technology to improve effectiveness and economy in Government operations in accordance with Public Law 89-306 (40 U.S.C. 759), relevant Executive Orders, and other directives; carries out this mission by managing the Federal Information Processing Standards Program, developing Federal ADP standards guidelines, and managing Federal participation in ADP voluntary standardization activities; provides scientific and technological advisory services and assistance to Federal agencies; and provides the technical foundation for computer-related policies of the Federal Government. The Institute consists of the following centers:

Programming Science and Technology — Computer Systems Engineering.

<sup>1</sup>Headquarters and Laboratories at Gaithersburg, MD, unless otherwise noted; mailing address Washington, DC 20234.

<sup>2</sup>Some divisions within the center are located at Boulder, CO 80303.

# CHARACTERIZATION OF HIGH TEMPERATURE VAPORS AND GASES Volume 1

---

Proceedings of the 10th  
Materials Research Symposium  
held at the National Bureau of Standards  
Gaithersburg, Maryland  
September 18-22, 1978

Edited by:

John W. Hastie

Center for Materials Science  
National Measurement Laboratory  
National Bureau of Standards  
Washington, DC 20234



---

U.S. DEPARTMENT OF COMMERCE, Juanita M. Kreps, Secretary

Luther H. Hodges, Jr., Under Secretary

Jordan J. Baruch, Assistant Secretary for Science and Technology

NATIONAL BUREAU OF STANDARDS, Ernest Ambler, Director

Issued September 1979



Library of Congress Catalog Card Number: 79-600152

**National Bureau of Standards Special Publication 561/1**

Nat. Bur. Stand. (U.S.) Spec. Publ. 561/1, 800 pages (Sept. 1979)

CODEN: XNBSAV

**U.S. GOVERNMENT PRINTING OFFICE**

**WASHINGTON: 1979**

---

For sale by the Superintendent of Documents, U.S. Government Printing Office, Washington, D.C. 20402

Stock No. 003-003-02124-5      Price \$20. (Sold in sets only)

(Add 25 percent additional for other than U.S. mailing)

## PREFACE

During the week of September 18-22, 1978, the 10th Materials Research Symposium was held at NBS, Gaithersburg, on the subject of "Characterization of High Temperature Vapors and Gases". The Symposium aim was to assess the state-of-the-art and future directions and characterization methods for high temperature vapors including, where appropriate, gases and, to a lesser extent, plasmas. Modern technology increasingly requires materials and processes to function at high temperatures--a condition where the vapor, gaseous or plasma phase becomes significant. For example, the future success of new energy technologies such as coal-fired magnetohydrodynamic generators, coal gasification, and nuclear fusion depends largely on materials performance in hot chemically reactive gaseous atmospheres. Characterization of such atmospheres, or components thereof, is a challenging problem requiring adaptation of existing and development of new experimental and theoretical techniques. An assessment of these techniques for application in modern science and technology had not been previously attempted. The Symposium addressed this question by assembling internationally recognized experts in the measurement science and technology of high temperature vapors, gases, flames, and, to a lesser extent, plasmas. Key foreign laboratories, including those of the USSR, France, England, Japan, West Germany, Canada and Mexico are represented in the formal proceedings. In the United States, academic, industrial and Government institutions each made a substantial contribution to the Symposium.

From this Symposium, a group of invited and pertinent contributed papers were selected for publication. Also, in order to prevent, as far as possible, serious omissions of important new or improved techniques a number of papers not delivered at the Symposium were solicited for inclusion in this publication. Each paper has been subjected to a critical review process. Further, those papers delivered verbally at the Symposium were discussed by the attendant body and the edited discussion included at the end of each paper. I believe that this interactive process between authors, reviewers, symposium attendees, and the editor has resulted in a valuable published account of the current status of "Characterization of High Temperature Vapors and Gases."

The discussion following most of the papers in these volumes was prepared as follows. During the Symposium both written (question and answer forms) and taped discussion material was generated. Editing of this material was designed mainly to eliminate remarks that were adequately covered in the main text. Additional constraints were imposed by the usual problems of incoherence and human error in taping. A light handed approach was used in the editing process in order to retain something of the conference atmosphere and the personalities involved. Those scientists involved in the discussion process may be located by reference to the list of Symposium Participants.

These volumes deal with both classical and recently developed experimental techniques, ranging from the historically significant and still active area of Knudsen effusion to sophisticated spectroscopic methods such as Coherent AntiStokes Raman Spectroscopy<sup>1,2</sup>. What results from such developments is the generation of new basic data and diagnostic techniques for monitoring complex laboratory or real-life systems<sup>3</sup>. Such data and measurement tools provide the necessary ingredients to develop and validate computer-based models of complex technologically important systems such as combustion, corrosion, materials preparation and so on. Though the main emphasis of these volumes is on characterization methods, a useful number of examples of application to practical problems through modeling have been included.

Researchers concerned both with the basic properties of hot vapors and gases and the applied problems resulting from the extremes of temperature, pressure and chemical activity should find these volumes of particular interest. Throughout, the authors have made an effort to cite useful follow-up references and I have listed here additional major reference sources representing the past decade of research in this or related areas<sup>4</sup>.

It is a particular pleasure to acknowledge the following members of the Symposium Review Committee who willingly and enthusiastically assisted with the important review process; in alphabetical order they are: Dr. Dave Bonnell, Dr. Ray Dils, Dr. Mike Drake, Dr. Dick Gann, Dr. Bob Hauge, Dr. Bill Horton, Dr. Marilyn Jacox, Mr. Ralph Krause, Dr. Ken McCulloh, Dr. Ernie Plante, Dr. Gerd Rosenblatt, and Dr. Pete Schenck. The mammoth task of formatting, typing and proofing the manuscripts was managed primarily by the NML Text Editing Facility. Other conference management activities were expertly arranged by the offices of Mr. Ron Johnson and Joanne Lordon.

---

<sup>1</sup>In the interests of accuracy and clarity in describing various items of equipment or apparatus, mention has been made of commercial sources or brand names. This in no way implies endorsement of such products by the U.S. Government.



<sup>2</sup>Units: Several systems of units are used in this publication. Conversion factors to the International System of Units (SI) may be found in the representative publications listed below. The more common units and their conversion factors, as used in this publication are as follows.

Physical Quantity	Unit	Equivalent SI Unit
length	inch	$2.54 \times 10^{-2}$ m
length	angstrom	$10^{-10}$ m
mass	pound	0.453 592 37 kg
mass	atomic mass unit	$\sim 1.66041 \times 10^{-27}$ kg
force	kilogram-force	9.806 65 N
pressure	atmosphere	$101\,325\text{ N m}^{-2}$
pressure	torr	$(101325/760)\text{ N m}^{-2}$
energy	calorie(thermochem.)	4.184 J
energy	electron volt	$\sim 1.6021 \times 10^{-19}$ J
temperature	Celsius	kelvin - 273.15

References: Manual of Symbols and Terminology for Physiochemical Quantities and Units, Pure and Applied Chemistry 21, 1-44 (1970). Policy for NBS Usage of SI Units, J. Chem. Ed. 48, 569-572 (1971). SI Units in Physico-Chemical Calculations, A. C. Norris, J. Chem. Ed. 48, 797-800 (1971).

<sup>3</sup>A recurrent theme throughout these proceedings is the very limited bank of basic high temperature data, and the widespread usage of the JANAF Thermochemical Tables.

<sup>4</sup>High Temperature Vapors and Gases--Major References:

- 1975 High Temperature Vapors (J. W. Hastie; Academic Press, New York)
- 1967 Characterization of High Temperature Vapors (J. Margrave, ed., Wiley, New York).
- 1967-1971 Advances in High Temperature Chemistry (series, Academic Press, New York)
- Current Symposium (Int.) Combustion (Combustion Inst., Pittsburgh, Pennsylvania).
- 1976 Combustion Measurements (R. Goulard, ed., Academic Press, New York).

John W. Hastie  
Editor and Symposium Chairman

Sy  
re  
te  
ap  
of  
ac  
re  
te  
se  
res  
no  
mer  
ma  
Lab  
pra  
des  
Exa  
the  
Nil  
str  
opu  
thi  
slar  
tect  
runt  
rece  
ever  
will  
lanc  
good

## WELCOME

Good morning. I am pleased to have this opportunity to welcome the participants in this Symposium on "Characterization of High Temperature Vapors and Gases." This is the first conference of its kind devoted to the important measurement problems associated with the high temperature gaseous phase. Our charter as the National Measurement Laboratory makes it quite appropriate that we host this unique conference.

Some of you may be visiting NBS for the first time and may not be familiar with the range of activities at the Bureau. I would like to take a few minutes to describe some of our activities.

The Bureau was established in 1901 to develop and disseminate the national standards of measurement, to determine physical constants and properties of important materials, to develop test methods, to aid in the establishment of standard practices, and to provide technical services to other government agencies. Recent legislation has given NBS new and specific responsibilities in the areas of materials conservation, energy conservation, computer technology, standard reference data, and fire research. A new organizational structure was implemented on April 9, 1978 at NBS. Presently, the work of the Bureau is carried out in three major organizational units: The National Measurement Laboratory, the National Engineering Laboratory, and the Institute for Computer Science and Technology. Measurements, standard practices, and accurate data are common themes in all of our work, and we are perhaps best described as the nation's measurement laboratory.

NBS also has a long history of involvement in characterizing hot vapors and gases. Examples of notable past activities include the early work of Broida on flame spectroscopy, the application of matrix isolation methods to high temperature species as carried out by Milligan and Jacox, the development of specialized microwave spectroscopic techniques for structural determinations of high temperature species by Lide and coworkers, and the development of metal vapor pressure standards by Paule and associates. Current NBS interests in this area range from understanding flame inhibition to the thermodynamic characteristics of slag vapors important in the development of new magnetohydrodynamic and coal gasification technologies.

In recent years this field has seen rapid development, as evidenced by the variety and number of papers to be delivered this week. In order that the reports of these new activities receive rapid and widespread attention the conference committee and support staff has made every effort to ensure a rapid publication of the proceedings. I believe that this conference will enhance greatly the understanding of high temperature gases and vapors and their importance in developing new technologies. Once again, welcome to NBS, Gaithersburg and have a good meeting.

John D. Hoffman, Director  
National Measurement Laboratory  
National Bureau of Standards,  
Washington, DC



## ABSTRACT

This book is based on the proceedings of the 10th Materials Research Symposium, held at the National Bureau of Standards, Gaithersburg, Maryland, September 18-22, 1978. The symposium was sponsored by the National Measurement Laboratory (formerly Institute for Materials Research). Modern technology increasingly requires materials and processes to function at high temperatures--a condition where the vapor, gaseous or plasma phase becomes significant. Characterization of such atmospheres, or components thereof, is a challenging problem requiring adaptation of existing and development of new experimental and theoretical techniques. The aim of the symposium was to assess the state-of-the-art and future directions and characterization methods for high temperature vapors including, where appropriate, gases and, to a lesser extent, plasmas. In order to prevent, as far as possible, serious omissions of important new or improved techniques, a number of papers not delivered at the Symposium were solicited for inclusion in this publication. A total of eighty-six papers (invited and contributed) or chapters representing nine countries are contained in these volumes. The discussion, which followed most of the delivered papers, is also included.

Key words: Combustion; equilibrium; high temperature; isolation; lasers; mass spectrometry; matrix; modeling; vapors.

## CONTENTS<sup>1</sup>

Preface . . . . .	iii
Welcome . . . . .	
J. D. Hoffman . . . . .	vii
Abstract . . . . .	viii

## VOLUME I

### I. CLASSICAL VAPORIZATION METHODS

THE EFFUSION METHOD AT AGE 69: CURRENT STATE OF THE ART . . . . .	3
E. David Cater	
GENERAL THEORETICAL ANGULAR NUMBER DISTRIBUTION FUNCTIONS OF KNUDSEN FLOW THROUGH THE FOLLOWING SINGLE AND DOUBLE-SLIT ORIFICE GEOMETRIES: CIRCULAR, RECTANGULAR, AND CYLINDRICAL . . . . .	39
F. Miller	
AUTOMATIC DATA ACQUISITION BY THE TORSION-EFFUSION METHOD . . . . .	67
J. G. Edwards	
APPLICATION OF LASER PULSE HEATING FOR THE STUDY OF HIGH TEMPERATURE VAPORS, PHASE TRANSITIONS AND EQUATION OF STATE . . . . .	83
R. W. Ohse, J. F. Babelot, L. Cercignani, P. R. Kinsman, K. A. Long, J. Magill, and A. Scotti	
A HIGH TEMPERATURE TRANSPIRATION APPARATUS FOR THE STUDY OF THE ATMOSPHERE ABOVE VISCOUS INCONGRUENTLY VAPORIZING MELTS . . . . .	111
D. M. Sanders and W. K. Haller	
VAPORIZATION THERMODYNAMICS AND KINETICS OF HEXAGONAL SILICON CARBIDE . . . . .	125
R. G. Behrens and G. H. Rinehart	
A VERY ACCURATE PYROMETER FOR GENERAL LABORATORY USE . . . . .	143
E. K. Storms and B. A. Mueller	
OPERATION OF NEAR IDEAL HEAT PIPES . . . . .	153
L. A. Melton	

### II. MASS SPECTROMETRIC TECHNIQUES--KNUDSEN EFFUSION

ATTAINMENT OF CHEMICAL EQUILIBRIUM IN EFFUSIVE BEAM SOURCES OF THE HETEROGENEOUS REACTION TYPE . . . . .	171
D. L. Hildenbrand	
THERMODYNAMIC AND PHYSICO-CHEMICAL BEHAVIOR OF THE INTERACTIONS BETWEEN KNUDSEN-EFFUSION-CELLS AND THE SYSTEMS UNDER INVESTIGATION. ANALYSIS BY HIGH TEMPERATURE MASS SPECTROMETRY . . . . .	181
C. Chatillon, M. Allibert, and A. Pattoret	

<sup>1</sup>The grouping of papers is based primarily on the method rather than the system under study. Papers having either a fundamental or review emphasis are usually grouped at the beginning of a section.

CHARACTERIZATION OF HIGH TEMPERATURE VAPORS BY ANGULAR DISTRIBUTION MASS SPECTROMETRY . . . . .	211
R. T. Grimley and J. A. Forsman	
THE HIGH TEMPERATURE VAPORIZATION AND THERMODYNAMICS OF THE TITANIUM OXIDES. XIV. RELATIVE IONIZATION CROSS-SECTIONS OF Ti, TiO, AND TiO <sub>2</sub> . . . . .	231
R. I. Sheldon and P. W. Gilles	
CONGRUENT VAPORIZATION AND THERMODYNAMICS IN THE PRASEODYMIUM-SULFUR SYSTEM . . . . .	237
E. D. Cater, B. H. Mueller, and J. A. Fries	
VAPOR PRESSURE MEASUREMENTS OF POTASSIUM OVER K <sub>2</sub> O-SiO <sub>2</sub> SOLUTIONS BY A KNUDSEN EFFUSION MASS SPECTROMETRIC METHOD . . . . .	265
E. R. Plante	
MASS SPECTROMETRIC INVESTIGATION OF VAPOR SPECIES OVER LIQUID GERMANIUM DIOXIDE . . . . .	283
T. Sasamoto, M. Kobayashi, and T. Sata	
MASS SPECTROMETRIC DETERMINATION OF ATOMIZATION ENERGIES OF INORGANIC MOLECULES AND THEIR CORRELATION BY EMPIRICAL MODELS OF BONDING . . . . .	289
K. A. Gingerich	
III. MASS SPECTROMETRIC TECHNIQUES--HIGH PRESSURE SAMPLING	
HIGH PRESSURE MOLECULAR BEAM MASS SPECTROMETRIC SAMPLING OF HIGH TEMPERATURE MOLECULES . . . . .	303
C. A. Stearns, F. J. Kohl, G. C. Fryburg, and R. A. Miller	
TRANSPIRATION MASS SPECTROMETRY OF HIGH TEMPERATURE VAPORS . . . . .	357
D. W. Bonnell and J. W. Hastie	
<u>IN SITU</u> ANALYSIS OF MINOR GASEOUS SPECIES IN CRYSTAL GROWTH AMBIENTS USING MOLECULAR BEAM MASS SPECTROMETRY . . . . .	411
H. Dun, B. L. Mattes, and D. A. Stevenson	
MOLECULAR BEAM MASS SPECTROMETRIC SAMPLING OF MINOR SPECIES FROM COAL DUST-AIR FLAMES . . . . .	431
F. T. Greene, J. E. Beachey, and T. A. Milne	
THE USE OF FLAMES AS MEDIA FOR THE STUDY OF ION-MOLECULE THERMOCHEMISTRY . . . .	443
W. J. Miller	
MASS SPECTROMETRIC DETERMINATION OF NEGATIVE AND POSITIVE ION CONCENTRATIONS IN COAL-FIRED MHD PLASMAS . . . . .	457
J. Wormhoudt and C. E. Kolb	
MASS SPECTROMETRIC SAMPLING OF CONDENSED SYSTEM FLAMES <sup>2</sup> . . . . .	479
O. P. Korobeinichev and A. G. Tereshenko	

<sup>2</sup>Not presented at Symposium.



#### IV. MOLECULAR STRUCTURE DETERMINATION--MATRIX ISOLATED SPECIES

MATRIX ISOLATION STUDIES OF HIGH TEMPERATURE SPECIES . . . . .	495
R. H. Hauge and J. L. Margrave	
THE CHARACTERIZATION OF HIGH TEMPERATURE MOLECULES USING MATRIX ISOLATION AND ISOTOPE FINE STRUCTURE . . . . .	511
J. S. Ogden	
MATRIX ISOLATION OF HIGH TEMPERATURE SPECIES AND MATRIX PERTURBATION EFFECTS . .	523
F. W. Froben	
MATRIX ISOLATION STUDY OF THE VIBRATIONAL AND ELECTRONIC SPECTRA OF PO AND HPO . . . . .	529
M. Larzilliere and M. E. Jacox	
ESR MATRIX ISOLATION OF $\text{AlH}^+$ FORMED DURING THE HIGH TEMPERATURE VAPORIZATION OF $\text{Al}_2\text{O}_3$ . . . . .	545
L. B. Knight, Jr., R. L. Martin and E. R. Davidson	
MATRIX ISOLATION STUDIES OF MAGNESIUM AND IRON ATOM REACTIONS WITH WATER . . .	557
R. H. Hauge, S. E. Gransden, J. W. Kauffman, and J. L. Margrave	
PHOTOSELECTIVE BIMETALLIC AGGREGATION: A NEW ROUTE TO BIMETALLIC CLUSTERS . . .	567
W. E. Klotzbucher and G. A. Ozin	
TRANSITION-METAL MOLECULES AND WALSH'S RULES--RATIONALIZATION OF OPTICAL AND ESR DATA . . . . .	587
W. Weltner, Jr.	

#### V. MOLECULAR STRUCTURE DETERMINATION--VAPOR SPECIES

THE DETERMINATION OF THE MOLECULAR SHAPES OF 'HIGH TEMPERATURE' SPECIES . . . .	597
I. Beattie and D. A. Greenhalgh	
RAMAN SPECTROSCOPY IN HIGH TEMPERATURE CHEMISTRY . . . . .	609
M. C. Drake and G. M. Rosenblatt	
RESONANCE RAMAN SPECTRA OF METAL HALIDE VAPOR COMPLEXES . . . . .	647
G. N. Papatheodorou	
INFRARED SPECTRAL MEASUREMENTS OF SPECIES IN A HIGH TEMPERATURE FLOW TUBE . . . . .	679
M. E. Gersh and C. E. Kolb	
ROTATIONAL SPECTROSCOPY OF HIGH TEMPERATURE MOLECULES <sup>3</sup> . . . . .	695
T. Topping and E. Tiemann	
MODERN HIGH-TEMPERATURE ELECTRON DIFFRACTION <sup>3</sup> . . . . .	711
V. P. Spiridonov and E. Z. Zasorin	
PHOTOIONIZATION MASS SPECTROMETRY AND PHOTOELECTRON SPECTROSCOPY OF HIGH TEMPERATURE VAPORS . . . . .	757
J. Berkowitz	

<sup>3</sup>Not presented at Symposium.

THE PHOTOELECTRON SPECTROSCOPIC CHARACTERIZATION OF VAPORS OVER HEATED INORGANIC SOLIDS . . . . .	771
R. A. Bowling, T. W. Lassiter, D. O. Vick, and G. K. Schweitzer	
AB INITIO MOLECULAR ORBITAL STUDIES OF SOME HIGH TEMPERATURE METAL HALIDE COMPLEXES . . . . .	791
L. A. Curtiss	
SYMPOSIUM PARTICIPANTS . . . . .	803
AUTHOR INDEX . . . . .	811

## VOLUME II

### VI. SPECTROSCOPIC DIAGNOSTIC TECHNIQUES--SPECIES CONCENTRATION

NEW OPTICAL DIAGNOSTIC TECHNIQUES FOR TEMPERATURE AND SPECIES CONCENTRATION MEASUREMENTS IN FLAMES . . . . .	817
J. R. McDonald, A. P. Baronavski, L. Pasternack, S. Lamont, and A. B. Harvey	
LASER-ABSORPTION METHODS FOR CHARACTERIZING HIGH TEMPERATURE GASES . . . . .	835
W. C. Gardiner, Jr.	
NEAR-RESONANCE RAYLEIGH SCATTERING AND ATOMIC FLAME FLUORESCENCE SPECTRO- SCOPY . . . . .	847
C. Chan and J. W. Daily	
LASER INDUCED REACTIONS OF LITHIUM IN FLAMES . . . . .	855
C. H. Muller, III, K. Schofield, and M. Steinberg	
OPTO-GALVANIC SPECTROSCOPY: A NEW LOOK AT ATOMS AND MOLECULES . . . . .	865
K. C. Smyth, P. K. Schenck, W. G. Mallard, and J. C. Travis	
SiCl <sub>2</sub> FLUORESCENCE AS A CHEMICAL VAPOR DEPOSITION REACTOR PROBE . . . . .	885
T. O. Sedgwick and G. U. Arbach	
RAMAN SCATTERING OF THE GASEOUS PHASE AT HIGH TEMPERATURE . . . . .	899
R. Hillel, J. Bouix, and A. Machaelides	

### VII. SPECTROSCOPIC DIAGNOSTIC TECHNIQUES AND TEMPERATURE MEASUREMENT

DIAGNOSTIC TECHNIQUES IN COMBUSTION MHD FLOWS . . . . .	915
S. A. Self	
CARS DIAGNOSTIC INVESTIGATIONS OF FLAMES . . . . .	943
A. C. Eckbreth and R. J. Hall	
COMPARISON OF THERMOCOUPLE, GAS SAMPLING AND RAMAN MEASURED TEMPERATURES IN AN AFTERBURNING TURBOJET ENGINE PLUME . . . . .	973
W. M. Roquemore and P. O. Yaney	
USE OF THERMOCOUPLES FOR GAS TEMPERATURE MEASUREMENTS IN GAS TURBINE COMBUSTORS . . . . .	1027
R. R. Dils and P. S. Follansbee	

MOVING THERMOCOUPLE MEASUREMENTS OF HEAT TRANSFER IN HOT GASES . . . . .	1071
L. W. Hunter, C. H. Hoshall, C. Grunfelder, and R. M. Fristrom	
APPLICATION OF THE TWO LINE ATOMIC FLUORESCENCE TECHNIQUE TO THE TEMPORAL MEASUREMENT OF SMALL VOLUME FLAME TEMPERATURES . . . . .	1079
J. Bradshaw, J. Bower, S. Weeks, K. Fujiwara, N. Omenetto, H. Haraguchi, and J. D. Winefordner	
A COMPARISON OF SPECTROSCOPIC FLAME TEMPERATURE MEASUREMENTS: Na-D LINE REVERSAL, ROTATIONAL AND VIBRATIONAL RAMAN, AND OH ABSORPTION SPECTROSCOPY . . .	1105
M. C. Drake, L. H. Grabner, and J. W. Hastie	
OPTICAL DIAGNOSTICS IN CVD REACTORS . . . . .	1135
G. H. Miller, A. J. Mulac, and P. J. Hargis, Jr.	
LASER-GENERATED OPTO-ACOUSTIC PULSES IN AN ATMOSPHERIC PRESSURE FLAME . . . . .	1153
W. R. Anderson, J. E. Allen, Jr., T. D. Fansler, and D. R. Crosley	
MEASUREMENT OF ROTATIONAL DISTRIBUTIONS WITHIN $\text{OH}(\text{A}^2\Sigma^+, v'=0)$ IN FLAMES . . . .	1171
M. A. DeWilde and D. R. Crosley	
ROTATIONAL DEPENDENCE OF TRANSITION PROBABILITIES IN THE OH A-X BAND SYSTEM . . . . .	1181
I. L. Chidsey and D. R. Crosley	

#### VIII. RATE PROCESSES IN GASES--HOMOGENEOUS SYSTEMS

CHEMICAL PROCESSES IN HIGH REYNOLDS NUMBER TURBULENT DIFFUSION FLAMES . . . . .	1195
D. E. Jensen	
MODELING STUDY OF FLAME STRUCTURE IN LOW-PRESSURE, LAMINAR, PRE-MIXED METHANE FLAMES . . . . .	1223
J. R. Creighton and C. M. Lund	
PREDICTIVE MODELING OF DIBORANE OXIDATION . . . . .	1249
W. M. Shaub and M. C. Lin	
NEW COMPUTATIONAL ALGORITHMS FOR CHEMICAL KINETICS <sup>4</sup> . . . . .	1265
D. T. Pratt	
MEASURES OF EFFECTIVENESS AND MECHANISMS FOR CHEMICAL AND PHYSICAL INHIBITION OF QUENCHED AND ADIABATIC PREMIXED FLAMES . . . . .	1281
J. J. Reuther	
INFLUENCE OF WATER VAPOR ON HYDROGEN COMBUSTION <sup>4</sup> . . . . .	1315
A. Feugier	
INHIBITION ON THE PROPAGATION OF FLAME <sup>4</sup> . . . . .	1327
T. Inomata, S. Okazaki, T. Moriwaki, and M. Suzuki	
MEASUREMENTS OF SOME ELEMENTARY HYDROCARBON REACTIONS AT HIGH TEMPERATURES . . .	1339
P. Roth and T. H. Just	
THE WALL-LESS REACTOR. A TECHNIQUE FOR THE STUDY OF GAS PHASE OXIDATIONS AND PYROLYSES OF HYDROCARBONS <sup>4</sup> . . . . .	1353
J. E. Taylor	

<sup>4</sup>Not presented at Symposium.

STUDIES OF THE ELEMENTARY REACTION KINETICS OF HIGH-TEMPERATURE SPECIES USING OPTICAL MEASUREMENT TECHNIQUES . . . . .	1359
A. Fontijn	
DIFFUSION OF CARBON DIOXIDE AT HIGH TEMPERATURES . . . . .	1373
J. R. Ferron, D. L. Kerr, and A. U. Chatwani	
IX. RATE PROCESSES IN GASES--HETEROGENEOUS SYSTEMS	
THE COMBUSTION OF PUVERIZED COALS--AN ASSESSMENT OF RESEARCH NEEDS . . . . .	1407
D. R. Hardesty and J. H. Pohl	
TRANSPORT, THERMODYNAMIC AND KINETIC ASPECTS OF SALT/ASH DEPOSITION RATES FROM COMBUSTION GASES . . . . .	1451
D. E. Rosner, K. Seshadri, J. Fernandez de la Mora, G. Fryburg, F. Kohl, C. Stearns, and G. Santoro	
THE MODELING OF MODERN HIGH PRESSURE ARC LAMPS . . . . .	1477
R. J. Zollweg	
THE FUTURE OF GAS TRANSPORT REACTIONS <sup>5</sup> . . . . .	1497
V. P. Orlovskii	
NEW MOLECULES INVOLVED IN CHEMICAL TRANSPORT REACTIONS: GASEOUS HALIDE COMPLEXES <sup>5</sup> . . . . .	1507
H. Schafer	
METAL HALIDE--GROUP III HALIDE VAPOR COMPLEXES WITH EMPHASIS ON ALUMINUM CHLORIDE <sup>5</sup> . . . . .	1517
H. A. Øye and D. M. Gruen	
FORMATION OF CHROMATES FROM THE REACTION OF ALKALI CHLORIDES WITH Cr <sub>2</sub> O <sub>3</sub> AND OXYGEN . . . . .	1539
C. Hirayama and C. Y. Lin	
CATALYTIC REACTIONS STUDIES BY A MATRIX ISOLATION TECHNIQUE: DECOMPOSITION OF HCOOH ON Pt . . . . .	1551
D. Tevault and M. C. Lin	
X. THERMODYNAMIC DATA AND APPLICATIONS	
REFERENCE DATA FOR HIGH TEMPERATURE SYSTEMS . . . . .	1571
L. N. Gevantman, H. J. White, Jr., and D. R. Lide, Jr.	
EVALUATION AND COMPILATION OF THE THERMODYNAMIC PROPERTIES OF HIGH TEMPERATURE SPECIES . . . . .	1581
M. W. Chase, J. R. Downey and A. N. Syverud	
DIMENSIONAL ANALYSIS OF PARTITION FUNCTIONS FOR IONIC MOLECULES: THERMODYNAMIC PROPERTIES OF VAPORS . . . . .	1597
D. J. Frurip and M. Blander	

<sup>5</sup>Not presented at Symposium.



THERMODYNAMICS OF NON-RIGID MOLECULES AT HIGH TEMPERATURE <sup>6</sup> . . . . .	1611
P. Ip and H. L. Strauss	
GRAPH THEORY PREDICTION OF THE PRESSURE SECOND VIRIAL COEFFICIENTS OF SOME HYDROCARBONS, FLUOROCARBONS, AND THEIR MIXTURES <sup>6</sup> . . . . .	1619
W. Brostow	
MECHANISMS OF OXIDATION AND HOT CORROSION OF METALS AND ALLOYS AT TEMPERATURES OF 1150 TO 1450 K UNDER FLOW . . . . .	1639
E. A. Gulbransen and G. H. Meier	
POTASSIUM SEED ACTIVITIES IN OPEN CYCLE MHD SYSTEMS: PREDICTIONS USING A MULTIPHASE MULTICOMPONENT SOLUTION MODEL . . . . .	1683
C. C. Hsu and C. E. Johnson	
COMPUTER MODELING OF GAS-CONDENSED PHASE EQUILIBRIA: PRESENT STATUS AND SOME FUTURE NEEDS IN SCIENCE AND TECHNOLOGY . . . . .	1707
M. Blander	
SYMPOSIUM PARTICIPANTS . . . . .	1717
AUTHOR INDEX . . . . .	1725

---

<sup>6</sup>Not presented at Symposium



## **I. CLASSICAL VAPORIZATION METHODS**

High  
Pressure  
Gases  
The  
eff  
est  
vol  
dur  
bec  
of  
in  
and  
ove  
vap  
Eff  
stu  
tor  
equ  
exp  
Thi  
of  
asc  
the  
anc  
who  
bwe  
d.  
—  
F



## THE EFFUSION METHOD AT AGE 69: CURRENT STATE OF THE ART

E. David Cater  
Department of Chemistry  
University of Iowa  
Iowa City, Iowa 52242

The effusion method for determining vapor pressures was introduced in 1909 by M. Knudsen [1]<sup>1</sup> and in its several variants has been the dominant tool for studying equilibria between gases and condensed phases at vapor pressures in the molecular flow region. In the ferment which occurred in high temperature chemistry from World War II through the 1960's the effusion method was the key to determining vapor pressures and dissociation energies and to establishing the vaporization processes of materials of very high melting point and low volatility. A number of studies investigating the validity of the assumptions were published during the 1960's and early 1970's. The mass spectrometric variant of the Knudsen method became widespread starting in the mid-1950's, and has given rise to insight and understanding of the chemical bonding of molecules of transition elements, of deviations from stoichiometry in high temperature solids, and of periodic trends in thermochemical values. Several reviews and surveys of effusion techniques and results appeared from 1967-1970, but no comprehensive overviews seem to have been published since. In this symposium devoted to high temperature vapors and gases it seems particularly appropriate to survey the scene and comment on "The Effusion Method at Age 69: Current State of the Art."

I do not propose to survey the extensive literature and present tabulations of systems studied and catalogs of thermochemical results. Instead I shall first present a few historical notes tracing the development of the effusion methods and presenting some fundamental equations to be used later. Then I shall attempt to cite what appear to be theoretical and experimental limitations of the method, generally, and of each variant of the effusion method. Third, I hope to indicate how these problems have been dealt with and where our understanding of them now lies, and to give estimates of the accuracy with which derived results can be ascribed. Finally, I shall mention some newer techniques which give some of the same results that have traditionally been obtained by effusion studies, try to place them in perspective, and perhaps suggest some future directions for effusion studies.

I am happy to acknowledge conversations and communications with a number of persons to whom I asked the question "Are we making better effusion measurements now than, say, ten or twenty years ago?" Particularly informative were the comments of J. Berkowitz, J. Drowart, J. G. Edwards, P. W. Gilles, K. A. Gingerich, R. T. Grimley, D. L. Hildenbrand, E. K. Storms,

---

<sup>1</sup> Figures in brackets indicate the literature references at the end of this paper.

R. J. Thorn, J. W. Ward, P. G. Wahlbeck and W. L. Winterbottom. In a sense these are co-authors of this paper, although, of course, I take responsibility for errors of fact and interpretation.

## 1. Historical Notes

### 1.1 Knudsen

In 1909 Martin Knudsen published two landmark papers [2,3] in which he explained theoretically and demonstrated experimentally the laws of transport of low pressure gases by molecular flow. In the first paper [2] he proposed the random (cosine) reflection of molecules upon collision with the container wall and showed that this assumption and the Maxwellian velocity distribution were sufficient to derive the law for flow through ideal orifices and long tubes, although his approach yielded only a qualitative result for the transmissivity of short tubes (or long orifices). In the second paper [3] he investigated the transition from molecular flow toward the then better understood hydrodynamical effusion as the ratio of mean free path to orifice diameter,  $\lambda/D$ , (now called the Knudsen number) decreased below about 10. In his third paper of 1909 [1], Knudsen applied what we now call the effusion or Knudsen method to the determination of the vapor pressure of mercury in a glass apparatus in the range 0-50 °C. He thereby assured himself a place in the affections of some of us at least equivalent to those occupied by his countrymen Niels Bohr and Hans Christian Anderson. Incidentally, his effusion measurement at 0 °C lasted 13 days, because his method of detection was to condense the effusing mercury vapor and then measure its volume at room temperature in a capillary tube attached below the condenser. His nonlinear vapor pressure equation, when extrapolated as high as 800 °C gave excellent agreement with vapor pressures measured in other ways.

Knudsen's subsequent "ingenious experiments" [5] contributed to the development of molecular physics in the era just before the quantum mechanical revolution, particularly in the area of the accommodation of energy [6,7,8] between colliding molecules and surfaces. On re-reading Knudsen's earliest papers from the vantage point of off-the-shelf, ultra-high vacuum components, one is struck by his sophisticated use of what seems very simple equipment and his remarks that at that time it was still uncertain how exactly the ideal gas law might apply in devices like McLeod gages. One recalls that the diffusion pump was not invented until 1915 (Gaede) or 1916 (Langmuir).

The well-known Knudsen equation (or Hertz-Knudsen equation) first derived by Hertz in 1882 [4]) relates the vapor pressure to the molar effusion rate through an ideally thin-edge orifice of area A

$$P = (Z/At)(2\pi RTM)^{1/2} \quad (1)$$

or to the mass effusion rate

$$P = (G/At)(2\pi RT/M)^{1/2} \quad (2)$$

## 1.2 Early measurements

The earliest effusion apparatuses, for example Egerton's in 1917 [10], were designed, as was Knudsen's, to condense the total effusate and so determine its amount. Egerton [11] in 1923 was one of the first to weigh the effusion cell to determine the mass loss to calculate the pressure. Nesmeyanov [12] gives details of some of the early apparatuses and techniques as well as later ones. The first application of target collection methods, in which a small known fraction of the effusate is condensed on a suitable collector placed coaxially with the orifice but some distance away, was made by Rudberg, who determined the vapor pressure of calcium in 1934 [13]. Target methods have the advantage that vapor pressures can be measured at a number of temperatures without disturbing the vacuum, and that exposure times can be accurately established by the use of suitable shutters. The fraction of the effusate collected by a circular target of radius  $R$  on the axis at a distance  $D$  from the orifice is proportional to  $R^2/(R^2 + D^2)$ . Thus analytical methods sensitive in the microgram range are necessary to obtain precise measurements, as will be mentioned again later.

## 1.3 The Cosine law; Clausing factors

Knudsen had predicted a cosine distribution of effusing molecules from ideal orifices. That is, the number of molecules per unit time effusing at angle  $\theta$  to the normal and into element of solid angle  $d\omega = 2 \sin \theta d\theta$ , is proportional to  $\cos \theta d\omega$ . H. Mayer in 1928-29 [14,15] used a delicate aluminum foil vane suspended on a quartz torsion fiber to explore the momentum distribution in front of a thin edged orifice, and so experimentally verified the cosine law, within his experimental error for the first time. He also studied the upper pressure bound to the effusion process and measured the vapor pressures of potassium and mercury [15] with his apparatus.

The calculation of transmission probabilities for molecular flow through long and short tubes [2], was attempted by Knudsen, but it was Clausing [16,17,18] who in 1929-32 published the first reliable results for short, cylindrical tubes and orifices. We still refer to these transmission probabilities as Clausing factors, and most authors use his symbol  $W$  for them. For finite orifice lengths, molecules not traveling parallel to the axis may strike the orifice wall and be returned to the cell, rather than passing on out after the collision. The measured mass loss is thus less than that expected for the pressure in the effusion cell, and the pressure calculated from the mass loss must be corrected by the Clausing factor,

$$P = (1/W)(G/At)(2\pi RT/M)^{1/2}. \quad (3)$$

Clausing also quantitatively predicted the departure from the ideal cosine distribution for beams effusing from these nonideal orifices. For about 25 years Clausing's  $W$  values were the only ones available. Later more sophisticated calculations [19-21] tabulate Clausing factors for cylindrical, and diverging and converging conical orifices, and for spherical ones [22]. For the cylindrical cases the results differ at most by a few percent from

Clausing's original values. Grimley [23] has discussed the modification of Clausing's angular distribution equations necessary to account for source and detector geometry in experimental angular distribution studies.

#### 1.4 Volmer and torsion effusion

Volmer and his dissertation students at the Technische Hochschule in Berlin invented the torsion effusion method, apparently initially as a way to determine molecular weights of slightly volatile organic compounds. This work was first published in 1931 [24]. Freeman [25] has given a complete and interesting review of the development of the torsion effusion method and related momentum measurements up to the mid 1960's. Edwards, in a later paper in this volume, presents its latest incarnation. The torsion cell was a major advance, for from purely geometrical and mechanical measurements it gives the total vapor pressure free of any assumptions about the molecular character of the vapor. This application is discussed in detail later.

#### 1.5 Knudsen cell mass spectrometry

The first applications of Knudsen cell mass spectrometry (KC/MS) followed immediately upon the mass spectrometric studies of the sublimation of graphite published by Chupka and Inghram [26] in 1953 and Honig [27] in 1954. Chupka and Inghram [28] at the University of Chicago established what was almost the "standard" high temperature mass spectrometric apparatus, employing a 60° sector magnetic deflection instrument, electron bombardment ionization, and electron multiplier detection. With several co-workers at Chicago and Argonne National Laboratory (many of whom continued similar studies elsewhere) they instituted a long series of studies of vaporization processes and thermodynamics of elements, oxides, halides and other high temperature materials. Simultaneously, Spedding, Johnson, and co-workers at the Ames Laboratory, Iowa State University, obtained the heats of vaporization [29,30] of rare earth metals, using a less versatile hot wire ionization technique. The rapid expansion of KC/MS studies in the 1950's and 60's is detailed in reviews by Brewer and Searcy [31], Margrave [32], Gilles [33], Drowart and Goldfinger [34], and a rather complete list of 280 high temperature systems studied up to 1964 is given by Grimley [35]. Drowart and Goldfinger's review article [36] is particularly useful.

The less expensive time-of-flight instruments which came on the market in about 1958-59 immediately made their appearance in the effusion field [37,38]. The much smaller and still cheaper quadrupole units are now also widely used, and most mass spectrometer manufacturers now can provide Knudsen cell input systems.

Because both the classical effusion techniques and mass spectrometry were well developed at the time they were combined, very rapid development occurred. On reading the pioneering papers and early review articles one finds that the techniques and interpretations differ very little from those found in the most recent papers. The two most fundamental problems, then and now, characteristic of KC/MS experiments are: (1) the identification of the parent gaseous species from which the observed ions are derived (the fragmentation problem) and



particularly (2) the determination of sensitivity constants to get absolute partial pressures (the cross section problem).

## 2. The effusion method

The procedures basic to all effusion studies are well known, and detailed reviews and description of experimental apparatus and procedures are available in several books [39-42]. The reader is referred to those reviews for details. In the present paper we shall consider the basic assumptions behind the effusion method in its several variants, and try to indicate the extent to which practice lives up to the assumptions and how some major problems are presently handled. Thus, I hope to indicate "how well we are doing."

In the effusion method I include all detection methods for measuring and/or analyzing the effusate from Knudsen cells at low pressures, which yield vapor pressures and thermodynamic data on the condensed phase(s) and the gaseous species.

### 2.1 Basic assumptions

A generalized effusion experiment occurs as follows. A solid or liquid sample of known stoichiometry is in equilibrium with its vapor in an initially evacuated, isothermal enclosure (Knudsen or effusion cell) of known temperature, in a good vacuum system. A small orifice of ideally thin edge, or of precisely known dimensions if not thin edged, opens through the wall or lid and vapor molecules escape into the surrounding vacuum at a rate assumed equal to the equilibrium rate of collision with the wall or the sample surface. One measures the rate of effusion of all species together, or of individual species, through the orifice and calculates the total effective vapor pressure or the partial pressures of the observed species at a number of different temperatures. Then, from the temperature dependence of the partial pressures and whatever auxiliary data are necessary, one derives the desired thermodynamic results. The experiment is really an irreversible transport process, and some of the basic assumptions may not be met in a given "real life" situation. The basic assumptions are these:

Isothermal cell, known temperature.

Equilibrium conditions are maintained.

- a. Thermal equilibrium.
- b. Constant collision density at all surfaces, no pressure gradient in the gas phase from sample surface to orifice.
- c. Chemical equilibrium
  - (1) constant, uniform composition in each phase.
  - (2) unit evaporation/condensation coefficients.
  - (3) equilibrium among the condensed phases and all vapor species.

Only collisional interactions with walls (the cell is "inert.")

- a. Random (cosine) reflection at all surfaces.

- b. No grain boundary or surface diffusion.
  - c. No chemical reaction with the cell.
  - d. No diffusion into or through the wall.
4. Ideal orifice
- a. Zero thickness, or, if not,
  - b. Orifice geometry well known and accurate transmission probabilities (Clausing factors) available.
5. Pressures in the molecular flow regime.

## 2.2 Real cells, samples, and orifices

The basic effusion equations involve the assumption of isotropic vapor within the cell and a constant collision rate at all surfaces. However, the open orifice acts as a sink for molecules, and must therefore establish a pressure gradient. The mean free path may be long in relation to cell dimensions and the sample is likely to be localized either on the floor or wall of the cell. If the orifice is in the top of the cell, most of the molecules effusing in the forward direction make one long jump directly from the sample surface and through the orifice without any collisions. If the orifice is not directly opposite the sample, as is likely with torsion cells, then most of the molecules effuse after making the last collision with the opposite wall. Yet for forty years users of the effusion method assumed that transport in Knudsen cells obeyed the isotropy assumption, i.e. the vapor in the cell behaved as though there were sufficient collisions between molecules to maintain equilibrium conditions. Because fair to good agreement is often obtained with several cell geometries, and by mass loss, collection, and torsion experiments, isotropy and equilibrium must be fairly closely approached in real cells. However, up to the mid-1960's no experimental tests of the angular distribution theory seemed to agree exactly with theoretical predictions (see Wang and Wahlbeck [85] for a review of the literature) although the agreement was often tantalizingly close. The general feeling was that the theory was good, and that understanding the deviations of the observations from the theory would go far toward understanding the problems of real vapor pressure measurements. The aspects of the problem studied have included shape of cell and orifice, nonunit evaporation coefficients, effects due to long mean free paths (wall collisions more important than gas phase collisions), effects due to short mean free paths as the flow goes from free molecular to transition to hydrodynamical, and effects due to temperature gradients, to surface diffusion, and due to specular reflection.

### 2.2.1 Cell geometry and vaporization coefficients

Whitman [43] and Motzfeldt [44] have considered the transport in cylindrical cells with sample in one end and orifice in the other, in which the sample may have non-unit vaporization coefficient  $\alpha$ . By different approaches they obtained the same equation relating the equilibrium vapor pressure  $P_{eq}$  to the observed mass loss pressure  $P_K$  calculated via the Knudsen equation. The Whitman-Motzfeldt equation incorporates the Clausing factor for the

orifice,  $W_o$ , a Clausing factor for the cell body  $W_c$ , calculated as though the cell body were itself an orifice, and also the areas of orifice and sample surface,  $A_o$  and  $A_s$ . The cross sectional area of the cell is often used for  $A_s$ .

$$P_{eq} = P_K \left[ 1 + \frac{W_o A_o}{A_s} \left( \frac{1}{\alpha} + \frac{1}{W_c} - 2 \right) \right] \quad (4)$$

For a cell of length equal to its diameter,  $W_c \approx 0.5$  and

$$P_{eq} = P_K (1 + W_o A_o / \alpha A_s) \quad (5)$$

Balson [45] obtained a similar result by using a more elaborate assumption for the form of the pressure gradient in the cell. Carlson, et al. [46] showed that the assumptions of Motzfeldt and Whitman were mutually contradictory, but their own numerical results for  $P_{eq}/P_K$  were almost identical to the others'. Ward and Fraser [47] simulated the real effusion process by Monte Carlo calculations, and found that eq. (4) has the correct form. For small  $\alpha$  and  $W_o$  their numerical results agree very closely with the Whitman-Motzfeldt result, even at very low pressures where gas phase collisions are few.

The effect of cell geometry is seen if we set  $\alpha$  and  $W_o = 1$ , i.e., ideal sample and orifice. Then all these authors predict values of  $P_K/P_{eq}$  in the ranges listed below for the given ratios of radii of orifice and cell body,  $R_o/R_c$ :

$R_o/R_c$	0.1	0.2	0.3	0.4
$P_K/P_{eq}$	0.99-1.00	0.96-0.97	0.92-0.94	0.87-0.90

Cater [48] has tabulated these results in more detail. Because most effusion cells have  $R_o/R_c$  in the range 0.1 to 0.2, one seldom finds any corrections made for the cell body itself in the literature.

By using orifices of different areas with a given effusion cell, one can obtain the vaporization coefficient  $\alpha$ . Thus, if several orifices are used and eq. (5) is applied, a plot of  $P_K$  vs  $P_K(W_o A_o / A_s)$  will have slope  $-1/\alpha$  and intercept  $P_e$ . The general feeling is that this approach is valid to obtain  $P_e$  and  $\alpha$ . However, one must be careful in interpreting the value of  $\alpha$  obtained. It was assumed in the derivation that  $\alpha$  is a material constant of the sample only, and so is "real." "Real"  $\alpha$ 's are the result of one or more slow steps in the vaporization process [49] and arise, for example, when a rearrangement of molecular structure must occur upon vaporization, as in the vaporization of  $As_4$  from solid arsenic [50], or when a large flat molecule such as cobalt phthalocyanine [51] must be moved from the bulk solid to the surface. In other cases one obtains "apparent"  $\alpha$ 's, which are really a function of the kind of reaction occurring and the way the experiment is run. Examples are the build-up of a second phase on the surface in an incongruent vaporization, or thermal gradients due to radiation of heat from too large an orifice, or poor heat transport through the sample to the surface.

The recent literature on vaporization of alkali and alkaline earth sulfites, sulfates, and carbonates [52-58] illustrates a variety of phenomena which can lead to misinterpretation due to kinetically rather than thermodynamically controlled effusion processes. Careful workers usually try to use data taken before appreciable decomposition products can build up on the surface. In evaluating evaporation coefficients, particularly from single crystal faces, it is more common to compare free evaporation rates with effusion rates [49], under the assumption that the effusion rates represent equilibrium vaporization, but more than one orifice area should be used to insure that  $P_e$  is being measured.

A possibility not usually considered is that surface diffusion within the effusion cell may lead to the observed increased values of  $P_K$  as smaller orifices are employed. As is discussed below, surface diffusion within the cell leads to enhanced rates of mass loss, which become relatively larger as orifice diameters are decreased, and are largest with knife-edged (near ideal) orifices.

The Monte Carlo simulations of Ward and co-workers [47,59-61] were accompanied by experiments in which the angular distribution of gold and plutonium, vaporizing from various cells, was measured by collecting the vapor on copper strips above the orifice, then sectioning the strips and determining the amount of condensate by radiochemical techniques. In general the results both of calculation and experiment agreed with the predictions of the Whitman-Motzfeldt and Clausing-type theories. A very interesting result is that when vapor pressures were so low that the mean free path was much longer than the cell dimensions, the distribution in angle of effusing molecules from cells with ideal orifices departs from the expected cosine distribution. Instead, the distribution obtained in each case mirrors the cell interior, that is it shows effects due to the corners where the walls meet the floor of the cell, and due to the location and shape of the sample itself. It appears that at the lowest pressures the best effusion method is some variant of the collection of vapor in a small solid angle coaxial with the orifice, with the sample itself on the floor opposite the orifice. As Ward, among others, has noted [62], in this case neither the Whitman-Motzfeldt nor Clausing corrections should be applied.

### 2.2.2 Surface diffusion

Surface diffusion, in which a molecule colliding with the wall might migrate along the surface before re-evaporating, became a prime suspect for causing deviations from the Clausing theory for the angular distribution and total rate of effusion. Winterbottom and Hirth and their co-workers [68-72] have analyzed flow in the effusion cell and in cylindrical and conical effusion orifices, including contributions from surface diffusion. Increased transport out the orifice and altered angular number distributions come about because more molecules are present on the orifice wall than would be available from arrival from the gas phase alone, thus enhancing the rate of emission of molecules from the wall. Also, particularly with near-ideal orifices in thin walls, surface diffusion carries molecules on the outside surface of the cell, where direct evaporation occurs.



To predict surface diffusion effects one needs to know the distribution of diffusion path lengths, or at least the mean diffusion distance  $\bar{x}$  travelled by molecules while adsorbed. To calculate  $\bar{x}$  one must have the free energy of desorption, the frequency of vibration of the adsorbed molecule at the surface, the evaporation coefficient, and the diffusivity of the molecules on the particular surface. These detailed quantities are usually not known, and values of  $\bar{x}$  from 0 to 0.02 cm have usually been used to estimate the surface diffusion effects. The principal documented case in which the requisite data were available was the case of silver effusing from a molybdenum cell. For an orifice of  $L/R = 0.1$  at 1000 K, Winterbottom and Hirth [68] predicted the increased total flux through the orifice due to surface diffusion. Boyer and Meadowcroft [73] seem to have verified the result experimentally.

Ward, Bivins, and Fraser [74], by including surface diffusion in their Monte Carlo techniques, verified Winterbottom and Hirth's mathematical analysis of surface diffusion contributions for cylindrical orifices, and also those of Dunham and Hirth [72] for divergent conical orifices. The Monte Carlo treatment provided greater detail than the other calculations in picturing the separate contributions to the effusate coming directly from the gas phase in the orifice entrance, and coming off the orifice wall both by diffuse reflection and after surface migration. By using  $\bar{x}$  from 0.005 to 0.01 cm, Ward, et al. [63] predicted angular distribution curves which deviated in the same way from Clausing theory as did the experimental results of Freeman [75], who studied the flow of He,  $N_2$ , and  $N_2O$  through conical orifices.

However, attempts to explain other observed effects by invoking surface diffusion have not been conclusive. In at least the following two cases, simpler explanations have proven more satisfactory than surface diffusion effects, which had earlier been proposed [70,71] to account for the observations. Adams, et al. [64,76] studied angular distributions of CsCl from cylindrical and conical orifices, and found a much lower flux than expected in the forward direction ( $\theta < 20^\circ$ ). Ward, et al. [63] found that Adams' data were what would be expected if virtually all the effusing vapor originated by diffuse reflections along the orifice wall, and if the contribution from the wall opposite the orifice were decreased because that wall was cooler than the rest of the cell. The experimental design made this last problem seem quite likely. Thus, surface diffusion was probably absent and temperature inhomogeneity played the critical role.

In the second case, Grimley, et al. [77-79] found by mass spectrometry that monomers and dimers vaporizing from KCl and CsCl effused through both short and long orifices with different angular distributions than predicted by Clausing theory. The monomers, which were the species of higher concentration, gave slightly more diffuse distributions than predicted; the dimers were concentrated in the forward direction and/or depleted at high angles. Adsorption and surface migration of monomers, which could then react on the wall to vaporize as dimers, would modify the distribution obtained from ordinary vapor transport. By reasonable choices of the adjustable parameters Winterbottom [70,71] obtained distributions in fair agreement with Grimley's observations. However, Voronin [80] and Liu and Wahlbeck [81] showed that surface transport need not be involved. Instead they assumed that equilibrium between monomers and dimers was established at every point along the orifice, and



the monomer/dimer ratio shifted according to the known equilibrium constants as the molecular density decreased along the orifice toward its exit. Presumably the equilibrium was established on the wall itself, as pressures were too low for many gas phase collisions to occur. By introducing the equilibrium of monomers and dimers into the flow equations they predicted angular distributions which were in good agreement with Grimley's data. Qualitatively, as the pressure drops along the orifice, the equilibrium should shift toward the monomers, so that at large angles from the orifice axis the vapor is enriched in monomers and depleted in dimers, as is observed. The observed distributions from near-ideal orifices, where equilibrium on the orifice wall is unlikely, were explained [82] in terms of the failure-of-isotropy theory, which involves only gas kinetic theory, as discussed below. However, in some other cases, such as in the vaporization of samarium, Grimley has found that bulk surface diffusion definitely does affect angular distribution curves with some Ta and BN cells [83], but not with others [84].

As an aid in correlating theoretical and experimental studies of the effect of surface diffusion, or correcting experimental effusion data for surface diffusion when the mean diffusion path  $\bar{x}$  is known, Ward, et al. [74] have condensed the results of their costly numerical calculations into an equation suitable for use with a pocket calculator. The following equation gives the transmission probability (Clausing factor) for right circular cylindrical orifices as a function of length L, radius R, and mean surface diffusion path length  $\bar{x}$ . The equation fits the Monte Carlo results within 1 percent for all L/R, and gives four figure agreement with the best other available Clausing factors for  $\bar{x} = 0$  (no surface diffusion).

$$W = P_1 + [P_2/(L/R + P_3)] + [P_4 + P_5/(L/R + P_6)] [P_7 + f(\bar{x})]^{1/2} \quad (6)$$

The quantities in the equation are:

$$\begin{array}{ll} f(\bar{x}) = (0.0125 \bar{x}/R) \quad (\text{in cm}) & P_4 = 0.4325264 \\ P_1 = 0.0204648 & P_5 = 0.4013835 \\ P_2 = 1.9906862 & P_6 = 0.6417474 \\ P_3 = 2.2555966 & P_7 = 2.924756 \times 10^{-6} \end{array}$$

Ward, et al. [63] tabulate W's for eight different conical orifices for  $\bar{x} = 0.0, 0.001, 0.005, \text{ and } 0.01 \text{ cm.}$ , but do not give a summary equation analogous to (6).

The effects of surface diffusion on effusion measurements may be summarized as follows:

(1) The transmission probability is both a property of orifice shape and of the nature of cell and sample materials.

(2) For all orifice geometries, if there is a single vapor species, the surface diffusion contribution to the flux near  $\theta = 0$  is smaller than it is for the total flux. Thus the angular distribution is more nearly cosine (enhanced more at large angles from the axis) than predicted by Clausing theory for cylindrical orifices.

(3) The overall transmission probabilities are increased over the usual Clausing predictions by surface diffusion. The enhancement is greater for cylindrical orifices of

smaller diameters and shorter lengths, for wider angles for conical orifices, and enhanced most of all for the most nearly ideal orifices. The relative surface diffusion contribution increases as pressure decreases and temperature increases.

(4) For interacting vapor species, e.g., monomers and dimers, surface diffusion probably increases the deviations from Clausing theory which already result from equilibrium determined by the density gradient in the orifice.

(5) Enhancement of effusion rates from a few to perhaps 60 percent are predicted for reasonable estimates of  $\bar{x}$  and frequently used geometries, with ideal, small diameter orifices being the most affected.

(6) For most materials the necessary data are unavailable to predict whether surface diffusion will be appreciable. Fortunately, for most controlled experiments it appears not to have been a factor. Chatillon and Allibert later in this volume describe experimental designs to obviate difficulties from surface diffusion in real cells.

Bulk surface flow, as distinguished from surface diffusion, has often been observed, particularly with liquid samples, most notably with liquid metals. This effect has been somewhat successfully countered by holding the samples in sharp edged cups in the Knudsen cell, by using cells machined from single crystal material to eliminate grain boundary effects, and generally by finding cells which are not wet by the sample of interest.

### 2.2.3. Specular reflection

Specular reflection has also been considered as a possible explanation for observed angular distributions which deviate from prediction. Wang and Wahlbeck [85] have reviewed the literature, and have studied angular distributions of CsCl from long orifices, and velocity distributions in the forward direction. They proposed that the enhanced flux of CsCl and increased numbers of high velocity molecules they observed in the forward direction were due to specular reflections of some faster molecules striking the wall at near grazing angles. They used a double effusion cell, in which the vapor density was fixed by the lower temperature of a reservoir compartment, and the effusion occurred from a second compartment at a temperature higher by  $\Delta T$ . The enhancement in the forward direction increased as  $\Delta T$  increased. Ward, et al. [63] included a provision for specular reflection in their Monte Carlo formulation, and examined a case with the geometry and pressures used by Wang and Wahlbeck. They concluded that specular reflection was a possible explanation, but that more information on the parameters determining the fraction of specular reflection would be needed for a quantitative treatment.

### 2.2.4. Failure-of-isotropy and the upper pressure limit

The upper limit of pressures reliably determined by the effusion method was set by Knudsen at pressures where the ratio of mean free path to orifice diameter,  $\lambda/D$ , was about 10. The ratio  $\lambda/D$  is called the Knudsen number. Above this pressure the rate of effusion at a given pressure increases above that predicted by the Knudsen equation as the transport goes

from free molecular flow to transitional flow, and finally to hydrodynamic effusion, when the rate of effusion becomes about 1.65 times that expected from the Knudsen equation [87,88]. Subsequent experiments reviewed by Wang and Wahlbeck [85] have indicated that transition flow begins from  $\lambda/D = 1.2 - 8.2$  for various gases and orifices.

Wahlbeck [89] has presented the Failure of Isotropy Theory (FISOT) which provides corrections to the simple Clausing theory for the angular number distribution of the effusing molecules as the mean free path decreases.

The theory is so named because the isotropic distribution of momentum is disturbed in the region in the cell from which the molecules can enter the orifice, as  $\lambda$  decreases and gas phase collisions become the dominant mechanism for sending molecules into the orifice. Standard kinetic theory considerations are employed. The important parameter used in calculating the angular distribution and transmission probabilities is designated by Wahlbeck [89] as  $\delta\bar{\omega}(0)/2\pi$ . This quantity is essentially the normalized flux density effusing into the element of solid angle along the axis ( $\theta = 0$ ) of an ideal orifice of radius  $R$ , and is related to  $\lambda/R$  by

$$\delta\bar{\omega}(0)/2\pi = 1 - (\pi R/2\lambda) [H_1(R/\lambda) - Y_1(R/\lambda)] + R/\lambda,$$

where  $H_1(x)$  is a Struve function and  $Y_1(x)$  is a Bessel function of the second kind. Because  $\lambda/R$  is half the reciprocal of the Knudsen number, it is apparent that the Knudsen number has a real theoretical significance in determining the change from molecular to transitional flow from an orifice. Wahlbeck concludes that the transition flow region extends from about  $\lambda/D = 8$  to 0.01. Wahlbeck comments that the different reported values of  $\lambda/D$  for the upper pressure limit to the Knudsen equation have been the result of different sensitivities with which the investigators could detect departure from molecular flow, and not the result of inherently different behavior of different chemical systems.

The transmission probability for an ideal orifice is given by Wahlbeck [89] as

$$W = 1 + 2/3[\delta\bar{\omega}(0)/2\pi]. \quad (7)$$

For cylindrical orifices  $W$  is the integral of a complicated function of  $L/R$  and  $(\delta\bar{\omega}(0)/2\pi)$  given by eq. 23 of ref. [89]. These transmission probabilities can be used with the Knudsen equation to obtain accurate vapor pressures well up into the transition region: at least for  $\lambda/D \geq 0.5$  for near ideal orifices and  $\lambda/D \geq 0.1$  for longer cylinders. Extension of the theory to include conical orifices as well should be possible.

Wey and Wahlbeck [90] experimentally measured transmission probabilities from the molecular flow regime to the hydrodynamic regime by measuring rates of effusion of CsCl through different orifices with length to diameter ratios of 0.02 to 9.5. For part of the work they used the simultaneous effusion apparatus of Macur, et al. [91] in which 14 identical effusion cells had been found to yield identical effusion rates within about 2 percent, thereby demonstrating that all cells were at the same temperature. In this way, Wey and Wahlbeck could compare the transmission probabilities of differently shaped orifices directly. They

obtained good agreement with the usual Clausing factors [19-21] for  $\lambda/D \geq 10$ , and good agreement with the FISOT calculations for  $10 \geq \lambda/D \geq 0.5$  or  $0.1$  as indicated above. Furthermore, Wey and Wahlbeck [82,90] showed that correction of effusion data for solid and liquid CsCl for vapor pressures from 0.003 to 1.0 Torr by using the FISOT transmission factors gave exact agreement ( $\pm 2.5$  percent) with accepted vapor pressures measured by static techniques [92]. The Failure-of-Isotropy Theory appears to provide the information required for understanding some of the controversies that occasionally arise due to application of the effusion method at pressures up to the order of 1 Torr.

Wey and Wahlbeck [82] have extended the theory to include gases containing several species, of different mass and size, e.g. monomers and dimers. The theory accurately predicts the different angular distributions found by Grimley and LaRue [93] for CsCl and  $\text{Cs}_2\text{Cl}_2$  from near-ideal orifices. The theory has not yet been extended to cases involving interaction of monomer and dimer on the orifice wall, as discussed above.

### 2.2.5 Temperature problems

So far no effects due to temperature have been considered; now we turn to these. The single problem most likely to be at fault when discrepancies are found in effusion data between laboratories or between experiments is inaccurately measured temperature or lack of temperature homogeneity within the cells. The partial pressure  $P_i$  of an effusing species gives to a good approximation a straight line dependence of  $\log P_i$  vs  $1/T$ , with slope given by  $-\Delta H/R$ . For a typical metal with  $\Delta H$  of vaporization of 100 kcal/mol, a temperature error of 5 K at an experimental temperature of 1000 K leads to a 25 percent error in  $P_i$ . Hence, small differences in temperature scales in different laboratories lead to different reported vapor pressures.

If temperature is not constant through the cell, some often unrecognized, but very significant, mass transport effects can occur. For example, solid samples migrate to colder regions by vapor transport, and decreased effusion rates ultimately result. Angular distributions of effusate also change, as colder surfaces have lower rates of emission than hotter ones. An interesting example was provided by Ward, et al. [63] who invoked such a low emission rate from a cold wall to explain quantitatively the departure of the experimental angular distribution measurements of Adams [64] from theoretical predictions. Cater, Gilles, and Thorn [65] reported a consistent difference of 20 percent between pressures calculated from target collection and mass loss measurements with  $\text{U}$  and  $\text{UO}_2$  in six experiments. Their effusion cell had a 10 K gradient [66], with temperatures pyrometrically measured in the massive bottom section lower than those measured in the orifice. The sample was located on the floor of the cell cavity. It seems likely that low rates of effusion at large angles to the forward direction, resulting from slightly cooler walls may at least in part account for this observation.

Storms [67] published the results of a number of experiments in which temperature gradients were deliberately introduced into cells heated by electron bombardment from three independently controlled filaments. He measured temperatures at several points along the cell with an optical pyrometer. He concluded that one should use as the temperature of



vaporization the value measured in a blackbody hole as near as possible to the sample surface. He also found that a filament configuration which gave no temperature gradients in one range of temperatures sometimes introduced temperature gradients outside that range. In general the effects of temperature gradients on derived thermodynamic data (slope heats, for instance) are unpredictable, and the experimenter should insure if at all possible that temperature gradients are absent. Unfortunately, gradients are sometimes necessary to prevent condensation in the orifice or for other experimental reasons. Chatillon and Allibert in a later paper in this volume also comment on temperature effects. The photon counting pyrometer described by Storms and Mueller, later in this volume, appears to be a major step forward in improving temperature measurement in effusion studies.

## 2.3 Summary

I conclude that the basic theory for transport in Knudsen cells and through their orifices is well established if the standard conditions are met: temperature homogeneity, molecular flow, and only diffuse (cosine-wise) reflection of molecules at the walls. Experimental deviations from the predicted angular distributions have been the rule rather than the exception until recently in attempts to verify the theoretical predictions. The main reasons for such deviations are now understood as effects of temperature inhomogeneity, surface diffusion, monomer/dimer equilibria established along the orifice wall, or failure of isotropy as the mean free path decreases. Corrections are available to deal with the last three of these problems, and the effects of the first are disastrous enough that the experimenter must insure against it by proper design.

## 3. The effusion techniques

Having considered the state of understanding of the effusion cell itself, we now shall examine the state of the art in the different individual effusion techniques.

### 3.1 Mass loss and collection techniques

These straightforward effusion procedures are well-known and adequately covered in the review articles already cited [39-42]. Only a few remarks on the techniques need be made here. Simple weighing of the cell at atmospheric pressure before and then after an effusion experiment gives the least precise and least reproducible vapor pressure measurements. However, this technique is often employed to determine the total amount effused, to be compared with integrated ion currents in mass spectrometers for calibration purposes. The relatively poor precision when a series of such measurements is made usually results from non-equilibrium mass loss due to such things as

- (1) poorly outgassed metal cells, which may lose excess weight through loss of oxide molecules containing cell material (e.g. Ta above 2000 °C),

- (2) "gettering" of background gas by the cell at temperatures lower than the outgassing temperature (e.g. Ta below 2000 °C),



(3) surface oxide films or dissolved oxygen in the sample, often observed as  $MO^+$  in mass spectrometers during early stages of a vaporization experiment.

The use of vacuum balances eliminates much of the scatter found when simple weighing is used at high temperatures.

The collection technique is generally to be preferred to direct weighing, if the major vapor species are condensible. The usual location of collector coaxial with the orifice and a few cm away from it is ideal from several standpoints.

(1) Neither Clausing nor Motzfeldt-type corrections need be applied if the angle subtended by the collector at the orifice is but a few degrees.

(2) The collector is exposed directly to the sample on the bottom of the cell in the usual arrangement, and so is likely to be sampling the saturation vapor pressure, which might not be true if molecules arrived at the collector only after collision with the wall.

(3) In general, condensation of vapor on the targets is quantitative, at least for the most important species in fairly simple chemical systems.

The chief disadvantage of the collection technique is that very sensitive analytical techniques must be available. Amounts on targets typically range from  $10^{-8}$  to  $10^{-4}$  gm. Various radiochemical counting techniques and neutron activation have been successfully used, as well as electrochemical and spectrophotometric analyses. Tuenge, Laabs, and Franzen [94] successfully used the electron microprobe as the analytical tool in their study of scandium sulfide. X-ray fluorescence has also been used [95], but the precision has not been as good as desired.

### 3.2 Torsion effusion

The torsion technique appears to be quite reliable and has the advantages of giving data over a large temperature range quickly and of providing an absolute measurement of the mean molecular weight of the vapor. For a typical cell, suspended at its midpoint and having two orifices of area  $A_1$  and  $A_2$  on opposite sides and displaced by perpendicular distances  $d_1$  and  $d_2$  from the point of suspension, rotated by the effusing molecular beams to angle  $\theta$  against the restoring torque of the suspension fiber, of torsion constant  $\tau$ , the total pressure is

$$P_T = 2\tau\theta / (A_1 d_1 f_1 + A_2 d_2 f_2); \quad (8)$$

The "force factors"  $f$ , which are analogous to Clausing factors, are tabulated in several publications [20,21,96,97]. As Volmer first recognized [24], if one can suspend the torsion cell from a balance and simultaneously measure torsion angle and rate of mass loss, equation (8) can be combined with the Knudsen equations (2) or (3) to give the molecular weight  $\bar{M}$  of the effusing vapor,

$$\bar{M} = \frac{2\pi RT}{(2\tau\theta)^2} \left[ \frac{G_1}{A_1 W_1 t} + \frac{G_2}{A_2 W_2 t} \right]^2 (A_1 d_1 f_1 + A_2 d_2 f_2)^2 \quad (9)$$

Here,  $G_1$  and  $G_2$  are the mass losses through orifices 1 and 2. If the orifices are identical the problem of determining the separate mass losses is obviated and the molecular weight is given by

$$\bar{M} = \frac{2\pi RT}{(2\tau\theta)^2} \left( \frac{G d_{12}^f}{wt} \right)^2, \quad (10)$$

where  $d_{12} = d_1 + d_2$ , the perpendicular distance between the orifice centers.

If (as is usually the case) there are more than one vapor species, say  $s$  of them,  $\bar{M}$  is an averaged molecular weight given by

$$\bar{M} = \left( \sum_{j=1}^s m_j M_j^{-1/2} \right)^{-2}, \quad (11)$$

where  $m_j$  is the mass fraction of species  $j$  in the effusing vapor. If the only molecules are monomer and polymers of the same species, for example  $KCl$ ,  $K_2Cl_2$ , etc., then [10] can be converted to the form

$$\bar{M} = \left( \sum_{j=1}^s x_j M_j^{1/2} \right)^{-2} \quad (12)$$

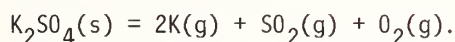
where  $x_j$  is the mole fraction of species  $j$ . If Knudsen mass loss pressures  $P_K$  are determined separately from the torsion experiments and calculated with an arbitrarily chosen molecular weight  $M^*$ , the mean molecular weight is obtained from the ratio of Knudsen and torsion pressures,

$$\bar{M} = M^* (P_K/P_T)^2. \quad (13)$$

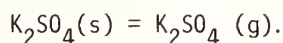
The direct determination of mean molecular weight by combining torsion and mass loss data is important in two ways. First, by itself it provides the necessary data for choosing the predominant vaporization process from several which might be possible, or for determination of concentrations where only two species are important. A typical recent example is the verification that  $MnS(s)$  vaporizes chiefly to  $Mn(g) + 1/2 S_2(g)$  at 1600 K [98], ( $\bar{M} = 88 \pm 8.3$  measured, 58.1 expected).

Secondly, and perhaps more importantly, such a mean molecular weight may provide the vital link between partial pressures and mass spectrometric ion currents, when several vapor species are present and/or extensive fragmentation in the ion source may occur. This second use of  $\bar{M}$  is illustrated nicely by the very recent study of Lau, Cubicciotti, and Hildenbrand [52] of the vaporization/decomposition of solid  $K_2SO_4$ . Their torsion and mass loss measurements gave  $\bar{M}$  as  $110 \pm 5$  between 1240 and 1260. A mass spectrometric study indicated that ions  $K_2SO_4^+$ ,  $K^+$ ,  $SO_2^+$ ,  $O_2^+$  were all due to primary vapor species, that  $K_2O^+$  was, and  $K^+$  might also be, a fragment ion. Furthermore, the temperature dependences of all were equal with

the experimental precision. Sufficient thermodynamic data were available to calculate the pressure expected from the decomposition reaction



The difference between the total (torsion effusion) pressure and this decomposition pressure could then be attributed to the direct sublimation process



Lau, et al. [52] calculated the overall stoichiometry of vaporization to be



The stoichiometry yields  $\bar{M} = 116 \pm 1$  in excellent agreement with the directly observed value. The mass spectrometric data on individual ions could then be used to obtain relative sensitivity constants for the vapor species and various thermodynamic data.

A number of cases can be found in the literature where the mean molecular weight determined by combined torsion effusion and mass effusion has been used to calculate relative proportions of monomers and dimers in effusing vapor, for example Pugh and Barrow's work on  $\text{Cl}_2$  [99]. One very interesting application of this sort was the double cell of Budininkas, Edwards, and Wahlbeck [100-102]. This consisted of a lower reservoir suspended by a hollow vertical tube from the actual torsion cell. The reservoir contained sulfur, selenium, or tellurium at one temperature. The saturated vapor from the reservoir passed up the tube into the effusion cell which was maintained at a much higher temperature. The total pressure was thus determined by the reservoir, but the equilibrium in the vapor at the higher temperature provided the effusive torque, which was measured.

In general, modern measurements of pressures by torsion effusion experiments are reliable and reproducible. One of my consultants claims he can get molecular weights to  $\pm 1$  percent or better, vapor pressures of metals reproducible to  $\pm 1/2$  percent and heats of vaporization from slopes to a few percent. In addition, measurements can be made rather rapidly. As an example, Myles and Aldred [103] determined partial pressures of iron over various alloys at each of eight temperatures between 1450 and 1700 K while holding the total weight loss to less than 0.2 percent.

Interestingly enough, in Volmer's original applications of torsion effusion studies [24] to the determination of molecular weights of slightly volatile organic compounds he obtained excellent results for benzophenone ( $M = 182$ ; experimental values  $183 \pm 7$  and  $188 \pm 7$  for two torsion wires) and azobenzene ( $M = 182$ ; experimental value  $182 \pm 2$ ). As Freeman [25] notes, Volmer, et al. had encountered and solved essentially all the problems associated with the technique except those associated with high temperatures.

The current high quality results have principally accompanied better torsion fibers, better cell and heater design, better isothermicity and temperature measurement. This last aspect is definitely required for accurate slope heats.

The problems of vapor returning non-randomly from heater walls are now better understood. The net result is an increased torque displayed by the cell and/or decreased mass loss. In surveying the literature McCreary and Thorn [104,105] found that torsion pressures were generally larger than mass loss pressures by 5-17 percent and concluded [106] that return of effusate to the cell caused the mass loss pressure to be too low rather than affecting the torsion pressure. The latter remained constant, while the former increased, up using a tantalum heating sleeve of larger diameter. These effects appear to be minimized if the heater is of tungsten or graphite mesh rather than a solid cylinder, and so is more or less transparent to the effusing molecules.

Cells are often designed with a divergent conical orifice ( $30^\circ$  apex angle), which provides the maximum momentum per unit mass loss. A big advance in reproducibility has been due to the use of flat ribbons of Pt(10 percent Ni) alloy designed originally as galvanometer suspensions, rather than the tungsten and quartz fibers used a decade ago and earlier. The ribbons are more uniform and their torsion constants more permanent. Effects of residual background gas at low pressure are suspected to cause some of the remaining problems but the effects are not yet understood. Another improvement has been the use of materials more nearly free of magnetic impurities which can affect the deflection by interaction with damping systems or fields due to heating currents.

The only real innovation in torsion effusion techniques since their origin about 1930 is the development of the dynamic or oscillating torsion effusion cell by Edwards and his co-workers [107,108]. In this technique the cell is deliberately caused to oscillate as a torsion pendulum, rather than to attain a steady deflection. Because the swing is alternately enhanced and retarded by the momentum of the effusing vapor, the pressure can be derived from the equation of motion. The oscillatory motion is reported to smooth out various experimental residual torques and thus may possibly give more reliable data. Direct observations [98,107], videotape [108], and most recently a ring of photocells, a laser beam, and direct connection to a computer have been used to obtain the requisite data for fitting the equation of motion. This last approach appears to offer real opportunities for direct computer control and data acquisition as discussed by Edwards later in this volume. A few electromagnetically nulled, static torsion effusion apparatuses have been proposed or described from time to time [25] but none seems to have been routinely operated.

### 3.3 Knudsen cell mass spectrometry (KC/MS)

The mass spectrometer is, of course, the most versatile device for detection of effusing molecules. Its application in effusion studies has been described in detail in the books already cited [39-42]. Additional review articles that emphasize particular aspects are those of Drowart and Goldfinger [36], an overall review of the method and its results, particularly the determination of thermodynamic properties of high temperature molecules; Chatillon, Pattoret, and Drowart [109], which emphasizes the study of activities in the vaporizing solids; of Stafford [110], who deals with the ionization and fragmentation



problems; of Ackermann and Rauh [111], who use their own work as examples to summarize the approach to the study of nonstoichiometry in oxide systems at high temperatures, the relation of ionization potential to sensitivity constant, and the use of isomolecular equilibria. Another review by Drowart, somewhat less accessible, [112] gives good, concise summaries of the behavior of different classes of chemical systems as determined by the KC/MS technique.

The current state of the art in KC/MS work can be summarized generally as follows.

(1) The factors peculiar to the mass spectrometer which limit the accuracy of partial pressure measurement are still, after 25 years, the problems of sensitivity constants (cross sections) and fragmentation.

(2) Larger errors in many cases are not inherent in the mass spectrometer, but are the control, measurement, and homogeneity of temperature in the effusion cell, and the attainment of chemical equilibrium within the cell (effects due to changing stoichiometry, and non-equilibrium in mixed solid phases).

(3) Many of the instruments in use are ten to twenty years old, but basic instrumentation has been pretty standard for that length of time. Improved precision and accuracy have resulted from refinement of technique and apparatus rather than from fundamental changes in approach. For example signal averaging, ion counting, and phase sensitive detection have increased the sensitivity and allowed determination of species in lower concentrations. Increased use of radiation rather than electron bombardment heating, and improved mechanical stability of effusion sources, seem to have also improved the precision available, while reducing noise.

(4) Investigators have determined partial pressures and thermodynamic properties of very minor species such as intermetallic molecules and polymeric species in a large variety of systems, mostly by designing effusion cells for higher temperature operation. Gingerich, later in this volume, deals with some of these results.

(5) We are beginning to understand the problems of sensitivity constants and how to measure them for molecules. Empirical rules have been developed for estimating ratios of sensitivity constants for atoms and molecules, and these have led to improved second law-third law agreement. New techniques to attack these problems and the related one of fragmentation include the electrochemical Knudsen cell [113,114] and angular distribution studies, which Grimley describes later in this volume.

(6) Automated data acquisition and treatment are viewed favorably, because they put the scientist closer to the details of the experiment. But the consensus is that complete automation of high temperature effusion studies is not possible because of the complex nature of the processes that can occur in the effusion cell, which require human decisions on what to do next.

I shall not attempt to cover the entire subject of the KC/MS technique, but I do want to discuss some aspects of the sensitivity constant problem, and say something about how isomolecular equilibrium studies have shed some new light on it. Then I shall discuss the approach to equilibrium in Knudsen cells, and finally, try to look briefly at the newer techniques of photoionization, chemiluminescent reactions, and laser fluorescence, and compare their results to those of effusion studies.



### 3.3.1 The sensitivity constant (cross section) problem

The relation between the partial pressure  $P_i$  of species  $i$  in the effusion cell and the ion current  $I_i$  measured in the mass spectrometer is

$$P_i = \frac{1}{X_i} I_i T, \quad (14)$$

where  $X_i$  is the sensitivity constant or ionization efficiency for species  $i$ . The quantity is essentially the product of an instrumental constant, the cross section  $\sigma_i$  for forming  $i$  from neutral molecules of the same formula at the energy used,  $\gamma_i$ , the electron multiplication efficiency, and, for quadrupole instruments, the transmission factor. This last quantity is not further discussed here. The term "ionization cross section" is much misused, because properly there are different cross sections for ionization from different atomic or molecular orbitals for forming ions in different excited states, and for different fragmentation patterns, and these all vary with the energy of the projectile electrons. Stafford [110] has an excellent discussion of these distinctions. I shall use the terms sensitivity constant and ionization efficiency for  $X_i$ , and only use the term cross section in a specific context.

If only atomic species were involved, one could employ ionizing electrons of 75-100 eV energy and use the ionization cross sections tabulated by Mann [115,116] and others [117,118]. Experimental and calculated values are in reasonable agreement for atoms at these energies, where the Born-Oppenheimer approximation is valid. Experience has shown that relative values from Mann's tabulation can be used for atoms at low energies also, provided measurements for each species are made at a constant increment (often 5 eV) above threshold or if the data are taken at low energies and corrected to plateau values by use of ionization efficiency curves determined in separate experiments.

Fragmentation of a molecule  $AB$  to give  $A^+ + B$  is always a possibility if the ionizing energy is greater than the sum of the dissociation energy of  $AB$  and the ionization potential of  $A$ . However, fragmentation often is not detected even at energies where it could be happening. Because bond dissociation energies encountered in effusion studies are in the 1-10 eV range and ionization potentials of metal atoms are in the range of 4 - 10 eV, it would be desirable to use electrons of less than about 10 or 12 eV energy. Often the molecules of interest also have ionization potentials of 4 - 10 eV, and so this is a viable solution. In addition, use of low ionization energies often eliminates undesirable signals from background gases in the mass spectrometer.

Several problems arise with the use of low ionizing energies. Non-metal atoms have ionization potentials much higher than metals in general, so use of electron energies low enough to avoid fragmentation may mean that not all the atomic species can be detected. Furthermore, working at low electron energies may mean working at energies on the steeply rising initial portion of the appearance potential (ionization efficiency) curve of some of the species, where a small variation in energy may mean a relatively large change in observed ion current. Another problem often encountered is that some species, particularly halides, undergo dissociative ionization almost exclusively and parent ions are observed in very small amounts.

amounts, if at all. This problem is particularly bad if polymeric species are present which also fragment.

If vaporization of binary compounds like  $A_nX_m$  or if isomolecular equilibria of the type  $AX + B = A + BX$  are studied, it is common to use energies from 7 to 15 eV or so, at which the ratios  $I(AX^+)/I(A^+)$  and  $I(BX^+)/I(B^+)$  are constant (which they typically are over a range of several volts), and not to attempt to ionize and measure the nonmetallic species. The partial pressures of X or  $X_2$  are then usually determined by stoichiometric considerations or from appropriate equilibrium constants.

If different molecular species have quite different appearance potentials, for example  $U^+$ ,  $UO^+$ ,  $UO_2^+$ , 5.4-6.1 eV, but  $UO_3^+$ , 10.6 eV [119] one can measure each ion at a constant energy, typically 5 eV, above its appearance potential as mentioned above with atoms. (It is of course necessary to establish that the appearance potential of each ion is due to direct ionization (A.P. = I.P.) and not due to the onset of fragmentation.)

Not infrequently one reads a paper in which it is not clear what energy was used or whether all species were measured at the same energy, and what sequence the data were taken in. If there is a possibility that the stoichiometry of the sample changes with time or with temperature (as in the case of a number of congruent vaporizations of nonstoichiometric compounds) then very poor second law results may be obtained if one species is measured at one energy over a range of temperatures before the next species is recorded.

The relation between ionization potentials and sensitivity constants has been explored for refractory oxide systems by Ackermann and Rauh [119]. They found (as had earlier workers in various cases) that significant differences occur between the ionization potentials of "saturated" oxide molecules and "unsaturated" ones. The saturated oxides are those with the highest attainable number of oxygen atoms per metal atom. The metal atoms and unsaturated oxide molecules have ionization potentials within about one eV of each other, whereas those of saturated oxides are significantly higher, presumably because all the valence electrons of the metal are involved in bonds. Typical examples given by Ackermann and Rauh [119] are for the titanium and uranium oxide systems: Ti (6.8 eV), TiO (6.4 eV), and  $TiO_2$  (10.2 eV); U (6.1 eV), UO (5.6 eV),  $UO_2$  (5.4 eV), and  $UO_3$  (10.6 eV). The effect on mass spectrometric effusion studies is that if ionizing energies of 10-12 eV are used, the higher oxides are on the initial, rising, portion of their ionization efficiency curves, and they may be assigned partial pressures that are too low if ordinary estimates of sensitivity constants are made. This explains, for example, the surprising sensitivity constants cited by Ackermann and Rauh: Ce/CeO/CeO<sub>2</sub>, 100/70/3 at 10.5 eV [120]; Th/ThO/ThO<sub>2</sub>, 100/75/14 at 12 eV [121]; and U/UO/UO<sub>2</sub>/UO<sub>3</sub>, 100/140/35/1.4 at 12 eV [122]. In all these systems extensive fragmentation occurs; for example the onset of formation of  $Th^+$  from ThO occurs at 13 eV and of  $ThO^+$  from ThO<sub>2</sub> at 15 eV, so that partial pressure measurements were made at the lower voltages cited above. Perhaps also the very low sensitivity constants found by Norman, et al. [123] for oxides of Ru, Rh, Ir, and Pt result from similar effects.

There are no theoretical methods available to calculate ionization cross sections or sensitivity constants for molecules at low energies. Early practitioners of the KC/MS art used the then best available atomic ionization cross sections from the tabulation of Otvos

and Stevenson [124]. For molecules they usually assumed the additivity rule, namely that cross sections for molecules are the sum of those for the constituent atoms. However, this rule has usually been found invalid for high temperature molecules, even when used with new cross sections. Sensitivity constants for molecules can be determined experimentally by comparing integrated ion currents with measured weight losses in systems where the stoichiometry of vaporization is well known, and only one vaporization process is involved. Examples of data obtained are listed below. The methods are described in more detail in the references already cited. Cater and Thorn's approach [125] has been used [126] for relative sensitivities of two species produced from a congruently subliming solid by such a process:  $AB(s) = z AB(g) + (1-z) A(g) + (1-z) B(g)$ . If  $z$  is temperature dependent, the relative sensitivities  $X_{AB}/X_A$  can be obtained from total rate of effusion measurements and ion current measurements at two or more temperatures. However, this method depends on precisely determining the differences in rates of change with temperature of the ion currents and the total effusion rate and works only if  $A$  and  $AB$  are of comparable importance in the vapor (i.e. if  $0.9 \geq z \geq 0.1$ ). Other methods that can be used when more than one important species is always present have been developed by Kohl, et. al. [173] and Sidorov [174]. The new technique of transpiration mass spectrometry can also yield cross section data, as shown by Bonnell and Hastie elsewhere in this volume.

Norman [127] obtained relative sensitivities for two species  $A$  and  $B$  by using phase sensitive detection to measure the changes in ion currents in the mass spectrometer when a separate ionizing electron beam was turned on between the effusion cell and the mass spectrometer's ion source. The ions formed in the auxiliary ionizing beam were deflected out of the molecular beam and thus reduced the number of molecules reaching the regular ion source. Then

$$X_A/X_B = \frac{\Delta I_A I_B}{\Delta I_B I_A}.$$

Enough examples have been measured by these and other approaches to give some general rules of thumb for estimating relative sensitivities in other cases as summarized below. First of all, it appears that sensitivity constants for homonuclear diatomic molecules are somewhat less than predicted by additivity. Some reported values, for example, are  $S_2/S$ , 1.34 [128] or 1.44 [36],  $O_2/O$ , 1.80 [36] or 1.5 [110];  $H_2/H$ , 1.44 [36];  $Al_2/Al$ , 1.75 [129] and  $Sb_2/Sb$ , 1.7 [130]. For monoxide and monosulfide molecules of metals, by contrast, the molecules usually seem to have lower sensitivity constants than the corresponding metal atoms. Some examples from the literature are:  $Y_2O/Y$ , 0.66 [131];  $LaO/La$ , 0.60 [131];  $TiO$ , 1 at low eV, 2.35 at 70 eV [132];  $UO/U$ , 0.70 [133]. Cater and co-workers [134-137] have used the estimated ratio  $X_{MS}/X_M = 0.80$  for the monosulfides of  $Sc$ ,  $Y$ ,  $La$ ,  $Pr$ , and  $Gd$ , and have justified this estimate by analogy with measured values for oxides and because better internal consistency and second-third law agreement were obtained than with ratios greater than unity. Smoes and coworkers [128,138] have also used ratios  $X_{MS}/X_M$  and  $X_{MSe}/X_M$  less than unity. For oxide molecules other than monoxides, similar considerations seem to apply, so long as the ionizing energy is appropriate. As examples we may cite the use [129] of  $X_{MO_2}/X_{MO} = X_{MO}/X_M = 0.7$  for  $Al-O$ ,  $Ti-O$ , and  $Ta-O$  species, and of  $X_{Al_2O}/X_{Al_2} = 0.75$ . For



halide species in the absence of extensive fragmentation values quoted lie in the range  $X_{MX_2}/X_{MX} = 0.7$  to  $1.8$  [36]. For nonmetallic monoxides the ratios are more like the

heteronuclear diatomics than like the metallic monoxides:  $X_{PO}/X_P = X_{NO}/X_N = 1.2$  [128]. Finally, for still more complex species containing polyatomic anions ionically bound to metal ions, like  $K_2SO_4$ , the sensitivity constants may be surprisingly low. For example from the combined torsion effusion and mass spectrometric data on  $K_2SO_4$ , Lau, et al. [52] found  $X_K/X_{K_2SO_4}$  to be about 10 at low energies. This last case may be another case analogous to

the saturated oxides mentioned above.

To conclude, it appears that the problem of uncertain sensitivity constants is still with us, but we have narrowed down the possible ranges of values and have general rules to guide in their estimation. However, when estimated sensitivity ratios are used a factor of two uncertainty is probably not excessively conservative.

### 3.3.2 Isomolecular equilibria

A very profitable way of minimizing the sensitivity constant problem has been the use of so-called isomolecular equilibria to determine dissociation energies and free energies of formation of diatomic molecules. The vapor effusing from appropriate mixed solid phases is analyzed. Reactions of the general type



where M and N are different metals studied, and the dissociation energy or  $\Delta G_f$  of the molecule MX is known and used to determine that of NX by second or third law methods. Because equal numbers of molecules appear on both sides of the reaction equation, the absolute pressure disappears from the equilibrium constant expression, which becomes

$$K = (I_M I_{NX} / I_{MX} I_N) \cdot (X_{MX} X_N / X_M X_{NM}) = K^+ \Sigma. \quad (15)$$

It is usually assumed that the ratio of sensitivity constants  $\Sigma$  can be taken to be unity within the usual precision, and thermodynamic treatments are then based on the ion current ratio  $K^+$ . Some of the best agreement between laboratories engaged in KC/MS studies has been obtained in measuring these ion current equilibrium constants for isomolecular equilibria. A typical example of such agreement is for the reaction  $GdS + Y = Gd + YS$ , for which three laboratories obtained the following respective values at 2150 K: 1.55 [136], 1.48 [139], and 1.24 [140]. (These were calculated from the three individual least squares fits of  $\log K^+$  vs  $1/T$ .) Such good agreement leads to agreement within about 1.0 kcal/mol in the third law heat of reaction, but respective slope heats and their standard deviations for this equilibrium were  $(1.0 \pm 1.1)$ ,  $(4.5 \pm 2.6)$ , and  $(-2.0 \pm 2.2)$  kcal/mol. Another example is afforded by the dissociation energy of LaS, which has been determined by effusion measurements on LaS(s)

[153] and by independent isomolecular equilibria involving US and YS [134] and SiS and CeS [141], as well as by a single collision chemiluminescent reaction of La(g) with OCS [142]. Jones and Gole [142] have recalculated the earlier results with newer auxiliary data where necessary. All the second and third law values for  $D_0^0(\text{LaS})$  lie within 3 kcal/mol of 136.0, and the lower bound from the chemiluminescence study was  $136.2 \pm 0.4$  kcal/mol.

I would call these results typical of interlaboratory agreement for mass spectrometric effusion measurements.

Two further comments should be made before leaving the subject of isomolecular equilibrium studies, one on using them to verify refined estimates of sensitivity constants, and the other on the degree to which chemical equilibrium is achieved in the effusion cell containing mixed solids. Ackermann and Rauh [143] have suggested that careful isomolecular equilibrium constant measurements on well defined systems are more precise than is implied by the assumption that the sensitivity constant ratio  $\Sigma=1$ . They noted that the atomic ionization cross sections are computed [115] as being proportional to the mean square radii of the atomic orbitals from which ionization occurs, and reasoned that some analogous quantity might be proportional to the sensitivity constant for a monoxide molecule. They chose as this parameter  $r^2$ , the square of the internuclear spacing in the molecule. Then they made precise measurements of nine isomolecular equilibria among the metal atoms and monoxides of Y, La, Ce, Zr, Hf, and Th. They calculated equilibrium constants on the assumptions that  $\Sigma = 1$  and that  $\Sigma = r_{\text{MO}}^2 \sigma_{\text{N}} / r_{\text{NO}}^2 \sigma_{\text{M}}$ . The atomic cross sections  $\sigma$  were taken from Mann [115]. For these molecules  $r$  is known from spectroscopy. The  $\Sigma$  values were in the range from 0.69 to 1.42, which correspond to a range of 3.0 kcal/mol in a third law heat calculated at 2100 K. Most of the variation was due to the differences in  $\sigma$  (7.76 to 12.91 on Mann's scale), rather than in  $r^2$  (2.96 to 3.39 Å<sup>2</sup>). Then, taking as standards their previously determined values of  $\Delta G_f^0$  and  $D_0^0$  for ThO and YO, they calculated the same quantities for the other monoxides at 2100 K or 2400 K. In every case Ackermann and Rauh found better agreement (within 1.4 kcal/mol) between third law  $\Delta G_f^0$  and  $D_0^0$  for CeO, LaO, ZrO, and HfO calculated with  $\Sigma = r_{\text{MO}}^2 \sigma_{\text{N}} / r_{\text{NO}}^2 \sigma_{\text{M}}$  than with  $\Sigma=1$ . For the equilibria involving the pairs Y/Th, Y/La, Y/Ce, Th/Zr, and Th/Hf better second law - third law agreement was also obtained by using the non-unity values for  $\Sigma$ . For the other four equilibria  $\Sigma$  differed from unity by no more than 3 percent.

Finally, Ackermann and Rauh compared second and third law values for the entropy of formation of the MO molecules at temperatures from 1800 to 2400 K. The third law values were calculated from spectroscopic energy levels which were available for all six of the monoxides and so did not involve estimations, except for CeO, for which only the ground state was known. The second and third law entropies of formation differed by only 0.1 to 0.5 cal·K<sup>-1</sup>·mol<sup>-1</sup>, for CeO, for which the difference of 0.8 cal·K<sup>-1</sup>·mol<sup>-1</sup> was in the direction expected if more than the known ground electronic state contributed to the entropy. This sort of estimation of the relative sensitivity constants can probably be applied whenever saturated oxide molecules are not involved. Furthermore the excellent agreement of second and third law entropies of formation suggests that second law entropies carefully determined from isomolecular equilibrium constants can be used to obtain reasonably accurate estimates of entropies of molecules for which electronic spectra are not available. Such entropy calculations in the past have usually given unsatisfactory results.



### 3.3.3 Chemical equilibrium in Knudsen cells

The final comments to be made while on the subject of isomolecular equilibrium measurements have to do with how closely chemical equilibrium is approached in the Knudsen cell. The comments also apply to other effusion methods. As mentioned earlier, it is the vapor over mixed condensed phases (or solid or liquid solutions) which is studied. Thermodynamic data on the gaseous species are obtained but nothing is learned about the condensed phases in the typical isomolecular equilibria study. The reasonable agreement in the literature among dissociation energies of molecules studied by more than one isomolecular equilibrium implies that chemical equilibrium is approached in the phases from which the molecules vaporize. The excellent agreement quoted above in the work of Ackermann and Rauh, and the good agreement quoted above for the sulfide equilibria attest to this. The mean free paths are usually too long under the conditions employed for any true gas phase equilibrium to occur, so that the mass spectrum really pictures the chemical nature of the sample surface. At least two studies have appeared in which the question of equilibrium among the solid phases has been discussed. Wu and Gilles [144] examined isomolecular equilibria among the mono-sulfides of Gd, Ho, and Sm over several two and three phase solid mixtures which had vastly different chemical potentials of sulfur. Equilibrium constants calculated for the various systems all agreed within factors of up to two, which corresponds to about 3 kcal/mol in the heats of reaction. Wu and Gilles concluded that equilibrium did exist in the Knudsen cell for these reactions.

Cater, Rauh and Thorn [145] studied the vaporization of mixtures of solid US and  $\text{UO}_2$  and of UOS, using various isotopic compositions of uranium and oxygen to trace the origin of the several observed molecular species, which were U,  $\text{UO}$ ,  $\text{UO}_2$ , US, UOS, and S. The mixture experiments gave much less reproducible results than the separate studies of US [65,126],  $\text{UO}_2$  [146] or U-US [147] and U- $\text{UO}_2$  [148] mixtures. Further, the degree to which equilibrium seemed to be approached by different vapor species varied considerably. A number of interesting conclusions were reached.

(1) Although steady state isotopic distributions in the molecules, and fairly reproducible partial pressures, were reached over the mixed solids at 2000 to 2200 K, it was not until the temperature was raised above the eutectic melting point of 2240 K that the isotopic distribution of each element in all the vapor species became the same as in the total condensed material.

(2) The gaseous species US,  $\text{UO}_2$ , and UOS, which corresponded to the ideal formulas of the solid phases, behaved much more reproducibly than species like U and  $\text{UO}$ .

(3) Because of the long mean free paths, the mass spectrometer was sampling some average situation existing at and in the condensed phase surface, which was apparently undergoing slow, long-term changes in composition, and in which different areas may have had different compositions. Still, the partial pressures of the species were usually reproducible within about a factor of two at any temperature, and so were not hugely aberrant.

A related topic is the large change in vapor pressures of some species which can occur with small composition changes. See, for example, the  $10^4$ -fold change in  $P_{\text{U}}$ ,  $P_{\text{UO}}$  or  $P_{\text{UO}_3}$

over vaporizing uranium dioxide as the composition goes from  $\text{UO}_{2.01}$  to  $\text{UO}_{1.99}$  [149].

These kinds of observations and the differences between the thermochemically calculated and actually observed ratios of  $P_M/P_{MO}$  and  $P_M/P_{MS}$  that I ran across in surveying the vaporization behavior of rare-earth compounds for a review article [150], convince me that lack of chemical equilibrium within the condensed phases of Knudsen cells is a major cause of the discrepancies in effusion data reported from different laboratories. The recent interest in measuring both extremely small [128] and appreciable [151] changes in the stoichiometry of congruently vaporizing solids at different temperatures has been made possible by the good precision now attainable in mass spectrometric studies. Hildenbrand, in a later chapter in this volume, discusses the problem of attaining equilibrium in effusion cells in which reactive flow situations are studied.

In a later chapter in this volume, Cater, Fries, and Holler show that it is probable that different phases,  $\text{PrS}$  and  $\text{Pr}_3\text{S}_4$ , are the congruently evaporating phase in the  $\text{Pr-S}$  system at different temperatures. I believe that in the future people will pay more attention to the condensed phase compositions, and that discrepancies in data from different laboratories will become smaller. Twenty-five years ago one of the pioneers of Knudsen cell mass spectrometry told me that there was so much to be learned from every new system, that he did not even try to determine things to better than a factor of two. The result is, as Ray Ackermann once remarked [152], that one finds precisely determined information on the vaporization of exotic materials which have been studied recently, while the data in the literature on some of the simple compounds may be quite unreliable.

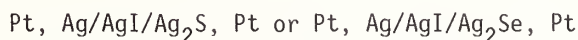
#### 3.3.4 Angular distribution mass spectrometric technique (ADMS)

The angular distribution technique developed by Grimley and co-workers has provided an extremely useful addition to the KC/MS technique for studying systems in which polymeric molecular species occur and in which fragmentation in the electron impact ion source occurs. The apparatus [78] consists of an elegant Knudsen cell which can be rotated about an axis in the exit plane of the orifice and thus can direct the molecules effusing at any angle from the normal into the ion source of a mass spectrometer. As mentioned earlier, Grimley and Meunow [154] discovered that the monomers and dimers of  $\text{KCl}$  and  $\text{CsCl}$  had distinctly different angular number distributions when effusing from cylindrical orifices. Because  $\text{K}^+$  and  $\text{KCl}^+$  had identical distributions they were both identified with the neutral molecule  $\text{KCl}$ , whereas  $\text{K}_2\text{Cl}^+$  was the only ion observed from neutral  $\text{K}_2\text{Cl}_2$ . This principle has been extended to more complex systems, and studies of the angular distributions as a function of temperature and ionizing electron energy enable one to sort out the contributions of different processes to give the observed ions. Then partial pressures can be derived. Grimley, Forsman, and Grindstaff [155] have developed the necessary equations to accomplish these analyses. Although it is the shifting equilibrium established among the molecular species on the orifice wall that gives rise to the different angular distributions, it is not necessary to know the equilibrium constants a priori to perform the calculations. As a brief example of application of ADMS analysis to a fairly complex system, we may cite some results on the

vaporization of LiF, in which the vapor species are LiF, Li<sub>2</sub>F<sub>2</sub>, and Li<sub>3</sub>F<sub>3</sub>. Grimley, et al. [155] showed that at 60 eV and 825 °C, the contributions to the Li<sup>+</sup> ion current from Li<sub>2</sub>F<sub>2</sub> and LiF are in the ratio 0.22, while at 60 eV and 785 °C they are in the ratio 0.15. At 18 eV and 825 °C the same ratio is 0.06, while at this lower voltage and 785 °C, it has increased to 0.12. The probability of fragmentation of LiF(g) to give Li<sup>+</sup> is about 3 times that for simple ionization to give LiF<sup>+</sup> from 18 to 60 eV. The probability for Li<sub>2</sub>F<sub>2</sub> to fragment to Li<sub>2</sub>F<sup>+</sup> instead of Li<sup>+</sup> is five times as great at 10 eV as it is at 40 eV. No evidence was found to confirm Snelson's matrix isolation work [156] which indicated that two isomers of Li<sub>2</sub>F<sub>2</sub>, a linear and a ring form, are present in the vapor. The ADMS results were compared to those from some seven conventional KC/MS studies from 1958 to 1977. The most careful and detailed of these other studies gave the same overall picture of the fragmentation behavior in the Li-F system, but none provided the information in such detail. In a later chapter in this volume Grimley and Forsman present a more detailed look at the theory and practice of the ADMS technique.

### 3.3.5. The electrochemical Knudsen cell

The electrochemical Knudsen cell method of Rickert and Drowart, et al. [113,114] is an ingenious example of a way to establish the chemical potential of one component in a vaporizing system and so fix the partial pressures. The apparatus has been realized and used to study the complex vapor systems of sulfur and selenium. It consists of a solid state galvanic cell of the type



built into the effusion cell of a mass spectrometer. Because AgI is an almost purely ionic conductor in which current is carried by migration of Ag<sup>+</sup>, it is possible to control the rate of vaporization of sulfur or selenium at the Ag<sub>2</sub>S or Ag<sub>2</sub>Se electrode by coulometrically removing Ag. This controls the equilibrium pressure in the Knudsen cell over a range of several orders of magnitude, and so controls the partial pressures of the species S<sub>n</sub> and Se<sub>n</sub>, where for both cases n was observed from 2 to 8. The partial pressures can be calculated from the chemical potentials obtained, and the thermodynamics of the various gaseous equilibria were studied in the mass spectrometer as the temperature of the cell was varied. The results yielded the mass spectrometric sensitivity constants of various species. Ionization cross section ratios of selenium species at 45-50 eV were found [113] to be Se<sub>5</sub>/Se<sub>6</sub>/Se<sub>7</sub>/Se<sub>2</sub> = 1.28/0.36/0.35/1. From the sulfur study [114] Drowart and Goldfinger (36) derive the following relative cross sections at 14 eV: S<sub>8</sub>/S<sub>7</sub>/S<sub>6</sub>/S<sub>2</sub> = 1.0/1.7/1.4/1.0. Clearly for these molecules the additivity rule does not hold.

The specialized nature of the electrochemical technique does not lend itself to the study of a large number of systems, but it should be applicable to other systems in which the chemical potential of one component in the vaporizing electrode phase can be controlled by migration of ions through the solid electrolyte. For example, the stoichiometry of an



incongruently vaporizing oxide could be maintained constant at chosen values by coulometrically titrating oxygen through a calcia-doped-zirconia electrolyte, from a standard oxide electrode like  $\text{Fe}$ ,  $\text{Fe}_{1-x}\text{O}$ . Or changes in stoichiometry of the vaporizing phase could be measured by measuring the emf of the electrochemical cell.

### 3.4 Comparison with newer techniques

New techniques which have shown particular promise in recent years of supplementing KC/MS for obtaining dissociation energies of high temperature molecules are photoionization mass spectrometry (PIM) and single collision chemiluminescence spectroscopy. It is worthwhile to compare results from these techniques with those from effusion methods.

#### 3.4.1 Photoionization mass spectrometry (PIM)

Berkowitz has published a review of this technique [157] and discusses it further in a later chapter in this volume. In photoionization mass spectrometry, vacuum ultraviolet techniques are used to impinge photons of varying frequency on a tenuous gas or molecular beam. The appearance of ions is detected mass spectrometrically, and the threshold energy,  $E_{\text{th}}$  is thus measured. Simple ionization gives accurate ionization potentials. Fragmentation leads to the obtaining of dissociation energies. For a molecule  $\text{MX}$  the reaction might be



Then if the ionization potential of  $\text{M}$  is known, the dissociation energy is given by

$$D(\text{MX}) = E_{\text{th}} - \text{IP}(\text{M}).$$

Correction must be made for the distribution of energies in the species at the temperature of the molecular beam, typically 2 to 4 kcal/mol, and the nature of the states involved when ionization occurs must be understood. Berkowitz notes that though the numbers obtained are much more precise than those from thermochemical or KC/MS techniques, "The price one must pay is the uncertainty in interpreting thresholds."

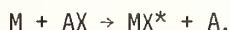
The experimental advantages of PIM are that equilibrium need not be achieved in the molecular source, and that one can often find convenient room temperature molecules that will fragment to yield the data on species of interest, whereas only complicated high temperature experiments will yield these species in effusion studies. For example,  $\text{C}_2\text{H}$  has been studied by the photoionization of acetylene [158],  $\text{C}_2\text{HCN}$ , and  $\text{CH}_3\text{CN}$  [159] at room temperature, and by mass spectrometric analysis [160] of the vapor effusing from a graphite cell at 1950-2230 K into which the gases  $\text{H}_2$ ,  $\text{C}_2\text{H}_2$ , and  $\text{CH}_4$  were introduced. The mass spectrometrically obtained heat of formation at 298 K was  $-130 \pm 5$  kcal/mol, while the PIM experiments gave 130 and  $127 \pm 1$  kcal/mol. However, these authors [158,159] cited a number of similar photoionization studies whose results led to erroneous values for this and some

related heats of formation. A recent example [162] of a combined KC/MS and PIM measurement of high temperature species is the determination of the atomization energies of CSe and CSe<sub>2</sub> at 1530-1870 K. The results, confirmed by both methods, were respectively 140.2 and 225.4 kcal/mol.

Berkowitz [157] summarizes the systems studied to 1971 and discusses the agreements and disagreements with KC/MS results for halide and chalcogen molecules. From about 1971 to the present few experiments were published on molecules obtained from high temperature sources, in part because of difficulties with noise due to heating by electron bombardment at temperatures above about 1000 °C [161]. However, development of radiant heating sources has led to renewed interest in this area. Future development of PIM will accompany the exploitation of synchrotron radiation and perhaps eventually tuneable ultraviolet lasers as light sources and advances in understanding threshold behavior.

### 3.4.2 Single-collision chemiluminescence reactions

This post-1970 method which yields dissociation energies and spectroscopic information for high temperature molecules was pioneered by Zare and co-workers [163] and has been exploited by Zare and by Gole, who has reviewed progress up to 1976 [164]. It involves the spectroscopic study of the light emitted by excited molecules which are formed in the reaction between an effusing beam of metal atoms and a low pressure oxidizing gas such as O<sub>2</sub>, O<sub>3</sub>, NO<sub>2</sub>, ClF, or OCS, which is either stationary or also in a molecular beam. A lower bound to the dissociation energy of the excited product molecule can be obtained in the following way. If M is a reactant metal atom and AX is the oxidant gas, the reaction is



From the experimental conditions one can compute the initial total kinetic energy  $E_t$  and the internal energies  $E_{int}(M)$  and  $E_{int}(AX)$ . The maximum internal energy of the product  $MX^*$  is calculated from the highest vibrational level identified in the emission spectrum. Usually no information is available on the final translational energies or the internal energy of the product A. Neglecting the unknown quantities, one obtains from an energy balance for the reaction

$$D_0^0(MX) \geq D_0^0(AX) + E_{int}(AX) + E_{int}(M) + E_t - E_{int}(MX).$$

Gole [164] compares the lower bounds for  $D_0^0$ 's by chemiluminescence for 22 monoxide and mono-halide molecules, with  $D_0^0$ 's determined by KC/MS and flame spectroscopic techniques. The values from chemiluminescence and KC/MS determinations for monoxides and monochlorides and Group IIIB monofluorides mostly agree within the expressed uncertainties of the KC/MS data. However, the chemiluminescence experiments give stabilities for the group IIA monofluorides that are significantly (6-10 kcal/mol) greater than those calculated from the effusion measurements. The dissociation energy of LaS from KC/MS experiments,  $136.0 \pm 3.0$  kcal/mol, is



supported by the lower bound from the chemiluminescence reaction [147]  $\text{La} + \text{OCS} \rightarrow \text{LaS}^* + \text{CO}$ . However, the lower bound for the dissociation energy of  $\text{EuO}$ ,  $131.4 \pm 0.7$  kcal/mol, from chemiluminescence work [165] while in agreement with earlier KC/MS results [131,166], is in conflict with the latest KC/MS value,  $111.9 \pm 2.4$  kcal/mol [167]. In conclusion it appears that the chemiluminescence technique gives good lower bounds to  $D_0^0$ 's when the spectroscopic observations can be unambiguously interpreted, but that skepticism is warranted in many cases.

Incidentally, the chemiluminescence reactions are serving as detectors for the effusing metal beam, so that the intensity of emitted light is related to the vapor pressure within the effusion cell. One might expect by analogy to the mass spectrometric equations that the heat of vaporization of the metal could be obtained from a plot of  $\ln(IT)$  vs  $1/T$ , where  $I$  is the intensity observed and  $T$  is the effusion cell temperature. In fact this does give an upper limit for  $\Delta H_{\text{vap}}$ ; the correct relation between  $\ln(IT)$  and  $1/T$  also includes the activation energy for the reaction producing the excited species and a weighted mean temperature between the effusing beam and the oxidant gas. Pruess and Gole [168-170] have discussed this aspect of chemiluminescence reactions, and have used the known heats of vaporization of metals to derive activation energies for the reactions and identify the electronic states from which emission takes place.

### 3.4.3 Laser induced fluorescence as a detector for effusion cells.

Fairbank, Haensch, and Shawlow [171] measured absolute vapor densities of Na atoms in the equilibrium vapor of sodium in a static oven by observing the fluorescence induced by a cw dye laser. The range of densities and temperatures was 100 atoms/cm<sup>3</sup> at 245 K to  $10^{11}$  atoms/cm<sup>3</sup> at 417 K. These concentrations correspond to pressures in the oven of  $3 \times 10^{-15}$  to  $6 \times 10^{-6}$  atm. By varying the temperature of the Oven, Fairbank, et al. [171] determined the heat of vaporization of Na by a third law method, obtaining excellent agreement with published values. Vu and Stwalley [172] are currently studying  $\text{Na}_2$  in sodium vapor in a heat pipe, and hope to extend the study to higher polymers.

These concentrations easily cover the range of densities in the effusing molecular beam from a Knudsen cell. For example at 1000 K and  $10^{-6}$  atm, with an orifice of 1 mm diam, the molecular beam density is  $3 \times 10^{10}$  molecules/cm<sup>3</sup> at a distance of 1 cm from the orifice, and  $3 \times 10^8$  at 10 cm. The extreme sensitivity of the laser fluorescence technique thus recommends it for future use with Knudsen cells at extremely low pressures or with vapor species in very minor concentrations. However, considerable information must be developed for the system under study if absolute measurements are to be made, because the absolute absorption coefficients are required, the vibrational and rotational states involved must be known and lasers of the appropriate frequencies are needed. Fairbank, et al. [171] list the wavelengths required to excite the most promising ground state transition of 73 different elements, and group these according to the type of laser needed.

## References

- [1] Knudsen, M., *Ann. Physik*, 28, 75-130 (1909).
- [2] Knudsen, M., *Ann. Physik*, 28, 999-1016 (1909).
- [3] Knudsen, M., *Ann. Physik*, 29, 179 (1909).
- [4] Hertz, H., *Ann. Physik*, 17, 177 (1882).
- [5] Leob, L. B., *The Kinetic Theory of Gases* (Dover Publications, Inc., 1961) (reprint of McGraw-Hill edition of 1934) Chapter VII.
- [6] Knudsen, M., *Ann. Physik*, 34, 593 (1911).
- [7] Knudsen, M., *Ann. Physik*, 48, 1113 (1915).
- [8] Knudsen, M., *Ann. Physik*, 6, 129 (1930).
- [9] Knudsen, M., *Kinetic Theory of Gases*, 3rd ed. (Methuen and Co., Ltd., London, 1950).
- [10] Egerton, A. C., *Phil. Mag.* 33, 33 (1917).
- [11] Egerton, A. C., *Proc. Roy. Soc.* 103A, 469 (1923).
- [12] Nesmeyanov, An. N., ref. 42, chap. 1.
- [13] Rudberg, E., *Phys. Rev.* 46, 763 (1934).
- [14] Mayer, H., *Z. Physik*, 52, 235 (1928); 58, 373 (1929).
- [15] Mayer, H., *Z. Physik*, 67, 240 (1931).
- [16] Clausing, P., *Physica*, 9, 65 (1929).
- [17] Clausing, P., *Z. Physik*, 66, 471 (1930).
- [18] Clausing, P., *Ann. Physik*, 12, 961 (1932).
- [19] Demarcus, W. C., The Problem of Knudsen Flow, report K-1302, part 3, Union Carbide Corp. Oak Ridge Gaseous Diffusion Plant, Oak Ridge, Tenn., 1957. Demarcus's summary equations are quoted by Cater, ref. 39, p. 39.
- [20] Iczkowski, R. P., Margrave, J. L., and Robinson, S. M., *J. Phys. Chem.* 67, 229 (1963).
- [21] Freeman, R. D., and Edwards, J. G., *The Characterization of High Temperature Vapors*, Margrave, J. L., ed., Appendix C (Wiley, New York, 1967).
- [22] Edwards, J. G., and Gilles, P. W., *J. Chem. Phys.* 44, 4426 (1966).
- [23] Grimley, R. T., and Wagner, L. C., *J. Phys. Chem.* 58, 402 (1973).
- [24] Volmer, M., *Z. Physik. Chem., Bodenstein Festband*, 863 (1931). The work originated in the dissertations of Teusher, W., (1923), Heller, S., (1930), and Neumann, K., (1930).
- [25] Freeman, R. D., *The Characterization of High Temperature Vapors*, J. L. Margrave, ed., chapter 7 (Wiley, 1967).
- [26] Chupka, W. A., and Inghram, M. G., *J. Chem. Phys.* 21, 371 (1953).
- [27] Honig, R. E., *J. Chem. Phys.* 22, 126 (1954).
- [28] Chupka, W. A., and Inghram, M. G., *J. Phys. Chem.* 59, 100 (1955).
- [29] Johnson, R. G., Hudson, D. E., Caldwell, W. C., Spedding, F. H., and Savage, W. R., *J. Chem. Phys.* 25, 917 (1956).
- [30] Savage, W. R., Hudson, D. E., and Spedding, F. H., *J. Chem. Phys.* 30, 221 (1959).
- [31] Brewer, L., and Searcy, A. W., *Ann. Rev. Phys. Chem.* 7, 259 (1956).
- [32] Margrave, J. L., *Ann. Rev. Phys. Chem.* 10, 457 (1959).
- [33] Gilles, P. W., *Ann. Rev. Phys. Chem.* 12, 355 (1961).

- [34] Drowart, J., and Goldfinger, P., *Ann. Rev. Phys. Chem.* 13, 459 (1962).
- [35] Grimley, R. T., in The Characterization of High Temperature Vapors, J. L. Margrave, ed. (Wiley, New York, 1967), ch. 8.
- [36] Drowart, J., and Goldfinger, P., *Angew. Chem., Int., Ed. in English*, 6, 581 (1967).
- [37] Goldstein, H. W., Walsh, P. N., and White, D., *J. Phys. Chem.* 65, 1400 (1961).
- [38] Cater, E. D., Rauh, E. G., and Thorn, R. J., *J. Chem. Phys.* 35, 619 (1961).
- [39] Cater, E. D., Chapter 2A, Winterbottom, W. L., Chapter 2B, Buchler, A., and Berkowitz Mattuck, J., Chapter 2D, and Honig, R. E., and Kramer, D. A., Appendix, in Physicochemical Measurements in Metals Research, R. A. Rapp, ed., Vol. IV, part 1, of Techniques in Metals Research, R. F. Bunshah, series editor (Wiley, New York, 1970).
- [40] Margrave, J. L., ed., The Characterization of High Temperature Vapors, (Wiley, New York, 1967) (Chapters 2-8 and appendix C, by P. W. Gilles; P. R. Clopper, R. L. Altman, and L. Margrave; K. D. Carlson; R. C. Pauie and J. L. Margrave; R. D. Freeman, R. T. Grimley; R. D. Freeman and J. G. Edwards, respectively).
- [41] Margrave, J. L., in Physicochemical Measurements at High Temperatures, J. O'M. Bockris, J. L. White, and J. D. Mackenzie, eds., chap. 10 (Butterworths, London, 1959).
- [42] Nesmeyanov, An. N., Vapor Pressures of the Elements, Transl. from Russian and published both by Academic Press, New York, 1963, and by American Elsevier Publ. Co., New York, 1963.
- [43] Whitman, C. J., *J. Chem. Phys.* 20, 161 (1952).
- [44] Motzfeldt, K., *J. Phys. Chem.* 59, 139 (1955).
- [45] Balson, E. W., *J. Phys. Chem.* 65, 115 (1961).
- [46] Carlson, K. D., Gilles, P. W., and Thorn, R. J., *J. Chem. Phys.* 38, 2064 (1963).
- [47] Ward, J. W., and Fraser, M. V., *J. Chem. Phys.* 49, 3743 (1968).
- [48] Cater, E. D., ref. 39, p. 45.
- [49] Winterbottom, W. L., ref. 39, p. 126.
- [50] Brewer, L. and Kane, J. S., *J. Phys. Chem.* 59, 105 (1955).
- [51] Bonderman, D. P., Cater, E. D., and Bennett, W. E., *J. Chem. Eng. Data* 15, 396 (1970).
- [52] Lau, K. H., Hildenbrand, D. H., and Cubicciotti, D., *J. Electrochem. Soc.* 126, 490 (1979).
- [53] Lau, K. H., Cubicciotti, D., and Hildenbrand, D. L., *J. Chem. Phys.* 66, 4532 (1977).
- [54] Mohazzabi, P., and Searcy, A. W., *J. Chem. Soc., Faraday Trans. 1*, 72, 290 (1978).
- [55] Knutsen, G. F., and Searcy, A. W., *J. Electrochem. Soc.* 125, 327 (1978).
- [56] Beruto, D., and Searcy, A. W., *Nature* 263, 221 (1976).
- [57] Gurvich, L. V., Dorofeeva, O. V., and Yungman, V. S., in *Proceedings of the Conference on High Temperature Science Related to Open-Cycle, Coal-Fired MHD Systems*, Argonne Nat. Lab. report ANL-77-21 (1977).
- [58] Gorokhov, L. N., Annual Report, Institute for High Temperatures, Academy of Sciences, USSR (1975).
- [59] Ward, J. W., Mulford, R. N. R., and Kahn, M., *J. Chem. Phys.* 47, 1710 (1967).
- [60] Ward, J. W., Mulford, R. N. R., and Bivens, R. L., *J. Chem. Phys.* 47, 1718 (1967).
- [61] Ward, J. W., *J. Chem. Phys.* 47, 4030 (1967).

- [62] Ward, J. W., Ohse, R. W., and Reul, R., J. Chem. Phys. 62, 2366 (1975).
- [63] Ward, J. W., Fraser, M. V., and Bivins, R. L., J. Vacuum Sci. and Tech. 9, 1056 (1972).
- [64] Adams, J. Q., Phipps, T. E., and Wahlbeck, P. G., J. Chem. Phys. 51, 920 (1969).
- [65] Cater, E. D., Gilles, P. W., and Thorn, R. J., J. Chem. Phys. 35, 608 (1961).
- [66] Cater, E. D., Argonne National Report ANL-6140 (1960).
- [67] Storms, E., High Temp. Sci. 1, 456 (1969).
- [68] Winterbottom, W. L., and Hirth, J. P., J. Chem. Phys. 37, 784 (1962).
- [69] Ruth, V., Winterbottom, W. L., and Hirth, J. P., Z. Angew. Phys. 16, 53 (1963).
- [70] Winterbottom, W. L., J. Chem. Phys. 47, 3546 (1967).
- [71] Winterbottom, W. L., J. Chem. Phys. 51, 5610 (1969).
- [72] Dunham, T. E., and Hirth, J. P., J. Chem. Phys. 49, 4650 (1968).
- [73] Boyer, A. J., and Meadowcroft, T. R., Trans. AIME 233, 388 (1965).
- [74] Ward, J. W., Bivins, R. L., and Fraser, M. V., J. Vacuum Sci. and Tech. 7, 206 (1970).
- [75] Freeman, R. D., Okla. State Univ., report ASD-TDR-63-754, Pt. III, Nov., 1967.
- [76] Adams, J. Q., Phipps, T. E., and Wahlbeck, P. G., J. Chem. Phys. 49, 1600 (1968).
- [77] Grimley, R. T., and Muenow, D. W., J. Chem. Phys. 46, 3260 (1967).
- [78] Muenow, D. W., and Grimley, R. T., Rev. Sci. Instr. 42, 455 (1971).
- [79] Grimley, R. T., Muenow, D. W., and LaRue, Jr., J. L., J. Chem. Phys. 56, 490 (1972).
- [80] Voronin, G. F., Russ. J. Phys. Chem. 41, 889 (1967); 43, 733 (1969).
- [81] Liu, M. B., and Wahlbeck, P. G., J. Chem. Phys. 59, 907 (1973); erratum, *ibid.*, 59, 5748 (1973).
- [82] Wey, S. J., and Wahlbeck, P. G., J. Chem. Phys. 57, 2937 (1972).
- [83] Grimley, R. T., Chakaborti, P. K., and Castle, P. M., J. Appl. Phys. 46, 4090 (1975).
- [84] Grimley, R. T., Wagner, L. C., and Castle, P. M., J. Phys. Chem. 79, 302 (1975).
- [85] Wang, K. C., and Wahlbeck, P. G., J. Chem. Phys. 49, 1617 (1968).
- [86] Wang, K. C., and Wahlbeck, P. G., J. Chem. Phys. 51, 2896 (1970).
- [87] Carlson, K. D., Gilles, P. W., and Thorn, R. J., J. Chem. Phys. 38, 2725 (1963).
- [88] Carlson, K. D., The Characterization of High Temperature Vapors, J. L. Margrave, ed., Wiley, New York, 1967, Chap. 5.
- [89] Wahlbeck, P. G., J. Chem. Phys. 55, 1709 (1971).
- [90] Wey, S. J., and Wahlbeck, P. G., J. Chem. Phys. 57, 2932 (1972).
- [91] Macur, G. J., Edwards, R. K., and Wahlbeck, P. G., J. Phys. Chem. 70, 2956 (1966).
- [92] Kelley, K. K., U.S. Bureau of Mines Bull. 383, p. 39 (1935).
- [93] Grimley, R. T. and LaRue, J. L., Advan. Appl. Mech., Suppl. 5, Vol. II, 1455 (1969).
- [94] Tuenge, R. T., Laabs, F., and Franzen, H. F., J. Chem. Phys. 65, 2400 (1976).
- [95] Wu, R. L. C., and Gilles, P. W., USAEC Report No. C00-1140-200, Univ. of Kansas, 1971.
- [96] Schulz, D. A., and Searcy, A. W., J. Chem. Phys. 36, 3099 (1962).
- [97] Cater, E. D., ref. 39, p. 42.
- [98] Puligandla, V., and Edwards, J. G., J. Chem. Phys. 62, 3875 (1975).
- [99] Pugh, A. C. P., and Barrow, R. F., Trans. Faraday Soc. 54, 671 (1958).
- [100] Budininkas, P., Edwards, R. K., and Wahlbeck, P. G., J. Chem. Phys. 48, 2859 (1968).
- [101] Budininkas, P., Edwards, R. K., and Wahlbeck, P. G., J. Chem. Phys. 48, 2867 (1968).



- [102] Budininkas, P., Edwards, R. K., and Wahlbeck, P. G., J. Chem. Phys. 48, 2870 (1968).
- [103] Myles, K. M., and Aldred, A. T., J. Phys. Chem. 68, 64 (1964).
- [104] McCreary, J. R., and Thorn, R. J., J. Chem. Phys. 50, 3725 (1969).
- [105] McCreary, J. R., Rassoul, S. A., and Thorn, R. J., High Temp. Science, 1, 4 (1969).
- [106] McCreary, J. R., and Thorn, R. J., High Temp. Science 3, 300 (1971).
- [107] Edwards, J. G., J. Vac. Sci. Technol. 11, 400 (1974).
- [108] Gates, A. S., and Edwards, J. G., J. Phys. Chem. 82, 2789 (1978).
- [109] Chatillon, C., Pattoret, A., and Drowart, J., High Temp. - High Pressures 7, 119 (1975).
- [110] Stafford, F. E., High Temp. - High Pressures 3, 213 (1971).
- [111] Ackermann, R. J., and Rauh, E. G., Canadian Metallurgical Quarterly 14, 205 (1975).
- [112] Drowart, J., Proc. Int. School on Mass Spec., Ljubljana, Yugoslavia, 1969, pp. 187-242.
- [113] Keller, H., Rickert, H., Detry, D., Drowart, J., and Goldfinger, P., Z. Phys. Chem. N.F. 75, 273 (1971).
- [114] Detry, D., Drowart, J., and Goldfinger, P., Keller, H., and Rickert, H., Z. Phys. Chem. N.F. 55, 314 (1967).
- [115] Mann, J. B., J. Chem. Phys. 46, 1646 (1967).
- [116] Mann, J. B., in Recent Developments in Mass Spectrometry, K. Ogata, T. Hayakawa, eds Univ. Park Press, Baltimore, MD, 1970.
- [117] Lin, S. S., and Stafford, F. E., J. Chem. Phys. 48, 3885 (1968).
- [118] Kieffer, L. J., and Dunn, G. H., Rev. Mod. Phys. 38, 1 (1966).
- [119] Ackermann, R. J., and Rauh, E. G., J. Chem. Phys. 60, 1396 (1974).
- [120] Ackermann, R. J., and Rauh, E. G., J. Chem. Thermodyn. 3, 609 (1971).
- [121] Ackermann, R. J., and Rauh, E. G., High Temp. Science 5, 463 (1973).
- [122] Blackburn, P. E., and Danielson, P. M., J. Chem. Phys. 56, 6156 (1972).
- [123] Norman, J. H., Staley, H. G., and Bell, W. E., Advan. Chem. Ser. 72, 101 (1968).
- [124] Otvos, J. W., and Stevenson, D. P., J. Am. Chem. Soc. 78, 546 (1956).
- [125] Cater, E. D., and Thorn, R. J., J. Chem. Phys. 44, 1342 (1966).
- [126] Cater, E. D., Rauh, E. G., and Thorn, R. J., J. Chem. Phys. 44, 3106 (1966); erratum ibid. 48, 538 (1968).
- [127] Norman, J. H., J. Chem. Phys. 52, 629 (1970).
- [128] Smoes, S., Drowart, J., and Welter, J. M., J. Chem. Thermodyn. 9, 275 (1977).
- [129] Smoes, S., Drowart, J., and Myers, C. E., J. Chem. Thermodyn. 8, 225 (1976).
- [130] Quoted by J. Drowart, S. Smoes, and A. Vanderauwera-Mahieu, J. Chem. Thermodyn. 10, 453 (1978).
- [131] Ames, L. L., Walsh, P. N., and White, D., J. Phys. Chem. 71, 2707 (1967).
- [132] Sheldon, R. I., and Gilles, P. W., paper in this volume.
- [133] Drowart, J., Pattoret, A., Smoes, S., Proc. Brit. Ceram. Soc. 8, 67 (1967).
- [134] Steiger, R. P., and Cater, E. D., High Temp. Sci. 7, 288 (1975).
- [135] Steiger, R. A., and Cater, E. D., High Temp. Sci. 7, 204 (1975).
- [136] Fries, J. A., and Cater, E. D., J. Chem. Phys. 68, 3978 (1978).



- [137] Cater, E. D., Mueller, B. H., and Fries, J. A., paper in this volume.
- [138] Smoes, S., Pattje, W. R., and Drowart, J., High Temp. Sci. 10, 109 (1978).
- [139] Wu, R. L. C., Ph.D. Thesis, Univ. of Kansas, 1971, available as R. L. C. Wu and P. W. Gilles USAEC Report No. C00-1140-200 (1971).
- [140] Smoes, S., Coppens, P., Bergman, C., and Drowart, J., Trans. Faraday Soc. 65, 682 (1969).
- [141] Coppens, P., Smoes, S., and Drowart, J., Trans. Faraday Soc. 63, 2140 (1967).
- [142] Jones, R. W., and Gole, J. L., Chem. Phys. 20, 311 (1977).
- [143] Ackermann, R. J., and Rauh, E. G., J. Chem. Phys. 60, 2266 (1974).
- [144] Wu, R. L. C., and Gilles, P. W., J. Chem. Phys. 59, 6136 (1973).
- [145] Cater, E. D., Rauh, E. G., and Thorn, R. J., J. Chem. Phys. 49, 5244 (1968).
- [146] Ackermann, R. J., Gilles, P. W., and Thorn, R. J., J. Chem. Phys. 25, 1089 (1956); *ibid.* 29, 237 (1958).
- [147] Ackermann, R. J., and Rauh, E. G., J. Phys. Chem. 73, 769 (1969).
- [148] Ackermann, R. J., Rauh, E. G., and Chandrasekharaiah, M. S., J. Phys. Chem. 73, 762 (1969).
- [149] Winslow, G. H., High Temp. Sci. 7, 81 (1975).
- [150] Cater, E. D., J. Chem. Educ. 55, 697 (1978).
- [151] Ackermann, R. J., and Rauh, E. G., J. Chem. Thermodyn. 3, 609 (1971); *ibid.* 3, 445 (1971); *ibid.* 5, 331 (1973).
- [152] Ackermann, R. J., Seventh Midwest High Temperature Chemistry Conference, Wichita, KS, June, 1977.
- [153] Cater, E. D., Lee, T. E., Johnson, E. W., Rauh, E. G., and Eick, H. A., J. Phys. Chem. 69, 2684 (1965); corrections in Cater, E. D and Steiger, R. P., J. Phys. Chem. 72, 2231 (1968).
- [154] Grimley, R. T., and Muenow, D. W., J. Chem. Phys. 46, 3260 (1967).
- [155] Grimley, R. T., Forsman, J. A., and Grindstaff, Q. G., J. Phys. Chem. 82, 632 (1978).
- [156] Snelson, A., J. Phys. Chem. 73, 1919 (1969).
- [157] Berkowitz, J., Adv. in High Temp. Chem. vol. 3, L. Eyring, ed., Academic Press, New York, 1971, p. 123.
- [158] Dibeler, V. H., Walker, J. A., and McCulloch, K. E., J. Chem. Phys. 59, 2264 (1973).
- [159] Okabe, H., and Dibeler, V. H., J. Chem. Phys. 59, 2430 (1973).
- [160] Wyatt, J. R., and Stafford, F. E., J. Phys. Chem. 76, 1913 (1972).
- [161] Berkowitz, J., personal communication.
- [162] Smoes, S. and Drowart, J., J. Chem. Soc. Faraday Trans. II 73, 1746 (1977).
- [163] Ottinger, C., and Zare, R. N., Chem. Phys. Lett. 5, 243 (1970).
- [164] Gole, J. L., Ann. Rev. Phys. Chem. 27, 311 (1977).
- [165] Dickson, C. R., and Zare, R. N., Chem. Phys. 7, 2707 (1975).
- [166] Smoes, S., Coppens, P., Bergman, C., and Drowart, J., Trans. Faraday Soc. 65, 682 (1970).
- [167] Murad, E., and Hildenbrand, D. L., Z. Naturforsch, Teil A 30, 1087 (1975).
- [168] Preuss, D. R., and Gole, J. L., J. Chem. Phys. 66, 2994 (1977).

- [169] Gole, J. L., and Pruess, D. R., J. Chem. Phys. 66, 3000 (1977).  
[170] Preuss, D. R., and Gole, J. L., J. Chem. Phys. 66, 880 (1977).  
[171] Fairbank, W. M., Haensch, T. W., and Schawlow, A. L., J. Opt. Soc. Am. 65, 199 (1975).  
[172] Vu, T. H., Ph.D. thesis research with W. C. Stwalley, Univ. of Iowa, Iowa City.  
[173] Kohl, F. J., Uy, O. M., and Carlson, K. D., J. Chem. Phys. 47, 2667 (1967).  
[174] Sidorov, L. N., Dokl. Akad. Nauk. SSSR 184, 889 (1969).

GENERAL THEORETICAL ANGULAR NUMBER DISTRIBUTION FUNCTIONS OF KNUDSEN  
FLOW THROUGH THE FOLLOWING SINGLE AND DOUBLE-SLIT ORIFICE GEOMETRIES:  
CIRCULAR, RECTANGULAR, AND CYLINDRICAL

Federico Miller  
Department of Chemistry  
Laredo Junior College  
Laredo, TX 78040

Exact, rigorous solutions in the form of angular number distribution functions have been theoretically derived for the problem of Knudsen flow through a circular orifice as well as rectangular and cylindrical double-slit orifices. The usual definitions of an ideal gas and the conditions characterizing a dilute gas (i.e., mean free path  $\gg$  orifice diameter) have been employed in the formulation of the theory. An additional assumption has been incorporated into the theory of Knudsen flow, defining the intensity at a point in space on the low pressure side of the orifice: "The intensity of the effusing particles of the dilute gas at a point P in space, a distance L from the geometric center of the orifice, is directly proportional to the 'effective area' of the orifice." The "effective area" is defined as the area of the conic section formed by the intersection of a plane and a cone. The plane contains the geometric center of the orifice and is perpendicular to the line connecting the geometric center and the point P. The cone is defined as a geometric figure having the orifice as its base and the point P as its apex.

The angular number distribution functions obtained for the three orifice geometries mentioned are thus functions of the "effective area." For an ideal circular orifice, the normalized angular number distribution function is given by the expression:

$$I(\theta)/I(0) = \cos \theta / [1 - (R/L)^2 \sin^2 \theta]^{3/2}$$

where R is the radius of the circular orifice and  $\theta$  is the zenith angle ( $0 \leq \theta \leq \pi/2$ ).

For an ideal rectangular orifice, the normalized angular number distribution function along a plane normal to the orifice plane and bisecting two opposite sides of the rectangular orifice is given by the expression:

$$I(\theta)/I(0) = \cos \theta / [1 - (R/L)^2 \sin^2 \theta]^2$$

where R is half the length of the orifice.

Complex angular number distribution functions have also been derived for ideal double-slit (no walls) rectangular and cylindrical orifices.

## 1. Introduction

Knudsen effusion [1]<sup>1</sup> is a physical phenomenon describing the effusion of a rarefied gas in equilibrium through an ideal orifice. An ideal orifice is one whose thickness is vanishingly small. The Knudsen effusion method is based on the mathematical formalism of the kinetic theory of dilute gases [2] used in the determination of the molecular flux at a dimensionless boundary.

The method has been used widely in the field of high temperature chemistry in the characterization of vapors in equilibrium with their condensed phases [3]. The Knudsen effusion method in combination with mass spectrometry as an analytical tool has become a powerful technique in obtaining equilibrium thermodynamic data for slightly volatile molecular and atomic species [4].

Knudsen effusion experimentally incorporates the use of single, double, and leak cells having near-ideal knife-edge, conical, and cylindrical orifices [4]. In the determination of equilibrium vapor pressures within cells containing channeled orifices, a correction factor known as the Clausing factor is required. The Clausing factor, or transmission probability, may be defined as the probability that a molecule entering through one orifice will emerge through the other orifice [5]. This factor has been the subject of extensive studies by Clausing [6] and others [5,7,8]. The non-ideality of Knudsen cell orifices is expressed by the use of such factors.

The effect that orifice geometry has on the rate of effusion has been studied by Clausing [6,9] and others [5,7,10]. Theoretical studies of the dependence of angular number distribution functions on orifice geometry have also been performed and compared with experiment [11,12,13,14]. A theoretical investigation has also been made of the density field for rarefied flow through thin square, rectangular, and circular orifices [15]. It is the subject of this paper to theoretically derive general equations for the angular number distribution functions of such orifices which not only hold for great distances from the orifices, but also for the vicinity of the orifices. In addition, the angular number distribution functions for the ideal double-slit (no walls) rectangular and ideal double-slit (no walls) cylindrical orifices are derived. In contrast to all previous theoretical derivations of angular number distribution functions for channeled orifices, the geometric center of the orifice, as opposed to the center of the orifice

---

<sup>1</sup>Figures in brackets indicate the literature references at the end of this paper.



on the low pressure side, is taken as the origin of the ray to a point P in space on the same side. The zenith angle  $\theta$  is then the angle formed by the ray with the normal axis through the orifice.

The choosing of the geometric center of the ideal double-slit (no walls) rectangular and cylindrical orifices as the critical point of the angular number distribution functions (figs. 3c, 3d, 5, 6, and 7) lends itself to the rigorous derivation of these functions. All functions derived in this paper, thus, do not contain contributions from the walls of the orifices. The functions are simple two-dimensional spatial distributions having molecular contributions strictly from within the cell. In the case of the double-slit cylindrical orifice, an exact Clausing factor has been derived from its definition [5].

## 2. Theory

The effusion of a gas through an orifice can be of two forms. Below a minimum pressure, the flow is described as Knudsen flow. Above this pressure, it is defined as hydrodynamic or Poiseuille flow and follows a completely different set of fluid dynamic equations [16]. The following assumptions are considered in developing the equations of Knudsen flow:

- (1) The gas is said to have unidirectional flow across the orifice from the region of high pressure to that of low pressure.
- (2) The mean free path of the molecules is greater than the diameter of the orifice.
- (3) The gas is in thermal as well as mechanical equilibrium with its surroundings.
- (4) The molecules do not undergo individual collisions in the vicinity of the orifice nor anywhere in the region of lower pressure.

These are the basic conditions of an effusing gas necessary to Knudsen flow.

In an effort to derive general angular number distribution functions which not only hold at great distances from the orifice, but also at the neighborhood of the orifice, an additional geometric assumption is introduced:

- (5) The molecular intensity at a point P in space on the low pressure side, a distance L from the geometric center of the orifice, is directly proportional to the "effective cross-sectional area" of the orifice.

This effective area, which contains the geometric center, forms the base of a cone having the point P as its apex. The effective area is perpendicular to a line containing the geometric center and the apex point P.

The concept used in the development of the fifth geometric assumption is based on the theory of the diffuse scattering of light [17]. The ideal gas molecules effusing through the ideal orifices are assumed to behave identically to photons isotropically scattered from a rough surface--a special case of diffuse scattering [18]. The only difference being that gas molecules are not traveling at the speed of light.

In the field of illumination engineering, simple mathematical calculations employing Lambert's Law (the Cosine Law) have been performed to determine the illumination onto planes from various geometries of illuminating sources such as circular disks and rectangles [19,20,21].

Additional calculations have also been performed to determine the illumination at a point on a plane parallel to the illuminating plane for extended sources of any shape [22,23] using the theoretical formula for illumination from a line source [20].

The behavior of effusing rarefied gas molecules is, thus, assumed to parallel the isotropic diffuse scattering of light photons from illuminating sources.

## 2.1 The ideal circular orifice

Figure 1 shows the geometry of the ideal circular orifice. The angle  $\theta$  is the zenith angle formed by the normal to the plane of the orifice and containing the geometric center of the orifice  $O$  and the ray  $L$  whose origin is the geometric center and whose terminus is the point  $P$ .  $P$  is the apex of either a right circular cone ( $\theta = 0$ ) or an oblique circular cone ( $0 < \theta < \pi/2$ ) whose base is the ideal circular orifice of radius  $R$ .

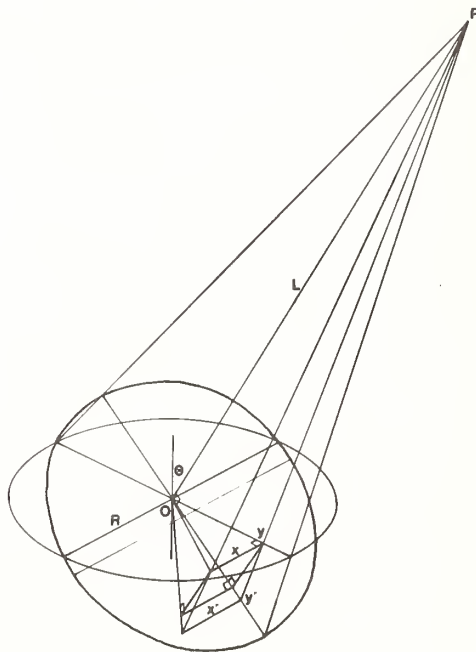


Figure 1. Geometry of the single ideal circular orifice. (See text for details.)

The effective area of the orifice is the conic section formed by the intersection of the cone and a plane containing the geometric center and having the ray  $L$  normal to it. The conic section is an ellipse [24].

In order to determine the area of the conic section, the geometric center  $O$  is chosen as the center of two coordinate systems. The points whose coordinates are  $(x,y)$  lie on the plane containing the ideal circular orifice. The points whose coordinates are  $(x',y')$  lie on the intersecting plane and are the projections of the points  $(x,y)$  from the point  $P$ .

Transformation projection formulas can be simply derived by the use of similar triangles. These formulas take the following forms:

$$x = \frac{Lx' \cos \theta}{y' \sin \theta + L \cos \theta} \quad (1)$$

$$y = \frac{Ly'}{y' \sin \theta + L \cos \theta} .$$

Substitution of these into the equation of a circle,  $x^2 + y^2 = R^2$ , and rearranging terms, gives rise to the following equation for an ellipse:

$$(L^2 \cos^2 \theta)x'^2 + (L^2 - R^2 \sin^2 \theta)y'^2 - (2LR^2 \sin \theta \cos \theta)y' - (L^2 R^2 \cos^2 \theta) = 0 . \quad (2)$$

The effective area is equal to the area of this ellipse. The area of the ellipse is equal to the product of  $\pi$ (pi) and the semiminor and semimajor axes. The semiminor axis  $\bar{y}'$  is defined as half the width of the ellipse along the line  $Oy'$ . The length of the semiminor axis can be obtained by setting  $x'$  equal to zero and solving for  $y'$ . Since the center of the orifice does not coincide with the center of the ellipse, two values of  $y'$  are obtained by solving the resulting quadratic equation. The length of the semiminor axis is obtained by taking the sum of the absolute values of both roots and dividing by two. The semiminor axis is then equal to the following expression:

$$\bar{y}' = \frac{R \cos \theta}{1 - (R/L)^2 \sin^2 \theta} . \quad (3)$$

To find the length of the semimajor axis  $x'$ , eq. (2) is rearranged to solve for  $x'$ . Taking the first derivative of  $x'$  with respect to  $y'$  and letting it equal to zero gives the value of  $y'$  at the maximum of  $x'$ :

$$y' = \frac{LR^2 \sin \theta \cos \theta}{L^2 - R^2 \sin^2 \theta} . \quad (4)$$

Substitution of this value into the expression for  $x'$ , immediately yields the value for the length of the semimajor axis  $x'$ :

$$\bar{x}' = \frac{R}{[1 - (R/L)^2 \sin^2 \theta]^{1/2}} \quad (5)$$

The effective area is now given by the following equation:

$$A = \frac{\pi R^2 \cos \theta}{[1 - (R/L)^2 \sin^2 \theta]^{3/2}} \quad (6)$$

According to assumption (5), the molecular intensity  $I(\theta)$  is directly proportional to the effective area  $A$ . Normalization of this intensity requires division of the effective area  $A(\theta \neq 0)$  by the effective area when  $\theta$  is equal to zero. This area is the area of the circular orifice  $\pi R^2$ . The normalized angular number distribution function for the ideal circular orifice is:

$$I(\theta)/I(0) = \cos \theta / [1 - (R/L)^2 \sin^2 \theta]^{3/2} \quad (7)$$

Table 1 gives theoretical values for the distribution function at several  $R/L$  ratios. Figure 2 shows the spatial distribution of the normalized angular number distribution for the ideal circular orifice for  $R/L$  ratios of 0.50 and 0.20.

The limit of eq. (7) as the ratio  $R/L$  approaches zero is the Cosine Law.

## 2.2 The ideal rectangular orifice

The derivation of the normalized angular number distribution function for the ideal rectangular orifice takes a different form to that of the ideal circular orifice. The derivation is simple and straightforward and does not necessitate the use of transformation formulas between two coordinate systems.

Figures 3(a) and 3(b) show the orifice geometry considered.  $R_1$  and  $R_2$  are expressed by the following equations:

$$\begin{aligned} R_1 &= L \cos \theta / (L/R + \sin \theta) \\ R_2 &= L \cos \theta / (L/R - \sin \theta) \end{aligned} \quad (8)$$

These equations are obtained by making use of the properties of similar triangles.  $W$  is the width of the orifice and  $R$  is half the length of the orifice.



Table 1. Normalized angular number distribution functions for the ideal circular orifice at several R/L ratios.<sup>a</sup>

$\theta$	$I(\theta)/I(0),$ R/L = 0.50	$I(\theta)/I(0),$ R/L = 0.20	$I(\theta)/I(0),$ R/L = 0.10	Cosine Law, R/L = 0.0
0.0	1.00000	1.00000	1.00000	1.00000
5.0	0.99904	0.99665	0.99631	0.99619
10.0	0.99605	0.98659	0.98525	0.98481
15.0	0.99071	0.96982	0.96690	0.96593
20.0	0.98247	0.94633	0.94134	0.93969
25.0	0.97058	0.91611	0.90874	0.90631
30.0	0.95406	0.87918	0.86928	0.86603
35.0	0.93170	0.83559	0.82321	0.81915
40.0	0.90215	0.78544	0.77082	0.76604
45.0	0.86392	0.72886	0.71244	0.70711
50.0	0.81549	0.66610	0.64849	0.64279
55.0	0.75546	0.59747	0.57940	0.57358
60.0	0.68271	0.52337	0.50568	0.50000
65.0	0.59660	0.44437	0.42788	0.42262
70.0	0.49721	0.36098	0.34660	0.34202
75.0	0.38549	0.27401	0.26248	0.25882
80.0	0.26337	0.18427	0.17621	0.17365
85.0	0.13368	0.09262	0.08847	0.08716
90.0	0.00000	0.00000	0.00000	0.00000

<sup>a</sup>Calculations were performed on a TI SR-51A hand calculator.

The effective cross-sectional area is a trapezoid (fig. 3(b)) whose height and average length are given as:  $R_1 + R_2$  and  $(a + b)/2$ , respectively, where  $a$  and  $b$  are the two parallel sides. The geometric expressions for  $a$  and  $b$  can be derived by projecting the similar triangles having the width  $W$  of the orifice, the edge  $a$ , and the edge  $b$  as bases, with a common apex at  $P$  on an imaginary plane perpendicular to the orifice and parallel to  $W$ . By comparing ratios of the projected sides of the similar triangles, the following equations for  $a$  and  $b$  are derived:

$$a = LW/(L + R \sin \theta)$$

$$b = LW/(L - R \sin \theta) \quad . \quad (9)$$

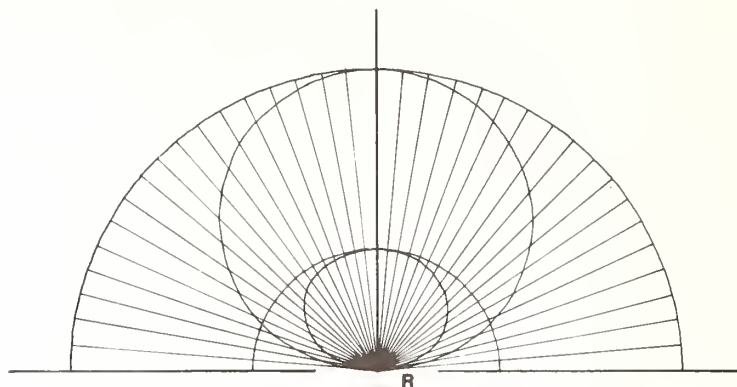


Figure 2. Graphs of normalized angular number distribution functions for the single ideal circular orifice for  $R/L$  ratios of 0.50 and 0.20.

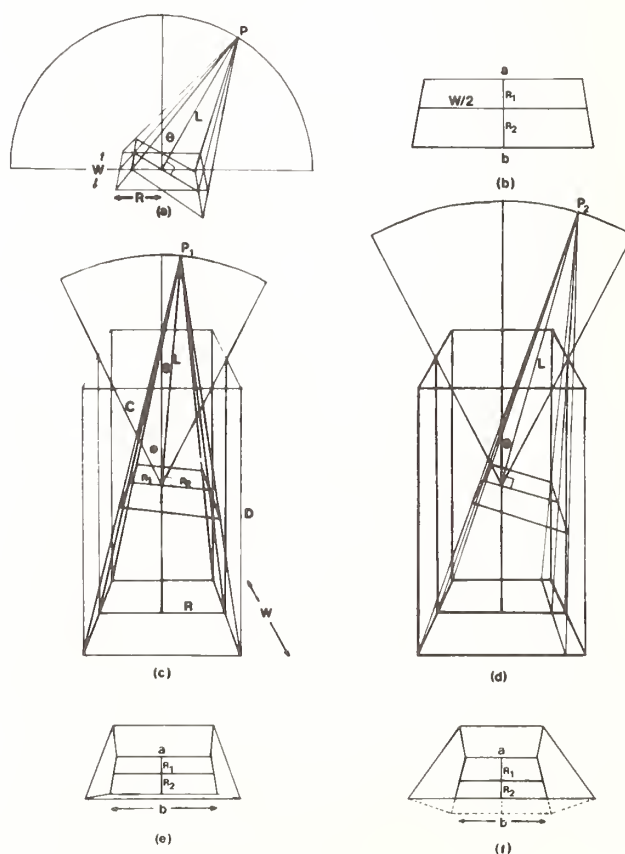


Figure 3. Geometries of the single ideal rectangular orifice and the ideal double-slit rectangular orifice. (See text for details.)

The effective area now takes the following form:

$$A = [(a + b)/2](R_1 + R_2) \quad (10a)$$

$$A = 2RW \cos \theta / [1 - (R/L)^2 \sin^2 \theta]^2. \quad (10b)$$

The normalized intensity for an ideal rectangular orifice is obtained by dividing eq. (8b) by the area of the orifice,  $2RW$ :

$$I(\theta)/I(0) = \cos \theta / [1 - (R/L)^2 \sin^2 \theta]^2. \quad (11)$$

The nondependence of this function on the width  $W$  can be noted.

The limit of this function as  $R/L$  approaches zero yields the Cosine Law. In table 2 are tabulated the values of the normalized angular number distribution function for the ideal rectangular orifice at several  $R/L$  ratios. Figure 4 shows plots of the normalized distribution for  $R/L$  values of 0.20 and 0.50.

Table 2. Normalized angular number distribution functions for the ideal rectangular orifice at several  $R/L$  ratios.

$\theta$	$I(\theta)/I(0),$ $R/L = 0.50$	$I(\theta)/I(0),$ $R/L = 0.20$	$I(\theta)/I(0),$ $R/L = 0.10$
0.0	1.00000	1.00000	1.00000
5.0	0.99999	0.99680	0.99635
10.0	0.99983	0.98719	0.98540
15.0	0.99911	0.97112	0.96722
20.0	0.99716	0.94855	0.94189
25.0	0.99301	0.91940	0.90955
30.0	0.98534	0.88361	0.87037
35.0	0.97255	0.84114	0.82457
40.0	0.95269	0.79201	0.77241
45.0	0.92357	0.73626	0.71423
50.0	0.88282	0.67406	0.65040
55.0	0.82811	0.60565	0.58135
60.0	0.75740	0.53141	0.50759
65.0	0.66926	0.45182	0.42965
70.0	0.56325	0.36752	0.34814
75.0	0.44024	0.27928	0.26372
80.0	0.30259	0.18795	0.17707
85.0	0.15416	0.09451	0.08891
90.0	0.00000	0.00000	0.00000

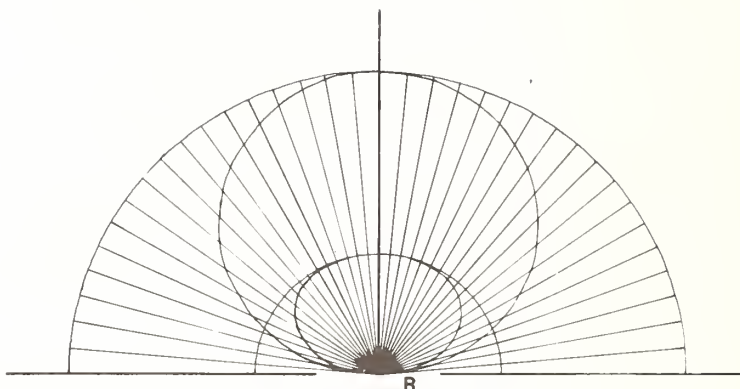


Figure 4. Graphs of normalized angular number distribution functions for the single ideal rectangular orifice for  $R/L$  ratios of 0.50 and 0.20.

### 2.3 The double-slit (no walls) rectangular orifice

This particular orifice is a composite of two identical ideal rectangular orifices placed one above the other. The effusing gas molecules are assumed to pass through both orifices without suffering collisions with the planes containing the ideal rectangular orifices. In the derivation of the normalized angular number distribution functions for this orifice, it is assumed that all the molecular trajectories intersect at the point  $P$  on the low pressure side, above the upper orifice (figs. 3(c) and (d)). Also, the effusing gas molecules are assumed to have velocity vectors whose magnitudes are less than some critical angle  $\theta$  defined below and shown on figures 3(c) and (d). Any gas molecules whose velocity vectors have magnitudes greater than  $\theta$  undergo collisions with the upper orifice plane. These, then, are assumed to suffer specular reflections in the region within the two orifice planes and, thus, not contribute to the total molecular flux across both orifices. The molecular intensity at a point  $P$  in space on the low pressure side of the orifice is then a function of that portion of the total molecular flux which passes through  $P$ .



Figures 3(c), (d), (e), and (f) show the details of the double-slit rectangular orifice.  $R$  is half the length of the orifice;  $W$  is the width;  $D$  is the depth or distance between the two identical ideal rectangular orifices;  $L$  is the ray from the geometric center of the orifice to the point  $P$  on the low pressure side of the orifice;  $C$  is a line segment connecting the geometric center of the orifice with the midpoint of the width for either ideal rectangular orifice. The value of  $C$  is  $1/2 (4R^2 + d^2)^{1/2}$  from geometric considerations. The angle  $\theta$  is the zenith angle;  $\phi$  is the upper limit of  $\theta$  and is geometrically defined as  $\tan^{-1}(2R/D)$ .  $R_1$ ,  $R_2$ ,  $a$ , and  $b$  are the borders of the effective area as seen from the point  $P$  (figs. 3(e) and (f)).

A similar treatment as done on the ideal rectangular orifice is performed, using similar triangles, on the double-slit rectangular orifice to derive the values of  $R_1$ ,  $R_2$ ,  $a$ , and  $b$ . As shown in figures 3(c) and (d), two cases must be considered.

$$\text{Case I. } 0 \leq \theta \leq \sin^{-1}(R/L).$$

This case considers the flux of all molecules which pass through the "lower" higher pressure orifice whose trajectories intersect at the point  $P$  on the lower pressure side of the orifice and are not impeded by any edge of the "upper" lower pressure orifice (fig. 3(e)).

The equations for  $R_1$  and  $R_2$  are given as:

$$\begin{aligned} R_1 &= L \sin(\phi - \theta) / [L/C + \cos(\phi - \theta)] \\ R_2 &= L \sin(\phi + \theta) / [L/C + \cos(\phi + \theta)] \end{aligned} \quad (12)$$

and for  $a$  and  $b$  are:

$$\begin{aligned} a &= 2W(L \cos \theta - R_1 \sin \theta) / (2L \cos \theta + D) \\ b &= 2W(L \cos \theta + R_2 \sin \theta) / (2L \cos \theta + D) . \end{aligned} \quad (13)$$

The effective area is a trapezoid (fig. 3(e)) whose area is given by eq. (10a). Substitution of eqs. (12) and (13) into eq. (10a) gives the unnormalized angular number distribution function for a double-slit rectangular orifice for  $0 \leq \theta \leq \sin^{-1}(R/L)$ :

$$\begin{aligned} A &= \left[ \frac{WL}{2L \cos \theta + D} \right] \left\{ 2 \cos \theta - \left[ \frac{\sin(\phi - \theta)}{L/C + \cos(\phi - \theta)} - \right. \right. \\ &\quad \left. \left. \frac{\sin(\phi + \theta)}{L/C + \cos(\phi + \theta)} \right] \sin \theta \right\} \\ &\quad \left[ \frac{L \sin(\phi - \theta)}{L/C + \cos(\phi - \theta)} + \frac{L \sin(\phi + \theta)}{L/C + \cos(\phi + \theta)} \right] . \end{aligned} \quad (14)$$

The effective area when  $\theta$  is equal to zero is:

$$A(\theta = 0) = 8L^2RW/(2L + D)^2 . \quad (15)$$

Division of eq. (14) by eq. (15) gives the normalized function:

$$\begin{aligned} \frac{I(\theta)}{I(0)} = & \left[ \frac{(2L + D)^2}{8R(2L \cos \theta + D)} \right] \left\{ 2 \cos \theta - \left[ \frac{\sin(\phi - \theta)}{L/C + \cos(\phi - \theta)} - \right. \right. \\ & \left. \left. \frac{\sin(\phi - \theta)}{L/C + \cos(\phi + \theta)} \right] \sin \theta \right\} \\ & \left[ \frac{\sin(\phi - \theta)}{L/C + \cos(\phi - \theta)} + \frac{\sin(\phi + \theta)}{L/C + \cos(\phi + \theta)} \right] . \end{aligned} \quad (16)$$

$$\text{Case II. } \sin^{-1}(R/L) \leq \theta \leq d.$$

The normalized angular number distribution function has a cusp at  $\theta = \sin^{-1}(R/L)$ . Case II considers the geometry of the orifice as shown by figures 3(d) and (f). For this geometry,  $R_1$ ,  $a$ , and  $b$  are identical to the expressions in eqs. (12) and (13). However,  $R_2$  takes the following form:

$$R_2 = L \sin(\phi - \theta) / [L/C - \cos(\phi - \theta)] . \quad (17)$$

Substitution of these values into eq. (10a) and normalizing gives the normalized angular number distribution function for  $\sin^{-1}(R/L) \leq \theta \leq \phi$ :

$$\begin{aligned} \frac{I(\theta)}{I(0)} = & \left[ \frac{(2L + D)^2}{8R(2L \cos \theta + D)} \right] \left\{ 2 \cos \theta - \left[ \frac{\sin(\phi - \theta)}{L/C + \cos(\phi - \theta)} - \right. \right. \\ & \left. \left. \frac{\sin(\phi - \theta)}{L/C - \cos(\phi - \theta)} \right] \sin \theta \right\} \\ & \left[ \frac{\sin(\phi - \theta)}{L/C + \cos(\phi - \theta)} + \frac{\sin(\phi - \theta)}{L/C - \cos(\phi - \theta)} \right] . \end{aligned} \quad (18)$$

Grouping eqs. (16) and (18) into one general equation expressing the normalized angular number distribution function for a double-slit (no walls) rectangular orifice gives:

$$\left[ \frac{I(\theta)}{I(0)} = \frac{(2L + D)^2}{8R(2L \cos \theta + D)} \right] \left\{ 2 \cos \theta - \left[ \frac{\sin(\phi - \theta)}{L/C + \cos(\phi - \theta)} - \frac{\sin(\phi \pm \theta)}{L/C \pm \cos(\phi \pm \theta)} \right] \sin \theta \right\} \left[ \frac{\sin(\phi - \theta)}{L/C + \cos(\phi - \theta)} + \frac{\sin(\phi \pm \theta)}{L/C \pm \cos(\phi \pm \theta)} \right]. \quad (19)$$

for  $0 \leq \theta_+ \leq \sin^{-1}(R/L) \leq \theta_- \leq \phi$ . Again, as in eq. (11), this function is not dependent on the width  $W$ .

The limit of eq. (19) as  $D$  approaches zero gives eq. (11) whose limit, in turn, as  $R/L$  approaches zero, is the Cosine Law.

Table 3 lists the values of the normalized angular number distribution function for a double-slit (no walls) rectangular orifice for particular values of the various parameters  $R$ ,  $L$ , and  $D$ . In figure 5 is drawn the spatial distribution function for these parameters.

#### 2.4 The ideal double-slit (no walls) cylindrical orifice

The total solution of the normalized angular number distribution function for the ideal double-slit cylindrical orifice contains a cusp at a value for the zenith angle  $\theta$  of  $\sin^{-1}(R/L)$ , just like the ideal double-slit rectangular orifice distribution function. As a result, the solution requires the consideration of two different orifice geometries. The first is described in figure 6 for the region  $0 \leq \theta \leq \sin^{-1}(R/L)$ . The second is shown in figure 7 for the region  $\sin^{-1}(R/L) \leq \theta \leq \theta = \tan^{-1}(2R/D)$ . The equations leading to the solutions within these two regions are developed below.

$$\text{Case I. } 0 \leq \theta \leq \sin^{-1}(R/L)$$

This case considers the same flux of ideal gas molecules as considered in Case I for the ideal double-slit rectangular orifice.

Table 3. Normalized angular number distribution function for a double-slit (no walls) rectangular orifice with the following parameters:

$R = 1$ ,  $L = 10$ , and  $D = 2$ .

$\theta$	$I(\theta)/I(0)$
0.0	1.00000
2.0	0.99963
4.0	0.99853
Cusp: $\sin^{-1}(R/L) = 5.7392$	0.99697
6.0	0.99150
8.0	0.94875
10.0	0.90466
12.0	0.85930
14.0	0.81272
16.0	0.76499
18.0	0.71620
20.0	0.66643
22.0	0.61575
24.0	0.56425
26.0	0.51202
28.0	0.45917
30.0	0.40578
32.0	0.35198
34.0	0.29786
36.0	0.24354
38.0	0.18914
40.0	0.13479
42.0	0.08062
44.0	0.02676
$\phi = \tan^{-1}(2R/D) = 45.0$	0.00000



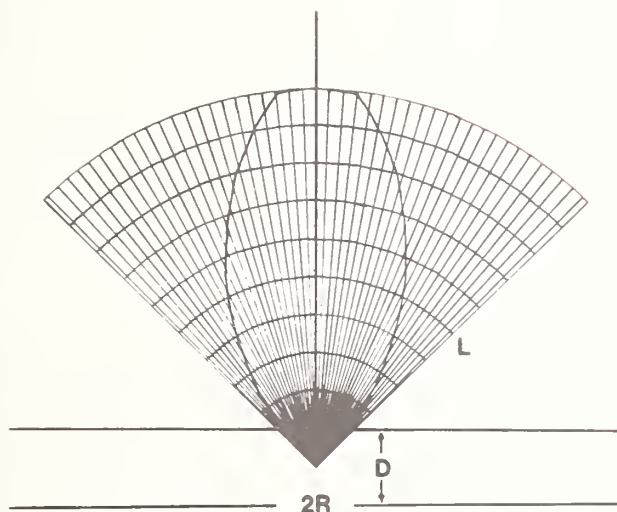


Figure 5. Graph of the normalized angular number distribution for the ideal double-slit rectangular orifice with the orifice parameters of  $R = 1$ ,  $L = 10$ , and  $D = 2$ .

The cylindrical orifice parameters for this region are shown in figure 6.  $D$  is the distance between the two ideal circular orifices forming the ideal cylindrical orifice.  $R$  is the radius of the cylinder.  $R_0$  is the radius of the circle formed by the intersection of a plane and the oblique circular cone having its base common with that of the cylinder and as its apex the point  $P$  on the low pressure side of the orifice. The intersecting plane contains the geometric center of the orifice  $O$  and is perpendicular to the axis of the cylinder. The constant  $k$  is the distance from the geometric center  $O$  to the center of this circle. The parameters  $\bar{x}'$  and  $\bar{y}'$  are the semimajor and semiminor axes, respectively, of the effective area. It follows from the geometry of intersecting planes and oblique circular cones that the effective area is an ellipse [24,25].

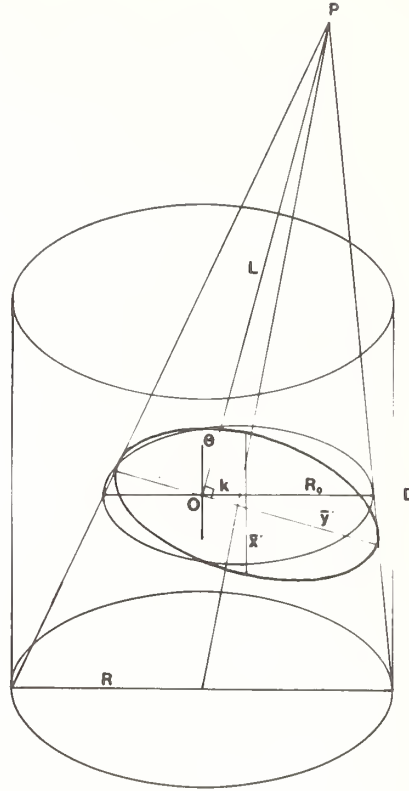


Figure 6. Geometry of the ideal double-slit cylindrical orifice for the region  $0 \leq \theta \leq \sin^{-1}(R/L)$ . (See text for details.)

Employing the properties of similar triangles, the following value of the constant  $k$  is obtained:

$$k = \frac{LD \sin \theta}{2L \cos \theta + D} \quad (20)$$

Likewise, a similar derivation can be used for the determination of the value for the radius  $R_o$ :

$$R_o = \frac{2RL \cos \theta}{2L \cos \theta + D} \quad (21)$$

In the derivation of the values for the semimajor and semiminor axes  $\bar{x}'$  and  $\bar{y}'$ , a similar treatment is performed as in the case of the ideal circular orifice using identical

transformation projection formulas (eq. (1)). However, the center of the circle does not coincide with the geometric center of the orifice 0. The equation for the ellipse can be obtained by substituting the same transformation formulas into the equation for the circle,

$$x^2 + (y - k)^2 = R_0^2 ,$$

and rearranging terms:

$$\begin{aligned} (L^2 \cos^2 \theta) x'^2 + [L^2 - 2Lk \sin \theta + (k^2 - R_0^2) \sin^2 \theta] y'^2 \\ - [2L^2 k \cos \theta - 2L(k^2 - R_0^2) \sin \theta \cos \theta] y' \\ + (k^2 - R_0^2) L^2 \cos^2 \theta = 0 . \end{aligned} \quad (22)$$

The effective area of the ellipse is obtained in an analogous fashion as is derived for the ideal circular orifice. The length of the semiminor axis  $\bar{y}'$  is derived by setting  $x'$  equal to zero and solving for the roots of the resulting quadratic equation. The length of the semiminor axis  $\bar{y}'$  is given by the expression:

$$\bar{y}' = \frac{R_0 L^2 \cos \theta}{L^2 - 2LK \sin \theta + (k^2 + R_0^2) \sin^2 \theta} . \quad (23)$$

The derivation of the expression for the semimajor axis  $\bar{x}'$  requires similar steps as used in the ideal circular orifice, also. The equation for  $\bar{x}'$  is then:

$$\bar{x}' = \frac{R_0 L}{[L^2 - 2LK \sin \theta + (k^2 - R_0^2) \sin^2 \theta]^{1/2}} . \quad (24)$$

Substitution of these values into the equation for the area of an ellipse,  $\pi \bar{x}' \bar{y}'$ , gives the effective area:

$$A = \frac{\pi R_0^2 L^3 \cos \theta}{[L^2 - 2LK \sin \theta + (k^2 - R_0^2) \sin^2 \theta]^{3/2}} . \quad (25)$$

The normalized angular number distribution function is obtained by dividing this expression by the effective area when the zenith angle  $\theta$  is equal to zero. This area can either be obtained from geometric considerations using the properties of similar triangles or by taking the limit of eq. (25) as  $\theta$  approaches zero. Both derivations give the same result. The effective area when the zenith angle  $\theta$  is equal to zero is:

$$A(r = 0) = \frac{4\pi R^2 L^2}{(2L + D)^2} \quad (26)$$

The normalized angular number distribution function for the ideal double-slit cylindrical orifice in the region  $0 \leq \theta \leq \sin^{-1}(R/L)$  is then defined as:

$$\frac{I(\theta)}{I(0)} = \left( \frac{2L + D}{2L \cos \theta + D} \right)^2 \times \frac{L^3 \cos^3 \theta}{[L^2 - 2LK \sin \theta + (k^2 - R_0^2) \sin^2 \theta]^{3/2}} \quad (27)$$

Case II.  $\sin^{-1}(R/L) \leq \theta \leq \theta$

In this region, the normalized angular number distribution function for the ideal double-slit cylindrical orifice takes a different form. The function rapidly approaches zero as the zenith angle  $\theta$  approaches the limiting value  $\theta$ .  $\theta$  again is equal to  $\tan^{-1}(2R/D)$ . Figure 7 shows the various orifice parameters of the cylindrical orifice employed in the determination of the various equations leading to the derivation of the distribution function. The parameters are defined below.

$R_1$  = the radius of the smaller circle formed by the intersection of a plane parallel to the base of the cylinder and containing the geometric center 0 with the oblique circular cone having the point P as its apex and the lower orifice as its base.

$R_2$  = the radius of the central projection (larger circle) of the upper orifice from the point P to the horizontal plane containing the geometric center 0.

$k_1$  = the distance from the geometric center 0 to the center of the smaller circle.

$k_2$  = the distance from the geometric center 0 to the center of the larger circle.

$d$  = the distance between the centers of the two ellipses (smaller and larger) on the visual plane and is equal to  $y_1' - y_2'$ .

$y_1'$  = the distance from the geometric center 0 to the center of the smaller ellipse.

$y_2'$  = the distance from the geometric center 0 to the center of the larger ellipse.  
 $\bar{x}_1'$  = the semimajor axis of the smaller ellipse.  
 $\bar{y}_1'$  = the semiminor axis of the smaller ellipse.  
 $\bar{x}_2'$  = the semimajor axis of the larger ellipse.  
 $\bar{y}_2'$  = the semiminor axis of the larger ellipse.  
 $y_0$  = (not shown on fig. 7) the distance from the center of the small ellipse to some point along a line connecting the two centers of the ellipses on the visual plane. This point is the midpoint of a line segment connecting the two points of intersection of the two ellipses.

The dotted line is the intersection of the visual plane with the horizontal plane and contains the geometric center 0.

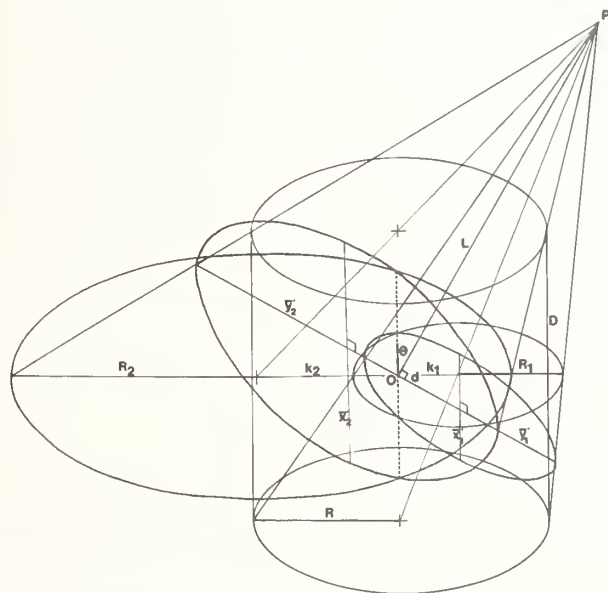


Figure 7. Geometry of the ideal double-slit cylindrical orifice for the region  $\sin^{-1}(R/L) \leq \theta \leq \emptyset$ . (See text for details.)

The equations for  $R_1$ ,  $k_1$ ,  $\bar{x}_1'$ , and  $\bar{y}_1'$  are identical in form as the expressions for  $R_0$ ,  $k$ ,  $\bar{x}'$ , and  $\bar{y}'$ , respectively, as in Case I.



By expressing eq. (22) in terms of  $x'$  and taking the first derivative of  $x'$  with respect to  $y'$  and setting it equal to zero, a value of  $y'$  can be obtained which gives the maximum value of  $x'$ . This value is the semimajor axis  $\bar{x}'_1$ . The value of  $y'$  is  $y'_1$  and is given as:

$$y'_1 = \frac{L^2 k_1 \cos \theta - L(k_1^2 - R_1^2) \sin \theta \cos \theta}{L^2 - 2Lk_1 \sin \theta + (k_1^2 - R_1^2) \sin^2 \theta} \quad (28)$$

where  $k_1$  and  $R_1$  were substituted for  $k$  and  $R_0$  in eq. (22). Now  $\bar{x}'_1$  and  $\bar{y}'_1$  take the following forms:

$$\bar{x}'_1 = \frac{R_1 L}{[L^2 - 2Lk_1 \sin \theta + (k_1^2 - R_1^2) \sin^2 \theta]^{1/2}} \quad (29)$$

$$\bar{y}'_1 = \frac{R_1 L^2 \cos \theta}{L^2 - 2Lk_1 \sin \theta + (k_1^2 - R_1^2) \sin^2 \theta} \quad (30)$$

For the larger circle, the equations derived for  $R_2$  and  $k_2$ , using similar triangles are the following:

$$R_2 = \frac{2RL \cos \theta}{2L \cos \theta - D} \quad (31)$$

$$k_2 = \frac{-LD \sin \theta}{2L \cos \theta - D} \quad (32)$$

The equation for the large ellipse on the visual plane is identical to that of the smaller ellipse (eq. (22)), but has  $k_2$  and  $R_2$  substituted in place of  $k$  or  $k_1$  and  $R_0$  or  $R_1$ , respectively.

A similar manipulation of the expression for  $x'$  as performed on the smaller ellipse yields an equation for  $y'_2$ :

$$y'_2 = \frac{L^2 k_2 \cos \theta - L(k_2^2 - R_2^2) \sin \theta \cos \theta}{L^2 - 2Lk_2 \sin \theta + (k_2^2 - R_2^2) \sin^2 \theta} \quad (33)$$

The value of  $y'_2$  is negative. Subtracting eq. (33) from eq. (28) yields  $d$ :

$$d = y_1' - y_2' . \quad (34)$$

The equation for the smaller ellipse can now be expressed as:

$$\frac{x^2}{\bar{x}_1'^2} + \frac{y^2}{\bar{y}_1'^2} = 1 \quad (35)$$

and for the large ellipse:

$$\frac{x^2}{\bar{x}_2'^2} + \frac{(y + d)^2}{\bar{y}_2'^2} = 1 . \quad (36)$$

The evaluation of  $y_0$  requires that eqs. (35) and (36) be solved for  $x$  and then set equal to each other. The solution of the resulting quadratic equation yields an expression for  $y_0$  when the positive root is kept.

The effective area in the region  $\sin^{-1}(R/L) \leq \theta \leq \emptyset$  is equal to the area of overlap of the smaller ellipse with the larger ellipse on the visual plane. This area is equal to the sum of two areas,  $A_1$  and  $A_2$ .  $A_1$  is a portion of the smaller ellipse in the overlap region that is bounded by the line segment connecting the two points of intersection of the two ellipses.  $A_2$  is a portion of the larger ellipse in the overlap region that is bounded by the same line segment.

$A_1$  is equal to the solution of the following integral:

$$A_1 = 2\bar{x}_1' \int_{-\bar{y}_1'}^{y_0} \left[ 1 - \left( \frac{y}{\bar{y}_1'} \right)^2 \right]^{1/2} dy \quad (37)$$

and is given as:

$$A_1 = \bar{x}_1' \bar{y}_1' \left\{ \frac{\pi}{2} + \sin^{-1} \left( \frac{y_0}{\bar{y}_1'} \right) + \left( \frac{y_0}{\bar{y}_1'} \right) \left[ 1 - \left( \frac{y_0}{\bar{y}_1'} \right)^2 \right]^{1/2} \right\} . \quad (38)$$

$A_2$  is equal to the integral

$$A_2 = 2\bar{x}_2' \int_{y_0 + d}^{\bar{y}_2'} \left[ 1 - \left( \frac{y}{\bar{y}_2'} \right)^2 \right]^{1/2} dy \quad (39)$$

whose solution is the following:

$$A_2 = \bar{x}_2' \bar{y}_2' \left\{ \frac{\pi}{2} - \sin^{-1} \left( \frac{y_0 + d}{\bar{y}_2'} \right) - \left( \frac{y_0 + d}{\bar{y}_2'} \right) \left[ 1 - \left( \frac{y_0 + d}{\bar{y}_2'} \right)^2 \right]^{1/2} \right\} \quad (40)$$

The normalized angular number distribution function for the ideal double-slit cylindrical orifice in the region  $\sin^{-1} (R/L) \leq \theta \leq \theta$  is defined as:

$$\frac{I(\theta)}{I(0)} = \frac{(2L + D)^2}{4\pi R^2 L^2} (A_1 + A_2) . \quad (41)$$

Table 4 lists the values of the normalized angular number distribution function for the ideal double-slit cylindrical orifice for a specific orifice geometry.

Consideration of the geometries of the two circles on the horizontal plane containing the geometric center 0 gives rise to an equation for the area of overlap A between these two. In the calculation of this area A, a transformation is performed from the visual plane to the horizontal plane. Letting  $y'$  be equal to the distance from the geometric center 0 to the midpoint of the line segment connecting the two points of intersection of the two ellipses, we can find a value of  $y$  which is equal to the distance from the geometric center to the midpoint of a line segment connecting the two points of intersection of the two circles. This value of  $y$  is obtained using the transformation projection equation for  $y$  (eq. (1)).

The parameter  $y'$  is defined as:

$$y' = y_1' + y_0 \quad (42)$$

and gives rise to the expression for  $y$ :

$$y = \frac{L(y_1' + y_0)}{(y_1' + y_0) \sin \theta + L \cos \theta} \quad (43)$$

Table 4. Normalized angular number distribution function for an ideal double-slit cylindrical orifice with the following orifice geometry parameters:  $R = 1$ ,  $L = 10$ , and  $D = 2$ .

$\theta$	$I(\theta)/I(0)^a$
0.0	1.00000
1.0	0.99999
2.0	0.99963
3.0	0.99916
4.0	0.99852
5.0	0.99767
Cusp: $\sin^{-1}(R/L) = 5.7392$	0.99696
6.0	0.99521
8.0	0.96253
10.0	0.91518
12.0	0.86292
14.0	0.80733
16.0	0.74971
18.0	0.69063
20.0	0.63064
22.0	0.57015
24.0	0.50953
26.0	0.44915
28.0	0.38936
30.0	0.33059
32.0	0.27329
34.0	0.21800
36.0	0.16540
38.0	0.11638
40.0	0.07210
42.0	0.03442
44.0	0.00681
$\emptyset = \tan^{-1}(2R/D) = 45.0$	0.00000

<sup>a</sup> The Clausing factor for this orifice is 0.1056 (eq. 49)).

Defining two new angles  $\alpha$  and  $\beta$  to be:

$$\alpha = \cos^{-1} \left( \frac{k_1 - y}{R_1} \right)$$

$$\beta = \cos^{-1} \left( \frac{-k_2 + y}{R_2} \right) \quad (44)$$

then the area of overlap  $A$  between the two circles is equal to:

$$A = R_1^2 (\alpha - \sin \alpha \cos \alpha) + R_2^2 (\beta - \sin \beta \cos \beta) . \quad (45)$$

#### 2.4.1 The Clausing factor

The transmission probability can easily be derived from the geometry of the double-slit cylindrical orifice. If a hemisphere is placed such that it circumscribes the upper orifice and has its center common with the center of the lower orifice, as shown in figure 8, then the Clausing factor is equal to the area of the hemisphere bounded by the upper orifice divided by the area of the hemisphere. The area of the hemisphere bounded by the upper orifice is:

$$H_1 = \int_0^{2\pi \tan^{-1}(R/D)} \int_0^{\alpha} (R^2 + D^2) \sin \alpha \, d\alpha \, d\beta \quad (46)$$

where  $\alpha$  is a zenith angle formed by the radius of the hemisphere with the normal through the orifice and  $\beta$  is the azimuthal angle. The area of the hemisphere is:

$$H_2 = 2\pi(R^2 + D^2) . \quad (47)$$

The Clausing factor  $W$  is then equal to  $H_1$  divided by  $H_2$ :

$$W = \frac{1}{2\pi(R^2 + D^2)} \int_0^{2\pi \tan^{-1}(R/D)} \int_0^{\alpha} (R^2 + D^2) \sin \alpha \, d\alpha \, d\beta . \quad (48)$$

Integration yields:

$$W = 1 - \left[ \frac{1}{(R/D)^2 + 1} \right]^{1/2} . \quad (49)$$



For large values of  $D$  compared to  $R$ ,  $W$  is asymptotic to zero and as  $D$  approaches zero,  $W$  converges on one. This is the case for the ideal circular orifice, whose Clausing factor is equal to one.

Equation (49) represents a lower limit to the actual Clausing factors for channeled orifices, since these also represent molecular contributions at a point  $P$  in space from molecules colliding with the walls of the orifice.

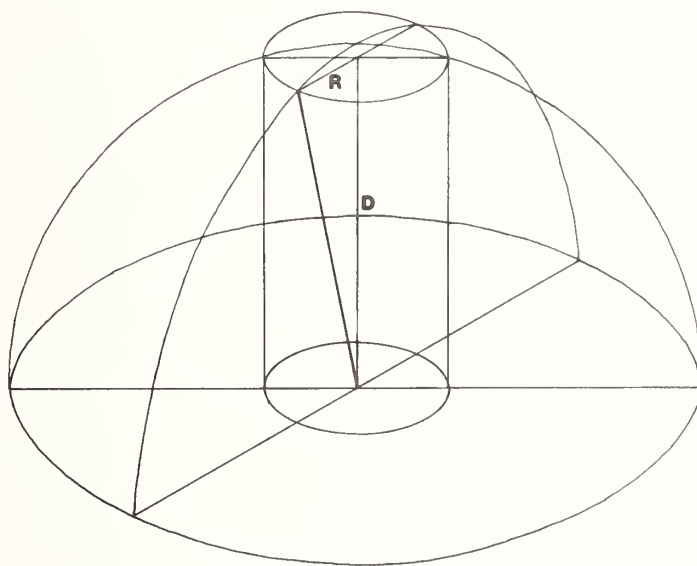


Figure 8. Geometry of the ideal double-slit cylindrical orifice used to find the transmission probability,  $W$ .

### 3. Conclusion

The general equations of the normalized angular number distribution functions for the various geometries described represent a closed set of functions. If the limit as the distance  $D$  between the ideal orifices forming the double-slit orifice geometries approaches,

zero is taken of the double-slit angular functions, the corresponding single ideal orifice distribution functions are obtained. The limit of these as the ratio  $R/L$  approaches zero yields the Cosine Law. This is a necessary result, since the distribution from a point source is the Cosine Law.

The theoretical results in this paper, thus, do not assume the Cosine distribution as was assumed originally by Clausen [26]. On the contrary, the Cosine Law is predicted from the limits of these theoretical distribution functions. The generality of these distributions is seen from their ability to predict results in the vicinity of the orifice, where orifice geometry is a major factor.

In the consideration of channeled orifices, Freeman and Edwards [27] have determined the area of overlap  $^*B$  of a horizontal cross-section with the projection at an angle  $\theta$  of the upper orifice unto the plane containing the horizontal cross-section. Assuming this horizontal cross-section to be the bottom orifice, the following result is obtained for a cylindrical orifice:

$$^*B = \pi R^2 - 2R^2 \sin^{-1} \left( \frac{D \tan \theta}{2R} \right) - D \tan \theta \ R^2 - \left[ \frac{D^2 \tan^2 \theta}{4} \right]^{1/2}. \quad (50)$$

Comparing this equation with eq. (45), it can be shown that the limit of  $A$  as the ratio  $R/L$  approaches zero is equal to eq. (50):

$$\lim_{R/L \rightarrow 0} A = ^*B \quad (51)$$

The existence of this limit proves that the area of overlap  $^*B$  is not equal to the area of overlap  $A$ , which is obtained by a transformation from the "effective area."

A key step in the derivations is the choosing of the geometric center of the orifice as the origin of the angular number distribution functions. The important assumption is that the intensity at a point in space is directly proportional to the "effective cross-sectional area."

---

I am highly appreciative to Professor Karl A. Gingerich for having given me the necessary encouragement and much needed incentive to pursue this subject during my graduate studies at Texas A & M University. Also, to Dr. Gollakota R. Somayajulu for his helpful advice. And, finally, to my wife, Lupita, for her moral support.

## References

- [1] Knudsen, M., Ann. Phys. 29, 179 (1909).
- [2] Kennard, E. H., Kinetic Theory of Gases (McGraw-Hill Book Co., New York, N.Y., 1938).
- [3] Carlson, K. Douglas, in Characterization of High Temperature Vapors, J. L. Margrave, ed. (Wiley-Interscience Publishers, New York, N.Y., 1967), pp. 115-129.
- [4] Grimley, R. T., in Characterization of High Temperature Vapors, pp. 195-243.
- [5] Iczkowski, R. P., Margrave, J. L., and Robinson, S. M., J. Phys. Chem. 67, 229 (1963).
- [6] Clausius, P., Physica 9, 65 (1929).
- [7] DeMarcus, W. C., Report K-1302, Parts 1-6, Oak Ridge Gaseous Diffusion Plant, Oak Ridge, Tenn. (1957).
- [8] Freeman, R. D. and Edwards, J. G., in Condensation and Evaporation of Solids, E. Rutner, P. Goldfinger, and J. P. Hirth, eds., Proceedings of an International Symposium, Dayton, Ohio, September 1962 (Gordon and Breach, New York, 1964).
- [9] Clausius, P. Ann. Phys. 12, 961 (1932).
- [10] Winterbottom, W. L., J. Chem. Phys. 47, 3546 (1967).
- [11] Winterbottom, W. L., J. Chem. Phys. 49, 106 (1968).
- [12] Grimley, R. T., Muenow, D. W., and LaRue, J. L., J. Chem. Phys. 56, 490 (1972).
- [13] Liu, M. B. and Wahlbeck, P. G., J. Chem. Phys. 59, 907 (1973).
- [14] Grimley, R. T., Wagner, L. C., and Castle, P. M., J. Phys. Chem. 79, 302 (1975).
- [15] Howard, W. M., Phys. of Fluids, 4, 521 (1961).
- [16] Prandtl, L., Essentials of Fluid Dynamics (Blackie, Glasgow, 1952).
- [17] Jenkins, F. A. and White, J. E., Fundamentals of Optics, 2nd edition (McGraw-Hill Book Co., Inc., New York, N.Y., 1950).
- [18] Beckmann, P. and Spizzichino, A., The Scattering of Electromagnetic Waves from Rough Surfaces (The MacMillan Book Company, New York, N.Y., 1963).
- [19] Moon, P., The Scientific Basis of Illuminating Engineering, 1st Edition (McGraw-Hill Book Co., Inc., New York, N.Y., 1936).
- [20] Cotton, H., Principles of Illumination (John Wiley and Sons, Inc., New York, N.Y., 1960).
- [21] Boast, W. B., Illumination Engineering, 2nd Edition (McGraw-Hill Book Co., Inc., New York, N.Y., 1953).
- [22] Higbie, H. H., Lighting Calculations (John Wiley and Sons, Inc., New York, N.Y., 1934).
- [23] Higbie, H. H., Trans. Illum. Eng. Soc. (N.Y.) 36, 79 (1941).
- [24] Stower, D. W., The Conics: The Geometric Approach (Houghton Mifflin Co., Boston, 1971).
- [25] Altshiller-Court, N., Modern Pure Solid Geometry, 2nd Edition (Chelsea Publishing Co., Bronx, N.Y., 1964).
- [26] Clausius, P., Z. Phys. 66, 471 (1930).
- [27] Freeman, R. D. and Edwards, J. G., in Characterization of High Temperature Vapors, Appendix C, pp. 508-529.



## AUTOMATIC DATA ACQUISITION BY THE TORSION-EFFUSION METHOD

Jimmie G. Edwards  
Department of Chemistry  
The University of Toledo  
Toledo, OH 43606

Data acquisition from torsion-effusion vapor pressure measurements has been automated by a video method and by a computer method. The torsion-effusion pendulum is suspended from a vacuum semimicrobalance for simultaneous Knudsen-effusion measurements. The pendulum is operated in the dynamic (or integral) mode; amplitudes are in the range 45-60° and periods are in the range 35-120 s. The video method involves recording pendulum motion on video tape for later observation with a video monitor. The computer method involves reflecting low-power laser beams from mirrors on the pendulum and detection of the reflected beams by photodetectors interfaced to a laboratory computer. In both methods, the times at which the pendulum reaches given positions are recorded and used to solve the equation of motion of the pendulum to obtain the vapor pressure. Theory, mathematical analyses, apparatus construction, and advantages of the methods are described and discussed. Ability to calculate pendulum rest points within  $\pm 0.01^\circ$  is reported. Vapor pressure measurements of MnS(s) without automation, in the ZnS(s)-Ga<sub>2</sub>S<sub>3</sub>(s) system by the video method, and of TiS(s) by the computer method are discussed and compared with simultaneous measurements by the Knudsen-effusion method.

### 1. Introduction

Freeman has given an excellent description and discussion of the torsion-effusion method for measuring vapor pressures [1]<sup>1</sup>. The method is conveniently used simultaneously with the Knudsen-effusion method when the torsion-effusion pendulum is suspended from one arm of a vacuum balance of appropriate capacity and sensitivity.

---

<sup>1</sup>Figures in brackets indicate the literature references at the end of this paper.



The torsion-effusion measurement gives the rate of momentum loss from the effusion cell and the Knudsen-effusion measurement gives the simultaneous rate of mass loss from the cell. When the nature of the effusing vapor is well known, either measurement yields the vapor pressure. From the torsion-effusion measurement

$$P = 2Q_e / \sum_{\ell=1}^L d_{\ell} f_{\ell} A_{\ell} \quad (1)$$

in which  $P$  is the vapor pressure,  $Q_e$  is the torque exerted on the torsion pendulum by effusing vapor,  $L$  is the number of orifices in the effusion cell, and  $d_{\ell}$  is the moment arm,  $f_{\ell}$  is the recoil force correction factor, and  $A_{\ell}$  is the area of orifice number  $\ell$ . From the Knudsen effusion measurement

$$P = (dg/dt)(2\pi RT/M)^{1/2} - \sum_{\ell=1}^L (W_{\ell} A_{\ell}) \quad (2)$$

in which  $dg/dt$  is the rate of mass loss from the effusion cell,  $M$  is the average molecular weight of the vapor,  $W_{\ell}$  is the transmission probability of orifice number  $\ell$ , and other symbols have their usual or already-defined meanings.

Three advantageous applications of the combined simultaneous Knudsen- and torsion-effusion methods are apparent. In the simple application with known  $M$ , one type of measurement of the vapor pressure serves to confirm the other. When the nature of the effusing vapor is not fully known, combination of mass-loss and momentum-loss data can yield the average molecular weight of the vapor [1-3]; if the vapor contains no more than two components, and the chemical nature of each component is known, the vapor composition can be calculated from the average molecular weight [4]. In differential pressure measurements with two opposed or antiparallel orifices [1], and samples of differing compositions; e.g., alloys, in the two chambers, combination of the two types of effusion data yields not only the differential pressure, but the vapor pressures in the two chambers.

The commercial availability of automatic vacuum semimicro- and micro-balances with automatic digital and stripchart outputs and capacities of 100 g makes a simultaneous application of the Knudsen- and torsion-effusion methods particularly convenient. A limitation, however, has been that no convenient and accurate method for automatically recording data from high-temperature torsion-effusion measurements has been readily available. The purpose of this paper is to describe methods used in this laboratory for automatically recording the position of a torsion-effusion pendulum and for calculating vapor pressures from the recordings.

## 2. Automation

A high-temperature vaporization experiment is complicated and requires the careful attention of the experimenter. In a simultaneous Knudsen- and torsion-effusion experiment, the motion of the torsion pendulum, the rate of mass loss, the temperature, the condition of the vacuum system, resetting the temperature and equilibration of the sample for each new experiment, and a number of details can occupy the experimenter. Automation of any of these operations can speed the experiments, make them more accurate, and make the results more dependable by removing stress from the experimenter.

Automation of the torsion-effusion method of vapor pressure measurement in its conventional form presents a difficult problem. With the apparatus configuration in most torsion-effusion experiments, in order to achieve a sensitivity of  $10^{-7}$ - $10^{-6}$  atm in vapor pressure, pendulum position must be measured within  $\pm 0.1^\circ$ . The usual means of achieving such accuracy has been some variation of the lamp and scale, or reflected light beam method. Another successful method has been to observe through a telescope a circular disk graduated in degrees and incorporated coaxially as part of the pendulum. The graduations on a disk with 5 cm diameter can easily be interpreted to within  $\pm 0.1^\circ$  with a small telescope.

Torsion-effusion measurements usually are made with the pendulum kept static by some damping device, often a magnetic one. Automation of data acquisition from a static pendulum requires continuous automatic measurement of pendulum position or measurement of a compensating torque required to maintain a null position. Several methods of continuous automatic measurement of a torsion pendulum's position have been reported [5-7], but none gave the angular precision needed for torsion-effusion measurements. A low-temperature, static, torsion-effusion apparatus was automated by the torque-compensation method [8,9].

Because of the difficulty of automating a static pendulum, we adopted, instead, the dynamic mode of pendulum operation, in which the pendulum oscillates undamped through any amplitude which does not damage the torsion fiber, and the times are measured at which the pendulum reaches certain discrete, accurately-known positions. The observed time-vs-position data then are used to solve the pendulum's equation of motion to deduce the torque exerted by effusing vapor, and thence the vapor pressure within the effusion cell.

## 3. The Dynamic Torsion-Effusion Method

The design and configuration of a torsion-effusion pendulum for dynamic measurements [2] is effectively the same as that for static measurements [1], except that the pendulum's motion is not damped and a means is provided for observing the motion of the pendulum. In our work, typical pendulum motion has been through amplitudes of  $45$ - $60^\circ$ . In one type of application, a disk graduated in degrees was part of the pendulum and its position was observed through a glass window in the vacuum wall. In another, a light-beam reflection method was used; a portion of the vacuum wall surrounding the pendulum was a section of

precision-bore glass tubing, and light beams were projected onto and reflected from mirrors on the pendulum to measure its position by a procedure described subsequently.

The equation of motion of an ideal torsion pendulum used for torsion-effusion vapor pressure measurements is given by Newton's second law of angular motion

$$I\ddot{\theta} = -k(\theta - \theta_r) + Q_e \quad (3)$$

in which  $I$  is the moment of inertia of the pendulum,  $\theta$  is the angular position and  $\ddot{\theta}$  is the angular acceleration of the pendulum at time  $t$ ,  $k$  is the torsion constant of the pendulum fiber,  $\theta_r$  is the position of the pendulum at rest with no vapor effusing, and  $Q_e$  is the torque exerted on the pendulum by vapor flowing from the effusion cell. The properties  $I$ ,  $k$ , and  $\theta_r$  are measured independently before vaporization experiments. The motion of an ideal torsion-effusion pendulum is influenced only by the energy stored in the pendulum, the moment of inertia of the pendulum, the torsion constant of the fiber, and the rate of momentum loss due to effusion of vapor.

Equation (3) is a second-order differential equation, and it contains the unknown  $Q_e$ , thus its solution requires at least three observations of the motion of the pendulum, two to provide boundary conditions and one to provide the value of  $Q_e$ . When a torsion-effusion pendulum is operated statically, the following simple conditions apply:

$$\ddot{\theta} = 0 \quad , \quad (4)$$

$$\dot{\theta} = 0 \quad , \quad (5)$$

and

$$(\theta - \theta_r) = Q_e/k \quad . \quad (6)$$

In eq. (5),  $\dot{\theta}$  is the angular velocity of the pendulum at time  $t$ . Thus, observation of the static position  $\theta$  yields  $Q_e$ .

When a torsion-effusion pendulum is operated dynamically, the times at which the pendulum is at certain discrete positions are observed. Since the acceleration is not observed, eq. (3) must be integrated to express  $\theta$  as a function of  $t$ ;

$$\theta - \theta_r - Q_e/k = C \sin \Omega t + D \cos \Omega t \quad , \quad (7)$$

in which  $C$  and  $D$  are integration constants and  $\Omega$  is  $(k/I)^{1/2}$  or  $2\pi/\tau$ , where  $\tau$  is the period of the pendulum. Observation of  $t$  at three values of  $\theta$  is sufficient to calculate  $C$ ,  $D$ , and the desired torque due to effusing vapor,  $Q_e$ , from eq. (7). If  $t$  is observed at more than three values of  $\theta$ , a statistical overdetermination of  $Q_e$  can be obtained by application of the linear least-squares method to eq. (7). The result is obtained by simultaneous solution of three equations in  $C$ ,  $D$ , and  $Q_e$ :

$$C \sum_{j=1}^J \sin^2 \Omega t_j + D \sum_{j=1}^J \sin \Omega t_j \cos \Omega t_j + (Q_e/k) \sum_{j=1}^J \sin \Omega t_j = \quad (8)$$

$$\sum_{j=1}^J (\theta_j - \theta_r) \sin \Omega t_j$$

$$C \sum_{j=1}^J \sin \Omega t_j \cos \Omega t_j + D \sum_{j=1}^J \cos^2 \Omega t_j + (Q_e/k) \sum_{j=1}^J \cos \Omega t_j = \quad (9)$$

$$\sum_{j=1}^J (\theta_j - \theta_r) \cos \Omega t_j$$

$$C \sum_{j=1}^J \sin \Omega t_j + D \sum_{j=1}^J \cos \Omega t_j + JQ_e/k = \sum_{j=1}^J (\theta_j - \theta_r) \quad (10)$$

in which J is the number of t vs  $\theta$  observations.

If extraneous torque [1,2,10] influences the motion of the pendulum, eq. (3) must be modified to account for the additional torque;

$$I\theta'' = -k(\theta - \theta_r) + Q_e + Q(\theta) \quad , \quad (11)$$

in which  $Q(\theta)$  represents the extraneous torque as a function of pendulum position. Solution of eq. (11) requires independent knowledge of the function  $Q(\theta)$ . In our work at temperatures above 1000 °C with torsion-effusion cells made of molybdenum or tungsten, we have found significant extraneous torque on the torsion pendulum due to interaction between 60 hz current in the resistance furnace and 60 hz induced current in the effusion cell. Blank experiments with empty cells showed that the inductive torque could be accurately represented by the equation

$$Q(\theta) = p + q \sin 2(\theta - \theta_0) \quad , \quad (12)$$

in which p, q, and  $\theta_0$  are parameters adjusted for best fit. The parameters p and q are strong functions of current in the resistance furnace, but  $\theta_0$  is only slightly dependent on that variable.

When eqs. (11) and (12) are combined, the resulting equation can be written as

$$\theta'' = a + b \theta + c \sin \theta , \quad (13)$$

in which

$$\theta = 2 (\vartheta - \vartheta_0) , \quad (14)$$

$$\theta'' = 2\vartheta'' , \quad (15)$$

$$a = (2k/I)(\vartheta_r - \vartheta_0) + 2 p/I + 2Q_e/I , \quad (16)$$

$$b = - k/I , \quad (17)$$

and

$$c = 2 q/I . \quad (18)$$

The coefficients  $b$  and  $c$  are known at the start of a torsion-effusion experiment, but  $a$  contains  $Q_e$  and thus is unknown.

Equation (13) must be solved numerically. We represent the position-dependent terms by a trigonometric series;

$$b\theta + c \sin \theta = \sum_{n=0}^N (\alpha_n \cos n\lambda t + \beta_n \sin n\lambda t) , \quad (19)$$

which yields, when combined with eq. (13),

$$\theta'' = a + \sum_{n=0}^N (\alpha_n \cos n\lambda t + \beta_n \sin n\lambda t) , \quad (20)$$

in which  $n$  is an index,  $N$  is an integer sufficiently large to give an accurate representation,  $\lambda$  is  $2\pi/\tau$ , and  $\alpha_n$  and  $\beta_n$  are constant coefficients. It is readily shown that  $\alpha_0 = -a$ . With this result, double integration of eq. (20) from  $t = 0$  to an arbitrary time  $t$  yields

$$\theta(t) - \theta(0) = \sum_{n=1}^N (n\lambda)^{-2} \left[ \alpha_n (\cos n\lambda t - 1) + \beta_n \sin n\lambda t \right] . \quad (21)$$



Equation (19) becomes

$$a + b\theta(t) + c\sin \theta(t) = \sum_{n=1}^N (\alpha_n \cos n\lambda t + \beta_n \sin n\lambda t) . \quad (22)$$

In principle the parameters  $\alpha_n$  and  $\beta_n$ ,  $n = 1, N$ , can be expressed in terms of two integration constants and  $\underline{a}$ , which contains  $Q_e$  and known quantities. This principle was exploited in nonautomated dynamic torsion-effusion experiments, in which as few as six time-vs-position data were available [2]. In automated experiments, because of the large number of time-vs-position data which are available, we have simply used the least squares method to obtain the parameters  $\alpha_n$ ,  $\beta_n$ , and  $\underline{a}$  from experimental data applied to eq. (22). We have found that  $N = 5$  gives accurate solutions; eleven parameters,  $\alpha_n$  and  $\beta_n$ ,  $n = 1, 5$ , and  $\underline{a}$ , must be obtained; thus a minimum of eleven observations of time vs position is required. In a typical automated experiment, time is recorded at 100 pendulum positions, and acceptable precision is obtained.

#### 4. The Dynamic Method Without Automation

In some experiments [2,10], the dynamic torsion-effusion method was used with direct observation of time vs position by the experimenter. Pendulum position was observed with a telescope focused through a glass window onto a disk which was graduated in degrees and which was part of the pendulum. Five stopwatches were started simultaneously at a preselected pendulum position. Each stopwatch was stopped at one of a set of preselected pendulum positions, and the time at each position was recorded. Thus, six time-vs-position data were obtained. With the aid of an additional stopwatch, which provided a continuous time base, the procedure above could be repeated to collect more than six data.

Application of this procedure to a study of the vapor pressure of  $\text{MnS(s)}$  was successful. It was, however, extremely time consuming; in some cases, collection of data for the vapor pressure at one temperature required three hours. Throughout this time, intense and exhausting concentration by the experimenter was required and sample was effusing and yielding little or no information. An automatic method of recording data, which would free the experimenter to attend to other parts of the experiment and would produce more data for a given expenditure of sample, power, etc., was called for.

#### 5. The Video Method

The video method [11] of automatic data acquisition simply involves recording an image of the oscillating pendulum on video tape. A video camera with a monitor and tape recorder is focused through a window in the vacuum system onto the disk to observe and record the pendulum motion. At a later time, the times at which the pendulum reaches certain positions

are observed by playing the video tape back on a video screen. Our application of this method is an extension of the dynamic method without automation described in the last section.

At the end of a series of vapor pressure experiments, the tape recordings of pendulum motions are played on the video monitor. The operator observes the recorded motions of the pendulum, and at preselected positions pushes a key which causes the time to be recorded on paper tape by a laboratory computer. Then the paper tape is read by a larger computer which matches pendulum positions with times, solves the equation of motion, and calculates  $Q_e$  and the vapor pressure.

The video method has the advantage that the important observations are recorded automatically and the experimenter is freed from that recording duty during the course of the experiment. The necessary observations at a given temperature can be recorded in a short time, usually within thirty minutes. Furthermore, a permanent, continuous record of pendulum motion is available for examination in any detail. The method has the disadvantage that final results are obtained only after the experiment is completed, and that data extraction requires investment by the observer of an amount of time almost equal to that required to produce the recordings. A method which would record time-vs-position in a computer and produce results in the course of the experiment is more desirable.

#### 6. The Computer Automated Acquisition of Data from Torsion-Effusion Experiments

The computer-automated data acquisition system is designed to observe and record times at which the dynamic torsion-effusion pendulum reaches preset discrete positions, to use those time-vs-position data along with known properties of the pendulum to solve the equation of motion of the pendulum to obtain  $Q_e$ , and thence to calculate and display the vapor pressure in the torsion-effusion cell. A light-beam reflection method is used to observe the pendulum. Low-power, He-Ne laser beams are cast through a glass portion of the cylindrical vacuum system wall surrounding the torsion-effusion pendulum, and reflected from mirrors mounted on the pendulum. The beams pass out through the glass wall and strike photodetectors at locations corresponding to known pendulum positions. The photodetector signals are transmitted to a laboratory computer where the mathematical analyses are done by means described previously in this paper.

The automatic data acquisition system has been described [12]; it is composed of eight parts: (1) four front-surface mirrors mounted on the torsion pendulum; (2) the light-beam generation and orientation system; (3) the photodetector mounting assembly; (4) the photodetector cells, each consisting of a defining slit, a light cavity, and a photodetector; (5) the photodetector circuits and signal shapers; (6) the photodetector signal encoder and computer interface; (7) a clock and computer interface; and (8) a laboratory computer.

The four front-surface mirrors are circular with 1-cm diameters. They are mounted on the rigid part of the pendulum, below the fiber, with the axis of rotation of the pendulum passing diametrically through the face of each mirror as shown in figure 1. The centers of the mounted mirrors are separated vertically by 1.5 cm, and the plane of the face of each mirror is oriented at  $90^\circ$  with respect to that (those) of its neighbor(s) such that one mirror faces into each quadrant. The mirrors, then, are on four levels separated by 1.5 cm. For reference, the mirrors and levels are assigned numbers 1-4 from top to bottom.

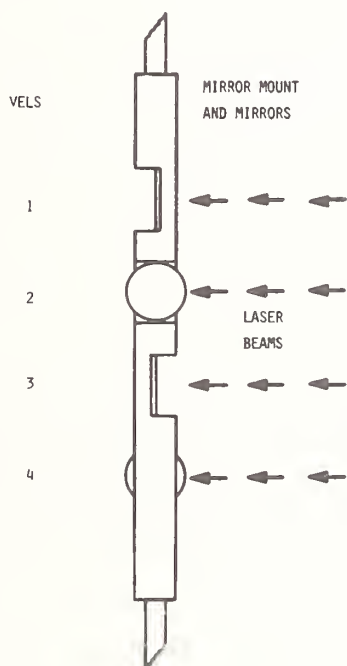


Figure 1. Arrangement of front-surface mirrors on the axis of the torsion pendulum to reflect laser beams onto photodetectors. The numbers of the mirror and beam levels are shown.

Four horizontal parallel laser beams in a vertical plane, one on each level, and correspondingly numbered 1-4, are cast radially through the cylindrical glass vacuum wall such that the pendulum axis is in the plane of the beams and such that one beam is directed at the center of each mirror. With this arrangement, one and only one beam is reflected acutely at any time, one is reflected obtusely, and two strike the mirror mount or the backs of mirrors. To avoid unwanted reflections, the mount, backs, and edges of the mirrors are painted black. The simple system which generates and orients the four beams has been described elsewhere [12].

The beam detection system, illustrated in figure 2, consists of four levels of photodetectors, one level for each beam and mirror and correspondingly numbered 1-4. Each level

is a  $175^\circ$  circular segment of 36 phototransistors equally spaced by  $5^\circ$ . The construction of the system is accomplished by setting the phototransistors in 36 vertical mounting posts each containing four detectors, one on each level, separated vertically by 1.5 cm. The posts are spaced at  $5^\circ$  intervals on a  $175^\circ$  circular segment on a supporting plate. The plate, in turn, sets on three vertically adjustable points on which it can be moved horizontally in any direction. This arrangement allows alinement of the detector system with the rest of the system.

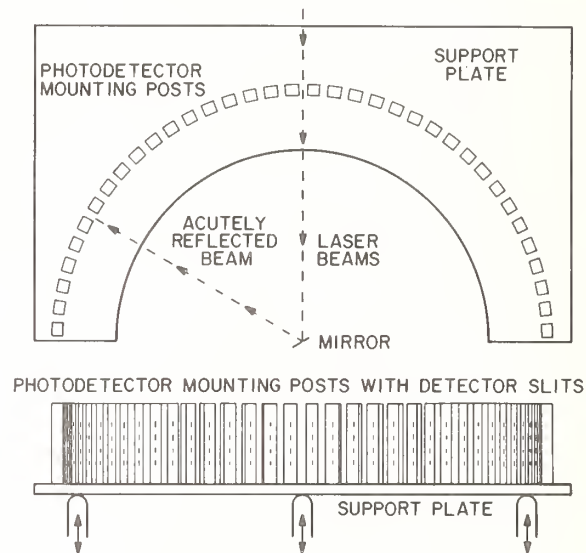


Figure 2. Top and front views of the photodetector system.

The four parallel laser beams are introduced radially through the center of the detector system between mounting posts 18 and 19. Thus, only the acutely reflected beam strikes the detector system. The spacing of detectors by  $5^\circ$  produces detection of pendulum position at  $2.5^\circ$  intervals because of the doubling effect of reflection of the beams from the mirrors.

The phototransistors are mounted in 5-mm-diameter holes drilled through the mounting posts. Over the end of the hole which faces toward the torsion pendulum and which is struck by the reflected beam are attached two razor blades separated by 0.5 mm to form a vertical slit which defines photodetector position. In the other end of the hole is placed the phototransistor. Into the interior of the hole, between the slit and the phototransistor, is placed a piece of 5-mm-diameter glass rod which disperses light and illuminates the cavity uniformly when a laser beam strikes the defining slit.

The electronics and interfacing to the laboratory computer are described elsewhere [12]. Their principle is discussed here. When a laser beam activates a photodetector, the electrical signal produced is conditioned by a preamplifier circuit on a small printed-circuit board attached to the back of the photodetector mounting post. The conditioned signal is transmitted to an encoder circuit which generates a binary number that is unique and identifies the active photodetector.

The principle by which the encoder functions is simple and is shown in figure 3 for the illustrative case of only seven photocells. Each OR gate in figure 3 represents a digit in a three-digit binary number. The preamplifier of each photodetector is wired directly to each OR gate which represents a digit in its unique binary number. Thus, detector 1 is wired only to gate 1, to produce the binary number 001 when it is active; detector 2 is wired to gates 1 and 2 to produce the binary number 011, etc., and detector 7 is wired to gates 1, 2, and 3 to produce the binary number 111. The encoder for the real photodetector system contains eight OR gates, because the number of detectors is 144, an eight-digit binary number. More wires are required for the real case, but no additional principle is involved.

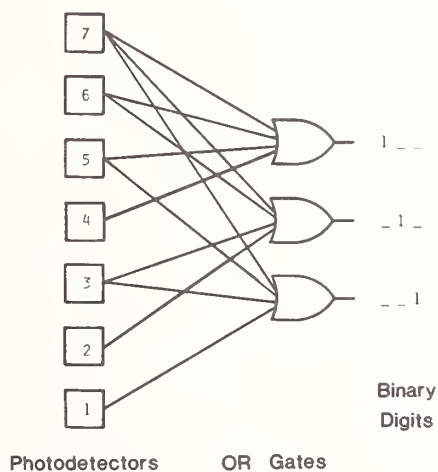


Figure 3. Illustrative example of a photodetector number encoder for the case of seven detectors.

The binary signal from the encoder is impressed on an eight-bit register in the interface board [13] of the laboratory computer [14]. The sensing of an active photodetector causes the register to be read by the computer and causes a 100 hz crystal clock on the same interface board to be read within a few machine cycles. The computer program which controls this reading also causes the clock to be read when the signal from the photodetector disappears. Thus, on each occasion when a photodetector is activated, the computer records the number of the active photodetector, the time it was activated, and the time it was deactivated.



The photodetector number is converted to pendulum position by multiplying its decimal value by  $2.5^\circ$ . The time at which the pendulum was at that position is calculated by averaging the activation time and the deactivation time. These time-vs-position data are stored in an array until the prescribed number have been collected, then they are analyzed by the methods already described. The computer can be programmed to skip observations such that time vs position is observed at intervals of any multiple of  $2.5^\circ$ .

As an example, we consider a typical experiment in which the rest position of the pendulum might be where the acutely reflected beam strikes near the center of detector level 1, and in which the amplitude might be near  $60^\circ$ . Suppose the computer is programmed to make observations at  $5^\circ$  intervals. As the pendulum oscillates through the rest point, the acutely reflected beam strikes detectors on level 1, until it leaves the detector bank and becomes obtusely reflected. Then the beam on level 2 or 4 (depending on pendulum direction) becomes acutely reflected and moves across detectors on its level until the pendulum is displaced by  $60^\circ$  from its rest point. Then the pendulum and reflected beams change direction and move to the other extreme, etc. In the course of these oscillations, the automatic system accumulates the prescribed number of time-vs-position data. Periods of the pendulums used in our experiments have been in the range 35-120 s. A typical period would be 60 s, and in that case, accumulation of 100 data under the conditions above would require 60 s.

## 7. Results

In a series of tests of the computer-automated data acquisition system conducted with the furnace off so that the effusion cell was at room temperature and no vapor effused, the rest position of the pendulum was reproduced within  $\pm 0.01^\circ$ . During actual vapor pressure measurements, calculated pendulum deflections at a given furnace setting varied by as much as  $\pm 0.1^\circ$  because of temperature variations and background gas effects.

The simultaneous Knudsen-effusion and dynamic torsion-effusion method was used without automatic collection of torsion-effusion data to measure the vapor pressure of  $\text{MnS(s)}$  [2]. The temperature range was 1536-1693 K, where the vaporization is congruent to produce  $\text{Mn(g)}$  and  $\frac{1}{2} \text{S}_2(\text{g})$  [15]. Combination of the Knudsen-effusion and torsion-effusion data gave the average molecular weight of the vapor to be  $61.6 \pm 4.9$ , a result which compares well with the value of 58.1 calculated for  $\text{Mn(g)} + \frac{1}{2} \text{S}_2(\text{g})$ . The third-law standard molar enthalpy of vaporization of  $\text{MnS(s)}$  at 298 K calculated from torsion-effusion data was  $563.7 \pm 0.3 \text{ kJ mol}^{-1}$ , in excellent agreement with the value from mass-loss data,  $562.8 \pm 0.2 \text{ kJ mol}^{-1}$ .

The simultaneous method was used with video observation of the dynamic torsion-effusion pendulum to study the vaporization of  $\text{ZnGa}_2\text{S}_4(\text{s})$  in the temperature range 1106 - 1209 K [4]. Vaporization was incongruent and produced a new solid,  $\text{ZnGa}_8\text{S}_{13}(\text{s})$ , and a two-component vapor phase containing the vapor of  $\text{ZnS}$ , viz.,  $\text{Zn(g)}$  and  $\frac{1}{2} \text{S}_2(\text{g})$ , and the vapor of  $\text{Ga}_2\text{S}_3$ , viz.,  $\text{Ga}_2\text{S(g)}$  and  $\text{S}_2(\text{g})$ .

Combination of the Knudsen-effusion and torsion-effusion data at each temperature gave an analysis of the vapor into its two components and allowed calculation of the partial pressure of each of the three constituents,  $\text{Zn(g)}$ ,  $\text{Ga}_2\text{S(g)}$ , and  $\text{S}_2\text{(g)}$ . Figure 4 is a graphical representation of the results in the form of least-squares lines from plots of logarithms of the partial pressures vs the inverse temperature. The vertical error bars represent standard deviations of the experimental points from the least-squares lines. The error bar for the  $\text{Ga}_2\text{S}$  line is relatively long because  $\text{Ga}_2\text{S(g)}$  constitutes only 10-20 percent of the vapor.

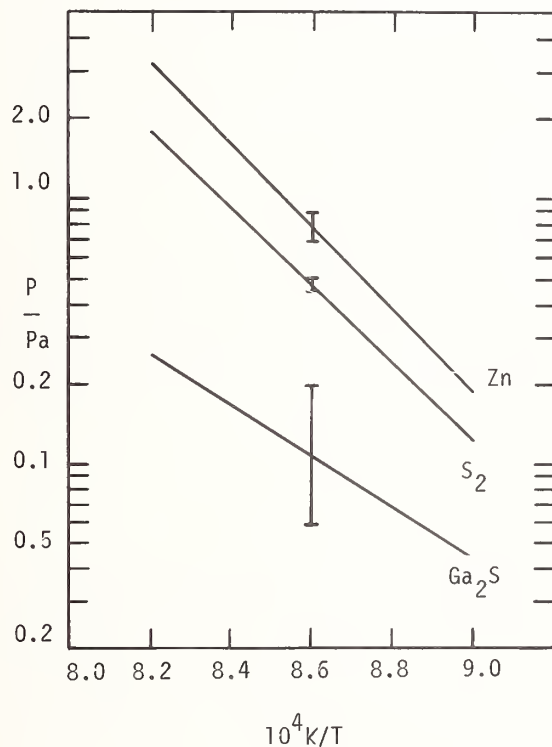


Figure 4. Least-squares straight lines from plots of partial pressures over  $\text{ZnGa}_2\text{S}_4\text{(s)} - \text{ZnGa}_8\text{S}_{13}\text{(s)}$  of  $\text{Zn(g)}$ ,  $\text{S}_2\text{(g)}$ , and  $\text{Ga}_2\text{S(g)}$  as functions of inverse temperature.

The simultaneous method was used with computer-automated acquisition of torsion-effusion data to study the vaporization of  $\text{TiS(s)}$  [16]. The temperature range was 2039-2168 K, where vaporization is congruent to produce vapor made up principally of  $\text{TiS(g)}$  and of  $\text{Ti(g)}$  and  $\text{S(g)}$  with minor amounts of  $\text{S}_2\text{(g)}$  and  $\text{TiS}_2\text{(g)}$  [17,18]. The average molecular weight of the vapor calculated from previous mass spectrometric results [18] was temperature dependent because of temperature dependence of vapor equilibria among the atoms and molecules, but over the present temperature range its average value was  $43.7 \pm 4.4$ . The average molecular weight from the present work without attention to temperature dependence was  $38.5 \pm 5.9$ . Third-law standard molar enthalpies of vaporization of  $\text{TiS(s)}$  to produce

TiS(g) were calculated by the method of Edwards, Franzen, and Gilles [18] from Knudsen-effusion and torsion-effusion data to be  $587.9 \pm 1.7 \text{ kJ mol}^{-1}$  and  $587.0 \pm 1.7 \text{ kJ mol}^{-1}$ , respectively. These values agree with the value  $586.6 \text{ kJ mol}^{-1}$  calculated [18] from previously reported target collection results [17].

## 8. Conclusion

The dynamic method of operating a torsion-effusion pendulum has proven to be practical and efficacious. Results obtained by that method were in good agreement with those from simultaneous experiments by the Knudsen-effusion method. The dynamic method affords a simple and accurate means of automating data acquisition from torsion-effusion experiments. That automation has been accomplished and described; its application to the high-temperature vaporization of  $\text{ZnGa}_2\text{S}_4(\text{s})$  and of  $\text{TiS}(\text{s})$  showed it to be efficient and accurate.

---

The author gratefully acknowledges the assistance and valuable suggestions of his colleagues and coworkers, particularly Dr. A. S. Gates and Dr. H. B. Thompson, in the development of the automatic methods described. This work was supported by NSF Grant ENG 75-19183.

## References

- [1] Freeman, R. D., in The Characterization of High Temperature Vapors, J. L. Margrave, ed. (John Wiley and Sons, Inc., New York, N.Y., 1967), Chapter 7.
- [2] Viswanadham, P. and Edwards, J. G., *J. Chem. Phys.* 62, 3875 (1975).
- [3] Hildenbrand, D. L. and Knight, D. T., *J. Chem. Phys.* 51, 1260 (1969).
- [4] Gates, A. S. and Edwards, J. G., *J. Phys. Chem.* 82, 2789 (1978).
- [5] Grady, P. L., Lord, P. R., London, C. R., and Smith, G. E., *Rev. Sci. Instrum.* 46, 1513 (1975).
- [6] Cooper, P. and Corti, C. W., *Rev. Sci. Instrum.* 47, 1337 (1976).
- [7] Zoller, P., Oppliger, H.-R., and Casalini, A., *Rev. Sci. Instrum.* 46, 695 (1975).
- [8] deKruif, C. G. and van Ginkel, C. H. D., *J. Phys. E*, 6, 764 (1973).
- [9] deKruif, C. G., van Ginkel, C. H. D., and Voogd, J., Conf. Int. Thermodyn. Chim., [C. R.], 4th, J. Rouquerol and R. Sabbah, eds. (Cent. Rech. Microcalorimetrie Thermochim. C. N. R. S., Marseilles, France, 1975), pp. 11-18.
- [10] Edwards, J. G., *J. Vac. Sci. Technol.* 11, 400 (1974).
- [11] Gates, A. S. and Edwards, J. G., *Rev. Sci. Instrum.* 48, 488 (1977).
- [12] Edwards, J. G., Heckler, M. K., and Thompson, H. B., *Rev. Sci. Instrum.* 50, 374 (1979).
- [13] Module Number DKC8-AA, Digital Equipment Corp., Maynard, Mass.
- [14] PDP-8/a Computer, Digital Equipment Corp., Maynard, Mass.

- [15] Wiedemeier, H. and Gilles, P. W., J. Chem. Phys. 42, 2765 (1965).  
[16] Pelino, M. and Edwards, J. G., to be published.  
[17] Franzen, H. F. and Gilles, P. W., J. Chem. Phys. 42, 1033 (1965).  
[18] Edwards, J. G., Franzen, H. F., and Gilles, P. W., J. Chem. Phys. 54, 545 (1971).

#### Discussion

Question (Gilles): Jim, what is your dynamic range?

Clarification (Edwards): By that you mean the amplitude of the pendulum?

Clarification (Gilles): No, in pressures. Can you go over a factor of a million or a factor of ten?

Response (Edwards): We are limited in our experiments, at the lower pressure end, by the sensitivity of the fiber that we use, and the accuracy with which we can measure angles, and our lower limit is very close to  $10^{-7}$  atmospheres. At the upper end we are limited by the requirement that we stay in the molecular flow region and that, of course, keeps us at about  $10^{-4}$  atmospheres, right in that range, so about a factor of a thousand.

Moderator (Cater): Would you care to take about one minute to tell us the advantages of doing torsion by oscillation?

Response (Edwards): Yes. I gave you the principal advantage. The principal advantage is that it makes it easy to automate the data acquisition. The other advantages, which I see, are that random effects tend to be averaged out vibrational effects. If you have thermal gradients in your furnace there is a tendency to average those out because the pendulum spends time at various orientations in the furnace, so that we can average out that sort of effect.

And in the case of effects such as inductive interactions with the cell: that is not a random effect, but it does vary over the position of the cell in the furnace, and that does tend to be averaged out also. You hit some high torques and then some low torques, so it is not necessary to map them quite so accurately if you look at the cell in several positions.

But I would say the principal advantage is that it makes the automation fairly straightforward, easy, and mostly easy to understand.





APPLICATION OF LASER PULSE HEATING FOR THE STUDY OF HIGH TEMPERATURE  
VAPOURS, PHASE TRANSITIONS AND EQUATION OF STATE

R. W. Ohse, J. F. Babelot, and C. Cercignani,<sup>1</sup>  
P. R. Kinsman, K. A. Long, J. Magill, and A. Scotti<sup>2</sup>

Commission of the European Communities  
Joint Research Centre  
European Institute for Transuranium Elements  
D-7500 Karlsruhe, Germany

A new dynamic laser pulse heating technique, allowing thermo-physical property measurement and equation of state studies above 3000 K has been described. The vapour pressure measurements of uranium oxide up to 5000 K, as required for reactor safety analysis are presented. The present state of experimental work above the melting point is summarized. A complete survey on predicted critical point data of uranium oxides reviewing the various theoretical models is given.

The various dynamic pulse heating techniques are outlined. For a study of the high temperature vapours and the gas dynamic expansion phenomena of the gas jet, the laser surface heating equipment has been extended to include high speed diagnostics such as multi-channel spectroscopy, time of flight mass spectrometry, and image converter photography in both the framing and streak recording mode.

The evaporation process and thermodynamic interpretation of the data are discussed. A kinetic theory description of the laser induced vapour jet using a monatomic gas dynamic model is given. The optical absorption in the gas jet, giving an upper temperature limit for the applicability of optical pyrometry has been calculated. The reduction of ionization potential was found to be of minor importance.

---

<sup>1</sup>Present address: Istituto di Matematica del Politecnico di Milano, Piazza Leonardo da Vinci, Milano, Italia.

<sup>2</sup>Present address: 21020 Centro Euratom di Ispra (Varese), Italia.

## 1. Introduction

One of the main tasks in nuclear safety analysis is to estimate the maximum energy release in a hypothetical core disruptive accident (HCDA) of a liquid metal fast breeder reactor (LMFBR). The effective amount of thermal energy released during a power transient and converted into mechanical energy depends on the rate of energy production and the time elapsed between initiating the prompt critical excursion and the disassembly process. Since the disassembly process, as a hydrodynamic shutdown mechanism, is mainly due to the pressure generation within the pin assembly and subsequent fuel motion, a "dynamic equation of state" of the irradiated fuel is required including the kinetics of the processes. As a first step in this direction, the vapour pressure of the pure fuel is measured up to temperatures of the order of 5000 K.

In principle, PVT data can be estimated by appropriate theoretical models, extrapolating measured data, or by purely thermodynamic calculations based on large extrapolations of low temperature data. Direct measurements under these extreme conditions of temperature and high rates of evaporation require the development of new dynamic pulse heating techniques and high speed diagnostics with adequate high spatial and temporal resolution.

The various theoretical approaches to predict the critical point data will be discussed in Section 2. The Principle of Corresponding States and Significant Structure Theory, being of a more phenomenological nature, were conceived for simple molecular liquids, whereas the more fundamental approach of the Monte Carlo Technique is based on the statistical mechanics of interacting molecules.

A description of the various dynamic pulse heating techniques, volume heating such as exploding wire technique, electron and neutron pulse heating, as well as laser surface heating is given in Section 3. The dynamic laser pulse surface heating technique has been chosen and developed in order to allow, in addition to total pressure measurements, a comprehensive mass spectrometric and spectroscopic study of the gaseous molecules as a function of temperature. The application of the laser surface heating technique has been demonstrated on uranium and plutonium oxides up to 5000 K. A detailed description of the technique, including the high speed diagnostics is presented.

The basic evaporation mechanism is discussed in Section 4. Section 5 deals with the gas dynamic expansion phenomena of the laser induced gas jet, starting on a steady state cylindrically symmetric evaporation of a monatomic gas.

Section 6 finally investigates the optical absorption in the gas jet by calculating the degree of ionization and possible reduction of the ionization potential, yielding a temperature limit for the applicability of optical pyrometry to  $\text{UO}_2$ .

## 2. Prediction of Critical Point Data by Theoretical Models

Table 1 and figure 1 summarize the prediction of critical point data of  $\text{UO}_2$ , as presented in the literature, using the principle of corresponding states (PCS), the law of rectilinear diameters (LRD), and significant structure theory (SST). As demonstrated in both figure 1 and

table 1, there are clearly considerable uncertainties in the values of the predicted critical temperature and pressure. The predictions range from 5000 K to 10,000 K. Additional research has therefore been started on the application of the Monte Carlo Technique (MCT) to  $\text{UO}_2$ . The basic details of the various models are discussed briefly.

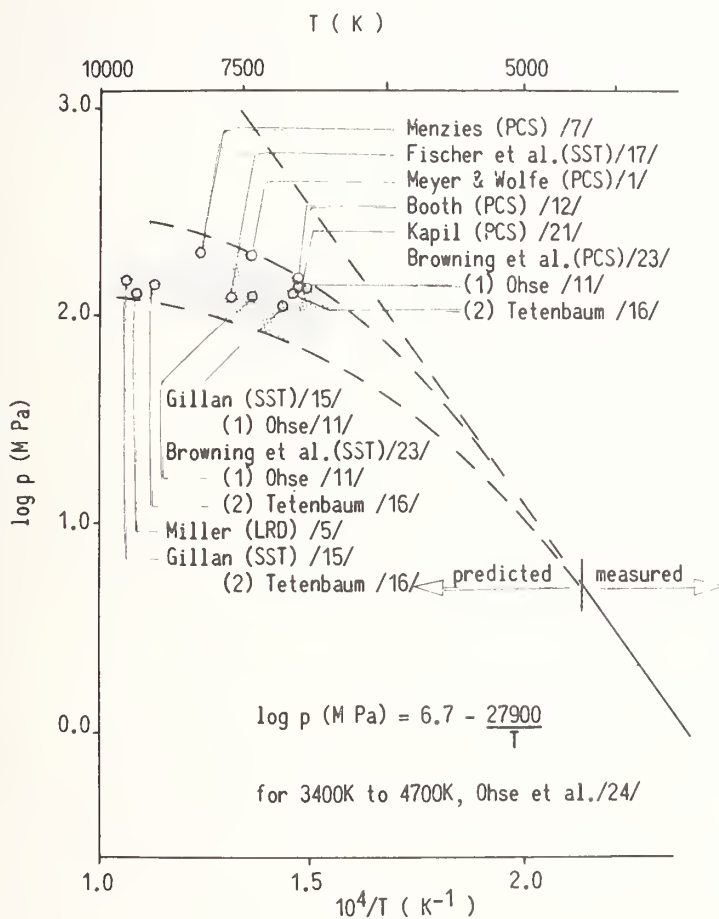


Figure 1. Degree of pressure deviation from linearity required to ensure consistency between the measured vapour pressures up to 4700 K and the predicted field of critical point data of  $\text{UO}_2$ .

## 2.1 The principle of corresponding states

The principle of corresponding states was originally formulated by Van der Waals [25]<sup>3</sup>. It states that materials at the same reduced temperature  $T_r = T/T_c$ , pressure  $P_r = P/P_c$ ,

<sup>3</sup>Figures in brackets indicate the literature references at the end of this paper.

Table 1. Predicted critical point data of  $UO_2$ .

Critical point data					Theoretical models			Input data	
$T_c$ (K)	$P_c$ (MPa)	$V_c$ ( $cm^3$ )	$\rho_c$ ( $g/cm^3$ )	$Z_c$	Method of evaluation	Author	Year	Data	Author
7300	194	85.5	3.01	0.27	PCS	Meyer, Wolfe [1]	1964	Melting point; density Saturated vapour pressure of a fluid Vapour pressure	Christensen [2] Hougen, et al. [3] Ackermann, et al. [4]
9115	125	170	1.59	0.27	LRD	Miller [5]	1965	Density Vapour pressure	Christensen [2] Ackermann, et al. [4]
8000	200	90	3.16	0.27	PCS	Menzies [7]	1966	Saturated vapour pressure of a fluid $UO_2$ data	Hougen, et al. [3] DEG Report [8]
5500-10000	100-200	96-120		0.20-0.40	PCS	Robbins [9]	1966	Density Heat of fusion Vapour pressure	Christensen [2] Christensen [2], Chikalla [10] Ackermann, et al. [4], Ohse [11]
6723	142	99	2.74	0.251	PCS	Booth [12]	1968, 1974	Melting point Density Vapour pressure Enthalpy of $UO_2$ solid	Hausner [13] Christensen [2] Ohse [11] Hein, et al. [14]
6960	108		1.64	0.308	SST	Gillan [15]	1974	Melting point Density Vapour pressure	Hausner [13] Christensen [2] Ohse [11]
9330	147		1.63	0.308	SST			Melting point Density Vapour pressure	Hausner [13] Christensen [6] Tetenbaum, et al. [16]
7560	123		1.66	0.316	SST	Fischer et al. [17]	1976	$UO_2$ molecule Vapour pressure Enthalpy of $UO_2$ solid	Abramowitz, et al. [18] Ohse [11] Kerrik, et al. [19], Affortit, et al. [20]
6744	142		2.74	0.25	PCS	Kapil [21]	1976	Melting point Density; linear expans. Vapour pressure	Hein, et al. [14] Christensen [2, 6] Ackermann, et al. [4] Ohse [11] Tetenbaum, et al. [16] Reedy, et al. [22]
6723 6820	140 138	98.7 98.4		0.25 0.24	PCS(1) PCS(2)	Browning, et al. [23]	1977	Vapour pressure (1)(2) Melting point data; liquid density, and expansion coefficient	(1) Ohse [11] (2) Tetenbaum [16] Hausner [13] Christensen [6]
7320 8840	126 142	152 158		0.32 0.31	SST(1) SST(2)			Vapour pressure (1)(2) Melting temperature, Vol. change of fusion, entropy of fusion at M.P. $UO_2$ molecular data	(1) Ohse [11] (2) Tetenbaum [16] Hausner [13] Christensen [6]

volume  $V_r = V/V_c$  show similar behaviour [26-29]. The compressibility factor  $Z = P_c V_c / RT_c$  should be an universal constant for all substances. This form is only successful for simple fluids (those consisting of spherical molecules interacting through potentials resembling the Lennard-Jones potential [36]). In an extended form of the principle, the variables are reduced by means of molecular constants, which describe more complicated intermolecular potentials. In this form, it is possible to introduce [29,30] additional parameters so as to extend the principle to the study of various types of molecules.

This method has been applied to  $UO_2$  by several authors (table 1), but since it relies on a correlation with liquids of similar properties, it is questionable whether it can be used for  $UO_2$ , because of the absence of suitable reference systems, partially ionic as assumed in the case of  $UO_2$  [31-33].

## 2.2 The law of rectilinear diameters

The law of rectilinear diameters is an empirical relationship [34,35], stating

$$1/2(\rho_L + \rho_V) = CT + D \quad (1)$$

where  $\rho_L$  and  $\rho_V$  are the saturated liquid and vapour densities, and C and D are constants. There is again the question of applicability of this law to ionic substances. Apart from this, application of the method to  $UO_2$  requires data on the densities of the liquid and gaseous phase as near as possible to the critical temperature, which are not available for most substances.

## 2.3 Significant structure theory

The significant structure theory as developed by Eyring [36,37], postulates a model of a liquid that describes the liquid as a mixture of solid-like and gas-like degrees of freedom. The aim of this theory is to predict the properties of liquids on the basis of the known properties of the corresponding solids and gases without explicit reference to intermolecular forces. The theory correlates a very wide range of properties (including transport properties) of a wide range of liquids. In this sense, it is an "engineering" type of approach to the prediction of critical point data.

The method has been applied to molten ionic salts and has given encouraging agreement with experiment [38-40]. The input data required is that for the construction of the solid and gas partition functions. For the solid partition function, these are  $V_s$  (the molar volume at the melting point of the solid),  $E_s$  (the solid binding energy), Einstein frequency of the vibrations in the solid  $\theta_e$ , and for the gas partition function, moments of inertia and vibration frequencies for polyatomic molecules. The parameters n and a, which describe the degeneracy factor, introduced due to the excess volume in the liquid are also needed. In the case where the substance is ionic an additional parameter  $\gamma$  is needed, although for



molten salts Lu, et al. set  $\gamma = 1/3$  [39]. If the gas contains dimers, a rate constant or equivalently  $\Delta H$  (heat of reaction) and  $\Delta S$  (entropy change) must be known. The method has the merit of yielding relatively simple analytic expressions for the Helmholtz free energy. It can be generalized by including such effects as electronic excitation, dissociation, and association in the gas phase. In practice, the method is relatively easy to apply and can yield most equilibrium thermodynamic data, including the equation of state.

This method has been applied to predict the critical point data of  $UO_2$  [15,17,23]. However, since all the data are not immediately at hand, experimental thermodynamic data were used to fix the values of  $E_s$ ,  $\theta_E$ ,  $n$ ,  $a$ , and  $\gamma$ . For the estimation of the critical constants, experimental data on the vapour pressure, the liquid expansion coefficient, together with the law of rectilinear diameters were used. In addition, the properties of the  $UO_2$  molecule were needed.

## 2.4 Monte Carlo technique

The Monte Carlo technique in statistical mechanics, particularly in the study of the equilibrium properties of simple liquids is by now well established. This method gives excellent agreement with experiment provided that sufficiently realistic (and complicated) potential energy functions are used [43]. Early results obtained encompass the description of hard sphere gases and Lennard-Jones fluids. Equations of state are obtained via averages computed following random walks in phase space, leading to the evaluation of two particle distribution functions. Detailed information, especially in the liquid state, is therefore obtained without any ad hoc assumptions. The basic input is the intermolecular potential which for more complex molecules and substances has to be either calculated or measured. Hence, in this case, the interaction potential has to be parameterized, and the calculations checked against available experimental data, heat of fusion, heat of evaporation, and vapour pressure. Since this has proved unsatisfactory for  $UO_2$  using a molecular or covalent type interaction, it is proposed to treat a model in which the Monte Carlo technique is applied to solve "exactly" an ionic type of description in which, however, polarizability of the ions is included so as to allow for the formation of bound molecules.

## 3. Dynamic Pulse Heating Techniques for EOS Studies of Uranium Oxide

### 3.1 Survey of experimental techniques

Experiments at high rates of evaporation, as occur above the melting point of refractory materials, require the application of a dynamic pulse heating technique. Four different methods of pulse heating have been applied: (a) isobaric resistive heating (IRH) (exploding wire technique), (b) neutron pulse heating (NPH), (c) electron pulse heating (EPH), and (d) laser surface heating (LSH). Each technique has particular advantages and disadvantages. A schematic outline of each technique is shown in figure 2.

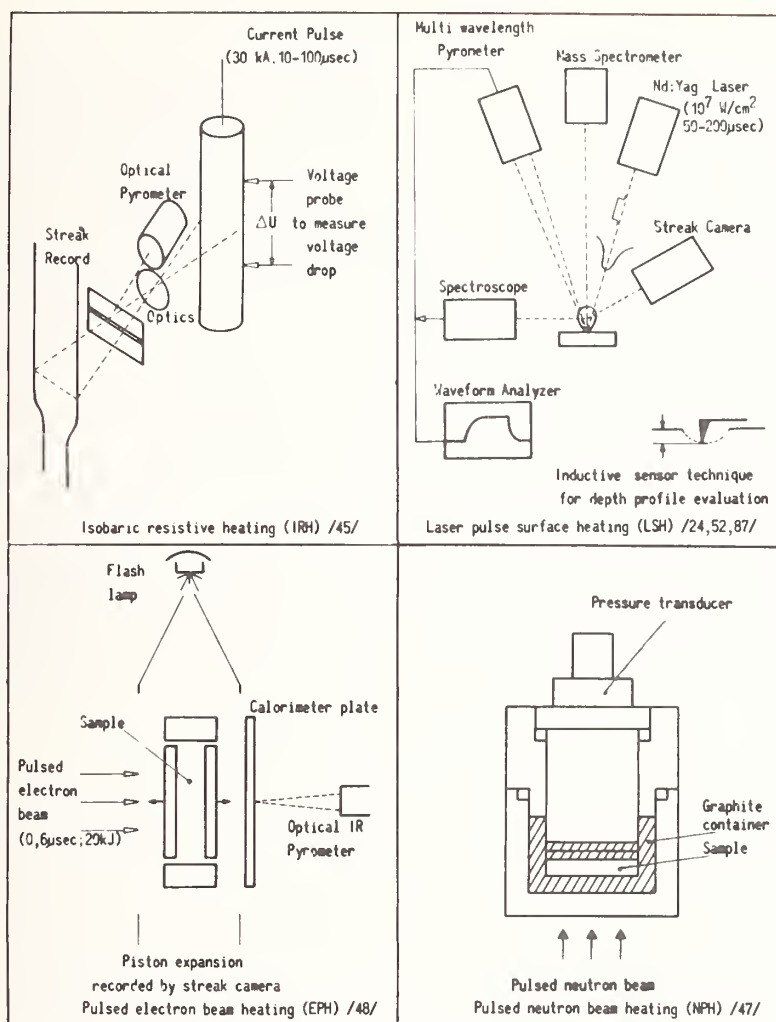


Figure 2. Schematic outline of the various dynamic pulse heating techniques.

### 3.2 Isobaric resistive heating (exploding wire technique)

High current pulsed heating of a wire or rod in the  $\mu\text{s}$  time scale has been applied in a number of laboratories [44,45,46] for thermal physical property measurements on sufficiently conductive materials. The sample is enclosed in a high pressure vessel filled with an inert gas or a transparent liquid, and heated by a capacitor bank discharge. Fast photography and pyrometry are used to determine thermal expansion and heat capacity at temperatures well above the melting point of the sample. One necessary sample requirement is a sufficiently high electrical conductivity, but even then it may be difficult to measure the energy deposited in the liquid column. Difficulties can also arise from nonuniform heating.

### 3.3 Neutron pulse heating

The intense neutron flux from a pulsed reactor can be used to uniformly heat small samples contained in a pressure cell [47]. A transducer is used to monitor the pressure generation in the cell during the millisecond heating time. The data are used to evaluate the vapour pressure as a function of input energy. Due to thermal losses and uncertainties in the energy of the neutron flux, the sample input energy is not clearly defined.

### 3.4 Electron pulse heating

This technique is similar to neutron heating in that a high intensity flux of particles is used to produce uniform heating within a small volume of the sample. At the Sandia Laboratories [48], a relativistic electron beam accelerator is used to deliver a specific energy of 300 joules per gram of sample in the  $\mu\text{s}$  time scale. The sample is contained in a cylindrical crucible sealed by two thin graphite pistons. By photographing the movement of these, and evaluating the energy input via pyrometric temperature measurement of a calorimeter plate, the vapour pressure can be determined as a function of input energy.

### 3.5 Laser surface heating

Laser pulse surface heating has been used by a number of laboratories [24,49,50,51] to determine vapour pressure as a function of temperature. Pulse times used have ranged from nanoseconds [49], microseconds [24], to milliseconds [50]. Various methods were applied for temperature determination. Though additional studies are required, as shown in Section 4, to elucidate the basic evaporation mechanism at high rates of evaporation, the advantages of spectroscopic and mass spectrometric studies of the gaseous molecules are attained. Vapour pressures have been measured successfully up to 5000 K [24,55].

#### 3.5.1 Experimental lay-out of laser surface heating

A schematic display of the experimental technique is shown in figure 3. A neodymium-doped YAG laser with four amplifying units and operating in the single transverse mode, delivering a Gaussian power profile, is used for heating in the pulse range 1  $\mu\text{s}$  to 5 ms. A focal spot diameter, defined as  $1/e^2$  of the peak height, of 2 mm, delivers a maximum power density of the order of  $10^8 \text{ W/cm}^2$ .

A high speed multi-wavelength pyrometer was specially constructed for this work, to permit a temporal resolution of the order of 10 ns and a spatial resolution of the order of 100  $\mu\text{m}$ .

Sets of four interference filters are mounted in front of two photomultipliers, allowing temperature measurements of 16 pairs of wavelengths. Each interference filter has a half width of 100 Å and a wavelength of peak transmissions determined to within  $\pm 20$  percent.

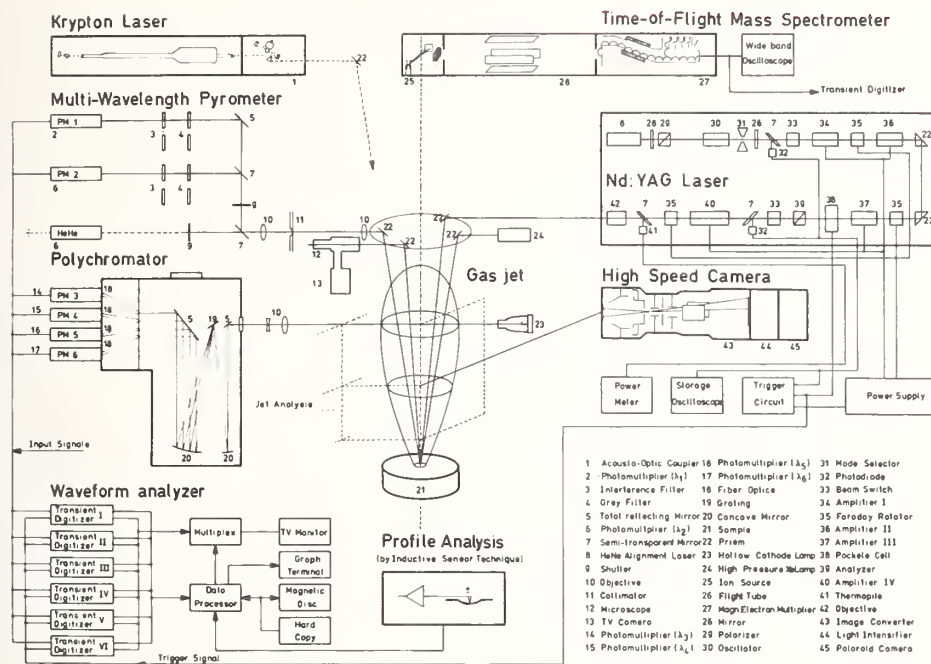


Figure 3. Schematic display of the lay-out of extended high speed diagnostics for thermophysical property measurements and the characterization of high temperature vapours induced by laser pulse heating.

The central temperature of the target was correlated to the central depth accounting for the Gaussian power profile of the laser beam. The effects of radiation from below the surface could be neglected [52]. The pyrometer was regularly calibrated against a tungsten ribbon standard lamp calibrated by the Physikalisch Technische Bundesanstalt standards laboratory. The output signals of the photomultipliers were recorded on transient digitizers interfaced to a disc storage system and a digital computer. A digital or graphical record of the temperature signal was stored. At 5000 K, a temperature resolution of the order of 5 degrees was achieved.

Additional diagnostic instrumentation includes a time of flight mass spectrometer for mass analysis of the laser induced vapour jet, and a 1 meter focal length grating polychromator. Four fast photomultipliers are connected to the output slit by optical fibers. This allows simultaneous recording of the variation in intensity of four spectral lines emitted by the vapour jet on the transient digitizers. Alternatively, absorption rather than emission measurements can be used for gas jet diagnostics. Spectroscopic measurements are foreseen to be necessary for gas temperature determinations above 500 K. Above 5000 K optical pyrometric surface temperature measurements are expected to become increasingly inaccurate because of absorption in the vapour jet. The gas dynamic model described in Section 4 allows the surface temperature to be deduced from measurements of the temperature distribution within the jet.



Finally, the high speed image converter camera equipped with an image intensifier can photograph the vapour jet in either the streak mode with speeds of up to 1 ns/mm, or in the framing mode at up to  $10^7$  frames/s. Experimental information on the time taken to establish the vapour jet and the luminous intensity distribution can be used to check the validity of the theoretical gas dynamic model.

### 3.5.2 Results on $\text{UO}_2$

Figure 4 summarizes all vapour pressure measurements on  $\text{UO}_2$  above its melting point of 3120 K. For comparison two series of measurements on  $(\text{U,Pu})\text{O}_2$  are given. A total of five sets of measurements on  $\text{UO}_2$  were made up to now.

The measurements of Reedy and Chasanov [22], using the transpiration technique up to 3400 K, refer to hypostoichiometric urania of  $\text{O/U} = 1.94$ . A normalization to  $\text{UO}_{2.00}$  will increase the total pressure.

The measurements of Asami, et al. [49], using a laser spike heating technique on a 15 nanosecond time scale, arrived at spectroscopically measured temperatures of up to 10,000 K, above the critical temperature of  $\text{UO}_2$ , indicating a possible interaction of the laser light with the ionized vapour jet.

The measurements of Ohse, et al. [24] with a laser pulse heating technique within the microsecond time scale used a well defined rectangular laser pulse, as described above, of a Gaussian power profile with the laser working in its single transversal mode. Liquid displacement was eliminated by applying a double pulse heating technique at sufficiently large focal spot diameters, thus achieving a fast temperature rise time [54]. The high speed multi-wavelength pyrometer was used to check the attainment of steady state conditions. First measurements of the spectral emissivity [55] at the melting point of  $\text{UO}_2$  at  $\lambda = 0.65 \mu\text{m}$  yielding  $\varepsilon = 0.84$  were confirmed by Bober, et al. [56].

Bober, et al. [50], using mechanically interrupted  $\text{CO}_2$  laser radiation on a millisecond time scale, moved their laser beam in circles to get around the formation of deep holes, which would lead to uncontrollable effects in vapour ejection. The large temperature gradients due to their comparatively small focal spot diameter, did, according to the authors [60], not allow the exclusion of radial liquid displacement necessary for steady state attainment.

Benson [48] applied electron beam heating as described above. Conversion of the measurements expressed in terms of pressure and energy to a pressure-temperature scale requires knowledge of the specific heat and thus involves the present uncertainty about the specific heat of the liquid  $\text{UO}_2$ , values of which vary over the range of  $0.437$  to  $0.50 \text{ J g}^{-1} \text{ K}^{-1}$  ( $28.2$  to  $32.2 \text{ cal mol}^{-1} \text{ K}^{-1}$ ).

Tsai, et al. [51] using laser pulse heating, obtained a heat of evaporation considerably lower than the values measured or extrapolated from measurements from below the melting point. According to the authors, the measured temperatures were believed to be too high, due to non-equilibrium radiation from the vapour.



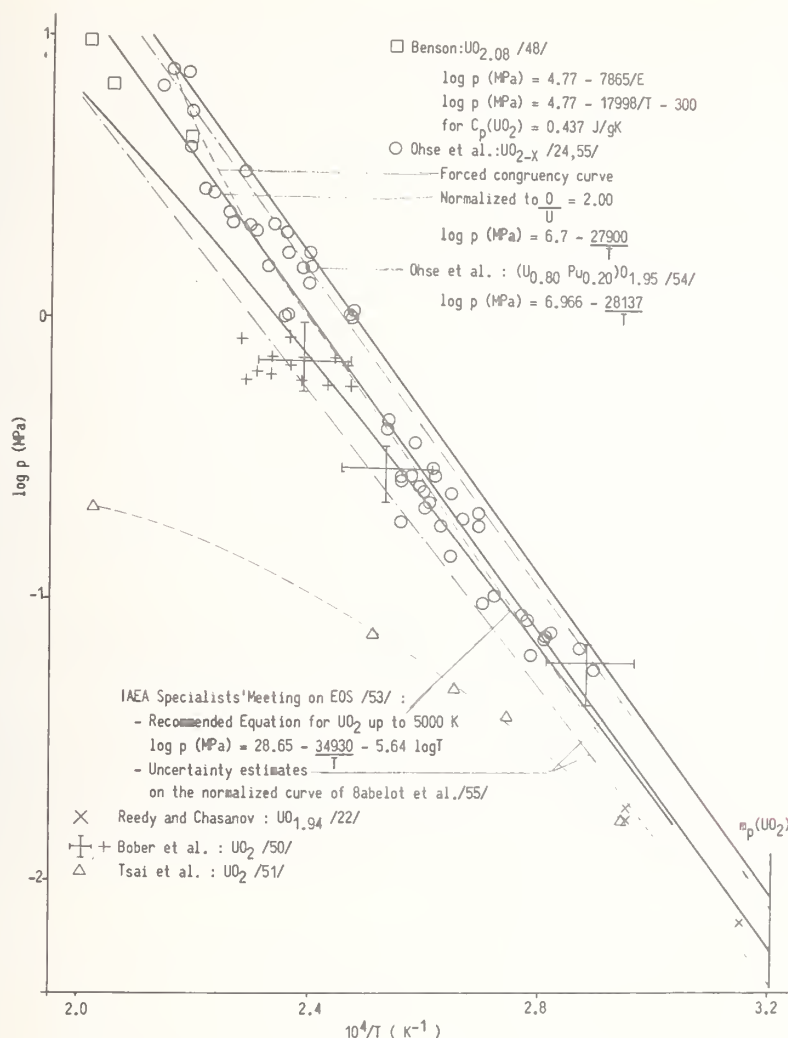


Figure 4. Total vapour pressure measurements over liquid uranium oxide, obtained by the transpiration technique [22], pulsed laser surface heating [24,55,49-51] and electron beam heating technique [48], including for comparison uranium plutonium oxide.

The best current estimate of the vapour pressure of  $\text{UO}_2(l)$  up to 5000 K was suggested by the IAEA Specialists' meeting of the International Working Group of Fast Breeder Reactor on Equation of State of Fast Reactor Materials at Harwell [53], held in June 1978, to be:

$$\log P(\text{MPa}) = 28.65 - 34930/T - 5.64 \log T .$$

This equation is based on the measurements given in figure 4, and law of mass action calculations, yielding a negative deviation from the linear  $\log P$  versus  $1/T$  plot, as indicated by the prediction of the critical point data using the various theoretical models, given in Section 2 (fig. 1).

Because of the large uncertainty in the prediction of the critical point data of  $\text{UO}_2$  ( $T_c$  runs from 5500 K to almost 10,000 K), and the necessity to extrapolate, for law of mass action calculations, the thermodynamic data over several thousand degrees, further measurements are required. Since the expected deviation from linear behavior at 5000 K is too small (fig. 1), compared to the scatter of the experimental data, extrapolations to beyond 5000 K can neither be obtained from the measurements within the present temperature range, nor from the thermodynamic data extrapolation. The recommended equation is therefore valid only up to 5000 K.

Calculations near the upper temperatures to which PVT data are required for fast breeder safety analysis should take into account the anomalous behaviour and non-ideality previously observed for various substances above  $0.8 T_c$ . Since the fast breeder oxide fuel does not consist of pure  $\text{UO}_2$  but the mixed oxides  $(\text{U,Pu})\text{O}_2$  with up to 40 mol percent of  $\text{PuO}_2$ , a substantially lower critical point temperature can be expected, possibly leading into the nonideality ( $0.8 T_c$ ) already below 5000 K. Investigation of such a departure from ideality again requires an extension of measurements to beyond 5000 K.

#### 4. Basic Evaporation Process at High Rates of Evaporation

The fact that the rate of evaporation  $\dot{n}_+$  of a substance into vacuum can be obtained from the saturated vapour pressure  $P_s$  and the evaporation coefficient  $\alpha_v$  was first shown by Hertz, Knudsen, and Langmuir from equilibrium considerations [57]. Conversely, the saturated vapour pressure of the material can be obtained by measuring the rate of evaporation, provided  $\alpha_v$  is known, through the relation

$$\dot{n}_+^{\text{net}} = \dot{n}_+ = \alpha_v \frac{1}{4} n_s \bar{v} = \frac{\alpha_v P_s}{(2\pi m k T)^{1/2}} \quad (2)$$

This is the basis of the Langmuir evaporation technique for measuring saturated vapour pressures of simple substances for the reaction  $\text{M(s)} \rightarrow \text{M(g)}$  under the assumption of molecular flow conditions.

At pressures greater than  $\approx 10^{-2}$  Torr, the assumption of molecular flow breaks down resulting in a hydrodynamic flow regime in the gas phase with associated density, pressure, and temperature gradients. The rate of evaporation from the solid is still given by eq. (2), but the net flux transfer from the solid phase into the gas phase can be considerably reduced due to the backscattering of particles from the gas phase back onto the surface. On the basis of a one dimensional steady state kinetic description of the evaporation of a simple solid, this net flux transfer can be shown to be [58,59] for  $\alpha_v = 1$

$$\dot{n}_+^{\text{net}} = \frac{n_s \bar{v}}{4} \left( 1 - \frac{b n_g \bar{v}}{n_s} \right) \quad (3)$$

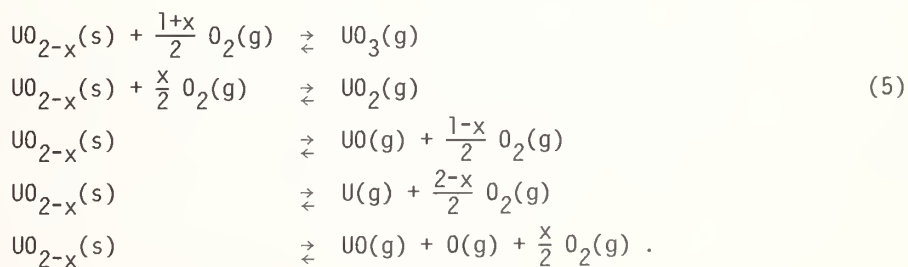
where the second term in brackets is the modification to eq. (2) required to account for the backscattered flux. Denoting this total backscatter coefficient by  $\beta$ , we can interpret it in terms of an equilibrium backscatter ( $n_g v_g / n_s \bar{v}$ ), a non-equilibrium backscatter  $b$  and a factor  $\tilde{F}^-$  which reduces the actual backscatter due to the forward motion in the gas phase. These are given by:

$$\begin{aligned}
 b &= (4S_\infty^2 - 2 - P_s/P_g) / \tilde{G}^- \\
 \tilde{F}^- &= \sqrt{\pi} S_\infty (-1 + \operatorname{erf} S_\infty) + e^{-S_\infty^2} \\
 \tilde{G}^- &= (2 S_\infty^2 + 1)(1 \pm \operatorname{erf} S_\infty) - \frac{2}{\sqrt{\pi}} S_\infty e^{-S_\infty^2} \\
 S_\infty &= u_\infty / (2RT_\infty)^{1/2} .
 \end{aligned} \tag{4}$$

It is interesting to note that at the sonic point  $S_\infty \rightarrow 1$ ,  $b \rightarrow 7.8$ ,  $\tilde{F}^- \rightarrow 8.5 \times 10^{-2}$ , and  $\beta$  the total backscatter coefficient  $\rightarrow 0.18$ . Thus, it can be seen that eq. (2) is still approximately valid (apart from an 18 percent correction) for the net flux transfer into the gas phase for the case of strong evaporation into vacuum under conditions of hydrodynamic flow.

Measurements of free evaporation rates have been a useful way of calculating equilibrium vapour pressures of "normal" solids at high temperature. In the case of dissociating multicomponent systems, measurement of the free evaporation rates alone (without more detailed kinetic studies) will, in general, not yield the equilibrium vapour pressure. In these systems, evaporation into vacuum can be completely different from that under equilibrium conditions.

This is precisely the situation encountered in the laser evaporation experiment on nuclear fuel materials discussed in this paper. A relationship between the equilibrium vapour pressure and the integrated mass loss must therefore be established. The approach taken in the Breitung calculation [60] is to assume complete thermodynamic equilibrium between the liquid and the gas (as in a closed box experiment) and consider the reactions



The partial pressures of the species can be calculated using the law of mass action. To close this system of equations, the oxygen potential calculated using Blackburn's model [61] and extrapolated over the required range in stoichiometry was used. Hence, for any

given stoichiometry, the partial pressures in the gas phase can be calculated as a function of temperature. However, at the high rates of evaporation encountered in laser surface heating experiments, the concept of forced congruent evaporation (FCE) is introduced whereby the (O/U) ratio in the gas phase must equal that in the bulk material. The consequence of imposing this condition on the gas composition in the above set of equations is that the solid composition in equilibrium with the gas is then fixed. To attribute the partial pressures and composition predicted by eq. (5) to the dynamic, non-equilibrium laser evaporation is clearly not sound, since they refer to equilibrium conditions.

As an alternative to this approach, the present authors do not assume thermodynamic equilibrium between the solid and gas but only in the gas itself. Thus, the gas reactions considered are:



again imposing the condition that  $(\text{O/U})_g = (\text{O/U})_{\text{bulk}}$  as stated earlier. It is clear, however, that an additional constraint is required to solve the system of eq. (6) together with the FCE condition, since there are six unknowns and only five equations. This is provided by gas dynamics, by equating the net mass flux leaving the surface to the mass flux at the sonic point, i.e.,

$$\dot{m}_+ = (\rho_g v_g)_{\text{sonic point}} = \rho_g \left( \frac{\gamma k T_g}{m} \right)^{1/2} \quad (7)$$

which provides the gas density evaluated at the sonic point. For any gas temperature  $T_g$ , the set of eqs. (6)-(7) together with the FCE conditions can be solved for the partial pressures of the various species at the sonic point in the gas phase. This approach is more appealing since through eq. (7) experimental information is input as a parameter in the calculation, and this is not included in the Breitung approach. The temperature used in eqs. (6)-(7) needs to be measured spectroscopically or be deduced from gas dynamic calculations. A gas dynamic calculation is underway to provide the temperature ratio and to provide the relationship between the saturated vapour pressure and the pressure at the sonic point calculated using eqs. (6)-(7).

## 5. Structure of an Evaporating Jet

This study of the structure of an evaporating jet is intended to give a simple kinetic theory description of vapour motion for arbitrarily strong evaporation rates from an interphase boundary of circular shape into a vacuum. The expansion is assumed to be a steady one.

The first step is to show that the solution of the problem of the jet structure may be reduced to the solution of three simpler problems. The starting point of the analysis is the Boltzmann equation [62,63] for the molecular distribution function  $f$ . The mean free path  $\ell_L$  at the interphase boundary is taken as a perturbation parameter, and this leads to a singular perturbation problem. The latter is handled by the now classical method of matched asymptotic expansions [64]. This leads to the recognition of the existence of three basic regions, where the dependence of the solution on the space variables and the mean free path  $\ell_L$  is different (fig. 5). Near the surface, the distribution function  $f$  varies considerably on the scale of the mean free path, and hence is to the lowest order in  $\ell_L$  a function of  $x/\ell_L$  ( $x$  denoting the Cartesian coordinate in a direction normal to the wall). At distances from the wall much larger than the mean free path ( $x \gtrsim 200 \ell_L$ ),  $f$  becomes practically independent of  $\ell_L$  and depends on  $r$  and  $\theta$ ,  $r$ ,  $\theta$  and  $\phi$  being the usual polar coordinates (the polar axis is along the normal to the wall). At even larger distances from the wall, the mean free path becomes so large that a new change of regime takes place; to lowest order, the dependence of the distribution function  $f$  on  $\ell_L$  is as follows [69]:

$$f = \ell_L^2 F(r\ell_L, \theta; \ell_L^{2/3} \underline{c}) \quad (8)$$

where  $\underline{c}$  denotes the random molecular velocity (i.e., the velocity with respect to the bulk motion of the gas).

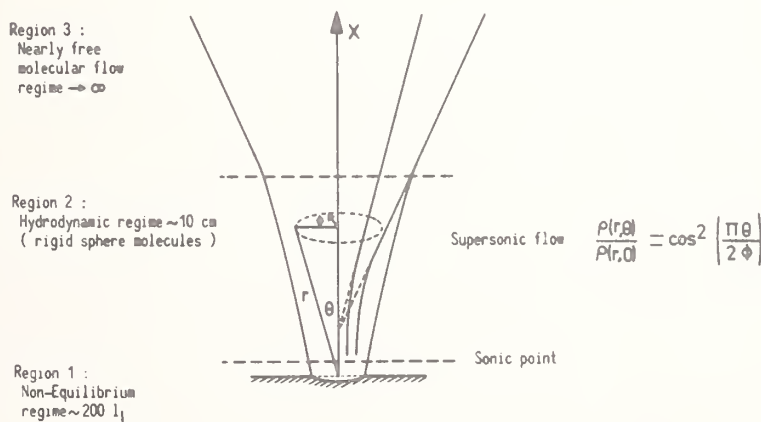


Figure 5. Schematic diagram of the laser induced gas jet showing the three regions considered in the Gas Dynamic model. (For clarity the scale of region 1 is largely magnified.)



Thus, three different problems have to be solved, one for each region and the three solutions matched. The theory so far has been restricted to the case of a single monatomic gas, but calculations for a binary mixture are under way and the study of the effects of internal degrees of freedom is planned for the near future.

The treatment of the region close to the evaporating boundary is based on an approximate method, first used by Ytrehus [59], which is the logical development of a simple calculation first carried out by Anisimov [58]. According to this treatment, the vapour cannot reach supersonic speeds in the region near the boundary and, as a consequence, the estimate of Anisimov that 18 percent of the emitted molecules are scattered back is confirmed. In addition, the study of this "inner" region shows that the thickness of the latter is of the order of  $200 \ell_L$  and allows a computation of the changes of the physical quantities to their values at the sonic point. In the "intermediate" region ( $x \gtrsim 200 \ell_L$ ), the flow is governed by the inviscid fluid equation, which has to be solved with the boundary conditions appropriate to an expansion from a disk where the flow is sonic and normal to the disk itself. Computations and approximate analytic solutions are available for this region [65-68].

Important properties of the sonic expansion into a vacuum are that the Mach number of the jet increases monotonically along the axis, and the computed flow exhibits a rather simple and self-similar development in the inertia-dominated region of high Mach number flow. The streamlines appear to radiate from a "source" in front of the sonic disk, and density decreases along each streamline in proportion to the inverse square of distance from the source.

The existence of the third or "outer" region is related to the fact that the increase in Mach number does not continue indefinitely, as predicted by the continuum theory; this circumstance is predicted by both theoretical and experimental work on free jet expansions [69-78]. As a consequence, the kinetic "temperatures" related to radial and transversal motions behave differently, the former tending to a nonzero constant, the latter to zero. The distance at which these effects become important depend strongly on the molecular law of interaction, a longer range leading to larger distances. For rigid sphere molecules, the continuum solution for an expansion of a gas with  $\ell_L = 10^{-6}$  cm from a disk of  $10^{-1}$  cm in diameter leads to a critical distance of the order of 10 cm.

The above analysis and evaluations are based on the assumption that all the molecules hitting the wall are adsorbed. The analysis may be extended to cover the case of a partially reflecting surface. In this case, the analysis presented by Ytrehus for the region close to the evaporating boundary is no longer sufficient and the estimate that 18 percent of the emitted molecules are scattered back is no longer valid. Computations show that the fraction  $\gamma$  of molecules scattered back, ranges from 18 percent (when the fraction  $\alpha$  of adsorbed molecules is unity), to 25 percent (when  $\alpha \rightarrow 0$ ). This leads to a mass defect in the molecules travelling downstream equal to  $\alpha\gamma$  and therefore ranging from 18 percent to 0. ( $\beta$  of Section 4 equals  $\gamma$  for  $\alpha = 1$ .)

## 6. Temperature Measurement by Optical Pyrometry and Spectroscopy

Optical pyrometry capable of both high temporal and spatial resolution, as previously shown [52], was found to be the most useful technique for temperature measurement under the extreme conditions of microsecond heating at high rates of evaporation. The limit of the applicability of optical pyrometry is clearly given by the absorption of the emitted light from the surface of the laser target in the gas jet. Therefore, a detailed analysis of optical absorption is required. Beyond the limits of optical pyrometry, the measurement of the gas temperature by spectroscopic techniques and the deduction of the surface temperature via a gas dynamic model may present a useful alternative at higher temperatures.

Laser induced gas jets at temperatures above 5000 K with laser power densities above  $10^7 \text{ W/cm}^2$  are partially ionized. Various physical phenomena can occur due to interaction between the incoming laser light and the gas jet [73-81], depending mainly on the intensity of the radiation. Further, the absorption of light has implications on temperature measurements.

For laser intensities below about  $10^7 \text{ W/cm}^2$ , the laser energy goes mostly into evaporation. The motion of the gas jet can be described by kinetic theory and hydrodynamic equations (Sections 4 and 5). The interaction of light with this gas jet can then be treated as a small perturbation, which has little influence on the gas flow. The following effects are of interest:

- i) the heating of the gas jet by absorption of the incoming laser light, introducing an error in the deduction of surface temperature from measured gas temperatures
- ii) absorption of light emanating from the surface, and its effect on pyrometric measurement of the surface temperature, and
- iii) the absorption of light emitted by atoms or molecules in the gas jet and its effect on spectroscopic temperature measurement.

For laser intensities above  $10^9 \text{ W/cm}^2$ , the gas dynamic description needs to be refined so as to include the strong absorption of laser light in the partially ionized gas jet. Due to the balance between absorption, temperature, and mass of material evaporated, there exists a stable optimum for the plasma thickness, usually taken as of unit optical thickness. This allows a self-similar solution to be constructed for the case in which the physical quantities,  $\underline{v}$  (velocity),  $T$  (temperature), and  $n$  (density) depend on one space coordinate  $x$  and time  $t$ . For temperatures below 5000 K, it is necessary to consider light interaction with the evaporating material as a perturbation that does not significantly affect the gas dynamical flow. In order to estimate the effects of light interaction with the gas jet, the degree of ionization and the absorption coefficient need to be calculated. The second approach to deduce the required surface temperature from spectroscopically determined gas temperatures is limited by the uncertainty of gas dynamic calculations on the temperature drop within the first region as described in Section 5. In addition, the accuracy of spectroscopic techniques under conditions of optical absorption, assuming cylindrical symmetry, needs further investigation.

## 6.1 Temperature limit of pyrometry due to optical absorption

### 6.1.1 The degree of ionization of the gas jet

The electron and ion density of a weakly ionized gas can be calculated as a function of total density and temperature by using the Saha equation [82], assuming ideal gas behaviour for  $UO_2$ . Neglecting dissociation,

$$\frac{n_i n_e}{n_m} = \left( \frac{2\pi m k T}{h^2} \right)^{3/2} \exp(-I/kT) , \quad (9)$$

where  $n_i$ ,  $n_e$ , and  $n_m$  are the densities of ions, electrons, and neutral molecules respectively. For single ionization,  $n_i = n_e$ , and  $n_T = n_m + n_i$  where  $n_T$  is the total density,  $m$  is the electron mass,  $T$  is the temperature,  $I$  is the ionization potential,  $k$  is Boltzmann's constant, and  $h$  is Planck's constant. If  $\alpha$  is the degree of ionization ( $\alpha \ll 1$ ), where

$$n_i = n_e = \alpha n_T \quad (10)$$

$$\alpha = (2/n_T)^{1/2} \left( \frac{2\pi m k T}{h^2} \right)^{3/4} \exp(-I/2kT) . \quad (11)$$

### 6.1.2 Reduction of the ionization potential

The use of the Saha equation with the ionization potential of isolated  $UO_2$  molecules yields too low a value for  $\alpha$  due to the presence of neighbouring molecules. There exist two simple methods of calculating the reduction in the ionization potential [83].

The nearest neighbour overlap approach. In this approach, the ionization potential is reduced because the potentials of neighbouring atoms overlap allowing excited electrons to move from one to the other, thus making them effectively free electrons [84]. The reduction is given by,

$$\Delta I_n = R a_0 / r , \quad (12)$$

where  $a_0$  is the Bohr radius and  $r = \left( \frac{4\pi}{3} n_T \right)^{-1/3}$ , and  $R$  is Rydberg's constant.

The Debye theory of the reduction in the ionization potential. In a plasma or ionized gas, charges of one sign tend to have, on the average, an excess charge of the opposite sign in their neighbourhood. The energy of ionization is diminished because both newly created charges are attracted by surrounding charges. The energy diminution depends upon the charges of the particles, the plasma density, and temperature, but not on the detailed structure of the atoms involved.

It can be shown [83] that the reduction is given by,

$$\Delta I_D = \frac{e^2}{4\pi\epsilon_0 \rho_0} , \quad (13)$$

where  $\epsilon_0$  is the dielectric constant of the vacuum, and  $\rho_0$  is the screening length,

$$\rho_0 = \left( \frac{\epsilon_0 kT}{e^2 2n_e} \right)^{1/2} . \quad (14)$$

In this case, the reduction must be calculated self consistently since  $n_e$  depends on  $\Delta I_D$  via the Saha equation.

At a surface temperature of 6000 K, implying a gas temperature (at the sonic point) of 4000 K (see Section 5), the reduction amounts to  $\Delta I_D = 0.27$  eV and  $\Delta I_n = 0.76$  eV. The nearest neighbour approach is usually considered to lead to too high reductions in the ionization potential [83], presumably due to the neglect of the electrostatic interaction. In laser surface heating, the kinetic energy of ions and electrons is of the same order as the electrostatic potential energy of interaction, and therefore the applicability of the Debye model can also be questioned. The influence of the reduction of the ionization potential has therefore been checked by using both values in Section 6.2.

#### 6.1.3 Absorption coefficient

The main processes as of absorption in a laser induced gas jet are photoionization and inverse Bremsstrahlung. The absorption coefficient for light with frequency  $\nu$  ( $K_\nu = (l)^{-1}$  where  $l$  is the photon mean free path), is given by [84],

$$K = \frac{10^{-7} n_T Z^2 \exp\{(h\nu - I_{\text{eff}})/kT\}}{T^2 (h\nu/kT)^3} \text{ cm}^{-1} , \quad (15)$$

where  $Z$  is the ionic charge equal to 1, and  $I_{\text{eff}} = I - \Delta I_{n,D}$ .

#### 6.1.4 Optical absorption

In order to estimate the limits of applicability of optical pyrometry, the total absorption in the gas jet needs to be calculated as a function of  $x$  by performing the necessary integrations, using the expression

$$I(x) = I(0) \left( \exp - \int_0^x K_\nu(y) dy \right) \quad (16)$$

where  $K_\nu$  is given by equation (15).

In order to determine an upper limit of applicability of optical pyrometry, it is sufficient to take the highest values of temperature and density in the gas, since these will clearly overestimate the absorption. A rapid temperature drop to the sonic point ( $T_g \approx 2/3 T_s$ ,



$n_g \approx \frac{1}{3} n_s$ ) is expected according to Anisimov [58] for a monoatomic gas. Since the first region extends over approximately 200 mean free paths [59], the absorption in this layer can be neglected.

Hence, the temperature and density at the sonic point have been taken as representative values for the gas jet, both decreasing with increasing  $x$ . It should also be noted that only the translational degrees of freedom of  $UO_2$  have been considered, and this amounts to assuming that the internal degrees of freedom are not relaxed at the sonic point.

Internal degrees of freedom, dissociation, and ionization will be incorporated into the gas dynamic model. The calculations have been carried out using the following procedure. The saturated number density ( $n_s$ ) is obtained from the vapour pressure equation and the ideal gas law at temperature  $T_s$  [52].  $K_v$  is calculated for the given values of  $n_g$ ,  $T_g$ , and  $I_{eff}(n_g, T_g)$ . The results are given in table 2 for  $K_v$ ,  $\alpha$ ,  $\Delta I_n$  at various temperatures. For a surface temperature of 6000 K,  $T_g$  is 4000 K,  $\Delta I_n = 0.76$  eV,  $\Delta I_D = 0.27$  eV, and  $K_v$  changes from  $1.66 \text{ cm}^{-1}$  to  $0.35 \text{ cm}^{-1}$ . Using  $\Delta I_D$  has a similar effect on other values of  $K_v$ .

To obtain a limiting value for  $K_v$ , radiation is considered to be coming from the surface of the target through the gas to the pyrometer. Then, the condition that no more than 5 percent of the radiation should be absorbed is imposed, such that  $K_v x = 0.05$  where  $x$  is the spatial coordinate. Taking  $x = 1 \text{ mm}$  (i.e. equal to radius of the focal spot), then  $K_v = 0.5 \text{ cm}^{-1}$ . From table 2, it can be seen that the limit is 6000 K (surface temperature), and hence it can be concluded that optical pyrometry can be used up to at least 5000 K.

Table 2. Degree of ionization, and photon mean free path for different temperatures.

$T_s$ (K)	$T_g$ (K)	$n_s (\text{cm}^{-3})$	$n_g (\text{cm}^{-3})$	$\Delta I$ (eV)	$I_{EFF}$ (eV)	$K_v^{-1} (\text{cm})$	$\alpha$ (%)
7500	5000	$9.5 \times 10^{21}$	$3.2 \times 10^{21}$	1.4	4.1	$1.4 \times 10^{-3}$	0.6
7000	4667	$5.3 \times 10^{21}$	$1.4 \times 10^{21}$	1.1	4.4	$1.6 \times 10^{-2}$	0.4
6000	4000	$1.3 \times 10^{21}$	$4.5 \times 10^{20}$	0.76	4.7	$6.0 \times 10^{-1}$	0.15
5000	3333	$1.5 \times 10^{20}$	$0.5 \times 10^{20}$	0.36	5.1	$1.4 \times 10^2$	0.05
4000	2667	$8.8 \times 10^{18}$	$2.9 \times 10^{18}$	0.14	5.36	$2.7 \times 10^5$	0.001

where  $T_s$  = temperature at the surface,

$T_g$  = temperature of the gas,

$n_s$  = saturated vapour density,

$\Delta I$  = reduction of the ionization potential,

$K_v$  = absorption coefficient for light with frequency, and

$\alpha$  = degree of ionization.



## 6.2 Deduction of surface temperature from spectroscopic measurements

Above a surface temperature of 5000 K where optical absorption becomes increasingly important, an alternative method is necessary to determine the surface temperature. This can be done by spectroscopic measurements of the gas temperature as a function of the distance from the surface, and deduction of the surface temperature by extrapolating down to the surface using a temperature variation deduced theoretically from a gas dynamic model. The accuracy of this surface temperature deduction procedure depends, on the one hand, on the validity of the gas dynamic model, which still needs to account for the multi-species vapour phase, relaxation of internal degrees of freedom and dissociation, and, on the other hand, on the accuracy of the spectroscopic technique employed. Three such techniques have been considered, namely, the relative line intensity method, the line reversal technique, and Doppler broadening.

### 6.2.1 Relative line intensity method

Let  $I_{K'K''}$  be the measured intensity of radiation due to a transition in an atom or molecule between states of energy  $E_{K'}$  and  $E_{K''}$ , where  $K'$  and  $K''$  are the quantum numbers of the states chosen. Using two lines, the relative intensity  $r = I_{K'K''}/I_{L'L''}$  is measured.

Then the temperature is given by Broida [85] and Griem [83] as

$$T = (E_{L'} - E_{K'}) / k(\ln r - \ln s - 4 \ln q) \quad (17)$$

where

$$s = A_{K'K''}/A_{L'L''} \quad , \quad q = \nu_{K'K''}/\nu_{L'L''}$$

$$\nu_{K'K''} = (E_{K'} - E_{K''})/h \quad , \quad \nu_{L'L''} = (E_{L'} - E_{L''})/h$$

and  $A_{K'K''} = g_{K'} a_{K'K''}$  where  $g_{K'}$  is the degeneracy of the state with energy  $E_{K'}$ ,  $a_{K'K''}$  is the transition probability for the transition  $K' \rightarrow K''$ ,  $h$  is Planck's constant, and  $k$  is Boltzmann's constant. This means that the relative transition probabilities must be known. By differentiating eq. (17)

$$\Delta T/T = \{kT/(E_{K'} - E_{L'})\} \Delta r/r \quad (18)$$

gives the error  $\Delta T$  in the temperature if  $\Delta r$  is the error in  $r$ . Errors can be reduced by taking  $E_{K'} - E_{L'}$  as large as possible and by using several transitions and making a Boltzmann plot. The radial temperature distribution can be determined by using the Abel inversion technique.

### 6.2.2 Line reversal technique

In this technique, the following two light intensities in a particular spectral region are compared: (i) the light intensity  $E_1$  emitted by the gas jet, and (ii) the total light intensity  $E_2$  emitted by the gas, and that from the reference source which has passed through the gas jet. Independently of the line shape of the gas jet radiation spectrum, the temperature of the gas jet  $T_g$ , is determined as in Soloukin [86]

$$T_g^{-1} = T_0^{-1} + (\lambda/C_2) \log(1-E_2/E_1) \quad (19)$$

where  $C_2$  is a constant, and  $T_0$  is the temperature of the reference source.

### 6.2.3 Line broadening

The width of a discrete spectral line depends, in part, upon the translational velocity distribution of the emitting particles. For a gas composed of atoms or molecules of atomic weight  $M$ , the Doppler width  $\Delta\lambda_D$  of a given spectral line, is measured. Then the temperature  $T$  can be obtained from the formula [85],

$$\Delta\lambda_D/\lambda_D = 7.2 \times 10^{-7} (T/M)^{1/2} . \quad (20)$$

This width is due to the Maxwell distribution of the velocities of the molecules. Any uniform motion of the gas will only give a frequency shift. The line reversal technique may be difficult to apply with pulsed laser surface heating. The line broadening technique works best at low densities where broadening due to other effects (pressure broadening, Stark effect) is small, and when molecules of low atomic weight are used (these give a larger value of  $\Delta\lambda_D$ ).

## 7. Conclusion

The measurement of thermophysical properties well above the melting point of refractory materials has been demonstrated on vapour pressure and equation of state studies, required as input data for reactor safety analysis. A survey on the critical point data of  $UO_2$ , predicted by various theoretical models, yielded a large uncertainty in the critical temperature, ranging from 5500 to almost 10,000 K, thus prompting the necessity of applying more appropriate models such as Monte Carlo technique or molecular dynamics. The laser pulse surface heating technique has proved to be a powerful instrument for high temperature research above the melting point. In addition to other dynamic techniques, such as exploding wire, electron, or neutron pulse techniques, the laser induced gas jet allows mass spectrometric and spectroscopic analysis under these extreme conditions. High speed optical pyrometry was found to be the only technique yielding adequate temporal and spatial resolution up to temperatures of the order of 5000 K. Above this limit, a deduction of

surface temperature from spectroscopic gas measurements, using gas dynamic relationships, seems the most promising method of approach. The experimental arrangement used for gas jet diagnostics is described.

#### References

- [1] Meyer, R. A. and Wolfe, B. E., Trans. Am. Nucl. Soc. 7 [1], 111 (1964).
- [2] Christensen, J. A., Thermal Expansion of Uranium Dioxide, HW-75148 (1962).
- [3] Hougén, O. A., Watson, K. M., and Ragatz, R. A., Chemical Process Principles, Vol. II, Thermodynamics, 2nd Ed. (J. Wiley, New York, 1959).
- [4] Ackermann, R. J., Gilles, P. W., and Thorn, R. J., J. Chem. Phys. 25, 1089 (1956).
- [5] Miller, D., ANL 7120 (1956).
- [6] Christensen, J. A., Thermal expansion and change in volume on melting for uranium dioxide, J. Am. Ceram. Soc. 46, 607 (1963).
- [7] Menzies, C., UKAEA Rep. TRG-1159(D) (1966).
- [8] Uranium Ceramics Data Manual DEG Report 120(R), (1960).
- [9] Robbins, E. J., UKAEA Rep. TRG-1344 (R) (1966).
- [10] Chikalla, T. D., The liquidus for the system  $UO_2$ - $PuO_2$ , HW 69832 (1961).
- [11] Ohse, R. W., J. Chem. Phys. 44, 1375 (1966); EUR 2166.e (1964).
- [12] Booth, D. L., UKAEA-TRG Report 1974 (R/X) (1968, 1974).
- [13] Hausner, H., J. Nucl. Mat. 15, 179 (1965).
- [14] Hein, R. A., Sjö Dahl, L. H., and Szwarc, R., J. Nucl. Mat. 25, 99 (1968).
- [15] Gillan, M. J., Thermodynamics of Nuclear Materials 1974, Vol. I, p. 269 (IAEA, Vienna, 1975).
- [16] Tetenbaum, M., and Hunt, P. D., J. Nucl. Mat. 34, 86 (1970).
- [17] Fischer, E. A., Kinsman, P. R., and Ohse, R. W., J. Nucl. Mat. 59, 125 (1976).
- [18] Abramowitz, S., Acquista, N., and Thompson, K. R., J. Phys. Chem. 75, 2238 (1971); 76, 648 (1972).
- [19] Kerrisk, J. F. and Clifton, D. G., Nuclear Technology, 16, 531 (1972).
- [20] Affortit, C. and Marcon, J., Rev. Int. Hautes Temp. et Refract. 7, 236 (1970).
- [21] Kapil, S. K., J. Nucl. Mater. 60, 158 (1976).
- [22] Reedy, G. T. and Chasanov, M. G., J. Nucl. Mat. 42, 341 (1972).
- [23] Browning, P., Gillan, M. J., and Potter, P. E., UKAEA Rep. AERE-R 8129 (1977).
- [24] Ohse, R. W., Berrie, P. G., Bogensberger, H. G., and Fischer, E. A., Thermodynamics of Nuclear Materials 1974, Vol. I, p. 307 (IAEA, Vienna, 1975).
- [25] Van der Waals, J. D., Doctoral Dissertation, Univ. of Leiden, 1873.
- [26] Scott, R. L., in Physical Chemistry - An Advanced Treatise: Liquid State, H. Eyring, D. Henderson, and W. Jost, eds. (Academic Press, New York), Vol. 8A, chap. 1.
- [27] Pitzer, K. S., J. Chem. Phys. 7, 583 (1939).
- [28] Lewis, G. N. and Randall, M., Thermodynamics (McGraw-Hill, New York, 1961) 2nd Edition, revised by K. S. Pitzer and L. Brewer.

- [29] Hirschfelder, J. O., Curtiss, C. F., and Bird, R. B., in Molecular Theory of Gases and Liquids (Wiley, New York, 1954).
- [30] Riedel, L., Chem. Ing. Tech. 26, 83, 257, 679 (1954).
- [31] Catlow, C. R. A. and Lidiard, A. B., in Proc. of Conference of Thermodynamics of Reactor Materials, Vol. II, p. 27 (IAEA, Vienna, 1974).
- [32] Blank, H., in Proc. of Conference of Thermodynamics of Reactor Materials, Vol. II, p. 45 (IAEA, Vienna, 1974).
- [33] Verbist, J. J., Plutonium and Other Actinides, H. Blank and R. Lindner, eds. p. 409 (North Holland, Amsterdam, 1975).
- [34] Partington, J. R., Treatise on Physical Chemistry, Vol. I, p. 639 (Longman, Green, 1949).
- [35] Cailletet, L. and Mathias, E., Compt. Rend. 102, 1202 (1886).
- [36] Eyring, H. and Jhon, M. S., Significant Liquid Structures (Wiley, New York, 1969).
- [37] Jhon, M. S. and Eyring, H., in Theoretical Chemistry, Advances and Perspectives, Vol. 3 H. Eyring and D. Henderson, eds., p. 56 (Academic Press, New York, 1978).
- [38] Carlson, C. M., Eyring, H., and Ree, T., Proc. Natl. Acad. Sci., 333 (1960).
- [39] Lu, W. C., Ree, T., Gerrard, V., and Eyring, H., J. Chem. Phys. 49, 797 (1968).
- [40] Vilcu, R. and Misdolea, C., J. Chem. Phys. 46, 906 (1967).
- [41] Wood, W. W., in Physics of Simple Liquids, H. N. V. Temperly, J. S. Rowlinson, G. S. Rushbrooke, eds., chap. 5 (North Holland, Amsterdam, 1968).
- [42] Ree, F. H., in Physical Chemistry, An Advanced Treatise, H. Eyring, et al. eds. p. 157 (Academic Press, New York, 1971).
- [43] Barker, J. A. and Henderson, D., Rev. Mod. Phys. 48, 581 (1976).
- [44] Cezairliyan, A., Morse, M. S., Berman, H. A., and Beckett, C. W., J. Res. NBS, 74A, 65 (1970).
- [45] Gathers, G. R., Shaner, J. W., and Brier, R. L., Rev. Sci. Instrum. 47, 471 (1976).
- [46] Seydel, U. and Fucke, W., Z. Naturforsch., 32a, 994 (1977).
- [47] Reil, K. O. and Cronenberg, A. W., Trans. Am. Nucl. Soc. 27, 576 (1977).
- [48] Benson, D. A., Application of pulsed electron beam vaporization to studies of  $\text{UO}_2$ , SAND-77-0429 (1977).
- [49] Asami, N., Nishikawa, M., and Taguchi, M., Thermodynamics of Nuclear Materials 1974, Vol. I, p. 287 (IAEA, Vienna, 1975).
- [50] Bober, M., Karow, H. U., and Schretzmann, K., Thermodynamics of Nuclear Materials 1974, Vol. I, p. 295 (IAEA, Vienna, 1975).
- [51] Tsai, H. C., Covington, A., and Olander, D. R., Materials and Molecular Research Division, Lawrence Berkeley Laboratory, California, Annual Report 1976, LBL-6016, UC-13, TID-4500-R65, 188.
- [52] Ohse, R. W., Babelot, J. F., Kinsman, P. R., Long, K. A., and Magill, J., High speed pyrometry and spectroscopy in laser pulse heating experiments at extreme rates of evaporation, VI European Conference on Thermophysical Properties of Materials, Dubrovnik, Yugoslavia, June 1978, to be published in High Temp.-High Press.
- [53] IWGFR Meeting on Equation of State of Materials of Relevance to the Analysis of Hypothetical Fast Breeder Reactor Accidents, Harwell, UK, June 1978.

- [54] Ohse, R. W., Berrie, P. G., Brumme, G. D., and Kinsman, P. R., 5th Int. Conf. on Plutonium and Other Actinides 1975, Baden-Baden, Sept. 1975, H. Blank and R. Lindner, eds. (North-Holland Publishing Company, Amsterdam, 1976).
- [55] Babelot, J. F., Brumme, G. D., Kinsman, P. R., and Ohse, R. W., Atomwirtschaft-Atomtechnik, Jahrgang XXII, Nr. 7-8, 387 (1977).
- [56] Bober, M., and Karow, H. U., Measurements of spectral emissivity of  $UO_2$  up to temperatures above the melting point, Colloque International sur les Oxydes Réfractaires pour Filières Energétiques de Haute Temperature, Odeillo, France, 1977.
- [57] Hertz, H., Ann. Physik, 17, 177 (1882).
- [58] Anisimov, S. I., Vaporization of a metal absorbing laser radiation, Soviet Physics JETP, 27, [1], 182-183 (1968).
- [59] Ytrehus, T., Kinetic theory description and experimental results for vapour motion in arbitrary strong evaporation, Von Karman Institute for Fluid Dynamics, Technical note 112, 1975.
- [60] Bober, M., Breitung, W., Karow, H. U., and Schretzmann, K., Reports KFK 2366 (1976), KFK 1276/3 (1976) Kernforschungszentrum Karlsruhe, Germany.
- [61] Blackburn, P. E., J. Nucl. Mat. 46, 244 (1973).
- [62] Cercignani, C., Theory and Application of the Boltzmann Equation (Scottish Academic Press, Edinburgh, and Elsevier, New York, 1975).
- [63] Cercignani, C., Mathematical Methods in Kinetic Theory (Plenum Press, New York, 1969).
- [64] Van Dyke, M., Perturbation Methods in Fluid Mechanics (Academic Press, New York, 1964).
- [65] Hill, R. and Pack, D. C., Proc. Roy. Soc. A 191, 524 (1947).
- [66] Smith, M. G., Quar. J. Mech. and Appl. Math., 12, 287 (1959).
- [67] Owen, P. L. and Thornhill, C. K., Aero. Res. Council Reports and Memoranda, 2616 (1968).
- [68] Ashkenas, H. and Sherman, F. S., in Rarefield Gas Dynamics, J. H. de Leeuw, ed., Vol. II, p. 84 (Academic Press, New York, 1966).
- [69] Hamel, B. S. and Willis, D. R., Phys. Fluids, 9, 829 (1966).
- [70] Freemand, N. C., AIAA J., 5, 1696 (1967).
- [71] Grundy, R. E., Phys. Fluids, 12, 2011 (1969).
- [72] Anderson, J. B. and Ferm, J. B., Phys. Fluids, 8, 780 (1965).
- [73] Krokhin, O. N., in Laser Handbook, F. T. Arrechi and E. O. Schulz-Dubois, eds. (North Holland, Amsterdam, 1972), p. 1371, PCh E7.
- [74] Kidder, R. E., in Proceedings of the Enrico Fermi Summer School of Physics, Physics of High Energy Density, P. Caldirola, ed., p. 306 (1971).
- [75] Caruso, A., in Proceedings of the Enrico Fermi Summer School of Physics, Physics of High Energy Density, P. Caldirola, ed., p. 353 (1971).
- [76] Gratton, R., in Proceedings of the Enrico Fermi School of Physics, Physics of High Energy Density, P. Caldirola, ed., p. 363 (1971).
- [77] Pert, G. J., Plasma Phys. 16, 1019 (1974).
- [78] Caruso, A. and Gratton, R., Plasma Phys. 10, 867 (1968).



- [79] Caruso, A. and Gratton, R., Plasma Phys. II, 839 (1969).
- [80] Caruso, A., Bertotti, B., and Guipponi, P., Nuovo Cimento, 45, 176 (1966).
- [81] Puell, H., Z. Naturforsch. 25a, 1807, 1815 (1970).
- [82] Landau, L. D. and Lifshitz, E. M., Statistical Physics, p. 323 (Pergamon Press, Oxford, 1969).
- [83] Griem, H. R., Plasma Spectroscopy, chap. 13 (McGraw-Hill, New York, 1964).
- [84] Zeldovich, Ya. B. and Raiser, Yu. P., Physics of Shock Waves and High Temperature Phenomena, W. D. Hayes and R. F. Probstein, eds., Vol. I, p. 131 (Academic Press, New York, 1967).
- [85] Broida, H. P., in Temperature-Its Measurement and Control in Science and Technology, H. C. Wolfe, ed., Vol. 2, p. 265 (Reinhold, New York, 1960).
- [86] Soloukin, R. I., in Gas Dynamics, P. P. Wegener, ed., Vol. 4, p. 313 (Dekker, New York, 1974).
- [87] Ohse, R. W. and von Tippelskirch, H., High Temp.-High Press. 9, 367 (1977).

#### Discussion

Question (Cater): I wonder why these curves (log pressure vs reciprocal temperature) are linear? There should be some heat capacity effects between this dense vapor and the liquid that, I would expect, make the vapor pressure curve non-linear.

Response (Ohse): These curves are actually not linear. As shown in figure 4, neither the measured, normalized, nor recommended vapor pressure curves are linear. The negative pressure deviation from the log p versus  $1/T$  plot, as indicated in figure 1 by the predicted critical point data, is however at 5000 K still too small, compared to the scatter of experimental data, to allow further extrapolation towards higher temperatures. Since law of mass action calculations would involve data extrapolations over several thousand degrees, reliable pressure data above 5000 K can only be obtained by an extension of measurements.

Question (Rosenblatt): Can you define the meaning of temperature under these extreme conditions? Do you have translational, vibrational and rotational equilibrium in the gas phase?

Response (Ohse): A gas dynamic program has been started, studying the structure and expansion of the laser induced gas jet into the vacuum, as shown in Section 5 of this paper. The theory will now be extended to the study of binary mixtures, and the effects of the various internal degrees of freedom. A first kinetic theory description of the vapor motion within the "inner" region, shown in figure 5, being of the order of 200 mean free paths, does not assume thermodynamic equilibrium between the solid and the gas. The gas temperature drops rapidly to  $2/3$  of the surface temperature at the sonic point. A nonequilibrium half plane cosine distribution changes by collisions into a spherical distribution, where thermodynamic equilibrium can now be assumed.

Question (Weltner): I realize this is for uranium oxide systems; have you ever tried a graphite system?

Response (Ohse): During the time we extended our equipment to include additional high speed diagnostics, as given in figure 3, such as multi-channel spectroscopy, time of flight mass spectrometry, and high speed photography, we did experiments on a series of inactive materials, such as stainless steel cladding materials and its Fe, Cr, Ni constituents. Extensive studies on graphite were not performed.

Question (Lincoln): What were the species you looked at in your mass spectrometer? We found lots of ions produced by the laser itself. Could you separate these on the basis of neutrals and ions?

Response (Ohse): The laser beam was focussed on to the surface under an angle sufficiently large to reduce laser light interaction to a minimum, and to avoid contamination of optical components by the evaporating gas jet. In addition, we were using a spike-free laser, thus avoiding the extreme spike power densities leading to high ionization. Preliminary examinations using a quadrupole mass spectrometer gave no evidence of large quantities of ions produced by laser light interaction with the gas jet. With our new equipment a Bendix time of flight mass spectrometer will be used to analyze the gaseous species. Gas dynamics will be used to interpret and relate results downstream.

is one  
the ad  
quieren  
range  
ticult  
materi

large  
pletect  
of sur  
through  
fresh

stirra  
the mo  
rium c  
light

ges is  
the co  
the me  
tor, a

tooth  
the wa  
the ga  
rle i

figure  
i atn

## A HIGH-TEMPERATURE TRANSPIRATION APPARATUS FOR THE STUDY OF THE ATMOSPHERE ABOVE VISCOUS, INCONGRUENTLY VAPORIZING MELTS

D. M. Sanders and W. K. Haller  
National Bureau of Standards  
Washington, DC 20234

### 1. Description of Apparatus

The entrainment of vapors in a carrier gas, commonly known as the transpiration method, is one of the oldest techniques for the measurement of vaporization behavior [1]<sup>1</sup>. Some of the advantages of the technique include experimental simplicity with no vacuum system requirement, straightforward control of atmosphere composition above the sample, and the wide range of partial pressures ( $10^2$ - $10^{-7}$  kPa or  $1$ - $10^{-9}$  atm.)<sup>2</sup> permitted. The technique is particularly useful in making studies of vaporization enhancement due to reactions between a material and its environment.

Despite these advantages, the high-temperature use of this method has been limited largely to congruently vaporizing substances because of the formation of surface layers depleted of more volatile components. One method used successfully to suppress the formation of surface layers during vaporization from glass melts involves bubbling the carrier gas through the melt [2]. The bubbling action serves the dual purpose of producing a continuously fresh surface and of circulating the melt. Since its original conception, the design of the stirrable transpiration apparatus (STA) has been modified to increase its versatility [3,4]. The most recent configuration is shown in figure 1. The apparatus consists of a Pt equilibrium chamber coaxially suspended in a double crucible. A high melting glass forms a gas-tight seal between the atmosphere above the sample and the external environment. Carrier gas is introduced through the central inlet tube, bubbles through the melt, and exits through the collection assembly whose details are shown in figure 2. In order to prevent foaming of the melt, sonic pulses produced by a loudspeaker, in turn, driven by a low-frequency generator, are directed at newly formed bubbles via the bubble breaking tube. The pulses are sawtooth shaped and have a frequency of 1 Hz. Polarity is such that the fast-rising side of the wave produces a movement of the loudspeaker membrane toward the equilibrium chamber. The gas leaves the broken bubbles and passes out of the equilibrium chamber through a 1 mm hole in a re-entrant capillary (figure 2). This restriction serves to increase the linear

<sup>1</sup>Figures in brackets indicate the literature references at the end of this paper.

<sup>2</sup>1 atm = 101.325 kPa.

flow velocity of the carrier gas minimizing the influence of diffusion of vapor from the equilibrium chamber. The re-entrant tube, furthermore, forces the flow of carrier gas to pass on the inside of the Pt collection tube. The alumina spacers, necessary to prevent Pt-Pt welding, are thus protected from exposure to the flow of carrier gas. (Diffusion of the entrained vapor species to the ceramic spacers is frequently negligible, but can be controlled when necessary [5] by adding a quench gas to inlet A in figure 2. The resulting gas flow indicated by arrows in figure 2 effectively suppresses diffusion of vapors to the ceramic spacer.) The collection tube, which is 6 mm o.d. by 33 cm long by 0.25 mm thick, is held, in turn, by a modified compression fitting in a collection tube holder made of Teflon. The entire assembly is sealed from the atmosphere with a double O-ring connector, as shown in figure 2.

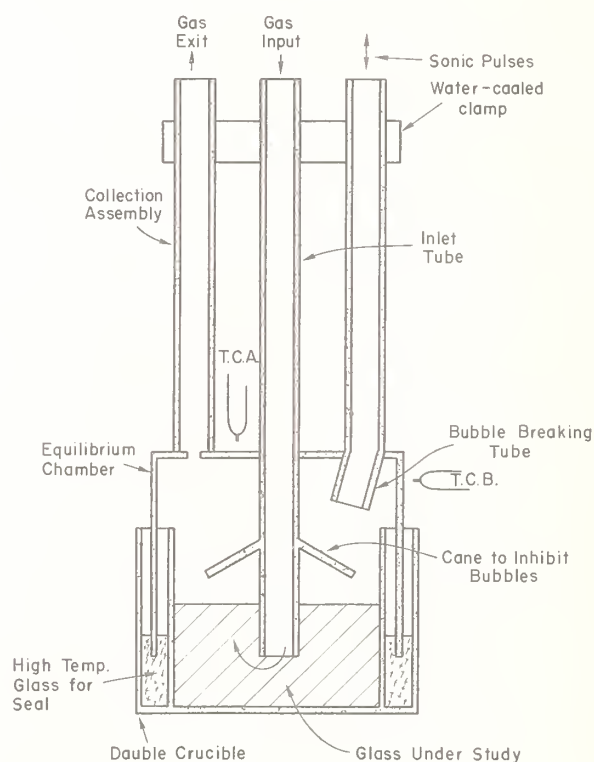


Figure 1. Schematic of stirrable transpiration apparatus.

The rate of gas flow is determined by a mass flow meter calibrated by the displacement of a Hg piston in a glass tube of known volume. All volumes and flow rates are normalized to STP<sup>3</sup>. Flow rates are maintained to within 0.3 percent with a 3-stage regulator and flow restriction produced by crushing stainless steel wire in 0.32 cm copper tubing. The carrier

<sup>3</sup>101.325 kPa 273 K.



gas is dried by passing through calcium sulfate and magnesium perchlorate before entering the equilibrium chamber. When required, water vapor was introduced to the carrier gas using a recondensing saturator described in [3]. The temperature of the saturator was held to within 0.01 °C with a thermostatic circulating fluid jacket. The volume of the water vapor was considered in the calculation of the total volume of the carrier gas.

Vaporized components are deposited mainly on the inside of the Pt collection tube where it enters the Teflon holder because the collection assembly is cooled at that point by the clamp (see figs. 1 and 2). Since all condensates are not trapped at this point, the gas leaving the Teflon collection tube holder is next passed through an electrostatic precipitator assembly, one module of which is pictured in figure 3. To provide for ease of washing, the precipitator modules are constructed so that only Teflon, platinum, and Viton are exposed to the carrier gas. During initial runs, as many as three modules were stacked in series

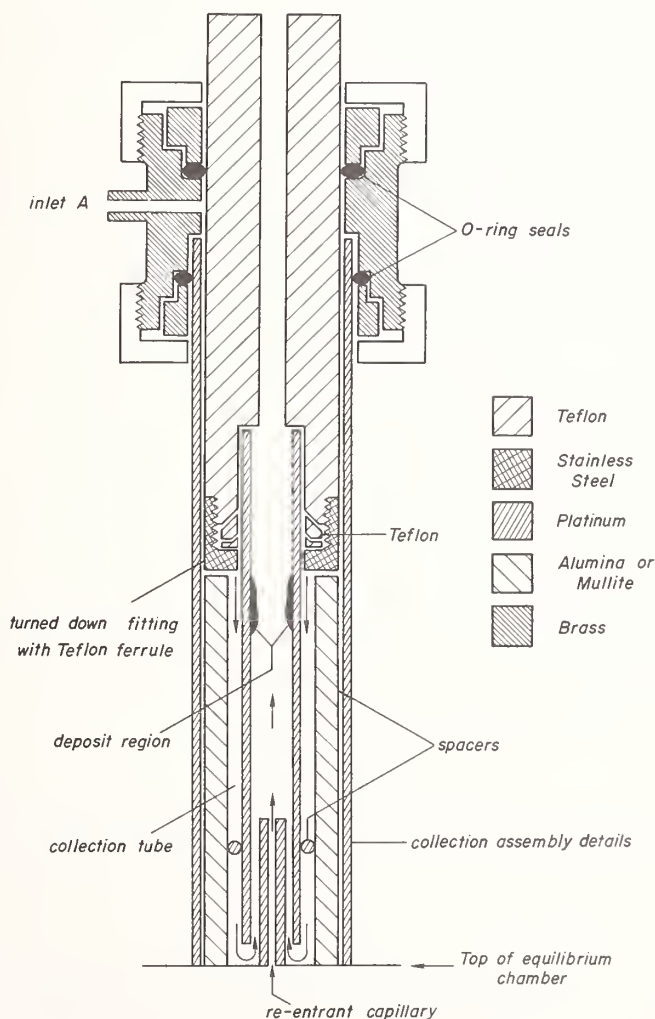


Figure 2. Details of collection assembly tube. Carrier gas can be introduced to inlet A to inhibit diffusion as described in the text.

with the amount of precipitate washed from each module being analyzed separately. It was found that the module closest to the furnace trapped 95 times more precipitate than the second module with the amount trapped in the third module being too small to measure. A two-module precipitator stack was therefore adopted. The solid condensates are washed from the collection tube with appropriate solvents (in the present case, 5 percent HF solution) and combined with the contents washed from the electrostatic precipitator. The resulting solutions are then analyzed using an atomic absorption-emission spectrophotometer.

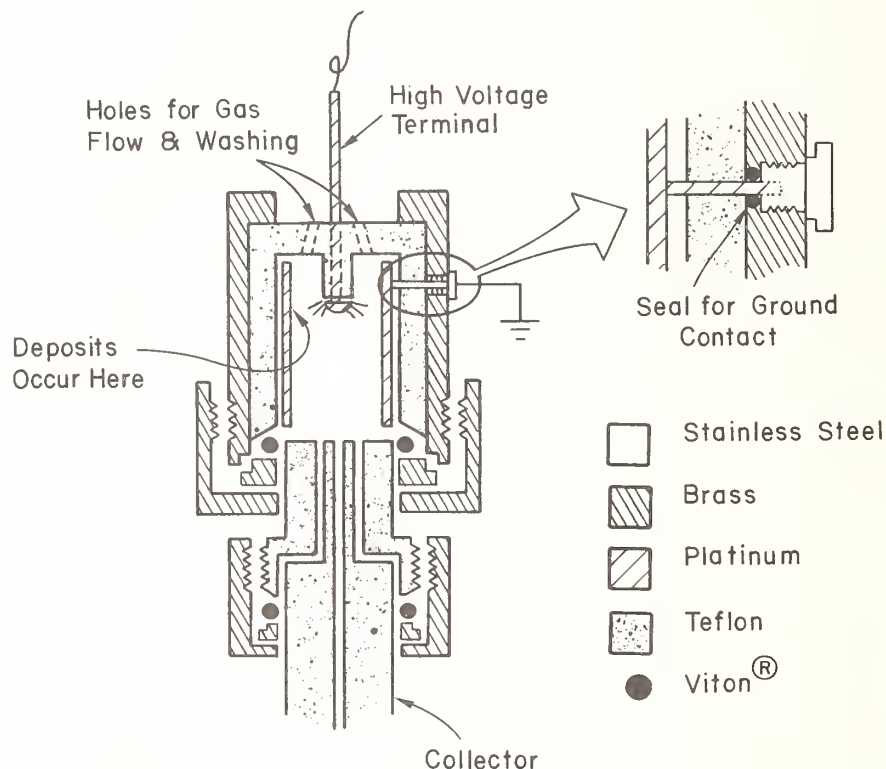


Figure 3. Schematic of a single module of the electrostatic precipitator assembly.

The figure shows this module on top of a Teflon interface which is, in turn, on a collector holder. The modules are designed to permit them to be nested in series to determine collector efficiency.

The collection bell and melt-crucible assembly are housed inside a box furnace using 10 SiC heating elements controlled by a Si rectifier. Two additional elements placed closer to the equilibrium chamber, near the top of the furnace cavity are powered by a separate autotransformer. The power to these elements is adjusted so that a thermocouple in position A (fig. 1) reads 2 °C hotter than a thermocouple in position B. A thermocouple introduced into the inlet tube so as to touch the melt produced a temperature reading within 0.5 °C of that from thermocouple B. The temperature reported in the present work was therefore read in position B.

Since a fresh surface is continually prepared by the bubbling through the melt, one would expect the formation of depleted films. However, insufficient stirring would be indicated by an increased apparent vapor density with increased stirring action. If it can be assumed that the stirring action is more vigorous when the carrier gas flow rate is increased, one would expect the apparent vapor density to increase with increasing flow rate. As will be discussed, this behavior does not occur, further indicating that the composition of the surface produced is indeed identical with that of the interior.

In addition to preventing the formation of depleted films, the experimental configuration must also have a useful range where vapor density is independent of carrier gas flow rate. In a traditional transpiration apparatus, proof that this condition is met results from plotting the rate of vaporization of one of the constituents with carrier gas flow rate. Figure 4 shows such a linear least-squares plot for a soda-lime-silica glass. The curve, produced without gas flow to inlet A (fig. 2) is linear and can be extrapolated near the origin. The small negative value for the intercept indicates a slight tendency for the transported vapor to diffuse to and react with the ceramic spacer. Other measurements at higher and lower temperatures indicate that this tendency is indeed temperature-sensitive with curves made below 1300 °C extrapolating through the origin and curves made above 1300 °C extrapolating through increasingly negative values. This explanation was checked by introducing  $N_2$  gas into side-arm A shown in figure 2. This caused gas to flow between the ceramic spacer and the outside of the collection tube, as indicated by the arrows in the figure. When this was done, curves similar to that in figure 4 having still larger negative intercepts retained the same slopes, but were shifted upward so that they, too, extrapolated through the origin.

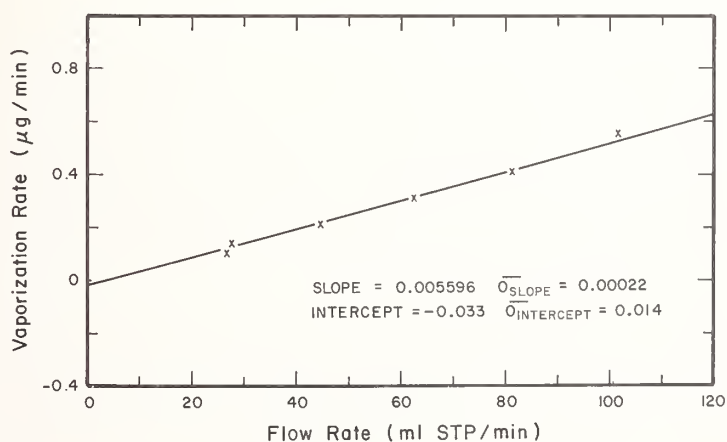


Figure 4. Transpiration curve obtained using present apparatus with dry Ar as carrier gas.

## 2. Activity of $\text{Na}_2\text{O}$ in the Binary $\text{Na}_2\text{SiO}_3$ System

The binary soda-silica system provides one of the simplest models for glass composition of industrial importance. One approach used to study this system involves the measurement of sodium vaporization as a function of glass composition. Preston and Turner [6], for instance, observed breaks in such plots which they attributed to the existence of stable compound-like species in the melts. Charles [7] used the same data coupled with thermodynamic considerations to explain the existence of liquid-liquid immiscibility. Since vaporization measurements on this system have proved useful and have typically been made using unstirred melts with poorly defined atmospheres above them [8], it seemed appropriate to employ the STA described here to check the validity of earlier measurements. Using vapor species information obtained in previous investigations [3,4], coupled with thermodynamic data from the literature [9,10], the activity of sodium oxide was calculated over the range of composition from 15 to 50 mol percent  $\text{Na}_2\text{O}$  for temperatures from 1100 to 1500 °C.

## 3. Experimental Considerations

In order to define the oxygen partial pressure, air was selected for the carrier gas. Water vapor at a partial pressure of 2.74 kPa or 0.027 atm was introduced using the reflux saturator described in [3]. The compositions of the glasses were analyzed before and after the vaporization measurements and found to be within 0.5 mol percent of the nominal melting composition. Calculation of the sodium oxide activities were made using the method described in [4]. Liquid sodium oxide was chosen as the standard state.

## 4. Results

Figure 5 shows representative plots of the natural logarithm of the vapor density of sodium compounds [ $\ln(g \text{ Na/ml carrier gas STP})$ ] as a function of  $1/T$ , where  $T$  is the absolute temperature. The data for any glass composition in this system are well represented by straight lines. Slope and intercepts are listed in table 1. An alternative method of presenting the same data involves the calculation of the sodium oxide activity as described in [4] for each individual data point. The results of this calculation are presented in table 2.

In order to compare data obtained using the method in this paper with others in the literature, it is necessary to reduce all the data to plots of the common logarithm of the sodium oxide activity as a function of glass melt composition. When necessary, data obtained by other authors for  $P_{\text{Na}}$  or  $P_{\text{NaOH}}$  were used to calculate  $\log a_{\text{Na}_2\text{O}}$  using liquid  $\text{Na}_2\text{O}$  as a standard state and the thermodynamic data from [9] and [10]. Figure 6 shows such a comparison. Curves 1, 2, and 6 were reproduced from a summary given in [7]. Curves 2 and 6 were derived from data obtained by Holmquist [11] and Pearce [12] using solubility calculations. Curve 1 was calculated by Charles using the data of Preston and Turner [6]. Curve 4 and singular point 5 show the results of more recent and direct studies based on optical

absorption [13] and Knudsen Mass Spectrometry [14]. These most recent measurements are in good agreement with the data presented in this work (curve 3). The present measurements differ in having been made over a wider range of glass compositions and temperatures and with vigorously stirred melts.

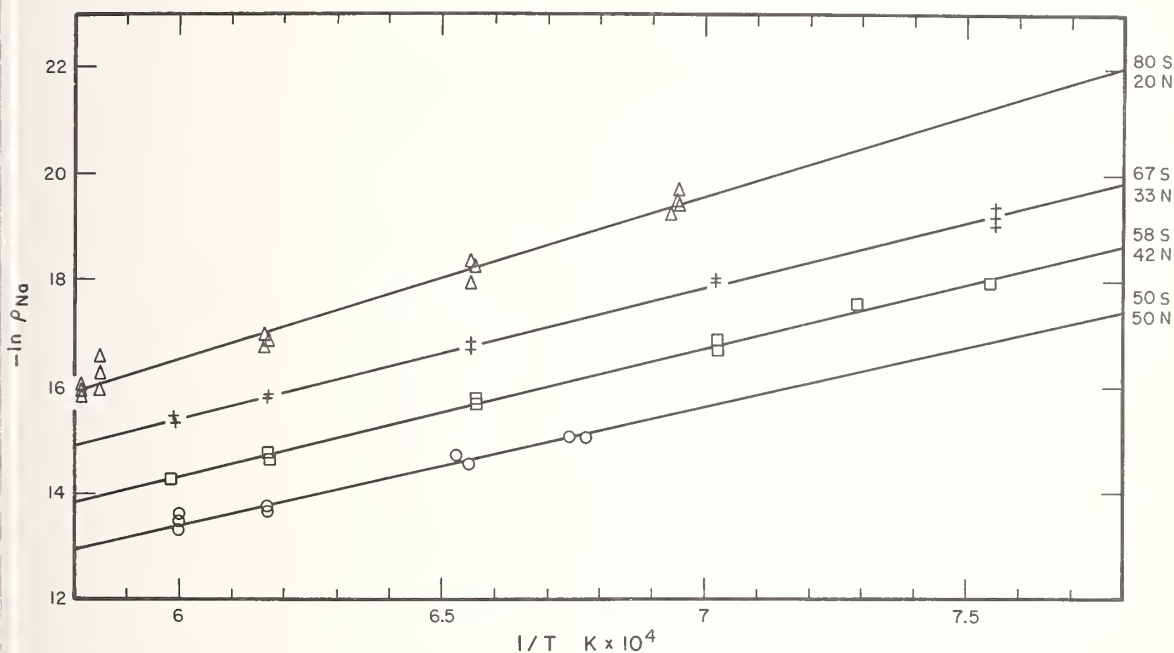


Figure 5. Plot of  $\ln$  sodium vapor density vs  $1/T$  K showing individual data points representative of that reported herein. The compositions are given in mol percent  $Na_2O$ .

An alternative method of determining relative values of  $a_{Na_2O}$  involves the measurement of the electric junction potential between half-cells of melts of different compositions. Borisov and Solov'ev [15] and Papadopoulos [16] have made such measurements using sodium disilicate and sodium trisilicate as reference half cells, respectively. Both measurements are in good agreement with each other. Since the EMF technique requires a value of  $a_{Na_2O}$  for the reference glass composition, this value was taken to be that of sodium disilicate from this work. The resulting curve 7 in figure 6 appears to have similar quantitative behavior to the curve 3 generated by the present study. This agreement suggests that, despite some possible problems (e.g., electrode polarization), the electrochemical technique appears to be extremely useful for the study of the composition dependence of  $a_{Na_2O}$  in inorganic glass systems.



Table 1. Results of linear regressions through plots of  $\ln p_{\text{Na}}$  vs  $1/T$  K.

Nominal Composition mol % $\text{Na}_2\text{O}$	Slope $\pm \sigma$	Intercept $\pm \sigma$	Correlation Coefficient (R)	Standard Error (Y-Y)	#PTS
15	$3.16 \pm 0.3 \times 10^4$	$-2.0 \pm 2$	0.93	0.28	17
20	$3.04 \pm 0.11 \times 10^4$	$-1.6 \pm 0.7$	0.99	0.2	19
23	$2.82 \pm 0.05 \times 10^4$	$-0.79 \pm 4$	0.998	0.12	13
24	$2.54 \pm 0.17 \times 10^4$	$0.64 \pm 1$	0.98	0.33	11
25	$2.48 \pm 0.09 \times 10^4$	$1.4 \pm 0.6$	0.99	0.17	13
27	$2.78 \pm 0.05 \times 10^4$	$-0.97 \pm 0.3$	0.998	0.10	14
30	$2.89 \pm 0.13 \times 10^4$	$-1.7 \pm 1$	0.99	0.21	19
33	$2.49 \pm 0.04 \times 10^4$	$0.48 \pm 0.3$	0.998	0.11	14
37.5	$2.42 \pm 0.07 \times 10^4$	$0.13 \pm 0.6$	0.999	0.11	8
42	$2.42 \pm 0.07 \times 10^4$	$-0.17 \pm 1$	0.998	0.81	15
50	$2.23 \pm 0.12 \times 10^4$	$0.03 \pm 1$	0.98	0.12	14

Table 2. Results of linear regressions through plots of  $\ln a_{\text{Na}_2\text{O}}$  vs  $1/T$  K.

Nominal Composition mol % $\text{Na}_2\text{O}$	Slope $\pm \sigma$	Intercept $\pm \sigma$	Correlation Coefficient	Std. Error	#PTS
15	$3.77 \pm 0.4 \times 10^4$	$-4.64 \pm 4$	0.83	0.56	17
20	$3.63 \pm 0.2 \times 10^4$	$-4.53 \pm 1$	0.98	0.4	39
23	$3.45 \pm 0.1 \times 10^4$	$-4.34 \pm 1$	0.99	0.25	13
24	$2.89 \pm 0.3 \times 10^4$	$-1.43 \pm 2$	0.94	0.65	11
25	$2.77 \pm 0.2 \times 10^4$	$0.69 \pm 1$	0.96	0.40	13
27	$3.37 \pm 0.1 \times 10^4$	$-4.69 \pm 0.6$	0.99	0.20	14
30	$3.57 \pm 0.1 \times 10^4$	$-6.08 \pm 1$	0.98	0.33	19
33	$2.72 \pm 0.1 \times 10^4$	$-1.4 \pm 1$	0.99	0.25	14
37.5	$2.54 \pm 0.2 \times 10^4$	$-1.87 \pm 1$	0.99	0.29	8
42	$2.64 \pm 0.1 \times 10^4$	$-3.05 \pm 0.6$	0.99	0.2	15
50	$2.42 \pm 0.2 \times 10^4$	$-3.67 \pm 2$	0.94	0.23	14

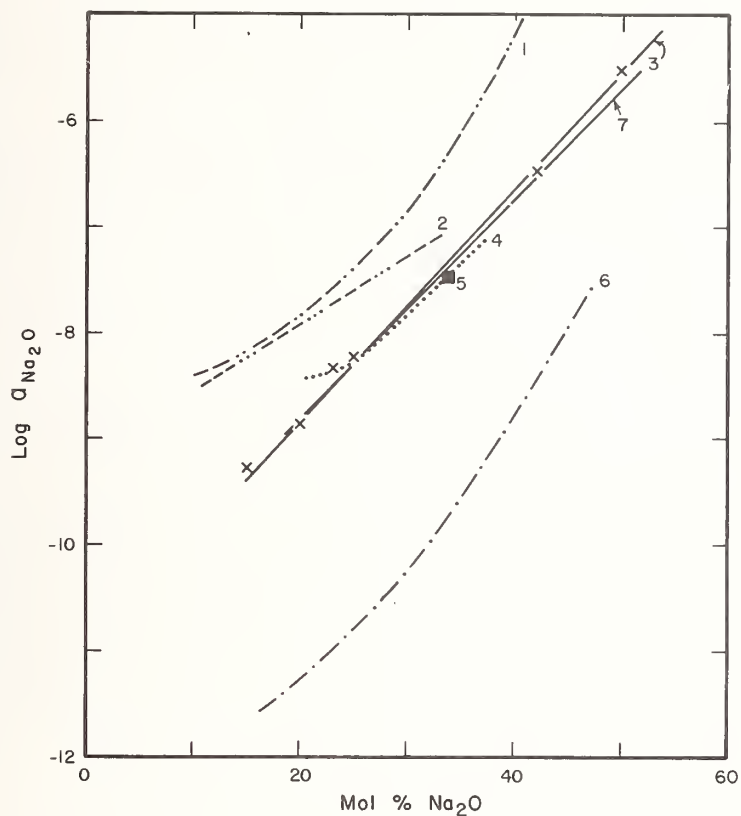


Figure 6. Comparison of the activity of sodium oxide as a function of composition at 1200 °C across the soda-silica system: (1) Charles [7] from Preston and Turner [6]; (2) Holmquist [11]; (3) This work; (4) Vidale [13]; (5) Piacente and Matousek [14]; (6) Pearce [12]; and (7) Borisov and Solov'ev [15].

## 5. Discussion

As stated, table 2 lists the results of a linear regression analysis through plots of the natural logarithm of sodium oxide activities vs  $1/T$ . The resulting slopes are proportional to the heat released when one mole of  $\text{Na}_2\text{O}$  is dissolved in an infinite amount of glass. This quantity is sometimes referred to as the partial molal enthalpy [17]. Figure 7 shows a plot of this enthalpy as a function of the mol percent  $\text{Na}_2\text{O}$  in the glass. With unreacting solute-solvent combinations, this value is on the order of 1-100 cal/mol. The much larger values reported here indicate extensive reaction between the sodium oxide and the solution. This is also suggested by the very small values of sodium oxide activity in

table 2. Within the relatively large scatter expected from enthalpies calculated from vaporization data, it appears that the heat content varies linearly with composition, increasing as the glass melt becomes more silica-rich. A more direct solution calorimetric technique will be required to discern detailed structure (see dashed line in fig. 3) which might be present in this dependence caused by compound-like complexes postulated by Preston and Turner [6] or Haller, Blackburn, and Simmons [18].

Using the values of tables 1 and 2, it is possible to explore the isothermal influence of glass composition on variables which can be calculated from the raw vaporization data. Figure 8, for instance, is a plot of  $\ln a_{\text{Na}_2\text{O}}$  vs mol percent  $\text{Na}_2\text{O}$  at other temperatures than the 1200 °C shown in figure 6. First (linear) and second degree polynomial regression curves are shown for the data at each temperature. Since these fits are quite similar with correlation coefficients in all cases  $> 0.99$ .

Using the STA, it can be concluded that the vaporization of sodium from binary soda-silica melts occurs such that  $\ln a_{\text{Na}_2\text{O}}$  varies linearly with composition over the range of compositions investigated in this study. The heat of mixing of  $\text{Na}_2\text{O}$  was also found to vary linearly with composition, roughly extrapolating to a value near zero for pure  $\text{Na}_2\text{O}$ . The breaks obtained by Preston and Turner [6] in plots of vapor pressure vs composition are not seen here and may therefore have been due to some phenomenon caused by the depletion of sodium at the surface of the unstirred melts used in that study. The large amount of scatter in the heat of mixing data presented in figure 7 suggests that possible irregular behavior may occur around 25 mol percent  $\text{Na}_2\text{O}$ . This behavior would best be explored by a more direct calorimetric technique.

The results presented for the  $a_{\text{Na}_2\text{O}}$  are in good agreement with measurements made on this system using mass spectrometry and optical absorption. They also compare well with data obtained from the electromotive force potentials produced between melt electrodes having different compositions. The good agreement between well stirred results, EMF measurements, and unstirred vaporization measurements made under complete saturation conditions is encouraging. As discussed, the transpiration technique is particularly useful in measurements which must be carried out at atmospheric pressure. The modification of this time-honored technique to permit stirring of the melt allows vaporization measurements to be made where there is chance of incongruent vaporization--the situation normally encountered in glass melting. Since the extension of STA measurements to other elements and other gas and glass compositions is straightforward, it is logical to extend this work to include studies of the relationships which exist between the extent of vaporization of various glass-melt components and the composition of the atmosphere above that melt during commercial glass melting operations.

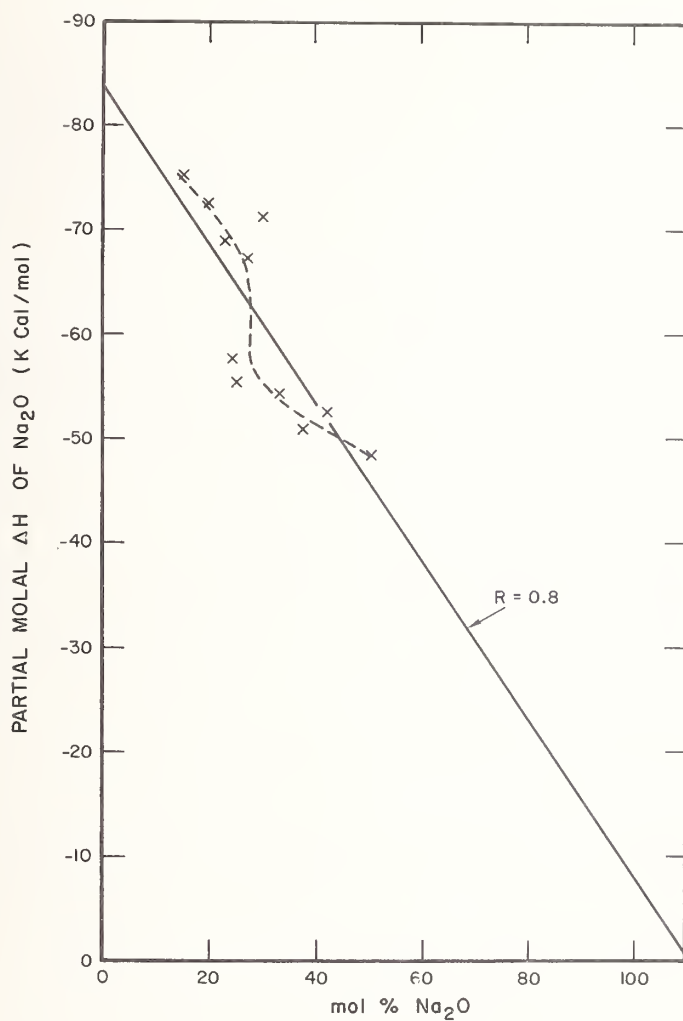


Figure 7. Partial molal enthalpy of sodium oxide vs composition. The solid line is a linear regression through the data points. The dashed line indicates possible structure which may be present due to compound formation in the melt. The errors of each data point can be calculated from table 2.

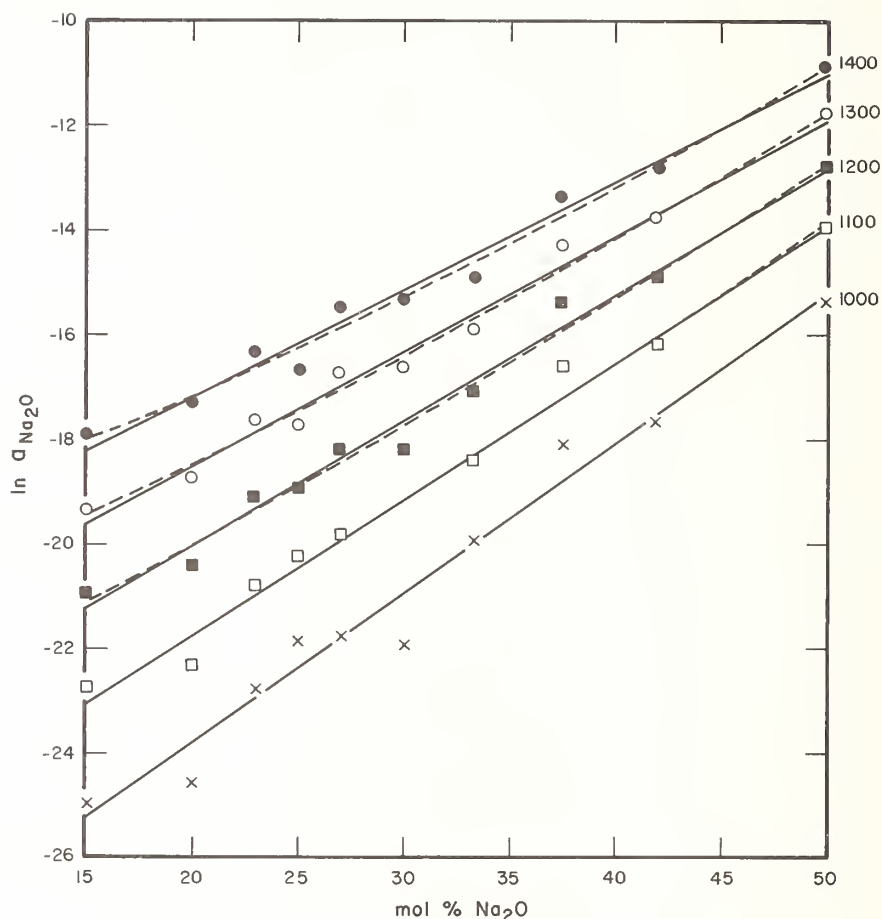


Figure 8. Plot of  $\ln a_{\text{Na}_2\text{O}}$  vs composition. As discussed in the text, a linear relationship (solid curve) appears to adequately fit the data. The dashed curves are second degree fits.

#### References

- [1] Merten, U. and Bell, W. E., in Characterization of High Temperature Vapors, J. L. Margrave, ed., pp. 91-114 (John Wiley, Inc., N.Y., 1967).
- [2] Sanders, D. M., Blackburn, D. H., and Haller, W. K., A high-temperature transpiration apparatus for study of viscous, incongruently vaporizing glass melts, *J. Amer. Ceram. Soc.* 59, 7-8, 366-368 (1976).
- [3] Sanders, D. M. and Haller, W. K., Effect of water vapor on sodium vaporization from two silica-based glasses, *J. Amer. Ceram. Soc.* 60, 3-4 (1977).



- [4] Sanders, D. M. and Haller, W., Influence of oxygen on vaporization of sodium disilicate glass at 1345 °C, submitted to J. Amer. Ceram. Soc.
- [5] Such diffusion should be independent of carrier gas flow rate and will, therefore, show up as a negative intercept in a plot of vaporization rate vs flow rate. The slope and, hence, vapor density is unaffected.
- [6] Preston, E. and Turner, W. E. S., Volatilization and vapor tension at high temperatures of the sodium silica-silicate glasses, J. Soc. Glass Technol. 16, 331-497 (1932).
- [7] Charles, R. J., Activities in  $\text{Li}_2\text{O}$ -,  $\text{Na}_2\text{O}$ -, and  $\text{K}_2\text{O-SiO}_2$  solutions, J. Amer. Ceram. Soc. 50, [12], 631-641 (1967).
- [8] Sanders, D. M. and Haller, W., The measurement of vaporization from soda-lime-silica glass melts, submitted to the Ceramic Bulletin.
- [9] JANAF Thermochemical Tables, 2nd Ed., D. R. Stull and H. Prophet, eds., No. NSRDS-NBS-37 (U.S. Government Printing Office, Washington, D.C., 1971).
- [10] Chase, M. W., Curnutt, J. L., Hu, A. T., Prophet, H., Syverud, A. N., and Walker, L. C., JANAF Thermochemical Tables, 1974 Supplement, J. Phys. Chem. Ref. Data, 3, [2], 311-480 (1974).
- [11] Holmquist, S., Sodium oxide activities in molten sodium sulfate and sodium silicate, presented at the Fall Meeting of the Glass Division, The American Ceramic Society, Bedford, PA., October 13, 1966 (Paper #15-G-66F). (For Abstract see Amer. Ceram. Soc. Bull., 45, [9], 815 (1966).)
- [12] Pearce, M. L., Calculation of oxygen ion activities in sodium silicate and sodium borate melts, J. Amer. Ceram. Soc. 48, [12], 611-13 (1965).
- [13] Vidale, G. L., The Measurement of the vapor pressure of atomic species from spectrometric measurements of the absorption of the resonance line III: The thermodynamics of vaporization of sodium from sodium silicate glasses, TIS Report R60SD390 Air Force Contract Nbr. AF 04(647)-269 (1960).
- [14] Piacente and Matousek, J., Mass spectrometric determination of sodium partial pressures over the system  $\text{Na}_2\text{O-SiO}_2$ , Silikaty 4, 269-279 (1973).
- [15] Borisov, A. F. and Solov'ev, U. I., Study of phase separation processes in sodium silicate system by the electromotive force method, Phase Separation Phenomena in Glasses, Structure of Glass, 8 (Consultants Bureau Translation), 69-73 (1973).
- [16] Papadopoulos, K., Kinetics of the sodium metasilicate-sand reaction by an EMF method, J. Amer. Ceram. Soc. 58, 9-10, 364-367 (1975).
- [17] Lewis, G. N., and Randall, M., in Thermodynamics (McGraw-Hill, N.Y., 1961), revised by K. S. Pitzer and L. Brewer.
- [18] Haller, W., Blackburn, D. H., and Simmons, J. H., Miscibility gaps in alkali-silicate binaries-data and thermodynamic interpretation, J. Amer. Ceram. Soc. 57, [3], 120-126 (1974).

## Discussion

Question (Hastie): I noticed in the comparison of data on the sodium oxide - silicon oxide mixtures, that your data agreed very well with mass spectrometric data. I assume that the mass spectrometric data were obtained using a Knudsen cell, and I don't believe that those experiments would have involved any stirring of the melt or anything like that, and it would seem, for that particular oxide system, that there is not much of a problem as far as retaining a homogeneous melt composition.

Response (Sanders): Well, in answer to your question, the measurements were a bit low, but relative to the other measurements, the agreement was reasonably good. There aren't that many measurements in the system, and I just showed you what is available.

There is a possibility of diffusion from the bulk to the surface if the Knudsen experiment is done properly. The trick is to figure out when it is done properly, and having the apparent vapor pressure being a constant with time is not a good test, but there are problems with not stirring some of these melts, and the problems become considerably more serious with the higher alkali contents. That one singular point was for the disilicate.

The optical work used a static technique where the sample was contained in a platinum tube with small holes for light passage. And again, apparently, diffusion of the vapor out of that chamber was small enough so that bulk diffusion to the surface restored its surface composition.

But the difficulty with any technique that does not stir the melt actively, is that you don't really know whether you are, indeed, measuring the composition which is characteristic of the bulk composition.

Question (Hastie): How isothermal is your sample container? What temperature accuracy do you think you have?

Response (Sanders): Well, we have a large glow-bar furnace and we take a small portion of it to make the measurement, and we have extra glow-bars which we fine tune the temperature with, and we can get the two thermocouples, which are shown in the apparatus figure at about the level of the glass melt, to be within half a degree, and if we probe inside the glass we get the same temperature, so we are within a degree. We feel because of the bulkiness of this apparatus that we have pretty good control over our temperature.

Question (Rosenblatt): Would you briefly describe the dynamic pressure range of the technique?

Response (Sanders):  $10^{-7}$  atmospheres to  $10^{-3}$  atmospheres, something like this. It has good dynamic range because you can increase the length of the transpiration time. It depends on what you are analyzing for, again. The alkali metals are analyzable to impressively small concentrations whereas boron is not so good.

## VAPORIZATION THERMODYNAMICS AND KINETICS OF HEXAGONAL SILICON CARBIDE<sup>1</sup>

Robert G. Behrens and Gary H. Rinehart  
University of California  
Los Alamos Scientific Laboratory  
Los Alamos, NM 87545

Mass spectrometer Knudsen effusion vaporization experiments over the temperature range 1835-2264 K confirm earlier mass spectrometric results that Si(g) is the predominant vapor species above the SiC-C two-phase region. Si<sub>2</sub>C(g) and SiC<sub>2</sub>(g) are found to be the next most important vapor species. Total vapor pressures using a gold calibrated mass spectrometer are measured to be a factor of 10-15 higher than values previously reported between 1800-2200 K. Partial pressures of Si(g), SiC<sub>2</sub>(g), and Si<sub>2</sub>C(g) lead to third-law enthalpies of formation for SiC<sub>2</sub>(g) and Si<sub>2</sub>C(g) which are in accord with previously recommended values.

Langmuir vaporization of SiC(hexagonal) (0001) single crystal faces in the mass spectrometer show ion intensities of Si<sup>+</sup> and SiC<sub>2</sub><sup>+</sup> that are time-independent after an initial induction period during which the intensities increase by a factor of 1.5 before attaining a steady-state value. The mass spectrometer studies between 2200-2500 K give activation enthalpies of  $\Delta H^*(2350) = 141.6 \pm 2.7 \text{ kcal mol}^{-1}$  for Si(g) and  $\Delta H^*(2350) = 166.2 \pm 3.5 \text{ kcal mol}^{-1}$  for SiC<sub>2</sub>(g) vaporization from the (0001) crystal face of hexagonal SiC.

Constant temperature total mass-loss Langmuir vaporization experiments using SiC (0001) crystal faces show a time-dependent rate of mass-loss. It is believed that this time-dependent behavior is caused by a decrease in the SiC(hexagonal) single crystal surface area and is not due to impedance of silicon vaporization by the graphite layer formed on the crystal surface during decomposition.

---

<sup>1</sup>Work performed under the auspices of the Department of Energy.

## 1. Introduction

Low atomic number ceramic solids have numerous potential uses in controlled thermo-nuclear reactor engineering applications [1-3]<sup>2</sup>. Ceramic materials being considered for such applications include SiC, Be<sub>2</sub>C, B<sub>4</sub>C, BN, Si<sub>3</sub>N<sub>4</sub>, Al<sub>2</sub>O<sub>3</sub>, and BeO. These materials are also of interest from a fundamental point of view as many of them vaporize by incongruent decomposition, often yield complex and unique vapor molecules at high temperatures, and are believed to exhibit vacuum vaporization rates lower than the equilibrium values.

The present paper reports the results of investigations on the vaporization thermodynamics of hexagonal silicon carbide using high temperature quadrupole mass spectrometry. Preliminary results of investigations using mass spectrometry to study the vaporization of hexagonal SiC single crystals are also reported. The vaporization thermodynamics and kinetics of hexagonal SiC were investigated because:

- (1) of the potential application of SiC as a first wall protective barrier in fusion reactors,
- (2) discrepancies exist in the literature regarding the vaporization thermodynamics of SiC and the composition of the equilibrium vapor,
- (3) the vaporization kinetics of SiC have not been previously established, and
- (4) single crystal wafers of hexagonal SiC can be readily obtained.

## 2. Summary of Previous Work on SiC

Silicon carbide, SiC, is believed to be the only compound formed in the SiC system [4,5]. SiC exists as two phases: an alpha or hexagonal phase and a beta or cubic phase. Cubic SiC is believed to be the thermodynamically stable phase at low temperatures. The cubic to hexagonal phase transition temperature is reported to lie between 2000-2300 K [6]. Thermodynamic stabilities of the two SiC phases are believed to be similar, their free energies of formation differing by about 0.5 kcal mol<sup>-1</sup> at 298 K. Hexagonal SiC forms numerous polytypic modifications which arise from different stacking sequences of the hexagonal SiC layers [7]. Differences in the thermodynamic stabilities of these polytypes have not been determined.

Quantitative data regarding the composition range over which SiC exists have not been reported. It is generally assumed that SiC exists as a line compound [5].

SiC vaporizes incongruently to form solid graphite as a reaction product. Vapor pressures in both the SiC-C and Si-SiC systems have been investigated since as early as 1926. Ruff and Konschak [8] and Ruff and Grieger [9] measured the vapor pressure of the SiC-C system between 2673-2990 K and 2565-2951 K, respectively. Assuming the vapor to consist of Si(g) and SiC(g), these authors were able to calculate Si(g) partial pressures for the SiC-C system.

---

<sup>2</sup>Figures in brackets indicate the literature references at the end of this paper.



Drowart, DeMaria, and Inghram [10] used mass spectrometry to establish the vapor composition in the SiC-C system between 2149-2316 K. They determined that Si(g) is the predominant vapor species with SiC<sub>2</sub>(g) and Si<sub>2</sub>C(g) being the next most predominant vapor species over their experimental temperature range. They also found Si<sub>2</sub>(g), SiC(g), Si<sub>2</sub>C<sub>2</sub>(g), Si<sub>3</sub>(g), Si<sub>2</sub>C<sub>3</sub>(g), and Si<sub>3</sub>C(g) to be minor species in the equilibrium vapor.

While investigating the spectroscopy of SiC molecules by matrix isolation techniques, Weltner and McLeod [11] found a relatively strong Si<sub>2</sub>C<sub>3</sub> spectrum. As they could not determine whether the strong spectrum was due to a high transition probability of the Si<sub>2</sub>C<sub>3</sub> bands in the visible region of the spectrum or to a concentration of Si<sub>2</sub>C<sub>3</sub> in the SiC-C vapor higher than that suggested by the mass spectrometry results of Drowart, et al., Weltner and McLeod suggested that the importance of this molecule in the high temperature equilibrium vapor of SiC-C be re-examined.

Knippenberg [5] measured the total vapor pressure of hexagonal SiC in a graphite crucible and determined the silicon content of the vapor at the normal sublimation temperature (3030 K from Knippenberg's work). On the basis of his analysis, Knippenberg concluded that the equilibrium gas phase composition of the SiC-C system is always rich in silicon in contrast to the results of the mass spectrometer studies of Drowart, et al., which indicate the Si/C ratios in the gas phase to be less than unity.

Drowart and DeMaria [12] measured the vapor pressure of the Si-SiC system using mass spectrometry and found Si(g) to be the major vapor species with Si<sub>2</sub>C(g) and SiC<sub>2</sub>(g) being the next most important vapor species below 2632 K. Enthalpies of formation of Si<sub>2</sub>C(g) and SiC<sub>2</sub>(g) calculated by a third-law analysis of the vapor pressure data are consistent with the corresponding third-law values from Drowart, et al.'s mass spectrometer work on SiC-C. Total vapor pressures extrapolated to the temperature range over which Ruff and co-workers [8,9] measured total vapor pressures of the Si-SiC system are in poor agreement with Ruff's results. Drowart and DeMaria attributed this discrepancy to the fact that silicon diffused through the crucible in Ruff's experiments causing their vapor pressures to be inordinately high.

Grievesson and Alcock [13] used a mass-loss effusion technique to measure the total vapor pressure of both hexagonal and cubic SiC. The measured total vapor pressures for each SiC phase were slightly higher than those reported by Drowart, et al. At temperatures above 1973 K, Grievesson and Alcock found that their vapor pressures for hexagonal SiC were higher than values calculated by extrapolating their low temperature data. This behavior may indicate that the low temperature vapor pressures are too low because of kinetic problems (i.e., a low vaporization coefficient).

Davis, Anthrop, and Searcy [14] measured the vapor pressures of cubic SiC by a mass-loss effusion technique using Drowart, et al.'s mass spectrometer results to calculate Si(g) partial pressures from their observed mass losses. They obtained total vapor pressures in agreement with the total vapor pressures measured by Grievesson and Alcock. Davis, et al. also report that they found no systematic change in the vapor pressure as a function of cell orifice area and concluded that the vaporization coefficient of Si(g) from cubic SiC was close to unity. They did, however, observe a time-dependent decrease in the



vaporization rate which they attributed to impedance of Si(g) vaporization by a graphite microlayer formed on the SiC particles during vaporization.

Mell and Brodsky [15] obtained the mass spectrum of silicon evaporating from a carbon-lined copper hearth under high vacuum (The temperature at which the mass spectrum was taken was not reported.). They observed peaks for most of the known Si-C and Si molecules but did not observe a peak attributable to SiC<sub>2</sub>(g).

Mass-loss effusion studies of SiC-C by Voronin, Makarova, and Yudin [16] give vapor pressures which are a factor of 20-30 below those of the previously discussed investigations. These results indicate a low vaporization coefficient in contradiction to the results of Davis, et al. Ghoshtagore [17] performed Langmuir vaporization experiments using hexagonal SiC single crystal wafers and reported vaporization rates a factor of 10<sup>4</sup> lower than those measured under equilibrium conditions.

### 3. Experimental Section

#### 3.1 Sample characterization

Knudsen effusion experiments are performed using 200 mesh SiC particles, 200 mesh SiC particles crushed to 325 mesh powder, or 325 mesh SiC powder mixed with 325 mesh H-451 reactor grade graphite powder. X-ray diffraction shows the SiC to be the hexagonal phase, most probably a mixture of polytypes. Cubic SiC may also be present as x-ray diffraction lines for the cubic phase are not clearly discernible from those for the hexagonal phase. The x-ray diffraction patterns also show that significant amounts of impurities are not present in the SiC samples.

Langmuir vaporization experiments are performed using hexagonal SiC single crystal wafers purchased from the Materials Research Corporation, Orangeburg, N.Y. The crystals are carbon arc grown, 6-8 mm in cross section and 1 mm thick with the c-axis oriented perpendicular to the large face. X-ray diffractometer scans confirm the crystals to be hexagonal SiC.

#### 3.2 Experimental apparatus

The mass spectrometer used for both the Knudsen effusion and Langmuir vaporization experiments is shown in figures 1 and 2. The mass spectrometer consists of an Extra-nuclear Laboratories field separation (ELFS) quadrupole mass filter. The quadrupole rods are 0.95 cm diameter by 20 cm long giving a mass range of 1400 amu with a resolution of approximately 1000 at m/e = 1000.

The electron impact ionizer is of cross-beam design; that is, the molecular beam from the high temperature source enters the ionizer region in a direction normal to the geometrical axis of the quadrupole rods and normal to the direction of ion extraction into the mass filter.

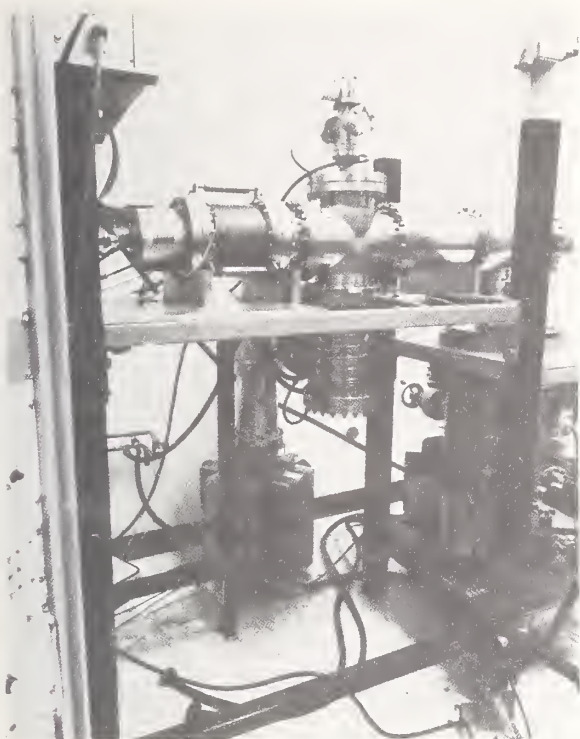


Figure 1. High temperature mass spectrometer. View 1.

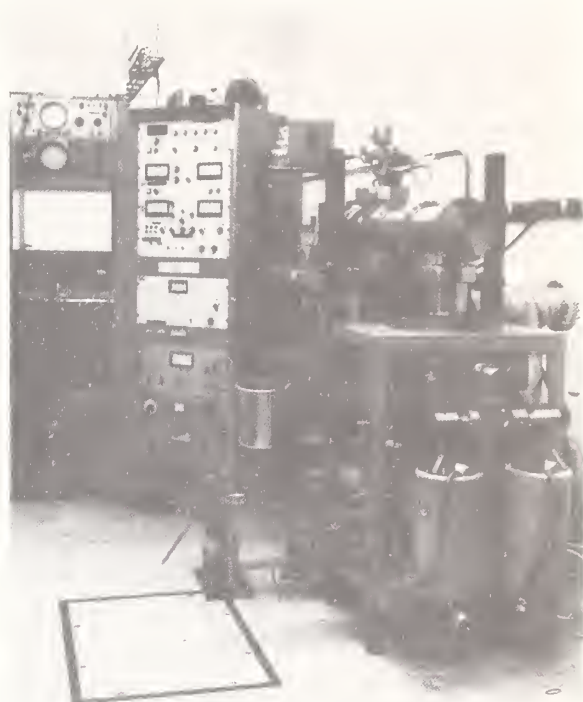


Figure 2. High temperature mass spectrometer. View 2.

Ion detection is achieved by a 21-stage copper-beryllium "venetian blind" electron multiplier mounted paraxial to and offset from the quadrupole transmission axis. Multiplier gains are determined in the usual manner using a Faraday plate detector.

Multiplied ion currents pass through a preamplifier, through a  $10^7$  or  $10^9$  ohm resistor, and into a dc electrometer. Output from the electrometer is displayed on an oscilloscope, X-Y recorder, or a strip chart recorder.

The electron multiplier-mass filter-ionizer assembly is mounted as a single unit on an 8-inch o.d. conflat flange through which electrical connections to the quadrupole power supply, ionizer control, and electrometer are made. The assembly is mounted horizontally on a 5.5-inch i.d. stainless steel bellows which can be adjusted to permit easy alignment of the ion source entrance hole with the molecular beam from the high temperature Knudsen cell region (see fig. 1).

The vacuum system is constructed entirely of 6-inch o.d. stainless steel tubing. Conflat flanges with copper gaskets are used in all vacuum connections. A Varian FC-12E vacuum station is used to pump on the ion source region. The station consists of  $200 \text{ l s}^{-1}$  of Triode VacIon pumping, a titanium sublimation pump (TSP), and a liquid nitrogen cryo-array. A poppet valve is located above the VacIon pumps and TSP to permit breaking of vacuum without turning off the pumps. Pumping of the Knudsen cell region is achieved

by a  $400 \text{ l s}^{-1}$  Thermionics Laboratory VacIon pump. Rough pumping of the system is achieved by three liquid nitrogen-cooled VacSorb pumps. These pumps are isolated from the main vacuum system by 1.5-inch polyimide-sealed ultra-high vacuum valves (see fig. 2).

Typical background pressures of  $5 \times 10^{-9}$  Torr are readily achieved in both the ion source and Knudsen cell regions after about six hours pumping from 10 microns pressure. Background pressures on the order of  $1 \times 10^{-7}$  Torr or better in the ion source region and  $1 \times 10^{-6}$  Torr or better in the Knudsen cell region are routinely achieved during operation with a graphite Knudsen cell at temperatures as high as 2300 K.

The Knudsen cell region is separated from the ion source region of the mass spectrometer by a water-cooled plate with a 0.25-inch diameter hole through its center. A stainless steel shutter blade with a 0.025-inch wide slit etched into it rests on top of the water-cooled plate and is moved across the path of the molecular beam from the Knudsen cell region by a linear-motion vacuum feedthrough.

A graphite Knudsen effusion cell or SiC single crystal situated in a graphite holder is heated by a tungsten spiral resistance heater mounted on an 8-inch o.d. conflat flange (fig. 3). A Sorenson high current, low voltage dc power supply is used to supply power to the tungsten heater. Water-cooled copper power feedthroughs for the tungsten heater are brought into the vacuum system through the 8-inch o.d. flange. A concentric arrangement of six tantalum and two tungsten shield cans, with molecular beam exit holes drilled through the center of their tops, is situated around the tungsten heater. Seven tantalum heat shields, with pyrometer sight holes drilled through their centers, are situated directly below the heater. The entire furnace arrangement fits into a 6-inch o.d. stainless steel housing which has 0.25-inch o.d. copper tubing brazed to the outside wall for water cooling.

The temperature of a Knudsen cell is measured using a calibrated Pyro optical pyrometer by sighting through an optical window onto a blackbody hole drilled into the bottom of the Knudsen cell. Single crystal temperatures are measured by sighting the pyrometer through a hole drilled in the bottom of a cylindrical graphite holder onto the underside of the single crystal. Observed temperatures are then corrected for optical window and prism effects.

Knudsen effusion cells used in the equilibrium vapor pressure measurements are machined from graphite and are of two types. The first type consists of a base with a lid, has a 1.3 cm outside diameter and is approximately 1.8 cm long. The cell lid contains a knife-edge circular orifice with an area of  $3.0 \times 10^{-3} \text{ cm}^2$  and a Clausing factor of 0.502. The second type of Knudsen effusion cell consists of a single piece of graphite 1.8 cm in length and 1.3 cm in outside diameter. A 0.48 cm long graphite plug with a cylindrical hole drilled through its center provides the orifice. The orifice area is  $0.027 \text{ cm}^2$  with a Clausing factor of 0.385.

Total mass-loss Langmuir vaporization experiments are performed with a SiC single crystal wafer sitting in a graphite holder. The crystal and holder are seated in the center of a water-cooled eddy-current concentrator on a Veeco vacuum pumping station. The current concentrator is coupled to induction coils from a Lepel 20 kW induction heating

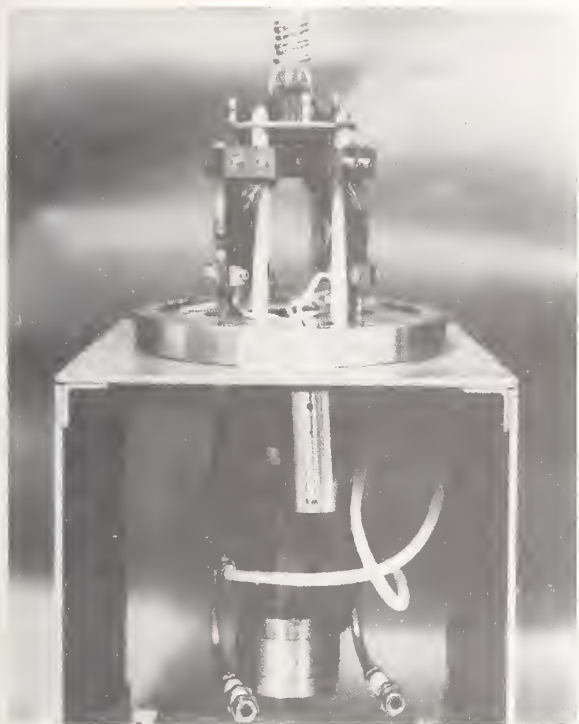


Figure 3. Tungsten spiral resistance heater on 8-inch conflat flange.

unit. The crystal surface temperature is measured by sighting a Pyro optical pyrometer through a quartz window located at the top of the concentrator onto the crystal surface. The mass change of the crystal after heating for a given time period is determined by removing the crystal from the concentrator and weighing it on a Mettler pan micro-balance.

### 3.3 Data treatment

Ion intensities from the SiC Knudsen effusion studies are converted to absolute partial pressures for each vapor species assuming the ion transmission efficiency of the mass filter is independent of  $m/e^3$ , using the results of a separate Knudsen effusion vaporization of gold from a graphite crucible, and using the relation

$$P_u = C_{Au} I_u T \frac{(\sigma \gamma f i)_{Au}}{(\sigma \gamma f i)_u} \quad (1)$$

where  $P_u$  is the pressure of molecular species  $u$  with measured ion intensity  $I_u$ ;  $C_{Au}$  is the instrument sensitivity;  $T$  is the thermodynamic temperature;  $\gamma$  is the electron multiplier

<sup>3</sup>Editor's note: This is not necessarily a good assumption, e.g., see Section 5.1 and the chapter by Bonnell and Hastie in this volume.



gain;  $f$  is the isotopic abundance;  $i$  is an emission current correction factor; and  $\sigma$  is the calculated ionization cross section at the working electron energy. The instrument sensitivity,  $C_{Au}$ , is obtained from the gold vaporization experiment and the known vapor pressure of gold [18].

Vapor pressures obtained using eq. (1) are fitted to the relation

$$R \ln(P/\text{atm}) = -\Delta H^\circ/T + \Delta S^\circ \quad (2)$$

by a least-squares calculation. Second-law values of  $\Delta H^\circ(298)$  and  $\Delta S^\circ(298)$  are calculated by a  $\Sigma'$  evaluation of the vapor pressures [19]. Third-law values of  $\Delta H^\circ(298)$  are obtained in the usual manner [20].

Time-independent ion intensities from the single crystal Langmuir vaporization studies are fitted to the relation

$$R \ln(IT) = -\Delta H^*/T + \text{Constant} \quad (3)$$

by a least-squares calculation. The quantity  $\Delta H^*$  is the activation enthalpy change for the vaporization process. The similar form of eqs. (2) and (3) permits  $\Delta H^*$  and  $\Delta H^\circ$  to be compared to yield an enthalpy barrier,  $\Delta H^* - \Delta H^\circ$ , for the kinetically slow step(s) in the vaporization process.

#### 4. Experimental Results

##### 4.1 Knudsen effusion mass spectrometer measurements on the SiC-C system

The most important vapor molecule in the SiC-C system over the experimental temperature range of 1835-2264 K is found to be Si(g) with Si<sub>2</sub>C(g) and SiC<sub>2</sub>(g) being the next most important molecules. Only trace amounts of shutterable Si<sub>2</sub>(g), Si<sub>2</sub>C<sub>2</sub>(g), Si<sub>3</sub>(g), Si<sub>3</sub>C(g), and C<sub>3</sub>(g) are detected to be present at 2275 K. Mass spectrum peaks attributable to ions of other silicon or silicon-carbon molecules are not detected. These results are in accord with the mass spectrometer results of Drowart, et al. [10]. X-ray analysis of the solid product remaining after complete vaporization of silicon shows it to be graphite.

Temperature coefficient plots for Si<sup>+</sup> (m/e = 28), SiC<sub>2</sub><sup>+</sup> (m/e = 52), and Si<sub>2</sub>C<sup>+</sup> (m/e = 68) are shown in figure 4 for a typical mass spectrometer experiment using a graphite effusion cell with a  $3 \times 10^{-3} \text{ cm}^2$  orifice area and 325 mesh SiC powder. For this particular experiment, electron energies of 13 eV are used for the Si<sup>+</sup> intensity measurements and 15 eV for the SiC<sub>2</sub><sup>+</sup> and Si<sub>2</sub>C<sup>+</sup> measurements. An emission current of 2.0 mA is used for all the measurements.

Figure 4 shows attenuation of the Si<sup>+</sup>, Si<sub>2</sub>C<sup>+</sup>, and SiC<sub>2</sub><sup>+</sup> intensities at high temperatures. This behavior is believed to be caused by intramolecular scattering in the molecular beam. Ion intensity attenuation caused by intramolecular scattering as predicted by a model developed by Meschi [21,22] is indicated in figure 4 by the dashed lines. The total



vapor pressure inside the SiC-containing graphite Knudsen cell at which attenuation is first observed is in good agreement with that predicted by Meschi's model. However, agreement between the magnitude of the observed attenuation and that predicted by Meschi's model is only qualitative. This discrepancy may be caused by incorrect assumptions contained in the model, incorrect assumptions concerning collision cross-sections for Si-C molecules used in the calculations, or by an added contribution due to scattering of molecules in the molecular beam by background gases.

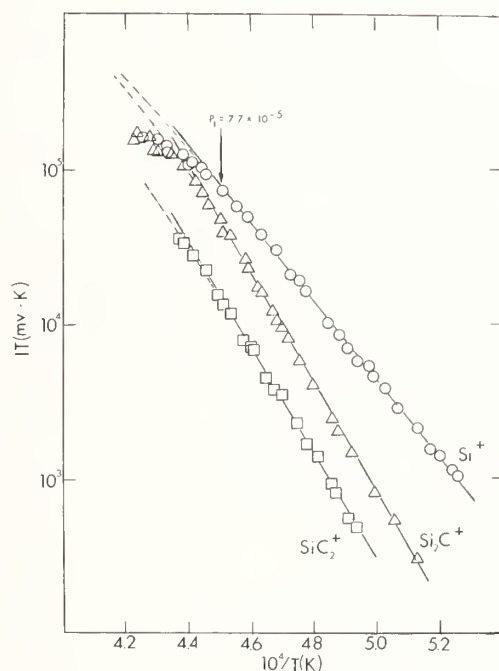


Figure 4. Temperature coefficient plot of  $\text{Si}^+$ ,  $\text{SiC}_2^+$ , and  $\text{Si}_2\text{C}^+$  for a typical mass spectrometer Knudsen effusion experiment using a graphite effusion cell with  $3 \times 10^{-3} \text{ cm}^2$  orifice area. Dashed lines indicate expected intensity attenuation calculated using Meschi's model for intramolecular scattering [21].

To assure that the observed ion intensity attenuation is not caused by some anomalous behavior of the mass spectrometer or by vaporization kinetic problems (e.g., solid state diffusion of silicon is determining the vaporization rate at high temperature), vaporization of molten gold from a graphite Knudsen cell was studied at temperatures where the gold vapor pressure is on the order of  $10^{-3}$ - $10^{-4}$  atmospheres. A temperature coefficient plot for this experiment is shown in figure 5 (data are taken using 20 eV electron energy,

3.0 mA emission current). Attenuation of the  $\text{Au}^+$  ( $m/e = 197$ ) intensities starts at gold vapor pressures predicted from Meschi's model (about  $5 \times 10^{-4}$  atmospheres). The magnitude of the attenuation is also comparable to that predicted by the model.

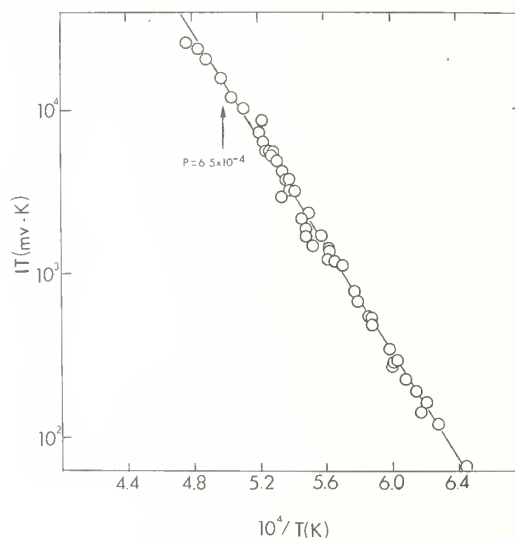
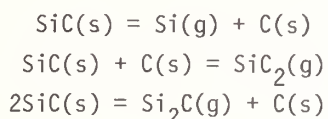


Figure 5. Temperature coefficient plot of  $\text{Au}^+$  data from mass spectrometer Knudsen effusion experiment using a graphite effusion cell with  $3 \times 10^{-3} \text{ cm}^2$  orifice area.

Measured partial pressures of  $\text{Si(g)}$ ,  $\text{SiC}_2(\text{g})$ , and  $\text{Si}_2\text{C(g)}$  are found to depend on both the SiC particle size and the size of the Knudsen cell orifice. SiC powder ground to 325 mesh (44 micron) and vaporized from a Knudsen cell with a  $3 \times 10^{-3} \text{ cm}^2$  orifice area gives the highest measured vapor pressures. A coarsely crushed hexagonal SiC single crystal vaporized from the crucible with a  $3 \times 10^{-3} \text{ cm}^2$  orifice area gives partial pressures 90 percent below vapor pressures obtained with the 325 mesh samples. Vapor pressures measured using 200 mesh SiC powder and a crucible with a  $0.027 \text{ cm}^2$  orifice area are 65 percent lower than those obtained using the 35 mesh powder in an effusion cell with a  $3 \times 10^{-3} \text{ cm}^2$  orifice area. Samples of 200 mesh SiC powder vaporized in the effusion cell with a  $3 \times 10^{-3} \text{ cm}^2$  orifice area give measured partial pressures the same as obtained with the 325 mesh samples.

Because of the orifice and particle size effects, thermodynamic quantities for SiC vaporization are calculated using data from those experiments with 200 and 325 mesh SiC powder and a  $3 \times 10^{-3} \text{ cm}^2$  orifice area. Second- and third-law enthalpies of vaporization at 298 K for the reactions



are summarized in table 1. These values are obtained as described in Section 3.3 and using JANAF [6] free energy functions. Vapor pressures computed using the present third-law enthalpy changes and JANAF free energy functions are given in table 2.

#### 4.2 Mass spectrometer and total mass-loss Langmuir vaporization experiments

Two mass spectrometer experiments, performed over the temperature range 2200-2500 K, investigated the Langmuir vaporization from the (0001) basal plane of two separate SiC single crystals. Shutterable ions observed are  $\text{Si}^+$ ,  $\text{SiC}_2^+$ , and  $\text{Si}_2\text{C}^+$ . Ion intensities are found to be independent of time after an initial induction period during which the intensity of  $\text{Si}^+$  (and presumably  $\text{SiC}_2^+$  and  $\text{Si}_2\text{C}^+$ ) increases with time. The steady-state  $\text{Si}^+$  intensity is a factor of 1.5 higher than that measured during the initial stages of heating. At 2400 K, measured steady-state ion intensities are a factor of 80-100 lower than intensities extrapolated from those measured in the Knudsen effusion experiments.

The measured temperature-dependence of  $\text{Si}^+$  and  $\text{SiC}_2^+$  intensities yield activation enthalpies of  $\Delta H^*(2350) = 141.6 \pm 2.7 \text{ kcal mol}^{-1}$  for  $\text{Si(g)}$  and  $\Delta H^*(2350) = 166.2 \pm 3.5 \text{ kcal mol}^{-1}$  for  $\text{SiC}_2\text{(g)}$  sublimation from the (0001) plane of hexagonal SiC. Comparison of these activation enthalpies with the corresponding equilibrium enthalpies obtained in the present work,  $\Delta H^0(2350) = 111.3 \text{ kcal mol}^{-1}$  and  $\Delta H^0(2350) = 143.7 \text{ kcal mol}^{-1}$ , respectively, gives enthalpy barriers of  $30.3 \text{ kcal mol}^{-1}$  and  $22.5 \text{ kcal mol}^{-1}$  for  $\text{Si(g)}$  and  $\text{SiC}_2\text{(g)}$  sublimation.

Results of a total mass-loss Langmuir vaporization study of the SiC (0001) face are shown for one experiment conducted at 2498 K in figure 6. The results show that the total mass-loss is time-dependent during the entire course of vaporization (i.e., from initial heat-up until all the silicon is vaporized from the crystal). Figure 7 shows the mass-loss data of figure 6 plotted against  $t^{1/2}$  indicating a parabolic time-dependence. Figure 8 shows the time-dependence of the apparent flux vaporizing from the (0001) crystal face calculated from the data shown in figure 6. It should be noted that the flux measured initially ( $0.31 \text{ mg min}^{-1} \text{ cm}^2$ ) is a factor of about  $10^4$  below the equilibrium flux of  $\text{Si(g)}$  at 2498 K, and that during the 1300 minute vaporization, the apparent flux drops by a factor of four. The flux then immediately drops to zero at which time it is believed that the silicon is completely depleted from the crystal.

Table 1. Comparison of vaporization enthalpies for the SiC(hex)-C system.

Reaction	$\Delta H^\circ(298)$ , second-law (kcal mol <sup>-1</sup> )		$\Delta H^\circ(298)$ , third-law (kcal mol <sup>-1</sup> )	
	<u>This work</u>	<u>Reference [10]<sup>a</sup></u>	<u>This work</u>	<u>Reference [10]<sup>a</sup></u>
SiC(s) = Si(g) + C(s)	119.2±2.1 <sup>b</sup>	136.9±0.7 <sup>b</sup>	115.2±0.8	124.6±0.3
2SiC(s) = Si <sub>2</sub> C(g) + C(s)	162.4±2.1	169.6±7.5	145.3±1.2	161.3±0.5
SiC(s) + C(s) = SiC <sub>2</sub> (g)	169.0±6.4	168.1±9.4	152.1±1.6	163.6±0.6

<sup>a</sup>Recalculated from partial pressures reported in reference [10] using JANAF free energy functions.

<sup>b</sup>All uncertainties are quoted as one standard deviation.

Table 2. Comparison of calculated equilibrium pressures in the SiC(hex)-C system.

Molecule	T(K)	P(atm)	
		<u>This work<sup>a</sup></u>	<u>Reference [10]<sup>a</sup></u>
Si	1800	1.2 × 10 <sup>-6</sup>	8.7 × 10 <sup>-8</sup>
	2000	2.9 × 10 <sup>-5</sup>	2.7 × 10 <sup>-6</sup>
	2200	3.8 × 10 <sup>-4</sup>	4.4 × 10 <sup>-5</sup>
SiC <sub>2</sub>	1800	3.6 × 10 <sup>-8</sup>	1.5 × 10 <sup>-9</sup>
	2000	2.3 × 10 <sup>-6</sup>	1.3 × 10 <sup>-7</sup>
	2200	6.6 × 10 <sup>-5</sup>	4.7 × 10 <sup>-6</sup>
Si <sub>2</sub> C	1800	1.2 × 10 <sup>-7</sup>	1.3 × 10 <sup>-9</sup>
	2000	5.7 × 10 <sup>-6</sup>	1.0 × 10 <sup>-7</sup>
	2200	1.4 × 10 <sup>-4</sup>	3.5 × 10 <sup>-6</sup>
P <sub>total</sub>	1800	1.4 × 10 <sup>-6</sup>	9.0 × 10 <sup>-8</sup>
	2000	3.7 × 10 <sup>-5</sup>	2.9 × 10 <sup>-6</sup>
	2200	5.9 × 10 <sup>-4</sup>	5.2 × 10 <sup>-5</sup>

<sup>a</sup>Calculated using third-law values of  $\Delta H^\circ(298)$  given in table 1 and JANAF free energy functions.

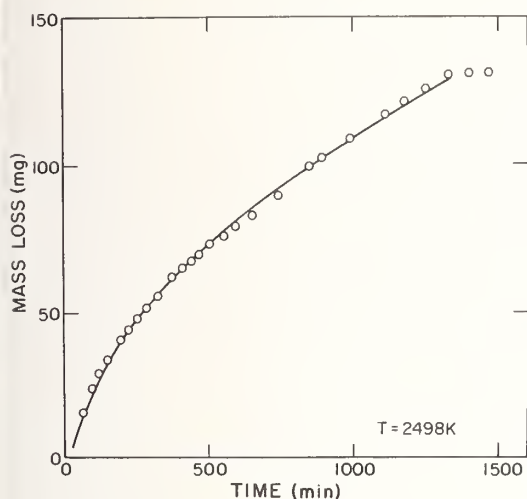


Figure 6. Time-dependence of total mass-loss from a freely vaporizing hexagonal SiC (001) single crystal face at 2498 K.

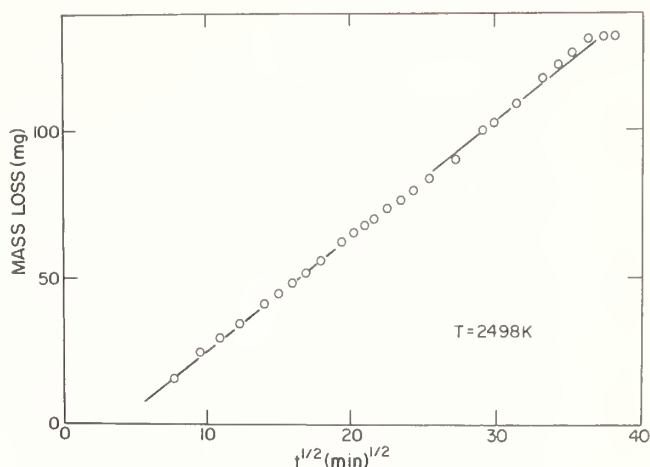


Figure 7. Total mass-loss data of figure 6 showing parabolic time-dependence.

The residue formed on the SiC single crystal substrate was investigated using x-ray diffraction and scanning electron microscopy (SEM). X-ray diffraction scans show the residue to be graphite. Broadening of the 002 and 004 graphite diffraction peaks indicates the graphite surface to be composed of small graphite crystallites. Scanning electron microscopy shows no pores to be present at magnification of up to 50,000X.

## 5. Discussion

### 5.1 Knudsen effusion mass spectrometer experiments

Over the temperature range 1800-2200 K equilibrium partial pressures of Si(g), SiC<sub>2</sub>(g), and Si<sub>2</sub>C(g) above SiC-C measured in the current work using a gold calibrated mass spectrometer are higher than pressures reported by Drowart, et al. [10] by factors of 10-15, 15-25, and 40-90, respectively. Accordingly, total vapor pressures of the present work are a factor of 10-15 higher than those of Drowart, et al. [10]. Present total vapor pressures extrapolated to 2800-2900 K are in excellent agreement with total pressures measured at these temperatures by Ruff and Konschak [8] and Ruff and Grieger [9].

Table 1 shows excellent agreement between present second- and third-law values of  $\Delta H^\circ(298)$  for reaction (1). Agreement between second- and third-law enthalpies for reactions (2) and (3) is not good, the second-law enthalpies being 17 kcal mol<sup>-1</sup> lower than the corresponding third-law values. Note, however, that the present second-law enthalpies for reactions (2) and (3) are in good agreement with the corresponding third-law enthalpies reported by Drowart, et al.



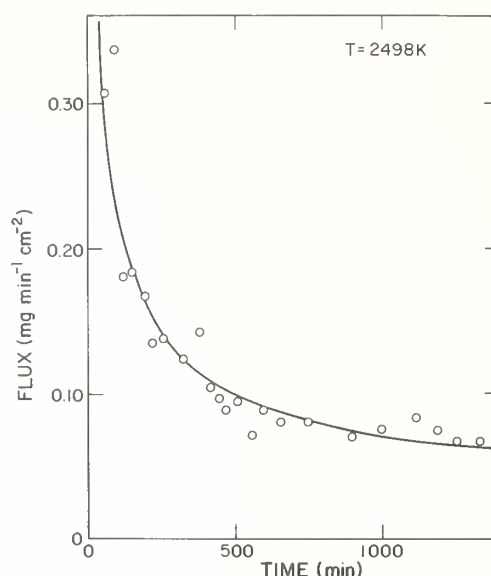


Figure 8. Time-dependence of total flux vaporizing from the (0001) SiC single crystal face at 2498 K. Calculated from data in figure 6.

The partial vapor pressures of Si(g), SiC<sub>2</sub>(g), and Si<sub>2</sub>C(g) reported in table 2 for the present work are believed to be too high and the corresponding third-law enthalpy changes are believed to be too low for the following reasons. Ion intensities from the mass spectrometer studies were converted to absolute partial pressures using the results of a separate gold calibration experiment assuming the ion transmission efficiency of the quadrupole mass filter to be independent of m/e. However, because of the wide mass range between Au<sup>+</sup> (m/e=197) and Si<sup>+</sup> (m/e=28), the transmission efficiency of the mass filter may not be independent of m/e thus leading to erroneous vapor pressures in the present work. Vapor pressures of the present work compared to those reported by Drowart, et al. suggest that the transmission Au<sup>+</sup> in our mass filter is about ten percent relative to the transmission of Si<sup>+</sup> (the transmission of Au<sup>+</sup> also appears to be about ten percent relative to the transmission of SiC<sub>2</sub><sup>+</sup> and Si<sub>2</sub>C<sup>+</sup> as well). Other indications of higher transmission efficiency for low mass ions than for high mass ions in the mass filter are:

1. The vapor pressure of C<sub>3</sub>(g) above graphite calculated from the present measure C<sub>3</sub><sup>+</sup> intensity at 2275 K and the gold calibration results is a factor of thirty higher than the vapor pressure calculated from thermodynamic data presented in the JANAF tables.

2. Mass spectrometer Knudsen effusion experiments on  $\text{Al}_4\text{C}_3(\text{s})$  and  $\text{Al}_4\text{SiC}_4(\text{s})$ , both of which vaporize incongruently to give  $\text{Al}(\text{g})$ , also indicate the transmission of  $\text{Au}^+$  to be approximately ten percent relative to  $\text{Al}^+(\text{m/e}=27)$ .
3. The enthalpy of formation of  $\text{SiC}$  (hexagonal) at 298 K computed from the present third-law enthalpy change given in table 1 for  $\text{Si}(\text{g})$  vaporization from  $\text{SiC}$  and the enthalpy of formation for  $\text{Si}(\text{g})$  given in the JANAF tables,  $107.7 \text{ kcal mol}^{-1}$  at 298 K, is  $-7.5 \text{ kcal mol}^{-1}$ . This value is  $9.4 \text{ kcal mol}^{-1}$  more positive than that recommended by JANAF based on the enthalpy of reaction for  $\text{SiC}(\text{hex}) + 4\text{F}_2(\text{g}) = \text{SiF}_4(\text{g}) + \text{CF}_4(\text{g})$  measured by fluorine bomb calorimetry.

Enthalpies of formation for  $\text{Si}_2\text{C}(\text{g})$  and  $\text{SiC}_2(\text{g})$  are computed to be  $130.3 \text{ kcal mol}^{-1}$  and  $144.6 \text{ kcal mol}^{-1}$ , respectively, using the present third-law enthalpy changes for reactions (1) through (3) given in table 1. Third-law values of  $\Delta H^\circ$  (298 K) for reactions (2) and (3) derived using a mass spectrometer calibration constant obtained by normalizing the present  $\text{Si}^+$  intensity at 2000 K to the partial pressure of  $\text{Si}(\text{g})$  above  $\text{SiC}(\text{hex})$  reported by Drowart, et al., give  $\Delta H_f^\circ(298 \text{ K}) = 121.1 \text{ kcal mol}^{-1}$  and  $144.8 \text{ kcal mol}^{-1}$  respectively for  $\text{Si}_2\text{C}(\text{g})$  and  $\text{SiC}_2(\text{g})$ . These are in excellent agreement with values recommended by JANAF based on the mass spectrometer results of Drowart, et al. [10,12],  $(128 \pm 6) \text{ kcal mol}^{-1}$  and  $(147 \pm 7) \text{ kcal mol}^{-1}$ , respectively.

## 5.2 Langmuir vaporization experiments

Activation enthalpy barriers of  $30.3 \text{ kcal mol}^{-1}$  for  $\text{Si}(\text{g})$  and  $22.5 \text{ kcal mol}^{-1}$  for  $\text{SiC}_2(\text{g})$  vaporization from the  $\text{SiC}(\text{hexagonal})$  basal plane lead to vaporization coefficients of  $1.5 \times 10^{-3}$  and  $8.1 \times 10^{-3}$ , respectively, at 2350 K if it is assumed there are no corresponding entropy barriers for the kinetically-slow step in the vaporization process (i.e.,  $\Delta S^\circ = \Delta S^*$ ).

The time-independent  $\text{Si}^+$  and  $\text{SiC}_2^+$  intensities observed in the mass spectrometer Langmuir single crystal experiments show that the porous graphite layer formed as a result of  $\text{SiC}$  decomposition has little or no effect on the transport rate of  $\text{Si}(\text{g})$  and  $\text{SiC}_2(\text{g})$  from the crystal surface. The parabolic time-dependence of the total mass-loss observed in the mass-loss Langmuir experiments is believed to be due to a decrease in the surface area of the single crystal as decomposition proceeds and not due to a diffusion-controlled rate-limiting step in the vaporization process. A time-dependent decrease in  $\text{Si}^+$ ,  $\text{SiC}_2^+$ , and  $\text{Si}_2\text{C}^+$  intensities due to a decrease in the single crystal surface area is not expected to be observed in the Langmuir mass spectrometer experiments as only a small portion of the vapor flux from the center of the  $\text{SiC}$  crystal surface is sampled by the mass spectrometer.

A simple model used to calculate the mass-loss of a cube with a surface area decreasing with time gives mass-losses in qualitative agreement with those observed experimentally. The data shown in figure 6 best fit the model at short times ( $t < 500$  minutes). At longer times, the model predicts a too-slow decrease in the surface area with time and, hence, too fast a loss of material in comparison with the experimental data.

Details concerning the mechanism for the decomposition of SiC cannot be presented at this time. However, on the basis of a model developed by Searcy for endothermic decomposition reactions which form porous solid reaction products, the preliminary vaporization data and SEM results reported here indicate that either a chemically activated mechanism of surface diffusion or a step involving the gaseous reaction products is rate-limiting [24,25].

---

We wish to thank Alan Searcy for helpful discussions concerning the kinetics of decomposition reactions and for informing us of Meschi's model for intramolecular scattering; MaryAnn David for performing some of the mass spectrometer Knudsen effusion measurements; and Terry Wallace for his support and interest in this project. We wish also to thank the Los Alamos Scientific Laboratory for providing funds under its New Research Initiatives Program.

#### References

- [1] Rovner, L. H. and Hopkins, G. R., Nuclear Tech. **29**, 274 (1976).
- [2] Hopkins, G. R., Low Atomic Number Materials for Fusion. An Assessment Study, General Atomic Company Report GA-A13306 (September 15, 1974).
- [3] McHargue, C. J. and Scott, J. L., Metall. Trans. A, **9A**, 151 (1978).
- [4] Scace, R. I. and Slack, G. A., J. Chem. Phys. **30**, 1551 (1959).
- [5] Knippenberg, W. F., Philips Research Reports, **18**, 161 (1963).
- [6] Stull, D. R. and Prophet, H., JANAF Thermochemical Tables, Second edition, National Bureau of Standards Publication NSRDS-NBS 37 (June 1971).
- [7] Addamino, A., Speculations on the origins of the polytypism of SiC, in Silicon Carbide-1973, 179 (Univ. of S. Carolina Press, Columbia, S.C., 1973).
- [8] Ruff, O. and Konschak, M., Z. Electrochem. **32**, 515 (1926).
- [9] Ruff, O., Trans. Electrochem. Soc. **68**, 87 (1935).
- [10] Drowart, J., DeMaria, G., and Inghram, M. G., J. Chem. Phys. **29**, 1015 (1958).
- [11] Weltner, W., Jr. and McLeod, D., Jr., J. Chem. Phys. **41**, 235 (1964).
- [12] Drowart, J. and DeMaria, G., Thermodynamic study of the binary system carbon-silicon using a mass spectrometer, in Silicon Carbide. A High Temperature Semiconductor, J. R. O'Connor and J. Smiltens, eds., p. 16 (Pergamon Press, 1960).

- [13] Grieveson, P. and Alcock, C. B., The thermodynamics of metal silicides and silicon carbide, in Special Ceramics, P. Popper, ed., p. 183 (Heywood and Company Ltd., London, 1960).
- [14] Davis, S. G., Anthrop, D. F., and Searcy, A. W., J. Chem. Phys. 34, 659 (1961).
- [15] Mell, H. and Brodsky, M. H., Thin Film Solids, 46, 299 (1977).
- [16] Voronin, N. I., Makarova, N. L., and Yudin, B. F., Issled. v Obl. Khim. Silikatov i Okislov, Akad. Nauk SSSR, Sb. Statei, 203 (1965).
- [17] Ghoshtagore, R. N., Solid-State Electronics, 9, 178 (1966).
- [18] Paule, R. C. and Mandel, J., Analysis of Interlaboratory Measurements on the Vapor Pressure of Gold, National Bureau of Standards Special Publication 260-19 (January, 1970).
- [19] Cubicciotti, D., J. Phys. Chem. 70, 2410 (1966).
- [20] Behrens, R. G. and Rosenblatt, G. M., J. Chem. Thermodynamics, 4, 175 (1972).
- [21] Meschi, D., J. Phys. Chem. 76, 2947 (1972).
- [22] Roberts, J. Jr., and Searcy, A. W., High Temperature Science, 4, 411 (1972).
- [23] Greenberg, E., Natke, C. A., and Hubbard, W. N., J. Chem. Thermodynamics, 2, 193 (1970).
- [24] Searcy, A. W. and Beruto, D., J. Phys. Chem. 80, 425 (1976).
- [25] Searcy, A. W. and Beruto, D., J. Phys. Chem. 82, 163 (1978).

#### Discussion

Question (Weltner): You spoke of Drowart's data; did you restrict yourself when you were thinking of the molecular species and their properties to Drowart's discussion of them? There has been some recent work on  $\text{SiC}_2$  by Verma and Nagaraj [Canadian J. Phys. 52, 1938 (1974)], and the vibrational frequencies have changed. Do you know of this?

Response (Rinehart): I am not aware of this.

Comment (Weltner): Well, the  $\text{SiC}_2$  molecule is now pinned down quite thoroughly, I think, and very well done. The low vibrational frequencies have shifted considerably from earlier data. Now, I really didn't notice how good your agreement was between second and third law, but I just thought you would be interested.

Question (Hildenbrand): You mentioned the change in transmission efficiency with your mass filter, with mass discrimination effects between gold and silicon. But of course that would also affect the evaluation of these minor species partial pressures as well.

Is it possible to make reliable corrections for mass discrimination that are stable and would be useful over a wide mass range. Lots of people publish data with quadrupole instruments and never mention this problem.

(Editor's note): The response was not recorded but the main text contains some discussion of this point. Further pertinent information can be found elsewhere in this volume (see Bonnell and Hastie).

Moderator (Rosenblatt): Do you expect the mass signal to be independent of surface area from the geometry of the sampling system and beam collimation used in the mass spectrometer.

Response (Rinehart): The crystal was fairly large, and I don't think we were really sampling it all. We sampled only a small portion of that.



## A VERY ACCURATE PYROMETER FOR GENERAL LABORATORY USE<sup>1</sup>

E. K. Storms and B. A. Mueller  
Los Alamos Scientific Laboratory  
University of California  
Los Alamos, NM 87545

Using commercially available equipment, a photon counting pyrometer was constructed which permits temperatures from 1400 K to above 2200 K to be measured routinely to within 0.5 K and 1.0 K, respectively, of the International Practical Temperature Scale.

### 1. Introduction

Planck's Law is used as the basis for extrapolating the temperature scale above the melting point of gold. Pyrometry in this temperature range, therefore, requires the measurement of radiation flux at a known wavelength. The most common laboratory pyrometers do this by using the eye to compare the unknown flux with that from a lamp of known characteristics. Advanced devices use a photomultiplier tube for this comparison, thereby significantly increasing the precision. However, in both cases the accuracy depends on knowing the characteristics of a lamp within the pyrometer.

This limitation can be removed by measuring the radiation flux directly using a photomultiplier tube which operates in either the digital or analog mode [1,2,3]<sup>2</sup>. With the availability of fast counting circuits and digital computers, the greater stability of the digital mode has made this technique attractive. In addition, calibration is very simple, requiring the use of a single known temperature and a variable, but uncalibrated source of radiation. Because a commercial instrument is not yet available, we have adapted those items which are available to construct a relatively inexpensive, but very accurate pyrometer for general laboratory use. This paper describes the adaptation and resulting performance.

We have described our experience with particular equipment in order to give the general principles which the reader may use in choosing other approaches. The manufactured items mentioned are not necessarily the best or the least costly of those available.

### 2. Description of Apparatus

In general terms, the design is very simple. Light from the object is focused onto a mirror through which a small hole has been drilled. The position of the hole relative to

<sup>1</sup>Work completed under the auspices of the Department of Energy.

<sup>2</sup>Figures in brackets indicate the literature references at the end of this paper.

the object is viewed through a magnifying lens situated at 90 degrees to the optical path. That light which passes through this hole is eventually detected by a photomultiplier tube. An interference filter is placed in front of the mirror so that the object can be focused using the wavelength of interest. Two levels of attenuation are placed in the optical path behind the mirror to extend the range.

Pulses produced by light striking the photomultiplier are amplified and counted using readily available pulse counting equipment having less than a 10 ns dead-time. This permits the measurement of counting rates up to  $10^7 \text{ s}^{-1}$  without excessive uncertainty in the corrected value. Figure 1 shows the general optical and electrical arrangement.

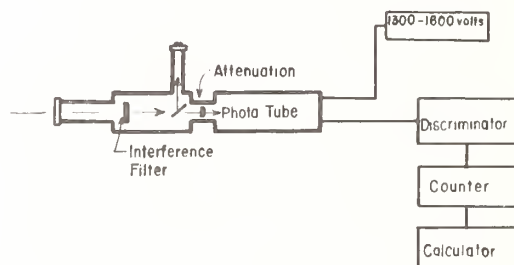


Figure 1. General diagram of optical and electrical arrangement.

Specifically, the optical system is an adaptation of the Pyro Micro Optical Pyrometer [5]. Figure 2 shows a photograph of the result.

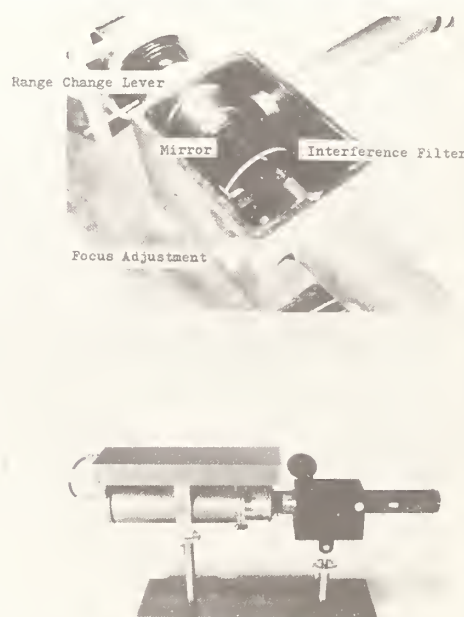


Figure 2. Photograph of photon counting pyrometer.

The mirror was fashioned from a glass microscope cover in which a 0.025 cm hole was drilled followed by the application of a reflective surface. A convex lens, located behind the mirror, causes the transmitted light to occupy a region approximately 1 cm in diameter on the face of the photomultiplier tube. This makes the count rate less sensitive to the presence of dust on the phototube or to a nonuniform photocathode sensitivity. Neutral density filters, located behind the mirror, are chosen to give suitable temperature ranges.

The 9810B photomultiplier [6] was operated at a voltage which was found to lie in the plateau region of the count rate-voltage curve. This was observed to occur at 1360 V and 1500 V for two different multiplier tubes of this type. A RF1-B-213 Phototube housing [6] containing the ML0 and M1 magnetic focusing assemblies was used and these reduced the background count rate to  $50 \text{ s}^{-1}$ . Pulses from the photomultiplier were conditioned and prescaled by 0.1 using a model 1121 amplifier-discriminator [7] and counted by a HP 5328A counter [8]. All count rates given in the paper are values before prescaling.

Calibration requires a single, known black-body temperature, for which the melting point of gold was used, and a value for the wavelength at the transmission maximum of the interference filter. The dead-time of the counting circuits and the light attenuation factors can be obtained in situ using any convenient source of radiation as described below.

Using an adjustable light source, a count rate ( $R_i$ ) is measured in the absence of a filter. A new count rate ( $R_{i+1}$ ) is measured with the filter in the light path. The attenuation factor ( $A_i$ ) and the dead-time ( $\gamma$ ) can be obtained from a series of such measurements by using the equation

$$R_i/R_{i+1} = A_{i+1} + R_i \gamma (A_{i+1}-1)$$

$$i = 1, 2, 3 \dots n$$

Attenuation factors for the other filters are found in a similar manner by using the other ratios.

The corrected count rate ( $R_c$ ) is calculated from the measured count rate ( $R_m$ ) using the equation

$$R_c = \prod_{i=1}^n A_{i+1} R_n / (1 - \gamma R_n)$$

where the attenuation factors for all lower scales are multiplied. Hence, the  $R_c$  term gives the count rate in the absence of a filter and with no dead-time. Planck's law relates the count rate and the unknown temperature ( $T_m$ ) through the approximate equation

$$T_m = 1/[(\ln R_s - \ln R_c) \lambda / C_2 + 1/T_s]$$

where  $R_s$  and  $T_s$  are the count rate and temperature at the calibration point, measured with no filter and corrected for dead-time, and  $\lambda$  is the wavelength of the interference filter.

### 3. Sources of Error

Table 1 lists the errors in those factors to which a statistical analysis can be applied. Multiple measurements were made of the dead-time and the scale attenuation. The error represents a one sigma variation from the mean.

Table 1. Values and uncertainties for the calibration variables.

<u>Variable</u>	<u>Value</u>	<u>Uncertainty</u>	Contribution to the Temperature Error at		<u>Source for Value</u>
			<u>1400 K</u>	<u>2200 K</u>	
Scale 2					
Attenuation	21.74	0.06	---	---	Measured <u>in situ</u>
Scale 3					
Attenuation	155.11	0.06	---	0.08	Measured <u>in situ</u>
Dead-time $10^{-9}$ s	14.4	0.2	0.00	0.36	Measured <u>in situ</u>
Count Rate at Gold Point count/s	77340	300	0.38	0.84	Isothermal Gold Furnace
Filter Wave Length, nm	0.5077	0.0001	0.30	0.42	Cary 14 Spectrophotometer
Melting Point of Gold, K	1337.58		---	---	IPTS-68
Plancks Constant, mK	0.014387865	$3 \times 10^{-9}$	0.00	0.00	CODATA Dec. 1973

Values for the interference filter wavelength were obtained from the manufacturer [9] and from our measurements using, in both cases, Cary 14 spectrophotometers which were calibrated using Hg lines and a H<sub>2</sub> high pressure lamp, respectively. Agreement between the two measurements was better than  $1 \times 10^{-10}$  m. Because the filter was not truly monochromatic, a value of  $5 \times 10^{-10}$  m was calculated and added to the value at the transmission center to give an effective wavelength for black-body radiation.

Calibration at the gold melting point involved multiple measurements of counting rate vs time during both cooling and heating through a transition lasting approximately 15 min. The two values, which differed by 0.4°, were averaged. The gold used in the graphite black-body furnace was better than 99.995 percent pure. A spectroqualitative analysis is given in table 2. We have assumed that this gold melts at an indicated temperature equal to that adopted by IPTS-68 (1337.58 K). A cross section view of the furnace assembly is shown in figure 3.

Table 2. Result of spectroqualitative analysis of gold used in the melting point furnace

Li < 4	Cr < 2	Zr < 6	Sb < 40
Be < 0.6	Mn < 20	Nb < 20	Ba < 1
B < 6	Fe < 2	Mo < 4	Ta < 60
Mg < 0.6	Co < 2	Ru < 6	W < 20
Al 0.6	Ni < 2	Rh < 6	Ir < 20
Si < 2	Cu < 0.6	Pd < 2	Pt < 60
K < 40	Zn < 60	Ag 1.5	Au MAJOR
Ca < 0.6	Ga < 2	Cd < 2	Tl < 20
Ti < 2	Ge < 6	In < 6	Pb < 6
V < 2	Sr < 0.6	Sn < 6	Bi < 4

< Symbol represents limit of detection. Values in µg/g.

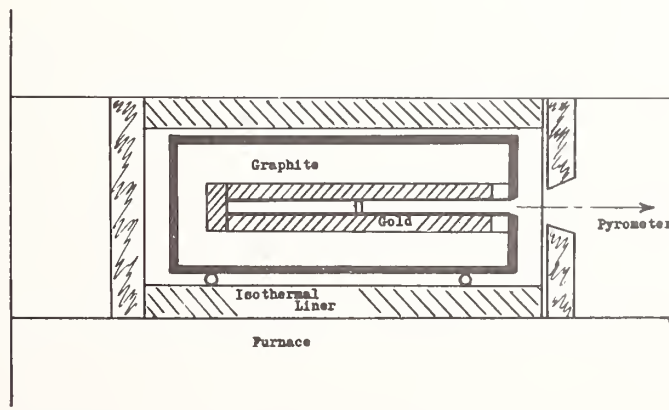


Figure 3. Cross section view of gold furnace.



A sufficient number of photons were measured (50) that the statistical error in the count rate was negligible.

#### 4. Comparison to Other Devices

Table 3a summarizes the results obtained by comparing the photon pyrometer with various calibrated sources. The origin of the calibrations is given in table 3b. The first four items are part of the CMB-3 group standards, items 5 and 6 are used by the Los Alamos Scientific Laboratory standards group, and number 7 is used by the Sandia Laboratory Standards Laboratory as a transfer standard from ten NBS calibrated lamps. All of the other pyrometers have been compared with various NBS calibrated strip lamps and the results show no differences outside the stated accuracy.

A furnace of a design similar to that used for gold was constructed and used to melt copper. The result, shown as the last entry on table 3a, was within  $0.26^\circ$  of the NBS certified value.

#### 5. Discussion

Photon counting pyrometry offers several advantages over conventional pyrometers. For example, calibration of the entire temperature range requires only a comparison to a single known temperature. The non-linearity of the device, caused by the dead-time of the counting circuits and the scale change produced when the neutral density filters are changed, can be measured easily to high accuracy using any source of light. Filter factors based on  $1/T_0 - 1/T_a$  ("A" values), as used in conventional devices, are unnecessary, thereby reducing the scale overlap error to about  $0.7^\circ$ . The use of an interference filter rather than a glass absorber, as is common, further increases the accuracy.

Based on our experience, the reproducibility of any reading is better than  $\pm 0.2^\circ$  and the long term drift in calibration is less than  $1^\circ$  if the dead-time is determined periodically. The absolute accuracy relative to the International Temperature Scale (1968), is better than  $2^\circ$  based on other calibrated devices and better than  $1^\circ$  based on a first principle calculation as shown in table 1. By using additional filters, the upper temperature range can be increased almost without limit. With proper design an instrument can be made which could reproduce the International Temperature Scale to within  $0.5^\circ$  at 2500 K and  $1^\circ$  at 3000 K. All this is possible in a routinely used laboratory instrument for a cost significantly below comparable devices.

A comparison to conventional, calibrated standards (summarized in table 3a and detailed in table 4) shows that the photon pyrometer is well within the stated error of these devices if the difference is averaged over the entire calibration range. However, as can be seen in table 4, the difference changes with temperature and scale by amounts which are unique to the particular pyrometer and, in some cases, are outside the expected error. In addition, the automatic pyrometers tended to read an excessively high value at the gold print. We conclude from this comparison that the photon pyrometer is internally more consistent and

Table 3a. Comparison between the photon pyrometer and various calibrated sources.

<u>Standard</u>	<u>Range, K</u>	<u>Stated Accuracy</u>	<u>Difference over the Range, std-photon</u>	<u>Precision</u>	<u>Number of Values</u>	<u>Measured T At Gold Point</u>
Black-body Gas Lamp	1923-2273	$\pm 0.2\%$	+ 5.4	+ 3.1	22	---
Black-body Vacuum Lamp	1473-1973	$\pm 0.2\%$	+ 2.5	$\pm 1.2$	18	---
Pyro M5399 <sup>a</sup>	1473-2373	$\pm 5$	- 1.2	$\pm 1.8$	20	---
Pyro M5108 <sup>a</sup>	1473-2373	$\pm 5$	+ 1.7	$\pm 1.4$	11	
LN 8642						1341.0 (M)
Serial 391 <sup>a</sup>	1386-2373	$\pm 5$	+ 0.5	$\pm 1.8$	18	1337.4 (L)
LN 8642						
Serial 390 <sup>a</sup>	1396-2439	$\pm 5$	- 1.4	$\pm 1.0$	17	1340.8 (L)
LN 8642 <sup>a</sup>	1050-1300	$\pm 1$	+ 2.5	$\pm 0.2$	10	
Sandia test						
NBS 45d Copper	1359.95	$\pm 0.5$	+ 0.26	$\pm 0.45$	10	(5 cooling + 5 heating)

<sup>a</sup>Comparison made using the black-body lamps.

Table 3b. Calibration information about the various sources.

<u>Standard</u>	<u>Source of Calibration</u>	<u>Year</u>	<u>Remarks</u>
BB Gas Lamp	National Physical Laboratory (England) Test # 100/71/Gas	1971	Calibration above 2320 K grossly in error.
BB Vac Lamp	National Physical Laboratory (England) Test # 100/70/VAC	1971	Construction described in Ref. [4].
M5399	National Bureau of Standards (USA) Test # 182836	1965	Lamp current calibrated, corrected to IPTS68.
Serial # 391	Sandia Laboratories Test # 4897G	1977	Automatic pyrometer.
Serial # 390	Sandia Laboratories Test # 2876G	1977	Automatic pyrometer.
Sandia	Direct Comparison to 10 NBS Calibrated Strip Lamps Test #4069C	1977	Automatic pyrometer.
NBS 45d Copper	National Bureau of Standards	1971	Melted in graphite.

at least as accurate as the standards we have available. However, if the photon pyrometer is used simply as a stable comparator between the various calibrated automatic pyrometers, the results suggest that such devices may have errors at some temperatures which are far outside the instrument precision and the stated accuracy of the calibration.

Table 4. Comparison to calibrated pyrometers.

LN # 391 Std-photon scale					LN # 390 Std-photon scale				
L	M	H	X	T,K	L	M	H	X	T,K
+ 2.4	+ 5.6			1386	- 0.5	+ 1.2			139
+ 2.7	+ 4.5			1433		- 1.5			150
	+ 2.3			1478		- 3.5			163
	- 0.6			1579		- 4.2			170
	- 1.8			1660		- 3.9	- 1.4		191
	+ 0.4			1720		- 3.9	- 1.5		207
	- 3.5			1787			- 0.3		206
	- 1.4	+ 2.9		1918			- 0.3		216
	0.0	+ 1.0		1966			- 2.1		227
	+ 1.4	+ 0.5		2023			- 0.5		226
		- 0.3		2123			- 1.4		231
	- 4.3			2323			+ 0.5	0.0	236
	- 3.7			2461			+ 0.5	0.0	241
Pyro M 5399					Pyro M 5108				
- 1.5				1471	+ 1.5				147
- 1.9	- 1.0			1569	+ 0.1				157
- 1.9	- 3.0			1670	+ 1.6	+ 0.5			167
	- 4.6			1770		- 2.3			177
	- 3.5			1821		- 0.6			187
	- 2.8			1869		+ 0.7			197
	- 2.1			1920		+ 5.7			207
	- 1.8			1970		+ 4.3			217
	- 2.7			2018		+ 5.8			227
	+ 2.4	+ 4.2		2068		+ 2.2			237
	- 2.2	+ 1.7		2118					
	+ 2.7	+ 6.4		2165					
		- 4.5		2267					
		- 4.9		2315					
		- 1.4		2361					

In addition to the errors noted above, the particular photon pyrometer used for the comparison showed a slight temperature variation with focal distance. Because this was not noted until after the study was made, the photon-standard comparison has an additional  $\pm 1^\circ$  uncertainty in the absolute accuracy. Improved optics based on inexpensive camera optics would eliminate this problem and make the device cheaper and more convenient.

## 6. Summary

This study has demonstrated the exceptional accuracy of the photon counting technique and has resulted in a comparison between the temperature standards used at NBS, Sandia Laboratories, and the Los Alamos Scientific Laboratories.

---

The authors wish to thank Allen Gauler (SP-14) and R. Foster (Sandia Laboratory) for their help and cooperation in calibrating the photon pyrometer.

## References

- [1] Treiman, L. H., Temperature--Its Measurement and Control in Science and Industry, 3, 523 (1962).
- [2] Quinn, T. J. and Ford, M. D., Proc. Roy. Soc. A312, 31 (1969).
- [3] Storms, E. and Mueller, B., J. Phys. Chem. 81, 318 (1977).
- [4] Quinn, T. J. and Barber, C. R., Metrologia, 3, 19 (1967).
- [5] Manufactured by Pyrometer Instrument Co., Inc., Bergenfield, NJ, USA.
- [6] Available from Gencom Division/Emitronics, Inc., 80 Express St., Plainview, NY 11803.
- [7] Manufactured by Princeton Applied Research Corp., P. O. Box 2565, Princeton, NJ 08540.
- [8] Manufactured by Hewlett-Packard, 1820 Embarcadero Rd., Palo Alto, CA 94303.
- [9] Ealing Corp., 22 Pleasant St., South Natick, MA 01760.

## Discussion

Moderator (Cater): The pyrometer you described is one which would be usable at lower temperatures than ordinary optical pyrometers, is that correct?

Response (Ed Storms): You could. It does require having a sufficient amount of light, and that of course is determined to some extent by the size of the little hole in the mirror and the wave length that you intend to use, but in principle you can go to much lower temperatures. How low, I don't know. We haven't really tried to push it at the lower end.

Question (Hildenbrand): Ed, what about possible systematic errors introduced by temperature gradients in the cell itself. I know you have done a lot of work on this, but has that been absolutely eliminated? What if you had studied a standard whose properties are very well established, such as gold, do we know that has been eliminated?

Response (Ed Storms): Well, we have, and this is in the boron studies where we went directly into the cell---. We have studied gold, unfortunately our particular instrument has possibilities for error -- in some of the early studies we did get close to gold, very close.



## OPERATION OF NEAR IDEAL HEAT PIPES

L. A. Melton

Department of Chemistry  
The University of Texas at Dallas  
Richardson, TX 75080

An analytical model has been developed to describe the operation of gas-loaded heat pipes and to assess the extent of deviations from ideal behavior due to diffusion, and sonic flow. The model predicts, with reasonable accuracy, the start-up power, the maximum heat transport, and the thermal regulation ( $=\Delta$  density/ $\Delta$  input power). Experimental results will be presented for Li/He heat pipes. This approximate analytical model should enable heat pipe users to design and operate heat pipes optimally without extensive and costly computer solutions of the full Navier-Stokes equations.

The model is based on approximate solutions of diffusion/convection equations, in which the convective velocity distribution of a nearly ideal heat pipe is assumed to be identical to that of an ideal heat pipe. The vapor is treated as a one-dimensional compressible fluid. Among the more important results are the following:

- 1) The start-up power, defined as the power required to bring the metal vapor density to 95 percent of  $n_0$  the stagnation density at the exit of the heated zone (or adiabatic zone if present), is virtually independent of  $n_0$ .
- 2) For a heat pipe whose thermal losses are dominated by radiation, the start-up power varies as  $T_0^{9/4}$ , where  $T_0$  the stagnation temperature is defined by  $n(T_0) = n_0$ .
- 3) The sonic or choked flow limit,  $Q_{CF}$ , may be approximated as  $Q_{CF} = 1/2 h_{fg} A n_0 c(T_0)$  where  $h_{fg}$  is the heat of vaporization per atom,  $A$  is the cross sectional area, and  $c(T_0)$  is the speed of sound at  $T_0$ .

Applications to the measurement of vapor pressure at high temperatures are discussed.

## 1. Introduction

In recent years, heat pipes have become popular as a convenient means for the stable confinement of reactive metal vapors under defined temperature and pressure conditions. They have been used in spectroscopic, energy transfer, and reaction studies [1-8]<sup>1</sup>. Throughout these studies, the heat pipes have been assumed to operate "ideally," in the sense of an isothermal metal vapor whose pressure is equal to that of the inert buffer gas and is unaffected by the power input through the heaters. Thus, the pressure in the metal vapor zone except for the sharply defined transition regions, may be determined by measurement of the buffer gas pressure in the low temperature, typically room temperature, regions.

In the spectroscopic literature, only Vidal has attempted to characterize the limitations of the "ideal" heat pipe assumptions, and his work concerns only the high power/low pressure operation [9]. Many experimental studies and computer solutions of the Navier-Stokes equations have appeared in the engineering literature, again primarily to characterize the maximum heat transport possible with a given heat pipe design [10-26]. Successful as these studies have been, they still fail to provide the experimentalist with a working, tractable, assessment of the "ideality" of his heat pipes. In Section 2 of this paper, we present data on the operating characteristics of cylindrical gas loaded heat pipes and compare the performance with that of "ideal" heat pipes. In Section 3, we develop an approximate analytical model of heat pipe operation, which is particularly useful in assessing low power operation. In Section 4, we describe how these approximate models can be used to define ranges of metal vapor pressure and heater power in which near ideal heat pipe operation is obtained. In particular, the functional dependence of the start-up power, the minimum power necessary for near ideal heat pipe operation, is shown to be very weakly dependent on the chosen buffer gas pressure. The intent of this paper is thus not the exact calculation of heat pipe performance, but rather the provision of approximate analytical solutions which, because they display explicitly their dependence on microscopic parameters (heats of fusion, atomic masses, collision cross sections, etc.) and macroscopic parameters (diameters, lengths, etc.), will be useful to spectroscopists and kineticists in designing, scaling, and operating near ideal gas loaded heat pipes.

## 2. Experimental

The data given in this paper were taken on a lithium heat pipe, operating in the 0.3-3.0 Torr range with He as a buffer gas.

### 2.1 Apparatus

#### 2.1.1 Heat pipe

The heat pipe, shown in figure 1, was constructed of 2-1/2 inch o.d. stainless steel pipe, type 304, 1/16 inch wall, 39 inches long. It was originally designed for use in

---

<sup>1</sup>Figures in brackets indicate the literature references at the end of this paper.

energy transfer measurements involving collisions of laser excited  $\text{LiH } A^1\Sigma$  with  $\text{Li}(^2S)$  atoms [7]. In order to reduce laser scattered light, the pipe was crossed at its midpoint by a 1-inch o.d., 1/16 inch wall stainless steel pipe. The wick was constructed of 2-3 layers of 60 mesh stainless steel, type 303, wire cloth. In addition, 2-3 inch long wicks were provided for the 1 in. cross pipe. Before lithium was added, the heat pipe was baked overnight under vacuum at 500-700 °C in order to clean the mesh and enhance the ease of wetting. Typically 30-50 grams of lithium were used in the heat pipe.

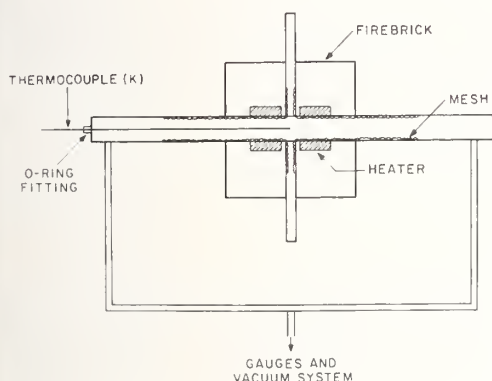


Figure 1. Heat pipe used in experimental studies.

The temperature in the heat pipe was monitored with a chromel-alumel thermocouple referenced to an ice bath temperature junction. The thermocouple, which was protected by a 1/8 inch diameter by 42 inch long stainless steel sheath, was inserted through an O-ring and could be moved continuously in and out of the vapor zones. In these measurements, particular care was taken to keep the thermocouple junction on the axis of the heat pipe, although checking measurements showed no measurable temperature difference (i.e.  $<0.2$  K) between the vapor and the wick. The thermocouple was calibrated against a Pt/Rh thermocouple, which in turn was calibrated against a NBS standard thermocouple. At 1000 K, agreement of  $\pm 2$  K was found between our thermocouples and the standards.

### 2.1.2 Other instrumentation and procedures

Pressures were measured with a Datametrics 1000 Torr full scale capacitance manometer. Pressures as low as 5 microns could be measured reliably. The power to drive the heat pipe was supplied by four semi-cylindrical heating elements, 3-1/2 inch long, 3 inch i.d., rated at 350 watts each, located as close as possible to the center of the pipe. The pipe and heaters were surrounded by insulating fire brick. The fire brick extended past the heaters by 2-1/4 inches on each side. Thermocouple voltages were measured to 0.01 mV with a Keithley model 190 digital voltmeter and were converted to temperatures by use of standard tables

[27]. Vapor pressures of Li atoms and  $\text{Li}_2$  molecules were calculated from the JANAF tables [28], or from the constants provided by Nesmeyanov [29].

## 2.2. Observation and results

In figure 2, we display the temperature profiles measured with He as a buffer gas, and at a series of powers ranging from just below the start-up power at 800 watts to full, near ideal operation, at 1900 watts. The profiles shown here exhibit many of the characteristics of simple gas loaded heat pipes which will be treated in the development of the analytical model in Section 3.

In figure 2a, the heat pipe is very much underpowered, the metal vapor is in equilibrium with the liquid, but no convective flow of metal vapor is present since a significant helium pressure exists even in the center of the heat pipe. Hence, the temperature profiles for helium pressures of 0.3, 1.0, and 3.0 Torr are almost identical.

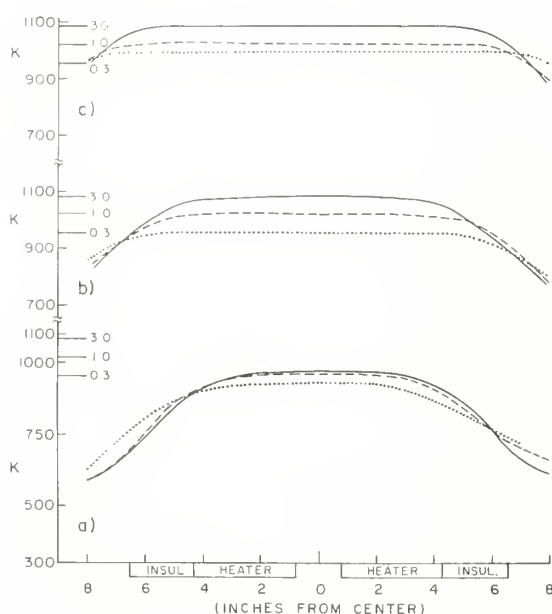


Figure 2. Temperature profiles for heat pipe at various buffer gas pressures and powers: (a) 800 watts, (b) 1300 watts, and (c) 1900 watts. Gas pressures, in Torr, are 3.0 (solid curve), 1.0 (broken curve), and 0.3 (dotted curve). Marks at left side indicate temperatures at which the designated total pressure of lithium vapor (monatomic and diatomic) is obtained. (JANAF Tables).

In figure 2b, the profiles for 0.3 and 1.0 Torr show the flat profiles which are widely regarded as the test of ideal heat pipe operation. The profile for 3.0 Torr, however, still shows a slightly rounded profile and a maximum temperature of 1082 K which is 5 degrees less than the calculated equilibrium value at this pressure. In the more stringent criterion use by Rohani and Tien [14], the 0.3 and 1.0 Torr profiles still represent underpowered heat pipes since the temperature begins to drop before the end of the adiabatic region is reached.

In figure 2c, the 1.0 and 3.0 Torr profiles show that these heat pipes, particularly the 1.0 Torr one, are operating very nearly ideally. The 0.3 profile shows that this heat

pipe is operating in the "choked flow" regime; the convective vapor flow velocity is near the local speed of sound, and the additional heat can only be moved by an increase in the vapor density. Because the vapor is in equilibrium with the liquid metal, the temperature also increases.

In figure 3, a different sort of data is shown. Here the thermocouple junction was located at the center of the heat pipe, radially and axially. For a given buffer gas pressure,  $P_0$ , the heater power was increased and the temperature of the junction was measured. Through use of tables [27,28], these thermocouple readings were converted to total vapor pressure,  $P_T$  (atoms and diatomics). The electrical power dissipated in the heaters is greater than the power convected through the heat pipe since a portion of the heat diffuses through the fire brick insulation. By use of the thermal conductivity of fire brick [27], this diffusive heat loss was estimated to be 100-150 watts; it is relatively insensitive to the operating temperature of the heat pipe.

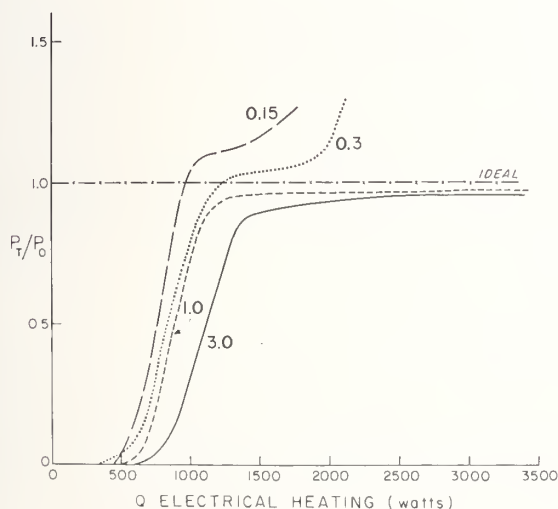


Figure 3. Pressure in center of heat pipe ( $x=0$ ) as a function of heater power for helium pressures of 0.15, 0.30, 1.00, and 3.00 Torr.

The curves shown in figure 3 exhibit the same characteristics shown in figure 2. At low powers, there is insufficient heat to drive the convection against the diffusion of He atoms into the metal vapor zone. Once a certain power is reached, typically the power for which  $P_T/P_0$  is approximately 0.9, the heat pipe "turns on" and  $P_T$  becomes nearly independent of the electrical power, or heat conducted. This ideal operation, however, depends very much on  $P_0$ , the buffer gas pressure. The curves for  $P_0 = 1.0$  and 3.0 Torr show an extensive plateau once the minimum, or "start-up," power is reached. The curves for 0.3 and 0.15 Torr, on the other hand, show very little in the way of a plateau region. Indeed, for these buffer gas pressures, there is very little separation between the minimum convected heat necessary,  $Q_{\text{START-UP}}$ , and the maximum convected heat possible at a metal vapor density corresponding to a buffer gas pressure  $P_0$ ,  $Q_{\text{CHOKED-FLOW}}$ . These heat pipes have essentially no range of input power for which they operate ideally. In Section 3, we shall see that  $Q_{\text{SU}}$



is only weakly dependent (logarithmically) on  $P_0$ , whereas  $Q_{CF}$  varies linearly with  $P_0$ . At high values of  $P_0$ ,  $Q_{CF} \gg Q_{SU}$ , and at sufficiently low values  $Q_{CF} \approx Q_{SU}$ . Near ideal operation is easily obtained for sufficiently large  $P_0$ , but is difficult to obtain for small  $P_0$ .

### 3. Approximate Analytical Model

This model is based on the experimental observations discussed above as well as on theoretical calculations involving computer solutions of the two-dimensional Navier-Stokes equations. The computer solutions, in this context, are experiments, also, since they correctly portray the operation of a heat pipe. However, their dependence on the metal vapor parameters and heat pipe dimensions is not explicit, and hence the utilization of these results in predicting heat pipe performance under very different conditions is difficult. We shall use the rough agreement obtained between the results of the model and the results of the laboratory and computer experiments as a means of confirming the model's overall validity. Since the dependence on fundamental parameters--density, temperature, diffusion coefficients, etc.--is explicit, these model equations, once developed and tested, can easily be applied to the design of heat pipes for operation under unfamiliar conditions.

#### 3.1 Basic convection/diffusion model

We take as our fundamental equation, the convection/diffusion balance for the buffer gas

$$n_B v_M - D_{B/M} \frac{dn_B}{dx} = J_B \quad (1)$$

where  $n_B$  is the number density of the buffer gas,  $v_M$  is the bulk flow velocity of the metal vapor,  $D_{B/M}$  is the diffusion coefficient for the diffusion of buffer gas through metal vapor,  $x$  is the distance from the center of the heat pipe, and  $J_B$  is the net flux of buffer gas. In steady state,  $J_B = 0$ .

We define the following working variables:

$$P = \frac{n_M}{n_0} \quad (2)$$

where  $n_0$  is the buffer gas density at the stagnation point,

$$D_{B/M} = \frac{D_R}{n_M} \quad (3a)$$

$$D_0 = \frac{D_R}{n_0} \quad (3b)$$

where  $D_R$  is the "reduced diffusion coefficient," i.e. the nondensity dependent portion of the diffusion coefficient.

Finally, we note that

$$n_B + n_M = n_0 \quad (4)$$

provided that the flow velocity  $v_M$  is sufficiently small that compressibility effects are negligible. In practice, this allows  $v_M < 0.3c$ , where  $c$  is the local speed of sound.

With these substitutions, eq. (1) yields

$$n_0(1-P)v_M - (D_R/P) \frac{d(1-P)}{dx} = 0 \quad (5)$$

Integration of this differential equation yields

$$\frac{P(x_2)}{1-P(x_2)} - \frac{P(x_1)}{1-P(x_1)} \exp. - \left[ \frac{1}{D_0} \int_{x_1}^{x_2} v_M(x) dx \right] = 0 \quad (6)$$

We adopt Rohani and Tien's [14] criterion for heat pipe start up, and require

$$x_2 = \ell_a \quad P(x_2) = 0.99 \quad (7a)$$

$$x_1 = \ell_c \quad P(x_1) = 0.01 \quad (7b)$$

where  $\ell_a$  is the exit of the adiabatic zone and  $\ell_c$  is the end of the primary condensation (cooling) zone (see fig. 4). Hence,

$$4D_0 \ln 10 = \int_{\ell_a}^{\ell_c} v(x) dx \quad (8)$$

Equation (8) is the basic result needed for the analysis of heat pipe start-up. Since  $v(x)$  depends on the heating power provided to the heat pipe, then by finding the functional dependence of  $v_M$  on  $Q$ , the input power, we can find the value of  $Q$  which satisfies (8). This will be  $Q_{\text{START-UP}} \equiv Q_{\text{SU}}$ .

The choice of  $P(x_2) = 0.99$  and  $P(x_1) = 0.01$  is somewhat arbitrary. However, because of the logarithmic dependence in eq. (8), reasonable choices will lead to acceptable estimates of  $Q_{\text{SU}}$ .

### 3.2 Velocity distribution in heat pipe

If the velocity distribution in the heat pipe were known exactly as a function of the input power  $Q$ , the calculation of density profile and  $Q_{SU}$  would be straight-forward. We may, however, approximate the velocity profile, and thus estimate  $Q_{SU}$ . At low power, the metal vapor behaves as an incompressible fluid, and we may postulate velocity profiles which match those calculated in exact computer solutions [24]. These idealized profiles are shown in figure 4 along with schematic representations of the true velocity profiles.

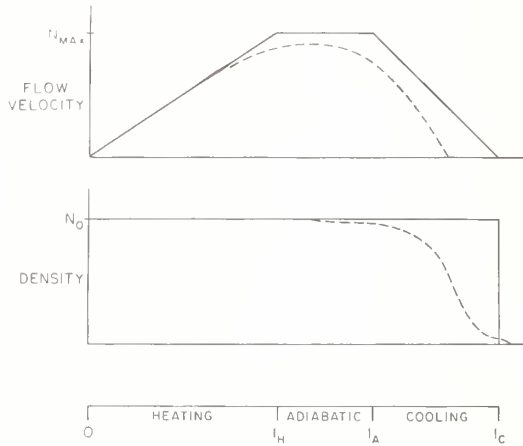


Figure 4. Velocity and density profiles — ideal heat pipe, no diffusion,  $\beta = 1$ ; ---- ideal heat pipe with diffusion,  $\beta = 1$ .

Mathematically, we may approximate the velocity distribution by

$$\frac{v(x)}{v_{MAX}} = \begin{cases} \frac{x}{l_H} & 0 \leq x \leq l_H \\ 1 & l_H \leq x \leq l_a \\ \frac{1}{\beta(l_c - l_{c,SU})} \left\{ [\beta(l_c - (l_{c,SU} - l_a)) - x] - (l_a - x) \right\} & l_a \leq x \leq l_c - (l_{c,SU} - l_a) \\ \frac{1}{\beta} \frac{(l_c - x)}{(l_{c,SU} - l_a)} & l_c - (l_{c,SU} - l_a) \leq x \leq l_c \\ 0 & l_c \leq x \end{cases} \quad (9)$$

where  $\beta = Q/Q_{SU}$ .  $\ell_c$  and  $\ell_{c,SU}$  are defined by the condition that the cooling must be complete at  $\ell_c$  or  $\ell_{c,SU}$  for input power  $Q$  or  $Q_{SU}$ , respectively.

In the case of a heat pipe whose heat rejection is dominated by radiative heat losses (almost certainly the case for these high temperature heat pipes), we have

$$(\ell_c - \ell_a)(2\pi r)\epsilon \sigma_{SB}(T_o^4 - T_R^4) = Q \quad (10)$$

as the defining equation for  $\ell_c$ .  $\epsilon$  is the emissivity of stainless steel, typically 0.8-0.9 for oxidized stainless steel and  $\sigma_{SB}$  is the Stephan-Boltzmann constant,  $r$  is the outer radius of the pipe,  $T_o$  is the stagnation temperature, i.e.  $n(T_o) = n_o$ , and  $T_R$  is room temperature. More generally, we have

$$Q = (\ell_c - \ell_a)/\alpha \quad (11)$$

where  $\alpha^{-1}$  is the heat loss per unit length of pipe.

For  $\beta = 1$ , we obtain the idealized profile shown in figure 4.

### 3.3 Relation of $v_{max}$ and $Q$

At low flow velocities, as might be expected under start-up conditions, the metal vapor behaves as an incompressible gas (see for example, Vidal's paper [9]). Under the conditions,

$$Q = v_{max} A n_o h_{fg} \quad (12a)$$

where  $A$  is the cross-sectional area of the heat pipe,  $n_o$  is the stagnation density (and the metal vapor density in this near ideal heat pipe).  $h_{fg}$  is the heat of vaporization of the metal vapor per atom.  $v_{max}$  is the flow velocity at the exit of the heater zone and throughout the adiabatic zone. Hence,

$$v_{max} = \frac{Q}{A n_o h_{fg}} \quad (12b)$$

### 3.4 Solution for $Q$

By using eqs. (9) and (12b) in eq. (8) with  $\beta = 1$ , we obtain

$$4 \ln 10 = \frac{v_M}{2D_o} (\ell_{c,SU} - \ell_a) \quad (13a)$$

$$= \frac{1}{2D_0} \left( \frac{Q_{SU}}{h_{fg} A n_0} \right) \propto Q_{SU} \quad (13b)$$

$$Q_{SU} = [(8D_0 (\ln 10) h_{fg} A n_0) / \alpha]^{1/2} \quad (14a)$$

If we use simple kinetic theory approximations for  $D_0 = \frac{1}{2} \bar{c} \left( \frac{1}{\sqrt{2} n_0 \sigma_c} \right)$  [30], where,  $\bar{c} = (8kT/\pi\mu)^{1/2}$ , is the mean relative velocity and  $\sigma_c$  is the collision cross section, and use eq. (10) to define  $\alpha$ , we obtain

$$Q_{SU} = [8 \ln 10 (\frac{1}{2} \bar{c} \frac{1}{\sqrt{2} n_0 \sigma_c}) h_{fg} (\pi r^2) n_0 (2\pi r) \varepsilon \sigma_{SB} (T_o^4 - T_R^4)]^{1/2} \quad (14b)$$

$$= \left\{ [4\sqrt{2} (\ln 10) \sigma_{SB} \pi^2] \left[ \frac{\bar{c} h_{fg} (T_o^4 - T_R^4)}{\sigma_c} \right] [\varepsilon r^3] \right\}^{1/2} \quad (14c)$$

In eq. (14c), the first factor in contains numerical constants, the second contains molecular properties, and third properties of the pipe itself.

Taking into account the  $T^{1/2}$  dependence of  $\bar{c}$ , we have

$$Q_{SU} \propto T_o^{9/4} r^{3/2} \quad (15)$$

In eq. (14b), the direct dependences on  $n_0$  cancel out, and the only remaining dependence is through  $T_o$ , which depends logarithmically on  $n_0$ , a very weak dependence. For example, increasing  $P_o$  from 0.3 Torr to 3.0 Torr, a factor of ten, increases  $T_o$  from 956 K to 1087 K, and  $Q_{SU}$  increases by a factor of only 1.33.

#### 4. Discussion

##### 4.1 Validation of model

In the heat pipe literature, only Rohani and Tien [14] have made full computer solutions to obtain the start up powers of gas loaded heat pipes. Their results pertain to a sodium/argon heat pipe at 848 K, with inner radius 2.5 cm. They do not assume radiative cooling, but rather assume a heat transfer coefficient of  $32 \text{ WM}^{-2} \text{ K}^{-1}$  into a heat sink at 400 K. This yields a value of  $\alpha^{-1} = 2.25 \times 10^8 \text{ ergs cm}^{-1} \text{ s}^{-1}$ . We assume  $\sigma_c = 30 \times 10^{-16} \text{ cm}^2$ , a reasonable value in terms of previous calculations [31], and  $h_{fg} = 1.66 \times 10^{-12} \text{ ergs/atom}$  [9]. Using these numbers, eq. (14a) yields  $Q_{SU} = 132 \text{ watts}$ . Rohani and Tien's work yields, after recalculation of the heat transfer rates from their primary input data,  $Q_{SU} = 110 \text{ watts}$ . This is a very good agreement.

We have also calculated  $Q_{SU}$  to compare with our experimental results as shown in figure 3. Taking  $\sigma_c = 30 \times 10^{-16} \text{ cm}^2$  [31],  $T_o = 1020 \text{ K}$ ,  $n_0 = 9.46 \times 10^{15} \text{ cm}^{-3}$  (1 Torr) [28],



$h_{fg} = 2.50 \times 10^{-12}$  ergs/atom [9], and  $\varepsilon = 0.8$ , we obtain  $Q_{SU} = 670$  watts. However, since the model has been developed for a heat pipe which is closed at  $x = 0$  and our experimental heat pipe is symmetrical about  $x = 0$ , the experimental  $Q_{SU}$  should be compared with twice this calculated value, i.e. 1340 watts. From figure 3, we obtain for  $P/P_0 = 0.95$  at  $P_0 = 1.0$  Torr He,  $Q = 1300 \pm 100$  watts, a level of agreement which is probably better than the theory deserves.

Finally, we test the  $T_0^{9/4}$  prediction of eq. (15). From figure 3, we estimate  $Q_{SU} = 1000 \pm 100$  watts at  $P_0 = 0.15$  Torr,  $1200 \pm 100$  watts at 0.3 Torr,  $1300 \pm 100$  watts at 1.0 Torr, and  $1500 \pm 100$  watts at 3.0 Torr. In figure 5, we plot  $Q_{SU}/Q_{SU}(0.15 \text{ Torr})$  versus  $[T_0/T_0(0.15 \text{ Torr})]^{9/4}$ . The values of  $T_0$  are determined from the JANAF tables [27]. The dashed line is the prediction of eq. (15). The agreement is, once again, quite good.

The agreement of this relatively crude model with the work of Rohani and Tien and with our own is excellent, and we regard the model, crude as it is, as a valid working description of heat pipe start-up.

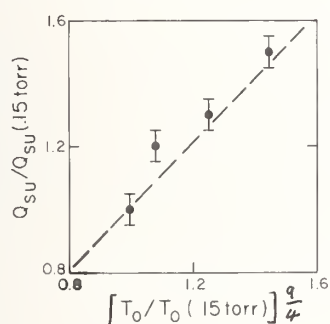


Figure 5. Test of eq. (15).  $Q_{SU}/Q_{SU}(0.15 \text{ Torr})$  is plotted against  $(T_0/T_0(0.15 \text{ Torr}))^{9/4}$ .

#### 4.2 Calculation of $P/P_0$ versus $Q$ curves

Our diffusion/convection model provides an adequate basis for the calculation of the low power portions of the curves in figure 3. We now show briefly that simple considerations yield useful calculation of the higher power behavior also.

In Vidal's treatment of sonic velocity limited "choked flow" operation of heat pipes, he showed that

$$n/n_0 = [1 + (\gamma-1)M^2/(1+\gamma M^2)] \quad (16)$$

where  $\gamma$  is the ratio of the specific heats at constant pressure and constant volume ( $=5/3$  for an ideal, monatomic gas) and  $M$  is the local Mach number ( $=v/c$ , where  $c$  is the local speed of sound). For  $M = 1$ ,  $n/n_0 = 1/2$ . In a simplistic model for  $Q_{\text{CHOKED FLOW}} \equiv Q_{CF}$ ,

$$Q_{CF} = (1/2)n_0 A c h_{fg} \quad (17)$$

Hence the heater power for which choked flow is obtained increases linearly (actually slightly faster than linearly since  $c \propto T_0^{1/2}$ ) with  $n_0$ . Surprisingly this crude, one dimen-

sional result, gives values within 10-20 percent of the excellent two-dimensional computer relations of DeMichele and Davis [10]. Similar results have been derived by Busse [11] and Tien [23]. For heater powers greater than  $Q_{CF}$ ,  $Q$  can only increase by increasing  $n$  (and  $c(T_0)$  slightly); hence, eventually the curve of  $n/n_0$  must begin to rise as the heater power is increased past this limit. In this simplistic model, at high power  $n/n_0$  is linearly proportional to  $Q$ .

For the heat pipe used in taking the data of figure 3, we calculate for pressures of 0.15, 0.5, 1.0, and 3.0 Torr helium,  $Q_{CF}$  is approximately 1500, 3000, 10,000, and 30,000 watts, respectively. From figure 3, we estimate  $Q_{CF}$  to be approximately 1000 and 1800 watts, at 0.15 and 0.30 Torr, respectively. Our experimental results are 30-40 percent below the calculated results. For our rough purposes, however, eq. (17) gives a decent estimate for the power at which choked flow effects become important.

#### 4.3 Use of heat pipes for measuring vapor pressures

Heat pipes offer a seemingly attractive device for the measurement of equilibrium vapor pressure curves as a function of temperature [32,33]. In an ideal heat pipe, once convective operation is obtained, the pressure in the high temperature, reactive, metal vapor zone is equal to that of the buffer gas in the room temperature environment, where pressures are easily measurable. Further, the extensive isothermal zone protects the thermocouple from radiation losses and leads to more accurate temperature measurements.

In practice, however, the technique offers the complications shown in figure 3. The higher buffer gas pressures may require heater power several times the start-up power to reach full plateau operation. At higher power--and flow velocities--the observed readings may be distorted by the increasingly important compressibility of the metal vapor. At low buffer gas pressures, a recirculating metal vapor flow can be maintained; however, this flow does not show the thermal regulation characteristic of a near ideal heat pipe. Since there is no plateau region, where  $dn/dQ \cong 0$ , the observed vapor pressure may be strongly dependent on the convected power. Under these conditions, the metal vapor pressure on the heated zone is not simply related to the measurable buffer gas pressure. Real heat pipes, marvelously stable and isothermal though they be, may not be sufficiently ideal for accurate vapor pressure measurements.

These warnings aside, it is tempting to interpret the plateau regions of the 1.0 and 3.0 Torr curves in figure 3 as regions of ideal behavior in which  $P/P_0$  ought to be unity. The deviation for unity is then an indication of a systematic error in temperature or pressure measurements, or in the vapor pressure tables. If one uses the constants given by Nesmeyanov [29] rather than those given by JANAF tables [28], the calculated values of  $P/P_0$  do indeed rise to values near unity. Whether these results indicate truly that Nesmeyanov's compilation is to be preferred is beyond our estimated experimental accuracy, since a 2 K error in our temperature readings could also yield  $P/P_0 = 1.00$ .

Finally, it should be noted that heat pipes may be used to provide highly isothermal environments for heating effusion cells, and thus contribute indirectly to vapor pressure measurements by other techniques [34].

## 5. Summary

We have shown that the start-up power of a gas loaded heat pipe can be reasonably modeled by a simple convection model in which the velocity distribution is approximated by that appropriate to an ideal heat pipe with no diffusion. The model predicts  $Q_{SU}$  should depend very weakly on the buffer gas density  $n_0$ , and, in particular, for radiation-cooled heat pipes,  $Q_{SU}$  ought to be proportional to  $T_0^{9/4}$ .

Further, the sonic limit to high power operation ought to be roughly linearly proportional to  $n_0$ . Busse has shown that the viscous limit, important primarily for long, narrow, heat pipes, varies as  $n_0^2$ , and consequently becomes controlling at low values of  $n_0$  [11]. In practice, this viscous limit is rarely important.

Figure 6 shows schematically these constraints on ideal heat pipe operation. The viscous limit increases quadratically with  $n_0$ , the sonic limit linearly with  $n_0$ , and the diffusion limit increases only logarithmically with  $n_0$ . At high buffer gas densities--and temperatures--the limit is primarily one of the strength of materials, either because of super-atmospheric pressures and/or enhanced corrosion at high temperatures. Thus, as shown in figure 6, a triangular region is available for the reasonably ideal operation of heat pipes. The contours indicate roughly that the most nearly ideal operation is obtained at power-density combinations well away from the limits. Further, figure 6 shows that near ideal heat pipe operation cannot be obtained at arbitrarily low buffer gas densities. A stable, recirculating flow is obtained, and the variation of metal vapor density with input heater power may be much less than with unstabilized metal evaporation. However, in the sense of a metal vapor density defined by the buffer gas density only and not at all by the heater power, near ideal heat pipe operation is not possible in this case.

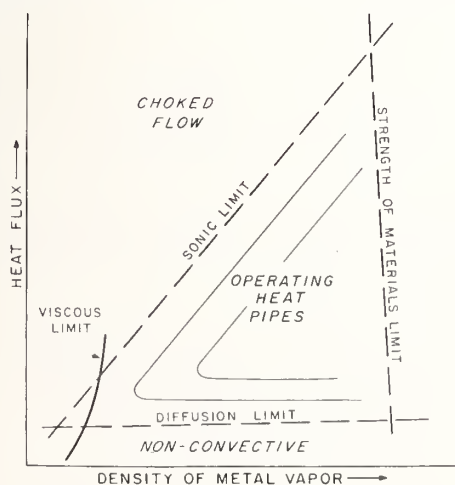


Figure 6. Schematic indication of combinations of power and density for which near-ideal heat pipe operation can be obtained. Spacing of contours indicates rate of deviation from ideal operation.

We thank the Robert A. Welch Foundation for their support of this work. P. H. Wine, K-J. Chung, and Charles Murray aided in taking the data.

## References

- [1] Hessel, M. M., Phys. Rev. Lett. 26, 215 (1971).
- [2] Hessel, M. M. and Jankowski, P., J. Appl. Phys. 43, 209 (1972).
- [3] Vidal, C. R. and Cooper, J., J. Appl. Phys. 40, 3370 (1969).
- [4] Vidal, C. R. and Haller, F. B., Rev. Sci. Instru. 42, 1779 (1971).
- [5] Vidal, C. R. and Hessel, M. M., J. Appl. Phys. 43, 2776 (1972).
- [6] Hessel, M. M. and Lucatorto, T. B., Rev. Sci. Instru. 44, 561 (1976).
- [7] Wine, P. H. and Melton, L. A., J. Chem. Phys. 64, 2692 (1976).
- [8] Luria, M., Eckstrom, D. J., and Benson, S. W., J. Chem. Phys. 64, 3103 (1976).
- [9] Vidal, C. R., J. Appl. Phys. 44, 2225 (1973).
- [10] DeMichele, D. W. and Davis, M. V., Nucl. Tech. 15, 366 (1972).
- [11] Busse, C. A., Int. J. Heat Mass Transfer, 16, 169 (1973).
- [12] Rohani, A. R. and Tien, C. L., Journal of Heat Transfer, 95, 377 (1973).
- [13] Tien, C. L. and Rohani, A. R., Journal of Heat Transfer, 94, 479 (1972).
- [14] Rohani, A. R. and Tien, C. L., AIAA Journal, 13, 530 (1975).
- [15] Sun, K. H. and Tien, C. L., Int. J. Heat Mass Transfer, 18, 363 (1975).
- [16] Williams, C. L. and Colwell, G. T., AIAA Journal 12, 1261 (1974).
- [17] Edwards, D. K. and Marcus, B. D., Journal of Heat Transfer, 94, 155 (1972).
- [18] Somagyi, D. and Yen, H. H., Journal of Heat Transfer, 95, 93 (1973).
- [19] Kotani, K., Tanicharo, Y., and Sumido, J., J. Nucl. Sci. Technol. 11, 159 (1974).
- [20] Asselman, G. A. A. and Green, D. B., Phillips Tech. Rev. 33, 104 (1973).
- [21] Levy, E. K. and Chow, S. F., J. Heat Transfer, 95, 218 (1973).
- [22] Fox, R. D., Caruthers, K. G., and Thompson, W. J., AIAA Journal, 10, 859 (1972).
- [23] Tien, C. L., Ann. Rev. Fluid Mechanics, 7, 167-185 (1975).
- [24] Tien, C. L. and Rohani, A. R., Int. J. Heat Mass Transfer, 17, 61 (1974).
- [25] Dunn, P. D. and Reay, D. A., Heat Pipes (Pergamon, Oxford, 1978).
- [26] Chi, S. W., Heat Pipe Theory and Practice (Hemisphere, Washington, 1976).
- [27] Handbook of Chemistry and Physics, 42nd ed. (Chemical Rubber Publishing Co., Cleveland, Ohio, 1960).
- [28] Stull, D. R. and Prophet, H., JANAF Thermochemical Tables, 2nd ed. (NSRDS-NBS37) (U.S. Government Printing Office, Washington, D.C., 1971).
- [29] Nesmeyanov, A. N., Vapor Pressure of the Elements (Academic, New York, 1963).
- [30] Adamson, A. W., A Textbook of Physical Chemistry (Academic, New York, 1973), p. 70.
- [31] Davies, R. H., Mason, E. A., and Munn, R. J., Phys. Fluids 8, 444 (1965).
- [32] Bohdanský, J. and Shin, H. E. J., J. Appl. Phys. 36, 3683 (1965).
- [33] Bohdanský, J. and Shin, H. E. J., J. Phys. Chem. 71, 215 (1967).
- [34] Chatillon, C., Allibert, M., Morachioli, R., and Pattoret, A., J. Appl. Phys. 47, 1690 (1976).



## Discussion

Question (Edwards): You mentioned a heat pipe on one of the space missions, would heat pipes be a useful technique for doing vaporization experiments in space?

Response (Melton): They will work in space. There is no gravity limitation. They were used on the Apollo capsule because you have got to keep the temperature the same on both sides of the capsule, or spin your capsule as you shoot it to the Moon, and spinning has a bad effect on astronauts.

A heat pipe would be an appropriate thermal transformer for such an application. The evaporator end could easily be fashioned to match the output of the solar reflector, and designs already exist for using heat pipes for isothermal heating of effusion cells depending upon the choice of working fluids, temperatures up to 2000 °C could be obtained.

Moderator (Cater): What sort of gases were they using; surely not liquid lithium.

Response (Melton): You need not run with metal vapors, you can run with liquid nitrogen in a heat pipe, and you have to choose a vapor depending upon the temperature operating range.

Question (Ferron): There are two other factors which contribute to non-equilibrium effects here at 0.15 and 0.3 Torr, and I wonder whether these were considered. One of them is the rate of flow of the liquid back through the porous medium. That, of course, has to keep up with the rate of vaporization. If it doesn't, then the boiling interface recedes into the porous medium and you have to consider the greater pressure of the smaller bubbles thus produced; you have to consider the temperature gradient through the porous medium that drives heat transfer.

The other point has to do with the mechanism of boiling that occurs at the hot end. There again the temperature gradient may be set up if the temperature difference between the internal surface and the interphase to boiling is sufficient. You have a range of phenomena, from natural convection effects at low rates to film boiling at very high rates of power transmission.

It is not clear to me what produces these non-plateau effects that you speak of. I notice in your curve fit, in which you use the sixth form in order to smooth the data, that you really don't get a linear form, you retain a sigmoidal form. I wonder whether these other non-equilibrium things may contribute?

Response (Melton): Okay. First of all, I think the answer to your first question is that the design of wicks is generally adequate to handle the flow. It can be a problem, particularly if one wants to crank large amounts of power through the heat pipes. The engineers have worried much more about this.



On your second question, I default. I can't tell you about boiling.

On the third question, we would have liked very much to drive the power to much higher regions and see if those things were actually sigmoidal or whether they are true plateaus, but we were at the limits of what we could crank through the heating elements.

## II. MASS SPECTROMETRIC TECHNIQUES-- KNUDSEN EFFUSION

Na  
Re  
Ga

no  
fus  
equ  
cor  
has  
gas  
and  
abu  
est  
pol  
Kau  
ed  
Th  
ini  
Fie

## ATTAINMENT OF CHEMICAL EQUILIBRIUM IN EFFUSIVE BEAM SOURCES OF THE HETEROGENEOUS REACTION TYPE<sup>1</sup>

D. L. Hildenbrand  
SRI International  
Menlo Park, CA 94025

Effusive beam sources derived from gas-solid reactions provide a very important pathway for widening the scope of high temperature thermodynamic studies, but the attainment of chemical equilibrium within these sources is problematical. Some of the underlying kinetic factors associated with the use of these sources are discussed. As one might expect, it is important to maximize the ratio of reactive surface area to exit orifice area. Equilibrium seems to be achieved more readily among the products of gas-solid reactions than among reactant and products, as suggested by the quasi-equilibrium model. Some experiences with the use of heterogeneous reaction sources are described, and two definitive tests for the establishment of equilibrium are outlined.

### 1. Introduction

One of the most reliable methods of determining the thermodynamic properties of gaseous molecules stable at high temperatures is based on the study of reaction equilibria in effusive beam sources. In most instances, thermodynamic data are derived from vaporization equilibria using the conventional Knudsen cell technique [1]<sup>2</sup>, once the identities of the condensed and vapor phases have been established. More recently, the Knudsen technique has been used to study complex gaseous equilibria [2-4], in which case a distribution of gaseous species is generated in the cell by the reaction of two or more condensed phases, and a selective detection method such as mass spectrometry is used to measure the relative abundances of the species. For thermodynamic applications, of course, it is necessary to establish that chemical equilibrium conditions prevail or to provide some means of extrapolating the results to equilibrium. The attainment of vaporization equilibrium within Knudsen cells has been discussed in some detail [5-7], and a useful model has been developed for treating nonequilibrium data [6]. This direct vaporization method has been used

<sup>1</sup>This research was sponsored by the Air Force Office of Scientific Research (AFSC), United States Air Force, under contract F 49620-78-C0033.

<sup>2</sup>Figures in brackets indicate the literature references at the end of this paper.

widely and it has gained acceptance as one of the most powerful methods available for thermodynamic studies. Most of the selected thermochemical data for gaseous metal oxides and halides have been obtained from Knudsen vaporization measurements on solid or liquid samples.

For a number of chemical systems to which one would like to apply the method, particularly with mass spectrometric analysis of the vapor, there are no suitable condensed phases or mixtures of condensed phases that will generate the desired distribution of gaseous species. This is especially true, for example, of many refractory metal halides that do not form stable, involatile condensed halides, and that cannot be generated by halogenation of the metal with another condensed metal halide because of unfavorable thermodynamics. Other examples are the many gaseous metal hydroxides that are stable only in the presence of the metal oxides and relatively high partial pressures of water. For many such systems, the only feasible reaction pathway involves generation of the desired gaseous species by addition of a reactive gas to the Knudsen effusion source containing a suitable condensed phase. Heterogeneous reaction beam sources of this type have been used to study gaseous species such as  $\text{HBO}_2$  [8],  $\text{LiOH}$  [9],  $\text{BeCl}$  [10],  $\text{BH}$  [11], and  $\text{WF}_x$  [12], along with many others, greatly increasing the variety of chemical systems that can be investigated by high temperature mass spectrometry. Unlike the direct vaporization sources, however, there has not been a generally accepted criterion for establishment of chemical equilibrium in gas-solid reaction sources, and there has been some skepticism from time to time about the validity of the results. Stafford [13], in fact, has cited the uncertain status of equilibrium attainment in gas inlet work as one of the major limitations in applying mass spectrometry to high temperature thermodynamic studies. As direct evidence of this, he refers to Knudsen cell studies of the reaction of  $\text{H}_2(\text{g})$  with  $\text{B}_4\text{C}(\text{s})$  that yielded concentrations of  $\text{BH}_3$  and alkylboranes far in excess of predicted equilibrium levels [11], although two other gaseous products,  $\text{BH}$  and  $\text{HBCl}_2$ , appear to be equilibrated.

Similar considerations apply to double cell experiments in which gaseous species vaporized from a low temperature chamber pass over a second sample in another chamber held at a higher temperature. Reactive vaporization in the hotter chamber yields the distribution of products to be sampled for equilibrium measurements. A good example of the difficulties that can be encountered is offered by two reported studies [14,15] of the gaseous equilibrium  $\text{Ge} + \text{SiO} = \text{GeO} + \text{Si}$ . First, a double cell study [14] in which  $\text{GeO}$  and  $\text{O}_2$  vaporized from a low temperature chamber containing  $\text{GeO}_2(\text{s})$  into the high temperature chamber containing  $\text{Si}(\text{s})$  yielded an apparent equilibrium constant of  $3.0 \times 10^{-4}$  for the gaseous reaction at 1500 K. Inconsistencies with other data on the thermochemical properties of  $\text{SiO}$  and  $\text{GeO}$  prompted a reexamination by the single Knudsen cell technique, using a mixture of  $\text{Si}(\text{s})$ ,  $\text{Ge}(\text{s})$  and  $\text{SiO}_2(\text{s})$  to generate the gaseous products; these single cell measurements [15] gave an equilibrium constant of  $4.6 \times 10^{-5}$  at 1500 K for the  $\text{SiO} - \text{GeO}$  gaseous exchange reaction and removed the earlier discrepancy. Failure to achieve gaseous equilibrium in the double cell experiments is the most probable reason for the difference.

In view of these concerns over the attainment of chemical equilibrium in heterogeneous reaction beam sources, it seemed worthwhile to review some of the pertinent background on



the subject, to discuss some recent experiences with the use of gas-solid reaction sources in thermodynamic studies, and to outline some useful criteria for establishing that chemical reaction equilibrium is attained. The objective is to improve the overall reliability of high temperature equilibrium measurements, thereby increasing the accuracy of the derived thermochemical data. This is an important item because equilibrium studies are one of the most powerful and widely used methods for characterizing high temperature vapors.

## 2. Typical Gas-Solid Reaction Sources

There are several different ways in which heterogeneous reaction sources can be used for equilibrium studies. In all cases, the experimental arrangement is simple in principle: The reactive gas is added to the base of a conventional Knudsen cell, where it interacts chemically with a condensed sample to produce one or more gaseous products. The resulting gas mixture is emitted from the cell exit orifice in the form of a molecular effusion beam, and is sampled by an instrument such as a mass spectrometer to obtain composition data and reaction equilibrium constants. In this paper we will be dealing exclusively with mass spectrometric detection, but the analysis applies to all other methods as well. The usual experimental procedure and data treatment methods have been described elsewhere [8,10,12], and will not be dealt with here, except as they bear on the equilibrium question. A sketch of a typical effusion cell with gas inlet is given by Meschi, et al. [8]. For convenience in discussing the kinetic aspects of gas-solid reaction sources, a differentiation is made between two types of applications as described below.

In the most obvious application, the added gas is a direct participant in the reaction under study. For example, the reaction  $\text{H}_2\text{O}(\text{g}) + \text{B}_2\text{O}_3(\text{l}) = 2\text{HBO}_2(\text{g})$  was investigated by admitting  $\text{H}_2\text{O}(\text{g})$  to a platinum cell containing  $\text{B}_2\text{O}_3(\text{l})$  [8]. Likewise, the gaseous species  $\text{LiOH}$  and  $(\text{OBF})_3$  have been characterized by the reaction of  $\text{H}_2\text{O}(\text{g})$  with  $\text{Li}_2\text{O}(\text{s})$  [9], and  $\text{BF}_3(\text{g})$  with  $\text{B}_2\text{O}_3(\text{l})$  [16]. These cases in which the added gas is a direct participant and must be present at equilibrium levels are labeled as Type I sources.

An important and useful variation is that in which the added gas and perhaps even the condensed phase serve only to generate a distribution of gaseous products by reactive vaporization, and it is the investigation of equilibria among these gaseous products that is of primary interest. As noted earlier, this technique allows one to study certain gaseous species that cannot be generated by the conventional single cell technique. For example  $\text{W}(\text{s})$  can be fluorinated by  $\text{SF}_6(\text{g})$  in a carbon or tungsten cell with gas inlet to yield a distribution of W-F and W-S-F gaseous species that varies with cell temperature [12]. With this arrangement it was possible to study gaseous equilibria such as  $\text{WF}_3 + \text{WF}_5 = 2\text{WF}_4$ ,  $\text{WF}_3 + \text{S} = \text{WF}_2 + \text{SF}$  and  $\text{WSF}_3 + \text{S} = \text{WF}_3 + \text{S}_2$ , and to use this information to characterize the W-F and W-S-F species thermochemically. Other examples are the Mo-F system  $[\text{Mo}(\text{s}) + \text{SF}_6(\text{g})]$  [17], the IIA metal iodides and bromides  $[\text{MO}(\text{s}) + \text{HI}(\text{g}) \text{ and } \text{HBr}(\text{g})]$  [18, 19] and the CF molecule  $[\text{C}(\text{s}) + \text{SF}_6(\text{g})]$  [20]. Under these conditions, the added gas need not be present at equilibrium levels, nor must the gaseous products necessarily equilibrate with the condensed phases present if only gaseous reactions are being studied; it is necessary only that

gaseous equilibrium be achieved. There have been examples of reaction products generated at partial pressures far above the equilibrium values [21,22], but in one of these it was demonstrated that gaseous equilibrium prevailed among the products [21]. Sources that are used to study equilibria among the gaseous reaction products are designated as Type II sources.

### 3. Kinetic Implications

Although our concern here is with the use of the gas inlet cell for equilibrium studies, it is worth noting that, at the other extreme, this arrangement has been used for purely kinetic studies. Benson, Golden and associates have developed the Very Low Pressure Pyrolysis (VLPP) technique into an effective kinetic tool [23]. In VLPP studies, a sample gas is admitted to a heated Knudsen cell with relatively large exit aperture under the usual molecular flow condition, and the steady state level of the sample and decomposition products effusing from the reactor are monitored by mass spectrometry. From measurement of the fraction of sample decomposed as a function of temperature for various reactor geometries, information about unimolecular rate constants and activation energies can be derived. It is worth noting that VLPP was conceived as a direct result of reports detailing the difficulties involved in achieving equilibrium in gas inlet work with Knudsen cells [24].

The analysis of Golden, et al. [23] emphasizes the importance of considering the collision number,  $Z$ , associated with a specific Knudsen cell reactor. This collision number is the average number of collisions made by a molecule during its transit through the cell, and is defined by the ratio  $Z = A_s/A_o$  where  $A_s$  is the interior surface area of the cell and  $A_o$  is the cell exit orifice area. For heterogeneous reactions,  $A_s$  is the surface area of the condensed sample in the cell, which may or may not include the surface of the cell itself. For a purely gas-phase thermal decomposition process, something on the order of at least 50 wall collisions are required before a molecule attains sufficient internal energy to undergo unimolecular reaction. To attain equilibrium,  $Z$  values of  $10^4$  or greater may be required, pointing up the importance of maximizing the ratio  $A_s/A_o$ . A strictly gas-phase decomposition process requires the walls to be chemically inert, but Golden, et al. [23] point out that wall effects are seldom a problem because heterogeneous reactions are generally far slower than the re-evaporation of unreacted species. The latter cannot be generally true, and clearly depends on the specific chemistry involved. In any event, the purely gas-phase decomposition process, a special case of the Type I source, is perhaps the most difficult to study under equilibrium conditions. Along these lines, severe difficulties in establishing dissociative equilibrium in Knudsen sources have been reported for gaseous  $SF_6$  [25,26], and  $B_2H_6$  [27].

Experiences with the attainment of chemical equilibrium among the products of gas-solid reactions, i.e., with the Type II source, have been much more favorable. This is in accord with the general kinetic behavior of gas-solid reactions, as exemplified by the quasi-equilibrium (QE) model [28]. According to the QE model, the rate limiting step is the adsorption and equilibration of the impinging gas molecule at the solid interface. Volatile reaction products are in equilibrium with the surface and are emitted in equilibrium proportions, at a rate governed by the rate of adsorption of the incoming reactive molecule.

The QE model appears to correlate the results of several metal oxidation [28] and metal fluorination [29,30] studies at high temperatures and low pressures quite well. In any event, there is kinetic evidence to support the expectation that chemical equilibrium can be achieved with the Type II source under optimum conditions. It must be demonstrated for each individual system, however, that equilibrium is in fact attained.

#### 4. Tests for the Attainment of Equilibrium

One of the most useful and definitive tests for equilibrium can be made by varying the flow or pressure of the reactive gas over a wide range at constant temperature and noting the effects on the derived equilibrium constant,  $K_{eq}$ . As pressure is varied, composition of the gas phase changes in accord with the mass action principle, but at equilibrium the values of  $K_{eq}$  derived from the species abundances and the reaction stoichiometry must be independent of overall changes in composition. This invariance of  $K_{eq}$  with composition defines the fundamental condition of equilibrium in terms of the law of mass action.

As an example of the mass action test, consider the results of some recent studies of the Sr-Al-I gaseous system [31], obtained by admitting HI(g) to a Knudsen cell containing a mixture of SrO(s), Al<sub>2</sub>O<sub>3</sub>(s) and AlB<sub>12</sub>(s). The cell contained a perforated partition at the center to prevent molecular streaming, but otherwise involved no special design features. In two measurements at 1762 K with different HI flow rates, the observed parent ion abundances of Sr<sup>+</sup>, SrI<sup>+</sup>, Al<sup>+</sup> and AlI<sup>+</sup> varied by factors of 1.2, 36, 0.87 and 25, respectively, but the derived equilibrium constants for the gaseous reaction  $Sr + AlI = SrI + Al$  were in good agreement (0.0376 and 0.0368), indicating the attainment of equilibrium. For this experiment, the abundances of Sr and Al were essentially fixed by the presence of the solid phases, but the gaseous iodides were dependent on the HI flow. Likewise, with similar studies [31] of the gaseous equilibrium  $Ba + GaI = BaI + Ga$ , the abundances of the parent ions Ba<sup>+</sup>, BaI<sup>+</sup>, Ga<sup>+</sup>, and GaI<sup>+</sup> changed by factors of 0.43, 2.4, 4.4 and 25, respectively, by shifting the HI flow at 1711 K but the derived equilibrium constants of 0.708 and 0.698 agree closely. The reader is referred to the original paper [31] for more details of the measurement. Another example of the use of the mass action test is afforded by the results of studies of gaseous equilibria in the Mo-S-F system, generated by the reaction of SF<sub>6</sub>(g) and Mo(s) in a Knudsen cell [17]. As noted in the paper [17], a positive indication of equilibrium was obtained. On the negative side, measurements of S-F gaseous reactions generated by passing SF<sub>6</sub>(g) through a graphite cell showed that an order of magnitude change in the SF<sub>6</sub> flow yielded apparent equilibrium constants for the reaction  $SF_6 + 2S = 3SF_2$  that differed by more than a factor of 100, while concordant results were obtained for the reaction  $S + SF_2 = 2SF$  [26]. The mass action criterion is a sensitive one, and it should always be applied as a test for equilibrium in heterogeneous reaction sources, preferably by varying the abundances of the more pressure sensitive species by at least a factor of ten. Departures from equilibrium in the double cell studies [14] of the Si-Ge-O system would have been apparent if the mass action test had been applied there.

A particularly revealing application of the mass action test is given in some recent studies of the heterogeneous reaction  $5/6 \text{ MoF}_6(\text{g}) + 1/6 \text{ Mo}(\text{s}) = \text{MoF}_5(\text{g})$  carried out by Knudsen cell mass spectrometry [32]. When  $\text{MoF}_6(\text{g})$  was admitted to the Mo cell packed with Mo wire initially, the ion current equilibrium quotient  $[\text{I}^+(\text{MoF}_5)]/[\text{I}^+(\text{MoF}_6)]^{5/6}$  at 440 K showed a substantial flow rate dependence, seen in the series I data of table I. After

Table I

EFFECT OF  $\text{MoF}_6$  FLOW RATE ON MOLECULAR ABUNDANCES<sup>a</sup>  
AND DERIVED DATA FOR THE EQUILIBRIUM  
 $5/6 \text{ MoF}_6(\text{g}) + 1/6 \text{ Mo}(\text{s}) = \text{MoF}_5(\text{g})$  at 440 K

$\text{I}^+(\text{MoF}_6)$	$\text{I}^+(\text{MoF}_5)$	$\frac{[\text{I}^+(\text{MoF}_5)]}{[\text{I}^+(\text{MoF}_6)]^{5/6}}$
<u>Series I</u>		
2.77	0.054	$2.31 \times 10^{-2}$
12.01	0.171	$2.15 \times 10^{-2}$
33.5	0.315	$1.69 \times 10^{-2}$
66.6	0.408	$1.23 \times 10^{-2}$
<u>Series II</u>		
11.3	0.047	$6.28 \times 10^{-3}$
12.4	0.051	$6.26 \times 10^{-3}$
36.4	0.151	$7.55 \times 10^{-3}$
45.0	0.162	$6.79 \times 10^{-3}$
50.5	0.191	$7.27 \times 10^{-3}$
106.1	0.365	$7.48 \times 10^{-3}$

<sup>a</sup>Abundances in arbitrary units.



vacuum outgassing of the cell for an hour at 1300 K and  $5 \times 10^{-7}$  Torr, the quotient dropped to a somewhat lower value but was essentially independent of  $\text{MoF}_6$  flow rate within experimental error. Apparently the molybdenum surface was initially covered with an oxide film, and this film severely limited the number of surface sites available for reactive vaporization. After vacuum outgassing, equilibrium behavior was observed, probably as a result of the increase in reactive surface sites. This phenomenon could be reproduced repeatedly by alternately exposing the molybdenum surface to background gas at about  $10^{-3}$  Torr, and later outgassing at 1300 K under high vacuum. The results point out the importance of considering the "clean" surface area  $A_s$  when maximizing the ratio  $A_s/A_0$ . Another implication of these results worth noting is that the chemical rearrangement and bond breaking step in the  $\text{MoF}_6 + \text{Mo}$  reaction is apparently faster than the surface accommodation of the impinging  $\text{MoF}_6$  molecule, even at the relatively low temperatures of these experiments. This is contrary to the assumptions of Golden, et al. [23] regarding the relative importance of surface reaction as opposed to re-evaporation, but is in accord with the quasi-equilibrium model of surface reactions.

One further test that can be useful in checking on the attainment of equilibrium involves the approach to the equilibrium position from different chemical compositions. This is a variation of the classical technique of approaching equilibrium from opposite directions: at equilibrium, the rates of the forward and reverse reactions must be equal, so that the derived equilibrium constants will be independent of the direction of approach. For the high temperature reactions of interest here, the reagents and products cannot be added separately, but it is possible to vary the beam source chemistry so as to give definitive information about equilibrium attainment. For example, in studies of the gaseous tungsten fluorides [12], the reactions  $\text{WF}_3 + \text{WF}_5 = 2\text{WF}_4$  and  $\text{WF}_4 + \text{WF}_2 = 2\text{WF}_3$  were studied by fluorinating  $\text{W(s)}$  with both  $\text{SF}_6(\text{g})$  and  $\text{WF}_6(\text{g})$ . Equilibrium data obtained with the two different sources were in close agreement [12]. A similar set of data for the Mo-F system [17], shown graphically in figure 1 provides evidence that the reactions of  $\text{MoF}_6(\text{g})$  and  $\text{SF}_6(\text{g})$  with  $\text{Mo(s)}$  yield identical equilibrium data for reactions among the Mo-F species. In yet another example, equilibrium data for the gaseous reaction  $\text{Sm} + \text{CaF} = \text{SmF} + \text{Ca}$  were found to be independent of whether approached by the reaction of  $\text{CaF}_2(\text{g})$  and  $\text{Sm}_2\text{O}_3(\text{s})$  in a double cell or by the reaction of  $\text{SmF}_3(\text{s})$ ,  $\text{CaF}_2(\text{s})$ , and  $\text{B(s)}$  in a single cell [33]. The double cell data yielded an equilibrium constant of 2.60 at 2200 K for the SmF-CaF exchange reaction, compared to a value of 2.49 from the single cell. These examples serve to show that conclusive evidence of equilibrium behavior also can be obtained by varying the beam source chemistry. The extra time required to make these tests is more than offset by the added confidence that can be attached to the results.

In conclusion, it goes without saying that the attainment of equilibrium in effusive sources never should be taken for granted. Fortunately when tests such as those described above are used routinely with gas-solid reaction sources, no assumptions need be made about the establishment of equilibrium.



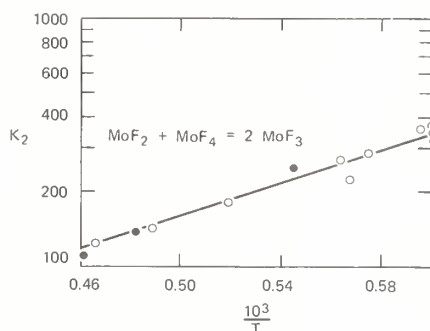
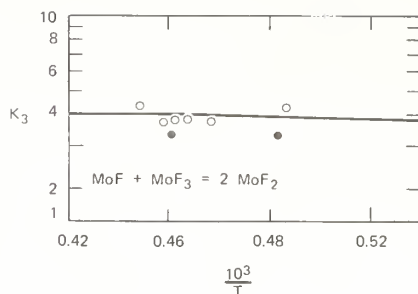


Figure 1. Plot of equilibrium constants for gaseous Mo-F reactions; open circles,  $\text{SF}_6(\text{g}) + \text{Mo}(\text{s})$ ; closed circles,  $\text{MoF}_6(\text{g}) + \text{Mo}(\text{s})$ .

#### References

- [1] Margrave, J. L., in Physicochemical Measurements at High Temperatures, chap. 10, p. 231 (Butterworths, London, 1959).
- [2] Ehlert, T. C., Blue, G. D., Green, J. W., and Margrave, J. L., J. Chem. Phys. **41**, 2250 (1964).
- [3] Hildenbrand, D. L. and Murad, E., J. Chem. Phys. **43**, 1400 (1965).
- [4] Ames, L. L., Walsh, P. N., and White, D., J. Phys. Chem. **71**, 2707 (1967).
- [5] Whitman, C. I., J. Chem. Phys. **20**, 161 (1952).
- [6] Motzfeldt, K., J. Phys. Chem. **59**, 139 (1955).
- [7] Stern, J. H. and Gregory, N. W., J. Phys. Chem. **61**, 1226 (1957).
- [8] Meschi, D. J., Chupka, W. A., and Berkowitz, J., J. Chem. Phys. **33**, 530 (1960).
- [9] Berkowitz, J., Meschi, D. J., and Chupka, W. A., J. Chem. Phys. **33**, 533 (1960).
- [10] Hildenbrand, D. L. and Theard, L. P., J. Chem. Phys. **50**, 5350 (1969).
- [11] Steck, S. J., Pressley, Jr., G. A., and Stafford, F. E., J. Phys. Chem. **73**, 1000 (1969).
- [12] Hildenbrand, D. L., J. Chem. Phys. **62**, 3074 (1975).
- [13] Stafford, F. E., High Temperatures-High Pressures **3**, 213 (1971).
- [14] Hildenbrand, D. L. and Murad, E., J. Chem. Phys. **51**, 807 (1969).
- [15] Hildenbrand, D. L., High Temperature Science **4**, 244 (1972).
- [16] Porter, R. F., Bidinosti, D. R., and Watterson, K. F., J. Chem. Phys. **36**, 2104 (1962).
- [17] Hildenbrand, D. L., J. Chem. Phys. **65**, 614 (1976).
- [18] Hildenbrand, D. L., J. Chem. Phys. **68**, 2819 (1978).

- [19] Hildenbrand, D. L., J. Chem. Phys. 66, 3526 (1977).
- [20] Hildenbrand, D. L., Chem. Phys. Lett. 32, 523 (1975).
- [21] Chupka, W. A., Berowitz, J., Meschi, D. J., and Tasman, H. A., Advan. Mass Spectrom., Vol. 2, p. 99 (Pergamon, London 1963).
- [22] Steck, S. J., Pressley, Jr., G. A., Lin, S. S., and Stafford, F. E., J. Chem. Phys. 50, 3196 (1969).
- [23] Golden, D. M., Spokes, G. N., and Benson, S. W., Angew. Chem. 12, 534 (1973).
- [24] Golden, D. M., Private communication.
- [25] Brackmann, R. T., Fite, W. L., and Jackson, W. M., Paper F-1, 18th Annual Conference on Mass Spectrometry and Allied Topics, San Francisco, California (1970).
- [26] Hildenbrand, D. L., J. Phys. Chem. 77, 897 (1973).
- [27] Sinke, E. J., Pressley, Jr., G. A., Bayliss, A. B., and Stafford, F. E., J. Chem. Phys. 41, 2207 (1964).
- [28] Batty, J. C. and Stickney, R. E., J. Chem. Phys. 51, 4475 (1969).
- [29] Philippart, J. T., Caradec, J. Y., Weber, B., and Cassuto, A., J. Electrochem. Soc. 125, 162 (1978).
- [30] Nordine, P. C., J. Electrochem. Soc. 125, 498 (1978).
- [31] Kleinschmidt, P. D. and Hildenbrand, D. L., J. Chem. Phys. 68, 2819 (1978).
- [32] Kleinschmidt, P. D., Lau, K. H., and Hildenbrand, D. L., J. Chem. Thermodynamics, in press.
- [33] Lau, K. H., Kleinschmidt, P. D., and Hildenbrand, D. L., unpublished data.

#### Discussion

Question (Cater): Do you have a problem with sorting out the fluoride species because of dissociation in the ion source?

Response (Hildenbrand): Not necessarily, for example in the tungsten case, they all formed parent ions. In some cases there is some fragmentation. But I think there aren't any overriding cases where we cannot sort this out.

Question (Ferron): Is there excess gas in these reactions, I guess at the interface?

Response (Hildenbrand): We are talking about very low pressure conditions. There is a free molecular flow ---.

(Editor's note): The record of this discussion is incomplete but the general concern was with possible nonequilibrium transport effects, the response was that this was usually not a problem.



THERMODYNAMIC AND PHYSICO-CHEMICAL BEHAVIOR OF THE INTERACTIONS BETWEEN  
KNUDSEN-EFFUSION-CELLS AND THE SYSTEMS UNDER INVESTIGATION:  
ANALYSIS BY HIGH TEMPERATURE MASS SPECTROMETRY

C. Chatillon and M. Allibert  
Domaine Universitaire, ENSEE, BP 44,  
38401 Saint Martin D'Heres, France

and

A. Pattoret  
Commisariat á l'Energie Atomique, SEAMA,  
92260 Fontenay-aux-Roses, France

1. Introduction

It would often be of benefit to limit the uncertainties involved in the measurements of vapor pressure by the Knudsen effusion method. Major uncertainties, specific to the system investigated or due to parasitic reactions may be suppressed by connecting a mass spectrometer. Nevertheless, some uncertainties persist, due to various causes that can be often identified but remain difficult to assess, and that are specific to the effusion method and the sampling mode. Apart from its analytical function, and due to its speed and dynamic range of measurement, in particular, the mass spectrometer seems particularly well adapted to detect and evaluate any parasitic phenomena that are likely to jeopardize the results.

The combination of an effusion cell and a mass spectrometer will often prove to be the sole reliable means of studying complex chemical systems at elevated temperature.

The precision required to investigate condensed phases means that measurements on the effusing gaseous species must be well mastered and the behavior of the sample-cell system must be sufficiently well understood. Even though effusion may be interpreted by gas kinetics, its practical use relies on a knowledge of the interactions between the sample and the cell.

Two types of Knudsen cell assembly that are used in our laboratories are shown in photos 1 and 2 on the following page.



Photo 1. Multiple Knudsen-cell with sodium heat pipe oven.



Photo 2. High temperature (up to 2500 °C) multiple cell furnace.

## 2. Knudsen-Cell as an Equilibrium System

To obtain the thermodynamic properties of the systems under investigation with Knudsen effusion cells, steady conditions are necessary, allowing a state as near as possible to those of a closed system.

### 2.1 A cell acts according to gas kinetics

When the mean free path  $\lambda$  of the gas is greater than the effusion hole dimensions, and the vaporizing surfaces are sufficiently large with respect to the effective effusion area, the different phases will be considered under equilibrium conditions. Thus, the steady-state effusion formula for gaseous molecules

$$\frac{dN}{dt} = \frac{PA}{\sqrt{2\pi MRT}} C = Z/n, \quad (1)$$



where  $P$  is the vapor pressure;

$T$ , the temperature;

$AC$ , the product of effusion area and Clausing factor;

$M$ , the molar mass; and

$R$ , the perfect gas constant,

may be established in different ways.

The first way is to consider the exchange between two sections  $ds_i$ ,  $ds_j$  in the gas phase according to the cosine law [1]<sup>1</sup>.

$$Z_{ij} ds_j = \frac{n\bar{C}}{4\pi} \cdot \frac{\cos \theta_{ij} \cos \theta_{ji}}{l_{ij}^2} ds_i ds_j \quad (2)$$

where  $n$  is the vapor density given by the number of molecules in a unity of volume,

$\bar{C}$  is the average thermal speed of these molecules,

$\cos \theta_{ij}$  and  $\cos \theta_{ji}$  the angles between the normal to the elementary surfaces,  $ds_i$ ,  $ds_j$  and the distance  $l_{ij}$  between them. The arbitrary surfaces are chosen suitable for integration according to the geometrical device used for the measurements:  $ds_i$  may be on elementary surface of the orifice area and  $ds_j$  of the cell walls and so appropriate integrations lead us to the Knudsen effusion formula as shown by (1).

The second way is to consider the emission of molecules after binary collisions, whose collision number is  $Z_{11}$ , occurring in an elementary volume of the gas phase [2]. So, for an isotropic gas, the number of molecules which escapes per second from the elementary volume and passes through the effusion hole, at distance  $L$  and angle  $\theta$ , is

$$dN_{\theta L} = 2Z_{11} A \cos \theta \frac{dw}{4\pi} \cdot \exp\left(-\frac{L}{\lambda}\right) dL$$

and after integration over  $L$  from 0 to  $\infty$ :

$$dN_{\theta} = 2 Z_{11} A \cos \theta \frac{dw}{4\pi} \lambda \quad (3)$$

or

$$dN_{\theta} = \frac{n\bar{C}}{4\pi} A \cos \theta dw$$

which is the usual form of the cosine law of effusion. For all the space outside the ideal orifice

<sup>1</sup>Figures in brackets indicate the literature references at the end of this paper.

$$N = \frac{n\bar{C}}{4\pi} \int_0^{2\pi} \int_0^\pi \cos \theta \sin \theta d\theta = \frac{PA}{\sqrt{2\pi MRT}}.$$

These two modes for setting up the Hertz-Knudsen equation for the flows escaping through an effusion orifice do not account for the true working of practical effusion cells. In fact, the flow of matter would be established from collisions in the gas phase and emission from the cell walls.

In a molecular beam application of the effusion method, only a fraction of the effusate is collected on a target or passes through the ion source of a mass spectrometer. Carlson proposes [1], in the case of an ideal orifice (thin wall edge) and a circular, coaxial and parallel plane detector, the relation for molecular flow:

$$Z = \frac{n\bar{C}}{4\pi} \Delta\Omega = \frac{n\bar{C}}{4\pi} \frac{\pi^2}{2} \left[ (L^2 + R_0^2 + R_1^2) - \sqrt{(L^2 + R_0^2 + R_1^2)^2 - 4R_0^2 R_1^2} \right]$$

where  $L$  is the depth of the cell, and  $R_0$  and  $R_1$  are the radii of the orifice and the evaporating material, respectively. In this approach, there are some ambiguities because umbra and penumbra effects must be taken into account to define the useful solid angle between the evaporating and detector surfaces through the effusion hole (fig. 1). We have carried out the integration from both elementary volumes in the gas phase and elementary surfaces of the walls in equilibrium with the gas. These calculations show that the molecular flow which reaches the detector through the effusion hole is always the same whatever the value of the mean free path. So it is always equivalent to an emission from the effusion hole, according to the conclusions quoted by [1]. Then  $L$ ,  $R_0$ , and  $R_1$  fix the solid angle defined by the effusion hole and the detector. Moreover, the number of molecules coming from binary collisions in the gas become rapidly important as shown in table 1 with the vaporization of silver.

Table 1. Ratio of the molecular flow entering the ion source  $\phi_T$  to that provided from collisions in the gas phase  $\phi_g$ .  $\lambda$ : mean free path for silver. Height of the cell: 20 mm.

$\lambda_{(mm)}$	T(K)	$\phi_T/n\bar{C}$	$\phi_g/\phi_T$ (%)
10000	1050	2.95 E-5	0.8
1000	1140	2.95 E-5	7.2
100	1240	2.95 E-5	48.3
38	1290	2.96 E-5	77.9
19	1325	2.97 E-5	92.1
5	1415	3.00 E-5	100
1.5	1490	2.95 E-5	100

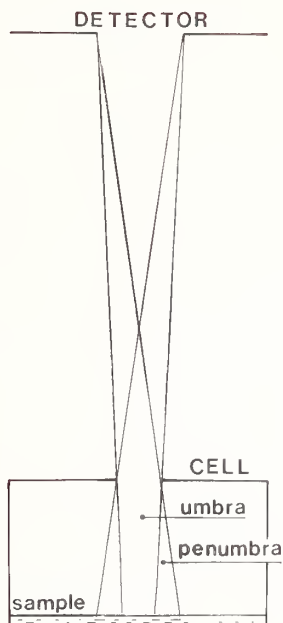


Figure 1. The area viewed by the detector through the effusion hole.

## 2.2 A cell acts in thermodynamic and physico-chemical equilibria

In high temperature measurements, the different equilibria between the studied sample and the vessels, spread quickly as temperature rises. So the different possible reactions can be regarded as in their final equilibrium state. Three principal types of equilibria take place: gas-sample, but also gas-vessel and sample-vessel.

### 2.2.1 Evaporation of the sample

The equilibrium between the sample and its vapor phase is the principal condition used to obtain thermodynamic properties. For the best approach to equilibrium conditions, the quantity and the state of the sample, and the shape of the cell have to maximize the back flow towards the evaporating surface.

For vaporizing liquids, generally the most suitable conditions favoring approach to equilibrium are:

- ° evaporation coefficients [3,4] near unity,
- ° wetting of the crucible to increase the evaporation area, and
- ° rapid homogenization of the melts.

But the interactions between the cell or product segregation may also maintain a "skin," continuous or otherwise, at the surface of the sample, which reduces the evaporation area. This could explain some observations when vaporizing metals [5] and alloys such as Al-Cu [6] and Al-Si [7], where activity measurements of Si and Al, with multiple effusion cells,

are distorted when calculated from  $\text{SiO}$  and  $\text{Al}_2\text{O}$  molecules. In the same manner, we observed with multiple effusion cells an activity of alumina as great as 5000 in the system  $\text{CaF}_2\text{-CaO-Al}_2\text{O}_3$  because the liquid  $\text{CaF}_2$  recovered alumina in the reference melt.

In the case of solid samples, the conditions needed to reach equilibrium are less favorable: condensation and evaporation coefficients [4,5-8] are often smaller, homogenization into and between separate phases is slower. The effective evaporation area can be somewhat increased by means of the shape or the state of the sample [9].

### 2.2.2 Interactions between crucible and sample

The reactivity of vaporizing products with the crucible or cell is governed by the partial free energies of all the constituents in each of the phases. The final state can be expressed by thermodynamics [10] and the composition of the different phases found from the phase diagram of the entire system, sample and cell. Figure 2 shows interactions between Si and C when vaporizing silicon in dense graphite or vitreous carbon. The activity of Si departs from unity as temperature rises, and this effect is very sensitive on high polymers. When more than two constituents are present in the whole system--crucible plus sample--preliminary thermodynamic calculations or estimations must be established in the complete system to fix different compatible composition ranges between the products and the crucibles. In the case of the vaporization of Al, alumina crucibles are certainly more suitable than any other oxides such as  $\text{BeO}$  [11], as shown in figure 3. For the study of the binary melts Al-Si, different cell materials have been chosen according to the composition ranges [7] (fig. 4).

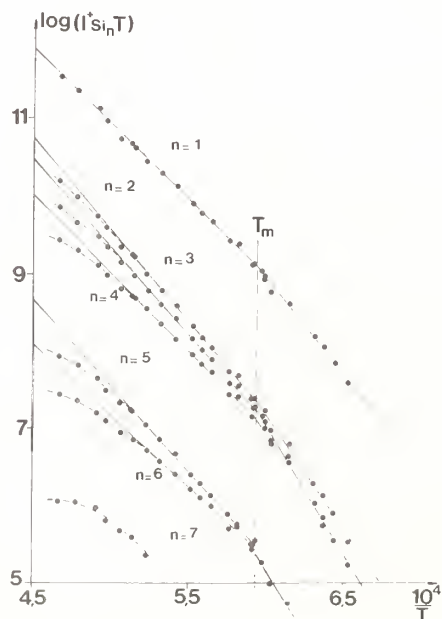


Figure 2. Evaporation of solid and liquid silicon in a vitreous carbon crucible. The chemical interaction between carbon and silicon is more obvious with high gaseous polymers.

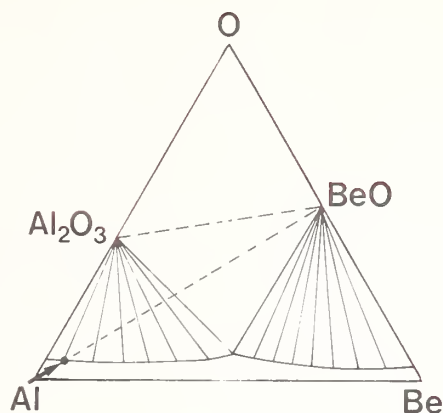


Figure 3. Hypothetical phase diagram for the equilibrium conditions when vaporizing Al in BeO crucibles. The system is stable when  $\text{Al}_2\text{O}_3$  coating is formed.

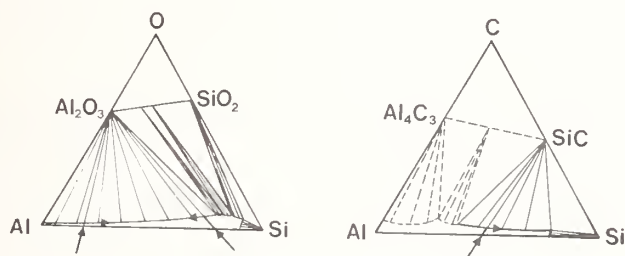
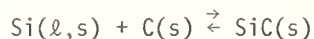


Figure 4. Ternary phase diagrams showing the equilibrium conditions in the whole system Al-Si-crucibles. The ternary eutectic valleys may be evaluated to determine temperature and composition ranges suitable to study Al-Si alloys.

The physico-chemical behavior of the crucible or Knudsen-cells is also important for the practicability of experiments. In the case of silicon, only dense graphite is suitable because no intergranular penetration occurs [12]. We have observed under the same conditions, and also with silicon in vitreous carbon, that the formation of an SiC coating acts as an effective barrier for silicon [13]. Then, the measurements with Si and Si-Al alloys rich in Si, have to be interpreted according to a reduced activity of carbon, defined for the system





Previous assumptions [14] of  $a_c = 1$ , in the equilibrium



seems to us erroneous. After correction from the free energy of formation of SiC, the value of the dissociation energy of AlSi(g) agrees with our value [15]:

$$D^\circ_{\text{AlSi}} = 51.5 \pm 7.2 \text{ kcal/mol (ref. [14])}$$

$$D^\circ_{\text{AlSi}} = 65.8 \pm 7.2 \text{ kcal/mol (ref. [14] corrected)}$$

$$D^\circ_{\text{AlSi}} = 59 \pm 3.0 \text{ kcal/mol (ref. [15]) .}$$

Considering the thermodynamics of equilibrium between the studied systems and the crucibles or Knudsen-cells, many experiments of vaporization in oxide crucibles may be regarded as possible by the formation of an inner component tight coating during the first heating [16].

The physical state of the cells is also important to maintain the cell as a closed system. This was shown in the case of U vaporization in melted Ta or monocrystal W [17] to avoid intergranular penetration. In the same manner, the vitreous states may limit the reactions between the sample and the crucible, chemical reactions, or creeping.

For the gaseous phase, chemical interactions with the cell material are only dependent on the chemical potential of each component, just as for the condensed-phase. The amount of matter involved to establish equilibrium conditions may take longer and, secondly, all the inner materials of the cell are concerned. In the absence of chemical interactions, a mass loss (diffusion through the walls, leakage, etc.) can create the situation of a non-closed system.

In all such cases, equilibrium conditions are not satisfied for the gaseous phase. The explanation of non-ideal angular distribution has been attributed to such wall effects [15, 18-21].

### 2.2.3 Interactions outside gaseous sample

Gases coming from the surroundings may enter through the effusion hole and react with the sample. Such disturbances have been quoted [24] with reducing residual gases when vaporizing CaO. Generally, part of the effusate will come back from the radiation shields. As these shields are often made of reducing metals (Ta), they may react with the effusate

and produce a flow of reducing matter through the effusion hole. In the case of multiple effusion cells, this type of disorder has been detected, but is generally of minor importance, (a few percent of the effusate) with a large sample.

### 2.3 A cell acts in thermal equilibrium

The pressure measurements are very sensitive to temperature. This sensitivity, due to large values for vaporization enthalpies is expressed through the Clausius-Clapeyron relation at mean temperature ( $T_m$ ):

$$\frac{\Delta P}{P} = \frac{\Delta H_{\text{vap}}}{RT_m} \frac{\Delta T}{T} \quad \text{or} \quad \cong 20 \frac{\Delta T}{T} < \frac{\Delta P}{P} < 60 \frac{\Delta T}{T} .$$

So the effusion cells must work without temperature gradients to achieve equilibrium conditions.

The effects of temperature gradients on pressures have been noted [22,23] for classical measurements with effusion cells. Transport phenomena may occur with temperature gradients and frequently the effusion holes are obstructed when their temperature is lower than the sample. So, many experimenters try to increase the temperature around the orifice.

An internal cause of temperature gradient may come from the heat flows required to vaporize the effusate. For low temperatures ( $T < 1000$  K), calculations [25] show the possibility of lowering the temperature of the vaporization surface when high pressures are measured with effusion cells, but the gradient can also be reduced when the cell is near a closed system. Such calculations are pessimistic, as shown for the Ag-Ge system [24] because, in fact, heat conduction must be taken into account. Moreover, for the higher effusion pressures, the "heat pipe" effect [27,28] could act in favor of temperature equilibrium. Measurements [23] show that the permissible magnitude of the apparent external gradient (measurements in the cell envelope) is related to its direction. Moreover, a suitable device [23] or heat pipe envelopes will reduce such effects on vapor pressure measurements.

### 3. Kundsén-Cell as an Irreversible System

The sampling of the gaseous phase by effusion prevents the complete system, cell and component, under investigation, from remaining at rigorous equilibrium conditions. This complete system is an open system, not only because effusion occurs, but also because other matter flow may be present; under conditions near equilibrium, this system may be considered as a succession of local equilibrium states [36]. So the cell operation implies taking several possible kinetic phenomena into account.

### 3.1 Gas conductance of the Knudsen-cell

The flow of gas from the vaporization area to the effusion orifice is subjected to a pressure gradient which can be evaluated according to gas kinetics. Some relations have been proposed which include the evaporation coefficients [29-32]. Carlson [33] attempts successfully to verify these formulae from the local assumptions of vaporization equilibrium, i.e., the cosine law of emission. The main results have been discussed in [1,33] and lead to the conclusion that the effusion orifice works as a source of molecules whose emission density is determined by the geometry of the cell and the evaporation coefficients.

In the case of high pressures, when the mean free path of the gaseous molecules is about the order of the orifice dimensions, the consequences of isotropic effects on the intensity of the molecular beam effusing from the cell should be considered [2,34]. However, we must mention that some measurements have been carried out successfully at high pressures [35]<sup>2</sup>.

### 3.2 Bulk diffusion and surface segregation

Generally, the effusion flows are not congruent with the composition of the condensed phase and so bulk diffusion may occur to restore equilibrium surface conditions for vaporization. Such phenomena have been observed through mass spectrometry [17(b),37,38,39]. An evaluation of surface concentrations has been established from the equality of matter flows at the vaporizing surface [40-44]. For these calculations, constant diffusion and activity coefficients are assumed. So corrections are only valid if the surface depletion is small. Calculations from these assumptions and relations show that bulk diffusion may occur easily with solids ( $D \approx 10^{-8} \text{ cm}^2/\text{s}$ ) but is generally avoided with liquids ( $D \approx 10^{-5} \text{ cm}^2/\text{s}$ ). Moreover, in this last case, convection favors homogenization.

As activation energies are lower for diffusion than for vaporization, the tendency to surface depletion increases with temperature and so the duration of the experiments at elevated temperatures must be shortened. Inversely, low temperatures may favor the homogenization of the melts. Temperature cycles may evidence this phenomenon and fix the best conditions for measurement at equilibrium (duration, cycles, etc.) [37].

In the case of liquids, some difficulties arise due to surface segregation caused by the incidence of surface tension on flows [45]. In this case, the Gibbs-Duhem relation is not suitable as used for the bulk phases, and the measurements of thermodynamic quantities for condensed phases may not be reliable; we observed this in Ag-Ge alloys when the temperature was increased; bulk diffusion would not explain our observations [26].

---

<sup>2</sup>Editor's note: For an extensive consideration of this point see the chapter by Bonnell and Hastie in this volume.

### 3.3 Matter flows other than effusion

In many vapor pressure determinations, experimenters observe that the results are dependent on the nature of the gaseous phase and on the cell material, through the choice of the Clausing factors [5]. In fact, the effusion orifice ensures a sharp discontinuity between the cell and the outside space only for vaporization and condensation equilibria.

First, calculations involving surface diffusion of the products along the walls and around the outside surface of the effusion hole, showed a possible and quite significant contribution to matter flow parallel to the effusion process: 30 percent in the case of Ag in Ni cells [46]. The permanence of this phenomenon does not allow the experimentalist to avoid these contributions, but only to minimize the consequences [3,46] or to make some corrections [47]. A more precise evidence of surface diffusion, around effusion orifices, has been found experimentally when analyzing the angular distribution in molecular beams [48-52].

In the case of liquid systems, creeping of the products may occur when the sample wets the cell material [7,17,53,54]. Solutions such as use of a sharp edge crucible [55] must be found. In practice, as the temperature rises, the number of possible solutions to this problem decrease. If we observe an effusion cell, we can see that it is an ideal device to favor creeping because the cell walls are quickly saturated with gases, and so generally creeping of liquids is observed when the temperature rises, that is, at higher pressures. At the same time, chemical interactions can become significant. But it is possible to establish conditions at the effusion orifice to restrain this creeping drastically: thin wall edges for effusion holes to stop any possible thin film of liquid, and surfaces around the effusion hole that are not saturated with the gaseous products which vaporize under Langmuir conditions outside the cell. Creeping may also occur through capillary joining. Dense or monocrystalline materials are more suitable [17] and joints must be made tight like vacuum seals or welded. Nevertheless, random creeping may be observed as we have shown in a comparative study on multiple cells by vaporizing pure gold in four identical cells (table 2).

As we pointed out, the entire analyzed system includes also the cell materials, and so, bulk or intergranular diffusion, or leakage, can occur through the walls [17,56,57]. This matter flow must not be neglected in order to understand the possible evolutions of the entire system.

### 3.4 Evolutions of the samples in the Knudsen-cells and congruent effusion

The studied sample will generally change its composition because of the non-congruency of matter flows escaping from the effusion cell (by effusion, diffusion, etc.). The evolution of the sample is always analyzed on the assumption of matter flow by effusion. In fact, the entire phenomenon must be regarded with all sorts of matter flows and according to irreversible thermodynamics [13]. The stationary states agree with the minimum of

entropy production relative to the independent thermodynamic strengths. To illustrate some possible evolutions, we chose some practical cases.

Table 2. Comparative measurements of the vaporization of gold in four dense graphite cells. Creeping or quick surface diffusion occurs on cell 1. The comparative response of the analyzer  $I_m^+/I_M^+$  (as described in [53]), shows the surface evaporation increases with cell 1.

$T^{\circ}\text{C}$	$I_1^+/I_2^+$	$(\frac{I_m^+}{I_M^+})_1/(\frac{I_m^+}{I_M^+})_2$	$I_1^+/I_2^{+a}$	$I_3^+/I_2^{+a}$	$I_4^+/I_2^{+a}$
1184	1.10	1.00	1.11	1.00	1.07
1069	1.18	0.96	1.14	0.95	1.17
1109	1.15	0.99	1.14	1.01	1.03
1142	1.19	1.05	1.25	1.01	1.07
1222	1.20	0.96	1.16	1.00	1.05
1248	1.29	0.91	1.18	0.99	1.03
1269	1.39	0.89	1.24	0.99	1.05
1299	1.54	0.84	1.29	0.99	1.03
1136	1.57	0.81	1.28	0.97	1.00
1310	1.57	0.77	1.214	0.98	1.00
1350	2.26	0.33	0.74	0.99	1.03

<sup>a</sup> Intensities corrected with the analyzer.

#### 3.4.1 Homogeneous chemical samples without interactions with the cell: ideal Knudsen-cell

This is the most common case and is generally taken, using isothermal evolutions, to analyze the gaseous phase and/or to calibrate the mass spectrometer. For example this method has been used extensively to solve complex gaseous phases with fragmentation patterns and to obtain partial pressures versus composition data, especially in mixed fluorides [39].

When the composition of the effusing matter flow is the same as the sample, the evolution has reached a steady state until all the sample is evaporated. This "congruent effusion" may be established from irreversible thermodynamics. Basic assumptions are presented in Appendix 1. This general result has been proposed [58] and used as a supplementary relation to determine relative ionization cross-sections [59].

#### 3.4.2 Homogeneous chemical samples with interactions with the crucible

In effusion cells, the composition of the gaseous phase is also dependent on the stability of the different gaseous molecules which can exist between the constituents of the sample and the crucible. For example, the evaporation of Al in stable oxide crucibles, such as BeO and ThO<sub>2</sub>, occurs as Al and Al<sub>2</sub>O molecules. The departure of oxygen with Al<sub>2</sub>O gas, maintains the consumption of the crucible and at the same time the metallic element



is solubilized, as we have observed [6]. The direction of the evolution is shown in figure 5. Through irreversible thermodynamics, we have established that the entire system, cell and sample, will reach a steady-state with no congruent effusion (Appendix 1).

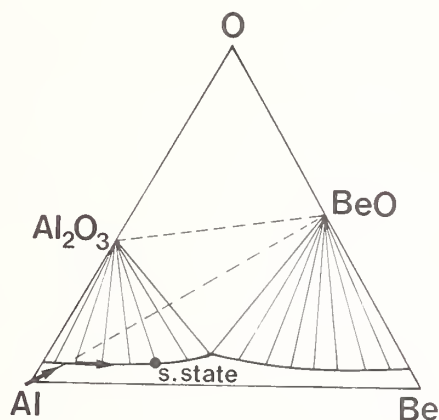


Figure 5. Isothermal evolution of the aluminium sample in BeO crucible. As the experimental time increases the sample becomes more rich in Be.

#### 3.4.3 Homogeneous samples with effusion flow and diffusion flow through the cell walls

Diffusion of one or several constituents through the cell walls and effusion may occur simultaneously. Those two processes have been suspected [60] and evaluated in the case of  $UO_{2\pm x}$  in tungsten-Knudsen-cells [17]. The final state of systems with effusion and diffusion flows could be evaluated with irreversible thermodynamics. Assumptions and calculations in Appendix 1 show, in the case of binary systems, that a possible stationary state is, of course, not a congruent effusion and depends largely on the geometry and the thermodynamics of the cell material. For example, in the case of oxide systems vaporizing in Mo or W cells, the competition between effusion and diffusion flows of oxygen shifts the composition of the gaseous phase towards a reducing range. Then, the crucible in the stationary state acts as if the chemical potential of oxygen is fixed at lower values than in the sample system proper without interactions.

#### 4. Molecular Beam Sampling With a View to High Temperature Mass Spectrometry

When sampling the molecular beam from effusion and ionizing, practical devices may introduce various parasitic contributions.

#### 4.1 Principle of the measurements and practical difficulties

We consider an elementary volume  $dv$  in the ionization zone which is defined by the intercept of a part  $d\phi$  of the molecular beam and a part of the electron beam with intensity  $i^-(M')$  (see fig. 6):

$$d\phi = \frac{n\bar{c}}{4\pi} d\Omega = \frac{n\bar{c}}{4\pi} \cdot \frac{ds \cos\theta ds' \cos\theta'}{L^2}.$$

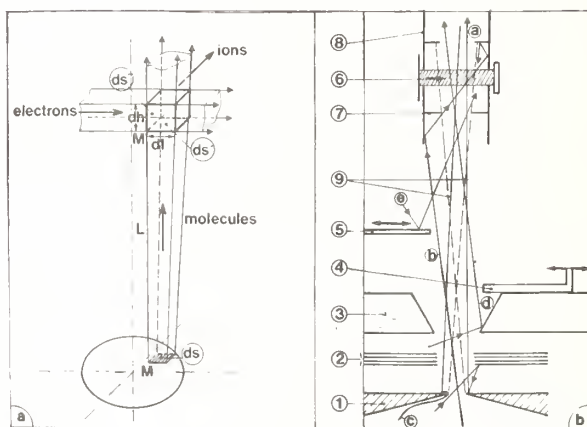


Figure 6. Principle of the ions production. Parasitic contributions to the molecular beam sampling may occur: (1) effusion cell, (2) radiation shield, (3) cold field diaphragm, (4) shutter sliding on the cold trap, (5) shutter, (6) electron beam, (7) entrance diaphragm of the ionization box, (8) ionization box, (9) representative molecular beam; (a) re-evaporations from shields, (b) re-evaporations in the source, (c) re-evaporations from surface diffusion or creeping, and (d) and (e) "shutter effect."

From the Beer-Lambert law, the number of ions produced is:

$$i^+_{(M')} dv = i^-_{(M')} \rho \sigma dL ds''$$

where  $\rho$  is the density of a gaseous molecule in the molecular beam,  $\sigma$  is the ionization cross-section of the molecule.

The quantity of detected ions is:

$$dI^+_{(M')} = i^+_{(M')} dv \gamma \eta_{(M')} f$$

where  $\gamma$  is the detector efficiency,  $f$  the isotopic abundance, and  $\eta_{(M')}$  the yield for extraction and transmission of the ion produced at  $M'$ .

Since  $\rho \bar{c} ds' = d\phi = \rho \bar{c} \frac{dI ds''}{dh}$  and  $P = nkT$ , the elementary ionic current coming from  $M'$  is:

$$dI^+_{(M')} = i^-_{(M')} \frac{P}{4\pi kT} \cdot \frac{dscos\theta ds' cos\theta'}{L^2} \sigma \gamma f \eta_{(M')} dh$$

The entire current is then:

$$I^+ = \frac{P}{4\pi kT} \cdot (\sigma \gamma f) \cdot \int_A \int_V i^-_{(M')} \eta_{(M')} \frac{dscos\theta ds' cos\theta'}{L^2} dh \quad (5)$$

where  $A$  is the effusion hole area, and  $V$  is the "effective" ionization volume, which is the usual formula  $I^+T = PS$ . The evaluation of the sensitivity  $S$  cannot usually be established because  $i^-_{(M')}$ ,  $\eta_{(M')}$  and the ionization volume are not known.

To establish these formulae the parasitic contributions have been set aside. These contributions come from the technological background as well as from the nature of the studied system. Figure 6 shows the different parasitic contributions:

- Evaporations from surfaces around the effusion orifice and possibly from deposits in the source.
- Interferences between residual gases and the molecular beam: absorption of the beam or difficulties in measuring gaseous species which exist also in the residual gases.
- Parasitic ions coming from the furnace and so-called "photo effects." These ions can be distinguished from those produced by electron impact [54].

## 4.2 Parasitic contributions from surface evaporations

So-called surface evaporations cover all the possibilities of re-emission of molecules towards the useful ionization zone. These molecules are not representative of the equilibrium conditions in the Knudsen-cell.

### 4.2.1 Emission of molecules from the effusion hole surroundings

The best conditions for sampling the molecular beam have been summarized [61], particularly in the case of sampling with sharp slits. In mass spectrometry, except in a few cases [62,67], the geometrical devices are rarely described with precision, and most often an observation of the drawings is the only source of information.

Usually the collimation of the molecular beam in the space between the effusion hole and the ionization zone is entirely defined by two diaphragms (in the restricted case of cylindrical symmetry) which limit, in the plane of the effusion orifice, the umbra and pen-umbra zone observable by the ion source [53]. Then, the source can also detect molecules

issuing from surfaces around the effusion hole. The different paths for molecules are shown in [53].

Many experimentalists have observed such surface evaporations (quoted in [53]) either when moving the shutter to make a shutter profile or when comparing cells with the system under investigation and empty cells [63,64]. We evidenced and calculated these surface evaporations by differential analysis of intensity distributions in the molecular beam [53]. The device is made of calibrated paddles (more sensitive than slits) which partially hide the observed area (fig. 7): the most significant position corresponds to the complete occultation of the effusion orifice. Then, if the ion current observed is no longer null, surface evaporations must be present.

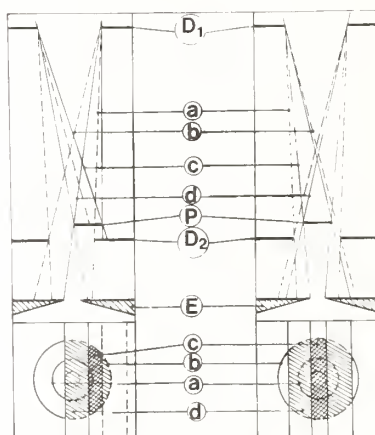


Figure 7. Differential molecular beam analyzer: E = effusion cell;  $D_2$  = field diaphragm;  $D_1$  = source diaphragm; a and b = umbra and penumbra zones of the collimation  $D_1D_2$ ; c and d = umbra and penumbra zones for the analyzer.

Estimations of the emissivity of the surfaces around the effusion orifice have been made for the different parasitic sources [53]. Creeping re-evaporation from radiation shields or conical cell envelopes involve practically constant surface emissivity. Surface diffusion along the orifice edges involves a rapid change in emissivity if going further away from the effusion hole [3,46] (fig. 8). In fact, this surface diffusion cannot be avoided as explained earlier (Section 3.3).

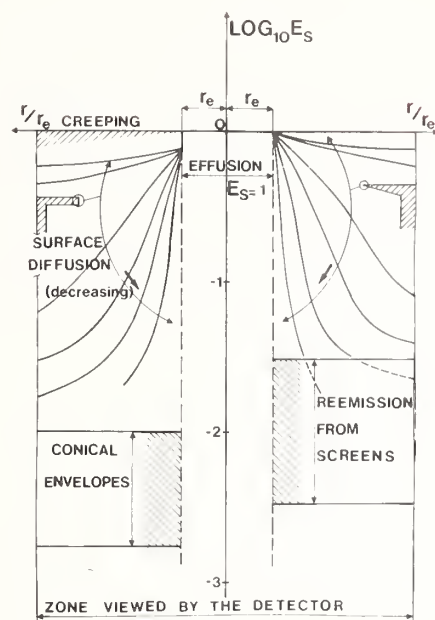


Figure 8. Comparison of the "surface emissivity"  $E_S$  for different parasitic surface evaporations.

These two kinds of parasitic flows produce very different contributions for the same collimation device and must be identified and then evaluated. Consequently, simple comparisons with a standard shutter profile [65] or simplifications [66] in the calculations lead to an underestimation.

Moreover, the accuracy of such an evaluation is restricted because the ionization and extraction yield in the ion source is not known. Thresholds for detection of these contributions have been quoted, such as 5 percent for constant emissivity and 15 percent to 20 percent for emissivity from surface diffusion with our mass spectrometer. However, when relative measurements are carried out (activity measurements, isomolecular equilibrium, etc.) accurate corrections may be made more easily [53].

#### 4.2.2 Re-emission of molecules in the ion source

The temperature of the ionization box may reach a few hundred degrees Celsius, ensured through the filament. So, when the studied systems vaporize in this temperature range, re-emission of molecules may occur from deposits on the different parts composing the ionization box. This phenomenon has been systematically observed with systems such as As, Sb, Se, and fluorides [67].



Generally, liquid nitrogen traps are arranged around the oven and the ion source, and they lower contributions from screens, vacuum housing, etc. [68,65]. Nevertheless, an important contribution may remain which is not shutterable if the molecular beam is not perfectly collimated. Such observations have been made on various systems [65] and we have observed something similar during the vaporization of  $\text{Sb}_2\text{O}_3$ . In fact, with usual high temperature mass spectrometers, it is difficult to avoid some deposits in the ionization box by collimation of the molecular beam. In our case [69], we had to build a kind of cold "nose" which enters the ionization box as close as possible to the electron beam. In this way, we were able to study the vaporization of  $\text{Sb}_2\text{O}_3$  without re-emitted molecules, over the entire temperature range, 250 to 500 °C, where the gaseous  $\text{Sb}_4\text{O}_6$  molecule is detectable.

#### 4.3 Residual gases: interferences and measurements on permanent gas

Attenuation due to collisions between residual gases and the molecules traveling in the useful molecular beam can be evaluated from Beer's law as pointed out by Estermann [61]. For gaseous species easily condensable on the walls or cold traps, and with good vacuum conditions, the molecular beam is not perturbed. When the measurements are made on permanent gases which exist in the residual atmosphere ( $\text{N}_2$ ,  $\text{O}_2$ , etc.), the production of these gases by effusion maintains a local increase of pressure between the cell and the first diaphragm. There is an optimum value for the distance between the cell and the first diaphragm as shown in [61] and solutions must be sought in different geometrical devices such as skimmers for high pressure sampling.

Difficulties occur with measurements on permanent gases because the relative sensitivity of the ion source, for an equal pressure, to the gases traveling with the molecular beam is several orders of magnitude ( $\sim 10^{-4}$ ) lower than to those coming from the residual gases: this is due mainly to the smallness of the solid angle to sample the molecular beam. These difficulties may be reduced with the best possible ultra-high vacuum and by lowering the ionization box temperature<sup>3</sup>.

When the intensities of the permanent gas molecules, coming from the effusion cell, are high enough to be detected, the so-called shutter effect [54] must be avoided. A difference in pressure of these molecules between the source and the oven housings leads to parasitic flow towards the ion source. So, if the displacement of the shutter modifies conductance between the two housings, the variation of this parasitic flow is taken into account with the molecular beam measurements. This shutter effect is cancelled either when the two housings are put at the same vacuum [70], or by a suitable design of the shutter device in the collimation system [13,53].

---

<sup>3</sup>Editor's note: Use of molecular beam modulation with phase sensitive detection is another approach e.g., see the chapter in this volume by Bonnell and Hastie and by Plante.

#### 4.4 Spatial discrimination in the ion sources

When moving the effusion orifice all around the axis of the molecular beam collimation, experimenters often observe maximum ion intensity when centering the cell. The position reached in this way is not always on the geometrical axis of the collimation. A study [71] of the influence of the displacement of the effusion hole on the ion intensity has been carried out with our mass spectrometer. Figure 9 shows the theoretical response for cylindrical symmetry with constant yield in the ionization zone, and practical observations where a dissymmetrical response appears. This phenomena is practically systematic with the ion source used.

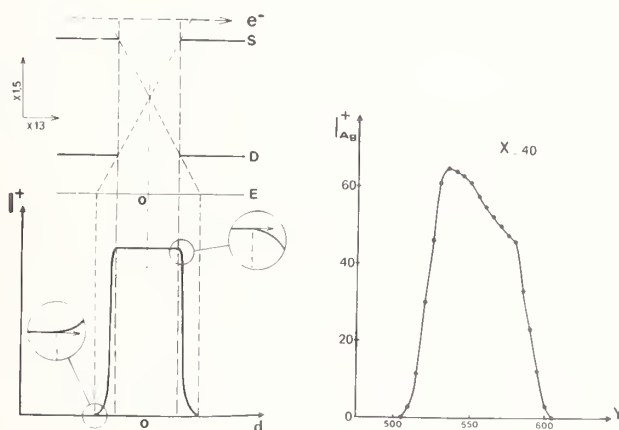


Figure 9. Theoretical and practical responses of the mass spectrometer when moving the effusion hole around the axis of the molecular beam collimation.

Taking into account a sharp collimation of the molecular beam by the entrance source diaphragm, it seems that the ionization volume is larger than the molecular beam according to eq. (5). Consequently, if the local ionization efficiency is not constant, the whole current is sensitive to the molecular beam position inside the ionization volume. The maximum of the response is always obtained when the molecular beam in the ionization zone is displaced towards the entrance slit of the electron beam where the electron density is highest.

So, in the case of comparative measurement, either taken successively [38,63,64] or with multiple cells [72,73] or two ovens [74,75], it is necessary to determine experimentally the effect of the location of the effusion hole for each Knudsen-cell ion source assembly, in order to define the accuracy of the determinations.

## 5. Improvements in the Principles of Vapor Pressure Measurements with High Temperature Knudsen-Cell Mass Spectrometry

Depending on the different interactions quoted between the sample and the cells, the parasitic contributions introduced by the molecular beam sampling and temperature considerations, different ways may be reported or proposed to ascertain or improve vapor pressure measurements. At the same time, recent partial results will be presented.

### 5.1 The true temperature of the inner cell and calibrations in situ

As explained in Section 2.3, many factors contribute to establish good thermal equilibrium conditions in the inner volume of the cell where the vaporization occurs. So it should be appropriate to carry out the temperature measurements in this volume to ascertain the most reliable  $P(T)$  measurements. If this is not possible, special precautions must be taken to avoid any temperature gradients between the inner cell temperature volume and the measurement points.

The influence of temperature measurements by pyrometry on the temperature of the cell is relatively small compared with other conduction and radiation leaks, as usually the radiations are emitted towards the pyrometer through a very small solid angle. Some recent developments [76] show that a sensitivity of  $0.2\text{ }^{\circ}\text{C}$  is possible with a pyrometer equipped with a photomultiplier detector whose accuracy is  $1\text{ }^{\circ}\text{C}$  up to  $2000\text{ }^{\circ}\text{C}$ <sup>4</sup>.

In the case of thermocouples, difficulties arise from thermal leakage along the thermocouple itself [77] and it is not surprising that melting points may be observed a few degrees below the true values [74]. Because thermal exchange between the cell and the thermocouples are subject to variations with temperature, and from one experiment to another, it is advisable to eliminate the thermal drop around the thermocouple junction. So, in addition to usual thermocouple calibrations, it is necessary to ascertain the best layout and thermal guard without significant thermal leak at the junction. Solutions have to be found, such as to roll the thermocouples into a coil in the cell envelope [17] or to tighten them by welding or with screws [26], while checking possible interactions of the materials.

Heat pipe devices, due to their design, can ensure rigorous isothermal conditions inside the cell envelope [78]. On the one hand, such a device will provide an ideal situation for vapor pressure measurements and, on the other hand, it is possible to control the identical response of thermocouples located under several cells<sup>5</sup>.

---

<sup>4</sup>Editor's note: See also the chapter by Storms and Mueller in this volume.

<sup>5</sup>Editor's note: A detailed discussion of heat pipes has been given by Melton in this volume.

For a long time, temperature calibrations have been carried out in situ by mass spectrometric observations of melting-points. Primary and secondary standards [79] are conveniently available for this purpose. But precautions must be taken to avoid any evolution of the reference sample, as quoted in Sections 2.2 and 3.4.

## 5.2 Comparative measurements for the best choice of cells

Before attempting to measure the vapor pressures of a system, some controls with multiple cells in the same oven may inform the experimentalist on the behavior of the entire system, sample plus cell.

The chemical reactivity between the sample and the crucible can be studied as a measurement of activities in a multicomponent system. The best conditions have been established in [72]. In the same manner, parasitic flow of matter through the walls of the cell can be evidenced, the best materials can be chosen, depending on composition and temperature ranges, and the true congruent effusion can be ascertained.

The study of equilibrium conditions may be performed by comparing cells with different evaporation area/effusion area ratios. Inversely, new development would be possible to analyze the evaporation behavior of systems [80] while the irreversibility of the cell increases.

The identity of temperatures between the cells is easily verified by mass spectrometry with the same sample in each cell. When viewing with collimating diaphragms, such as those described later, through the different effusion orifices, we have measured strictly identical ionic currents. But in the case of classical collimation, the surface evaporations generally lead to different and unexpected responses which can vary with the temperature.

The presence of surface evaporations may be pointed out by comparison between different cells as already shown [53]: cells with collimating holes and conventional cells. To evaluate these parasitic contributions more exactly, conventional cells having effusion holes inside the penumbra zone may be compared with a cell whose effusion hole allows direct viewing inside the cell by means of a sharp and suitable collimating system.

## 5.3 Absolute vapor pressure and equilibrium constant measurements

When measuring vapor pressures or sublimation enthalpies, frequently the results from the second and third law of thermodynamics are consistent only with a low confidence factor. A typical example is given by interlaboratory analysis measurements [81] of silver vapor pressures. The temperature measurements cannot be solely incriminated to explain such discrepancies. On the other hand, ionic current measurements can be accurate and known, especially in the case of discriminate ion pulse counting. Under these conditions, it seems justified to attribute the uncertainties chiefly to surface evaporations and nonequilibrium conditions. According to relative enthalpies for vaporization and surface diffusion, the parasitic contributions would lead to serious deviation for the second law and a drift for the third law data.

### 5.3.1 Chemical trapping with hot collimators

A solution proposed consists in trapping [7,15] the parasitic flow of matter with a series of hot collimators put just over the effusion hole to cut off evaporations from its surroundings towards the ion source (fig. 10a) or to prevent all parasitic matter flow from leaving this assembly (fig. 10b). The collimators and the different parts inside must be chemically reactive with the gases. As some saturation effects may appear, it is advisable to control with a molecular beam analyzer (as shown in fig. 7) if some surface evaporation occurs. Good results were obtained when studying the evaporation of silicon in vitreous carbon surrounded by dense graphite [13] as shown in figure 2. The results would be obtained from the third law with a sensitivity factor including a transmission coefficient established from the useful solid angle (fig. 10b).

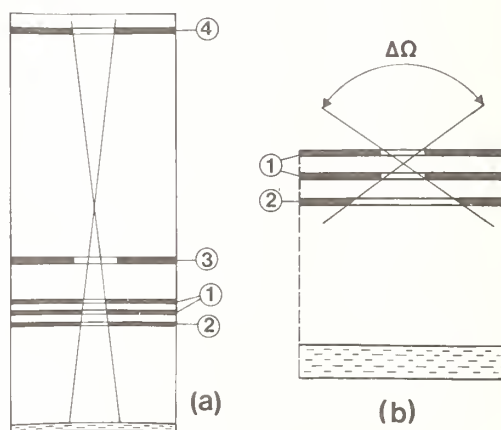


Figure 10. Principle of the molecular beam sampling with hot collimators:  
(1) hot collimators, (2) effusion hole, (3) field diaphragms, (4) detector.  
(a) sampling without parasitic flow for the detector.  
(b) sampling for weight loss measurements.

### 5.3.2 Permanent cold collimation

The chemical trapping of gases issuing from the sample is not always possible, especially if the system under investigation is not reactive enough, as we have observed for silver-germanium alloys [26]. This case is more frequent with low temperature systems. So, as for activity measurements, it is preferable to build a collimation such that the ion source can view only inside and through the effusion hole (fig. 11). This solution is being used at present to study the sublimations of Pb, PbSe, and cubic  $\text{Sb}_2\text{O}_3$ . The second law data is obtained with a notable accuracy and the standard deviations of the second and third law data overlaps for a confidence factor 0.95:



$$\Delta H_{298 \text{ subl. Pb}} = 45.561/\text{kcal/mol} \quad S = 0.386 \text{ (second law)}$$

$$= 46.586/\text{kcal/mol} \quad S = 0.208 \text{ (third law)}$$

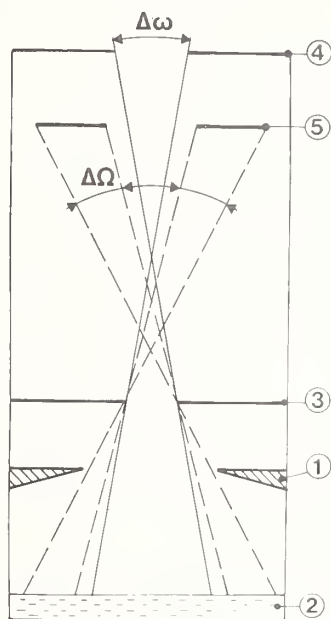


Figure 11. Sampling of the same molecular beam for mass spectrometry ( $\Delta\omega$ ) and condensation ( $\Delta\Omega$ ) without parasitic contributions.

For the third law, a moderate uncertainty remains because with such a collimating system the total weight loss used to establish absolute pressures includes the parasitic matter flows. To solve this difficulty, partial condensation of the effusate can be achieved as already carried out [17,37] simultaneously with the measurement in an analogous sampling using mass spectrometry (fig. 11). With such a device, the measurements are not sensitive to the spatial discrimination in the ion source, related to the location of the effusion hole. The useful molecular beam is always directed into the ion source at the same place. Moreover, when moving the furnace, the experimenters can evidence the different surface evaporations for all the components, as observed with  $\text{Al}_2\text{O}_3\text{-CaO}$  system (fig. 12).

## 6. Conclusion

Numerous recent studies have resulted in appreciable progress in our understanding of the actual working of the effusion cell. They concern, in particular, gaseous flows and their spatial distribution, the chemical interactions between cell and sample, and flows other than effusion. At the same time, there have been decisive technical developments allowing an effective experimental grasp of all the main phenomena involved.

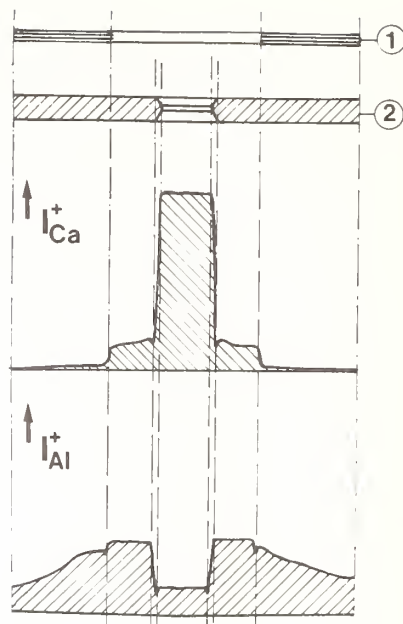


Figure 12. Response of the mass spectrometer when moving the effusion hole with a sharp collimation viewing through the effusion hole. The surface evaporations are shown more important with Al, for the studied system  $\text{Al}_2\text{O}_3\text{-CaO}$ .

To obtain reliable and precise information on effusion, the behavior of the cell-sample system and parasitic flows must be taken into account. Solutions exist for reducing the difference between the true equilibrium pressure and that actually measured under dynamic conditions. The irreversible character of the Knudsen cell introduces a deviation in relation to an "ideal" closed system which should be measured and assessed more accurately.

The most powerful application of the effusion method involves the connection of a mass spectrometer, which is a choice detector in that it affords a sensitive, speedy and continuous means of monitoring the composition of the gas phase as well as the parasitic flows, such as surface evaporation, which seem responsible for major errors.

Since pyrometric measurements are sensitive detectors, temperature gradients can be precisely controlled and practically eliminated and the temperature can be known with a precision almost as exact as its thermodynamic definition allows. Ion pulse counting techniques can be used to assign a mathematical uncertainty to ion current measurements.

Consequently, it would seem possible to attain good measurement accuracy once parasitic phenomena are detected, evaluated or suppressed by the quality of the cell-collimators-ion source assembly.

## References

- [1] Carlson, K. D., in The Characterization of High-Temperature Vapors (John Wiley and Sons, Inc., New York, 1967).
- [2] Wahlbeck, P. G., J. Chem. Phys. 55, 1709 (1971).
- [3] Winterbottom, W. L. and Hirth, J. P., in Condensation and Evaporation of Solids, p. 348 (Gordon and Breach, New York, 1964).
- [4] Pound, G. M., J. Phys. Chem. Ref. Data, 1, 135 (1972).
- [5] Ward, J. W., Report LA-3509 (1966).
- [6] Perakis, J., Thesis Docteur Ingenieur, Universite Scientifique et Medicale de Grenoble, Grenoble-France (1973).
- [7] Chatillon, C., Allibert, M., and Pattoret, A., High Temp. High Pressures, 7, 583 (1975).
- [8] Alcock, C. B. and Peleg, M., Trans. Brit. Ceram. Soc. (May 1967).
- [9] Rosenblatt, G. M., J. Electrochem. Soc. 110, 563 (1963).
- [10] Kubachewski, O., Rev. Hautes Temp. et Refract. 3, 229 (1966).
- [11] Brewer, L. and Searcy, A. W., J. Amer. Chem. Soc. 73, 5308 (1951).
- [12] Drowart, J. and DeMaria, G., in Silicon Carbide, p. 16 (Pergamon Press, New York, 1960).
- [13] Chatillon, C., Thesis, Universite Scientifique et Medicale de Grenoble, France, No. A-0-11.591 (1975).
- [14] Stearns, C. A. and Kohl, F. J., High Temp. Science, 5, 113 (1973) and Report NASA-TN-D-7123 (1972).
- [15] Chatillon, C., Allibert, M., and Pattoret, A., C. R., Acad. Sc. Paris, 280, C 1505 (1975).
- [16] Grimley, R. T., Burns, R. P., and Inghram, M. G., J. Chem Phys. 34, 664 (1961).
- [17a] Pattoret, A., Drowart, J., and Smoes, S., Trans. Faraday Soc. 65, 98 (1969).
- [17b] Pattoret, A., Thesis, Universite Libre de Bruxelles, Belgium (1969).
- [18] Ward, J. W., Mulford, R. N. R., and Kahn, M., J. Chem. Phys. 47, 1710 (1967).
- [19] Ward, J. W., Mulford, R. N. R., and Bivins, R. L., J. Chem. Phys. 47, 1718 (1967).
- [20] Ward, J. W., J. Chem. Phys. 47, 4030 (1967).
- [21] Ward, J. W. and Fraser, M. V., J. Chem. Phys. 49, 4743 (1968).
- [22] Buchler, A. and Berkowitz-Mattuck, J., J. Chem. Phys. 39, 286 (1963).
- [23] Storms, E. K., High Temp. Sci. 1, 456 (1969).
- [24] Babeliowsky, T. P., J. Chem. Phys. 38, 2036 (1963).
- [25] Littlewood, R. and Rideal, E., Trans. Faraday Soc. 52, 1598 (1956).
- [26] Martin-Garin, L., Chatillon, C., and Allibert, M. (J. Less Common Metals), to be published.
- [27] Chisholm, D., The Heat Pipe (Mills and Boon Ltd., London, 1971).
- [28] Dunn, P. D. and Reay, D. A., Heat Pipes (Pergamon Press, Oxford, G.B., 1976).
- [29] Whitman, C. I., J. Chem. Phys. 20, 161 (1952); 21, 1407 (1953).
- [30] Rossman, M. G. and Yarwood, J., J. Chem. Phys. 21, 1406 (1953); Brit. J. Appl. Phys. 5, 7 (1954).

- [31] Motzfeld, K., J. Phys. Chem. 59, 139 (1955).
- [32] Balson, E. W., J. Phys. Chem. 65, 1151 (1961); Iczkowsky, R. P., Margrave, J. L., and Robinson, S. M., J. Phys. Chem. 67, 229 (1963).
- [33] Carlson, D. K., Gilles, P. W., and Thorn, R. J., J. Chem. Phys. 38, 2064 (1963).
- [34] Carlson, K. D., Gilles, P. W., and Thorn, R. J., J. Chem Phys. 38, 2725 (1963).
- [35] Hager, J. P. and Hill, R. B., Metall. Trans. 1, 2723 (1970).
- [36] Ackerman, R. J., Thorn, R. J., and Winslow, G. H., Report AN6-6663 (1962).
- [37] Pattoret, A., Drowart, J., and Smoes, S., Bull. Soc., Fr. Ceram. 77, 75 (1967).
- [38] Storms, E. K., in Thermodynamics, 1, 309 (IAEA, Vienna, Austria, 1966).
- [39] Sidorov, L. N. and Shol'ts, V. B., Int. J. Mass Spectrom. Ion Phys. 8, 437 (1972).
- [40] Walsh, W. J., Ph.D. Thesis, Iowas State University (1964).
- [41] Roy, P. and Hultgren, R., Trans. Metall. Soc. AIME 233, 1811 (1965).
- [42] Shroeder, D. L. and Elliott, J. F., Trans. Metall. Soc. AIME 236, 1091 (1966).
- [43] Chang, Y. A., Wilhelm, G. G., Lathrop, M., and Gyuk, I., Acta Metall. 19, 795 (1971).
- [44] Jaeger, J. C. and Carslow, H. S., in Conduction of Heat in Solids (Oxford University Press, 1959).
- [45] Defay, R. and Prigogine, I., Surface Tension and Adsorption (Longmans, Grenn, and Co. Ltd., London, 1966).
- [46] Winterbottom, W. L. and Hirth, J. P., J. Chem. Phys. 37, 784 (1962).
- [47] Boyer, J. and Meadowcroft, T. R., Trans. Metal. Soc., AIME 233, 388 (1965).
- [48] Winterbottom, W. L., J. Chem. Phys. 47, 3546 (1967).
- [49] Winterbottom, W. L., J. Chem. Phys. 49, 106 (1968).
- [50] Winterbottom, W. L., J. Chem. Phys. 51, 5610 (1969).
- [51] Dunham, T. E. and Hirth, J. P., J. Chem. Phys. 49, 4650 (1968).
- [52] Wagner, L. C. and Grimley, R. T., Chem. Phys. Letters, 29, 594 (1974).
- [53] Chatillon, C., Allibert, M., and Pattoret, A., High Temp. Science, 8, 233 (1976).
- [54] Inghram, M. B. and Drowart, J., in High Temperature Technology, p. 219 (McGraw Hill, New York, 1959).
- [55] Erway, N. D. and Simpson, O. C., J. Chem. Phys. 18, 953 (1950).
- [56] Gokcen, N. A., J. Phys. Chem. 69, 3538 (1965).
- [57] Panish, M. B., J. Chem. Eng. Data, 6, 592 (1961).
- [58] Searcy, A. W. and Williams, W. S., J. Chem Phys. 32, 957 (1960).
- [59] Cater, E. D. and Thorn, R. J., J. Chem Phys. 44, 1342 (1966).
- [60] White, D., Walsh, P. N., Ames, L. L., and Goldstein, H. W., in Thermodynamics of Nuclear Materials, p. 417 (IAEA, Vienna, Austria, 1962).
- [61] Estermann, I., Rev. Modern Phys. 18, 300 (1946).
- [62] Cater, E. D., Rauh, E. G., and Thorn, R. J., J. Chem. Phys. 35, 619 (1961).
- [63] Storms, E. K. and Griffin, J., High Temp. Science, 5, 423 (1973).
- [64] Storms, E. K. and Griffin, J., High Temp. Science, 5, 291 (1973).
- [65] Murray, J. J., Pupp, C., and Pottie, R. F., J. Chem. Phys. 58, 2569 (1973).
- [66] Bartosik, D. C., Ph.D. Thesis, Evanston, U.S.A., No. 71-30, 739 (1971).

- [67] Vasile, M. J., Jones, G. R., and Falconer, W. E., Adv. Mass Spectrom. 6, 557 (1974), Applied Science Publishers Ltd., Barking, Essex, G.B.
- [68] Drowart, J., Goldfinger, P., Detry, D., Rikert, H., and Keller, H., Adv. Mass Spectrom. 4, 499 (The Elsevier Publishing Co., New York, 1969).
- [69] Mass Spectrometer type 12-90 HT, Nuclide Corporation, 642 East College Avenue, State College, Pa. 16801.
- [70] Paule, R. C., High Temp. Science, 8, 257 (1976).
- [71] Chatillon, C., Senillou, C., Allibert, M., and Pattoret, A., Rev. Sci., Instrum. 47, 334 (1976).
- [72] Chatillon, C., Allibert, M., and Pattoret, A., Adv. Mass Spectrom. 7A, 615 (Heyden and Son Ltd., London, 1978).
- [73] Chatillon, C., Pattoret, A., and Drowart, J., High Temp. High Pressures, 7, 119 (1975).
- [74] Grimley, R. T., and Joyce, T. E., J. Phys. Chem. 73, 3047 (1969).
- [75] Joyce, T. E., Ridley, T. Y., and Grimley, R. T., Rev. Sci., Instrum. 41, 1789 (1970).
- [76] Storms, E. K. and Mueller, B., J. Phys. Chem. 81, 318 (1977).
- [77] White, D., Sommer, A., Walsh, P. N., and Goldstein, H. W., Adv. Mass Spectrom. 2, 110 (Pergamon Press, Ltd., Oxford, G.B., 1963).
- [78] Chatillon, C., Allibert, M., Moracchioli, R., and Pattoret, A., J. Appl. Phys. 47, 1690 (1976).
- [79] Metrologia, 5, 35 (1969).
- [80] Storms, E. K. and Mueller, B., J. Phys. Chem. 82, 51 (1978).
- [81] Paule, R. C. and Mandel, J., Pure Appl. Chem. 31, 395 (1972).
- [82] Allibert, M., Chatillon, C., and Lourtou, R., Colloque Int. CNRS-IUPAC, Odeillo, France, (28 June-1 July, 1977).

## Appendix 1

### Evolutions of Systems in Knudsen-Cells

#### A. Congruent effusion for homogeneous samples without interactions with the cell

For a flux-tube  $i$  between the effusion area and any semi-permeable surface with constant pressure in the molecular beam, the entropy production can be calculated:

$$P_{S_i} = \phi_i \int_{\text{orifice}}^{\text{surface at constant pressure}} \text{grad} \left( \frac{\mu_i}{T} \right)$$

where the elementary strength  $dX_i = \text{grad} \left( \frac{\mu_i}{T} \right) = R \text{ grad} (\ln P_i)$ ,  $X_i = R \ln \frac{P_i^{(o)}}{P_i^\infty}$  and  $\phi_i$  is the effusion flow;  $P_i^{(o)}$  is the pressure at the orifice, and  $P_i^\infty$  the pressure on a



surface (like housing) sufficiently distant from the orifice. The entire entropy production is:

$$P_S = \sum_{i=1}^n \phi_i R \ln \frac{P_i^{(o)}}{P_i}$$

The steady state is reached when the derivation of  $P_S$  on regard to independent strength is nul. The  $n$  strengths obey the Gibbs-Duhem relation at the vaporization and so

$$d_X P_S = \sum_{i=1}^{n-1} \left( \phi_i - \phi_n \frac{x_i}{x_n} \right) d \ln P_i = 0$$

leads to  $(n-1)$  relations for the stationary state:

$$\begin{aligned} \phi_i - \phi_n \frac{x_i}{x_n} &= 0 \\ \vdots \\ \phi_n - 1 - \phi_n \frac{x_n - 1}{x_n} &= 0 \end{aligned} \quad \text{or} \quad \frac{\phi_i}{\phi_n} = \frac{x_i}{x_n} \quad 1 \leq i \leq n-1$$

Then the composition of the fluxes is the same as the condensed phase ( $x_i$ ). The stationary state is a "congruent effusion," and we can write:

$$\frac{\gamma_i P_i^0}{\gamma_n P_n^0} = \sqrt{\frac{M_i}{M_n}} \quad 1 \leq i \leq n-1$$

$\gamma_i$  is the activity coefficient and  $P_i^0$  is the pressure in standard state for the  $i$ th element.

#### B. Homogeneous samples with equilibrium interactions with its crucible

When the reaction between the sample and the crucible occurs:

$$P_S = R \sum_{i=1}^n \phi_i \ln \frac{P_i}{P_i^0} - R \sum_{i=1}^n \lambda_i \ln \frac{a_i}{A_i}$$

where  $\lambda_i$  is the flow of matter between the sample (activity  $a_i$ ) and the crucible (activity  $A_i$ ). Generally, in the effusion cells the flow of matter is limited by the effusion only and the second part of the equation will be reduced to

$$R \sum_{i=1}^n \phi_i \ln \frac{p_i}{p_i^\infty} .$$

The minimum of entropy production is obtained after elimination of non-independent strengths which are related by the Gibbs-Duhem relation in the sample:

$$\sum_{i=1}^n x_i d \ln a_i$$

and in the crucible:

$$\sum_{i=1}^n X_i d \ln A_i$$

So:

$$d_X P_S = R \sum_{i=1}^{n-2} \left[ \left( \phi_i - \frac{x_i}{x_n} \phi_n \right) - \frac{\phi_{n-1} - \frac{x_{n-1}}{x_n} \phi_n}{x_{n-1} - x_n \frac{x_{n-1}}{x_n}} \left( x_i - x_n \frac{x_i}{x_n} \right) \right] d \ln a_i$$

and in the stationary state:

$$\frac{\left( \frac{\phi_i}{\phi_n} - \frac{x_i}{x_n} \right)}{\left( \frac{\phi_{n-1}}{\phi_n} - \frac{x_{n-1}}{x_n} \right)} = \frac{\left( \frac{x_i}{x_n} - \frac{x_i}{x_r} \right)}{\left( \frac{x_{n-1}}{x_n} - \frac{x_{n-1}}{x_n} \right)} \quad 1 \leq i \leq n-2 .$$

The  $n-2$  conditions are the barycentric rule for the composition of the effusion flow and of the different phases.

When the reaction between the sample and the crucible is slow,

$$d_X P_S = R \sum_{i=1}^{n-1} \left[ (\phi_i - \lambda_i) - (\phi_n - \lambda_n) \frac{x_i}{x_n} \right] d \ln a_i + R \sum_{i=1}^{n-1} (\lambda_i - \lambda_n \frac{x_i}{x_n}) d \ln A_i$$

and the  $2(n-1)$  conditions for stationary state are:

$$\frac{\lambda_i}{\lambda_n} = \frac{x_i}{x_n} \quad 1 \leq i \leq n-1$$

$$\frac{\phi_i - \lambda_i}{\phi_n - \lambda_n} = \frac{x_i}{x_n} \quad 1 \leq i \leq n-1$$

The flow matter which goes from the solid crucible to the sample has the same composition as the solid crucible. The composition of the sample is constant and equal to the difference of entering and escaping flows.

In the two cases, fast or slow reactions, the composition of the fluxes are different for the two phases (sample and crucible), and the steady state is not a "congruent effusion."

### C. Homogeneous systems with effusion and diffusion competitive flows

If we choose to integrate along flux tubes for the diffusion through the cell walls,

$$P_S = -\frac{1}{T} \int_0^L \sum_{\text{tubes}} \sum_{i=1}^{n-1} (J_i - J_n \frac{x_i}{x_n}) \text{grad } \mu_i \, d\ell$$

The quantities  $J_i$  and  $J_n$  are constant along the tubes, the molar fractions are those in the walls, depending of the coordinate  $\ell$  as well as the  $\text{grad } \mu_i = RT \, d \ln A_i$ ;  $A_i$  is the activity in the walls. So when coupling with effusion, the derivative of the entropy production cannot be obtained if the diffusion process is not known, because the integration is not possible. But, at the "whole congruency," one can write the relation:

$$\frac{J_i + \phi_i}{J_j + \phi_j} = \frac{x_i}{x_j}$$

In this relation, the boundary conditions (inner cell, oven, etc.) may be solved for each device. Then, each cell has its "own whole congruency." The effusion is no longer congruent.

## CHARACTERIZATION OF HIGH TEMPERATURE VAPORS BY ANGULAR DISTRIBUTION MASS SPECTROMETRY

Robert T. Grimley and James A. Forsman  
Department of Chemistry  
Purdue University  
W. Lafayette, IN 47907

### 1. Introduction

During the past two decades the mass spectrometer has become the most frequently used tool in the quantitative investigation of high temperature vapor systems. Most of the techniques and procedures used in the early stages of development of the mass spectrometric method continue to be employed. While earlier existing techniques have been improved, newer and more powerful methods have been developed.

If one could develop a successful mass spectrometric technique capable of the characterization of a vapor system, it would involve determination of (a) the types of vapor species and (b) the amounts of each species present in the vapor phase. The process of characterization can be divided quite arbitrarily into three steps:

- (a) identification of the ionic species in the mass spectrum,
- (b) identification of the vapor species from the mass spectrum, and
- (c) determination of the amount of each species present in the vapor phase.

The latter two steps constitute the problem areas in the characterization process. Unfortunately, one frequently finds great concern with the problems of converting ion intensities into partial pressures for systems in which the neutral species and the fragmentation processes have not been identified. The purpose of this paper is to consider the methodology by which the identities of the neutral vapor species are obtained from mass spectral data. The cross-section problem (that of converting ion intensities into partial pressures) will not be considered.

### 2. Conventional Methods

The identification process involves the association of each ion in the mass spectrum with one or more of the neutral vapor species which evaporate from the condensed phase. While several ionization methods are feasible, electron impact ionization has been used in high temperature mass spectrometry almost to the exclusion of other methods. Photoionization has been used sparingly, but it represents a more difficult experimental technique than electron bombardment.

The established or conventional methods which have been employed to determine the identity of the neutral vapor species include:

- (a) ionization efficiency curves,
- (b) thermodynamic methods, and
- (c) modulated beam techniques.

The two parameters of ionization efficiency curves which have been used in species identification are (a) the appearance potential and (b) the shape of the ionization efficiency curve. The use of these parameters has been described in previous reviews [1-3]<sup>1</sup>.

Thermodynamic methods encompass a group of approaches which employ the thermodynamic properties of the system. The most useful of these involves the interpretation of ion intensity data or ratios as a function of temperature. If several ionic species are produced from one neutral vapor species, the  $\ln I^+T$  plot for each of these ions should yield the same value for the heat of vaporization. This interpretation, however, may be complicated by several factors. First, the possibility exists that two or more species in a system may have experimentally indistinguishable heats of vaporization. In this event both ions could be interpreted as arising from one neutral species. The possibility also exists that an ionic species may be formed from more than one neutral vapor species. Since the heat of vaporization for the multisource ion would be different than the values of the contributing neutrals, the ion could be attributed to a separate vapor species. An assumption normally involved in the application of thermodynamic methods is that the ionization cross-section is independent of temperature. The presence of a temperature dependent process can lead to erroneous conclusions regarding the gas phase composition.

Numerous other thermodynamically-based procedures have been reported. Many are specific to one system and, therefore, lack generality of application.

Modulated beam techniques have been used for signal enhancement but only occasionally has species identification been attempted [4].

A review of the literature on high temperature mass spectrometry shows that species identification by the conventional techniques is often more guesswork than science. In few cases have the fragmentation contributions been determined with any degree of accuracy. The flow characteristics of molecules through non-ideal orifices have provided us with a newer and somewhat more powerful technique in the angular distribution method.

### 3. Angular Distribution Method

#### 3.1 Introduction

According to the kinetic theory of gases, the ratio of the number of molecules of a given type which pass through an ideal orifice at an angle  $\theta$  to the orifice normal to those which pass through in the direction of the orifice normal is equal to  $\cos \theta$ . The variation of the molecular flux with the effusion angle is commonly referred to as the angular or spatial distribution. The basic Knudsen equation which relates the rate of mass loss to the vapor pressure assumes that vapor transport occurs through an ideal orifice. Real orifices

---

<sup>1</sup>Figures in brackets indicate the literature references at the end of this paper.



are of finite length and, therefore, non-ideal; most experimental orifices are of cylindrical geometry. The theoretical treatment by Clausing of molecular flow through cylindrical orifices predicts that the angular distribution is a function of the orifice geometry only. The validity of these results has in the past been accepted and continues at present to be accepted in many quarters. However, the first mass spectrometric angular distribution measurements reported by Grimley and Muenow [5] over a decade ago clearly indicated the inadequacy of the Clausing theory [6]. It is the failure of real systems to follow Clausing theory that interests us.

There are several aspects of mass spectrometrically determined angular distribution data which one might consider. These include:

- (a) the experimental determination of transmission probabilities and the relationship to the quantitative determination of thermodynamic properties,
- (b) the use of experimental data to test possible theoretical models of flow through non-ideal orifices,
- (c) the use of angular distribution data in the identification of the neutral vapor species present in complex systems, and
- (d) the determination of ion intensity contributions resulting from fragmentation in the ion source of the mass spectrometer.

The latter two aspects are important in the characterization of the vapor phase and will be considered here.

The basic assumption of angular distribution mass spectrometry (ADMS) is that, within a given system, the angular distribution is unique for each vapor species effusing from a non-ideal orifice. The basic data required in angular distribution measurements include:

(a) the polar angle  $\theta$  which is the angle between the position of the detector and the normal to the plane of the orifice, (b) the Knudsen cell temperature  $T$ , and (c) the ion beam intensity  $I_k^+(T, \theta)$  for a given ionic species  $k$  as a function of the temperature and detector angle. The beam intensities are normalized to the ion intensity at  $\theta = 0$  by taking the ratio of the intensity at each angle  $\theta$  to the intensity at  $\theta = 0^\circ$ . The relative intensities for a given temperature  $T$ ,  $D_k(T, \theta) = I_k^+(T, \theta)/I_k^+(T, 0)$ , are then plotted as a function of the angle  $\theta$ , and the resultant plots are referred to as normalized angular distribution or AD curves.

## 3.2 Experimental

### 3.2.1 Rotary cell assembly

The experimental determination of the angular distribution of the molecular flux requires either (a) a fixed molecular beam source with a movable detector or (b) a movable molecular beam source with a fixed detector. In this work the detector was a  $60^\circ$  sector field, 30.5 cm radius-of-curvature direction focusing mass spectrometer. Because of the size of the mass spectrometer, it was necessary that the beam source be movable. The choice of this design configuration was necessitated by the unavailability of small and electronically stable mass spectrometers at the time this work was initiated. Furthermore,

since there was some question as to whether research in this area would prove fruitful, the beam source was designed to operate only up to temperatures of reasonable design convenience ( $\sim 1000^\circ\text{C}$ ). Extension of angular distribution measurements to higher temperatures is experimentally feasible with current technology. The simplest approach would likely involve the use of a fixed beam source and a movable detector.

The movable beam source used in this work has been called the rotary Knudsen cell system to distinguish it from the conventional fixed or static Knudsen cell. The Knudsen cell is capable of angular rotation about an axis contained within the plane and along a diameter of the outer face of the effusion orifice. The most important features of the high temperature rotary cell assembly can be seen in figures 1 and 2. Except where noted, components were made of Inconel 600 or 304 stainless steel.

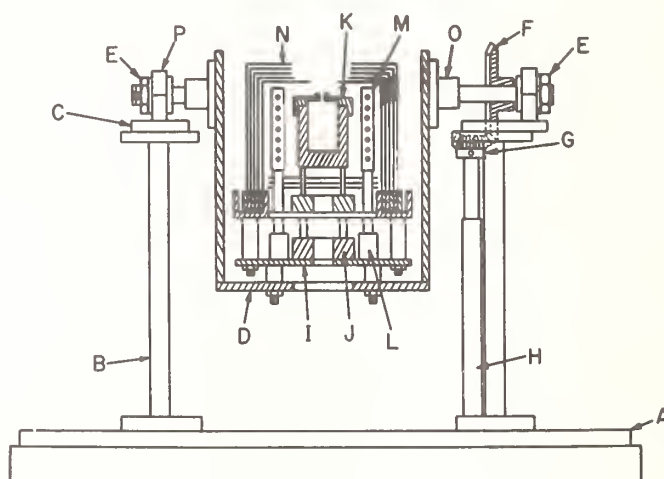


Figure 1. Cross-sectional view of high temperature rotary Knudsen cell.

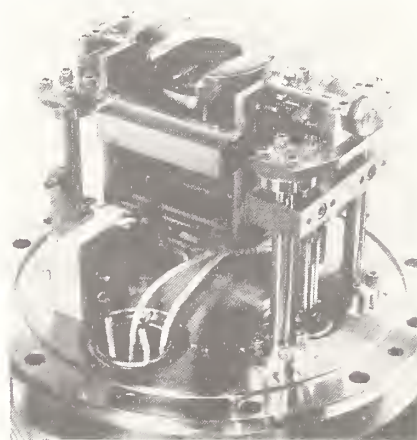


Figure 2. View of the complete rotary unit.

The rotary furnace assembly is mounted on a base plate, A, by means of four vertical support rods, B. The horizontal cross member and pillow block assemblies, C, which are attached to the vertical support rods, form the cradle in which the U-shaped furnace assembly, D, is rotated. To prevent galling of the shafts at high temperatures, each of the pillow blocks is fitted with graphite bushings. The location of the rotary furnace is rigidly maintained by locknuts, E. Rotation of the carriage assembly is accomplished by means of a pinion-bevel gear arrangement, F,G. The pinion gear is attached to a drive shaft, H, which is driven by a modified Ultek model 80-334 high vacuum rotary feedthrough.

The cell and furnace are mounted on the support plate, I. The furnace support rod holders, L, are attached to the support plate, and each support holder positions and holds a Lucalox furnace rod, M. The furnace element consists of a bifilarly wound platinum--10 percent rhodium resistor wire. The heat shields, N, consist of a set of five nested concentric cylinders with slotted caps and are fabricated from 0.051 mm tantalum foil. A variety of cell designs and supports have been used, one of which is shown in the cross-sectional view, J,K. Temperature measurements of the Knudsen cell were made by means of chromel-alumel thermocouples.

### 3.2.2 Measurement reliability checks

A major concern during the design of the apparatus was the possibility that the design of the system might introduce some spurious effect in the measurements. As a result, the design was evaluated with regard to: (1) the reliability of the angle calibration, (2) the effect of the radiation shield configuration, and (3) the effect of temperature gradients on temperature measurement in the Knudsen cell.

#### 3.2.2.1 Angle calibration

It is important that the off-axis angle of the Knudsen cell be known accurately for the various dial settings of the feedthrough. Because of backlash in the gears and also because the motion was transmitted through a rotary bellows seal, the dial indicated cell angle was compared with the actual cell angle. Bench calibration of the angle setting was first carried out. The rotation angle was set on the feedthrough dial and then compared with the true rotation as determined by accurate measurements with a vernier height gage. In order to determine whether angular settings could be reproduced under high vacuum and high temperature conditions, additional tests were performed. No change in the bench calibration values was observed under any test condition. The angle of rotation may be set to an uncertainty of  $\pm 0.1^\circ$ . Since the rotary seal involves a bellows, the possibility that the feedthrough would fail to hold the calibration was considered to be likely. After some slight initial change, periodic recalibration checks revealed a stable calibration curve.

### 3.2.2.2 Heat shield design

Modification of the conventional shield configuration is necessary to prevent the effusing molecular beam from being intercepted by the shields when the cell is rotated to an off-axis angle. The design of the heat shields was finalized after a series of experiments in which the effect of shield configuration on angular distribution curves was determined. The standard shield configuration which has been used for all studies exhibited no scattering contribution when used with a near-ideal orifice geometry ( $L/R = 0.1$ ).

### 3.2.2.3 Thermal gradients

A requirement of high temperature effusion studies is that the effusion cell be maintained under isothermal conditions. The temperature of the effusion cell, assumed to be the condensed phase-vapor phase equilibration temperature, is usually determined by a temperature sensing device located somewhere on the exterior surface of the effusion cell. Typical measuring devices employed in effusion studies are: (a) thermocouples or thermistors with suitable operating temperature ranges, and (b) thermo-optic devices (e.g., optical pyrometer) which are usually employed where thermoelectric devices are unsuitable. Unfortunately, these devices sample only a small portion of the effusion cell and, as such, may not detect thermal gradients which exist in the interior of the cell. In addition, when materials with different thermal conductivities are employed in a single effusion cell, large thermal gradients between cell components may be expected.

Several temperature profile studies have been conducted in this laboratory using a variety of cell materials and cell designs. The thermal gradients introduced by an  $Al_2O_3$  liner and lid fitted into an aluminum (6061-T6) cell body and trap lid were measured in vacuo using two previously calibrated chromel-alumel thermocouples. One of the thermocouples was peened into the base of the aluminum cell and served as the reference temperature for the other thermocouple. The second thermocouple was positioned at various locations on the interior surfaces of the  $Al_2O_3$  liner and lid. A thermal gradient of less than 1 °C was observed within the  $Al_2O_3$  cell cavity. However, a difference of several degrees was observed between the interior of the  $Al_2O_3$  cavity which had a nominal temperature of 110 °C and the reference thermocouple mounted in the base of the aluminum cell.

When an Inconel cell body and lid were employed in a higher temperature study, a 2 °C gradient was observed on the interior surface of the effusion cell. With the effusion cell interior operating at 560 °C, the reference thermocouple (peened into the base of the Inconel cell) measured a temperature approximately 6 °C lower than the nominal interior surface temperature.

### 3.2.3 Special instrumental requirements

Two instrumental factors which most significantly affect the reproducibility and sensitivity of the ADMS technique are: (1) control of the Knudsen cell temperature, and (2)



the stability of the ion current (for a given atomic or molecular beam flux). The variation in the Knudsen cell temperature has been minimized by the use of a specially designed temperature controller. Improved stability of accelerating, focusing, and high voltage power supplies in conjunction with a dc integration system has appreciably reduced the short term instabilities of the measured ion current.

### 3.2.3.1 Temperature control method

The calibrated chromel-alumel thermocouple which is used to measure the nominal Knudsen cell temperature also provides the input signal to a specially designed temperature controller. The choice of thermocouple material allows one to operate the effusion cell from room temperature to 1000 °C. However, it has been observed that vacuum operation will change the calibration of this type of thermocouple resulting presumably from the vaporization of chromium out of solution in the positive element [7]. If the thermocouple is annealed in an inert atmosphere prior to calibration, the rate of vaporization of chromium appears to be reduced. Even with the adverse effect of vacuum operation of a chromel-alumel thermocouple, the large Seebeck coefficient ( $\sim 40 \mu\text{V}/^\circ\text{C}$ ) and the relative chemical inertness of this type of thermocouple makes it more desirable than others.

The input signal from the thermocouple is compared with a high-stability, low noise ( $\pm 0.02 \mu\text{V}/\text{hr}$ ) reference voltage using a low-noise, low-drift ( $0.2 \mu\text{V}/\text{month}$ ) operational amplifier. The reference voltage is manually adjusted to the desired cell temperature. The differential output of the comparator is amplified using a second high stability operational amplifier with a large open loop gain ( $500 \text{ V}/\text{mV}$ ). The output of the second operational amplifier is used to drive silicon pass transistors whose function is to control the supply current to the furnace element from a regulated dc power supply. Temperature control of  $\pm 0.008 \text{ }^\circ\text{C}$  ( $\pm 0.2 \mu\text{V}$ ) of the nominal cell temperature, 75-1000 °C, may be obtained with this type of temperature controller.

If this type of temperature stability is to be realized, one must also take special precautions to minimize stray emf pickup on the thermocouple and extension leads. Several sources of stray emfs typically encountered are: (a) junction potentials resulting from dissimilar metal contact, (b) reference junction fluctuations, and (c) pickup on the extension leads from the reference junction to the temperature controller.

Fluctuations in the input signal to the temperature controller as a result of dissimilar vacuum feedthrough material and/or extension wires from the feedthrough to the reference junction have been observed. To reduce these fluctuations chromel-alumel feedthrough wires and extension leads to the reference junction have been used. In addition, the extension leads are shielded by a copper coaxial sheath which is terminated at the reference junction.

It has been observed in this laboratory that an electromechanical reference junction (Joseph Kaye and Co., Inc., Model RCS4) induces a short term cyclic pulse on the input signal to the temperature controller. Modification of this ice point reference standard could only reduce the cycle to  $\pm 3 \mu\text{V}/\text{min}$ . Since this was unsatisfactory, a carefully prepared



ice-water reference was employed whose stability was better than the noise band of the emf measurement device ( $\pm 0.2 \mu\text{V}$ ). The reference junction was maintained at  $0^\circ\text{C}$  for 10-12 hours without any change in temperature or stability. Mercury filled tubes served to make electrical contact between the chromel-alumel extension leads and the copper conductors used to connect the reference junction to the temperature controller.

Coaxial cable (RG-59/U) was used as the copper extension leads which connected the reference junction to the temperature controller. The braided shield of the coaxial cable was terminated on one end by the chromel-alumel protective sheath and on the other end by the temperature controller's earth ground. In addition, the coaxial wire was isolated from other conductors by an aluminum conduit system.

#### 3.2.3.2 Ion intensity measurements

Intensity data were collected using a 16-stage Cu-Be electron multiplier (non-activated) as the detector. The output current of the electron multiplier ( $10^{-15}$  -  $3 \times 10^{-5}$  amperes) is converted to a voltage by a 640 Keithley vibrating capacitor electrometer in series with a 399 Keithley isolating amplifier. Stability of the electrometer is better than  $5 \times 10^{-17}$  amperes/day with non-cumulative long term drift. The output of the isolating amplifier is simultaneously fed to a strip chart recorder (for monitoring purposes) and to a VFC (voltage to frequency converter). The VFC is a Hewlett-Packard model 2212-A with a stability of better than 0.02 percent FS on all ranges. The output of the VFC is measured with a Mech-Tronics Nuclear 715 Dual Scaler. One scaler is used as a preset time base and the other scaler functions as a frequency counter. The maximum counting rate of the scaler is 20 MHz with an accuracy of  $\pm 1$  count.

The VFC and dual scaler function as a dc integrator with a variable time base. By varying the integration times it is possible to maintain approximately the same average deviation for a wide variety of peak intensities and signal to noise ratios.

### 3.3 Factors affecting angular distribution curves

Many different shapes of angular distribution (AD) curves are observed. The different shapes of AD curves may be explained using approaches similar to those used in the treatment of the thermodynamic properties of matter. One may choose to approach the explanation of AD curves either from the molecular or phenomenological point of view. The phenomenological approach is most useful in our attempts to use AD curves as a tool in the identification of the vapor species.

Up to the present, six factors affecting AD curves have been identified, and the six factors may be classified into the two general categories of orifice related effects and detector related effects. The orifice related factors include:

- (1) orifice geometry,
- (2) nature of the vapor species,
- (3) temperature, and
- (4) orifice composition.

The detector related factors include:

- (1) ionizing energy and
- (2) detector geometry.

### 3.3.1 Orifice related factors

#### 3.3.1.1 Orifice geometry

The effect of orifice geometry on the AD curves of the KCl vapor system was examined by Grimley, Muenow, and LaRue [8]. All parameters except the orifice geometry were fixed, and the AD curves for cylindrical orifices with length to radius ratios ( $L/R$ ) of 1, 2, 3, and 4 were determined for vapor species of the system as shown in figures 3 and 4. The shapes of the experimental curves were in qualitative agreement with the predictions of the Clausing theory [6] in that the molecular beam became more highly focused as the  $L/R$  ratio of the orifice was increased. This finding is significant in the identification process only when considered in conjunction with other factors.

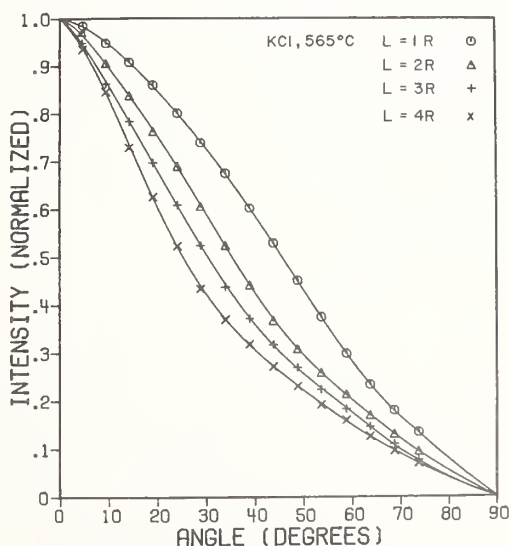


Figure 3. Angular distribution curves for KCl at a cell temperature of 565 °C using orifice geometries of  $L/R = 1, 2, 3$ , and 4.

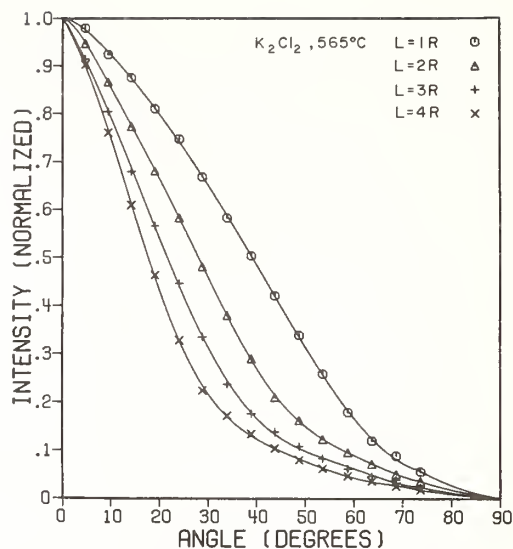


Figure 4. Angular distribution curves for  $K_2Cl_2$  at a cell temperature of 565 °C using orifice geometries of  $L/R = 1, 2, 3$ , and 4.

### 3.3.1.2 Nature of the vapor species

The species effect is probably the most important single factor in the application of AD curves to the identification of the vapor species. By species effect we mean that, for the systems studied to date, each vapor species in a given system has exhibited a unique angular distribution. A typical example is seen in the AD curves for the LiF vapor system shown in figure 5.

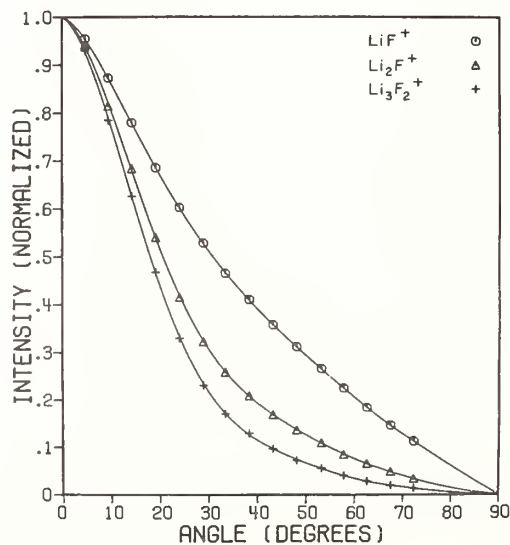


Figure 5. Average angular distribution curves for  $LiF^+$ ,  $Li_2F^+$ , and  $Li_3F_2^+$  (18-75 eV) at a cell temperature of 825 °C.

The choice of the experimental orifice geometry requires the simultaneous consideration of the effects of orifice geometry and the species effect. Measurements of the KCl system [9] have shown that the species effect is minimal for near-ideal orifices and become greater as  $L/R$  increases. However, the peak intensities diminish as  $L/R$  increases. We have, therefore, two competing factors to consider. In most of our studies we have found that an  $L/R = 4$  orifice geometry is a reasonable compromise for data gathering.

#### 3.3.1.3 Temperature effects

The AD curve of each species became more diffuse or less focused as the temperature of the system was increased. It is important, therefore, that the temperature be maintained constant during the investigation of other parameters affecting the shape of the AD curves.

#### 3.3.1.4 Composition of the orifice

In each study an attempt was made to select an orifice material that would not react with the system under investigation. In the investigation of the KCl system [10], several orifice materials were used, and within the accuracy of our measurements no effect of orifice material on the AD curves was observed. However, the AD curves for the species of the Bi vapor system [11] were substantially different for Ta and  $Al_2O_3$  orifices. The AD curves which resulted when an  $Al_2O_3$  orifice was used were clustered and somewhat difficult to distinguish. Similarly, the nature of the orifice material was important in studies of the S and Se vapor systems [12,13].

The goal in the selection of the orifice material is to maximize the separation of the AD curves for the various vapor species. The implication of vapor-surface interaction is obvious. However, our understanding of these processes is so limited as to make impossible any attempt at preselection of the orifice material. The selection of the orifice material, for the moment, is on a trial and error basis.

#### 3.3.2 Detector related factors

##### 3.3.2.1 Ionizing energy

Up to this point we have approached the discussion as if each AD curve determined by mass spectrometric detection were the distribution of a neutral vapor species. In order to use the AD curves for identification of the vapor, it is necessary to consider the processes which occur in the ion source of the mass spectrometer. If an ion, either a parent or fragment, is formed as the result of electron bombardment of only one neutral species, then the AD curve will be representative of that neutral species only. In such a case, changing the energy of the ionizing electrons will have no effect on the observed distribution since a change in the ionization cross-section merely changes the number of ions formed by the same proportion at each detector angle. If two or more vapor species ionize to produce the same ion, however, the observed AD curve will be a superposition of the AD curves of the

contributing vapor species. The occurrence of such a process may be detected by the determination of AD curves at different ionizing energies. It is highly unlikely that the ionization potentials and the ionization efficiency curves of the involved species would be identical. As a result one would expect the AD curve for an ion formed from more than one neutral species to change with the energy of the ionizing electrons. Examples of this phenomenon are numerous [14-16], and some specific examples will be considered shortly.

### 3.3.2.2 Detector geometry

The correct form of the angular distribution is obtained only if measurements are made with a point detector. In this work the source slits define the detector geometry. The effect of a slit detector on the angular distribution has been discussed by Grimley and Wagner [17]. Fortunately, the distortion of the AD curves as a result of non-ideal detector geometry is unimportant insofar as species identification is concerned. In the quantitative analysis of ion intensities from fragmentation, however, some error will result from non-ideal detector geometry.

## 3.4 Application of the ADMS technique

In the determination of the vapor phase composition for a given system, one normally obtains preliminary AD curves for all ionic species observed in the mass spectrum at several ionizing energies. As mentioned in the previous section, if an ionic species is invariant with changes in ionizing energy, then the ion most probably results from the ionization or fragmentation of a single neutral molecule. As an example, consider the LiF vapor system which has four ions of measurable intensity ( $\text{Li}^+$ ,  $\text{LiF}^+$ ,  $\text{Li}_2\text{F}^+$ , and  $\text{Li}_3\text{F}_2^+$ ) [14]. Of these ions only  $\text{LiF}^+$ ,  $\text{Li}_2\text{F}^+$ , and  $\text{Li}_3\text{F}_2^+$  have angular distributions which are invariant with changes in electron bombardment energy. The AD curves and AD data for these ions are shown in figure 5 and in table 1 for several ionizing energies. All data were obtained with a nickel cell and orifice which was maintained at 825 °C. Since each ion has a unique normalized distribution, it is fairly certain that each of the three ions results from different molecules. From the stoichiometry it would appear that the  $\text{LiF}^+$ ,  $\text{Li}_2\text{F}^+$ , and  $\text{Li}_3\text{F}_2^+$  ions result from electron bombardment of LiF,  $\text{Li}_2\text{F}_2$ , and  $\text{Li}_3\text{F}_3$ , respectively.

If an ionic species has multiple precursors, then the resulting AD curve will be a function of the average speeds, ionization cross-sections, and molecular or atomic fluxes. The ion intensity contributions of each of the neutral species to a given ion can be determined using a method developed for the LiF vapor system [14].

The total ion intensity from all sources  $j$  to a given ion  $k$  is given by

$$I_k^+(T, \theta) = \sum_j I_{jk}^+(T, \theta) \quad (1)$$

Index  $k$  refers to the ionic species, and index  $j$  serves to identify the neutral vapor species



Table 1. Normalized angular distribution data for  $\text{LiF}^+$ ,  $\text{Li}_2\text{F}^+$ , and  $\text{Li}_3\text{F}_2^+$ , at 825 °C and ionizing electron energies of 18, 25, 40, and 60 eV.

Angle	Ion: $\text{LiF}^+$				Ion: $\text{Li}_2\text{F}^+$				Ion: $\text{Li}_3\text{F}_2^+$			
	18eV	25eV	40eV	60eV	18eV	25eV	40eV	60eV	18eV	25eV	40eV	60eV
0.0	1.000	1.000	1.000	1.000	1.000	1.000	1.000	1.000	1.000	1.000	1.000	1.000
4.6	0.952	0.961	0.950	0.959	0.949	0.946	0.950	0.948	0.946	0.941	0.947	0.943
9.4	0.871	0.874	0.872	0.876	0.830	0.822	0.827	0.828	0.806	0.800	0.805	0.804
14.2	0.776	0.780	0.780	0.784	0.688	0.682	0.683	0.685	0.636	0.624	0.626	0.624
19.1	0.685	0.683	0.685	0.690	0.549	0.541	0.539	0.536	0.459	0.457	0.460	0.455
24.0	0.606	0.600	0.600	0.606	0.421	0.418	0.413	0.413	0.323	0.325	0.324	0.323
28.9	0.527	0.525	0.532	0.534	0.328	0.325	0.321	0.320	0.232	0.229	0.233	0.230
33.4	0.465	0.463	0.467	0.468	0.264	0.262	0.256	0.256	0.172	0.171	0.170	0.171
38.3	0.409	0.410	0.412	0.414	0.212	0.211	0.207	0.206	0.132	0.129	0.129	0.129
43.2	0.358	0.357	0.360	0.359	0.171	0.172	0.167	0.167	0.098	0.097	0.096	0.096
48.1	0.310	0.310	0.313	0.317	0.139	0.138	0.135	0.135	0.074	0.072	0.074	0.073
53.2	0.266	0.265	0.268	0.267	0.112	0.111	0.107	0.108	0.056	0.056	0.056	0.056
57.8	0.224	0.223	0.225	0.229	0.087	0.087	0.084	0.084	0.042	0.041	0.042	0.041
62.6	0.187	0.185	0.183	0.182	0.067	0.066	0.065	0.065	0.029	0.029	0.030	0.029
67.5	0.148	0.144	0.148	0.148	0.049	0.049	0.048	0.048	0.020	0.020	0.020	0.020
72.3	0.113	0.116	0.114	0.113	0.035	0.034	0.033	0.033	0.014	0.012	0.015	0.014

which form ion k upon ionization. For the selenium system index k runs from 1 to 8 and refers to ions of the form  $\text{Se}_k^+$ . Initially one assumes that all neutral species  $\text{Se}_j$  ( $j = 1-8$ ) are possible. Since the partial ion intensities  $I_{jk}^+(T, \theta)$  cannot be measured directly, an indirect approach is required. The ion intensity fraction  $F_{jk}(T, \theta)$  of the total ion intensity  $I_k^+(T, \theta)$  is defined by

$$F_{jk}(T, \theta) = I_{jk}^+(T, \theta) / I_k^+(T, \theta). \quad (2)$$

To evaluate the  $F_{jk}(T, \theta)$  terms one must make use of the normalized AD data. In general, it is possible to identify the precursor molecules j whose normalized distributions are defined by the equation

$$D_j(T, \theta) = I_{jj}^+(T, \theta) / I_{jj}^+(T, 0). \quad (3)$$

This is most easily done by varying the ionizing energy and determining which ionic species results from ionization of single molecules. From this information the identity of all the neutral vapor species is generally available. The angular distribution for each ionic species k is similarly defined by

$$D_k(T, \theta) = I_k^+(T, \theta) / I_k^+(T, 0). \quad (4)$$

It was demonstrated in the LiF study that equation (1) may be written in the form

$$D_k(T, \theta) = \sum_j f_{jk}(T) D_j(T, \theta). \quad (5)$$

The  $f_{jk}(T)$  coefficients are determined by using a least-squares fitting procedure which utilizes the normalized distribution terms. It has also been demonstrated that a relationship exists between  $f_{jk}(T)$  and  $F_{jk}(T, \theta)$ .

$$F_{jk}(T, 0) = f_{jk}(T) \quad (6)$$

The  $f_{jk}(T)$  coefficients are equal to the ion intensity fractions  $F_{jk}(T, \theta)$  when the mass spectrometer is placed in a position along the orifice normal (i.e.,  $\theta = 0$ ).

The  $\text{Se}_2^+$  ionic species observed in the mass spectrum of the hexagonal selenium vapor system at 210 °C has a spatial distribution which shows an electron ionizing energy dependence. Angular distribution curves for  $\text{Se}_2^+$  formed by electron impact of selenium vapor effusing from an  $\text{Al}_2\text{O}_3$  orifice ( $L/R = 4$ ) are shown in figure 6 for several ionizing energies and a cell temperature of 210 °C. Below 10 eV the  $\text{Se}_2^+$  AD curve becomes invariant with any further decrease in electron ionizing energy. This would indicate that at 10 eV and lower energies the  $\text{Se}_2^+$  ion results from ionization of a single neutral species. From the stoichiometry of the ionic species, the position of the normalized distribution curve at 10 eV,

and the difference in the spatial distribution from those of all other neutral molecules, the major source of  $\text{Se}_2^+$  at 10 eV and below is most probably  $\text{Se}_2$ . The other neutral species which contributes to  $\text{Se}_2^+$  may be determined by a comparison of the  $\text{Se}_5$  spatial distribution (experimentally obtained from the  $\text{Se}_5^+$  normalized distribution) and the  $\text{Se}_2^+$  AD curve. At 35 eV and higher ionizing energies the  $\text{Se}_2^+$  and  $\text{Se}_5^+$  AD curves are virtually identical which would indicate that the predominant source of  $\text{Se}_2^+$  at these energies is  $\text{Se}_5$ .

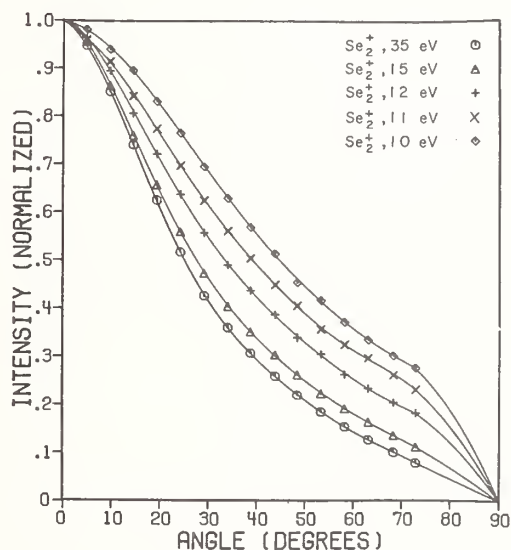


Figure 6. Angular distribution curves for  $\text{Se}_2^+$  at 10, 11, 12, 15, and 35 eV and a cell temperature of 210 °C.

From equations (5) and (6) cited above and the normalized  $\text{Se}_2^+$  (10 eV) and  $\text{Se}_5^+$  AD curves one may determine ion intensity fractions and contributions of  $\text{Se}_2$  and  $\text{Se}_5$  to the  $\text{Se}_2^+$  ion. The ion intensity fractions and ion intensity contributions for  $\text{Se}_2^+$  from  $\text{Se}_2$  and  $\text{Se}_5$  are given in table 2 for several ionizing energies and a Knudsen cell temperature of 210 °C.

The effects of the orifice material on the relative location of the normalized distribution curves for the Se vapor system are shown in figures 7 and 8 for  $\text{Al}_2\text{O}_3$  and Ta orifices, respectively. All data were obtained at a cell temperature of 210 °C. The fragmentation processes were identical for both cell materials. However, the relatively small separation of the AD curves for the various vapor species effusing from a Ta orifice makes a quantitative analysis of the fragmentation processes quite difficult. In the case of the monoclinic sulfur vapor system, use of a nickel cell and orifice makes any type of fragmentation analysis impossible due to near identical AD curves for the various species.

Table 2. Ion intensity fractions<sup>a</sup> and ion intensity contributions (arbitrary units) for  $\text{Se}_2^+$  from  $\text{Se}_2$  and  $\text{Se}_5$ .

Ionizing Energy eV	$F_{22}$ (210°C,0)	$F_{52}$ (210°C,0)	$I_{22}^+$ (210°C,0) $\times 10^{-3}$	$I_{52}^+$ (210°C,0) $\times 10^{-3}$
18	0.076	0.924	25.45	309.42
15	0.167	0.833	22.37	111.57
14	0.230	0.770	19.77	66.19
12	0.500	0.500	12.52	12.52
11	0.769	0.231	8.41	2.53
10	1.000	0.000	5.09	0.00

a. Data were taken at a detector angle of  $\theta = 0$ .

However, when an  $\text{Al}_2\text{O}_3$  (L/R = 4) orifice is employed, distinguishable AD curves for the ionic species may be obtained and used for an analysis of the fragmentation processes and a determination of the vapor phase composition.

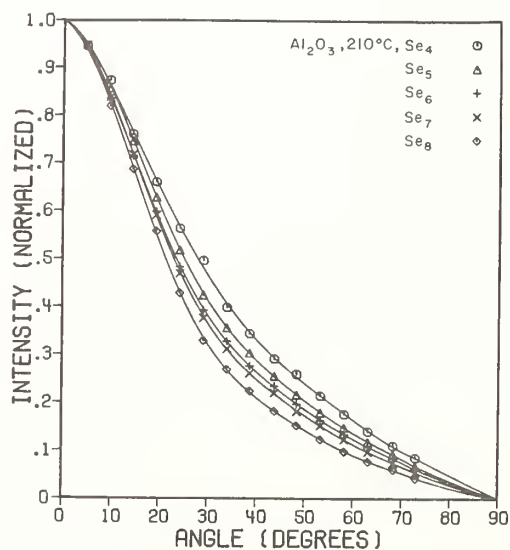


Figure 7. Angular distribution curves for  $\text{Se}_4$ ,  $\text{Se}_5$ ,  $\text{Se}_6$ ,  $\text{Se}_7$ , and  $\text{Se}_8$  at a cell temperature of 210 °C using an  $\text{Al}_2\text{O}_3$  orifice.

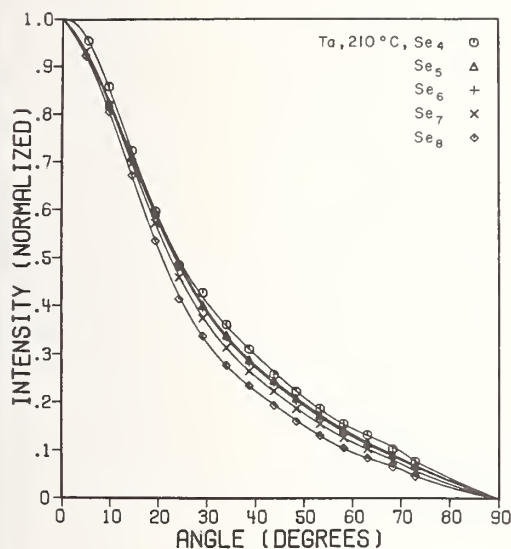


Figure 8. Angular distribution curves for  $\text{Se}_4$ ,  $\text{Se}_5$ ,  $\text{Se}_6$ ,  $\text{Se}_7$ , and  $\text{Se}_8$  at a cell temperature of 210 °C using a Ta orifice.

The effect of cell temperature on the  $D_j(T, \theta)$  and/or  $D_k(T, \theta)$  terms may be ascertained by comparing the normalized distribution curves for a given species at several temperatures and a fixed ionizing energy. The relative change in the position of the AD curve as a function of the cell temperature is determined by the temperature dependence of the molecular fluxes of the precursor molecules, the average speeds, and the ionization cross-sections. A relatively large variation of the AD curve for the  $\text{Se}^+$  ion ( $\text{Al}_2\text{O}_3$  orifice) was observed as a function of temperature and is shown in figure 9. The  $\text{Se}^+$  ionic species results from ionization and fragmentation of  $\text{Se}$ ,  $\text{Se}_2$ , and  $\text{Se}_5$ . A smaller and more typical variation in temperature shifting of the  $\text{S}_8^+$  distribution is shown in figure 10.

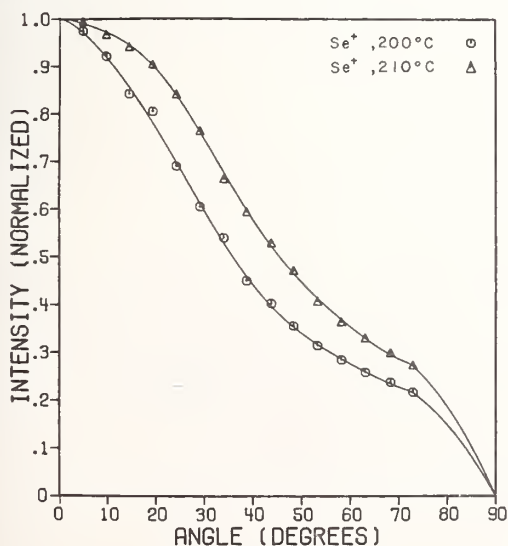


Figure 9. Angular distribution curves for  $\text{Se}^+$  at 10 eV and cell temperatures of 200 and 210 °C.



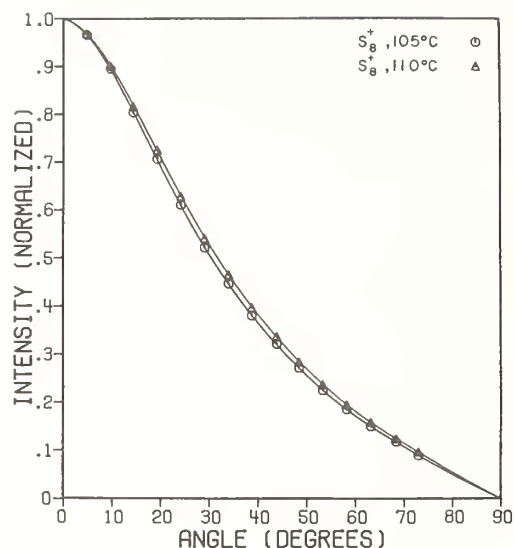


Figure 10. Angular distribution curves for  $S_8^+$  at 75 eV and cell temperatures of 105 and 110 °C.

#### References

- [1] Inghram, M. G. and Drowart, J., Mass spectrometry applied to high temperature chemistry, in Proceedings of International Symposium on High Temperature Technology, Asilomar, CA (McGraw-Hill Book Co., NY, 1959).
- [2] Grimley, R. T., Mass spectrometry, in The Characterization of High Temperature Vapors, J. L. Margrave, ed. (Wiley, NY, 1967).
- [3] Drowart, J. and Goldfinger, P., *Angew. Chem.* **6**, 581 (1967).
- [4] Boyer, M. H., Murad, E., Inami, Y. H., and Hildenbrand, D. L., *Rev. Sci. Instrum.* **39**, 26 (1968).
- [5] Grimley, R. T. and Muenow, D. W., *J. Chem. Phys.* **46**, 2360 (1967).
- [6] Clausing, P., *Ann. Phys. (Leipzig)* **12**, 961 (1932).
- [7] Thermocouple Reference Tables, NBS Monograph 125 (1974).
- [8] Grimley, R. T., Muenow, D. W., and LaRue, J. L., *J. Chem. Phys.* **56**, 490 (1972).
- [9] Grimley, R. T., Wagner, L. C., and Castle, P. M., *J. Phys. Chem.* **79**, 302 (1975).
- [10] Grimley, R. T. and LaRue, J. L., *Ber. Bunsenges. Phys. Chem.* **80**, 167 (1976).
- [11] Wagner, L. C. and Grimley, R. T., *Chem. Phys. Lett.* **29**, 594 (1974).
- [12] Grimley, R. T., DeMercurio, T. A., and Forsman, J. A., to be published.
- [13] Grimley, R. T., Grindstaff, Q. G., and Forsman, J. A., to be published.

- [14] Grimley, R. T., Forsman, J. A., and Grindstaff, Q. G., J. Phys. Chem. 82, 632 (1978).  
 [15] Wagner, L. C. and Grimley, R. T., J. Phys. Chem. 76, 2819 (1972).  
 [16] Wagner, L. C., Robert, P., Grindstaff, Q., and Grimley, R. T., Int. J. Mass Spectrom. Ion Phys. 15, 255 (1974).  
 [17] Grimley, R. T. and Wagner, L. C., J. Chem. Phys. 58, 402 (1973).

## Discussion

Question (Beattie): How does the angular distribution mass spectrometric (ADMS) technique compare with a chopped molecular beam mass spectrometer using time of flight of neutrals and phase sensitive detection? The latter method seems to have been little used for studies of high temperature species. Is the main problem the distribution of velocities?

Response (Grimley): Chopped beam techniques were used some years ago by Don Hildenbrand, he used it on lithium fluoride, and Don can perhaps address you more readily on the subject than I can.

Comment (Hildenbrand): It can be used to assign molecular precursors but is a bit more difficult to use, I think, than this technique (ADMS). It probably should be used more.

Comment (Rosenblatt): In response to Prof. Beattie's question, we (P. Kleinschmidt and G. M. Rosenblatt, Proc. Ann. Conf. Mass Spectrometry 1977) used the modulated beam technique to look at vaporization of  $\text{As}_2(\text{g})$  and  $\text{As}_4(\text{g})$  from  $\text{As}(\text{III})$  single crystals. Langmuir studies are, of course, an example of conditions where the angular distribution technique is not applicable. The phase-sensitive modulated beam technique was very helpful in distinguishing the  $\text{As}_2^+$  ion current arising from  $\text{As}_2(\text{g})$  from possible fragmentation of  $\text{As}_4$  to give  $\text{As}_2^+$  ( $\text{As}_2$  is present in about 1 percent relative to  $\text{As}_4$ ).

(Editor's note): Elsewhere in this volume Bonnell and Hastie, and Plante describe their apparatus for phase sensitive mass spectrometry and citation of earlier work is also given.

Question (Hildenbrand): I wanted to ask what would the lithium ion look like in those lithium fluoride curves? It would seem that it has several contributions perhaps?

Response (Grimley): The  $\text{Li}^+$  ion, yes, has two contributions. One of these is definitely the monomer; the other is a higher polymer, and normally if we shift the electron energies enough we can get the curves to move completely from one to the other. The lithium system however won't move all the way. And we couldn't positively identify whether it (the molecular precursor) was a dimer or a trimer. I suspect it is a dimer in this case, but it could be the trimer. Definitely the monomer is there, because we can shift it all the way to the monomer, but we cannot get it all the way back to the higher species. We can get pushing towards the dimer, but not totally up to it or past it to indicate that there was perhaps trimer contribution.

Question (Hastie): Have you looked at NaCl?

Response (Grimley): We looked at sodium chloride some time ago. It looks the same as KCl. The  $K^+$  and the  $KCl^+$  come from the monomer. The  $K_2Cl^+$  comes from the dimer and the same is true with the sodium chloride system.

(Editor's note): See elsewhere in this volume further discussion along these lines by Bonnell and Hastie.

THE HIGH TEMPERATURE VAPORIZATION AND  
THERMODYNAMICS OF THE TITANIUM OXIDES. XIV.  
RELATIVE IONIZATION CROSS-SECTIONS OF Ti, TiO, AND TiO<sub>2</sub>

Robert I. Sheldon and Paul W. Gilles

Department of Chemistry

University of Kansas

Lawrence, KS 66045

Usually, the largest uncertainties in values for thermodynamic quantities which are obtained from high temperature mass spectrometric vaporization studies arise from uncertainties in the electron impact cross-sections. The purpose of the present work was to measure these relative cross-sections for Ti and TiO which are the principal species over the titanium oxides less rich in oxygen than Ti<sub>2</sub>O<sub>3</sub>.

In recent work [1]<sup>1</sup> the authors reported values for equilibrium pressures of Ti(g) and TiO(g) over stoichiometric titanium monoxide at 1806 K. These pressures were measured in two separate vaporization experiments at the same constant temperature. In the first experiment 0.57 mg of a 10.24-mg sample of stoichiometric titanium monoxide was vaporized in vacuum from a tungsten Knudsen cell. The vapor was collected on a water-cooled quartz cap surrounding the cell, and the total amount of titanium deposited on the cap was determined colorimetrically. The second constant temperature experiment was a mass spectrometer experiment designed to measure the vapor composition over stoichiometric titanium monoxide and thus apportion between Ti and TiO the titanium found in the first experiment. The largest source of uncertainty in the calculation of these pressures arises from uncertainties in the relative electron impact ionization cross-sections of Ti(g) and TiO(g). In the previous work [1], maximum ionization cross-sections for titanium and oxygen reported by Mann [2] were used to calculate relative ionization cross-sections for Ti(g) and TiO(g) assuming the additivity rule of Otvos and Stevenson [3] to be appropriate for TiO(g). Because ionization cross-sections reported by Mann are at different electron energies than used in our previous work and because additivity of elemental cross-sections to give molecular cross-sections is questionable, experiments reported here were undertaken.

Ionization cross-sections of Ti(g) and TiO(g) were measured relative to the ionization cross-section of Ag(g) in two separate mass spectrometric vaporization experiments, one for Ti(g), the other for TiO(g). In the first experiment 1.25 mg of silver and 1.30 mg of titanium were loaded together in a tungsten Knudsen cell and were successively

---

<sup>1</sup>Figures in brackets indicate the literature references at the end of this paper.

vaporized in a Nuclide mass spectrometer. The silver was vaporized first at temperatures ranging from 1346 K to 1772 K, and then the titanium was vaporized at temperatures ranging from 1776 K to 2368 K. In the second experiment 1.79 mg of silver and 0.70 mg  $\text{Ti}_3\text{O}_5$  were vaporized in the mass spectrometer at temperatures ranging from 1319 K to 1402 K and 1953 K to 2009 K, respectively. Intensities of important vapor species were measured at ionizing electron energies of 9.7, 11.7, 13.7, 21.7, 31.7, 41.7, and 71.7 eV. The electron energy was calibrated from the appearance potential of  $\text{Hg}^+$ . The mass spectrometer and samples of silver and titanium, Laboratory designation Ti-6, have been described elsewhere [4]. The  $\text{Ti}_3\text{O}_5$  sample, designated PJH-7, whose composition was  $\text{Ti}_{3.015}\text{O}_5$  as determined by oxygen combustion analysis. This sample was chosen because its composition was closer to  $\text{Ti}_3\text{O}_5$  than any other available.

The calculation of the relative ionization cross-sections is based on a mass balance. The appropriate equations are:

$$\frac{\gamma_{\text{Ti}} \sigma_{\text{Ti}}}{\gamma_{\text{Ag}} \sigma_{\text{Ag}}} = \frac{f_{\text{Ag}}}{f_{\text{Ti}}} \left( \frac{M_{\text{Ti}}}{M_{\text{Ag}}} \right)^{1/2} \frac{(A_{\text{Ti}})_{\text{sf}}}{(A_{\text{Ag}})_{\text{sf}}} \frac{m_{\text{Ag}}}{m_{\text{Ti}}} \quad (1)$$

$$\frac{\gamma_{\text{TiO}} \sigma_{\text{TiO}}}{\gamma_{\text{Ag}} \sigma_{\text{Ag}}} = \frac{f_{\text{Ag}}}{f_{\text{TiO}}} \frac{\sqrt{M_{\text{TiO}}} + 2\sqrt{M_{\text{TiO}_2}}}{\sqrt{M_{\text{Ag}}}} \frac{(A_{\text{TiO}})_{\text{sf}}}{(A_{\text{Ag}})_{\text{sf}}} \frac{m_{\text{Ag}}}{m_{\text{Ti}_3\text{O}_5}} \quad (2)$$

where  $\gamma_{\text{Ti}}$ ,  $\sigma_{\text{Ti}}$ ,  $f_{\text{Ti}}$ ,  $M_{\text{Ti}}$ , and  $m_{\text{Ti}}$  are respectively the electron multiplier gain, ionization cross-section, isotopic fraction of the ion whose intensity was measured, molecular weight and sample mass for titanium. The quantity  $(A_{\text{Ti}})_{\text{sf}}$  is the time integrated product of the titanium intensity and square root of temperature from the "start" to "finish" of the experiment. The other quantities are similarly defined for the indicated species. Equations (1) and (2) are based on the assumption that all the sample is vaporized, that there are no leaks in the cell except the orifice, and that fragmentation of molecules undergoing electron impact ionization is negligible; and further for equation (2) that stoichiometric  $\text{Ti}_3\text{O}_5(\text{s})$  vaporizes congruently to give two molecules of  $\text{TiO}_2(\text{g})$  and one of  $\text{TiO}(\text{g})$ . Transport of oxygen from the cell as tungsten oxides, though perceptible, is negligible.

The measured products of electron multiplier gain and ionization cross-section of  $\text{Ti}(\text{g})$  and  $\text{TiO}(\text{g})$  relative to silver are given in the second and fourth columns in table 1. The uncertainties in these results based on uncertainties in the masses, multiplier gains, and A-values, are estimated to be about 10 percent. The relative ionization cross-sections shown in the third and fifth columns of table 1 have been calculated from the results and the measured electron multiplier gains,  $\gamma_{\text{Ti}} = (4.30 \pm 0.08) \times 10^4$ ,  $\gamma_{\text{TiO}} = (4.34 \pm 0.05) \times 10^4$ ,  $\gamma_{\text{TiO}_2} = (4.77 \pm 0.16) \times 10^4$ , and  $\gamma_{\text{Ag}} = (2.68 \pm 0.02) \times 10^4$ . The relative



ionization cross-section  $\sigma_{\text{TiO}}/\sigma_{\text{Ti}}$  in the final column is obtained by division. The value at 13.7 eV of 1.17 is insignificantly different from the ratio 1.15 used previously [1]; hence, changes in the pressures are insignificant.

Table 1. Relative electron impact cross-sections of Ti and TiO.

Electron Energy (eV)	$\frac{\sigma_{\text{Ti}}}{\sigma_{\text{Ag}}}$	$\frac{\sigma_{\text{Ti}}}{\sigma_{\text{Ag}}}$	$\frac{\sigma_{\text{TiO}}}{\sigma_{\text{Ag}}}$	$\frac{\sigma_{\text{TiO}}}{\sigma_{\text{Ag}}}$	$\frac{\sigma_{\text{TiO}}}{\sigma_{\text{Ti}}}$
9.7	2.32	1.45	2.29	1.41	0.97
11.7	2.09	1.30	2.20	1.36	1.05
13.7	2.00	1.25	2.37	1.46	1.17
21.7	1.58	0.98	2.41	1.49	1.52
31.7	1.30	0.81	2.18	1.35	1.67
41.7	1.19	0.74	2.15	1.33	1.80
71.7	0.86	0.54	2.05	1.27	2.35

The results in table 1 are subject to systematic errors, both for Ti and TiO. Uncertainty about possible interaction with the tungsten crucible leads to an uncertainty in the Ti result, and uncertainty about the exact composition of the  $\text{Ti}_3\text{O}_5$  congruently vaporizing solution leads to uncertainty in the TiO result. The phase diagram for the titanium-tungsten system given by Hansen [5] indicates these two components form a solid solution over the entire temperature range of the experiment. If the cell retains some of the titanium, the results reported for the cross-section of Ti in table 1 will be too low, and the ratio too high.

For the first 265 minutes of the vaporization of titanium the temperature was 1776 K followed by a 379-minute period at 1810 K. Over the first constant temperature period the titanium intensity was fairly constant, decreasing slowly by 10 percent. Over the second constant temperature period the titanium intensity remained constant for about 100 minutes then dropped by a factor of about five. Subsequent elevations of the temperature resulted in a rapid increase in the titanium intensity followed by a slow continuous decrease of the mass spectrometer signal.

If it is assumed the equilibrium pressure of titanium metal was established the first 365 minutes, the mass of titanium lost during this period may be calculated from the equilibrium vapor pressure of the metal which is independent of the ionization cross-section. The calculation indicates 56 percent of the titanium vaporized.

On the other hand this initial 365 minute period represents about 80 percent of the contribution to the integral  $(A_{\text{Ti}})_{\text{sf}}$ , thus indicating that the effect of this systematic error is not more than about 24 percent.

An uncertainty in the TiO results arises from the uncertainty in the composition of the congruently vaporizing solution near  $\text{Ti}_3\text{O}_5$ . At the beginning of the experiment the intensity of TiO rose quickly to a maximum and then fell to a steady value, indicating a possible slight shift to a higher oxygen-to-titanium ratio than the initial  $\text{TiO}_{1.672}$ . If the shift were as large as to give  $\text{TiO}_{1.68}$ , the error in the cross-section would be about four percent.

Only a few measurements of  $\text{TiO}_2^+$  in the experiment with  $\text{Ti}_3\text{O}_5$  were made because the main thrust of the effort was directed toward the  $\text{TiO}^+$  measurements. The  $\text{TiO}_2^+$  measurements at eV are not inconsistent with a cross-section ratio for  $\text{TiO}_2/\text{TiO}$  given previously [4] as 1/2.2. We estimate this ratio to be uncertain by about 50 percent.

#### References

- [1] Sheldon, R. I. and Gilles, P. W., J. Chem. Phys. 66, 3705 (1977).
- [2] Mann, J. B., Proceedings of the International Conference on Mass Spectroscopy, K. Ogata and T. Hagakawa, eds. (University of Tokyo Press, 1970).
- [3] Otvos, J. W. and Stevenson, D. P., J. Amer. Chem. Soc. 78, 546 (1956).
- [4] Gilles, P. W. and Hampson, P. J., J. Chem. Phys. 55, 3712 (1971).
- [5] Hansen, M., Constitution of Binary Alloys, Second edition (McGraw-Hill, New York, 1958).

#### Discussion

Question (Edwards): Paul, what evidence do you have that  $\text{TiO}_2^+$  doesn't fragment to give  $\text{TiO}^+$ ? When you monitored  $\text{TiO}^+$ , and  $\text{Ag}^+$ , the cross-sections you measure would be somewhat affected if  $\text{TiO}^+$  was fragmenting or if  $\text{TiO}_2^+$  was fragmenting to give  $\text{TiO}^+$ .

Response (Gilles): We have some earlier evidence obtained, I believe, by Bruce Kotter. He found that  $\text{TiO}_2$  undergoes insignificant fragmentation in the mass spectrometer, even at 70 eV.

Moderator (Hauge): I believe Joe Berkowitz had some comments that he wanted to make in relation to ionization cross-sections.

Comment (Berkowitz): This is a very old question and it gets re-addressed all the time. I think what I would like to do here is distinguish between the practicality--the necessity of having some phenomenological cross-section to use in high temperature Knudsen cell mass spectrometric studies--and what are the real cross-sections and what they mean in electron impact ionization. There have been apparently all kinds of semi-empirical techniques used to decide what is an appropriate cross-section.

There was an early calculation by Otvos and Stevenson using mean square radii and a rather approximate calculation. People have used polarizabilities of materials to determine what relative cross-sections are. There are even some kinds of theoretical support for the things, but they only go so far. And then there comes the additivity question.

Mann's calculations, I am not sure whether they aren't more accurate values of mean square radii for atoms because, it seems to me, one of the slides this morning did in fact indicate something like that. Somebody else mentioned using for molecules the inter-nuclear distance as a measure of relative cross-sections. These all perhaps have some validity for the case in point, but I think they missed the boat on just what these cross-sections really are.

Another thing that I wanted to put some emphasis on, has been mentioned also, is the influence of fragmentation. At best, when you are talking even semi-empirically about a cross-section, you must be meaning total cross-sections for ionization. But if you ionize a molecule and it breaks up in various pieces, you ought to at least add up all the pieces that are present ---.

Nat'l  
Res  
Lait

Few  
rep

was

PrS

who

re-

four

ear

cial

(S,

bet

300

effe

and

for

dem

Pre

Pre

Fig

## CONGRUENT VAPORIZATION AND THERMODYNAMICS IN THE PRASEODYMIUM-SULFUR SYSTEM

E. David Cater, Barbara H. Mueller<sup>1</sup>, and James A. Fries<sup>2</sup>

Department of Chemistry

The University of Iowa

Iowa City, IA 55242

### 1. Introduction

Many binary inorganic systems have one congruently subliming phase; many have none. Few systems have two congruently subliming compositions. The cerium-sulfur system is reported [1]<sup>3</sup> to be such a system. Our initial interest in the praseodymium-sulfur system was in the thermodynamics of vaporization of PrS(s) and the dissociation energy of PrS(g) in connection with a systematic study of the rare earth monosulfides [2]. However, when it was found that both PrS and Pr<sub>3</sub>S<sub>4</sub> are congruently subliming, as described below, we re-examined some of our earlier unpublished observations on the lanthanum-sulfur system and found evidence that La<sub>3</sub>S<sub>4</sub> may be congruently subliming in addition to LaS, which we had earlier shown to be congruent [3,4].

All the rare earths from La to Tm form MS phases of NaCl-type structure with appreciable ranges of stoichiometry, with the composition MS<sub>1.00</sub> as the upper phase boundary [5,6]. The elements La to Sm have as their next higher sulfide a phase that extends between the limiting compositions M<sub>3</sub>S<sub>4</sub> and M<sub>2</sub>S<sub>3</sub>. The structure of M<sub>3</sub>S<sub>4</sub> is Th<sub>3</sub>P<sub>4</sub>-type BCC; M<sub>2</sub>S<sub>3</sub> has the same structure with ordered metal vacancies [6].

In this paper, we present the thermochemical results of vaporization studies by mass effusion and mass spectrometry of the Pr-S system for the compositions  $0.75 < S/Pr < 1.36$ , and a discussion of congruent and incongruent sublimation in rare earth-sulfur systems. For this latter purpose figure 5 presents schematic pressure-composition phase diagrams demonstrating various possible vaporization modes.

<sup>1</sup>Present address: Los Alamos Scientific Laboratory, Los Alamos, NM 87544

<sup>2</sup>Present address: Northern State College, Aberdeen, SD 57401

<sup>3</sup>Figures in brackets indicate the literature references at the end of this paper.



## 2. Experimental Details

### 2.1 Materials

Experimental samples were prepared by reaction of praseodymium metal filings and powdered sulfur in sealed, evacuated silica-glass tubes at 725 K for periods of several hours or days, followed by annealing in a tungsten crucible in vacuum for several hours above 1700 K. The crucible lid contained a sight hole and the crucible was, in effect, a large Knudsen cell. Various samples were analyzed for sulfur content by acid evolution of  $\text{H}_2\text{S}$  which was absorbed in standard silver nitrate solution, followed by titration of the excess silver. Some samples were analyzed for praseodymium content as well. However, after mass spectrometric vaporization studies demonstrated the absence of appreciable oxygen in the samples, only sulfide analyses were performed. Samples richer in Pr than  $\text{PrS}_{1.00}$  lost Pr on prolonged vaporization in tungsten Knudsen cells, yielding  $\text{PrS}_{1.00 \pm .02}$ . Samples richer in sulfur than  $\text{Pr}_3\text{S}_4$  lost sulfur preferentially on vaporization, giving residues of  $\text{Pr}_3\text{S}_4$  ( $\text{S/Pr} = 1.33$  to  $1.34 \pm 0.02$ ). Mixtures of the  $\text{PrS}$  and  $\text{Pr}_3\text{S}_4$  phases were obtained when equimolar mixtures of Pr and  $\text{Pr}_3\text{S}_4$  were subjected to prolonged heating in a Knudsen cell at 2200-2225 K. However, monophasic  $\text{PrS}$  could be prepared by mixing  $\text{Pr}_3\text{S}_4$  with metal filings and heating in vacuum above 2350 K. In appearance,  $\text{PrS}$  is gold and metallic, while  $\text{Pr}_3\text{S}_4$  is a shiny purple-black color. In residues of partially vaporized mixtures the two phases retained their characteristic appearances and could easily be distinguished visually.

Table 1 lists details of various experimental materials involved in the vaporization studies. The lattice parameters were determined at room temperature by x-ray diffraction in Debye-Scherrer cameras of 114.6 mm diameter, using copper  $K\alpha$  x-rays of wavelengths taken to be  $K\alpha_1 = 1.54050$  and  $K\alpha_2 = 1.54434$  Å. The quoted uncertainty of each lattice parameter is the standard deviation obtained in the least squares extrapolation of the parameter, as calculated from each back reflection line, to  $\theta = 90^\circ$  against the function  $(\cos^2\theta/\theta + \cos^2\theta/\sin\theta)$  [7].

The data of table 1 and the discussions below of the vaporization experiments indicate that both  $\text{PrS}$  and  $\text{Pr}_3\text{S}_4$  are congruently subliming at the stoichiometric compositions, within an estimated uncertainty of  $\pm 0.02$  in the  $\text{S/Pr}$  ratio. Flahaut [6] indicates that the  $\text{PrS}$  phase has composition limits  $0.84 \leq \text{S/Pr} \leq 1.0$ . We did not attempt to determine the lower phase boundary of the  $\text{PrS}$  phase, but the room temperature lattice parameter of a sample of overall composition  $\text{S/Pr} = 0.75$ , whose initial vaporization rate indicated the presence of  $\text{Pr}(1)$  at high temperatures, was significantly smaller than that of congruently subliming  $\text{PrS}$ . The upper phase boundary of  $\text{PrS}$  (annealed with  $\text{Pr}_3\text{S}_4$ ) must be very close to the congruently subliming composition, because their lattice parameters are the same, within one standard deviation. Similarly, the congruently subliming composition of  $\text{Pr}_3\text{S}_4$  is very nearly the same as its lower phase boundary composition, as indicated by their equal lattice parameters. Average lattice parameters with standard deviations are:

PrS (lower phase boundary)	5.7266±0.0010	° A
PrS (congruently subliming)	5.7330±0.0004	° A
PrS (upper phase boundary)	5.7337±0.0012	° A
Pr <sub>3</sub> S <sub>4</sub> (lower phase boundary)	8.5673±0.0004	° A
Pr <sub>3</sub> S <sub>4</sub> (congruently subliming)	8.5668±0.0007	° A .

The melting points, based on various experimental observations, are PrS, above 2421 K and Pr<sub>3</sub>S<sub>4</sub>, 2310 ± 10 K.

## 2.2 Vacuum balance experiments

Rates of effusion in vacuum from a tungsten Knudsen cell were measured as a function of temperature for Pr-S samples in four different phase regions: Pr(l) + PrS(s), PrS(congruent), PrS(s) + Pr<sub>3</sub>S<sub>4</sub>(s), and Pr<sub>3</sub>S<sub>4</sub>(congruent). The inductively heated cell was suspended from one arm of an Ainsworth automatic, recording, semi-micro balance, type RV-AU-2. The apparatus was the same as used in our studies of LaS [3] and YS [8]. The effusion cells, obtained from Phillips Metalonic, were machined from copper-impregnated tungsten, from which residual copper was removed by induction heating to 2400 °C in vacuum. The effusion cells were somewhat porous, so that molten samples diffused through the walls giving excessive rates of weight loss. Experiments showed that with solid samples such effects were negligible compared with effusion through the orifice. The orifice was a right circular cylinder of diameter 0.127±0.001 cm and length 0.251±0.001 cm. The diameter was measured with a traveling microscope and the length with a micrometer, before and after each vaporization run, but no measurable changes in dimensions occurred. Temperatures were measured by means of a calibrated optical pyrometer sighted through a window and prism of known transmissivity into a blackbody hole drilled into the thick bottom of the cell. Auxiliary experiments showed that if the cell were properly located within the induction coil, temperatures so measured were identical within experimental error (± 2 K) with temperatures read in the orifice. However, there were rims around the top and bottom of the cell, through which the suspension wires passed, and these probably kept the ceiling of the cells slightly hotter than the walls due to their induction heating characteristics. The cell suspension had to be clamped during heating because of forces on the effusion cell in the induction field. Weighing was begun immediately upon shutting off the heating power. The time for each weight loss was measured from the time heating power was applied. No correction was applied for heat-up time (approximately one minute), which was short compared with the times at high temperature, most of which were from 30 to 300 minutes. Weights were recorded to ± 0.02 mg, and observed weight losses were from 0.5 to 13 mg, with most in the range 2-4 mg.

From each weight loss an "effective pressure"  $P_E$  was calculated from the Knudsen equation:

$$P_E(\text{atm}) = \frac{w}{K_C A t} \sqrt{2\pi RT/M} = 0.02256 \frac{w}{K_C A t} \sqrt{T/M} \quad (1)$$

where  $w$  is in gm,  $A$  is in  $\text{cm}^2$ ,  $t$  is in s, and the Clausing correction [9]  $K_C = 0.360$  for the orifice used. The molecular weight of PrS,  $M = 172.97$ , was used. Plots of  $\log P_E$  vs  $10^4/T$  are given in figure 1 for each of the series of experiments. Experimental details for the vacuum balance and mass spectrometric experiments are summarized in table 1.

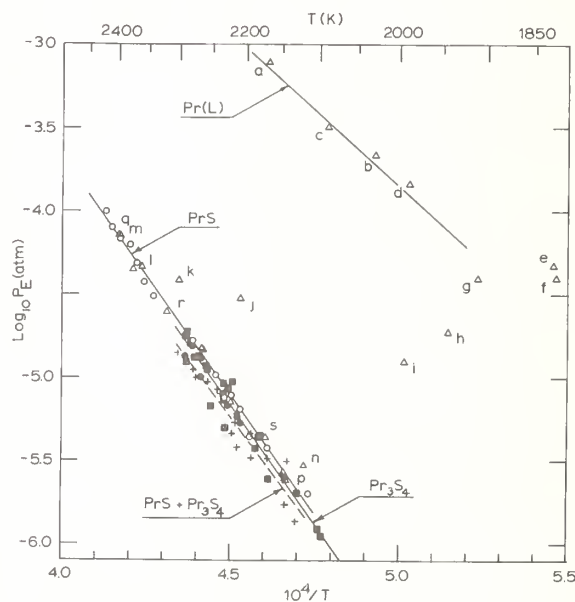


Figure 1. Vacuum balance data. Effective vapor pressure vs temperature for praseodymium-sulfur systems. Data marked  $\Delta$  from sample initially Pr + PrS, mole ratio S/Pr = 0.75 (VB-1). Data points lettered in chronological order; there is no point lettered  $\underline{o}$ . Data marked  $\circ$  from sample initially PrS (VS-7). Data marked  $\blacksquare$  and  $\bullet$  from sample initially  $\text{Pr}_3\text{S}_4$  (VB-5, 6). Data marked  $+$  from a mixture of PrS +  $\text{Pr}_3\text{S}_4$  (VB-8). Line marked Pr(L) is the vapor pressure of liquid Pr from Haberman and Daane, reference [10]. Other lines are from eqs. (2-4).

### 2.3 Vacuum balance results

In the first experimental run, VB-1, the sample was a mixture of metal and PrS phases with overall composition  $\text{S/Pr} = 0.75 \pm 0.02$ . The temperatures were all above the melting point of Pr. Figure 1 shows initially very high effusion rates (points a-g) which give

Table 1. Summary of experimental conditions: evidence for congruent sublimation.

Expt., vac. bal. or mass spec.	Initial Sample			Final Residue				Symbol fig. 1	Comments
	S/Pr ( $\pm 0.02$ )	Phases	Lattice parameter ( $\text{\AA}$ )	Temperature range (K)	% Wt. loss	S/Pr ( $\pm 0.02$ )	Phases	Lattice parameters ( $\text{\AA}$ )	
VB-1	0.75	$\left\{ \begin{array}{l} \text{Pr} \\ \text{PrS} \end{array} \right\}$	5.7261 $\pm 0.0006$	1830-2400	40	1.00	PrS	5.7327 $\pm 0.0013$	Residue used in MS-1H
VB-2	1.325	$\text{Pr}_3\text{S}_4$	8.5690 $\pm 0.0006$	2125-2334	>10	-	-	-	Exceeded M.P.-- Diffusion into wall
VB-3	"	"	"	2079-2144	<10	1.32	$\text{Pr}_3\text{S}_4$	8.5678 $\pm 0.0004$	Electronics problems. Residue used in mass spec.
VB-4	"	"	"	2138-2205	>10	-	$\text{Pr}_3\text{S}_4$	8.5667 $\pm 0.0003$	Vacuum problems
VB-5	"	"	"	2207-2289	20	1.34	$\text{Pr}_3\text{S}_4$	8.5664 $\pm 0.0003$	8 expt. points
VB-6	1.34	$\text{Pr}_3\text{S}_4$	8.5704 $\pm 0.0004$	2095-2308	40	-	-	-	27 expt. points exceeded MP at end of run
VB-7	-	$\left\{ \begin{array}{l} \text{PrS} \\ \text{PrS} \end{array} \right\}$	5.7333 $\pm 0.0005$	2112-2398	75	-	$\left\{ \begin{array}{l} \text{PrS} \\ \text{PrS} \end{array} \right\}$	5.7334 $\pm 0.0005$	22 expt. points
VB-8	-	$\left\{ \begin{array}{l} \text{PrS} \\ \text{Pr}_3\text{S}_4 \end{array} \right\}$	5.7340 $\pm 0.0011$	2129-2303	80	-	$\text{Pr}_3\text{S}_4$	5.7341 $\pm 0.0012$	18 expt. points
MS -1, 2H	1.00	PrS	8.5668 $\pm 0.0004$	1942-2433	-	-	PrS	8.5676 $\pm 0.0005$	Appeared to have melted
			5.7327 $\pm 0.0013$					5.7333 $\pm 0.0005$	

Table 1. (continued)

Expt., vac. bal. or mass spec.	Initial Sample			Final Residue				
	S/Pr ( $\pm 0.02$ )	Phases	Lattice parameter ( $\text{\AA}$ )	Temperature range (K)	% Wt. loss	S/Pr ( $\pm 0.02$ )	Phases	Lattice parameters ( $\text{\AA}$ )
MS -3, 4H	-	PrS	5.7333 $\pm 0.0005$	1980-2362	-	-	PrS	5.7326 $\pm 0.0006$
MS -4-11 F	-	Pr <sub>3</sub> S <sub>4</sub>	8.5695 $\pm 0.0004$	1887-2104	-	1.36	Pr <sub>3</sub> S <sub>4</sub>	8.5664 $\pm 0.0003$
MS -12C	-	{ PrS Pr <sub>3</sub> S <sub>4</sub>	-	1913-2119	-	-	{ PrS Pr <sub>3</sub> S <sub>4</sub>	5.7321 $\pm 0.0004$ 8.5675 $\pm 0.0008$
								Appeared not to have melted
								45 expt. points



pressures in good agreement with the vapor pressure of liquid Pr reported by Habermann and Daane [10]. The pressures decreased rapidly after point g and by point m were indistinguishable from pressures obtained in run VB-7 with monophasic PrS. The total weight loss from a through l corresponded within 2 percent to the excess of Pr over  $\text{PrS}_{1.00}$  in the initial sample. The final residue after VB-1 was monophasic  $\text{PrS}_{1.00}$  as shown by its x-ray pattern and sulfide analysis. Run VB-7, in which 75 percent weight loss occurred, started and ended with a single phase sample of PrS, whose lattice parameter did not change, and which agreed well with that of the residue from VB-1 and those from mass spectrometric residues. We conclude that PrS is congruently subliming at very near the stoichiometric composition.

Experimental runs VB-2 to VB-6 involved monophasic  $\text{Pr}_3\text{S}_4$ . Two different initial samples, of compositions  $\text{S/Pr} = 1.325$  and  $1.34 \pm 0.02$ , were used ( $\text{Pr}_3\text{S}_4$  is  $\text{S/Pr} = 1.333$ ). Two final residues were analyzed after 10 and 20 percent, respectively, of the samples were vaporized. Their compositions were  $\text{S/Pr} = 1.32$  and  $1.34 \pm 0.02$ . Lattice parameters did not change even upon vaporization of up to 80 percent of a sample. Residues from mass spectrometric and vacuum balance runs had identical lattice parameters as listed in table 1. We conclude that  $\text{Pr}_3\text{S}_4$  is also congruently subliming at very near its stoichiometric composition. Data from runs VB-2 to 4 were not used in the final calculations and are not plotted in figure 1. In run VB-2 the sample was melted and diffused into the heavy wall and bottom of the sintered tungsten cell. In VB-3 and 4 the apparatus suffered respectively from vacuum and electronics problems. Near the end of run 6 at 2308 K an abnormally high value of  $P_E$  was obtained when the sample apparently melted and diffused into and through the wall. This point was not used.

In experiment VB-8, the sample as synthesized was a mixture of gold PrS and purple  $\text{Pr}_3\text{S}_4$ . The sample was not chemically analyzed, but both phases were visually present and the x-ray patterns of both were of comparable intensity. After the run the sample was found to have been deposited as a hollow cylinder around the interior wall of the cell. The color next to the wall was the gold of PrS, while the color on the inside of the cylinder was almost entirely the purple of  $\text{Pr}_3\text{S}_4$  with small areas of gold PrS. This was the only experiment in which  $\text{Pr}_3\text{S}_4$  was formed by vapor deposition, and the only VB experiment in which appreciable amounts of material deposited on the walls.

Linear least squares fits to the data gave the following equations with the indicated standard deviations of slopes and intercepts. The least squares lines are shown in figure 1.

For congruently subliming PrS, from VB-7 and points m-x of VB-1:

$$\log P_E(\text{PrS, atm}) = -(28400 \pm 412)/T + (7.68 \pm 0.18). \quad (2)$$

For congruently subliming  $\text{Pr}_3\text{S}_4$ , from VB-5 and 6:

$$\log P_E(\text{Pr}_3\text{S}_4, \text{ atm}) = -(28410 \pm 880)/T + (7.62 \pm 0.40). \quad (3)$$

For the  $\text{PrS-Pr}_3\text{S}_4$  mixture, from VB-8:

$$\log P_E(\text{mix, atm}) = -(26860 \pm 1460)/T + (6.85 \pm 0.74). \quad (4)$$

In discussing the vapor pressures, one should note that  $P_E$ , which is convenient to calculate and plot, is related to the partial pressures of the three vapor species identified by mass spectrometry via the equation

$$P_E = P_{\text{PrS}} + P_{\text{Pr}}(M_{\text{Pr}}/M_{\text{PrS}})^{1/2} + P_{\text{S}}(M_{\text{S}}/M_{\text{PrS}})^{1/2}. \quad (5)$$

The thermodynamically more meaningful total vapor pressure, on the other hand, is

$$P_T = P_{\text{PrS}} + P_{\text{Pr}} + P_{\text{S}}. \quad (6)$$

Thus,  $P_T$  is always greater than  $P_E$ . In the effusion cell, where  $P_{\text{S}}$  is reduced relative to  $P_{\text{Pr}}$  by the stoichiometric requirement of congruent effusion,  $P_T$  is about 16 percent higher than  $P_E$  for congruent  $\text{PrS}$ ; about 22 percent higher for congruent  $\text{Pr}_3\text{S}_4$ .

As seen in figure 1, the  $P_E$ 's of the congruent sulfide phases and of the mixture are nearly equal over the range of measurement. The least squares analysis places them in the order  $\text{PrS} > \text{Pr} > \text{mixture}$ , but the  $P_E$ 's overlap somewhat within the statistical uncertainties. For example, using three standard deviations in  $\log P_E$  as the uncertainty, at 2150 K, the values of the  $P_E$ 's are, respectively

$$\begin{aligned} P_E(\text{PrS}, 2150) &= 3.0 \times 10^{-6} \text{ atm} \pm 10\% \\ P_E(\text{Pr}_3\text{S}_4, 2150) &= 2.6 \times 10^{-6} \text{ atm} \pm 13\% \\ P_E(\text{mix}, 2150) &= 2.3 \times 10^{-6} \text{ atm} \pm 21\%. \end{aligned}$$

Thermodynamically, the total pressure (or  $P_E$ ) over the mixture must be higher than that over the congruent  $\text{PrS}$  and  $\text{Pr}_3\text{S}_4$ , with the limitation, however, that the partial pressure of  $\text{Pr(g)}$  decrease and that of  $\text{S(g)}$  increase in the order  $\text{PrS(congruent)} \rightarrow \text{mixture} \rightarrow \text{Pr}_3\text{S}_4(\text{congruent})$ . Also, the partial pressure of  $\text{PrS(g)}$  must be a maximum over stoichiometric  $\text{PrS(s)}$  [11]. The partial pressures derived later from the mass spectrometric studies indicate that  $P_E(\text{mix})$  cannot be more than about 1.1 or 1.2  $P_E(\text{PrS})$ . Given the difficulties inherent in effusion studies with solid mixtures at high temperatures, the slightly low values of  $P_E(\text{mix})$  are probably not a bad result at all. A further discussion of the pressure-composition diagrams of the  $\text{Pr-S}$  system is included later.

## 2.4 Mass spectrometric measurements

The vaporization of each of the four  $\text{Pr-S}$  phase regions and of a  $\text{PrS/YS}$  solid solution were observed by means of a time-of-flight mass spectrometer. Samples were vaporized from

single crystal tungsten cells heated by electron bombardment. The effusate was continuously ionized [12] by electrons of 12 and 18 eV energy. Temperatures were measured by an optical pyrometer sighted through a calibrated prism and window into the orifice. Details of the instrument and technique have appeared earlier [2,3].

Appearance potential measurements showed that all the observed species,  $\text{Pr}^+$ ,  $\text{S}^+$ ,  $\text{PrS}^+$ ,  $\text{PrO}^+$ ,  $\text{Y}^+$ ,  $\text{YS}^+$ ,  $\text{YO}^+$  were primary, and no evidence of fragmentation was obtained in the range 12-18 eV. However, above 20 eV,  $\text{Pr}^{++}$  ions were observed. The  $\text{PrO}^+$  or  $\text{YO}^+$  signal apparently arose from  $\text{PrO(g)}$  or  $\text{YO(g)}$  and appeared during the initial states of each vaporization. However, they soon decreased to background level in each experiment, showing that oxide was only a surface containment in all the experimental samples. We infer that the vacuum balance data also correspond to vaporization of only  $\text{Pr(g)}$ ,  $\text{S(g)}$ , and  $\text{PrS(g)}$  from the solid samples.

The vaporization processes of the congruent phases are thus



The dissociation equilibrium



is, of course, simultaneously observed. The samples used were both new preparations and residues from vacuum balance or previous mass spectrometric experiments. Because congruent vaporization of  $\text{PrS}$  and  $\text{Pr}_3\text{S}_4$  had been demonstrated in the vacuum balance experiments, less attention was devoted to analysis of the samples in the mass spectrometric studies. Table 1 contains information on those materials for which chemical and x-ray analyses were performed.

#### 2.4.1 $\text{Pr(l)}-\text{PrS(s)}$

The few observations made in the  $\text{Pr(l)}-\text{PrS(s)}$  region showed that the ratio of  $\text{Pr}^+$  to  $\text{PrS}^+$  was many times the ratio over  $\text{PrS(congruent)}$  in accord with the discussion of figure 1.

#### 2.4.2 $\text{Pr}_3\text{S}_4(\text{congruent})$

The most careful measurements were made with  $\text{Pr}_3\text{S}_4(\text{congruent})$ . Ion currents were measured as a function of temperature at 12 eV ionizing energy with a single sample over

several days. In all cases, after each new temperature was set, one-half hour was allowed for equilibration before ion currents were recorded. Data were recorded for long enough times to insure that the ion currents were constant. Precise measurement of  $S^+$  was difficult because of the low ionization efficiency of  $S(g)$  at 12 eV and a residual background signal at  $m/e = 32$ . Data were taken at 45 different temperatures from 1887 to 2104 K of the ion currents,  $I_{Pr}^+$  and  $I_{PrS}^+$ . Only 27 data on  $I_S^+$  were recorded. All are plotted as  $\log I^+T$  vs  $10^4/T$  in figure 2. Least squares fits to the data gave the following equations in which the uncertainties are standard deviations:

$$\log I_{Pr}^+T = -(28422 \pm 269)/T + (15.188 \pm 0.135) \quad (7)$$

$$\log I_{PrS}^+T = -(29181 \pm 261)/T + (15.601 \pm 0.131) \quad (8)$$

$$\log I_S^+T = -(29338 \pm 1217)/T + (14.57 \pm 0.60) \quad (9)$$

The relation of ion current to partial pressure for species  $i$  is  $I_i^+T = X_i P_i$ , where  $X_i$  is the overall sensitivity constant of the mass spectrometer to species  $i$ . These ion current data were converted to partial pressures of  $Pr(g)$ ,  $PrS(g)$ , and  $S(g)$  by use of the vacuum balance data as discussed below. The equilibrium constants for the dissociation of  $PrS(g)$  calculated from these results on  $Pr_3S_4$ (congruent) were also used to calculate the partial pressures over  $PrS$ (congruent) and over the mixture of  $PrS$  and  $Pr_3S_4$ .

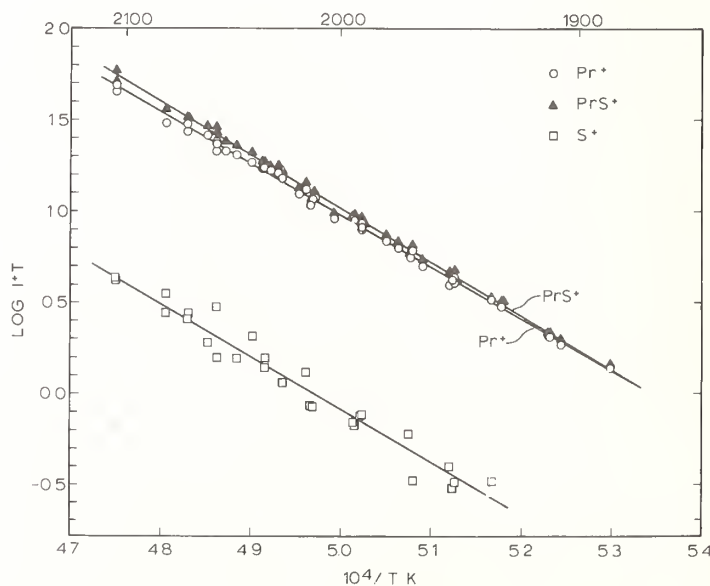


Figure 2. Mass spectrometric results at 12 eV ionizing energy. Plot of  $\log I^+T$  vs  $10^4/T$  for species observed in equilibrium with congruently vaporizing  $Pr_3S_4$ .

### 2.4.3 PrS(congruent)

Several mass spectrometric experiments were performed with monophasic PrS. Ion currents of  $\text{Pr}^+$  and  $\text{PrS}^+$  and a few measurements of  $\text{S}^+$  were made between 1940 and 2406 K. Least squares treatments of  $\log I^+T$  vs  $1/T$  were made and thermodynamic quantities were calculated from them. The slopes of  $\text{Pr}^+$  and  $\text{PrS}^+$  were, respectively, higher and lower than that of  $\text{P}_E$ , but quite poor second law-third law agreement was obtained for the heats of atomization of  $\text{PrS(s)}$  and dissociation of  $\text{PrS(g)}$ , reactions (II) and (V), respectively. The ratio  $I_{\text{Pr}}^+/I_{\text{PrS}}^+$  increased from 1.15 at 2000 K to 1.75 at 2200 K. It was later concluded that the temperature range had been repeatedly traversed too fast for equilibrium to have been attained, and that probably the partial pressures of  $\text{Pr(g)}$  were increasingly too high by up to 30 percent above their equilibrium values as the temperature was increased. This implies that the equilibrium composition of the stoichiometrically subliming phase at high temperatures is  $\text{PrS}_{1-x}$ , where  $x$  is probably quite small and increases with temperature. If true, this behavior is similar to that of europium monosulfide, recently shown by Smoes, et al. [13] to have a ratio  $\text{S/Eu}$  which decreases by about 0.08 percent from 1830 to 2260 K. A very small deviation from the equilibrium composition could lead to higher Pr pressure than the equilibrium values, until the excess Pr were lost, even though PrS pressures would be little affected [13,14].

Therefore, the mass spectrometric data for PrS(congruent) are not further reported here. Instead,  $\text{P}_E(\text{PrS})$  from eq. (2) is apportioned into the partial pressures of PrS, Pr, and S by assuming congruent sublimation at  $\text{S/Pr} = 1.00$  and use of the equilibrium constant for dissociation of  $\text{PrS(g)}$  obtained from the  $\text{Pr}_3\text{S}_4$ (congruent) data. Using the partial pressures so derived and a consistent ratio of sensitivity constants, one can calculate ion current ratios that would correspond to equilibrium mass spectrometric data. These (presumably) equilibrium ratios are essentially equal to the observed ratio at 2000 K (calculated ratio  $I_{\text{Pr}}^+/I_{\text{PrS}}^+ = 1.14$ ) and remained nearly constant with increasing temperature (calculated ratio  $I_{\text{Pr}}^+/I_{\text{PrS}}^+ = 1.10$  at 2200 K). The calculations are detailed below.

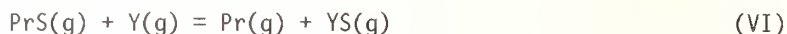
### 2.4.4 PrS- $\text{Pr}_3\text{S}_4$ mixture

Nine measurements of the ion currents due to  $\text{PrS}^+$  and  $\text{Pr}^+$  from a vaporizing mixture of the solids PrS and  $\text{Pr}_3\text{S}_4$  were taken in the temperature range 1913 to 2177 K, with a nominal ionizing energy of 12 eV. The ratio  $I_{\text{Pr}}^+/I_{\text{PrS}}^+$  was constant within experimental precision over the temperature range, the average and its standard deviation being  $I_{\text{Pr}}^+/I_{\text{PrS}}^+ = 1.96 \pm 0.13$ . Unfortunately, the Knudsen cell assembly was removed from the mass spectrometer, which was converted to a different use, before it was realized that this ratio of ion currents is not consistent with congruent sublimation of both phases. Thus, this interesting result was not followed up experimentally, but its implications are discussed in a later section.



## 2.4.5 PrS/YS isomolecular equilibrium study

As an independent check on  $D_0^0(\text{PrS})$ , an equimolar mixture of  $\text{PrS(s)}$  and  $\text{YS(s)}$  was placed in the Knudsen cell of the mass spectrometer and ion currents of  $\text{Pr}^+$ ,  $\text{PrS}^+$ ,  $\text{Y}^+$ , and  $\text{YS}^+$  were measured at 27 temperatures from 1970 to 2280 K. The ion intensities were in the order  $\text{Pr}^+ > \text{PrS}^+ > \text{Y}^+ > \text{YS}^+$  with  $I_{\text{Pr}}^+/I_{\text{YS}}^+$  ratios from 6 to 10. The  $\text{YS(s)}$  sample has been prepared earlier by Steiger [8]. From the measured ion currents, equilibrium constants were calculated for the isomolecular reaction

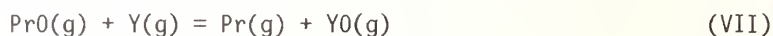


at each temperature. The assumption was made that the ratios of overall detection efficiency for  $\text{PrS}^+/\text{Pr}^+$  and  $\text{YS}^+/\text{Y}^+$  were equal. Thus, the equilibrium constants were defined by:

$$K(\text{PrS/YS}) = I_{\text{YS}}^+ I_{\text{Pr}}^+ / I_{\text{Y}}^+ I_{\text{PrS}}^+ \quad (10)$$

At the end of the experiment, the majority of the sample was a metallic gold solid solution of NaCl-type structure, whose lattice parameter indicated a composition  $\text{Pr}_{0.47}\text{Y}_{0.53}\text{S}$  on the assumption that lattice parameter varies linearly with  $x$  in  $\text{Pr}_{1-x}\text{Y}_x\text{S}$ . A small amount of purple material of complex powder pattern was also present in the residue.

During the initial heating of the sample  $\text{PrO}^+$  and  $\text{YO}^+$  were of comparable intensity to the other species, and five equilibrium constants for the reaction



were measured before the oxide species began to fade rapidly to background level.

Plots of  $\log K$  vs  $10^4/T$  for the  $\text{PrS/YS}$  and  $\text{PrO/YO}$  equilibria appear in figure 3. The first five data for  $\text{PrS/YS}$ , taken simultaneously with the five data for  $\text{PrO/YO}$ , are indicated by filled circles. The presence of oxide apparently did not affect the sulfide equilibrium. Least squares fits give the lines in figure 3 and the following equations:

$$\log K(\text{PrS/YS}) = (730 \pm 140)/T - (0.128 \pm 0.055) \quad (11)$$

$$\log K(\text{PrO/YO}) = - (2970 \pm 650)/T + (0.388 \pm 0.308) \quad (12)$$

## 2.5 Thermochemical calculations

### 2.5.1 $\text{Pr}_3\text{S}_4$ (congruent)

The most nearly complete and (we believe) most reliable measurements in the  $\text{Pr-S}$  system were made with  $\text{Pr}_3\text{S}_4$ (congruent). We have combined the vacuum balance data and mass spectrometric data on  $\text{Pr}_3\text{S}_4$ (congruent) with the assumption of three-to-four stoichiometry

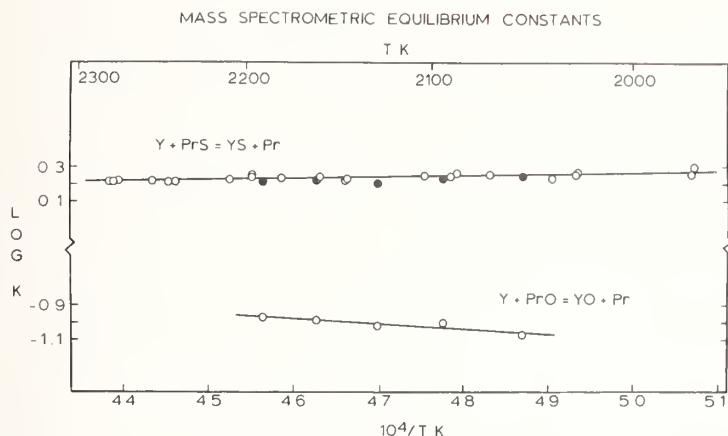


Figure 3. Plot of  $\log K$  vs  $1/T$  for the isomolecular reactions  $Y + \text{PrS} = \text{YS} + \text{Pr}$  and  $Y + \text{PrO} = \text{YO} + \text{Pr}$ . Electron ionizing energy 12 eV.

and the estimated ratio of sensitivity constants  $X_{\text{PrS}}/X_{\text{Pr}} = 0.8$  to calculate the partial pressures and thermodynamics in this system. (This sort of ratio has been justified in earlier papers [2,8,13,15] and agrees with current usage that MX molecules ionize less easily than M atoms.) Then, the equilibrium constants for dissociation of  $\text{PrS(g)}$  calculated from the  $\text{Pr}_3\text{S}_4$ (congruent) results are used with  $P_E$  data to deal with  $\text{PrS(congruent)}$  and the  $\text{PrS/Pr}_3\text{S}_4$  mixtures. Finally, a best value of  $D_0^0(\text{PrS})$  is obtained by considering both the  $\text{Pr}_3\text{S}_4$ (congruent) data and the isomolecular equilibrium data.

Rather than estimate a relative sensitivity constant for  $\text{S(g)}$  at the low electron energies used, we choose to calculate  $P_S$  at 2100 K from the assumption of stoichiometric effusion, which requires that the molar effusion rates  $Z$  of the three vapor species be related by

$$3Z_S = 4Z_{\text{Pr}} + Z_{\text{PrS}} \quad (13)$$

Then, at any temperature the partial pressures will be given by:

$$P_{\text{PrS}} = P_E \left[ A + B(X_{\text{PrS}}/X_{\text{Pr}})(I_{\text{Pr}}^+/I_{\text{PrS}}^+) \right]^{-1} \quad (14)$$

$$P_{\text{Pr}} = P_{\text{PrS}}(I_{\text{Pr}}^+/I_{\text{PrS}}^+)(X_{\text{PrS}}/X_{\text{Pr}}) \quad (15)$$

and

$$P_S = 1/3 P_{\text{PrS}}(M_S/M_{\text{PrS}})^{1/2} + 4/3 P_{\text{Pr}}(M_S/M_{\text{Pr}})^{1/2} \quad (16)$$

In (14) the constants A and B are given by  $A = 1 + M_S/3M_{\text{PrS}}$  and  $B = (M_{\text{Pr}}/M_{\text{PrS}})^{1/2} + 4M_S/3(M_{\text{Pr}}M_{\text{PrS}})^{1/2}$ .

From the above relations and the least squares equations for  $\log IT$  for  $\text{Pr}^+$  and  $\text{PrS}^+$ , the partial pressures tabulated in table 3 were obtained at 2100 K, a temperature at which the vacuum balance and mass spectrometric studies overlapped. In order to make explicit use of the temperature coefficients of eqs. (7) and (8), we normalize those equations to the pressures just calculated and so derive equations for  $\log P_{\text{Pr}}$  and  $\log P_{\text{PrS}}$  vs  $1/T$ . For  $\text{Pr}_3\text{S}_4$ (congruent):

$$\log P_{\text{PrS}}(\text{atm}) = -(29181 \pm 261)/T + (7.709 \pm 0.184) \quad (17)$$

$$\log P_{\text{Pr}}(\text{atm}) = -(28422 \pm 269)/T + (7.199 \pm 0.188) \quad (18)$$

The standard deviations of the intercepts have been increased by three standard deviations of  $\log P_E$  at the normalization temperature, to reflect the absolute uncertainty in pressure. The corresponding equation for sulfur is derived from the above calculated  $P_S$  at 2100 K, the stoichiometry implied by eq. (13), and eqs. (17) and (18) for  $P_{\text{PrS}}$  and  $P_{\text{Pr}}$ . The uncertainties here are estimated. For  $\text{Pr}_3\text{S}_4$ (congruent):

$$\log P_S(\text{atm}) = -(28600 \pm 300) + (7.208 \pm 0.200). \quad (19)$$

Had one derived the equation for  $\log P_S$  vs  $1/T$  from eq. (9) as was done for  $\text{PrS}$  and  $\text{Pr}$  above, the numerical values of  $P_S$  would be within 4 percent of those given by (19), but the uncertainty of the slope would be four times greater. The overall stoichiometry of the effusion process at 2100 K is thus  $\text{Pr}_3\text{S}_4(\text{s}) = 1.68\text{PrS}(\text{g}) + 1.32\text{Pr}(\text{g}) + 2.32\text{S}(\text{g})$ .

Equations (17-19) combine to give the following for the dissociation equilibrium constant of  $\text{PrS}(\text{g})$ :

$$\log K(\text{PrS}) = -(27841 \pm 480)/T + (6.698 \pm 0.263) \quad (20)$$

Second and third law enthalpies and entropies of reaction obtained from these equations are given in table 2. Estimated thermodynamic quantities for  $\text{PrS}(\text{g})$  were based on the rigid-rotor, harmonic oscillator model, with the following estimated molecular parameters. The vibrational frequency,  $443 \text{ cm}^{-1}$ , is 0.570 times that of gaseous  $\text{PrO}$  [16]; the internuclear spacing is  $2.29 \text{ \AA}$ , 80 percent that in solid  $\text{PrS}$ ; and the ground state degeneracy is 4, that of  $\text{PrO}(\text{g})$  [17]. We have justified these estimation methods before [2,18]. For solid  $\text{Pr}_3\text{S}_4$  we have estimated  $S_{298}^\circ = 60.9 \text{ cal K}^{-1} \text{ mol}^{-1}$  by the method of Gronvold and Westrum [19] from lattice contributions and the magnetic susceptibility [20]. An average heat capacity of  $49.0 \text{ cal K}^{-1} \text{ mol}^{-1}$  (7.0 per atom in the formula [21]) was used above 298 K. The heat of sublimation of  $\text{Pr}$  is from Habermann and Daane [22]. Other data for  $\text{Pr}(\text{g})$  were obtained from Feber and Herrick [23] and for sulfur, from the JANAF Tables [24]. Uncertainties listed in table 2 are based on statistical standard deviations and estimated uncertainties in the auxiliary assumptions.

Table 2. Thermodynamics of vaporization of  $\text{Pr}_3\text{S}_4$ (congruent) and  $\text{PrS}$ (congruent). The results for  $\text{Pr}_3\text{S}_4$  are based on mass spectrometric and vacuum balance data. The results for  $\text{PrS}$  are based on vacuum balance data, stoichiometry, and the results for  $\text{Pr}_3\text{S}_4$ . Units of  $\Delta H$  are  $\text{kcal mol}^{-1}$ . Units of  $\Delta S$  are  $\text{cal K}^{-1}\text{mol}^{-1}$ . Gas constant  $R = 1.9873 \text{ cal K}^{-1}\text{mol}^{-1}$ .

Reaction	"Second Law" Results			"Third Law" Results		
	$\Delta H_{2100}^\circ$	$\Delta H_{298}^\circ$	$\Delta H_0^\circ$	$\Delta S_{2100}^\circ$	$\Delta H_{2100}^\circ$	$\Delta S_{2100}^\circ$
IV. $\text{Pr}_3\text{S}_4(\text{s}) = 3\text{Pr}(\text{g}) + 4\text{S}(\text{g})$	914 ± 9	939 ± 21	-	230.8 ± 12.4	885 ± 21	901 ± 37
V. $\text{PrS}(\text{g}) = \text{Pr}(\text{g}) + \text{S}(\text{g})$	127.4 ± 2.2	-	121.6 ± 2.8	30.65 ± 1.51	123.9 ± 4.0	118.1 ± 4.0
$3\text{Pr}(\text{s}) + 4\text{S}(\text{rh}) = \text{Pr}_3\text{S}_4(\text{s})$	-	392 ± 12	-	-	-	400 ± 15
I. $\text{PrS}(\text{s}) = \text{PrS}(\text{g})$	130.8 ± 2.7	-	138.7 ± 3.3	34.17 ± 1.14	130.5 ± 4.0	138.4 ± 5
II. $\text{PrS}(\text{s}) = \text{Pr}(\text{g}) + \text{S}(\text{g})$	258.2 ± 3.9	-	260.2 ± 5.0	64.82 ± 1.61	254.4 ± 4.0	256.4 ± 5
V. $\text{PrS}(\text{g}) = \text{Pr}(\text{g}) + \text{S}(\text{g})$	127.4 ± 4.6	-	-	30.65 ± 5.2	123.9 ± 4.0	-
$\text{Pr}(\text{s}) + \text{S}(\text{rh}) = \text{PrS}(\text{s})$	-	-111 ± 4	-	-	-	-107 ± 4

Auxiliary Data: Estimates for  $\text{PrS}(\text{s})$

$$\begin{aligned}
 C_p &= 13 \text{ cal} \cdot \text{K}^{-1} \text{mol}^{-1} \quad (298-2100 \text{ K}) \\
 S_{298}^\circ &= 19.4 \text{ cal} \cdot \text{K}^{-1} \text{mol}^{-1} \\
 S_{2100}^\circ &= 44.78 \text{ cal} \cdot \text{K}^{-1} \text{mol}^{-1} \\
 H_{2100}^\circ - H_0^\circ &= 26054 \text{ cal} \cdot \text{mol}^{-1} \\
 H_{298}^\circ - H_0^\circ &= 2630 \text{ cal} \cdot \text{mol}^{-1}
 \end{aligned}$$

Estimates for  $\text{Pr}_3\text{S}_4(\text{s})$

$$\begin{aligned}
 C_p &= 49 \text{ cal} \cdot \text{K}^{-1} \text{mol}^{-1} \quad (298-2100 \text{ K}) \\
 S_{298}^\circ &= 60.9 \text{ cal} \cdot \text{K}^{-1} \text{mol}^{-1} \\
 S_{2100}^\circ &= 156.6 \text{ cal} \cdot \text{K}^{-1} \text{mol}^{-1} \\
 H_{2100}^\circ - H_{298}^\circ &= 88200 \text{ cal} \cdot \text{mol}^{-1}
 \end{aligned}$$

The least accurate estimates are those for  $\text{Pr}_3\text{S}_4(\text{s})$ ; accordingly, we accept the second law results as the best values for reactions involving  $\text{Pr}_3\text{S}_4$ . The heat of atomization (reaction IV) is  $\Delta H_{\text{atom},2100}^{\circ}(\text{Pr}_3\text{S}_4) = 914 \pm 9$  kcal/mole or  $305 \pm 3$  kcal/gm-atom Pr. At room temperature these become  $\Delta H_{\text{atom},298}^{\circ}(\text{Pr}_3\text{S}_4) = 939 \pm 21$  kcal/mol or  $313 \pm 7$  kcal/gm-atom Pr. The heat of formation is  $\Delta H_{\text{f},298}^{\circ}(\text{Pr}_3\text{S}_4) = -392 \pm 12$  kcal/mol or  $-131 \pm 4$  kcal/gm-atom Pr. This value agrees well with the only calorimetrically determined heat of formation of a  $\text{M}_3\text{S}_4$  phase, namely  $\text{Ce}_3\text{S}_4$ , for which [25]  $\Delta H_{\text{f},298}^{\circ} = -131.6 \pm 1.0$  kcal/gm-atom Ce.

The dissociation energy of  $\text{PrS}(\text{g})$  from the second law data on  $\text{Pr}_3\text{S}_4(\text{congruent})$  is  $D_{2100}^{\circ}(\text{PrS}) = 127.4 \pm 2.2$  kcal/mol or  $D_0^{\circ}(\text{PrS}) = 121.6 \pm 2.8$  kcal/mol. Third law values, calculated from the partial pressures at 2100 K and the estimated free energy functions or entropies are  $D_{2100}^{\circ}(\text{PrS}) = 123.9 \pm 4.0$  and  $D_0^{\circ}(\text{PrS}) = 118.1 \pm 4.0$  kcal/mol. A best value for  $D_0^{\circ}(\text{PrS})$  is selected below by consideration of both the  $\text{Pr}_3\text{S}_4(\text{congruent})$  data and the  $\text{PrS/YS}$  isomolecular data.

### 2.5.2 $\text{PrS}(\text{congruent})$

For reasons discussed earlier, the experimental mass spectrometric results on  $\text{PrS}(\text{congruent})$  are not used in calculating the thermodynamics of vaporization. Instead, we use the assumption of sublimation at exactly  $S/\text{Pr} = 1.00$ , which requires that in the Knudsen cell  $P_{\text{Pr}}/P_{\text{S}} = (M_{\text{Pr}}/M_{\text{S}})^{1/2}$ ,  $P_{\text{E}}(\text{PrS})$  from eq. (2), the dissociation constant  $K(\text{PrS})$  from eq. (20), and eq. (5) which gives  $P_{\text{E}}$  in terms of the partial pressures, to calculate the partial pressures at 2000 and 2100 K. The following equations are obtained in this way. For  $\text{PrS}(\text{congruent})$ :

$$\log P_{\text{PrS}} = -28584/T + 7.468 \quad (21)$$

$$\log P_{\text{Pr}} = -28212/T + 7.244 \quad (22)$$

$$\log P_{\text{S}} = -28212/T + 6.922 \quad (23)$$

Optimistic estimates of uncertainties are  $\pm 600$  for the slopes and  $\pm 0.250$  for the intercepts. As was mentioned earlier, these equations and the ratio of sensitivity constants  $\chi_{\text{PrS}}/\chi_{\text{Pr}} = 0.80$ , predict ratios of ion currents  $I_{\text{Pr}}^+/I_{\text{PrS}}^+$  which are essentially those observed over  $\text{PrS}(\text{congruent})$  at 2000 K, but which are lower by 30 percent than those observed at 2200 K. The eqs. (20)-(22) derived here were used to obtain the second law enthalpy and entropy changes for  $\text{PrS}(\text{congruent})$  tabulated in table 2. Partial pressures over  $\text{PrS}(\text{congruent})$  at 2100 K are listed in table 3. Note that the relative partial pressures of the three vapor species vary in the correct way from  $\text{PrS}(\text{congruent})$  to  $\text{Pr}_3\text{S}_4(\text{congruent})$ .



Table 3. Isomolecular reactions and dissociation energies of PrS and PrO.

Reaction	T (K)	Method	$\Delta H_T^\circ$ kcal/mol <sup>-1</sup>	$\Delta H_0^\circ$ kcal/mol <sup>-1</sup>	$D_0^\circ(\text{PrS})$ kcal/mol <sup>-1</sup>
PrS + Y = Pr + YS	2150	Second Law	$-3.36 \pm 0.64$	$-1.53 \pm 1.6$	$123.9 \pm 2.8^a$
	1970-2280	Third Law	$-4.29 \pm 1.6$	$-2.46 \pm 0.18$	$122.9 \pm 3.7^a$
PrS = Pr + S	2100	Second Law	$127.4 \pm 2.6^b$	$121.6 \pm 2.6^b$	$121.6 \pm 2.6^b$
	2100	Third Law	$123.9 \pm 4.0^c$	$118.1 \pm 4.0^c$	$118.1 \pm 4.0^c$
Selected "Best" Value of $D_0^\circ(\text{PrS})$					$122.0 \pm 3.0$

Reaction	T (K)	Method	$\Delta H_T^\circ$ kcal/mol <sup>-1</sup>	$\Delta H_0^\circ$ kcal/mol <sup>-1</sup>	$\Delta D_0^\circ(\text{PrO})$ kcal/mol <sup>-1</sup>
PrO + Y = Pr + O	2125	Second Law	$13.6 \pm 3.0$	$11.8 \pm 3.0$	$179.8 \pm 3.4^d$
	2053-2191	Third Law		$10.0 \pm 0.4$	$178.0 \pm 3.0^d$
Selected "Best" Value of $D_0^\circ(\text{PrO})$					$178.9 \pm 2.5$

<sup>a</sup> Based on  $D_0^\circ(\text{YS}) = 125.4 \pm 2.5$  kcal/mol [10].

<sup>b</sup> Uncertainty is standard deviation.

<sup>c</sup> Uncertainty allows for factor of 2 in  $K(\text{diss})$ .

<sup>d</sup> Based on  $D_0^\circ(\text{YO}) = 168.0 \pm 1.5$  kcal/mol [29].

## Auxiliary Data

Molecule	T (K)	$S_T^\circ$	$-(G_T^\circ - H_0^\circ)/T$ (cal K <sup>-1</sup> mol <sup>-1</sup> )	r (Å)	w (cm <sup>-1</sup> )	$g_0$
PrS(g)	2000	78.358	69.715	2.29	443	4
	2100	78.802	70.145			
	2200	79.213	70.544			
YS(g)	2000	75.369	66.751	2.19	483	2
	2100	75.804	67.172			
	2200	76.218	67.573			

This way of partitioning  $P_E(\text{PrS})$  into partial pressures is consistent with the dissociation energy of  $\text{PrS(g)}$  calculated from either the second or third law data for  $\text{Pr}_3\text{S}_4(\text{congruent})$ . It is less consistent with the final value of  $D_0^\circ(\text{PrS})$ , which is a composite value from both the  $\text{Pr}_3\text{S}_4(\text{congruent})$  data and the  $\text{PrS/YS}$  isomolecular equilibrium data. However, this approach yielded better overall consistency among the  $\text{Pr-S}$  data than any other of the several calculations made with various  $D_0^\circ(\text{PrS})$ 's, various sensitivity constant ratios, and other choices of starting points.

Table 2 also lists the various estimated thermodynamic parameters of  $\text{PrS(s)}$  used to obtain the heats and entropies of reaction given there. The average heat capacity  $13 \text{ cal K}^{-1} \text{ mol}^{-1}$  has given good results for other rare earth monosulfides [2,8,18]. The entropy at 298 was estimated by Gronvold and Westrum's method [19] from the magnetic susceptibility [6]. The enthalpy difference  $(H_{298}^\circ - H_0^\circ) = 2630 \text{ cal K}^{-1} \text{ mol}^{-1}$  was estimated from the calorimetric value [25] for  $\text{CeS(s)}$ ,  $2590 \text{ cal K}^{-1} \text{ mol}^{-1}$ .

The reasonable agreement between second and third law heats and entropies for reactions involving  $\text{PrS(s)}$ , and the fact that the partial pressures at 2100 K in table 3 vary in the right direction for all three vapor species relative to their pressures over  $\text{Pr}_3\text{S}_4$ , supports the validity of the calculations.

We suggest as best values the following. For sublimation of  $\text{PrS}$  (reaction I)  $\Delta H_{2100}^\circ = 131 \pm 3 \text{ kcal/mol}$ , and  $\Delta H_0^\circ = 138 \pm 4 \text{ kcal/mol}$ . For atomization of  $\text{PrS}$  (reaction II),  $\Delta H_{2100}^\circ = 256 \pm 4 \text{ kcal/mol}$ , and  $\Delta H_0^\circ = 260 \pm 5 \text{ kcal/mol}$ . The  $\Delta H_0^\circ$ 's have been adjusted to agree with the "best" value of  $D_0^\circ(\text{PrS})$  chosen below. The second law values of the dissociation energy of  $\text{PrS(g)}$  are just the input data from  $\text{Pr}_3\text{S}_4(\text{congruent})$ . The heat of formation may be taken to be  $\Delta H_{f,298}^\circ(\text{PrS,s}) = -110 \pm 4 \text{ kcal/mol}$ . This last is very close to the calorimetrically determined [25] value for  $\text{CeS}$ ,  $-109.1 \pm 1.0 \text{ kcal/mol}$ .

The results of  $\text{PrS}$  in the brief abstract published by Gordienko and Fenochka [28] are in reasonable agreement with ours. They give  $\Delta H_{298}^\circ = 143.2$  for sublimation,  $269.0$  for atomization, and  $125.8$  for dissociation, all in  $\text{kcal/mol}$ , with no uncertainties listed.

These thermochemical results for the  $\text{PrS}$  phase fit nicely into the patterns of periodicity in the rare earth monosulfides which are governed by the energy of the first  $4f \rightarrow 5d$  transition in the metal ion. Cater [27] and Fries and Cater [2] have published recent discussions of this periodicity. The numbers given by Fries and Cater [2] for enthalpies of reaction involving  $\text{PrS}$  were based on a preliminary analysis of the present work and differ by about  $2 \text{ kcal/mol}$  from the present numbers.

### 2.5.3 $\text{PrS} - \text{Pr}_3\text{S}_4$ mixture

A materials balance at 2100 K using  $P_E(\text{mix})$  from eq. (4), the observed ion current ratio,  $I_{\text{Pr}}^+/I_{\text{PrS}}^+ = 1.96$ , and  $K(\text{PrS})$  from eq. (20) leads to the partial pressures given in table 3 for the vapor in equilibrium with the  $\text{PrS} - \text{Pr}_3\text{S}_4$  mixture. The corresponding process in the effusion cell has the stoichiometry:

$$\text{PrS(s)} = 0.16\text{Pr}_3\text{S}_4\text{(s)} + 0.19\text{PrS(g)} + 0.34\text{Pr(g)} + 0.18\text{S(g)}. \quad (24)$$

Stoichiometries calculated at 2000 and 2200 K are very similar. The ion current ratio and eq. (24) imply that  $\text{PrS(s)}$  is not congruently subliming, but dissociates to  $\text{Pr}_3\text{S}_4\text{(s)}$  plus vapor of S/Pr ratio less than 1.0.

#### 2.5.4 Isomolecular equilibria and $D_0^\circ(\text{PrS})$ and $D_0^\circ(\text{PrO})$

The slope and intercept of eq. (11) were converted to second law enthalpy and entropy changes, which are tabulated in table 4. The mean temperature of 2150 K was used for calculation. Use of appropriate thermal functions for  $\text{Pr(g)}$  from Feber and Herrick [23], for  $\text{S(g)}$  from JANAF [24] and for the molecules from the estimates listed in table 4 permitted calculation of the second law  $\Delta H_0^\circ$ . Third law values of  $\Delta H_0^\circ$  were calculated from the individual equilibrium constants by means of the appropriate free energy functions. These third law values are plotted in figure 4 at the temperatures of measurement, and show no apparent drift. Their average is given in table 4. The dissociation energy of  $\text{YS(g)}$ , reported by Steiger and Cater [8] to be  $125.4 \pm 2.5$  kcal/mol, was added to the two values of  $\Delta H_0^\circ$  to obtain the following dissociation energies of  $\text{PrS(g)}$ : second law,  $D_0^\circ(\text{PrS}) = 123.9 \pm 2.8$  and third law,  $D_0^\circ(\text{PrS}) = 122.9 \pm 2.7$  kcal/mol, where estimated errors of the thermal functions have been added to the statistical uncertainties. These numbers are compared to the same quantities from the  $\text{Pr}_3\text{S}_4$ (congruent) results in table 4. The "best" value from these combined data is taken to be  $D_0^\circ(\text{PrS}) = 122.0 \pm 3.0$  kcal/mol. This differs by 2 kcal/mol from the preliminary value from this work included in reference [2].

Table 4. Comparison of partial and total pressures at 2100 K in effusion cells containing  $\text{PrS}(\text{congr.})$ ,  $\text{Pr}_3\text{S}_4(\text{congr.})$  and for the  $\text{PrS} + \text{Pr}_3\text{S}_4$  mixed phases. The last set of pressures is inconsistent with the others as indicated in the text. Pressures are given in atmospheres.

	$\text{PrS}(\text{congruent})$	$\text{Pr}_3\text{S}_4(\text{congruent})$	$\text{PrS} + \text{Pr}_3\text{S}_4$
$P_{\text{PrS}}$	$7.19 \times 10^{-7}$	$6.53 \times 10^{-7}$	$4.44 \times 10^{-7}$
$P_{\text{Pr}}$	$6.44 \times 10^{-7}$	$4.63 \times 10^{-7}$	$6.95 \times 10^{-7}$
$P_{\text{S}}$	$3.07 \times 10^{-7}$	$3.88 \times 10^{-7}$	$1.76 \times 10^{-7}$
$P_{\text{Total}}$	$1.67 \times 10^{-6}$	$1.50 \times 10^{-6}$	$1.32 \times 10^{-6}$
$P_{\text{E}}$	$1.43 \times 10^{-6}$	$1.23 \times 10^{-6}$	$1.15 \times 10^{-6}$

Corresponding numbers for the PrO/YO isomolecular equilibrium are also given in table 4 and plotted in figure 4. Based on  $D_0^{\circ}(\text{YO}) = 168.0 \pm 1.5$  kcal/mol, from Ackermann and Rauh [29], the "best" value for PrO from this work is taken to be  $D_0^{\circ}(\text{PrO}) = 178.9 \pm 2.5$  kcal/mol. This value is in good agreement with  $D_0^{\circ}(\text{PrO}) = 181 \pm 5$  kcal/mol obtained by Ames, et al. [17] from isomolecular equilibria involving TbO and NdO.

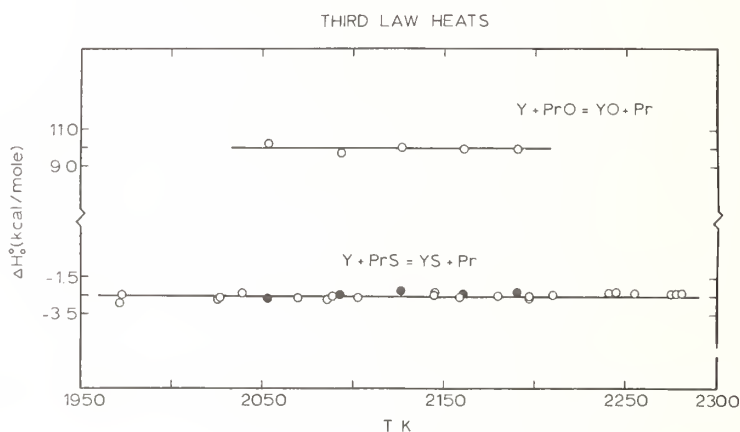


Figure 4. Third law heats of reaction for PrS/YS and PrO/YO isomolecular equilibria. Lines show average values. For  $(\text{Y} + \text{PrS} = \text{YS} + \text{Pr})$ :  $\Delta H_0^{\circ} = 122.9 \pm 3.7$  kcal/mol. For  $(\text{Y} + \text{PrO} = \text{YO} + \text{Pr})$ :  $\Delta H_0^{\circ} = 10.0 \pm 0.4$  kcal/mol.

### 3. Summary and Survey of Vaporization of Rare Earth Sulfides

We now summarize the vaporization behavior of the Pr-S system and other rare earth-sulfur systems by means of figure 5(A-D), which presents schematic pressure-composition diagrams.

#### 3.1 Pr-S

The quantitative vaporization data, the chemical analyses, and the lattice parameters presented above are convincing evidence of congruent sublimation of both PrS and  $\text{Pr}_3\text{S}_4$  as shown schematically in figure 5(A). The phase separation of the residue after VB-8 is also consistent with figure 5(A), as the PrS phase, having the higher  $P_E$ , should have disappeared before  $\text{Pr}_3\text{S}_4$  from the inside surface of the cylinder, by effusion through the orifice. Also consistent is the observation that equimolar mixtures of Pr(s) and  $\text{Pr}_3\text{S}_4(\text{s})$  when heated above 2350 K yielded monophasic PrS(s).

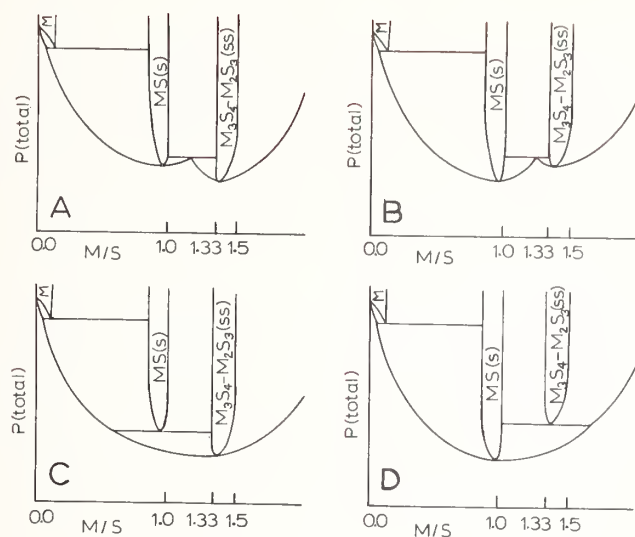


Figure 5. Schematic pressure-composition diagrams for high temperature vaporization of rare-earth sulfur systems. Systems and their corresponding phase diagrams are: La-S: (B) or (D). Ce-S: (B). Pr-S: (A), possibly (C) below 2225 K. Sm-S: (C). Eu-S: possibly (B) or (D). Gd-S: (D) with  $M_2S_{3-x}$  instead of  $M_3S_4$ . Lu-S: (C), with much broader MS region and very narrow  $M_3S_4$  region.

However, equimolar mixtures of  $Pr(s)$  and  $Pr_3S_4(s)$  when heated at 2225 K or below yielded solid  $PrS-Pr_3S_4$  mixtures. In the abbreviated mass spectrometric study of such a mixture in the range 1913 to 2177 K, both phases remained in the residue and the ratio of ion currents  $I_{Pr}^+/I_{PrS}^+$  correspond to the incongruent decomposition of  $PrS(s)$  to give  $Pr_3S_4(s)$  plus effusing vapor of overall composition  $S/Pr = 0.70$ . Both of these observations imply the phase diagram of figure 5(C) rather than 5(A).

Given the nearly equal vapor pressures over  $PrS(s)$ ,  $Pr_3S_4(s)$ , and the mixture, and the slowly varying ratios of  $P_{Pr}$ ,  $P_{PrS}$ , and  $P_S$  across this composition region, and the large contribution of  $PrS(g)$  to the total vapor composition, one may conclude that the free energy-composition diagrams of the components are rather flat across this region. Thus, the different behaviors in figures 5(A-D) are not very different energetically, and, in fact, different diagrams may apply at different temperatures. For the Pr-S system, a transition from incongruent to congruent sublimation of  $PrS(s)$ , i.e., from figure 5(C) to 5(A), may occur between 2225 and 2350 K. The vacuum balance and mass spectrometric results were convincing evidence for congruent behavior, but possible incongruency below 2225 K may have been masked by the repeated equilibration of the samples at the higher temperatures, where much higher effusion rates occur. The results derived for  $PrS(\text{congruent})$



in this paper are believed to be valid, but the possibility of incongruency below 2225 should be kept in mind.

It seems likely that a definitive answer, if based on Knudsen cell studies, would require exhaustively long vaporization times at different temperatures, to insure large enough fractional mass losses for equilibrium to occur. And, of course, the questions of possible compositional or phase changes on quenching from the high temperatures remain.

### 3.2 La-S

The La-S and Ce-S systems appear to behave similarly to the Pr-S system. We have published vaporization data on LaS(congruent) [3,4], for which the equilibrium vapor consists of about 80 percent LaS(g) and 20 percent La(g) + S(g) from 2100 to 2500 K. Figure 6 shows the least squares line for  $\log P_E(\text{LaS})$  vs  $10^4/T$  determined from vacuum balance data (shown as triangles) and mass spectrometric data (not shown here). If this line were plotted on figure 1, it would lie nicely among the PrS-Pr<sub>3</sub>S<sub>4</sub> mixture points. Previously unpublished measurements of  $P_E$  from successive vaporizations of LaS-La<sub>3</sub>S<sub>4</sub> mixtures, determined by weighing a tungsten effusion cell before and after heating in vacuum, are shown as circles. Two new data points from a sample of LaS(congruent) determined in the same way are shown as squares as an indicator of the precision. New mixture samples were introduced before a, e, and m. Filled circles are from vaporizations whose residues contained both phases as identified by their x-ray patterns. Eventually, the La<sub>3</sub>S<sub>4</sub> phase disappeared from the residues. In several cases, crystals of gold LaS grew from the vapor below the lid of the Knudsen cell. The La-S system may thus exhibit congruent sublimation of both LaS and La<sub>3</sub>S<sub>4</sub> according to figure 5(B) or incongruent sublimation according to figure 5(D).

### 3.3 Ce-S

Both CeS and Ce<sub>3</sub>S<sub>4</sub> are reported [1] to be congruently subliming in the cerium-sulfur system. From the very brief report of that work, one finds that  $P_E(\text{Ce}_3\text{S}_4)$  is about twice  $P_E(\text{CeS}) = 7 \times 10^{-7}$  atm at 2150 K, so figure 5(B) would apply. Gilles and Petzel [30] have apparently confirmed this. A thermochemical analysis [2] predicts that the vapor of CeS(congruent) is about 80 percent CeS(g), very similar to LaS(congruent).

### 3.4 Nd-S, Pm-S

Vaporization studies on the Nd-S system, and, of course, the PmS system have not been published.

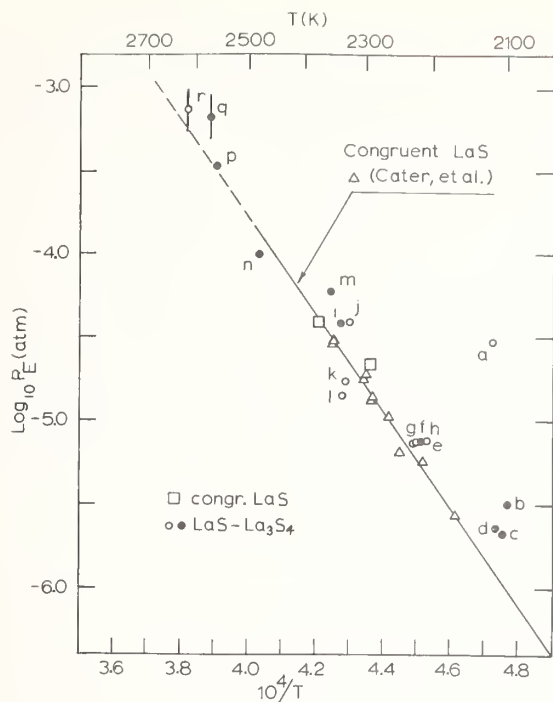


Figure 6. Plot of  $\log_{10} P_E$  vs  $1/T$  for LaS (congruent) and LaS -  $\text{La}_3\text{S}_4$  mixtures. Line is least squares fit for LaS (congruent) from reference [3,4] to vacuum balance data ( $\Delta$ ) and mass spectrometric data (not shown). Data plotted as circles ( $\bullet$  and  $\circ$ ) are from successive vaporization of LaS +  $\text{La}_3\text{S}_4$  mixtures. Squares ( $\square$ ) are new data on LaS (congruent). X-ray diffraction patterns of residues from data marked  $\bullet$ , showed both LaS and  $\text{La}_3\text{S}_4$ ;  $\circ$ , only LaS.

### 3.5 Eu-S

EuS sublimes congruently at near stoichiometric compositions as shown by Smoes, et al. [13], Hariharan and Eick [31], and Kaldis [32]. Because of the low dissociation energy of  $\text{EuS(g)}$ ,  $P_{\text{EuS}}$  makes only a small contribution to the vapor, about 8 percent of  $P_{\text{Eu}}$  at 2150 K according to Smoes, et al. [13].  $\text{Eu}_3\text{S}_4$  loses sulfur to form EuS on sublimation.

### 3.6 Sm-S

SmS is the only incongruently vaporizing monosulfide in the first half of the rare earths. We have found that SmS, and also its solid solutions in which the pnictides are substituted for some of the sulfur [33], lose Sm preferentially to give the  $\text{Sm}_3\text{S}_4$  phase. Others [34,35] have reported similar behavior. However, Gordienko and Fenochka have published an abstract [28] listing heats of sublimation and atomization and partial pressure ratios over presumably congruently subliming SmS at 1600 to 2000 K. Petzel and Greis [34]

were able to prepare stoichiometric SmS by passing the vapor of vaporizing metal over  $\text{Sm}_3\text{S}_4$  in a two-chambered Knudsen cell. It seems most likely that the incongruent behavior of figure 5(c) characterizes the Sm-S system.

### 3.7 Gd-S

Vaporization studies of only the Gd-S and Lu-S systems have been made in the second half of the rare earth sulfides. Near-stoichiometric GdS is congruently subliming [2,36]. No  $\text{Gd}_3\text{S}_4$  composition has been found to be stable, but Wu [36] has shown that  $\gamma\text{-Gd}_2\text{S}_3$  loses sulfur to form GdS (congruent). This corresponds to figure 5(D), with the modification that the  $\text{M}_2\text{S}_3$  phase does not extend down to  $\text{M}_3\text{S}_4$ .

### 3.8 LuS

The Lu-S system is quite different from any of those described so far. Hariharan and Franzen [37] have determined there is no congruent composition in the LuS phase, which extends from  $\text{LuS}_{0.75}$  to  $\text{LuS}_{1.30}$ .  $\text{Lu}_3\text{S}_4$  is congruently subliming, but its structure is not the  $\text{Th}_3\text{P}_4$ -type BCC of the other  $\text{M}_3\text{S}_4$  phases. Instead, it has a superlattice of ordered metal vacancies on the rock salt-type LuS structure. Apparently, it is a line phase whose lattice parameter is discontinuous from the upper phase boundary of  $\text{LuS}_{1+x}$ . An intriguing feature of this system is that  $P_{\text{Lu}}$  and  $P_{\text{S}}$  vary quite widely across the LuS composition range, but  $P_{\text{LuS}}$  is nearly constant. Perhaps this may be taken as illustrative of the broad chemical potential curves that must govern the species in the rare earth-sulfur systems so that more than one congruent phase is found in several of them.

## 4. Conclusion

In conclusion, it is not clear just what are the critical factors which determine the congruent composition in one of these systems, or, indeed whether there will be one or more. The frequently quoted generalization that a stable gaseous molecule of formula AB tends to lead to a congruently subliming solid of the same composition must be applied with care. The most stable rare earth monosulfide molecules are LaS, CeS, PrS, GdS, and LuS. The least stable are EuS, SmS, and YbS. In the first four of these systems the MS phase does sublime congruently. But, so also does the  $\text{M}_3\text{S}_4$  phase for the first three. In the fifth system, only  $\text{M}_3\text{S}_4$  is congruent. EuS(s) is congruently subliming, SmS(s) is not. Statistical mechanical models [38], whose energy parameters are fit to experimental vaporization data (e.g., partial pressures of the elements) can "predict" phase boundary compositions in some systems with some success, even though the assumed defect structures on which they are based may not quite correspond to the best experimental results [14b]. It appears that very accurately measured partial pressures are required for successful calculation of congruently subliming compositions in this way [14b]. Merrick and Franzen

[39] have shown that Madelung energy calculations based on point charge models, combined with configurational entropy calculations, do not predict that  $\text{Sc}_{0.81}\text{S}$  should be the congruently subliming composition in the Sc-S system, although Tuenge and Franzen [40] have found experimentally that it is. Clearly, much work must be done before the nature of congruent sublimation is completely understood.

---

This work was supported in part by the United States Atomic Energy Commission under Contract AT(11-1)-1182 with the University of Iowa. E.D.C. thanks the University of Iowa for support through an Old Gold Summer Fellowship during the writing of this paper. Discussion with Professors H. F. Flanzen and C. E. Meyers aided in the interpretation of the phase behavior.

#### References

- [1] Eastman, E. D., Brewer, L., Bromley, L. A., Gilles, P. W., and Lofgren, N. L., J. Am. Chem. Soc. 72, 2248 (1950).
- [2] Fries, J. A. and Cater, E. D., J. Chem. Phys. 68, 3978 (1978).
- [3] Cater, E. D., Lee, T. E., Johnson, E. W., Rauh, E. G., and Eick, H. A., J. Phys. Chem. 69, 2684 (1965).
- [4] Cater, E. D. and Steiger, R. P., J. Phys. Chem. 72, 2231 (1968).
- [5] Samsonov, G. V., High Temperature Compounds of the Rare Earths with Nonmetals (Consultants Bureau Enterprises, 1965), chap 5.
- [6] Flahaut, J. and Laruelle, P., in Progress in the Science and Technology of the Rare Earths, Vol. 3, L. Eyring, ed. (1969), chap 5.
- [7] Klug, H. P. and Alexander, L. E., X-Ray Diffraction Procedures, 2nd Ed. (Wiley-Interscience, New York, 1974), p. 594.
- [8] Steiger, R. A. and Cater, E. D., High Temp. Sci. 7, 204 (1975).
- [9] Iczkowski, R. P., Margrave, J. L., and Robinson, S. M., J. Phys. Chem. 67, 229 (1963).
- [10] Habermann, C. E. and Daane, A. H., J. Chem. Phys. 41, 2818 (1964).
- [11] See, for example, the treatment of Edwards, R. K., High Temperature Science, 1, 232 (1969).
- [12] Studier, M. H., Rev. Sci. Instrum. 34, 1367 (1963).
- [13] Smoes, S., Drowart, J., and Welter, J. M., J. Chem. Thermodyn. 1977, p. 275.
- [14] See also the numerous papers on partial pressures over  $\text{UO}_{2-x}$ , e.g., Edwards, R. K., et al., High Temp. Sci. 1, 98 (1969); and Winslow, G. H., High Temp. Sci. 7, 81 (1975).
- [15] Rauh, E. G. and Ackermann, R. J., J. Chem. Phys. 60, 1396 (1974).
- [16] Hertzberg, G., Spectra of Diatomic Molecules (D. Van Nostrand and Co., Princeton, NJ, 1950), p. 564.
- [17] Ames, L. L., Walsh, P. N., and White, D., J. Phys. Chem. 71, 2707 (1967).

- [18] Steiger, R. P. and Cater, E. D., High Temp. Sci. 7, 288 (1975).
- [19] Gronvold, F. and Westrum, E. F., Inorg. Chem. 1, 36 (1962).
- [20] Picon, M. and Flahaut, J., C. R. Acad. Sci. Paris, 243, 2074 (1956).
- [21] Kelley, K. K., U. S. Bur. Mines Bull. No. 371 (1934).
- [22] Habermann, C. E. and Daane, A. H., J. Chem. Phys. 41, 2818 (1964).
- [23] Feber, R. C. and Herrick, C. C., Los Alamos Scientific Laboratory Report LA-3184 (1965).
- [24] JANAF Thermochemical Tables, 2nd Ed., D. R. Stull, ed., NSRDS-NBS37 (U.S. Government Printing Office, 1971).
- [25] Montgomery, R. L., U. S. Bur. Mines, Reports of Investigations No. 5468 (1959), recalculated from M. W. Evans, in Chemistry and Metallurgy of Miscellaneous Materials, Thermodynamics, L. L. Quill, ed. (McGraw-Hill, New York, 1950), p. 312.
- [26] King, E. G. and Weller, W. W., U. S. Bur. Mines, Reports of Investigations No. 5485 (1959).
- [27] Cater, E. D., J. Chem. Educ. (1978), in press.
- [28] Gordienko, S. P. and Fenochka, B. V., Russ. J. Phys. Chem. 48, 291 (1974), translated from Zhur. Fiz. Khim. 48, 494 (1974).
- [29] Ackermann, R. J. and Rauh, E. G., J. Chem. Thermodyn. 5, 331 (1973).
- [30] Gilles, P. W. and Petzel, T., unpublished report, University of Kansas, cited in reference [36], p. 5.
- [31] Hariharan, A. V. and Eick, H. A., High Temp. Sci. 3, 123 (1971).
- [32] Kaldis, E., J. Cryst. Growth, 17, 3 (1972).
- [33] Beeken, R. B., Savage, W. R., Schweitzer, J. W., and Cater, E. D., Phys. Rev. B, 17, 1334 (1978).
- [34] Petzel, T. and Greis, O., Z. Anorg. Allg. Chem. 396, 95 (1973).
- [35] Tien, V. V. and Khodadad, P., Bull. Soc. Chim., France, 89, 2888 (1970).
- [36] Wu, R. L. C., Vaporization and Thermodynamics of Rare Earth Sulfides, Ph.D. Thesis, University of Kansas, 1971, available as Wu, R. L. C. and Gilles, P. W., USAEC Report No. C00-1140-200.
- [37] Hariharan, A. V. and Franzen, H. F., current work at Iowa State University, Ames, private communication.
- [38] Anderson, J. S., Proc. Royal Soc. (London) A185, 69 (1946).
- [39] Merrick, J. and Franzen, H. F., current work at Iowa State University, Ames, private communication.
- [40] Tuege, R. T. and Franzen, H. F., J. Chem. Phys. 65, 2400 (1976).

#### Discussion

Comment (Berkowitz): This was such a comprehensive talk that I hesitate to pick minor points for some comment, but in the interest of historical accuracy, there was one point I wanted to make. On the photo-ionization and photoelectron spectroscopy of high temperature vapors, the two are not the same, and photoelectron spectroscopy, in contrast to having had a quiescent period after 1969, really began in about 1972 and has continued to be very active since.



The other point I wanted to make was having to do with ionization cross-sections. I think it is a semantic problem, "the ionization cross section," because people conventionally work at 70 or 75 electron volts ionization energy and they call this, "the ionization cross-section"; and then sometimes they work near the ionization threshold, not the same increment above it, and they sometimes call that, "the ionization cross-section," and neither one is "the ionization cross-section." Unfortunately, it is a complicated business which is slowly beginning to be understood, and it has to even be folded in with something else, namely the fragmentation process for different systems, so that the total ionization cross-section may be one thing, but the cross-section for the species you are looking at is quite another, and the fact that these are so energy dependent and if they could be compared on some comprehensive basis over a large energy range, it would be more meaningful. It is something that needs to be kept in mind.

Moderator (Hastie): Did you want to make any remarks, Dave?

Response (Cater): Yes. I apologize for not making the distinction between photoionization and photoelectron spectroscopy. I did not intend to imply the latter is a dying art, and certainly your comments are well taken about ionization cross-sections being a function of the energy involved. I tried to write the energies down on the numbers I just quoted.

Comment (Gingerich): I want to make an additional comment about ionization cross-sections. I think they should be compared for maximum ionization. We have routinely, in later years, corrected our ion currents to maximum ionization and then you can apply the rules you gave namely that they (the molecular cross-sections) are a little bit less than additivity or something like that (modified Otvos-Stevenson rule). And it is really misleading, like these papers you showed on the uranium oxide, if one really doesn't have in mind the fact that you should compare cross-sections at maximum ionization.

The second comment is also for accuracy, although it is a minor one. You mentioned non-stoichiometry has been considered after 1969, but we did quite a bit of work in the early 1960's on it.

Response (Cater): Well, I agree with both of those statements too. In fact, the pictures I showed for the thorium system were some that were done in 1962, or so, by Ackerman, Thorne and Rauh; but I have no quarrel with you at all.

Moderator (Hastie): I think we are done with the discussion of this particular paper because a lot of these questions will come up again in some of the other papers. I know that Paul Gilles will talk again on this cross-section problem and we will probably want to make some more comments at that time.



VAPOR PRESSURE MEASUREMENTS OF POTASSIUM OVER  $K_2O-SiO_2$  SOLUTIONS BY A  
KNUDSEN EFFUSION, MASS SPECTROMETRIC METHOD

E. R. Plante  
Center for Materials Science  
National Measurement Laboratory  
National Bureau of Standards  
Washington, DC 20234

Measurements of the K pressure over  $K_2O-SiO_2$  solutions were carried out using a modulated beam--quadrupole mass spectrometer. Pressure measurements were made as a function of composition and temperature and covered the composition range 43.9 to 11.9 wt percent  $K_2O$  and the temperature range 1300-1800 K. The composition variable was determined through use of the integrated  $^{39}K$  ion current. In the above composition range, all of the data were well represented by a master equation with a single slope and a composition term in mole fraction squared. At still lower  $K_2O$  content, deviations from the master equation were apparent. The detailed data are presented.

## 1. Introduction

The concept of using MHD to obtain high efficiency combined-cycle energy conversion systems has led to a need for data which can be used to estimate the activity of  $K_2O$  dissolved in coal slag. Although  $K_2O$  is generally only a minor constituent of coal slags, the interaction of slags with the potassium seed required for MHD makes slags containing much larger concentrations of  $K_2O$  of interest. Since most coal slags contain of the order of 50 wt percent  $SiO_2$ , solutions of  $K_2O$  in  $SiO_2$  can serve as a simplified model reference slag.

There are few data in the literature relevant to the activity of  $K_2O$  in  $SiO_2$  solutions. Preston and Turner [1]<sup>1</sup> measured rates of evaporation in air of various  $K_2O-SiO_2$  melts as well as apparent pressures as a function of flow rate by the transpiration method. At the time their measurements were made, it was customary to obtain equilibrium pressures by extrapolation to zero flow rate, but this method has since been shown [2] to lead to pressures which are too high because of diffusion effects. Attempts to derive activity data

<sup>1</sup>Figures in brackets indicate the literature references at the end of this paper.

based in whole or in part on Preston and Turner's rate of evaporation data have been made by Callow [3], Charles [4], and Eliezer, et al. [5]. Charles, and Eliezer, et al., recognized that the enthalpy change based on the rate of vaporization data was not consistent with evaporation of K and  $O_2$  from the melts and concluded that the measurements would be better interpreted in terms of reaction with water vapor to form KOH(g).

While MHD applications require data for very complicated slag solutions which may contain up to six components, the use of a simplified two component solution as a standard may be helpful. The major objective of this paper will therefore be to describe the measurement technique and present the basic data obtained in studies on the evaporation of K and  $O_2$  from  $K_2O-SiO_2$  solutions.

## 2. Description of Mass Spectrometric System

The mass spectrometric system was the same as that previously used and described by Paule [6], but additional description of the system will be made to be in keeping with the emphasis of this volume on methodology.

The quadrupole mass spectrometer was constructed from components manufactured by Extranuclear Corp., Pittsburgh, Pa. The beam modulation system was constructed at NBS from commercially available components and consisted of a Wavetek model 130 function generator, a Bogen model Mo100A amplifier and a Globe Industries model 18A108 synchronous motor equipped with high vacuum bearings, which rotated a 10 toothed wheel to alternately pass or scatter the molecular beam effusing into the ion source from the Knudsen cell. A reference signal dependent on wheel position was generated by an HEI optical switch and fed to the reference circuit of an Ithaco model 391A lock-in amplifier. A small fraction of the neutral vapor species was ionized, focussed by the ion optics, and either transmitted or rejected by the quadrupole lens assembly depending on the mass selected. Molecules originating from the Knudsen cell traversed the mechanical chopping disc and bore a definite phase relationship to the reference signal. The phase angle for maximizing the amplitude was determined from an approximate phase angle by offsetting the selected phase angle by  $90^\circ$ , adjusting the phase control for 0 amplitude, and offsetting again by  $90^\circ$ . This procedure is used because the change in amplitude with phase angle is greatest at  $\phi = 0$ .

The distance from the Knudsen cell to the modulation disc was about 5 cm and from the modulation disc to the ion source was 10 cm. Although this system is theoretically capable of using phase sensitive detection to determine whether ion species are formed by direct ionization or fragmentation of a greater molecular weight precursor, such measurements were not necessary in this work and no attempt was made to use this capability of the modulation system. During the measurements, a constant modulation frequency of about 600 Hz was used.

The vacuum system was constructed from commercially available stainless steel components. Vacua were maintained using two liquid nitrogen trapped, four-inch, oil diffusion pumps. Two 4 inch gate valves allowed the system to be opened to the atmosphere without shutting down the diffusion pumps. The system differed from most mass spectrometric systems in that it did not make use of differential pumping. It was assumed that this arrangement

could help to avoid modulation of signals caused by the flow of background gases from a relatively high pressure Knudsen chamber ( $10^{-7}$  Torr) to a low pressure mass spectrometric chamber ( $10^{-8}$  Torr). However, the differential pumping effect could not be entirely eliminated because the Knudsen cell and furnace assembly were contained in a water-cooled copper chamber which had a high gas conductivity to one pump and lower gas conductivity to the second. In spite of this, pressures as measured by ionization gages which had line of sight connection to the respective regions usually did not differ significantly during experiments and were in the  $10^{-7}$ - $10^{-8}$  Torr range.

Figure 1 shows a schematic of the mass spectrometer system. The quadrupole mass filter (QMF) is mounted about 1-1/2 inches off center on a 6-inch flange in a horizontal position. The Knudsen cell and furnace are contained within a water-cooled copper chamber in order to eliminate effects of outgassing during the experiments. This appears to be a worthwhile technique because the relatively poor thermal conductivity of stainless steel makes external cooling relatively ineffective. The water-cooled motor (M) which drives the modulation disk (MD) and the optical switch (OS) are located below the mass filter. It was found that water cooling of the motor essentially eliminated outgassing during operation. The location of ion gauges (I.G.), and a shutter (S) for protecting the window (W) are also indicated. A prism (P) on the top flange deflected the radiant energy emitted from the Knudsen cell into an optical pyrometer for temperature measurement, while temperature stability was monitored by a thermocouple (T.C.) fed through the bottom flange. The water-cooled electrodes for heating the furnace are insulated from the flange using Teflon sleeves and Swagelock fittings (details not shown). All other vacuum feedthroughs are made using commercial fittings.

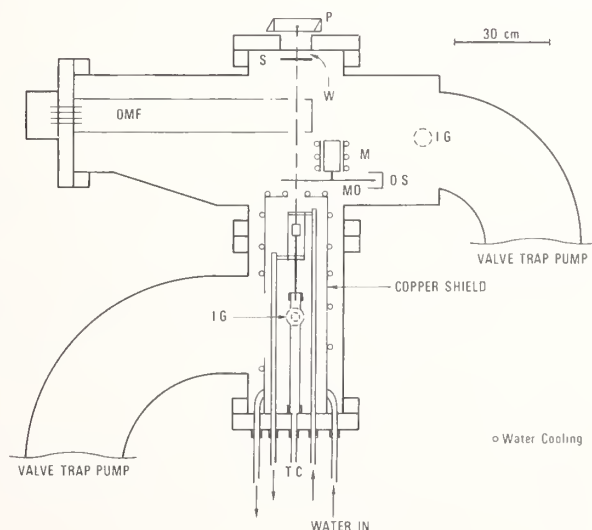


Figure 1. Schematic of vacuum enclosure and mass spectrometric system.



Figure 2 shows a schematic diagram of the Knudsen cell and furnace. The Knudsen cell was made of 0.025 cm Pt sheet and was of welded construction. It was 0.80 cm o.d. by 1.90 cm high and was welded to a 0.32 cm o.d. platinum mounting tube about 2.5 cm long. The top of the cell was made from 0.015 cm Pt sheet, the outer edge of which was bent in a mold to form a lip so that the lid fit snugly inside the effusion cell body (note detail in fig. 2). After loading the cell, the lid was spotwelded in numerous places around the lip to eliminate leakage.

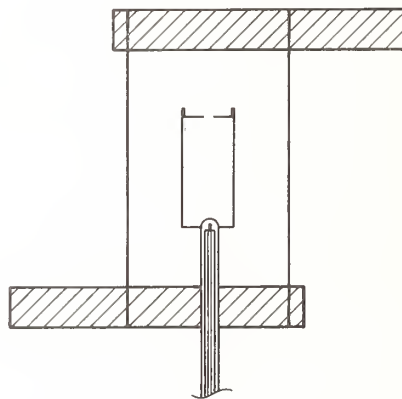


Figure 2. Schematic of furnace and Knudsen cell.

The furnace was made from 0.005 cm Ta sheet sandwiched between 0.62 x 1.6 diam x 0.05 cm Ta support rings at the ends and 0.62 x 0.05 cm Ta current leads which were connected to 1.25 cm o.d. water-cooled copper electrodes. In the first three series of measurements, the furnace was 5 cm long and the Knudsen cell was centrally located coaxially and vertically in the furnace.

After the first three series, the furnace was lengthened to 7.5 cm and the diameter of the furnace support rings was increased to 1.9 cm o.d. The latter change was made because most of the heat is absorbed by the lateral surface area of the effusion cell, and increasing the distance between the effusion cell and heater has the effect of smoothing temperature gradients in the effusion cell caused by temperature inhomogeneities in the heater or centering errors in the effusion cell. The cell position was biased upward by 0.6 cm to ensure that the base of the effusion cell was not in a cooler zone of the furnace and to compensate for heat losses due to the support. In all measurements, a single longitudinal radiation shield approximately 0.3 cm from the furnace and extending 2.5 cm below the furnace was used to increase the efficiency of the heater as well as to provide a more uniform hot zone.

Besides an increase in the furnace length, several changes in cell support were made as the measurements progressed. In the first series (1104), the Knudsen cell was mounted

on a 0.25 cm o.d. Mo rod which fitted snugly inside the Pt mounting tube. Because of the possibility that this could lead to undue cooling of the base of the effusion cell, an  $\text{Al}_2\text{O}_3$  thermocouple insulation tube was installed and used as a support in subsequent work. A Pt/Pt, 10 percent Rh thermocouple was installed at the same time with the thermocouple hot junction in proximity but not touching the base of the cell in order to avoid sticking problems. Comparison between the optical pyrometer and thermocouple temperatures showed that the thermocouple systematically read low. This was probably due to poor thermal contact between the thermocouple junction and the cell.

With a furnace length of 7.5 cm starting with series 1122, agreement between the thermocouple temperature and the optical pyrometer temperature was more satisfactory than with the shorter furnace. The major use of the thermocouple was to indicate whether the cell temperature was constant. This was achieved by feeding the output of the thermocouple to a Doric Trendicator 400 Type S digital indicator which constantly displayed the thermocouple output in  $^{\circ}\text{C}$ . This allowed an almost instantaneous check to be made to determine if increases or decreases in the ion intensity were correlated with temperature changes of the effusion cell.

Power was controlled by a Stabiline constant voltage transformer. With all leads securely tightened on the low voltage-high amperage side of the power supply, temperature control was usually better than  $2^{\circ}\text{C}$ .

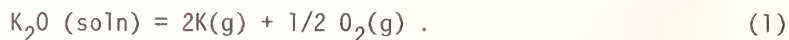
Temperature measurements were made using a Pyro-Micro-optical pyrometer, the temperature scale of which was verified by comparison with a bandlamp calibrated by the Temperature Physics Section at NBS. Temperatures were read through a prism, window, the ion source, and the modulation disc of the mass spectrometer, and into the black body orifice at the top of the effusion cell. Corrections of  $-1.25 \times 10^{-5} \text{K}^{-1}$  for the window and prism, and  $-3.13 \times 10^{-5} \text{K}^{-1}$  for the 50 percent transmission modulation disc were added to the reciprocal apparent absolute temperature to obtain a temperature on the IPTS-68 scale.

### 3. Procedure

Vapor pressure measurements over solutions would ideally be carried out by determining the pressure variation with composition at a number of isotherms or by determining the pressure variation with temperature at a number of constant compositions. Neither of these ideals was achieved, but at the lower temperatures, compositions are constant for all practical purposes and a large fraction of the change in composition takes place at the highest temperature points.

Because  $\text{K}_2\text{Si}_2\text{O}_5$  is somewhat hygroscopic, the sample was dried overnight at  $500^{\circ}\text{C}$  prior to use and undue exposure to the atmosphere was minimized during loading of the effusion cell, cell alignment in the mass spectrometer, and weighing. In the initial measurements when the sample was first being heated, special care was taken to attempt to observe phase locked signals corresponding to  $\text{H}_2\text{O}$ ,  $\text{KOH}$  which might be formed by reaction of  $\text{K}_2\text{Si}_2\text{O}_5$  with absorbed water, and  $\text{CO}_2$  which would be formed by residual, unreacted  $\text{K}_2\text{CO}_3$ . However, no appreciable signals resulting from vaporization of these impurities were detected, indicating that sample purity was satisfactory.

The predominant vaporization process can be written as:



Throughout the range of these measurements, the loss of  $\text{SiO(g)}$  or K-bearing molecules was insignificant. After vaporization of sufficient sample to give an accurately measurable weight loss, the mass spectrometer calibration constant was determined by equating the pressure from the mass spectrometer equation:

$$P_i = k_i I_i^+ T \quad (2)$$

to the pressure calculated in a gravimetric Knudsen measurement,

$$P_i = \frac{m_i}{cat} \sqrt{\frac{2\pi RT}{M_i}} \quad (3)$$

in which  $P_i$  is the pressure of some species  $i$ ,  $k_i$  is the mass spectrometer constant,  $T$  the absolute temperature,  $m_i$  is the mass loss,  $c$  the Clausing factor,  $a$  the orifice area,  $t$  the elapsed time,  $R$  the gas constant, and  $M_i$  the molecular weight of species  $i$ . It should be noted that the mass spectrometer constant defined in eq. (2) implicitly assumes that the isotopic abundance  $A_i$ , is taken into account when only a single isotopic species is observed (in this case  $^{39}\text{K}$ ). Equating (2) to (3) and inserting the isotopic abundance factor gives,

$$k_i = [m_i A_i (2\pi R)^{1/2}] / [cat I_i^+ (M_i T)^{1/2}] . \quad (4)$$

In practice, the sum of weight losses for a number of experiments at different temperatures and for different periods of time are observed so that eq. (4) need be cast in the form,

$$k_i = [GA_i (2\pi R)^{1/2} \Sigma m_i] / [ac \sqrt{M_i} \Sigma I_i^+ t \sqrt{T}] . \quad (5)$$

For vaporization of  $\text{K}_2\text{O}$  from  $\text{K}_2\text{O-SiO}_2$  solutions,  $\Sigma m_i$  is the weight loss of  $\text{K}_2\text{O}$  and  $G$  is a gravimetric factor to convert the weight loss of  $\text{K}_2\text{O}$  to  $\text{K}$ . For each experimental point, the composition of the evaporating solution was determined from the known starting composition and the summation of  $I_i^+ t \sqrt{T}$  terms. At the higher temperatures, there was a measurable decrease in the pressure (ten percent) and change in solution composition with time, but the change in pressure was essentially linear with time. The pressure and  $\text{K}_2\text{O}$  concentration calculated at the mean time interval were accepted for each observation in most cases, but in a few of the earlier runs, pressures were extrapolated to a known composition.

Each time the Knudsen cell was removed from the mass spectrometer, it was weighed so that the weight loss and  $\Sigma I^+ t \sqrt{T}$  data could be used to calculate the mass spectrometer sensitivity constant. Three mass spectrometer constants and the series designation they were used for are listed in table 1. In the last series of data, 1214, a valid calibration constant was not obtained because deformation of the furnace in the latter part of the experiment caused excess weight loss due to vaporization of platinum from the crucible. The calibration constant used in this series was the average of the three previously determined values.

Table 1. Mass spectrometer constants.

Series Designation	k
	Microvolts atm <sup>-1</sup> K <sup>-1</sup>
1104	1.96 E-11
1110-1115	1.47 E-11
1122-1129	1.83 E-11
1214	1.75 E-11 <sup>a</sup>

<sup>a</sup>Average of previous three values.

In spite of the modulated beam system, some extraneous phase locked mass 39 signals at low pressures ( $P_k < 10^{-7}$  atm) were apparent. Because a rapid increase in this signal coincided with the increase in power to the furnace and slowly decayed away, it appeared likely that it was due to desorption of residual hydrocarbon off the furnace walls. Because of this effect, some of the mass 39 observations at low ion intensities were rejected in the analysis of the data. Also, in order to improve the signal-to-noise ratio at lower ion intensities, an ionizing energy of 20 volts was used throughout the measurements.

Crystalline  $K_2Si_2O_5$  was prepared by the solid state reaction at 800 °C of Brazilian Optical Quality  $SiO_2$  (purity > 99.99 percent as determined by NBS spectrochemical analysis) and anhydrous  $K_2CO_3$  in weighed amounts corresponding to the appropriate composition. Repeated grinding and firing gave a product whose x-ray diffraction pattern showed only  $K_2Si_2O_5$ .

Preliminary vapor pressure measurements [7] were carried out by a gravimetric effusion method employing a Mettler Microbalance System using a platinum effusion cell with a nominal 1 mm diam orifice. Additional unpublished preliminary measurements were made using a modulated beam Bendix time-of-flight mass spectrometer in which the effusion cell employed a 1/2 mm diam effusion orifice (B5 experiments). The latter measurements yielded pressures significantly higher than the former, and the partial molal heat for formation of  $2K(g) + 1/2 O_2(g)$  from the solution was significantly less than for the microbalance measurements. This suggested that the microbalance measurements were in error because a temperature dependent rate process (probably diffusion through the melt)



governed the apparent pressure. As a further check, mass spectrometer measurements using the Bendix system were made on a sample contained in a cell with a 1 mm diam orifice (B1 experiments). These data were consistent with the microbalance data in that the rate of vaporization decreased more rapidly with composition and the heat of vaporization was greater than for the measurements employing a 1/2 mm diam orifice. In the preliminary microbalance measurements, it was concluded on the basis of currently available thermodynamic data that the  $K_2O-SiO_2$  system would be binary and that only K and  $O_2$  would be important vaporization products. This was shown to be the case in the B5 and B1 measurements by the observation that the ratio of  $O_2/K$  pressures as indicated by the  $O_2^+/K^+$  ion current ratio was constant with temperature and composition.

#### 4. Results

Absolute temperatures, the bulk  $K_2O$  weight percent in the melt, and the potassium pressures<sup>2</sup> are listed in table 2 in the order taken. Low temperature points rejected from consideration are not tabulated. All of the data in series 1214 were obtained at temperatures and compositions at which a crystalline silica phase and a silica saturated solution would exist if thermodynamic equilibrium were established. Also, some data points in series 1123 through 1129 belonging in the two phase region are identified with an a. The data were broken up into eight series for analysis in an attempt to determine if the partial molal heat of evaporation was composition dependent. Data were grouped into different series if changes had been made in the experimental arrangement or a different mass spectrometer constant was used. Some of the data were arbitrarily divided if it appeared that sufficient change in the composition of the solution had taken place to allow a reasonable estimate of the dependence of pressure on composition to be made.

The data from each series were fit by least squares to the empirical equation,

$$\log P_K = B_0 + B_1/T + B_2 \cdot N^2, \quad (6)$$

where  $B_0$ ,  $B_1$ , and  $B_2$  are constants and  $N$  is the mole fraction of  $K_2O$  that would exist if the sample were a homogeneous solution. Table 3 lists the series identification, the number of data points, the range of  $K_2O$  bulk composition, the values of the above constants and their standard deviations, and the standard deviation in  $\log P_K$ . The value of  $B_1$ , which is related to the partial molal heat of evaporation of  $K_2O$  from the solution, appears to be constant within a reasonable error limit for all the data through series 1129, while the constant  $B_2$  which accounts for the variation in pressure with composition averages out to be about ten excepting the deviant values for series 1122 and 1129. The standard deviation in  $B_2$  in both these series is higher than in the other series, possibly because of too narrow a composition range in series 1122 and phase separation in series 1129. It was found that all the data through series 1129 could be fit to a single master equation with only a modest increase in the standard deviation of  $\log P_K$ . However, the series 1214 data does



not fit the master equation, the constant B2 indicating that the variation in pressure with composition becomes greater in this composition range. In addition, the decrease in the B1 constant might also be indicative of separation of the solution into two phases.

The data for each of the series are plotted in figures 3a through 3h. Each plot shows the composition range for points of varying designations. On each data point, the direction of temperature change between points is noted. An upward tic on a data point shows that the temperature was being increased during the run while a downward tic indicates that temperatures were being decreased. Each figure shows two lines which represent the pressures calculated from the master equation for the higher and lower  $K_2O$  bulk composition range shown on the graph with the exception of figure 3h. For the 1214 series, the two lines represent the higher and lower  $K_2O$  bulk compositions calculated from the least squares fit for the 1214 data only. In figures 3a through 3g, the fit of the data to the master equation appears to be excellent. The major deviation from the equation appears in series 1122 (fig. 3d) in which the data clearly deviate from the upper line. A redetermination of the mass spectrometer constant was made at this juncture in the data and this could account for the deviation. However, the deviation is only about ten percent.

According to the phase equilibrium diagram accepted for the  $K_2O-SiO_2$  system [8], the concentration of  $K_2O$  in the silica saturated solution varies from 23 to 5 wt percent  $K_2O$  as the temperature increases from 1273 to 1873 K. As noted above, some of the data in series 1123 through 1129 were taken at temperatures and compositions which would lead to precipitation of cristobalite or tridymite and the formation of a silica saturated solution richer in  $K_2O$  than the composition corresponding to the bulk  $K_2O$  composition. All of the data in the 1214 series correspond to compositions and temperatures which would place the melt composition in the two phase region. If equilibrium were established in the two-phase region at an appropriate rate, it might be observed in the mass spectrometer measurements because of shifts in the composition of the saturated solution. For example, an increase in temperature would lead to an initial increase in the pressure which would slowly decrease as silica dissolved in the melt until equilibrium was reattained. Conversely, if the temperature were decreased, after an initial drop, the K pressure would slowly increase as silica precipitated from the melt in order to re-establish equilibrium. Attempts to observe these effects along the liquidus curve were not successful. It should be noted that even though the pressure of K still depends on the liquidus composition, the K pressure is uniquely determined by the temperature alone in this region of the phase diagram under equilibrium conditions.

The observation that the K pressure continued to fall with decrease in bulk composition of  $K_2O$  in series 1214 is of itself evidence that equilibrium was not established. Failure to achieve equilibrium could be due to unsaturation effects in the Knudsen cell

---

<sup>21</sup> 1 atmosphere = 101325 pascals.

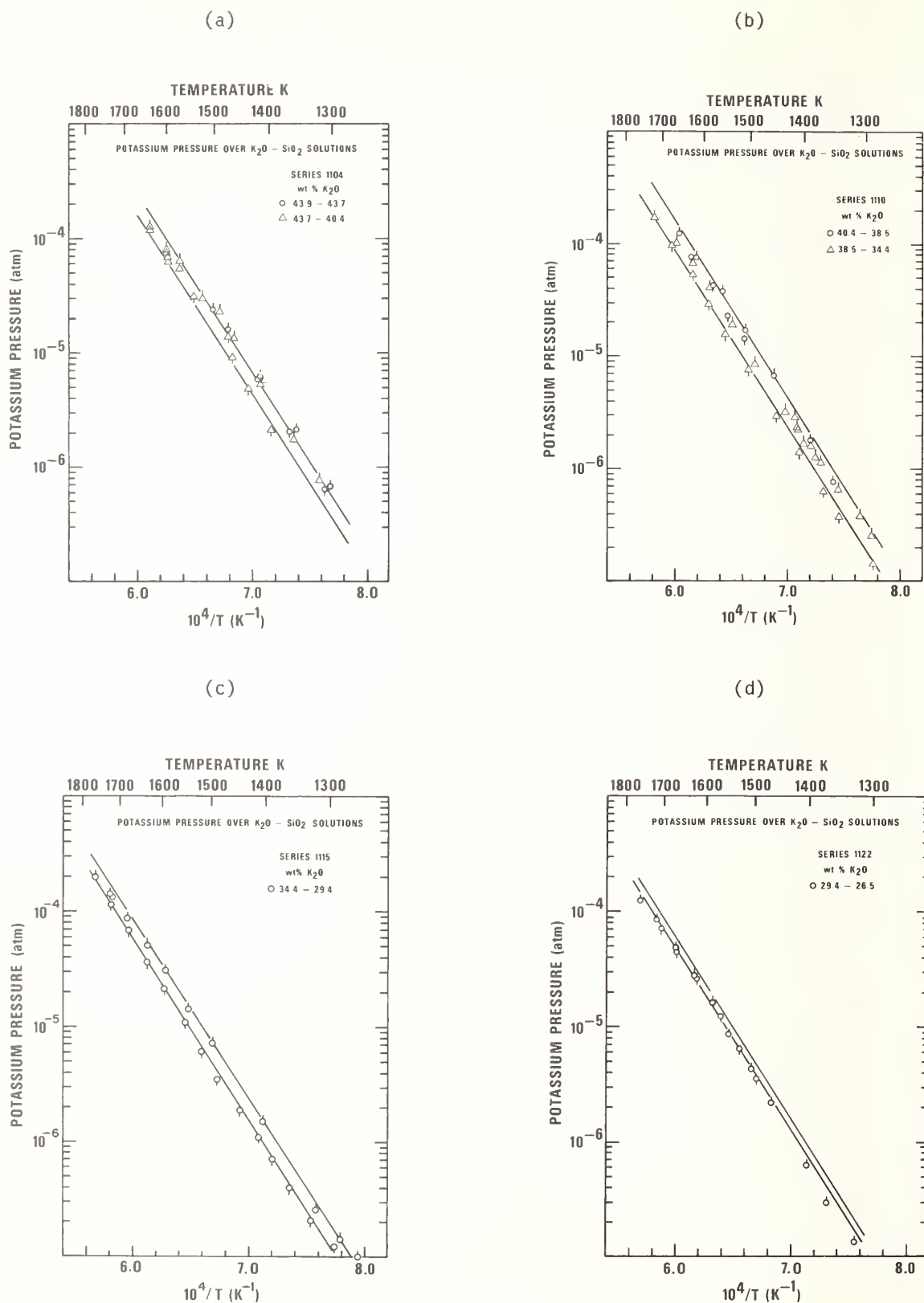
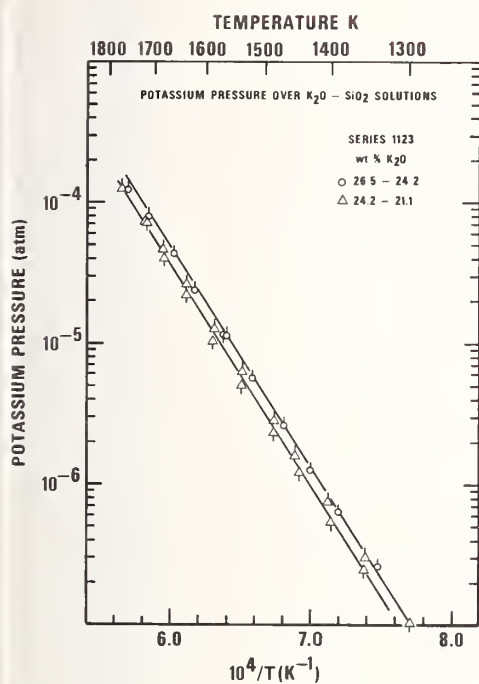
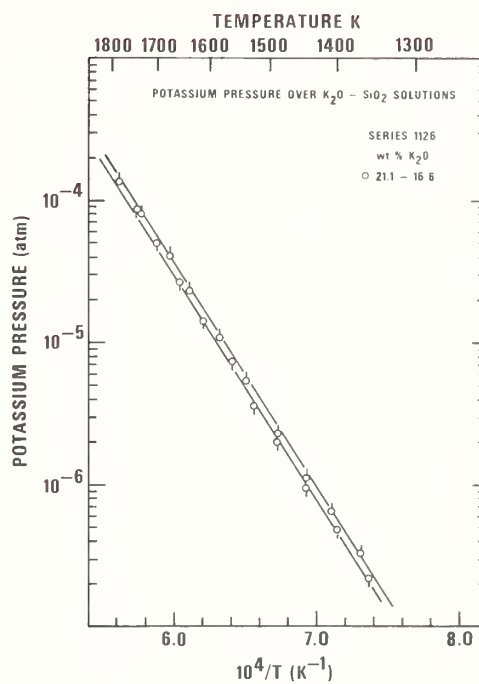


Figure 3.  $\log P_K$  vs  $1/T$  plots with lines representing pressures at upper and lower compositions based on master equation (a-g) or individual fit of data (h).

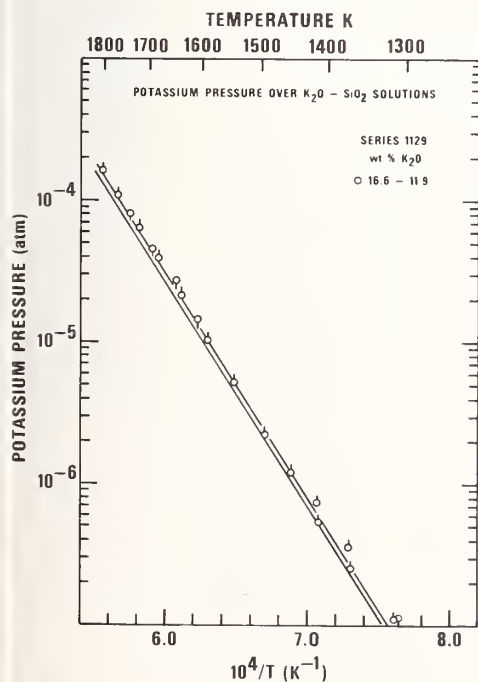
(e)



(f)



(g)



(h)

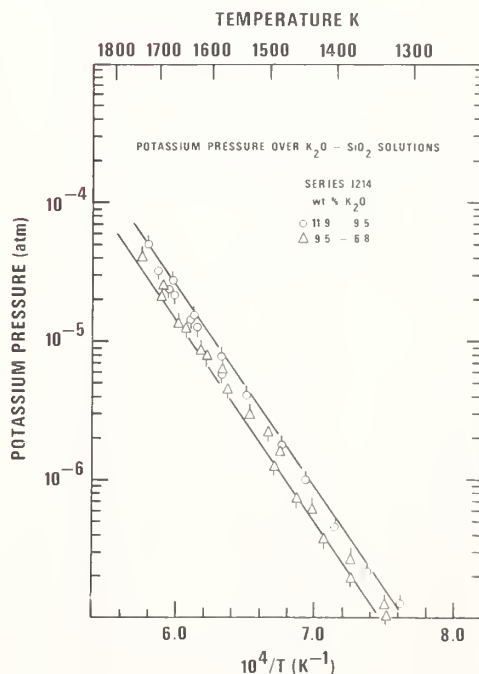


Figure 3. Continued

Table 2. Compilation of Data.

Series 1104			T,K	Wt % K <sub>2</sub> O	P <sub>K</sub> (atm)
T,K	Wt % K <sub>2</sub> O	P <sub>K</sub> (atm)			
			1489	38.31	8.79E-6
			1537	38.21	1.95E-5
1302	43.94	6.91E-7	1585	37.93	4.14E-5
1356	43.93	2.18E-6	1625	37.52	6.71E-5
1414	43.92	6.30E-6	1663	36.94	1.05E-4
1475	43.84	1.59E-5	1720	36.00	1.77E-4
1504	43.76	2.41E-5	1674	35.23	9.88E-5
1419	43.72	5.99E-6	1624	34.89	5.53E-5
1366	43.70	2.04E-6	1585	34.66	2.95E-5
1311	43.70	6.44E-7	1550	34.50	1.62E-5
1320	43.70	7.77E-7	1503	34.42	7.66E-6
1359	43.68	1.81E-6	1450	34.39	3.04E-6
1414	43.64	5.44E-6	1408	34.38	1.43E-6
1462	43.59	1.38E-5	1366	34.36	6.40E-7
1493	43.48	2.28E-5	1343	34.36	3.88E-7
1407	43.33	5.75E-6	1289	34.36	1.43E-7
1473	43.20	1.39E-5			
1524	43.04	3.02E-5		Series 1115	
1571	42.93	6.44E-5			
1571	42.51	5.63E-5	1259	34.36	1.00E-7
1601	42.51	8.22E-5	1283	34.36	1.43E-7
1601	42.02	7.73E-5	1320	34.35	2.59E-7
1640	42.02	1.29E-4	1404	34.34	1.53E-6
1640	41.32	1.22E-4	1435	34.34	2.27E-6
1594	41.32	6.91E-5	1496	34.30	7.28E-6
1594	40.99	6.32E-5	1544	34.24	1.43E-5
1542	40.73	3.16E-5	1592	34.03	3.12E-5
1466	40.44	9.21E-6	1631	33.74	5.17E-5
1436	40.39	4.91E-6	1681	33.40	8.92E-5
1396	40.36	2.16E-6	1723	32.81	1.42E-4
			1719	32.03	1.32E-4
			1765	31.18	2.03E-4
			1722	30.51	1.14E-4
1352	40.34	7.58E-7	1677	30.10	6.93E-5
1389	40.34	1.80E-6	1633	29.82	3.66E-5
1456	40.31	6.87E-6	1595	29.66	2.17E-5
1508	40.24	1.74E-5	1549	29.54	1.10E-5
1560	40.10	3.77E-5	1517	29.45	6.28E-6
1615	39.78	7.62E-5	1482	29.40	3.52E-6
1657	39.22	1.22E-4	1445	29.38	1.90E-6
1630	38.77	7.69E-5	1411	29.36	1.10E-6
1580	38.62	4.26E-5	1388	29.36	7.16E-7
1547	38.52	2.30E-5	1361	29.36	4.05E-7
1513	38.46	1.47E-5	1328	29.35	2.09E-7
1308	38.44	3.89E-7	1292	29.35	1.22E-7
1342	38.43	6.72E-7			
1369	38.43	1.17E-6		Series 1122	
1388	38.42	1.64E-6			
1416	38.42	2.90E-6	1294	29.34	9.48E-8
1292	38.41	2.65E-7	1325	29.34	1.36E-7
1413	38.40	2.43E-6	1369	29.34	3.00E-7
1379	38.38	1.34E-6			
1400	38.36	1.74E-6			
1411	38.35	2.23E-6			
1432	38.34	3.33E-6			

Table 2. (Continued)

T, K	Wt % K <sub>2</sub> O	P <sub>K</sub> (atm)	T, K	Wt % K <sub>2</sub> O	P <sub>K</sub> (atm)
1403	29.34	6.31E-7	1443	21.10	1.11E-6
1465	29.33	2.20E-6	1487	21.08	2.31E-6
1506	29.30	4.36E-6	1538	21.04	5.44E-6
1550	29.24	8.80E-6	1583	20.98	1.10E-5
1585	29.12	1.63E-5	1637	20.83	2.36E-5
1626	28.94	2.74E-5	1676	20.58	4.12E-5
1669	28.65	4.83E-5	1732	20.00	8.11E-5
1717	28.26	8.64E-5	1783	19.19	1.37E-4
1760	27.74	1.26E-4	1743	18.44	8.67E-5
1705	27.22	7.08E-5	1702	17.95	5.01E-5
1666	26.88	4.63E-5	1656	17.56	2.69E-5
1621	26.68	2.67E-5	1613	17.28	1.42E-5
1568	26.59	1.26E-5	1656	17.05	2.64E-5
1527	26.54	6.53E-6	1612	16.83	1.39E-5
1496	26.52	3.64E-6	1561 <sup>a</sup>	16.72	6.41E-6
Series 1123			1524 <sup>a</sup>	16.67	3.57E-6
1337	26.50	2.62E-7	1488 <sup>a</sup>	16.64	2.01E-6
1388	26.50	6.35E-7	1443 <sup>a</sup>	16.62	9.50E-7
1428	26.48	1.28E-6	1400 <sup>a</sup>	16.62	4.97E-7
1469	24.46	2.64E-6	1359 <sup>a</sup>	16.62	2.20E-7
1521	26.40	5.71E-6	1310 <sup>a</sup>	16.62	9.59E-8
1562	26.33	1.13E-5	Series 1129		
1620	26.18	2.45E-5	1373 <sup>a</sup>	16.60	3.64E-7
1660	25.92	4.37E-5	1416 <sup>a</sup>	16.60	7.52E-7
1713	25.48	7.92E-5	1308 <sup>a</sup>	16.59	1.15E-7
1758	24.74	1.26E-4	1313 <sup>a</sup>	16.59	1.11E-7
1568	24.24	1.15E-5	1316 <sup>a</sup>	16.59	1.11E-7
1352	24.20	3.22E-7	1368 <sup>a</sup>	16.59	2.60E-7
1403	24.20	7.70E-7	1410 <sup>a</sup>	16.58	5.71E-7
1451	24.18	1.67E-7	1454 <sup>a</sup>	16.58	1.22E-6
1484	24.17	2.91E-6	1494 <sup>a</sup>	16.56	2.27E-6
1535	24.14	6.50E-6	1543 <sup>a</sup>	16.52	5.36E-6
1584	24.06	1.30E-5	1589	16.42	1.05E-5
1634	23.90	2.64E-5	1636	16.25	2.18E-5
1681	23.58	4.68E-5	1681	15.94	3.90E-5
1722	23.16	7.56E-5	1723	15.50	6.37E-5
1770	22.55	1.30E-4	1767	14.88	1.10E-4
1717	21.96	7.14E-5	1800	13.93	1.65E-4
1679	21.61	4.08E-5	1741	13.02	8.16E-5
1634	21.38	2.25E-5	1693 <sup>a</sup>	12.47	4.59E-5
1587	21.24	1.07E-5	1646 <sup>a</sup>	12.10	2.74E-5
1537	21.18	5.14E-6	1608 <sup>a</sup>	11.92	1.47E-5
1484	21.16	2.40E-6	Series 1214		
1446	21.14	1.24E-6	1315 <sup>a</sup>	11.86	1.29E-7
1398	21.14	5.42E-7	1295 <sup>a</sup>	11.86	8.18E-8
1356 <sup>a</sup>	21.14	2.51E-7	1357 <sup>a</sup>	11.85	2.14E-7
1298 <sup>a</sup>	21.14	1.04E-7	1401 <sup>a</sup>	11.84	4.58E-7
Series 1126			1444 <sup>a</sup>	11.84	1.00E-6
1368 <sup>a</sup>	21.13	3.33E-7	1482 <sup>a</sup>	11.82	1.79E-6
1409	21.12	6.51E-7	1538 <sup>a</sup>	11.77	4.11E-6
			1582 <sup>a</sup>	11.68	7.81E-6
			1635 <sup>a</sup>	11.52	1.55E-5
			1678 <sup>a</sup>	11.21	2.70E-5
			1727 <sup>a</sup>	10.88	4.79E-5
			1707 <sup>a</sup>	10.64	3.21E-5
			1628 <sup>a</sup>	10.40	1.26E-5

<sup>a</sup>Compositions and temperatures corresponding to 2-phase region.



Table 2. (Continued)

T, K	Wt % K <sub>2</sub> O	P <sub>K</sub> (atm)
1672 <sup>a</sup>	10.16	2.11E-5
1640 <sup>a</sup>	9.96	1.47E-5
1685 <sup>a</sup>	9.70	2.42E-5
1582 <sup>a</sup>	9.46	5.77E-6
1335 <sup>a</sup>	9.40	1.22E-7
1379 <sup>a</sup>	9.39	2.60E-7
1435 <sup>a</sup>	9.38	6.12E-7
1484 <sup>a</sup>	9.36	1.61E-6
1534 <sup>a</sup>	9.32	2.88E-6
1582 <sup>a</sup>	9.30	6.14E-6
1620 <sup>a</sup>	9.10	8.53E-6
1664 <sup>a</sup>	8.88	1.37E-5
1702 <sup>a</sup>	8.77	2.16E-5
1738 <sup>a</sup>	7.88	4.00E-5
1696 <sup>a</sup>	7.36	2.39E-5
1649 <sup>a</sup>	7.08	1.32E-5
1612 <sup>a</sup>	6.96	7.62E-6
1571 <sup>a</sup>	6.88	4.28E-6
1524 <sup>a</sup>	6.83	2.16E-6
1493 <sup>a</sup>	6.80	1.26E-6
1457 <sup>a</sup>	6.78	7.11E-7
1416 <sup>a</sup>	6.77	3.77E-7
1379 <sup>a</sup>	6.77	1.98E-7
1335 <sup>a</sup>	6.76	1.01E-7

Table 3. Least squares fit of K(g) pressures over K<sub>2</sub>O-SiO<sub>2</sub> (ℓ) solutions.

Series	No. Pts.	K <sub>2</sub> O wt. %	B0	S.D.	B1	S.D.	B2	S.D.	S.D.
1104	28	43.9-40.4	4.482	.131	-15637	192	12.02	1.29	.041
1110	38	40.3-34.4	4.790	.092	-15843	115	10.17	.66	.038
1115	26	34.4-29.4	4.559	.076	-15485	98	10.42	.83	.034
1122	18	29.3-26.5	5.349	.141	-15958	218	- 2.89	3.53	.047
1123	31	26.5-21.1	4.491	.067	-15305	93	10.35	1.05	.029
1126	23	21.1-16.6	4.784	.081	-15706	113	8.65	1.76	.030
1129	20	16.6-11.9	4.735	.092	-15226	182	- 9.77	5.46	.042
1214	37	11.9- 6.8	3.841	.076	-14654	116	52.76	4.27	.041
1104-1129	184	43.9-11.9	4.721	.047	-15624	72	9.32	.13	.057

caused by too large a ratio of orifice/sample area which would lead to a diffusion controlled vaporization process and/or because the rate of crystallization of cristobalite or tridymite is too slow. However, the deviation from equilibrium conditions may not be too great because the lower slope observed in the 1214 data would be expected if equilibration along the liquidus curve actually took place.

At the conclusion of the vaporization measurements, the residues remaining in the effusion cells used in two of the preliminary experiments and this experiment were examined by x-ray diffraction and/or using the SEM. The residue from the B5 experiment had a  $K_2O$  bulk composition of 20.5 wt percent. Its x-ray diffraction pattern showed only a broad peak characteristic of a  $K_2O-SiO_2$  glass. The residue from the B1 experiment had a  $K_2O$  bulk composition of 18.8 wt percent  $K_2O$ . As noted earlier, it was concluded that there was a significant deviation from equilibrium conditions in this experiment. The x-ray diffraction pattern of this residue showed the presence of the broad peak characteristic of the  $K_2O-SiO_2$  glass and a moderately strong pattern of a crystalline phase which was identified as low cristobalite. The x-ray pattern of the residue from the current experiment, which had a  $K_2O$  bulk composition of 6.8 percent, showed a strong pattern characteristic of low cristobalite as well as one weak peak characteristic of tridymite.

All three effusion cells showed signs of some migration of the sample. The bulk of the sample was contained in the bottom of the effusion cell but many small globules had wet the platinum and were distributed over the lower half of the cell. The globules were either clear and glassy or had a slightly milky appearance. A number of these from the B1 experiment were examined in situ by a SEM, but all appeared the same under magnification. At high magnification some crystallinity was apparent. The EDX spectra of globules selected at random showed the presence of Si and K with the K intensity somewhat less than might be expected, but did not reveal any significant variation in composition of various globules.

Under the conditions where the phase diagram indicates that cristobalite or tridymite should crystallize from the melt, low cristobalite which is a metastable phase was observed. Although the composition of the melt in metastable equilibrium with low cristobalite is not well known, Kracek, Bowen, and Morey [9] indicate a melt composition several percent poorer in  $K_2O$  than for the stable equilibrium. It is doubtful, however, that metastable equilibrium throughout the two phase region was actually achieved because the vaporization behavior would be expected to be similar to that for thermodynamic equilibrium. Quite a bit of data taken in the two phase region, however, does appear to represent equilibrium pressures in that the data agree satisfactorily with data representing the homogeneous solution. Substitution of the saturated solution composition for the calculated bulk composition would have little effect on the fit of the data to the master equation because the pressure is fairly insensitive to composition as the phase boundary is approached. The series 1214 data, however, probably yields low K pressures simply because there is insufficient sample left in the effusion cell to yield equilibrium pressures.

As stated earlier, the potassium pressure measurements can be used to determine the activity of  $K_2O$  in the  $K_2O-SiO_2$  solution. For some calculations, an activity defined with

respect to a reference state of K(g) and O<sub>2</sub>(g) may be useful and an activity may be defined as:

$$A_{K_2O} \text{ (ref. to vapor)} = P_K^2 P_{O_2}^{1/2} . \quad (7)$$

For these experiments,  $P_{O_2} = 0.226 P_K$  and substitution of this into the master equation yields the equation

$$\log A_{K_2O} \text{ (ref. to vapor)} = 11.482 - 39060/T + 23.30 N^2. \quad (8)$$

which represents the activity of K<sub>2</sub>O in the solution from a wt. fraction of 0.44 to the saturated solution phase boundary referenced to the vapor state. For other calculations, K<sub>2</sub>O [ℓ] will a more useful reference state and eq. (8) may be modified to

$$\log A_{K_2O} \text{ (ref to } K_2O(\ell)) = \log A_{K_2O} \text{ (ref. to vapor)} - \log K_{eq} \quad (9)$$

in which  $K_{eq}$  is the equilibrium constant for reaction (1) when K<sub>2</sub>O is a pure liquid.

## 5. Discussion

The results obtained in this work in general have good internal as well as external consistency. For example, the mass spectrometer constants were quite reproducible and their constancy during the measurements is shown by the fact that data from various experiments show the proper trend with composition, i.e., decreasing pressure with decreasing K<sub>2</sub>O content. The partial molal heat of evaporation of K<sub>2</sub>O from the melt is constant within error and is 178.7 kcal mol<sup>-1</sup> which is quite consistent with the heat of solution of K<sub>2</sub>O in SiO<sub>2</sub> to form K<sub>2</sub>Si<sub>2</sub>O<sub>5</sub>(-ℓ) (-68 kcal/mol<sup>-1</sup>) estimated from Kelley's [10] compilation and the heat of formation of K<sub>2</sub>O of -109 kcal mol<sup>-1</sup> both at 1500 K. The heat of formation is based on the JANAF [11] K<sub>2</sub>O (c) table to the melting point, the heat of fusion reported by Natola and Touzain [12] and an estimated  $C_p$  of 25 cal mol<sup>-1</sup>K<sup>-1</sup> for liquid K<sub>2</sub>O.

The measurements presented provide activity data for K<sub>2</sub>O in SiO<sub>2</sub> solutions from approximately 44 wt percent K<sub>2</sub>O to the phase boundary and at temperatures from about 1300-1800 K. Some rough estimates of the overall possible systematic errors in the measurements may be useful. The largest error is undoubtedly due to error in temperature measurement which probably does not exceed 20 K. The error in composition is estimated to be not in excess of two percent at the starting composition and five percent at the final composition. At 1500 K, the estimated 20 K error yields an error in K pressure of about 40 percent.

It would be of scientific interest to measure the K<sub>2</sub>O activity starting from the K<sub>2</sub>O·SiO<sub>2</sub> composition and to make additional careful measurements using still smaller effusion orifices in the saturated silica solution area in order to cover a broader range

and to attempt to achieve equilibrium measurements in this difficult region of the system. The measurements here, however, cover most of the range of importance to MHD research for this simple system.

---

The author wishes to acknowledge the help of Dr. L. P. Cook for preparation of the  $K_2O \cdot 2SiO_2$  sample and the SEM measurements, C. L. McDaniel for the x-ray measurements, and A. B. Sessoms for assistance in the mass spectrometer measurements. This work was funded in part by the Department of Energy, MHD Division.

#### References

- [1] Preston, E. and Turner, W. E. S., J. Soc. Glass Tech. 17, 122 (1933).
- [2] Merten, U. and Bell, W. E., chapter 4: in, The Characterization of High Temperature Vapors, J. L. Margrave, ed. (J. Wiley & Sons, Inc., New York, 1967).
- [3] Callow, R. J., Trans. Faraday Soc. 46, 663 (1950).
- [4] Charles, R. J., J. Am. Ceram. Soc., 50, 631 (1967).
- [5] Eliezer, N., Howald, R. A., Marinkovic, M., and Eliezer, I., Conference on High Temperature Sciences Related to Open-Cycle, Coal Fired MHD Systems, ANL-77-21 (1977).
- [6] Paule, R. C., High Temp. Sci. 8, 257 (1976).
- [7] Plante, E. R., Olson, C. D., and Negas, T., Sixth International Conference on Magneto-hydrodynamic Electrical Power Generation, Washington, D.C., II, 211 (1975).
- [8] Kracek, F. C., Bowen, N. L., and Morey, G. W., J. Phys. Chem. 41, 1183 (1937).
- [9] Kracek, F. C., Bowen, N. L., and Morey, G. W., J. Phys. Chem. 33, 1857 (1929).
- [10] Kelley, K. K., Heats and Free Energies of Formation of Anhydrous Silicates, U.S. B.M. RI 5901 (1962).
- [11] JANAF Thermochemical Tables, Dow Chemical Co., Midland, Michigan.
- [12] Natola, F. and Touzain, Ph., Can. J. Chem. 48, 1955 (1970).





## MASS SPECTROMETRIC INVESTIGATION OF VAPOR SPECIES OVER LIQUID GERMANIUM DIOXIDE

Tadashi Sasamoto, Michio Kobayashi<sup>1</sup>, and Toshiyuki Sata  
Research Laboratory of Engineering Materials,  
Tokyo Institute of Technology  
Meguro-ku, Tokyo 152, Japan

The vaporization of liquid  $\text{GeO}_2$  was studied using a double-focusing mass spectrograph.  $\text{GeO}$  and  $\text{GeO}_2$  were found to be parent species vaporized from liquid  $\text{GeO}_2$ .

### 1. Introduction

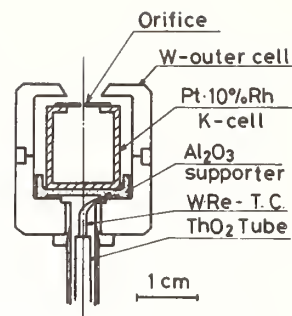
It is well known that  $\text{GeO}$  is the main gaseous species vaporized from liquid germanium dioxide. However, the identification of other gaseous species over liquid germanium dioxide is ambiguous, mainly because the vaporization experiments were done under reducing conditions. In this report, we identify gaseous species other than  $\text{GeO}$  under neutral conditions.

### 2. Experimental

The sample used was hexagonal  $\text{GeO}_2$  (99.99 percent purity). A Matauch-Herzog type double-focusing mass spectrograph (JMS-01BM, Japan Electron Optics Laboratory) equipped with a Knudsen source was used for the measurements. As details of the instrument have been reported elsewhere [1]<sup>2</sup>, only the Knudsen cell which is illustrated in figure 1 will be described here.  $\text{GeO}_2$  (about 200 mg) was placed in a Knudsen cell (Pt 90%-Rh 10%) which had an effusion hole diameter of 0.3 mm. The Knudsen cell was indirectly heated by the radiation from a tungsten outer cell which was heated by electron bombardment. The temperature of the cell was measured by a W 5 percent Re/W 26 percent Re thermocouple positioned at the bottom of the cell. Temperature calibration was made using an optical pyrometer and a carbon cell.

<sup>1</sup>Present address: Department of Materials Science and Technology, Technological University of Nagaoka, Nagaoka, Niigata 949-54 Japan.

<sup>2</sup>Figures in brackets indicate the literature references at the end of this paper.



Knudsen Cell

Figure 1. Knudsen cell.

The collimated beam of the gaseous species effusing from the cell was ionized by electrons of 20 eV except when measuring appearance potentials. The shutter effect was used to verify that the gaseous species originated from within the Knudsen cell.

The ratio of the vapor pressure ( $p_x$ ) of gaseous species  $x$  to that ( $p_s$ ) of reference species  $s$  is given by eq. (1)

$$p_x/p_s = (\sigma_s/\sigma_x)(S_s/S_x)(j_{y_s}^i/i_{y_x}^i)(i_{I_x}^+/j_{I_s}^+)(T_x/T_s) \quad (1)$$

where  $\sigma_x$  is relative ionization cross section for species  $x$ ,  $S_x$  is the sensitivity of the detector for  $x$ ,  $i_{y_x}^i$  is the isotope ratio of mass number  $i$  of species  $x$ ,  $i_{I_x}^+$  is the observed ion current of  $x^+$  with mass number  $i$ , and  $T_x$  is the temperature of the Knudsen cell where the gaseous species  $x$  originates. We used the following values for relative ionization cross sections [2,3];

$$\sigma_{\text{Ge}} = 5.71, \sigma_0 = 1.27, \sigma_{\text{GeO}} = \sigma_{\text{Ge}} + \sigma_0 = 6.98$$

$$\sigma_{\text{GeO}_2} = \sigma_{\text{Ge}} + 2\sigma_0 = 8.25, \sigma_{\text{Ge}_3\text{O}_3}/\sigma_{\text{GeO}} = 2.1,$$

and we assumed the sensitivity of the secondary electron multiplier was  $S = 1$  for all species.

### 3. Results and Discussion

Based on the experimental conditions described above, we assume that the vaporization experiment was performed under neutral oxidizing conditions.

Figure 2 shows the mass spectra obtained from  $\text{GeO}_2$  at 1380 °C when the shutter is opened (upper) and closed (lower). The comparison of these two mass spectra establishes the ion contribution from the effusion cell. They are  $\text{Ge}^+$ ,  $\text{GeO}^+$ ,  $\text{GeO}_2^+$ ,  $\text{Ge}_2\text{O}^+$ ,  $\text{Ge}_2\text{O}_2^+$ ,  $\text{Ge}_3^+$ ,  $\text{Ge}_3\text{O}^+$  and  $\text{Ge}_3\text{O}_3^+$ . The observed peak height ratio for each isotopic species compares well with the corresponding calculated isotope abundance ratios. The existence of the  $\text{GeO}_2^+$  species is, though not clear in figure 2, evident from figure 3 where the peaks with arrows are assigned to  $\text{GeO}_2^+$  (other intense peaks are due to background). The peak height ratio of the peaks with arrows in figure 3 corresponds well with the abundance ratio of germanium given in figure 2.

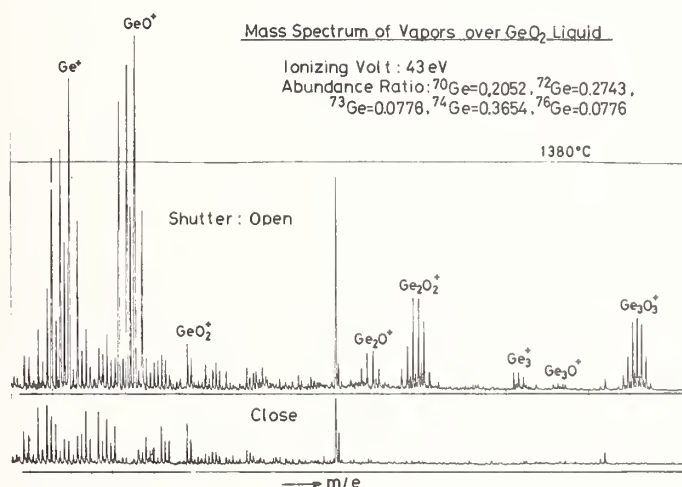
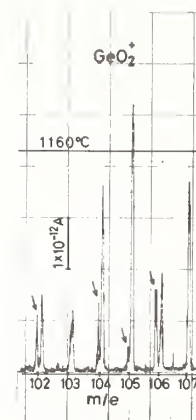


Figure 2. Mass spectrum of vapors over  $\text{GeO}_2$  liquid.

Mass spectral ions from liquid  $\text{GeO}_2$ , namely  $\text{GeO}_2^+$ ,  $\text{Ge}_2\text{O}^+$ ,  $\text{Ge}_2\text{O}_2^+$ ,  $\text{Ge}_3^+$ ,  $\text{Ge}_3\text{O}^+$ , and  $\text{Ge}_3\text{O}_3^+$  were observed for the first time under neutral oxidizing conditions. The ions  $\text{Ge}_3^+$  and  $\text{Ge}_3\text{O}^+$  were not previously observed in the system,  $\text{GeO}_2(\text{hex}) + \text{Ge}(\text{c})$ , although  $\text{Ge}_2\text{O}^+$ ,  $\text{Ge}_2\text{O}_2^+$ , and  $\text{Ge}_3\text{O}_3^+$  were observed.

The approximate appearance potentials were obtained by the linear extrapolation method, the energy scale being calibrated with the appearance potential (12.6 eV) of the  $\text{H}_2\text{O}^+$  ion. They are  $\text{Ge}^+$ , 16.4;  $\text{GeO}^+$ , 13.4;  $\text{GeO}_2^+$ , 13.4;  $\text{Ge}_2\text{O}_2^+$ ,  $15.8 \pm 3$ ;  $\text{Ge}_3\text{O}_3^+$ , 12.4 eV. Although our values of the appearance potentials are several eV higher than those by Drowart, et al. [3], the relative magnitude of our appearance potentials for the two main gaseous species  $\text{Ge}^+$  and  $\text{GeO}^+$  compares well with that by Drowart, et al. [3]. That is, the appearance potential of  $\text{Ge}^+$  is several eV higher than that of  $\text{GeO}^+$ . We, therefore, consider that  $\text{GeO}^+$  is the parent ion and  $\text{Ge}^+$  is a fragment ion from  $\text{GeO}$  as Drowart, et al. suggested. From similar reasoning we consider that  $\text{GeO}_2^+$  and  $\text{Ge}_3\text{O}_3^+$  are parent ions.  $\text{Ge}_2\text{O}^+$ ,  $\text{Ge}_3^+$  and  $\text{Ge}_3\text{O}^+$  are safely considered to be fragment ions judging from their unusual



Isotope Peaks of  $\text{GeO}_2^+$

Figure 3. Isotope peaks of  $\text{GeO}_2^+$ .

composition, though their appearance potentials were not measured. The abundance ratios of gaseous parent species are  $\text{GeO}_2(\text{g})/\text{GeO}(\text{g}) = 0.001$  and  $\text{Ge}_3\text{O}_3(\text{g})/\text{GeO}(\text{g}) = 0.002$  at about  $1300^\circ\text{C}$ .

Additional evidence that  $\text{GeO}_2^+$  is a parent ion is that the abundance ratio of gaseous species,  $\text{MO}_2(\text{g})/\text{MO}(\text{g})$ , over condensed  $\text{MO}_2(\text{c})$  decreases regularly for higher members of group IV ( $\text{M} = \text{C}, \text{Si}, \text{Ge}, \text{Sn}$ ). That is:  $\text{CO}_2(\text{g})/\text{CO}(\text{g}) \gg 1$ ,  $\text{SiO}_2(\text{g})/\text{SiO}(\text{g}) = 0.01$  [4],  $\text{GeO}_2(\text{g})/\text{GeO}(\text{g}) = 0.001$ , and  $\text{SnO}_2(\text{g})/\text{SnO}(\text{g}) = 0.0$  [5].

The vapor pressure of  $\text{GeO}_2(\text{g})$  as estimated from eq. (1) is given by

$$\log[P(\text{GeO}_2(\text{g}), \text{atm})] = 6.05 - (1.88 \times 10^4/T) \quad (2)$$

#### References

- [1] Watanabe, E., Naitoh, M. and Aoyama, T., *Kogyo Kagaku Zasshi*, **67**, 1778 (1964).
- [2] Mann, J. B., *J. Chem. Phys.* **48**, 1645 (1967).
- [3] Drowart, J., Degreve, F., Verhaegen, G., and Colin, R., *Trans. Faraday Soc.* **61**, 1072 (1965).
- [4] Porter, R. F., Chupka, W. A., and Inghram, M. G., *J. Chem. Phys.* **23**, 216 (1955).
- [5] Colin, R., Drowart, J., and Verhaegen, G., *Trans. Faraday Soc.* **61**, 1364 (1965).

## Discussion

Moderator (Gilles): Do you have a good feeling for when one should use a single focusing magnetic instrument or a double focusing magnetic instrument?

Response (Sasamoto): Yes, our resolution power is about 2,600 double focusing. This enables one to separate out hydrocarbon background gases from the mass spectra of interest.

Moderator (Gilles): Thank you. I think Dr. Kohl and R. Stearns have a double focusing instrument. What do you folks see as the principal advantage of using a double focusing instrument? Is it useful?

Response (Stearns): Yes, we recently added beam modulation and we find the high resolution useful.





## MASS SPECTROMETRIC DETERMINATION OF ATOMIZATION ENERGIES OF INORGANIC MOLECULES AND THEIR CORRELATION BY EMPIRICAL MODELS OF BONDING

Karl A. Gingerich  
Department of Chemistry  
Texas A&M University  
College Station, TX 77843

The application of the Knudsen effusion method combined with mass spectrometry for the measurement of atomization energies of inorganic molecules is described. Recent results with emphasis on molecular metals, intermetallic molecules and metal carbides are presented. The use and limitations of various empirical models of bonding is illustrated by comparing experimental values with those calculated by the various models.

### 1. Introduction

The work reported summarizes mass spectrometric determinations of bond energies performed in our laboratory, for species such as molecular gaseous nitrides, molecular intermetallic compounds and polyatomic metal carbides. For these investigations a Knudsen cell mass spectrometer that combines high sensitivity and high temperature capability was required. The large dynamic range for partial pressures achieved in many of the measurements permitted the investigation of minor vapor components present in concentrations of  $10^{-2}$  to  $10^{-6}$  relative to that of the major components.

First, a brief discussion of the method and the instrument used will be given. Then, selected results will be presented and discussed in terms of empirical models of bonding. These models permit interpretation of the measured bond energies and predictions about new molecules.

### 2. Knudsen Cell Mass Spectrometric Method

The Knudsen cell mass spectrometric method has been pioneered by Ionov [1]<sup>1</sup>, Chupka and Inghram [2], and Honig [3]. This method and its principal results have been described in many reviews, for instance references [4-9]. Critical examination of the method limitations has been made by Drowart [7] and by Stafford [10]. Today, Knudsen cell mass spectrometry is considered an important versatile method for equilibrium studies of high temperature systems

---

<sup>1</sup>Numbers in brackets indicate the literature references listed at the end of this paper.

to temperatures of about 3000 K. We [11-18] have made contributions, together with Kohl and Stearns [19] to extend its range of application to above 2700 K, while maintaining high sensitivity. There is no other method presently available that permits the measurement of bond energies of minor molecular vapor components at such high temperatures.

Our measurements were performed with a modified Nuclide Corporation 12-90 HT mass spectrometer, that resembles the one described by Chupka and Inghram [2]. The magnet orientation was changed to allow a horizontal positioning of the analyzer tube. This resulted in a 90° configuration of ion beam and molecular beam, and permitted viewing of the Knudsen cell orifice through a window at the top of the ionization tube. By pyrometric viewing of blackbody holes in the cell side and bottom, through appropriately located windows, accurate measurements of cell temperature gradients were possible. All windows, when not in viewing use, are protected by magnetically operated shutters.

Radiation from a thoriated tungsten spiral resistance furnace heats the Knudsen cell. The noninductively wound tungsten spiral is made of 2.5-mm-diameter rod and extends above and below the Knudsen effusion cell in order to obtain an even temperature distribution along the cell. The electrodes leading to the heater are water-cooled. A bent thoriated tungsten rod supports the upper terminal turn of heater in order to minimize sagging during operation at high temperatures. This heater results in Knudsen cell temperatures up to approximately 2700 °C without the disturbing influence of high electrical fields such as would be required for employed electron beam heating. These spurious fields are particularly troublesome when atoms or molecules with comparatively low ionization potentials are studied. The inner heat-shield cans and the lower shields of the heat shield assembly are fabricated from tungsten sheet instead of the commonly used tantalum.

Differential pumping is used to provide high vacuum to the analyzer, ion source, and Knudsen cell regions. A slit valve, separating the source region from the analyzer tube permits continuous pumping of the analyzer section while changing samples. To minimize the background at very high temperatures or when vaporizing substances that yield non-condensable species, such as N<sub>2</sub> or As<sub>4</sub> a liquid nitrogen trap may be inserted into the ion source region. In this case the Knudsen cell cannot be viewed through the ion source aperture during the experiment.

The Knudsen effusion cell is mounted vertically and its position can be horizontally adjusted during an experiment through an externally operated mechanism that permits a 0.25-in. motion in directions normal to each other by means of two micrometers. This adjustment can be done either by viewing the orifice at a moderate temperature before the vaporization of condensable gases sets in or, at high temperatures and high rates of vaporization, by adjusting to maximum beam intensity with the shutter in the "open" position.

A movable shutter, externally operated by means of a micrometer, permits partial or complete interception of the collimated molecular beam originating from the Knudsen cell and allows one to differentiate beam signals from those due to the background or shield re-evaporation. The molecular beam is ionized by electron impact with the electron energy variable between 0 and 100 eV. Generally an electron beam energy of about 20 eV and ion accelerating potential of 4.5 kV are used.

Samples are contained in Knudsen cells, e.g., tungsten [20] or graphite lined tantalum cells [21].

Temperatures are measured by focusing a calibrated optical pyrometer on a black body hole in the bottom of the Knudsen cell. Corrections are made for optical absorption of the viewing window and deflection prism used. The optical pyrometer can be calibrated at the freezing point of gold under in situ experimental conditions.

Identification of the ions with the corresponding molecular precursors is usually done by measurement of their mass-to-charge ratio, isotopic abundance distribution, shutter profile, appearance potential and ionization efficiency.

The measured ion currents are correlated with the corresponding partial pressures using well established instrument calibration procedures, e.g. see the discussion by Chatillon, et al. elsewhere in this volume. Expressing the partial pressures in terms of reaction equilibrium constants,  $K_{eq}$  allows for the determination of reaction enthalpies  $\Delta H_T^0$  by the third law method, using the equation

$$\Delta H_T^0 = -RT \ln K_{eq} - T[\Delta(G_T^0 - H_T^0)/T]$$

where the bracketed term is the Gibbs energy function. When a large enough temperature range can be covered, the second-law method can also be used, i.e.,

$$d \ln K_{eq} / d(1/T) = - \Delta H_T^0 / R$$

Further details on the instrument, experimental procedure and data evaluation are given elsewhere [20,22].

### 3. Results and Discussion

In the following discussion our experimental and estimated data will be used to illustrate various empirical models for correlating and predicting bond energies. These models include: (1) the  $\alpha$ -parameter method applied to transition metal mononitrides, (2) the Pauling model of a polar single bond using intermetallic gold compounds as an example, (3) a valence bond approach for calculating bond energies of diatomic intermetallic compounds with multiple bonds, and (4) bond additivity and other concepts that are illustrated using recent data for gaseous transition metal carbides. Most of the experimental data shown could not have been obtained by any other presently available method.

#### 3.1 The $\alpha$ -parameter method

An empirical correlation between the atomization energy,  $\Delta H_{298,at}^0$ , of a solid compound AB and the dissociation energy,  $D_{298}^0$ , of its corresponding gaseous diatomic molecule is:

$$\alpha = 0.5 \Delta H_{298,at}^0[AB(s)] / D_{298}^0[AB(g)]$$

Colin and Goldfinger [23] showed its application for groups of binary compounds with a sizable ionic bonding component, such as diatomic halides and oxides. The predictive power of this method is illustrated using transition metal mononitrides as an example (table 1) [24-28]. When we measured the first dissociation energy of a gaseous metal nitride, UN [28], we also determined the atomization energy of solid UN, and derived an  $\alpha$ -parameter of 1.23. Using this value, the dissociation energies (in  $\text{kJ mol}^{-1}$ ) of gaseous ZrN and ThN were predicted as  $586 \pm 42$  and  $582 \pm 42$ , respectively. At that time JANAF [29] had predicted the dissociation energy of ZrN to be  $368 \text{ kJ mol}^{-1}$ . In subsequent investigations the predictions by the  $\alpha$ -parameters method for the dissociation energies of ZrN [20] and ThN [11] were confirmed. Additional predictions [11] for gaseous transition metal mononitrides were based on  $\alpha = 1.24$  derived from the experimental data for UN, ZrN and ThN. In table 1, the predicted dissociation energies are compared with the corresponding experimental values obtained later. The  $\alpha$ -parameter method has also been used to predict the dissociation energies of selected diatomic metal carbides [12] and borides [13].

Table 1. Predicted dissociation energies of selected diatomic transition metal nitrides using the  $\alpha$ -parameter method and comparison with experimental values subsequently obtained. Values are in  $\text{kJ mol}^{-1}$ .

Molecule MN	$D_{298}^0(\text{MN})$ (Predict.) <sup>a</sup>	$D_{298}^0(\text{MN})$ (Exper.)	Ref. (Exper.)
TiN	$515 \pm 42$	$476.1 \pm 33$	[24]
ZrN	$586 \pm 42^b$	$564.8 \pm 25$	[20]
HfN	$590 \pm 42$	$535 \pm 30$	[25]
ThN	$582 \pm 42^b$	$577.4 \pm 33$	[11]
VN	$485 \pm 42$	$477.4 \pm 17$	[26]
CrN	$402 \pm 42$	$377.8 \pm 19$	[27]

<sup>a</sup>Ref. [11];  $\alpha = 1.24$

<sup>b</sup>Ref. [28]; predictions correspond to  $D_0^0$ .

### 3.2 The Pauling model of a polar single bond

The Pauling model of a polar single bond [30] has been found applicable to heteronuclear diatomic molecules, AB, if the electronegativity difference is less than 1.5 on the Pauling scale.

According to the model, the bond energy,  $D(\text{A-B})$  of a diatomic molecule, AB, may be expressed by the relation:

$$D(\text{A-B}) = 1/2 [D(\text{A-A}) + D(\text{B-B})] + 96(\chi_{\text{A}} - \chi_{\text{B}})^2 \text{ (in kJ mol}^{-1}\text{)} ,$$



where  $D(A-A)$  and  $D(B-B)$  are single bond energies of the component elements A and B, respectively, and  $\chi_A$  and  $\chi_B$  are the respective electronegativities on the Pauling scale [30]. In our laboratory we have studied the applicability of the model to intermetallic compounds, with emphasis on gold containing molecules. In connection with the investigation of  $MAu_2$  molecules [31], we have shown that the model can be applied to each individual bond in the molecule. In table 2 examples for calculated and experimental values are given for some MAu and  $MAu_2$  molecules where both are available [31-35]. A more detailed discussion of the application of the Pauling model and its limitation has been given elsewhere [36].

Table 2. Comparison of the experimental and calculated bond energies of diatomic and triatomic metal-aurides. Values are in  $\text{kJ mol}^{-1}$ .

M	$D_0^0(M-Au)$ (Calcul.) <sup>a</sup>	$D_0^0(M-Au)$ (Exper.)	$D_0^0(M-Au_2)$ (Exper.)	Ref.
Al	274.9	$322.2 \pm 6.3$	$253.1 \pm 12.6$	[32,33]
Eu	274.5	$238.9 \pm 10.5$	$274.9 \pm 8.4$	[34]
Tb	292.9	$289.5 \pm 33.5$	$291.2 \pm 20.9$	[35]
Ho	267.8	$263.6 \pm 33.5$	$266.5 \pm 20.9$	[35]
Lu	297.1	$328.4 \pm 16.7$	$301.2 \pm 16.7$	[31]

### 3.3 Valence bond approach for diatomic intermetallic compounds with multiple bonds

Intermetallic compounds for which the Pauling model predicts too low dissociation energies are diatomic platinum metal molecules with rare earth, actinide or group IV transition metals. In such molecules multiple bond formation is indicated and the experimental dissociation energies can be interpreted by an empirical valence bond approach [15,16]. This empirical method is based on the valence bond theory and is analogous to the one used by Brewer for calculating bond energies per electron in condensed metals [37,38].

Each of the two atoms forming the molecule is promoted to a valence state with two to four unpaired electrons that are suitable for multiple bond formation. Electron pair bonds are then allowed to form between the unpaired electrons of the two atoms in their valence states. The resulting bond energy per electron pair per mole is then taken to be the same as the determined valence state bonding enthalpy per mole of electrons for the corresponding type of electrons in the respective condensed metal. The individual values for the latter are taken from the Brewer curves [38] which show the variation of s or p and d valence state bonding enthalpies per mole of electrons with atomic number and with principal quantum number, and in case of d-electrons, also with the number of d-electrons participating in the bonding. Wengert [39] has also conveniently tabulated such values obtained from the Brewer curves.

The bonding energies of all bonds formed are then added. From this total, the sum of the valence state promotion energies is subtracted. The resulting value represents the calculated dissociation energy. The necessary valence state promotion energies are taken from

the literature [40,41]. They are evaluated in a manner analogous to the one shown by Brewer [38,42]. In table 3 experimental [43-47] and calculated values for some diatomic intermetallic compounds with multiple bonds are compared. The agreement between experimental and calculated values is good with two notable exceptions: one concerns ThRu [45] for which quadruple bond formation was assumed, yielding a calculated value of  $657 \text{ kJ mol}^{-1}$  for the dissociation energy. An assumed triple bond formation would yield a calculated value of  $531 \text{ kJ mol}^{-1}$ . The experimental value  $587.9 \pm 42 \text{ kJ mol}^{-1}$  [45], is between the values calculated assuming a quadrupole bond or triple bond, respectively. Apparently, quadrupole bonding is approached in ThRu(g) but not fully achieved. The second notable exception concerns the platinum compounds. This is a consequence of the lack of a suitable valence state of platinum for triple bond formation; therefore, the calculation had to be based on assumed double

Table 3. Comparison of calculated and experimental dissociation energies of selected diatomic intermetallic compounds with multiple bonds. Values are in  $\text{kJ mol}^{-1}$ .

Molecule	Assumed Bond Order	$D_0^0$ (Calcul.)	$D_0^0$ (Exper.)	Ref.
LaRh	3	540	$525 \pm 17$	[43]
CeRu	3	544	$527 \pm 25$	[16]
CeRh	3	544	$546 \pm 25$	[44]
CePd	2	326	$318 \pm 17$	[22]
CeOs	3	536	$503 \pm 33$	[16]
CeIr	3	565	$581 \pm 25$	[44]
CePt	2	423	$551 \pm 25$	[44]
EuRh	2	272	$230 \pm 33$	[34]
ThRu	4	657	$588 \pm 42$	[45]
ThRh	3	531	$510 \pm 21$	[46]
ThIr	3	556	$571 \pm 42$	[15]
ThPt	2	456	$547 \pm 42$	[15]
TiRh	3	385	$387 \pm 16$	[47]

bond formation. The high experimental bond energies for the platinum compounds suggest a strong interaction between the electron rich 5d orbitals of the platinum and the electron deficient 5d or 6d orbitals of cerium or thorium, respectively, effecting a bond order larger than two. The application of the molecular orbital approach offers further qualitative explanation for these apparent discrepancies. A recent critical discussion of the valence bond approach as applied to multiply bonded intermetallic molecules, its limitations and its range of application, has been given elsewhere [48].

### 3.4 Gaseous Metal Carbides

Several empirical correlations for the bond energies of gaseous metal carbides can be shown. DeMaria and coworkers have extensively discussed the analogy between the  $C_2$ -radical and the oxygen atom (which was proposed originally by Chupka, et al. [49]) and have extended it to the tetracarbides of the rare earth metals. Kohl and Stearns have extended this concept to several d-block transition metal dicarbides and tetracarbides. Balducci, et al. [50] have derived an approximate expression on the basis of this analogy relating the relative concentration of an  $MC_2$  species, with respect to the metal atom at a given temperature, to the dissociation energy of the corresponding monoxide and other thermodynamic data. Gingerich and associates have extended the pseudo oxygen concept of the  $C_2$ -radical to the platinum dicarbides [51,52]. In table 4 the  $M-C_2$  bond energies are compared with those for the corresponding MO molecules taken from Brewer and Rosenblatt [53]. It appears that the  $M-C_2$  bond is somewhat stronger than the corresponding  $M-O$  bond, whereas in case of the more electropositive transition and inner transition metals the  $M-C_2$  bond is somewhat weaker than the corresponding  $M-O$  bond. This observation may be attributed to the less pronounced ionic character of the respective bonds in the platinum metal compounds.

Table 4. Comparison of experimental  $M-C_2$  bond energies with those of the corresponding platinum metal monoxides.

Metal M	$D_o^0(M-C_2)$	$D_o^0(MO)^a$ Ref. [53]	$D(M-C_2)$ Ref.
Ru	$525.5 \pm 38$	$477 \pm 63$	[51]
Rh	$439.3 \pm 21$	$327 \pm 63$	[52]
Os	$575 \pm 29$	$\leq 590$	[16]
Ir	$\leq 494 \pm 42$	$\leq 389$	[51]
Pt	$490 \pm 42$	$343 \pm 33$	[51]

For the transition metal tricarbides,  $MC_3$ , measured by Stearns and Kohl [54] ( $LaC_3$ ) and by Gingerich and associates [55] ( $CeC_3$ ,  $ThC_3$ ), the bond additivity concept can be applied to the assumed  $C-M-C_2$  structure. Here, the atomization energies are obtained by adding the  $M-C$ ,  $M-C_2$  and  $C_2$  bond energies of the individual "component" molecules [55]. In table 5 the atomization energies thus calculated are given for transition metal tricarbides for which experimental or estimated values for the corresponding monocarbide and dicarbide are available.

Table 5. Calculated atomization energies of gaseous metal tricarbonides and comparison with experimental values.

Metal	$D_0^0(MC_2)$ Exper.	$D_0^0(MC)$ Exp. or (est.)	$D_0^0(MC_3)$	
			Calcul.	Exper.
La	$1257 \pm 8^a$	$(502 \pm 63)^b$	1759	$1759 \pm 31$
Ce	$1274 \pm 8^c$	$452 \pm 29^b$	1726	$1800 \pm 33$
Th	$1289 \pm 25^d$	$483 \pm 25^e$	1772	$1840 \pm 33$
Hf	$1258 \pm 28^e$	$\leq 536 \pm 25^e$ ( $544 \pm 63$ ) <sup>b</sup>	1794	
Sc	$1155 \pm 21^f$	$389 \pm 63$	1544	
Ti	$1157 \pm 21^e$	$\leq 432 \pm 25^e$ ( $473 \pm 63$ ) <sup>b</sup>	1589	
V	$1165 \pm 18^g$	$(464 \pm 63)^b$	1629	
Y	$1229 \pm 17^h$	$(414 \pm 63)^b$	1643	
Zr	$1164 \pm 24^e$	$\leq 556 \pm 25^e$ ( $527 \pm 63$ ) <sup>b</sup>	1691	
Ru	$1119 \pm 38^i$	$632 \pm 13^k$	1751	
Rh	$1033 \pm 21^l$	$579 \pm 10^{l,k}$	1612	
Os	$1116 \pm 21^m$	$645 \pm 13^m$	1761	
Ir	$\leq 1088 \pm 42^i$	$623 \pm 11^n$	1711	
Pt	$1084 \pm 42^i$	$605 \pm 11^n$	1689	

References: a[54]; b[12]; c[56]; d[55]; e[19]; f[57]; g[58]; h[59]; i[51]; k[60]; l[52]; m[16]; n[15].

The bond additivity concept may also be expected to apply to the higher cerium carbides  $CeC_5$  and  $CeC_6$  which were observed together with a host of other species over the Ce-Rh-Ru-Os-graphite system [61]. A set of the observed cerium and ruthenium containing species is given in table 6 as an example. The possibility of measuring simultaneously such a large number of vapor components over a dynamic range of six orders of magnitude, under equilibrium conditions, is an unique feature of the method. Only in the case of  $CeC^+$  was there a serious fragmentation problem. In table 7 the atomization energies for the  $CeC_n$  species [61] are listed together with the bond energies  $D(CeC_n) - D(CeC_{n-1})$  that correspond to each successive addition of a C-atom to Ce or a monocerium carbide molecule. The observed alteration of these successive bond energies, e.g., 500-540 kJ mol<sup>-1</sup> for the Ce-C bond and 760-700 for the Ce-C<sub>2</sub> bond is suggestive of one Ce-C bond and two Ce-C<sub>2</sub> bonds in the molecule  $CeC_5$  and of 3 Ce-C<sub>2</sub> bonds in  $CeC_6$ . However, such possibilities as  $C_2M-C_3$  and  $C_3-M-C_3$  structures for  $MC_5$  and  $MC_6$  molecules, respectively, must also be considered. Further investigations into the bonding and structure of such higher transition metal carbides are presently in progress in our laboratory for the uranium, thorium [62] and scandium carbides [63].

Table 6. Set of relative ion currents measured at 2733 K over Ce-Ru-Rh-Os-graphite system with 20 eV electrons for cerium and ruthenium containing species.<sup>a</sup>

Ce <sup>+</sup>	8.37	Ce <sub>2</sub> C <sup>+</sup>	4.5x10 <sup>-5</sup>	Ru <sup>+</sup>	2.63x10 <sup>-1</sup>
CeC <sup>+</sup>	9.68x10 <sup>-3</sup> b	Ce <sub>2</sub> C <sub>2</sub> <sup>+</sup>	9.9x10 <sup>-5</sup>	RuC <sup>+</sup>	2.88x10 <sup>-1</sup>
CeC <sub>2</sub> <sup>+</sup>	8.52	Ce <sub>2</sub> C <sub>3</sub> <sup>+</sup>	1.20x10 <sup>-4</sup>	RuCe <sup>+</sup>	1.83x10 <sup>-2</sup>
CeC <sub>3</sub> <sup>+</sup>	4.90x10 <sup>-2</sup>	Ce <sub>2</sub> C <sub>4</sub> <sup>+</sup>	2.15x10 <sup>-3</sup>	RuCeC <sup>+</sup>	8x10 <sup>-5</sup>
CeC <sub>4</sub> <sup>+</sup>	3.80x10 <sup>-1</sup>	Ce <sub>2</sub> C <sub>5</sub> <sup>+</sup>	3.40x10 <sup>-4</sup>	RuCeC <sub>2</sub> <sup>+</sup>	2.9x10 <sup>-4</sup>
CeC <sub>5</sub> <sup>+</sup>	5.60x10 <sup>-3</sup>	Ce <sub>2</sub> C <sub>6</sub> <sup>+</sup>	6.9x10 <sup>-5</sup>	RuCeC <sub>3</sub> <sup>+</sup>	3x10 <sup>-5</sup> c
CeC <sub>6</sub> <sup>+</sup>	2.20x10 <sup>-3</sup>				

<sup>a</sup> The ion currents correspond to <sup>140</sup>Ce and <sup>102</sup>Ru.

<sup>b</sup> After correction for fragmentation the ion current is ~ 1x10<sup>-3</sup>.

<sup>c</sup> Measured at 2784 K.

Table 7. Atomization energies and derived bond energies of CeC<sub>n</sub> molecules [61] (in kJ mol<sup>-1</sup>).

Molecule	Assumed		D <sub>a,o</sub> <sup>0</sup> (CeC <sub>n</sub> ) -		D <sub>a,o</sub> <sup>0</sup> (CeC <sub>n</sub> )/
	No. of Bonds	D <sub>a,o</sub> <sup>0</sup>	D <sub>a,o</sub> <sup>0</sup> (CeC <sub>n-1</sub> )		No. of Bonds
CeC	1	500	500		500
CeC <sub>2</sub>	2	1263	763		632
CeC <sub>3</sub>	3	1799	536		600
CeC <sub>4</sub>	4	2551	752		638
CeC <sub>5</sub>	5	3074	523		615
CeC <sub>6</sub>	6	3777	703		630

### 3.5 Diatomic group V and VI transition metal molecules

Finally, examples from our current work on diatomic group V and group VI containing transition metal molecules are presented [64]. Thermodynamic, chemical and electronic properties of such molecules are of fundamental relevance to chemisorption and heterogeneous catalysis by highly dispersed transition metals and alloys. However, experimental studies of molecules of the refractory metals, Nb, Mo, W, etc., are either lacking entirely or have been unsuccessful.



We have been able to identify the molecules  $\text{Mo}_2$ ,  $\text{MoNb}$ ,  $\text{Nb}_2$  and  $\text{AuV}$  and determine their dissociation energies (in  $\text{kJ mol}^{-1}$ ) as  $404 \pm 20$  [17],  $448 \pm 25$  [18],  $523 \pm 42$  and  $238 \pm 12$ , respectively. The molecules  $\text{VNb}$ ,  $\text{VMo}$ ,  $\text{CrNb}$  and  $\text{CrMo}$  could not be observed because of the large disparity of the vapor pressure of Nb and Mo and that of V and Cr. For  $\text{CrMo}$  and  $\text{MoV}$  upper limit values for  $D_0^0$  have been derived as 469 and 452, respectively. The investigation of the  $\text{Mo}_2$  molecule [17] is the only example in literature where a second and third law evaluation has been made using data all measured above 2700 K.

---

The author thanks his associates, R. M. Atkins, U. V. Choudary, D. L. Cocke, H. C. Finkbeiner, S. K. Gupta, R. Haque, J. E. Kingcade, and J. Kordis, for their contributions to the results reported and the National Science Foundation and the Robert A. Welch Foundation for their financial support.

#### References

- [1] Ionov, N. I., Dokl. Akad. Nauk SSSR 59, 467 (1948).
- [2] Chupka, W. A. and Inghram, M. G., J. Chem. Phys. 21, 371, 1313 (1953); *ibid.* 22, 1472 (1954); J. Phys. Chem. 59, 100 (1955).
- [3] Honig, R. E., J. Chem. Phys. 22, 126 (1954).
- [4] Inghram, M. G. and Drowart, J., High Temperature Technology, p. 219-240 (McGraw-Hill Book Company, Inc., New York, 1960).
- [5] Grimley, R. T., in Characterization of High Temperature Vapors, J. L. Margrave, ed., p. 195-243 (Wiley-Interscience Publishers, New York, 1967).
- [6] Drowart, J. and Goldfinger, P., Angew. Chem. 79, 589 (1967); Angew. Chem. Intern. Edn. 6, 581 (1967).
- [7] Drowart, J., in Proc. Int. School Mass Spectrom., Lubljana, Yugoslavia, J. Marsel, ed., p. 187-242 (August 19-29, 1969).
- [8] Gingerich, K. A., J. Crys. Growth, 9, 31 (1971).
- [9] Chatillon, C., Pattoret, A., and Drowart, J., High Temp-High Pressures, 7, 119 (1975).
- [10] Stafford, F. E., High Temp-High Pressures, 3, 213 (1971).
- [11] Gingerich, K. A., J. Chem. Phys. 49, 19 (1968).
- [12] Gingerich, K. A., J. Chem. Phys. 50, 2255 (1969).
- [13] Gingerich, K. A., High Temp. Science, 1, 258 (1969).
- [14] Gingerich, K. A., J. Chem. Phys. 53, 746 (1970).
- [15] Gingerich, K. A., Chem. Phys. Letters, 23, 270 (1973).
- [16] Gingerich, K. A., and Cocke, D. L., Inorg. Chimica Acta 28, L171 (1978).
- [17] Gupta, S. K., Atkins, R. M., and Gingerich, K. A., Inorg. Chem. 17 (1978).
- [18] Gupta, S. K. and Gingerich, K. A., J. Chem. Phys. 69 (1978).
- [19] Kohl, F. J. and Stearns, C. A., High Temp. Science, 6, 284 (1974).
- [20] Gingerich, K. A., J. Chem. Phys. 49, 14 (1968).

- 21] Gingerich, K. A., J. Chem. Phys. 54, 2646 (1971).
- 22] Cocke, D. L. and Gingerich, K. A., J. Phys. Chem. 76, 2332 (1972); Erratum, 4042.
- 23] Colin, R. and Goldfinger, P., in Condensation and Evaporation of Solids, E. Rutner, P. Goldfinger and J. P. Hirth, eds., p. 165-179 (Gordon and Breach, New York, 1964).
- 24] Stearns, C. A. and Kohl, F. J., High Temp. Science, 2, 146 (1970).
- 25] Kohl, F. J. and Stearns, C. A., J. Phys. Chem. 78, 273 (1974).
- 26] Farber, M. and Srivastava, R. D., J. Chem. Soc. Faraday I, 69, 390 (1973).
- 27] Srivastava, R. D. and Farber, M., High Temp. Science, 5, 489 (1973).
- 28] Gingerich, K. A., J. Chem. Phys. 47, 2192 (1967).
- 29] JANAF Thermochemical Tables, Sec. Ed., NSRDS-NBS37.
- 30] Pauling, L., The Nature of the Chemical Bond, 3rd Ed. chap. 3. (Cornell Univ. Press, Ithaca, N.Y., 1960).
- 31] Gingerich, K. A., Chem. Phys. Letters, 13, 262 (1972).
- 32] Gingerich, K. A. and Blue, G. D., J. Chem. Phys. 59, 185 (1973).
- 33] Gingerich, K. A., Cocke, D. L., Finkbeiner, H. C., and Chang, C. -A., Chem. Phys. Letters, 18, 102 (1973).
- 34] Cocke, D. L., Gingerich, K. A., and Kordis, J., High Temp. Science, 7, 61 (1975).
- 35] Kordis, J., Gingerich, K. A., and Seyse, R. J., J. Chem. Phys. 61, 5114 (1974).
- 36] Gingerich, K. A., Chimica, 26, 619 (1972).
- 37] Brewer, L., Science, 161, 115 (1968), and references quoted therein.
- 38] Brewer, L., in Phase Stability in Metals and Alloys, P. S. Rudman, J. Stringer, and R. I. Jaffee, eds., p. 39-61, 241-49, 344-46 and 560-68 (McGraw-Hill, New York, 1967).
- 39] Wengert, P. R., Ph.D. Thesis, Table XII (University of California, Berkeley, 1969).
- 40] Moore, C. E., Atomic Energy Levels, Nat. Bur. Stand. U.S. Circular 467, Vols. 1-3 (U.S. Govt. Printing Office, Washington, 1949, 1952, 1958).
- 41] Brewer, L., J. Opt. Soc. Am. 61, 1101 (1971).
- 42] Brewer, L., in High Strength Materials, V. F. Zackay, ed., p. 12-103 (Wiley, New York, 1965).
- 43] Cocke, D. L., Gingerich, K. A., High Temp. Science, 5, 474 (1973).
- 44] Gingerich, K. A., J. Chem. Soc. Faraday Trans. II, 70, 471 (1974).
- 45] Gingerich, K. A., Chem. Phys. Letters, 25, 523 (1974).
- 46] Gingerich, K. A. and Gupta, S. K., J. Chem. Phys. 69, 505 (1978).
- 47] Cocke, D. L. and Gingerich, K. A., J. Chem. Phys. 60, 1958 (1974).
- 48] Gingerich, K. A., Int. J. Quant. Chem. Symposium No. 12, 1978, in press.
- 49] Chupka, W. A., Berkowitz, J., Giese, C. F., and Inghram, M. G., J. Phys. Chem. 62, 611 (1958).
- 50] Balducci, G., DeMaria, G., and Guido, M., Proc. 1st Intern. Conf. Calorimetry and Thermodynamics, p. 415-421 (Polish Scientific Publishers, Warsaw, 1970).
- 51] Gingerich, K. A., J. C. S. Chem. Comm., 198 (1974).
- 52] Cocke, D. L. and Gingerich, K. A., J. Chem. Phys. 57, 3654 (1972).
- 53] Brewer, L. and Rosenblatt, G. M., in Advances in High Temperature Chemistry, L. Eyring, ed. Vol. 2, p. 1-83 (Academic Press, New York, 1969).

- [54] Stearns, C. A. and Kohl, F. J., J. Chem. Phys. 54, 5180 (1971).
- [55] Gingerich, K. A., Chem. Phys. Letters, in press.
- [56] Balducci, G., Capalbi, A., DeMaria, G., and Guido, M., J. Chem. Phys. 50, 1969 (1969).
- [57] Kohl, F. J. and Stearns, C. A., J. Chem. Phys. 54, 1414 (1971).
- [58] Kohl, F. J. and Stearns, C. A., J. Phys. Chem. 74, 2714 (1970).
- [59] Kohl, F. J. and Stearns, C. A., J. Chem. Phys. 52, 6310 (1970).
- [60] McIntyre, N. S., Vander Auwera-Mahieu, A., and Drowart, J., Trans. Faraday Soc. 64, 3006 (1968).
- [61] Gingerich, K. A., Cocke, D. L., and Kingcade, J. E., Inorg. Chimica Acta 17, L1 (1976).
- [62] Gupta, S. K. and Gingerich, K. A., to be published.
- [63] Haque, R. and Gingerich, K. A., to be published.
- [64] Gupta, S. K. and Gingerich, K. A., presented at the Annual ACS Meeting, Miami Beach, Florida, Sept. 10-15, 1978.

### **III. MASS SPECTROMETRIC TECHNIQUES-- HIGH PRESSURE SAMPLING**





## HIGH PRESSURE MOLECULAR BEAM MASS SPECTROMETRIC SAMPLING OF HIGH TEMPERATURE MOLECULES

Carl A. Stearns, Fred J. Kohl, George C. Fryburg, and Robert A. Miller  
National Aeronautics and Space Administration  
Lewis Research Center  
Cleveland, OH 44135

### 1. Introduction

Modern technology is increasingly requiring the characterization of high temperature gaseous environments. Usually, the need is to identify, both qualitatively and quantitatively, all components of the environment in relation to system variables such as temperature, pressure, time, etc. For some systems, such characterization can be a relatively straightforward, albeit arduous, task. However, the task becomes considerably more formidable for high pressure systems, dynamic systems, and systems containing condensable high temperature molecules, unstable gaseous species, or ions.

Mass spectrometry is ideally suited for application to gaseous environment characterization problems because this single technique can be used to measure all species (both stable and unstable) and it provides direct, positive identification. Other spectroscopic techniques may not be applicable to such problems if the species of interest exist at very low concentrations and/or the relevant spectroscopic parameters are unknown.

Because mass spectrometers are low pressure devices, their application to higher pressure systems requires that a sample must be extracted from the system and transferred to the mass spectrometer for analysis. The transfer must be made in such a way that the chemical and dynamic integrity of the sample are not altered in an unpredictable way. This requirement limits the number of sampling techniques that can be employed. Meaningful results cannot be obtained with batch and microprobe methods for systems containing reactive and condensable high temperature species. Knudsen-type sampling through a small diameter orifice is precluded for higher pressure systems because the flow is not effusive. The resulting beam is not a true representation of the source gas: actually, it is mainly characteristic of the boundary layer composition in the region of the orifice. The so-called high pressure free-jet expansion sampling technique appears to satisfy the requirement of not altering the sample's chemical characteristics in an unpredictable way. With this technique, sampling is accomplished (continuously or intermittently) from a high pressure (a few Torr or greater) source through a relatively large orifice into a vacuum. The gas forms a supersonic beam through a free-jet expansion. As the expansion proceeds a molecular beam is formed, which after suitable skimming and collimating, is compatible with the mass spectrometer operating pressure ( $<10^{-5}$  Torr).

The high pressure free-jet expansion sampling technique has been successfully employed by a number of investigators in quite diverse research areas. These applications will be reviewed after the rudimentary theoretical aspects of the technique are established. While the theoretical considerations and review are not intended to be exhaustive, it is our hope that they will serve as a good starting place for the neophyte. Finally, the high pressure sampling apparatus in use at the Lewis Research Center will be described and evaluated. This apparatus has been used in various studies of the chemistry involved in hot corrosion processes. Some of our results will be considered in order to convey the potential of the sampling technique as applied to high temperature gaseous systems.

## 2. Theoretical Aspects of High Pressure Sampling

### 2.1 Beam formation

When sampling a gas system through an orifice that is not in thermodynamic equilibrium with the source gas, the orifice size should be selected to insure that the sample represents the bulk source gas and not a stagnant boundary layer near the orifice. For orifice Knudsen numbers,  $Kn_0$ , less than about  $10^{-2}$ , boundary layer effects are insignificant [1,2]<sup>1</sup> and therefore the orifice diameter,  $D_0$ , should be sized to satisfy the criterion  $Kn_0 < 10^{-2}$  for the source gas and conditions of pressure,  $P_0$ , and temperature,  $T_0$ . The orifice Knudsen number is related to the orifice diameter through the mean free path length,  $\lambda_0$ , of the source gas molecules [3], i.e.,

$$Kn_0 = \frac{\lambda_0}{D_0} \quad (1)$$

When gas flows through an orifice into a lower pressure region, the type of gas flow (effusive, transitional, slip, or continuum) is dictated by the value of  $Kn_0$ . For  $Kn_0 < 10^{-2}$  the source gas expands into the low pressure region by continuum flow [2]. The flow produces a supersonic jet if the pressure ratio across the orifice is greater than about two for most gases [4]. (For most beam systems the pressure ratio is usually made as high as practical,  $>10^4$ , to minimize scattering by background gas in the low pressure region.) The expansion is termed "free-jet" if the orifice has no flow controlling constraints on its down-stream side. Because a finite pressure exists in the low pressure region, the supersonic flow field is bounded by a shock system consisting of a barrel shock and a Mach disk or normal shock front. The flow field and shock system are shown schematically in figure 1. The size and shape of the shock system has been studied by Bier and Hagena ([5] and references cited therein) who showed that these parameters are a function of the pressure ratio across the orifice. Ashkenas and Sherman [6] have established that the location of the

<sup>1</sup>Figures in brackets indicate the literature references at the end of this paper.

Mach disk is independent of the source gas properties. The location of the Mach disk is given by the equation

$$X_M = 0.67 D_0 \left( \frac{P_0}{P_1} \right)^{1/2} \quad (2)$$

where  $X_M$  is the distance downstream from the orifice to the plane of the Mach disk and  $P_1$  is the pressure in the region downstream of the orifice. Thus we see that the higher the pressure ratio, the further downstream the jet proceeds before being interrupted by the normal shock.

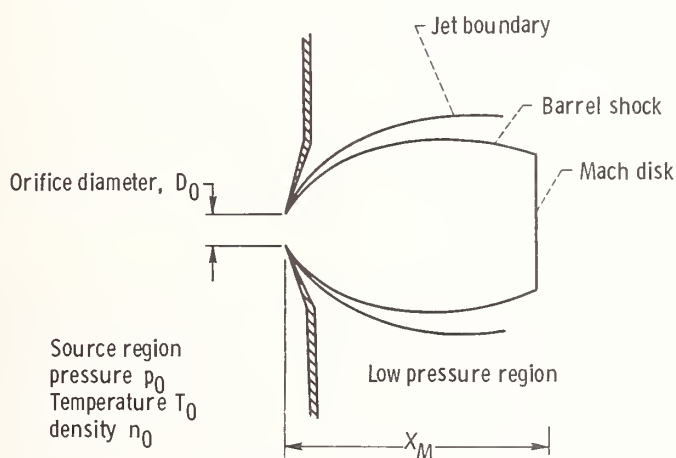


Figure 1. Free-jet expansion shock structure.

## 2.2 Continuum flow beam gas history

The gas history (time or distance-temperature-pressure-density relations) of a free-jet expansion can be approximated as an isentropic expansion where the gas leaves the source as a classical bulk fluid characterized by thermodynamic parameters. In the continuum flow region molecules collide with each other in such a way that the mass flow becomes highly directed and forms a jet. In the flow process the random thermal energy (enthalpy) of the colliding gas molecules is converted to directed kinetic energy and adiabatic cooling of the gas takes place. As the expansion proceeds downstream, the jet density and temperature decrease until a region is reached where collisions become so infrequent that essentially collisionless flow prevails. In this nearly collisionless flow regime a supersonic molecular beam is formed.

A knowledge of the aerodynamics of the supersonic beam is necessary if one expects to estimate the time involved in the beam formation process and the gas history. Extensive research by numerous investigative groups has established an almost complete understanding

of the aerodynamics. Excellent reviews and detailed analyses are contained in the literature ([4,6-10] and references cited therein). Our analysis of the beam formation process as presented here is not intended to start with first principles or be all inclusive. Instead we will deal only with those aspects needed to provide a general background for understanding the general principles of the sampling system.

The one-dimensional compressible flow analysis of a perfect gas with complete relaxation (equilibrium), as provided by fluid mechanics [11], yields the following fundamental isentropic expansion equations relating the expanded gas properties to the flow Mach number,  $M$ , and the source gas properties

$$\frac{n}{n_0} = \left[ 1 + \frac{(\gamma - 1)}{2} M^2 \right]^{1/(1-\gamma)} \quad (3)$$

$$\frac{P}{P_0} = \left[ 1 + \frac{(\gamma - 1)}{2} M^2 \right]^{\gamma/(\gamma-1)} \quad (4)$$

$$\frac{T}{T_0} = \left[ 1 + \frac{(\gamma - 1)}{2} M^2 \right]^{-1} \quad (5)$$

$$\frac{n}{n_0} = \left( \frac{P}{P_0} \right)^{1/\gamma} = \left( \frac{T}{T_0} \right)^{1/(\gamma-1)} \quad (6)$$

The density  $n$ , pressure  $P$ , and temperature  $T$  refer to source conditions when subscripted by zero and to expanded gas conditions at  $M$  when not subscripted. The specific heat ratio for the gas is denoted by  $\gamma$ . For incomplete relaxation, an effective  $\gamma$  may be used. Mach number is defined as the ratio of the local flow velocity,  $V$ , to the local speed of sound in the fluid,  $c$ , i.e.,

$$M = \frac{V}{c} \quad (7)$$

Ashkenas and Sherman [6] have derived an expression relating the centerline flow Mach number to the distance  $X$  downstream in the expansion from the orifice. Their expression is

$$M = A \left( \frac{X}{D_0} - \frac{X_0}{D_0} \right)^{\gamma-1} - \frac{\frac{1}{2} \left( \frac{\gamma+1}{\gamma-1} \right)}{A \left( \frac{X}{D_0} - \frac{X_0}{D_0} \right)^{\gamma-1}} \quad (8)$$

where  $A$  and  $(X_0/D_0)$  are constants whose value depends on  $\gamma$  as shown in table I. From equation (8) it is seen that it is convenient to express distance downstream from the orifice in terms of orifice diameters  $(X/D_0)$ . For distances  $(X/D_0) > 4$ , the centerline Mach number can be approximated by

$$M = A \left( \frac{X}{D_0} \right)^{\gamma-1} \quad (9)$$

for values of  $\gamma = 5/3$ ,  $7/5$ , or  $9/7$ . For Mach numbers large in comparison to unity, Knuth [12] suggests the following equation for all specific heat ratios:

$$M = \left( \frac{2.2}{\sqrt{\gamma(\gamma-1)}} \right)^{(\gamma-1)/2} \left( \frac{\gamma+1}{\gamma-1} \right)^{(\gamma+1)/4} \left( \frac{X}{D_0} \right)^{\gamma-1} \quad (10)$$

TABLE I.- Mach number expansion equation constants [6].

$\gamma$	$X_0/D_0$	A
5/3	0.075	3.26
7/5	.04	3.65
9/7	.85	3.96

While Ashkenas and Sherman's expression (eq. (8)) has been shown experimentally to be quite accurate at several orifice diameters downstream [6,13], it has been shown [13] that this equation does not apply in the transonic region near the orifice. The transonic flow problem is still unsolved but characterization of this flow has been approximated by various sink flow models [10,14], by extrapolation of Ashkenas and Sherman's results [15], and by empirical expressions derived from experimental measurements [4,16]. We have chosen to characterize the flow from the subsonic region upstream of the orifice to the hypersonic region downstream by smoothly extrapolating equation (8) for  $M < 4$  while assuming sonic flow ( $M = 1$ ) at the orifice plane. Although this extrapolation is not based on a physical model, we believe that the results are an adequate approximation for our purposes.

The extrapolation is performed by fitting the Mach number to a third degree polynomial in  $(X/D_0)$ . The polynomial

$$M = a_0 + a_1(X/D_0) + a_2(X/D_0)^2 + a_3(X/D_0)^3 \quad (11)$$

was fitted in two ranges of  $(X/D_0)$  by specifying certain conditions for each range. The first range was  $0 \leq (X/D_0) \leq (X/D_0)_{M=4}$  where  $(X/D_0)_{M=4}$  is the distance for  $M = 4$  as calculated by equation (8). In this range the specified conditions were: (1) the flow is choked by the orifice, i.e.,  $M = 1$  at  $(X/D_0) = 0$ ; (2) a point of inflection exists at the orifice, i.e., at  $(X/D_0) = 0$  the second derivative,  $d^2M/d(X/D_0)^2$ , is zero; (3) at  $M = 4$  the polynomial and equation (8) co-locate; and (4) at  $M = 4$  the polynomial and equation (8) have the same slope. Inspection of the polynomial reveals that condition (1) sets  $a_0 = 1.000$  and condition (2) fixes  $a_2 = 0.000$ .



The second range for fitting the polynomial extended from  $(X/D_0) = 0$  to some distance upstream from the orifice designated  $(X/D_0)_r$  which is the root of the polynomial for the second range. Conditions specified for fitting in this range were: (1) the flow is choked by the orifice, (2) the polynomials for the first and second range co-locate at the orifice, (3) the polynomials have equal slopes at the orifice, (4) the second polynomial has an inflection point at the orifice, and (5) at  $(X/D_0)_r$  the slope is zero.

For all conditions specified, the following general polynomials result for the two ranges

$$\text{Range 1:} \quad M = 1 + a_1(X/D_0) + a_3(X/D_0)^3 \quad (12)$$

$$\text{Range 2:} \quad M = 1 + a_1(X/D_0) - \frac{4}{27} a_1^3 (X/D_0)^3 \quad (13)$$

The root of the second polynomial is  $(X/D_0)_r = -\frac{3}{2a_1}$ , and the polynomials obtained for  $\gamma = 5/3, 7/5$ , and  $9/7$  are presented in table II. The polynomials and equation (8) were used to calculate the Mach number against distance plots shown in figure 2. These curves show,

TABLE II.- Polynomials for extrapolating Mach number to subsonic flow regime.

$\gamma$	Range	Polynomial
5/3	$0 \leq (X/D_0) \leq 1.665$	$M = 1.000 + 1.671(X/D_0) + 0.047_1(X/D_0)^3$
5/3	$-0.897_7 \leq (X/D_0) \leq 0$	$M = 1.000 + 1.671(X/D_0) - 0.691_2(X/D_0)^3$
7/5	$0 \leq (X/D_0) \leq 2.228$	$M = 1.000 + 1.441(X/D_0) - 0.019_0(X/D_0)^3$
7/5	$-1.041 \leq (X/D_0) \leq 0$	$M = 1.000 + 1.441(X/D_0) - 0.443_3(X/D_0)^3$
9/7	$0 \leq (X/D_0) \leq 2.852$	$M = 1.000 + 1.174(X/D_0) - 0.015_0(X/D_0)^3$
9/7	$-1.278 \leq (X/D_0) \leq 0$	$M = 1.000 + 1.174(X/D_0) - 0.239_8(X/D_0)^3$

as we initially assumed, that the gas expansion actually begins slightly upstream of the orifice and this is in substantial agreement with experimental measurements and results obtained by other approximations.

The results presented in figure 2 provide a characterization of the aerodynamics of the free-jet expansion which can be used to estimate the gas history. The hydrodynamic flow velocity is given by

$$V = Mc = D_0 \frac{d(X/D_0)}{dt} \quad (14)$$

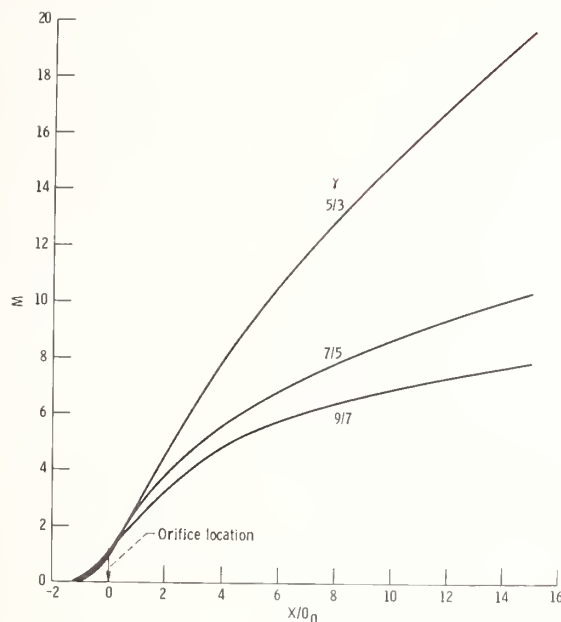


Figure 2. Mach number variation with downstream distance,  $X/D_0$ , for three values of the specific heat ratio  $\gamma$ .

and the speed of sound is a function of the local gas temperature,  $T$ , and molecular weight,  $M$  [3],

$$c = \left( \frac{\gamma R T}{M} \right)^{1/2} \quad (15)$$

where  $R$  is the gas constant ( $8.3143 \text{ J K}^{-1} \text{ mol}^{-1}$ ). For the isentropic expansion the local gas temperature of the jet can be expressed in terms of the source gas temperature (by eq. (5)) giving

$$c = \left( \frac{\gamma R}{M} \right)^{1/2} T_0^{1/2} \left[ 1 + \frac{(\gamma - 1)}{2} M^2 \right]^{-1/2} \quad (16)$$

or

$$c = c_0 \left[ 1 + \frac{(\gamma - 1)}{2} M^2 \right]^{-1/2} \quad (17)$$

where  $c_0$  is the speed of sound in the source gas. From equations (14) and (17) it follows that

$$\frac{c_0}{D_0} dt = \left[ \frac{1}{M^2} + \frac{(\gamma - 1)}{2} \right]^{1/2} d(X/D_0) \quad (18)$$

Integration of this equation yields the time-distance profile for the expanding gas. The profiles obtained by numerical integration of equation (18) for the specific heat ratios 5/3, 7/5, and 9/7 are shown in figure 3. In this figure time is plotted as the dimensionless flow time parameter  $c_0 t/D_0$  and distance is scaled in terms of orifice diameters.

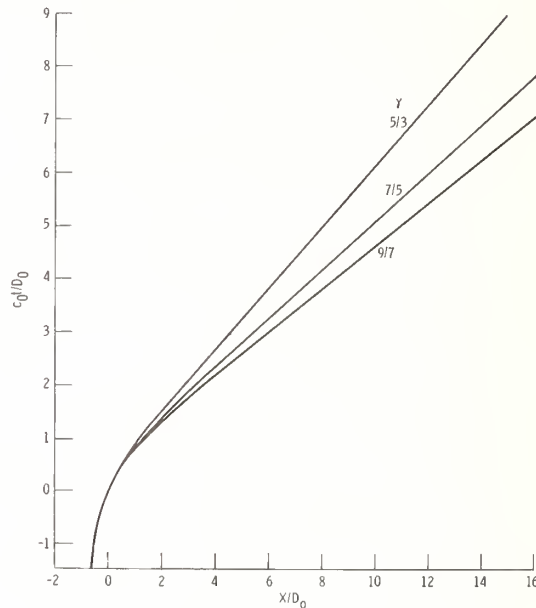


Figure 3. Dimensionless flow time  $c_0 t/D_0$  variation with downstream distance,  $X/D_0$ , for three values of the specific heat ratio  $\gamma$ .

Combining the data of figures 2 and 3 with the appropriate isentropic expansion relation (eqs. (3) to (6)) allows one to determine the temperature, density, or pressure at any point or time in the expansion. These various relations are shown graphically in figures 4 and 5 where the parameters ratioed to source conditions are plotted against time and distance, respectively. While these figures clearly indicate the rapidity of the expansion, a more tangible appreciation of the time involved can be obtained by considering an actual gas on a real time basis. The expansion history of argon source gas expanding through a 0.025 centimeter diameter orifice is shown in figure 6. Here, we see that major reductions in temperature, density, and pressure take place in only a few microseconds. This feature of the free-jet expansion accounts for the applicability of this technique to sampling [14,17].

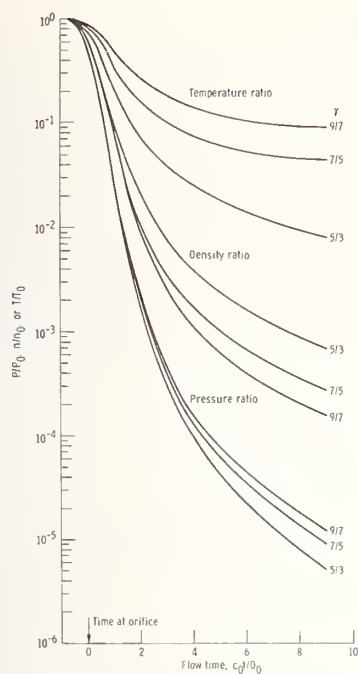


Figure 4. Variation of pressure, density, and temperature with dimensionless flow time for three values of the specific heat ratio  $\gamma$ .

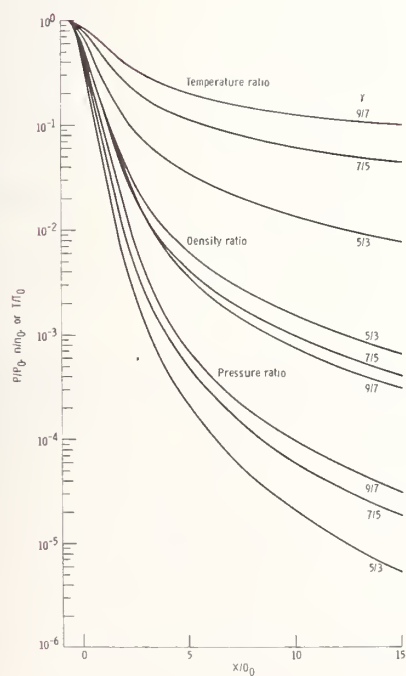


Figure 5. Variation of pressure, density, and temperature with downstream distance for three values of the specific heat ratio  $\gamma$ .

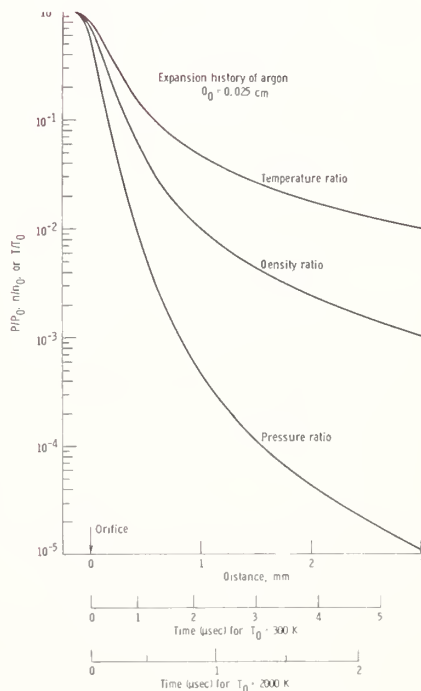


Figure 6. Expansion of argon source gas.

## 2.3 Beam gas history beyond continuum flow region

From the preceding discussion one might intuitively presume that at sufficiently large distances from the jet source the density becomes so low that there are essentially no collisions. Theoretical and experimental studies have shown that there is a limiting region in the flow field beyond which further cooling and acceleration are precluded by the rarefied nature of the flow [4]. Thus, there is a transition from the collision dominated continuum flow to a nearly collisionless molecular flow regime. Extensive effort has been directed to understanding the transition flow regime and as pointed out by Anderson [4] there is a hierarchy of theories. This hierarchy is based on the degree of accuracy and detail provided by the theories. The direct simulation Monte Carlo method as applied by Bird [18] has provided an almost complete understanding of the transition flow regime, but a detailed analysis of this regime is beyond the scope of our presentation. For our purposes it is only necessary to comprehend certain aspects of transition flow. To this end we will consider a simplified treatment which has proven to be adequate for predicting some jet properties.

Anderson and Fenn [19] measured velocity distributions of molecular beams extracted from free jets. They found that the transition to free molecular flow could for convenience be compared to phenomenon occurring in effusive flow. For effusive flow the velocity distribution in the axial direction does not change with increasing distance from the molecular beam source. The axial (parallel) molecular velocity distribution is thus said to be "frozen in." Conversely, the radial (perpendicular) distribution approaches zero with increasing distance from the source. (This is a consequence of the fact that the molecules travel in straight line paths and there are no collisions.) For the effusive source the distribution of velocities is anisotropic with a wide distribution in the parallel direction and a narrow distribution in the perpendicular direction.

For continuum flow the distribution of velocities is isotropic with equal parallel and perpendicular distributions. No freezing of the parallel distribution takes place in continuum flow and the velocity spread of the distribution decreases with increasing distance from the jet source.

In considering expanding source flow it is useful to define a parallel temperature,  $T_{||}$ , and a perpendicular temperature,  $T_{\perp}$ . These are the temperatures of a two-dimensional Maxwellian distribution function which describes the local distribution of molecular speeds in the radial direction and in a direction perpendicular to the radial direction. For continuum flow where the speed distribution is isotropic,  $T_{\perp} = T_{||}$ . The transition flow problem then can be considered as one of determining how  $T_{||}$  and  $T_{\perp}$  vary in the expansion as the transition regime is passed through.

## 2.4 Terminal Mach number

In the "free molecular flow" region of a free-jet expansion Anderson and Fenn [19] showed that a freezing of the parallel distribution occurred. They found non-isotropic distributions where the perpendicular direction had a narrower distribution width than that of the parallel direction. Their model of the transition regime yielded an expression for a



terminal Mach number,  $M_T$ , that was in substantial agreement with their experimental observations and those from other laboratories. The terminal Mach number expression was derived by considering the point in the expansion beyond which the temperature cannot change as rapidly as required for isentropic continuum behavior. The Mach number at this point,  $M_1$ , represents the value where collision domination of the jet flow ceases. The terminal Mach number then represents the asymptotic value which the Mach number approaches at infinite distances downstream from the source. Anderson and Fenn's terminal Mach number can be expressed in the generalized form

$$M_T = \left( \frac{\gamma}{\gamma - 1} \right) \left( \frac{2}{A} \right)^{1/\gamma} \left( \frac{8}{\gamma\pi} \right)^{(\gamma-1)/2\gamma} \left( \frac{Kn_0}{\varepsilon} \right)^{(1-\gamma)/\gamma} \quad (19)$$

where  $A$  is the constant in Ashkenas and Sherman's Mach number expression (eq. (8)) and  $\varepsilon$  is the collision effectiveness. For  $\gamma = 5/3$ ,  $7/5$ , and  $9/7$ , the respective terminal Mach numbers reduce to

$$M_{T(\gamma=5/3)} = 2.03 \left( \frac{Kn_0}{\varepsilon} \right)^{-0.400} \quad (20)$$

$$M_{T(\gamma=7/5)} = 2.48 \left( \frac{Kn_0}{\varepsilon} \right)^{-0.286} \quad (21)$$

$$M_{T(\gamma=9/7)} = 2.85 \left( \frac{Kn_0}{\varepsilon} \right)^{-0.222} \quad (22)$$

Anderson and Fenn's experimental data for  $\gamma = 5/3$  yielded a value for the collision effectiveness of  $\varepsilon = 0.25$ . Their equation for  $M_1$  can be expressed in the generalized form

$$M_1 = \frac{M_T}{\gamma} \quad (23)$$

and the distance from the source orifice to where  $M_1$  is reached can be calculated from equation (8).

## 2.5 Beam intensity

Thus far in our analysis of the beam formation process no consideration has been given to the question of beam intensity. From a practical point of view, intensity is a key parameter if free-jet expansion techniques are to be used in sampling. With a conventional effusive or oven beam source, the maximum attainable intensity in the collimated molecular beam is limited by two factors for any given oven temperature. These factors are: (1) the effusion through the orifice and (2) geometrical factors involved in obtaining a collimated beam from the random initial velocities of the effusing molecules. Kantrowitz and Grey [20] suggested that these limitations could be overcome by placing a collimating element in the

flow from a sonic nozzle. Their analysis indicated that the mass motion from a sonic orifice provides an initial collimation which improves the flow rate and geometrical factors so that a net beam intensification results. Their work provided much of the impetus for development of the free-jet expansion sampling technique.

### 2.5.1 Continuum flow at the skimmer

The Kantrowitz and Grey analysis is based on four critical assumptions: (1) the continuum flow field extends to the first collimating element (hereafter called the skimmer); (2) the continuum flow is isentropic; (3) the flow at the skimmer is parallel and undisturbed by the presence of the skimmer; and, (4) the flow downstream from the skimmer is collisionless. On the basis of these assumptions, and by neglecting the component of the random molecular thermal velocity in the direction of the mass flow, Kantrowitz and Grey derived expressions for the velocity distribution and "precollimation gain" in beam intensity. Parker, et al. [21] made a similar analysis without making the mathematical simplification of neglecting the random thermal velocity component parallel to the beam. For Mach numbers greater than three the results of both analyses are essentially the same.

The axial differential number density can be expressed as

$$\frac{dn(u)}{du} \propto u^2 \exp \left[ - \left( \frac{u - V}{\alpha} \right)^2 \right] \quad (24)$$

where  $u$  is the molecular velocity,  $V$  is the flow velocity, and  $\alpha$  is the most probable thermal velocity at the translational temperature  $T$  which is given by the isentropic flow relation (eq. (5)). The most probable velocity of the supersonic molecular beam,  $u_{mp}$ , is obtained by determining the maximum for the distribution given by equation (24),

$$u_{mp} = \frac{1}{2} \left[ V + (V^2 + 4\alpha^2)^{1/2} \right] \quad (25)$$

Thus it is apparent that for the supersonic beam the distribution is narrower than the Maxwellian distribution for an effusive beam where  $M = 0$  and  $V = 0$ . Also, the supersonic distribution is seen to move to higher velocities and become narrower as  $M$  increases. At the limit of infinite Mach number the distribution is monoenergetic with velocity  $V$ .

The theoretical equation for the centerline flux at a detector, located a distance  $\ell$  downstream from the skimmer, derived by Parker, et al. is given by

$$J_d = \frac{n_s A_s c_0}{4\pi\ell^2} \left[ \frac{M_s (3 + \gamma M_s^2) (1 + \operatorname{erf} \sqrt{\gamma M_s^2/2}) + \sqrt{2/\gamma\pi} (2 + \gamma M_s^2) \exp \left( -\frac{\gamma M_s^2}{2} \right)}{[1 + (\gamma - 1) M_s^2/2]^{1/2}} \right] \quad (26)$$

where  $n_s$  is the density at the skimmer,  $A_s$  is the area of the skimmer orifice, and  $M_s$  is the

Mach number at the skimmer. This equation is based on the four idealization assumptions of Kantrowitz and Grey. For  $M_s > 3$ , the centerline flux at the detector can be approximated by

$$J_d = \frac{n_s A_s c_0}{2\pi\ell^2} \left\{ \frac{M_s (\gamma M_s^2 + 3)}{[1 + (\gamma - 1)M_s^2/2]^{1/2}} \right\} \quad (27)$$

or

$$J_d = \frac{n_s A_s V_s}{2\pi\ell^2} (\gamma M_s^2 + 3) \quad (28)$$

where  $V_s$  is the flow velocity at the skimmer.

Because the mass spectrometer detector used in our apparatus is a density sensitive device, we are concerned with detector signals which are proportional to number density. In terms of number density at the detector,  $n_d$ , equation (28) can be expressed as

$$n_d = \frac{n_s A_s}{2\pi\ell^2} (\gamma M_s^2 + 3) \quad (29)$$

Knuth [10] and Anderson, et al. [19] recognized that beam divergence would affect beam intensity at the detector and derived equations to account for divergence. Their analysis again assumes continuum flow to the skimmer and collisionless flow downstream from the skimmer. For the usually encountered experimental case where the orifice to skimmer distance,  $X_s$ , is much smaller than the skimmer to detector distance,  $\ell$ , Knuth derives the distribution

$$\frac{dn_d}{du} = \frac{2}{\sqrt{\pi}} \left( \frac{X_s}{\ell} \right)^2 n_s \cos \beta \sin \beta \, d\beta \frac{u^2}{\alpha^3} \exp \left\{ - \left[ \frac{u^2}{\alpha^2} - \frac{2u}{\alpha} \cos \beta + S_s^2 \right] \right\} \quad (30)$$

where  $S_s = M_s \sqrt{\gamma/2}$  and  $\beta$  is the half angle subtended by the skimmer at the source as shown in figure 7. When equation (30) is integrated over all velocities,  $u = 0$  to  $u = \infty$ , and over  $\beta$  from 0 to  $\beta$ , a general equation for the number density at the detector results

$$n_d = \left[ \frac{n_s}{4} \left( \frac{X_s}{\ell} \right)^2 \frac{1}{S_s^2} \right] \left[ (1 - 2S_s^2 \cos^2 \beta) (1 + \operatorname{erf} S_s \cos \beta) \exp(-S_s^2 \sin^2 \beta) \right. \\ \left. + \frac{2}{\sqrt{\pi}} (1 - \cos \beta) S_s \exp(-S_s^2) + (2S_s^2 - 1)(1 + \operatorname{erf} S_s) \right] \quad (31)$$

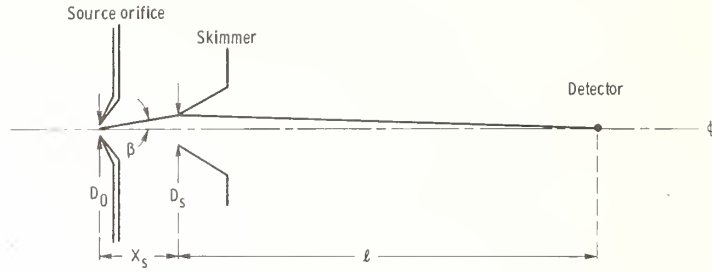


Figure 7. Orifice, skimmer, detector geometry.

For small skimmer openings and high Mach numbers at the skimmer, i.e.,  $\cos \beta \cong 1$ ,  $S_s \cos \beta \gg 1$  and  $2S_s^2 \gg 1$ , equation (31) can be reduced to the more tractable approximate form

$$n_d = n_s \left( \frac{x_s}{\ell} \right)^2 [1 - \cos^2 \beta \exp(-S_s^2 \sin^2 \beta)] . \quad (32)$$

If parallel flow to the skimmer is assumed (i.e., if divergence is neglected) so that  $\sin \beta = \beta$  and  $\cos \beta = 1$ , equation (30) can be integrated to give

$$n_d = \frac{n_s A_s}{2\ell^2 \pi^{3/2}} \left[ \sqrt{\pi} \left( S_s^2 + \frac{1}{2} \right) (1 + \operatorname{erf} S_s) + S_s \exp(-S_s^2) \right] . \quad (33)$$

Equations similar to (32) and (33) have been derived by LeRoy and Govers [22], Hagena and Morton [23], Anderson [4], and French [24]. The above equations can be used to calculate an "idealized" theoretical density at the detector for the case where the skimmer is placed close enough to the source orifice to be in the continuum flow field. In practice however, this case is usually avoided for high pressure sampling systems. Generally, the skimmer is positioned relatively far from the orifice to provide adequate pumping in this region and to reduce skimmer interference. (Usually the experimenter measures intensity as a function of  $X$  to find where the experimental maximum occurs.) Experimental considerations thus dictate the necessity for having skimmer to orifice distances sufficiently large to preclude continuum flow to the skimmer. Therefore, we must now examine the case where the transition from continuum flow takes place upstream of the skimmer.

### 2.5.2 Transition flow upstream of the skimmer

Downstream from the onset of translational freezing a relatively broad velocity distribution is found in the radial direction, and this greatly influences the axial beam intensity at the detector. Experimental determinations of  $T_{\perp}$  show a dependence on orifice to skimmer distance which is intermediate between the collision dominated form ( $T_{\perp} = T_{\parallel} \propto x_s^{-4/3}$ ) and

that expected in the free molecular limit ( $T_{\perp} \propto X_s^{-2}$ ). The variation of  $T_{\perp}$  with downstream distance from the orifice has been attributed to the removal of collision partners from the beam core caused by the relatively large transverse velocities imparted by collisions after the onset of translational freezing [25].

Hamel and Willis [26] presented a physical explanation of the situation which is useful to follow. As the gas expands  $T_{\perp}$  decreases due to the geometrical effect of the source flow spherical expansion but in the collision dominated range energy is transferred between the parallel and perpendicular modes of motion because  $T_{\parallel} > T_{\perp}$ . The collisional drain of energy cools  $T_{\parallel}$  so in the collision dominated limit  $T_{\parallel} = T_{\perp}$  and these temperatures vary in proportion to the reciprocal of the distance from the orifice to the 4/3 power. As collisions become less frequent  $T_{\perp}$  still decreases due to geometric expansion but collisional cooling of  $T_{\parallel}$  decreases and eventually freezes. A relatively small collisional transfer of energy still takes place after translational freezing occurs, but because  $T_{\parallel} \gg T_{\perp}$  this has a small effect on  $T_{\parallel}$ , but a discernible effect on the perpendicular temperature and  $T_{\perp}$  does not decay as expected in the free molecular case. Thus, collisions are more effective in the rarefied regime in inhibiting the decay of  $T_{\perp}$ . Therefore,  $T_{\perp}$  does not decrease as the reciprocal of distance squared as expected in the free molecular limit.

From the preceding discussion we can see that the beam core does not become collisionless and this effects the intensity at the detector. Sharma, et al. [27] and LeRoy, et al. [25] give the expression for the density at the detector as

$$n_d = n_s \left( \frac{X_s}{\ell} \right)^2 \left[ 1 - \exp \left( -S_{\perp}^2 \beta^2 \right) \right] \quad (34)$$

where  $S_{\perp}$  is the perpendicular speed ratio at the skimmer, i.e., the flow speed divided by the most probable random speed perpendicular to the flow velocity at the skimmer. In the derivation of equation (34) it was assumed that  $X_s \ll \ell$ ,  $\sin \beta = \beta$  and  $\cos \beta = 1$ . Remembering that  $S = M\sqrt{\gamma/2}$  and approximating  $\beta = r_s/X_s$ , where  $r_s$  is the radius of the skimmer opening, equation (34) can be written as

$$n_d = n_s \left( \frac{X_s}{\ell} \right)^2 \left[ 1 - \exp \left( -M_{\perp}^2 \frac{\gamma}{2} \frac{r_s^2}{X_s^2} \right) \right]. \quad (35)$$

We shall use this equation to calculate idealized theoretical densities because it is relatively easy to apply and because the comparisons made by LeRoy and Govers [22] indicate that it is a reasonable approximation for our purposes.

When using equation (35) we use two different methods of determining  $M_{\perp}$ . The first method is based on a sudden freeze approximation while the second method is based on expressions derived by Sharma, et al. [27] from correlations with experimental data. The first method, when applied to our experimental conditions, yields theoretical densities



which are about three times greater than our experimentally measured densities. However, the second method predicts theoretical densities which are in good agreement with our experimental measurements.

#### (1) Sudden freeze approximations for $M_{\perp s}$

For this method the expansion is assumed to be isentropic to some distance,  $X_q$ , downstream from the orifice. When the orifice to skimmer distance,  $X_s$ , is greater than  $X_q$ , the Mach number at  $X_q$  is taken as the terminal Mach number, i.e.,  $M_T = M_q$ , and

$$M_q = A \left( \frac{X_q}{D_0} \right)^{\gamma-1} . \quad (36)$$

This use of  $M_T$  is equivalent to assuming continuum flow upstream of  $X_q$  and molecular flow downstream from this point. With this assumption it follows that  $T_{\perp}/T_q = (X_q/X_s)^2$ , where  $T_q$  is the translational temperature at  $M_q$  calculated from isentropic relations, and

$$M_{\perp s} = M_q \left( \frac{X_s}{X_q} \right) . \quad (37)$$

At  $X_q$  the density  $n_q$  is calculated from

$$n_q = n_0 \left[ 1 + \frac{(\gamma-1)}{2} M_q^2 \right]^{1/(1-\gamma)} \quad (38)$$

and the density at the skimmer is assumed to decrease according to

$$n_s = n_q \left( \frac{X_q}{X_s} \right)^2 . \quad (39)$$

Therefore, the idealized density at the detector can be calculated for a given system geometry and source gas conditions, i.e., given  $X_s$ ,  $\ell$ ,  $D_0$ ,  $r_s$ ,  $\gamma$ ,  $n_0$ ,  $P_0$ , and  $T_0$ .

#### (2) Experimental Correlations for $M_{\perp s}$

Sharma, et al. [27] correlate experimental results for monatomic gases to obtain equations for calculating  $M_{\perp s}$ . The data on perpendicular temperatures indicate that this temperature decreases as though the expansion were isentropic to a transition point located several times as far from the source as is the point at which  $T_{\parallel}$  begins to deviate for an isentropic expansion. The distance downstream from the source orifice to this transition point is given by

$$\frac{x_{j1}}{D_0} = 4.58 \left( \frac{D_0}{\tau_0 c_0} \right)^{0.6} \quad (40)$$

where  $\tau_0$  is the characteristic time for translational relaxation of the gas species as given by

$$\tau_0 = \frac{15}{8} \left( \frac{1}{\sqrt{2} n_0 \pi \sigma^2} \right) \left( \frac{\pi M}{8RT_0} \right)^{1/2} \quad (41)$$

Here  $\sigma$  is the collision diameter and  $M$  is the molecular weight of the source gas at temperature  $T_0$  and with density  $n_0$ . From the argon jet data of Habets, et al. [28], Sharma, et al. develop the expression

$$M_{1s} = \frac{2.50}{\sqrt{Y}} \left( \frac{D_0}{\tau_0 c_0} \right)^{-0.2} \left( \frac{x_s}{D_0} \right) \quad (42)$$

For the second method of calculation equation (42) is used to obtain the value of  $M_{1s}$  used in equation (35) and  $n_s$  is calculated exactly the same as for method one.

## 2.6 Other considerations

The idealized conditions assumed in the preceding analyses are not entirely realized in practice and a variety of aerodynamic and other effects can operate to reduce beam intensity and alter sample integrity. These error-inducing effects include shocks, non-ideal expansion (boundary layer contamination and other wall-induced effects), Mach number focusing, skimmer interactions, background scattering, diffusive species separation, chemical reactions, chemical relaxation, and condensation. Most of these effects are related to the beam formation and propagation process. Other sources of error can be associated with sampling probe-gas system interactions and the mass spectrometer-ion source-detector combination. The relevancy to any individual investigator of each error-inducing effect depends in large measure on the nature and objective of the particular experimental investigation. The state-of-the-art of high pressure mass spectrometric sampling is advanced to the point where it is now possible to diagnose and adequately take into account most sources of error. Each error-inducing effect should be dealt with in the design, construction, evaluation, and application of a particular experimental apparatus. Those effects which alter beam intensity are readily handled by in situ calibration techniques [29-32]. Of more concern are effects which complicate the interpretation of data or alter the integrity of the sample. The scope of such effects and estimates of their magnitude have been made by a number of investigators [10,27,32-48].

### 3. Review of Applications

Numerous versions of the high temperature, high pressure, free-jet expansion molecular beam mass spectrometric sampling technique have been used successfully in quite diverse research areas. A summary of these past studies is given in table III. The general, if somewhat arbitrary, criteria used in setting up table III were: (1)  $T_0 > 500^\circ\text{C}$ , (2)  $P_0 > 1$  Torr, (3)  $Kn_0 < 10^{-2}$ , and (4) use of a mass spectrometer as a detector. Because these are only approximate criteria, some of the work cited does not satisfy all four requirements. The citations are presented in an approximately chronological order. Table III should be considered as an updated supplement to more general reviews of high pressure sampling presented previously by Milne and Greene [17,47,169] and Knuth [10]. No attempt was made in table III to include work devoted only to the aerodynamics associated with free-jet expansion, etc.

As is evident from table III, one of the most fertile areas of investigation has been the chemical characterization of combustion systems. Reviews of the flame structure studies of uncharged species have been presented recently by Hastie [45] and Biordi [133,134]. It is apparent from the literature that early applications of the technique to high temperature studies were devoted almost exclusively to sampling stable reactants and products, free radical, and intermediate molecules in laboratory flames. Combustion-type applications have now been extended to include studies of liquid and solid rocket propellant systems, internal combustion engines, N- and S-containing pollutant formation, coal-dust flames, and chemically-inhibited flames. Flames have also been used as wall-less containers for the study of chemical equilibria and for the derivation of thermodynamic properties for metal-containing molecules. Considerable effort has been devoted to the sampling of ions in flames where ion extraction and focusing present additional complications to the technique.

Other more recent applications include studies of gas-surface reactions, chemical vapor deposition systems, high pressure flow reactors and transpiration systems, thermal decomposition of solids, and laser pyrolysis of solids.

### 4. Lewis Research Center Apparatus

#### 4.1 General description

The high pressure modulated molecular beam mass spectrometric sampler being used at the Lewis Research Center was built to facilitate sampling and characterization of gaseous molecular species from various sources at pressures up to one atmosphere. The need for the apparatus derived from our desire to study certain chemical reactions considered fundamental in the hot corrosion process which can occur in gas turbine engines. Envisioned experiments would involve the sampling of doped flames and flowing gas reaction tube systems. Species to be directly identified and measured would include stable gases, reactive intermediates associated with flames, and metal-containing high temperature molecules. Therefore, prerequisites for the apparatus were: (1) capability of sampling systems at atmospheric pressure, (2) capacity to sample condensable high temperature gaseous species, (3) mass

TABLE III.- Summary of high pressure, high temperature molecular beam mass spectrometer sampling investigations. References marked with an \* give descriptions of the apparatus.

Organization; Personnel	Type of Study	Source Pressure	Species Observed	Reference
Shell Development; Eltenton	Low pressure flames and thermal decom- position of hydro- carbons	30-120 torr 0.01-100 torr	Combustion products, radicals, $\text{CH}_3$ , $\text{CH}_2\text{O}$ , $\text{C}_2\text{H}_5$ Decomposition products, radicals, $\text{CH}_3$	49 50*
John Hopkins Univ.; Foner, Hudson	$\text{H}_2/\text{O}_2$ , $\text{CH}_4/\text{O}_2$ flames	60,76 torr	Combustion products, radicals, $\text{CH}_3$ , $\text{H}$ , $\text{OH}$ , $\text{C}_2\text{H}_2$ , $\text{CO}$ , $\text{C}$ , $\text{CH}_2\text{O}$ , $\text{C}_2\text{H}_6$ , $\text{CH}_4\text{O}$ , $\text{C}_4\text{H}_2$	51*
Univ. Cambridge; Knewstubb, Sugden	(1) $\text{C}_2\text{H}_2/\text{O}_2/\text{N}_2$ , $\text{C}_2\text{H}_4/\text{O}_2/\text{N}_2$ , $\text{CH}_4/\text{O}_2/\text{N}_2$ , $\text{C}_2\text{H}_3\text{O}_2/\text{O}_2/\text{N}_2$ flames (2) $\text{H}_2/\text{O}_2/\text{N}_2$ flame (3) Metal-seeded $\text{H}_2/\text{O}_2/\text{N}_2$ flames (4) $\text{H}_2/\text{O}_2/\text{N}_2/\text{C}_2\text{H}_2$ flame (5) $\text{CH}_4/\text{O}_2$ flame (6) $\text{CO}/\text{O}_2/\text{C}_2\text{H}_2$ flame (7) $\text{C}_2\text{H}_2/\text{O}_2/\text{N}_2$ , $\text{CH}_4/\text{O}_2/\text{N}_2$ flames	1 atm 1 atm 1 atm 1 atm 1 atm 1 atm 1 atm	Many ions  $\text{H}_3\text{O}^+$ , $\text{NH}_4^+$ , $\text{NO}^+$  $\text{OH}^-$ , $\text{Cl}^-$ , $\text{NO}_2^-$ , $\text{CO}_3^-$ , $\text{O}^-$ , $\text{O}_2^-$ , $\text{OH}_2\text{O}^-$ , $\text{HO}_2^-$ , $\text{C}_2\text{O}_2\text{H}^-$ , $\text{HCO}_3^-$ , $\text{NO}_3^-$ , $\text{O}_3^-$ , $\text{SO}_2^-$  Many ions  Negative ions, $\text{C}_2\text{H}_3\text{O}^+$ , $\text{CH}_3^+$ , $\text{CH}_3\text{O}^+$ , $\text{C}_2\text{HO}^+$ , $\text{C}_3\text{H}_3^+$ , $\text{H}_3\text{O}^+$ , $\text{CHO}^+$  $\text{CHO}^+$ , $\text{H}_3\text{O}^+$ , $\text{O}^-$ , $\text{CO}_3^-$ , $\text{Cl}^-$  $\text{H}_2\text{CN}^+$ , $\text{H}_3\text{O}^+$ , $\text{CN}^-$ , $\text{Cl}^-$ , $\text{NO}^+$ , $\text{NH}_4^+$ , $\text{C}_3\text{H}_3^+$	52  53*  54 55  56,59  57 58
Shell Research; Sugden, et al.				
Morley				

TABLE III.- Continued

Organization; Personnel	Type of Study	Source Pressure	Species Observed	Reference
Univ. Louvain; Deckers, van Tiggelen, et al.	(1) C <sub>2</sub> H <sub>2</sub> /O <sub>2</sub> /N <sub>2</sub> flame	40 torr	H <sub>3</sub> O <sup>+</sup> , H <sub>2</sub> O <sup>+</sup> , CO <sup>+</sup> , NO <sup>+</sup>	60*
	(2) Hydrocarbon/O <sub>2</sub> /N <sub>2</sub> flames, C <sub>2</sub> H <sub>2</sub> /N <sub>2</sub> O/O <sub>2</sub> , C <sub>2</sub> H <sub>2</sub> /NH <sub>3</sub> /O <sub>2</sub> /N <sub>2</sub> , C <sub>2</sub> H <sub>3</sub> Cl/O <sub>2</sub> flames	10-40 torr to 1 atm	Many ions	61, 62, 63
	(3) NH <sub>3</sub> /O <sub>2</sub> /N <sub>2</sub> flame	1 atm	NH <sub>4</sub> <sup>+</sup> , H <sub>3</sub> O <sup>+</sup> , NO <sup>+</sup> , HNO <sup>+</sup>	65
Peeters, Mahnen	(4) CH <sub>4</sub> /O <sub>2</sub> flames	40 torr	CH <sub>4</sub> , O <sub>2</sub> , CO, CO <sub>2</sub> , H <sub>2</sub> O, CH <sub>2</sub> O, CH <sub>3</sub> , CH <sub>3</sub> O <sub>2</sub> , CH <sub>3</sub> OH, O, OH, H <sub>2</sub> , H, HO <sub>2</sub> , CHO	43* 67
	(5) C <sub>2</sub> H <sub>2</sub> /O <sub>2</sub> /Ar flames	40 torr	C <sub>2</sub> H <sub>2</sub> , O <sub>2</sub> , CO, H <sub>2</sub> O, CO <sub>2</sub> , OH, H <sub>2</sub> , O, H, CH <sub>2</sub> O, CH <sub>3</sub> , C <sub>2</sub> H <sub>2</sub> O, CH <sub>2</sub> , C <sub>2</sub> H <sub>3</sub> , C <sub>2</sub> H <sub>4</sub> O, C <sub>2</sub> H <sub>4</sub> OH, Ar, CH, CH <sub>2</sub> , C	64, 69
	(6) CO/H <sub>2</sub> /O <sub>2</sub> flame	40 torr	CO, H <sub>2</sub> , O <sub>2</sub> , CO <sub>2</sub> , H <sub>2</sub> O, O, H, OH, HO <sub>2</sub>	66
	(7) C <sub>2</sub> H <sub>4</sub> , C <sub>2</sub> H <sub>6</sub> , CH <sub>4</sub> / O <sub>2</sub> /N <sub>2</sub> , Ar flames	16.5, 18-43 torr	NO, O, OH, H, CH, CH <sub>2</sub> , C <sub>2</sub> , C <sub>2</sub> H, C, CH <sub>2</sub> O, plus combustion products	67, 68
	(1) He-, Ne-, Ar-seeded CH <sub>4</sub> /air flames	1 atm	Combustion products, He, Ne, Ar	70*, 71*
Midwest Reserach Institute; Milne, Greene, Beachey	(2) BCl <sub>3</sub> /H <sub>2</sub> /O <sub>2</sub> flame	1 atm	Combustion products, Cl, HCl HB02	14, 70*, 71*
	(3) Cl <sub>2</sub> /CO/O <sub>2</sub> /Ar flame	1 atm	Combustion products, Cl, Cl <sub>2</sub> , O	14, 70*, 71*, 74*
	(4) CH <sub>4</sub> /O <sub>2</sub> /Ar flame	1 atm	H <sub>2</sub> , H <sub>2</sub> O, CO, O <sub>2</sub> , CO <sub>2</sub> , Ar, O, OH	14, 73, 74*, 76*, 81*



TABLE III.- Continued

Organization; Personnel	Type of Study	Source Pressure	Species Observed	Reference
Midwest Research Institute; Milne, Greene, Beachey (Cont.)	(5) H <sub>2</sub> /O <sub>2</sub> /N <sub>2</sub> flame	1 atm	O, OH, O <sub>2</sub> , H <sub>2</sub> O, H, H <sub>2</sub> , N <sub>2</sub> , NO	14,73,74*
	(6) CH <sub>3</sub> Br-seeded CH <sub>4</sub> /O <sub>2</sub> flame	1/20 atm	Combustion products, HBr, Br	72,74*
	(7) CO <sub>2</sub> -, HCl-seeded H <sub>2</sub> /O <sub>2</sub> /N <sub>2</sub> flames	1 atm	Combustion products, HCl, Cl, H	73
	(8) H <sub>2</sub> S-, SO <sub>2</sub> -seeded H <sub>2</sub> /O <sub>2</sub> flames	1 atm	Combustion products, SO, S, SO <sub>2</sub> , SH, SH <sub>2</sub>	73
	(9) TiCl <sub>4</sub> -seeded C <sub>2</sub> N <sub>2</sub> /O <sub>2</sub> flame	1 atm	Cl	74*
	(10) Hg/Ar, Li/Ar, CsCl/Ar	1 atm	Hg, Ar, Hg <sub>2</sub> , Li, Li <sub>2</sub> , CsCl, Cs <sub>2</sub> Cl <sub>2</sub>	75
	(11) CO/O <sub>2</sub> flame	1 atm	O, O <sub>2</sub> , CO, CO <sub>2</sub>	73,74*,76*
	(12) Heated He, Ar	1 atm	He, Ar	76*
	(13) Heated C <sub>4</sub> H <sub>10</sub> /Ar	up to 1 atm	Butane plus fragment ions in M.S.	48*
	(14) Coal dust/air flames	1 atm	CO <sub>2</sub> , H <sub>2</sub> O, O <sub>2</sub> , N <sub>2</sub> , NO, HCN, NO <sub>2</sub> , H <sub>2</sub> S, SO, SO <sub>2</sub> , CH <sub>4</sub> , K, KOH	77*,78,79, 80,82*
	(15) K-, P-inhibited CH <sub>4</sub> /air flames	1 atm	K, KOH, P, PO	78
	(16) KHC0 <sub>3</sub> -seeded CH <sub>4</sub> /air flame	1 atm	K, KOH(?), combustion products	79
	(17) Laser plume from polymers, composites	1 atm	Combustion and pyrolysis products, hydrocarbons, boron oxides	183*

TABLE III.- Continued

Organization; Personnel	Type of Study	Source Pressure	Species Observed	Reference
Univ. Göttingen; Homann, Wagner, et al.	(1) Hydrocarbon flames	20 - 60 torr	Combustion products, CH <sub>2</sub> , CH <sub>3</sub> , C <sub>2</sub> H, C <sub>3</sub> H <sub>2</sub> , C <sub>4</sub> H, C <sub>2</sub> H <sub>5</sub> , others	83*, 84
	(2) Oxidation of CS <sub>2</sub>	1-60 torr	CS <sub>2</sub> , O <sub>2</sub> , CO, CO <sub>2</sub> , SO <sub>2</sub> , O, S, CS, SO, COS, S <sub>2</sub> O, S <sub>2</sub> O <sub>2</sub> , S <sub>2</sub> -S <sub>8</sub> , Ar	85*
	(3) CCl <sub>2</sub> F <sub>2</sub> /F <sub>2</sub> flame	77 torr	CCl <sub>2</sub> F <sub>2</sub> , F <sub>2</sub> , ClF, CClF <sub>3</sub> , Cl <sub>2</sub> , CF <sub>4</sub> , HCl	86
	(4) C <sub>2</sub> H <sub>4</sub> /O reaction	1.8-4.8 mbar	O <sub>2</sub> , C <sub>2</sub> H <sub>2</sub> , CO, H, C <sub>3</sub> H <sub>4</sub> , C <sub>4</sub> H <sub>2</sub> , C <sub>6</sub> H <sub>2</sub> , C <sub>4</sub> H <sub>4</sub> , CH <sub>2</sub> O, C <sub>4</sub> H <sub>6</sub> , C <sub>5</sub> H <sub>4</sub> , C <sub>8</sub> H <sub>2</sub> , CH <sub>2</sub> , C <sub>2</sub> H <sub>2</sub> O, C <sub>3</sub> H <sub>6</sub> , C <sub>3</sub> H <sub>4</sub>	87
AeroChem; Calcote	(1) C <sub>2</sub> H <sub>2</sub> /O <sub>2</sub> flame	1-6 torr	Ions, H <sub>3</sub> O <sup>+</sup> , C <sub>3</sub> H <sub>3</sub> <sup>+</sup> , C <sub>2</sub> H <sub>2</sub> O <sup>+</sup> , C <sub>3</sub> H <sub>6</sub> <sup>+</sup>	88*, 89*
Jensen	(2) Alkali-, B-seeded H <sub>2</sub> /O <sub>2</sub> /N <sub>2</sub> flames	1 atm, 100 torr	Li <sup>+</sup> , Na <sup>+</sup> , K <sup>+</sup> , BO <sub>2</sub> <sup>-</sup> , BO <sup>-</sup> , Cl <sup>-</sup>	90, 93, 98
	(3) Sn-seeded H <sub>2</sub> /O <sub>2</sub> /N <sub>2</sub> flames	1 atm	SnOH <sup>+</sup> , Sn <sup>+</sup>	91
	(4) K-, W-seeded H <sub>2</sub> /O <sub>2</sub> /N <sub>2</sub> flames	1 atm	WO <sub>3</sub> <sup>-</sup> , HWO <sub>4</sub> <sup>-</sup>	92*
Miller, Jensen	(5) K-, Mo-seeded H <sub>2</sub> /O <sub>2</sub> /N <sub>2</sub> flames	1 atm	MoO <sub>3</sub> <sup>-</sup> , HMoO <sub>4</sub> <sup>-</sup>	94
	(6) K-, Cr-seeded H <sub>2</sub> /O <sub>2</sub> /N <sub>2</sub> flames	1 atm	Cl <sup>-</sup> , CrO <sub>3</sub> <sup>-</sup> , HCrO <sub>3</sub> <sup>-</sup> , CrO <sub>2</sub> <sup>-</sup>	95
	(7) K-, Re-seeded H <sub>2</sub> /O <sub>2</sub> /N <sub>2</sub> flames	1 atm	ReO <sub>3</sub> <sup>-</sup> , ReO <sub>4</sub> <sup>-</sup>	96
Gould, Miller				

TABLE III.- Continued

Organization; Personnel	Type of Study	Source Pressure	Species Observed	Reference
Rocket Propulsion Establishment (Cont.); Jensen, Jones	(8) Sr-seeded H <sub>2</sub> /O <sub>2</sub> /N <sub>2</sub> flames (9) K-, Cs-, HCl-seeded H <sub>2</sub> /O <sub>2</sub> /N <sub>2</sub> flames	1 atm 1 atm 100 torr	Sr <sup>+</sup> , SrOH <sup>+</sup> K <sup>+</sup> , Cs <sup>+</sup> , OH <sup>-</sup> , Cl <sup>-</sup>	97 99
Univ. Cambridge; Hayhurst, Kittelston, Telford, Burdett	(1) Salt-seeded H <sub>2</sub> /air flames (2) Salt-seeded H <sub>2</sub> /O <sub>2</sub> /N <sub>2</sub> flames	1 atm 1 atm	OH <sup>-</sup> , Cl <sup>-</sup> , K <sup>+</sup> , Na <sup>+</sup> , Li <sup>+</sup> , H <sub>3</sub> O <sup>+</sup> , NH <sub>4</sub> <sup>+</sup> , KH <sub>2</sub> O <sup>+</sup> , NaH <sub>2</sub> O <sup>+</sup> , LiH <sub>2</sub> O <sup>+</sup> Na <sup>+</sup> , K <sup>+</sup> , Cs <sup>+</sup> , OH <sup>-</sup> , Cl <sup>-</sup> , Br <sup>-</sup> , I <sup>-</sup> , I <sup>+</sup> , ClH <sub>2</sub> O <sup>-</sup> , Br <sup>+</sup> , Br <sub>2</sub> <sup>+</sup> , IH <sub>2</sub> O <sup>+</sup> , I <sub>2</sub> <sup>+</sup> , I <sup>+</sup> 2, H <sub>3</sub> O <sup>+</sup> , Ca <sup>+</sup> , Sr <sup>+</sup> , CaOH <sup>+</sup> , SrOH <sup>+</sup> , Li <sup>+</sup> , MH <sub>2</sub> O <sup>+</sup> , MOH(H <sub>2</sub> O) <sup>+</sup> 1,2,3,4; M = alkali	100* 101*,102, 103,105, 106,107, 110*,113, 114
Univ. Sheffield; Hayhurst, Burdett, Morley, Telford	(3) CHCl <sub>3</sub> -, CCl <sub>4</sub> - NO- seeded H <sub>2</sub> /C <sub>2</sub> H <sub>2</sub> , CH <sub>4</sub> /O <sub>2</sub> /N <sub>2</sub> , Ar flames	1 atm	Na <sup>+</sup> , H <sub>3</sub> O <sup>+</sup> , NO <sup>+</sup> , Cl <sup>-</sup>	104,108, 109,111, 112,115
Univ. California, Berkeley; Sawyer, et al.	Hydrazine/chlorine pentafluoride flame	20 atm	HF, HCl, N <sub>2</sub> , NH <sub>3</sub> , H <sub>2</sub> , ClF, O <sub>2</sub> , Ar, H <sub>2</sub> O.	116*
UCLA; Knuth, Young, et al.	(1) Arc-heated Ar (2) Internal combustion engine (3) CH <sub>4</sub> /air flame	1 atm <323 PSIA 1 atm	Ar N <sub>2</sub> , O <sub>2</sub> , C <sub>3</sub> H <sub>8</sub> , CO <sub>2</sub> , H <sub>2</sub> O, NO, CO N <sub>2</sub> , NO, CO, CO <sub>2</sub> , O, O <sub>2</sub> , H <sub>2</sub> CO, HCO	117 10*,117, 118*,119* 120*

TABLE III.- Continued

Organization; Personnel	Type of Study	Source Pressure	Species Observed	Reference
Arnold Engineering Development Center; MacDermott, Dix McCay, Powell, Busby	(1) Low density wind tunnel	3.7-20.8 atm	N, O, N <sub>2</sub> , NO, O <sub>2</sub> , Ar	121*
	(2) MMH/N <sub>2</sub> O <sub>4</sub> rocket engine exhaust		Combustion products	122*, 123*
Edwards Air Force Base; Goshgarian, et al.	(1) CH <sub>4</sub> /O <sub>2</sub> /Ar flame	1 atm	Combustion products, O, OH, C <sub>2</sub> H <sub>2</sub>	30*
	(2) Fluorocarbon/F <sub>2</sub> / NH <sub>3</sub> flame	1 atm	N <sub>2</sub> , CF <sub>4</sub> , CF, CF <sub>2</sub> , C <sub>4</sub> F <sub>8</sub> , C <sub>3</sub> F <sub>8</sub> , F <sub>2</sub> , HF, FCN, COF <sub>2</sub> , C <sub>2</sub> N <sub>2</sub> , NF <sub>3</sub>	124*
Bureau of Mines; Biordi, Lazzara, Papp	(1) CF <sub>3</sub> Br-CH <sub>4</sub> /O <sub>2</sub> /Ar flames	32 torr	CH <sub>4</sub> , O <sub>2</sub> , CO, CO <sub>2</sub> , H <sub>2</sub> O, H <sub>2</sub> , H <sub>2</sub> CO, CF <sub>3</sub> Br, HBr, Br, HF, COF <sub>2</sub> , OH, CH <sub>2</sub> CF <sub>2</sub> , H, O, CH <sub>3</sub> , HCO, HO <sub>2</sub> , CF <sub>2</sub>	29*, 125*, 129, 130, 131, 132, 133, 134
	(2) CH <sub>4</sub> /O <sub>2</sub> /Ar flames	32 torr	CH <sub>4</sub> , O <sub>2</sub> , CO, CO <sub>2</sub> , H <sub>2</sub> O, H <sub>2</sub> , O, H, OH, CH <sub>3</sub> , HCO, H <sub>2</sub> CO, C <sub>2</sub> H <sub>6</sub> , C <sub>2</sub> H <sub>4</sub> , C <sub>2</sub> H <sub>2</sub> , CH <sub>3</sub> OH	125, 126, 127, 128, 131, 132, 133, 134
NBS; Hastie	(1) SbBr <sub>3</sub> , SbCl <sub>3</sub> -seeded CH <sub>4</sub> /O <sub>2</sub> /N <sub>2</sub> flames	1 atm	Combustion products, SbX <sub>3</sub> , HX, CH <sub>3</sub> X, X, Sb, SbO; X = Br or Cl	135
	(2) CH <sub>4</sub> /O <sub>2</sub> and CH <sub>4</sub> /O <sub>2</sub> /N <sub>2</sub> flames	1 atm	CO <sub>2</sub> , CO, H <sub>2</sub> , H <sub>2</sub> O, CH <sub>4</sub> , H <sub>2</sub> CO, C <sub>2</sub> H <sub>2</sub> , CH <sub>3</sub> , OH, H, C <sub>4</sub> H <sub>2</sub>	136*
	(3) TPPO-seeded flame	1 atm	Combustion products, P, HPO, PN, HPO <sub>2</sub> , P <sub>3</sub> P <sub>4</sub> , P <sub>2</sub> , P <sub>4</sub> , P <sub>2</sub> O <sub>5</sub>	137
	(4) H <sub>2</sub> /O <sub>2</sub> /N <sub>2</sub> flames	1 atm	Combustion products, HO <sub>2</sub>	138
	(5) NaCl; Na <sub>2</sub> SO <sub>4</sub> transpiration	1 atm	NaCl, Na <sub>2</sub> Cl <sub>2</sub> , Na, SO <sub>2</sub> , O <sub>2</sub>	139

TABLE III.- Continued

Organization; Personnel	Type of Study	Source Pressure	Species Observed	Reference
Space Sciences; Farber, Srivastava	(1) W-, Mo-, K-seeded H <sub>2</sub> /O <sub>2</sub> flames	1 atm	H, H <sub>2</sub> , O, O <sub>2</sub> , OH, H <sub>2</sub> O, K, H <sub>2</sub> MoO <sub>4</sub> , K <sub>2</sub> MoO <sub>4</sub> , K <sub>2</sub> MoO <sub>4</sub> , H <sub>2</sub> WO <sub>4</sub> , K <sub>2</sub> WO <sub>4</sub> , WF <sub>6</sub> , MoF <sub>6</sub> , HF, K <sup>+</sup> , MoO <sub>3</sub> , WO <sub>3</sub> , MoO <sub>2</sub> , MoO, WO <sub>2</sub> , WO	140*
	(2) V-, Cr-, K-seeded H <sub>2</sub> /O <sub>2</sub> flames	1 atm	K, H <sub>2</sub> VO <sub>3</sub> , KHV <sub>3</sub> O <sub>3</sub> , H, K <sub>2</sub> VO <sub>3</sub> , H <sub>2</sub> CrO <sub>4</sub> , KHCrO <sub>4</sub> , K <sub>2</sub> CrO <sub>4</sub> , V, VO, CrO <sub>3</sub> , CrO <sub>2</sub> , CrO	141
	(3) Fe-, Re-, K-seeded H <sub>2</sub> /O <sub>2</sub> flames	1 atm	Fe, FeO, H <sub>2</sub> FeO <sub>2</sub> , ReO, ReO <sub>2</sub> , ReO <sub>3</sub> , HReO <sub>4</sub> , K <sub>2</sub> FeO <sub>2</sub> , K <sub>2</sub> FeO <sub>2</sub>	142
	(4) Al-seeded H <sub>2</sub> /O <sub>2</sub> flames	1 atm	Al, AlO, AlOH, AlO <sub>2</sub> , HA10 <sub>2</sub>	143
	(5) As-, Sb-, K-seeded H <sub>2</sub> /O <sub>2</sub> flames	1 atm	AsO, HAsO <sub>3</sub> , H <sub>3</sub> AsO <sub>4</sub> , Sb, SbO, HSB <sub>3</sub> , H <sub>3</sub> SbO <sub>4</sub> , KH <sub>2</sub> AsO <sub>4</sub> , KH <sub>2</sub> SbO <sub>4</sub>	144
	(6) Al-, F-seeded H <sub>2</sub> /O <sub>2</sub> flames	1 atm	AlO, AlO <sub>2</sub> , AlOH, FA10, HA10 <sub>2</sub> , AlF	145
	(7) Plateau burning propellants con- taining Pb and Cu	1 atm	Combustion products, Pb, PbO, PbO <sub>2</sub> , H <sub>3</sub> PbO <sub>4</sub> , Cu, CuO, H <sub>2</sub> CuO <sub>2</sub>	146
Rocket Propulsion Establishment; Williams, Wilkins	CH <sub>4</sub> /HClO <sub>4</sub> flame	15 torr	CH <sub>4</sub> , O, CO, O <sub>2</sub> , HCl, H <sub>2</sub> O, CO <sub>2</sub> , ClO, HClO <sub>4</sub> , Cl	2*
Univ. Orleans; Delfau, et al.	(1) CH <sub>4</sub> /O <sub>2</sub> /N <sub>2</sub> and CH <sub>4</sub> /O <sub>2</sub> /NH <sub>3</sub> , NO flames		Combustion products, H <sub>3</sub> O <sup>+</sup> (H <sub>2</sub> O) <sub>1,2,3</sub> , NH <sub>4</sub> <sup>+</sup> , NO <sup>+</sup>	147
	(2) C <sub>2</sub> H <sub>2</sub> /O <sub>2</sub> flame	18-21 torr	Combustion products, C <sub>3</sub> H <sub>3</sub> <sup>+</sup> , CH <sub>3</sub> <sup>+</sup> , H <sub>3</sub> O <sup>+</sup>	148



TABLE III.- Continued

Organization; Personnel	Type of Study	Source Pressure	Species Observed	Reference
Jet Propulsion Lab; Houseman, Young	(1) $N_2O_4/N_2H_4$ -pro- pellant rocket engine exhaust	60 PSIA	$N_2$ , $H_2O$ , $H_2$ , $O_2$ , $NO$ , $NH_3$ , $NO_2$ , $N_2O_4$ , $N_2H_4$	149*
Ryason	(2) $N_2O_4/N_2H_4$ rocket engine exhaust	100 PSIA	$N_2$ , $H_2O$ , $H_2$ , $O_2$ , $NO$ , $NH_3$ , $O$ , $N_2O_4$ , $N_2H_4$	150*, 151*
Univ. Salford; Price, et al.	Pyrotechnic flame	1 atm	$N_2$ , $O_2$ , $CO_2$ , $H_2O$	152*
AMMRC; Lin	(1) $Si_3N_4$ oxidation (2) Si nitridation (3) $Al_2O_3$ CVD (4) $HCl$ -Si/ $SiO_2$ interaction (5) $Si_2ON_2$ oxidation (6) $Si_3N_4$ CVD	< 175 torr 50-425 torr 50 torr to 1 atm 100-400 torr 140-340 torr 50-200 torr	$O_2$ , $N_2$ , $NO$ $N_2$ , $SiO$ $Cl_2$ , $Cl$ , $Al_2Cl_6$ , $AlCl_3$ , $HCl$ , $Al$ , $N_2$ , $O_2$ , $AlCl_3$ , $H_2O$ , $H_2$ $N_2$ , $HCl$ , $SiO$ , $SiCl_4$ , $O_2$ , $SiCl_2$ , $SiCl_3$ $O_2$ , $N_2$ , $NO$ $N_2$ , $H_2$ , $NH_3$ , $SiF_4$ , $SiF_2$ , $Si_2F_6$ , $SiF_3NH_2$ , $Si_3F_8(NH)_2$ , $Si_2F_6NH$ , $(SiF_4)_2$	153 154* 155* 156 157 158*
Institute of Gas Technology; Pertel	$CH_4$ /air flame	1 atm	$N_2$ , $H_2O$ , $CO_2$ , $CH_4$ , $O_2$ , $CH_2O$ , $CHO$ , $C_2$ , $CN$ , $H_2O_2$ , $H_2O$ , $NO$ , $NO_2$	159*
NASA LeRC; Stearns, Kohl, Fryburg, Miller	(1) $NaCl(g)/O_2/H_2O$ reaction with $Cr_2O_3$ and Mo	1 atm	$O_2$ , $(NaCl)_1,2,3,4$ , $(NaCl)_1,2,3CrO_3$ , $Na_2Cr_2O_7$ , $NaClNa_2Cr_2O_7$ , $CrO_2(OH)_2$ , $(NaOH)_1,2CrO_3$ , $NaOHNa_2Cr_2O_7$ , $(MoO_3)_3,4$ , $(NaCl)_1,2(MoO_3)_3$ , $NaOH$ $(MoO_3)_3$	160

TABLE III.- Continued

Organization; Personnel	Type of Study	Source Pressure	Species Observed	Reference
NASA LeRC (Cont); Stearns, Kohl, Fryburg, Miller	(2) Na-, S-seeded CH <sub>4</sub> /O <sub>2</sub> flame; NaCl(g)/O <sub>2</sub> /SO <sub>2</sub> / H <sub>2</sub> O flow tube	1 atm	O <sub>2</sub> , H <sub>2</sub> O, CO <sub>2</sub> , SO <sub>2</sub> , CO, HCl, Na, SO <sub>3</sub> , NaCl, Na <sub>2</sub> SO <sub>4</sub> , NaSO <sub>2</sub> , NaSO <sub>3</sub>	161
	(3) Na-, K-, S-seeded CH <sub>4</sub> /O <sub>2</sub> flames	1 atm	Molecules in 2 plus KOH, K, K <sub>2</sub> SO <sub>4</sub>	162
	(4) NaCl(g)/HCl/O <sub>2</sub> /H <sub>2</sub> O interaction with Na <sub>2</sub> SO <sub>4</sub>	1 atm	O <sub>2</sub> , H <sub>2</sub> O, Na <sub>2</sub> SO <sub>4</sub> , (NaCl) <sub>1,2,3</sub> , SO <sub>2</sub> , HCl, NaClNa <sub>2</sub> SO <sub>4</sub>	163
	(5) KCl(g)/O <sub>2</sub> /H <sub>2</sub> O re- action with Cr <sub>2</sub> O <sub>3</sub> and LaCrO <sub>3</sub>	1 atm	(KCl) <sub>1,2,3</sub> , CrO <sub>3</sub> , KOH, CrO <sub>2</sub> (OH) <sub>2</sub> , (KCl) <sub>1,2,3</sub> CrO <sub>3</sub> , (KOH) <sub>1,2</sub> CrO <sub>3</sub> , K <sub>2</sub> Cr <sub>2</sub> O <sub>7</sub> , KClK <sub>2</sub> Cr <sub>2</sub> O <sub>7</sub>	164
Stanford Univ.; Stevenson, Mattes, Dun	H <sub>2</sub> /fused quartz reactor	1 atm	H <sub>2</sub> O, SiO, CH <sub>4</sub> , CO, CO <sub>2</sub>	165*
Aerodyne; Kolb, Wormhoudt, et al.	K <sub>2</sub> CO <sub>3</sub> -seeded coal/ CH <sub>4</sub> /air flame	1 atm	Combustion products, K <sup>+</sup> , KO <sup>+</sup> , Na <sup>+</sup> , Rb <sup>+</sup> , Cs <sup>+</sup> , CsO <sup>+</sup> , PO <sub>3</sub> <sup>-</sup> , PO <sub>2</sub> <sup>-</sup> , BO <sub>2</sub> <sup>-</sup> , OH <sup>-</sup> , SH <sup>-</sup> , HCrO <sub>3</sub> <sup>-</sup> , HMoO <sub>4</sub> <sup>-</sup> , HWO <sub>3</sub> <sup>-</sup>	166*
Aberdeen ARBRL; Beyer	Laser pyrolysis of NC and HMX/PU	1-200 mtorr	N <sub>2</sub> O, NO <sub>2</sub> , HCN, H <sub>2</sub> CO, NO, CO <sub>2</sub>	167
Akademiia Nauk SSSR; Korobeinichev, et al.	APC, PMMA catalyst com- bustion			168

TABLE III - Continued

Organization; Personnel	Type of Study	Pressure	Species Observed	Reference
Australian National University; Crane, Stalker	Shock tunnel hypersonic flow	> 1 atm	He, N <sub>2</sub> , N, O <sub>2</sub> , O, CO, CO <sub>2</sub> , NO, Ar, Ne	180*
United Tech. Res. Center; Seery, Zabielski	CH <sub>4</sub> /air flames	0.1 atm	Combustion products, NO	181
CSIRO, Australia; McAllister, et al	H <sub>2</sub> /N <sub>2</sub> /acetone flame	1 atm	CO <sub>3</sub> <sup>-</sup> , HCO <sub>3</sub> <sup>-</sup> , HCO <sub>4</sub> <sup>-</sup> , O <sub>2</sub> (H <sub>2</sub> O) <sub>n</sub> <sup>-</sup> , NO <sub>2</sub> <sup>-</sup> , NO <sub>3</sub> <sup>-</sup> , OH <sup>-</sup> , O <sub>2</sub> <sup>-</sup>	182

spectrometric detection to provide direct identification of sampled species and to measure their concentration, (4) sensitivity of parts per million or better, and (5) ability to maintain the chemical and dynamic integrity of the species being sampled. Our apparatus was designed in consultation with Drs. F. T. Greene and T. A. Milne of the Midwest Research Institute. Details of the apparatus hardware are presented elsewhere [170] so only a brief general description is given here.

A schematic cross-sectional view of the beam path portion of the sampler is shown in figure 8. The atmospheric pressure gas to be sampled enters the system through the sampling orifice located at the bottom of the vertical configuration. For sampling orifice Knudsen number less than  $10^{-2}$  the gas expands into stage I as a free jet. Stage I vacuum pumping maintains pressure ratios greater than  $10^5$  across the sampling orifice (0.025 cm diameter). The conical skimmer intercepts the gas flow and passes the central portion or core of the flow into stage II where the core is periodically interrupted by a toothed rotating disk beam chopper. Pressure in stage II is less than  $10^{-5}$  Torr. The chopped gas beam enters the stage III differential pumping vacuum chamber through a collimating aperture. Pressure in stage III is less than  $10^{-6}$  Torr. The beam exits from stage III through another aperture and passes into stage IV and the ionizer of the quadrupole mass spectrometer. Pressure in stage IV is less than  $10^{-7}$  Torr. Ions formed in the electron bombardment ionizer are electrically focused and transmitted to the quadrupole mass filter. Selected ions transmitted by the filter are electrically deflected into the off-axis electron multiplier whose output is electronically monitored. Thus a gas sample at high pressure is continuously transferred

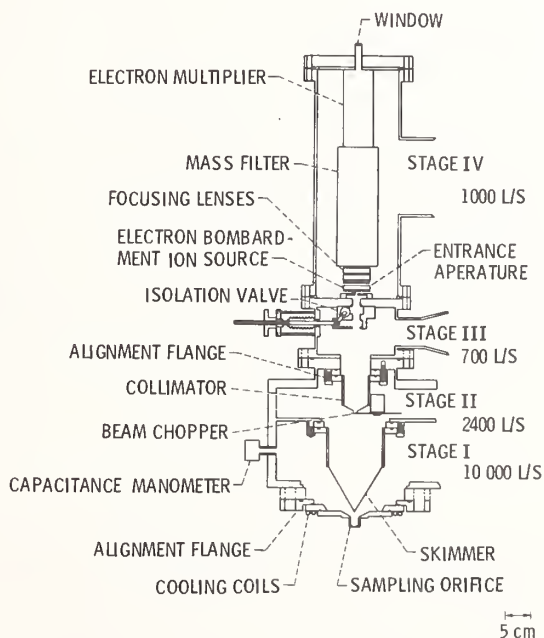


Figure 8. Schematic cross section of high pressure mass spectrometric sampler.

to the low pressure mass spectrometer where the gas is analyzed on the basis of the mass-to-charge ratio of its constituents. An Extranuclear Laboratories, Inc. quadrupole mass spectrometer system with electron bombardment ion source is used in our apparatus. The mass filter has a nominal range from 0 to 500 AMU but in practice we have been able to operate to above 600 AMU. Beam modulation and phase sensitive detection techniques are used to increase signal-to-noise ratio in processing the spectrometer electron multiplier output signal. The quadrupole mass spectrometer is one for which all settings of the ionizing, focusing, and mass filtering elements must be determined by the experimenter. The detection of low level signals depends very strongly upon the adjustment of these elements. Optimum adjustment corresponds to maximizing the signal-to-noise ratio (S/N) rather than just maximizing the signal. Our experience has indicated that the two controls which most strongly affect maximization of S/N are the emission current and the ion energy. Although, in general, the signal strength increases as each of these parameters is increased, a point is reached where the noise level begins to increase more rapidly than the signal level. We have found that optimum S/N is achieved at relatively low emission current (typically about 3 mA) and ion energy (typically 10 V at 32 AMU).

Tuning is accomplished by observing an intense peak on the oscilloscope and adjusting the controls to produce the proper peak shape. This is usually done by observing the nitrogen peak while sampling ambient laboratory air. A fast repetitive sweep rate is used and the resolution control is set to a low value so that the peak is about eight centimeters wide on the oscilloscope screen. The tuning controls are adjusted so that the top of the peak is flat, the high mass side of the peak is vertical, and the low mass side is a straight line with maximum slope. These features of the peak shape are sought while also endeavoring to maintain as large a peak amplitude as possible. The ideal shape is shown in figure 9 by the heavy solid line. Once the tuning is optimized, the resolution can be increased considerably before the peak amplitude is affected. As the resolution is increased, the position of the low mass side of the peak should move toward higher mass as shown by the dashed lines in figure 9. When the low mass side of the peak just intercepts the high mass side, e.g., point A in figure 9, the spectrometer is tuned to the highest resolution which gives the maximum S/N. Increasing the resolution control further increases the resolution but only at the expense of a loss in sensitivity, e.g., point B in figure 9.



Figure 9. Idealized focusing peak shape.

Optimum resolution and sensitivity at low AMU does not necessarily represent the optimum at high AMU. The control which most strongly affects the ratio of the low to high AMU



resolution is the  $\Delta M$  control. We have found that for our spectrometer a setting of  $\Delta M = 0$  should be used to obtain resolutions which are equally satisfactory at low and high AMU while maintaining good sensitivity. The intensity and resolution are usually checked daily by observing a one atmosphere oxygen beam. The oxygen used contains a low level xenon impurity which provides a suitable signal at relatively high AMU. The oxygen peak and one of the xenon peaks are alternately observed while fine tuning. Typical resolutions (defined using the full-width at half-maximum), used when detecting low level signals, are 1X to 2X the mass number in the AMU region near xenon and 2X the mass number in the region near oxygen.

Beam modulation is an important part of our apparatus which contributes to overall sensitivity. Therefore, it is instructive to consider certain aspects of the technique as applied to high pressure sampling where we have supersonic beams. Fite [171] has pointed out that in selecting a chopping frequency for performing modulated beam mass spectrometric measurements two physical considerations govern. First, the frequency should be made sufficiently high to insure that the Fourier component of the background gas pressure fluctuations is negligibly small. Second, the frequency should be made sufficiently low to insure that coherence of the modulated beam is not destroyed as the result of velocity spreading of the beam pulses. For effusive molecular beams where there is a broad distribution of velocities, the second consideration above is of critical importance. Fite and Brackman [172], Harrison, et al. [173,174], and Yamamoto and Stickney [175] have analyzed the effusive beam case and worked out the dependence of the amplitude and phase shift on frequency, molecular mass, and flight path length. For supersonic beams, Miller [176] has shown that the second consideration above is not critical. Miller showed that amplitude corrections are minor when the Mach number is greater than about five. This results from the fact that at high Mach numbers the velocity distribution is sufficiently narrow that the spread in velocities does not affect the coherence of the beam even at relatively high chopping frequencies, e.g., 1400 hertz.

Because our sampling system produces a high Mach number supersonic beam, we have only considered background gas pressure fluctuation effects in selecting a chopping frequency. We have used the analysis of Fite [171] to estimate the ratio of amplitudes of pressure fluctuations, in the stage II vacuum chamber, for a chopped beam as compared to an unchopped beam. The stage II vacuum system's time constant is approximately 40 milliseconds. At a chopping frequency of 150 hertz the pressure fluctuation amplitude is attenuated by a factor of about 40 and at a frequency of 400 hertz the attenuation factor is 100.

## 4.2 Evaluation

The general performance of our sampling system was initially assessed by sampling the ambient laboratory atmosphere. The orifice-to-skimmer distance was arbitrarily set to correspond to  $X_s/D_0 = 50$ . These initial tests demonstrated that the vacuum pumping systems met the design criteria and were adequate for ambient temperature, atmospheric pressure sampling through a 0.025-centimeter diameter orifice. The pressure in stage I was about 1.5 microns, and this value corresponds to the region where the 10-inch diffusion pumps

begin to achieve their maximum pumping speed. This result indicates that the 0.025-centimeter diameter orifice is about the maximum that can be used on our sampler with the stage I pumping provided. The pressure in stages II, III, and IV was  $2 \times 10^{-5}$ ,  $3 \times 10^{-7}$ , and  $< 10^{-8}$  Torr, respectively.

A portion of a typically recorded spectrum for the laboratory ambient atmosphere is shown in figure 10. The peaks at 32, 33, 34 AMU are due to oxygen and those at 36, 38, and 40 AMU are due to argon which exists in the atmosphere at about 0.93 percent by volume. An estimate of the sampling system's sensitivity was ascertained by observing that the  $\text{Ar}^{38}$  isotope was readily identified and measured here with the spectrometer and electronics set to only an intermediate sensitivity level. This isotope is of the order of five parts per million (ppm) in the ambient atmosphere.

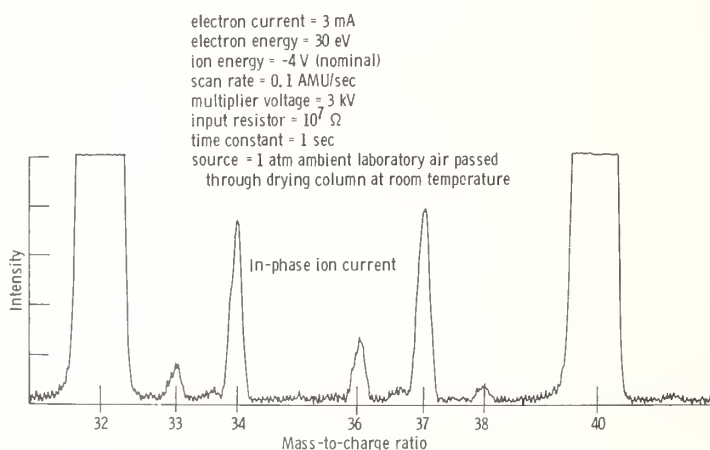


Figure 10. Portion of mass spectral scan for ambient laboratory air.

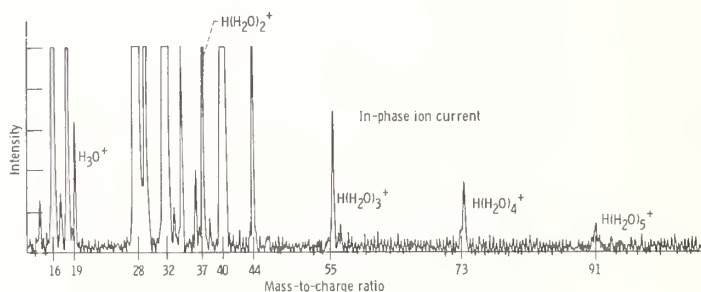


Figure 11. Mass spectral scan of ambient laboratory air.

The 37 AMU peak in figure 10 was attributed to the ion species  $\text{H}(\text{H}_2\text{O})_2^+$ . A subsequent scan of ambient air was made to higher AMU and is shown in figure 11. This scan was at a higher sweep rate and lower sensitivity than that shown in figure 10. The water and water cluster peaks are clearly visible and in accord with observations made by other investigators

[177]. To confirm these observations we sampled ambient air which was first passed through a drying column. A scan of the dry air sample is shown in figure 12. The water peak at 18 AMU is seen to be greatly reduced and the water cluster peaks are absent. The scans shown in figures 11 and 12 were made at the same sensitivity, scan speed, and time constant. At higher sensitivity, slower scan speed, and increased time constant the dried air sample still showed some water clustering peaks and this demonstrated that, as expected, the drying was not complete.

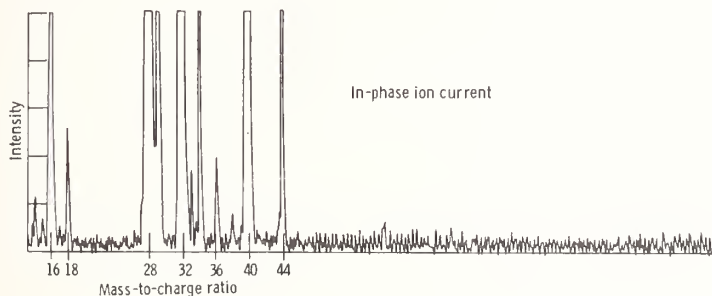


Figure 12. Mass spectral scan of ambient laboratory air passed through a drying column.

After the preliminary testing described above, experiments were performed to determine (1) how measured intensity varied as a function of  $X_s/D_0$  and source pressure,  $P_0$ , (2) how the measured intensity of an argon beam compared to theoretically calculated intensity, and (3) the ultimate sensitivity of the sampling system. For these experiments a vertically translatable sampling orifice assembly was installed on the sampler. Experiments were performed with argon, nitrogen, or oxygen as the room temperature source gas.

#### 4.2.1 Argon

Argon was sampled at various source pressures and the in-phase ion current was measured as a function  $X_s/D_0$ . Typical results at three source pressures are presented in figure 13. The intensity of the argon signal is seen to pass through a rather broad maximum near  $X_s/D_0 = 120$  and then fall sharply at lower values of  $X_s/D_0$ . The sharp drop in intensity at lower orifice to skimmer distances is similar to that reported by other investigators [35], and this drop is usually attributed to skimmer interference and shock effects [35,36]. We believe that in our case the drop in intensity at low values of  $X_s/D_0$  may also be due to background gas scattering effects because at small orifice-to-skimmer distances the pumping in the region of the orifice is probably somewhat restricted. The gradual decrease in intensity at  $X_s/D_0$  values beyond the maximum may be due to the decreased density at the skimmer entrance resulting from the increasing orifice-to-skimmer separation. According to the idealized theoretical analysis of Parker, et al. [21], the flux at the detector varies as

$(X_s/D_0)^{-2/3}$  for argon. This is in reasonable agreement with our observations for  $X_s/D_0$  values greater than where the maximum intensity occurs.

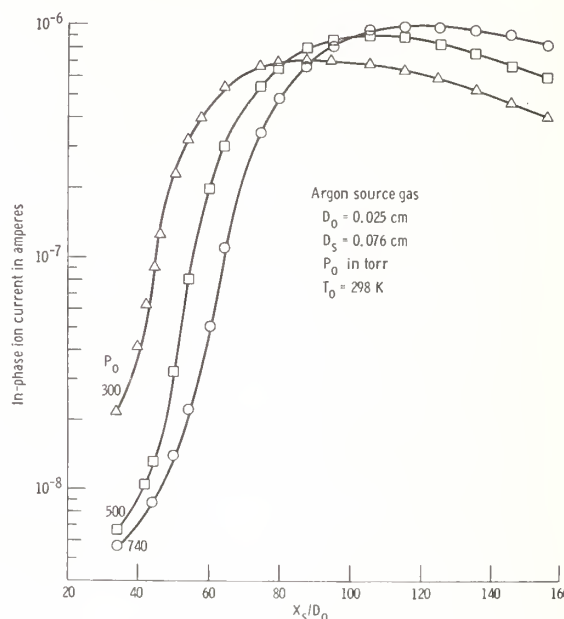


Figure 13. Argon beam intensity variation as a function of orifice-to-skimmer distance and source pressure.

It is interesting to note that if one makes a simplistic calculation of a skimmer Knudsen number at the point of maximum intensity, a value is obtained which is about equal to that usually considered to be a criterion for free molecular flow. For example, consider the case of argon with  $P_0 = 700$  Torr and  $X_s/D_0 = 120$ . As will be shown later, the number density at the skimmer is calculated to be  $n_s = 2.35 \times 10^{14}$  atoms  $\text{cm}^{-3}$ . The mean free path at the skimmer,  $\lambda_s$ , is calculated to be 0.71 centimeter from the expression  $\lambda_s = (\sqrt{2} \pi \sigma^2 n_s)^{-1}$  where the collision cross section  $\sigma$  is taken to have the value  $3.67 \times 10^{-8}$  cm. For the 0.076 centimeter skimmer diameter, the skimmer Knudsen number,  $\text{Kn}_s$ , is calculated from  $\text{Kn}_s = \lambda_s/D_s$  to be 9.3. Because a value of  $\text{Kn}_s = 10$  is taken as the criterion for free molecular flow, it is reasonable to conclude that for our example free molecular flow prevailed where maximum intensity was achieved. Upstream of where free molecular flow prevails, collisions still play a role and shock or scattering effects would be expected to attenuate the beam as previously postulated. Thus this qualitative picture in general can explain the experimentally observed shapes of the intensity versus  $X_s/D_0$  curves. Furthermore, this approach is in general accord with the findings of other investigators who observed similar curve shapes [37,38]. For example, Scott and Drewry [38] concluded that experimental results rise to a maximum and tend to approach theoretical predictions as  $\text{Kn}_s$  increases.

Our measured dependence of intensity on source pressure for  $X_s/D_0 = 120$  is shown in figure 14. For pressures below about 600 Torr the intensity is seen to be directly

proportional to source pressure and this is in accord with theoretical considerations. The fall-off of intensity at higher pressures was not expected. We speculated that this might be related to stage I pumping. At these higher pressures the stage I pressure is in the region where the diffusion pumps just begin to attain their maximum pumping speed. However, the stage I pressure is almost linearly related to source pressure, as shown in figure 15, even to source pressures of 800 Torr. One would expect to see a departure from linearity at higher pressures if the diffusion pumps were not pumping at their maximum speed.

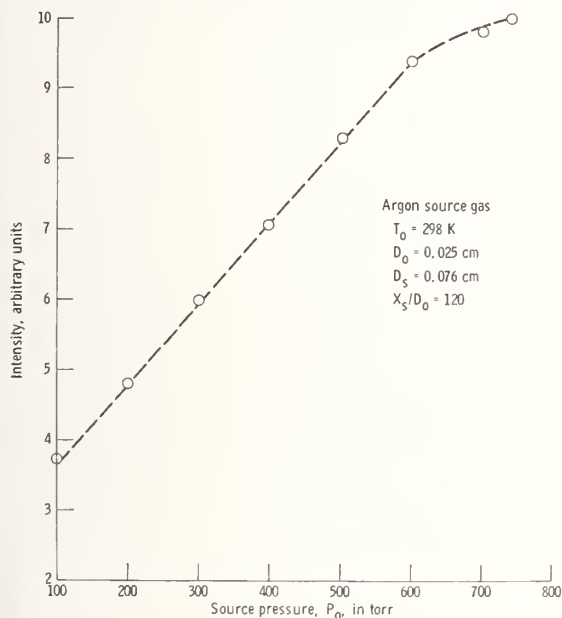


Figure 14. Argon beam intensity variation with source pressure.

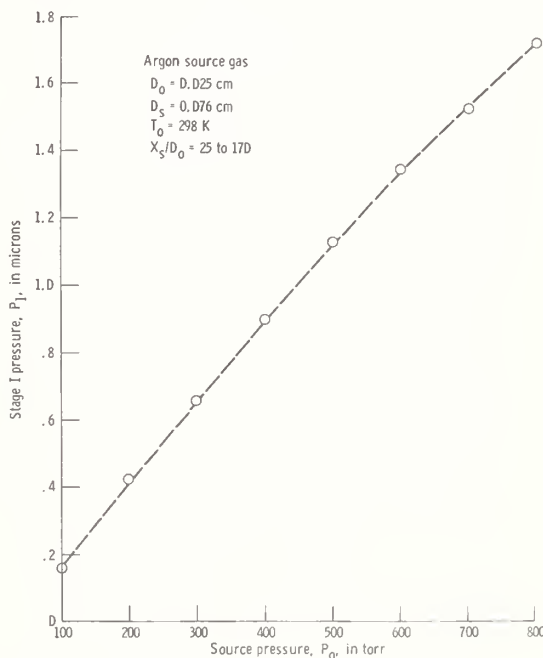


Figure 15. Variation of first stage expansion pressure as a function of source pressure.

To compare measured intensities with theoretically calculated values it is necessary to relate measured ion current to beam flux or number density which can be expressed in terms of source conditions. Because the ion source of the mass spectrometer is a density sensitive detector, we chose to characterize the beam in terms of number density  $n$ . The center-line number density at the ion source,  $n_d$ , is proportional to the measured ion current,  $I$ ,

$$n_d = CI \quad (43)$$

where  $C$  is the proportionality constant and the current is the in-phase component of the modulated beam current. The proportionality constant may be a function of molecular species but for any given species, such as argon, the proportionality is taken to be equally applicable to an effusive or supersonic beam. If the effusive beam is subscripted by  $E$  and the supersonic (nozzle) beam is subscripted by  $N$ , we can write for a particular species  $i$ ,



$$i^C = \frac{i_{dE}^n}{i_{I_E}} = \frac{i_{dN}^n}{i_{I_N}} \quad (44)$$

Effusive argon beams were produced by sampling argon source gas at pressures in the micron range and the results are shown in figure 16. Generally, effusive flow is considered to exist for orifice Knudsen numbers above about 10, but our data was found to be very linear to source pressures near 400 microns where the Knudsen number is approximately 0.5.

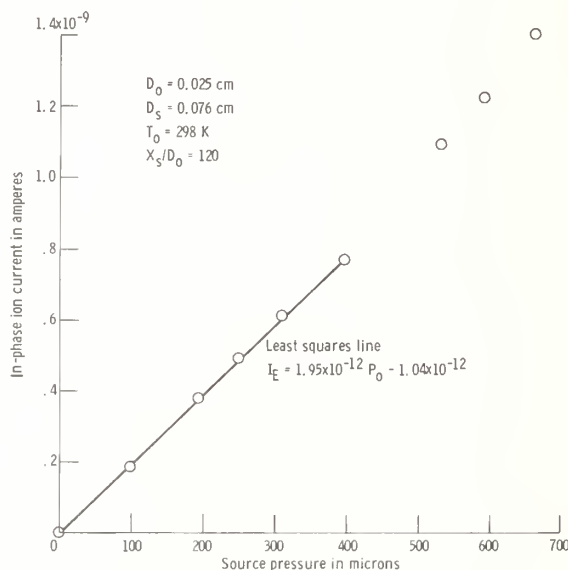


Figure 16. Argon beam intensity as a function of source pressures in the effusive range.

At a source pressure of 30 microns the number density at the detector (ion source) was calculated to be  $Ar_{dE}^n = 1.81 \times 10^7 \text{ molecules cm}^{-3}$  for  $X_s/D_0 = 120$  and a skimmer-to-detector distance,  $\ell$ , equal to 42.82 centimeters. From the least squares line equation a source pressure of 30 microns results in a beam current of  $5.75 \times 10^{-11}$  ampere. The proportionality constant  $Ar^C$  is then calculated to be  $Ar^C = 3.15 \times 10^{17} \text{ molecules cm}^{-3} \text{ ampere}^{-1}$ .

Supersonic argon beams resulting from a source pressure of 700 Torr were measured as a function of  $X_s/D_0$  and the measured ion currents,  $Ar_{I_N}$ , were converted to number density,  $Ar_{dN}^n$ , by multiplying  $Ar_{I_N}$  by  $Ar^C$ . Results are presented in figure 17 where it can be seen that the maximum density occurs at  $X_s/D_0 = 120$  where  $Ar_{dN}^n = 3.07 \times 10^{11} \text{ molecules cm}^{-3}$ .

Theoretical densities at the detector can be calculated by equation (35) and the techniques described in the section of beam formation. Calculations were made for the source conditions  $P_0 = 700$  Torr of argon,  $T_0 = 298 \text{ K}$ ,  $D_0 = 0.025$  centimeter,  $X_s/D_0 = 120$ ,  $D_s = 0.03$  centimeter, and  $\ell = 42.82$  centimeters. When  $M_{\perp S}$  was calculated according to equation (37)

$[M_{\perp_s} = M_T(X_s/X_q)]$  and the first method, we obtained  $Ar^{nd}_N = 1.03 \times 10^{12}$  molecules  $cm^{-3}$  for a theoretical density. This value is a factor of about 3.4 higher than our measured value.

When  $M_{\perp_s}$  was calculated according to the second method and equation (42) ( $M_{\perp_s} = (2.50/\sqrt{Y})(X_s/D_0)[D_0/(\tau_0 C_0)]^{-0.2}$ ), we obtain  $Ar^{nd}_N = 3.24 \times 10^{11}$  molecules  $cm^{-3}$  which is only five percent higher than our measured value. It must be recognized that while both theories are based on many idealized assumptions, the second method calculation results from a theory derived from correlations with experiment. Therefore, it is not surprising that the density derived from the second calculation is in better agreement with our measurements.

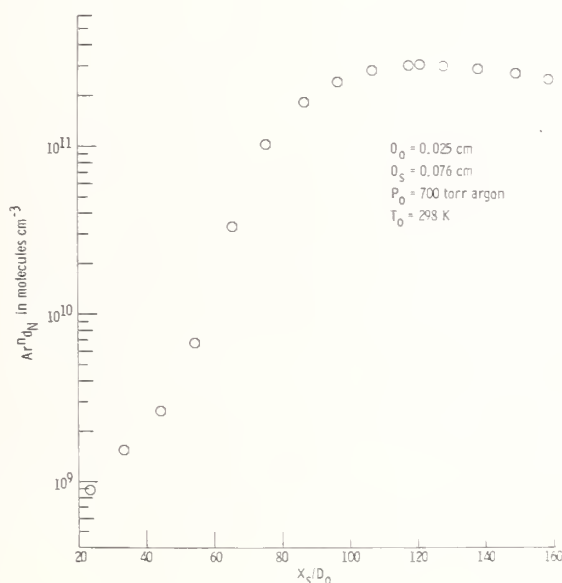


Figure 17. Argon beam density at the detector plotted versus orifice-to-skimmer distance.

For either method of calculation of the theoretical density at the detector, the agreement with experiment is considered to be good and an indication that at  $X_s/D_0 = 120$  skimmer interference is not a serious problem in our apparatus. The calculations also yield additional information which gives some insights into the sampler's operation. For the source conditions noted  $M_T = 30.2$  and the transition to "collisionless flow" occurs near  $X_q/D_0 = 28$  where  $n_q = 4.26 \times 10^{15}$  molecules  $cm^{-3}$ . The density at the skimmer is  $n_s = 2.35 \times 10^{14}$  molecules  $cm^{-3}$ .

A final series of argon beam experiments were performed to ascertain if abnormal condensation effects existed in our sampling system beam formation process. Condensation phenomenon are an important consideration in high pressure sampling and extensive research [39-42 and references cited therein] has been devoted to this subject. While most aspects of condensation in free jets is beyond the scope of our discussion, Milne and Greene [39] have shown how measurement of the argon dimer-to-monomer ratio can be used to evaluate the performance of a

sampler. Argon source gas was sampled at room temperature through a 0.025 centimeter diameter orifice. Orifice-to-skimmer distance was held constant at the optimum determined previously, i.e.,  $X_s/D_0 = 120$ . In-phase ion currents were measured for the argon monomer and dimer. Measured ion currents were not corrected for mass spectrometer mass discrimination, multiplier gain or sampler mass discrimination because such corrections were considered to be relatively small for the short range from 40 to 80 AMU. At a source pressure of one atmosphere we measured an argon dimer to monomer ratio of  $3.6 \times 10^{-3}$ . This value is in good agreement with Milne and Greene's data [39] (see fig. 5), extrapolated to our orifice size. We therefore conclude that for the orifice size, source pressure and temperature, and orifice to-skimmer distance used we had a relatively undisturbed free-jet expansion and beam formation.

#### 4.2.2 Nitrogen

Nitrogen was used as a source gas to perform experiments similar to those done with argon. Pressures in the various vacuum chambers as a function of source pressure and  $X_s/D_0$  were in substantial agreement with those measured with argon as the source gas. Intensity also varied with  $P_0$  and  $X_s/D_0$  in a fashion similar to argon. Effusion experiments yielded a value for the proportionality constant  $N_2 C = 2.97 \times 10^{17}$  molecules  $\text{cm}^{-3}$  ampere $^{-1}$ . The measured density at the detector,  $N_2 n_{dN}$ , is plotted as a function of  $X_s/D_0$  in figure 18 for a source pressure of 700 Torr. Again, the density is seen to pass through a broad maximum which peaks at  $X_s/D_0 = 120$ . The maximum density for nitrogen is  $1.26 \times 10^{11}$  molecules  $\text{cm}^{-3}$ .

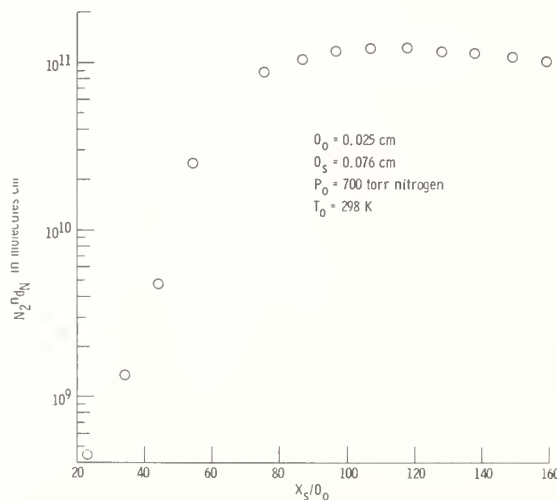


Figure 18. Nitrogen beam density at the detector plotted versus orifice-to-skimmer distance

The maximum density measured at the detector for argon beams is about a factor of 2.5 higher than that measured for nitrogen beams under the same conditions. If one calculates a theoretical density by the methods of equation (35), a higher density is obtained for nitrogen compared with argon. The value of such calculations for nitrogen are, however, somewhat suspect because the theoretical equations were developed mainly on the basis of a monatomic gas.

#### 4.2.3 Oxygen

Preliminary experiments with oxygen as the source gas indicated that a xenon impurity contained in the oxygen might be useful for determining the ultimate sensitivity of our sampling system. Therefore, a number of experiments were performed with oxygen. Missile grade tank oxygen was used at atmospheric pressure with a 0.025-centimeter sampling orifice diameter and with  $X_5/D_0 = 120$ . The oxygen was independently analyzed by conventional mass spectrometric techniques which had a sensitivity of about 1 ppm. No xenon was detected in that analysis and we therefore took the xenon level to be 1 ppm.

When the oxygen was sampled with our sampling system xenon was readily identified. A typically recorded spectrum of the xenon isotopes is given in figure 19. The total current (upper trace) was obtained at maximum spectrometer sensitivity for acceptable resolution, i.e., maximum electron multiplier gain and maximum electrometer sensitivity. The major xenon isotopes are just discernible and for the 132 isotope the signal-to-noise ratio is about two. However, the in-phase current (lower trace) clearly shows the xenon isotopes and the signal-to-noise ratio for the 132 isotope is about 10. The in-phase current was measured with the lock-in amplifier sensitivity set a factor of 10 below maximum and a 10 second time constant was used. Figure 19 demonstrates the signal-to-noise ratio enhancement that is

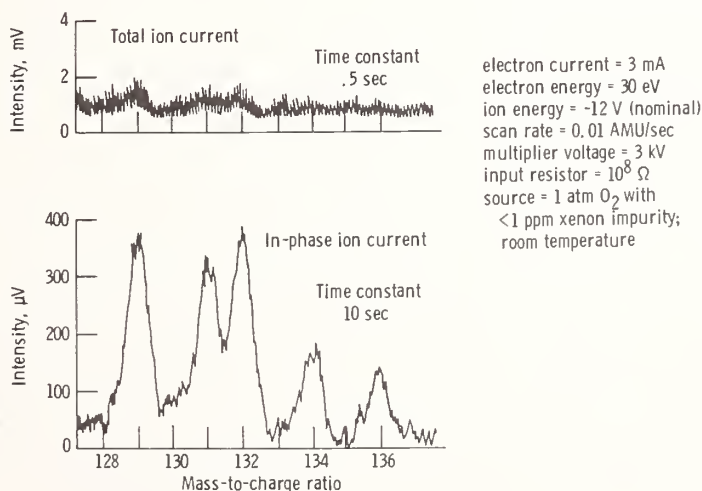


Figure 19. Mass spectral scan of xenon isotopes.

achieved by beam modulation and phase sensitive detection. Had a longer time constant and slower scan rate been used, an even greater enhancement could have been attained. The  $^{132}$  xenon isotope is about one-fourth of the total xenon level and thus for the presumed xenon impurity level of 1 ppm the  $^{132}$  signal represents about 0.25 ppm. Clearly, if the  $^{132}$  signal were one-fourth the level shown in figure 19, it would still be easily measurable at the sensitivities employed. On this basis we therefore expect an ultimate sensitivity for our sampling system in this general mass range to be on the order of 0.05 ppm.

## 5. Sampling of High Temperature Systems

We have used our sampling apparatus to study reaction product formation in flames and flowing gas systems [161-163] as well as to study volatile products emanating from metal samples subjected to various gaseous environments at elevated temperatures [160,164]. For these experiments atmospheric pressure gases were sampled through a 0.020 to 0.025 centimeter diameter orifice in the apex of a 0.6 centimeter high sampling cone welded to a 2-centimeter diameter by 1.5 centimeter high stainless steel tube attached to the flange plate. The skimmer diameter was 0.081 centimeter and  $X_s/D_0 = 144$ . For this arrangement the stage I and II pressures were  $1.5 \times 10^{-3}$  and  $8 \times 10^{-6}$  Torr, respectively, with room temperature atmospheric pressure source gas. When the gas temperature was 1000 °C, these pressures were  $7 \times 10^{-4}$  and  $1 \times 10^{-6}$  Torr, respectively. Stage III and IV pressures were less than  $10^{-7}$  and  $10^{-8}$  Torr, respectively, for both source gas temperatures. The various experimental results presented here are considered to be qualitatively correct even though quantitative aspects are preliminary. Reported ion intensities have not been adjusted to account for mass discrimination resulting from Mach-number focusing, quadrupole mass filter transmission, or multiplier gain variations as a function of  $m/e$ . Calibrations to correct for these factors have not yet been performed. Ion intensities have, however, been corrected for estimated relative ionization cross sections.

The formation of gaseous alkali sulfate molecules in flames was studied with methane-oxygen flames seeded with sodium or potassium salts and sulfur compounds. The systems studied are shown in table IV. The fuel-lean flat flames were produced with a specially designed burner. Gaseous sulfur compounds could be added to the methane-oxygen mixture and inorganic metal salts in an aqueous solution could be aspirated and nebulized into the flowing gas mixture. Gaseous flame reaction products were measured by recording the in-phase ion current at appropriate values of AMU. Composition profiles were determined by measuring each species' ion current as a function of vertical distance between the sampling orifice and burner surface. Clogging of the sampler orifice by condensable species was a problem which limited the duration of each sampling experiment to about 30 minutes.

Measured composition profiles for two seeded flames are shown in figures 20 and 21. The  $O_2$ ,  $H_2O$  and  $CO_2$  profiles are similar to those reported by other investigators for methane-oxygen flames in general. The direct identification in flames of the gaseous species  $Na_2SO_4$ ,  $K_2SO_4$ ,  $NaSO_2$ , and  $NaSO_3$  are new findings. The latter two species are intermediates and until now their existence was only postulated [178,179]. Shapes of the measured profiles are discussed in references [161] and [162].



TABLE IV.- Alkali metal- and sulfur-containing compound additions to methane-oxygen flames.

Flame System	Fuel	Reactant Gas Composition (mole %)	Oxidant	Fuel/Oxidant Mass Ratio	Calculated Adiabatic Flame Temperature (K)	Flame* Speed (cm sec <sup>-1</sup> )
NaCl-SO <sub>2</sub>	8.9 CH <sub>4</sub>		84.1 O <sub>2</sub>	0.072	2032	45
	0.92 SO <sub>2</sub>		5.9 H <sub>2</sub> O			
			0.18 NaCl			
NaCl-CH <sub>3</sub> SH	5.3 CH <sub>4</sub>		87.3 O <sub>2</sub>	0.046	1678	43
	1.0 CH <sub>3</sub> SH		6.2 H <sub>2</sub> O			
			0.19 NaCl			
Na <sub>2</sub> CO <sub>3</sub> -SO <sub>2</sub>	9.3 CH <sub>4</sub>		83.6 O <sub>2</sub>	0.077	2097	44
	1.0 SO <sub>2</sub>		6.0 H <sub>2</sub> O			
			0.051 Na <sub>2</sub> CO <sub>3</sub>			
KCl-SO <sub>2</sub>	9.3 CH <sub>4</sub>		83.5 O <sub>2</sub>	0.076	2088	44
	1.0 SO <sub>2</sub>		6.0 H <sub>2</sub> O			
			0.19 KCl			
K <sub>2</sub> CO <sub>3</sub> -SO <sub>2</sub>	9.3 CH <sub>4</sub>		83.8 O <sub>2</sub>	0.075	2101	45
	0.92 SO <sub>2</sub>		5.9 H <sub>2</sub> O			
			0.025 K <sub>2</sub> CO <sub>3</sub>			

\*The flame speed,  $V_0$  in cm sec<sup>-1</sup>, was calculated on the basis of NTP flow velocity of the reactant gases.

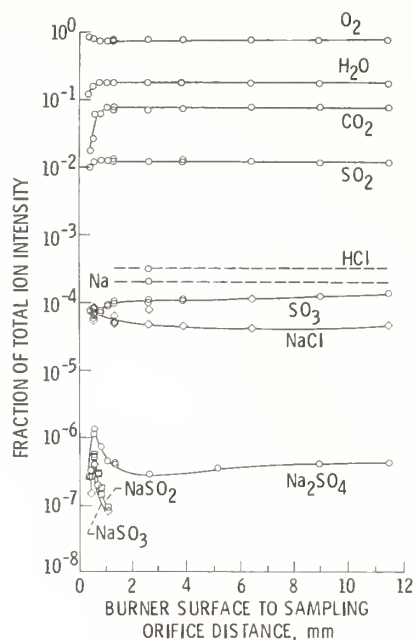


Figure 20. Composition profiles for  $\text{CH}_4\text{-O}_2\text{-H}_2\text{O-NaCl-SO}_2$  flame. Reactants (mole %): 8.9  $\text{CH}_4$ , 84.1  $\text{O}_2$ , 5.9  $\text{H}_2\text{O}$ , 0.18  $\text{NaCl}$ , and 0.92  $\text{SO}_2$ .

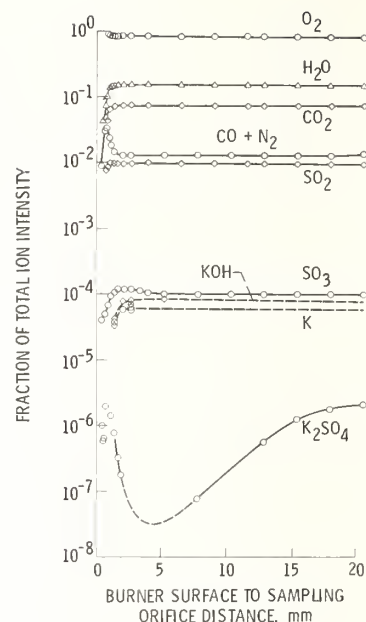


Figure 21. Composition profiles for  $\text{CH}_4\text{-O}_2\text{-H}_2\text{O-K}_2\text{CO}_3\text{-SO}_2$  Flame. Reactants (mole %): 9.3  $\text{CH}_4$ , 83.8  $\text{O}_2$ , 5.9  $\text{H}_2\text{O}$ , 0.025  $\text{K}_2\text{CO}_3$ , and 0.92  $\text{SO}_2$ .

The formation of  $\text{Na}_2\text{SO}_4(\text{g})$  was also studied in a flowing gas reaction tube at 1413 K. The reaction tube was positioned at the sampler inlet in such a way that the sampling orifice extended into the tube and hot zone. The orifice was heated for some time before the water-saturated oxygen,  $\text{SO}_2$  and  $\text{NaCl}(\text{g})$  were flowed through the hot reaction zone and sampled. Intensities were measured for the gaseous species,  $\text{O}_2$ ,  $\text{H}_2\text{O}$ ,  $\text{SO}_2$ ,  $\text{SO}_3$ ,  $\text{NaCl}$ ,  $\text{Na}_2\text{SO}_4$ , and  $\text{NaSO}_3$  with known flows of  $\text{O}_2$ ,  $\text{SO}_2$ ,  $\text{H}_2\text{O}$ , and known concentrations of  $\text{NaCl}(\text{g})$  (fig. 22). The species  $\text{NaOH}(\text{g})$  and  $\text{HCl}(\text{g})$  with parent ions at  $m/e$  40 and 36, 38 could not be measured because large in-phase background peaks were present at these  $m/e$  values. These background peaks were due to argon which is a 2300 ppm impurity in the missile grade oxygen that was used. Equilibrium thermodynamic calculations of the composition of the reaction products were made as a function of temperature. In the calculations the composition of the reactant was held constant at the weight fractions 0.96  $\text{O}_2$ ,  $1.2 \times 10^{-5}$   $\text{NaCl}$ , 0.012  $\text{H}_2\text{O}$ , and 0.032  $\text{SO}_2$ . Experimental reaction product ion intensity fractions are compared with the equilibrium calculated mole fractions in the histogram shown in figure 22. Considering that the measured intensities were not corrected for sampling factors, the quality of agreement between experiment and calculation is considered quite good.

Our sampler has proven to be valuable in studying the atmospheric pressure oxidation of various metals subjected to various contaminant gases added to the oxygen environment [160, 164]. The high pressure mass spectrometric sampling technique has been used to identify volatile products emanating from the metal samples. For these experiments the metal

specimen is suspended in the reaction tube and the sampling orifice is located 1 to 2 centimeters above the specimen. An example of the type of results obtained is shown in figure 23 for the system chromium specimen plus  $O_2 + NaCl(g) \pm H_2O(g)$  at 1020 °C. With this system the new species  $(NaCl)_xCrO_3$  with  $x = 1, 2$ , or 3,  $(NaOH)_yCrO_3$  with  $y = 1$  or 2,  $NaClNa_2Cr_2O_7$ , and  $NaOHNa_2Cr_2O_7$  were readily identified. At first glance one might suspect that these complexes are the product of gas phase reactions occurring in the sampling

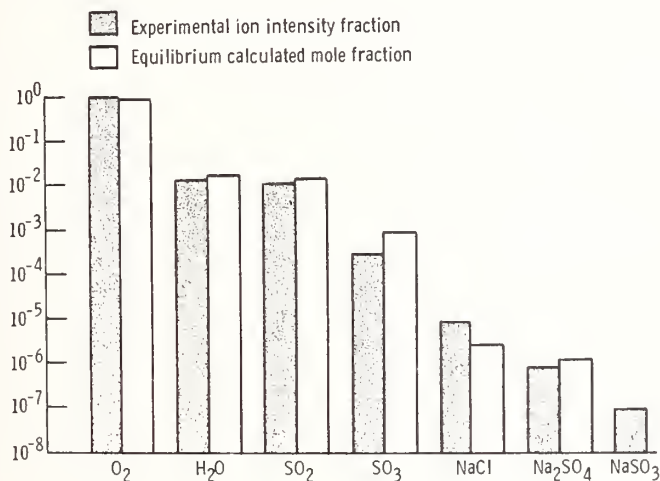


Figure 22. Comparison of measured and equilibrium calculated reaction products produced at 1413 K in a flowing gas mixture of  $NaCl(g) + SO_2(g) + H_2O(g) + O_2(g)$ .

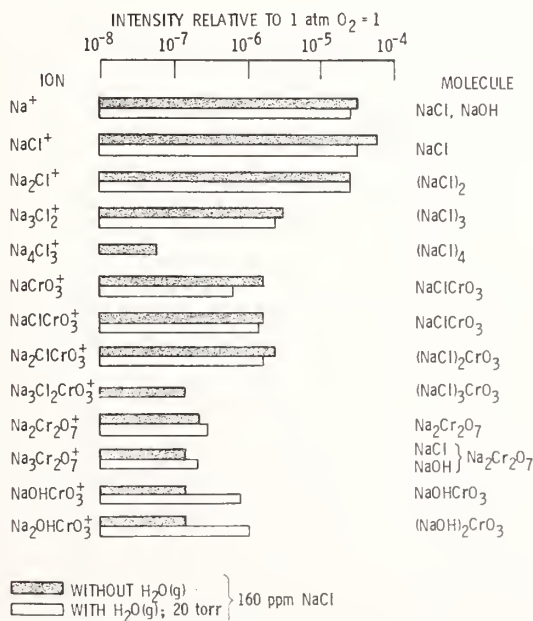


Figure 23. Mass spectrum of vapors over  $Cr_2O_3(s) + O_2(g) + NaCl(g) \pm H_2O(g)$  at 1020 °C.

process, but independent evidence obtained by a target collection technique [160] establishes that this is not the case. Even in the case of the NaCl polymers, condensation clustering does not seem reasonable when one considers the low NaCl(g) pressure and the fact that the gas is at elevated temperature [44]. In similar studies of the  $\text{Cr}_2\text{O}_3(\text{s}) + \text{KCl}(\text{g}) + \text{O}_2(\text{g}) + \text{H}_2\text{O}(\text{g})$  system, the molecules  $(\text{KCl})_x\text{CrO}_3(\text{g})$  and  $(\text{KOH})_y\text{CrO}_3(\text{g})$  were identified (fig. 24). Here  $x = 1, 2, \text{ or } 3$  and  $y = 1 \text{ or } 2$ .

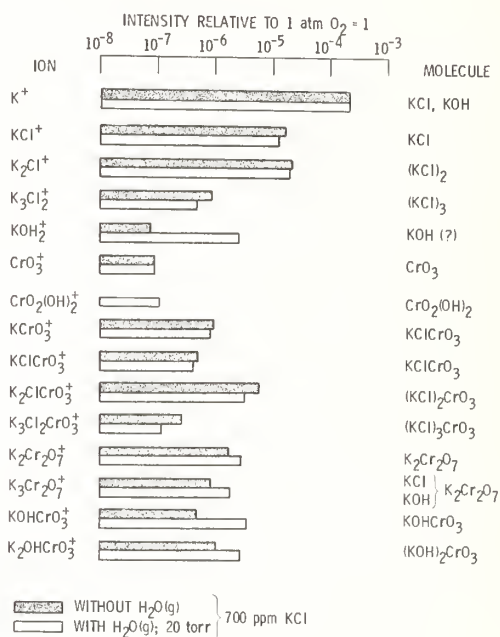


Figure 24. Mass spectrum of vapors over  $\text{Cr}_2\text{O}_3(\text{s}) + \text{O}_2(\text{g}) + \text{KCl}(\text{g}) \pm \text{H}_2\text{O}(\text{g})$  at  $1204^\circ\text{C}$ .

Studies of the system  $\text{MoO}_3(\text{s}) + \text{NaCl}(\text{g}) + \text{O}_2(\text{g}) + \text{H}_2\text{O}(\text{g})$  has revealed the existence of the high temperature gaseous molecules  $(\text{MoO}_3)_{3,4}$ ,  $(\text{NaCl})_{1,2}$ ,  $(\text{MoO}_3)_3$ ,  $\text{MoO}_2(\text{OH})_2$ , and  $\text{NaOH}(\text{MoO}_3)_3$  [160].

## 6. Concluding Remarks

The results presented above indicate some of the potential of high pressure mass spectrometric sampling as applied to several areas of high temperature chemistry. To this end the Lewis Research Center apparatus has proven to be a valuable tool. Experience with this apparatus has indicated shortcomings and limitations as well as directions for future improvement. Orifice clogging is an annoying but not limiting problem. For certain types of experiments so-called "metastable noise" [82] has proven to be a source of sensitivity limitation. It is our hope that changing from a coaxial to cross-beam configuration will alleviate this problem. Optimization of the apparatus performance would be greatly facilitated if it were possible to change the orifice-to-skimmer separation remotely while operating the sampler. Finally, the vast quantity of data that can be generated with this apparatus makes it highly desirable to computerize the system.

In the future we look forward to a continued and broader application of the high pressure sampling technique to problems in high temperature chemistry. The development of more compact and even portable apparatus could open new areas of application. There is a need for such instrumentation to monitor industrial processes and combustion systems. Applications may also exist in environmental pollution engineering.

Some indication of the nature and direction of future advances in this area is evident in papers presented at this conference. High pressure mass spectrometric sampling is now another well-established tool to be used in the characterization of high temperature vapors and gases.

#### References

- [1] Diesen, R. W., *J. Chem. Phys.* 44, 3662 (1966).
- [2] Williams, G. J. and Wilkins, R. G., *Combust. Flame*, 21, 325 (1973).
- [3] Dushman, S., *Scientific Foundations of Vacuum Technique*, 2nd ed., J. M. Lafferty, ed., pp. 80-81 (John Wiley and Sons, Inc., 1962).
- [4] Anderson, J. B., in *Molecular Beams and Low Density Gas Dynamics*, P. P. Wegener, ed., pp. 1-91 (Marcel Dekker, Inc., 1974).
- [5] Bier, K. and Hagena, O. F., *Rarefied Gas Dynamics*, Proc. of Third Intl. Symposium. Vol. 1, J. A. Laurmann, ed., pp. 478-496 (Academic Press, 1963).
- [6] Ashkenas, H. and Sherman, F. S., *Rarefied Gas Dynamics*, Proc. of Fourth Intl. Symposium, Vol. 2, J. H. deLeeuw, ed., pp. 84-105 (Academic Press, 1966).
- [7] Knuth, E. L., *Appl. Mech. Rev.* 17, 751 (1964).
- [8] Anderson, J. B., Andres, R. P., and Fenn, J. B., *Adv. Chem. Phys.* 10, 275 (1966).
- [9] Anderson, J. B., Andres, R. P., and Fenn, J. B., *Adv. At. Mol. Phys.* 3, 345 (1965).
- [10] Knuth, E. L., in *Engine Emissions: Pollutant Formation and Measurement*, G. S. Springer and D. J. Patterson, eds., pp. 319-363 (Plenum Publishing Co., 1973).
- [11] Hansen, A. G., *Fluid Mechanics*, pp. 223-296 (John Wiley & Sons, Inc., 1967).
- [12] Knuth, E. L., Dept. Eng. Report 64-53, University of California, Los Angeles (1964).
- [13] Anderson, J. B., Andres, R. P., Fenn, J. B., and Maise, G., *Rarefied Gas Dynamics*, Proc. of Fourth Intl. Symposium, Vol. 2, J. H. deLeeuw, ed., pp. 106-127 (Academic Press, 1966).
- [14] Milne, T. A. and Greene, F. T., 10th Symposium (Intl.) on Combust., pp. 153-159 (The Combustion Institute, 1965).
- [15] Calo, J. M., *J. Chem. Phys.* 62, 4904 (1975).
- [16] Anderson, J. B., *AIChE J.* 13, 1188 (1967).
- [17] Milne, T. A. and Greene, F. T., *Adv. High Temp. Chem.* 2, 107 (1969).
- [18] Bird, G. A., *AIAA J.* 8, 1998 (1970).
- [19] Anderson, J. B. and Fenn, J. B., *Phys. Fluids*, 8, 780 (1965).
- [20] Kantrowitz, A. and Grey, J., *Rev. Sci. Instrum.* 22, 328 (1951).
- [21] Parker, H. M., Kuhlthau, A. R., and Zapata, R., *Rarefied Gas Dynamics*, Proc. First Intl. Symp., F. M. Devienne, ed., pp. 69-79 (Pergamon Press, 1960).



- [22] LeRoy, R. L. and Govers, T. F., *Can. J. Chem.* 48, 1743 (1970).
- [23] Hagen, O. F. and Morton, Jr., H. S., *Rarefied Gas Dynamics*, Proc. of Fifth Intl. Symp., Vol. II, C. L. Brundin, ed., pp. 1369-1384 (Academic Press, 1967).
- [24] French, J. B., *AGARDOGRAPH-112* (1966).
- [25] LeRoy, R. L., Govers, T. R., and Deckers, J. M., *Can. J. Chem.* 48, 927 (1970).
- [26] Hamel, B. B. and Willis, D. R., *Phys. Fluids*, 9, 829 (1966).
- [27] Sharma, P. K., Knuth, E. L., and Young, W. S., *J. Chem. Phys.* 64, 4345 (1976).
- [28] Habets, A. H. M., Beijerinck, H. C. W., and Verster, N. F., *Rarefied Gas Dynamics*, Proc. of Ninth Intl. Symposium, Vol. I, M. Becker and M. Fiebig, eds., pp. B.6-1 to B.6-11 (DFVLR Press, 1974).
- [29] Biordi, J. C., Lazzara, C. P., and Papp, J. F., Bureau of Mines RI 7723 (1973).
- [30] Goshgarian, B. B. and Solomon, W. C., *AFRPL-TR-72-30* (1972).
- [31] Lin, S.-S., *Molecular Beam Sampling Conference* (Midwest Research Institute, 1972).
- [32] Hayhurst, A. N. and Telford, N. R., *Proc. Roy. Soc. London*, 322A 483 (1971).
- [33] Hayhurst, A. N. and Telford, N. R., *Combust. Flame*, 28, 67 (1977).
- [34] Hayhurst, A. N., Kittelson, D. B., and Telford, N. R., *Combust. Flame*, 28, 123 (1977).
- [35] Bossel, U., PhD Thesis, Report A6-68-6, University of California, Berkeley (1968).
- [36] McLean W. J., PhD Thesis, Report TS-71-7, University of California, Berkeley (1971).
- [37] Fenn, J. B. and Deckers, J., *Rarefied Gas Dynamics*, Proc. Third Int. Symposium, Vol. I, J. A. Laurmann, ed., pp. 497-515 (Academic Press, 1963).
- [38] Scott, J. E., Jr. and Drewry, J. E., *Rarefied Gas Dynamics*, Proc. Third Intl. Symposium, Vol. I, J. A. Laurmann, ed., pp. 516-538 (Academic Press, 1963).
- [39] Milne, T. A. and Greene, F. T., *J. Chem. Phys.* 47, 4095 (1967).
- [40] Milne, T. A., Greene, F. T., and Beachey, J. E., *J. Chem. Phys.* 56, 5340 (1972).
- [41] Beylich, A. E., *Rarefied Gas Dynamics*, Proc. of Ninth Intl. Symp., M. Becker and M. Fiebig, eds., pp. F.5-1 to F.5-10 (DFVLR Press, 1974).
- [42] Hagen, O. F., *Molecular Beams and Low Density Gas Dynamics*, P. P. Wegener, ed., pp. 93-181 (Marcel Dekker, Inc., 1974).
- [43] Peeters, J. and Mahnen, G., 14th Symp. (Intl.) on Combust., pp. 133-146 (The Combustion Institute, 1973).
- [44] Hagen, O. F. and Obert, W., *J. Chem. Phys.* 56, 1793 (1972).
- [45] Hastie, J. W., *Int. J. Mass Spectrom. Ion Phys.* 16, 89 (1975); *High Temperature Vapors*, p. 256 (Academic Press, 1975).
- [46] Biordi, J. C., Lazzara, C. P., and Rapp, J. F., *Combust. Flame*, 23, 73 (1974).
- [47] Greene, F. T. and Milne, T. A., *Adv. Mass Spectrom.* 3, 841 (1964).
- [48] Milne, T. A., Beachey, J. E., and Greene, F. T., *J. Chem. Phys.* 56, 3007 (1972).
- [49] Eltenton, G. C., *J. Chem. Phys.* 10, 403 (1942).
- [50] Eltenton, G. C., *J. Chem. Phys.* 15, 455 (1947).
- [51] Foner, S. N. and Hudson, R. L., *J. Chem. Phys.* 21, 1374 (1953).
- [52] Knewstubb, P. F. and Sugden, T. M., 17th Symp. (Intl.) on Combust., pp. 247-253 (Butterworths, 1959).
- [53] Knewstubb, P. F. and Sugden, T. M., *Proc. Roy. Soc.* 255A, 520 (1960).

- [54] Knewstubb, P. F. and Sugden, T. M., *Nature*, 196, 1311 (1962).
- [55] Green, J. A. and Sugden, T. M., 9th Symp. (Intl.) on Combust., pp. 607-620 (The Combustion Institute, 1963).
- [56] Sugden, T. M., Goodings, J. M., Jones, J. M., and Parkes, D. A., Combustion Institute European Symp., F. J. Weinberg, ed., pp. 250-255 (Academic Press, 1973).
- [57] Morley, C., *Vacuum*, 24, 581 (1974).
- [58] Morley, C., *Combust. Flame*, 27, 189 (1976).
- [59] Goodings, J. M., Bohme, D. K., and Sugden, T. M., 16th Symp. (Intl.) on Combust., pp. 891-902 (The Combustion Institute, 1977).
- [60] Deckers, J. and van Tiggelen, A., 7th Symp. (Intl.) on Combust., pp. 254-255 (Butterworths, 1959).
- [61] Deckers, J. and van Tiggelen, A., *Nature* 181, 1460 (1957); *ibid.* 182, 863 (1958).
- [62] de Jaegere, S., Deckers, J., and van Tiggelen, A., 8th Symp. (Intl.) on Combust., pp. 155-160 (Williams and Wilkins, 1962).
- [63] Feugier, A. and van Tiggelen, A., *Combust. Flame*, 11, 234 (1967).
- [64] Peeters, J. and Mahnen, G., Combustion Institute European Symp., F. J. Weinberg, ed., pp. 53-58 (Academic Press, 1973).
- [65] Bertrand, C. and van Tiggelen, P. J., *J. Phys. Chem.* 78, 2320 (1974).
- [66] Vandooren, J., Peeters, J., and van Tiggelen, P. J., 15th Symp. (Intl.) on Combust., pp. 745-753 (The Combustion Institute, 1975).
- [67] Peeters, J. and Vinckier, C., 15th Symp. (Intl.) on Combust., pp. 969-977 (The Combustion Institute, 1975).
- [68] Blauwens, J., Smets, B., and Peeters, J., 16th Symp. (Intl.) on Combust., pp. 1055-1064 (The Combustion Institute, 1977).
- [69] Vandooren, J. and van Tiggelen, P. J., 16th Symp. (Intl.) on Combust., pp. 1133-1144 (The Combustion Institute, 1977).
- [70] Milne, T. A., Brewer, J., and Greene, F. T., JANAF Working Group on Thermochemistry, 1st Meeting, pp. 123-138 (1963).
- [71] Greene, F. T., Brewer, J., and Milne, T. A., *J. Chem. Phys.* 40, 1488 (1964).
- [72] Milne, T. A., Midwest Research Institute Report FS-127-P (1966).
- [73] Milne, T. A. and Greene, F. T., *J. Chem. Phys.* 44, 2444 (1966).
- [74] Greene, F. T. and Milne, T. A., Midwest Research Institute Summary Technical Report, February 1, 1967, Contract No. Nonr-3599(00).
- [75] Milne, T. A. and Greene, F. T., Midwest Research Institute Summary Technical Report, July 27, 1967, Contract No. Nonr-3599(00).
- [76] Milne, T. A., Greene, F. T., Bennett, S. L., and Beachey, J. E., AFML-TR-69-225 (1969).
- [77] Milne, T. A., Greene, F. T., Beachey, J. E., Western States Section/The Combustion Institute, Spring Meeting, 1974.
- [78] Milne, T. A. and Beachey, J. E., Western States Section/The Combustion Institute, Spring Meeting, 1976.
- [79] Milne, T. A. and Beachey, J. E., FE-2288-12 (1977).

- [80] Milne, T. A. and Beachey, J. E., *Combust. Sci. Tech.* 16, 139 (1977).
- [81] Milne, T. A. and Beachey, J. E., *Combust. Sci. Tech.* 16, 123 (1977).
- [82] Greene, F. T., Beachey, J. E., and Milne, T. A., FE-2288-19 (1977).
- [83] Homann, K. H., Mochizuki, M., and Wagner, H. Gg., *Z. Phys. Chem. N.F.* 37, 299 (1963).
- [84] Homann, K. H. and Wagner, H. Gg., *Ber. Bunsenges. Phys. Chem.* 69, 20 (1965).
- [85] Homann, K. H., Krome, G., and Wagner, H. Gg., *Ber. Bunsenges. Phys. Chem.* 72, 998 (1968).
- [86] Homann, K. H. and MacLean, D. I., *J. Phys. Chem.* 75, 3645 (1971).
- [87] Homann, K. H., Warnatz, J., Wellmann, C., 16th Symp. (Intl.) on Combust., pp. 853-860 (The Combustion Institute, 1977).
- [88] Calcote, H. F. and Reuter, J. L., *J. Chem. Phys.* 38, 310 (1963).
- [89] Calcote, H. F., 9th Symp. (Intl.) on Combust., pp. 622-633 (Academic Press, 1963).
- [90] Jensen, D. E., *Trans. Faraday Soc.* 65, 2123 (1969).
- [91] Jensen, D. E., *J. Chem. Phys.* 51, 4674 (1969).
- [92] Jensen, D. E. and Miller, W. J., *J. Chem. Phys.* 53, 3287 (1970).
- [93] Jensen, D. E., *J. Chem. Phys.* 52, 3305 (1970).
- [94] Jensen, D. E. and Miller, W. J., 13th Symp. (Intl.) Combust., pp. 363-370 (The Combustion Institute, 1971).
- [95] Miller, W. J., *J. Chem. Phys.* 57, 2354 (1972).
- [96] Gould, R. K. and Miller, W. J., *J. Chem. Phys.* 62, 644 (1975).
- [97] Jensen, D. E. and Jones, G. A., *J. Chem. Soc., Faraday Trans. I* 71, 149 (1975).
- [98] Miller, W. J. and Gould, R. K., *Chem. Phys. Letters* 38, 237 (1976).
- [99] Miller, W. J. and Gould, R. K., *J. Chem. Phys.* 68, 3542 (1978).
- [100] Hayhurst, A. N. and Sugden, T. M., *Proc. Roy. Soc. Lond.* 293A, 36 (1966).
- [101] Hayhurst, A. N., Mitchell, F. R. G., and Telford, N. R., *Int. J. Mass Spectrom. Ion Phys.* 7, 177 (1971).
- [102] Hayhurst, A. N. and Kittelson, D. B., *J. Chem. Soc., Chem. Comm.* 422 (1972).
- [103] Hayhurst, A. N. and Telford, N. R., *J. Chem. Soc., Faraday Trans. I*, 68, 237 (1972).
- [104] Burdett, N. A. and Hayhurst, A. N., *Nature, Phys. Sci.* 245, 77 (1973).
- [105] Hayhurst, A. N. and Kittelson, D. B., *Combust. Inst. European Symp.*, F. J. Weinberg, ed., pp. 261-265 (Academic Press, 1973).
- [106] Hayhurst, A. N. and Kittelson, D. B., *Proc. Roy. Soc. Lond.* 338A, 155 (1974).
- [107] Hayhurst, A. N. and Kittelson, D. B., *Proc. Roy. Soc. Lond.* 338A, 175 (1974).
- [108] Burdett, N. A., Hayhurst, A. N., and Morley, C., *Chem. Phys. Letters*, 25, 596 (1974).
- [109] Hayhurst, A. N. and Telford, N. R., *J. Chem. Soc., Faraday Trans. I*, 70, 1999 (1974).
- [110] Hayhurst, A. N., *IEEE Trans. Plasma Sci.* PS-2, 115 (1974).
- [111] Hayhurst, A. N. and Telford, N. R., *J. Chem. Soc., Faraday Trans. I*, 71, 1352 (1975).
- [112] Burdett, N. A. and Hayhurst, A. N., 15th Symp. (Intl.) on Combust., pp. 979-990 (The Combustion Institute, 1975).
- [113] Burdett, N. A. and Hayhurst, A. N., *Chem. Phys. Letters* 48, 95 (1977).
- [114] Burdett, N. A. and Hayhurst, A. N., *Proc. Roy. Soc. Lond.* 355A, 377 (1977).

- [115] Burdett, N. A. and Hayhurst, A. N., 16th Symp. (Int.) on Combust., pp. 903-915 (The Combustion Institute, 1977).
- [116] Sawyer, R. F., McMullen, E. T., and Purgalis, P., AIAA J. 6, 2111 (1968).
- [117] Young, W. S. and Knuth, E. L., Entropie, No. 30, 25 (1969).
- [118] Young, W. S., Wang, Y. G., Rodgers, W. E., and Knuth, E. L., in Technology Utilization Ideas for the 70's and Beyond, American Astronautical Society, pp. 281-289 (1971).
- [119] Young, W. S., Rodgers, W. E., Cullian, C. A., Wang, Y. G., and Knuth, E. L., Proc. of the 2nd Intl. Clean Air Congress, pp. 418-424 (Academic Press, 1971).
- [120] Gay, R. L., Young, W. S., and Knuth, E. L., Combust. Flame, 24, 391 (1975).
- [121] MacDermott, W. N. and Dix, R. E., AIAA J. 10, 494 (1972).
- [122] McCay, T. D., Powell, H. M., and Busby, M. R., AIAA 15th Aerospace Sci. Meeting, AIAA Paper No. 77-154, American Institute of Aeronautics and Astronautics, 1977.
- [123] McCay, T. D., Powell, H. M., and Busby, M. R., J. Spacecraft and Rockets, 15, 133 (1978).
- [124] Goshgarian, B., Selph, C., and O'Pray, J., AIAA/SAE 10th Propulsion Conf., AIAA Paper No. 74-1141, American Institute of Aeronautics and Astronautics, 1974.
- [125] Biordi, J. C., Lazzara, C. P., and Papp, J. F., 14th Symp. (Int.) on Combust., pp. 367-381 (The Combustion Institute, 1973).
- [126] Lazzara, C. P., Biordi, J. C., and Papp, J. F., Combust. Flame, 21, 371 (1973).
- [127] Lazzara, C. P., Biordi, J. C., and Papp, J. F., Bureau of Mines RI 7766 (1973).
- [128] Biordi, J. C., Papp, J. F., and Lazzara, C. P., J. Chem. Phys. 61, 741 (1974).
- [129] Biordi, J. C., Lazzara, C. P., and Papp, J. F., Bureau of Mines RI 8029 (1975).
- [130] Biordi, J. C., Lazzara, C. P., and Papp, J. F., A.C.S. Symp. Series, No. 16, American Chemical Society, pp. 256-294 (1975).
- [131] Biordi, J. C., Lazzara, C. P., and Papp, J. F., Combust. Flame, 26, 57 (1976).
- [132] Biordi, J. C., Lazzara, C. P., and Papp, J. F., Bureau of Mines RI 8222 (1977).
- [133] Biordi, J. C., Prog. Astronaut. and Aeronaut. 53, 125 (1977).
- [134] Biordi, J. C., Prog. Energy Combust. Sci. 3, 151 (1977).
- [135] Hastie, J. W., Combust. Flame, 21, 49 (1973).
- [136] Hastie, J. W., Combust. Flame, 21, 187 (1973).
- [137] Hastie, J. W., J. Res. N.B.S. 77A, 733 (1973).
- [138] Hastie, J. W., Chem. Phys. Letters, 26, 338 (1974).
- [139] Bonnell, D. W. and Hastie, J. W., this volume (1979).
- [140] Farber, M. and Srivastava, R. D., Combust. Flame, 20, 33 (1973).
- [141] Farber, M. and Srivastava, R. D., Combust. Flame, 20, 43 (1973).
- [142] Farber, M., Harris, S. P., and Srivastava, R. D., Combust. Flame, 22, 191 (1974).
- [143] Farber, M., Srivastava, R. D., Frisch, M. A., and Harris, S. P., Faraday Discussions Symp. 8, 121 (1974).
- [144] Farber, M. and Srivastava, R. D., Combust. Flame, 25, 101 (1975).
- [145] Farber, M. and Srivastava, R. D., Combust. Flame, 27, 99 (1976).
- [146] Farber, M. and Srivastava, R. D., Combust. Flame, 31, 309 (1978).



- [147] Delfau, J. L., Vacher, J. R., Thomas, R., and Barassin, A., Combust. Inst. European Symp., F. J. Weinberg, ed., pp. 256-260 (Academic Press, 1973).
- [148] Tse, R. S., Michaud, P., and Delfau, J. L., Nature, 272, 153 (1978).
- [149] Houseman, J. and Young, W. S., Proc. 4th Int. Symp. Mol. Beams, pp. 125-140 (1973).
- [150] Ryason, P. R., AIAA 11th Prop. Conf., AIAA Paper No. 75-1270, American Institute of Aeronautics & Astronautics (1975).
- [151] Ryason, P. R., 13th JANNAF Combust. Meeting, Vol. 3, pp. 63-78 (1976).
- [152] Price, D., Lippiatt, J. H., Brown, R. W., and Izod, D. C. A., Adv. Mass Spectrom. 6, 551 (1974).
- [153] Lin, S.-S., J. Amer. Ceram. Soc. 58, 160 (1975).
- [154] Lin, S.-S., J. Amer. Ceram. Soc. 58, 271 (1975).
- [155] Lin, S.-S., J. Electrochem. Soc. 122, 1405 (1975).
- [156] Lin, S.-S., J. Electrochem. Soc. 123, 512 (1976).
- [157] Lin, S.-S., J. Amer. Ceram. Soc. 58, 273 (1976).
- [158] Lin, S.-S., J. Electrochem. Soc. 124, 1945 (1977).
- [159] Serauskas, R. V., Brown, G. R., Pertel, R., Int. J. Mass Spectrom. Ion Phys. 16, 69 (1975).
- [160] Fryburg, G. C., Miller, R. A., Kohl, F. J., and Stearns, C. A., J. Electrochem. Soc. 124, 1738 (1977); NASA TM X-73476 (1976) and NASA TM X-73599 (1977).
- [161] Stearns, C. A., Miller, R. A., Kohl, F. J., and Fryburg, G. C., J. Electrochem. Soc. 124, 1145 (1977); NASA TM X-73600 (1977).
- [162] Fryburg, G. C., Miller, R. A., Stearns, C. A., and Kohl, F. J., in High Temperature Metal Halide Chemistry, D. L. Hildenbrand and D. D. Cubicciotti, eds., The Electrochemical Society Softbound Symp. Series, Vol. 78-1, pp. 468-483 Princeton, NJ (1978); NASA TM-73794 (1977).
- [163] Stearns, C. A., Kohl, F. J., Fryburg, G. C., and Miller, R. A., in High Temperature Metal Halide Chemistry, D. L. Hildenbrand and D. D. Cubicciotti, eds., The Electrochemical Society Softbound Symp. Series, Vol. 78-1, pp. 555-573 Princeton, NJ (1978); NASA TM-73796 (1977).
- [164] Kohl, F. J., Miller, R. A., Stearns, C. A., Fryburg, G. C., and Dillard, J. G., in High Temperature Metal Halide Chemistry, D. L. Hildenbrand and D. D. Cubicciotti, eds., The Electrochemical Society Softbound Symp. Series, Vol. 78-1, pp. 595-607 Princeton, NJ (1978); NASA TM-73795 (1977).
- [165] Stevenson, D. A., Mattes, B. L., and Dun, H., Center for Materials Research, Stanford Univ., Technical Report CMR-77-4 (1977).
- [166] Kolb, C. E., Yousefian, V., Wormhoudt, J., Haimes, R., Martinez-Sanchez, M., and Kerrebrock, J. L., Aerodyne Research, Inc., ARI-RR-116 (1978).
- [167] Beyer, R. A., U.S. Army Armament Research and Development Command Memorandum Report ARBRL-MR-02816 (1978).
- [168] Korobeinichev, O. P., Zenin, A. A., Tereshchenko, A. G., and Puchkov, V. M., Fiz. Goreniia i Vzryva 13, 335 (1978); translation: Combustion, Explosion, and Shock Waves 13, 273 (1978).



- [169] Milne, T. A. and Greene, F. T., Adv. Chem. Ser. 72, 68 (1968).
- [170] Stearns, C. A., Kohl, F. J., Fryburg, G. C., and Miller, R. A., NASA TM 73720 (1977).
- [171] Fite, W. L., Selection of Frequency in Modulated Beam Mass Spectrometry, Extra-nuclear Laboratories, Inc., Res. Note 2.
- [172] Fite, W. L. and Brackman, R. T., Phys. Rev. 112, 1141 (1958).
- [173] Harrison, H., Hummer, D. G., and Fite, W. L., J. Chem. Phys. 41, 2567 (1964).
- [174] Harrison, H., Hummer, D. G., and Fite, W. L., Sci. Memo 26, Boeing Sci. Res. Labs. (1963).
- [175] Yamamoto, S. and Stickney, R. E., J. Chem. Phys. 47, 1091 (1967).
- [176] Miller, R. A., Crossed Molecular Beam Reactive Scattering of Barium and Samarium with Sulfur Dioxide. PhD. Thesis, Case Western Reserve Univ. (1976).
- [177] Milne, T. A., Beachey, J. E., and Greene, F. T., AFCRL-70-0341 (1970); AD-709229.
- [178] Fenimore, C. P., 14th Symp. (Intl.) on Combust., pp. 955-963 (The Combustion Institute, 1973).
- [179] Durie, R. A., Johnson, G. M., and Smith, M. Y., 15th Symp. (Intl.) on Combust., pp. 1123-1133 (The Combustion Institute, 1975).
- [180] Crane, K. C. A. and Stalker, R. J., J. Phys. D.: Appl. Phys. 10, 679 (1977).
- [181] Seery, D. J. and Zabielski, M. F., Western States Section/The Combustion Institute, Fall Meeting, 1977, WSS/CI Paper 77-30.
- [182] McAllister, T., Nicholson, A. J. C., and Swingler, D. L., Int. J. Mass Spectrom. Ion Phys. 27, 43 (1978).
- [183] Greene, F. T., AFML-TR-77-15 (1977).

### Bibliography

The citations listed below are not referred to in the text above, but contain descriptions of apparatus and/or discussions of the high pressure molecular beam mass spectrometric sampling technique. They are listed here for completeness.

- [1] Milne, T. A., High-Pressure Sampling Conference Report (Midwest Research Institute, 1965); AD-618566.
- [2] Dimiduk, P. W., AFML-TR-67-97 (1967); AD-815499.
- [3] Chang, J. H., AIAA 7th Aerospace Sci. Meeting, AIAA Paper No. 69-94, American Institute of Aeronautics and Astronautics (1969).
- [4] Kahrs, J., AFRPL-TR-70-28 (1970); AD-870956.
- [5] Williams, G. J., Rocket Propulsion Establishment, England, Tech. Memo 546 (1970); AD-891866.
- [6] Greene, F. T., Molecular Beam Sampling Conference (Midwest Research Institute, 1972).
- [7] Williams, G. J. and Wilkins, R. G., Rocket Propulsion Establishment, England, Tech. Rept. No. 72/6 (1972); AD-914035.
- [8] Lin, S. S., AMMRC TR 73-9 (1973).
- [9] Zabielski, M. F., United Aircraft Research Laboratories, UAR-N186 (1974).

[10] Intl. J. Mass Spectrom. Ion Phys. 16, No. 1/2 (1975).

[11] White, K. J. and Reynolds, R. W., U.S. Army Ballistic Research Laboratories Memo. Rept. No. 2497 (1975); AD-A013372.

#### Discussion

(Editor's note): A question from an unidentifiable source was raised concerning office plugging.

Response (Stearns): We do have condensation of material on the skimmer. This has never caused us any problems. Routinely, when we open the system to clean the sampling orifice, we will wipe material off the skimmer. But I can't say that we have ever had any problems with it. We have a rather large orifice in our skimmer. It is 30 mil diameter.

Question (written) (Hastie): In the flame composition profile shown for the NaCl-seeded flame, how do the authors account for the difference in value of NaCl measured (too low) and that calculated by the equilibrium code? And, second, why was only a single point shown for the HCl profile?

Response (written) (Stearns and Kohl): The way the NaCl seed is added to the flame (aspirated aqueous solution) introduces uncertainty as to the actual concentration of NaCl to be used in the equilibrium calculations for the system. Also, the profile is for the  $\text{NaCl}^+$  ion only and no contribution from the  $\text{Na}^+$  fragment ion is included [C. A. Stearns, R. A. Miller, F. J. Kohl and G. C. Fryburg: J. Electrochem. Soc. 124, 1145 (1977)].

With regard to the second point, missile grade oxygen gas was used for the  $\text{CH}_4\text{-O}_2\text{-SO}_2\text{-H}_2\text{O-NaCl}$  flame. This grade of oxygen contains a high argon impurity level of 2300 ppm. This argon level results in a high (in-phase) background signal at 36, 38, and 40 amu. The 36 and 38 background signals make the measurement of HCl signals difficult and therefore we do not normally profile this species.

Comment (Steinberg): I have a comment that addresses the point made with respect to calibrating the aspirator-burner combination. If you simply inject your sodium chloride with your aspirator or nebulizer, and then look at the emission of the sodium and get a curve of growth, it is linear for a while as you increase the sodium concentration and then it goes square root dependence on the sodium. The point where it goes from linear to square root is calculable and that gives you an absolute calibration then of the sodium injection into your flame. Try it, it is simple.

Question (Hastie): Have you looked at lean flames, since for that case what Dr. Steinberg says would apply very well?

Response (Stearns): We haven't, John.



## TRANSPIRATION MASS SPECTROMETRY OF HIGH TEMPERATURE VAPORS

D. W. Bonnell and J. W. Hastie  
National Bureau of Standards  
Washington, DC 20234

Material transport via vapor phase species at high temperature and pressure is an important phenomenon in materials science and technology. The preparation of high purity semiconductor and ceramic materials utilizes vapor transport to advantage, whereas the corrosion of power plant boilers, gas turbines and other advanced energy devices results from reactive vapor transport. To understand and control these transport phenomena, it is essential to be able to identify and measure the key chemical species present in the vapor phase systems. However, in the past, classical characterization methods such as transpiration and Knudsen or Langmuir effusion have been limited because they do not establish the molecular identity of transport species or because low pressures are necessary to make effusion measurements.

We have developed a new technique - Transpiration Mass Spectrometry (TMS) - that overcomes both of these limitations by combining the basic features of transpiration and mass spectrometry. With this technique, it is possible to sample reactive gases directly from high-temperature, high-pressure atmospheres for qualitative and quantitative characterization with a mass spectrometer. To demonstrate the method, the thermodynamic equilibrium vaporization of the salts  $\text{Na}_2\text{SO}_4$  and  $\text{NaCl}$  was studied at total pressures up to an atmosphere using  $\text{N}_2$  or Ar as carrier gases. The molecular composition of the vapors was determined over a wide range of temperature and pressure and the results indicated no measurable perturbation of the vaporization equilibria due to the presence of a molecular beam sampling probe. In fact the accuracy of data obtained by the TMS method is competitive with that of established, lower dynamic range, techniques.



## 1. Introduction

### 1.1 Technological background

Many high temperature processes of technological importance rely upon, or are adversely affected by, chemically active heterogeneous subsystems. One such case involves chemical interaction of a multicomponent high temperature (e.g.,  $\sim 500$ - $2000$  K) high pressure (e.g.,  $\sim 0.1$ - $100$  atm) gas mixture with a solid or liquid substrate. This interaction frequently leads to the formation of intermediate species containing elements of both the gaseous and substrate materials. These reaction intermediates can be transported in the presence of temperature, concentration, or momentum (e.g., forced convection) gradients. Transport to another regime of temperature, pressure, or concentration can lead to a reaction-reversal or the introduction of secondary processes. In many instances, this changing chemistry along gradients results in a deposition of intermediate species with the overall result that the initial substrate has been physically transported to another part of the system.

Such material transport can have either an undesirable or beneficial effect on the system of interest. Examples in modern technology include, respectively:

- (1) Hot corrosion of gas turbines, jet engines, rockets, coal gasifiers, magneto-hydrodynamic channels, coal fired boilers, and numerous pyrometallurgical systems.
- (2) Controlled material transport for production of crystals and films, extractive metallurgy, flame inhibition and fire extinguishment, combustion modification such as smoke and antiknock control with additives, and regenerative lamp cycles.

A detailed recent discussion of these and other examples of high temperature materials transport has been given elsewhere [1]<sup>1</sup>.

In order to understand these heterogeneous processes for development of new or improved control strategies, it is necessary to define at a molecular level the transport mechanisms and particularly the reaction intermediates. To date, extensive reliance has been placed on speculation and empirical observations based solely on macroscopic variables defining the initial and final state of the system. For instance, current understanding of hot corrosion derives from metallurgical examination of the clean and corroded material under ambient conditions. Extrapolation of these observations to the actual conditions of usage requires many assumptions about the corrosion mechanisms. However, detailed mechanistic information is practically nonexistent. A further inaccuracy occurs because standard test procedures (e.g., use of laboratory burner rigs) simulate only part of the actual system. To properly relate test results to practical usage would require a knowledge of scale-up factors derived from a detailed mechanistic description of both the test and the end-use systems.

Information on reaction mechanisms, including the intermediate transport species, has been practically nonexistent heretofore because of the measurement problems associated with these extreme conditions. Very limited molecular-specific information can be obtained using optical spectroscopic methods at high temperature and pressure. In principle the broad spectrum of gaseous and vaporized species present could be identified and their spatial and temporal concentrations determined by the high pressure sampling mass spectrometric (HPMS)

---

<sup>1</sup>Figures in brackets indicate the literature references at the end of this paper.

technique. This molecular beam technique, which uses a sonic nozzle for sample extraction, has been amply demonstrated by us [2] and others for homogeneous systems, including flames. A summary of recent work in this area has been given by Stearns, et al. elsewhere in this volume [3]. For heterogeneous systems, the gas is saturated by condensible species. In this case, the nozzle probes used to interface the hot gas and the mass spectrometer become part of the reaction system and severe limitations arise. Conventional use of the HPMS technique (homogeneous systems) has required probe temperatures to be considerably less than for the sample system. With saturated gases, this leads to condensation of inorganic species at the probe tip and results in physical blockage of the small entrance orifice or in corrosive loss of the probe.

We have developed a procedure for avoiding this difficulty, in addition to providing other advantages, as described in Section 2. Basically, the sample, probe and skimmer (to a lesser degree) are maintained isothermal by an external heat source. Maintenance of a steady state (and constant pressure) between gas and substrate requires a continuous replenishment of the gas extracted by the sampling process. This leads naturally to a transpiration procedure, where the input flow rate matches the gas extraction rate through the small-orifice probe. The technique therefore combines the basic features of both the transpiration [4] and the HPMS methods.

## 1.2 Scope of application

In the following sections we describe this technique of transpiration mass spectrometry (TMS) and its application to the characterization of high temperature vapors. We have demonstrated that it is a nonperturbing method<sup>2</sup>, which is always an important concern with probe methods. The method extends the dynamic range of classical vaporization and vapor transport techniques by many orders of magnitude; at least four orders with respect to Knudsen effusion mass spectrometry. We believe that TMS should be applicable as a quantitative measurement tool for laboratory simulations of most of the technological transport systems mentioned above and eventually may be applicable to plant-scale systems.

With regard to systems of initial academic interest, one can most likely expect this technique to be a useful means of producing novel high temperature species in a spectroscopically cool form, resulting from free jet expansion cooling. This would greatly extend the utility of thermally sensitive molecular beam spectroscopic methods. In particular, electron diffraction, microwave, laser fluorescence, Raman, photoelectron, and photoionization spectroscopy, as well as matrix isolation methods, would benefit from a coupling with the TMS technique. The extended high pressure range should also allow for the study of basic thermodynamic properties of novel complexes and adducts of the type suggested indirectly from gas-solid solubility studies (e.g., see Hastie, pp. 126-148; pp. 73-87 [1]). Future extension to even greater pressures should permit definitive molecular characterization of systems in their critical state and greatly supplement equation of state studies and the fundamental understanding of fluids.

---

<sup>2</sup>At least for the equilibrium systems studied, and this is most likely the case for many nonequilibrium systems.

## 2. Apparatus

### 2.1 The mass spectrometer system

Figure 1 shows a schematic of the mass spectrometer (stage II) and vacuum system layout with the transpiration apparatus attached (stage I). The aluminum walled vacuum system is partitioned into two differentially pumped stages. The stage labeled I utilizes a 6 in diffusion pump (Varian/NRC VHS-6)<sup>3</sup> with a cold trap (Granville-Phillips Model 270-6) and gate valve (NRC 1279-6) close-coupled to the base of the vacuum chamber. Net pumping speed at the bottom of the chamber is calculated to be  $\sim 800$  l/s. The backing system for this pump-stack uses a Roots blower (Leybold-Hereaus WA250) and a rotary two stage vane pump (Sargent-Welch 1375). Use of a blower in series maintains, even for high gas loads, a pressure at the diffusion pump outlet well below the  $\sim 10^{-4}$  atm<sup>4</sup> critical backing pressure. This assures that the diffusion pump will continue to pump near its rated speed into the  $10^{-5}$  atm pressure range. A high sensitivity thermocouple gage controller (Hastings-Raydist model SL-1R) and tube (type DV-8M) was used to monitor this pressure range.

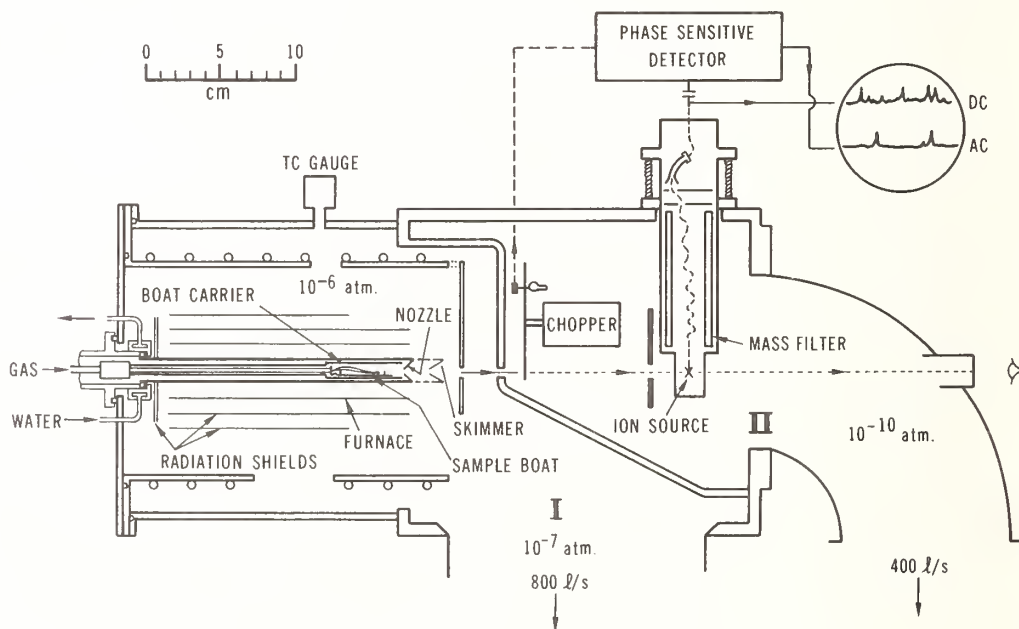


Figure 1. Detailed schematic of assembled transpiration reactor-mass spectrometer system.

<sup>3</sup>Commercial sources are identified only for purposes of accuracy and do not imply endorsement by the U. S. Government nor that they are the most suitable product for the work performed.

<sup>4</sup>1 atm =  $1.01325 \times 10^2$  kPascal; see introduction to this volume for SI unit conversions.

A mechanical shutter separates stages I and II, acting as a valve to isolate the stages during removal of the transpiration reactor assembly. In addition, there are a variety of differential pump apertures (three hole sizes) in the shutter plate for control of the molecular beam diameter and stage I to II pressure difference. The aperture used for transpiration experiments is 0.05 cm in diameter and is located 4 cm from the skimmer orifice.

Stage II, the high vacuum mass spectrometer section, is pumped by a stack consisting of a 4 in diffusion pump (Varian/NRC VHS-4), a 4 in cold trap (Granville-Phillips Model 270-4) and a butterfly valve (Vacoa BFV-4). This stage has an approximate pumping speed of 400 l/s at the vacuum chamber base. No-load vacuum in both stages is  $<5 \times 10^{-11}$  atm. The background mass spectrum at this pressure shows the 18 amu ( $\text{H}_2\text{O}^+$ ) ion as the major peak ( $\sim 50$  percent of total ions) which arises from  $\text{H}_2\text{O}$  desorption from the aluminum-walled vacuum system. At maximum load ( $\sim 50$  sccm [standard cubic centimeters per minute]) the stage I and II pressures are  $\sim 5 \times 10^{-6}$  atm and  $\sim 5 \times 10^{-9}$  atm, respectively. A titanium sublimation pump (Granville-Phillips TSP series 287 in a 214-669 chamber) and an ion pump (Ultek Model 10-250), not shown in figure 1, are used as holding pumps on the stage II section when the diffusion pump is valved off to cycle the cold trap. This periodic trap cleaning procedure minimizes release of trapped reactive gas back into the mass spectrometer chamber.

The beam modulation chopper system, located in the stage II region, is a toothed wheel (3 or 24 teeth) driven by an AC synchronous motor (Globe 75-121-2) which has been cleaned for vacuum service. A reference signal, needed for phase sensitive detection, is generated by the wheel interrupting light from a small incandescent bulb (GE number 40) impinging on a photo transistor (GE-L14B). A sine wave oscillator (Donner model 1202) supplies the drive frequency to a chopper drive system [Extranuclear Laboratories (EL)] which produces the capacitively shifted two phase 115 V power to drive the chopper motor. The three tooth chopping wheel yields beam modulation frequencies from  $\sim 40$  to 270 Hz. Higher frequencies can be obtained with the twenty-four tooth wheel. The actual chopping frequency is normally selected by observing a very weak modulated beam mass spectral peak and adjusting for minimum noise interference from the 60 Hz line frequency. For these studies a chopping frequency of  $214 \pm 1$  Hz was used.

The mass spectrometer itself is a quadrupole mass filter (EL-Model 270-9) with a crossed-beam configuration ion source (EL Model 041-2). We have modified the commercial ion source by mounting a stainless steel plate at the ion source entrance for additional neutral beam collimation. Standard quadrupole power supply (EL model 011-1) and ionizer control electronics (EL type II) are used. The mass analyzed ion beam is deflected to a channeltron electron multiplier (Galileo Electro-Optics, model 4700) mounted off axis and operated at a nominal 1700 volts dc. Since the final amplifier is a frequency and phase sensitive lock-in detector (Ithaco Model 393), the multiplier gain is set for optimum signal to noise ratio at the lock-in, rather than for maximum gain. Total system gain using a fast electrometer amplifier (EL Model 031-2) is  $\sim 4 \times 10^{11}$ ; signal to noise, rather than total signal being the sensitivity limiting factor.

This mass filter system is supported by a 6 in flange (conflat) mounted on a large welded bellows assembly which allows three-axis positioning of the ion source entrance



aperture. In practice, a pinhole and collimator alignment assembly is mounted on the beam axis with a He-Ne laser directed along the same axis. The mass filter assembly is then positioned so that the ion source entrance and exit apertures are centered on the laser beam. Final molecular beam alignment is achieved by adjusting both the mass spectrometer and the molecular beam source angle position to obtain maximum ion intensity of a non-scatterable beam component. This alignment procedure proved to be a critical phase of the experiment.

## 2.2 The transpiration reactor

The transpiration reactor is located in stage I of the overall assembly (see fig. 1). Essential features of this reactor include: a sample container or boat, a boat carrier, a thermocouple for temperature measurements, a carrier gas inlet system, and a gas extraction system or probe. The boat carrier allows for boat removal from the reactor without need for a complete disassembling of the transpiration system. Molecular beam sonic probes are typically conical nozzles with design details determined by reasonably well established gas dynamic criteria, as outlined in Section 3. However, for highly reactive systems, we also found it desirable to develop a relatively more robust capillary probe, at the possible expense of sampling fidelity. Pertinent gas dynamic considerations for this type of probe are given in Section 2.3. Below we describe the construction details of these probes and the transpiration assembly in general.

### 2.2.1 Reactor internal details

Figure 2 shows a schematic view of a typical transpiration reactor assembly, including details of the assembled boat carrier and boat. A platinum tube, with outside diameter 1.23 cm, wall thickness 0.075 cm, and length 5 cm is used as a boat carrier. This tube has machined ridges at each end to allow a snug fit with the main chamber walls for prevention of diffusion losses. Welded to the rear of the carrier is a section of 0.64 cm diameter platinum tube through which the carrier gas passes. This carrier gas tube is sealed to an SS304 1/4 in stainless steel tube via a SWAGELOK joint machined to fit inside the 1.27 cm i.d. of the main chamber. The seal is 21 cm from the front of the boat carrier. This long path length allows the gas to reach thermal equilibrium with the walls before interacting with the sample. The platinum section of the carrier gas tube also serves as a guide for introduction of an alumina sheathed Pt-Pt/10 percent Rh thermocouple to the sample area.

The boat, which is fabricated from welded platinum sheet, has a slanted base ( $\sim 5^\circ$  to the front) to allow liquid samples to be preferentially retained in the front of the boat (fig. 3). The gas baffle shown in figure 2 is located  $\sim 0.75$  cm behind the boat, and serves to interrupt the fast gas flow into the boat region, thereby allowing the gas maximum time to equilibrate thermally before passage at a relatively slow rate over the sample. The baffle also supports the tip of the alumina thermocouple sheath so that only bare wires are brought into the boat region, thereby minimizing exposure of potentially reactive ceramic to the system.



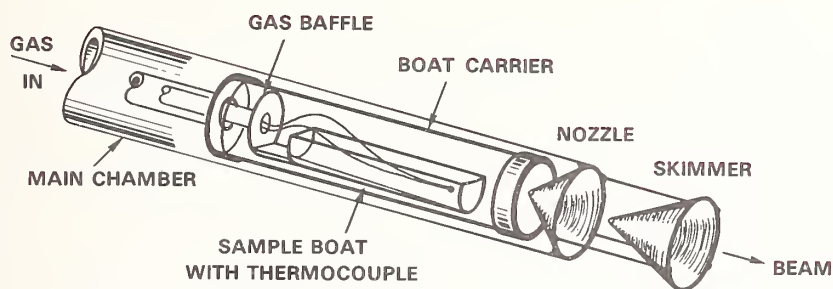


Figure 2. Transpiration reactor showing internal details.

### 2.2.2 Conical sampler

Details of the nozzle-skimmer arrangement are shown in figure 3. Nozzle cones are constructed by alternate pressing and heat annealing of thick platinum disks (2 cm x 0.1 cm) in steel dies until a 45° half angle cone with a relatively sharp tip (~0.1 cm radius) is obtained. Minor surface machining is followed by ELOX drilling of a hole in the tip to achieve an orifice 0.006-0.009 cm in diameter with a maximum hole channel length of 0.004 cm. The tip exposed to the source gas normally has a flat face ~0.1 cm wide. We discontinued use of knife edge machined nozzles since they occasionally failed in service due to cracking in the wall close to the orifice. Experience showed that gas leaking through such cracks created serious disturbances in the expanding gas flow and sufficiently disrupted the trajectory of the initial high intensity jet to lower its density, after passage through the skimmer, by three to four orders of magnitude. We believe that micro cracks originate during the cone-forming and machining process and that these cracks propagate as a result of the combined effects of thermal cycling under pressure and reactive gas mixtures (nonoxidizing). The design of a sturdier probe (snubnosed), such as that depicted in figure 3, avoided this problem which was particularly severe for slag and strongly basic samples.

The skimmer (shown in fig. 3) was fabricated in a manner similar to the nozzle, using 30° half angle dies. Finish machining specified a sharp-edged hole since cracking would not be a problem and minimal flow disturbance is mandatory for skimmers. The skimmer hole was drilled with a high speed twist drill (number 69-0.074 cm). Clogging of the skimmer was a primary concern in the use of supersonic beam sampling, since at high temperatures and source pressures a single experiment could be expected to deposit condensable material on a cool skimmer at a rate of several hundred mg/hr. Such deposits were avoided by physically attaching the skimmer to the nozzle assembly with thin platinum support struts (not shown in fig. 3). Skimmer temperatures were then within 50 K of the nozzle temperature. This arrangement also provided an essentially permanent alinement of skimmer and nozzle.

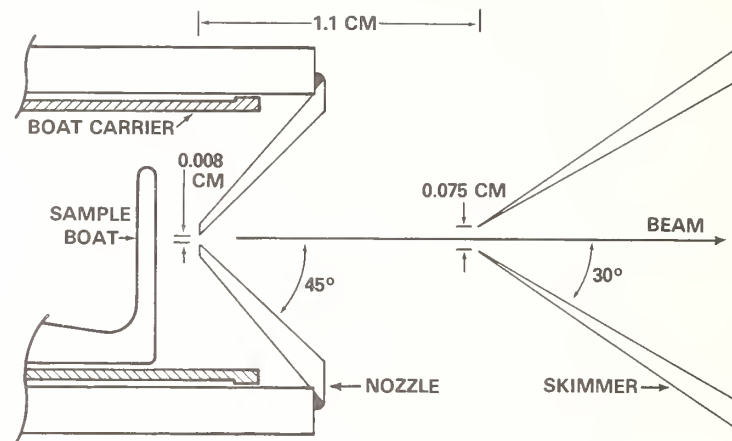


Figure 3. Schematic of conical sampler construction details and relative location of internal components. Forward edge of skimmer is attached to outer edge of chamber exterior with 3 thin (0.2 cm thick) platinum struts (not shown in fig.). For clarity, not all dimensions are drawn to scale.

### 2.2.3 Capillary sampler

A capillary sampler, shown in figure 4, was fabricated to be interchangeable with the conical nozzle-skimmer assembly. Note the absence of a skimmer with the capillary method. This omission was possible since beam velocity distribution measurements [5] with short channels (length to orifice diameter ratio of 2) and no skimmer have indicated formation of a well developed isentropic expansion leading to a high Mach number supersonic beam. Our longer channel (corresponding ratio of 30) capillary also produces a good quality supersonic beam (see Section 3.4.2).

Capillary fabrication involved first welding a 0.32 cm diameter platinum rod to the center of a 2 cm x 0.1 cm thick platinum disk. Then, using a 0.013 cm wire, a hole was drilled from the disk side by the ELOX process to a depth of  $\sim 0.5$  cm. Overcut from the ELOX process produced a converging capillary, as shown in figure 4. The rod was then cut at the bottom of the hole and crushed in steel dies to reduce the hole to the approximate dimensions shown (see fig. 4). ELOX machining smoothed any irregularities from the postforming process. The entire assembly was then welded to the main chamber tube, using a jig to maintain proper alignment. System alignment procedure was essentially identical to that used for the conical sampler system.

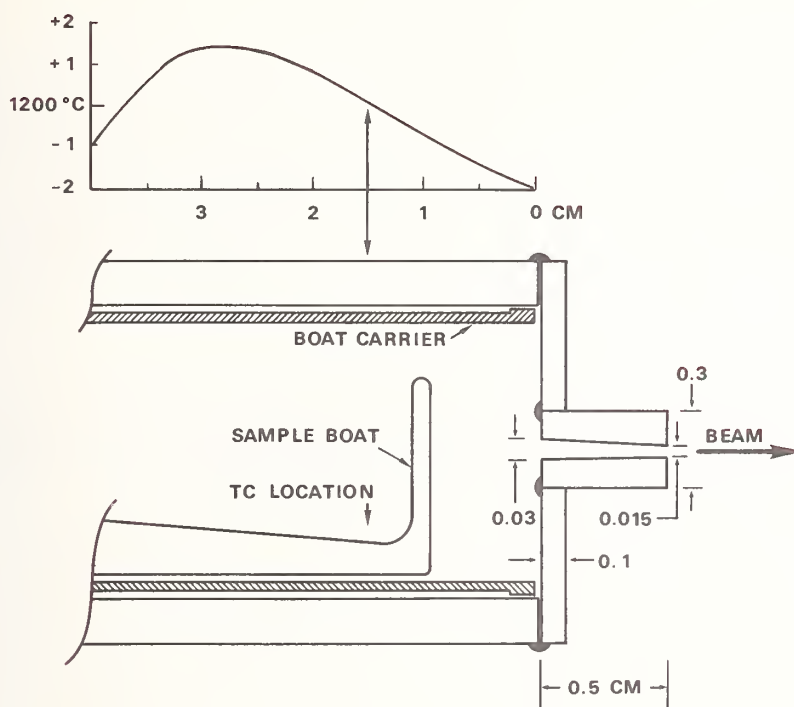


Figure 4. Schematic of capillary sampler showing construction details and relative location of internal components. Channel not drawn to scale for clarity. A typical temperature profile, obtained along the central axis of the chamber, is also shown.

#### 2.2.4 Reactor external details

The complete transpiration assembly is shown in figure 5. Attachment to the support flange is made with a 1.59 cm (commercial 5/8 in) CAJON O-ring fitting. Initially a large stainless steel SWAGELOK fitting was used to make this connection, but differential expansion on heating caused unacceptable leaks. To protect the VITON O-ring from thermal degradation, the CAJON nut was water jacketed. A rigid connection was provided by compressing a machined bridge (an integral part of the main chamber) between the nut and O-ring. With this protection, the system could operate even at the  $\sim 1700$  K maximum temperature for many hours. However, the large temperature gradient resulting from the location of this water cooled connection only 15 cm from the sample area, required careful optimization of the position of the Ta foil furnace and its radiation shields. By careful positioning of a partial shield (see fig. 5) at the rear of the furnace, it was possible to control the temperature gradient to  $< 10$  K over the length of the boat (3 cm) at the highest operating temperature. Gradients between the thermocouple location and the nozzle were much less, as shown in figure 4, and constituted a negligible source of experimental error.

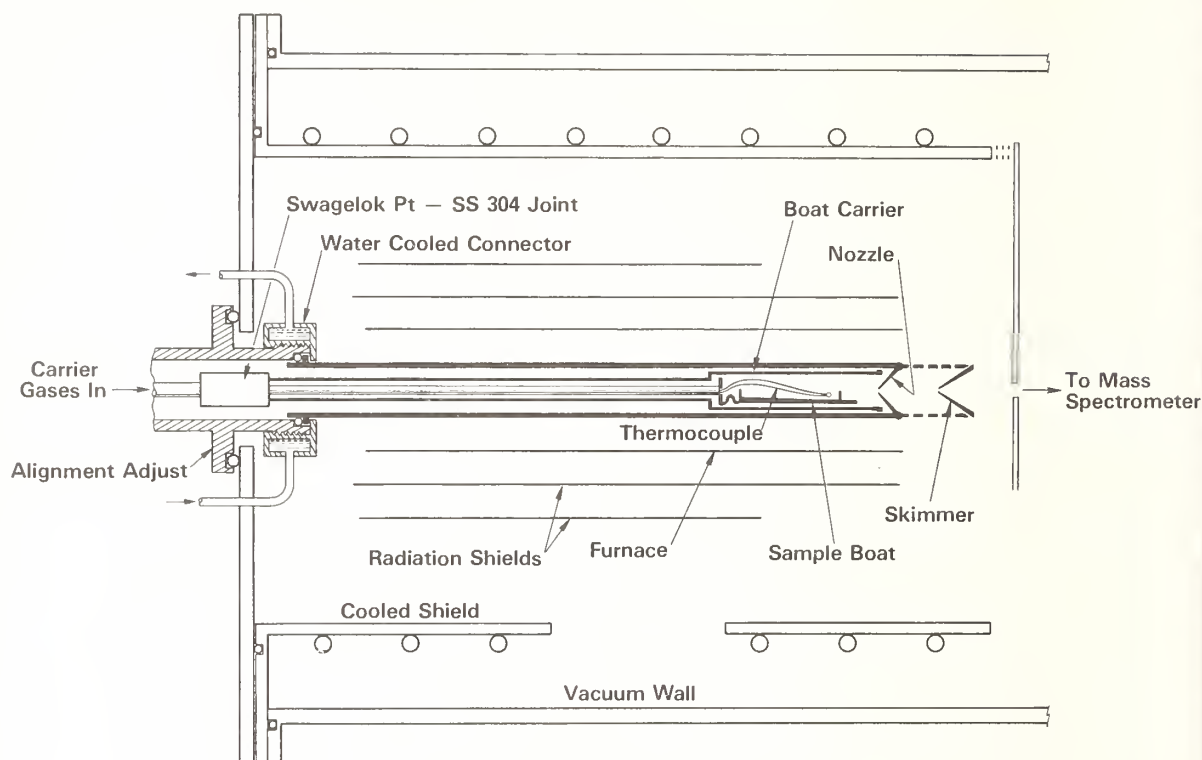


Figure 5. Transpiration inlet assembly showing details of furnace, radiation shield and assembly proportions.

The main body of the furnace is supported by water cooled bus bars (not shown in fig. 5) which are sealed to the support flange via SWAGelok compression of TEFLON sleeves against the bus bars. Power to the furnace is supplied by a 208 V, 20 amp variable autotransformer driving a 20:1 stepdown transformer. Typically, 250-300 amperes is required to attain 1700 K. Precise temperature adjustment with this arrangement is only marginally acceptable. However, alternative use of phase angle fired controllers creates unacceptable noise in the mass spectrometer signal amplifier circuit, and zero crossing controllers cannot fire into the inductance presented by the stepdown transformer. Several remedies to improve temperature control are under investigation.

A water cooled copper jacket surrounding the furnace assembly condenses high temperature species scattered by the skimmer. The front plate of this jacket is mounted on copper stand-off legs to improve pumping access to the furnace region (see fig. 5). The entire transpiration assembly is flange mounted and attached to the vacuum system as a unit, as shown in figure 1.

### 2.3 Reactor alinement

Alinement of the skimmer to the nozzle is performed by mounting the sampler (i.e., transpiration reactor) assembly in a jig with the same type CAJON fitting used for the vacuum seal at the support flange. This jig is carefully machined to have a rear face perpendicular to the sampler axis. A small He-Ne laser is then alined by reflection to project its beam parallel to the sampler axis. The laser is then translated, maintaining parallelism, until the beam is centered on the orifice. It is then a simple matter to deform the skimmer struts slightly to obtain a visually perfect circular diffraction pattern through the skimmer. This adjustment is very sensitive and can detect alinement errors of a few hundredths of a millimeter.

Approximate centering of the sampler on its support flange is achieved by translating the entire sampler on its mount until the nozzle-skimmer-line is centered in the aperture of the front plate of the water cooled shield. This initial alinement is facilitated by shining a light down the sampler and positioning the light viewed through the nozzle and skimmer. With the entire assembly mounted and evacuated, a final tuning of the initial alinement is made by telescopic observation of the light passing through the nozzle, skimmer and mass spectrometer ion source. The sampler is then centered on the differential pump aperture (separating stage I and II). Final alinement is achieved by moving the quadrupole mass filter assembly and adjusting for maximum observed beam intensity. This is a very minor adjustment, requiring movement of the mass filter by less than 1 mm.

### 2.4 Carrier gas system

Mass flow meters (Tylan Corporation model FM 360) and mass flow controllers (Tylan model FC 260) are used to provide carrier gas and mixed gas flow to the sampler. The flow controllers are slaved electronically to the carrier gas output to ensure constant and reproducible ( $\pm 0.5$  percent) gas mixture compositions. These mixtures can contain from 40 to  $2 \times 10^5$  ppm of each of as many as three solute gases in the carrier gas stream. Flow controller ranges can be readily changed from 0.2-10 sccm to 20-1000 sccm to achieve these dilutions. During a transpiration run, gas flows of typically 3-30 sccm are used. The flow meter controllers are calibrated against a mercury piston volume gage to better than 2 percent absolute sccm. The mixed gases are metered to the sampler through a rotameter-type flowmeter (Matheson series 600; 602 flow tube) and valve (NRS number 1). Before passage through this flow meter, excess carrier gas is exhausted through a metering valve and a fixed differential pressure check valve to a hood system. The total gas pressure at the sampler inlet is measured by a capacitance pressure transducer (Rosemount model 1332A4, 0-30 psia) calibrated to read directly in atmospheres. Gage sensitivity is 0.002 atm and long term accuracy is  $\pm 0.003$  atm (0.15 percent).



### 3. Gas Dynamic Aspects of High Pressure Sampling

The design of an effectively non-perturbing high pressure molecular beam sampling device, and subsequent data analysis, relies heavily on fundamental gas dynamic principles. In deciding on an optimum nozzle (probe)--skimmer geometry, consideration must be given to system pumping capacity, source pressure and temperature, desired beam intensity, and the characteristic thermodynamic and dynamic properties of the sample gas. Stearns, et al., elsewhere in this volume [3], have discussed this subject in some detail and cited the pertinent literature. The following treatment deals primarily with those aspects necessary to system design and data analysis considerations.

Following the landmark paper of Kantrowitz and Grey [6] which suggested that intense molecular beams could be obtained from small supersonic nozzles, a number of theoretical and experimental verifications [7-11], have laid the groundwork for extending this technique to studies of high pressure-high temperature systems. The primary advantages over conventional effusive techniques provided by the use of a supersonic beam source are, enhanced beam intensity resulting from the use of higher source pressures, and the narrower angular distribution (better beam collimation) obtained as a consequence of the conversion of random thermal motion to ordered motion in the expansion process. A possible disadvantage results from changes in the distribution of translational velocity, rotational and vibrational population during the initial free jet expansion stage.

#### 3.1 Free-jet relaxation effects

Factors affecting the final beam characteristics include: the nature of the free-jet expansion process (e.g., time to reach a collision free condition), down-stream effects (shock boundaries, background pressure, geometry, etc.), and the gas heat capacity(s). Inferences made concerning pre-expansion source conditions (i.e., composition of the sample gas of interest) from observations on the final molecular beam are highly dependent on an awareness of these factors and their relationship to source conditions and system design.

##### 3.1.1 Relaxation of internal modes

In the supersonic sampling process, isentropic conditions generally govern the gross mass flow characteristics of the beam (pressure, temperature and density). In an excellent review article, Morris [12] discusses relaxation phenomena under isentropically expanding hypersonic conditions. Using the Navier-Stokes equations, which have been shown [13] to satisfactorily describe the flow properties, Morris [12] estimated the translational relaxation time  $\tau_t$  for rigid non-attracting spheres to be

$$\tau_t = 5/4 \tau_c \quad ,$$

where  $\tau_c$  is the mean collision time based on the number of gas collisions. By assuming that molecular collisions are non-adiabatic with respect to rotation, it can be shown that rotational relaxation should readily occur. Experimental data for simple molecules such as  $N_2$ ,  $NH_3$ , and  $CH_4$  indicate the ratio

$$\tau_r/\tau_c < 50, \text{ where } \tau_r = \text{rotational relaxation time.}$$

Even  $H_2$  relaxes rotationally in 400 collisions. As the collision controlled expansion time is of the order of  $10^{-7}$ s, for the rapid expansions typical of the supersonic sampling process, both the translational and rotational degrees of freedom are essentially equilibrated [3].

On the other hand, vibrational relaxation is a relatively much slower process with times ranging from  $10^2$  to  $10^7 \tau_c$  [12]. Higher temperatures should increase the vibrational relaxation rates. Only binary collisions appear to be important and polyatomic species typically have a single characteristic vibrational relaxation time. For the very fast expansions characteristic of supersonic sampling, the degree of vibrational relaxation depends mainly on the gas mixture used and may vary for different constituents. Bray [14] points out that the falling temperature and pressure as the gas passes through the nozzle both tend to increase the vibrational relaxation time, and the vibrational temperature can be represented by a sudden freezing approximation.

### 3.1.2 Chemical relaxation

Chemical relaxation is of paramount concern in the application of free-jet expansion methods to the analysis of species identity and concentration in high pressure sources. Bray's [14] one-dimensional sudden freezing model of chemically reacting expanding gases, where the reaction is at equilibrium upstream and frozen downstream provides a reasonable approximation to finite rate non-equilibrium systems. This model is also supported by the experimental results of Wegener [15] who used a low expansion ratio<sup>5</sup> one-dimensional nozzle system. The reaction studied



is quite fast, with a half life of  $\sim 10^{-7}$ s [15]. In spite of the fact that the expansion time for Wegener's nozzle was about  $3 \times 10^{-3}$ s, i.e., relatively long, he observed major departures from the expansion flow equilibrium--expected for an infinitely fast relaxation rate. Hence, even for reactions of the order of  $10^4$  times faster than the expansion process, much of the chemical information may be frozen with respect to the source composition--which is the desired condition for high pressure sampling.

<sup>5</sup>Number density ratio for pre and post expansion regimes (see Section 3.2.2).

A more critical test for chemical relaxation effects is given by the very fast ion-molecule reactions studied by Hayhurst and Telford [16]. Their nozzle system geometry is similar to ours. Using a 1 atm flame source they monitored the reaction



which has an estimated forward rate relaxation time of  $2 \times 10^{-9}$  s. The concentration ratio  $[\text{H}_5\text{O}_2^+]/[\text{H}_3\text{O}^+]$  observed was much higher than the equilibrium concentration expected in the sampled flame. Using a three-dimensional method-of-characteristics solution to the expansion flow field, they obtained results which were in good agreement with one dimensional solution. Although they found significant evidence for boundary layer perturbations, caused by the water cooled nozzle, they concluded that flow equilibrium had prevailed during the early phase of expansion. They also suggested as a general criterion for ideal unperturbed sampling that the reactions of interest have a relaxation time significantly longer than continuum flow time.

For normal gas-gas and condensed-gas reactions involving uncharged species, reaction times are typically greater than  $10^{-5}$  s. As continuum flow times of  $10^{-7}$  s are typical for modern sampling systems, including ours, the criterion for minimal sampling perturbation should apply for most molecular systems of interest. In the absence of chemical reaction kinetic data, however, it is desirable to provide experimental verification of sampling fidelity. This has been done for the TMS system, as described in Section 4.

### 3.2 Beam flux and sensitivity--conical probes

#### 3.2.1 Beam flux-source pressure dependence

Greene, et al. [17] showed that the flux through the skimmer of an isentropically expanding gas from a supersonic nozzle (i.e., conical probe) has the functional form of effusive flow multiplied by a function dependent only on the gas specific heat and the Mach number at the skimmer. Experimentally it has also been shown [18] that, to a good approximation, the dilute components of a gas mixture undergoing supersonic expansion are accelerated with the characteristics of the solvent carrier gas. In the absence of mass separation effects (see Section 3.3) these results suggest that the usual mass spectrometer relationship, based on effusive flow, can be applied to the supersonic jet sampling process. That is,

$$P_0 = kIT_0$$

where  $I$  is the observed ion intensity,

$T_0$  the source temperature,

$k$  the effective mass spectrometer sensitivity constant, and

$P_0$  the source pressure.

As will be shown by our data, the functional dependence of beam flux on specific heat and Mach number can be empirically absorbed into the  $k$  factor when this "constant" is obtained from the observed ion intensity for the carrier gas at known conditions of  $P_0$  and  $T_0$ . In practice,  $k$  is measured at every temperature and pressure of an experimental run. The  $k$ 's obtained show a minor variation with temperature and pressure, reflecting small changes in the expansion process including mass separation effects.

### 3.2.2 Nozzle characteristics

The size of main chamber tube (see fig. 2) and sample which could be accommodated in the current vacuum system design, and the need to assure saturation of the carrier gas, determined the transpiration gas flow range (less than 40 sccm). In the physical design of the sampling system, available pumping speed and desired expansion ratio governed the choice of nozzle orifice size. Experimentally, it was determined for the chosen nozzle geometry and available pumping speed, that an orifice diameter of 0.008 cm, required a nitrogen carrier gas flow rate of <10 sccm to maintain a stage I pressure of  $\sim 5 \times 10^{-7}$  atm.

The Knudsen number ( $Kn_0$ ) can be determined from its definition,

$$Kn_0 = \frac{\lambda_0}{d_0}$$

where  $\lambda_0 = [(2)^{1/2} \pi \sigma^2 n_0]^{-1}$  = mean free path,

$d_0$  is the nozzle orifice diameter,

$\sigma$  is the collision diameter, and

$n_0$  is the carrier gas number density.

Using  $\sigma \sim 3.7 \times 10^{-8}$  cm [19],  $Kn_0$  for this system is 0.003 at 1 atm and 1000 K. This value is well within the limit for continuum flow which is generally taken as  $Kn_0 \leq 0.1$ . To insure that the sample beam represents the bulk source gas and not a stagnant boundary layer near the orifice, the Knudsen number should be small enough that boundary layer effects can be ignored. For  $Kn_0 \leq 0.01$  these effects are minimal [20]. In the present system, where the nozzle is maintained at  $T_0$ , this Knudsen number constraint is probably of lesser importance than the continuum flow requirement.

Pumping speed in the nozzle-skimmer region can be calculated from

$$F_0 = n_I S_I$$

where  $F_0$  is the net flow rate in molecules/s from the source,

$n_I$  is the stage I number density in molecules/cm<sup>3</sup>, and

$S_I$  is the pumping speed in cm<sup>3</sup>/s.

For the above conditions, the pumping speed in the nozzle region is calculated as  $\sim 330$  L/s. Conductance estimates, based on the stage I geometry, indicated the net pumping speed in the nozzle region should be  $\sim 300$ -400 L/s in good agreement with the above flow rate determination.



The nozzle expansion ratio for the sonic conical nozzle can be given by the ratio of source number density to stage I number density, i.e.,

$$\frac{n_0}{n_I} = \left( \frac{P_0 \cdot 298}{P_I \cdot T_0} \right) \sim 5 \times 10^5 ,$$

at typical conditions of  $P_0 = 0.8$  atm and  $T_0 = 1000$  K. This ratio is essentially constant as long as  $S_I$  and the nozzle-skimmer geometry are fixed. It was not feasible to construct a real-time variable distance nozzle-skimmer system for the following reason. The high flux of condensibles from the transpiration zone at high temperatures precluded the more conventional use of a room temperature or cooled skimmer [21] since plugging of the skimmer orifice would be quite rapid (see Section 2.1). This problem was avoided by mounting the skimmer directly onto the heated nozzle, just outside the furnace zone. The high available pumping speed of 800 L/s in stage I, outside the nozzle-skimmer region, produces an operating mean free path of  $\sim 15$  cm. A simple plate, with an orifice for line of sight transmission (see fig. 1, region I) allows the skimmer itself to behave as a differential pumping barrier with the stage I pump performing double duty. The disadvantage of a higher post-skimmer pressure is more than offset by the system simplification provided, and since the skimmer orifice would be located about 4 cm from the differential pump aperture, this nozzle-skimmer arrangement seemed to be a reasonable compromise.

### 3.2.3 Skimmer characteristics

Location of the skimmer should be well upstream of the Mach disc to avoid beam scattering through a detached shock. Ashkenas and Sherman [9] have experimentally confirmed the relation determining the Mach disc location, in nozzle diameters, as

$$\frac{Z}{d_0} = 0.67 \left( \frac{P_0}{P_I} \right)^{1/2}$$

for distance  $Z$  from the nozzle orifice, at room temperature expansion ratios to  $\sim 17,000$  and  $T_0 = T_I$ . This expression places the Mach disc in our system at  $\sim 475$  nozzle diameters or  $\sim 4$  cm from the nozzle. Greene, et al. [17] have successfully utilized a system with similar nozzle size, geometry, and expansion ratio parameters. Their determination of beam intensity dependence on nozzle to skimmer distance indicated a maximum intensity at 120 nozzle diameters for 1 atm pressure. At smaller  $Z/d_0$  the intensity dropped sharply but at greater distances the decline was gradual. In order to avoid rapid changes in instrument sensitivity with pressure the skimmer-nozzle spacing was somewhat larger than for the maximum intensity condition, i.e., 1.1 cm ( $Z/d_0 \sim 140$ ). An estimated 30 percent of the maximum beam intensity was sacrificed with this arrangement. This spacing also placed us well within the expected Mach disc location, thus providing a safety margin against a possible over-estimate of the expansion ratio. It is also desirable to locate the skimmer downstream of the "freeze-in" point,



where essentially collisionless flow begins, to minimize shock induced scattering in the downstream regions of the skimmer.

Anderson and Fenn [8] have developed an expression for estimating the location at which the terminal Mach number occurs. At this location the Mach number has a maximum rate of change and the collision dominated region of the expansion ends. Stearns, et al. [20] have calculated, using the derivations of Anderson and Fenn [8], expressions for the terminal Mach number for typical ratios of the gas heat capacity  $\gamma$ ,

$$M_t (\gamma=5/3) = 2.03 \left( \frac{Kn_o}{\varepsilon} \right)^{-0.400}$$

$$M_t (\gamma=7/5) = 2.48 \left( \frac{Kn_o}{\varepsilon} \right)^{-0.286}$$

$$M_t (\gamma=9/7) = 2.85 \left( \frac{Kn_o}{\varepsilon} \right)^{-0.222}$$

where  $\varepsilon$  is a collision effectiveness parameter, measured by Anderson and Fenn [8] for monatomic gases to be  $\sim 0.25$ . This terminal Mach number can be applied in the general semi-empirical expression for center-line Mach number

$$M = A(\gamma) \left( \frac{Z}{d_o} \right)^{\gamma-1}, \quad (M > 4)$$

where  $A(\gamma)$  is 3.26 for  $\gamma=5/3$ , 3.65 for  $\gamma=7/5$ , and 3.96 for  $\gamma=9/7$ . Using the  $\gamma=7/5$  expression for our nozzle, a value of  $M_t \sim 10.7$  is calculated.  $Z_t/d_o$  is then about 15. Thus our choice of  $Z/d_o \sim 140$  is well downstream of the point of translational freezing.

Using the sudden-freeze approximation of Stearns, et al. [20], the number density at the end of the isentropic expansion process can be calculated from

$$n_t = n_o \left[ 1 + \frac{(\gamma-1)}{2} M_t^2 \right] (1-\gamma)^{-1}$$

which for typical conditions ( $n_o = 2.2 \times 10^{19}$  molecules/cm<sup>3</sup>) in our system gives  $n_t \sim 3.6 \times 10^{15}$  molecules/cm<sup>3</sup>. The number density ( $n_s$ ) at the skimmer is derived from molecular flow considerations as,

$$n_s = n_t \left( \frac{Z_t}{Z_s} \right)^2$$

giving  $n_s \sim 4 \times 10^{13}$  molecules/cm<sup>3</sup>. With a skimmer orifice size of 0.08 cm, the skimmer Knudsen number is  $\sim 56$ , indicating that flow into the skimmer is well into the effusive range.

The choice of skimmer aperture size was based on an expected core beam with a half angle spread of  $\sim 4^\circ$ . Since the skimmer could not be readily adjusted during an experiment, additional beam attenuation due to downstream scattering for this relatively large skimmer

orifice would be a lesser problem than loss of the beam due to shifting of the skimmer during thermal cycling. This has proved to be the case since we routinely monitor the low abundance isotopes  $^{36}\text{Ar}$  and  $^{14,15}\text{N}$  which are 0.3 and 0.7 percent of the carrier gases, respectively, and find these signals to be 3 or 4 orders of magnitude above the minimum detectable signal for high background regions of the spectrum. That is, minimum sensitivity is about 1 ppm.

### 3.3 Capillary probe sampling

For the converging nozzle geometry of our capillary, two descriptions of the flow conditions can be used. The standard isentropic relations, assuming adiabatic conditions, yield expressions identical to those for the sonic nozzle, since the isentropic solution is independent of channel length when the exit pressure is lower than the critical pressure,  $P_c$ <sup>6</sup>. For this case, the pressure drop across the capillary channel is given by,

$$\frac{P_c}{P_0} = \left(\frac{2}{\gamma+1}\right)^{\gamma/(\gamma-1)}$$

and the exit velocity is sonic, i.e., the Mach number is 1. A simple graphical treatment of the velocity function along the capillary suggested that in the early phases of expansion, the isentropic temperature drop might occur in a time scale where vibrational relaxation could play a role. This could manifest itself, for example, as an apparent temperature error in Clausius-Clapeyron plots of pressure versus temperature data.

Another possible treatment is to consider that for a narrow channel wall collisions should be important. Thus, energy transfer should occur and since the capillary is essentially at  $T_0$ , the flow description should be isothermal. The solution for the isothermal case is a straightforward problem, very similar to the isentropic case, and yields a pressure drop along the nozzle channel of,

$$\frac{P_c}{P_0} = e^{-1.2} = 0.606.$$

The flow velocity yields an exit Mach number of  $M_y^{-1/2}$ . These conditions are very similar to the isentropic case and thus one would expect expansion in the stage I vacuum chamber to be indistinguishable from isentropic expansion within the channel. In practice both the conical and capillary samplers showed similar, though not identical, gas dynamic character.

---

<sup>6</sup>This critical pressure is the minimum pressure which can exist within the channel for a given initial pressure at the channel entrance.

### 3.4 System mass discrimination

#### 3.4.1 Contributing factors

In order to make quantitative measurements of species partial pressures, it was necessary to determine the magnitude of possible mass discrimination effects in our system. One such effect is inherent in the free-jet expansion process and results from differences in the perpendicular velocity component for various beam species, leading to radial diffusion and depletion of low mass species in the beam. In practice, this effect is superimposed on the normal mass discrimination effects of the quadrupole mass analyzer and electron multiplier.

The radial diffusion effect, often referred to as "Mach number focusing," has been explained by Stern, et al. [22] as follows. As the expansion progresses, the translational temperature falls and random velocities in the beam decrease. However, lighter gases near the axis (and elsewhere) will have a higher net velocity and thus a larger perpendicular velocity component with respect to the beam axis. Qualitatively, then, one would expect to observe in the regions where the flow is collision dominated, a depletion in the beam of the lighter mass species. Past the collision dominated region, reverse diffusion would be expected to gradually reduce this process.

Reis and Fenn [23] observed mass separation effects in nitrogen-hydrogen mixtures which could be attributed to formation of a detached shock. A theoretical analysis by Sherman [24] indicated agreement with the results of Reis and Fenn [23] where the bow shock was swallowed (by the skimmer); but where a detached shock was formed, a much higher separation of light and heavy species was predicted. He concluded that large separation effects result from a probe perturbation and vary proportionally to the inverse of the Reynolds number.

A first power dependence of mass separation with molecular weight was observed by Green, et al. [17] which suggested that the lesser dependence observed by Stern, et al. [22] may be due to skimming downstream of the Mach disc location. However, this is not the case in the work of Reis and Fenn [23], and the large separations observed by Greene, et al. [17] might have a similar explanation, even though the conditions are quite different. Greene, et al. [17] used rather small pumps and the skimmer region pressures were such that the mean free path was of the order of 0.5 cm. A calculated Reynolds number at their skimmer, based on their reported background gas pressure, is  $\sim 0.08$ . Even though collisional interaction in their beam presumably ceased well upstream of the skimmer, shock production and detachment at the skimmer were still possible, and the above arguments could then apply at least qualitatively.

#### 3.4.2 Experimental observations

In combination, the various mass discrimination effects are taken into account by calibration with a commercially prepared (Matheson) standard gas mixture analyzed (Matheson) against gravimetric standards. This gas mixture contains  $\sim 1$  percent of each of the rare gases, helium, neon, argon, krypton, and xenon in nitrogen and has been analyzed to 0.01 percent of the gas composition. The overall mass discrimination function, as obtained in the temperature and pressure region of operation and normalized to the carrier gas ( $N_2$ ), is used

to correct the ion intensity and, hence, pressure data (see Section 4.2). Table 1 gives the gas mixture analysis (as supplied by Matheson). This analysis was independently confirmed by us using GC analysis.

Table 1. Calibration gas mixture characteristics.

Gas	Fraction of mix <sup>a</sup>	Ionization cross section <sup>b</sup>	Isotope mass (amu)	Isotope abundance
N <sub>2</sub>	0.9489	1.18 ± 0.1	28	0.9892
			29	0.0072
He	0.0102	0.08 ± 0.03	4	1.00
Ne	0.0100	0.11 ± 0.03	20	0.905
			22	0.092
Ar	0.0104	2.6 ± 0.3	36	0.0034
			40	0.9959
Kr	0.0104	3.8 ± 0.6	84	0.570
			86	0.173
Xe	0.0105	6.2 ± 2	129	0.264
			132	0.270
			134	0.105

<sup>a</sup>Gas chromatographic analysis (Matheson) calibrated against gravimetric standards.

<sup>b</sup>Kieffer and Dunn [39];  $\sigma$  taken from their graphs at 30 eV, errors estimated from their data spread.

A typical plot of normalized ion intensities versus mass number, at several temperatures and pressures, is given in figure 6. The normalization of ion intensities,  $I_m$ , for species  $i$  to the nitrogen carrier gas (using the <sup>29</sup>N<sub>2</sub> isotopic species) is made using the expression

$$I_m(\text{norm}) = \frac{I_m}{f_m \cdot A_m \cdot \sigma_m} \frac{f_{29} \cdot A_{29} \cdot \sigma_{29}}{I_{29}},$$

where  $f_m$  is the mole fraction,

$A_m$  the isotopic abundance, and

$\sigma_m$  the ionization cross section at 30 eV (see table 1).

The mass spectrometer resolution used was sufficient to separate (>10% valley) each xenon isotope. It should be noted that the <sup>36</sup>Ar isotope concentration in the mixture is only

34 ppm. This mass peak is relatively noisy due to background argon and other unidentified residual gas components. However, with reasonable integration times (4 s), a signal-to-noise ratio significantly better than 10 could be obtained, indicating a conservative detection limit of <10 ppm. The reference discrimination curve (see effusive curve of fig. 6) was obtained under effusive conditions at a pressure of less than  $10^{-5}$  atm using a large orifice cell. This curve may be used as a measure of the mass discrimination effects present in the quadrupole filter and detector.

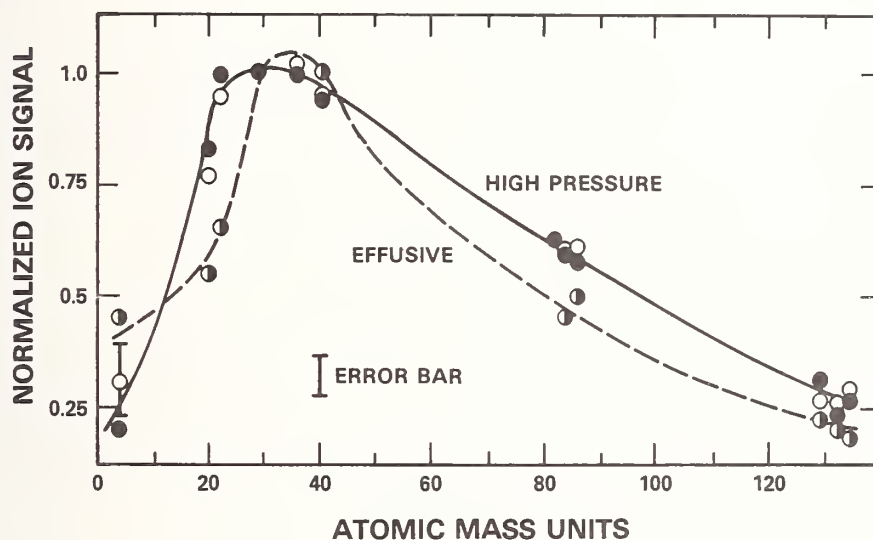


Figure 6. Mass discrimination behavior obtained using a standard gas mixture of: He(1.02%), Ne(1.00), Ar(1.04), Kr(1.04), Xe(1.05), and  $N_2$ (94.85): open circles - conical sonic orifice sampler at 1065 K and 0.6 atm, closed circles - capillary sampler at 800 K and 0.3 atm, and half closed circles - effusive source at 295 K and  $<10^{-5}$  atm. Error bar represents worst case for variations in ion signal; most abundant isotope of each species normally exhibits variations less than half this amount. An exception is  $^{20}Ne$ , where contributions from  $^{40}Ar^{2+}$  and the narrow peak width limit the signal to noise ratio. Ion intensities measured at 30 eV ionizing electron energy and normalized with respect to  $^{29}N_2^+$ .

Figure 6 shows a small enhancement ( $\sim 10\%$ ) of higher mass species in supersonic beams which agrees qualitatively with the arguments outlined in Section 3.4.1, considering an early onset of collisional "freezing" and the relatively large skimmer-orifice separation used. The rapid signal fall-off at He is mainly a mass spectrometer resolution effect. Instrument tuning conditions produce very narrow peaks below 12 amu and consequent difficulties in



dwelling on the peak maximum. The effective coincidence of the mass separation curves for the conical and capillary probes (see fig. 6) suggests that both probe types are effectively isentropic in their expansion characteristics.

To account for the combined mass discrimination effects of mass separation in the expanding jet and quadrupole mass filter discrimination, a sensitivity factor,  $S_{\text{Na}^+(\text{NaCl})}$ , for example, was obtained from

$$S_{\text{Na}^+(\text{NaCl})} = \left( \frac{S_h - S_e}{S_e} \right) 58 \text{ amu} + (S_e)_{23 \text{ amu}}$$

where h and e refer to the high pressure and effusion curves of figure 6, respectively.

It should be noted that the experimental mass discrimination function is essentially fixed for a given set of quadrupole mass filter operating parameters. However, when the mass spectrometer is re-tuned by varying the ion source and resolution settings a new discrimination function is obtained.

### 3.5 Aggregation effects

Besides mass discrimination effects, other perturbations are possible in supersonic free jet expansion. Condensation or species aggregation is a particularly well known case, e.g., see [10,25] and cited references. A particularly useful test of species aggregation is to monitor the formation of  $\text{Ar}_2$  in the expansion process. However, the single pump differential pumping scheme employed by us in the nozzle-skimmer region did not allow operation in a low scattering condition at pressures where the  $\text{Ar}_2^+$  intensity would be above our detection limit. Bier and Hagena [10] give limiting criteria for minimizing condensation, based on the source pressure-nozzle diameter product  $P_0 \cdot d_0$ . At a source temperature of 295 K,  $P_0 \cdot d_0$  should be less than 60 Torr-mm for  $\text{CO}_2$ , 85 Torr-mm for argon, and 500 Torr-mm for nitrogen. At atmospheric pressure and room temperature our system operates at  $P_0 \cdot d_0 < 60$  Torr-mm and, consequently, condensation should be minimal or non-existent, particularly at higher temperatures.

### 3.6 Pressure operating characteristics

Figure 7 shows the behavior of the detected ion signal as a function of source pressure. For this instrument, the expansion ratio is essentially constant, set by the available pumping speed, and the turnover of the unit slope portion of the curves, marked by arrows on figure 7 occurs consistently at an observed pressure of  $P_I \sim 2 \times 10^{-6}$  atm. The fact that this turnover occurs for both the capillary (no skimmer) and conical sampling system at the same stage I pressure, independent of temperature, suggests the effect is a post-expansion scattering phenomenon dependent primarily on the mean free path. This argument is also consistent with the sensitivity of the turnover point onset to the skimmer alignment relative to the nozzle.

It appears possible, as Green, et al. [17] showed, to operate at pressures where scattering is significant and still maintain sampling fidelity; our data also indicate this (see Sections 4 and 5). However, the majority of our experimental runs were made in a pressure

range where scattering was relatively low, i.e., within the linear region of the intensity-pressure curves such as those shown in figure 7.

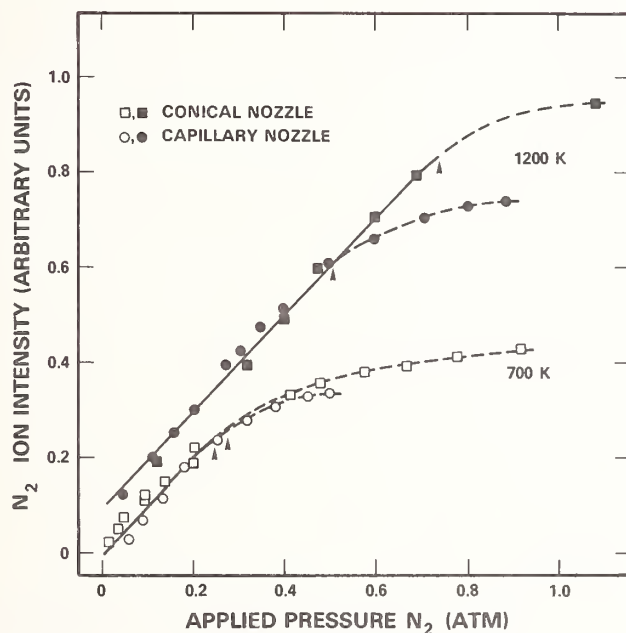
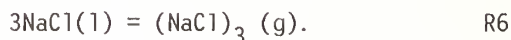
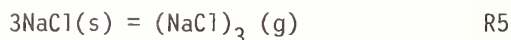
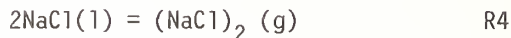
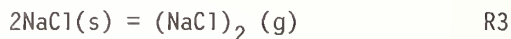


Figure 7. Dependence of carrier gas ion intensity on applied pressure and temperature. The 1200 K data have been offset vertically +0.1 div for clarity. Solid curves are lines of unit slope and zero intercept in accord with the theoretical relationship. Arrows indicate where stage I pressure exceeds  $2 \times 10^{-6}$  atm. The capillary curve deviates from linearity at lower pressure because the total flow rate is higher through the relatively large capillary orifice.

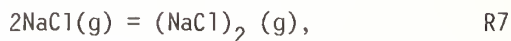
#### 4. The NaCl System: Results and Discussion

This system was chosen to test the validity and accuracy of the transpiration mass spectrometric technique, since the literature data for NaCl is extensive, reasonably self-consistent, and has been critically evaluated and formatted as thermochemical tables by JANAF [26].

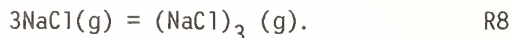
Between about 800-1600 K the significant reactions in the equilibrium NaCl vaporization process are



Reactions R1 - R4 can be expressed in homogeneous form as



and similarly



This variety of reactions, involving both homogeneous and heterogeneous equilibria should provide a stringent test of the TMS technique, and particularly where the second law method of data analysis is used.

Barton and Bloom [27] measured the total pressure of NaCl(l) by a boiling point method and reported excellent agreement with the results of earlier workers. Vaporization of NaCl from a copper Knudsen cell was reported by Miller and Kusch [28] who used a velocity profile analysis on effusive vaporization and determined the presence of substantial amounts of dimer  $(\text{NaCl})_2 \text{ (g)}$ . More recently, Milne and Klein [29] measured heats of sublimation and dimerization for the alkali chlorides, including NaCl, using the mass spectrometric Knudsen effusion method. By incorporating selected literature data with their results they were able to make an extrapolation to the liquidus region. Second law heats of vaporization for the monomer (reaction R2) differ between laboratories by no more than 3.5 k cal/mol. This uncertainty is sufficiently low that the reaction may be used to test the temperature dependent characteristics of the transpiration reactor sampling system.

Certified reagent grade (A.C.S.) sodium chloride (Fisher lot number 757984) was used without further treatment. Lot analysis indicated contaminants of less than 0.1 percent and no impurity ion signals were observed in the mass spectra.

#### 4.1 NaCl mass spectral fragmentation data

The characteristic mass spectral fragmentation pattern for NaCl vapor has been reasonably well established by others using Knudsen effusion mass spectrometry [29,30] over solid

samples. A potential problem with this system arises from the presence of both NaCl and (NaCl)<sub>2</sub> in the vapor, where either of these species could be a precursor for the ions Na<sup>+</sup> and NaCl<sup>+</sup>. Feather and Searcy [31] have considered the possible contribution to NaCl<sup>+</sup> from (NaCl)<sub>2</sub>. They showed that if one assumes the dimer as the NaCl<sup>+</sup> progenitor, a 35 percent change in the ratio  $R = \text{Na}^+/\text{NaCl}^+$  should result over the temperature range 870 to 1020 K. However, within a 15 percent uncertainty, they observed no temperature dependence in the observed R value of about two. Our Knudsen effusion data (see Section 4.5) support this observation; R values of about 1.5 were practically invariant over the same temperature range (see fig. 10, in Section 4.5). Hence, NaCl<sup>+</sup> can be used as a measure of the monomer partial pressure<sup>7</sup>. Typical mass spectral fragmentation data are summarized in table 2.

Table 2. Typical mass spectral ion intensities<sup>a</sup> for the NaCl system.

Na <sup>+</sup>	NaCl <sup>+</sup>	Na <sub>2</sub> Cl <sup>+</sup>	R <sup>b</sup>	Cell	T(K)	eV	Source
1.00	0.49	0.88	2.0	Cu-Knudsen	968	70	[31]
1.00	0.73	0.91	1.4	Cu-Knudsen	~960	20	[29]
1.00 <sup>c</sup>	0.66	0.66	1.5	Pt-Knudsen	957	30	Section 4.4
1.00 <sup>d</sup>	0.04	0.08	25.0	Pt-transp. <sup>e</sup>	1312	30	Section 4.3
1.00 <sup>g</sup>	0.03	0.14	33.3	Pt-transp. <sup>f</sup>	1360	30	

<sup>a</sup>Normalized to I<sub>Na<sup>+</sup></sub>, and corrected for Cl-isotope fractions.

<sup>b</sup> $R = I_{\text{Na}^+}/I_{\text{NaCl}^+}$ .

<sup>c</sup>Equivalent to a signal intensity of 920 μV(10<sup>7</sup>Ω).

<sup>d</sup>Equivalent to a signal intensity of 1.8x10<sup>4</sup> μV.

<sup>e</sup>Carrier gas N<sub>2</sub> at 0.54 atm; I<sub>29N<sub>2</sub></sub> = 1.00 (=1.8x10<sup>4</sup> μV) and  $k_{\text{N}_2} = 1.66 \times 10^{-10}$  μV/atm K.

<sup>f</sup>Transpiration weight loss run. Note S factors differ to e.  $k_{\text{N}_2} = 3.7 \times 10^{-11}$  μV/atm K (0.65 atm).

<sup>g</sup>Equivalent to a signal intensity of 1.9x10<sup>4</sup> μV.

The transpiration mass spectrometric data for the vapors over solid NaCl (i.e., at temperatures more compatible with Knudsen effusion data) showed no measurable NaCl<sup>+</sup> ion. However, while the 23 amu Na<sup>+</sup> ion is at a low noise position, NaCl<sup>+</sup> at 58 and 60 amu is relatively noisy (an order of magnitude greater than for 23 amu) and R values of about 2 cannot be ruled out on this basis. But, well into the liquid range, where the ion signals at both 23 and 58 amu are strong and relatively noise-free, we observe  $R \sim 26 \pm 4^8$ . This ratio

<sup>7</sup>Recent angular distribution mass spectrometric measurements (~10-70 eV) also indicate NaCl as the predominant (>99 %) precursor for Na<sup>+</sup> and NaCl<sup>+</sup>, as well as (NaCl)<sub>2</sub> for Na<sub>2</sub>Cl<sup>+</sup>. (R. Grimley, Purdue Univ., personal communication (Nov. 1978)).

<sup>8</sup>Error is standard deviation for data above 1170 K.

varies slightly between experimental runs. The average ratio above 1200 K is quite constant within a variable temperature run and shows no significant variation from ~1200 - 1500 K, even with carrier gas pressures varying over the range 0.35-0.8 atm.

That the relatively high  $\text{Na}^+$  signal intensities are not an artifact of the external geometry of the sampling system, such as NaCl-furnace interaction, is evidenced from the following observations. If the furnace power is suddenly turned off, the transpiration sampler cools much more slowly than the furnace and the  $\text{Na}^+$ ,  $\text{NaCl}^+$  and  $\text{Na}_2\text{Cl}^+$  signals respond to the sampler temperature, not the furnace, thus precluding a decomposition mechanism involving the hotter furnace. Salt does not deposit on the exterior of the sampler elements since, with the sampler cool, a sudden heating of the furnace does not produce significant signals of sodium-containing species until the lagging sampler has reached an internal temperature where these species are normally observed. As a final test of the absence of external deposits, the sampler can be cycled down in temperature, the sample boat and boat-carrier removed, and the sampler immediately returned to a high temperature. The small amount of residual salt in the sampler produces ion signals of less than 4 percent of those obtained at the same temperature with a normal sample level present, and the ion signal decays rapidly to barely detectable levels.

Ion intensity ratios can also depend on mass discrimination differences between individual species, as was discussed in Section 3.4. However, for the ions in question the mass discrimination curves of figure 6 indicate only small differences between the 23 and 58 amu species.

It appears, then, that the high  $\text{Na}^+/\text{NaCl}^+$  ion intensity ratio, with respect to those characteristic of Knudsen effusion measurements, are not an artifact of the sampling process. The remaining explanation must be associated with the electron impact ionization process and the non-thermal nature of the molecular beam. A possible pertinent observation in this regard was made by Berkowitz, et al. [32] for the related case of LiF, using Knudsen effusion mass spectrometry, where a factor of three decrease in  $\text{Li}^+/\text{LiF}^+$  was observed for a 300 K temperature increase. It was suggested that the tendency for LiF to yield  $\text{Li}^+$  in a state of excess energy increased with temperature and that the ion source discriminated against these excess energy ions thereby yielding lower  $\text{Li}^+/\text{LiF}^+$  ratios at higher temperatures. In sharp contrast to effusive beams, the supersonic beam used for our TMS studies had an effective temperature of the order of 10 percent of the transpiration source temperature. We speculate that this large difference in temperature between effusive and supersonic beams might well produce a similar ion source discrimination effect for NaCl. That is, the effectively much cooler (translationally and probably vibrationally) NaCl species produced by high pressure sampling would ionize to form  $\text{Na}^+$  with relatively less excess energy, and the ion source would produce higher relative amounts (with respect to  $\text{NaCl}^+$  and  $\text{Na}_2\text{Cl}^+$ ) of  $\text{Na}^+$  for mass analysis and detection, leading to high R values. On the other hand, the effusive molecular beams obtained using Knudsen cells remain at high temperature during passage to the ionizer and low R values would result from the effect of excess energy discrimination. That R is essentially temperature independent for a TMS experiment may be explained from the known



properties of supersonic beams where the final beam temperature does not vary to nearly the same degree as the source temperature.

This explanation of apparently anomalous mass spectral fragmentation warrants further investigation with the TMS technique, possibly including other alkali halide species such as LiF. However, as will become evident from the discussion to follow, a definitive explanation of the apparent high R values obtained by TMS is not necessary to successful application of the technique to thermodynamic studies.

#### 4.2 NaCl vaporization and pressure calibration

The effective temperature insensitivity of the  $\text{Na}^+/\text{NaCl}^+$  ratio, R, together with auxiliary appearance potential data (not presented here as it basically agrees with earlier work), leads to the conclusion that both  $\text{Na}^+$  and  $\text{NaCl}^+$  may be used as a measure of the NaCl partial pressure without significant interference from electron impact fragmentation of the  $(\text{NaCl})_2$  dimer species<sup>9</sup>. Typical partial pressure data for NaCl derived on this basis are shown in figure 8. This plot represents a number of sets of data obtained using either Ar or  $\text{N}_2$  as carrier gases, with total pressures varying from 0.35-0.75 atm and 0.4-0.8 atm, respectively. Two different conical orifice samplers of similar, but not identical, construction were used. Also, the data plotted in the liquid range include pressures calculated from both  $\text{Na}^+$  and  $\text{NaCl}^+$  ion intensities. The essential concordance between these various data sets support the ion-precursor assignments and all other aspects of the procedure adopted for converting ion intensities to partial pressures. Note also in figure 8 the good agreement between the experimental and literature melting points ( $T_m$ ), indicative of accurate temperature measurement.

##### 4.2.1 Partial pressure-ion intensity relationships

There are three methods by which the mass spectral ion intensity data were converted to absolute pressures in the present study:

- (a) classical transpiration,
- (b) integrated ion intensity-time method, and
- (c) reference gas ion intensity comparison.

With method (a) the salt mass loss is measured (gravimetrically) for a known volume of transpiration carrier gas at a fixed temperature and total pressure. Typical data are given in table 3. To convert these data to a partial pressure for the NaCl species, a small correction was made for the dimer species  $(\text{NaCl})_2$  using the JANAF [26] thermochemical data. Subsequent analysis of our own data for the dimer-monomer equilibrium reaction (Section 4.5) will indicate that this dimer correction may be too high but is still within the quoted uncertainty for  $P_{\text{NaCl}}$  given in table 3.

<sup>9</sup>The similar T dependence of  $\text{Na}^+$  and  $\text{NaCl}^+$ , but not  $\text{Na}_2\text{Cl}^+$ , shown in figure 10 (Section 4.5) also supports this claim, as do similar data reported in the literature.

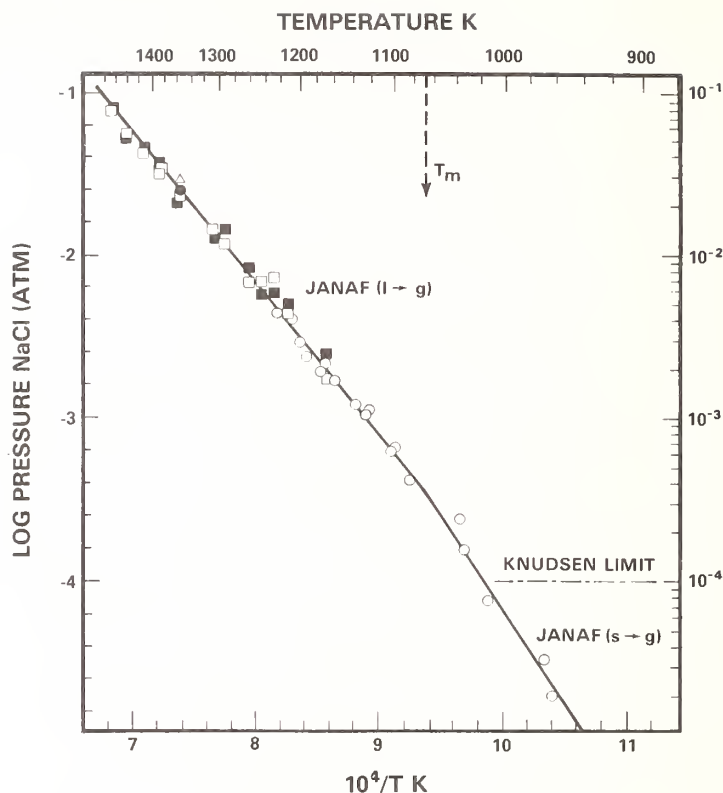


Figure 8. Vapor pressure curves for NaCl (s and l) obtained by TMS.

Open squares -  $P_{\text{NaCl}}(\text{Na}^+)$  in  $\text{N}_2$  carrier gas, total pressure 0.4-0.8 atm, at 30 eV. Closed squares -  $P_{\text{NaCl}}(\text{NaCl}^+)$  in  $\text{N}_2$  carrier gas total pressure 0.4-0.8 atm, at 30 eV. Open circles -  $P_{\text{NaCl}}(\text{Na}^+)$  in Ar carrier gas, total pressure 0.35-0.75 atm, at 70 eV. The data points  $\Delta$  and  $\bullet$  were obtained using the integrated ion intensity (b) and classical transpiration (a) methods, respectively (see Section 4.2.1). All other points were obtained using the ion intensity comparison method (c). Solid curve represents data from the JANAF compilation [26]. The broken line labeled Knudsen limit was calculated assuming a typical orifice diameter of 0.1 cm.

Method (b) is an adaptation of the integrated ion intensity method often used with Knudsen effusion cells as described in Section 4.4. In the present case use is made of equation 4.1 and the relationship

$$k_{\text{NaCl}} = R \left( \frac{n}{V} \right) \Delta t / \Sigma I \Delta t$$

where  $R$  is the Universal gas constant,  $n$  the number of moles of salt transported as  $\text{NaCl}$  species, and  $V$  the volume of carrier gas transported for time  $t$  and constant temperature  $T$ .

Table 3.  $\text{NaCl}$  Absolute Pressure Calibration

transpiration mass loss data:

time 172 min  
 $\text{N}_2$  flow rate 7.9 sccm  
 $T = 1360 \text{ K}$   
 $\text{N}_2$  pressure 0.7 atm  
 $\text{NaCl}$  mass loss 0.193 gm

auxiliary input data:

average mol wt 72<sup>a</sup>  

$$P_{\text{Na}_2\text{Cl}_2} / (P_{\text{Na}_2\text{Cl}_2} + P_{\text{NaCl}}) = 0.23^a$$

derived pressures:<sup>b</sup>

$$P_{\text{NaCl}}^{\text{total}} = [n_{\text{NaCl}} / (n_{\text{NaCl}} + n_{\text{N}_2})] P_{\text{total}} = 2.96 (\pm 0.6) \times 10^{-2} \text{ atm}$$

$$P_{\text{NaCl}} = 2.28 (\pm 0.4) \times 10^{-2} \text{ atm}$$

<sup>a</sup>Derived from JANAF [26] data and also self consistent with independent Knudsen and TMS data from the present study.

<sup>b</sup> $n$  refers to moles of gas transported.

Method (c) utilizes the known pressure and ion intensity of the carrier gas ( $\text{Ar}$  or  $\text{N}_2$ ), but relative mass discrimination factors and ionization cross sections are needed. For the relatively straightforward case of  $\text{Na}^+$  as a measure of  $\text{NaCl}$ , ion intensities were converted to partial pressures as follows. The partial pressure of  $\text{NaCl}$  is given by,

$$P_{\text{NaCl}}(\text{Na}^+) = k_{\text{NaCl}} \cdot I_{\text{Na}^+} \cdot T, \quad (4.1)$$

where  $k_{\text{NaCl}}$  is a constant which takes into account mass spectrometer sensitivity ( $k'$ ), mass discrimination ( $S$ ) and ionization cross section ( $\sigma$ ) effects;  $I_{\text{Na}^+}$  is the measured  $\text{Na}^+$  ion intensity at the sample temperature,  $T$ . The constant  $k_{\text{NaCl}}$  can be derived from a knowledge of the carrier gas pressure and ion intensity, i.e.,

$$P_{\text{Ar}} = k_{\text{Ar}} \cdot I_{\text{Ar}^+} \cdot T, \quad (4.2)$$

and

$$k_{Ar} = P_{Ar} / (I_{Ar}^+ \cdot T) \quad (4.3)$$

then

$$k_{NaCl} = k_{Ar} \left( \frac{\sigma_{Ar}}{\sigma_{NaCl}} \right) \left( \frac{S_{Ar}}{S_{NaCl}} \right) (\bar{S})^{-1} \quad (4.4)$$

The term  $\bar{S} (\leq 1)$  is an empirical correction factor discussed in Section 4.2.3.

For the case of  $NaCl^+$  as a measure of NaCl, an average R value, denoted as  $\bar{R}$ , was used as a scaling factor (necessary for the total ionization cross section argument to be valid) to avoid overwhelming the  $NaCl^+$  variations by the large  $Na^+$  contribution. The  $P_{NaCl}(NaCl^+)$  data were obtained from the expression

$$P_{NaCl}(NaCl^+) = [(1 + \bar{R}) \cdot I_{NaCl}^+] k_{NaCl} \cdot T \quad (4.5)$$

Figure 8 shows the pressures derived from this expression to be equivalent to those using the  $Na^+$  ion intensity data [and eq. (4.1)].

#### 4.2.2 Ionization cross sections

Values of  $\sigma$  for the reference gases  $N_2$  and Ar are known from the literature [39]. However, no such data exist for the high temperature species NaCl and  $(NaCl)_2$ . Expressions of the type 4.4 can be used to obtain ratios of ionization cross sections. Values of  $\sigma$ , relative to Ar, were measured for  $N_2$ ,  $O_2$ ,  $SO_2$  and NaCl using the TMS technique and the results are summarized in table 4. The data for  $N_2$  and  $O_2$  agree with the literature results within the combined experimental errors. Also the measured  $\sigma$ 's for  $SO_2$  and NaCl seem reasonable in comparison with data for electronically similar species. To derive  $\sigma_{NaCl}$ ,  $k_{NaCl}$  was obtained using expression 4.1 and the value of  $P_{NaCl}$  obtained by transpiration [method (a)].

Table 4. Ionization Cross Sections ( $\pi a_0^2$  units [39])<sup>a</sup>

	30 eV	70 eV
Ar	-- (2.6) <sup>b</sup>	-- (4.0)
$N_2$	1.48 (1.2)	3.0 (2.8)
$O_2$	1.26 (1.0)	2.8 (2.8)
$SO_2$	1.3	--
Na	-- (4.6 $\pm$ 0.3)	-- (4.0 $\pm$ 0.2)
NaCl	1.00 ( $\pm$ 0.3) <sup>c</sup>	--
$(NaCl)_2$	1.5 <sup>d</sup>	--

<sup>a</sup>Experimental values determined from expressions of the type 4.4 using Ar as reference  $\sigma_j$ .

<sup>b</sup>Literature values of Kieffer and Dunn [39] given in parentheses. Typical uncertainty  $\pm 0.2$ .

<sup>c</sup>Based on  $\bar{S} = 0.6$ , as determined in Section 5.2.

<sup>d</sup>Determined from literature empiricism for dimer to monomer cross section ratio of  $\sim 1.5$  (Meyer and Lynch [40]); probable uncertainty  $\pm 0.2$ .

#### 4.2.3 Pressure correction due to gas scattering

The empirical factor  $\bar{S}$  contained in expression 4.4 corrects for a differential gas scattering effect. This effect, which is characteristic of our TMS system, arises as follows.

In the working pressure range of our system, the beam number density at the skimmer is only four times higher than for the background. Since the differential pump aperture does not completely limit the solid angle viewed by the ion source to beam species, some of the carrier gas ( $N_2$  or Ar) admitted arises from the scattered background (in region I) and not the beam itself. This would not be the case for the condensible salt species. Hence, since the ion intensities of salt species are normalized against the carrier gas signal [by expressions (4.3) and (4.4)], as part of the pressure calibration procedure, they would be underestimated by the degree that scattered carrier gas competes with beam gas. Thus, in treating ion signals of condensible species relative to the carrier gas signal, we need to include an empirically determined multiplying factor of about 1.67 ( $\bar{S} = 0.6$ ) as a calibration constant, e.g., in expression 4.4. This factor is essentially invariant with total pressure since the ratio of background to beam pressure remains constant for our unthrottled pumping system (see Section 3.2). We have applied this correction factor to all condensible species partial pressures included in this study.

An independent test and verification of this correction procedure will be demonstrated for the  $Na_2SO_4$  system in Section 5. We should emphasize, however, that even without this correction the agreement between our data and the JANAF [26] values is well within that usually expected for vapor pressures of complex high temperature systems.

#### 4.2.4 Data comparison with JANAF [26]

Below the melting point, the sublimation data (fig. 8) fit the least squares expression:

$$\log P_{NaCl}(\text{atm}) = 7.8(\pm 1.6) - 11970(\pm 1500)/T.$$

It follows that the enthalpy and entropy of sublimation (reaction R1) are, respectively,

$$\Delta H_s = 54.8 \pm 7 \text{ kcal/mol and } \Delta S_s = 35.6 \pm 8 \text{ cal/deg mol at 1000 K.}$$

For the liquid region, the corresponding data-fit is given by:

$$\log P_{NaCl}(\text{atm}) = 4.85(\pm 0.3) - 8820(\pm 200)/T,$$

and for reaction R2,

$$\Delta H_v = 40.4 \pm 0.9 \text{ kcal/mol and } \Delta S_v = 22.2 \pm 1.4 \text{ cal/deg mol at 1290 K.}$$

The enthalpy of sublimation compares favorably with the JANAF [26] selection of  $51.6 \pm 2.4$  kcal/mol where the uncertainty represents the standard deviation in the second law data analyzed by JANAF [26]. For the liquid region, the literature data are based on total



pressure measurements (i.e., not molecular specific) which have been corrected for dimer contribution by extrapolating mass spectrometric data obtained over solid NaCl. JANAF [26] selects  $\Delta H_V = 42.7 \pm 3.5$  kcal/mol and  $\Delta S_V = 24.2 \pm 0.5$  cal/deg mol at 1290 K for reaction R. Both sets of data are in very good agreement.

The key uncertainty in the present data arises from the cross section and  $\bar{S}$  terms in expression 4.4. However, the agreement between NaCl pressures obtained by the methods (a) - (c) at 1360 K and a subsequent check on  $\bar{S}$  using  $\text{Na}_2\text{SO}_4$  strongly support the pressure calibration procedure and hence the entropy data.

In view of the sparsity of molecular specific measurements in the liquid range by other investigators, the general agreement between JANAF [26] and our data is excellent. Further, this appears to be the first report of measurements in the temperature range from the melting point to 1250 K. This result demonstrates an additional advantage of TMS over the classical effusion (e.g., Knudsen effusion mass spectrometry) and total pressure (e.g., conventional transpiration) methods in its ability to bridge the  $10^{-4}$  -  $10^{-3}$  atm gap in existing partial pressure measurement capability at high temperature. The temperature range of >450 K covered by our measurements is exceptionally large, and measurements over an even wider range are feasible with this technique.

#### 4.3 NaCl dimerization and test for homogeneous equilibrium

The NaCl sublimation and vaporization reactions represented by the data in figure 8 provide a convincing test of the attainment of heterogeneous equilibrium, for condensible vapor species, in the transpiration reactor and their faithful sampling into the mass spectrometer. However, in the absence of additional experimental insight, it is conceivable that the sampling process could perturb homogeneous vapor phase chemical equilibria. A sensitive test of the system fidelity in this regard can be made using the known equilibrium represented by reaction R7.

It is well established from the literature, and our results support this, that the  $\text{Na}_2\text{Cl}^+$  ion may be used as a measure of the dimer species  $(\text{NaCl})_2$ . Our appearance potential and temperature dependence data indicate that  $\text{Na}_2\text{Cl}^+$  is a fragment ion of  $(\text{NaCl})_2$  and that any  $\text{Na}^+$  or  $\text{NaCl}^+$  arising from dimer electron impact fragmentation is negligible (for present purposes). The equilibrium constant for the dimerization process (R7) is then given by:

$$K_d = \frac{I_{\text{Na}_2\text{Cl}^+}}{(I_{\text{Na}^+} \text{ or } I_{\text{NaCl}^+}^*)^2 k_{\text{Na}_2\text{Cl}_2} \cdot T} \quad (4.6)$$

where  $k_{\text{Na}_2\text{Cl}_2}$  includes the relative ionization cross section, mass spectrometer sensitivity, differential gas scattering and beam segregation factors for the monomer and dimer species, discussed previously. The term  $I_{\text{NaCl}^+}^*$  refers to the scaled  $\text{NaCl}^+$  ion intensity, i.e., as in expression 4.5. In practice, where  $I_{\text{Na}^+}$  and  $I_{\text{Na}_2\text{Cl}^+}$  are used as measures of monomer and dimer, respectively,  $k_{\text{Na}_2\text{Cl}_2} = 4.0 k_{\text{Na}}$ .

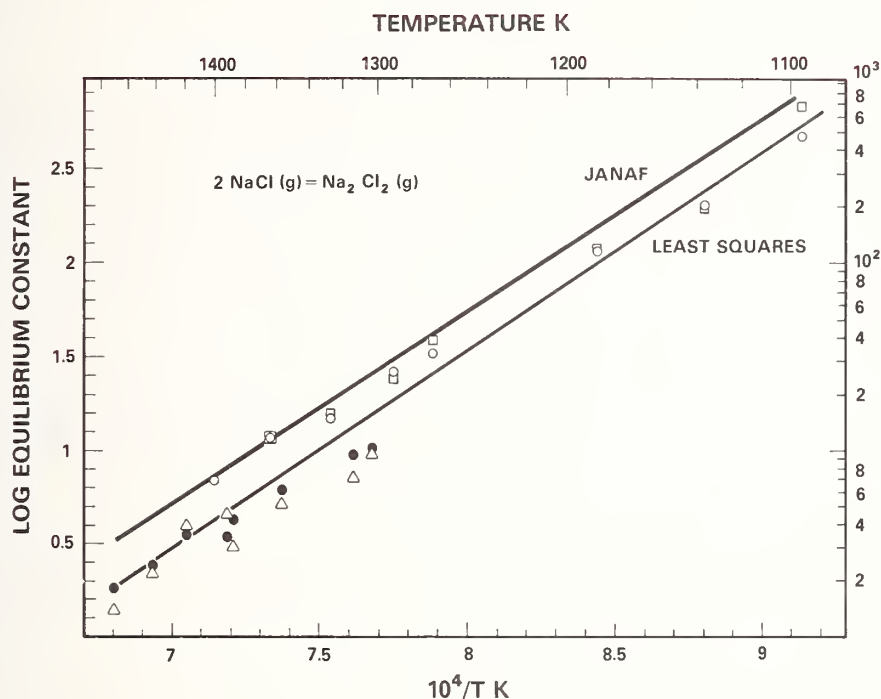


Figure 9. TMS data, at 30 eV with  $\text{N}_2$  carrier gas for NaCl monomer - dimer equilibrium. Open circles and squares using capillary sampler at 0.3-0.5 atm with  $\text{Na}^+$  and  $\text{NaCl}^+$  (scaled--see text) as measures of  $P_{\text{NaCl}}$ , respectively. Closed circle and open triangle obtained with conical sampler, 0.4-0.6 atm, using  $\text{Na}^+$  and  $\text{NaCl}^+$  (scaled--see text), respectively [see eq. (4.6) in main text].

Typical data sets for  $K_d$  as a function of temperature are given in figure 9. These data were obtained using both the conical and the capillary-type samplers. Note the satisfactory agreement between the various  $K_d$  data sets and the JANAF [26] literature curve, indicating good control over the various effects discussed earlier as contributing errors in converting ion intensity to partial pressure, or equivalent equilibrium constant, data. Both the  $I_{\text{Na}^+}$  [as per eq. (4.1)] and the scaled  $I_{\text{NaCl}^+}^*$  [as per eq. (4.5)] signals were used as measures of  $P_{\text{NaCl}}$ . The least squares line shown in figure 9 is an average of individual least squares fits to each data set, giving

$$\log K_d = 10640 (\pm 400)/T - 6.97 (\pm 0.4).$$

The calculated enthalpy of dimerization (reaction R7) at 1265 K is then  $\Delta H_d = -48.7 (\pm 1.8)$  kcal/mol, which is in good agreement with the selected JANAF [26] value of -47.1 kcal/mol, particularly since the corresponding literature data span a difference of more than 7 kcal/mol (see JANAF [26]). Our data for the conical probe were obtained at carrier gas

pressures varying over the range 0.4-0.6 atm and gas flow rates in the range 3-10 sccm. The capillary probe data, were obtained at pressures of 0.3-0.5 atm and gas flow rates in the range 15-40 sccm. That there is agreement between these data sets over a range of flow rates suggests saturated flow conditions in the transpiration reactor.

The isentropic expansion model discussed earlier (see Section 3.3) for the capillary sampler suggested that a temperature decrease of a few percent might occur in the early gas expansion phase along the capillary, while the velocity in the channel was still low enough that a re-adjustment of simple gas equilibria might be kinetically feasible. However, the generally good agreement between the capillary and conical samplers, and between the JANAF [26] literature data, suggests that during the early expansion period the isothermal model is a better description of capillary flow. That is, isentropic expansion dominates only when the remaining residence time in the capillary is a few microseconds and the flow velocity approaches unit Mach number. Direct computer modeling is required to predict more definitively the early flow conditions for this type of sampling orifice. However, the empirical approach adopted seems to satisfy present requirements.

#### 4.4 NaCl vaporization at low pressures using Knudsen effusion mass spectrometry

At the outset of the transpiration mass spectrometric studies we considered the accuracy of the literature data for NaCl vaporization, as compiled by JANAF [26], to be more than adequate for demonstrating and calibrating the TMS technique. However, small, but systematic, differences persisted between our measured dimerization reaction enthalpies and entropies and those recommended by JANAF [26]. That this difference occurred for different reactor and furnace geometries, different probe types, carrier gas flow rates and pressures, temperatures, thermocouples, mass spectrometers, ion sources, and sample loadings, seemed to rule out systematic error as an explanation. Closer inspection of the original literature data concerning the NaCl dimerization process revealed the thermodynamic data to be less definitive than suggested by the JANAF [26] compilation. The data for the liquidus NaCl region relied heavily on an extrapolation of solid NaCl data through the melting phase transition. We therefore considered it desirable to check the original dimerization data, as obtained over solid NaCl by Knudsen effusion mass spectrometry, using a similar technique ourselves. Such an experiment also served the useful purpose of providing an independent check on the  $\text{Na}^+/\text{NaCl}^+ (=R)$  characteristics for a thermal effusion beam of NaCl, as distinct from the non-thermal cool supersonic beams generated by the TMS method.

For these Knudsen effusion studies a lightweight platinum Knudsen cell with a leak free welded lid-seal was used in a vertical orientation. A Pt-Pt +10 %Rh thermocouple was used to measure the cell temperature at the base and an optical pyrometer (calibration traced to NBS standards) used to measure the effusion orifice temperature. These two independent temperature measurements agreed to within the pyrometer reading uncertainty of 5 K. As the thermocouple readings were of higher precision they were used as the primary source of

temperature data. A 33 mg sample was completely vaporized from a cell volume of  $0.7 \text{ cm}^3$  through an orifice  $0.051 \text{ cm}$  diameter drilled in a lid of  $0.01 \text{ cm}$  thickness.

Figure 10 shows the ion intensity-temperature dependence plots for the major ion species-- $\text{Na}^+$ ,  $\text{NaCl}^+$ ,  $\text{Na}_2\text{Cl}^+$  and  $\text{Na}_3\text{Cl}_2^+$ <sup>10</sup>. Near the end of the experiment unsaturation effects were noted; see the high temperature region in figure 10. The sequence of loss-of-saturation followed the expected order of species loss, i.e., trimer > dimer > monomer. Note also in figure 10 that during the unsaturation period, both  $\text{Na}^+$  and  $\text{NaCl}^+$  continue to increase with temperature even though the dimer  $\text{Na}_2\text{Cl}^+$  and trimer  $\text{Na}_3\text{Cl}_2^+$  ion intensities fall off dramatically. This observation further supports the earlier assignments of ions to their neutral precursors. These data also show an essentially constant R ratio, even during unsaturation. As was mentioned earlier (Section 4.1) the magnitude of this ratio is considerably less than that obtained by TMS. If the higher ratio found by TMS was related solely to sample temperature we should have expected the Knudsen effusion data to show a trend towards larger R values with increasing temperature. Thus our earlier interpretation of the corresponding TMS ratios seems consistent with these Knudsen data.

Conversion of the ion intensities to partial pressures was made using relationships of the same form as (4.1). The proportionality constant  $k_i$ , for species i, was determined using the established integrated signal-weight loss method [33] which can be expressed in the form:

$$k_i = \frac{G_i A_i (2\pi R)^{1/2} W}{a C (M_i)^{1/2} \sum [I_i(T)^{1/2} \Delta t]} \quad (4.7)$$

where

- G is a gravimetric factor,
- A an isotopic abundance factor,
- R the universal gas constant,
- W the weight loss,
- a the orifice area,
- C the orifice Clausing factor,
- M the molecular weight,
- I the ion intensity,
- T the temperature, and
- $\Delta t$  the elapsed time.

The contribution of the trimer to observed weight loss was neglected (<1 percent error). To calculate the individual  $k_i$ 's for  $\text{NaCl(g)}$  and  $(\text{NaCl})_2(\text{g})$  it was necessary to estimate the relative concentrations for each species. Based on relative cross section estimates and the quadrupole mass discrimination for monomer and dimer species and their ion intensities (given in fig. 10), we partitioned the weight loss as  $\sim 20 (\pm 5)$  percent dimer and  $\sim 80$  percent monomer.

<sup>10</sup>Note that the  $\text{Na}_3\text{Cl}_2^+$  ion was not routinely monitored during TMS experiments owing to its relatively low intensity and the preferential instrument tuning for low amu species.

This partitioning was considered acceptable as it produced NaCl monomer partial pressures in good agreement with JANAF [26]. From this partitioning estimate the above  $k_i$  expression (4.7) leads to

$$k_{(\text{Na}^+ + \text{NaCl}^+)} = 1.00 \times 10^{-11} (\pm 30 \%) \mu\text{V/atm K}, \text{ and}$$

$$k_{(\text{Na}_2\text{Cl}^+)} = 4.15 \times 10^{-12} (\pm 30 \%) \mu\text{V/atm K}.$$

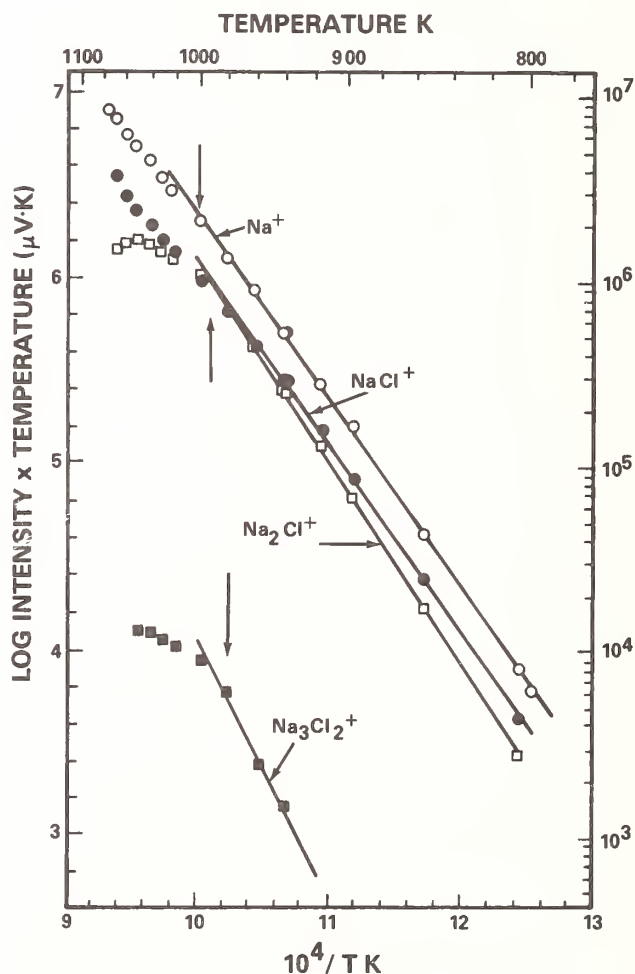


Figure 10. Kundsén effusion mass spectrometric data, expressed in the form of Clausius-Clapeyron plots, for vaporization of NaCl(s). Open circles -  $\text{Na}^+(\text{NaCl})$ , closed circles -  $\text{NaCl}^+(\text{NaCl})$ , open squares -  $\text{Na}_2\text{Cl}^+(\text{Na}_2\text{Cl}_2)$ , closed squares -  $\text{Na}_3\text{Cl}_2^+(\text{Na}_3\text{Cl}_3)$ . The Cl-containing species refer only to the  $^{35}\text{Cl}$  isotopic species. Vertical arrows denote the end of saturated vaporization and the highest temperature included in the least squares fit. Experimental chronology was in the direction of increasing temperature.



These constants were used to convert the ion intensity data (fig. 10) to partial pressures, as shown in figure 11. The least squares lines have the algebraic form,

$$\log P_{\text{NaCl}} (\text{atm}) = 5.75 (\pm 0.14) - 10170 (\pm 120)/T$$

$$\log P_{(\text{NaCl})_2} (\text{atm}) = 5.81 (\pm 0.11) - 11050 (\pm 100)/T$$

and yield, at ~900 K, in comparison with corresponding literature data (in parentheses)

$$\Delta H_s (\text{R1}) = 46.5 \pm 0.6 (52.3 [26]) \text{ kcal/mol}$$

$$\Delta S_s (\text{R1}) = 26.3 \pm 0.6 \text{ cal/deg mol}$$

$$\Delta H_s (\text{R3}) = 50.6 \pm 0.5 (57.0 [26]) \text{ kcal/mol, and}$$

$$\Delta S_s (\text{R3}) = 26.6 \pm 0.5 \text{ cal/deg mol.}$$

For the trimer (fig. 10 data),

$$\Delta H_s (\text{R5}) = 62 \pm 5 (62.2 \pm 2.3 [31]) \text{ kcal/mol.}$$

The monomer data are in good agreement with the JANAF [26] results (see fig. 11) but the corresponding dimer data show a significant, though not excessive, difference.

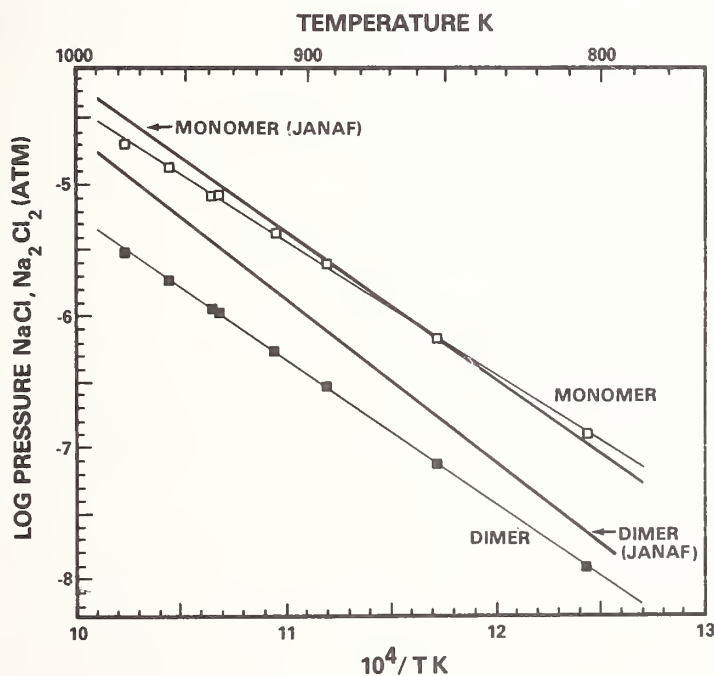


Figure 11. Vapor pressure of NaCl monomer and dimer obtained via Knudsen effusion mass spectrometry. Heavy curves represent the JANAF [26] data. Open squares -  $P_{\text{NaCl}}(\text{NaCl}^+ + \text{Na}^+)$ , closed squares -  $P_{\text{Na}_2\text{Cl}_2}(\text{Na}_2\text{Cl}^+)$ .

#### 4.5 Comparison of Knudsen effusion and TMS-NaCl dimerization data

The various Knudsen effusion and TMS data sets have been replotted in the form of  $K_d$  (R7), as shown in figure 12. Table 4 summarizes the essential thermodynamic parameters represented by the various individual and combined data sets given in figure 12.

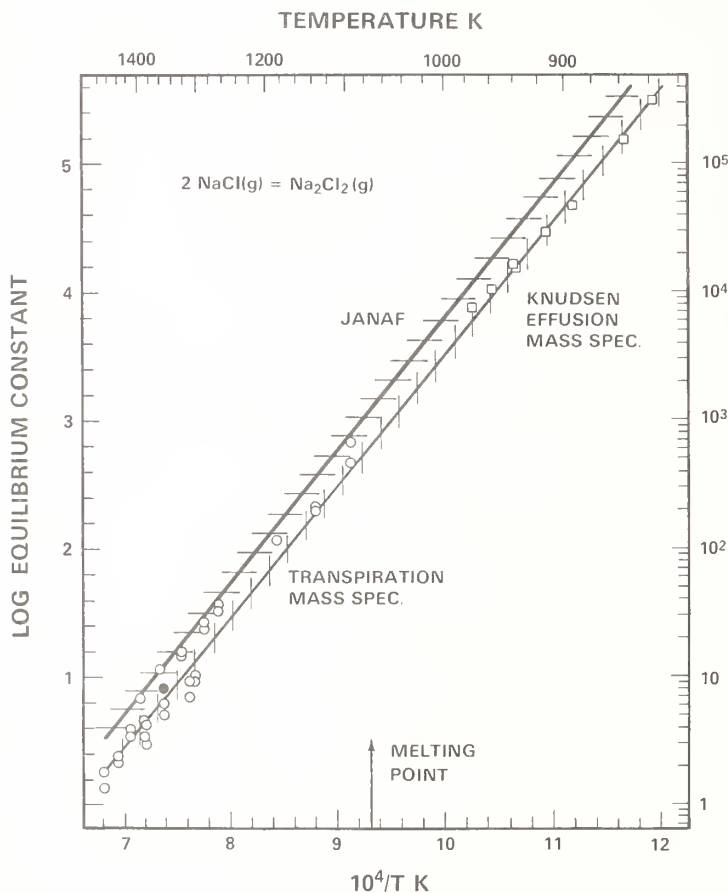


Figure 12. Comparison of various data sets for NaCl dimerization (reaction R7) (see also table 4). Horizontal and vertical bars indicate (to a good approximation) the slope uncertainties for the JANAF [26] and experimental curves, respectively (see text). The closed circle data point was obtained using calibration method (a) (see Section 4.2.1).

Table 4. Comparison of dimerization data (reaction R7).

	$\log K_d$ $\text{atm}^{-1}$	$-\Delta H_d$ $\text{kcal/mol}$	$-\Delta S_d$ $\text{cal/deg mol}$	T Range K	Data source
<u>9300 (<math>\pm 200</math>)</u>	$-5.70 (\pm 0.2)$	$42.5 \pm 0.8$	$26.1 \pm 0.9$	820-980	Knudsen MS (fig. 11)
<u>10640 (<math>\pm 400</math>)</u>	$-6.97 (\pm 0.4)$	$48.7 \pm 1.8$	$31.9 \pm 1.8$	1100-1480	TMS (fig. 9)
<u>10312 (<math>\pm 150</math>)</u>	$-6.49 (\pm 0.1)$	$47.1 \pm 3.5$	$29.7 \pm 1.0$	800-1600	JANAF [26]
<u>10140 (<math>\pm 150</math>)</u>	$-6.60 (\pm 0.13)$	$46.4 \pm 0.7$	$30.2 \pm 0.6$	820-1480	Knudsen + TMS (fig. 12)

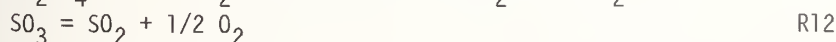
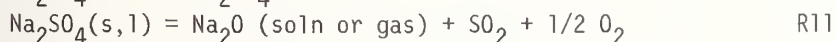
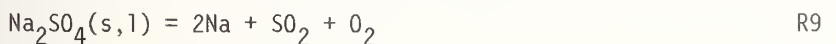
Note (in fig. 12) that our Knudsen effusion data extrapolate almost perfectly to the liquidus data curve obtained by TMS. Thus both the Knudsen effusion and TMS data sets appear to be more consistent with each other than with the JANAF [26] data, though the difference is not disturbingly great and is almost within the combined data uncertainties (see fig. 12). Such agreement between widely differing measurement techniques clearly establishes the TMS method as reliable and accurate, and capable of extending the pressure range of conventional effusion methods by four orders of magnitude or greater. The temperature range is also naturally extended by such a high pressure sampling capability.

## 5. The $\text{Na}_2\text{SO}_4$ System: Results and Discussion

Most practical systems adaptable to characterization by the TMS technique are heterogeneous, involving equilibria between reactive gases and volatile substrates. Experience with Knudsen effusion mass spectrometric studies of gas-solid (or liquid) systems has indicated a need to exercise great care in achieving, and then demonstrating, thermodynamic equilibrium<sup>11</sup>. On the other hand, considerable experience has shown that equilibria involving only condensible vapor species and their substrates are generally attainable in Knudsen cells.

With the TMS technique, the results for the NaCl system clearly demonstrated the presence of a thermodynamic equilibrium between condensible vapor species and the corresponding substrate. However, these data showed the need for a small, but noticeable, correction factor in relating partial pressures of condensible NaCl species to the carrier gas pressure (see fig. 8). This effect was attributed to mass spectral contributions of non-beam scattered carrier gas. Such an effect should also be present in heterogeneous systems where the scatterable gas is one of the reaction components. To further test our interpretation and data correction procedure for this effect, and to validate the TMS technique for the more general, but more difficult, case of heterogeneous gas-solid (or liquid) equilibria, we selected the  $\text{Na}_2\text{SO}_4$  system as a test case.

This system is known [34-38] to vaporize according to one or more reactions:



Historically, there has been considerable disagreement among researchers concerning the relative contribution of each reaction to the overall vaporization process (see table 5 in Section 5.5). It now appears that container reactions (catalytic or otherwise), temperature, sample treatment, and gas composition (e.g., external  $\text{O}_2$  or  $\text{SO}_2$  present), all contribute to the overall process defined by reactions R9-R12. For the high temperature ( $>1360$  K) conditions of interest to the present study, we can readily eliminate reaction R12 as a contributing process. Previous mass spectrometric observations of Kohl, et al. [37] indicate that above 1300 K,  $\text{SO}_3$  dissociation is favored and this species forms less than 10 percent of the

<sup>11</sup>For example, see the chapter by Hildenbrand elsewhere in this volume - "Attainment of Chemical Equilibrium in Effusive Beam Sources of the Heterogeneous Reaction Type."

vapor. Our own observations indicate  $\text{SO}_3$  to be barely detectable at  $\sim 1100$  K and virtually absent at higher temperatures.

As will be shown later (Sections 5.4 and 5.5), for most conditions reaction R9 is usually predominant. This is a very convenient reaction for a critical test of TMS sampling of gas-condensed phase equilibria. In addition to carrying out temperature dependence studies for the isolated system, it is possible to externally control the concentration of product species  $\text{SO}_2$  and  $\text{O}_2$  and provide an isothermal mass action (or Le Chatelier effect) test for equilibrium. With our particular design of external gas supply multiple mass flow meter/controller system we were able to introduce either  $\text{SO}_2$ ,  $\text{O}_2$  or their mixtures at concentrations, with respect to the  $\text{N}_2$  or Ar carrier gas, in the range of  $\sim 0.02$ -4 percent. Usually we maintained a constant  $\text{O}_2$  pressure and varied the  $\text{SO}_2$  concentration. The capability for varying the  $\text{SO}_2$  partial pressure over a range of two orders of magnitude was more than adequate for a mass action test of equilibrium sampling.

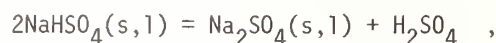
### 5.1 Sample preparation and side reactions

Certified ACS grade anhydrous  $\text{Na}_2\text{SO}_4$ , supplied by Fisher Scientific Company (lot number 770832), was used as a starting material. Initial preparation techniques for our transpiration runs involved melting  $\text{Na}_2\text{SO}_4$  into the transpiration boat at 1200 K using a muffle furnace under ambient conditions. Observations of  $\text{Na}^+$  and  $\text{CO}_2^+$  in the initial mass spectra at relatively low temperatures of 900-1100 K lead us to the conclusion that a small quantity of the salt reacted with atmospheric  $\text{CO}_2$  to form  $\text{Na}_2\text{CO}_3$ . Under vacuum vaporization conditions,  $\text{Na}_2\text{CO}_3$  decomposes according to the reaction:



leading to much higher Na pressures at low temperatures than for reaction R9. These impurity signals disappeared during the pre-run bake out period.

Another impurity reaction noted by Fryxell, et al. [34] is



followed at elevated temperatures by



Consistent with this process we observed, during the initial measurement phase with fresh samples, impurity signals of  $\text{SO}_2$  and  $\text{H}_2\text{O}$  at temperatures of about 1300 K. However, these impurities could be readily removed by a period of outgassing prior to commencement of a measurement run.

The presence of trace amounts of water in the system, either in the sample itself or as an impurity in the carrier gas, could alter the  $\text{Na}_2\text{SO}_4$  vaporization process according to

the reaction



To remove water from the sample, the salt was heated for a 6-12 hour period at 400 °C in the assembled transpiration system prior to beginning an experimental run. This in situ drying process was monitored mass spectrometrically by following the decay of the  $\text{H}_2\text{O}^+$  ion signal. Background  $\text{H}_2\text{O}$  from the aluminum walls of the stage I vacuum region limited ultimate  $\text{H}_2\text{O}$  detection sensitivity to ~25 ppm. The zero grade nitrogen and pre-purified argon contained <3 ppm  $\text{H}_2\text{O}$  (Matheson supplied specification). This specification was verified by us where a dew point of less than -80 °C was found. Even using our limited detection sensitivity as an upper limit for  $P_{\text{H}_2\text{O}}$ , and allowing reaction R13 to set the values for  $P_{\text{SO}_2}$  and  $P_{\text{O}_2}$ , we can show from the JANAF [26] values of  $K_p(\text{R13})$  that  $P_{\text{NaOH}}$  is negligible. During experimental runs with nitrogen as a carrier gas we periodically monitored the ions 40 ( $\text{NaOH}^+$ ), 39 ( $\text{NaO}^+$ ), 80 [ $(\text{NaOH})_2^+$ ] and 79 ( $\text{Na}_2\text{O}_2\text{H}^+$ ) amu but no evidence for these species was found, in agreement with the thermodynamic prediction.

The following arguments can be made concerning the possible competition of reactions R10 and R11 with reaction R9. Cubicciotti and Keneshea [35] have calculated reaction R11, with  $\text{Na}_2\text{O}(\text{g})$  as a product, to be ~10 orders of magnitude less significant than reaction R9. We can also show the corresponding reaction leading to  $\text{Na}_2\text{O} (\text{soln})$  to be insignificant in this system. From JANAF [26], the equilibrium constant for the reaction



at 1500 K has a calculated value of

$$\log K_p(\text{R14}) = \log \left[ \frac{P_{\text{Na}}^2 P_{\text{O}_2}^{1/2}}{a_{\text{Na}_2\text{O}}} \right] = -5.9;$$

similarly for reaction R9 at 1500 K,

$$\log K_p(\text{R9}) = \log \left[ \frac{P_{\text{Na}}^2 \cdot P_{\text{SO}_2} \cdot P_{\text{O}_2}}{a_{\text{Na}_2\text{SO}_4}} \right] = -16.4.$$

With the reasonable assumption that the activity  $a_{\text{Na}_2\text{SO}_4} \sim 1$ , and congruent vaporization, reaction R9 requires a materials balance

$$1/2 P_{\text{Na}} = P_{\text{SO}_2} = P_{\text{O}_2}.$$



Hence, the sodium pressure can be given as

$$P_{\text{Na}} = [4 K_p(\text{R9})]^{1/4} \sim 1 \times 10^{-4} \text{ atm (at 1500 K).}$$

Substitution of this value into the equilibrium constant expression for reaction R14 with the approximation that  $1/2 P_{\text{Na}} = P_{\text{O}_2}$  (valid if reaction R9 is dominant) predicts

$$a_{\text{Na}_2\text{O}} < 4 \times 10^{-5}.$$

This predicted low activity of the basic oxide is supported by the observations of Fryxell, et al. [34] that their post-run salt exhibited a neutral pH. Likewise, our post-run samples, even for experiments as short as 2-3 hr, did not exhibit any basic pH character.

From these considerations we can eliminate reactions R11-R14 as possible contributing factors to  $\text{Na}_2\text{SO}_4$  vaporization.

## 5.2 Closed system temperature dependence

Under closed system conditions, i.e., no external reactive gas load applied, we observe reaction R9 as the predominant process in the temperature range ca 1400-1700 K. The measured temperature dependence of the equilibrium constant,

$$K_p(\text{R9}) = P_{\text{Na}}^2 \cdot P_{\text{O}_2} \cdot P_{\text{SO}_2} \quad (5.1)$$

is shown in figure 13, where an excellent agreement with the JANAF [26] curve is indicated. The right-hand side axis represents an equivalent partial pressure of sodium calculated from the observed  $K_p(\text{R9})$  using  $P_{\text{Na}} = [4K_p(\text{R9})]^{1/4}$ . This is a useful representation of  $K_p(\text{R9})$  for making comparisons with the literature data, as will be shown in Section 5.5.

The partial pressures were obtained using the established relation,

$$P_i = k_i I_i^{+T}$$

for conversion of the ion intensities for  $\text{Na}^+$  (23 amu),  $\text{SO}_2^+$  (64 amu), and  $\text{O}_2^+$  (32 amu).  $k_i$  was derived from  $k_{\text{Ar}}$  or  $k_{\text{N}_2}$  at each temperature T where

$$k_{\text{Ar}} = \frac{P_o \cdot f_i}{I_{36\text{Ar}} \cdot T} \text{ and } k_{\text{N}_2} = \frac{P_o \cdot f_i}{I_{29\text{N}_2} \cdot T},$$

$P_0$  is the source pressure of carrier gas (Ar;  $N_2$ ),

$I_{^{36}\text{Ar}}$  the ion intensity of the argon isotope at 36 amu,

$I_{^{29}\text{N}_2}$  the ion intensity of the nitrogen isotope at 29 amu,

$f_i = 0.0034$  is the  $^{36}\text{Ar}$  isotope fraction of argon gas, and

$f_i = 0.0072$  is the  $^{29}\text{N}_2$  isotope fraction of  $N_2$  gas.

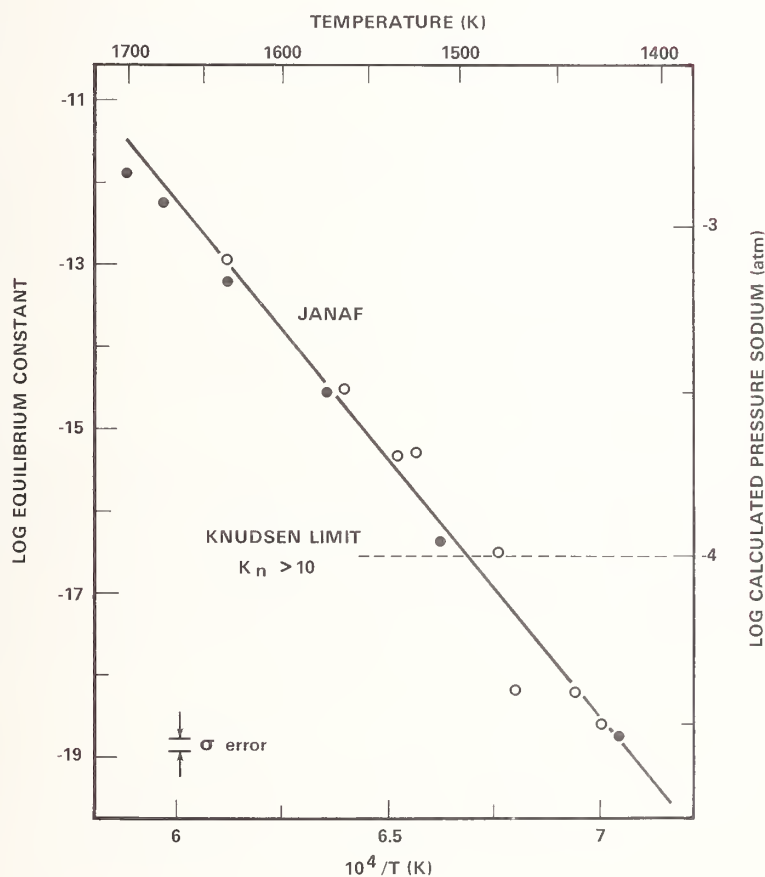


Figure 13. Temperature dependence of the equilibrium constant for reaction  $\text{Na}_2\text{SO}_4(l) = 2\text{Na} + \text{SO}_2 + \text{O}_2$  from TMS observations of  $\text{Na}^+$ ,  $\text{SO}_2^+$  and  $\text{O}_2^+$ . Data taken at 30 eV ionizing electron energy using Ar carrier gas at pressures of 0.4 atm (closed circles) and 0.5 - 0.8 atm (open circles). The solid line is taken from JANAF [26]. The Knudsen limit was estimated for a cell with  $\sim 0.1$  mm orifice diameter. The right-hand side axis has been calculated, assuming congruent vaporization, as  $P_{\text{Na}} = [4K_p(R9)]^{1/4}$ .

A typical data point for figure 13 is given by the experimental parameters:

$= 1563$  K,  $P_{\text{Ar}} = 0.81$  atm,  $I_{^{36}\text{Ar}} = 26 \times 10^3$ ,  $I_{\text{Na}} = 2100$ ,  $I_{\text{SO}_2} = 500$  and  $I_{\text{O}_2} = 2300$   $\mu\text{V}$ .

These data agree within experimental error with the JANAF  $K_{\text{Na}_2\text{SO}_4}$  data if a scattering

factor of  $\bar{S} = 0.6 (\pm 0.06)$  is assumed. That this factor has the same magnitude as for the NaCl study tends to establish its use as a universal correction factor for our particular TMS system.

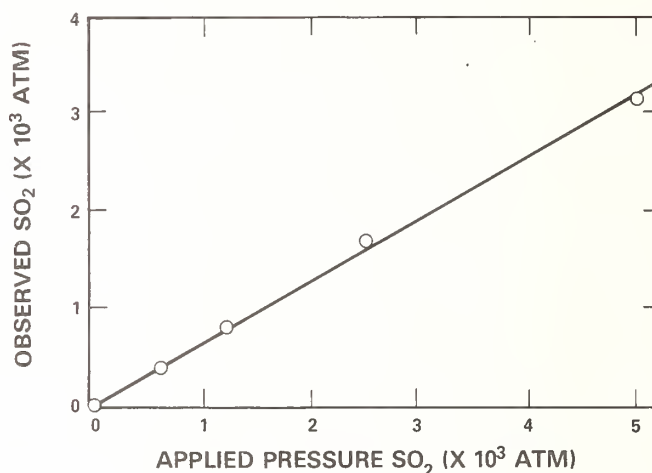


Figure 14. Dependence of "observed"  $SO_2$  on externally applied partial pressure; where  $P_{SO_2}(\text{obs}) = k_{N_2} \cdot I_{SO_2} \cdot T$ . Data taken at 30 eV ionizing electron energy and 1485 K using  $N_2$  carrier at  $\sim 0.6$  atm in the presence of  $Na_2SO_4$ . The least squares fit yields the relationship  $P_{SO_2}(\text{appl}) = 1.55 (\pm 0.5) k_{N_2} I_{SO_2} \cdot T + 2.5 (\pm 0.2) \times 10^{-5}$  atm.

The constants  $k_i$  are then derived as follows. For the case of  $k_{SO_2}$ , use can be made of the system response to a known external pressure of  $SO_2$ . Figure 14 indicates the relationship between calculated and "observed" pressures for  $SO_2$ , where the observed data refer to  $k_{N_2}$  as the proportionality constant. The figure shows the excellent linear response of the mass spectrometer system to known concentrations of reactive gas species and gives a direct relation between observed intensity and true pressure. These data may be used to derive cross sections, such as those given in table 4. From the slope of the line in figure 14 we obtain,

$$\frac{P_{SO_2}(\text{obs})}{P_{SO_2}(\text{appl})} = \frac{k_{N_2} \cdot I_{SO_2} \cdot T}{k_{SO_2} \cdot I_{SO_2} \cdot T} = \frac{1}{1.55} ;$$

hence,  $k_{SO_2} = 1.55 k_{N_2}$  (at 30 eV). With the mass discrimination function of figure 6, the

cross section data of table 4, and the scattering correction (multiplication factor of 1.67) obtained from the NaCl TMS data, the equilibrium constant is then

$$K_p(R9) = 4.8(k_{Ar}T)^4 (I_{Na+})^2 \cdot I_{SO_2+} \cdot I_{O_2+} \quad (5.2)$$

The data represented in figure 13 were obtained at various argon carrier gas pressures  $P_0$ , in the range of 0.4 - 0.8 atm. Separate least squares fits to the low (0.4 atm) and high (0.5 - 0.8 atm)  $P_0$  data points yield, respectively (in terms of Na):

$$\Delta H_V = 69 \pm 1 \text{ and } 71 \pm 4 \text{ kcal/mol}$$

$$\Delta S_V = 27.5 \pm 1.5 \text{ and } 28.1 \pm 4 \text{ cal/deg mol (for reaction R9).}$$

The good fits within and between various total pressure-ranges is indicative of saturated sampling conditions since the carrier gas flow rate is proportional to  $P_0$  at constant T. Also, the excellent agreement with the JANAF [26] data for both  $\Delta H_V$  and  $\Delta S_V$  (evident in fig. 13) is consistent with a non-perturbing sampling process.

### 5.3 Open system, isothermal, variable $SO_2$ conditions

The effect of variable  $SO_2$  pressure on the equilibrium constant for reaction R9 at near isothermal conditions ( $1475 \pm 7$  K) is shown in figure 15. Note that the least squares curve has zero slope [required by definition of  $K_p(R9)$ ] and is located very close to the JANAF [26] curve. There are two contributing factors to the data scatter observed in figure 15. First, during the runs, the VARIAC driven furnace system allowed a temperature variation of  $\pm 7$  K, due partly to fluctuations in line power and to interaction of variable background  $SO_2$  with the thin-foil tantalum furnace. The second factor resulted from a slow response of  $I_{SO_2+}$  to changes in applied  $P_{SO_2}$  from high to low  $SO_2$  concentrations. This slow response is believed to result from  $SO_2$  dissolving, and being retained, in the liquid  $Na_2SO_4$ .

### 5.4 Closed-system Knudsen effusion mass spectrometric results

There appears to be considerable discrepancy in the data obtained by various methods, and in different laboratories, concerning the relative contribution of reactions R9 and R10 to the overall  $Na_2SO_4$  vaporization process (e.g., see later in table 5). For the TMS studies considered so far, emphasis has been on reaction R9. No attempt was made to study reaction R10 in this work; in fact the mass spectrometer tuning was optimized for the low mass range needed for Na,  $O_2$  and  $SO_2$  rather than for the species  $Na_2SO_4$ . In order to be sure that reaction R10 does not compete appreciably with reaction R9 for our TMS conditions, we undertook a Knudsen effusion mass spectrometric study of  $Na_2SO_4$ . The apparatus and experimental procedures used were very similar to those indicated for the NaCl study (Section 4.4). A all-platinum Knudsen cell was used to avoid the sample-cell interaction problems reported by others (e.g., see table 5).

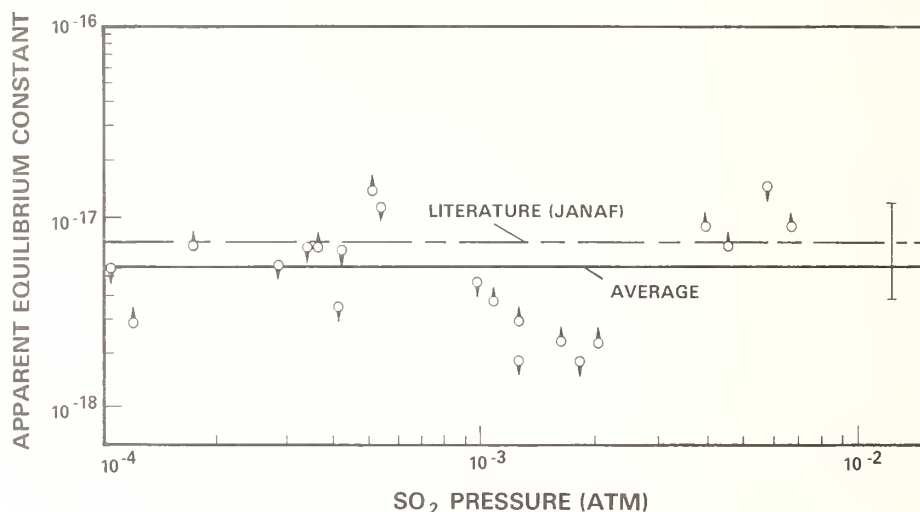


Figure 15. Isothermal equilibrium behavior of  $K_p(R9)$  with variable  $SO_2$  partial pressure at 1475 ( $\pm 7$ ) K, using  $N_2$  carrier gas at 0.5 atm and 30 eV ionizing electron energy. Error bar on JANAF [26] value (broken line) represents the change in  $K_p(R9)$  for the experimental temperature variation of  $\pm 7$  K. The solid line is the average of all measurements; a two parameter fit yields a similar result with a statistically insignificant pressure dependent term. Arrows on data symbols indicate the direction of change of applied  $SO_2$  pressure. Three symbols with double arrows denote the turning points of the two cycles of variation in  $SO_2$ .

Our mass spectrometric results, plotted as  $\log(I \cdot T)$  vs  $1/T$  for the principal ions  $Na^+$  and  $Na_2SO_4^+$  are given in figure 16. The  $Na^+$  curve gives an enthalpy of vaporization (R9) as sodium of  $72.3 \pm 4$  kcal/mol at 1165 K, in excellent agreement with the JANAF [26] data. From the  $Na_2SO_4^+$  curve we obtain a second law enthalpy for reaction R10 of

$$\Delta H_{Na_2SO_4} = 65.1 \pm 3.5 \text{ kcal/mol},$$

which is in very good agreement with the result of Kohl, et al. [37] (shown in table 5). The location of their least squares curves for  $Na_2SO_4^+$  (relative to  $Na^+$ ) are indicated for comparison in figure 16, using the same relationship between  $Na_2SO_4^+$  and  $Na^+$  as given in their reported mass spectrum. The agreement for the relative importance of  $Na_2SO_4$  and Na between the laboratories of Kohl, et al. [37] and ours is quite satisfactory. Also within the errors quoted, and considering the differences in mean temperature, both mass spectrometric studies are in good agreement with the transpiration measurements of Cubicciotti and Keneshea [35].



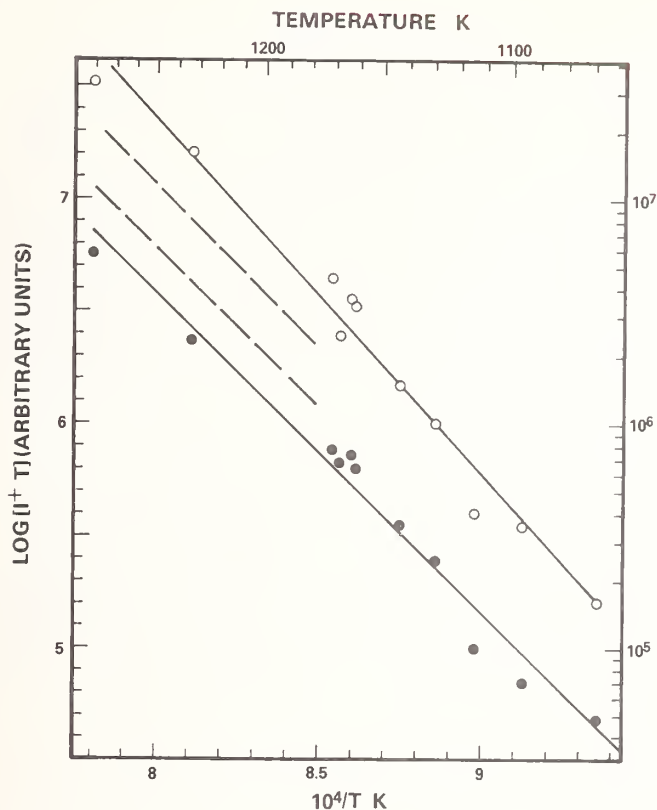


Figure 16. Knudsen effusion mass spectrometric data for  $I_{\text{Na}^+ + \text{T}}$  and  $I_{\text{Na}_2\text{SO}_4 + \text{T}}$  from  $\text{Na}_2\text{SO}_4(1)$ . Open circles are  $I_{\text{Na}^+ + \text{T}}$  and closed circles are  $I_{\text{Na}_2\text{SO}_4 + \text{T}}$  data, corrected by effusive mass discrimination plot of figure 6. Due to a substantial time difference, and instrumental changes between obtaining the figure 6 data and these results, the relative locations of the two lines could be uncertain by a factor of 2. Broken lines represent two sets of  $I_{\text{Na}_2\text{SO}_4 + \text{T}}$  data from Kohl, et al. [37] located relative to our fitted  $I_{\text{Na}^+ + \text{T}}$  line using their reported mass spectral relative intensities [their fig. 2(b)].

### 5.5 Data summary and literature comparison

Table 5 summarizes the most recent literature for the  $\text{Na}_2\text{SO}_4$  vaporization process(es). As total vaporization techniques do not monitor individual species, they usually do not identify the separate contributions from reactions R9 and R10. The data reviewed, including molecular specific results, are therefore expressed in terms of  $P_{\text{Na}}$  for comparison with the literature total vaporization data. The decomposition data (reaction R9) have been converted using the assumption of congruent vaporization, i.e.,  $P_{\text{Na}} = 2P_{\text{SO}_2} = 2P_{\text{O}_2}$  as discussed above. In the case of the data reported by Ficalora, et al. [36], their cited result

Table 5. Comparison of data among various investigators<sup>a</sup>

Authors	Range K	Method	System materials	Carrier gas	Vapor species	Results <sup>b</sup>
Fryxell Trythall Perkins [34]	1227 - 1477 $\bar{T} = 1340$	transpiration (wt loss)	platinum, mullite	air	$\text{Na}_2\text{SO}_4$	$\text{Log } P = 6.04 - 15870/T$ $\Delta H = 72.6 \pm 3.5$ $\Delta S = 27.6 \pm 2.5$
Cubicciotti Keneshea [35]	1400 - 1625 $\bar{T} = 1504$	transpiration (collection)	platinum	$\text{O}_2 + \text{SO}_2$	$\text{Na}_2\text{SO}_4$	$\text{Log } P = 5.86 - 15540/T$ $\Delta H = 71.1 \pm 1.7$ $\Delta S = 26.8 \pm 0.7$
	$\bar{T} = 1518$			$\text{N}_2$	$2\text{Na} + \text{SO}_2 + \text{O}_2$ as $\text{Na}$	$\text{Log } P = 7.11 - 16480/T$ $\Delta H = 75.4 \pm 1.7$ $\Delta S = 32.4 \pm 1.0$
Uhlig Davis Graham [38]	1175 - 1375 $\bar{T} = 1267$	transpiration free evaporation	platinum		$\text{Na}_2\text{SO}_4$	$\text{Log } P$ not obtained $\Delta H = 71$
Ficalora, uy Muenow Margrave [36]	1020 - 1150 $\bar{T} = 1081$	Knudsen ms w/shutter	tantalum, alumina		$2\text{Na} + \text{SO}_2 + \text{O}_2$ as $\text{Na}$	$\text{Log } P$ not given $\Delta H = 74.8 \pm 1.3$
Kohl Stearns Fryburg [37]	1196 - 1400 $\bar{T} = 1290$ 1175 - 1375 $\bar{T} = 1267$	Knudsen ms w/shutter	platinum, alumina		$2\text{Na} + \text{SO}_2 + \text{O}_2$ as $\text{Na}$ $\text{Na}_2\text{SO}_4$	$\text{Log } P$ not given $\Delta H = 73.5 \pm 2.5$ $\text{Log } P = 4.87 - 14440/T$ $\Delta H = 65.9 \pm 3$ $\Delta S = 22.3 \pm 2.8$
JANAF [26]	1400 - 1700 $\bar{T} = 1536$	selected	--		$\text{Na}_2\text{SO}_4(1) =$ as $\text{Na}$	$\text{Log } P = 6.49 - 15670/T$ $\Delta H = 71.7 \pm 0.6$ $\Delta S = 29.7$

Table 5 (continued)

this work	1069 - 1281 $\bar{T} = 1165$	Knudsen modulated beam ms	platinum	$2\text{Na} + \text{SO}_2 + \text{O}_2$ as $\text{Na}_2\text{SO}_4$	LOG P not obtained $\Delta H = 72.3 \pm 4$
	1400 - 1701 $\bar{T} = 1550$	transpiration modulated beam	platinum, trace alumina $\text{N}_2$ or Ar	$2\text{Na} + \text{SO}_2 + \text{O}_2$ as $\text{Na}_2\text{SO}_4$	LOG P not obtained $\Delta H = 65.1 \pm 3.5$
					LOG P = $6.16 - 15300/T$ $\Delta H = 69.8 \pm 3$ $\Delta S = 27.8 \pm 3$

<sup>a</sup>Underlined species observed directly.<sup>b</sup>p in atm;  $\Delta H$  in kcal/mol;  $\Delta S$  in cal/deg mol, at  $\bar{T}$   
(1 atm =  $1.01325 \times 10^5$  kpasca; 1 cal = 4.184 J).

for  $\Delta H_{\text{Na}}$  ( $= 78.8 \pm 3.3$  kcal/mol) was not in agreement with the result calculable from their raw data (their fig. 3), and we have listed the latter in table 5.

In the study of Ficalora, et al. [36] no ion attributable to  $\text{Na}_2\text{SO}_4(\text{g})$  was observed and they concluded that reaction R9 together with the gas phase equilibrium R12 best described the vaporization of  $\text{Na}_2\text{SO}_4(\text{s})$ . The work of Kohl, et al. [37] included tests for sample interaction with tantalum and tungsten cells using  $\text{ZrO}_2$  liners, and with platinum cells with or without  $\text{Al}_2\text{O}_3$  liners. Their results indicated a significant enhancement of  $\text{Na}^+$  and  $\text{SO}_2^+$  signals relative to  $\text{Na}_2\text{SO}_4^+$  from the  $\text{ZrO}_2$  lined tantalum and tungsten cells, and formation of additional species due to sample reduction by the tungsten cell. They concluded that Ficalora, et al. [36] failed to identify  $\text{Na}_2\text{SO}_4^+$  because of a cell-interaction enhancement of reaction R9.

Transpiration data, in an all-platinum apparatus, were obtained by Cubicciotti and Keneshea [35]. They distinguished between reactions R9 and R10 by using, separately, an atmosphere of pure  $\text{N}_2$  and of  $1/2 \text{SO}_2 + 1/2 \text{O}_2$ . Uhlig, et al. [38] assert that the only vapor species present in their studies is  $\text{Na}_2\text{SO}_4$ , as no dependence of vaporization rate on an applied  $\text{O}_2$  partial pressure was observed. This result is inconsistent with our data and indeed the bulk of the literature. Their static technique is highly surface layer diffusion controlled, as evidenced by the fact that the actual weight-loss rate is much lower than expected from a saturated flow or vacuum evaporation system.

In conclusion, the summary of table 5 clearly indicates the inherent and historical problems associated with the  $\text{Na}_2\text{SO}_4$  vaporization system and, in comparison, the quality of the TMS data must be considered very good. The reliability of the TMS technique for heterogeneous gas-liquid (or solid) systems, as demonstrated for the very demanding  $\text{Na}_2\text{SO}_4$  system, appears to outweigh that of alternative approaches.

---

We wish to acknowledge the able technical assistance provided by Mr. Art Sessoms during the course of this study. Support by the Department of Energy under contract EA-77-A-01-601 is also acknowledged.

#### References

- [1] Hastie, J. W., High Temperature Vapors: Science and Technology (Academic Press, New York, 1975).
- [2] Hastie, J. W., Intl. J. Mass Spectrom. Ion Phys. 16, 89 (1975); Combust. Flame, 21, 49 (1973).
- [3] Stearns, C. A., Kohl, F. J., and Fryburg, G. C., this volume (1979).
- [4] Merten, U. and Bell, W. E., in The Characterization of High Temperature Vapors, J. L. Margrave, ed., p. 91 (Wiley, 1967).
- [5] Gordon, R. J., Lee, Y. T., and Herschbach, D. R., J. Chem. Phys. 54, 2393 (1971).
- [6] Kantrowitz, A. and Grey, J., Rev. Sci. Instr. 22, 328 (1951).

- [7] Parker, H. M., Kuhlthau, A. R., Zapata, R., and Scott, J. E., Jr., Rarefied Gas Dynamics, Proc. First Int. Symp., F. M. Devienne, ed., 1, 69 (1960).
- [8] Anderson, J. B. and Fenn, J. B., Phys. Fluids, 8, 780 (1965).
- [9] Ashkenas, H. and Sherman, F. S., Rarefied Gas Dynamics, Proc. Fourth Int. Symp., J. H. deLeeuw, ed., 2, 84 (1966).
- [10] Bier, K. and Hagen, O., ibid, 200 (1966).
- [11] Knuth, E. L., Appl. Mech. Rev. 17, 751 (1964).
- [12] Morris, J. F., The Chemistry of Propellants, AGARD Symposium, S. S. Penner and J. Ducarme, eds., 410 (Pergamon Press, N. Y., 1960).
- [13] Sherman, F. S., Second Biennial Gas Dynamics Symposium, Am. Rocket Soc. (Northwestern University, 1957).
- [14] Bray, K. C. N., Ninth Symposium (International) on Combustion, 770 (Academic Press, N. Y., 1963); and J. Fluid Mech. 6, 1 (1959).
- [15] Wegener, P. P., Combustion and Propulsion, Fourth AGARD Symposium, A.C. Jourmatte, A. H. Lefebvre and A. M. Rothrock, eds., 261 (Pergamon Press, N. Y., 1961).
- [16] Hayhurst, A. N. and Telford, N. R., Proc. Roy. Soc. London, A322, 483 (1971).
- [17] Greene, F. T., Brewer, J., and Milne, T. A., J. Chem. Phys. 40, 1488 (1964).
- [18] Abuaf, N., Anderson, J. B., Andres, R. P., Fenn, J. B., and Marsden, D. G. H., Science, 156, 997 (1967).
- [19] This collision diameter is from Anderson and Fenn (ref [8]) for monatomic gases  $\delta = 5/3 = C_p/C_v$ . A larger collision diameter for diatomic  $N_2$  makes  $Kn_0$  smaller. The choice of  $3.7 \times 10^{-8}$  cm for this calculation shows  $Kn_0 < 0.01$  for argon which was used for some studies.
- [20] Stearns, C. A., Kohl, F. J., Fryburg, G. C., and Miller, R. A., NASA Technical Memorandum 73720 (1977) and references cited therein.
- [21] Brown, R. F. and Heald, J. H., Jr., Rarefied Gas Dynamics, Proc. Fifth Int. Symp., 1407 (1966).
- [22] Stern, S. A., Waterman, P. C., and Sinclair, T. F., J. Chem. Phys. 33, 805 (1960).
- [23] Reis, V. H. and Fenn, J. B., J. Chem. Phys. 39, 3240 (1963).
- [24] Sherman, F. S., Phys. Fluids, 8, 773 (1965).
- [25] Milne, T. A. and Greene, F. T., J. Chem. Phys. 47, 4095 (1967).
- [26] JANAF Thermochemical Tables, 2nd ed., NSRDS-NBS 37 (1971), U. S. Govt. Printing Office, Washington, D.C.
- [27] Barton, J. L. and Bloom, H., J. Phys. Chem. 60, 1413 (1956); ibid. 63, 1785 (1959).
- [28] Miller, R. C. and Kusch, P., J. Chem. Phys. 25, 860 (1956); ibid. 27, 981 (1957).
- [29] Milne, T. A. and Klein, H. M., J. Chem. Phys. 33, 1628 (1960).
- [30] Akishin, P. A., Gorokhov, L. N., and Sidorov, L. N., Russian J. Phys. Chem. 33, 2822 (1959).
- [31] Feather, D. H. and Searcy, A. W., High Temp. Sci. 3, 155 (1971).
- [32] Berkowitz, J., Tasman, A. A., and Chupka, W. A., J. Chem. Phys. 36, 2170 (1962).
- [33] Margrave, J. L., ed., The Characterization of High Temperature Vapors, p. 38 (Wiley, New York, 1967).



- [34] Fryxell, R. E., Trythall, C. A., and Perkins, R. J., Corrosion-NACE, 29, 423 (1973).
- [35] Cubicciotti, D. and Keneshea, F. J., High Temp. Sci. 4, 32 (1972).
- [36] Ficalora, P. J., Uy, O. M., Muenow, D. W., and Margrave, J. L., J. Amer. Ceram. Soc. 51, 574 (1968).
- [37] Kohl, F. J., Stearns, C. A., and Fryburg, G. C., Metal-Slag-Gas Reactions and Processes, Z. A. Foroulis and W. W. Smeltzer, eds., p. 649 (The Electrochemical Society, 1975); also NASA TMS 71641.
- [38] Uhlig, G. F., Davis, H. H., and Graham, H. C., J. Amer. Ceram. Soc. 58, 201 (1975).
- [39] Kieffer, L. J. and Dunn, G. H., Rev. Mod. Phys. 38, 1 (1966).
- [40] Meyer, R. T. and Lynch, A. W., High Temp. Science, 5, 192 (1973).

#### Discussion

Moderator (Green): You showed that the partial pressure in the high pressure molecular beam sampling system was proportional to the intensity times the temperature, which is a little bit surprising, though I expect it is right. But you actually used this relationship?

Response (Bonnell): Yes, we do. What we actually do is monitor the carrier gas along with everything that moves with it, i.e., the transported vapor. We use the carrier gas (known pressure) through  $P=kIT$  to back-calculate an effective instrument constant,  $k$ , for every data point taken. (Actually when we do this at every temperature we simply use ion intensity ratios.) The real point is that the beam characteristics outside of the effusive nature of that function are carrier gas dependent. And one really does need to take a measurement of the carrier gas each time.

We find that the function (i.e.,  $k$ ) varies slowly with  $T$  and  $P$ . We could, in fact, process our data with the average of all the instrument constants ( $k$ ) we calculate. But, it is rougher. There is actually a dependence on the expansion process that is observable as a change in instrument constant, particularly as a function of temperature in the transpiration cell.

Question (Hildenbrand): I didn't understand the explanation for your sodium chloride total pressures. You said they were low by about 50 percent relative to the JANAF data.

Response (Bonnell): The current interpretation is that molecular beam collimating system is not particularly a restriction in the beam only. The beam that actually enters the mass spectrometer ion source is of the order of the size of the entrance of the mass spectrometer itself. This arrangement allows scattered carrier gas, in addition to beam carrier gas, to enter the ion source and give too high a reference gas signal. I would like to make the argument that 50 percent agreement is pretty good. I mean, that is quite typical of ordinary Knudsen cell work. This question is discussed more fully in the main text.

Question (Hildenbrand): Do you expect the same kind of disparity over other condensible species?

Response (Bonnell): Yes, as a matter of fact, in the sodium sulphate case, we apply that correction to the sodium partial pressure. We do not need to apply it to the sulphur dioxide or the oxygen.

Moderator (Greene): Did you do any diagnostics such as varying the orifice size in your study of sodium chloride monomer-dimer equilibrium?

Response (Bonnell): All right, varying orifice size is a little tricky. These are platinum cones and we take what we can get when we drill holes. We did use two totally different samplers with approximately 30 percent difference in orifice size and there seems to be no difference in the data.

We have changed the skimmer to orifice distance slightly. This is not something that is easily done. We are, in fact, depending upon measurements by a number of other people as to where the maximum expansion ratio occurs, which is typically like 120 nozzle diameters. So we haven't made a systematic change in orifice size. We are really not equipped with the pumping to do it yet. That is coming. (It should be noted that the nozzle-skimmer geometry is very similar to that used earlier for flame sampling and other 1 atm pressure studies as reported on by Hastie).

Comment (Hastie): I think the interesting thing about this work is represented by the figure where we show data over about an 800 degree temperature range for sodium chloride and about six orders of magnitude in pressure--that is, the data from the conical and the capillary sampler both fall on the same line (Clausius-Clapeyron relationship). The really striking thing was that we were able to get this kind of data with a capillary. We thought the capillary would be much cruder and we were originally interested in the capillary just because it would be a more robust type of sampling probe for very extreme environments. But it does seem to give pretty good thermodynamic data.



IN SITU ANALYSIS OF MINOR GASEOUS SPECIES IN CRYSTAL GROWTH  
AMBIENTS USING MOLECULAR BEAM MASS SPECTROMETRY

Haiping Dun, Brenton L. Mattes<sup>1</sup>, and David A. Stevenson  
Department of Materials Science and Engineering  
Stanford University  
Stanford, CA 94305

A molecular beam-mass spectrometry system has been designed for high temperature (600-1100 °C) atmospheric pressure gas sampling. A sharp conical nozzle was adopted as a sampling probe and the gas dynamics of the expansion was thoroughly characterized. Both advantages and disadvantages of this sampling method, in contrast to the conventional thin plate orifice or sonic nozzle, are discussed. One of the most significant features of this sampling method is the effect of mass separation; the concentration of the sampled beam will, in general, differ from the concentration of the sample itself. Experimental data and analysis of this mass separation as a function of the mass number are presented and guidelines given for suitable correction factors.

With this sampling method, resolution in the parts per million range are obtainable. The high temperature chemical transport reactions were studied for a typical crystal growth reactor system containing graphite, purified hydrogen gas, and fused quartz. Both kinetic and thermodynamic aspects of relevant chemical transport reactions were investigated. The implications of these reactions on the impurity incorporation in conventional liquid phase epitaxial crystal growth techniques are discussed.

## 1. Introduction

There is considerable practical interest in the accurate analysis of vapor species in high temperature chemical process environments. These environments typically contain reactive gaseous species at elevated temperatures and a total pressure around one atmosphere. In the present paper, we are concerned about the characterization of the gaseous environment in typical crystal growth processes for semiconducting materials. Because of the stringent requirements for extremely high purity, there is concern over species present in the vapor in very small concentrations since the incorporation of impurities in the crystal

---

<sup>1</sup>Present address: Department of Electrical and Computer Engineering, University of Michigan.

exerts a significant influence on the crystal properties. We focus, in particular, on the liquid phase epitaxial (LPE) GaAs growth process. It has been established that Si, C, and O are unintentional impurities in LPE GaAs crystals and their presence exerts a significant influence on the crystal properties [1-6]<sup>2</sup>. It has been suggested that these elements are present in the crystal as a result of specific impurities in the gaseous environment during crystal growth. Species such as CO, H<sub>2</sub>O and SiO may be present in the purified protective atmosphere or may arise from chemical reactions during growth and are a source of impurities in the final crystals. Direct in situ analysis of the crystal growth ambient, however, has not been made for this system.

Techniques for in situ analysis of crystal growth systems have recently been revised [7] with emphasis on two general techniques: Raman and fluorescence spectroscopy; and mass spectrometry. In this paper we are concerned with the use of mass spectrometry for the analysis of high temperature-atmospheric pressure systems. In the use of mass spectrometry as an analytical tool, it is necessary to introduce a representative sample into a detection chamber which operates at a pressure of  $\sim 10^{-6}$  Torr. As a consequence, for a system at atmospheric pressure, it is necessary to meter the sample into the detector chamber with an appropriate device.

Common techniques for accomplishing this include: a simple capillary; a selective membrane; and a chromatographic column. For high temperature systems, however, all of these systems may perturb the chemistry during sampling. A solution to this problem is the formation of a molecular beam by free jet expansion through a sampling orifice. This has traditionally been done by expansion through a thin plate orifice (a pinhole) or a sonic nozzle. However, recently a conical nozzle has been adapted for use in molecular beam mass spectrometry (MBMS) [8,9,10]. This type of sampling orifice has two distinct advantages: (i) the sharp tip of the conical nozzle may be positioned at critical locations, such as adjacent to a reactor wall or near a substrate surface in a deposition system; and (ii) in flow systems, the conical geometry perturbs the flow less than with other sampling orifices and allows sampling at different angles to the flow direction. A disadvantage, in some instances, is the geometrical confinement of the flow at the throat of the conical nozzle. This will influence the rate of expansion and, consequently, the number of collisions that occur prior to the formation of the molecular beam. In addition, confined expansion will lead to substantial differences in the beam characteristics, such as the molecular density distribution and the composition change upon sampling. Although there are extensive studies on the gas dynamics of the two other types of sampling orifices, relatively little work has been done to characterize the conical nozzle orifice.

In the present paper, we summarize observations on the use of this type of nozzle for molecular beam sampling with particular reference to the following points: the density profile in the expansion stage; the sampling time and the system response time; composition change upon sampling; and the sensitivity and accuracy of the method.

The relevance of this method for characterization of crystal growth environments is explored for the case of gallium arsenide liquid phase epitaxial growth. In particular, the

---

<sup>2</sup>Figures in brackets indicate the literature references at the end of this paper.



purity of palladium diffused hydrogen and the reactions between purified hydrogen and quartz at elevated temperatures were studied and the possible influence of the observed impurities in the gas phase upon the final crystal properties of LPE grown GaAs are discussed.

## 2. Molecular Beam Mass Spectroscopy Apparatus and Method

Every molecular beam mass spectrometer (MBMS) has its individual characteristics which are a result of its geometry, vacuum system, and detector system and it is important to characterize each system. We briefly describe the present MBMS system.

A schematic representation of the experimental system is shown in figure 1. The system consists of three differentially pumped stages. The gas in question, for example, in a crystal growth furnace, is expanded through a conical sampling orifice (0.08 mm diameter) into the first stage at  $10^{-3}$  Torr (2400 L/S diffusion pump)<sup>3</sup>. After expansion, the center of the gas stream passes through a conical skimmer orifice (0.12 mm diameter), into the second stage which is maintained at  $10^{-5}$  Torr (260 L/S turbomolecular pump). The beam is chopped in this stage for phase lock detection and then passes through the final beam channel into the third stage at  $\sim 10^{-7}$  Torr (ion pumped at 500 L/S). The third stage contains a quadrupole mass analyzer (Uthe Technology International, UTI 100C) as the gas detector.

The nozzle and skimmer cones were made of General Electric type 204 fused quartz and were designed to have half-cone angles of  $40^\circ$  and  $25^\circ$ , respectively. The fabrication process followed a method described by Thomas [8]. A cylindrical fused quartz tube was initially shaped into a cone with the desired angle. The tip was then drawn out to form a tapered capillary and ground to expose a circular hole as a gas entrance, with a tolerance of  $\pm 0.0005$  mm. The fabrication process introduced a short narrow channel between the entrance and expansion region with an inner half cone angle  $\sim 5^\circ$  which expands to  $40^\circ$ . The influence of this geometry on the expansion is discussed later. The skimmer, with a larger orifice, was fabricated by the same process. Both tips were polished by a small torch to obtain a smooth surface.

---

<sup>3</sup>Appropriate conductance losses must of course be considered, along with the rated pump speeds, in order to calculate the pumping speed and steady state pressure of each stage. For the first stage, the combined pumping speed is  $\sim 200$  L/S, with a calculated first stage pressure for sampling atmospheric air of  $2 \times 10^{-3}$  Torr as compared with an observed pressure of  $8 \times 10^{-3}$  Torr. The second stage pressure depends on the gas density (or the related mach number) at the skimmer. For a typical mach number of 10, we calculate a pressure  $\sim 4 \times 10^{-6}$  Torr, with observed values in the range of  $5 \times 10^{-5}$  to  $8 \times 10^{-6}$  Torr for typical skimmer locations.

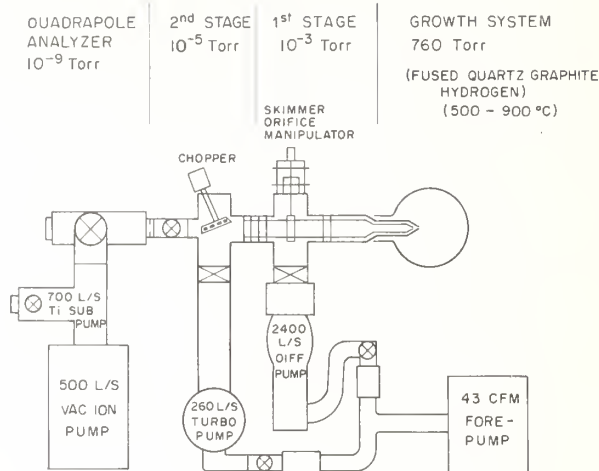


Figure 1. A schematic representation of the molecular beam mass spectrometer.

The axis of the conical nozzle, which determines the direction of the expansion flow, is adjustable in the x-y dimension with a set of three bolts and the skimmer is adjustable in three dimensions with a micrometer manipulator with an accuracy of 0.015 mm.

The detector chamber entrance is a stainless steel tube (21 mm i.d. and 12 cm long) located ~40 inches downstream of the skimmer orifice and may be moved in the X-Y direction. The preliminary alignment of the three inlets was made by using a laser beam, and the fine adjustment was accomplished by monitoring the maximum signal from the mass analyzer. The ability to move the skimmer continuously in three dimensions facilitates the characterization of the expansion zone and the achievement of good beam performance.

To minimize the influence of the background, beam chopping and phase-lock detection are used. A chopper, which consists of two wide slots 2-1/2 x 1-3/8 in. on a cylindrical column, is mounted vertically between the skimmer orifice and the detector (fig. 2). The column is driven by a DC motor (Electro-Craft Corp. Model E-650) through the shaft of a ferrofluidic rotary seal (Ferrofluidics Corporation, Model SB253). The operation frequency of the motor is set at 16.2 Hz, which corresponds to a 33.3 Hz chopping frequency. The chopping frequency is selected to avoid 60 Hz harmonics.

The mass signal detected in the quadrupole analyzer is comprised of two parts: a modulated AC part and a static DC part from the ambient background. The output of the mass analyzer is connected to the signal channel of a lock-in amplifier (Princeton Applied Research Model 124A or Model 5204) and a synchronized reference signal is generated by an incandescent bulb and a photocell. The modulated beam is phase-lock detected and separated from the background (fig. 2).

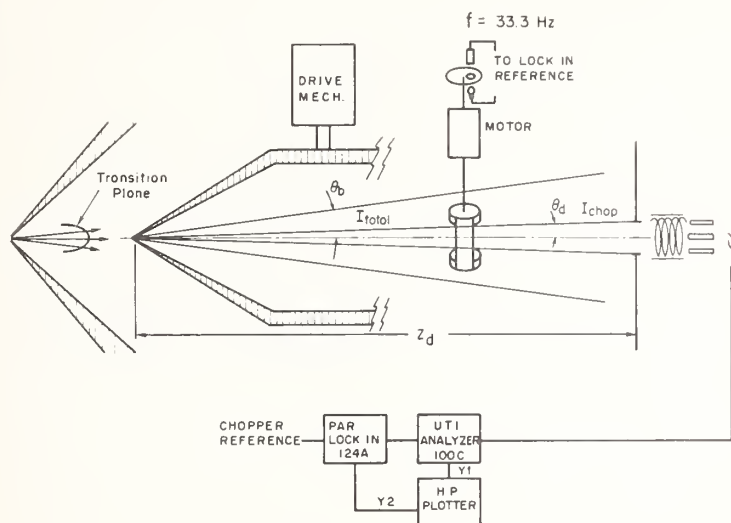


Figure 2. The interior of the molecular beam mass spectrometer.

### 3. Experimental Results and Interpretation

#### 3.1 The far flow field of a conical nozzle

The jet expansion flow field inside the conical sampling nozzle was profiled by manipulating the skimmer in the expansion cone. The flux through the skimmer orifice was calculated in the expansion cone from the measured pressure directly above the turbo pump (fig. 1) and from the pumping speed. The observed variations of density with axial position for air (25 °C), and  $H_2$  (25 °C and 410 °C) are displayed in figure 3; and figure 4 shows the measured transverse density distribution. Several important conclusions can be drawn from these figures.

(i) A nearly radial expansion pattern is obtained in the far flow field, where the normalized density for each streamline is given on figure 4. It is found that the density distribution is more concentrated for high Reynolds number gas (air, 25 °C) than for low Reynolds number gas ( $H_2$ , 410 °C).

(ii) The relationship between the axial position variable,  $\zeta$ , ( $\zeta \equiv (z - z_c)/d^*$ , with  $z$  the distance downstream of the sampling orifice and  $d^*$  the orifice diameter), and the density,  $\rho$ , at the center of the beam axis (fig. 3) may be represented empirically by the relation:  $\zeta \propto K\rho^{-1/2}$  ( $r = 0$ ). The quantity  $z_c$  is an apparent source point for gas expansion in the inertia-dominated (farfield) region and  $K$  is a characteristic constant for a given gas and temperature. The constant  $K$  increases with the source Reynolds number of the respective gas.

(iii) The observed dependence of the density in the transverse direction for a given value of  $\zeta$  (fig. 4) is expressed empirically by the expression  $\rho(r,z)/\rho(0,z) = f(\theta) = (1-K^2\theta^2)$ , for  $f(\theta) < 0.6$ , where  $\tan \theta = r/z$ . The constant  $K$ , obtained empirically and individually for the fit to the axial and radial profile is numerically identical for the two cases, which implies geometric similarity.

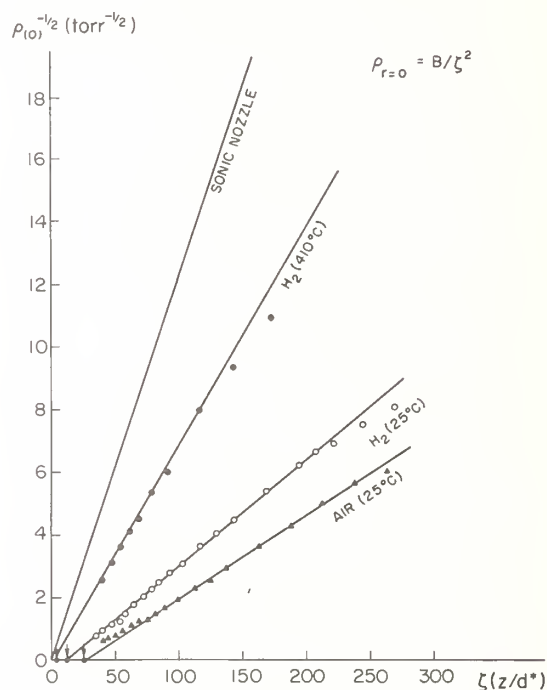


Figure 3. The variation of the expansion gas density along the jet axis of the conical nozzle versus the nozzle-skimmer distance.

Combining (ii) and (iii), the density distribution can be formulated in terms of the stagnation density,  $\rho_0$ , as:

$$\frac{\rho(r,z)}{\rho_0} = D \frac{f(\theta)}{(\zeta/K)^2} \quad (1)$$

In this equation,  $K$ ,  $D$ , and  $z_c$  are parameters that are characteristic of the specific gas sampled; the values for air,  $H_2$  (25 °C) and  $H_2$  (410 °C) are given in table 1 along with the source Reynolds number,  $Re_0$ , for comparison. For values of  $\theta$  larger than  $\sim 10^\circ$ , nonradial flow behavior becomes significant and more terms in  $\theta$  are necessary to express  $f(\theta)$ .

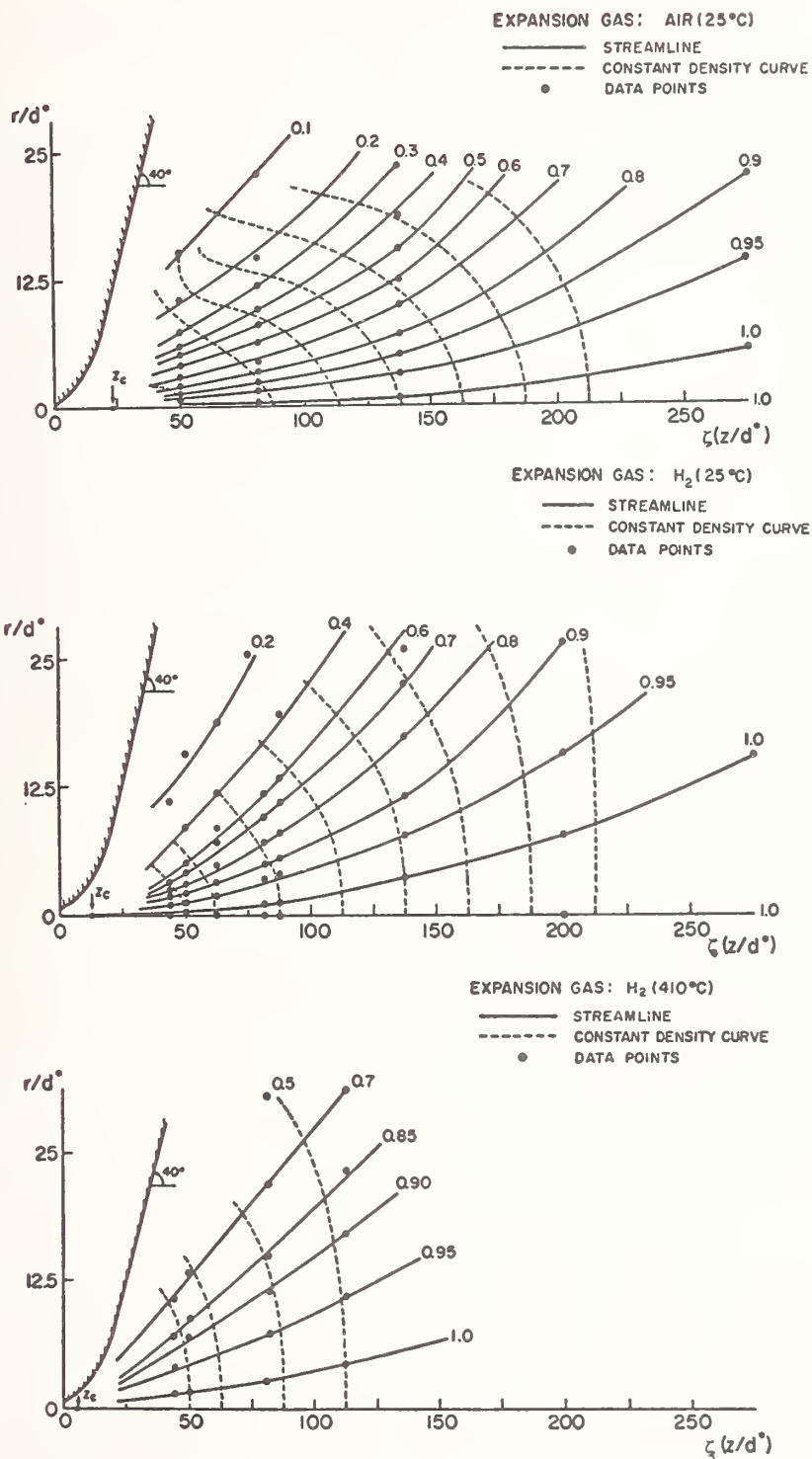


Figure 4. The expansion flow field of a conical nozzle for air (25 °C), H<sub>2</sub>(25 °C), and H<sub>2</sub>(410 °C). The solid lines are the streamlines and the dotted lines are the constant density curves.



Table 1. The conical nozzle parameters  
(eq. (1))

	$\underline{K}$	$\underline{D}$	$\underline{(z_c/d^*)}$	$\underline{A}$	$\underline{Re_o(r^*c_o/v_o)}$
Air (24 °C)	6.3	0.052	24.5	1.95	1000
H <sub>2</sub> (25 °C)	3.2	0.096	12.5	2.20	535
H <sub>2</sub> <sup>*</sup> (410 °C)	1.9	0.070	4.4	2.85	205

The most significant difference in the expansion flow pattern for the conical nozzle, compared with a sonic nozzle, is the elongation in the axial direction and the contraction in the transverse direction. This more concentrated flow pattern has been explained by the following model. The initial gas expansion in the throat region is confined by the nozzle walls as well as a boundary layer built up along the wall (fig. 5). These factors produce a nearly parallel flow up to several nozzle diameters in distance. After a certain degree of nearly parallel expansion, the pressure drops and the flow becomes supersonic. The angle of divergence of the wall increases toward 40° and, at a specific point downstream, the expansion is no longer confined by the geometry, but instead by a shock boundary; the enhanced radial expansion establishes a radial flow component with a shock boundary formed due to the expanding gas colliding with the background gas.

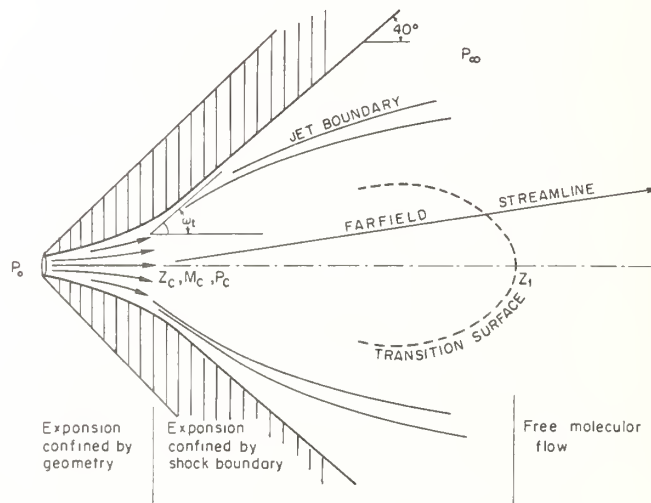


Figure 5. The cross section of the miniature conical nozzle with  $z_c$  given as an apparent source point for subsequent expansion in the inertia-dominated region.

In summary, the flow pattern of a conical nozzle is quite different from a sonic nozzle with the flow pattern elongated in the axial direction and contracted in the transverse direction. The concentration of the flow pattern along the axial direction results in a

slower rate of expansion which consequently gives a slower quenching rate and a slower increase in the Mach number with distance.

### 3.2 Composition change upon sampling of a dilute gas mixture

During the molecular beam sampling process, there is the possibility of a significant change in composition. This is particularly important for the sampling of a minor species in a matrix of a gas of significantly different molecular weight. In this study, we are concerned about the sampling of a species in a hydrogen matrix and the observed enrichment of the heavier molecular species upon sampling.

In order to find the possible mechanism for mass separation, we compare established models for a sonic nozzle with our results with a conical nozzle. In particular, we consider the difference that arises from the slower change of the Mach number with distance and a more concentrated streamline for the conical nozzle. There are four mechanisms that are proposed to explain the mass separation phenomenon in molecular beam sampling and the relative importance of these mechanisms are summarized as follows:

(i) Pressure Diffusion [11]: According to the theory for pressure diffusion, a sonic nozzle with a source Reynolds number of 500 gives an enhancement factor of 1.34 for dilute  $N_2$  in  $H_2$  and 1.58 for Ar in  $H_2$ . In the case for our conical nozzle, with a slower increase of the axial Mach number with distance, the enhancement factor would be smaller than this factor and less than the observed linear mass ratio.

(ii) Skimmer Induced Shock Separation [12]: This is not significant when the skimmer is located downstream from the transition plane and when the skimmer geometry is designed to minimize shock.

(iii) Molecular Diffusion [13]: Enhancement due to free molecular diffusion after the beam is formed by the skimmer, as analyzed by Greene, Brewer and Milne [14], Sharma, Knuth and Young [15], and French and O'Keefe [16], appears to be the dominant mass separation mechanism.

(iv) Background Penetration [17]: This mechanism is important when the expansion gas pressure is comparable to the background pressure. Lighter species, which are enriched in the background and have higher random velocity, will penetrate the jet plume to a greater extent than the heavier species. At the final stage of expansion, the background penetration becomes significant.

The enhancement factor,  $\alpha$ , was measured by preparing calibrated mixtures of 1 percent Ar (or  $N_2$ ) in  $H_2$  by controlled flow of the respective gases and then sampling the controlled gas mixture with the sampling nozzle. The resulting beam was chopped and the modulated AC signal was detected with a lock-in amplifier. The recorded mass concentration ratio of Ar (or  $N_2$ ) to  $H_2$  was divided by the actual calibrated concentration to obtain the experimental separation factor,  $\alpha$ :

$$\alpha = \frac{(I_h/I_l)_d}{(I_h/I_l)_o} \quad , \quad (2)$$

where the subscripts h, l denote "heavy" and "light" species and d, o denote "detected" and "originally present in the stagnation ambient," respectively. The value of  $\alpha$  is plotted in figure 6 as a function of the reduced nozzle-skimmer separation,  $\zeta$ . Over a range of  $\zeta$  values,  $\alpha$  is a constant and is linearly proportional to the mass ratio. This is obviously due to molecular diffusion from the beam after the gas passes the skimmer. When the skimmer position is located further upstream or further downstream from this range,  $\alpha$  decreases. The decrease of  $\alpha$  downstream is attributed to background penetration whereas the decrease of  $\alpha$  upstream is attributed to either skimmer interference or the streamline divergence effect.

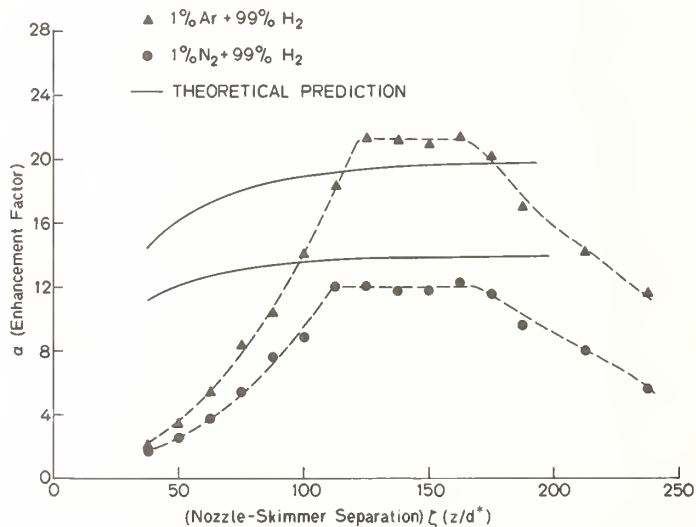


Figure 6. The mass separation factor plotted as a function of the reduced nozzle-skimmer separation.

### 3.3 Sources of error and correction factors

The error introduced by composition change upon sampling can be corrected using the mass ratios of the molecular species when the skimmer is properly located, as was previously discussed. Other sources of error include detector errors and vacuum interference. The detector errors arise from the different ionization efficiency, quadrupole transmission

coefficient and detector sensitivities for different gas species. We have used the data provided by UTI Corporation for these corrections.

The vacuum interference arises from the difference between the ambient pressure in the detector stage and the composition of the molecular beam. This disparity arises from the different pumping speeds and the different rates of adsorption and desorption in the detector stage for different species. The vacuum interference is relatively difficult to predict; however, this effect is substantially eliminated with the beam chopping technique. For non-condensable species that are not efficiently pumped in the detector chamber, there is a pressure build-up in the third stage which masks the beam pressure and gives a correspondingly high DC signal for those species. For condensable or unstable species and for species that are efficiently pumped in the detector chamber, the steady state background pressure is low compared to the effective beam pressure and there is a correspondingly low DC signal.

An illustration of the vacuum interference is provided by the results for the detection of the composition of air using both the steady DC signal, representative of the background, and the phase locked AC signal, representative of the beam. The composition of the air has been accurately measured previously [18] and is a convenient calibrated source. The air in our laboratory, however, contains a higher concentration of hydrogen because of the extensive use of hydrogen in crystal growth furnaces in the same room. The detected air spectrum is shown in table 2, with peak ratios normalized to the nitrogen peak.

Table 2. Air composition

	<u>Standard</u>	<u>AC Signal</u>	<u>DC Signal</u>
N <sub>2</sub>	1	1	1
O <sub>2</sub>	26.8%	23.1%	12.7%
Ar	1.2%	1.5%	4.9%
CO <sub>2</sub>	0.042%	0.049%	0.26%
H <sub>2</sub>	0.64 ppm	0.44%	13.5%
H <sub>2</sub> O	-	1.22%	2.5%
(H <sub>2</sub> O) <sub>3</sub> H <sup>+</sup>	-	40 ppm	-
(H <sub>2</sub> O) <sub>4</sub> H <sup>+</sup>	-	35 ppm	-

It is seen that the AC technique gives air compositions close to the standard value, whereas the DC signal leads to considerable errors. Peaks at mass 37, 55, 73, etc., which are observed only in the AC mode, are water vapor clusters nucleated during the nozzle expansion process.

### 3.4 Sensitivity and response time

To obtain high sensitivity, the vacuum should be as perfect as possible to avoid background interference. The background pressure of the particular vapor species influences the actual sensitivity for that species. Careful baking and outgassing of the system was done in the present work to achieve this objective. The sensitivity for water vapor, which is

the worst case because of high background pressure, can be as low as  $\sim 1$  ppm with beam chopping (or  $\sim 200$  ppm without chopping). Because of the mass separation effect, there is a higher sensitivity in a light gas matrix and a lower sensitivity in a heavy gas matrix. For example, the sensitivity for oxygen in a hydrogen ambient is as low as 0.5 ppm, while in argon it is around 10 ppm.

The MBMS is, in principle, capable of response time of  $\sim 10$   $\mu$ s; for our system; the nozzle-skimmer separation is  $\sim 1$  cm, the terminal velocity for hydrogen is  $\sim 10^5$  cm/s, thus, the change from continuous to molecular flow is  $\sim 10$   $\mu$ s. However, the quadrupole mass analyzer detector response time is only 1 ms, and the beam modulation technique further reduces the response time. The system response time is related to the sensitivity and accuracy. Table 3 gives the response time-sensitivity characteristic of the system using the lock-in amplifier.

Table 3. Response time of the MBMS system in the chopping mode.

sensitivity (ppm)	1	10	100	1000	1%
response time (s)	3	1	0.3	0.1	0.03%

Figure 7 gives a comparison of the response time of the MBMS and a commercial zirconia tube oxygen sensor. Initially, a known amount of oxygen was mixed with pure nitrogen by adjusting the flow rate of the gases until steady state was established. At a specific time, the oxygen flow was terminated and the decay of the mass 32 signal was measured versus time. Assuming a laminar flow inside the furnace, the relaxation time,  $t_c$ , is the volume of the gas between the furnace inlet and the sampling nozzle divided by the gas flow rate. The calculated  $t_c$  is consistent with the observed MBMS response. It is obvious that the present system has a more rapid response time than a zirconia oxygen sensor in this partial pressure regime. The slow response of the latter is due to many factors, including transport, interface kinetics, and the resistance and capacitance of the electrode and electrolyte.

#### 4. Analysis of The Gaseous Ambient Liquid Phase Gallium Arsenide Growth

There have been extensive studies made to identify the origin of the residual donor or acceptor in liquid phase epitaxial (LPE) gallium arsenide, and it is concluded that silicon, carbon, and oxygen are the principal contaminants in GaAs LPE layers. Examples of impurity centers that have been proposed are: native defect donor [19], oxygen related donor [4,5], silicon donor [6], silicon acceptor [1,2], carbon acceptor [3], and vacancy-impurity complex [20].

A typical LPE growth system contains the following chemical components: palladium cell diffused hydrogen; a quartz reactor tube ( $\text{SiO}_2$ ); the growth cell (quartz, graphite or boron nitride); the gallium melt saturated with arsenic; and a gallium arsenide substrate. Contamination may arise from the starting materials (such as palladium cell diffused



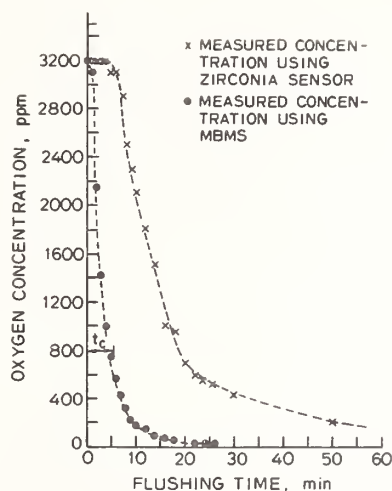
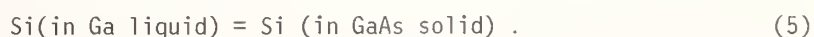
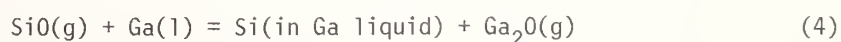
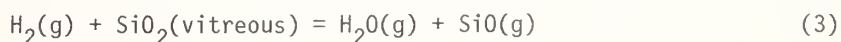


Figure 7. Comparison of the response time of the MBMS with a zirconia sensor.

hydrogen, the gallium melt, the gallium arsenide source and substrate) and from the side chemical reactions during high temperature growth. Examples of these side reactions are: hydrogen reduction of quartz; the reaction of gallium with the boat materials (graphite, BN, quartz); the contamination of Ga and the system by oxidation; water adsorption during loading; air leaks during growth; and residual organic solvents used in cleaning.

#### 4.1 Possible silicon incorporation reactions

Hicks and Greene [1] proposed that the reduction of quartz is a source of Si contamination in GaAs. A kinetic study of this mechanism was reported by Weiner [2], who explained the observed level of contamination ( $\sim 10^{14}/\text{cm}^3$ ) by a model relating thermodynamic quantities to variables such as flow rate and bake out time. The same reaction was proposed to explain the silicon contamination in GaP LPE growth [21]. The key reactions proposed in these papers are the following:



Several groups have reported that high purity gallium arsenide layers grown by the LPE technique are n-type and they attribute this to an oxygen donor [3,4]. The work of Mattes,

et al. [22] showed the pre-growth bake-out of the gallium melt, influences the layer properties and, in fact, the carrier type may change from n to p. This n-p transition phenomena depends on the bake-out conditions, such as bake-out temperature and time and the hydrogen flow rate, but it is not too sensitive to the growth conditions. By careful control of the bake-out temperature and time and the other growth parameters, a layer with carrier concentration  $<10^{14}/\text{cm}^3$  could be achieved by close compensation between impurity donors and Si acceptors [22]. It was proposed that Si is incorporated in the melt during bake-out and subsequent incorporation in the crystal during growth, with the acceptor form of Si dominating. However, there has been no direct observation of Si species arising from the quartz-hydrogen reaction as proposed in eq. (3) at the bake out temperature ( $\sim 800^\circ\text{C}$ ). This gas-solid reaction might proceed very slowly because of slow interface kinetics. The role of SiO vapor may be elucidated using MBMS.

#### 4.2 The purity of palladium cell diffused hydrogen and reaction quartz

The major impurity species found in palladium cell diffused hydrogen by the MBMS system were  $\text{H}_2\text{O}$ , Ar,  $\text{CH}_4$ , and mass 28 (which could be either  $\text{N}_2$  or CO). The mass 28 peak was identified as CO using both ionization potential and fragmentation methods, with the detection limit being in the 0.5 ppm range. (A molecular sieve trapping system was used to analyze species below this level.) When purified hydrogen is exposed to quartz at temperatures above  $800^\circ\text{C}$ , there are measurable changes in gas composition arising from chemical reaction and outgassing (fig. 8). For example, at  $890^\circ\text{C}$ , we observe potassium vapor, oil vapor fragments ( $\text{C}_3$  and  $\text{C}_4$ ), and a peak at mass 44. The potassium is attributed to contamination of the quartz furnace chamber from the molecular sieve during adsorption-desorption experiments and the oil vapor is attributed to residual organic solvent or grease from the glass joints. The observed increase of mass 44 with temperature is assigned to SiO arising from the hydrogen reduction of quartz; although  $\text{CO}_2$  has the same mass number, it is unstable at high temperature in a hydrogen ambient.

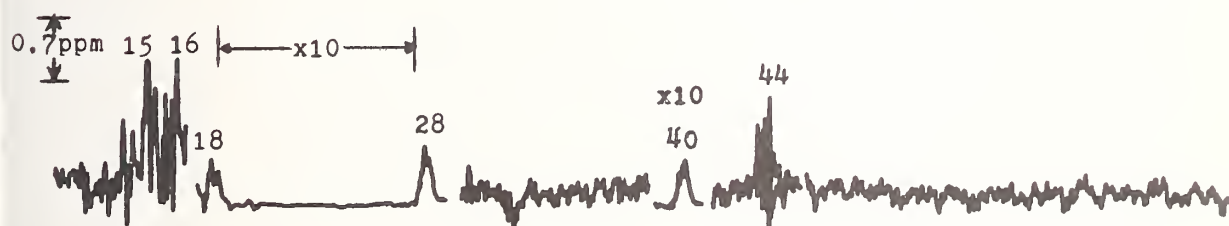
The observed dependence of SiO pressure upon temperature, shown in figure 9, is somewhat higher than present literature data [23,24]. Part of this discrepancy may be attributed to the higher free energy state for quartz in our present study, since it is in an amorphous state [25]. The increase in the concentration of water at different temperatures is in excess of that implied from the SiO partial pressure which indicates that water vapor is desorbed from the quartz and/or arises from the reduction of  $\text{SiO}_2$  leaving a residual dissolved SiO in the quartz.

#### 4.3 The role of impurity incorporation in LPE GaAs growth

In the LPE growth procedure, the exposure of the Ga melt to air, when the substrates are loaded or unloaded, causes oxidation of the Ga surface. When the melt is subsequently

de-oxidized with hydrogen, side reactions such as quartz reduction and hydrocarbon decomposition may introduce carbon and/or silicon into the melt which may be subsequently incorporated in the GaAs crystal.

PALLADIUM CELL DIFFUSED HYDROGEN + QUARTZ FURNACE (GE 204)  
at 25°C



at 890°C

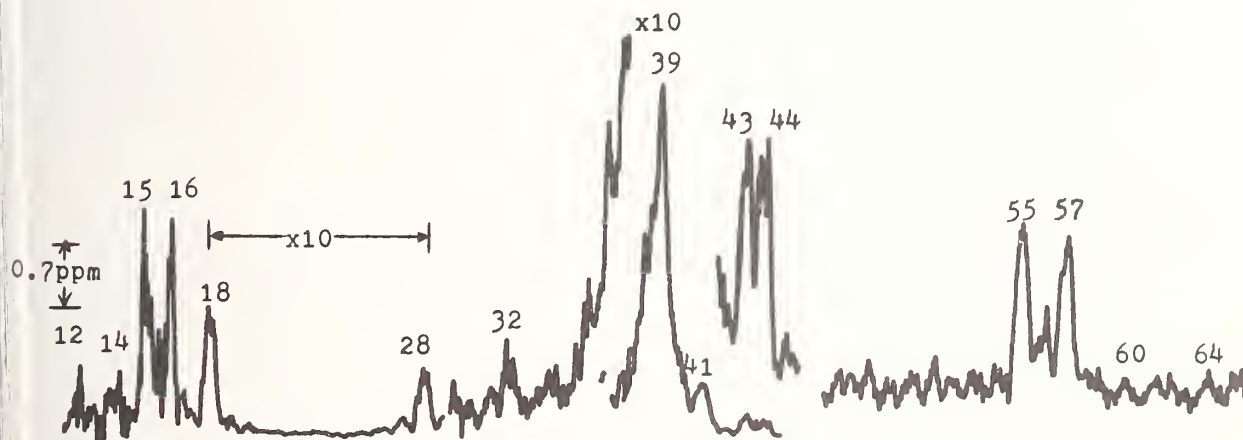


Figure 8. Comparison of palladium cell diffused hydrogen plus quartz system at 25 °C and 890 °C.

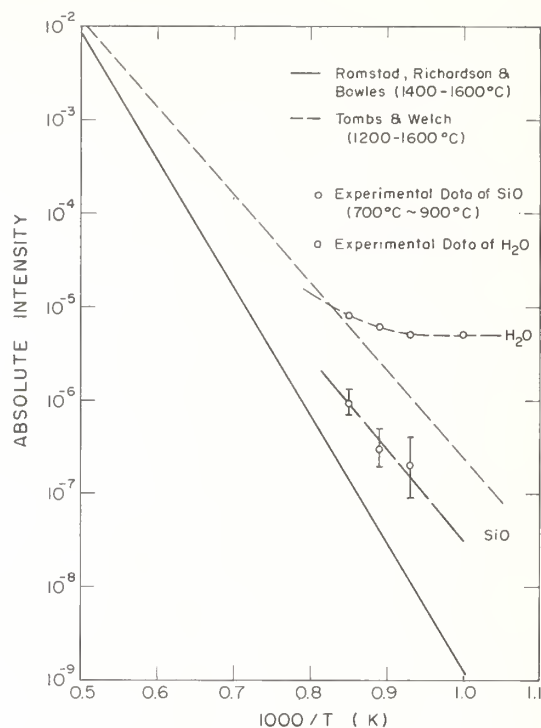


Figure 9. The comparison of the detected  $H_2O$  and  $SiO$  vapor pressure in a  $H_2$ -quartz system with the data obtained from the literature.

The following is a tentative explanation of impurity incorporation in LPE GaAs. Short time or low temperature bake-outs produce n-type layers due to an oxygen related donor and long time and high temperature bake-outs produce p-type layers due to the incorporation of the acceptor species, carbon incorporated on an arsenic site ( $C_{As}$ ) or silicon incorporated on an arsenic site ( $Si_{As}$ ) (which at growth temperature less than 890 °C is assumed to be the dominant Si incorporation reaction, rather than  $Si_{Ga}$  [26]). In order to grow high purity GaAs LPE layers, the key task is to reduce the oxygen level without introducing impurities from side chemical reactions.

## 5. Conclusions and Summary

The characteristics of molecular sampling using a diverging conical nozzle has been described as well as the capabilities of the MBMS system. The system is capable of detecting ppm levels of condensable species, such as water vapor at high temperatures (e.g., 900 °C). This technique was applied to the analysis of growth ambient of liquid phase epitaxial gallium arsenide at different temperatures. The following is a summary of the important results of the study.

(i) For a conical nozzle, in contrast to a sonic nozzle, there is a slower expansion rate and a flow pattern that is elongated in the axial direction and contracted in the transverse direction. The flow pattern depends on the geometry in the vicinity of the throat, the background pressure in the expansion chamber, and the characteristics of the gas that is sampled. For the small nozzle orifice and narrow throat used in the present study, the viscous effect is significant, as evidenced by the change of the flow patterns for gas samples of different Reynolds number.

(ii) The mass separation phenomenon, which was shown to be primarily a result of molecular diffusion, gives significant differences between the measured gas composition and the sampled gas composition for gas samples containing species of different masses. When the skimmer is placed in a region free from shock interference and background penetration, the mass separation is found to be approximately proportional to the mass ratio. In order to obtain high beam intensity, the skimmer is positioned as close to the nozzle as possible without encountering significant skimmer interference.

(iii) The beam modulation technique has advantages for quantitative analysis by minimizing the influence of the background. It is essential for the detection of condensable, reactive and metastable species.

(iv) The major gaseous species detected in a typical LPE gallium arsenide growth ambient ( $\sim 890^\circ\text{C}$ ) are  $\text{H}_2\text{O}$ ,  $\text{SiO}$ ,  $\text{CO}$ ,  $\text{CH}_4$ , and oil vapor. It is proposed that these impurities are the source of C, O, and Si impurities in LPE GaAs crystals and the hydrogen de-oxygenation process actually introduces compensating Si and/or C acceptors into the LPE GaAs crystals.

---

This work was supported by the Office of Naval Research under Contract N00014-75-C-0887.

#### References

- [1] Hicks, H. G. B. and Greene, P. E., in Proceedings of the Third International Symposium on GaAs. Inst. Phys. Phys. Soc., p. 92 (Academic Press, NY, 1971).
- [2] Weiner, M. E., J. Electrochem. Soc. 119, 4, 496 (1972).
- [3] Ashen, D. J., Dean, P. J., Harle, D. T., Mullin, J. B., White, A. M., and Green, P. D., J. Phys. Chem. Solids, 36, 1041 (1974).
- [4] Solomon, R., in Proceedings of the Second International Symposium on GaAs, Inst. Phys. Phys. Soc., p. 11 (Academic Press, NY, 1969).
- [5] Vilms, J. and Garrett, J. D., Solid State Elec. 15, 443 (1972).
- [6] Wolfe, C. M., Korn, D. M., and Stillman, G. E., Appl. Phys. Lett. 24, 2, 78 (1974).
- [7] Sedgewick, T. O. and Smith, J. E., J. Electrochem. Soc. 123, 254 (1976).
- [8] Thomas, R. W., Mass Spectrometry Technique and Their Application to Integrated Circuits, Final Report 01746902, Rome Air Force Development Center (1971).



- [9] Pertel, Richard, International J. of Mass, Spec. and Ion Phys. 16, 39 (1975).
- [10] Brown, R. W., Lippiatt, J. H., Price, D., and Izod, D. C. A., International J. of Mass. Spec. and Ion Phys. 16, 101 (1975).
- [11] Sherman, F. S., Phys. Fluids, 8, 773 (1965).
- [12] Reis, V. H. and Fenn, J. B., J. Chem. Phys. 19, 3240 (1963).
- [13] Waterman, P. C. and Stern, S. A., J. Chem. Phys. 31, 405 (1959).
- [14] Green, F. T., Brewer, J., and Milne, T. A., J. Chem Phys. 40, 1488 (1964).
- [15] Sharma, P. K., Knuth, E. L., and Young, W. S., J. Chem. Phys. 64, 11, 4345 (1976).
- [16] French, J. B. and O'Keefe, D. R., in 4th Symposium on Rarefied Gas Dynamics, J. H. deLeeuw, ed., p. 298 (Academic Press, NY, 1966).
- [17] Camparague, R., J. Chem. Phys. 52, 1975 (1970).
- [18] Handbook of Chemistry and Physics, 56th Ed., p. F-206 (CRC Press Inc., Ohio, 1975).
- [19] Williams, E. W. and Blacknall, D. M., Trans. Met. Soc., AIME, 239, 387 (1967).
- [20] Wolfe, C. M. and Stillman, G. E., Appl. Phys. Lett. 27, 10, 564 (1975).
- [21] Lorimor, O. G., Haszko, S. E., and Dapkus, P. D., J. Electrochem. Soc. 122, 1230 (1975).
- [22] Mattes, B. L., Houg, Y. M. and Pearson, G. L., J. Vac. Sci. Tech. 12, 4, 869 (1975).
- [23] Ramstad, H. F., Richardson, F. D., and Bowles, P. T., AIME, 221, 1021 (1961).
- [24] Tombs, N. C. and Welch, A. J. E., J. Iron Steel Inst. 172, 69 (1962).
- [25] van der Steen, G. H. A. M., Phillips Res. Repts. 30, 309 (1975).
- [26] Teramoto, I., J. Phys, Chem. Solids, 33, 2089 (1972).

#### Discussion

Question (Rosenblatt): What impurities are present?

Response (Stevenson): -- Carbon, oxygen and silicon, and we have some clues now on how we may control these.

Question (Rosenblatt): Is there any chance that there are any other impurity elements that are also concerned?

Response (Stevenson): You may have noticed that we did find some sulphur. We used a trap desorption technique to improve the sensitivity. We essentially trapped over a long period of time at low temperatures in a molecular sieve to trap polar species and then desorbed over a short period of time and by making some approximations we have determined H<sub>2</sub>S in the parts per billion regime.

Now, sulphur would also be an electrically active species. But the ones that are most suspect are carbon, silicon and oxygen, and for pretty good reasons.

Question (Spencer): The data on the gas composition of Pd-purified  $H_2$  passing over fused quartz at low and high temperatures shows SiO at high temperatures. The origin of SiO is presumably  $SiO_2 + H_2 \longrightarrow SiO + H_2O$ , and the data show an increase in  $H_2O$  at the higher temperature. However, the increase in  $H_2O$  is much greater than the concentration of SiO. This indicates a progressive reduction of the quartz surface. Have you investigated continued SiO evolution after the  $H_2$  flow is stopped and replaced by inert carrier gas, or investigated any memory of the quartz if the experiment is repeated?

Response (Stevenson): No, we haven't done that, but there are data in the literature. There are reports of partial reduction of quartz to give you more SiO and more  $H_2O$  corresponding to SiO. Essentially,  $SiO_2$  is stoichiometric and, furthermore, I am sure part of this is simply out-gassing of the system. But we haven't looked at the memory effect. It is a good point.



## MOLECULAR BEAM MASS SPECTROMETRIC SAMPLING OF MINOR SPECIES FROM COAL DUST-AIR FLAMES

Frank T. Greene, Jacob E. Beachey, and  
Thomas A. Milne  
Midwest Research Institute  
Kansas City, MO 64110

### 1. Introduction

It has been demonstrated in work in this laboratory that unaugmented, unconfined, premixed coal dust-air flames can be stabilized on small conical or flat, Meeker type burners [1-3]<sup>1</sup>. Since these flames are laminar, they can be used to study the kinetics of various processes in coal combustion and related areas such as understanding mechanisms of fireside corrosion and of flame and explosive inhibition. Some of the current work with these flames is directed toward identification and measurement of minor alkali metal and other species responsible for fireside corrosion. In order to make these measurements, molecular beam mass spectrometric sampling techniques have been adapted for use with these heterogeneous flames. In this paper, the equipment and techniques used are reviewed and some preliminary results presented.

### 2. Molecular Beam Mass Spectrometric Sampling of Flames

Our molecular beam mass spectrometric sampling equipment and techniques, and their application to the study of a variety of high pressure systems, have been previously reported and will, therefore, not be discussed in detail here [4-19]. A current bibliography of applications of molecular beam mass spectrometric studies of high pressure systems has also been completed by Stearns, et al. and described elsewhere in this volume [20].

In the molecular beam sampling of high pressure system, the gas is extracted in continuum flow through a sonic orifice and expanded into a reduced pressure region as a free-jet. In all of our past work, the pressure has been sufficiently low that the free-jet can be allowed to expand to low density, essentially collisionless flow before being collimated into a molecular beam. This avoids most problems with shock waves in the supersonic flow. After collimation, the beam passes through several stages of differential pumping and is introduced into the ion source of the mass spectrometer. For almost all studies, the molecular beam is chopped and phase sensitive detection employed to improve the signal-to-noise ratio and to eliminate the contribution of background gases and scattered gases from the beam. Time-of-flight velocity analysis and changes in the

---

<sup>1</sup>Figures in brackets indicate the literature references at the end of this paper.

sampling system parameters can be used to deduce sampling perturbations as indicated in the references given above.

Although the study of flames was one of the first applications of molecular beam mass spectrometry [21], significant problems can still arise in the sampling of premixed flames, and some of the errors are not always recognized. When heterogeneous flames are to be sampled, additional problems are introduced by the presence of particulates in the sampled gas and, at least in the case of butuminous coal-air flames, by rapid plugging of the sampling orifice. As a result, it proved to be necessary to develop new equipment for the study of coal dust-air flames.

### 3. The Molecular Beam Sampling System

#### 3.1 General considerations

In previous work in this laboratory [1-3], it was found that the high loading of particulates in coal dust-air flames, particularly in the early ignition and pyrolysis regions where the coal particles are sticky, caused rapid plugging of even relatively large sampling orifices. However, by using orifices of 0.02 to 0.03 in. diameter in conjunction with periodic (automatic) orifice cleaning, satisfactory operation could be achieved. These large orifices do, of course, require handling very large gas loads in the initial expansion stage. There is also an increased chance of reactions during the free-jet expansion changing the gas composition and of other sampling perturbations becoming important. The problems of free-jet, molecular-beam formation from sampling probes that involve large gas loads (either because of high pressure or large diameter) have been summarized by White [22].

Two major choices appear to be available, each with its disadvantages. Ideally, one would like a pumping capability in Stage 1 sufficient to maintain the pressure below  $1 \times 10^{-6}$  Torr for the maximum gas loads anticipated. At such pressures, the free-jet expansion can proceed to collisionless flow before encountering the skimmer. In this way, shocks at the skimmer are avoided and the minimum number of collisions for a given orifice diameter and system pressure will occur. The problem is that for a 0.03 in. orifice extracting gas at one atmosphere, an extremely large high vacuum pump would be needed (gas loads up to 70 Torr L/s may be encountered), requiring large pumping ducts and resulting in large beam distances from gas source to mass spectrometer. Prohibitive costs and physical bulkiness ruled out this approach for this work.

A second choice, which was selected for this work, involves operating Stage 1 at pressures in the 0.01 to 0.1 Torr range with placement of the skimmer in either the post-Mach disk continuum flow region of the free-jet or insertion of the skimmer into the free-jet ahead of the Mach disk. In this pressure range the Mach disk will be located approximately 0.2 to 0.5 cm downstream of the orifice. In either case, one risks the complications of shock wave perturbation of species concentrations, although it should be possible to avoid this problem by placing a properly designed skimmer upstream of the Mach disk. In this configuration, it should also be possible to approach molecular flow through



the skimmer, and avoid any complications resulting from a secondary expansion downstream of the skimmer. The advantage is that one can use much less costly, and more moderately sized pumps for Stage 1, such as booster diffusion pumps or blowers.

A third choice, which appears to be theoretically possible, and which is included for completeness, involves the initial free-jet expansion of the sampled gas into pressures of the order of 1 to 100 Torr, followed by a secondary free-jet expansion of the gas through the skimmer into essentially collisionless flow. The principal advantage of this arrangement appears to be in the relatively small pumps and vacuum components required. The major disadvantages include the difficulty in probing the high density supersonic jet without introducing a shock wave in the path of the sampled gas, and the larger number of collisions which will probably be produced in the free-jet expansion. Although, to our knowledge, this approach has not been successfully applied to molecular beam sampling, some preliminary data recently obtained in this laboratory indicate that this arrangement may be feasible [23].

### 3.2 Apparatus

The basic molecular beam sampling system, designed according to the criteria discussed above, is shown schematically in figures 1 and 2. Figure 1 shows the system in a configuration which was selected to minimize the distance between the sampling probe and mass spectrometer in order to maximize sensitivity. This arrangement yielded excellent sensitivity but proved to be unsatisfactory for use with coal dust flames and other particulate laden systems, as discussed below, and it was therefore modified by the positioning of a quadrupole in the crossed beam position and by the addition of another stage of differential pumping as shown in figure 2. In this configuration, the quadrupole is inserted into the vacuum system through one of a pair of identical bellows mounted on opposite sides of the chamber and held apart by a movable external frame. Since the very large forces produced by atmospheric pressure on the bellows are balanced, the quadrupole can be easily moved in small increments to obtain optimum alignment of the quadrupole ion source with the molecular beam and to insure that the beam does not strike any of the ion source surfaces and thereby allow particulate or metastable ionization to occur.

The housings for the quadrupole mass spectrometer and sampling system were fabricated from stainless steel, with the entire system designed to be rotated through either 90 or 180 degrees in order to accommodate upward, downward, or horizontally flowing systems. The mini-slide valve, which was pneumatically operated, was designed especially for this system. The motor-chopper-photocell for beam modulation and phase-sensitive detection were patterned after the system used in previous work [11]. The skimmer cone was formed by wrapping thin nickel foil (0.00035 in. thick) onto a support cone of 60-degree angle, so that the desired diameter of hole remains at the apex. This procedure produces a very sharp-edged cone facing the supersonic flow from the orifice. The flame sampling orifices are fabricated by drilling holes in the apex of spun copper cones, which are silver soldered into a water-cooled plate. The orifices are kept open by the solenoid operated orifice cleaner mounted on the vacuum side of the water-cooled plate as shown in figure 3. This cleaner "reams" the orifice at preset intervals, which were typically 1-10 s.

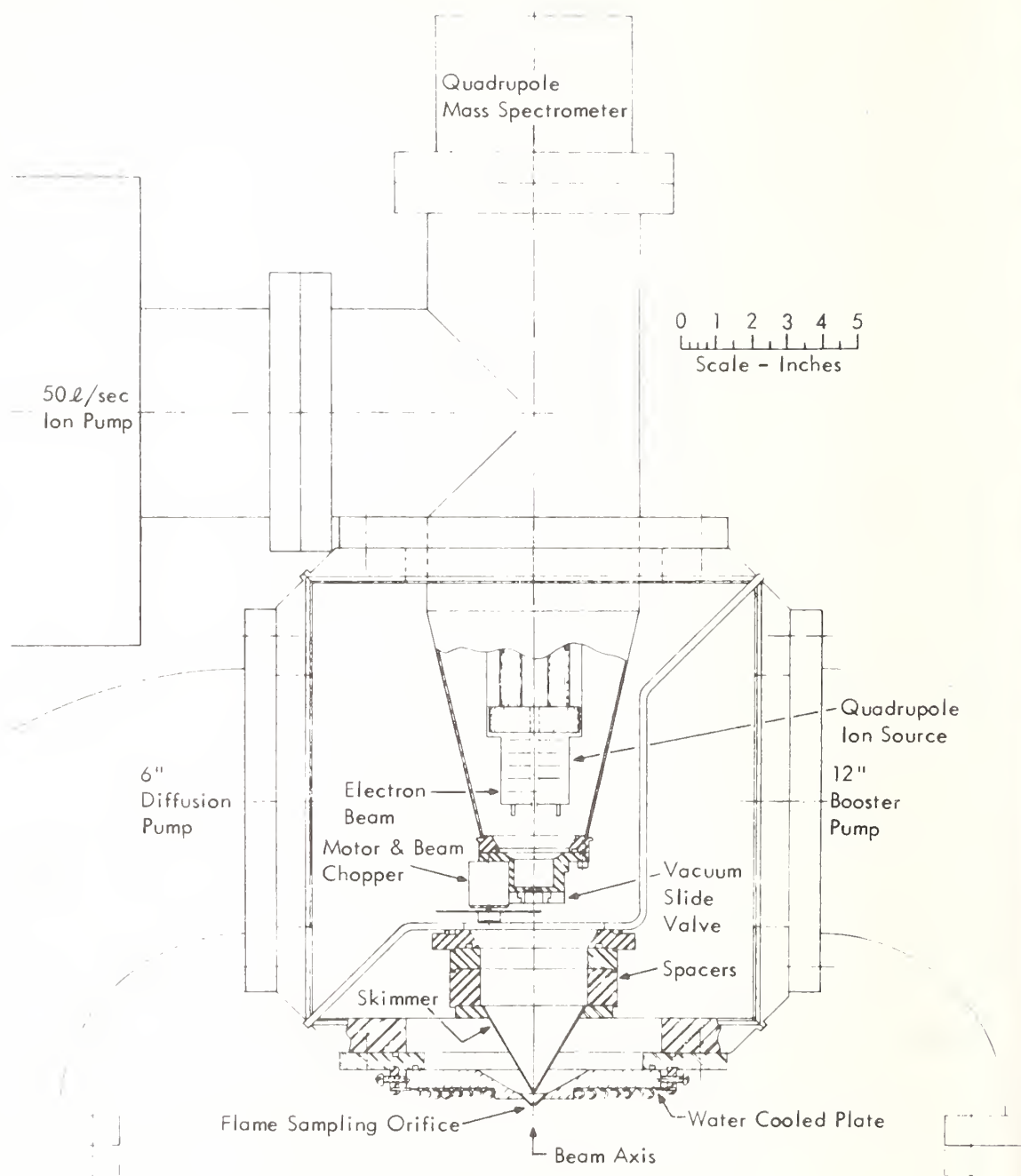


Figure 1. Schematic of axial, molecular-beam, mass spectrometric sampling system.

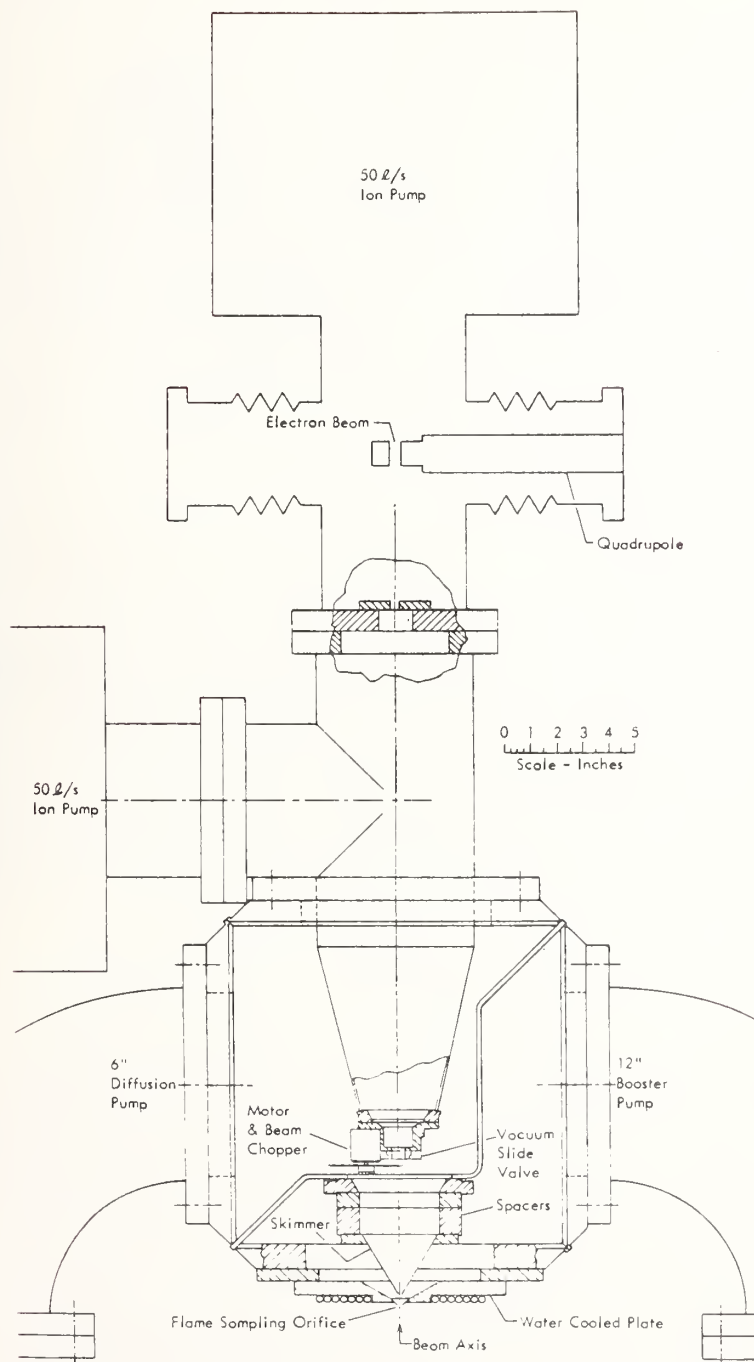


Figure 2. Molecular beam sampling system as modified for use with a quadrupole in the crossed beam mode.

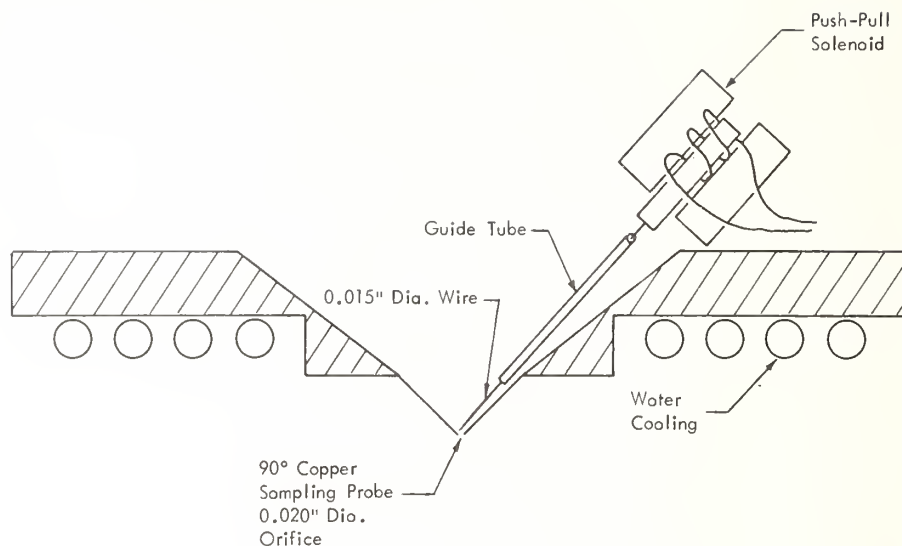


Figure 3. Water-cooled orifice and orifice cleaner assembly.

In this system, Stage 1 was pumped by an Edwards 1834 4,000 L/s booster pump, which maintained pressures of the order of  $4 \times 10^{-2}$  Torr when a 0.03 in. orifice was used to sample  $\text{CH}_4$ -air or coal dust-air flames. Stage 2 was pumped by a NRC NHS6 1,500 L/s conventional diffusion pump, which maintained pressures of less than  $2 \times 10^{-5}$  Torr. Both of these pumps were isolated from the sampling system by mechanically refrigerated baffles cooled to below  $-40^\circ\text{C}$ . Stages 3 and 4 were maintained below  $1 \times 10^{-6}$  Torr by 50 L/s ion pumps.

#### 4. Sampling System Performance

##### 4.1 General tests

The sampling configuration selected for this work represents a substantial change in gas dynamic conditions from those previously used since the skimmer may intercept the free-jet in a transition or viscous flow regime rather than in essentially collisionless flow. The free-jets were also larger than those in earlier work, and, therefore, more likely to introduce sampling perturbations. A series of tests of the sampling system using room temperature gases and atmospheric pressure flames was therefore carried out.

When room temperature air and  $\text{CH}_4$ -air flames at atmospheric pressure were sampled using 0.02 in. orifice, strong beams were obtained which exhibited normal dependence on orifice-to-skimmer distance as shown in figure 4. A typical set of data obtained when  $\text{CH}_4$ -air flames were sampled is shown in figure 5. When a 0.03 in. orifice was used to sample air at atmospheric pressure, substantially higher Stage 1 pressures were obtained and the beam intensity showed an abrupt decrease at large orifice-to-skimmer distances, suggesting the presence of a well defined Mach disk. When both the 0.02 and 0.03 in. orifices were moved laterally, the

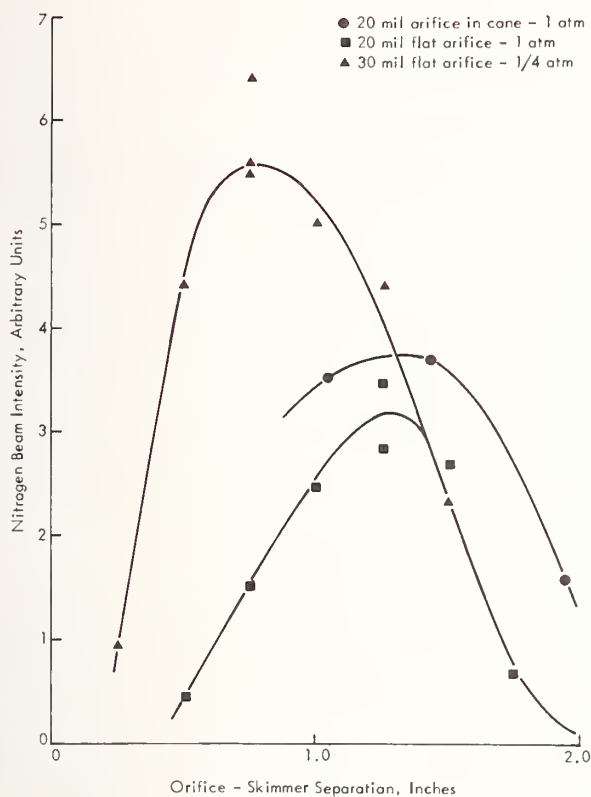


Figure 4. Variation of modulated molecular beam intensity with orifice-to-skimmer separation for room-temperature air. Relative peak intensities for different conditions are not significant.



Figure 5. Variation of modulated molecular beam intensity with orifice-to-skimmer separation for a lean, one atmosphere,  $\text{CH}_4$ -air flame and 20 mil orifice.



profiles obtained were normal, indicating that the beams were indeed being formed directly from the free-jet.

In our past work, we have found the mole fraction of clusters formed during a free-jet expansion to be a good indication of an undisturbed free-jet. The possibility of either a "bow-shock" across the skimmer entrance or a Mach disk producing partial randomization of the sampled gas is of particular concern here. The probe geometry could also influence the expansion. Consequently, the quality of the free-jet expansion was tested by sampling room temperature argon at atmospheric pressure. Past work [10,13] with smaller orifices has indicated a good correlation of observed  $\text{Ar}_2^+/\text{Ar}^+$  ion ratios with  $P_0^2 d$ , the square of the source pressure times the orifice diameter. Table 1 shows the results of sampling pure argon under two different conditions and compares the dimer ratio with this correlation. The results indicate a substantially undisturbed, isentropic free-jet expansion for the flat 0.03 in. orifice. The conical 0.02 in. orifice yields less than the expected dimer, perhaps due to expansion effects in the cone, differential scattering at the higher Stage 1 pressures, or to perturbation of the expansion by the large quantities of clusters formed.

Table 1. Dimer/monomer ratios observed in free-jet expansion of room temperature argon gas.

Orifice	Pressure	Measured Dimer Mole Fraction	Dimer
			Mole Fraction from Correlation
0.030 in. flat	1/4 atm	$2.6 \times 10^4$	$2.5 \times 10^4$
0.020 in. conical	1 atm	$2.2 \times 10^3$	$3.8 \times 10^{-3}$

Tests of the usable sensitivity of the system were made by comparing the observed noise level with the signal obtained from Ar in a  $\text{CH}_4$ -air flame. The noise level at a "clean" mass was found to correspond to 0.2 ppm with a 3 s 12 dB filter. This noise level is necessarily increased by statistical noise from background peaks, so the useful sensitivity at several peaks of interest were checked. This was always better than 1 ppm, which appeared adequate for the measurements in coal dust-air flames. Longer integration times could, of course, be used to increase the sensitivity.

#### 4.2 Metastable and particulate impact ionization

Initial tests were made using the axial system shown in figure 1. It was found that, when sampling air or  $\text{CH}_4$ -air flames, a small but significant phase-locked signal was observed which was independent of mass and of the analyzer settings, but which appeared only when the electron gun was on. Since this signal was monotonically dependent on the mole fraction of

Ar in the sampled gas, it was attributed to metastable Ar and possibly other species striking surfaces in the vicinity of the multiplier. A much more serious problem appeared when coal dust-air flames were sampled as the result of "particulate impact ionization." Particulate impact ionization, which has previously been investigated in this laboratory [19], occurs when high velocity particulates strike a plate, producing alkali metal ions. Even though the multiplier was located off the beam axis, the phase-locked signals produced by the effect reached levels corresponding to species constituting 10 percent of the beam. This background level clearly prohibited the detection of trace species in the flame. Attempts to swallow the particulate beam (through the analyzer) and to trap the particulate ions were unsuccessful, and so the sampling system was modified as shown in figure 2. With this configuration, metastable and particulate impact ionization were undetectable. Although the sensitivity of the system was reduced, it was found to be adequate for the detection of species at ppm levels as discussed above.

#### 4.3 Tests for other sampling perturbations

In addition to the general tests discussed above, tests were also made for several sampling perturbations which appeared to be of particular concern in this work, including entrainment of random gases from Stage 1 in the free-jet and the modulation of background peaks as the result of nonlinear behavior of the ion source. Tests for perturbation of the sampled gas by conduction to the sampling probe and reactions in the large free-jet expansions employed here are discussed in the following section. Other possible sampling perturbations have been discussed by Greene [19].

Some entrainment of random gases from Stage 1 in the free-jet is inevitable, if not necessarily significant. This error is of particular concern here both because of the high Stage 1 pressures used and the need to detect minor species. The level of entrainment in the free-jet was therefore determined by leaking known pressures of  $\text{CO}_2$  and  $\text{CHF}_2\text{Cl}$  into Stage 1 and measuring their level in a beam formed by the expansion of nitrogen through a 0.03 in. sampling orifice. It was found that the entrainment by species present in Stage 1 at pressures of  $1 \times 10^{-3}$  Torr would produce concentrations of less than 1 ppm in the beam. Since hydrocarbons and other species likely to interfere with minor flame species are unlikely to reach this pressure in Stage 1, this error should be negligible.

Modulation of background peaks by changes in ion source efficiency resulting from the presence of a strong molecular beam has been previously observed [18]. Tests for this effect with the quadrupole equipped with a high efficiency ion source were made by leaking n-hexane into the ion source region, and examining the resulting peaks, which resulted only from the random gas in the ion source, for modulation at the beam chopping frequency. Significant modulation, which would correspond to 0.01 to 0.1 percent species in the beam, were observed for the stronger background peaks. This problem was eliminated by reduction in the density of the electron beam.

## 5. Molecular Beam Sampling of Coal Dust-Air and Other Flames

Preliminary measurements were made of species in premixed gaseous and coal dust-air flames. A limited number of measurements were made of potassium species in  $\text{CH}_4$ -air and  $\text{CH}_4$ - $\text{O}_2$  flames seeded with a dry KCl aerosol. The only potassium species definitely identified were K and KOH. In these measurements, the KOH/K ratio was always below that calculated from existing thermochemical data, as has been previously observed [24,25]. This ratio was found to be independent of orifice size and probe temperature, so sampling perturbations do not appear to be responsible. The discrepancy may be due to extensive fragmentation at these high temperatures or to errors in the thermochemical data.

A limited number of measurements have been made of species in coal dust-air flames. In general, the molecular beam sampling system performed satisfactorily, with the automatic orifice cleaner keeping even the 0.02 in. orifice sufficiently open in stoichiometric Freeport seam coal flames. Profiles of Na extending to concentration levels as low as 1 ppm were obtained through these flames. Other species observed included K, KOH, SO,  $\text{SO}_2$  and  $\text{H}_2\text{S}$ .

## 6. Conclusions

Molecular beam mass spectrometric sampling systems can be designed to operate satisfactorily with relatively large sampling orifices and high pressures in the expansion region. The preliminary data obtained using this system indicate that molecular beam mass spectrometry can be used to measure concentrations of even minor species in coal dust-air flames and other intractable systems containing high concentrations of particulates.

---

This work was supported by the Department of Energy, Contract No. E(49-18)-2288.

## References

- [1] Milne, T. A., Greene, F. T., and Beachey, J. E., Pulverized Coal Combustion Studies on Flat-Flame Burners, paper preprinted and presented at the Western States Section/The Combustion Institute, 1974 Spring Meeting, May 6 and 7 at Pullman, Washington.
- [2] Milne, T. A. and Beachey, J. E., Laboratory Studies of the Combustion, Inhibition, and Quenching of Coal Dust-Air Mixtures, paper preprinted and presented at the Western States Section/The Combustion Institute, 1976 Spring Meeting, April 19 and 20, Salt Lake City, Utah.
- [3] Milne, T. A. and Beachey, J. E., Exploratory Studies of Flame and Explosion Quenching, Summary Technical Progress Report, June 30, 1972 - December 31, 1975, U.S. Bureau of Mines Contract No. H0122127, June 25, 1976.
- [4] Greene, F. T. and Milne, T. A., Mass spectrometric detection of polymers in supersonic molecular beams, J. Chem. Phys. 39, 3150 (1963).

- [5] Greene, F. T., Brewer, J., and Milne, T. A., Mass spectrometric studies of reactions in flames. I. Beam formation and mass dependence in sampling one atmosphere gases, J. Chem. Phys. 40, 1488 (1964).
- [6] Milne, T. A. and Greene, F. T., Mass spectrometric sampling of one atmosphere flames, Tenth Symposium (International) on Combustion, p. 153 (The Combustion Institute, 1965).
- [7] Greene, F. T. and Milne, T. A., Mass spectrometric sampling of high pressure-high temperature sources, Advances in Mass Spectrometry, 3, p. 841 (The Institute of Petroleum, 1966).
- [8] Greene, F. T. and Milne, T. A., Mass spectrometric studies of reactions in flames. II. Quantitative sampling of free radical from one atmosphere flames, J. Chem. Phys. 44, 244 (1966).
- [9] Milne, T. A. and Greene, F. T., The mass spectrometric detection of dimers of nitric oxide and other polyatomic molecules, J. Chem. Phys. 47, 3668 (1967).
- [10] Milne, T. A. and Greene, F. T., Mass spectrometric observations of argon clusters in nozzle beams. I. General behavior and equilibrium dimer concentrations, J. Chem. Phys. 47, 4095 (1967).
- [11] Milne, T. A. and Greene, F. T., Direct mass spectrometric sampling of high pressure systems, in Applications of Mass Spectrometry in Inorganic Chemistry, Advances in Chemistry Series, John Margrave, ed. (American Chemical Society, 1968).
- [12] Milne, T. A. and Greene, F. T., Molecular beams in high temperature chemistry, in Advances in High Temperature Chemistry, 2, Leroy Eyring, ed. (Academic Press, New York, 1969).
- [13] Milne, T. A., Vandegrift, E., and Greene, F. T., Mass spectrometric observations of argon clusters in nozzle beams. II. The growth kinetics of dimer, J. Chem. Phys. 52, 1552 (1970).
- [14] Milne, T. A., Beachey, J. E., and Greene, F. T., A study of relaxation in free jets using temperature dependence of n-butane mass spectra, J. Chem. Phys. 56, 3007 (1972).
- [15] Milne, T. A., Greene, F. T., and Beachey, J. E., Detection of argon cluster fragmentation in a time-of-flight mass spectrometer, J. Chem. Phys. 45, 5340 (1972).
- [16] Milne, T. A., Beachey, J. E., and Greene, F. T., Empirical observations of dimer formation in free-jet expansion, J. Chem. Phys. 57, 2221 (1972).
- [17] Milne, T. A. and Greene, F. T., Mass Spectrometer Study of Metal-Containing Flames, Contract No. Nonr-35990(00) Midwest Research Institute, Kansas City, Missouri (1968).
- [18] Milne, T. A., Beachey, J. E., and Greene, F. T., Mass Spectrometric Studies of Graphite Vaporization at High Temperatures, Technical Report AFML-TR-74-75, Midwest Research Institute, Kansas City, Missouri (1974).
- [19] Greene, F. T., Basic Research on Laser Plume Characterization, Technical Report AFML-TR-77-15, Midwest Research Institute, Kansas City, Missouri, March 1977.
- [20] Stearns, C. A., Kohl, F. J., Fryburg, G. C., and Miller, R. A., High Pressure Molecular Beam Mass Spectrometer Sampling of High Temperature Molecules, paper presented at the 10th Materials Research Symposium, National Bureau of Standards, Gaithersburg, MD, September 18-20, 1978.



- [21] Foner, S. N. and Hudson, R. L., J. Chem. Phys. 21, 1374 (1953).
- [22] White, K. and Reynolds, R. W., Apparatus for Detecting Interior Ballistic Combustion Products, BRL Memorandum No. 2497, USA Ballistic Research Laboratories, Aberdeen Proving Ground, Maryland (July 1975).
- [23] Greene, F. T., Direct Sampling and Characterization of Gaseous Species Responsible for Fireside Corrosion in Fossil Fuel-Fired Systems, Fifth Quarterly Progress Report, Contract No. E(49-18)-2288 (May 1978).
- [24] Greene, F. T., Beachey, J. E., and Milne, T. A., Direct Sampling and Characterization of Gaseous Species Responsible for Fireside Corrosion in Fossil Fuel Fired Systems, Annual Report FE-2288-19, Midwest Research Institute (August 1977).
- [25] Fryburg, G. C., Miller, R. A., Stearns, C. A., and Kohl, F. J., Formation of  $\text{Na}_2\text{SO}_4$  and  $\text{K}_2\text{SO}_4$  in Flames Doped With Sulfur and Alkali Chloride and Carbonates, NASA TM-73794, NASA, Lewis Research Center, Cleveland, Ohio (October 1977).

#### Discussion

Question (Lincoln): Did I understand you to say for the first system you saw a lot of noise from particles and beam swallowing didn't help, but on your second system, you did show a beam swallowing pump.

Response (Greene): Okay, it is not clear, the only conclusion I can reach is that our beam swallowing is kind of on a jury-rigged basis and was inadequate in the first system. I really think you can make that kind of on-axis system work which has some real advantages in terms of quadrupole sensitivity, but I think one has to be a great deal more careful with the geometry and on paper we should have swallowed the particulate beam and we were still seeing noise. But there was no easy explanation.

Question (Lincoln): But your beam swallowing system did work.

Response (Greene): Only in the second system. I think it probably would have worked even if we hadn't put the particulates into an ion pump. At that point, we were determined to do everything we could. We have similar systems, I just might add. Similar problems occur in the magnetic mass spectrometer and again we are able to, for sure, get the particulate beam through the ion source without hitting a surface. We do not see this particulate ionization.

So, it is just a matter of getting a well enough collimated beam.



## THE USE OF FLAMES AS MEDIA FOR THE STUDY OF ION-MOLECULE THERMOCHEMISTRY

W. J. Miller  
AeroChem Research Laboratories, Inc.  
P. O. Box 12  
Princeton, NJ 08540

The chemistry of charged species is of considerable interest in many practical combustion-related processes. The behavior of MHD generators, rf communication systems in rocketry, and gas chromatographic flame ionization detectors, for example, can only be predicted from knowledge of charged species kinetics and thermodynamics. Laboratory test flames, by virtue of their inherent similarity to practical systems, are very appropriate media for the determination of this information.

This paper briefly describes a series of flames and diagnostic techniques that have been extensively employed for high temperature thermochemical studies and offers some examples of the results of those studies. It is also shown how, through the use of these charged species diagnostics, neutral free radical concentrations and reaction rates can be determined in previously uncharacterized flames.

### 1. Introduction

Equilibrium constant measurements in flames have been pursued for a long time for a variety of different reasons. Probably, the first and most obvious motivation for such investigations of flame chemistry was to secure the information necessary to solve some problem associated with the use of the flame itself. Subsequently, when the bulk flame properties had been suitably well characterized, a number of combustion systems became appropriate media for the determination of thermochemical data of general applicability in high temperature material science. The results of these flame studies now constitute a considerable contribution to the existing thermodynamic data base for high temperature gases including many charged species.

The extensive flame characterization work and studies of alkali metal ionization phenomena [1-6]<sup>1</sup> in premixed  $H_2/O_2/N_2$  flames by Sugden, Padley, and a host of their

<sup>1</sup>Figures in brackets indicate the literature references at the end of this paper.

coworkers at Cambridge have provided an especially versatile and dependable set of laboratory test flames in which to measure equilibrium constants for high temperature ion and electron-neutral interactions. A number of dissociative electron attachment reactions and charge transfer processes have been examined including several not readily accessible through other techniques because of difficulties associated with the production of appropriate neutral species. The approach taken in such studies is identical to all equilibrium constant determinations in flames in that one endeavors to measure at some well-defined temperature(s), the concentrations of as many of the species involved in an equilibrated process as possible.

Practical considerations often preclude the neutral species measurements, however, and the accuracy of the determination becomes largely dependent on calculated combustion product distributions based on data from other sources. Unfortunately, there are instances in which this information is highly uncertain or confounded with unresolved controversy; in such cases, the charged species measurements can only provide additional clues.

Once the thermodynamic data for a given ion-molecule reaction are well-established, the reaction itself offers the potential for determining the relative concentrations of its participant neutrals through measurements of only the ionic species densities. Moreover, since ion-molecule reactions are typically very rapid, this can be done even in systems where the neutral species concentrations are far from equilibrium. The criteria for applying this technique as a diagnostic for the investigation of uncharacterized flames are outlined below following a description of the flames, a summary of instrumental considerations, and a tabulation of some prior work.

## 2. Experimental Methods

### 2.1 The flames

The laboratory test flames employed as the media for most of these investigations comprise an extensive series of  $\text{H}_2/\text{O}_2/\text{N}_2$  flames which has been exhaustively studied and applied as a tool for thermochemical and kinetic research for more than 20 years (see, e.g., [1-6]), a set of less well-characterized  $\text{CO}/\text{O}_2/\text{N}_2$  flames [7] and a number of low pressure hydrocarbon  $\text{H}_2/\text{O}_2$  flames [8]. They are all premixed, laminar flames supported on annular circular burners (see fig. 1) to give an inner test flame to which the materials of interest are added, surrounded by an outer shield flame of the same bulk composition and temperature to prevent complications due to the entrainment of external gases and the presence of steep temperature and concentration gradients at the edges of the test flame. Some examples of these flames are given in tables 1 and 2, which include unburned and burned gas compositions and temperatures. These examples, and the other 15 or so members of both series, collectively afford the experimenter an overall temperature range at 1 atm of about 1500-2600 K and, within subsets covering less than 100 K, independent variations in  $[\text{H}]$  and  $[\text{H}_2]$  greater than a factor of 100. The changes in radical concentrations with flow time in these flames also have been quite accurately determined [8,9], and thus, the

detailed local composition at points in any flame corresponding to reaction times up to about 5 ms are reasonably well established.

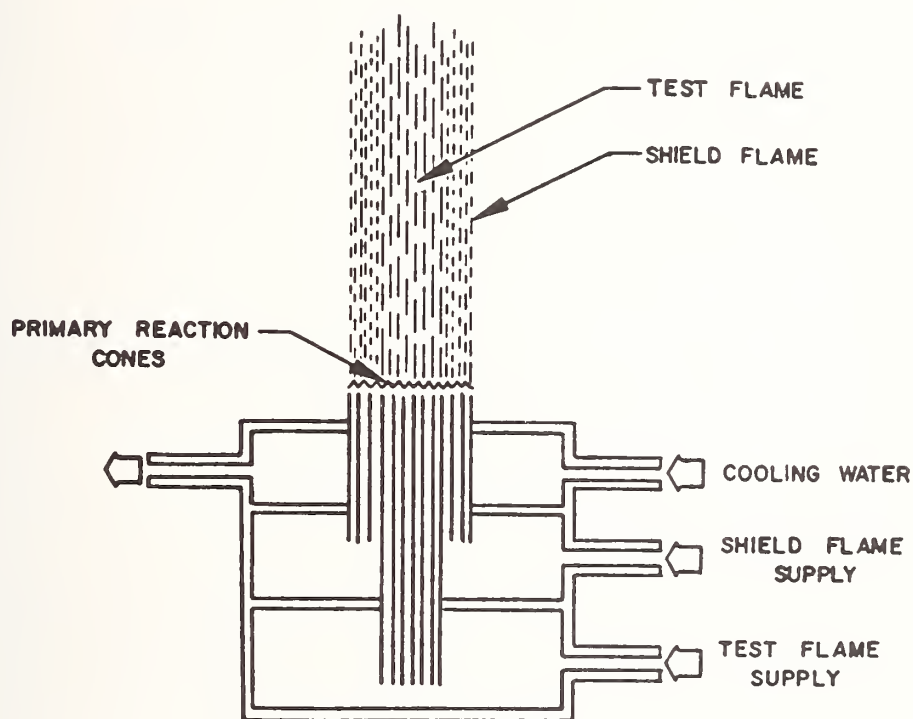


Figure 1. Annular burner.

Table 1. Flame temperatures and compositions<sup>a</sup>--H<sub>2</sub> flames.

Flame	H <sub>2</sub> /O <sub>2</sub> /N <sub>2</sub> (unburned)	T, K	[H <sub>2</sub> ]	[H <sub>2</sub> O]	[H] × 10 <sup>3</sup>	[OH] × 10 <sup>4</sup>
P6	3.5/1.0/6.0	1815	0.16	0.21	1.1	0.9
U4	4.0/1.0/4.0	2020	0.25	0.25	3.5	3.6
P3	3.5/1.0/3.0	2250	0.23	0.31	6.8	14
O2	3.4/1.0/2.0	2475	0.25	0.37	13.3	38
F2	2.6/1.0/2.0	2605	0.13	0.41	16.7	128

<sup>a</sup>Concentrations expressed as mole fractions. Data given for a position 3 cm downstream of primary reaction zones.

Table 2. Flame temperatures and compositions<sup>a</sup>--CO flames  
(0.5% H<sub>2</sub>O).

$\text{CO}/\text{O}_2/\text{N}_2$ (unburned)	T, K	$[\text{CO}] \times 10^2$	$[\text{CO}_2]$	$[\text{H}] \times 10^4$	$[\text{H}_2] \times 10^4$
1.7/1.0/2.4	2460	4.6	0.34	2.3	1.0
1.6/1.0/3.7	2180	0.67	0.28	2.2	0.25
1.9/1.0/3.7	2190	1.7	0.31	0.40	0.60
2.0/1.0/2.3	2490	8.4	0.38	3.2	1.9
2.1/1.0/3.7	2260	3.6	0.32	0.85	1.2
2.4/1.0/3.7	2240	1.7	0.31	0.40	0.61

<sup>a</sup>Concentrations expressed in mole fractions. Data given at position of maximum temperature, in all cases between 1.5 and 3.0 cm from burner.

The low pressure flames of H<sub>2</sub> and hydrocarbon fuels, as well, have been much more the subject of investigation than tools for other studies. Because of the importance of three-body heat releasing reactions in H<sub>2</sub> combustion, low pressure greatly increases the deviations from equilibrium in these flames and gives rise to extremely high radical concentrations [9,10]. The addition of a small amount of hydrocarbon alters the overall flame chemistry and temperature only slightly, but has a large accelerating effect on the rate of ionization of seed materials [10,11]. This is an important contribution to the use of low pressure flames for ion-molecule studies since the kinetics of alkali metal ionization which are fairly rapid at 1 atm are too slow to provide a convenient ion source at low pressure. Low pressure H<sub>2</sub> flames containing both hydrocarbon and alkali metal additives thus provide additional media for ion-molecule reaction studies under conditions of much lower temperatures and higher free radical concentrations; the extent to which these conditions have been documented is much smaller, however, than for 1 atm flames.

## 2.2 Charged species diagnostics

The diagnostic techniques employed in these studies for the determination of individual charged species concentrations are described below only briefly; detail is available elsewhere. They include microwave cavity resonance for the determination of free electron densities, electrostatic probes for total positive ion concentrations, and a direct sampling mass spectrometer for determinations of relative ion concentrations. Collectively, these methods offer many opportunities for cross-checking and calibrating results.

### 2.2.1 Microwave cavity resonance

The cavity resonance technique that has proven most useful is one in which the cavity is of a geometry suitable to surround the flame as shown in figure 1 and operated in the TM(010) mode at a specific microwave frequency,  $\omega$ , between 1 and 4 GHz. In practice [12-15], these cavities are annuli about 10 cm in diameter and a few millimeters high. The hole in the center can be as large as about 3 cm without seriously affecting performance. The spatial resolution of electron concentration measurements made along the flame axis is typically about the same as the cavity height except in the region of the flame close to the burner where the Q factor of the cavity is influenced by the presence of the burner itself. Microwave power from a tunable klystron, is fed into the cavity through antennae placed opposite one another near the circumference. A parallel impedance is provided by a crystal diode rectifier through which current flow ( $I$ ) is measured. An analysis of the electrical properties of the cavity shows that the Q of the cavity as measured by the diode current,  $I$ , is related to the electron concentration,  $n_e$ , through the expression

$$(I_0/I)^{1/2} - 1 = C n_e \quad (1)$$

where  $I_0$  is the diode current without electrons in the flame and  $C$  is a number of combined constants determined by direct calibration.

The accuracy of this technique is as good as this calibration and the sensitivity is a direct function of the cavity constant. In its implementation, the method has proven useful, practically, in the range  $10^8 < n_e < 10^{12} \text{ ml}^{-1}$ . At the lower limit of this range, the system must be very noise-free and stable; even with well-designed (high Q) cavities, at  $n_e = 10^8 \text{ ml}^{-1}$ , one must be able to detect a change in  $I$  of a few parts per  $10^3$  or less. The most severe limitation on the usefulness of the method, however, is that the flame must be a part of the cavity, and thus the overall dimensions of the apparatus must be large relative to those of the flame. This restriction effectively precludes the use of cavities in low pressure flames where large burners are required.

### 2.2.2 Electrostatic probes

The current-vs-voltage probe curves obtained from small cylindrical or spherical electrostatic probes, in principle, can be interpreted to yield local values of both positive and negative charged species concentrations and electron temperatures. The use of very small probes [16-20] at variable collection voltages has produced the greatest proportion of our present knowledge of the detailed plasma properties of high-temperature combustion systems. The probes themselves are fairly easy to build; the minimum necessary instrumentation includes only a variable dc voltage source and an electrometer of some sort. The data are deceptively simple to collect; and, if anything, there is an overabundance of theories available with which to interpret the results.



Figure 2 illustrates a typical probe of cylindral geometry. The quartz tubing provides the insulation, which is protected by the silver cooling jacket from dielectric degradations due to heating. The probe wire itself must be of a material refractory to flame constituents and temperature. It also should be non-catalytic with respect to atom and radical recombination to preclude overheating due to these effects. In flames of hydrogen-containing fuels, noble metal alloys such as Pt/Rh are very satisfactory. The data collected comprise a curve of current flow between the probe and its surroundings (e.g., burner, pressure vessel, and, preferably, a screen of large area downstream of the probe) as a function of probe voltage. The charged species concentration  $n_{\pm}$  is then computed from an equation of the form

$$n_{\pm} = j_{\pm} e^{-1} \left( \frac{2\pi m_{\pm}}{RT} \right)^{1/2} (1 + B) \quad (2)$$

where  $j_{\pm}$  is the current flux due to the species in question obtained by extrapolating the appropriate part of the current vs voltage curve back to the plasma potential,  $m_{\pm}$  is the mass of the charged species,  $e$  is the electronic charge, and  $B$  is any of a variety of terms derived for specific probe sizes and configurations, flame conditions, and mass transport effects.

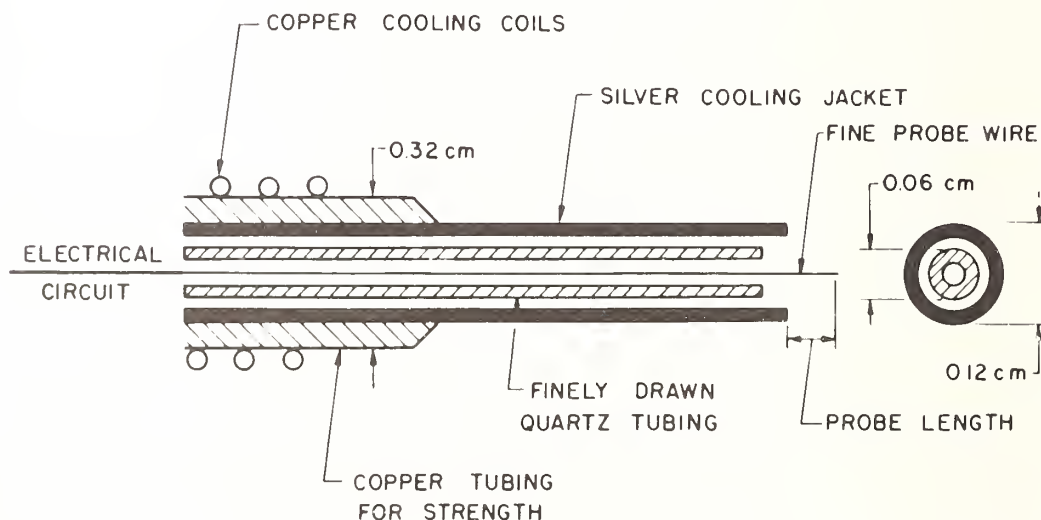


Figure 2. Electrically and thermally insulated probe.

The biggest problems encountered in the use of probes derive from the fact that the current collected is almost always limited by the mobility of the massive positive ions regardless of the polarity of the voltage on the probe. When the probe is biased positively, then, to collect electrons, a very large "ground" or negative electrode must be present in and around the flame to allow the electron transport to the probe to be current limiting as it must be. In practice, this condition is difficult to obtain and electron concentration measurements are often wrong for this reason. Absolute, dependable positive ion measurements can be made quite readily.

### 2.2.3 Mass spectrometry

Direct sampling mass spectrometers, i.e., instruments with no ion source of their own, have become the primary diagnostic in many investigations of charged species including those in flames. An example of such an instrument [21] is shown in figure 3. The principles of operation are analogous to those involved in molecular beam sampling devices for the analysis of neutrals. In both cases, a gas sample is withdrawn, frozen chemically and the species of interest separated from the remainder of the sample. The first of these goals is accomplished by expanding the gas through a nozzle or orifice into a vacuum. The reduction in pressure accompanying the expansion effectively freezes all but the most rapid chemistry by decreasing the molecular collision frequency; the corresponding decrease in temperature also retards all chemical reactions except those with little or no activation energy. In molecular beam work, the central portion of the expanding gas jet (comprising molecules which have not undergone collisions with the walls) is then separated from the remainder of the gas by a skimmer, which allows the molecules near the jet axis to flow into a second chamber containing the mass spectrometer and its ion source. In the sampling of ions, the function of the skimmer is performed by electrostatic lenses. The whole process of ion sampling, thus, is simplified by two factors: the absence of gas dynamic problems associated with the skimmer and the elimination of an ion source within the instrument.

The extent to which the flame chemistry in the sampled gas is frozen is the major concern in both ion and neutral sampling. An analysis of this problem by Hayhurst and Telford [22], using a simple gas dynamic model of the sampling process, indicates the critical available time during which unwanted chemical reactions (i.e., those which occur under conditions not representative of the combustion system, e.g., at lower temperature) can occur is of the order  $10^{-7}$  s. This number provides a basis for estimating whether or not significant errors of this nature are possible. For example, in the instance of a typical ion-molecule reaction with a rate coefficient of  $10^{-9}$  ml molecule<sup>-1</sup> s<sup>-1</sup>, a significant amount of reaction will occur within this time period only if the neutral reaction partner is present in the expanding sampled gas at a concentration greater than about  $10^{15}$  ml<sup>-1</sup>. Although many flame constituents including such reactive entities as H atoms and OH radicals frequently exceed this threshold value, errors of this sort are encountered only when, in addition, the forward and reverse rates of a reaction have distinctly different

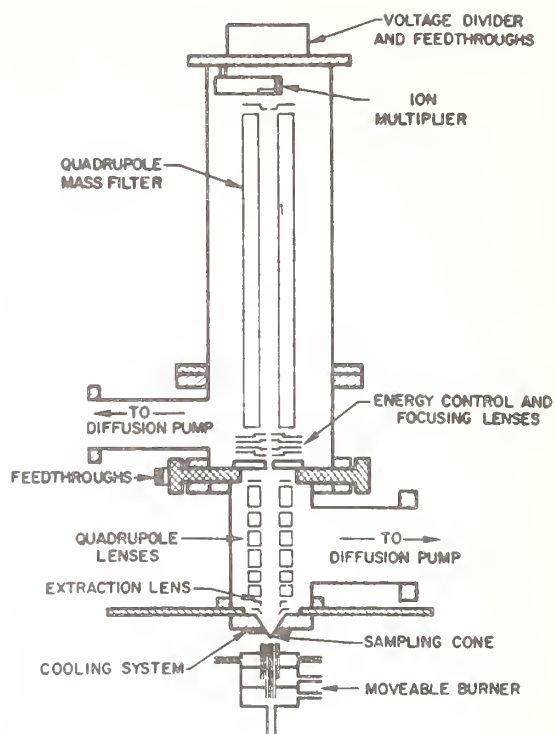


Figure 3. Flame-ion mass spectrometer.

temperature coefficients [22,24,25]. When this combination of circumstances does not occur and sampling errors are thus absent or small, the mass spectrometer alone can be sufficient instrumentation for these studies.

### 3. Results

#### 3.1 Negative ion thermochemistry

The fundamental thermochemical properties sought in these experiments are high temperature equilibrium constants from which the standard state free energies and enthalpies of formation for the negative ions are obtained. These fundamental parameters are deduced from the data in two ways. First, the equilibrium constants ( $K_i$ ) for a given process are computed from the instrumental results and bulk gas composition data, as indicated above, in a number of different flames spanning as wide a range of temperature as practicable. These values of  $K_i$  are then plotted vs  $T^{-1}$  and the slope of the best resultant straight line used to compute a "second law" value [26] of  $\Delta H$  (reaction) within that range of  $T$ . The  $\Delta H_0^0$  for the reaction under consideration is then derived by estimating the change in heat capacity associated with the process.

The alternative "third law" calculation of  $\Delta H_0^0$  involves selecting the single best measured  $K_i$  and extracting the basic heat change by computing  $T\Delta S$  from the ratios of the electronic, translational, vibrational and rotational partition functions as indicated by the mass action expression.

Our prior work has produced thermochemical data for the electron attachment and ion-molecule reactions listed in table 3. Derived electron affinities are given in table 4. The values of the equilibrium constants governing formation of  $\text{BO}_2^-$ ,  $\text{MoO}_3^-$ ,  $\text{CrO}_3^-$ ,  $\text{WO}_3^-$ ,  $\text{HMoO}_4^-$ , and  $\text{HWO}_4^-$ , illustrate the high stabilities of these ions. Boron, molybdenum and tungsten are all more electrophilic in these flames than chlorine.

Table 3. Equilibrium constants and enthalpy changes for formation of negative ions and compounds.

Reaction	Equilibrium Constant	$\Delta H_o^a$ (kJ mol <sup>-1</sup> )	Reference
$\text{HCl} + e^- \rightleftharpoons \text{Cl}^- + \text{H}$	180 exp(-7600/T)	+ 74	[27]
$\text{HBO}_2 + e^- \rightleftharpoons \text{BO}_2^- + \text{H}$	1500 exp(-10000/T)	+ 94 ± 20	[29]
$\text{H}_2\text{MoO}_4 + e^- \rightleftharpoons \text{HMoO}_4^- + \text{H}$	24 exp(500/T)	+ 50 ± 40	[30]
$\text{H}_2\text{WO}_4 + e^- \rightleftharpoons \text{HWO}_4^- + \text{H}$	25 exp(1300/T)	+ 40 ± 40	[21]
$\text{HCrO}_3 + e^- \rightleftharpoons \text{CrO}_3^- + \text{H}$	2500 exp(-13400/T)	+125	[31]
$\text{HReO}_4 + e^- \rightleftharpoons \text{ReO}_4^- + \text{H}$	2500 exp(-6200/T)	+ 16	[32]
$\text{HMoO}_4^- + \text{H} \rightleftharpoons \text{MoO}_3^- + \text{H}_2\text{O}$	0.85 exp(10400/T)	- 60 ± 40	[30]
$\text{HWO}_4^- + \text{H} \rightleftharpoons \text{WO}_3^- + \text{H}_2\text{O}$	0.87 exp(5700/T)	- 22 ± 40	[21]
$\text{CrO}_3^- + \text{H}_2 \rightleftharpoons \text{HCrO}_3^- + \text{H}$	1.7 exp(-9900/T)	+ 78	[31]
$\text{ReO}_4^- + \text{H} \rightleftharpoons \text{ReO}_3^- + \text{OH}$	$2.8 \times 10^{-5} \exp(18,400/T)$	+115	[32]

<sup>a</sup> $\Delta H_o^0$  is the standard enthalpy change at 0 K. Reactions of chlorine-containing species are included for purposes of comparison.

### 3.2 Neutral species concentrations from ionic tracers

If the sampling problems described above can be avoided then, in principle, the ratios of ion currents observed mass spectrometrically often can be used to compute neutral species concentrations. For example, the array of protonated species observed [20] in and near the primary reaction zones of hydrocarbon flames are probably in equilibrium with one another [33]. Thus, the ion currents, I, at, say, masses 31 ( $\text{CH}_3\text{O}^+$ ) and 29 ( $\text{CHO}^+$ ) can be used to obtain the local relative concentrations of  $\text{CH}_2\text{O}$  and CO through the expression

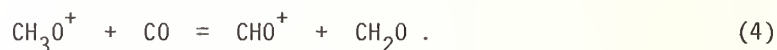
Table 4. Electron affinities.

Ion	Electron affinity (kJ mol <sup>-1</sup> )
Cl <sup>-</sup>	365
BO <sub>2</sub> <sup>-</sup>	393 ± 20
BO	≥ 240
HMoO <sub>4</sub> <sup>-</sup>	410 <sup>a</sup>
MoO <sub>3</sub> <sup>-</sup>	249 ± 40
HWO <sub>4</sub> <sup>-</sup>	400 <sup>a</sup>
WO <sub>3</sub> <sup>-</sup>	351 ± 40
CrO <sub>3</sub> <sup>-</sup>	230 ± 50
HCrO <sub>3</sub> <sup>-</sup>	390 ± 50
ReO <sub>3</sub> <sup>-</sup>	275 ± 50
PO <sub>2</sub> <sup>-</sup>	355 ± 40

<sup>a</sup>Error limits not given due to uncertainties in H-O bond dissociation values.

$$\frac{[\text{CH}_2\text{O}]}{[\text{CO}]} = K_4 \frac{I(\text{CH}_3\text{O}^+)}{I(\text{CHO}^+)} \quad (3)$$

where  $K_4$  is the equilibrium constant for the reaction



Unfortunately, most equilibrium constants of this nature are not available. Some (like  $K_4$ ) can be estimated on the basis of known proton affinities, but even this information is lacking for most of the observed intermediates.

The use of small amounts of additives with known ion thermochemistry that give rise to more than one ion provides an extremely effective diagnostic method for H atoms or other radicals [10,34]. It can be seen from the data in table 3, for instance, that Mo compounds are especially suitable; the reaction



is only slightly exothermic, has a small temperature dependence, and is therefore not subject to serious disturbances during the sampling process. Moreover, one of the neutrals involved,  $\text{H}_2\text{O}$ , is a major constituent of the flame and not subject to large changes in concentration--at least in the burned gas region. The equilibrium constant together with



the known  $[H_2O]$  value for the flame conditions of interest can therefore be used, together with the observed ratio of the two ions, as an H atom concentration probe. This method has been employed successfully with other additives in 1 atm flames [34] and at low pressure [10].

In the case of low pressure hydrocarbon flames, the natural flame ionization provides its own diagnostic for H atom and other radicals. It can be seen from figure 4 that [8] the negative ion profiles in the downstream regions of these flames are dominated by the species  $O_2^-$ ,  $O^-$ , and  $OH^-$ . As is the case with positive ions downstream of the flame front, equilibrium is apparently established among the negative ions. The reactions dominating the negative ion equilibria may be considered to be those paralleling the H/O neutral species equilibria,

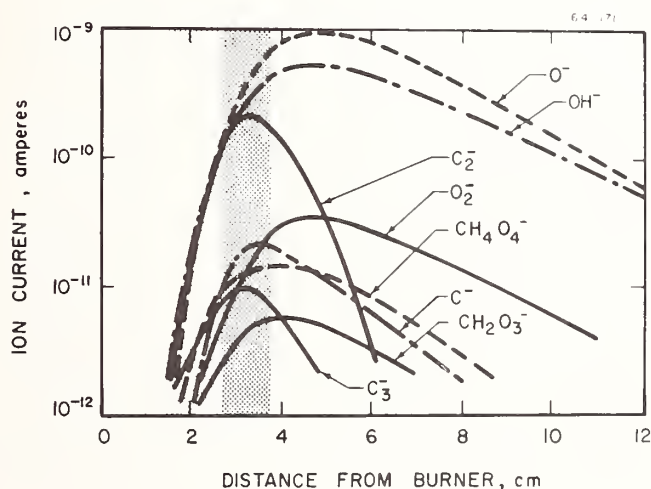


Figure 4. Negative ion profiles in low pressure stoichiometric hydrocarbon/oxygen flames.

These ion-molecule reactions are only slightly exothermic in the forward direction and are almost certainly very rapid in both directions. The ions, then, are in equilibrium with the neutral species, whether the overall neutral equilibria are established or not, and a detailed examination of the negative-ion content downstream of the flame front should be an accurate indication of neutral free radical concentrations.

The  $[\text{OH}]/[\text{H}]$  ratios in the flames of figure 5 may be calculated from observed negative ion ratios and the equilibrium constants for reaction (6) at the appropriate flame temperatures:

$$\frac{[\text{OH}]}{[\text{H}]} = K_6^{-1} \frac{[\text{O}_2^-]}{[\text{O}^-]} \quad (8)$$

Similarly, the observed ratio of  $[\text{OH}^-]/[\text{O}^-]$  together with the equilibrium constants for reaction (7) will give  $[\text{H}]/[\text{H}_2]$ . The results of these calculations for the flames of figure 5 are given in table 5. Comparison of the concentration ratios, thus derived from the experimental data with those calculated assuming complete equilibrium reveals that, although the  $[\text{OH}]/[\text{H}]$  ratios appear to be well equilibrated, the  $[\text{H}]$  in every case is appreciably above equilibrium. Thus, in these low-pressure flames, H and OH both appear to be present at concentrations above equilibrium to about the same extent--a factor of from 5 to 10. These conclusions are consistent with a number of other results in similar flames.

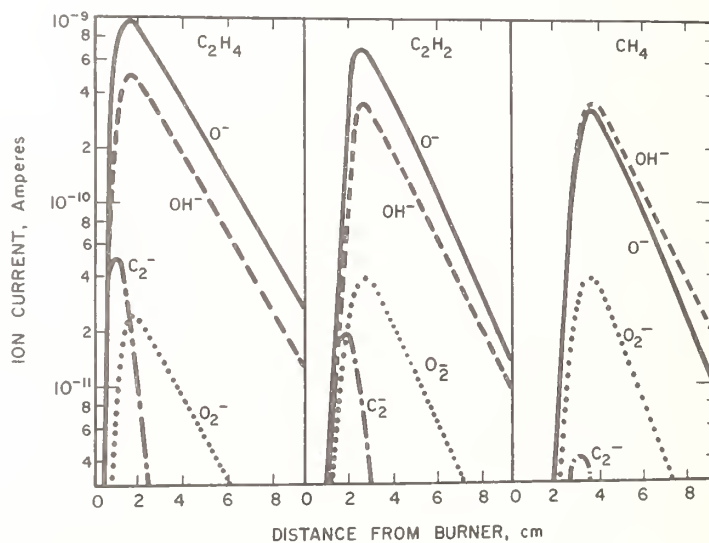


Figure 5. Negative ion profiles in low pressure stoichiometric hydrocarbon/oxygen flames.

Table 5. Equilibrium and negative-ion inferred [H] and [OH] in low pressure flames<sup>a</sup>.

Flame	T, K	Observed Ion Ratio		[H]/[H <sub>2</sub> ]		[OH]/[H]	
		[OH <sup>-</sup> ]/[O <sup>-</sup> ]	[O <sup>-</sup> ]/[O <sub>2</sub> <sup>-</sup> ]	Exp.	Equil.	Exp.	Equil.
C <sub>2</sub> H <sub>2</sub> /O <sub>2</sub>	2500	0.5	43	8.8	1.83	0.64	0.69
C <sub>2</sub> H <sub>4</sub> /O <sub>2</sub>	2300	0.7	22	5.4	0.72	1.5	1.5
CH <sub>4</sub> /O <sub>2</sub>	2000	0.2	11	2.2	0.25	4.1	3.6

<sup>a</sup>Pressure = 2.5 Torr.

#### References

- [1] Bulewicz, E. M., James, C. B., and Sugden, T. M., *Proc. Roy. Soc. A* **235**, 89 (1956).
- [2] Bulewicz, E. M. and Sugden, T. M., *Trans. Faraday Soc.* **52**, 1415, 1481 (1956).
- [3] Halstead, C. J. and Jenkins, D. R., *Twelfth Symposium (International) on Combustion*, p. 979 (The Combustion Institute, Pittsburgh, 1970).
- [4] Padley, P. J., *Trans. Faraday Soc.* **56**, 449 (1960).
- [5] Schofield, K. and Sugden, T. M., *Trans. Faraday Soc.* **67**, 1054 (1971).
- [6] Padley, P. J. and Sugden, T. M., *Proc. Roy. Soc.* **248**, 248 (1958).
- [7] Hollander, T., Self-absorption, ionization and dissociation of metal vapour in flames, Thesis, Utrecht, 1964.
- [8] Calcote, H. F. and Miller, W. J., in *Reactions Under Plasma Conditions*, Vol. II., M. Venugopalan, ed., p. 327 (John Wiley & Sons, New York, 1971).
- [9] Eberius, K. H., Hoyer mann, K., and Wagner, H. G., *Thirteenth Symposium (International) on Combustion*, p. 713 (The Combustion Institute, Pittsburgh, 1971).
- [10] Miller, W. J. and Gould, R. K., *Chem. Phys. Lett.* **38**, 237 (1976).
- [11] Hayhurst, A. N. and Telford, N. R., *J. Chem. Soc. Faraday I*, **71**, 1352 (1975).
- [12] Jensen, D. W., Microwave and optical studies of metallic derivatives in flames, Ph.D. Dissertation, Cambridge University, Cambridge, England, 1965.
- [13] Padley, P. J. and Sugden, T. M., *Eighth Symposium (International) on Combustion*, p. 164-179 (Williams & Wilkins, Baltimore, 1962).
- [14] Sugden, T. M. and Thrush, B. A., *Nature*, **168**, 703 (1951).
- [15] Sugden, T. M. and Wheeler, R. C., *Disc. Faraday Soc.* **19**, 76 (1955).
- [16] Calcote, H. F., *Ninth Symposium (International) on Combustion*, p. 623 (Academic Press, New York, 1963).
- [17] Travers, B. E. L. and Williams, H., *Tenth Symposium (International) on Combustion*, p. 657 (The Combustion Institute, Pittsburgh, 1965).

- [18] Silla, H. and Dougherty, T. J., *Combust. Flame*, 18, 65 (1972).
- [19] Wortberg, G., Tenth Symposium (International) on Combustion, p. 651-655 (The Combustion Institute, Pittsburgh, 1965).
- [20] Calcote, H. F., Kurzius, S. C., and Miller, W. J., Tenth Symposium (International) on Combustion, p. 605 (The Combustion Institute, Pittsburgh, 1965).
- [21] Jensen, D. E. and Miller, W. J., *J. Chem. Phys.* 53, 3287 (1970).
- [22] Hayhurst, A. N. and Telford, N. R., *Proc. Roy. Soc.* A322, 483 (1971).
- [23] Ferguson, E. E., Fehsenfeld, F. C., and Schmeltekopf, A. L., *Adv. Atomic Molec. Phys.* 5, 1 (1969).
- [24] Hayhurst, A. N. and Telford, N. R., *Combust. Flame*, 28, 67 (1977).
- [25] Hayhurst, A. N. and Kittleson, D. B., *Combust. Flame*, 28, 137 (1977).
- [26] Sugden, T. M., *Trans. Faraday Soc.* 52, 1465 (1956).
- [27] JANAF Thermochemical Tables, Dow Chemical Co., Midland, MI, continuously updated.
- [28] Jensen, D. E., *Trans. Faraday Soc.* 65, 2123 (1969).
- [29] Jensen, D. E., *J. Chem. Phys.* 52, 3305 (1970).
- [30] Jensen, D. E. and Miller, W. J., Thirteenth Symposium (International) on Combustion, p. 363 (The Combustion Institute, Pittsburgh, 1971).
- [31] Miller, W. J., *J. Chem. Phys.* 57, 2354 (1971).
- [32] Gould, R. K. and Miller, W. J., *J. Chem. Phys.* 62, 644 (1975).
- [33] Calcote, H. F. and Jensen, D. E., in Ion-Molecule Reactions in the Gas Phase, Advances in Chemistry Series No. 58, p. 291 (American Chemical Society, 1966).
- [34] Jensen, D. E. and Jones, G. A., *J. Chem. Soc. Faraday I*, 71, 149 (1975).

#### Discussion

Question (Cater): I noticed on your table of reactions involving molecule-ion reactions, the pre-exponential factors you gave for the equilibrium constants seem to vary by orders of magnitude for reactions which have similar numbers of reactants and products, where I would have expected the entropy changes would be comparable. Could you speak to that?

Response (Miller): The most notable violator in that list was the electron exchange between  $\text{PO}_2$  and  $\text{Cl}$ , I think. The rest of them are fairly reasonable. That one is out of line. And it turns out it is out of line because at the time that number was derived, the neutral species that was thought to be predominant in that flame was  $\text{PO}_2$ . That is what the JANAF tables would tell you because they are missing the species  $\text{HPO}_2$  which now John Hastie has found in flames.

In re-analyzing that data and including the  $\text{HPO}_2$  rather than  $\text{PO}_2$  as the attacking species the numbers came out much more reasonable. Those results should be in *J. Chem. Phys.* next month (Oct. 1978).

## MASS SPECTROMETRIC DETERMINATION OF NEGATIVE AND POSITIVE ION CONCENTRATIONS IN COAL-FIRED MHD PLASMAS

J. C. Wormhoudt and C. E. Kolb  
Center for Chemical and Environmental Physics  
Aerodyne Research, Inc.  
Bedford, MA 01730

A molecular beam mass spectrometric sampling system developed to sample neutral and ionic species from atmospheric pressure, high temperature plasmas produced in the combustion of coal and/or gaseous fuels seeded with alkali salts will be described. Used in conjunction with a laboratory scale pulverized coal/seed burner, this sampling system has been able to identify both the positive and negative ions characteristic of the plasma which will form the working fluid in the direct, coal-fired MHD generators now under development. These measurements have served as the first direct experimental validation of extensive thermochemical and kinetic computer codes which have been developed to characterize MHD plasmas.

A brief review of the high temperature plasma chemical effects which may adversely affect the operation of full-scale, coal-fired MHD generators will also be presented. The feasibility of using molecular beam, mass spectrometric sampling to characterize full-scale MHD combustor and generator flow will be discussed.

### 1. Introduction

Coal is a complex chemical substance containing variable amounts of both metallic and nonmetallic species in addition to the desired carbon and hydrogen fuel elements. The work described in this paper is part of an experimental and theoretical effort designed to understand how these nonfuel components of coal will affect the electron and alkali seed chemistry in the high temperature coal combustion systems envisioned for direct-fired magnetohydrodynamic (MHD) electrical generating systems.

To date, theoretical analyses have identified two separate mechanisms through which small amounts of vaporized inorganic ash components may have a seriously adverse impact on the conductivity of coal combustion plasmas, and thus, on the efficiency of direct-fired MHD generators. Both of these mechanisms are predicted to become more serious with



increasing generator size as residence times increase and the higher operating temperatures projected for commercial scale generators are approached. Due to this scaling effect, these plasma chemical complications are difficult to study in the small test scale MHD systems presently in operation. Thus, their potential effects on the demonstration scale systems now being designed, as well as planned commercial scale facilities, must presently be estimated by utilizing complex computer codes to understand the coupled chemical fluid mechanical and MHD interactions in the core flow of large scale generators. The most comprehensive computer code of this type is the PACKAGE (Plasma Analysis, Chemical Kinetics And Generator Efficiency) code developed at Aerodyne Research, Inc. (ARI) [1,2]<sup>1</sup>.

However, a complex computer code such as PACKAGE, which includes extensive use of incompletely determined high temperature thermochemical, chemical kinetic, and electron scattering data, requires extensive and detailed experimental validation. Direct measurements of important neutral and ionic plasma constituents from laboratory and, eventually, field scale plasma generators, must be made and compared with calculated quantities before the validity of computer predicted plasma chemical phenomena and their calculated effects on generator design can be fully credible.

The two potential ash vapor-induced effects on MHD coal plasma conductivity will be briefly reviewed in the following section. This review will be followed by a description of the molecular beam mass spectrometer sampling system and laboratory scale coal plasma combustor which have yielded the first direct measurement of many of the deleterious ash vapor species predicted by computer codes such as PACKAGE.

After analysis of preliminary laboratory results on the positive and negative ion species found in laboratory produced, atmospheric pressure, coal combustion plasmas, a discussion of the feasibility of using molecular beam, mass spectrometric sampling techniques to characterize the plasmas produced in full-scale, coal-fired MHD combustors and generators will be presented.

## 2. Vaporized Ash Effects on MHD Conductivity

At least two major plasma chemical effects due to minor coal constituents have been predicted to cause potentially important reductions in combustion plasma conductivities under full-scale generator conditions. If realized, these conductivity reductions would have a major impact on the design parameters of high efficiency, direct, coal-fired MHD generators.

### 2.1 Negative ion formation

The first plasma chemical effect, the formation of ash-related negative ion species, which reduce free electron concentrations and increase electron scattering, was initially explored by Spencer and co-workers using equilibrium models [3]. Since that time, a great

---

<sup>1</sup>Figures in brackets indicate the literature references at the end of this paper.

deal of information on the thermochemical properties of inorganic negative ion species have become available [4-6]. This additional information has allowed updated calculations on the effects of inorganic oxide negative ion species which demonstrate that, under equilibrium conditions, major reductions in high temperature plasma conductivities can be caused by negative ions formed from oxides of iron, boron, phosphorous and aluminum [7-9].

While some stable negative ions may be formed from hydrocarbon combustion species ( $\text{OH}^-$ ), the bulk of the stable negative ions are expected to be formed from oxidized inorganic coal slag constituents ( $\text{FeO}_2^-$ ,  $\text{PO}_2^-$ ,  $\text{AlO}_2^-$ , etc.). Since an MHD generator extracts electricity produced by the rapid motion of electrons through a magnetic field, negative ion formation can affect the conductivity through two mechanisms. The first is simple depletion of the electron population by attachment to negative ion precursor molecules, while the second is a slowing of the average directed electron velocity due to Coulombic scattering by the negative ions.

Model calculations indicate that conductivity reductions at a given plasma temperature often range between 10 and 40 percent depending on ash type and loading [1,2,3,8,9]. This effect has serious implications for the channel length needed to extract viable enthalpy levels from the working plasma and could significantly impact the cost of commercial scale generators.

## 2.2 Slag nucleation catalysis of electron/ion recombination

The second chemical effect which may affect plasma conductivity is the greatly enhanced rate of electron-ion recombination that may be catalyzed by slag condensation nuclei. This phenomenon has recently been modeled by Martinez-Sanchez, Kolb, and Kerrebrock and may seriously decrease conductivity in the back end of full-scale generators [10,11].

In fact, if reasonable assumptions about the rate of refractory oxide homogeneous condensation and the effective work function of the resulting condensation nuclei are correct, vaporized slag fractions which compose as little as  $10^{-4}$  of the combustion plasma may catalytically deplete up to 80 percent of the plasma electrons over significant portions of the generator channel's back end as the slag condenses [11].

Analysis of both of these plasma chemical effects requires a detailed knowledge of the levels of vaporized inorganic oxides found in coal-fired plasma under generator conditions. Traditionally, these levels have been calculated using chemical equilibrium codes [7-9].

A computer program designated the PACKAGE (Plasma Analysis, Chemical, Kinetics, And Generator Efficiency) code, designed to compute the detailed composition and conductivity of coal-fired plasmas and to establish the effects of plasma composition on conductivity and generator efficiency has recently been developed at ARI [1,2]. This code is designed to calculate the neutral and ionic constituents of coal combustion plasmas under both equilibrium and finite rate dominated conditions.

The measurements described in the remainder of this paper are designed to calibrate and validate the results of PACKAGE calculations so the code may serve as a design tool for the MHD community.

### 3. Description of Laboratory Apparatus

Typical MHD generator conditions involve coal/seed/air combustion gases at pressures of one to ten atmospheres and temperatures between 2800 and 1800 K. Typical electron and ion concentrations are on the order of  $10^{14}$ - $10^{11}$  cm<sup>-3</sup>. PACKAGE code and other computer calculations clearly indicate that inorganic neutral and ionic species with concentrations as low as one part per million (ppm) under these conditions may significantly affect plasma conductivity.

Any laboratory apparatus designed to simulate plasmas similar to those expected in MHD channels must produce coal/seed combustion products with pressures of at least one atmosphere and temperatures in excess of 1800 K. Furthermore, sampling of the laboratory plasma must be performed with sufficient sensitivity to quantify a wide variety of ionic and neutral plasma constituents present at levels as low as one ppm.

This section describes a methane augmented, pulverized coal and alkali seed combustor which can prepare and maintain one atmosphere coal/seed combustion plasmas at temperatures up to 2300 K and maintain these conditions at residence times long enough to insure chemical equilibrium.

The chemical state of the plasma produced in this manner is sampled via a supersonic nozzle expansion and skimmer system producing a molecular beam of plasma constituents suitable for ionic and neutral mass spectral analysis. If sampling conditions are carefully controlled, such nozzle expansion systems are capable of providing chemically "frozen" molecular beams which contain species distributions nearly identical to those present in the bulk of the high pressure source.

Supersonic expansion molecular beam mass spectrometers similar to the one described below are uniquely suited to the chemical characterization of near atmospheric pressure, high temperature gaseous systems. They are currently undergoing development and utilization in a number of laboratories for this purpose. Notable applications include studies of the neutral chemistry of atmospheric pressure gaseous flames by Hastie [12], and Pertel and co-workers [13], analysis of the ionic chemistry of atmospheric pressure gaseous flames by Hayhurst and co-workers [14], determination of the chemistry of pulverized coal flames by Milne and co-workers [15], the characterization of condensation and vaporization systems which affect gas turbine corrosion by Kohl and co-workers [16], analysis of interior ballistic combustion products by White and Reynolds [17], and detection of rocket exhaust flow species by Powell and co-workers [18], and Ryason [19]; see also the review of Stearns et al. and related chapters in his volume. Thus, supersonic expansion molecular beam mass spectrometry appears to be evolving as a major diagnostic suitable for high temperature gaseous systems at pressures up to several atmospheres.

Schematic diagrams of the coal burner assembly and the molecular beam mass spectrometer used in MHD studies are shown in figures 1 and 2. This section will discuss the apparatus components in order, beginning with the coal flame and ending with the ion detection.

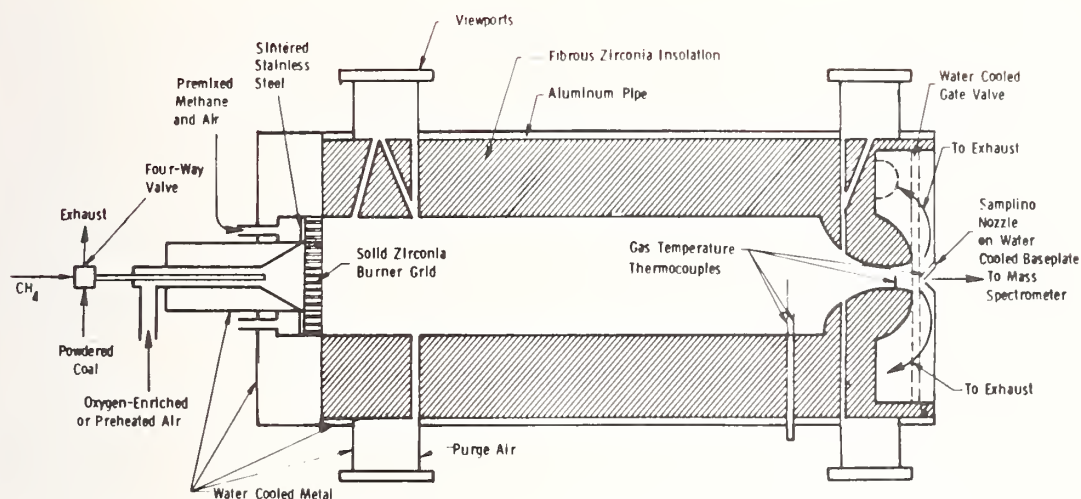


Figure 1. Coal burner, channel, and exhaust assembly schematic.

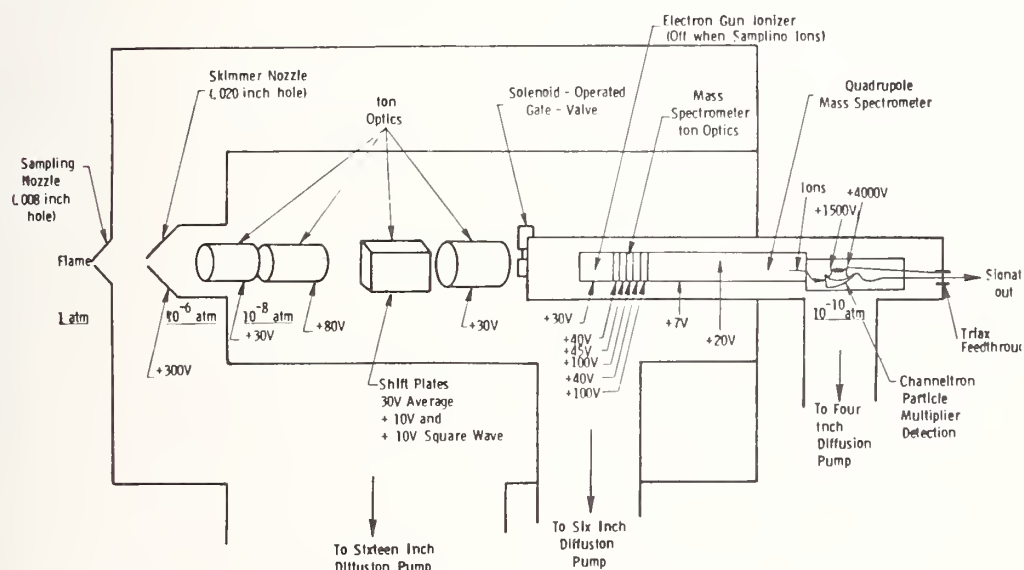


Figure 2. Molecular beam mass spectrometer schematic. Configuration shown is for detection of flame negative ions.



### 3.1 Coal/seed combustor flow train

The coal combustor (fig. 1) is divided into burner, channel, and exhaust sections made out of aluminum pipe lined with refractory insulation. The outside of the aluminum pipe is water-cooled by wrapping with copper tubing which is cemented to the pipe with heat-conducting epoxy. The burner is supported by a metal framework, which in turn rests on an aluminum plate which forms the top of a table supported by I-beams. This table in turn, supports a gas handling panel and a framework holding protective shielding panels, all not shown in the figure. In the rear of the apparatus this shielding is 3/16 inch thick steel plate, while in those areas where visibility is important, it is composed of Lexan sheets backed by heavy perforated metal screens. The framework also supports an exhaust hood, which is vented to the outside through a blower on the roof.

Powdered coal and seed mixtures are fed into the burner using a Plasmadyne Model 1000A Roto-Feed Hopper. In this device, a rotating perforated disc at the bottom of the hopper causes some of the powder to drop through a small hole and become entrained in a stream of air. To insure positive feeding, a small tamping hammer can be used which operates automatically as the disc rotates. Although this introduces a periodic pulse into the feed rate, it is found that with the hammer, feed rates can be calibrated to around ten percent. Using the roto-feeder coal feed rates 1 to 15 g/min have been obtained. The coal and all other powders feed must be sieved through a 100 mesh screen to prevent clogging of the feeder.

On its way to the burner, the coal and air stream passes through a solenoid-operated four-way valve, whose controlling switch is located near the mass spectrometer detection electronics. The third arm of the valve leads to a filter bottle, while the fourth is either capped or attached to a methane feed line. This feature allows a steady flow of the coal to be set up, collecting in the filter bottle, which can be quickly switched into the burner. This maximizes the running time before coating of the sampling nozzle with seed and slag components, in particular potassium salts, causes plugging of the sampling orifice. In the case where methane is fed into the burner through the valve when the coal is being exhausted, a second solenoid valve in the methane line is shut by the same switch so that methane does not flow into the filter bottle when coal is being fed into the burner.

The burner is actually two concentric burners, an inner one through which particles of coal and seed can be fed, and an outer ring which burns only methane and air with the purpose of protecting the inner coal flame from heat loss to the walls. The exhaust gases are pulled through two exhaust ports by the same blower which serves the hood. On their way out, they pass through a water-jacket section of the exhaust manifold whose inner wall is perforated to provide a water spray. This spray cools the gas and carries any particles with it into a collection tank. The water is recirculated through a filter by a pump which feeds the water-spray manifold. The exhaust then passes through the water tank and through a fiber filter on its way to the blower.



### 3.2 Molecular beam mass spectrometer pumping configuration

The hot atmospheric pressure combustion gases traveling down the center of the channel are sampled into the vacuum chamber through a small hole in the tip of a stainless steel cone soldered to a water-cooled copper base plate shown schematically at the left of figure 2. The center of this expanding gas is sampled through another small hole in the tip of the molybdenum skimmer cone into a second vacuum chamber, forming a molecular beam. Here the ions are focused and steered by a system of ion optics. This beam passes through a hole which can be covered by an electrically-operated gate valve in a third and even lower pressure chamber which houses the ionizer and quadrupole mass spectrometer. The electron gun ionizer is used only in detecting neutrals and is turned off when studying ions. Directly behind the ionizer are more ion optics to bring the ions from whatever source onto the axis of the quadrupole.

The first and highest pressure vacuum chamber is pumped by a Varian HS Series 16-inch diffusion pump with a nominal pumping speed of 10,000 liters/s. With the present 0.008 inch sampling hole, a typical pressure in the first chamber is  $6 \times 10^{-4}$  Torr. The second vacuum chamber, containing the ion optics, is pumped by a Varian VHS Series 6-inch diffusion pump, with a nominal pumping speed of 2400 liters/s. Both of the outer chamber pumps use a silicone pump oil, Varian DC 704. The mass spectrometer chamber is pumped by a Varian M Series 4-inch diffusion pump with a nominal pumping speed of 800 liters/s. The pump is topped by a Granville-Phillips Series 278 Cryo Clean 4-inch liquid nitrogen trap and an Airco Temescal Series 5010 4-inch gate valve. The mass spectrometer pump uses Monsanto Santovac pump oil, a polyphenyl ether, in order to avoid build up of a dielectric film which can defeat mass spectrometer ion optics. The 16-inch diffusion pump is backed by a Stokes Microvac Model 149-4 mechanical pump with a nominal pumping speed of 38 liters/s. The two small diffusion pumps are backed by a NRC Type 15-5 mechanical pump with a nominal pumping speed of 14 liters/s. A typical pressure in the second chamber is  $1 \times 10^{-5}$  Torr, and in the third,  $2 \times 10^{-7}$ . The three diffusion pumps have individual temperature interlocks which shut off the pump if it overheats, as well as a waterflow interlock which monitors the cooling water to them and the Stokes mechanical pump. In addition, the mass spectrometer diffusion pump can be interlocked to the filament of the ionization gage for that chamber, so that the pump is shut down in the event of a large leak.

### 3.3 Combustor operating parameters

Returning to the cross-sectional view of the coal burner as given in figure 1, in the central coal burner the coal dust and air stream from the feeder (and any added methane) enters through the small central tube while the bulk of the burner air (preheated, or oxygen augmented as the case may be) enters through the larger concentric tube. The swirl vanes in this tube serve to keep the coal suspended inside the burner tube. We have never had trouble with coal dust building up behind the burner grid or with clogging of the holes

in the grid. The concentric outer burner serves to isolate the coal flame from the walls by burning premixed methane and air. The outer burner grid is presently constructed of fibrous zirconia board with a number of drilled 1/16 inch holes, while the inner grid is of solid zirconia of similar design. Its higher thermal conductivity and consequent lower temperature helps to prevent flashbacks. The outer guard flame burner also has a ring of porous stainless steel which prevents flashback into the premixed methane and air. The ratio of surface areas, and of hole areas, for the guard and coal burners is close to two to one.

To reduce heat losses, the viewports at the burner end have been covered with insulation except for two small holes which allow viewing of the burner grid and of the channel wall for the purpose of measuring its temperature. One other hole in the wall allows entry of the pilot flame from a propane torch, which is turned off once the methane flame is stable. To avoid explosions, the back and sides of the methane burner chamber as well as the sleeve which holds the coal burner tube are water-cooled.

The gas handling system for the coal burner includes separate flow meters on the air and oxygen lines to each burner, allowing reliable mixing of oxygen with the air. A typical set of flow rates is given in table 1, which will serve as nominal operating parameters for future discussions. (The feed lines up to the regulating valves are normally run at 40 and 50 pounds pressure, but the flow rates of table 1 are at standard temperature and pressure.)

Table 1. Typical air/methane burner gas flow rates.

Burner Methane	3.5 liters/min
Guard Flame Methane	5.5
Burner Air	35
Guard Flame Oxygen	0
Guard Flame Air	55
Rear Window Purge Air	5
Front Window Purge Air	5
Coal Feeder Air	8

The use of insulating walls made from fibrous refractory cylinders with very low thermal conductivity as well as small thermal mass, together with minimization of the area of open holes to the outside which reduces radiation losses, essentially preserves the gas at combustion temperatures all the way to the combustor exit. The main channel section is a 4-inch i.d. porous zirconia tube, which gently expands to 4-1/2 inches at the guard flame burner. It is inserted inside a low density alumina-silica tube, which in turn is supported inside the aluminum pipe by spacers cut from alumina-silica board and by wrappings of fibrous alumina blanket. A large alumina cylinder forms an insulating liner for the exhaust port assembly. Three concentric zirconia tubes were joined with zirconia cement

and sculpted into a nozzle at the channel exit, which carries the flow directly onto the sampling cone. The nozzle is so constructed that the cold outer walls are not visible from the main part of the channel, and in particular, not from parts which are visible from the outside through small (1/4 inch diameter) holes cut through the liner at the viewports. These holes allow viewing of the inner walls with the optical pyrometer. Using the methane guard flame of table 1 to heat the walls, typical pyrometer readings of 1620 to 1670 K are obtained.

Figure 1 also shows the exhaust and sampling end of the channel. Again, to direct the flow of hot gas toward the sampling cone and prevent the formation of a cloud of stagnant gas in front of the sampling orifice, the channel is formed into a nozzle or constriction with an inner diameter of one inch. This small size also minimizes radiation losses. The flow through this narrowing is still smooth and quiet, and is calculated to cool very little before reaching the sampling cone. A platinum/platinum-rhodium thermocouple is mounted at the end of the constriction extending into the center of the flow. Others sample the flow further back in the channel, as well as the gas passing by the sampling nozzle. For the basic methane and airflow rates given in table 1, the temperature read on these thermocouples does not much exceed 1670 K. This temperature must be corrected for the balance between convective heating of the thermocouple and the losses through radiation and conduction. At this temperature, the losses are essentially radiative, and the correction raises the observed temperature by around 180 K to 1850 K. Temperatures up to 2300 K can be obtained by replacing portions of the combustion air with oxygen.

When not sampling, the sampling cone is protected from the flame by a water-cooled gate valve. The small volume enclosed by the gate valve and the base plate can be filled with a reference gas such as argon during sensitivity checks. Analyses of isotopic distributions of atmospheric Ar and O<sub>2</sub> sampled from room air show that the apparatus currently has a sensitivity of approximately 1 ppm for neutral species.

### 3.4 Molecular beam mass spectrometer detail

The present sampling cone is of stainless steel, machined in our own shop, with the hole in the tip simply drilled. The 0.008-inch hole diameter allows the large diffusion pump to operate in a more comfortable pressure range. The skimmer cone was originally made entirely out of stainless steel. However, it is apparent that the use of this material, and many others, can degrade the transmission of ions through small holes [20,21]. This appears to be a surface chemistry effect which is not well understood. One of the few materials which has been found to avoid this problem is molybdenum [20,21], so a portion of the cone closest to the beam was removed and replaced by an identical piece of molybdenum.

Figure 2 includes a schematic of the ion optics system used to carry the ion beam from the skimmer to the ion lenses at the front of the mass spectrometer. All pieces are made from thin sheets of stainless steel supported by insulating plastic. The first two 1.5-inch diameter cylinders form a simple two-tube lens. This is followed by four shift plates

in the form of a box. The intention of this design is that the cylinder lenses focus the beam near the entrance to the mass spectrometer chamber, and the shift plates move it around until it passes through the hole. Typical voltages for negative ions are given in the figure. After the shift plates, and extending almost up to the gate valve covering the entrance to the mass spectrometer, is a two-inch diameter cylinder. The end nearest the gate valve is capped with a stainless steel plate with a half-inch hole in the center. This was originally done to make this cylinder a more efficient Faraday cup, a collector of the charged beam which can be used with the picoammeter to measure the beam current arriving at this intermediate point in the system. Now that this beam attenuation measurement has been made (roughly half the attenuation occurs from the skimmer to the third lens, the other half in going to the inner vacuum chamber and through the mass spectrometer) the third lens acts as another collimating and focusing element.

The skimmer requires a large drawout voltage. The first cylinder lens is now running at a low potential, so that with the second cylinder an accelerating focusing lens is formed. From the second lens to the plate covering the mass spectrometer chamber all surfaces are floated on one voltage supply, usually run at around 30 volts. Batteries and voltage dividers are also floated at this base voltage to allow for individual variations. Chopping of the ion beam can be achieved by floating a square wave generator in the circuit for two of the shift plates. A square wave amplitude of ten volts is quite adequate. The ion lens data which give nominal voltages for the desired focal lengths can be found in standard texts [22,23], but maximization of signal must be done empirically.

The mass filter used in this work is an Extranuclear Laboratories quadrupole mass spectrometer. The mass spectrometer ion optics immediately follow the axial electron beam ionizer, which is used to create positive ions from neutral molecules. These ion optics have a large effect on the sensitivity and resolution of the mass spectrometer. When looking at ion beams, the ionizer is turned off, but the ion lenses can still have a large effect on the ion signal. The ions then travel down the axis of the quadrupole filter where the proper DC and RF voltages applied to the poles serve to select particles with a certain mass to charge ratio. It should be noted that the reason that all surfaces, including the mass spectrometer casing and the quadrupole, must be floated at a small attractive potential is that flame ions are created at ground potential, while ions from the electron beam ionizer were formed at a small potential above ground.

The charged particles are then drawn into the Channeltron particle multiplier, shown at the right in figure 2. The multiplier is mounted off-axis, but the high voltage applied to the front is sufficient to reach through the hole in the mass spectrometer casing and cause the particles to turn two fairly sharp corners to arrive at the multiplier. Photons, and other uncharged particles are intended to pass straight through a smaller on-axis hole in the Faraday plate without striking the detector. (However, we seem to have some problem with large signals at random masses, whenever particles are introduced into the flames.) The multiplier operates by electron emission from its surface when struck by an energetic particle. These electrons are drawn back along the horn by the potential



gradient applied to the multiplier, creating a growing cascade of electrons which is taken out through the signal lead as multiplier current.

When detecting positive ions, this current and the signal lead are at ground potential, and any one of several methods may be used to detect it. For weak signals, we take the current out directly and measure it with a picoammeter. Stronger signals can be converted to voltages by measuring across a load resistor, often the 1 M ohms internal resistance of the oscilloscope. The ramp output of the oscilloscope can be used to repeatedly sweep a desired portion of the spectrum. Or, the beam can be chopped, either with a mechanical rotating chopper for neutrals or by imposing a square wave voltage on the shift plates for ions. The mass spectrometer can be scanned very slowly and the chopped signal detected by a lock-in amplifier for high sensitivity.

There is one very significant difference in the case of negative ion detection. Now the front end of the particle multiplier must be at a high positive voltage, to draw out the negative ions from the particle multiplier. However, the back of the multiplier must still be at a high positive potential with respect to the front, to move the electrons along as they multiply. This leaves the signal lead at a very large positive voltage with respect to ground, typically 4000 volts. This requires several modifications (which are shown in fig. 3).

Any spurious signals caused by leakage currents at the vacuum feed-through from the signal lead through the insulation to ground must be avoided. This is done by separating signal and ground with a guard ring which is held at the same high potential as the signal. Leakage from signal to guard ring is zero, while leakage from the guard ring (connected directly to the high voltage power supply) to ground does not affect the signal. The presence of this guard ring means that the signal feed-through is a tri-axial connector. Such a connector was constructed by potting MHV connectors into the vacuum chamber flange (and is shown in fig. 3).

A second problem is that the signal must be detected through a high voltage coupling capacitor. This in turn means that the signal must be modulated, either by chopping the beam or by rapidly scanning a mass spectrum. Further, we note that the high voltage blocking capacitor we were able to obtain is so small that when it is coupled to an ordinary high impedance input like that of an oscilloscope, the resulting time constant is extremely short and only derivative signals would be seen. To avoid this, a high impedance current preamplifier is used.

A final problem associated with obtaining a signal from negative ion mass spectrometry is that we must float the mass spectrometer casing and multiplier housing off ground. This causes it and the signal to be most susceptible to pickup of the quadrupole RF fields. To filter this out, a simple RC circuit is used.

### 3.5 Mass discrimination calibration for ion sampling

The direct detection of positive and negative ion species from the coal/seed combustion plasmas is subject to a number of potential mass discrimination effects which



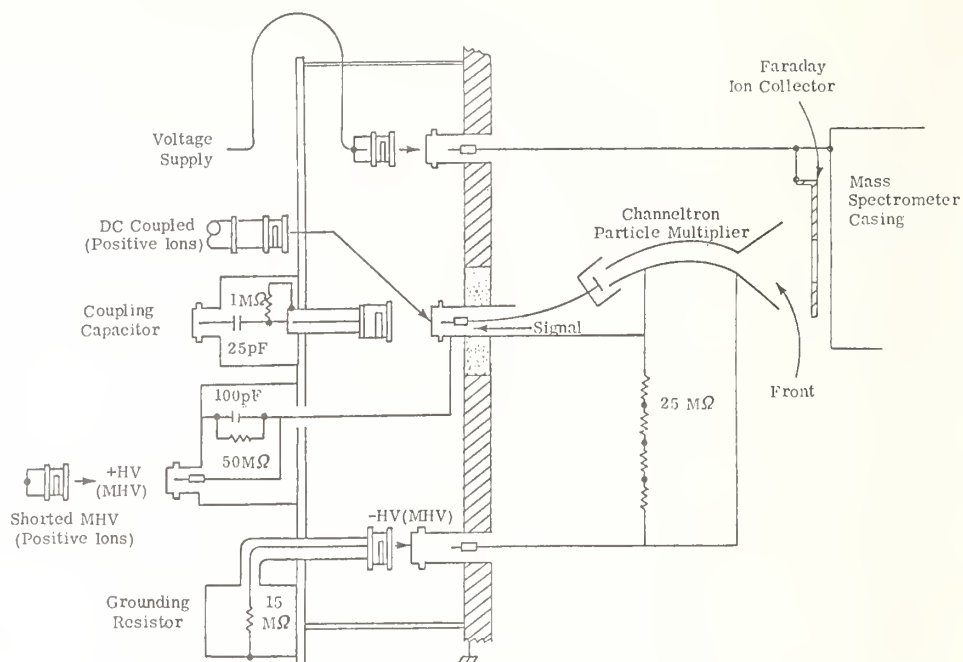


Figure 3. Triaxial particle multiplier output circuitry.

preclude direct identification of mass spectrum peak heights with plasma ion concentrations. While the direct detection of thermal ions does not suffer from the usual electron impact ionizer, neutral mass spectroscopy problems of variable ionization cross-sections and fragmentation patterns, potential (and variable) mass discrimination effects in the supersonic expansion, ion optics and mass filter still require a straightforward technique to adjust observed peak heights for mass discrimination effects.

This is accomplished by seeding a standard burner methane flame in known amounts of sodium, potassium and cesium carbonate diluted in powdered charcoal. This arrangement allows the production of plasmas with known temperature, stoichiometry and alkali loading. A PACKAGE calculation is performed for the appropriate combustor conditions, yielding predicted concentrations of atomic ions, atoms and molecules (predominately hydroxides) for each alkali. Comparisons of the predicted  $\text{Na}^+/\text{K}^+/\text{Cs}^+$  ratios with those measured for various plasma temperatures and equivalence ratios then allows a systematic determination of mass discrimination effects. Since the nozzle expansion and ion lens focusing systems are identical in the positive and negative ion sampling mode the mass discrimination effects observed for the simple positive ion system (where alkali atomic ions are the only major species) are assumed to be valid for the more complex negative ion mass spectra.

#### 4. Examples of Ion Mass Spectra

The coal/seed/methane burner described in the previous section has proved to be a rich source of slag and seed-derived flame plasma thermal ions. In fact, after initial

periods of use, a rather constant level of characteristic slag and seed positive and negative ions are produced during methane combustion runs, without simultaneous addition of slag and seed. The source of these ions appears to be alkali-enriched deposits of slag deposited on the burner surfaces.

The production of seed-enriched deposits of condensed slag which contain up to 18 weight percent potassium is a process often observed in MHD-related studies. A review of this "seed/slag interaction" phenomena may be found in reference [2].

While absolute levels of both positive and negative ions do go up dramatically when coal and seed are actively fed into the combustion plasma, a persistent "memory" of ions remains upon their cessation. These "memory ions" have proved to be a useful source of signal for maximization of ion lens transmission, as well as for investigation of the equivalence ratio and temperature dependences of individual ion peaks. These "memory ions" do form a significant background in our apparatus and will probably also fill a similar role in larger scale MHD devices.

In practice, since the ion peak ratios, particularly in the negative ion channels, change relatively little from the coal/seed on to coal/seed off conditions, it is often convenient to study negative ion characteristics without actively feeding the coal/seed mixture to avoid clogging of the sampling nozzle and the additional noise levels associated with high particle loadings. It is, of course, necessary to perform measurements during active coal/seed feeding in order to fix absolute levels of ions for coal/seed/air mixtures directly relevant to actual MHD plasma conditions.

#### 4.1 Positive ion mass spectra

As noted in the preceding section, the positive ion spectrum expected for this device is rather simple, and subject to calculation. Figure 4 shows the positive ion mass spectra produced from the alkali-enriched slag on the burner under the methane flame conditions characterized in table 1. The vastly predominant ion is  $K^+$ , with traces of other alkali atomic ions  $Na^+$ ,  $Rb^+$ , and  $Cs^+$ . The non-potassium alkali species arise from trace impurities in both the  $K_2CO_3$  seed and the coal ash, as well as from the mass calibration feeding runs described in Section 3.

The only surprise in the positive ion mass spectrum is the small peak near  $m/e = 56$ , tentatively identified as  $KOH^+$ . Various assignments for this peak, including  $KO^+$ ,  $KOH^+$ ,  $Ca^+$ ,  $Mn^+$ , and  $Fe^+$  have been added to PACKAGE calculations, but none reach the observed concentration level. If the peak is  $KOH^+$ , which is the largest calculated peak in that mass region, some adjustment to the accepted  $KOH^+$  thermochemistry will be necessary. Further experiments with known additions of ion precursor materials and higher mass resolution will be necessary to confirm this peak's identity.

Figure 5 contains a higher resolution scan of the potassium ion peak, demonstrating that the minor  $K^+$  isotope at  $m/e = 41$  can be resolved from the parent peak at  $m/e = 39$ . The peak height ratio for the two  $K^+$  isotopes is in good agreement with the known isotopic ratio.

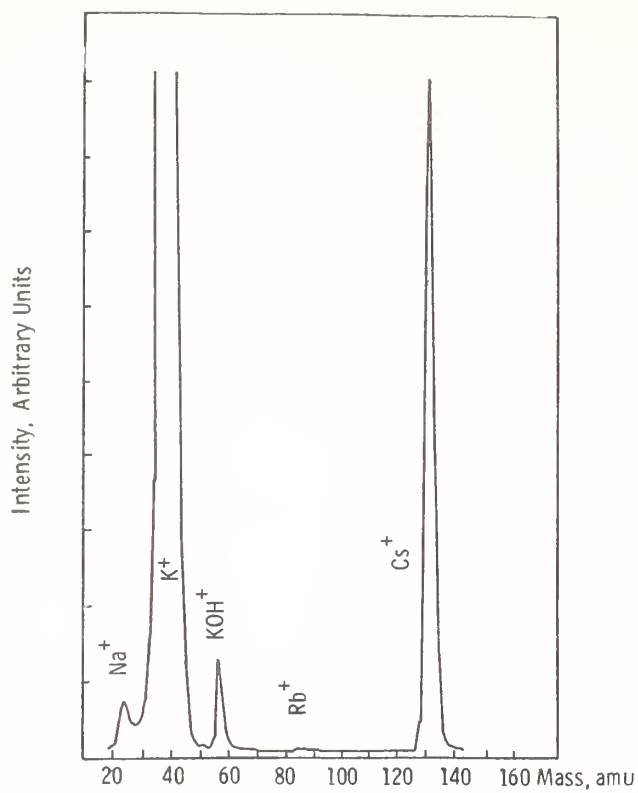


Figure 4. Mass spectrum of positive ions found in a methane flame seeded by evaporation from the burner walls.

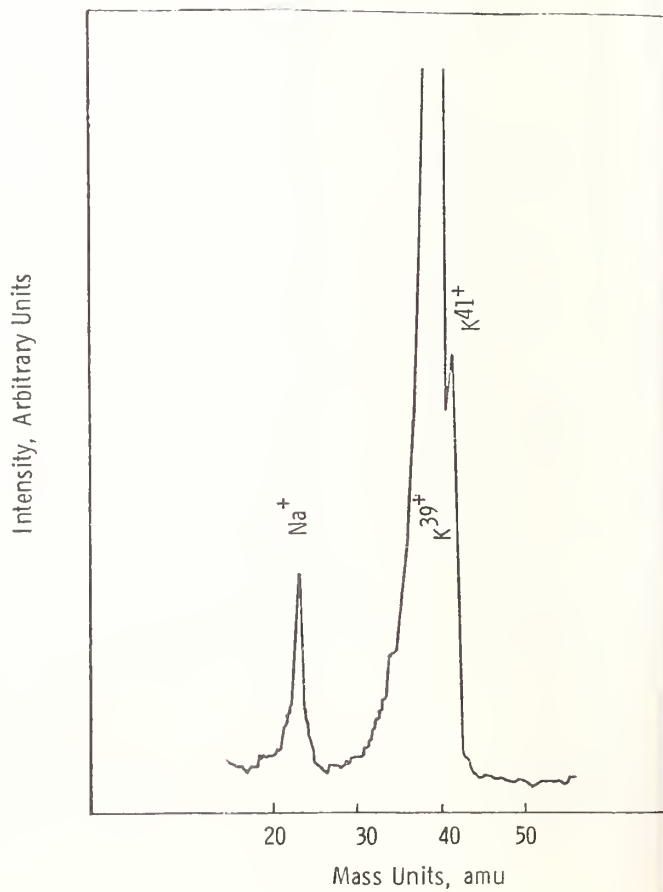


Figure 5. Mass spectrum of positive ions at higher resolution.

## 4.2 Negative ion mass spectra

The negative ion mass spectra found in the plasma combustor are a good deal richer than the correlated positive ion spectra. Figure 6 shows a typical negative ion spectrum obtained under conditions similar to the positive ion spectrum shown in figure 4. As noted above, the relative heights of the various negative ion peaks remain similar whether the coal/seed feed is on or off, so figure 6 is similar in appearance, but not amplitude, to spectra measured during coal/seed feeding under similar conditions.

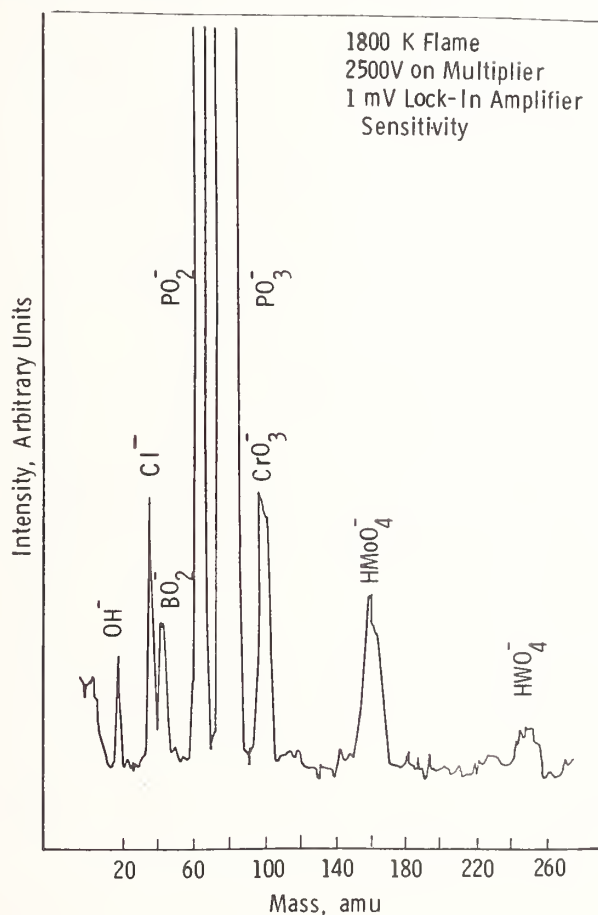


Figure 6. Mass spectrum of negative ions found in a methane flame seeded by the slag and seed vaporized from the burner walls-preliminary species assignments are indicated.

The negative ion mass spectra are very sensitive to both plasma temperature and flame equivalence ratio. This is illustrated, for moderately low plasma temperatures, in figure 7 which shows PACKAGE calculations of the ten most abundant negative ions for the laboratory combustor under typical methane/seed/coal feed conditions for an overall equivalence ratio of 0.9. Over most of the 1700 to 2100 K temperature range shown, PO<sub>3</sub><sup>-</sup>, a gas phase species not previously characterized, is predicted to be the dominant negative ion species. At higher equivalence ratios, less highly oxidized ions such as

$\text{PO}_2^-$  and  $\text{SH}^-$  are predicted to be important; while at higher temperatures, refractory oxide ions such as  $\text{FeO}_2^-$  and  $\text{AlO}_2^-$  are expected to predominate [3,7,8,9].

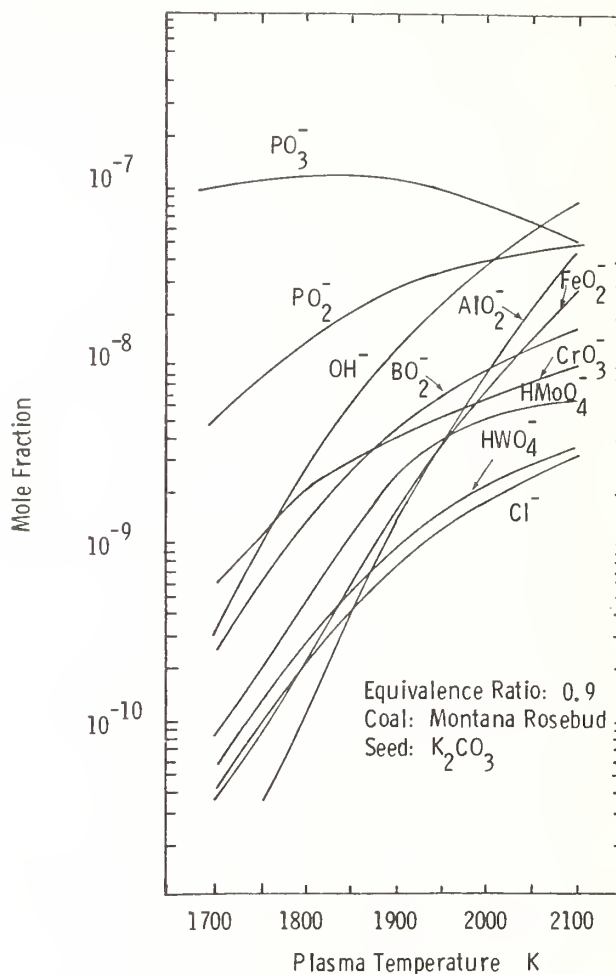


Figure 7. PACKAGE predictions for negative ion mole fractions prod.

Table 2 compares measured negative ion ratios ( $\text{PO}_3^- = 1$ ) averaged from four experimental spectra to PACKAGE predictions at 1850 K and an equivalence ratio of 0.9. In general, the agreement is fair. From the ratios to  $\text{PO}_3^-$ , there are indications that the computer program is significantly overpredicting levels of  $\text{PO}_2^-$ ,  $\text{OH}^-$ ,  $\text{FeO}_2^-$ , and  $\text{AlO}_2^-$ . However, from comparison of the calculated ratio of total negative ions to positive ions that observed, the code may be overpredicting  $\text{PO}_3^-$ . In terms of absolute levels (compare with positive ion production) the PACKAGE calculation predicts a negative to positive ion ratio of 0.79 at this temperature and equivalence ratio, while our tentative measurements suggests 0.20. This result may be due to overprediction of  $\text{PO}_3^-$  and  $\text{PO}_2^-$  levels due to a basic ignorance of their thermochemistry. Still, both the  $\text{PO}_2^-$  and  $\text{PO}_3^-$  concentrations are predicted to be very strong functions of equivalence ratio, with  $\text{PO}_3^-$  decreasing sharply from 0.9 and  $\text{PO}_2^-$  increasing.



Table 2. Comparison of Predicted and Measured Negative Ion Ratios  
Plasma Temperature 1850 K. Equivalence Ratio 0.9

Ion	m/E	Relative Ion Intensity		Assumed Ion Thermochemistry		
		Measured Avg.	PACKAGE Prediction	$-\Delta H_f^0$ 298 (kcal/mole)	EA(eV)	Ref.
$\text{PO}_3^-$	79	1.0	1.0	-190	3.5	-
$\text{PO}_2^-$	63	0.05	0.16	-135	3.0	a, b
$\text{OH}^-$	17	0.02	0.048	- 35	1.8	c
$\text{CrO}_3^-$	100	0.05	0.027	-165	4.0	d
$\text{BO}_2^-$	43	0.003	0.019	-165	4.25	c
$\text{HMoO}_4^-$	161	0.004	0.0068	-245	4.25	e
$\text{FeO}_2^-$	88	0.000	0.0044	- 50	2.85	f, g
$\text{HWO}_4^-$	249	0.002	0.0042	-260	4.35	h
$\text{Cl}^-$	35	0.003	0.0033	- 55	3.6	c
$\text{AlO}_2^-$	59	0.000	0.0033	-140	4.0	c

- Drowart, J., Myers, C.E., Swarc, R., Vander Auwera-Mahieu, A., Uy, O.M., J. Chem. Soc., Faraday Trans. II, **68**, 1749 (1972).
- Reference 6.
- JANAF Thermochemical Tables, Dow Chemical Co.
- Miller, W.J., "Electron Attachment and Compound Formation in Flames V. Negative Ion Formation in Chromium and Potassium", J. Chem. Phys. **57**, 2351 (1972).
- Jensen, D.E., and Miller, W.J., "Electron Attachment and Compound Formation in Flames. IV. Negative Ion Formation in Flames Containing Potassium and Molybdenum", Thirteenth Symposium on Combustion, The Combustion Institute, Pittsburgh, Pa., p.363 (1961).
- Hildenbrand, D.L., Chem. Phys. Lett. **34**, 325 (1975).
- Reference 4.
- Jensen, D.E., and Miller, W.J., "Electron Attachment and Compound Formation in Flames. III. Negative Ion and Compound Formation in Flames Containing Tungsten and Potassium", J. Chem. Phys. **53**, 3287 (1970).

The thermochemical model parameters used in the PACKAGE calculation are also shown in table 2. The coal and coal ash model used is described in references [1] and [7], and may be responsible for errors on the order of factors of two in abundance ratios for minor species containing trace elements such as B, Cl, Cr, W, and Mo. In considering the results given in table 2, a more significant source of uncertainty is differences in composition between the coal ash and the eventual composition of the slag which has deposited on the burner.

These preliminary comparisons of measured and calculated levels of coal-derived negative ions in combustion plasma are only illustrative. A much wider range of

measurements, in both plasma temperature and flame equivalence ratio, will be performed to guide modifications of the calculations input data.

#### 5. Mass Spectrometric Sampling of Full-Scale MHD Flows

Final calibration and validation of plasma chemical MHD generator design codes such as PACKAGE will require detailed sampling of full-scale MHD combustor and channel flows. A preliminary design for a supersonic expansion, molecular beam mass spectrometer sampling system for full-scale systems is presented in reference [2].

Major innovations include an additional pumping stage to turn the expanding flow so that diagnostic apparatus may operate perpendicular to the plasma flow direction and a nozzle plug cleaner to allow clearing of the sampling nozzle when it is plugged by condensing slag or seed particles. This latter feature is similar to the device pioneered by Milne and co-workers in their study of pulverized coal flames [15].

These design changes are now being incorporated into the laboratory sampling device described in Section 3, and will be tested before a final design for a full-scale mass spectrometric sampling system is finalized next year.

It is not anticipated that mass spectrometric sampling of MHD combustor and channel plasmas will become a routine diagnostic for either demonstration or commercial MHD facilities. However, it appears certain that systematic mass spectrometric measurements on selected demonstration facilities are crucial to the development of reliable design and performance computer codes for full-scale, direct coal-fired MHD generator systems.

---

This work was funded by the MHD Division of the U.S. Department of Energy under Contract No. EX-76-C-01-2478. The advice and support of M. Sluyter and L. Sullivan of the MHD Division is gratefully acknowledged.

This work benefited from numerous valuable technical suggestions tendered by M. Camac and J. L. Kerrebrock, fluid dynamic analyses performed by M. Martinez-Sanchez and J. Moran, and the technical and construction skills of S. Kallelis. Preliminary design tasks were performed by D. Mann.

#### References

- [1] Yousefian, V., Wormhoudt, J., Kolb, C. E., Martinez-Sanchez, M., and Kerrebrock, J. L., Computer modeling of the effects of coal ash chemistry on the performance of MHD generators, Seventeenth Symposium on Engineering Aspects of MHD, Paper C.4, Stanford University, March 1978.
- [2] Kolb, C. E., et al., Characterization of Open-Cycle, Coal-Fired MHD Generators, Report No. ARI-RR-116, Aerodyne Research, Inc. (January 1978).

- [3] Spencer, Jr., F. E., Hendrie, J. C., and Bienstock, D., Equilibrium electron density of coal-combustion mixtures - computer study and comparison with experiment, Thirteenth Symposium on the Engineering Aspects of MHD, Paper VII-4, Stanford University, March 1973.
- [4] Lineberger, W. C. and Engelking, P. C., Negative Ion Energetics, Conference on High Temperature Sciences Related to Open-Cycle, Coal-Fired MHD Systems, Report No. ANL-77-21, p. 67, Argonne National Laboratory, April 1977.
- [5] Miller, W. J., Thermodynamic properties of some negative ions and gaseous K-compounds from the combustion of coal impurities, Fifteenth Symposium on the Engineering Aspects of MHD, Paper IX-8, University of Pennsylvania, May 1976.
- [6] Miller, W. J., Mass Spectrometric Investigations of the Ion Chemistry of Certain Coal Impurities, Conference on High Temperature Sciences Related to Open-Cycle, Coal-Fired MHD Studies, Report No. ANL-77-21, p. 43, Argonne National Laboratory, April 1977.
- [7] Kolb, C. E., et al., Characterization of Open-Cycle, Coal-Fired MHD Generators - Third Quarterly Technical Summary, Report No. ARI-RP-32, Aerodyne Research, Inc., April 1977.
- [8] Kolb, C. E., et al., Characterization of Open-Cycle, Coal-Fired MHD Generators - Fourth Quarterly Technical Summary, Report No. ARI-RP-33, Aerodyne Research, Inc., July 1977.
- [9] Lu, C-L, et al., Thermochemical Effects in the Determination of Electrical Conductivity in Coal-Fired MHD Plasmas, Conference on High Temperature Sciences Related to Open-Cycle, Coal-Fired MHD Studies, Report No. ANL-77-21, p. 54, Argonne National Laboratory, April 1977.
- [10] Martinez-Sanchez, M., Kolb, C. E., and Kerrebrock, J. L., Theoretical Analysis of the Effects of Slag Condensation of Plasma Conductivity in Open-Cycle, Coal-Fired MHD Generators, Conference on High Temperature Sciences Related to Open-Cycle, Coal-Fired MHD Studies, Report No. ANL-77-21, p. 38, Argonne National Laboratory, April 1977.
- [11] Martinez-Sanchez, M., Kolb, C. E., and Kerrebrock, J. L., Potential effects of coal slag condensation on plasma conductivity in MHD generators, J. of Energy, 2, 311 (1978).
- [12] Hastie, J. W., Mass spectrometric analysis of 1 atm flames: apparatus and  $\text{CH}_4\text{-O}_2$  system, Combust. and Flame, 21, 187 (1973); *ibid*, p. 49.
- [13] Serauskas, R. U., Brown, G. R., and Pertel, R., A supersonic molecular beam atmospheric pressure flame system, Int. J. Mass. Spec. and Ion Phys. 16, 69 (1975).
- [14] Hayhurst, A. N. and Telford, N. R., Mass spectrometric sampling of ions from atmospheric pressure flames - I: Characteristics and calibration of the sampling system, Combust. and Flame, 28, 67 (1977).
- [15] Milne, T. A. and Beachey, J. E., The microstructure of pulverized coal-air flames. I. Stabilization on small burners and direct sampling techniques, Combust. Sci. and Tech., in press.

- [16] Stearns, C. A., Kohl, F. J., Fryburg, G. C., and Miller, R. A., A High Pressure Modulated Molecular Beam Mass Spectrometric Sampling System, Report No. NASA TM-73720, NASA-Lewis Research Center (July 1977).
- [17] White, K. J. and Reynolds, R. W., Apparatus for Detecting Interior Ballistic Combustion Products, Report No. BRL-2497, U. S. Army Ballistic Research Laboratories (July 1975).
- [18] McCary, T. D., Powell, H. M., and Busby, M. R., Direct Mass Spectrometric Measurements in a Highly Expanded Rocket Exhaust Plume, Paper 77-154, AIAA Fifteenth Aerospace Sciences Meeting, Los Angeles, CA, January 1977.
- [19] Ryason, P. R., Molecular beam sampling of liquid rocket engine exhaust, in preparation.
- [20] Ferguson, E. E., Fehsenfeld, F. C., and Schmeltekopf, A. L., Flowing afterglow measurements, Advances in Atomic and Molecular Physics, Vol. 5, D. R. Bates and L. Estermann, ed. (Academic Press, New York, 1969).
- [21] Kaufman, F., private communication, 1977.
- [22] Klemperer, O., Electron optics, Cambridge University Press, London, England, 1971.
- [23] El-Kareh, A. B. and El-Kareh, J. C. J., Electron beams, lenses, and optics (Academic Press, New York, 1970).

## Discussion

Moderator (Kohl): I have one question. Bill Miller mentioned the  $\text{HPO}_2^-$  as being an important species. Can you tell in your system if  $\text{HPO}_2^-$  is present?

Response (Wormhoudt): I would say that if there were  $\text{HPO}_2^-$  formed that is something we really could see if we went to high resolution--and used mass markers, too, like halide negative ions.

Question (Gilles): Have you ever seen  $\text{AlO}_2^-$ ?

Response (Wormhoudt): I have never seen  $\text{AlO}_2^-$ . We would not expect to see it at the low temperatures that have been at so far. We have hopes to go to higher temperatures, and we intend to seed that flame with trimethyl aluminum so that if it were there, we would see it.

Question (Hauge): I am curious in your calculations from your equilibrium measurements to what extent you need to involve yourself in attempting to estimate the entropy of your negative ions to arrive at electron affinities. Do you need to know low lying excited states? How happy are you with the error bars on those electron affinities? I mean, do you feel like there are some real questions involved there?

Response (Wormhoudt): I think it has been my job to invent structures of excited electronic states, etc., for all of these and those are minor perturbations on the answer of how much there is. The big uncertainty is in the heat of formation.





## MASS-SPECTROMETRIC SAMPLING OF CONDENSED SYSTEM FLAMES

O. P. Korobeinichev and A. G. Tereshenko  
Institute of Chemical Kinetics and Combustion  
Novosibirsk 630090, USSR

### 1. Introduction

Combustion of condensed systems is a complex multistaged process including a number of correlated physical (melting, diffusion, heat transfer) and chemical (consecutive-concurrent reactions) processes. Investigations of combustion wave structure are very important for identification of the combustion mechanism, selection of combustion catalysts and inhibitors, and determination of the principal chemical stages and their kinetic parameters in combustion zones for development of a combustion model. So far the main quantitative method used to study the internal structure of combustion waves of condensed systems (CS) was the investigation of temperature distribution using fine wire thermocouples [1]<sup>1</sup>. This method, however, gives no information on the nature of the principal processes in the combustion zones nor on their kinetics. Lately, investigators have used the spectroscopic method [2] to study the chemical structure of CS combustion zones where the absence of flame perturbations is an advantage. However, there are some species in flames which cannot be observed by this method because their spectra are too complex. Moreover, the spatial resolution of this method does not exceed 0.1 mm, i.e., is comparable with the width of the CS combustion zone. The sampling is not performed locally, but along a straight line; hence, the method can be applied only to homogeneous one-dimensional systems with strictly parallel fronts (deviations from parallelism must be less than 0.1 mm).

The mass-spectrometric method has a number of advantages for studying CS combustion. Being universal, mass-spectrometry is one of the most popular and effective methods to study flames and combustion processes; it has been successfully used for two decades to investigate combustion zone structures, combustion mechanisms, and kinetics in gas system flames [3-5]. However, there are some additional difficulties in investigations of solid fuel combustion zones. Unlike gas systems (GS), in the case of condensed systems with short combustion times, it is difficult to stabilize the burning surface relative to the probe. Second, in CS combustion zones there are often present solid particles and condensible vapours (metals and their compounds) which precipitate on the probe walls, and block the probe orifice. To understand the CS combustion mechanism, it is very important

<sup>1</sup>Figures in brackets indicate the literature references at the end of this paper.

to know (at least qualitatively) the chemical composition of the gas phase in the CS reaction layer which can be solid, liquid or foam.

Note that maximum temperatures in CS combustion are as a rule higher than those in GS combustion and exceed the fusion temperature of quartz and higher-temperature materials. Therefore, the problem is to create a heat resistant probe which, at the same time, is miniature and causes minimum perturbation of the combustion process. Perhaps, because of these difficulties, there are few workers in the field and no reliable results.

In one of the first CS flame investigations [6], sampling was performed in the combustion zones of solid double-base propellant at high pressures (10-20 atm) by a capillary probe at a distance of 1 mm from the burning surface into an evacuated vessel. Then, a mass-spectrometric analysis was carried out. The burning surface was held at a constant level by a gold wire or quartz fiber restraint upon the propellant strand, which was pressed from below by a compressed spring. Since the burning surface melted, the wire pressed through it and influenced the combustion process. The burning surface was only approximately at a constant level. The composition of combustion products in the "dark" zone was determined at 10-13 atm pressure and a distance of 4-16 mm from the burning surface. It was shown that in the "dark" zone, the gas composition changes negligibly. Sampling of the "foam" zone adjoining the surface and of the flame zone could not be done because of their small widths.

Hertzberg [7] reported sampling of ammonium perchlorate (AP) and AP-polymethylmethacrylate (PMMA) sandwich composite flames. Steady-state combustion of the above system was kept at pressures of 20 Torr - 1 atm by a  $\text{CO}_2$ -laser which created a heat flux of 10-20  $\text{cal/cm}^2\text{s}$  to the burning surface. Data was obtained on the composition of AP combustion products at various pressures and 1 mm distance from the burning surface. Qualitative data was given on the structure of the diffusion flame. Peaks observed at m/e 15, 29, and others, indicated depolymerization in the flame of the composite propellant sandwich.

More recent workers [8] made an unsuccessful attempt to sample flames of pyrotechnic systems directly into the ion source of a time-of-flight mass-spectrometer (TOFMS). Experiments have shown that the probe inlet becomes blocked by solid deposits in 3-11 s after ignition. No peaks characterizing the pyrotechnic system were observed.

Amongst other papers dealing with CS combustion, two studies [9,10] of the structure of diffusion flames of PMMA and epoxide resin are noteworthy. Each of these methods only allow CS flame sampling at distances of 1 mm or more and with little accuracy. The width of CS combustion zones, as a rule, does not exceed 1 mm.

In the present paper, a new method of mass-spectrometric sampling for condensed system flames [11-13] which eliminates some of the above difficulties, is described.

## 2. Experimental

Figure 1 represents the setup for mass-spectrometric sampling of CS flames at pressures below 1 atm. The apparatus consists of a quartz combustion chamber (5) connected with the

detector of a TOFMS (1). The combustion chamber includes a device to move the strand (4). The strand is mounted on one end of a rod (8); the other end is rigidly connected with a piston (6) which can move inside a tube (9). The piston moves due to the difference of pressures (external atmospheric pressure and that inside the combustion chamber). Uniform motion of the strand is wound up round the shaft (11) of the engine. Sampling was performed by a microprobe (3) (quartz cone with apex angle of  $30^\circ$ , apex hole 0.02-0.03 mm diameter and 0.1 mm outer diameter) connected directly with the ion source of the TOFMS, which was evacuated by a diffusion pump (17) with a pumping speed of 500 l/s. At a distance of 0.02 mm from the top of the probe there is a platinum-rhodium micro-thermocouple (7) (0.007 mm thick ribbon). The strand is ignited by a nichrome spiral (12) heated by electric current and rigidly connected to a fixed tube (14). To prevent blocking the probe inlet with solid deposits, the tube is placed at a distance of 10-15 mm from the probe. After ignition of the sample and blowup of the spiral, the sample moves rapidly (with speed of several mm per sec) to the probe until the distance between the probe and the burning surface is 1-2 mm. Then the sample speed slows to a value which depends on the strand burning rate; at which the speed of the burning surface relative to the microprobe (which equals the difference between the strand motion speed and the burning rate) equals 0.1-0.2 mm/s. This allows us to scan a 0.1-0.2 mm wide combustion zone during about 1 s, which is sufficient to obtain an accurate intensity distribution of mass peaks. With a 30 frame/s rate of filming, we could make about 30 measurements of the mass-spectra in the combustion zone. To prevent catalytic and mechanical influence of the spiral on the thermocouple and the probe, the spiral ends were pulled aside by a ring (13) (placed between the spiral and the strand and rigidly connected to the rod) during the rapid travel of the burning strand towards the probe. The strand was blown with argon whose flow velocity was controlled with valve (15). Pressure in the combustion chamber was controlled with the valve (16) through which the combustion chamber was evacuated by a mechanical pump. The pressure in the combustion chamber was measured with a mercury pressure gauge. To maintain a constant pressure during the strand combustion, the combustion chamber was connected with a 20-liter vessel. The strand could be preliminarily heated to a required temperature with a furnace which consisted of nichrome wire wound round the glass tube of the combustion chamber. The probe with the strand was photographed by a camera with four-fold magnification. The frame marker signals from both cameras as well as the thermocouple signal were recorded by a loop oscillograph. This allowed us to find the mass-spectrum, the distance between the probe and the burning surface at the moment of sampling, and the temperature of the flame at the place of sampling.

Below we present results of combustion wave structure investigations of a number of model condensed systems--ammonium perchlorate (AP) and its mixtures with polymethylmethacrylate (PMMA) and copper oxide (catalyst), and double-base propellant. Combustion of these systems has been investigated in detail for many years. Samples of AP and its mixtures with PMMA were prepared by a standard method by pressing and have the form of 6 x 6 x 10 mm parallelepiped. A teflon film is used as armoured protection. The

dispersion of the components is AP - 0.005 mm, PMMA - 0.003 mm. The samples of double-base propellant ("N" powder) had the form of cylinders with diameter 6 mm and length 10 mm

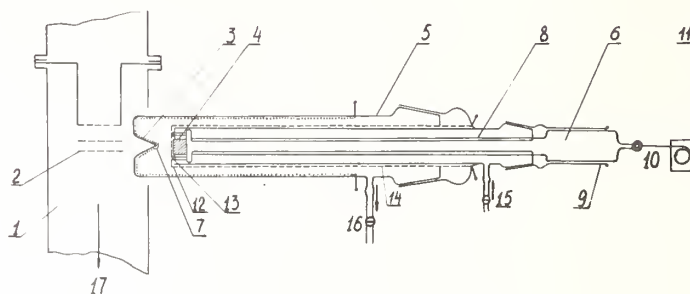


Figure 1. Schematic of apparatus.

### 3. Experimental Results and Discussion

Table 1 lists the experimental conditions--pressure (P), initial temperature ( $t_0$ ), burning rate (U)--for the system under study. Figure 2 represents one of the frames of the microprobe and the burning surface during their approach. When analyzing the data, one should remember that for a number of components the mass peaks may overlap. Normally the peak intensities in the mass spectrum  $I_i$  are related to the component concentration through the expression  $I_i \sim n_i \cdot \sqrt{T}$  where T is the gas temperature at the place of sampling.<sup>2</sup>

Table 1

No.	Composition	P, Torr	$t_0$ , °C	U mm/s
I	84% AP - 16% PMMA	100	20	0.15
II	84% AP - 16% PMMA - 2% CuO	100	20	0.22
III	AP	450	260	0.3
IV	AP - 2% CuO	450	20	0.45
V	"N" powder	480	120	1.9

<sup>2</sup>Editor's note: The origin of the  $I_i$  expression is unclear; see chapter by Bonnell and Hastie in this volume for an alternative expression.





Figure 2. Photo (single frame) of sample approaching microprobe.

Figure 3 represents the intensity profiles, measured relative to the sample surface, of the mass peaks of reactants and reaction products in combustion of 84 percent AP - 16 percent PMMA mixture at 100 mm Hg. As the probe approaches the burning surface, concentrations of the combustion products in the flame decreases:  $\text{HCl}$  ( $m/e - 36$ ),  $\text{CO}_2\text{-N}_2\text{O}$  (44),  $\text{NO-N}_2\text{O}$  (30), ( $\text{CO-N}_2$  (28) not shown in the figure); and those of the gasification products increase:  $\text{NH}_3$  (16)<sup>3</sup>,  $\text{ClO}_2$  (67),  $\text{C}_5\text{H}_8\text{O}_2$  (100,41),  $\text{O}_2$  (32).

When approaching the burning strand, the microprobe passes through all combustion zones including that of flame and the reaction layer of the K-phase. At a certain moment, the probe comes into contact with the burning surface and then moves inside the reaction porous layer of the K-phase (porousness of the surface layer has been determined by microscopic studies of extinguished samples). The curves of concentration distribution in the combustion zones show maxima of oxidant ( $\text{ClO}_2$ ,  $\text{NH}_3$ ) and fuel methylmethacrylate (MMA) gasification products. Coordinates corresponding to these peculiarities are denoted in figure 3 as  $S_1$  and  $S_2$ . These are 0.1 mm distant from each other.

Microfilming of the moment when contact occurred between the burning surface and the probe allowed us to localize the burning surface on the concentration curve. At the moment of contact of the burning surface and the probe, the intensity of the peak with  $m/e - 67$  equals 0.8 of the maximum value achieved in the interior of the reaction layer at

<sup>3</sup>Editor's note: apparently  $\text{NH}_2^+$  is being referred to here.

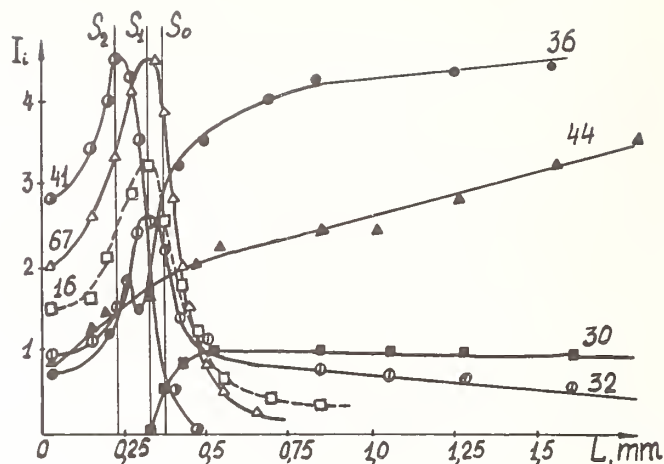


Figure 3. Intensity profiles, measured relative to the sample surface.

a distance of 0.05 mm from the burning surface ( $S_0$  in fig. 3). Note that the above conclusion on the location of the concentration maximum of gasification products has been found to agree with an analysis of the differential material balance equation of oxidant gasification products in the porous reaction layer.

The maximum oxidant gasification rate is in the interior of the reaction layer; at the surface this rate must equal zero. The oxidant surface is the burning surface. This follows from the fact that the fuel gasification occurs earlier and with higher rate than that of the oxidant. It also follows from noncoincidence of the concentration maxima of the oxidant and the fuel gasification products in the reaction layer as well as from the multistage character of AP-PMMA system decomposition (PMMA gasification is the first stage, AP gasification is the second). The above fact has been observed by direct experiments on thermal decomposition of AP-PMMA system at heating rates of 100-300 K/s, realized in a combustion wave of these mixtures at pressures below atmospheric [14].

A decrease of MMA concentration in the reaction layer of the K-phase may be associated with dilution of MMA by AP decomposition products in the course of increasing the porosity of the K-phase due to gasification reactions. This very fact may account for the non-monotonic trend of HCl and  $\text{CO}_2$  concentration curves in this layer.

In figure 4, HCl partial pressure distribution (relative scale) in the flame zone is plotted using the temperature profile and the data of figure 3, taking  $P_{\text{HCl}} \sim I_{\text{HCl}} \cdot \sqrt{T}$ . The HCl partial pressure in the region of  $S_1$  equals 30 percent and in the region of  $S_0$ , 43 percent of the HCl partial pressure in the burnt mixture.

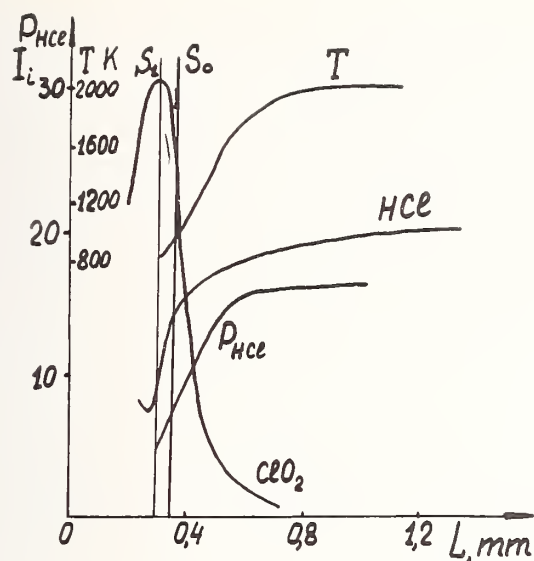


Figure 4. Distribution of HCl,  $\text{ClO}_2$ , and T for flame system I (see table 1).

Figure 5 represents the distribution of the intensities of mass peaks observed for the reagents and the reaction products in combustion of system II (see table 1) with a catalyst at 100 mm Hg. The catalyst  $\text{CuO}$  increases the combustion rate by a factor of  $\sim 1.5$ . It is seen that in the presence of the catalyst, even the form of the curves changes qualitatively. When approaching the burning surface, the HCl (36) and  $\text{CO}_2\text{-N}_2\text{O}$  (44) concentrations decrease to a minimum then increase to a maximum and fall again.

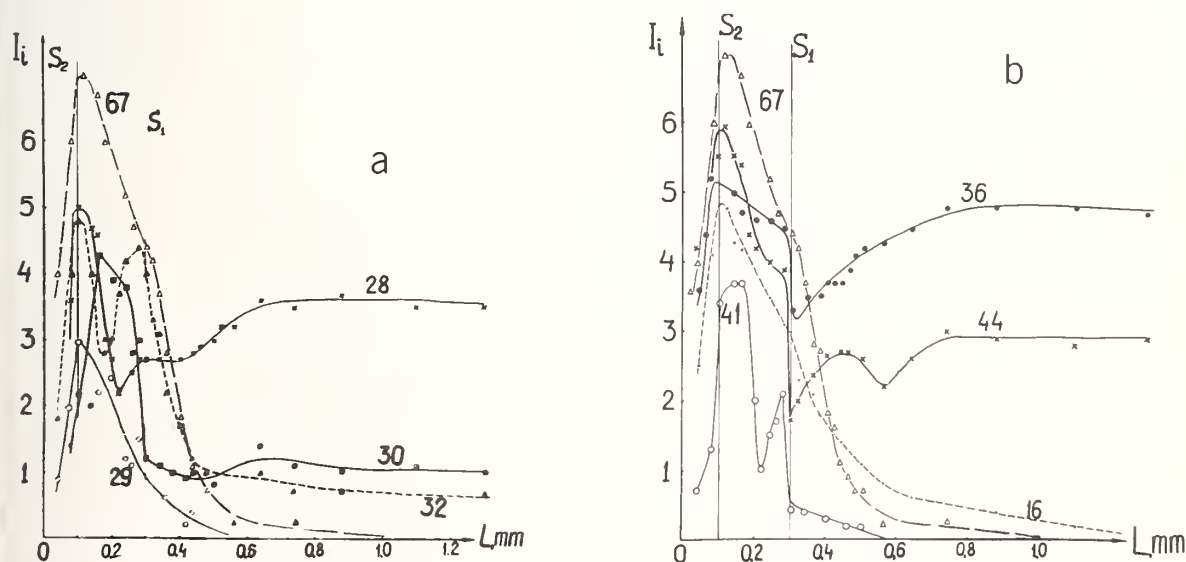
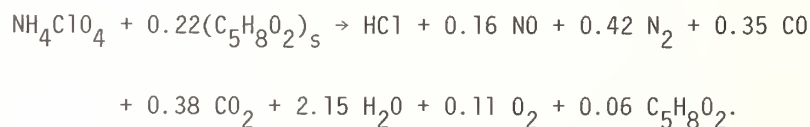


Figure 5. Distribution of reactant and product species for flame system II (see table 1).

All the curves change sharply at the  $S_1$  point which is perhaps situated in the interior of the reaction layer (the burning surface is not localized in this case). HCl partial pressure at the  $S_1$  point is 45 percent of the maximum pressure in the flame zone, whereas in the experiments on this system without a catalyst, this value is 30 percent. This means that the degree of decomposition in the K-phase for the system with a catalyst (or the portion of AP decomposed to HCl) is approximately 0.45 both in  $S_1$  and  $S_2$  (i.e., in the region of concentration maxima of the oxidant gasification products). Thus, in the presence of a catalyst, the degree of reaction in the K-phase increases approximately by a factor of 1.5. Note that in the presence of a catalyst, the concentration maxima of oxidant and fuel gasification products practically coincide. In the region of concentration maxima of the fuel gasification products ( $S_2$  in figs. 3 and 5b), the ratio of the mass peak intensities,  $I_{41}/I_{67}$ , which is proportional to that of the fuel and oxidant gasification products, decreases in the presence of a catalyst. This supports the conclusion that the processes of fuel oxidation in K-phase are intensified.

When the probe moves through the porous reaction layer (with a catalyst), the concentrations of all components increase. This can be associated with increasing the pressure in the porous reaction layer of the K-phase due to intensification of the gasification process. An analysis shows that the partial pressures in the interior of the layer at the  $S_2$  point are 1.5-2 times higher than those at the burning surface at the  $S_1$  point. It is also necessary to note that considerable amounts of formaldehyde ( $\text{CH}_2\text{O}$ , m/e 30) are generated in the reaction layer of the K-phase in combustion of the system with a catalyst. Thus, the above data establish that this catalyst reacts in the K-phase.

Using the concentration curves (the sensitivity coefficients for the components were taken from [15] and also obtained in the present study) and the balance equations with respect to the elements, we composed the following equation of system I combustion,



The ratio between CO and  $\text{N}_2$  was found using chromatography. Unbalance with respect to oxygen is 20 percent. This is perhaps associated with the fact that nonreacted MMA written in the right-hand side of the equation is present as the monomer oxidative degradation products which can be observed only in a molecular beam system. The thermal effect and the combustion temperature were evaluated by the combustion equation with the formation heats of the compounds being taken from thermodynamic tables. The results of the calculations depend essentially on the value set for the methylmethacrylate formation heat. The literature data [16,17] differ nearly by a factor of 2. If we take the average of the published data,  $\Delta H_{(\text{C}_5\text{H}_8\text{O}_2)_s} = -220 \text{ kcal/mol}$ , then the combustion heat would be 80 kcal/mol (575 cal/g). Setting the heat capacity of the K-phase equal to 0.3 cal/(gK), we obtain  $T_g = 2000 \text{ K}$  which does not contradict  $T_g \sim 2000 \text{ K}$  given above (fig. 4).

Analogous calculations were performed to determine the composition of the gasification products.

Solving the material balance equation, we find that the primary chlorous product of the oxidant gasification is perchloric acid, not the  $\text{ClO}_2$  observed spectrometrically. This contradiction can be accounted for by the possibility that perchloric acid--a very unstable product--decomposes on the hot walls of the probe into  $\text{ClO}_2 + \text{HO}_2$  due to the heterogeneous-catalytic reaction:



$\text{HO}_2$  radicals probably decay at the probe walls by recombination and thus are not registered in the mass-spectrum. This explanation is corroborated by the observation of a complete transformation of  $\text{HClO}_4$  to  $\text{ClO}_2$  in vacuum [18].

Figure 6 represents results of AP flame sampling.  $\text{NH}_3$  (m/e-16) and  $\text{ClO}_2$  (m/e-67) are observed as the major gasification products. However, for the above reasons, ammonia and perchloric acid may be the primary products of AP gasification. These products form the basis of many theories of combustion of AP and its mixtures with other compounds. Together with the above products of AP dissociation, products of its decomposition-- $\text{HCl}$  (36),  $\text{Cl}_2$  (70),  $\text{O}_2$  (32),  $\text{H}_2\text{O}$  (18),  $\text{NO}$  (30),  $\text{N}_2\text{O}$  (44,30),  $\text{NO}_2$  (46,30),  $\text{N}_2$  (28)--are observed near the burning surface.

When moving out from the burning surface, the concentrations of AP dissociation products increase and those of the final products decrease. Nitrogen dioxide concentration has a maximum which is an evidence for  $\text{NO}_2$  being an intermediate product in an AP flame.

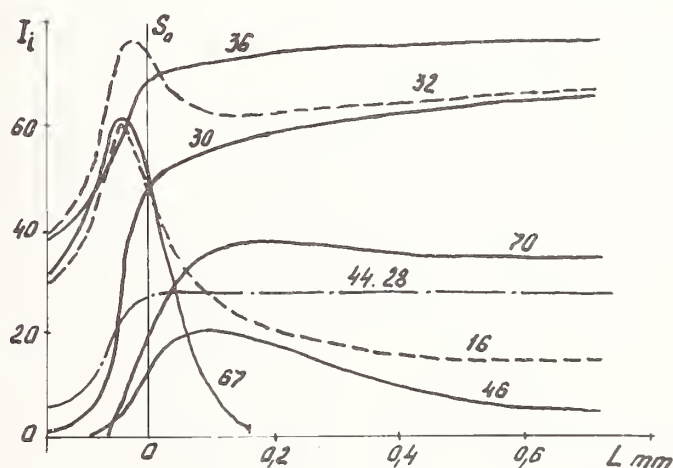


Figure 6. Distribution of species in an AP flame.



Figure 7 represents results of sampling of AP flame with CuO as a catalyst. In this case (unlike the system without CuO), no nitrogen dioxide was observed; nitrogen concentration increased and that of nitrogen oxide decreased compared to AP without the catalyst. The ratio of the intensity peak of ammonia to that of  $\text{ClO}_2$  on the burning surface decreased by a factor of 2 with catalyst present. This suggests that CuO has a great influence both on the rate and direction of the decomposition reaction in the condensed phase by accelerating ammonia oxidation and increasing the reduction of nitrogen oxides to nitrogen.

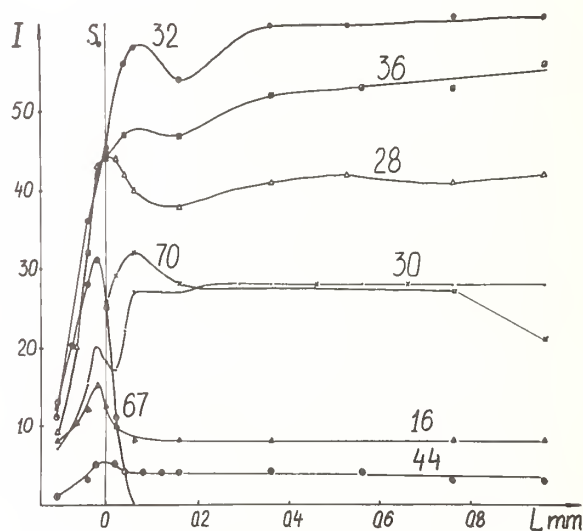


Figure 7. Distribution of species in an AP flame with CuO as a catalyst (system IV, table 1).

Figure 8 shows distribution of mass peak intensities in the combustion zones of double-base propellant ("N" powder).  $\text{CH}_2\text{O}$  (29,30) is one of the major "N" powder gasification products. Its formation is probably the main reaction in the so-called "foam" zone adjoining the burning surface.  $\text{N}_2 + \text{CO}$  (28),  $\text{NO}$  (30),  $\text{N}_2\text{O}$  (30,44),  $\text{CO}_2$  (44),  $\text{NO}_2$  (46) and also small amounts of nitroglycerin (76,46) and dinitrotoluol (62,89) are additional gasification products. Although formaldehyde generation in double-base propellant combustion was suspected earlier [2,19], in the present work this supposition has been verified experimentally. It is necessary to note that we did not observe a large amount of nitroglycerin (NGC) and  $\text{NO}_2$  from mass-spectrometry of "N" powder thermal decomposition in vacuum [20]. The data of figure 8 shows that the intensity of the peak with  $m/e$ -46, which is characteristic of NGC and  $\text{NO}_2$ , increases sharply within the reaction layer of burning propellant. Thus, NGC and  $\text{NO}_2$  decomposition reactions take place, primarily in the surface layer of burning propellant.

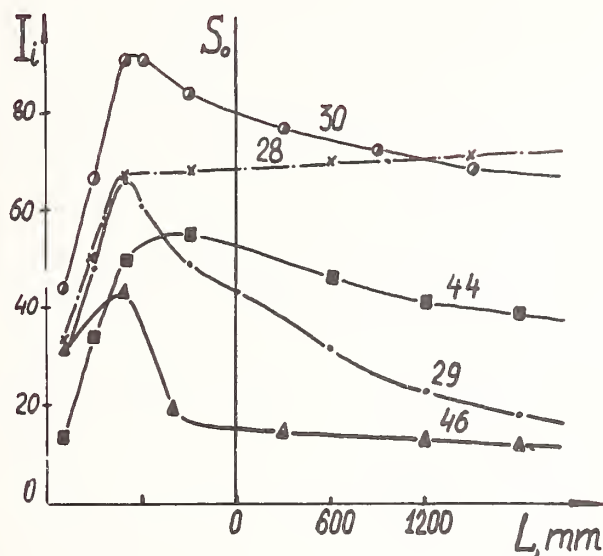
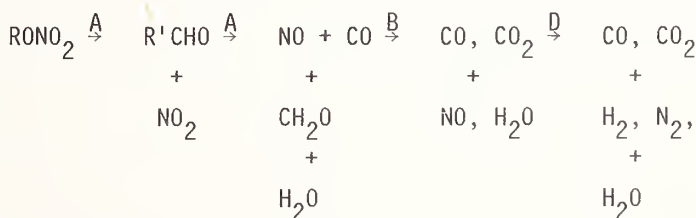


Figure 8. Distribution of species in a double base propellant ("N" powder) flame (system V, table 1).

Figure 9 presents the distribution of mass peak intensities in "N" powder flame at 20 atm pressure. Here, we used a system of two-step sampling with an intermediate chamber evacuated with a mechanical pump. Since in this case the strand, which initially was placed near the quartz microprobe, was fixed and the burning surface moved away from the probe at the rate of combustion, then the initial increase in the mass peak intensities is mainly associated with the approach to steady-state conditions after ignition. Comparison of the data given in figure 8 and figure 9 shows that the degree of reduction of NO to nitrogen increases with pressure. This reaction, as seen from figure 9, is the basic one in the flame zone (according to published data, the width of the "dark" zone is 4 mm at 20 atm). Our data confirm the following reaction scheme in the combustion zones which differs from that given in [21] mainly in the place where it occurs:



Here, A is the surface reaction zone, B is the foam zone, and D is the flame zone.

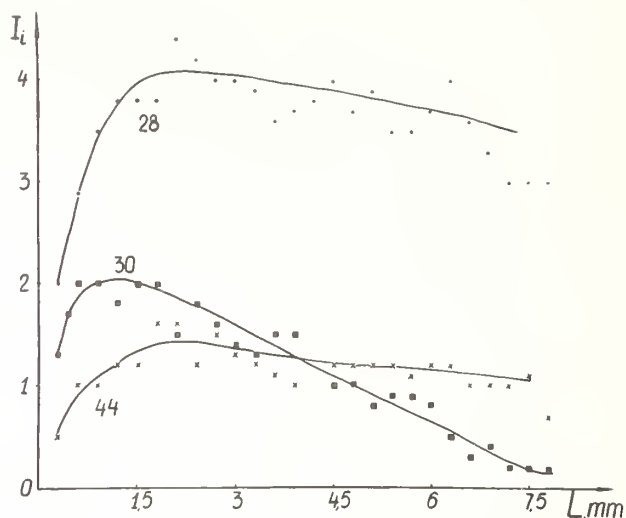


Figure 9. Distribution of species in a double-base propellant at 20 atm.

#### References

- [1] Zenin, A. A., *Phys. Combust. and Explosion* (Russ.), 3, 67 (1966).
- [2] Davidchuk, E. L. and Maltsev, V. M., *Phys. Combust. and Explosion* (Russ.), 5, 656 (1974).
- [3] Fristrom, R. M. and Westenberg, A. A., *Flame Structure* (McGraw-Hill, New York, 1965).
- [4] Hastie, J. W., *Intern. J. Mass Spectr. Ion Phys.* 16, 89 (1975).
- [5] Biordi, J. C., Lazzara, C. P., and Papp, J. F., in *Fourteenth Symposium (International) on Combustion* (The Comb. Inst., Pittsburgh, PA, 1973), p. 367.
- [6] Heller, C. A. and Gordon, A. S., *J. Phys. Chem.* 8, 59, 773 (1955).
- [7] Hertzberg, M., *Oxidation and Comb. Reviews*, 5, 1 (1971).
- [8] Brown, R. W., Lippiatt, J. H., Price, D., and Izod, D. C. A., *Intern. J. Mass Spectr. Ion Phys.* 16, 101 (1975).
- [9] Fenimore, C. P. and Martin, F. J., in *The Mechanisms of Pyrolysis, Oxidation and Burning of Organic Materials*, NBS Publ. 357, p. 159, (1972).
- [10] Efremov, V. L., Kolesnikov, B. Ya., Shapyrin, V. A., Manzhos, V. K., and Ksandopulo, G. I., *Khimicheskaya fizika protsessov goreniya i vzryva. Gorenje geterogennyh i gazovyh sistem*, Chernogolovka, p. 14 (1977).
- [11] Korobeinichev, O. P., Tereshenko, A. G., and Puchkov, V. M., *Phys. Combust. and Explosion* (Russ.) 3, 335 (1977).
- [12] Korobeinichev, O. P., Zenin, A. A., Tereshenko, A. G., and Puchkov, V. M., *Phys. Combust. and Explosion* (Russ.), 3, 335 (1977).
- [13] Koroveinichev, O. P. and Tereshenko, A. G., *Khimicheskaya fizika protsessov goreniya i vzryva. Gorenje kondensirovannyh sistem*. Chernogolovka, p. 73 (1977).

- 14] Korobeinichev, O. P., Kovalenko, K. K., and Lesnikovitch, A. I., Phys. Combust. and Explosion (Russ.), 4, 550 (1977).
- 15] American Petroleum Inst. Research Project 44, Mass Spectral Data, NY (1952).
- 16] Shteinberg, A. S. and Ulybin, V. B., et al., in, Gorenje i vzryv, Moscow, Nauka, p. 12b (1972).
- 17] Krishnamurthy, Z. and Williams, F. A., Fourteenth Symposium (International) on Combustion (The Comb. Inst., Pittsburgh, PA, 1973), p. 151.
- 18] Korobeinichev, O. P., Karpenko, Yu. Ya., and Boldyrev, V. V., Izv. AN SSSR, ser. khim. 7, 1663, (1970).
- 19] Bent, H. A. and Crawford, B., J. Phys. Chem. 63, 941 (1959).
- 20] Korobeinichev, O. P. and Hlevnoi, S. S., Phys. Combust. and Explosion (Russ.), 3, 404 (1970).
- 21] Cubota, N., Ohlemiller, T. J., Caveny, L. H., and Summerfield, M., AIAA, Paper No. 74-124 (1974).





#### **IV. MOLECULAR STRUCTURE DETERMINATION-- MATRIX ISOLATED SPECIES**

mona  
ear  
then

St

labl

1995

at

of

1108

1998

488

8

10

1

100

10

10

544

15

0

Tag

Med

22

10

15

140

1

1

1

The

18

There

130

1

10

1

1

1

## MATRIX ISOLATION STUDIES OF HIGH TEMPERATURE SPECIES

R. H. Hauge and J. L. Margrave  
Rice University  
Houston, TX 77001

### 1. Introduction

Studies of the spectroscopy of matrix isolated high temperature molecules have provided valuable insight into the bonding characteristics and reactivity of many high temperature species. We have referenced some of the more recent reviews and books which discuss matrix isolation applications and technique [1-17]<sup>1</sup>. Our discussion will concern itself with the use of infrared and ESR isolation techniques as practiced in our laboratory. This seems appropriate since it is our interest in the characterization of high temperature molecules which led us to use matrix isolation. We will also discuss possible new directions in matrix isolation.

A long standing interest has been the isolation and spectroscopic study of species which can be directly vaporized or produced by reaction at high temperatures. Our studies have dealt with the halides of groups IA [18], IIA [19], IIIA [20], IVA [21-26], IVB [27-28], first row transition metals [29-31], rare earth metals [32-33], uranium [34], oxides of group IIA [35-37], sulfides of groups IA [38], IIIA [38] and cyanides of group IA [39-41]. A more recent interest has been the study of the reactivity of high temperature species with themselves and with other species. This is possible since a number of reactive collisions can occur on the matrix surface during isolation. The extent of reaction is controlled by adjusting the matrix to reactant mole ratio as well as the nature of the matrix. We have studied the reactions of alkali metals with carbon monoxide [42], silicon monoxide [38], carbon monosulfide [38], silicon difluoride [38], carbon dioxide [38], carbon disulfide [38], water, ammonia [43,44], uranium fluorides [45], uranium tetrafluoride with fluorine [46], magnesium difluoride with alkali and alkaline earth fluorides [47], and carbon monoxide with metal fluorides [48].

### 2. Experimental

The application of matrix isolation to high temperature species involves the use of high vacuum, cooling and heating techniques. The various spectroscopic techniques also have different requirements in the design of the trapping surface. For infrared and visible-ultraviolet spectroscopy, the matrix may be deposited on a transparent window or a mirror

---

Figures in brackets indicate the literature references at the end of this paper.

surface as shown in figure 1. We much prefer the use of polished Cu metal surfaces because of the increased number of trapping surfaces and shorter trapping times. Other advantages are lack of thermal gradients and window transmission problems especially for the far IR. However, the use of reflective trapping surfaces does require a mirror system such as the one shown in figure 2 which is used with a Beckman IR-9 and IR-11. We have successfully used a Beckman source mirror for mirror A.

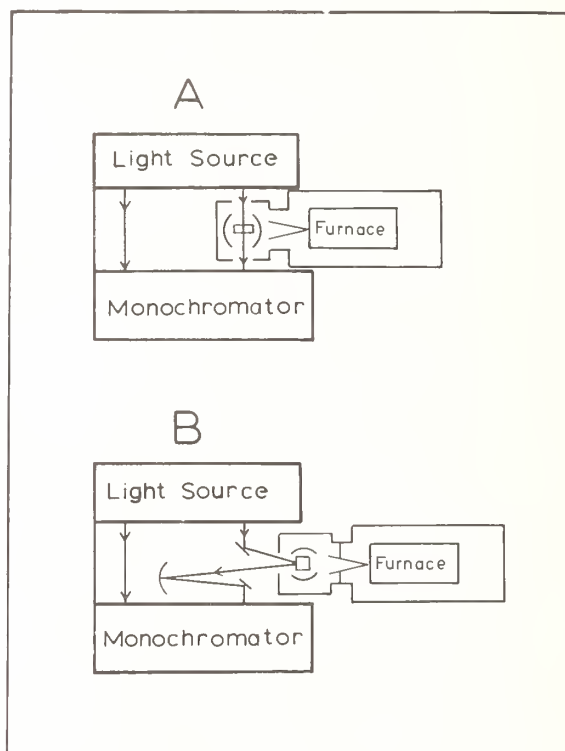


Figure 1. Schematic of transmission (A) and reflection (B) forms of isolation apparatus.

A schematic of our apparatus is shown in figure 3. The closed cycle He refrigerator can be rotated 360 degrees. There are four polished Cu surfaces with a shutter attached to the outer shield in front of each surface. The refrigerator takes approximately one hour to cool to  $\approx 12$  K. The shutters are left closed during cooldown in order to prevent condensation due to system outgasing. The vacuum prior to cooldown is  $\approx 1 \times 10^{-6}$  Torr and decreases to  $\approx 5 \times 10^{-7}$  Torr after cooldown. The pumping system consists of a gate valve, water-cooled baffle, 2 in -175 l/s diffusion pump and forepump. The furnace is constructed from 25 micron Ta foil. A ceramic liner or graphite cloth is used to electrically isolate metal crucibles from the Ta foil. The current leads are constructed from 0.5 mm Ta foil and are clamped to water-cooled copper vacuum feed throughs. Power is provided with a thirty ampere variac coupled to a 10/1 stepdown one kilowatt transformer. The furnace temperature is monitored with appropriate thermocouples or with an optical pyrometer.

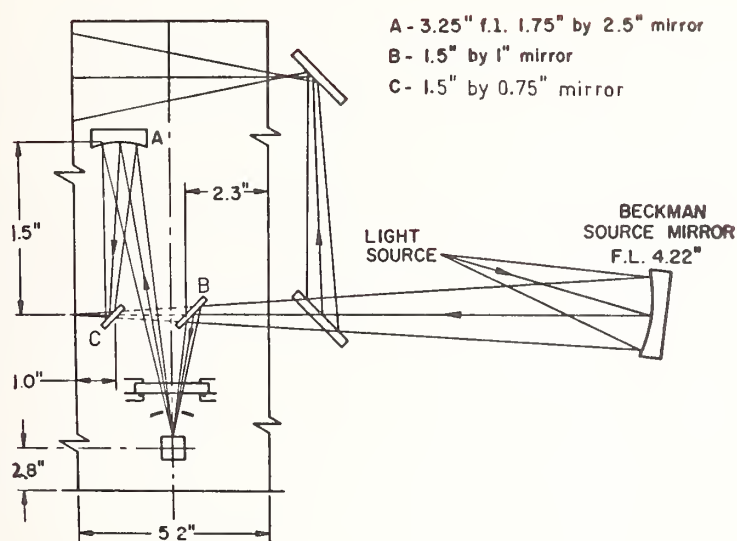


Figure 2. Mirror system for infrared reflection matrix isolation spectroscopy.

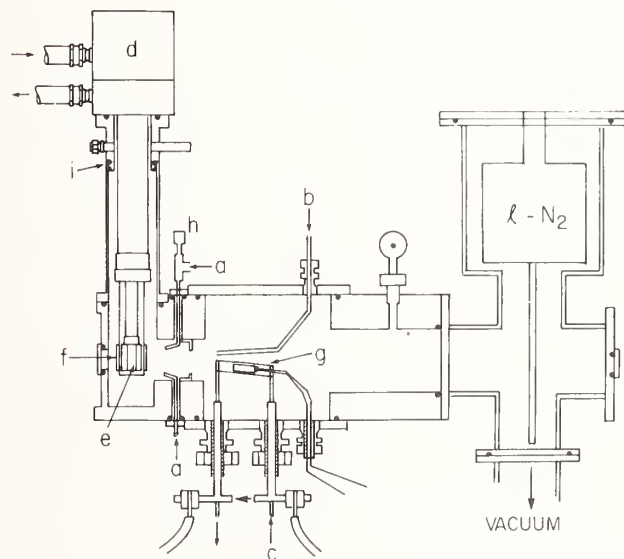


Figure 3. Matrix isolation apparatus: (a) matrix gas inlet; (b) reactant gas inlet; (c) water cooling for furnace leads; (d) closed cycle He refrigerator, Air Products Model CS202; (e) polished copper surfaces; (f) shutter; (g) Ta foil furnace; (h) thermocouple gage to monitor matrix gas input; and (i) rotatable double o-ring seal.



The matrix gas is taken directly from a research grade lecture bottle with a pressure regulator, passed through a liquid nitrogen trap and then through 0.125 in. tubing into the vacuum system. The matrix gas exits above and below the trapping surface  $\approx 5$  cm from the surface. A thermocouple gage is placed  $\approx 13$  cm upstream from one of the exit points and serves as a monitor of the matrix gas trapping rate. A nominal matrix gas trapping rate is 0.5 cc/min. Trapping times are from 0.5 to 2 hours with resulting matrices 10-50 microns in thickness.

Argon and nitrogen are the most often used matrix materials and are condensed at  $\approx 15$  K. Nitrogen appears to allow less surface reaction than argon during trapping perhaps due to increased interaction with the trapped species. Krypton and xenon are useful materials but are considerably more costly and result in higher light scattering than for argon or nitrogen. Their transparency can be improved by using a higher trapping temperature, i.e., 25-30 K. Neon gives the most transparent matrix and least interaction with the trapped species but condensation requires a temperature  $< 10$  K. Reactive matrices such as oxygen, fluorine, carbon monoxide, and methane can be condensed with conditions similar to argon.

Problems most often encountered are poor matrix transparency or impurities from leaks, system outgasing, and backstreaming of pump oils. Poor matrix transparency is usually caused by dirty surfaces. Occasionally, we have matrices peel away from the surface. The cause of this is uncertain, but we have found that it primarily occurs when the trapping surface is colder than is normally used. Water is always present in a matrix to a lesser or greater extent depending on the extent of exposure to room air and the length of time the system is pumped on prior to trapping. As a result, very long trapping times, i.e., days, at low matrix gas inlet rates may result in water complexing with the trapped species. Visual observation of the trapping surface during trapping is highly desirable since the success of the experiment can often be gauged by the appearance of the matrix. For reaction studies a system design which allows photolysis during trapping is very useful as it tends to maximize the production of reaction products. Finally, table I shows typical operating parameters for various cooling techniques.

### 3. Examples

There are now numerous examples in the literature of spectral studies of matrix isolated high temperature species, see references [2,3]. Vis.--UV and EPR spectroscopic studies have often given a definitive identification of the electronic ground state of species where more than one low lying electronic state exists. Infrared and Raman studies of many metal fluorides and chlorides have been published as have many of the metal oxides. In most instances, molecular geometry and force constant information were derived from isotopic shifts and measured frequencies. Data are generally lacking for the metal bromides, iodides, and chalcogenides.

TABLE I

Typical Operation and Costs for Cooling Techniques Useful in Matrix Isolation Studies

Cooling Method	Liquid He Capacity (liters)	Liquid He use for Cooldown (liters)	Liquid He use Rate (liters/hour)		Total Liquid He Used for 8 Hour Exp. (liters)		Cooldown Time (hours)	Temperature Variability	Initial Cost (\$)
			4.2 K	15.0 K	4.2 K	15.0 K			
Liquid He Reservoir	5	1.0	0.2	0.2	2.6	2.6	≈1	Difficult	2,000-5,000
Continuous Liquid He	25-100	0.3	0.8	0.3	6.7	2.7	0.2	Easy	1,000-5,000
Refrigerated Cycle Refrigerator	0	0	-	0	-	0	≈1	Easy	5,000-10,000

Infrared spectra and/or Raman spectra without isotopic information can, in some cases, provide a definitive assignment of molecular symmetry. For instance, the question of linear or planarity may be settled by the observation of a symmetric vibrational mode for metal halides and trihalides, respectively.

This was possible for the rare earth trifluorides [32] as shown in figure 4. In this case, assignment of two bands to monomeric  $\text{MF}_3$  was only possible after careful study of their dependence on trapping rates. This was necessary so as to eliminate the possibility of oligomers of  $\text{MF}_3$  being responsible for one of the two bands.

The infrared spectrum of  $\text{CrF}_2$ , as shown in figure 5, illustrates the effect of metal isotopes on the asymmetric vibration,  $\nu_3$ , of a  $\text{XY}_2$  molecule. The isotope product rule is the following relationship for the  $\nu_3$  mode.

$$\left(\frac{w_3^i}{w_3}\right)^2 = \frac{m_x m_y (m_x^i + 2m_y^i \sin^2 \alpha)}{m_x^i m_y^i (m_x + 2m_y \sin^2 \alpha)}$$

It can be shown that the isotopic shift has a much greater dependence on the bond angle ( $2\alpha$ ) than at 0 degrees than at 180 degrees. Thus, smaller angles can be more accurately measured for a given isotopic shift.

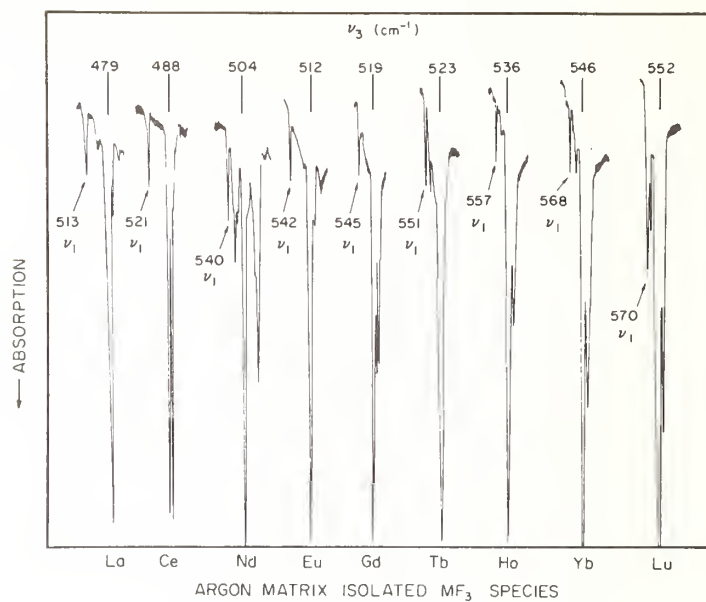


Figure 4. Metal fluorine stretching modes for rare earth trifluorides isolated in an argon matrix.

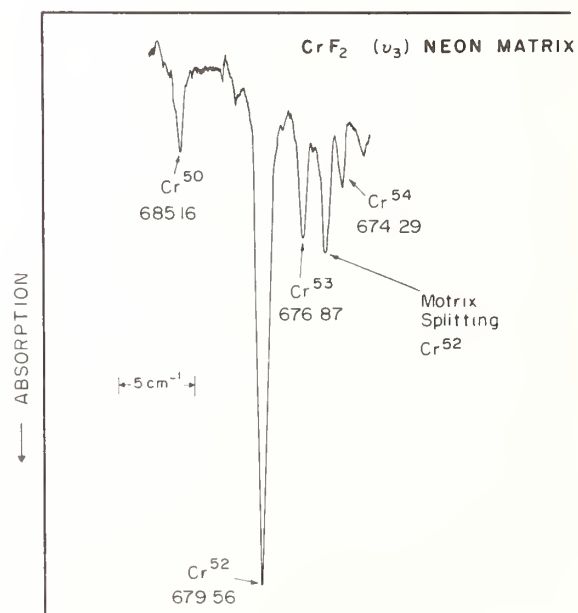


Figure 5. Asymmetric stretching mode of  $\text{CrF}_2$  isolated in a neon matrix.

It has also been shown that use of measured frequencies rather than zero order frequencies results in the calculated angle being a lower limit to the true value for isotopic substitutions at X and an upper limit for substitution at Y [50]. A useful check on the importance of an anharmonic correction can be made by assuming the anharmonicity to be  $0.01 \nu_3$  and its mass dependence to vary as  $(\nu_3^i/\nu_3)^2$ . Thus,  $w_3 = \nu_3 + 0.01 \nu_3$  and  $\Delta \nu_3 = \Delta \nu_3 + 0.01 \nu_3 [1 - (\nu_3^i/\nu_3)^2]$ . Table II illustrates the anharmonic correction for  $\text{CrF}_2$ . It is seen that inclusion of an approximate anharmonicity term does provide good agreement with calculated shifts for a linear molecule. The estimation of gas phase frequencies cannot be accomplished in any rigorous manner at present. Currently, it seems best to assume the gas phase value lies to the opposite side of the neon matrix value from that in an argon matrix. Where the gas phase value is known, primarily for diatomics, adding  $0.7 (\nu_{\text{Ar}} - \nu_{\text{Ar}})$  has given a reasonable estimate of it.

TABLE II

Comparison of Experimental and Calculated Isotope Shifts

Isotopes	Exp.	Calc. (163°)	$\Delta$	Calc. (180°)	$\Delta$	Corr. Exp.	Calc. (180°)	$\Delta$
$\text{Cr}^{50}-\text{Cr}^{54}$	10.92	10.92	.0	11.06	+ .14	11.25	11.22	- .03
$\text{Cr}^{50}-\text{Cr}^{53}$	8.35	8.33	- .02	8.39	+ .04	8.60	8.52	- .08
$\text{Cr}^{50}-\text{Cr}^{52}$	5.60	5.64	+ .04	5.71	+ .11	5.77	5.79	+ .02
$\text{Cr}^{52}-\text{Cr}^{54}$	5.27	5.33	+ .06	5.39	+ .12	5.44	5.48	+ .04
$\text{Cr}^{52}-\text{Cr}^{53}$	2.69	2.67	- .02	2.71	+ .03	2.70	2.75	+ .05
$\text{Cr}^{53}-\text{Cr}^{54}$	2.55	2.60	+ .05	2.63	+ .08	2.56	2.67	+ .11
			+ .09		+ .52			+ .11

Alkali metal atom reactions have been used extensively as a means of extracting a halogen to produce and study the resulting free radical species [13]. Alkali and alkaline earth metals have also been used to create unusual cation-anion molecules [51]. We have recently studied alkali metal reactions with  $\text{UF}_6$  [45] as shown in figure 6. The spectra are interpreted as being due to a contact pair and a separated ion pair. The spectra of  $\text{UF}_6^-$  for the separated ion pair is expected to be invariant with a change of the alkali metal as is apparent for the  $520 \text{ cm}^{-1}$  band. Only a few molecules may be expected to form separated ion pairs as the electron affinity needs to be quite high.

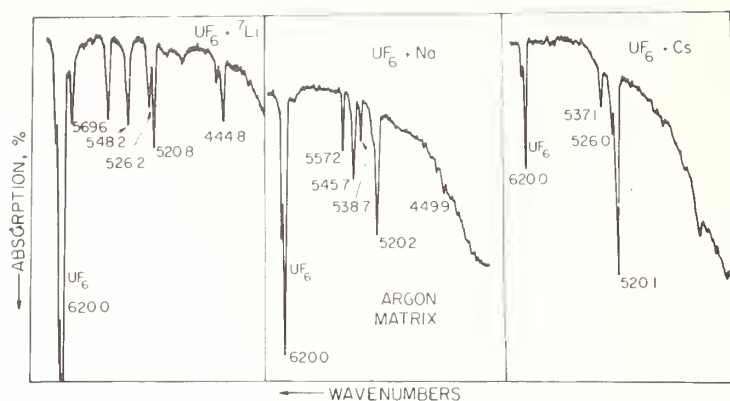


Figure 6. Reactions of  $\text{UF}_6$  with alkali metals.

Studies of  $\text{UF}_4$  with fluorine, see figure 7, illustrate the usefulness of matrix isolation in the study of reaction mechanisms [46]. It seems that  $\text{UF}_4$  reacts with fluorine with little or no activation energy and does not add both fluorines in a single step to form  $\text{UF}_6$ . Finally, the reaction of alkali metals with water have shown it possible to form a weak adduct with water through the oxygen without any further reaction [44]. Photolysis with visible radiation of the lithium-water adduct does cause it to react further to form lithium hydroxide and a hydrogen atom. The measured lithium hydroxide values are given in table III. Calculations of isotopic shifts indicate  $\text{LiOH}$  is linear.

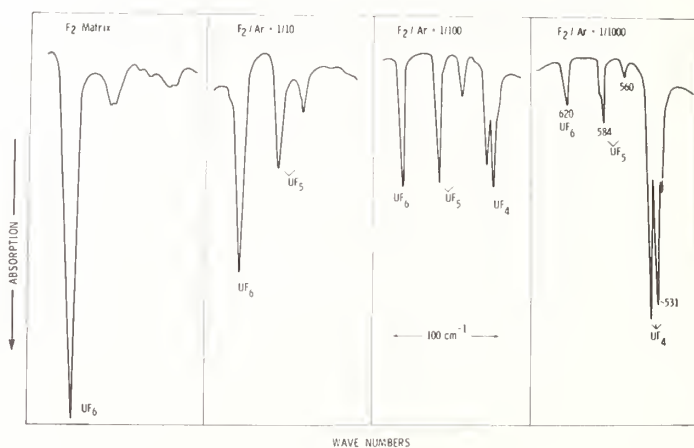


Figure 7. Reaction of  $\text{UF}_4$  with fluorine in an argon matrix.



TABLE III

Lithium Hydroxide Frequencies ( $\text{cm}^{-1}$ )

Compound	Measured	Corrected <sup>a</sup>	Calculated <sup>b</sup>
<sup>7</sup> LiOH	874.0 882.0	889.8	889.2
<sup>6</sup> LiOH	922.8 931.8	940.2	--
<sup>6</sup> Li <sup>18</sup> OH	911.1 920.0	928.2	927.2
<sup>7</sup> LiOD	865.6 873.9	881.0	882.0
<sup>6</sup> LiOD	915.1 924.1	932.5	933.4

- a. The measured values have been increased by twice the anharmonic constant where  $\omega_e x_e$  equals 8.8 for <sup>6</sup>LiOH and  $\omega_e x_e^i = \mu/\mu^i(\omega_e x_e)$ .  $\mu$  is the reduced mass of lithium hydroxide with the hydroxide treated as a single mass.
- b. The values were calculated with a triatomic linear model. The isotopic shifts for the hydrogen stretching mode were taken as  $(\mu^i/\mu)^{1/2}$  for the diatomic hydroxide.

## 4. Possible New Applications

It is of some interest to speculate as to other uses of the matrix isolation technique. We would like to discuss three promising areas of application in respect to high temperature chemistry. They are high pressure sampling with matrix isolation, the matrix isolation of pulsed laser heated thin film mixtures, and matrix isolation photoelectron spectroscopy.

The matrix isolation of species existing at high temperature and high pressure should present no more difficulty than that of mass spectrometric sampling. Vacuum requirements are less demanding since the trapping device acts as a pump. A schematic of an apparatus designed for high pressure sampling is shown in figure 8. The matrix gas could be added to the trapping stage or originate at the high pressure zone. Species sensitivity would depend on the spectroscopic technique used. Vis.--UV fluorescence and EPR spectroscopy should allow the study of species presence in the ppm range. Infrared and Raman spectroscopy would require concentrations in the parts-per-thousand and parts-per-hundred range, respectively. Its value with respect to a mass spectrometric study of the same system could derive from the additional structural and frequency information that matrix isolation spectroscopic techniques can provide.

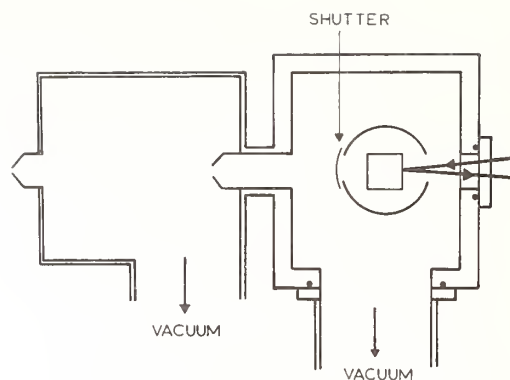


Figure 8. Schematic of a hypothetical high pressure sampling matrix isolation system.

The matrix isolation technique has made it possible to study most high temperature species and their chemistry at low temperatures. It has also made it possible to create mixtures of any number of reactive components without concern for their volatility or solubility. The chemistry necessary involves processes with low activation energy such as electron transfer or associative type reactions. Matrix chemists are accustomed to warming their matrices slightly to promote further reaction; however, the matrix volatility sets an upper limit of  $\approx 40$  K in the case of argon and nitrogen. Thus, many important high temperature reactions cannot be studied. However, it appears that a matrix can be pulse heated by a laser to any desired temperature and subsequently recondensed on a second cold surface as shown in figure 9. This would then cycle the reactions through a momentary high pressure-high temperature state where important high temperature reaction intermediates could form and be subsequently studied by matrix isolation techniques. For instance, an appropriate mixture of metals, hydrocarbons and hydrogen might be co-condensed as a model of a high pressure-high temperature catalytic hydrogenation system.

Finally, it appears possible to study the electron spectroscopy of isolated negative ions as indicated in figure 10. In fact, photoelectron emission from inert gas matrices has been previously observed [52]. The experiment would involve initial preparation of a metallic surface from which electrons can be photo-ejected by radiation  $h\nu_1$  into the matrix where they are captured by a matrix isolated species. A chopper then turns  $h\nu_1$  off and  $h\nu_2$  on, and the electron emission is monitored as a function of the frequency of  $h\nu_2$ . The metallic film is chosen so that its work function is greater than the energy available in  $h\nu_2$ . Spectra would be subject to the usual matrix perturbations but should give reasonable measures of negative ion excited states, electron affinity, and possibly low lying excited states of the neutral species.

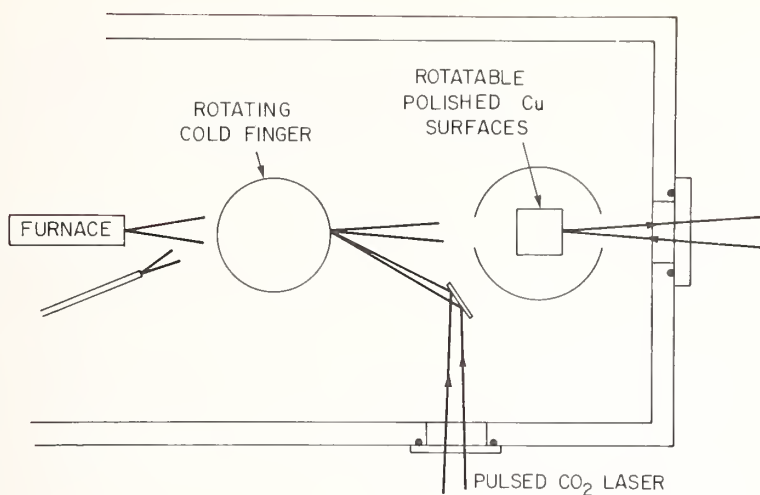


Figure 9. Schematic of a cryogenic mixture-laser pulse heated-matrix isolated system.

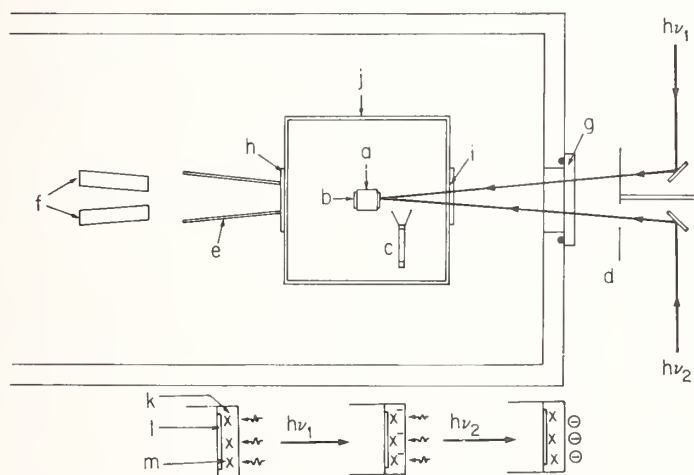


Figure 10. Schematic of a photoelectron emission matrix isolation system: (a) cold metal block; (b) metal coated sapphire window; (c) channeltron; (d) chopper; (e) liquid N<sub>2</sub> cooled collimator; (f) furnaces; (g, i) windows; (h) shutter; and (j) liquid N<sub>2</sub> shield.

We thank the National Science Foundation, the U. S. Army Research Office (Durham), and the Robert A. Welch Foundation for financial support.

#### References

- [1] International Conference on Matrix Isolation Spectroscopy, Berlin (1977), Ber. Bunsenges., Phys. Chem. 82 (1978).
- [2] Weltner, Jr., W., Matrix isolation applied to high temperature and interstellar molecules: a review, Ber. Bunsenges., Phys. Chem. 82, 80-89 (1978).
- [3] Cryo Chemistry, M. Moskovits and G. A. Ozin, eds. (Wiley, N.Y., 1976).
- [4] Vibrational Spectroscopy of Trapped Species, H. E. Hallam, ed. (Wiley, N.Y., 1973).
- [5] Snelson, A., Infrared studies of vaporizing molecules trapped in low temperature matrices, in Vibrational Spectroscopy of Trapped Species, H. E. Hallam, ed. (Wiley, N.Y., 1973), pp. 203-244.
- [6] Downs, A. H. and Peake, S. C., Matrix isolation, in Molecular Spectroscopy, Vol. I (Chem. Soc., Burlington House, London, 1973), pp. 523-607.
- [7] Perutz, R. N. and Turner, L. J., Pulsed matrix isolation, Faraday Soc. II, 69, 452 (1973).
- [8] Carstens, D. H. W., Brashear, W., Eslinger, D. R., and Gruen, D. M., The correlation between gaseous atomic spectra and the absorption spectra of atoms isolated in noble-gas matrices, Applied Spectroscopy, 26, 184-217 (1972).
- [9] Milligan, D. E. and Jacox, M. E., Matrix isolation spectroscopy, in International Review of Science: Spectroscopy, Phys. Chem. Ser. 1, Vol. 3, D. A. Ramsay, ed. (Butterworths, London, 1972), pp. 1-32.
- [10] Milligan, D. E. and Jacox, M. E., Infrared and ultraviolet spectroscopic studies of a number of small free radicals and molecular ions, Adv. High Temp. Chem. 4, 1-42 (1971).
- [11] Kasai, P. H., Generation and electron spin resonance study of charged species in rare gas matrices, Acct. Chem. Res. 4, 329 (1971).
- [12] Meyer, B., in Low Temperature Spectroscopy (American Elsevier, N.Y., 1971).
- [13] Andrews, L., Infrared spectra of free radicals and chemical intermediates in inert matrices, Ann. Rev. Phys. Chem. 22, 109 (1971).
- [14] Ogden, J. S. and Turner, L. J., Matrix isolation, Chemistry in Britain, 7, 186 (1971).
- [15] Hastie, J. W., Hauge, R. H., and Margrave, J. L., Matrix isolation spectroscopy, in Spectroscopy in Inorganic Chemistry, Vol. 1, C. N. R. Rao and J. R. Ferraro, eds. (Academic Press, 1970), pp. 57-106.
- [16] Hastie, J. W., Hauge, R. H., and Margrave, J. L., High temperature chemistry: stabilities and structures of high temperature species, Ann. Rev. Phys. Chem. 21, 475 (1970).

- [17] Formation and Trapping of Free Radicals, A. M. Bass and H. P. Broida, eds. (Academic Press, N.Y., 1960).
- [18] Ismail, Z. K., Hauge, R. H., and Margrave, J. L., Infrared spectra of sodium and potassium fluorides by matrix isolation, *J. Inorg. Nucl. Chem.* **35**, 3201 (1973).
- [19] Hauge, R. H., Kana'an, A. S., and Margrave, J. L., IR spectra of matrix  $\text{MgF}_2$ , *J. Chem. Soc. Trans. Faraday II*, **71**, 1082 (1975).
- [20] Hastie, J. W., Hauge, R. H., and Margrave, J. L., Infrared spectra of matrix-isolated species in the gallium-fluorine system, *J. Fluorine Chemistry*, **3**, 285 (1973).
- [21] Hastie, J. W., Hauge, R. H., and Margrave, J. L., Infrared spectra of  $\text{SiF}_2$  in neon and argon matrices, *J. Amer. Chem. Soc.* **91**, 2536 (1969).
- [22] Hastie, J. W., Hauge, R. H., and Margrave, J. L., Infrared vibrational properties of  $\text{GeF}_2$ , *J. Phys. Chem.* **72**, 4492 (1968).
- [23] Hauge, R. H., Maass, G., and Margrave, J. L., The IR spectrum of matrix isolated  $\text{SiBr}_2$  and  $\text{SiCl}_2$ , *Z. fur anorg. und allg. Chemie*, **392**, 295 (1972).
- [24] Maltsev, A. K., Nefedov, P. M., Hauge, R. H., Seyferth, D., and Margrave, J. L., Matrix-isolation study of the pyrolysis of bromosubstituted organomercury compounds. Infrared spectra of the chlorobromocarbene and free radicals  $\text{CCl}_2\text{Br}$  and  $\text{CClBr}_2$ , *J. Phys. Chem.* **75**, 3984 (1971).
- [25] Maltsev, A. K., Mikaelian, R. G., Nefedov, O. M., Hauge, R. H., and Margrave, J. L., Pyrolysis of organomercury compounds: investigation by the method of matrix isolation, *Proc. Nat. Acad. Sci., USA*, **68**, [12] 3238-3241 (1971).
- [26] Hauge, R. H., Hastie, J. W., and Margrave, J. L., Infrared spectra of matrix isolated tin and lead difluorides, *J. Mol. Spec.* **45**, 420 (1973).
- [27] Hastie, J. W., Hauge, R. H., and Margrave, J. L., Infrared spectra and geometry of  $\text{TiF}_2$  and  $\text{TiF}_3$  in rare gas matrices, *J. Chem. Phys.* **51**, 2648 (1969).
- [28] Hauge, R. H., Hastie, J. W., and Margrave, J. L., Infrared spectra of matrix isolated  $\text{ZrF}_2$ ,  $\text{ZrF}_3$ , and  $\text{ZrF}_4$  species, *High Temp. Sci.* **5**, 89 (1973).
- [29] Hastie, J. W., Hauge, R. H., and Margrave, J. L., Vibrational frequencies and valence force constants of first-row transition-metal di-fluorides, *Chem. Comm.* **1969**, 1452 (1969).
- [30] Hastie, J. W., Hauge, R. H., and Margrave, J. L., Infrared spectra and geometry of the difluorides of Co, Ni, Cu and Zn isolated in neon and argon matrices, *High Temp. Sci.* **1**, 76 (1969).
- [31] Hastie, J. W., Hauge, R. H., and Margrave, J. L., Infrared spectra and geometries for the dichlorides of Ca, Sc, Ti, V, Cr, Mn, Fe, and Ni, *High Temp. Sci.* **3**, 257 (1971).
- [32] Hauge, R. H., Hastie, J. W., and Margrave, J. L., Force constants and geometries of matrix isolated rare-earth trifluorides, *J. Less-Common Metals*, **23**, 359 (1971).
- [33] Hastie, J. W., Hauge, R. H., and Margrave, J. L., Geometries and entropies of metal trifluorides from infrared spectra:  $\text{ScF}_3$ ,  $\text{YF}_3$ ,  $\text{LaF}_3$ ,  $\text{EuF}_3$ , and  $\text{GdF}_3$ , *J. Less-Common Metals*, **39**, 309 (1975).



- [34] Kunze, K. R., Hauge, R. H., Hamill, D., and Margrave, J. L., Studies of matrix-isolated uranium tetrafluoride and its interaction with frozen gases, *J. Phys. Chem.* 81, 1664 (1977).
- [35] Hastie, J. W., Hauge, R. H., and Margrave, J. L., Infrared spectra and geometry of  $\text{SO}_2$  and  $\text{SeO}_2$  in rare gas matrices, *J. Inorg. Nucl. Chem.* 31, 281 (1969).
- [36] Hastie, J. W., Hauge, R. H., and Margrave, J. L., Reactions and structures of matrix-isolated SiO species at low temperatures from infrared spectra, *Inorg. Chem. Acta*, 3, 601 (1969).
- [37] Muenow, D. W., Hastie, J. W., Hauge, R. H., Bautista, R., and Margrave, J. L., Vaporization, thermodynamics and structures of species in the tellurium-oxygen system, *Trans. Faraday Soc.* 65, 3210 (1969).
- [38] Hauge, R. H. and Margrave, J. L., unpublished data.
- [39] Hauge, R. H., Ismail, Z. K., and Margrave, J. L., IR study of matrix isolated lithium isocyanide, *J. Chem. Phys.* 57, 5137 (1972).
- [40] Ismail, Z. K., Hauge, R. H., and Margrave, J. L., The IR spectra of matrix-isolated NaCN and KCN, *J. Mol. Spec.* 45, 304 (1973).
- [41] Hauge, R. H., Ismail, Z. K., and Margrave, J. L., IR studies of matrix isolated sodium and potassium chloride and cyanide dimers, *J. Mol. Spectroscopy*, 54, 402 (1975).
- [42] Krishnan, C. N., Thesis, IR and ESR studies of reactions involving matrix isolated species (Rice University, Houston, 1975).
- [43] Hauge, R. H., Meier, P. F., and Margrave, J. L., Matrix isolation IR and EPR studies of reaction intermediates: lithium atom reactions with  $\text{H}_2\text{O}$ ,  $\text{CH}_3\text{OH}$ , and  $\text{NH}_3$ , *Ber. Bunsenges., Phys. Chem.* 82, 102 (1978).
- [44] Meier, P. F., Hauge, R. H., and Margrave, J. L., Electron spin resonance studies of the reaction of lithium atoms with Lewis bases in argon matrices: formation of reactive intermediates. 1. Water and ammonia, *J. Amer. Chem. Soc.* 100, 2108 (1978).
- [45] Kunze, K. R., Hauge, R. H., Hamill, D., and Margrave, J. L., Co-condensation reactions of uranium tetrafluoride and hexafluoride with alkali metals and alkali-metal fluorides in low-temperature argon matrices, *J. Chem. Soc., Dalton Trans.*, 5, 433 (1978).
- [46] Kunze, K. R., Hauge, R. H., and Hamill, D., IR matrix study of reactions of  $\text{UF}_4$  with fluorine, *J. Chem. Phys.* 65, 2026 (1976).
- [47] Kana'an, A., Hauge, R. H., and Margrave, J. L., Infrared spectra of matrix isolated species: reactions of  $\text{MgF}_2$  with group I-group II fluorides, *J. Chem. Soc., Faraday II*, 72, 1991 (1978).
- [48] Hauge, R. H., Gransden, S. E., and Margrave, J. L., The interaction of carbon monoxide with alkali, alkaline earth, transition metal and lanthanide fluorides in an argon matrix, *J. Chem. Soc., Dalton Trans*, submitted for publication (1978).
- [49] Wilson, Decius, and Cross, Molecular Vibrations (McGraw-Hill, N.Y., 1955).
- [50] Allavena, M., Rysnik, R., White, D., Calder, G. V., and Mann, D. E., Infrared spectra and geometry of  $\text{SO}_2$  isotopes in solid krypton matrices, *J. Chem.* 50, 3399 (1969).

- [51] Andrews, L., Infrared and Raman spectroscopic studies of alkali-metal-atom matrix-reaction products, in Cryo-Chemistry, M. Moskovits and G. A. Ozin, eds. (Wiley, N.Y., 1973), pp. 195-229.
- [52] Ophir, Z., Raz, B., Jortner, J., Saile, V., Schwentner, N., Koch, E., Skibowski, M., and Steinman, W., Photoemission from doped rare gases, J. Chem. Phys. **62**, 650 (1975).

### Discussion

Question (Berkowitz): Do you have an idea of the structure of  $\text{UF}_5$ ?

Response (Hauge): The idea should be credited to the Los Alamos people. There was also work done where they photolysed  $\text{UF}_6$  in a matrix at the same time we did ours. I think it is almost certain that the structure of  $\text{UF}_5$  is square pyramidal. The other structure, of course, would be trigonal bipyramid. --- There are three known frequencies for  $\text{UF}_5$ . The two we observed were the strongest. There is another weak one, when you go back and look hard you find it. That has been verified by Raman spectroscopy too which verified the structure.

Question (Berkowitz): You can use isotopic labeling in that case, I guess?

Response (Hauge): No, neither one has a decent isotope to work with that you can see. We have put a chlorine in there and the structure for  $\text{UF}_4\text{Cl}$  is trigonal bipyramidal, we think.

Question (Klotzbucher): The question is actually in two stages. Number one, did you use a number of your reflecting surfaces during one experiment?

Response (Hauge): Yes.

Question (Klotzbucher): Number two, do you see an effect of matrix gas deposit on the front creeping around to the back? Does your baseline rise from that?

Response (Hauge): The answer is some argon often gets around the side--very little condensibles get around---there is no contamination.

Question (Klotzbucher): Did you consider the effect of what would happen if you are blasting off part of the surface on to the second cold finger, what would that do to your base line?

Response (Hauge): I don't know. We would have to try it and find out. But the baseline isn't the problem. You are not worried about losing a little light.



## THE CHARACTERIZATION OF HIGH TEMPERATURE MOLECULES USING MATRIX ISOLATION AND ISOTOPE FINE STRUCTURE

J. S. Ogden  
Department of Chemistry  
University of Southampton  
Southampton SO9 5NH, U.K.

### 1. Introduction

The difficulties encountered in the direct study of high temperature vapours are well known. Basically, these fall into three main areas connected broadly with production, detection, and characterization, and for many systems these areas are interlinked. Thus, the chemical reactivity of many high temperature species often places a severe constraint on the study of closed systems owing to the lack of a suitable container material. When this problem is by-passed by working at low pressures in a molecular beam, the resulting low concentrations may present serious detection problems, notably for ir or Raman spectroscopy. The third problem is concerned with the sheer complexity and abundance of information present in many high resolution gas phase studies. For all but the simplest molecules, a complete analysis of the electronic, vibrational, or pure rotational spectrum will present a formidable task if there is significant thermal population of low lying vibrational (or electronic) states and if, as is often the case, the composition of the vapour is unknown. Lower resolution studies, with the possible exception of gas phase Raman measurements, are generally rather inconclusive as spectral features are often broad and ill-defined. Matrix isolation [1-3]<sup>1</sup> offers a number of advantages in all three areas, and its application to high temperature molecules has been extensively reviewed [4-5]. However, before describing the characterization of such species in detail, it is useful to summarize the essential features of this technique.

In a matrix isolation study on a typical high temperature system, the species of interest are generated in a Knudsen cell, and traverse a distance of  $\sim 10$ -20 cm, before impinging on a suitable deposition surface cooled to cryogenic temperatures. Isolation of these species is achieved by simultaneously condensing a large excess ( $\times 500$ ) of inert gas on the cooled surface where it solidifies and traps the species of interest in an inert rigid matrix. Nitrogen or argon are generally used as matrix materials, and the low temperatures are most conveniently achieved using closed cycle refrigerators operating at  $\sim 10$  K. Under these conditions, the high temperature molecules have a very extended lifetime, and may be studied at leisure. Sample deposition typically takes place slowly

<sup>1</sup>Figures in brackets indicate the literature references at the end of this paper.

over periods of  $\gtrsim 1$  hour and this cumulative effect means that a variety of traditional spectroscopic methods may be used, including ir, uv/vis., Raman, e.p.r., m.c.d., and Mössbauer.

However, experiments on stable vapour phase molecules show that the presence of the matrix cage has a small but distinct effect on the spectroscopic properties of the trapped species, and this is clearly important if we are to apply data obtained from matrix studies to vapour species. Thus, for the majority of compounds, molecular rotation is completely quenched in the matrix, and the frequencies of vibrational or electronic transitions are found to be slightly shifted from the gas phase values. In addition, degeneracies may be lifted, and the possibility of different trapping sites may also lead to multiplet features. These perturbations, however, are usually small, and in vibrational studies, for example, are comparable to the effects produced by a non-coordinating solvent. One additional aspect of matrix isolation which may complicate spectral interpretation is the readiness shown by some molecules to undergo a limited amount of polymerization during sample deposition. Unexpected features due to this behaviour may often be confirmed by then allowing a small amount of further polymerization to take place under conditions of controlled diffusion. This may often be achieved simply by warming the matrix to 25-50 K and noting any changes in relative band intensities.

## 2. Vibrational Spectroscopy

One of the most widely used physical methods for characterizing high temperature molecules in matrices is infrared spectroscopy, and this has recently been supplemented by an increasing use of Raman. These techniques together offer a unique combination of features which bridge the gap between basic species identification (e.g., by mass spectrometry) and a detailed knowledge of structure. Firstly, owing to the lack of molecular rotation, vibrational transitions in matrix isolated species are frequently single sharp ( $\sim 1 \text{ cm}^{-1}$  wide) bands, and the selection rules governing their occurrence may be used in exactly the same way as in gas phase studies. In addition, the sharpness of the lines means that vibrational isotope effects may be observed for a wide range of elements (e.g., up to Xe). This vibrational fine structure may be used both qualitatively and quantitatively to obtain a definitive characterization.

If we consider the introduction of isotopes  $Y'$  and  $Y''$  in a random manner into the molecule  $XY_n$ , a total of  $n + 1$  different molecular species will result assuming that all  $Y$  atoms are chemically equivalent. The relative proportion of these isotopomers will be determined by the relative abundances of  $Y'$  and  $Y''$  and will, in general, follow a distribution governed by the binomial theorem. For each non-degenerate mode involving the set of equivalent  $Y$  atoms, isotope enrichment will therefore yield a multiplet of  $n + 1$  lines with relative intensities proportional to abundances. Thus, in a  $C_{2v}$  or  $D_{\infty h}$  dichloride  $MCl_2$  the  $^{35}\text{Cl}:^{37}\text{Cl}$  abundance ratio of  $\sim 3:1$  will result in a 9:6:1 isotope pattern for the ir active stretching modes, and this triplet pattern would be repeated for any isotopic variation of  $M$ . In this way, an absorption band may sometimes be assigned quite unambiguously to a



particular molecular species. Typical examples of double isotope labelling are to be found in the halides of Gp II elements [6] and of the first series transition metals [3], and in favorable cases, precise measurements of these isotope shifts may be used to estimate [7] bond angles without any knowledge of the force field.

For degenerate vibrations, such as the  $E'$  stretching mode in  $XY_3$  species, the effect of two different isotopes  $Y'$  and  $Y''$  in general produces a pattern which shows a clear departure from a binomial intensity distribution. This is because the degeneracy is invariably lifted in the partially substituted species, and the resulting spectrum either contains more than  $n + 1$  distinct lines, or alternatively shows an anomalous intensity pattern as a result of band overlap. Fortunately, the form of this "anomalous" pattern may be calculated fairly readily, and in fact used to characterize degenerate modes in, for example, high temperature trichlorides [8,9]. Many of the essential steps in the characterization of high temperature molecules using matrix isolation may be illustrated by considering in more detail the silicon oxide system.

### 3. Silicon Oxides

Early high temperature mass spectrometric studies on the vapours above heated  $SiO_2$  or  $SiO$  established [10] that the principal silicon-containing molecule is diatomic  $SiO$ , and that smaller amounts of molecular  $SiO_2$  or  $Si_2O_2$  may also be detected. Subsequent calculations on the thermodynamics of these high temperature systems generally assumed [11] linear geometries for all three species, but it was not until the electric deflection studies of Kaufman, *et al.* [12] that any experimental evidence was obtained in favor of the  $SiO_2$  model for  $SiO_2$ .

Two matrix isolation studies on these systems were carried out independently [13,14] and almost simultaneously, and figure 1 summarizes the principal findings. When the vapours present above heated  $SiO$  are condensed at low temperatures in a nitrogen matrix [13], the infrared spectrum of the deposit typically shows four prominent bands in the spectral region  $1000-1300\text{ cm}^{-1}$ . Varying the matrix deposition rate or switching to a different matrix material (e.g., Ar) produces changes in the relative intensities of some of these features, with the result that at least three different molecular species may be distinguished. Figure 1(i) shows a typical spectrum in which two of these species are identified by single bands A and C, whilst species B is characterised by two relatively closely spaced bands. When this sample is allowed to warm to  $\sim 27\text{ K}$ , a limited amount of diffusion takes place within the matrix, and after recooling, the spectrum shown in figure 1(ii) is obtained. Clearly, C has increased dramatically, whilst B has decreased, and optical density measurements show that A has also decreased slightly. On diffusion, therefore, the reaction  $A + B \rightarrow C$  seems probable, and these changes in relative band intensities form the basis for the typical "diffusion plots" by which monomer or dimer species may be distinguished from higher polymers.

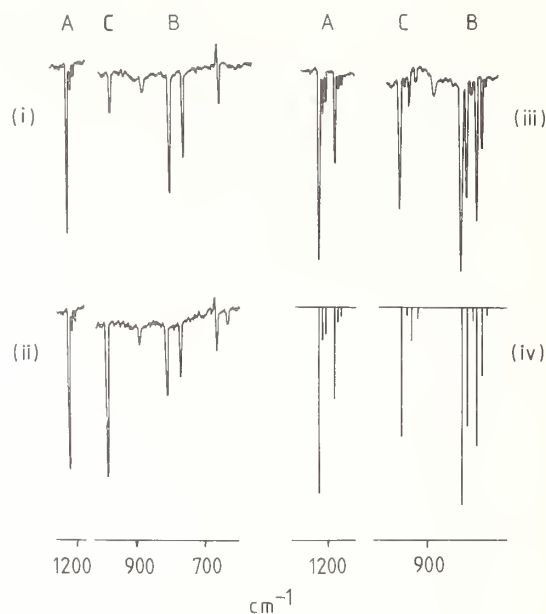


Figure 1. Infrared spectra of matrix isolated silicon oxides: (i)  $\text{N}_2$  matrix spectrum at 20 K before diffusion; (ii) the same sample after warming to 27 K; (iii)  $\text{N}_2$  matrix spectrum of 20 percent  $^{18}\text{O}$  enriched silicon oxides; and (iv) calculated spectrum assuming A is  $\text{SiO}$ , B is  $\text{Si}_2\text{O}_2$  ( $\text{D}_{2h}$ ) and C is  $\text{Si}_3\text{O}_3$  ( $\text{D}_{3h}$ ).

At this stage, only one of these species may be identified with any confidence. Band A lies at  $1223.9\text{ cm}^{-1}$ , some  $6\text{ cm}^{-1}$  away from the fundamental transition expected for diatomic  $^{28}\text{Si}^{16}\text{O}$  on the basis of an analysis of its vapour phase electronic spectrum. In addition, this band shows two small satellites on the low frequency side, which under high resolution, are seen to correspond almost exactly in terms of both position and relative intensity to those expected for  $^{29}\text{Si}^{16}\text{O}$  and  $^{30}\text{Si}^{16}\text{O}$  in natural abundance.

$^{18}\text{O}$  isotope experiments provide practically all the answers regarding the basic characterization of species B and C, and figure 1(iii) shows a typical spectrum obtained for  $\sim 20$  percent enrichment. As expected, two prominent bands due to  $\text{Si}^{16}\text{O}$  and  $\text{Si}^{18}\text{O}$  are now observed in the region of A, with an intensity ratio of 4:1, and each of these bands shows silicon isotope fine structure. A total of six bands is observed in the region of B. Here, it is evident that two triplets have replaced the original pair, and both the number of components and their relative intensities strongly suggest that B contains two equivalent oxygen atoms. It was similarly shown from a study of the silicon isotope fine structure that B also contained two silicon atoms, and B is therefore identified as  $\text{Si}_2\text{O}_2$ . In the original work on this system, C was identified as an  $\text{E}'$  mode of  $\text{Si}_3\text{O}_3$  primarily as a result of the matrix diffusion reaction. This was subsequently confirmed [15] by an analysis of the isotope pattern, which clearly shows a departure from the simple binomial

pattern of band intensities, and indicates a degenerate vibration. This particular molecule has not yet been detected in the vapour phase, and its presence here serves as a reminder that, in general, the distribution of species found in mass spectrometric studies on high temperature vapours may not always correspond to the species ultimately trapped in the matrix.

The line diagram in figure 1(iv) illustrates the final stage in the analysis of many matrix vibrational studies. The characterization of molecular SiO is significantly over-determined, but for B and C the observed frequencies may be used quantitatively to discriminate between several possible geometries consistent with the observed number of vibrational fundamentals. In this way, the linear  $D_{\infty h}$  model proposed originally for  $Si_2O_2$  is discounted, and the most probable structure is found to be a planar four-membered ( $D_{2h}$ ) ring. C is identified as the six-membered ring species  $Si_3O_3$  ( $D_{3h}$ ) where the ir active stretching modes have  $E'$  symmetry, and the quantitative agreement between observed and calculated frequencies for both these species is very satisfactory.

However, this final stage of characterization in which an exact correspondence between observed and calculated frequencies is sought, and usually obtained, occasionally requires such a large number of arbitrarily fixed parameters in relation to experimental observables that it may lose credibility, and as new high temperature systems are explored, this situation may initially become more widespread. It is therefore interesting to explore how one might use the isotope patterns obtainable from matrix isolation as a method of characterization when only a very limited number of fundamentals is available. The examples below outline some very recent results where the main emphasis is on pattern recognition rather than a detailed frequency fit.

#### 4. $M_4O_6$ Cage Units: The Characterization of $V_4O_{10}$ .

The identification of doubly degenerate modes via their characteristic isotope patterns has been described for a number of simple  $MCl_3$  species [9] and also for ring molecules such as  $Si_3O_3$ ,  $Ge_3O_3$ , and  $Li_3F_3$  [15]. It is therefore interesting to explore whether triply degenerate modes may similarly be identified, and we have chosen to study molecules containing the  $T_d$   $M_4O_6$  unit. A list of such species would include  $As_4O_6$ ,  $P_4O_6$ ,  $P_4O_{10}$ , and perhaps  $V_4O_{10}$  which is believed to be present in the vapour above heated vanadium pentoxide.  $As_4O_6$  and  $P_4O_6$  are well-studied molecules which are relatively easy to handle, and matrix isolation ir studies have shown [16] that one of the most prominent absorptions is the highest  $F_2$  stretching mode. In addition, it is relatively straightforward to synthesize  $^{18}O$  enriched  $As_4O_6$ , and we have selected this mode on which to base a series of isotope calculations designed to find out whether it will, in general, give rise to a characteristic pattern.

Figure 2(i) shows the type of pattern predicted for 50 percent  $^{18}O$  enrichment in a species  $M_4O_6$  where the atomic mass of M is taken to be 51. This pattern has been generated using a force field based on a fixed  $F_2$  mode at  $830\text{ cm}^{-1}$  and other frequencies close to those observed in  $As_4O_6$ . However, it proves to be rather insensitive both to the exact

position of these lower fundamentals and to the mass of  $M$ , and it would therefore seem that this isotope pattern might be used to characterize the  $M_4O_6$  cage unit. Figure 2(ii) shows the isotope pattern obtained experimentally [16] for  $\sim 50$  percent  $^{18}O$  enriched  $As_4O_6$  in the region of the highest  $F_2$  mode, and the correspondence is very satisfactory. Similar patterns have also been observed for  $^{18}O$  enriched  $P_4O_6$  and  $P_4O_{10}$  and this approach was therefore extended to the high temperature vanadium oxide system.

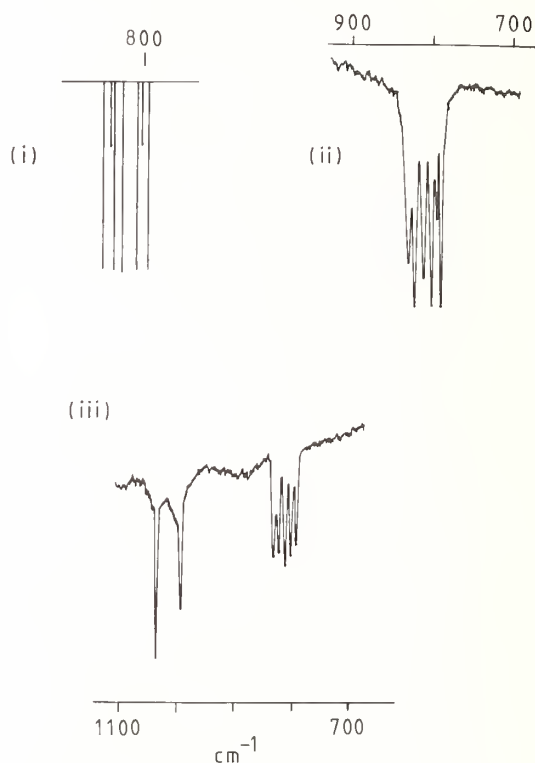


Figure 2. Infrared isotope patterns for highest  $F_2$  mode in  $M_4O_6$  cage species: (i) calculated spectrum assuming 50 percent  $^{18}O$  enrichment; (ii) Ar matrix spectrum  $\sim 50$  percent enriched  $As_4O_6$ ; and (iii)  $N_2$  matrix spectrum of  $\sim 50$  percent enriched  $V_4O_{10}$ .

When solid  $V_2O_5$  is heated to  $\sim 1000$  K, partial decomposition to a lower oxide and oxygen takes place, but the mass spectrum of the vapour [17] shows prominent ions  $V_4O_{10}^+$  and  $V_4O_8^+$  indicating that at least one vanadium oxide species is present. Matrix isolation studies under similar vapourization conditions [18] result in a relatively simple ir spectrum consisting of two strong bands at  $1029.9$  and  $828.4$   $cm^{-1}$ , and a much weaker feature at  $\sim 626$   $cm^{-1}$ . Varying the deposition rate or matrix gas established that these absorptions could all be assigned to the same trapped species, but it is clear that this three-line spectrum is rather limiting if one wishes to confirm the existence of  $V_4O_{10}$ . The results



from the  $^{18}\text{O}$  enriched material are shown in figure 2(iii). The highest frequency band now appears as a basic doublet suggesting that only one terminal  $\text{V}=\text{O}$  unit is present, but the  $840\text{ cm}^{-1}$  band yields an almost equally spaced quintet in which the five components have approximately equal intensities. This feature is in the general region expected for  $\text{V}-\text{O}-\text{V}$  stretching modes, and the quintet pattern is very similar to that predicted for a  $\text{V}_4\text{O}_6$   $\text{Td}$  cage. The presence of this unit dictates that there be at least four terminal  $\text{V}=\text{O}$  bonds, and the appearance of a basic doublet in the terminal  $\text{V}=\text{O}$  region arises because of weak coupling between these four terminal motions. This is a common feature in molecules containing heavy central atoms (e.g., in  $\text{OsO}_4$ ) and is also found in cage molecules such as  $\text{P}_{10}$  [18]. Clearly, we are still a long way from a complete vibrational characterization of  $\text{V}_4\text{O}_{10}$ , but this kind of experiment illustrates that certain basic questions concerning molecular shape and band assignment may be obtained fairly readily from the isotope patterns of quite complex species.

As a final example of the use of isotopes to provide basic structural information, consider briefly some results recently obtained on high temperature salts of the type  $\text{PO}_3$ .

#### 5. Vapour Phase $\text{MXO}_3$ Species: The Shapes of $\text{KNO}_3$ and $\text{NaPO}_3$

Vapour phase nitrates of general formula  $\text{MNO}_3$  ( $\text{M}$  = alkali metal,  $\text{Tl}$ ) have been known for many years but uncertainty still remains concerning many of their shapes [19]. For these species, it is generally assumed that the anion coordinates through oxygen, and this leads to two popular binding models: a bidentate structure with  $\text{C}_{2v}$  symmetry, and a monodentate structure for which the highest possible symmetry is also  $\text{C}_{2v}$ . For both these structures  $\Gamma_{\text{vib}} = 4\text{A}_1 + 3\text{B}_2 + 2\text{B}_1$  ( $\text{B}_1$  out of plane) and for a general  $\text{MXO}_3$  complex, the two highest frequency modes are expected to be the  $\text{A}_1 + \text{B}_2$   $\text{X}-\text{O}$  stretching modes which correlate with the  $\text{E}'$  mode in free  $(\text{D}_{3h})\text{XO}_3^-$ . In the ir spectrum, these two modes are expected to be of similar intensity and figure 3(i) illustrates this schematically. The only distinguishing feature between these two line diagrams concerns the relative positions of the  $\text{A}_1$  and  $\text{B}_2$  modes.

Chemical arguments indicate that in a bidentate complex, the unique terminal  $\text{X}=\text{O}$  bond will have a higher force constant than the  $\text{X}-\text{O}$  bridge bonds. This leads to the prediction that in a bidentate case  $\nu_{\text{A}_1} > \nu_{\text{B}_2}$  and it may similarly be argued that the converse is true for monodentate binding [20]. This distinction is not readily available from the ir spectrum and at the present time the most satisfactory vibrational method of identifying the symmetries of these bands would be the positive identification of a polarized band in the Raman. In practice, however, this would be quite difficult for this type of system and we have therefore attempted to identify the symmetries of these bands using characteristic isotope patterns in a matrix infrared study.

Figure 3(ii) shows typical line diagrams expected for 25 percent  $^{18}\text{O}$  enrichment for mono and bidentate  $\text{MXO}_3$  species. For these particular calculations, cation motion was



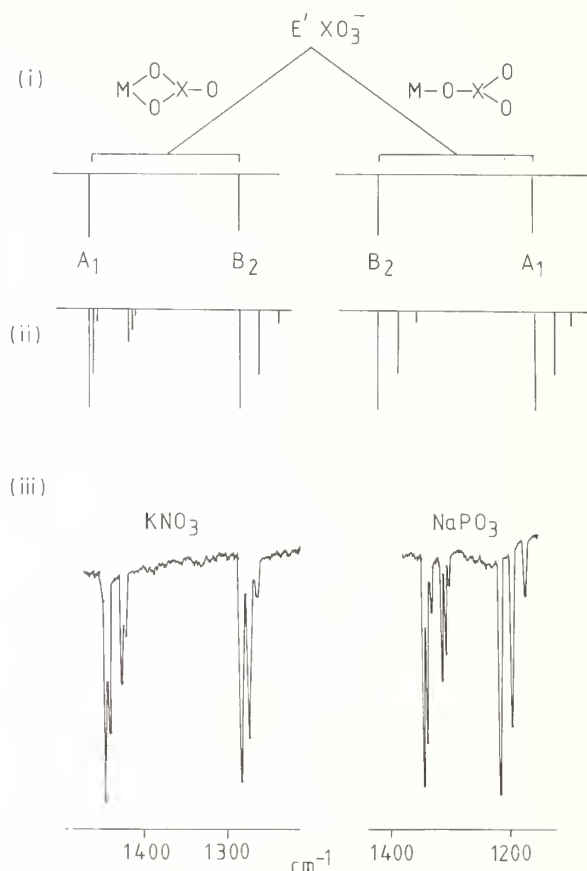


Figure 3. Infrared isotope patterns in monodentate and bidentate  $MXO_3$  species: (i) highest frequency bands in  $MXO_3$  in relation to free  $XO_3^-$ ; (ii) calculated isotope patterns for 25 percent  $^{18}O$  enrichment; and (iii) ir matrix spectra of  $\sim 20$  percent  $^{18}O$  enriched  $KNO_3$  and  $\sim 30$  percent  $^{18}O$  enriched  $NaPO_3$ .

completely ignored and, in general, these patterns turn out to be relatively insensitive to the remaining vibrational fundamentals. They may, therefore, be used to distinguish between mono and bidentate binding. In particular, bidentate complexes are characterized by a basic high frequency doublet, each component of which is expected to show fine structure, whilst in monodentate complexes, the highest frequency band should appear as a well defined triplet. For 25 percent  $^{18}O$  enrichment, the basic doublet has an intensity ratio  $\sim 3:1$ , whilst the triplet shows a  $9:6:1$  pattern.

Figure 3(iii) shows some recent experimental results on  $^{18}O$  enriched  $KNO_3$  and  $NaPO_3$  isolated in low temperature matrices [21,22]. Here the enrichment is  $\sim 20$  percent and  $\sim 30$  percent, respectively, and the spectra point clearly to bidentate binding in both species. Detailed numerical analysis of all the isotope shifts confirms this and the

Table below shows a comparison of observed and calculated isotope bands for  $\text{NaPO}_3$  together with their assignments. This type of characterization by isotope pattern recognition is therefore quite powerful, and may easily be extended to other complex salt vapours.

Table 1. Infrared frequencies ( $1100\text{--}1400\text{ cm}^{-1}$ ) and assignments for  $^{18}\text{O}$ -enriched  $\text{NaPO}_3$  isolated in an Argon matrix at 10 K

Observed	Calculated	Assignment <sup>a</sup>
1341.7	1341.6	$\text{Na}^{16}\text{O}^{16}\text{O} \text{ P}^{16}\text{O}$
1338.0	1337.5	$\text{Na}^{16}\text{O}^{18}\text{O} \text{ P}^{16}\text{O}$
1333.2	1332.8	$\text{Na}^{18}\text{O}^{18}\text{O} \text{ P}^{16}\text{O}$
1312.2	1311.6	$\text{Na}^{16}\text{O}^{16}\text{O} \text{ P}^{18}\text{O}$
1307.5	1306.6	$\text{Na}^{16}\text{O}^{18}\text{O} \text{ P}^{18}\text{O}$
1302.0	1300.4	$\text{Na}^{18}\text{O}^{18}\text{O} \text{ P}^{18}\text{O}$
1211.2	1210.9	$\text{Na}^{16}\text{O}^{16}\text{O} \text{ P}^{16}\text{O}$
	1210.9	$\text{Na}^{16}\text{O}^{16}\text{O} \text{ P}^{18}\text{O}$
1193.3	1193.1	$\text{Na}^{16}\text{O}^{18}\text{O} \text{ P}^{16}\text{O}$
	1192.5	$\text{Na}^{16}\text{O}^{18}\text{O} \text{ P}^{18}\text{O}$
1173.5	1173.0	$\text{Na}^{18}\text{O}^{18}\text{O} \text{ P}^{16}\text{O}$
	1173.0	$\text{Na}^{18}\text{O}^{18}\text{O} \text{ P}^{18}\text{O}$

<sup>a</sup> assuming  $\text{C}_{2v}$  bidentate structure.

## 6. Conclusions

The examples discussed in this paper have been chosen specifically to illustrate how matrix isolation may be used to characterize high temperature vapours, and it is clear that in addition to the stabilization and detection of such species by routine spectrometric methods, the principal advantage lies in the ability to obtain well-resolved vibrational isotope fine structure. For small, light molecules this data can lead to a fairly reliable estimate of interbond angles, and for more complex species these isotope patterns provide a valuable guide to molecular structure. In addition, the standard methods of vibrational analysis via symmetry selection rules are available. However, the small perturbations inevitably produced in a trapped species by the matrix environment undoubtedly mean that

beyond a certain level of characterization, more direct methods of studying high temperature species will be required. Until that time matrix isolation remains one of the most useful and straightforward methods of studying high temperature molecules.

#### References

- [1] See, for example, Downs, A. J. and Peake, S. C., Molecular spectroscopy, Specialist Periodical Report of the Chemical Society, London, I, 523 (1973); also Chadwick, B. M. ibid., III, 281 (1975).
- [2] Vibrational Spectroscopy of Trapped Species, H. E. Hallam, ed. (Wiley and Sons, London, 1973).
- [3] Hastie, J. W., Hauge, R. H., and Margrave, J. L., in Spectroscopy in Inorganic Chemistry, Vol. I, C. N. R. Rao and J. R. Ferraro, eds. (Academic Press, 1970) p. 58.
- [4] Weltner, Jr., W., Adv. High Temp. Chem., 2, 85 (1969).
- [5] Snelson, A., Infrared studies of vaporizing molecules trapped in low temperature matrices, chap. 6 in reference [2].
- [6] See, for example, Loewenschuss, A., Ron, A., and Schnepf, O., J. Chem. Phys. 49, 272 (1968); White, D., Calder, G. V., Hemple, S., and Mann, D. F., J. Chem. Phys. 59, 6645 (1973).
- [7] Allavena, M., Rysnik, R., White, D., Calder, G. V., and Mann, D. E., J. Chem. Phys. 50, 3399 (1969).
- [8] Ogden, J. S., Ber. Bunsenges, Phys. Chem. 83, 76 (1978).
- [9] Beattie, I. R., Blayden, H. E., Hall, S. M., Jenny, S. N., and Ogden, J. S., Dalton, J.C.S., 666 (1976).
- [10] Porter, R. F., Chupka, W. A., and Inghram, M. G., J. Chem. Phys. 23, 216 (1955).
- [11] Schick, H. L., Chem. Rev. 60, 331 (1969).
- [12] Kaufman, M., Muentzer, J., and Klemperer, W., J. Chem. Phys. 47, 3365 (1967).
- [13] Anderson J. S. and Ogden, J. S., J. Chem. Phys. 51, 4189 (1969).
- [14] Hastie, J. W., Hauge, R. H., and Margrave, J. L., Inorg. Chim. Acta, 3, 601 (1969).
- [15] Ogden, J. S., Spectrochim. Acta, 33A, 1059 (1977).
- [16] Jenny S. N. and Ogden, J. S., to be published.
- [17] Berkowitz, J., Chupka, W., and Inghram, M. G., J. Chem. Phys. 27, 87 (1957); Farber, M., Uy, O. M., and Srivastava, R. D., J. Chem. Phys. 56, 5312 (1972).
- [18] Beattie, I. R., Ogden, J. S., and Price, D. D., Inorg. Chem., in press.
- [19] Moore, J. C. and Devlin, J. P., J. Chem. Phys. 68 826 (1978).
- [20] Hester, R. E. and Grossman, W. F. L., Inorg. Chem. 5, 1308 (1966); Brintzinger, H. and Hester, R. E., Inorg. Chem. 5, 980 (1966).
- [21] Beattie, I. R., Ogden, J. S., and Price, D. D., J.C.S. Dalton, submitted for publication.
- [22] Jenny, S. N. and Ogden, J. S., J.C.S. Dalton, submitted for publication.

## Discussion

Question (Gingerich): How did you make sodium phosphite?

Response (Ogden): We heated it.

Question (Gingerich): Did you see other molecular species?

Response (Ogden): It depends which phosphate you take. I can talk to you a long time about all the different sorts of phosphates that we started with. But we vaporized  $\text{Na}_3\text{PO}_4$ .

Now, when you melt that, I think it is true to say that you retain that stoichiometry in the melt. That is not true of meta- and pyro-phosphates. It is an area that we have really only started to explore. I can say that the spectra are certainly different from other phosphates.

Comment (Gingerich): I can say from our studies that we had  $\text{NaPO}_2$  as a major species but followed by  $\text{NaPO}_3$ .

Counter Question (Ogden): I just wondered where the reduction came from?

Response (Gingerich): We had an alumina liner in a molybdenum cell and eventually the liner broke, I think, and we had a reduction.

Question (Cater): I just want to ask a very simple minded question for my own personal information. It looks like the sodium nitrate and the potassium nitrate species have a different structure as molecules. Is there any indication of directionality of bonding in solid nitrates?

Response (Ogden): I don't think you can compare these vapor species with the solid nitrates at all. Basically, when you take these things up into the vapor phase, you just have an ion pair -- I think in the solid, the nitrate ion is fairly close to being roughly  $\text{D}_{3h}$  symmetry.

tion  
sear  
the

T

bus

opic

ced

atrix

stant

zati

I

ura

ure

A

ides

reacti

T

ther

conden

see f

can be

tion.

to

vacu

s

A

ura

ort

ich

add

resolu

is very

freque

plastic

figure



## MATRIX ISOLATION OF HIGH TEMPERATURE SPECIES AND MATRIX PERTURBATION EFFECTS

F. W. Froben  
Institut für Molekülphysik  
Freie Universität Berlin  
Berlin, Germany

The characterization of unstable high temperature molecules of great importance in combustion, plasmas and chemical reactions, depends very much on the knowledge of spectroscopic data. Observations in the gas phase by emission/absorption spectroscopy are complicated by the population of many excited states. This difficulty can be overcome using the matrix-isolation-technique. Especially for high temperature molecules, it has the unique advantage of long sampling times for molecules with low gas phase concentrations and stabilization in an inert environment where the species can be studied at leisure spectroscopically. In many instances, its advantages outweigh the greater sensitivity which is still favorable even when the sensitivity for detection is of mass spectroscopy and laser induced fluorescence.

As large molecules are discussed by J. S. Ogden [1]<sup>1</sup> and inorganic small hydrides, oxides and fluorides by W. Weltner [2], this article will be restricted to experiments where reactions with nitrogen are involved.

The experimental arrangement is shown in figure 1. The molecules can be produced either in an oven heated by direct current or in a fast flow discharge system. They are condensed on a cold window at about 10 K. The window is attached to the He-mixing chamber (see fig. 1) of the cryostat. By regulation of the cold-valve or pumping, the temperature can be varied between 4 and 100 K. The window can be rotated and moved in a vertical direction. The cryostat is inserted into a Fourier IR-Spectrometer (Bruker IFS 114 wavelength 0 to 4000  $\text{cm}^{-1}$  maximal resolution 0.12  $\text{cm}^{-1}$ ). The cryostat can be decoupled from the molecule production line and moved into an EPR-machine to measure IR and EPR spectra of the same sample.

As Fourier IR-measurement of matrix isolated species are still limited to very few laboratories, some advantages and disadvantages will be summarized here [3]. The most important advantage of a Fourier IR-Spectrometer is connected with the optical throughput, which is much larger than for conventional instruments. Due to the computer control and the adding of many scans in the memory, the signal to noise ratio can be improved and a high resolution spectrum recorded in about 1/5 of the time needed for a grating instrument. This is very important for samples at low temperature. Another advantage is the accuracy of the frequency scale due to the He-Ne laser used as a standard and the possibility of data manipulation with the dedicated computer.

Figures in brackets indicate the literature references at the end of this paper.

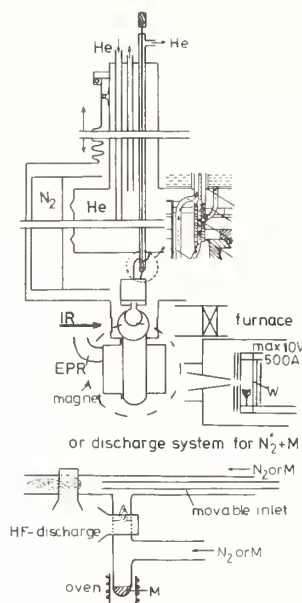


Figure 1. Cryostat and molecule production for matrix isolation spectroscopy.

The Bruker FIR-Spectrometer adds two additional benefits: first, the optical beam is focused on the sample and the beam splitter; and second, the Michelson mirror is on both sides of the movable support to reduce the necessary retardation for a given resolution. But, in spite of all these facts, there are some restrictive disadvantages. Though the system is, in principle, simple, many of the components can produce difficulties. The most serious difficulty is caused by vibrations of the instrument, due, for example, to vacuum pumps, liquid He, even cars or elevators. The vibrations recorded in the Fourier interferogram are folded into the frequency spectrum, so that the spectra have to be recorded with different velocities to distinguish between absorption lines and disturbances.

The data known for diatomic nitrenes are given in table 1. The production of the molecules by simple heating is difficult because the nitrenes decompose during evaporation. One exception is PN, which has been produced by pyrolysis of  $P_3N_5$  by Atkins and Timms [11], with a band at  $1323\text{ cm}^{-1}$  and a  $\sim 10\text{ cm}^{-1}$  half-width assigned to PN.

PN and also other diatomics of group V of the periodic system can be produced by mixing the trihalides with nitrogen in a discharge system. The mixing of gas ( $N_2 + Kr$  or  $N_2 + Ar$ ) with the trihalide vapor before the discharge is somewhat more effective for nitrene production than the reaction of the discharged gas with the vapor. But, in both cases, the nitrene is produced. Besides the mononitrenes, other molecules, like monohalogens, are produced as can be seen by their absorption in the matrix. Figure 2 shows the IR-spectra of PN and PCl in Kr as an example [6].

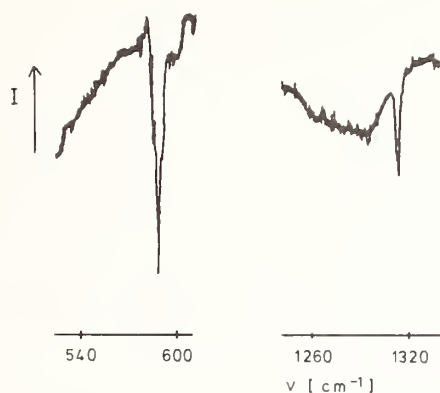


Figure 2. IR spectra of PCl (left) and PN (right) in a Kr matrix.

Table 1. Diatomic nitrenes,  $\omega_e$ -values ( $\text{cm}^{-1}$ ) for gas phase (g) and matrix (m).

I - V	III - V	IV - V	V - V	VI - V	VII - V
NH $^3\Sigma$	BN $^3\Pi$	CN $^2\Sigma$	PN $^1\Sigma$	NO $^2\Pi$	NF $^3\Sigma$
g 3203.2	1514.6	2068.7	1337.2	1904	1141.4
m 3122	1288 <sup>a</sup>	2069.4	1312 <sup>b</sup>	1874	1115
		SiN $^2\Sigma$	AsN $^1\Sigma$	NS $^2\Pi$	NCI $^3\Sigma$
		g 1151.36	1068.5	1219.1	827
		m 1186 <sup>b</sup>			819
			SbN $^1\Sigma$	NSe $^2\Pi$	NBr $^3\Sigma$
			g 864.8	957.5	691.7
					m 689
			BiN		NI
			-		-
			m 668 <sup>b</sup>		595 <sup>c</sup>
	UN	TiN $^2\Sigma$			
	-	g 1080			
	m 1000.9 <sup>d</sup>	1037 <sup>b</sup>			
		ZrN <sup>e</sup>	NbN <sup>f</sup>		

<sup>a</sup> not indicated the data are taken from reference [4]. <sup>a</sup> $\Delta G$  1/2 reference [5].  
Reference [6]. <sup>c</sup>Reference [4]. <sup>d</sup>Reference [8]. <sup>e</sup>Reference [9]. <sup>f</sup>Reference [10].

If the interaction between matrix molecules and the isolated species is small, then vibrational frequencies closely approximate the gas phase values. This is true for most of the diatomics. Table 2 gives some examples.

However differences can be large in certain matrices, see for example MgO and CuO, which are blue shifted. There are several possibilities which explain this. One possibility is that interactions of the ground state with low lying electronic states undergo a change in the matrix, which causes a change in the vibrational spacing of the ground state.

The use of matrix data may not be sufficient to describe the behavior of larger molecules in the gas phase at high temperatures, where the geometry and vibrational frequencies may be different. For example, a linear structure and the measured vibrational frequencies cannot explain the microwave spectra of KCN at high temperatures [19,20]. It is hoped that some of these difficulties can be solved by laser induced fluorescence studies of the matrix isolated species and future microwave spectroscopy [20].

Though matrix isolation spectroscopy has been proven to be extremely valuable for measuring unstable high temperature molecules, it has, in some cases, added new questions. The best understanding of molecular structure and behavior can be achieved by preparing the molecule of interest with a variety of techniques. Characterization of the species should be carried out with as many methods as possible.

Table 2. Comparison of  $\omega_e$  between gas phase and matrix isolation.

<u><math>\Delta\omega_e &lt; 11 \text{ cm}^{-1}</math></u>				
Molecule	State	Gas phase	Matrix	Reference
CN	$X^2\Sigma$	2068.7	2069.6	[12]
	$A^2\Pi$	1814.4	1813	
	$B^2\Sigma$	2164.1	2165.9	
TiO	$X^3\Delta$	1008	1005	[13]
<u><math>\Delta\omega_e &gt; 10 \text{ cm}^{-1}</math></u>				
CuO	$X^2\Pi$	631.5	663	[14]
	$A^2\Sigma$		620	
	$B^2\Pi$	601	605	
MgO	$X^1\Sigma$	785.1	828	[15,16]
	$a^3\Pi$	648		
	$A^1\Pi$	664.4		
	$B^1\Sigma$	824		
PCl	$X^3\Sigma$	552.3 (577)	587	[6,17,18]

## References

- [1] Ogden, J. S., this volume.
- [2] Weltner, W., Jr., this volume.
- [3] For a full evaluation: Green, D. W. and Reedy, G. T., Fourier Transform Infrared Spectroscopy, Vol. 1, I. R. Ferraro and L. J. Basile, ed. (Academic Press, 1978) p. 1.
- [4] Data from: Rosen, B., Spectroscopic Data of Diatomic Molecules (Pergamon Press, 1970). Additions by Barrow, R. F. (1973) and (1975), Suchard, S. N., Spectroscopic Data (Plenum Press, 1975).
- [5] Mosher, O. A. and Frosch, R. P., J. Chem. Phys. 52, 5781 (1970).
- [6] Froben, F. W., to be published.
- [7] Minkwitz, R. and Froben, F. W., Chem. Phys. Lett. 39, 473 (1976), and unpublished results.
- [8] Green, D. W. and Reedy, G. T., J. Chem. Phys. 65, 2921 (1976).
- [9] Bates, J. K. and Dunn, T. M., Can. J. Phys. 54, 1216 (1976).
- [10] Dunn, T. M. and Rao, K. M., Nature, 222, 266 (1969).
- [11] Atkins, R. M. and Timms, P. L., Spectrochim. Acta, 33A, 853 (1977).
- [12] Bondybey, V. E., J. Chem. Phys. 66, 995 (1977).
- [13] Brom, J. M., Jr. and Broida, H. P., J. Chem. Phys. 63, 1718 (1975).
- [14] Griffiths, M. J. and Barrow, R. F., J. Chem. Soc. Faraday Trans. II, 73, 943 (1977).
- [15] Ikeda, T., Wong, N. B., Harris, D. O. and Field, R. W., J. Mol. Spectr. 68, 452 (1977).
- [16] Andrews, L., Prochaska, E. S. and Ault, B. S., J. Chem. Phys. 69, 556 (1978).
- [17] Coxon, J. A. and Wickramaaratchi, M. A., J. Mol. Spectr. 68, 372 (1977).
- [18] Basco, N. and Yee, K. K., Spectrosc. Lett. 1, 19 (1968).
- [19] Ismail, Z. K., Hauge, R. H. and Margrave, J. L., J. Mol. Spectr. 54, 402 (1975).
- [20] Ehlert, T. C. (Marquette Univ.) and Törring, T. (Freie Universität Berlin): personal communication; see the discussion by Törring, T., this volume.

## Discussion

Comment (Hauge): Bill Weltner, Jr. could probably expound on this best of anyone, but it is probably too complicated to really get into. I want to point out that this blue matrix shift is really surprising in the case of copper oxide and magnesium oxide. All other shifts that we have seen have been to the red of the gas phase value. I am not sure that that doesn't say that there is something peculiar about MgO and CaO.

One thought I had was that--my concept of matrix shifts for ionic species is that it depends very much on the dipole moment change in going from the ground state to the first vibrationally excited state. The concept there is that your dipole moment increases slightly in the excited state and so you have a greater interaction of the excited state



with the matrix and so you have a reduced spacing between the two states. Now, if in fact the spacing increases, that suggests the dipole moment has decreased in the excited state which makes  $\text{MgO}$  a very unusual species and  $\text{CaO}$  also.

I am not sure that you could get away with saying that low lying excited states have become the ground state in the matrix. That, I don't think has ever been shown to be a case in point.

Moderator (Weltner): I would like to congratulate you on making all of those nitrates. We tried and failed. You really got them, did you? (Laughter.)

MATRIX ISOLATION STUDY OF THE VIBRATIONAL AND ELECTRONIC  
SPECTRA OF PO AND HPO<sup>1</sup>

Michel Larzilliere<sup>2</sup> and Marilyn E. Jacox

National Bureau of Standards

Washington, DC 20234

On vacuum ultraviolet photolysis of PH<sub>3</sub> isolated in an argon matrix at 14 K, an infrared absorption assigned to the bending fundamental of PH<sub>2</sub> and visible-ultraviolet absorptions associated with the A-X transitions of PH<sub>2</sub> and PH and with the C-X transition of P<sub>2</sub> appeared. In the presence of N<sub>2</sub>O, which provided a photolytic source of O atoms, bands from three electronic transitions of PO also appeared, as did a complicated pattern of infrared absorptions. Detailed isotopic substitution studies have supported the assignment of an absorption at 1218 cm<sup>-1</sup> to the vibrational fundamental of ground-state PO and of absorptions at 1188 and 2100 cm<sup>-1</sup> to the two stretching fundamentals of ground-state HPO. These assignments have received further support from studies of the rapid quenching in an excess of argon at 14 K of the products of the reaction of PH<sub>3</sub> with an Ar:O<sub>2</sub> mixture which had been passed through a low power microwave discharge. Other infrared absorptions present in these experiments may be contributed by such species as PO<sub>2</sub>. The techniques employed in these experiments can also be applied to the stabilization of the simple oxides and oxyhydrides of other Group IV and Group V elements in concentrations sufficient for observation of their vibrational and electronic absorption spectra.

1. Introduction

Although the chemical and spectroscopic properties of the nitrogen oxides have been quite well characterized, those of the phosphorus oxides are comparatively obscure. The already complex chemistry of the nitrogen-oxygen system is still further complicated by the potential participation of the d orbitals of the phosphorus atom in chemical bonds, leading

<sup>1</sup>This research was supported by the Planetary Atmospheres program of the National Aeronautics and Space Administration under Grant W-13424.

<sup>2</sup>Guest worker at the National Bureau of Standards, 1975. Present address: Equipe de Spectroscopie, C.N.R.S., Saint-Etienne, France.

to a large number of stable  $P_xO_y$  species. To study the simplest phosphorus oxides and oxyhydrides, it has heretofore been necessary to work with high-temperature vapors, resulting in broad infrared and ultraviolet absorption bands and significant "hot band" contributions to the spectrum. In practice, such absorption spectra are not available in the scientific literature; analysis of the even more complicated emission spectra of PO and HPO, observed in flames and high-temperature vapors, has provided the most definitive information on the vibrational and electronic energy levels of these two compounds. Further spectroscopic studies of the simple phosphorus oxides and oxyhydrides would advance our understanding of the role of the  $d$  orbitals of third-row elements in determining the structures and energy levels of their compounds. Such studies would also be of interest in relation to energy generation processes and to the chemistry of planetary atmospheres. Reactions involving PO and HPO are believed to play an important role in flame inhibition by phosphorus compounds [1]<sup>3</sup>. The presence of phosphorus impurity in the fossil fuels mandates the consideration of the phosphorus oxides in the characterization of MHD power generation systems. Compounds of phosphorus with oxygen and hydrogen may also play significant roles in the chemistry of the atmospheres of the outer planets. Phosphine has been detected in the atmospheres of both Jupiter [2] and Saturn [3,4]. In regions of the outer planetary atmospheres where water is also present, the oxides and oxyhydrides of phosphorus may be formed.

The matrix isolation technique affords important advantages for studies of the absorption spectra of simple P-O-H compounds. Because atoms can diffuse through rare-gas matrices at 14 K but molecules cannot, spectral contributions from the larger phosphorus oxides and oxyhydrides should be minimal. At the low temperatures used for such studies, "hot bands" are completely eliminated from the absorption spectrum. Typically, infrared and ultraviolet absorptions lie within about 1 percent of the gas-phase band centers, and the infrared absorptions are sufficiently sharp to permit the resolution of isotopic shifts and splittings in studies of oxygen-18 enriched systems. Such data are crucial to the positive identification of the product species and sometimes also permit the derivation of approximate structures. In consideration of the need for spectroscopic data for these species and of these advantages of matrix isolation experiments, photolytic and discharge sampling techniques have been devised for stabilizing observable concentrations of simple compounds of the Group IV and Group V elements with oxygen and hydrogen in solid argon at cryogenic temperatures. The application of these techniques to infrared and ultraviolet spectroscopic studies of the P-O-H system is described in the following discussion.

## 2. Experimental Details<sup>4</sup>

$PH_3$  and  $PD_3$  were prepared by the reaction of zinc phosphide with  $H_2O$  and  $D_2O$ ,

---

<sup>3</sup>Figures in brackets indicate the literature references at the end of this paper.

<sup>4</sup>Certain commercial instruments and materials are identified in this paper in order to specify adequately the experimental procedure. In no case does such identification imply recommendation or endorsement by the National Bureau of Standards, nor does it imply that the instruments or materials identified are necessarily the best available for the purpose.

respectively. The product of this reaction was dried by passage through a column packed with  $\text{P}_2\text{O}_5$ . Trace impurities of relatively volatile gases were removed by condensing the dried product at 77 K and pumping on the solid material.  $\text{N}_2\text{O}$  and  $\text{O}_2$  (Matheson Co., Inc.) and their oxygen-18 enriched counterparts (Miles Laboratories, Inc.) were used without further purification, as was the argon used as matrix material in all of the experiments. Gas mixtures were prepared using standard manometric procedures. All observations were conducted at 14 K.

The first series of experiments was concerned with the infrared and ultraviolet spectroscopic characterization of the products of the 1216-Å photolysis of  $\text{Ar:PH}_3$  and  $\text{Ar:PD}_3$  samples of mole ratio ranging from 200 to 500. The photolysis procedures used in these experiments have previously been described [5]. The second series of experiments involved the addition of a small concentration of  $\text{N}_2\text{O}$  to the sample to provide a photolytic source of atoms, which can migrate through the argon matrix.  $\text{Ar:PH}_3\text{:N}_2\text{O}$  mole ratios ranging from 100:1:1 to 800:1:1 were employed in this series of experiments. The third series of experiments involved the codeposition of an  $\text{Ar:PH}_3 = 200$  sample with an  $\text{Ar:O}_2 = 100$  sample that had been passed through a microwave discharge. The discharge configuration used for these studies was similar to that used in previous studies of the products of the interaction of excited argon atoms with small molecules [6,7]. The  $\text{Ar:O}_2$  mixture was admitted into the discharge tube at a controlled low pressure of approximately 1 Torr. A 2450 MHz discharge was maintained in this tube at a 20-30 W power level. The excited gas mixture streamed out of the discharge tube through a pinhole of approximately  $2 \text{ mm}^2$  area and mixed with the  $\text{Ar:PH}_3$  sample, which was introduced at a controlled low pressure through an annular ring which was concentric with the pinhole. The reaction products were frozen onto the 14 K observation surface approximately 2 cm downstream from the pinhole. Backstreaming of the  $\text{PH}_3$  into the discharge region was minimized by the pinhole, which also helped to maintain a suitable discharge pressure at a sufficiently low  $\text{Ar:O}_2$  flow rate to avoid warming of the cryogenic surface during condensation of the sample.

The infrared spectra of the resulting deposits were studied between 400 and  $4000 \text{ cm}^{-1}$  using a Beckman IR-9 infrared spectrophotometer. Under typical scanning conditions, the resolution and the absolute and relative frequency accuracies are estimated to be  $1 \text{ cm}^{-1}$  between 400 and  $2000 \text{ cm}^{-1}$  and  $2 \text{ cm}^{-1}$  between 2000 and  $4000 \text{ cm}^{-1}$ .

Absorption studies between 1900 and 5500 Å were conducted using an 0.8 m evacuated Bert-Fastie scanning monochromator equipped with 50 micron slits, with a grating blazed at 3000 Å, and with an EMI 6255S photomultiplier detector. A deuterium background source was used between 1900 and 3650 Å and a tungsten background source between 3650 and 5500 Å. The estimated error in the determination of relatively sharp band maxima was 2.5 Å, corresponding to  $62 \text{ cm}^{-1}$  at 2000 Å,  $40 \text{ cm}^{-1}$  at 2500 Å,  $27 \text{ cm}^{-1}$  at 3000 Å,  $16 \text{ cm}^{-1}$  at 4000 Å, and  $10 \text{ cm}^{-1}$  at 5000 Å. Certain of the absorptions were comparatively broad, increasing the error associated with the determination of their positions.

### 3. Observations

#### 3.1 Ar:PH<sub>3</sub> photolysis

Typical absorption spectra observed between 5100 and 4000 Å and between 3600 and 3100 Å for Ar:PH<sub>3</sub> and Ar:PD<sub>3</sub> samples deposited at 14 K with concurrent hydrogen-discharge photolysis are shown in figures 1 and 2, and the positions and assignments of these absorptions are summarized in table 1. The absorption maxima of the broad, structured bands observed between 5500 and 4200 Å in photolyzed Ar:PH<sub>3</sub> samples are red-shifted by approximately 100 cm<sup>-1</sup> from the band origins of the 0v'0-000 progression of the A-X transition of PH<sub>2</sub>, reported by Berthou and co-workers [8]. Similarly, the absorption maxima observed between 5100 and 4100 Å in photolyzed Ar:PD<sub>3</sub> samples correspond well with the gas-phase band centers for the corresponding progression of PD<sub>2</sub>, reported by Vervloet and Berthou [9]. The determination of the absorption maxima for the matrix-isolated samples is somewhat complicated by the structure of the bands. Possibly the sharp long-wavelength edge and the partly resolved peak associated with it, evident for the PH<sub>2</sub> bands having relatively small values of v', are associated with the zero phonon transitions, with the broad absorptions at slightly shorter wavelengths corresponding to the phonon wings of the vibronic bands. Since simple hydrides can rotate in the argon lattice at 14 K, the broad, shorter wavelength peaks may also result from the excitation of low-J rotational structure. The trapping of PH<sub>2</sub> in several distinct types of site in the argon lattice may also contribute to the breadth and structure of the observed bands. The very prominent absorption at 3448 Å (29,002 cm<sup>-1</sup>) and the weaker absorptions.

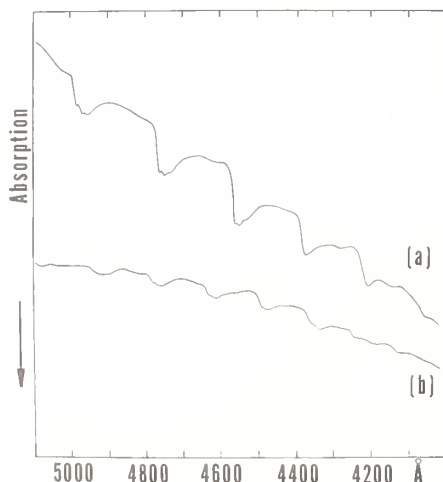


Figure 1. (a) Ar:PH<sub>3</sub> = 200. 14 K. 74.9 μmol PH<sub>3</sub> deposited over period of 282 min with concurrent hydrogen-discharge photolysis. (b) Ar:PD<sub>3</sub> = 200. 14 K. 46.5 μmol PD<sub>3</sub> deposited over period of 197 min with concurrent hydrogen-discharge photolysis.



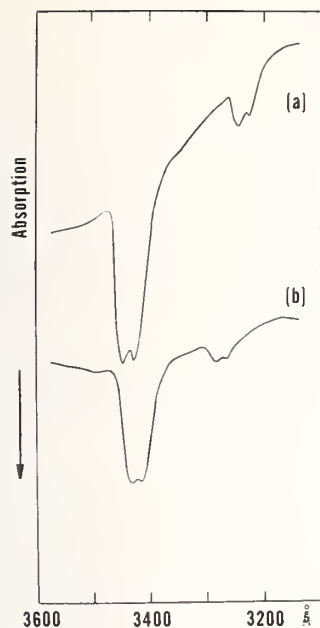


Figure 2. (a) Ar:PH<sub>3</sub> = 200. 14 K. 33.2 μmol PH<sub>3</sub> deposited over period of 150 min with concurrent hydrogen-discharge photolysis. (b) Ar:PD<sub>3</sub> = 200. 14 K. 17.7 μmol PD<sub>3</sub> deposited over period of 75 min with concurrent hydrogen-discharge photolysis.

Table 1. Absorptions<sup>a</sup> which appear between 5500 and 3000 Å on 1216-Å photolysis of phosphine isolated in an argon matrix at 14 K.

Table 1a. Ar:PH<sub>3</sub> = 200

$\lambda$ (Å)	$\nu$ (cm <sup>-1</sup> )	$\Delta\nu^b$ (cm <sup>-1</sup> )	$\nu_{\text{gas}}$ (cm <sup>-1</sup> )	Assignments
5498w	18,188		18,277	PH <sub>2</sub> A-X 000-000
5222w	19,150		19,226	PH <sub>2</sub> A-X 010-000
4975sh	20,101			
4961m	20,157*		20,165	PH <sub>2</sub> A-X 020-000
4948m	20,210	931		
4755sh	21,030			
4742m-s	21,088*		21,094	PH <sub>2</sub> A-X 030-000
4728m-s	21,151	904		
4555sh	21,954			
4547m-s	21,992*		22,010	PH <sub>2</sub> A-X 040-000
4530sh	22,075	891		
4370m	22,883*		22,911	PH <sub>2</sub> A-X 050-000
4278vw,br	23,375	898		
4205w-m	23,781*		23,800	PH <sub>2</sub> A-X 060-000
4145vw,br	24,125			
3448vs	29,002*			PH A-X 0-0
3428vs	29,172	1815		
3245m	30,817*			PH A-X 1-0
3225m	31,008			

Table 1 (Continued)

Table 1b. Ar:PD<sub>3</sub> = 200

$\lambda$ (Å)	$\nu$ (cm <sup>-1</sup> )	$\Delta\nu^{(b)}$ (cm <sup>-1</sup> )	$\nu_{\text{gas}}$ (cm <sup>-1</sup> )	Assignments
5078vw	19,693*	665	19,646	PD <sub>2</sub> A-X 020-000
4912w,br	20,358*		20,326	PD <sub>2</sub> A-X 030-000
4780sh	20,921	659		
4758w-m	21,017*		20,999	PD <sub>2</sub> A-X 040-000
4630sh	21,598	684		
4608-m	21,701*		21,666	PD <sub>2</sub> A-X 050-000
4490sh	22,272	645		
4475m	22,346*		22,322	PD <sub>2</sub> A-X 060-000
4365w-m	22,910*	564	22,972	PD <sub>2</sub> A-X 070-000
4335w-m	23,068			
4242w	23,574*	664	23,606	PD <sub>2</sub> A-X 080-000
4190vw,br	23,866			
4130w,br	24,213*	639	24,233	PD <sub>2</sub> A-X 090-000
3432vs	29,138*			PD A-X 0-0
3414vs	29,291	1294		
3286m	30,432*			PD A-X 1-0
3262m	30,656			

<sup>a</sup>vw--very weak; w--weak; m--medium; s--strong; vs--very strong; sh--shoulder; br--broad.

<sup>b</sup>Separations between starred absorptions.

absorption at 3245 Å (30,817 cm<sup>-1</sup>) in the Ar:PH<sub>3</sub> studies correspond well with the 0-0 and 1-0 band centers of the A-X transition of gas-phase PH, observed by Rostas and co-workers [10] at 29,318 and 31,152 cm<sup>-1</sup>, respectively. There is a similar correspondence between the 3432 Å (29,138 cm<sup>-1</sup>) and 3286 Å (30,432 cm<sup>-1</sup>) product absorptions of the Ar:PD<sub>3</sub> studies and the corresponding bands of gas-phase PD, reported by these same workers at 29,379 and 30,736 cm<sup>-1</sup>, respectively. Red-shifts of approximately 300 cm<sup>-1</sup> are typical of argon-matrix observations in the near ultraviolet.

The absorption spectra of photolyzed Ar:PH<sub>3</sub> and Ar:PD<sub>3</sub> samples in the 1900-3000 Å spectral region are relatively complicated. The positions and approximate relative intensities of the peaks in this spectral region are summarized in table 2. The most prominent progression, with band spacings of about 450 cm<sup>-1</sup>, has its onset near 2145 Å. The absorption band system, shown in figure 3, can be detected even in the early stages of photolysis. In one experiment, it began to appear on exposure of an unphotolyzed deposit to

Table 2. Absorptions<sup>a</sup> which appear between 3000 and 1900 Å on 1216-Å photolysis of phosphine isolated in an argon matrix at 14 K.

PH <sub>3</sub>			PD <sub>3</sub>			Assignments
λ (Å)	ν (cm <sup>-1</sup> )	Δν <sup>b</sup> (cm <sup>-1</sup> )	λ (Å)	ν (cm <sup>-1</sup> )	Δν <sup>b</sup> (cm <sup>-1</sup> )	
2950w,br	33,898		2942w,br	33,990		P0 B'(D')-X 1-0
			2910w,sh	34,364*		P0 B-X 3-0
			2892w	34,578	972	
2832w	35,311*		2830vw	35,336*		P0 B-X 4-0
2798w,br	35,740	987			1028	
			2772w	36,075		
2755w	36,298*		2750w	36,364*		P0 B-X 5-0
2732vw	36,603	1043			977	
2678w-m	37,341*		2678w-m	37,341*		P0 B-X 6-0
2655w-m	37,665	973			944	
2610w-m	38,314*		2612w	38,285*		P0 B-X 7-0
		871	2590w-m	38,610	931	
2552w	39,185*		2550w	39,216*	945	P0 B-X 8-0
			2520w-m	39,683		
			2490w-m	40,161*		P0 B-X 9-0
			2465w	40,568		
			2432w	41,118*		P0 B-X 10-0
			2412vw	41,459		
			2302vw	43,440*	847	P0 C'-X 0-0
			2258w	44,287*	880	P0 C'-X 1-0
2220w,br			2214w-m	45,167*	768	P0 C'-X 2-0
2172w,br			2177w-m	45,935*		P0 C'-X 3-0
2145w-m	46,620*	417	2142w-m	46,685*	440	P <sub>2</sub> C-X 0-0
2126w-m	47,037*	469	2122m-s	47,125*	471	P <sub>2</sub> C-X 1-0
2105w-m	47,506*	456	2101m-s	47,596*	498	P <sub>2</sub> C-X 2-0
2085w-m	47,962*	464	2081s	48,054*	443	P <sub>2</sub> C-X 3-0
2065w-m	48,426*	474	2062s	48,497*	475	P <sub>2</sub> C-X 4-0
2045w	48,900*		2042s	48,972*	435	P <sub>2</sub> C-X 5-0
			2024m-s	49,407*	443	P <sub>2</sub> C-X 6-0
			2006m-s	49,850*	452	P <sub>2</sub> C-X 7-0
			1988m	50,302*	459	P <sub>2</sub> C-X 8-0
			1970m	50,761*	469	P <sub>2</sub> C-X 9-0
			1952w-m	51,230*	396	P <sub>2</sub> C-X 10-0
			1937w	51,626*		P <sub>2</sub> C-X 11-0

<sup>a</sup>vw--very weak; w--weak; m--medium; s--strong; br--broad.

<sup>b</sup>Separations between starred absorptions.

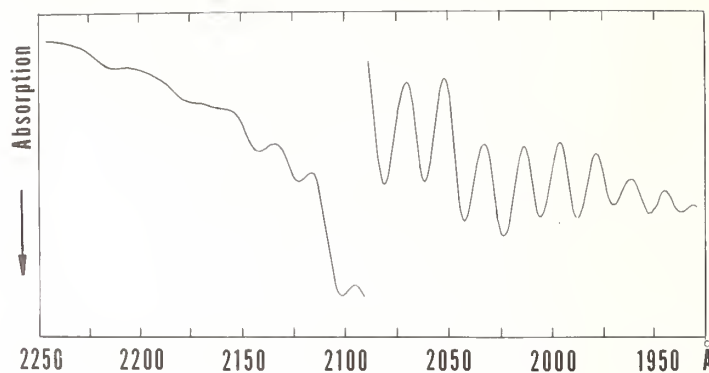


Figure 3. Ar:PD<sub>3</sub> = 400. 14 K. 13.4 μmol PD<sub>3</sub> deposited over period of 111 min with concurrent hydrogen-discharge photolysis.

the deuterium background lamp for a study of the initial absorption pattern of the sample. Creutzberg [11] has found values  $T_e = 46,941.33 \text{ cm}^{-1}$ ,  $w_e = 473.92 \text{ cm}^{-1}$ , and  $w_e x_e = 2.34 \text{ cm}^{-1}$  for the  $C \Sigma_u^+$  state of P<sub>2</sub> in the gas phase. The band assignment given in table 2 for the progression observed between 2142 and 1937 Å in the matrix experiments corresponds very well with the gas-phase assignment for the  $C \Sigma_u^+ - X \Sigma_g^+$  transition of P<sub>2</sub>, with a red shift of approximately  $300 \text{ cm}^{-1}$  in the argon matrix. Relatively weak absorptions between 3000 and 2170 Å varied in prominence from one experiment to another. Except for a weak, broad absorption at 2798 Å in the Ar:PH<sub>3</sub> study summarized in table 2, all of these bands were unshifted on deuterium substitution in the molecule. As is indicated in table 2, it is possible to assign virtually all of them to three electronic transitions of P<sub>0</sub>. With allowance for small matrix shifts, these bands correspond well with the positions of the corresponding gas-phase absorptions of P<sub>0</sub> calculated using the spectroscopic constants summarized by Ngo and co-workers [12]. Their detailed assignment will be considered in a separate publication [13]. The photolysis of traces of water desorbed from the walls of the deposition system would provide a suitable source of O atoms for reactions in the matrix leading to the stabilization of P<sub>0</sub>.

The infrared spectrum of photolyzed Ar:PH<sub>3</sub> samples is relatively simple. A product absorption at  $1103 \text{ cm}^{-1}$ , on the low-frequency shoulder of the relatively broad  $1115 \text{ cm}^{-1}$  absorption of PH<sub>3</sub>, corresponds very well with the value  $\nu_2 = 1101.4 \text{ cm}^{-1}$  reported for gas-phase PH<sub>2</sub> by Dixon, Duxbury, and Ramsay [14], providing still further evidence for the stabilization of PH<sub>2</sub> in these experiments. No absorptions attributable to PH<sub>2</sub> appeared in the PH stretching region, nor did an infrared absorption of PH appear near  $2276 \text{ cm}^{-1}$ , the position calculated for the ground-state vibrational fundamental of PH from the constants given by Rostas and co-workers [10]. The only other photolysis product absorptions were two moderately intense peaks at  $1218$  and  $1188 \text{ cm}^{-1}$ . The molecular constants given for

ground-state PO by Ngo and co-workers [12] yield a value  $\Delta G(1/2) = 1220.26 \text{ cm}^{-1}$ , in excellent agreement with the observed absorption at  $1218 \text{ cm}^{-1}$  in the argon-matrix experiments. The analysis of the emission spectrum of HPO by Lam Thanh and Peyron [15] has yielded a value of  $179 \text{ cm}^{-1}$  for the ground-state PO stretching fundamental of this species, in reasonable agreement with the  $1188 \text{ cm}^{-1}$  product absorption of the argon-matrix experiments. Evidence presented in the following discussion supports this assignment.

### 3.2 Ar:PH<sub>3</sub>:N<sub>2</sub>O photolysis

Ultraviolet spectra obtained in Ar:PH<sub>3</sub>N<sub>2</sub>O photolysis experiments were similar to those characteristic of Ar:PH<sub>3</sub> photolysis experiments, except that the absorptions assigned to the three PO transitions were more prominent. The visible absorption band system of HPO was undetectably weak. In contrast, addition of N<sub>2</sub>O to the sample resulted in the development of a rather complex pattern of infrared absorptions. Spectral regions of especial interest in a typical experiment are shown in figure 4. The absorptions of residual unphotolyzed PH<sub>3</sub> and N<sub>2</sub>O are indicated, as are the peaks already assigned to PH<sub>2</sub> and PO. In addition, the  $1188 \text{ cm}^{-1}$  peak is readily assigned to HPO. The  $1218$  and  $1188 \text{ cm}^{-1}$  peaks were considerably more prominent in the Ar:PH<sub>3</sub>:N<sub>2</sub>O experiments than in the Ar:PH<sub>3</sub> experiments, where their presence resulted from traces of water impurity. The peak optical densities of all of the infrared product absorptions characteristic of the presence of an oxygen-atom source in the sample are summarized in table 3. All of the absorptions persisted in the most dilute samples studied, but in the highest mole ratio sample the PO absorption was more than twice as intense as any other product absorption. The contours of the  $863\text{-}8$  and  $1320\text{-}5 \text{ cm}^{-1}$  absorptions also changed as the sample was diluted. Lam Thanh and Peyron [15] have identified the ground-state bending fundamental of HPO at  $983 \text{ cm}^{-1}$ . This absorption was not observed in the present study, presumably because it is weak. It may also have been overlapped by the prominent  $994 \text{ cm}^{-1}$  absorption of PH<sub>3</sub>.

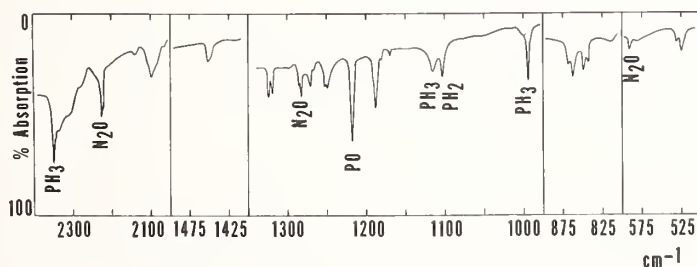


Figure 4. Ar:PH<sub>3</sub>:N<sub>2</sub>O = 400:1:1. 14 K. 21.7  $\mu\text{mol}$  PH<sub>3</sub> deposited over period of 346 min with concurrent hydrogen-discharge photolysis.



Table 3. Peak optical densities of product absorptions in typical studies<sup>a</sup> of the reaction of O atoms with PH<sub>3</sub> in an argon matrix.

cm <sup>-1</sup>	Ar: PH <sub>3</sub> : N <sub>2</sub> O			Ar: PH <sub>3</sub> = 200 + (Ar: O <sub>2</sub> ) <sup>*</sup> = 100	
	200:1:1	400:1:1	800:1:1	Initial	Hg Photolysis
461	0.047	0.023	0.014	0.039	0.039
525	0.071	0.048	0.033	0.053	0.091
849	0.149	0.103	0.063	0.083 <sup>c</sup>	0.151
863-8	0.288	0.119	0.091 <sup>b</sup>	...	...
1188	0.337	0.166	0.064	0.160	0.196
1218	0.401	0.291	0.230	0.114	0.162
1250	0.176	0.073	0.049	0.059	0.083
1271	0.107	0.068	0.094	0.037	0.054
1320-5	0.157	0.089	0.085 <sup>b</sup>	0.055 <sup>b</sup>	0.079 <sup>b</sup>
1450	0.109	0.048	0.026	0.084	0.114
2100	0.196	0.101	0.043	0.054	0.078

<sup>a</sup>Ar: PH<sub>3</sub>: N<sub>2</sub>O samples deposited with concurrent 1216-Å photolysis. Ar: PH<sub>3</sub> = 200 sample codeposited with Ar: O<sub>2</sub> = 100 sample that had been passed through a microwave discharge; sample subsequently exposed to mercury-arc radiation.

<sup>b</sup>868, 1320 cm<sup>-1</sup> peaks more prominent, used for optical density calculation.

<sup>c</sup>Shoulder on 843 cm<sup>-1</sup> peak.

In studies of the photolysis of Ar:PD<sub>3</sub>:N<sub>2</sub>O samples, the 1103 cm<sup>-1</sup> absorption of PH<sub>2</sub> was replaced by a weak absorption at 797 cm<sup>-1</sup> which can be assigned to PD<sub>2</sub>. The 1218 cm<sup>-1</sup> absorption of PO was, of course, unshifted. The analog of the 1188 cm<sup>-1</sup> absorption of HPO was shifted by only 2 cm<sup>-1</sup>, to 1186 cm<sup>-1</sup>, in agreement with the observations of Lam Thanh and Peyron [15]. These workers also assigned the ground-state bending fundamental of DPO at 749 cm<sup>-1</sup>. A weak absorption at 749 cm<sup>-1</sup> in the matrix experiments was probably contributed by DPO. The absorptions at 461, 525, 849, and 2100 cm<sup>-1</sup> did not appear in the Ar:PD<sub>3</sub>:N<sub>2</sub>O photolysis studies. A new, moderately intense absorption at 1531 cm<sup>-1</sup>, with a shoulder at 1525 cm<sup>-1</sup>, can be correlated with the 2100 cm<sup>-1</sup> absorption of the Ar:PH<sub>3</sub>:N<sub>2</sub>O experiments; the ratio of the two frequencies is 0.73, a typical value for the ratio of a deuterium- to a hydrogen-stretching frequency. The 863-8, 1271, 1320-5, and 1450 cm<sup>-1</sup> peaks were unshifted on deuterium substitution in the system, but the 1250 cm<sup>-1</sup> peak was replaced by a pair of absorptions at 1241 and 1256 cm<sup>-1</sup>.

In still other experiments utilizing both PH<sub>3</sub> and PD<sub>3</sub>, oxygen-18 enriched N<sub>2</sub>O was substituted. Only the general outline of the observations on these systems will be present here; the detailed numerical data are of particular importance in the spectroscopic analysis which will form the subject of a separate publication [13]. The absorption of P<sup>18</sup>O was

readily identified at  $1173\text{ cm}^{-1}$ . The constants given for ground-state  $\text{P}^{18}\text{O}$  by Ngo and coworkers [12] yield a gas-phase value  $\Delta G(1/2) = 1175\text{ cm}^{-1}$ . The red shift of  $2\text{ cm}^{-1}$  for  $\text{P}^{18}\text{O}$  in an argon matrix is equal to that observed for  $\text{P}^{16}\text{O}$ . The  $\text{PO}$  stretching fundamental of  $\text{P}^{18}\text{O}$ , previously unreported, was observed at  $1143\text{ cm}^{-1}$ , and that of  $\text{DP}^{18}\text{O}$  was observed at  $1142\text{ cm}^{-1}$ . A very weak absorption at  $746\text{ cm}^{-1}$  could also be assigned to  $\text{DP}^{18}\text{O}$ . The  $2100\text{ cm}^{-1}$  absorption of the  $\text{Ar:PH}_3:\text{N}_2\text{O}$  studies and its counterpart at  $1531\text{ cm}^{-1}$  in the  $\text{PD}_3:\text{N}_2\text{O}$  studies were unshifted when  $\text{N}_2^{18}\text{O}$  was used. The  $863\text{-}8\text{ cm}^{-1}$  absorptions were shifted to  $825\text{-}30\text{ cm}^{-1}$  in studies utilizing 89 percent oxygen-18 enriched  $\text{N}_2\text{O}$ , but a very complicated absorption pattern resulted in studies utilizing 25 percent oxygen-18 enriched  $\text{N}_2\text{O}$ . In studies on the 89 percent oxygen-18 enriched  $\text{N}_2\text{O}$  sample, the relatively broad  $1050\text{ cm}^{-1}$  peak was shifted to  $1205\text{ cm}^{-1}$ , the sharper  $1271\text{ cm}^{-1}$  peak to  $1235\text{ cm}^{-1}$ , the  $120\text{-}5\text{ cm}^{-1}$  pair of absorptions to  $1281\text{-}6\text{ cm}^{-1}$ , with a weak intermediate pair of absorptions at  $1301\text{-}7\text{ cm}^{-1}$ , and the  $1450\text{ cm}^{-1}$  peak to  $1408\text{ cm}^{-1}$ .

### 3.3 $\text{Ar:PH}_3 + \text{Ar:O}_2$ discharge studies

Regions of especial interest in the infrared spectrum of an  $\text{Ar:PH}_3$  sample which was deposited with an  $\text{Ar:O}_2$  sample that had been passed through a low-power microwave discharge are shown in figure 5. A prominent pair of absorptions near  $1040\text{ cm}^{-1}$  was readily assigned to the expected  $\text{O}_3$  product, and a moderately strong absorption at  $805\text{ cm}^{-1}$  and a weaker, broad peak at  $791\text{ cm}^{-1}$  behaved appropriately on isotopic substitution for assignment to the antisymmetric stretching fundamental of  $\text{O}_3^-$  [16]. A sharp, prominent peak at  $1388\text{ cm}^{-1}$  can be assigned to  $\text{HO}_2$  [17,18]. The  $1102\text{ cm}^{-1}$  absorption of  $\text{HO}_2$  would overlap the  $1103\text{ cm}^{-1}$  absorption of  $\text{PH}_3$ . Although the extent of  $\text{PH}_3$  decomposition was significantly less than in the photolysis experiments, the yield of oxidation products was comparable to that in the earlier studies. Absorptions in the  $400\text{-}550\text{ cm}^{-1}$  spectral region were relatively well developed in the discharge experiments. The  $863\text{-}8\text{ cm}^{-1}$  absorptions did not appear, but a moderately intense, structured absorption appeared at  $910\text{ cm}^{-1}$ . As is shown in the broken-line trace of figure 5, irradiation of the sample deposit with the full light of a medium-pressure mercury arc led to the photodecomposition of  $\text{O}_3$  and  $\text{O}_3^-$  and to a growth in the intensities of most of the product absorptions which were common to the photolysis studies. Peak optical densities of these absorptions before and after mercury-arc irradiation of a typical sample are summarized in table 3. The contours of several of the peaks, including those at  $843$ ,  $1321$ ,  $1450$ , and  $2100\text{ cm}^{-1}$ , differed from those typical of the photolysis experiments, quite possibly because of the different types of site in which products may be trapped in the presence of approximately 1 percent of  $\text{O}_2$  in the deposit.

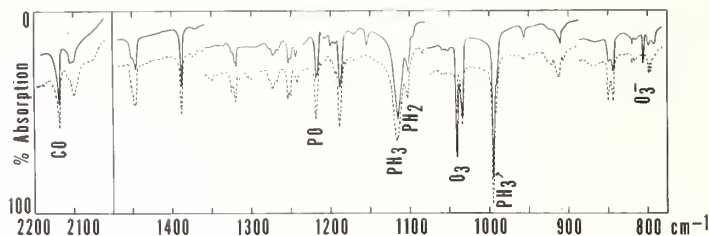


Figure 5.  $\text{Ar:PH}_3 = 200 + \text{Ar:O}_2 = 100$ . 14 K. 20.9  $\mu\text{mol}$   $\text{PH}_3$  codeposited over period of 312 min with 47.1  $\mu\text{mol}$   $\text{O}_2$  that had been passed through a microwave discharge. — Initial deposit. ----- 33 min subsequent mercury-arc photolysis.

Isotopic substitution studies utilizing  $\text{PD}_3$  and  $\text{O}_2$  enriched to 55 percent in oxygen-18 were conducted in the discharge sampling experiments. These studies will be reported in greater detail in a separate publication [13]. Because the 55 percent oxygen-18 enrichment favored the formation of mixed oxygen-isotopic products, these experiments were particularly useful in determining the number of oxygen atoms in the various product molecules. The participation of only one oxygen atom in the vibrational absorptions previously assigned to PO and to HPO and DPO was confirmed. The appearance of one intermediate pair of absorption between the  $1321\text{-}6\text{ cm}^{-1}$  absorption pair of the  $\text{N}_2^{16}\text{O}$  experiments and the  $1281\text{-}6\text{ cm}^{-1}$  absorption pair of the  $\text{N}_2^{18}\text{O}$  experiments suggests the participation of two symmetrically equivalent oxygen atoms in the vibration responsible for that absorption. Since there was single absorption, at  $1430\text{ cm}^{-1}$ , between the  $1450\text{ cm}^{-1}$  absorption of the unenriched samples and the  $1408\text{ cm}^{-1}$  absorption of heavily oxygen-18 enriched samples, the vibration responsible for this absorption also involves two symmetrically equivalent oxygen atoms.

#### 4. Discussion

The many studies of the gas-phase photochemistry of  $\text{PH}_3$  have recently been summarized by Di Stefano and co-workers [19]. The energy of the 1216-Å radiation of the hydrogen discharge photolysis source used in these experiments is far in excess of the threshold for the photodissociation of  $\text{PH}_3$  into  $\text{PH}_2 + \text{H}$  or into  $\text{PH} + \text{H}_2$ . Secondary photodecomposition of either  $\text{PH}_2$  or  $\text{PH}$  could lead to the production of P atoms which, unlike diatomic and polyatomic photofragments, can migrate through the argon lattice, resulting in the observed stabilization of  $\text{P}_2$ . Because of the demonstrated presence of  $\text{P}_2$ , it cannot be inferred that all of the product absorptions in the photolysis experiments are contributed by species containing a single P atom. The extent of decomposition of  $\text{PH}_3$  was much less in the discharge experiments, possibly decreasing the contributions of products containing two or more P atoms to the spectrum. Because the background lamp used for the ultraviolet absorption studies had a significant output down to 1900 Å and itself led to the production

of  $P_2$ , it was not possible to obtain a quantitative estimate of the extent of  $P_2$  formation in the discharge experiments.

While species containing a single P atom are likely to be somewhat favored in the discharge experiments, products with several O atoms would most certainly be favored in this experimental system. The single O atom produced by the photolysis of  $N_2O$  would be able to migrate through the argon lattice, and there would be a significant probability for the formation of products containing more than one O atom, but this must be balanced against the probability of reaction of  $PH_3$  with excited  $O_2$  or with  $O_3$  before the products are quenched on the cold surface in the discharge sampling experiments.

The identification of PO in these experiments is convincing. The infrared absorptions of both  $P^{16}O$  and  $P^{18}O$  are shifted by only  $2\text{ cm}^{-1}$  from the  $\Delta G(1/2)$  values of the ground-state molecule in the gas phase. Ultraviolet absorptions can be correlated with three band systems for the gas-phase molecule, with only a small matrix shift [13].

The assignment of the  $PO'$  stretching fundamental of ground-state HPO is also convincing. The present series of measurements has contributed previously unreported values for the ground-state PO stretching frequencies of both  $HP^{18}O$  and  $DP^{18}O$ . Although progressions in the ground-state bending vibration were prominent in the gas-phase emission spectra of both HPO and DPO [15], in the infrared the bending fundamental absorptions were weak. The prominent  $2100\text{ cm}^{-1}$  absorption in the matrix experiments behaved appropriately for assignment to a PH stretching fundamental. Although this peak did not appear in Ar: $PH_3$  photolysis studies in the absence of an O-atom source, it was unshifted on oxygen-18 substitution in the system. With allowance for its contour in the discharge experiments, which can be attributed to interactions with  $O_2$  trapped in nearby sites in the argon lattice, its appearance can be correlated with that of the  $1188\text{ cm}^{-1}$  fundamental of HPO. In their 1963 paper, Lam Thanh and Peyron [15] assigned the PH stretching fundamental of ground-state HPO at  $2308\text{ cm}^{-1}$ . Examination of their data indicates that this value should instead be associated with the PH stretching fundamental of HPO in the excited state, as has previously been noted by Herzberg [20]. The appearance of the PH stretching absorption of ground-state HPO at  $2100\text{ cm}^{-1}$ , an atypically low position for a PH stretching fundamental, has its analog in the behavior of the closely related molecule HNO in its ground state. The NH stretching fundamental of HNO trapped in solid argon has been identified at  $2716\text{ cm}^{-1}$  [21], and the gas-phase band center has been assigned at  $2684.7\text{ cm}^{-1}$  [22]. The position of the NH stretching absorption of HNO in the matrix is exceptionally sensitive to the presence of trace impurities of nitrogen.

Present data do not suffice for a definitive identification of the other products. Either the  $1320\text{-}6$  or the  $1450\text{ cm}^{-1}$  absorption would have the appropriate behavior on isotopic substitution for assignment to the antisymmetric stretching fundamental of  $PO_2$ , for which only estimates of the positions of the vibrational fundamentals have previously been available [23]. However, similar oxygen-isotopic shifts would be expected for the species  $(PO)_2$ , also expected to be stabilized in these experiments.

The stabilization of  $O_3^-$  in the discharge experiments suggests that phosphorus oxide anions may also be present. Although phosphorus compounds have frequently been found to have



relatively high electron affinities, it is likely that photodetachment would lead to a decrease in the intensities of absorptions due to phosphorus oxide anions when the sample is exposed to the full light of a medium-pressure mercury arc. However, most of the product absorptions were observed to grow in intensity under these conditions.

## 5. Conclusions

The 1216-Å photolysis of  $\text{PH}_3$  isolated in an argon matrix leads to the stabilization of  $\text{PH}_2$ , of PH, and of  $\text{P}_2$ , evidenced by the appearance of electronic absorptions shifted by less than 1 percent from the corresponding gas-phase band origins. In the presence of a photolytic source of O atoms, PO, HPO, and other phosphorus oxides and oxyhydrides are also stabilized. Similar products are also obtained when an Ar: $\text{PH}_3$  sample is mixed with an Ar: $\text{O}_2$  sample which has been passed through a microwave discharge and the products are rapidly frozen on an observation surface maintained at 14 K. Products containing more than one P atom are somewhat favored in the photolysis experiments and products with more than one O atom in the discharge experiments. These two techniques afford the advantage of ready introduction of oxygen-18 into the sample, potentially of interest in spectroscopic studies of the simple oxides and oxyhydrides of other Group IV and Group V elements. PO has been identified in absorption in both the infrared and the ultraviolet, and HPO has been seen in absorption in the infrared. The PH stretching fundamental of ground-state HPO appears at  $2100\text{ cm}^{-1}$ , an atypically low value which has its precedent in the exceptionally low NH stretching fundamental frequency of ground-state HNO. Further studies may lead to the spectroscopic identification of other products such as  $\text{PO}_2$ .

## References

- [1] Hastie, J. W., J. Res. Natl. Bur. Std. 77A, 733 (1973).
- [2] Ridgway, S. T., Bull. Am. Astron. Soc. 6, 376 (1974).
- [3] Gillett, F. and Forrest, W., Astrophys. J. 187, L37 (1974).
- [4] Bregman, J. D., Lester, D. F., and Rank, D. M., Astrophys. J. 202, L55 (1975).
- [5] Milligan, D. E. and Jacox, M. E., J. Chem. Phys. 47, 5146 (1967).
- [6] Jacox, M. E., Chem. Phys. 7, 424 (1975).
- [7] Jacox, M. E., Rev. Chem. Intermed. 2 (1978).
- [8] Berthou, J. M., Pascat, B., Guinebaut, H., and Ramsay, D. A., Can. J. Phys. 50, 2265 (1972).
- [9] Vervloet, M. and Berthou, J. M., Can. J. Phys. 54, 1375 (1976).
- [10] Rostas, J., Cossart, D., and Bastien, J. R., Can. J. Phys. 52, 1274 (1974).
- [11] Creutzberg, F., Can. J. Phys. 44, 1583 (1966).
- [12] Ngo, T. A., Da Paz, M., Coquart, B., and Couet, C., Can. J. Phys. 52, 154 (1974).
- [13] Larzilliere, M. and Jacox, M. E., to be submitted to J. Mol. Spectrosc.
- [14] Dixon, R. N., Duxbury, G., and Ramsay, D. A., Proc. Roy. Soc. A296, 137 (1967).



- [15] Lam Thanh, M. and Peyron, M., J. Chim. Phys. 59, 688 (1962); 60, 1289 (1963); 61, 1531 (1964).
- [16] Jacox, M. E. and Milligan, D. E., J. Mol. Spectrosc. 43, 148 (1972).
- [17] Milligan, D. E. and Jacox, M. E., J. Chem. Phys. 38, 2627 (1963).
- [18] Jacox, M. E. and Milligan, D. E., J. Mol. Spectrosc. 42, 495 (1972).
- [19] Di Stefano, G., Lenzi, M., Margani, A., Mele, A., and Nguyen Xuan, C., J. Photochem. 7, 335 (1977).
- [20] Herzberg, G., Molecular Spectra and Molecular Structure. III. Electronic Spectra and Electronic Structure of Polyatomic Molecules, p. 589 (Van Nostrand, Princeton, NJ, 1966).
- [21] Jacox, M. E. and Milligan, D. E., J. Mol. Spectrosc. 48, 536 (1973).
- [22] Clough, P. N., Thrush, B. A., Ramsay, D. A., and Stamper, J. G., Chem. Phys. Lett. 23, 155 (1973).
- [23] Drowart, J., Myers, C. E., Szwarc, R., Vander Auwera-Mahieu, A., and Uy, O. M., J. Chem. Soc., Faraday Trans. 2, 68, 1749 (1972).



# ESR MATRIX ISOLATION OF $\text{AlH}^+$ FORMED DURING THE HIGH TEMPERATURE VAPORIZATION OF $\text{Al}_2\text{O}_3$

L. B. Knight  
Department of Chemistry  
Furman University  
Greenville, SC 29613  
and

Richard L. Martin and Ernest R. Davidson  
Department of Chemistry  
University of Washington  
Seattle, WA 98105

The vaporization products of  $\text{Al}_2\text{O}_3$  from a tungsten-rhenium Knudsen cell at 2550 K were matrix isolated in solid neon at 4 K and investigated by electron spin resonance (ESR) spectroscopy. The initial vaporization of a non-dried sample of  $\text{Al}_2\text{O}_3$  produced a paramagnetic species which is assigned to the  $\text{AlH}^+$  radical with the following parameters:  $\text{Al}$  ( $I=5/2$ ),  $A_{||}=1009(3)$  MHz;  $A_{\perp}=877(3)$  MHz and  $\text{H}$  ( $I=1/2$ ),  $A_{||}=A_{\perp}=283(3)$  MHz;  $g_{||}=2.002(1)$ ,  $g_{\perp}=2.000(1)$ .

The quantities  $|\psi(0)|^2$  and  $\frac{3 \cos^2 \theta - 1}{r^3}$  were obtained from ab initio CI and SCF type calculations and compared with experimental results. A comparison of  $\text{AlH}^+$  with the isoelectronic  $\text{MgH}$  radical is also presented.

$\text{AlH}^+$  is the first paramagnetic molecular cation studied via rare gas matrix isolation ESR spectroscopy.

## 1. Introduction

Over the past twelve years the rare gas matrix isolation technique has been utilized for electron spin resonance (ESR) investigations of numerous high temperature ( $>1000$  K) radicals. The coverage of this paper will be limited to ESR studies of rare gas matrix isolated diatomic radicals. Other presentations will describe recent results of larger radicals. Experimental procedures and equipment descriptions for this application of the matrix isolation spectroscopic method have been presented in detail elsewhere [1]<sup>1</sup>.

<sup>1</sup>Figures in brackets indicate the literature references at the end of this paper.

Table 1 lists all metal containing diatomic radicals observed to date. Several important non-metallic diatomic radicals include CN [25], KrF [26] and XeF [27]. Tri-atomic metal containing radicals include  $BC_2$  [28], MgOH [29], BeOH [30], CdCN, HgCN [31] and  $CuF_2$  [1] as well as numerous transition metal species [3]. The trapped molecules have been produced by co-deposition of metal atoms and thermally generated hydrogen atoms [7].

Table 1. Metallic Diatomic Radicals.

<u>Fluorides</u>	<u>Hydrides</u>	<u>Oxides</u>	<u>Miscellaneous</u>
MgF (2) <sup>a</sup>	BeH (6)	ScO (13)	ScS (20)
CaF (2)	MgH (7)	YO (13)	YS (20)
SrF (2)	CaH (7)	LaO (13)	BS (21)
BaF (2)	SrH (7)	VO (14)	RhC (22)
MnF (3)	BaH (7)	BO (15)	CaCl(23)
ZnF (4)	ZnH (8)	AlO (16)	AgZn(24)
CdF (4)	CdH (8)	RbO (17)	AgCd(24)
YbF (5)	HgH (8)	CsO (17)	AgHg(24)
CrF (3)	PdH (9)	NbO (18)	
	YbH (10)	MnO (19)	
	MnH (11)		
	CrH (12)		
	AlH <sup>+</sup>		

<sup>a</sup>Reference Numbers.

A few diatomic molecular anions (ion pairs) have been studied by matrix isolation spectroscopy including  $C_2^-$  [32],  $Cl_2^-$  [33],  $F_2^-$  [34],  $O_2^-$  [35],  $Br_2^-$ ,  $I_2^-$  [36], and  $NO^-$  [37]. Earlier ESR work established the feasibility of isolating atomic and molecular ions in rare gas hosts [38]. A review of matrix isolated ionic species has been presented [39], as well as an analysis of the energetics of ion formation and stabilization [38,40].

The  $AlH^+$  species discussed in this report is particularly interesting since no positively charged diatomic radical has been reported to date. Infrared bands have been assigned to the species  $HAr_n^+$  in argon matrices [41], although other workers have assigned similar bands to interstitial H atoms [42].

The matrix isolation method for ESR studies of high temperature vapors is especially important since direct gas phase ESR detection of high temperature radicals (>1000 K) has apparently not been accomplished. Also, observations at such high temperatures would be considerably more complicated to interpret. Unfortunately, radicals having orbitally degenerate ground electronic states have not been detected in rare gas matrices although ESR detection of isolated boron, aluminum, gallium and scandium atoms in quenched states has been reported [43]. All the diatomics listed in table 1 have sigma ground electronic

states. It might be possible in future studies to intentionally quench the orbital angular momentum by co-depositing a perturbing species (i.e. ion pairs) along with the orbitally degenerate diatomic or linear polyatomic radical. However, this strategy might alter to an unacceptable degree the electronic properties of the radical of interest.

The  $\text{AlH}^+$  molecule has been characterized by optical spectroscopy [44] and quantum calculations have been reported [45]. The ESR results for diatomic molecules form an important body of experimental data for testing theoretical calculations. Thus far, such comparisons have only been made for  $\text{BeH}$  [6] and  $\text{MgH}$  [7]. A comparison of ab initio CI type calculations and experimental parameters for  $\text{AlH}^+$  is presented.

## 2. Experimental

The high temperature matrix isolation apparatus for ESR studies employed in this laboratory is based on earlier designs [1]. Our apparatus contains the following modifications: (1) the use of a commercial Varian cavity employing 100 kHz modulation in place of 200 Hz; (2) an Air Product's closed cycle helium refrigerator instead of liquid helium; and (3) a construction design that does not require separating the Dewar portion from the furnace section in order to position the matrix deposition surface in the microwave cavity and magnetic field. The apparatus is permanently installed between the pole faces of a 6-inch magnet. This feature offers a real experimental advantage since the time required to investigate subsequent deposits is considerably reduced. The microwave bridge of the V-4500 Varian spectrometer is operated in the low power configuration without the use of superheterodyne detection. The microwave cavity is not cooled, but is operated near room temperature, in contrast to the other experimental designs. The use of 100 kHz modulation produces a substantial improvement in the signal-to-noise ratio compared to 200 Hz. However, the microwave power cannot be lowered in the homodyne mode to the degree possible with the superheterodyne detection system. Hence, homodyne operation can be a distinct disadvantage for those species with long relaxation times.

The neon studies of  $\text{AlH}^+$  were conducted on a liquid helium cryostat [25]. The use of a mechanical refrigerator in place of liquid helium prevents the formation of neon matrices since operating temperatures below 12 K cannot be achieved. The production of the species assigned to  $\text{AlH}^+$  occurred inadvertently during initial vaporization of a  $\text{Al}_2\text{O}_3(\text{s})$  sample from a resistively heated tungsten-rhenium Knudsen cell at 2600 K. On subsequent vaporizations the intensity of the signals assigned to  $\text{AlH}^+$  decreased significantly.  $\text{AlH}^+$  argon and krypton experiments are in progress as well as efforts to produce other paramagnetic molecular positive ions by more direct approaches.

## 3. Results

The ESR spectrum assigned to  $\text{AlH}^+$  in neon at 4 K is presented in figure 1. The spectrum is complicated by the presence of  $\text{AlO}$ , weak aluminum atom features near 3400 gauss, methyl radicals (labeled m) and hydrogen atoms. The six parallel and six perpendicular lines of the  $^2\Sigma$   $\text{AlO}$  molecule are denoted by the single arrows. The sextet structure



results from large nuclear hyperfine splitting (hfs) of  $^{27}\text{Al}(I=5/2, \mu=3.8365 \text{ n.m.})$ . The  $\text{AlO}$  molecule has been extensively studied via optical, infrared and ESR spectroscopy in neon, argon, and krypton matrices and has been observed in the absence of the other ESR features shown in figure 1 [16]. The connected arrows indicate the six parallel and six perpendicular doublet features of  $\text{AlH}^+$ . The 101(1) gauss doublet splitting of each aluminum  $M_I$  value is due to hydrogen hfs. The hydrogen hfs is expected to be nearly isotropic since the dipolar splitting for the hydrogen 2p electron,  $A_{\text{dip}}$ , is only 3 gauss and a very small amount of hydrogen 2p character should be involved [6,7].

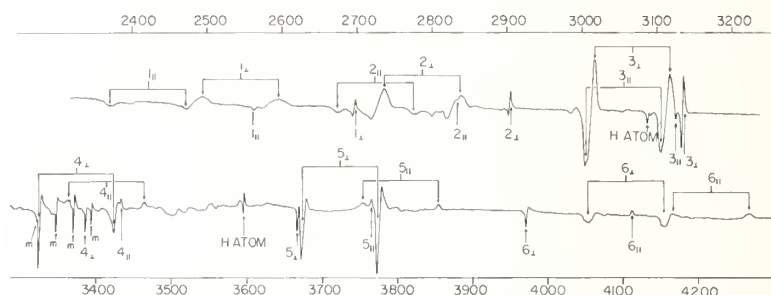


Figure 1. ESR spectra of  $\text{AlH}^+$  and  $\text{AlO}$  in a neon matrix at 4 K. Connected arrows indicate the hydrogen doublet of each  $^{27}\text{Al } M_I$  component.

The observed lineshape for the assigned  $\text{AlH}^+$  lines follows an ideal powder pattern type behavior. Note that the phase of the low field parallel and perpendicular lines are reversed relative to the high field lines as expected. Note how the perpendicular lines sharpen and increase in height as the accompanying parallel transition of the same  $M_I$  value approaches. It is also obvious from figure 1 that the linewidth of the  $\text{AlH}^+$  transitions is several times greater than that for  $\text{AlO}$  or H atoms.

The observed hfs is reasonably small relative to the applied magnetic field. Hence, the usual second-order solution to the axial spin Hamiltonian with neglect of nuclear Zeeman terms has been used to extract the final A and g values [46]. The agreement between calculated and observed line positions is given in table 2. The agreement is good considering the magnitude of the A values and the experimental uncertainty in measuring the relatively broad  $\text{AlH}^+$  lines. The parameters,  $A_{\text{iso}}$  and  $A_{\text{dip}}$ , which are compared to theoretical results are obtained from the experimental values of  $A_{\parallel}$  and  $A_{\perp}$  as follows:

$$A_{\text{iso}} = \frac{A_{\parallel} + 2A_{\perp}}{3} = \left(\frac{8\pi}{3}\right)g\beta_N\beta_N|\psi(0)|^2$$

$$A_{\text{dip}} = \frac{A_{\parallel} - A_{\perp}}{3} = g\beta_N\beta_N \left\langle \frac{(3\cos^2\theta - 1)}{2r^3} \right\rangle$$

Table 3 lists all the magnetic parameters for  $\text{AlH}^+$  and  $\text{AlO}$ .

Table 2. Observed vs Calculated Line Positions for  $\text{AlH}^+$  (gauss).<sup>a</sup>

<sup>27</sup> $\text{Al}(M_I)$				
	Observed	Calculated	Observed	Calculated
5/2	2541	2538	2422	2422
3/2	2784	2784	2723	2723
1/2	3062	3063	3052	3054
-1/2	3373	3376	3413	3414
-3/2	3722	3723	3804	3803
-5/2	4105	4103	4224	4222

<sup>a</sup>Positions are for the center of the hydrogen doublet splitting.

Table 3. Magnetic Parameters (MHz).<sup>a</sup>

	$g_{  }$	$g_{\perp}$	$b_{A_{  }}$	$b_{A_{\perp}}$	$A_{iso}$	$A_{dip}$
$\text{AlH}^+$	2.002(1)	2.000(1)	1009(3)	877(3)	921(3)	44(3)
			<sup>c</sup> 283(3)	<sup>c</sup> 283(3)		
$\text{AlO}$	2.0015(3)	2.0004(5)	872(1)	713(1)	766(2)	53(1)

<sup>a</sup>Neon -- 4 K.

<sup>b</sup>The signs of the hyperfine components are assumed to be positive since absolute signs cannot be determined by these experiments.

<sup>c</sup>Hydrogen hfs.

The preferential orientation characteristics of isolated molecules have been discussed in detail [1,14,15]. Although a full and satisfactory explanation of the phenomena has not been presented, its occurrence can be used advantageously in correlating transitions that belong to the same species. Figure 2 gives an expanded view of the fifth set of transitions in figure 1 for two different orientations of the flat sapphire deposition surface in the magnetic field. Figure 2A is for  $\theta=0$  and figure 2B is for  $\theta=90$  where  $\theta$  is the angle between a line normal to the deposition surface and the external magnetic field. All parallel transitions of  $\text{AlO}$  exhibit intensity maxima for  $\theta=0$  and intensity minima for  $\theta=90$ . The perpendicular lines of  $\text{AlO}$  show the reverse effect. The degree of preferential orientation of  $\text{AlO}$  in neon is not large compared to other oriented diatomics but its characteristics are the same. In contrast to the preferential orientation of  $\text{AlO}$ ,

all  $\text{AlH}^+$  lines are nearly superimposable for all angles. Practically all diatomics that have been generated at high temperatures and trapped in a neon matrix have demonstrated preferential orientation. It is interesting that  $\text{AlH}^+$  is not preferentially oriented. Ionic interaction between  $\text{AlH}^+$  and its counter anion might be dominant over whatever crystalline forces are responsible for preferential orientation. This ionic interaction might also account for the increased linewidth of  $\text{AlH}^+$  relative to neutrals trapped in neon.

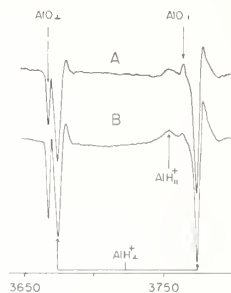


Figure 2. Demonstration of the preferential orientation of  $\text{AlO}$  in neon matrix and the random orientation of  $\text{AlH}^+$ . A and B refer to different orientations of the sapphire rod in the magnetic field. See text.

#### 4. Discussion

The accidental production of the unlikely species  $\text{AlH}^+$  from the high temperature vaporization of  $\text{Al}_2\text{O}_3$  can be rationalized by at least two different mechanisms. Mass spectrometric studies of the dissociative vaporization of  $\text{Al}_2\text{O}_3(\text{s})$  indicate that under neutral conditions the dominant vapor species are  $\text{AlO}$ , oxygen, and aluminum atoms [47]. The likely presence of water in our poorly outgassed sample and the occurrence of hydrogen atoms suggest that  $\text{AlH}$  might be formed. Aluminum is known to wet tungsten cells and copious amounts of hydrogen can be released from metals at such high temperatures. Hence,  $\text{AlH}$  could be formed from at least two different sources. On numerous occasions we have observed the ESR spectra of unexpected diatomic hydrides when a source of metal atoms was present at temperatures above 2200 K. Even under strongly reducing conditions such as the high temperature cracking of  $\text{ZnF}_2(\text{g})$  and  $\text{CdF}_2(\text{g})$  into  $\text{ZnF}$  and  $\text{CdF}$  the  $\text{ZnH}$  and  $\text{CdH}$  radicals have dominated the ESR spectrum [4]. Other workers have reported the production of  $\text{MgH}$  when  $\text{H}_2$  gas was passed over  $\text{MgO}$  at 2200 K in a tungsten Knudsen cell [29]. It is very pertinent to our following argument to point out that  $\text{Mg}^+$  was also trapped under these conditions and conclusively identified without external photolysis. The ten percent natural abundance of the  $^{25}\text{Mg}^+$  isotope with  $I=5/2$  was detected and shown to have properties similar to a "free"  $\text{Mg}^+$  ion.

Based upon the above observations it is proposed that  $\text{AlH}^+$  might be formed by an electron transfer process from  $\text{AlH}$  to some electron acceptor such as  $\text{O}$ ,  $\text{O}_2$  or  $\text{OH}(\text{X})$ .

Hence the ion pair  $\text{AlH}^+$  and  $\text{X}^-$  are trapped in the neon lattice at sufficiently large distances to preserve the characteristics of the free ion  $\text{AlH}^+$ , but close enough to provide substantial Coulombic stabilization. The energetics of such a situation and the "free" ion properties of such species have been clearly elucidated [38,40]. The degree of interaction or distance between  $\text{AlH}^+$  and  $\text{X}^-$  cannot be determined from these studies. If the distance is small or we have what Brus and Bondybey refer to as chemically bonded (nearest neighbor) ion pairs, the Coulombic attraction is quite large [38]. Since the ESR spectra yield data fairly consistent with a "free"  $\text{AlH}^+$  species we will examine the energetics of non-nearest neighbor ion pairs.

The ionization energy of  $\text{AlH}$  is not known with high accuracy but has an approximate value of  $8 \pm 0.5$  eV [45]. An alternate, and more energetically favorable, mechanism would involve the initial formation of  $\text{Al}^+$  from  $\text{Al}$  neutral followed by reaction with hydrogen atoms. The ionization energy of  $\text{Mg}$  atoms is 7.5 eV while  $\text{Al}$  is only 6.0 eV.  $\text{Al}^+$  would not be detected via ESR as  $\text{Mg}^+$  was in the work described above.

A feature of the experimental arrangement that might be essential to the success of either mechanism (especially  $\text{AlH}$  ionization) is the photolytic capability of the 2600 K vaporization cell itself. Non-nearest neighbor ion pair formation is usually not observed prior to photolysis [38].  $\text{AlH}$  absorbs at  $4230 \text{ \AA}$  ( $^1\pi \leftarrow ^1\Sigma$ ) and  $\text{Al}$  at  $3945 \text{ \AA}$  ( $^2S \leftarrow ^2P$ ). A black-body radiator at 2600 K has a small, but non-negligible, radiant output at these wavelengths which constantly irradiates the rare gas matrix at a distance of  $\approx 6$  inches. Even with quite small donor-acceptor distances, 6-7  $\text{\AA}$ , the sum of the Coulombic attractive term and the electron affinity of either  $\text{O}$ ,  $\text{O}_2$ , or  $\text{OH}$  is  $\approx 3$  eV less than the ionization energy of  $\text{AlH}$  from its ground electronic state. This energy deficiency can just be met by considering photo assisted ionization from the excited states of  $\text{AlH}$  or  $\text{Al}$  atoms. The neglect of neon matrix solvation energies is not sufficient to significantly alter the above qualitative discussion [40]. Energetically, it is even more difficult to explain the appearance of  $\text{Mg}^+$  without external photolysis than  $\text{AlH}^+$  since the electronic excitation of  $\text{Mg}$  ( $^1P \leftarrow ^1S$ ) occurs at  $2852 \text{ \AA}$  where radiant output from the cell is substantially reduced. Another mechanism of ion production that should be considered is the possibility of a complex vaporization phenomena on the tungsten-rhenium vaporization surface.

## 5. A Tensors and Chemical Bonding

Molecular values of  $A_{\text{iso}}$  and  $A_{\text{dip}}$  can be compared to corresponding atomic values to estimate the percent "s" and "p" character, respectively, of the molecular orbital containing the unpaired electron. Neglecting the minor influence of d orbitals and contributions to the dipolar operator from orbitals centered on the other nucleus, the results for  $\text{AlH}^+$  are: 33 percent s and 49 percent p for the aluminum 3s and 3p orbitals and 20 percent s for hydrogen 1s. The molecular aluminum percentages based upon  $\text{Al}^+$  instead of  $\text{Al}$  are 18 percent s and 36 percent p [48]. Both of these crude approximations indicate an aluminum  $3p_{\text{O}}$  to 3s ratio of  $\approx 2:1$ . Also note, that the unpaired electron is practically fully accounted for utilizing only  $\text{Al}$  and  $\text{H}$  orbitals. This observation, although based on a simple theoretical model,



lends support to the spectroscopic assignment of the species as "free"  $\text{AlH}^+$ . The 13 electron  $\text{MgH}$  radical, isoelectronic to  $\text{AlH}^+$ , shows a reverse in the  $3p_\sigma$  to  $3s$  ratio of 1:2 ( $\approx 66$  percent  $s$  and 33 percent  $p$ ) [7]. Interestingly, the hydrogen  $1s$  character is virtually 20 percent for both species. The observed changes in the ratio follow general expectations since the  $3p$  orbital for the ground state  $\text{Mg}$  atom is not occupied while it is for  $\text{Al}$ . For both molecules a significant degree of metallic hybridization as well as covalency is evident from these interpretations. By comparison,  $\text{AlO}$  has 28 percent " $s$ " and 72 percent " $p$ " for aluminum orbitals based on  $\text{Al}^0$  and 15 percent " $s$ " and 43 percent " $p$ " based on  $\text{Al}^+$  [16]. The similarity in the totals of " $s$ " and " $p$ " for  $\text{AlH}^+$  and  $\text{AlO}$  is interesting and might suggest a similar ionic description for both molecules, i.e.  $\text{Al}^{++}\text{O}^{--}$  and  $\text{Al}^{++}\text{H}^-$ . However, such an extreme ionic model for  $\text{AlH}^+$  is certainly not realistic given the magnitude of the observed hydrogen hyperfine structure.

Only a few comparisons between experiment and ab initio type calculations for molecular  $A_{\text{iso}}$  and  $A_{\text{dip}}$  parameters have been reported. Table 4 lists the results of such a comparison for  $\text{BeH}$ ,  $\text{MgH}$  and  $\text{AlH}^+$ . The SCF and CI calculations for  $\text{AlH}^+$  utilized a Gaussian basis set described previously except for the utilization of only one aluminum  $3d$  and one hydrogen  $2p$  function [49]. The calculations were conducted at the experimentally reported equilibrium internuclear distance of  $1.601 \text{ \AA}$  for the ground  $^2\Sigma$  state. The calculated dipolar quantity for  $\text{AlH}^+$  shows excellent quantitative agreement with experiment. The hydrogen  $|\psi(0)|^2$  value has proven to be an especially difficult quantity to calculate accurately. The agreement is fair considering its inherently small value and the relative insensitivity of the total energy to electron density charges in the vicinity of the hydrogen nucleus. The disagreement between the calculated and observed values of  $|\psi(0)|^2$  for aluminum is quite apparent. The matrix value is observed to be  $\approx 66$  percent of the calculated value. However, the calculations do predict that large aluminum hfs should be observed. The hfs for  $\text{Mg}^+$  in argon was observed to be reduced about 14 percent relative to the gaseous ion [29]. Hence, matrix shifts coupled with uncertainties in the theoretical method might account for the 34 percent discrepancy. The large aluminum  $A_{\text{iso}}$  value for  $\text{AlO}$  varied from 766 to 899 to 920 MHz going from neon to argon to krypton matrices. Since the dipolar term depends entirely on the difference between the two large splitting parameters,  $A_{\parallel}$  and  $A_{\perp}$ , matrix effects might tend to cancel thus explaining why such good agreement with theory is observed. Based upon the general characteristics of the ESR spectrum and the probable identity of the counter ion, we do not feel that significant unpaired spin density is transferred to the counter ion of  $\text{AlH}^+$ .

## 6. g Tensor

The  $g$  values observed for  $\text{AlH}^+$  are consistent with theory [50]. The  $g_{\parallel}$  value should have essentially the free spin value of 2.0023. Spin-orbit coupling between the known  $^2\pi_r$  excited state at  $27,500 \text{ cm}^{-1}$  and the ground  $^2\Sigma$  state should produce a slight decrease in  $g_{\perp}$  relative to  $g_e$ . If we use the observed molecular spin-orbit coupling constant for the  $^2\pi$  state and assume that the  $^2\pi$  state involves only  $\text{Al } 3p_x$  character, then a  $g_{\perp}$  value of 1.999



is predicted if overlap terms are neglected. This calculated result is based on a 40 per-  
cent  $3p_{\sigma}$  character for the ground electronic state. The result is consistent within  
experimental uncertainty to the observed  $g_{\perp}$  value of 2.000 [1].

Table 4. Comparison of Experimental Quantities with Ab Initio Calculations.<sup>a</sup>

$$|\psi(0)|^2$$

$$\frac{3 \cos^2 \theta - 1}{r^3}$$

Molecule		Experimental	SCF	CI	Experimental	SCF	CI
<sup>b</sup> BeH	Be	.317(2)	.283	0.322	0.12(3)	0.113	--
	H	0.0434(2)	0.0165	0.0367	±0.012(4)	-0.0019	--
<sup>c</sup> MgH	Mg	0.800(8)	0.645	0.764	0.18(6)	--	--
	H	0.0663(2)	0.0199	0.0379	0.0034(6)	--	--
<sup>d</sup> AlH <sup>+</sup>	Al	0.791(3)	1.21	1.22	0.64(4)	0.676	0.715
	H	0.0633(7)	0.048	0.094	<0.008	0.013	0.0072
<sup>e</sup> AlO	Al	0.658(2)	--	--	0.76(2)	--	--

<sup>a</sup>Atomic Units.

<sup>b</sup>Argon Matrix Reference No. 6.

<sup>c</sup>Argon Matrix Reference No. 7.

<sup>d</sup>Neon Matrix.

<sup>e</sup>Neon Matrix Reference No. 16.

The authors wish to express their appreciation to Professor W. Weltner, Jr. for the  
use of the liquid helium cryostat and for many helpful discussions. The support of the  
National Science Foundation is gratefully acknowledged. (CHE 76-18587).

#### References

- [1] Weltner, W., Jr., Adv. High Temp. Chem. 2 (Academic Press, New York, NY, 1969); Kaisai,  
P. H., Whipple, E. B., and Weltner, W., Jr., JCP, 44, 2581 (1966); Jen, C. K., Foner, S.  
N., Cochran, E. L., and V. A. Bowers, Phys. Rev. 112, 1169 (1958).

- [2] Knight, L. B., Easley, W. C., Weltner, W., Jr., and Wilson, M., J. Chem. Phys. 54, 322 (1971).
- [3] DeVore, T. C., Van Zee, R. J., and Weltner, W., J. Electrochemical Soc. (in press); and DeVore, T. C., Van Zee, R. J., and Weltner, W., Jr., J. Chem. Phys. 68, 3522 (1978).
- [4] Knight, L. B., Jr., Mouchet, A., Beaudry, W. T., and Duncan, M., J. Mag. Res. (1978), in press.
- [5] Van Zee, R. J., Seely, M. L., DeVore, T. C., and Weltner, W., Jr., J. Phys. Chem. 82, 1192 (1978).
- [6] Knight, L. B., Brom, J. M., and Weltner, W., J. Chem. Phys. 56, 1152 (1972).
- [7] Knight, L. B. and Weltner, W., Jr., J. Chem. Phys. 54, 3875 (1971).
- [8] Knight, L. B. and Weltner, W., Jr., J. Chem. Phys. 55, 206 (1971).
- [9] Knight, L. B. and Weltner, W., Jr., J. Mol. Spectr. 40, 317 (1971).
- [10] Van Zee, Richard J., Seely, Mikell L., and Weltner, W., Jr., J. Chem. Phys. 67, 861 (1977).
- [11] Van Zee, R. J., DeVore, T. C., Wilkerson, J. L., and Weltner, W., Jr., J. Chem. Phys. (1978), in press.
- [12] Weltner, W., Jr., private communication.
- [13] Weltner, W., Jr., McLeod, D., Jr., and Kasai, P. H., J. Chem. Phys. 46, 3172 (1967).
- [14] Kasai, P. H., J. Chem. Phys. 49, 4979 (1968).
- [15] Knight, L. B., Easley, W. C., and Weltner, W., Jr., J. Chem. Phys. 54, 1610 (1971).
- [16] Knight, L. B. and Weltner, W., Jr., J. Chem. Phys. 55, 5066 (1971).
- [17] Lindsay, D. M., Herschbach, D. R., and Kwiram, A. L., J. Chem. Phys. 60, 315 (1974).
- [18] Brom, J. M., Jr., Durham, C. H., Jr., and Weltner, W., Jr., J. Chem. Phys. 61, 970 (1974).
- [19] Ferrante, R. F., Wilkerson, J. L., Graham, W. R. M., and Weltner, W., Jr., J. Chem. Phys. 67, 5904 (1977).
- [20] McIntyre, N. S., Lin, K. C., and Weltner, W., Jr., J. Chem. Phys. 56, 5576 (1972).
- [21] Brom, J. M., Jr., and Weltner, W., Jr., J. Chem. Phys. 57, 3379 (1972).
- [22] Brom, J. M., Jr., Graham, W. R. M., and Weltner, W., Jr., J. Chem. Phys. 57, 4116 (1972).
- [23] Martinez de Pinillos, J. V. and Weltner, W., Jr., J. Chem. Phys. 65, 4256 (1976).
- [24] Kasai, P. H. and McLeod, D., Jr., J. Phys. Chem. 79, 2324 (1975).
- [25] Easley, W. C. and Weltner, W., Jr., J. Chem. Phys. 52, 197 (1970); Cochran, E. L., Adrian, F. J., and Bowers, V. A., J. Chem. Phys. 36, 1938 (1962).
- [26] Falconer, W. E., Morton, J. A., and Streng, A. G., J. Chem. Phys. 41, 902 (1964).
- [27] Morton, J. A. and Falconer, W. E., Proc. Chem. Soc. 95 (1963).
- [28] Easley, W. C. and Weltner, W., Jr., J. Chem. Phys. 52, 1489 (1970).
- [29] Brom, J. M., Jr. and Weltner, W., Jr., J. Chem. Phys. 58, 5322 (1973).
- [30] Brom, J. M., Jr. and Weltner, W., Jr., J. Chem. Phys. 64, 3894 (1973).
- [31] Knight, L. B., Jr. and Lin, K. C., J. Chem. Phys. 56, 6044 (1972).

- [32] Milligan, D. E., Jacox, M. E., and Abouaf-Marguin, L., J. Chem. Phys. 46, 4562 (1967); Milligan, D. E. and Jacox, M. E., J. Chem. Phys. 51, 1952 (1969); Frosch, R. P., J. Chem. Phys. 54, 2660 (1971); Bondybey, V. and Nibler, J. W., J. Chem. Phys. 56, 4719 (1972); Lineberger, W. C. and Patterson, T. A., Chem. Phys. Lett. 13, 40 (1972); Graham, W. R. M., Dismuke, K. I., and Weltner, W., Jr., J. Chem. Phys. 61, 4793 (1974); Brus, L. E. and Bondybey, V. E., J. Chem. Phys. 63, 3123 (1975).
- [33] Howard, W. F., Jr. and Andrews, L., J. Am. Chem. Soc. 95, 2056 (1973); Inorg. Chem. 14, 767 (1975); Martinez de Pinillas, J. V. and Weltner, W., Jr., J. Chem. Phys. 65, 4256 (1976); Andrews, L., J. Am. Chem. Soc. 98, 2147 (1976).
- [34] Howard, W. F., Jr. and Andrews, L., J. Am. Chem. Soc. 95, 3045 (1973); Inorg. Chem. 14, 409 (1976); Andrews, L., J. Am. Chem. Soc. 98, 2147 (1976).
- [35] Andrews, L., J. Phys. Chem. 73, 3922 (1969); Andrews, L., J. Chem. Phys. 50, 4288 (1969); Smardzewski, R. R. and Andrews, L., J. Chem. Phys. 57, 1327 (1972); Adrian, F. J., Cochran, E. L., and Bowers, V. A., J. Chem. Phys. 59, 56 (1973); Lindsay, D. M., Herschbach, D. R., and Kwiram, A. L., Chem. Phys. Lett. 25, 175 (1974).
- [36] Andrews, L., J. Am. Chem. Soc. 98, 2152 (1976).
- [37] Milligan, D. E. and Jacox, M. E., J. Chem. Phys. 55, 3404 (1971).
- [38] Kasai, P. H., Acc. Chem. Res. 4, 329 (1971).
- [39] Milligan, D. E. and Jacox, M. E., Adv. High Temp. Chem. 1971 4, 1-42; Mol. Spectros. Mod. Res. 1972, 259-86, K. N. Rao, ed. (Academic, NY).
- [40] Brus, L. E. and Bondybey, V. E., J. Chem. Phys. 63, 3123 (1975).
- [41] Milligan, D. E. and Jacox, M. E., J. Mol. Spectros. 46, 460 (1973).
- [42] Bondybey, V. E. and Pimentel, G. C., J. Chem. Phys. 56, 3832 (1972).
- [43] Knight, L. B., Easley, W. C., and Weltner, W., Jr., J. Chem. Phys. 52, 1607 (1970); Ammeter, J. H. and Schlosnagle, D. C., J. Chem. Phys. 59, 4784 (1973); Graham, W. R. M. and Weltner, W., Jr., J. Chem. Phys. 65, 1516 (1976); Scandium; Knight, L. B., unpublished work.
- [44] Herzberg, G., Spectra of Diatomic Molecules (Van Nostrand, Princeton, NJ, 1950).
- [45] Rosmus, P. and Meyer, W., J. Chem. Phys. 66, 13 (1977).
- [46] Low, W., Paramagnetic Resonance in Solids (Academic, New York, 1960).
- [47] Drowart, J., Demaria, G., Burns, R. P., and Inghram, M. G., J. Chem. Phys. 32, 1366 (1960).
- [48] See reference 16 for details concerning the Al and Al<sup>+</sup> parameters employed to obtain these percentages.
- [49] Meyer, W. and Rosmus, P., J. Chem. Phys. 63, 2356 (1975).
- [50] Stone, A. J., Proc. Roy. Soc. (London), A271, 424 (1963).

#### Discussion

Comment (Weltner): I would like to make a comment. I don't know whether the audience appreciates what a great thing this is. I mean, to trap ionic species in matrices is

something we would like to do and there have been very few really. Marilyn Jacox has trapped a lot of ions and we had a discussion about ions because, you know, we were talking about ionic species and how important they are in plasmas and so on, so we would like to learn about them and the same thing applies to the gas phase.

If one can see simple species like this in ionic form, it is difficult to study them in the gas state, to do ESR in the gas phase in these terms is not possible now. So, I just wanted to praise the work.

Response (Knight): There is a whole other story on the argument of why we are seeing an ion here and why we are not seeing a charged matrix. There is a counter-ion, most definitely. But this is the first para-magnetic diatomic molecule, ion molecule, that has been seen. There have been para-magnetic ions that have been seen and there have been numerous negative ions and some more complex positive ions investigated by infra-red work, but as far as I know this is the first diatomic ion, positive ion, that has been trapped.

## MATRIX ISOLATION STUDIES OF MAGNESIUM AND IRON ATOM REACTIONS WITH WATER

R. H. Hauge, S. E. Gransden, J. W. Kauffman, and J. L. Margrave

Department of Chemistry

Rice University

Houston, TX 77001

### 1. Introduction

A study of the matrix reactions of metal atoms and small metal clusters with water could serve as a useful guide in efforts toward understanding the reaction mechanisms of other molecules interacting with metal atoms and metal surfaces.

Previous studies of alkali metal atom reactions with water demonstrated initial formation of an atom-molecule adduct where the interaction occurs through the water oxygen [3a]<sup>1</sup>. Quantum mechanical calculations suggest the lithium-water adduct is planar with 2 kcal bond strength [3b,4,5]. Infrared studies [2,3] have shown that the bending mode of water shifts down in frequency and parallels a decrease in metal s orbital character for alkali unpaired electron. The lithium-water adduct can be readily photolyzed by visible radiation to produce lithium hydroxide and a hydrogen atom.

Reactions of water with divalent metals are expected to be more complex than those with alkali metals. Possible reactions are as follows:

		Est. $\Delta E$ (Mg, Fe) kJ/m
A.	$M + OH_2 \rightarrow M \cdots OH_2$	---
B. 1.	$M \cdots OH_2 \xrightarrow{h\nu} MOH + H$	+80
2.	$M \cdots OH_2 \xrightarrow{h\nu} HMOH$	-80
3.	$M \cdots OH_2 \xrightarrow{h\nu} MO + H_2$	+80
C.	$M + HMOH \xrightarrow{h\nu} HMOMH$	-80

shift in the water bending mode has been measured for iron and magnesium water adducts. The resulting adducts and photolysis products have been studied as a function of metal concentration. We will focus on the primary reactions at low metal concentrations.

### 2. Experimental

The matrix isolation equipment has been described in an adjoining paper [6]. Magnesium was vaporized from a stainless steel cell over a temperature range of  $350 \pm 50$  °C.

Figures in brackets indicate the literature references at the end of this paper.



Iron was vaporized from a sapphire tube over a temperature range of  $1350 \pm 50$  °C. Photolysis was carried out with a medium pressure 100 watt Hg lamp. A water-pyrex filter was used. With the lamp focused on the matrix surface, a photolysis time of thirty minutes caused essentially complete reaction of the metal-water adducts.

### 3. Data

When magnesium atoms are co-condensed with water, a new band at  $1578\text{ cm}^{-1}$  is observed. At a slightly higher magnesium trapping rate, a band at  $1577\text{ cm}^{-1}$  begins to appear in addition to the  $1578\text{ cm}^{-1}$  band. At even higher trapping rates, a third band at  $1581\text{ cm}^{-1}$  appear and becomes the dominant band at very "high" magnesium trapping rates. The one to one magnesium-water adduct is the most probable species at low magnesium concentration and the  $1578\text{ cm}^{-1}$  band assigned to it. The  $1577\text{ cm}^{-1}$  band may be due to diatomic magnesium and the  $1581\text{ cm}^{-1}$  band to small magnesium clusters. The bands have been labeled a, b, and c, respectively, and are shown in figure 1. The  $1578\text{ cm}^{-1}$  band is removed and new bands grow in when photolyzed by radiation of wavelength  $< 500\text{ nm}$ . The  $1581\text{ cm}^{-1}$  band can be removed when photolyzed by radiation of wavelength  $< 600\text{ nm}$ . The  $1577\text{ cm}^{-1}$  band appears to have a lower threshold than the  $1581\text{ cm}^{-1}$  band but not as low as that of the  $1578\text{ cm}^{-1}$  band. Figure 2 shows bands in the  $1500\text{ cm}^{-1}$  region which result upon photolysis. The bands are labeled with respect to the initial bands which disappear upon photolysis.

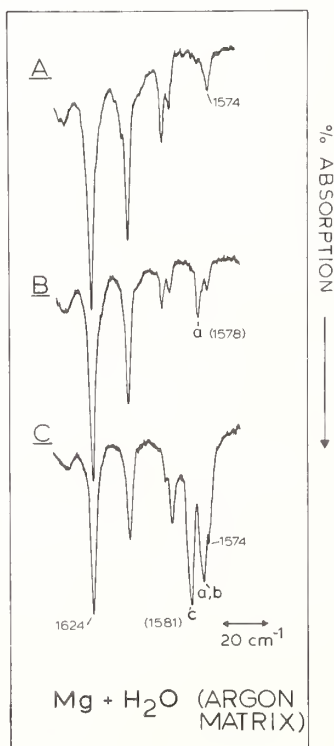


Figure 1. (A) Rotation-vibration bands of the water bending mode for water in an argon matrix, (B) water plus low magnesium concentration, and (C) water plus high magnesium concentration.

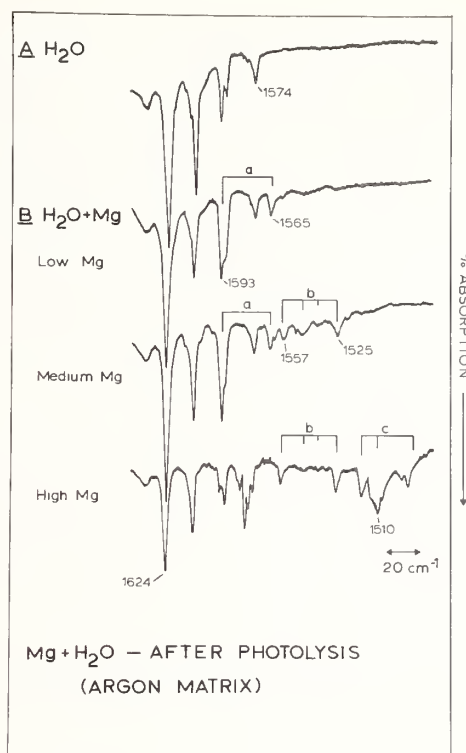


Figure 2. (A) Water only, and (B) water plus photolysis products from magnesium and water condensation in an argon matrix.

As seen in figure 2, with low magnesium concentrations only two bands are observed at  $593\text{ cm}^{-1}$  and  $1565\text{ cm}^{-1}$  in the  $1500\text{ cm}^{-1}$  region. Under these conditions, bands also appear at  $742\text{ cm}^{-1}$  and  $937\text{ cm}^{-1}$  as shown in figure 3. A band also appears at  $545\text{ cm}^{-1}$  at slightly higher magnesium trapping rates and results from photolysis of the  $1587\text{ cm}^{-1}$  "b" band. Isotopic studies indicate that species responsible for the  $742$  and  $937\text{ cm}^{-1}$  bands contain only one oxygen atom as seen in figure 3. Deuterium substitution clearly indicates the presence of two equivalent protons in the species responsible for the  $937\text{ cm}^{-1}$  band, as shown in figure 4. Deuterium substitution also indicates the presence of two nonequivalent protons in the species responsible for the  $742\text{ cm}^{-1}$  band. The respective frequencies for each species are given in table 1 along with calculated isotopic shifts for the molecular species  $\text{HMgOMgH}$  and  $\text{HMgOH}$ . The oxygen isotopic shift for the  $937\text{ cm}^{-1}$  band can only be explained by a structure such as  $\text{HMgOMgH}$  with a  $\text{OMgO}$  bond angle of  $164^\circ$ . The deuterium shift for the  $742\text{ cm}^{-1}$  band eliminates the possibility of its assignment to  $\text{MgOH}$  or  $\text{MgO}$  which would result from reactions B(1) or B(3) and strongly suggests the molecular species is  $\text{HMgOH}$ .

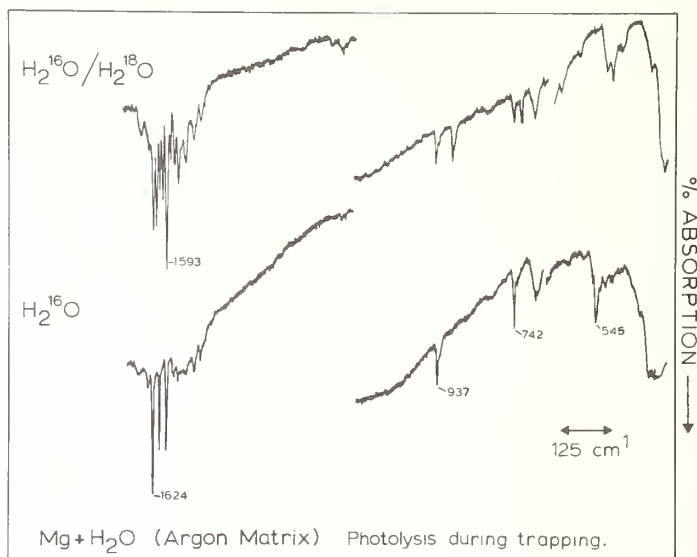


Figure 3. Spectrum from a magnesium-water co-condensation with photolysis during trapping in an argon matrix.

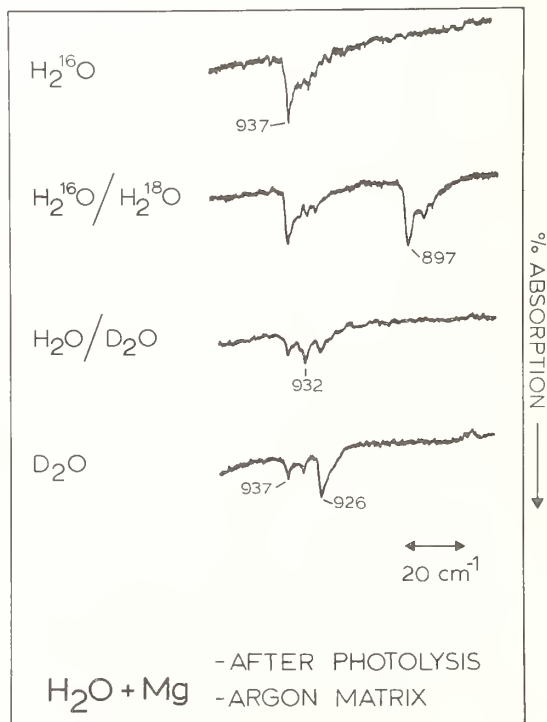


Figure 4. Spectrum in the 900  $\text{cm}^{-1}$  region from photolysis of a water-low magnesium trapping in an argon matrix.

Observed Frequencies for Mg + H<sub>2</sub>O Species

	Meas. (cm <sup>-1</sup> )		Meas. <sup>a</sup>		Calc. <sup>b</sup>	Meas.	
HMgOH	1592.9	742.3	1657.9	750.3	---	HMgOMgH	1564.1 937.1
HMg <sup>18</sup> OH	1592.9	721.5	1657.9	730.0	726.4	HMg <sup>18</sup> OMgH	1564.1 897.0
DMgOH	1163.4	731.9	1207.2	739.6	737.8	DMgOMgH	931.8
HMgOD	1592.9	723.5	1657.9	731.3	737.8	DMgOMgD	1145.3 926.0
DMgOD	1163.4	714.5	1207.2	722.1	725.3		

a. The measured values have been corrected for anharmonicity as follows. Anharmonic constants,  $2\omega_e x_e$ , of 65 and 8 cm<sup>-1</sup> were estimated from the diatomic molecules MgH and MgF. The mass effect was assumed to be that of a diatomic where either the MgH or OH is treated as a single mass.

b. The calculated values were obtained from the isotopic product rule for a linear triatomic XYZ molecule.

When iron atoms are co-condensed with water, new bands appear at  $1562\text{ cm}^{-1}$  and  $1590\text{ cm}^{-1}$  as shown in figure 5 along with the oxygen-18 counterparts. The  $1562\text{ cm}^{-1}$  band disappears completely with photolysis by radiation of wavelength  $> 350\text{ nm}$ . The  $1590\text{ cm}^{-1}$  band is only partially decreased even after prolonged photolysis and is probably not due to an iron-water adduct. At the lowest iron concentration, photolysis gives bands at 1731, 680, 654, and  $455\text{ cm}^{-1}$  for mixed oxygen isotopes as shown in figure 6. Also formed is a weak set of bands at 737, 727, and  $714\text{ cm}^{-1}$  with intensities in a 1-2-1 ratio which indicates the presence of two equivalent oxygen atoms. The 1731, 680, 654, and  $455\text{ cm}^{-1}$  bands can be assigned to the HFeOH species by analogy to the magnesium reaction, and the 737, 727, and  $714\text{ cm}^{-1}$  bands can be tentatively assigned to the  $\text{Fe}(\text{OH})_2$  species. At higher iron concentrations, the 915 and  $870\text{ cm}^{-1}$  bands are increased relative to the 680 and  $654\text{ cm}^{-1}$  set and are assigned to the HFeOFeH species. A number of new bands are observed in the  $1700\text{ cm}^{-1}$  region at higher iron concentration; however, a definite species assignment has not yet been made. Assigned bands and calculated isotopic shifts are listed in table 2. The oxygen isotopic shift for HFeOFeH indicates an FeOFe bond angle of  $144^\circ$ .

TABLE II

Observed Frequencies for Fe + H<sub>2</sub>O Species

		Meas.	( $\text{cm}^{-1}$ )	Calc.
HFeOH	1731.3	680.0	455.0	---
HFe <sup>18</sup> OH	1731.3	654.2	455.0	657.8 <sup>a</sup>
HFeOFeH	1723.4	914.6		---
HFe <sup>18</sup> OFeH	1723.4	869.5		869.5 <sup>b</sup>
H <sup>18</sup> OFeOH	727.3			
H <sup>18</sup> OFe <sup>18</sup> OH	714.4			712.9 <sup>c</sup>

- a. The calculation assumes the molecule is linear and treats the OH as a single mass in an XYZ molecule.
- b. For a OFeO bond angle of  $144^\circ$ .
- c. The calculation assumes the molecule is linear and treats the OH groups as a single mass in an XY<sub>2</sub> molecule.



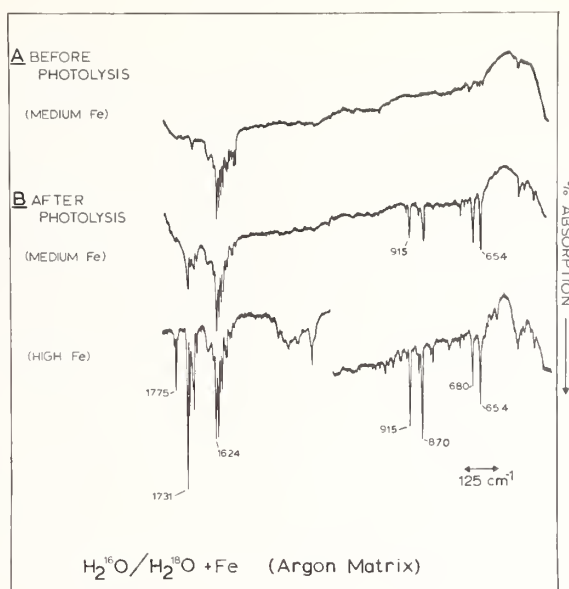


Figure 5. Spectrum of products from the co-condensation of iron with water in an argon matrix for the  $1500\text{--}1800\text{ cm}^{-1}$  region, before and after photolysis.

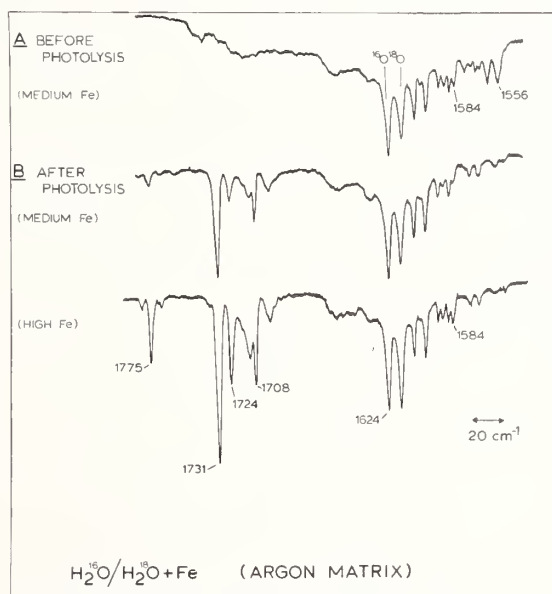


Figure 6. Spectrum of products from the co-condensation of iron with water in an argon matrix for the  $400\text{--}1800\text{ cm}^{-1}$  region, before and after photolysis.

#### 4. Discussion

It is helpful to consider the type of interaction which occurs between water and the metal atom. Previous studies of the alkali atoms [1-5] have shown that the interaction involves sigma electron donation from the oxygen to the metal. This would primarily involve the  $3a_1$  orbital of water which is strongly bonding. The bending mode of water changes from  $1595$  to  $975\text{ cm}^{-1}$  and the bond angle changes from  $104^\circ$  to  $180^\circ$  when an electron is removed from the  $3a_1$  orbital [7,9]. This suggests that the bending mode may be a very sensitive indicator of the extent of sigma bonding between a water molecule and metal atom or surface. Table 3 lists the measured value for the bending mode of water when complexed with various metals. For lithium and sodium, interaction energies have been calculated [4,5] and are given in the last column. The change in the bending mode parallels that of the interaction energy for lithium and sodium. If this simple relationship is general, one might predict other interaction energies as also shown in table 3. However, further tests of the relationship are clearly needed.

The observed bands for the magnesium and iron species may be compared to analogous modes for simpler molecules as shown in table 4. The respective metal fluoride vibrations closely resemble the metal hydroxide modes, as expected. A trend to smaller bond angles for heavier elements of the group IIIA series also appears to exist for the HMOMH species. The low frequency band at  $455\text{ cm}^{-1}$  for  $\text{HFeOH}$  could be assigned to either the  $\text{HFeO}$  bending mode or the  $\text{FeOH}$  bending mode, however, assignment to the  $\text{HFeO}$  mode would seem to be favored since the  $\text{FeOH}$  bending mode would be expected to occur at a lower frequency by analogy to  $\text{RbOH}$  [8] for which  $\nu_2$  is  $309\text{ cm}^{-1}$ .

---

We thank the National Science Foundation, the U.S. Army Research Office (Durham), and the Robert A. Welch Foundation for financial support.

TABLE III

Variation of  $\nu_2$  in Water + Metal Adducts

	$\text{H}_2\text{O}(\nu_2, \text{cm}^{-1})$	$\Delta\nu_2 (\text{cm}^{-1})$	Est. E(kJ/m)	Calc. <sup>4,5</sup> E(kJ/m)
$\text{OH}_2$	1593.3			
$\text{Li}\cdots\text{OH}_2$	1575.8	17.5	--	50
$\text{Na}\cdots\text{OH}_2$	1585.9	7.4	21	22
$\text{K}\cdots\text{OH}_2$	1586.7	6.6	19	--
$\text{Cs}\cdots\text{OH}_2$	1590.6	2.7	8	--
$\text{Mg}\cdots\text{OH}_2$	1577.7	15.6	45	--
$\text{Fe}\cdots\text{OH}_2$	1562.4	30.9	88	--

TABLE IV

Comparison of Related Molecules to Products From  
Metal Atom-Water Molecule Reactions

MgH*	MgF*	HMgOH	$\text{Al}_2\text{O}$	HMgOMgH	$\text{FeF}_2$	$\text{Fe}(\text{OH})_2$
1432		1593	994	937	731	738
	710	742	145° (<MOM)	164		
FeH	FeF*	HFeOH	$\text{Ga}_2\text{O}$	HFeOFeH		
--		1725	809	915		
	655	680	140 (<MOM)	144		

\* These values are for the gas phase species. All other values were measured in an argon matrix.

## References

- [1] Meier, P. F., Hauge, R. H., and Margrave, J. L., J. Amer. Chem. Soc. 100, 2108 (1978).
- [2] Hauge, R. H., Meier, P. F., and Margrave, J. L., Ber. Bunsenges., Phys. Chem. 82, 102 (1978).
- [3] a. Hauge, R. H. and Margrave, J. L., to be published; b. Meier, P. F., Hayes, E. F., and Margrave, J. L., to be published.
- [4] Trenary, M., Schaefer III, H. F., and Kollman, P. A., J. Am. Chem. Soc. 99, 3885 (1977).
- [5] Trenary, M., Schaefer III, H. F., and Kollman, P. A., J. Chem. Phys. 68, 4047 (1978).
- [6] Hauge, R. and Margrave, J. L., Matrix isolation studies of high temperature species, Proceedings of 10th Materials Research Symposium, NBS (1978-1979).
- [7] Turner, D. W., Baker, C., Baker, A. D., and Brundle, C. R., Molecular Photoelectron Spectroscopy (Wiley-Interscience, New York, 1970).
- [8] Acquista, N. and Abramowitz, S., J. Chem. Phys. 51, 2911 (1969).
- [9] Potts, A. W. and Price, W. C., Proc. Roy. Soc. Lond. A 326, 181 (1972).

## PHOTOSELECTIVE BIMETALLIC AGGREGATION: A NEW ROUTE TO BIMETALLIC CLUSTERS

Werner E. Klotzbücher and Geoffrey A. Ozin  
Lash Miller Chemical Laboratories and Erindale College  
University of Toronto  
Toronto, Ontario, Canada

Codeposition of transition metal atoms with weakly interacting, low-temperature matrices has led to the isolation and UV-visible spectroscopic identification of monatomic, diatomic, and polyatomic clusters, both of the unimetallic and bimetallic type. An intriguing new technique, termed "cryophotoaggregation," has been discovered for initiating, controlling, and spectroscopically observing the embryonic stages of transition metal atom nucleation to cluster sizes difficult to achieve by metal atom deposition and bulk annealing techniques. A process of atomic excitation, electronic-to-lattice energy transfer via matrix exciplex formation, localized matrix softening and ensuing short-range bulk diffusion is proposed to rationalize the observed photoaggregation of metal atoms to small unimetallic and bimetallic clusters. Semiempirical molecular orbital techniques are employed to probe the electronic and bonding properties of these unique bimetallic combinations. The ramifications of these types of "mini-cluster" experiments to the concepts of alloy and bimetallic cluster catalysis are briefly discussed.

### 1. Introduction

As a result of recent theoretical and experimental developments, interest in the physical and chemical properties of small molecular aggregates has risen tremendously: advanced computer techniques now allow more reliable quantum mechanical calculations for moderately large clusters and experimental innovations yield UV-visible and photoelectron spectra on small clusters. It has been recognized for some time that studies of very small transition metal clusters of precisely-defined dimensions have implications on a wide range of research areas, most notably in the fields of heterogeneous catalysis [1]<sup>1</sup>,

<sup>1</sup>Figures in brackets indicate the literature references at the end of this paper.



nucleation theory [2], photographic processes [3], and chemisorption simulation by use of localized models for the interaction between adsorbate and adsorbent [4].

By adopting the metal atom cryosynthetic route, one can, in principle, generate and spectroscopically probe "adsorbate-adsorbent" interactions on "mini-transition metal surfaces" ranging from single to few-atom sites [4c,4d]. In this way, some illumination may be brought to bear on the still controversial subject of the chemisorption bond, particularly, whether it should be treated as a collective property of an infinite ordered array of metal atoms or rather as a local phenomenon characterized by a limited group of metal atoms in the vicinity of the chemisorption site [1,5].

To lay out the groundwork for this kind of research, we have performed in-depth studies of the embryonic stages of the aggregation of transition metal atoms to small clusters of unimetallic or bimetallic composition. Already, some matrix-isolated atoms have been spectroscopically identified by UV-visible, luminescence, esr, and Mössbauer spectroscopy [6,17]. However, their assignment had often been hampered by the accidental trapping of diatomic or polyatomic cluster species. We discovered that by carefully monitoring the metal flow via a quartz crystal microbalance (essentially a metal atom-matrix gas titration), metal clusters can be formed conveniently in large quantities under matrix isolation conditions. The bands associated with these entities can be readily identified, using a novel technique that employs the fact that the metal atoms being deposited with a matrix gas at low temperatures are capable of diffusion either on the matrix surface or within a narrow region (the reaction zone) near the surface, before their kinetic energy is dissipated sufficiently to immobilize them. This process is amenable to analysis in terms of either a quenched reaction kinetic model, or one that assumes that at constant deposition rate of matrix material a steady state exists in the concentration of the various species within a highly mobile, moving reaction zone [4d]. Metal dimers and higher aggregates form within the reaction zone to a much higher extent than one would calculate from a statistical analysis based upon the matrix ratio. Using this technique we have, more or less successfully, attempted to investigate most of the first and second row transition metals, studying in depth some of the more interesting groups. Let us briefly review the present state-of-the-art.

Some lines of the scandium atom spectrum had been reported by Weltner [7a]; we positively identified the spectra of scandium atoms and dimers [7b]. The spectra of titanium of Gruen, et al. [8] was verified and the  $Ti_2$  absorptions ascertained [7b]. As we have been unable to obtain absolutely impurity-free zirconium and hafnium metals, only their atom spectra could be secured [58]. Vanadium has been investigated by De Vore [9,10]. The atomic, diatomic, and triatomic species were identified by our group [11,12]. It was observed that the metal atom would not appreciably photoaggregate on irradiation into an atomic ( $\sim 320$  nm) absorption [40b]. Early absorption spectra of niobium [13] were shown to actually be spectra of niobium atoms and diniobium [14]. Graham and Weltner [15a] isolated tantalum atoms in argon, and Schoch, et al. in xenon [15b] matrices. Our own studies [58] confirm their assignments of more than forty atomic features which make

search for the diatomic species a truly Herculean task. In their studies on several transition metal atoms, Mann and Broida [16] reported part of the spectrum of chromium, as did Gruen [17]. The atomic and diatomic species were identified by Kündig, et al. [18].  $\text{Cr}_3$  has been characterized recently [19]. The absorption spectra of molybdenum atoms in inert gas matrices were reported by Green, et al. [20], as well as Schoch, et al. [15b], and we could confirm their results and identify  $\text{Mo}_2$  [14]. The spectrum of tungsten atoms has been reported for xenon matrices [15b]. It is very similar to the tantalum spectrum in that it consists of a multitude of absorptions which make the identification of dimeric species unpractical [58]. Manganese was one of the first metals to be studied using matrix-isolation techniques [21], with several other groups contributing [16,22]. A band in the spectrum at 650 nm has been assigned to  $\text{Mn}_2$  [23]. No reports are available on the atomic spectra of technetium or rhenium. Quite a number of workers have studied the spectrum of iron in noble gas matrices [16,17,24-27]. However, the absorption spectrum of  $\text{Fe}_2$  is still a source of discrepancies [23,28], although the Mössbauer spectrum seems quite secure [27].

We have been unable to evaporate ruthenium and osmium metal by the resistive heating method. Both metals alloy quickly with tantalum or tungsten supports and their evaporation rate is satisfactory only from the melt. It is no surprise then that we could not locate a reference to the matrix atomic spectra in the literature.

A part of the atom spectrum of cobalt has been reported by Mann and Broida [16] and has been the subject of an extensive study in our group [28,29]. The spectrum is quite complex with a large number of absorptions between 200 and 400 nm. Absorptions of  $\text{Co}_2$  have been located around 340, 320, 280, 270 nm, and  $\text{Co}_3$  at 316, 287 nm [29].

A brief report by Weltner, et al. [30] mentions the spectrum of matrix-isolated rhodium atoms in neon, which in a later study from our group, was shown to actually consist of a mixture of Rh and  $\text{Rh}_2$  absorptions [31]. Data on the multitude of lines for iridium atoms are available in the thesis work of Hanlan [39].

Investigation of the UV-visible absorptions of nickel, palladium, and platinum was our first venture into the matrix-isolated metal atom field [32]. The stronger lines of nickel were observed by Mann and Broida [16], who also claimed to have observed the palladium spectrum. The latter data were found to actually belong to a different species, a dinitrogen complex of palladium [32]. Absorption of platinum atoms was originally reported by Gruen, et al. [33]. As a result of some recent work by two groups,  $\text{Ni}_2$  and  $\text{Ni}_3$  absorptions have been identified [34].  $\text{Pt}_2$  has been claimed [35].

The UV-visible spectrum of copper atoms isolated in solid supports have been reported by numerous workers [6,33,36,37,38,45], some of which found evidence for the existence of  $\text{Cu}_2$  [38-40] and higher clusters [40a,40b]. Excitation studies are providing new insights into the aggregation and photodissociation properties of  $\text{Cu}_2$  [40b]. Similarly, silver has been under investigation by several groups [15b,36,41-45], which also reported on the higher clusters [44,60]. Fluorescence data of matrix isolated silver atoms [56] as well

as the Raman spectra of  $\text{Ag}_2$  and  $\text{Ag}_3$  [64] have been claimed. The atomic absorption spectra of matrix isolated gold is known [6,25,36,43,45a,45d,46] and the clusters of gold are part of studies reported in this paper [58]. The spectra of zinc, cadmium and mercury have been extensively reviewed by Gruen [17] and have, so far, not been investigated by our group.

Just as accurate electronic spectral information for transition metal homonuclear diatomic molecules will undoubtedly provide a useful reference point for theoretical studies of electronic, geometric, chemisorptive and catalytic properties of larger metal aggregates, it is our contention that the corresponding data for heteronuclear diatomics will prove to be equally valuable for theoretically modeling bimetallic clusters [1] as a function of cluster size and geometry. We, therefore, have initiated a program to study the simultaneous cocondensation of "two different metal atomic vapors" with weakly interacting matrix supports as a controlled synthetic route to heteronuclear diatomic and higher bimetallic clusters, which will be discussed in this paper.

## 2. Experimental

Our set-up for bimetal-atom deposition techniques has been described previously [47]. Chromium and silver were both evaporated from tantalum Knudsen cells, palladium and gold from tungsten supports, and molybdenum from 0.01 inch filaments. All metals were of better than 99.99 percent purity, with the metal flow quantitatively monitored by a dual quartz crystal microbalance assembly. Research grade gases (99.995 percent) were supplied by Matheson of Canada; high-purity alkanes were obtained from Aldrich Chemical Co. A Displex closed-cycle helium refrigerator was used to cool a NaCl optical window to 10-12 K, with the temperature being monitored by a thermocouple embedded in the window. UV-visible spectra were recorded on a Unicam SP 8000 spectrophotometer in the range of 200-700 nm. In photoaggregation experiments, the light of either a 450-watt Oriel xenon lamp or a 550-watt Hanovia medium pressure lamp was focused through a 10-cm water cell onto the entrance slit of a Schoeffel GM 100 grating monochromator.

## 3. Results

### 3.1 Cr-Mo aggregates

The molecules  $\text{Cr}_2$  and  $\text{Mo}_2$  had been identified in previous experiments [14,18] (figs. 1A,1B). The results of a typical mixed Cr/Mo atom matrix cocondensation experiment with  $\text{Cr/Mo/Ar} \simeq 1/1/1000$  are displayed in figure 1C. A new and remarkably clear spectral feature can be observed at 485/488 nm which is essentially midway between the corresponding electronic absorptions of  $\text{Cr}_2/\text{Mo}_2$  at 460/516 nm, respectively. Weaker spectral features can be observed in the higher energy regions. After a series of experiments, these features have been assigned to the heteronuclear diatomic molecule CrMo. Comparisons with gas phase data as well as Extended Hückel Molecular Orbital (EHMO) and Self-Consistent Field (SCF)- $X\alpha$ -SW calculations on this molecule have been reported in detail [47].

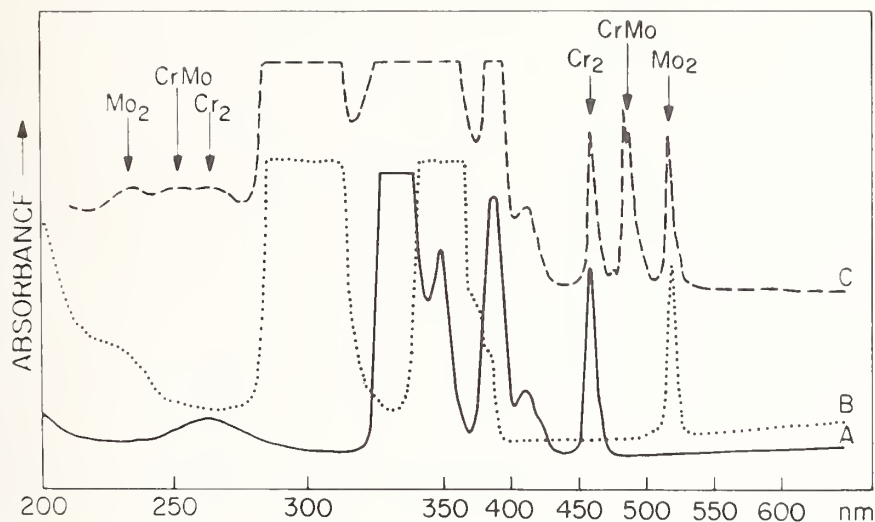
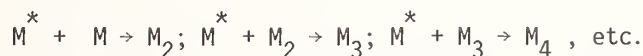


Figure 1. The UV-visible absorption spectra of the matrix depositions: (A) Cr/Ar  $\approx$  1/1000; (B) Mo/Ar  $\approx$  1/1000; and (C) Cr/Mo/Ar  $\approx$  1/1/1000 at 10-12 K showing the bands of Cr<sub>2</sub>, Mo<sub>2</sub>, and CrMo molecules in the presence of Cr and Mo atoms.

Cryophotoaggregation of metal atoms is a new technique pioneered in our laboratory, whereby matrix-entrapped transition metal atomic species are photomobilized and photoaggregated at low temperatures, thus allowing one to achieve cluster size distributions not hitherto accessible by conventional metal deposition-bulk thermal annealing procedures. By selectively exciting metal atomic species isolated in weakly interacting, low-temperature supports, at energies corresponding to their atomic resonance transitions, one can observe (for example, by optical spectroscopy) a highly controlled photocustering phenomenon, whereby metal atom absorptions gradually decay and metal cluster absorptions concomitantly grow-in [19,44,48]. Employing this method, we have synthesized and identified Mo<sub>2</sub> and Mo<sub>3</sub> [19], Cr<sub>2</sub> and Cr<sub>3</sub> [19] as well as a metastable species with a half-lifetime of approximately 30 minutes at 10 K. This intriguing species has not yet been unambiguously assigned; it may be either a metastable Cr-Ar site or a metastable, weakly interacting Cr...Cr<sub>2</sub> combination [19].

The photoaggregation process can be visualized as a reaction of a photomobilized metal atom within the substrate:



In all of the above, M<sup>\*</sup> represents the photomobilized metal atom which is assumed to diffuse in the system. Thus, the photomobilization and the diffusion processes would control the rate of growth of metal clusters. In this discussion, we present information



on the question of selective photomobilization of metal atoms. The mixed metal cluster system  $\text{Cr}_n\text{Mo}_m$  (where  $m = 3$  to  $0$  and  $n = 0$  to  $3$ ) is selected for study because details of the optical spectra of the various metal atom combinations in an argon matrix are known. Spectra in a krypton matrix are essentially the same except for a small frequency shift.

In experiments described here, a dilute mixed metal/krypton matrix of atom ratio  $\text{Cr/Mo/Kr} \approx 1/1/10^4$  and a more concentrated atom matrix of composition  $\text{Cr/Mo/Kr} \approx 1/1/10^3$  were irradiated with light of 335 nm. Such radiation should selectively photomobilize Cr atoms. Radiation at 295 nm used in a separate experiment should selectively photomobilize Mo atoms. In Kr, the  $\text{Cr}(3d^5 4s^1) \rightarrow \text{Cr}(3d^4 4s^1 4p^1)$  band maximum lies at roughly 341 nm, while the  $\text{Mo}(4d^5 5s^1) \rightarrow \text{Mo}(4d^4 5s^1 5p^1)$  band maximum lies at 295 nm. There is, however, some non-selective excitation with irradiation at 335 nm because other transitions of Mo,  $(4d^5 5s^1 \rightarrow 4d^5 5p^1)$  lie at 340, 358, and 364 nm. The starting matrix prepared in solid Kr at 12 K clearly displayed the characteristic absorptions of Cr, Mo,  $\text{Cr}_2$ ,  $\text{CrMo}$ ,  $\text{Mo}_2$ ,  $\text{Cr}_3$ ,  $\text{Cr}_2\text{Mo}$ ,  $\text{CrMo}_2$ , and  $\text{Mo}_3$ . The spectrum of each species in a Kr matrix (apart from the  $\text{Cr}_2\text{Mo/CrMo}_2$  combination) was reasonably well resolved. In a solid Ar matrix, the  $\text{Cr}_2\text{Mo/CrMo}_2$  combinations were also resolvable (table 1).

When a matrix of known composition was irradiated at 295 nm to excite Mo, major decay of molybdenum absorptions was observed (fig. 2(I) C) and selective growth of  $\text{CrMo}$ ,  $\text{CrMo}_2$ ,  $\text{Mo}_2$ , and  $\text{Mo}_3$  (fig. 2(I) D) [65] was observed. Only slight decay of Cr (fig. 2(II) B,C) was noted along with approximate constancy of  $\text{Cr}_2$ , and  $\text{Cr}_3$ . These observations argue strongly for selective photoexcitation and photomobilization of Mo atoms by radiation at 295 nm.

Table 1. Low energy optical absorptions (wavelength units-nm) of  $\text{Cr}_n\text{Mo}_m$  in solid argon and krypton matrices.

	<u><math>\text{Cr}_2</math></u>	<u><math>\text{CrMo}</math></u>	<u><math>\text{Mo}_2</math></u>	<u><math>\text{Cr}_3</math></u>	<u><math>\text{Cr}_2\text{Mo}</math></u>	<u><math>\text{CrMo}_2</math></u>	<u><math>\text{Mo}_3</math></u>
Ar	460/469	486/486	518/524	477	494	498	534
Kr	457/468	496	510/526	479	496	496	538

Similarly, photoexcitation of Cr using radiation at 335 nm results in a major decrease in the chromium absorptions (fig. 2(II) D) and selective growth of  $\text{Cr}_3$  and  $\text{Cr}_2\text{Mo}$  (fig. 2(I) E) [66] was observed. Only slight decay of Mo (fig. 2(II) D) was noted along with slight growth of  $\text{Cr}_2$  and approximate constancy of  $\text{Mo}_2$  and  $\text{Mo}_3$  (fig. 2(I) E). A schematic representation of these photoselectivity effects is illustrated in figure 3. These observations provide a strong case for selective photoexcitation and photomobilization of Cr atoms by radiation at 335 nm.



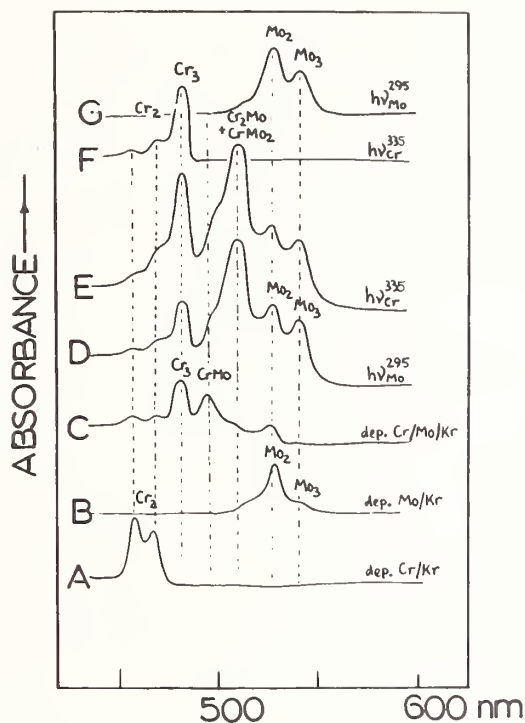


Figure 2-I. The low energy optical spectra of: (A)  $\text{Cr/Kr} = 1/10^3$ ; (B)  $\text{Mo/Kr} = 1/10^3$ ; (C)  $\text{Cr/Mo/Kr} = 1/1/10^3$  mixtures all deposited at 12 K showing the characteristic absorptions of  $\text{Cr}_2$ ,  $\text{Cr}_3$ ,  $\text{CrMo}$ ,  $\text{Cr}_2\text{Mo}$ ,  $\text{CrMo}_2$ ,  $\text{Mo}_2$ , and  $\text{Mo}_3$ ; (D) the result of 10 minutes  $h\nu_{\text{Mo}}^{295}$  photolysis of sample (C); (E) the result of 5 minutes  $h\nu_{\text{Cr}}^{335}$  photolysis of sample (D); (F) the result of 3 minutes  $h\nu_{\text{Cr}}^{335}$  photolysis of sample (A); and (G) the result of 30 minutes  $h\nu_{\text{Mo}}^{295}$  photolysis of sample (B).

Noteworthy support for these proposals can be considered to stem from the simultaneous Cr/Mo atomic excitation (350 nm) control experiments, which displayed the expected growth patterns for all cluster species concomitant with decay of both Cr and Mo atomic species, that is designed non-photoselectivity. The corresponding high dilution  $\text{Cr/Mo/Kr} \approx 1/1/10^4$  experiments also very effectively support our case for a highly selective photoaggregation process [67].

The  $\text{Cr}_n\text{Mo}_m$  series of small, naked clusters was genuinely bimetallic in the Sinfelt terminology but related to metallic components which were partially miscible in the bulk phase [49], owing to their similar electronic structures and minimal size difference. Nevertheless, the usefulness of the method for studying the interaction between two different metals in very small cluster-form by UV-visible (our work), ESR (Kasai, McLeod [30]) and Mössbauer spectroscopy (Montano [51]) was established and the way was set for

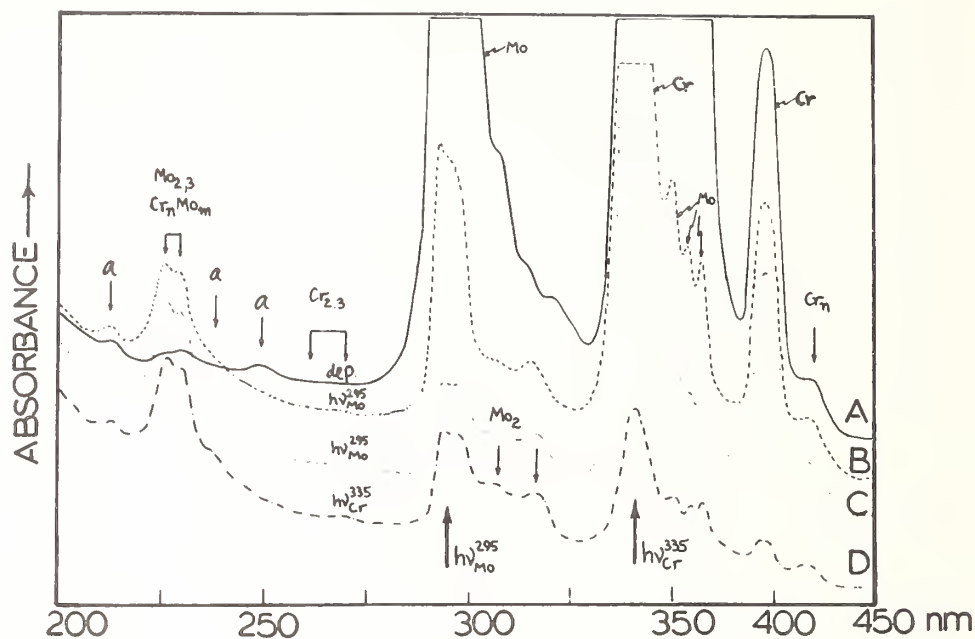


Figure 2-II. (A) The high energy optical spectra of Cr/Mo/Kr  $\approx 1/1/10^3$  mixtures deposited at 12 K showing the known absorptions of Cr, Mo, Cr<sub>2</sub>, Mo<sub>2</sub>, and Mo<sub>3</sub>. (B) and (C) the results of 50 and 130 minutes of  $h\nu_{\text{Mo}}^{295}$  photolysis of sample (A), and (D) the result of a further 22 minutes of  $h\nu_{\text{Cr}}^{335}$  photolysis of sample (C). Note that the bands labeled "a" could be associated with mixed clusters Cr<sub>n</sub>Mo<sub>m</sub>.

an excursion to the more pertinent general class of immiscible and low-miscibility metallic combinations.

### 3.2 Ag-Cr aggregates

In our next study, we chose to investigate the rather discrepant atomic combination silver-chromium, two transition metals which in the bulk exhibit fcc and bcc crystal structures, respectively, which are of quite different atomic size and whose phase diagrams demonstrate very low miscibility properties [49]. Furthermore, these metals are from opposite sides of the periodic tables, with electronic configurations and energy levels distinctly different. From a cryochemical standpoint, this is an ideal test combination, as Cr and Ag atoms have been individually investigated by metal concentration, bulk

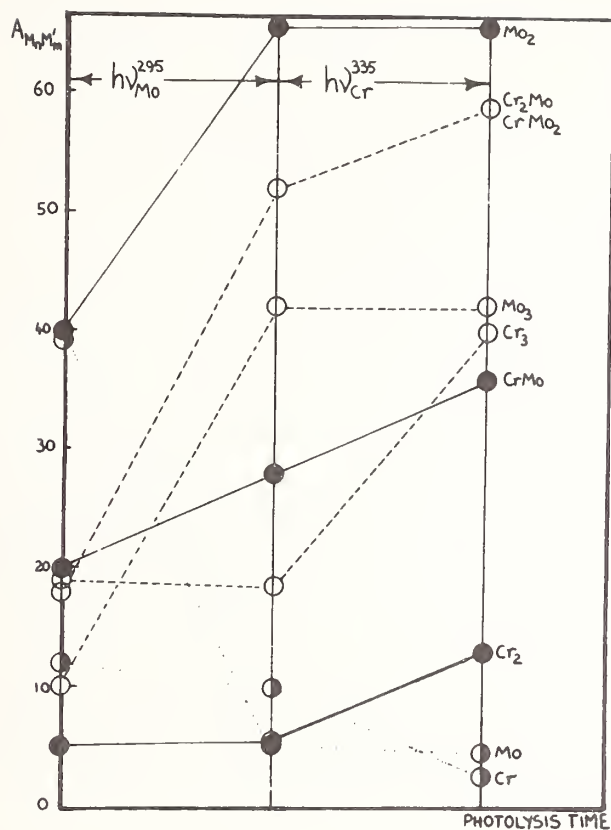


Figure 3. A schematic representation of the photoselectivity experiments involving  $Cr/Mo/Kr \approx 1/1/10^3$  mixtures deposited at 12 K and then sequentially subjected to  $h\nu_{Mo}^{295}$  and  $h\nu_{Cr}^{335}$  photolyses. Note that the Cr and Mo atom absorbances are recorded on a scale 10X smaller than that used for the  $Cr_nMo_m$  clusters.

annealing, and photoaggregation matrix techniques. Moreover, the optical spectroscopy of  $Cr_2$  and  $Cr_3$  [47,48] and  $Ag_{2,3,4}$  [44] naked clusters is reasonably well understood. The results of a typical mixed  $Ag/Cr$  atom matrix cocondensation experiment are displayed in figure 4 together with the spectra of the parent systems. The most striking observation is the appearance of a new spectral feature centered at 283 nm, which, from concentration and photoaggregation experiments, has been associated with the first stage of  $Ag/Cr$  clustering, that is,  $ArCr$  [52].

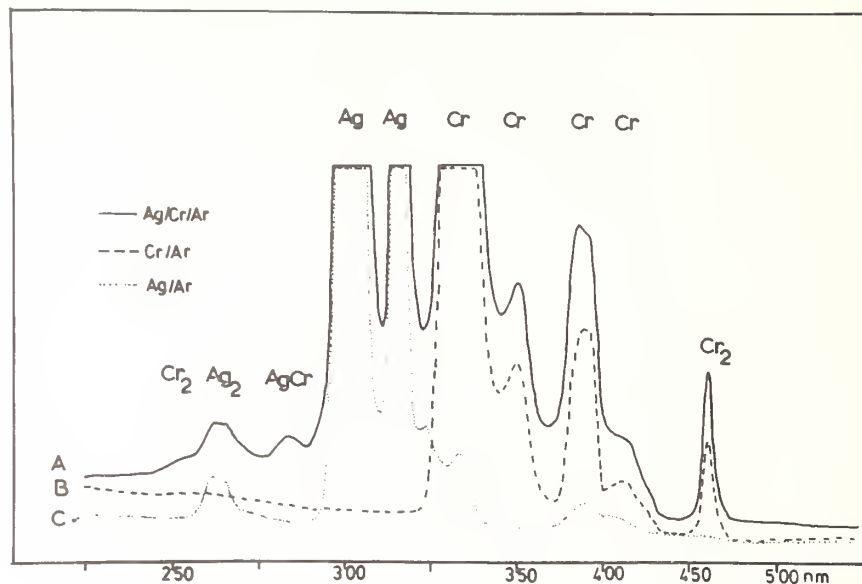


Figure 4. The UV-visible absorption spectra of the products of the matrix codeposition of (A) Ag/Cr/Ar  $\approx 1/1/1000$ , (B) Cr/Ar  $\approx 1/1000$ , and (C) Ag/Ar  $\approx 1/1000$  mixtures deposited at 10-12 K displaying the bands of Cr<sub>2</sub>, Ag<sub>2</sub>, and AgCr molecules in the presence of Ag and Cr atoms.

Let us now turn our attention briefly to the Ag/Cr bimetallic photoaggregation experiments. Figure 5A shows the Ag/Cr/Ar = 1/1/1000 systems after deposition at 10-12 K. As in figure 4, one observes mainly Cr<sub>2</sub>, Ag<sub>2</sub>, and AgCr on deposition. Narrow-band Cr ( $3d^5 4s^1 \rightarrow 3d^4 4s^1 4p^1$ ) excitation causes a large decrease in the Cr atomic resonance lines with a concomitant, but much smaller, loss of the Ag atomic resonance lines. Under these conditions, both stable and metastable Cr<sub>3</sub> species grow in, as in the pure Cr/Cr<sub>2</sub>/Ar system, along with a notable increase in the intensity of the AgCr (283 nm) absorption. Figure 5B displays the situation 30 minutes after irradiation when the metastable Cr<sub>3</sub> has decayed to zero. Significantly, the Ag<sub>2</sub> absorptions remain essentially unchanged during Cr atom photoexcitation and the characteristic Ag<sub>3</sub> absorptions at 245/440 nm do not grow in. All the evidence, therefore, points in favour of photoselective bimetallic aggregation upon Cr photomobilization in the presence of Ag, Ag<sub>2</sub>, AgCr, and Cr<sub>2</sub> species.

Focusing attention on sequential Ag atom photoexcitation as depicted in figure 5C, one observes a marked decrease in the Ag atomic resonance absorbances with concomitant, but much smaller, loss of the Cr atomic resonance lines. Especially gratifying is the observation of growth of Ag<sub>2</sub> and AgCr, together with the appearance of Ag<sub>3</sub> and a striking new spectral feature at 276 nm as a shoulder on the AgCr absorption at 283 nm. The results once again emphatically point to the existence of a photoselective bimetallic

aggregation phenomenon. Moreover, from a series of sequential Cr, Ag atomic photoexcitations, one can conclude that the new absorption at 276 nm is associated with the triatomic mixed-metal cluster  $\text{Ag}_2\text{Cr}$ . An absorption unequivocally ascribable to  $\text{Cr}_2\text{Ag}$  has not yet been observed in this system. Additional experimental support for the concept of photoselectivity in this bimetallic system and the spectral assignment of  $\text{AgCr}$  and  $\text{Ag}_2\text{Cr}$  stemmed from a series of experiments similar to those described in figure 5, except that the aggregation was initiated by Ag rather than Cr photoexcitation.

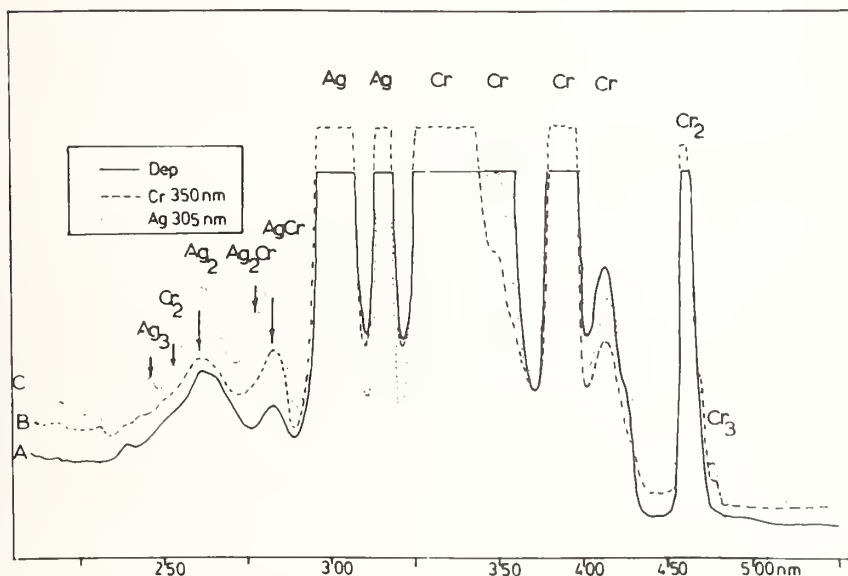


Figure 5. The UV-visible spectrum of a  $\text{Cr/Ag/Ar} \approx 1/1/1000$  mixture: (A) deposited at 10-12 K showing Cr, Ag,  $\text{Cr}_2$ ,  $\text{Ag}_2$ , and  $\text{AgCr}$ ; (B) after Cr atom 350 nm photoexcitation and 30 minutes relaxation time showing the growth of  $\text{Cr}_3$ , and  $\text{CrAg}$ ; and (C) after Ag atom 305 nm photoexcitation showing the growth of  $\text{Ag}_2$ ,  $\text{Ag}_3$ ,  $\text{AgCr}$ , and  $\text{Ag}_2\text{Cr}$ .

Still further support for our proposals stemmed from a control experiment in which a  $\text{Cr/Ag/Ar} \approx 1/1/1000$  matrix of the type illustrated in figure 5A was photolyzed with broad-band irradiation covering the region 250-600 nm. Under these conditions, both Cr ( $3d^5 4s^1 \rightarrow 3d^4 4s^1 4p^1$ ) and Ag ( $4d^{10} 5s^1 \rightarrow 4d^{10} 5p^1$ ) electronic transitions were simultaneously excited. The outcome was non-selective photoaggregation in which both Cr and Ag atomic lines showed concurrent major decay accompanied by the growth of  $\text{Ag}_2$ ,  $\text{Ag}_3$ ,  $\text{Cr}_3$ ,  $\text{AgCr}$ , and  $\text{Ag}_2\text{Cr}$ .

We have previously reported EHMO results on  $\text{Cr}_2$ ,  $\text{Mo}_2$ , and  $\text{CrMo}$  and compared them to SCF-X $\alpha$ -SW calculations on the same molecules [47]. We had found, that EHMO calculations, spectroscopically parameterized to quantitatively fit the observed electronic transitions of  $\text{Cr}_2$  and  $\text{Mo}_2$ , would reproduce not only bond distances and dissociation energies within the range of experimental error for the homonuclear molecules, but also predicted reasonably well



the electronic transitions, bond length, and dissociation energy of the heteronuclear molecule CrMo. However, the Cr<sub>2</sub>, Mo<sub>2</sub>, and CrMo calculations concerned component atoms which are neighbors in the periodic table, exhibiting similar molecular orbital energies and electronic configurations; close correlation between experiment and theory was, therefore, not totally unexpected. The application of the EMO approach to two atoms of quite disparate electronic properties, such as Ag and Cr, provided a more stringent test case. Straightforward transference of the optimized EMO parameters derived for Ag<sub>2</sub> and Cr<sub>2</sub> to the AgCr molecule led to a molecular orbital scheme [52] which closely resembles the ground state, spin-restricted X $\alpha$  descriptions [53]. In essence, one finds that the 3d orbitals of Cr and 4d orbitals of Ag are non-interacting in AgCr, with the Cr 4s and Ag 5s orbitals the main contributors to the silver-chromium bond. The minimum energy geometry for AgCr was computed at 2.9 Å, considerably elongated with respect to the multiply-bonded Cr<sub>2</sub> (1.7 Å) and slightly longer than the singly-bonded Ag<sub>2</sub> (2.7 Å).

### 3.3 Ag-Mo aggregates

Let us now briefly make an excursion to some work still in progress. We have seen that Cr/Mo and Cr/Ag cocondensations led to the bimetallic species CrMo and AgCr. The next obvious step involved a mixed Ag/Mo experiment. The results of a typical Ag/Mo/Ar 1/1/1000 cocondensation reaction are shown in figure 6C. One feature, an absorption at 213 nm, has grown in prominently and, under the conditions chosen, can be given the a priori assignment of AgMo. We envisage securing more definite assignments for Ag<sub>n</sub>Mo<sub>m</sub> clusters from Ag/Mo concentration and photoaggregation studies currently underway.

### 3.4 Au-Ag aggregates

We have seen from our cluster studies that both copper and silver aggregate upon deposition and photoexcitation into the  $^2S_{1/2} \rightarrow ^2P_{1/2,3/2}$  atomic resonance lines. So it was just a matter of time to investigate the remaining group IB metal, gold. With an atomic mass nearly double that of silver, one would anticipate its diffusion characteristics in the reaction zone of the growing matrix surface on deposition to be different from those of Cu and Ag. A typical result of cocondensation of gold atoms with argon (Au/Ar  $\simeq$  1/5000) at 10-12 K is displayed in figure 7A, that is, a simple, three line gold atom matrix spectrum. Only when employing higher concentration (Au/Ar  $\simeq$  1/500) and an enhanced deposition temperature of 20 K (the choice of temperature is crucial) can new absorptions be observed at 189, 207, 295, 312, and 365, 471 nm which we tentatively associate with Au<sub>2</sub> and Au<sub>3</sub> gold clusters, respectively (fig. 7B). An example of a preliminary Ag/Au/Ar cocondensation study is traced in figure 7C to indicate the kind of overlap problem that we are encountering in this system. Noteworthy here, is the region between 260 and 295 nm, which we presently suspect to contain new features associated with small, bimetallic gold-silver clusters.

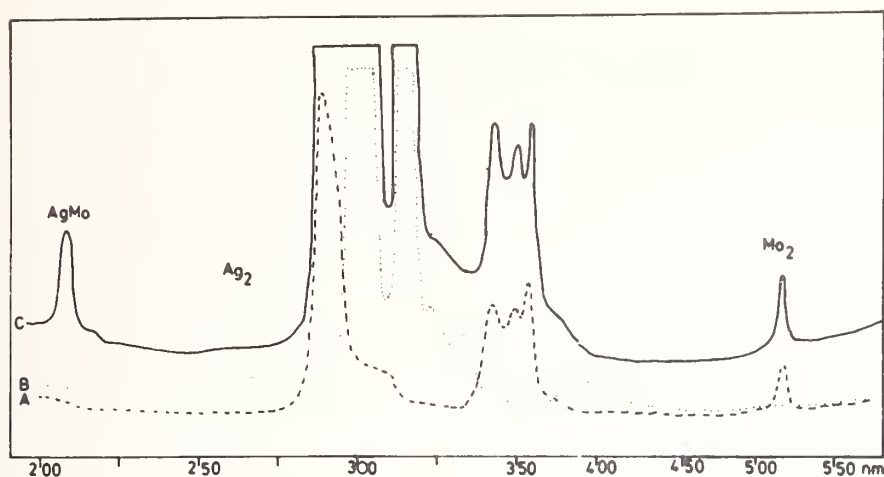


Figure 6. The UV-visible absorption spectra of the matrix cocondensation products of: (A) Mo/Ar  $\approx$  1/1000; (B) Ag/Ar  $\approx$  1/1000; and (C) Ag/Mo/Ar  $\approx$  1/1000 at 10-12 K, showing the bands of Ag<sub>2</sub>, Mo<sub>2</sub>, and AgMo in the presence of Ag and Mo atoms.

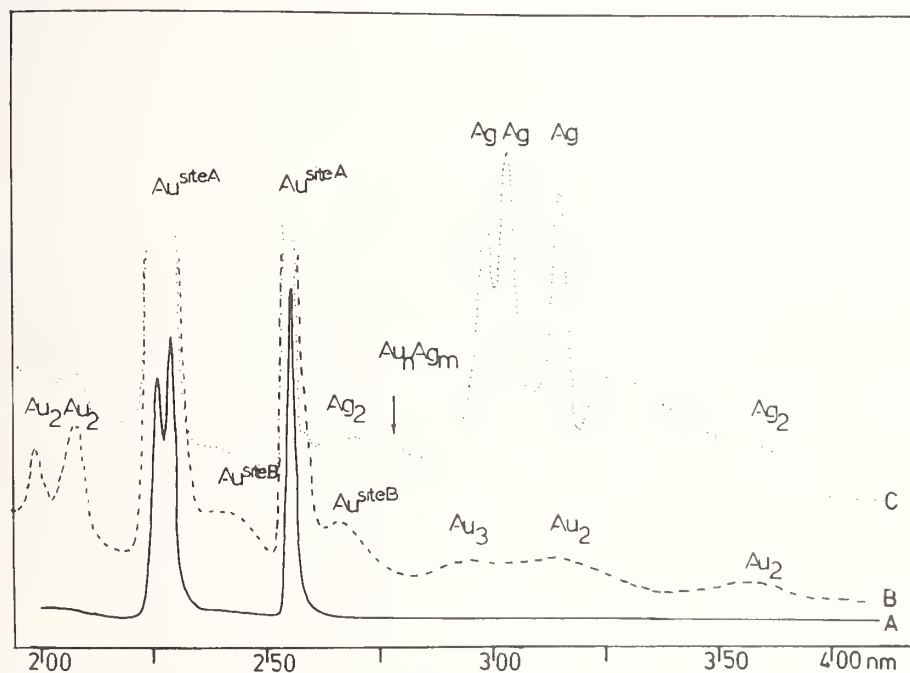


Figure 7. The UV-visible spectra of the matrix cocondensation products of: (A) Au/Ar 1/5000 at 10 K; (B) Au/Ar  $\approx$  1/500 at 20 K; and (C) Ag/Au/Ar  $\approx$  1/1/500 at 20 K showing the presence of absorptions tentatively assigned to Au<sub>2</sub>, Au<sub>3</sub>, and a suspected region of Au<sub>n</sub>Ag<sub>m</sub> bimetallic cluster formation. Two different matrix sites A and B of atomic gold are indicated with arrows.

### 3.5 Pd-bimetallic aggregation attempts

A metal not yet discussed, but highly interesting because of its known, catalytically significant, alloys with silver and other metals is palladium. The isolated palladium atom in a variety of inert gas matrices has been a mystery for quite some time. Its spectrum was first reported by Mann and Broida [16], subsequently shown to be erroneous (in fact, mistaken for  $\text{Pd}(\text{N}_2)_{1,2}$ ) and reassigned [32]. Further studies [54] proved that the spectrum actually consisted of a doublet of triplets, where one triplet would collapse on warm-up, indicating that the switch over was due to a matrix site change (fig. 8). Atomic palladium has a ground state electronic-configuration of  $d^{10}s^0$ . From simple molecular orbital theory, one might expect it to form a weakly bonded dimer with silver ( $d^{10}s^1$ ). However, neither Ag/Pd cocondensation experiments (fig. 9B) nor photoexcitation of silver atoms in low temperature Ag/Pd/Ar composite matrices (fig. 9C) has given any reason to indicate bimetallic cluster formation at the atomic level. Furthermore photoexcitation of the palladium  $^1S_0 \rightarrow ^1P_1$ ,  $^3D_1$ , and  $^3P_1$  atomic resonance transitions in Ag/Pd/Ar composite matrices, although involving energies greater than  $40,000 \text{ cm}^{-1}$ , has not led to bleaching of the spectrum nor to any other sign of photoaggregation. Similarly, the cocondensation and selective atomic photoexcitation of palladium with molybdenum in solid argon at 10-12 K produces a spectrum which is essentially a superposition of the Pd, Mo atomic spectra (fig. 10C).

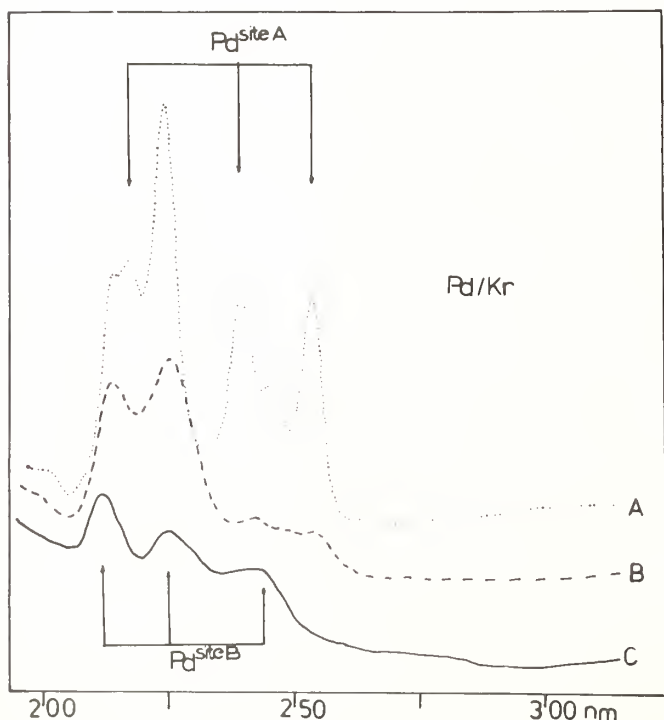


Figure 8. The UV-visible absorption spectra of the cocondensation of palladium atoms with krypton: (A) after deposition at 10-12 K, (B) after warm-up to ca. 17 K, and (C) final structure after warm-up to 20 K. Two different matrix sites A and B of atomic palladium are indicated with arrows.

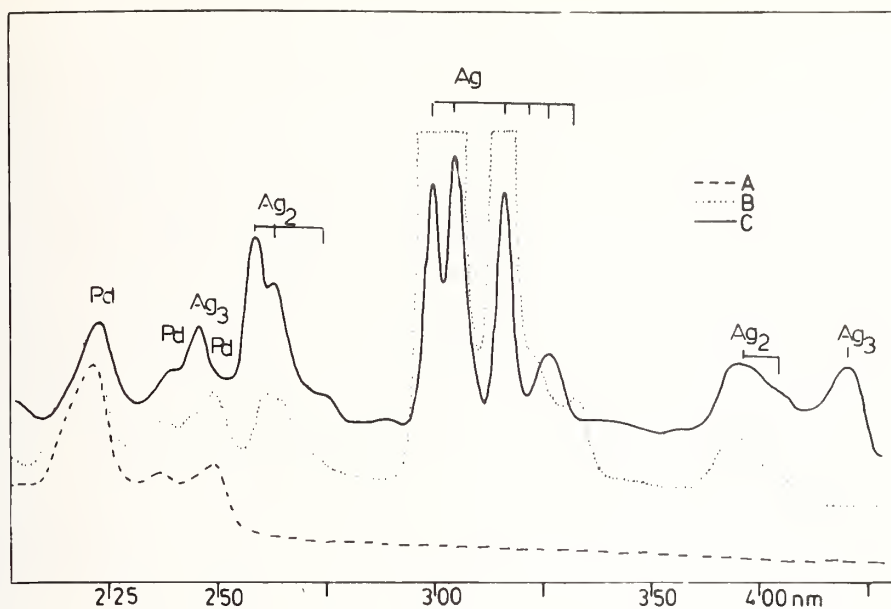


Figure 9. The UV-visible absorption spectra of the matrix cocondensation products at 10-12 K of: (A) Pd/Ar  $\approx$  1/1000, (B) Ag/Pd/Ar  $\approx$  1/1/1000, and (C) after subsequent prolonged irradiation in the 300 nm Ag atomic resonance line.

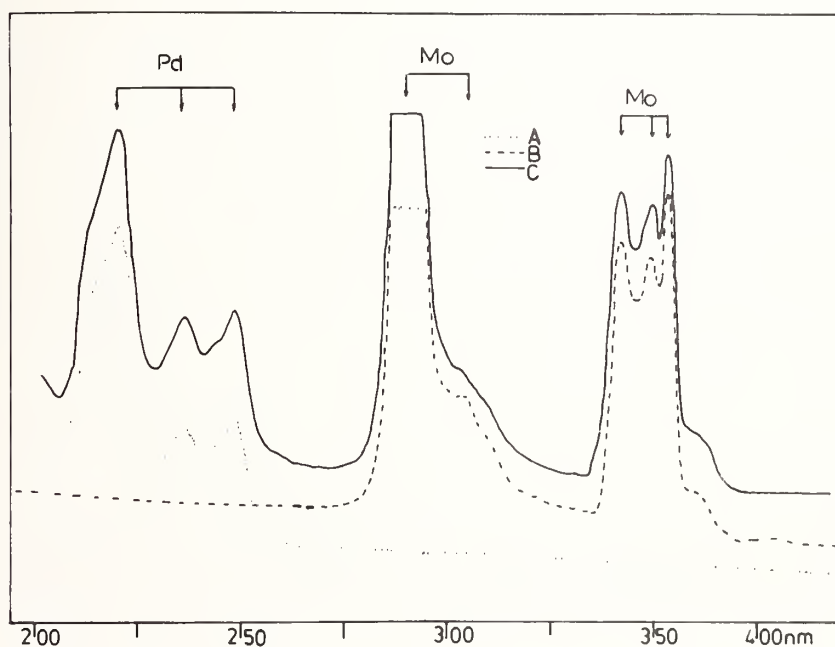


Figure 10. The UV-visible absorption spectra of the matrix cocondensation products of: (A) Pd/Ar  $\approx$  1/1000, (B) Mo/Ar  $\approx$  1/1000, and (C) Mo/Pd/Ar  $\approx$  1/1/1000 at 10-12 K showing essentially a superposition of the parent spectra of Pd and Mo atoms with little evidence for bimetallic cluster formation.

#### 4. Conclusion

Apart from the unequivocal demonstration of photoselective bimetallic aggregation in the Ag/Cr and Cr/Mo systems, probably the single most impressive discovery is the fact that "molecular bimetallic  $M_n M'_m$  clusters" actually have an independent and real existence in solid rare gas matrices. In view of the fact that Ag/Cr and Ag/Mo mixtures constitute bulk alloy systems which are categorized as of the immiscible variety [49], our discovery of "few-atom  $Ag_m Cr_n$  and  $Ag_m Mo_n$  bimetallic molecules" must be construed to provide strong evidence in favour of a direct interaction between Ag/Cr and Ag/Mo atomic combinations for Sinfelt-type, highly dispersed and supported Ag/Cr and Ag/Mo bimetallic clusters, with a genuine and direct electronic (bonding) interaction between the different metal atoms, rather than a simple additive combination of the separate metal clusters. On the other hand, the apparent non-interaction between palladium and silver or molybdenum will force us to contemplate more about the metal concentration, deposition temperatures, and metal atomic electronic configurations required to promote metal-metal bond formation, especially as closely related Fe/Ag, Co/Ag, and Ni/Ag immiscibles have been purported to form bimetallic clusters in patent publications [55].

Clearly, a thorough understanding of the energy transfer and diffusion characteristics of metal atoms in solid matrices upon photoexcitation is a basic requirement for further bimetallic aggregation studies. The recently reported fluorescence spectra of silver atoms in krypton matrices [56], which showed large Stokes shifts of the excited silver atom, as well as our own studies [57] on some of the metals employed in our bimetallic studies, will hopefully aid us in our understanding of the excimeric bond between the excited atom and the noble gas cage. Furthermore, other metallic combinations need to be investigated as a function of cluster size, and we fully intend to undertake such a program of research with a general thrust towards an electronic, structural and chemical characterization of small, bimetallic and eventually trimetallic clusters by ir, UV-visible, Raman, esr, and time-resolved emission spectroscopy in combination with EHMO/SCF- $X\alpha$ -SW molecular orbital techniques.

---

We gratefully acknowledge the financial assistance of the National Research Council of Canada's Operating, New Ideas and Strategic Energy Programs, the Atkinson Foundation, the Connaught Fund, Imperial Oil of Canada, Erindale College, and the Lash Miller Chemical Laboratories for support of this research.



## References

- [1] (a) Sinfelt, J. H. and Cusumano, J. A., in Advanced Materials in Catalysis, J. J. Burton and R. L. Garten, eds., p. 1-3 (Academic Press, 1977) and references cited therein; (b) Burton, J. J. and Garten, R. L., in Advanced Materials in Catalysis, p. 33-65 (Academic Press, 1977); (c) Sinfelt, J. H., Acc. Chem. Res. **10**, 15 (1977) and references cited therein; (d) E. Drauglis and R. I. Jaffee, eds., The Physical Basis of Heterogeneous Catalysis (Plenum Press, 1975); (e) Sachtler, W. M. H. and Van Santen, R. A., Adv. in Catal. **26**, 69 (1977), and references cited therein.
- [2] Abraham, F. F., Homogeneous Nucleation Theory (Academic Press, 1974), and references cited therein.
- [3] (a) Hamilton, J. F., J. Vac. Sci. Techn. **13**, 319 (1976); (b) Hamilton, J. F. and Logel, P. C., Photograph. Sci. and Engin. **18**, 507 (1974); (c) Baetzold, R. C., Photograph. Sci. and Engin. **17**, 78 (1973).
- [4] (a) Blyholder, G., Surf. Sci. **42**, 249 (1974); (b) Hulse, J. E. and Moskovits, M., Surf. Sci. **57**, 125 (1976); **61**, 302 (1976); (c) Ozin, G. A., Catal. Rev. Sci. and Engin. **16**, 191 (1977); Acc. Chem. Res. **10**, 21 (1977); (d) Moskovits, M. and Hulse, J. E., J. Chem. Soc. Faraday Trans. II, **73**, 471 (1977).
- [5] (a) R. B. Anderson and P. T. Dawson, eds., Characterization of Surfaces and Adsorbed Species, Vol. 3 (Academic Press, 1976); Vol. 3; (b) Somorjai, G. A., Adv. Catal. **26**, 2 (1976); Angew. Chem. Int. Ed. **16**, 92 (1977).
- [6] Meyer, B., Low Temperature Spectroscopy (American Elsevier, 1971).
- [7] (a) Weltner, W., McLeod, D., and Kasai, P. H., J. Chem. Phys. **46**, 3172 (1967); (b) Busby, R., Klotzbuecher, W., and Ozin, G. A., J. Am. Chem. Soc. **98**, 4013 (1976).
- [8] Gruen, D. M. and Carstens, D. H. W., J. Chem. Phys. **54**, 5206 (1977).
- [9] DeVore, T., Ph.D. Thesis, Iowa State University (1975).
- [10] DeVore, T. C., J. Chem. Phys. **62**, 520 (1975).
- [11] Ford, T. A., Huber, H., Klotzbücher, W., Kündig, E. P., Moskovits, M., and Ozin, G. A., J. Chem. Phys. **66**, 524 (1977).
- [12] Klotzbücher, W. E., Mitchell, S. A., and Ozin, G. A., Inorg. Chem. **16**, 3063 (1977).
- [13] Green, D. W. and Gruen, D. M., J. Chem. Phys. **57**, 4462 (1972).
- [14] Klotzbücher, W. and Ozin, G. A., Inorg. Chem. **16**, 984 (1977).
- [15] (a) Graham, W. R. M. and Weltner, W., Jr., J. Chem. Phys. **56**, 4400 (1972); (b) Schoch, F. and Kay, E., J. Chem. Phys. **59**, 718 (1973).
- [16] Mann, D. M. and Broida, H. P., J. Chem. Phys. **55**, 84 (1971).
- [17] Gruen, D. M. Spectroscopic identification and characterization of matrix isolated atoms, in Cryochemistry, M. Moskovits and G. A. Ozin, eds., chapter 10 (John Wiley, 1976).
- [18] Kündig, E. P., Moskovits, M., and Ozin, G. A., Nature, **254**, 503 (1975).
- [19] Klotzbücher, W. and Ozin, G. A., J. Mol. Catal., **3**, 195 (1977).
- [20] Green, D. W. and Gruen, D. M., J. Chem. Phys. **60**, 1797 (1974).

- [21] Schniepp, O., J. Phys. Chem. Solids, 17, 188 (1961).
- [22] Lee, E. L. and Gutmacher, R. G., J. Phys. Chem. Solids, 23, 1823 (1962).
- [23] DeVore, T. C., Ewing, A., Franzen, H. F., and Calder, V., Chem. Phys. Lett. 35, 78 (1975).
- [24] Carstens, D. H. W., Kozlowski, J. F., and Gruen, D. M., High Temp. Sci. 4, 301 (1972).
- [25] Shirk, J. S. and Bass, A. M., J. Chem. Phys. 49, 5156 (1968).
- [26] Kuene, W. and Luescher, E., Solid State Comm. 8, 811 (1970).
- [27] Micklitz, H. and Barrett, P. H., Phys. Rev. B 4, 3845 (1971).
- [28] Klotzbücher, W., McLaren, C., and Ozin, G. A., unpublished results.
- [29] Ozin, G. A., Hanlan, A. J. L., and Mitchell, S., in Vibrations in Adsorbed Layers, Conference Report Kernforschungsanlage Jülich (1978), in press.
- [30] Brom, Jr., J. M., Graham, W. R. M., and Weltner, W., Jr., J. Chem. Phys. 57, 4116 (1972).
- [31] Hanlan, A. J. L. and Ozin, G. A., Inorg. Chem. 16, 2848 (1977).
- [32] Klotzbücher, W. and Ozin, G. A., Inorg. Chem. 15, 292 (1976).
- [33] Carstens, D. H. W., Brashear, W., Eslinger, D. R., and Gruen, D. M., Appl. Spec. 26, 184 (1972).
- [34] (a) Huber, H., Ozin, G. A., and Power, W. J., J. Am. Chem. Soc. 98, 6508 (1976);  
(b) Moskovits, M. and Hulse, J. Chem. Phys. 66, 3988 (1977); (c) Ozin, G. A., Power, W. J., Goddard, III, W. A., and Upton, T. H., J. Am. Chem. Soc. 100, 4750 (1978).
- [35] Jansson, K. and Scullman, R., J. Mol. Spectr. 61, 299 (1976).
- [36] Brewer, L. and King, G., J. Chem. Phys. 53, 3981 (1970).
- [37] Kolb, D. M., Leutloff, D., and Schulze, W., J. Chem. Phys. 66, 2806 (1977).
- [38] Huber, H., Kündig, E. P., Moskovits, M., and Ozin, G. A., J. Am. Chem. Soc. 97, 2097 (1975).
- [39] Ozin, G. A., Appl. Spectr. 30, 573 (1976).
- [40] (a) Moskovits, M. and Hulse, J. E., J. Chem. Phys. 67, 4271 (1977); (b) Mitchell, S. and Ozin, G. A., unpublished data.
- [41] Brewer, L., King, B. A., Wang, J. L., Meyer, B., and Moore, G. F., J. Chem. Phys. 49, 5209 (1968).
- [42] Schulze, W., Kolb, D. M., and Gerischer, H., J. Chem. Soc. Faraday Trans. 271, 1763 (1975).
- [43] Forstmann, F., Kolb, D. M., Leutloff, D., and Schulze, W., J. Chem. Phys. 66, 2806 (1977).
- [44] Ozin, G. A. and Huber, H., Inorg. Chem. 17, 155 (1978).
- [45] (a) King, B. A., Ph.D. Thesis, Univ. of Calif., 1968; (b) Chang, C. A., Ph.D. Thesis, Univ. of Calif., 1970; (c) Mann, D. M., Ph.D. Thesis, Univ. of Calif., 1970; (d) Morel, A., Ph.D. Thesis, Univ. of Washington, Seattle, 1970.
- [46] Gruen, D. M., Gaudioso, S. L., Beth, R. L., and Lerner, J. L., J. Chem. Phys. 60, 89 (1974).
- [47] Klotzbücher, W., Ozin, G. A., Norman, J., Jr., and Kolari, H. J., Inorg. Chem. 16, 2871 (1977).

- [48] Klotzbücher, W. E. and Ozin, G. A., J. Am. Chem. Soc. 100, 2262 (1978).
- [49] Hansen, M., Constitution of Binary Alloys (McGraw-Hill, N.Y., 1958), and supplements.
- [50] Kasai, P. and McLeod, D., J. Phys. Chem. 82, 1554 (1978).
- [51] Montano, P. A., J. Appl. Phys. 49, 1561 (1978).
- [52] Ozin, G. A. and Klotzbücher, W. E., Inorg. Chem. (submitted).
- [53] McIntosh, D., Messmer, R. P., and Ozin, G. A. (in preparation).
- [54] Ozin, G. A. and Klotzbücher, W. E. (in preparation).
- [55] Sinfelt, J. H., et al., U.S. Patent 3,871,997 (March 1975); 3,901,827 (August 1975); 3,429,619 (December 1975); 3,953,368 (April 1976).
- [56] Kolb, D. M. and Leutloff, D., Chem. Phys. Lett. 55, 264 (1978).
- [57] Farrel, J., Huber, H., Klotzbücher, W., Mitchell, S., Ozin, G. A., and Wallace, G. K. (unpublished results).
- [58] Klotzbücher, W. and Ozin, G. A. (unpublished data).
- [59] Hanlan, A. J. L., Ph.D. Thesis, Univ. of Toronto, 1978.
- [60] Schulze, W., Becker, H. U., and Abe, H., Ber. Bunsenges. Phys. Chem. 82, 138 (1978).
- [61] Zhitnikov, R. A. and Melnikov, N. I., Opt. Spect. (USSR), (Eng. Transl.) 24, 53 (1965).
- [62] Kevon, L., Hue, H., and Kawabata, K., J. Chem. Phys. 66, 3834 (1977).
- [63] Forstmann, F., Kolb, D. M., and Schulze, W., J. Chem. Phys. 64, 2552 (1976).
- [64] Schulze, W., Becker, H. W., Minkwitz, R., and Manzel, K., Chem. Phys. Lett. 55, 59 (1978).
- [65] As  $\text{Cr}_2$  remains essentially invariant under these circumstances, we favour  $\text{Mo}^* + \text{CrMo} \rightarrow \text{CrMo}_2$  rather than  $\text{Mo}^* + \text{Cr}_2 \rightarrow \text{Cr}_2\text{Mo}$ .
- [66] As  $\text{Mo}_2$  remains essentially invariant under these circumstances, we favour  $\text{Cr}^* + \text{CrMo} \rightarrow \text{Cr}_2\text{Mo}$  rather than  $\text{Cr}^* + \text{Mo}_2 \rightarrow \text{CrMo}_2$ .
- [67] It is important to note here, that under a wide variety of concentration conditions in separate Cr/Kr(Ar), Mo/Kr(Ar), Cr/Mo/Kr(Ar) experiments, bulk diffusion incurred by thermal annealing (12-40 K for Ar, 12-60 K for Kr leads only to "catastrophic-clustering" as seen by the general decay of all  $\text{Cr}_n$ ,  $\text{Mo}_m$ ,  $\text{Cr}_n\text{Mo}_m$  spectral absorbances (presumably arising from non-selective diffusion-aggregation processes, leading mainly to high clusters characterized by broad bulk metal-like, far UV-absorptions). This could imply "thermally activated clustering" for the lower diatomic, triatomic etc., species which might well be kinetically impeded at the low temperatures employed in our matrix experiments. Incidentally, this is not the case for silver, where at least  $\text{Ag}_{2,3,4,5}$  clusters can be generated by thermal-annealing techniques in Ar, Kr, Xe, and  $\text{CH}_4$ . It is, therefore, conceivable, that the facile photogeneration of CrMo,  $\text{Mo}_2$ ,  $\text{Cr}_3$ ,  $\text{Cr}_2\text{Mo}$ ,  $\text{CrMo}_2$ , and  $\text{Mo}_3$  is, in fact, the outcome of "photoactivated" nucleation events involving either electronically excited or "thermally hot" atomic/cluster moieties. Further research is required to establish this pertinent aspect of photo-aggregation.

## Discussion

Question (Berkowitz): Correct me, that was entirely electronic absorption spectroscopy rather than vibrational. So, you don't see any fine structure that would enable you to give a vibrational or rotational analysis, right?

Response (Klotzbücher): Yes, electronic. The resolution on our instruments is not high enough for that fine structure.

Question (Berkowitz): So, you have various schemes for being able to say that it is  $\text{Mo}_2$  instead of  $\text{Mo}_3$ .

Response (Klotzbücher): We are doing concentration studies of the metallic position; from the slope we can tell if we form a dimer or trimer.

What we have done and the important part in this is we have formed bimetallic clusters, bimetallic dimers of metals which are supposed to be not miscible.

Question (Berkowitz): Okay, one question that I have. You did some calculations also, X-alpha, you say, and extended Hückel and I don't know how those calculations relate to your experiment. And the other question I have is how do those diatomics that have been observed in equilibrium in high temperature studies relate to the diatomics that you see? For example,  $\text{Au}_2$  or  $\text{Ag}_2$  have been observed in high temperature mass spectrometry many years ago; many of these others now have too.

Response (Klotzbücher): Can I give you an example? Okay, Dr. Gingerich was showing you a couple of the dimers today. Extended Hückel is a method where you are just plugging in some numbers. What we have done is we have taken those numbers and say, okay, I know my electronic position for dichromium. Now, let me adjust the parameters, just the energy levels such a way that those fit. How good is this? Can it predict now CrMo, by just using the parent values (i.e.,  $\text{Mo}_2$  and  $\text{Cr}_2$ )? Can I create the sum of them? The answer is yes. What it has done is predict the electronic transitions, the bond lengths and the bond strength, the dissociation energy. I will give you an example.  $\text{Cr}_2$  according to Dr. Gingerich is around 36 kcal/mol. I predicted 37 kcal/mol from my calculations.  $\text{Mo}_2$ : 96 from Gingerich again. Predicted from the calculations: 82-83 kcal/mol. Using just extended Hückel. It's just playing and it is a game. We were surprised ourselves that it works and it works for silver-chromium too. It is fantastic in a certain sense because we hadn't expected it.

Chromium-molybdenum, for example, again it works: 46 kcal/mol and the bond length, 1.7 Å for dichromium; 2.1 Å for dimolybdenum; and 1.9 Å for CrMo.



TRANSITION-METAL MOLECULES AND WALSH'S RULES--RATIONALIZATION  
OF OPTICAL AND ESR DATA

William Weltner, Jr.  
Department of Chemistry  
University of Florida  
Gainesville, FL 32611

The electronic and molecular structures of the transition-metal difluoride, dioxide, and dihydride molecules are rationalized or predicted from proposed molecular orbitals and Walsh-type diagrams based upon optical and ESR spectroscopic data.

1. Introduction

The electronic and molecular structures of the transition-metal dihalides is a rather old topic, where an increasing amount of experimental data has revealed some interesting variations. Much less is known about the dioxides, since few have been studied spectroscopically. The dihydrides also fall in this class, with the additional disadvantage that there is little experimental knowledge of the electronic states of the monohydrides [1]<sup>1</sup>.

There will be no attempt made here to review all of the data on these molecules, since there are several recent sources [2-5]. The gist of the difluoride data is that: (i)  $\text{TiF}_2$  is definitely bent and all heavier first-row difluorides are probably linear (see, however, the discussion of  $\text{NiF}_2$  in references [2] and [4]; and (ii) the trend of the multiplicities of the ground states are similar to the metals themselves. The few dioxides studied in Groups IVB - VIB are bent, but  $\text{MnO}_2$  is linear with a  $4\Sigma_g$  ground state [6].  $\text{CrH}_2$ <sup>7</sup> and  $\text{MnH}_2$ <sup>8</sup> are bent, with probable  $5A_1$  and  $6B_2$  ground states, respectively.

Some years ago Hayes [9] suggested a Walsh-type diagram [10] to explain the linearity of the  $\text{MnF}_2$  molecule, and we detailed a crude set of MO's for linear and bent  $\text{TaO}_2$  [11]. With more recent data in hand it is appropriate to revise and extend that theory to other transition-metal molecules. The difference, of course, between these molecules and those studied by Walsh, is in the occupancy of d orbitals. It should be noted here that ligand-field theory was early applied to the dihalides [12-14] with some success in the discussion of their optical spectra. Also, Drake and Rosenblatt [3] have successfully applied a polarizability model to correlate the geometries of dihalides (and trihalides).

<sup>1</sup>Figures in brackets indicate literature references at the end of this paper.



## 2. Difluorides and Dioxides

Experimental evidence indicates that a bent to linear structural change occurs at  $\text{TiF}_2$  to  $\text{VF}_2$ ; i.e., from 18 to 19 valence electrons. (Valence electrons here include 3d, 4s on the metal and 2s, 2p on the ligand.) One then predicts that such a change in geometry would occur in the dioxides between  $\text{CrO}_2$  and  $\text{MnO}_2$ . Although the structure of  $\text{CrO}_2$  is not known, that of  $\text{MnO}_2$  is linear [6] and that of  $\text{TiO}_2$  is bent [15]. However, there is support for the proposal that the dioxides straighten out in going from  $\text{CrO}_2$  to  $\text{MnO}_2$  in the observations of the heavier metal dioxides, since Mo [16] and W [17], in the same Group as Cr, both have bent dioxides. Although detailed wavefunctions are yet to be calculated (except for perhaps  $\text{NiF}_2$  [18]), an approximate set for the linear and bent molecules are given in table I.

Table I. Molecular orbitals<sup>a</sup> of linear and bent  $\text{MX}_2$ .

Linear ( $D_{\infty h}$ , sym. axis = z)		Bent ( $C_{2v}$ , $C_2$ axis = y)	
$s' + (s + s)$	$s_1$	$s' + (s + s)$	$s_1$
$s - s$	$s_2$	$s - s$	$s_2$
$s' + (p_z + p_z)$	$\sigma_g$	$s' + (p + p)_1$	$a_1'$
$p_z - p_z$	$\sigma_u$	$(p - p)_1$	$b_2'$
$d_{xz} + (p_x - p_x)$	$\pi_g$	$d_{xz} + (p_x - p_x)$	$a_2''$
$d_{yz} + (p_y - p_y)$		$d_{yz} + (p - p)_2$	$b_2'$
$p_x + p_x$	$\pi_u$	$p_x + p_x$	$b_1''$
$p_y + p_y$		$d_{x^2 - y^2} + (p + p)_2$	$a_1'$
$d_{x^2 - y^2}$	$\delta_g$	$d_{x^2 - y^2} - (p + p)_2$	$\bar{a}_1'$
$d_{xy}$		$d_{xy}$	$b_1''$
$d_{xz} - (p_x - p_x)$	$\bar{\pi}_g$	$d_{xz} - (p_x - p_x)$	$\bar{a}_2''$
$d_{yz} - (p_y - p_y)$		$d_{yz} - (p - p)_2$	$\bar{b}_2'$
$s' - (p_z + p_z)$	$\bar{\sigma}_g$	$s' - (p + p)_1$	$\bar{a}_1'$

<sup>a</sup> Over closed shells; e.g., includes 3d, 4s on metal and 2s, 2p on ligand.

4p on metal is neglected.  $s'$  is a hybrid 4s +  $3d_{z^2}$  orbital.

$\text{TiF}_2$  (and presumably  $\text{CrO}_2$ ), with 18 electrons, is bent, and one concludes that the bending influences of the  $\pi_u$  and  $\pi_g$  orbitals depicted in the Walsh-type diagram [10] in figure 1 more or less determine the geometry. The orbitals are filled up through the  $b_1''(\pi_u)$  with a  ${}^3B_1$  ground state resulting from two additional unpaired electrons in the  $b_1''$  and  $\bar{a}_1'$  orbitals [19]. These are essentially non-bonding  $d\delta_g$  orbitals in the linear molecule oriented perpendicular to the plane of the bent  $\text{TiF}_2$  molecule.

Addition of another electron into the scheme in figure 1 results in a linear  $\text{VF}_2$  (or  $\text{MnO}_2$ ) molecule, from experimental evidence [4,6]. Clearly, occupation of the antibonding  $\bar{\sigma}_g$  level, which must favor a bent molecule, will not cause the 19 valence-electron molecule to be linear. Since from ESR evidence both  $\text{VF}_2$  and  $\text{MnO}_2$  have  ${}^4\Sigma_g$  ground states, their

configurations (over closed shells) must be either  $\sigma\delta^2$  or  $\sigma\pi^2$ . Since  $\sigma\delta^2$  does not favor a linear structure, one must place the three unpaired electrons in the  $\bar{\sigma}_g$  and  $\bar{\pi}_g$  orbitals, the latter then stabilizing the observed linear geometry. The rationalization of this shift from  $\delta d$  to  $\pi d$  occupation from  $\text{TiF}_2$  to  $\text{VF}_2$  must be provided by higher d-d repulsion in the former. Such effects are known to be of great importance in ordering the many possible low-lying states in transition-metal molecules [1]. Also, although we earlier favored the  $\sigma\delta^2$  configuration for  $\text{MnO}_2$  [6], it appears that our reasoning was incorrect, which may have resulted from assuming the hyperfine splitting constants  $A_{||}(\text{Mn})$  and  $A_{\perp}(\text{Mn})$  to be positive.

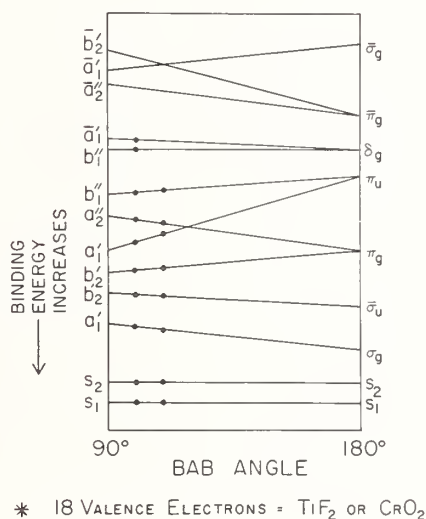


Figure 1. Walsh-type diagram for a BAB molecule where A is a transition-metal.

Single prime means that the orbital is symmetric with respect to reflection in the plane of the molecule, a double prime that it is anti-symmetric.

Note that the new experimental evidence for the structures of the early members of the series makes necessary a change in Hayes's logic about the bonding orbitals determining the structure [9]. It must be that the antibonding orbitals are the real culprits in producing linearity.

Figure 2 then gives the MO scheme for linear  $\text{VF}_2$  utilizing the orbitals in table I. The ordering of the levels  $\sigma_g$ ,  $\sigma_u$ ,  $\pi_u$ ,  $\pi_g$  is not established, but  $\pi_g$  has been placed below  $\pi_u$  here because the participation of  $d_{xz,yz}$  is expected to lead to increased bonding in the former (see fig. 4 in reference [5] for an illustration). The scheme for isoelectronic  $\text{MnO}_2$  should be the same as figure 2 except that one expects the 3d levels to be lower for Mn.

Judicious addition of further electrons then gives  $\text{CrF}_2$  and  $\text{FeO}_2$  ( $\sigma\pi\delta^2$ ,  $^5\Pi$ ) and  $\text{MnF}_2$  and  $\text{CoO}_2$  ( $\sigma\pi\delta^2$ ,  $^6\Sigma$ ). Only for  $\text{MnF}_2$  has this assignment been verified [20]. Since  $\text{CuF}_2$  is also linear [21], it is presumed that  $\text{FeF}_2$ ,  $\text{CoF}_2$ , and  $\text{NiF}_2$  are also. (For  $\text{NiF}_2$ , this disagrees with some theory and experiments [4,18]). Correspondingly,  $\text{ScO}_2$ ,  $\text{TiO}_2$ , and  $\text{VO}_2$  are expected

to be bent, as discussed earlier [5]. A summary of these predicted, and the few established ground states for the difluorides and dioxides is given in table II.

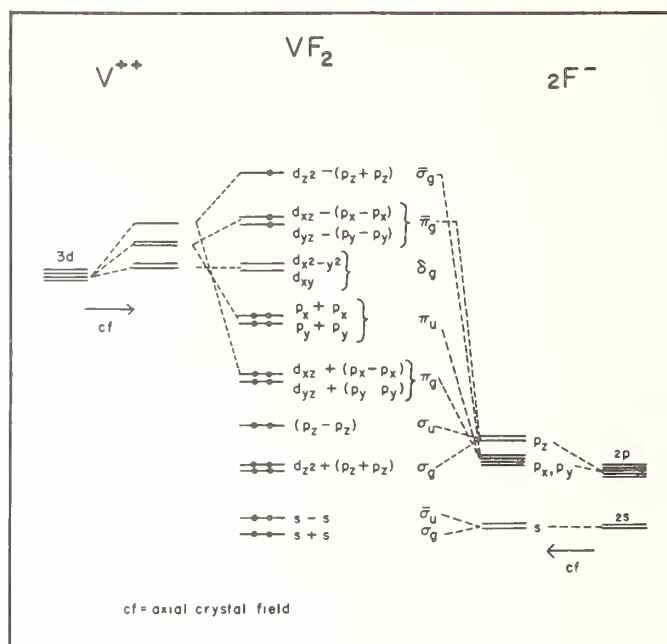


Figure 2. Approximate molecular orbitals of  $\text{VF}_2$  (or isoelectronic  $\text{MnO}_2$ ). The 19 valence electrons occupy the orbitals as indicated.

Table II. Configurations and Ground States of Transition Metal Difluorides and Dioxides.

Valence Electrons	Configuration and Ground State	Difluoride	Dioxide
15	$(b_1'')$ $2B_1$		$\text{ScO}_2$
16	$(b_1''^2)$ $1A_1$		$\text{TiO}_2$
17	$(b_1'')$ $2B_1$	$\text{ScF}_2$	$\text{VO}_2$
18	$(\bar{a}_1' b_1'')$ $3B_1^*$	$\text{TiF}_2$	$\text{CrO}_2$
19	$(\sigma\pi^2)$ $4\Sigma_g^*$	$\text{VF}_2$	$\text{MnO}_2$
20	$(\sigma\pi\delta^2)$ $5\Pi$	$\text{CrF}_2$	$\text{FeO}_2$
21	$(\sigma\pi^2\delta^2)$ $6\Sigma_g^*$	$\text{MnF}_2$	$\text{CoO}_2$
22	$(\sigma^2\delta^2\pi^2)$ $5\Sigma_g$	$\text{FeF}_2$	$\text{NiO}_2$
23	$(\sigma^2\delta^2\pi^2)$ $4\Delta$	$\text{CoF}_2$	$\text{CuO}_2$
24	$(\sigma\delta^4\pi^3)$ $3\Pi$	$\text{NiF}_2$	
25	$(\sigma\delta^4\pi^4)$ $2\Sigma$	$\text{CuF}_2$	

\*Consider as an established ground state.

### 3. Dihydrides

Among the diatomic hydrides, only the spectra of CrH ( $^6\Sigma$ ), MnH ( $^7\Sigma$ ), CuH ( $^1\Sigma$ ), and ZnH ( $^2\Sigma$ ) have been analyzed in any detail [1]. Theoretical studies have been made by a few workers [22-26] and reviewed recently by Scott and Richards [1]. In general, they find many low-lying states and therefore an uncertainty in identifying the ground state in most cases. High-spin MnH is an exception, both theoretically and experimentally, in that its optical spectrum has been analyzed, and the electronic properties of the ground  $^7\Sigma$  state derived from theory [24] agree rather well with the ESR data of Van Zee, et al. [8]. In MnH, the metal 3d nonbonding levels remain almost degenerate and lie lower than the next higher level ( $7\sigma$ ) by about 6 eV [24]. This  $7\sigma$  bonding orbital is about 16 percent Mn 4s, 8 percent Mn 4p and 72 percent H 1s. About 3.5 eV higher lies the  $8\sigma$  nonbonding orbital made up of about 60 percent Mn 4s, 38 percent Mn 4p and 2 percent H 1s. (ESR [8] indicated more like 40 percent Mn 4s.) Except for the bonding  $7\sigma$  orbital, the electrons are unpaired in the metal 3d and 4sp orbitals with the 3d lying lowest.

Addition of another H atom to form MnH<sub>2</sub> is analogous to the formation of isoelectronic FeH, but its ground state is also not known. Theory [26] indicates that the electron added to MnH goes into the 3d $\delta$  orbital to yield a  $^6\Delta$  ground state, but that the  $^6\Sigma$  and  $^6\Pi$  states, where the electron is added to the 3d $\sigma$  or 3d $\pi$  orbitals, are also candidates. It then follows that MnH<sub>2</sub> will probably have the same electron configuration as MnH but with an additional electron in one of the 3d orbitals.

Our IR evidence [8] on matrix-isolated MnH<sub>2</sub> and its deuterated counterparts indicates that it is bent at an angle of  $117 \pm 30^\circ$ . Extrapolating from the MnH orbitals, one arrives at those in table III (revised slightly from an earlier version [8]) and the probable Walsh-type diagram in figure 3.

Table III. Molecular orbitals<sup>a</sup> of linear and bent MH<sub>2</sub>.

Linear (D <sub>∞h</sub> , sym. axis = y)			Bent (C <sub>2v</sub> , C <sub>2</sub> axis = z)	
$\left. \begin{array}{l} d_{z^2} - x^2 \\ d_{xz} \end{array} \right\}$	$\delta_g$		$d_{x^2} + s_M$	$a_1'$
			$d_{xz}$	$b_1''$
$\left. \begin{array}{l} d_{yz} \\ d_{xy} \end{array} \right\}$	$\pi_g$		$d_{yz} + (1s - 1s)$	$b_2'$
			$d_{xy}$	$a_2''$
$d_{y^2}$	$\sigma_g$		$d_{z^2} - y^2 + (1s + 1s)$	$a_1'$
$s_M + (1s + 1s)$	$\sigma_g$		$p_z + (1s + 1s)$	$a_1'$
$p_y + (1s - 1s)$	$\sigma_u$		$p_y + (1s - 1s)$	$b_2'$
$\left. \begin{array}{l} p_z \\ p_x \end{array} \right\}$	$\pi_u$		$s_M$	$a_1'$
			$p_x$	$b_1''$

<sup>a</sup> Over closed shells, i.e., includes 3d, 4s, and 4p orbitals on the metal atom.

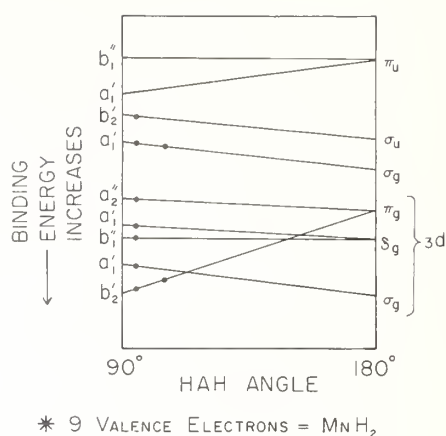


Figure 3. Walsh-type diagram for a  $AH_2$  molecule where A is a transition-metal. Single prime means that the orbital is symmetric with respect to reflection in the plane of the molecule, a double prime that it is anti-symmetric.

When  $MnH_2$  is bent, the  $d_{yz}$  ( $\pi_g$ ) orbital can be effective in the bonding, which must be the essential factor stabilizing the non-linear shape. (This is analogous to the  $\pi_u$  orbital (at higher energy in fig. 3) which drops in energy so drastically in bent non-transition-metal molecules [10].) The higher-lying orbitals in table III have been written to include specific metal 4p character, as in Bagus and Schaefer's [24] calculation for  $MnH$ , which is probably more correct than those given in table V of reference [8]. Then, from table III and figure 3, the most probable configuration of  $MnH_2$  is  $(b_2')^2(a_1')(b_1'')(a_1'')(a_2'')(a_1')^2(a_1')$  yielding a  ${}^6B_2$  ground state. Correspondingly,  $FeH_2$ ,  $CoH_2$ ,  $NiH_2$  and  $CuH_2$  would all be bent, with decreasing multiplicities as the 3d shell is filled across the Periodic Table. Removing electrons from  $MnH_2$  to form the lighter transition-metal dihydrides should result only in loss of 3d electrons and a lowering of the multiplicity. The bent character would then be retained as long as the lowest  $b_2'$  orbital was occupied which would always be the case in this model. However, in the lighter metal hydrides the 3d levels lie higher [1], but it is likely that they will still be bent.

#### 4. Conclusion

Lacking *ab initio* calculations on these triatomic species, an attempt has been made here to provide some understanding of the theoretical basis for their structures and ground electronic states. It remains to be seen whether further experimental data will support the proposed simple molecular orbital schemes and Walsh-type diagrams.



Over many years, the principal contributors to this research in our laboratory have been T. C. DeVore, R. F. Ferrante, W. R. M. Graham, W. D. Hewett, Jr., N. S. McIntyre, K. R. Thompson, R. J. Van Zee, and J. L. Wilkerson. Their research formed the basis for this theoretical discussion. The author is also grateful to the Air Force Office of Scientific Research (Grant No. AFOSR 76-2906) and the National Science Foundation (Grant No. CHE76-17564) for their support.

## References

- [1] Scott, P. R. and Richards W. G., Chemical Society, London Specialist Periodical Reports, Molecular Spectroscopy Vol. 4, pp. 70-95 (The Chemical Society, London, 1976).
- [2] Hastie, J. W., Hauge, R. H. and Margrave, J. L., Ann. Rev. Phys. Chem. 21, 475 (1970).
- [3] Drake, M. C. and Rosenblatt, G. M., in Proceedings of Symposium on High Temperature Metal Halide Chemistry, Proc. Vol. 78-1, D. L. Hildenbrand and D. D. Cubicciotti, eds., p. 234 (The Electrochem. Soc., Princeton, N.J., 1978).
- [4] DeVore, T. C., Van Zee, R. J. and Weltner, S. Jr., in Proceedings of Symposium on High Temperature Metal Halide Chemistry, Proc. Vol. 78-1, D. L. Hildenbrand and D. D. Cubicciotti, eds., p. 187 (The Electrochem. Soc., Princeton, N.J., 1978).
- [5] Weltner, W. Jr., Berichte der Bunsen-Gesellschaft fur phys. Chem. 82, 80 (1978).
- [6] Ferrante, R. F., Wilkerson, J. L., Graham, W. R. M. and Weltner, W. Jr., J. Chem. Phys. 67, 5904 (1977).
- [7] Van Zee, R. J., DeVore, T. C. and Weltner, W. Jr. (unpublished work).
- [8] Van Zee, R. J., DeVore, T. C., Wilkerson, J. L. and Weltner, W. Jr., J. Chem. Phys. (in press).
- [9] Hayes, E. F., J. Phys. Chem. 70, 3740 (1966).
- [10] Walsh, A. D., J. Chem. Soc. 2260, 2266 (1953).
- [11] Weltner, W. Jr. and McLeod, D. Jr., J. Chem. Phys. 42, 882 (1965).
- [12] Hougen, J. T., Leroi, G. E. and James, T. C., J. Chem. Phys. 34, 1670 (1961).
- [13] Smith, D. W., Inorg. Chim. Acta, 5, 231 (1971).
- [14] Gruen, D. M., Progr. Inorg. Chem. 14, 119 (1971).
- [15] McIntyre, N. S., Thompson, K. R. and Weltner, W. Jr., J. Phys. Chem. 75, 3242 (1971).
- [16] Hewett, W. D. Jr., Newton, J. H. and Weltner, W. Jr., J. Phys. Chem. 79, 2640 (1975).
- [17] Weltner, W. Jr. and McLeod, D. Jr., J. Molec. Spectr. 17, 276 (1965).
- [18] Besnainou, S. and Thitten, J. L., paper given in 32nd Symposium on Molecular Spectroscopy, Columbus, Ohio, TH1, June 14, 1977. This work gives the angle in  $\text{NiF}_2$  as  $162^\circ$ , while we are taking it to be linear. There is contradictory experimental evidence about the structure of this molecule. Electric deflection indicates it is linear, and optical spectra place the angle as somewhere between  $152$  and  $180^\circ$  [2,4].
- [19] DeVore, T. C. and Weltner, W. Jr., J. Am. Chem. Soc. 99, 4700 (1977).
- [20] DeVore, T. C., Van Zee, R. J. and Weltner, W. Jr., J. Chem. Phys. 68, 3522 (1978).

- [21] Kasai, P. H., Whipple, E. B. and Weltner, W. Jr., J. Chem. Phys. 44, 2581 (1966).  
[22] Henderson, G. A., Das, G. and Wahl, A. C., J. Chem. Phys. 63, 2805 (1975).  
[23] Walker, J. H., Walker, T. E. H. and Kelly, H. P., J. Chem. Phys. 57, 2094 (1972).  
[24] Bagus, P. S. and Schaefer, H. G. III, J. Chem. Phys. 58, 1844 (1973).  
[25] Scott, P. R. and Richards, W. G., J. Phys. B: Atom Molec. Phys. 7, 1679 (1974); 7, 50 (1974); 7, L347 (1974).  
[26] Scott, P. R. and Richards, W. G., J. Chem. Phys. 63, 1690 (1975).

#### Discussion

Comment (Hauge): Bill, I guess a couple of comments. I think we did try pretty hard to get nickel difluoride to be linear by putting in some anharmonic corrections in the isotopic shift calculations and it seemed like you really had to get out of the range of possible anharmonic corrections to get nickel difluoride to be linear by that type of mechanism. So, we ended up by concluding that we thought it was in the region of 160 degrees too.

The other thought, we did measure bending frequencies for all of those difluorides and they varied all over and we had no obvious explanation for it. I wondered if your scheme for molecular orbital populations would suggest a certain variation in bending frequency.

Response (Weltner): Yes, I hadn't thought about it Bob (Hauge), but you know you put electrons into antibonding orbitals and it would correspondingly change the bending frequency. I will have to look at that.

5

**V. MOLECULAR STRUCTURE DETERMINATION--  
VAPOR SPECIES**



## THE DETERMINATION OF THE MOLECULAR SHAPES OF HIGH TEMPERATURE SPECIES

I. R. Beattie and D. A. Greenhalgh

Department of Chemistry

The University

Southampton SO9 5NH, U.K.

### 1. Introduction

In this paper, we briefly outline the main techniques for studying high temperature vapours with reference to polyatomic molecules. We also attempt to draw attention to the problems (and advantages) associated with each technique. We then consider the new technique of coherent Raman spectroscopy and likely future developments.

Many laboratory experiments examine "high temperature" molecules in idealized situations which may have little relevance to the equilibrium vapour above a solid at high temperature. There is also the interesting philosophical--and fundamental scientific problem--of "floppy" molecules that the chemist may wish to conveniently categorize as planar or linear, for example, but where the molecule spends most of the time in a pyramidal or bent configuration. The following principal methods for the generation of vapours from solids may be considered.

### 2. Species Production

#### 2.1 Gases in furnaces

This appears at first sight to be the ideal equilibrium situation. However, there are major problems of containment, window materials, background thermal radiation, broadening of spectral lines due to population of many excited states (notably for molecules with large partition functions), and increased Doppler velocities. Raman spectroscopy at temperatures to 1000 °C is relatively routine and because the principal bands are normally totally symmetric vibrations showing only the Q-branches, useful information may be obtained from high temperature systems [1]<sup>1</sup>. Variable temperature studies in closed systems can be particularly valuable where dissociation or polymerization phenomena occur, and may aid the interpretation of mass spectrometric or matrix isolation studies (including the effects of diffusion in matrices).

---

<sup>1</sup>Figures in brackets indicate the literature references at the end of this paper.



## 2.2 Effusion cells<sup>2</sup>

Effusion is the passage of gas through a small orifice whose diameter is small compared with the mean free path. In many experiments based on "Knudsen cells," although conditions may appear to be similar among various workers, radical differences occur. Thus, in mass spectrometric studies, orifices are frequently in the range 0.03 to 0.3 mm diameter and because of the extreme sensitivity of the technique (say  $10^{-11}$  Torr detection limit) conditions close to true effusion may occur. The pressure in the source chamber (into which effusion is occurring) may be of the order of  $10^{-5}$  Torr. Contrast this with an electron diffraction experiment where the orifice may be of the order of 0.3 mm diameter and an electron beam of say 0.1 mm diameter passes as close to the orifice as possible. However the pressure of sample required in the interaction volume element is of the order of 1 Torr, giving a mean free path of less than 0.01 mm. For matrix isolation experiments the effusion cell is frequently a hollow tube of perhaps 1 cm diameter, sealed at one end and containing the sample. The solid sublimates in a fairly high vacuum (say  $10^{-4}$  Torr) while the inlet gas is bled independently into the co-condensation chamber. Clearly, the conditions are close to free evaporation in this case, while polymerization reactions may occur during the trapping process.

## 2.3 Dynamic situations<sup>3</sup>

These occur in flames, plasmas, and shock tubes for example. Where the interest lies in the study of materials introduced into the flame or plasma, the attainment of a homogeneous distribution may be difficult and concentrations rather low. There is also the problem of luminescence from the flame, including particulates.

## 3. Spectroscopic Techniques

### 3.1 Rotational spectroscopy<sup>4</sup>

The study of molecules ranges from the rigorous determination of molecular geometry to the qualitative assignment of shape. Some idea of the problems involved may be obtained by considering the dispute over the planarity [2] of  $\text{AlCl}_3$  or the linearity [3] of  $\text{MgF}_2$ . The ideal approach from a fundamental point of view is a rotational analysis of a pure rotational spectrum, a vibrational spectrum, or an electronic spectrum. For molecules of low symmetry the analysis of the spectra can be a formidable problem. Experimentally, for microwave spectroscopy, the molecule must have a permanent electric dipole. Although all molecules other than spherical tops formally show a pure rotational Raman spectrum, there is no instrumentation yet available to resolve the bands of heavy molecules. Also the Raman effect is weak so that studies on molecular beams, even of the expansion-cooled type (see Section 5)

<sup>2</sup>See also elsewhere in this volume chapters by Cater and by Chatillon, et al.

<sup>3</sup>See also chapter of Gersh and Kolb.

<sup>4</sup>See also chapter of Topping and Tiemann.

represent a formidable problem other than for pure gases. In considering the problem of the populations of excited states, it must be remembered that a temperature of only 10 K is equivalent to  $7 \text{ cm}^{-1}$ , and the rotational constant of  $\text{HgCl}_2$  for example would be about  $0.05 \text{ cm}^{-1}$ . The most attractive experiment for molecules which cannot be studied by microwave spectroscopy, and which do not absorb in the visible or near uv region of the spectrum, appears to be high resolution infrared spectroscopy.

### 3.2 Electron diffraction<sup>5</sup>

The next widely applicable (though not so utilized) technique yielding quantitative structural information is electron diffraction. Essentially, each pair of atoms in the molecule leads to coherent molecular scattering with an intensity variation observed as a damped sine wave whose period is related to the interatomic distance (with the additional complication of a phase angle change on scattering, where the atomic numbers are widely disparate). It is possible to calculate the molecular scattering pattern (based on realistic models) and to compare this with that experimentally observed. The principal objection raised is usually that the interatomic distances are averaged over all thermal vibrations. An alternative approach would be that it is a reflection of the mean molecular geometry from which amplitudes of vibration and vibrational frequencies can ideally be found [3a]. In general, bond lengths are less easily deformed than bond angles. Consider a molecular residue  $\text{XY}_2$  with a bond angle  $\text{YXY}$  of  $\alpha$ . If the molecule vibrates by  $\pm\Delta\alpha$  about the mean angle  $\alpha$ , the ... Y distance shrinkage is given approximately by:

$$d_e [\cos(\Delta\alpha/2) - 1] \quad (1)$$

where  $d_e$  is the equilibrium Y .. Y non-bonded distance corresponding to the angle  $\alpha$  (and the bond length X-Y is assumed to be fixed). It is also interesting to note that for a planar trigonal molecule  $\text{XY}_3$  where  $\alpha$  is again the  $\text{YXY}$  angle, if  $\beta$  is the angle an XY bond makes with the  $\text{C}_3$  axis then

$$\sin \beta = \left( \frac{2}{\sqrt{3}} \right) \sin(\alpha/2). \quad (2)$$

Thus, if the molecule is pyramidal to the extent that all of the XY bonds are  $5^\circ$  out of plane, the bond angle  $\text{YXY}$  changes by only  $0.75^\circ$  (from  $120^\circ$  to  $119.25^\circ$ ).

### 3.3 Molecular beam electric deflection

Proceeding to more qualitative experiments, the electric deflection of a molecular beam using a quadrupole focusser may be used to examine whether a molecule has a permanent dipole [4], although complications can arise due to vibrationally induced dipoles, for example [5]. For a molecule with a second order Stark effect, a quadrupole focusser acts like a

<sup>5</sup>See also chapter of Spiridonov and Zasorin

lens. Non-observation of an electric deflection was used, for example, to suggest that the molecule  $\text{Cs}_2\text{SO}_4$  does not possess a permanent dipole [6].

### 3.4 Photo electron spectroscopy<sup>6</sup>

Photo-electron spectroscopy of high temperature polyatomics has not been extensively studied. However, recent work [7] on heavier metal tetrafluorides illustrates the potential of this experiment. The 2s electrons of fluorine lie well below the 2p electrons energetically. The fluorine  $2p_\sigma$  orbital combinations transform as  $a_1 + t_2$  while the corresponding  $2p_\pi$  orbitals transform as  $e + t_1 + t_2$ . For elements with a  $d^0$  configuration, five bands are thus predicted in this region arising from  $a_1 + e + t_1 + 2t_2$  (the p orbitals on the metal transforming as  $t_2$  and the d-orbitals as  $e + t_2$ ). Any lowering of symmetry from  $T_d$  to  $D_{2d}$  (for example) would lift some of the degeneracies, resulting in the observation of more bands if coincidences did not occur and providing the distortion was sufficient to cause observable effects. Complications arise in the interpretation of such spectra due to spin-orbit coupling and Jahn-Teller effects in the excited state, for example.

### 3.5 Matrix isolation<sup>7</sup>

Finally, matrix isolation infrared spectroscopy has many advantages (which is one of the reasons why the papers on this subject are relatively numerous). The experiment is easy though matrix effects may complicate data interpretation, corrosion problems are minimized, well resolved spectra of various isotopic species may be obtained and the spectroscopy may be carried out over extended periods using closed cycle refrigeration systems. In certain cases, using intensities and frequencies (preferably including isotopic substitution), it is possible using reasonable force-field approximation to estimate bond angles. Recent results, pertinent to high temperature species structure, include the bidentate interaction of  $\text{NO}_3^-$  [8] or  $\text{PO}_3^-$  [9] with  $\text{K}^+$  and  $\text{Na}^+$ , respectively, and the likely (bidentate)  $D_{2d}$  structure for sodium, potassium and cesium sulphates [10,11]. There is also an extensive literature on Raman, electronic, epr, and Mössbauer spectroscopy of species isolated in matrices.

### 3.6 Combined methods

Clearly, a combination of several spectroscopic techniques is to be preferred. Certainly, for routine characterization of vapours and an indication of molecular shape, a combination of mass spectrometry and matrix isolation infrared spectroscopy is very powerful. One major difficulty in matrix isolation infrared spectroscopy in the absence of characteristic isotope patterns is the unambiguous assignment of molecular identity to a spectral feature. An analogous difficulty occurs with mass spectrometry where electron impact fragmentation can complicate molecular assignment. This latter problem can be largely eliminated

<sup>6</sup>See also elsewhere in this volume the articles by Berkowitz and by Bowling, et al.

<sup>7</sup>See also elsewhere in this volume articles by Ogden, Hauge and Froben.

by the use of time of flight of neutrals in a chopped molecular beam phase sensitive mass spectrometer [12]<sup>8</sup>. Alternatively, angular distributions from the Knudsen cell may be examined [13]<sup>9</sup>.

#### 4. Coherent Raman Phenomena<sup>10</sup>

##### 4.1 Theoretical Considerations

The introduction of lasers revolutionized spontaneous Raman spectroscopy approximately a decade ago. However, this was essentially the replacement of one light bulb by a very much better light bulb: the experimental technique from being rather difficult became almost routine. By contrast, although the study of coherent Raman effects may once again revolutionize certain aspects of Raman spectroscopy, the experiment in our experience is at least an order of magnitude more difficult for the average chemist. It is perhaps worth describing a few coherent Raman phenomena before discussing our own experiments.

Figure 1(a) illustrates the spontaneous Raman effect where the sample is irradiated by (laser) light of frequency  $\nu_1$ . (The thick solid line represents an incident laser, the irregular line  $\wedge$  represents spontaneous emission from the intermediate state). If the intensity of  $\nu_1$  is increased or the sample is irradiated with two lasers simultaneously, one or both of which is capable of producing a high power density at the sample, many other phenomena may be observed notably if  $|\nu_1 - \nu_2|$  is tuned to a Raman active molecular transition frequency. Figure 1(b) represents this case, where both  $\nu_1$  and  $\nu_2$  now are incident lasers. Where  $\nu_1$  is intense and amplification of  $\nu_2$  is observed, the effect has been described by many names including stimulated Raman spectroscopy and stimulated Raman gain spectroscopy. We prefer to shorten this term to Raman gain spectroscopy. Where  $\nu_2$  is intense and absorption in  $\nu_1$  is observed, this (for historical reasons) has been termed inverse Raman spectroscopy. Similarly we prefer the term Raman loss spectroscopy. In both cases an exponential term in the loss (or gain) may be regarded as the analogue of the more familiar term in the Beer-Lambert Law. Thus, for Raman gain spectroscopy

$$I_2(\ell) = I_2(0)e^{I_1 G \ell}, \quad (3)$$

and for Raman loss spectroscopy

$$I_1(\ell) = I_1(0)e^{-I_2 g \ell} \quad (4)$$

where

$$G = g \left[ \frac{\nu_2}{\nu_1} \cdot \frac{n_2}{n_1} \right] \quad (5)$$

<sup>8</sup> Editor's note: see also elsewhere in this volume articles by Plante, and by Bonnell and Hastie.

<sup>9</sup> Editor's note: see also elsewhere in this volume the article by Grimley and Forsman.

<sup>10</sup> Editor's note: additional discussion of this effect and its applications may be found elsewhere in this volume, e.g., see McDonald, et al., and Eckbreth and Hall.



the suffixes referring to the incident lasers  $\nu_1$  and  $\nu_2$ . Here

$$g = \Delta \cdot N \cdot \frac{d\sigma}{d\Omega} / n_2^2 2hc^2 \Gamma \nu_2^3 ; \quad (6)$$

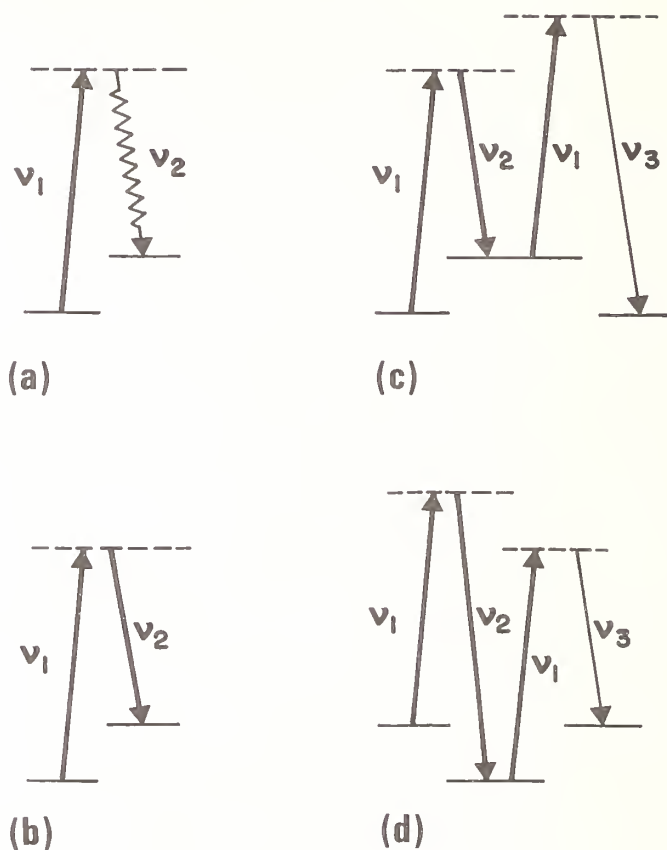


Figure 1. Thick line  $\nu_1$  represents incident laser light. Raman spectroscopic schemes: (a) spontaneous Raman, (b) Raman gain, (c) CARS, (d) CSRS.

$n_1$ ,  $n_2$  are refractive indices at  $\nu_1$  and  $\nu_2$ ;  $h$  = Planck's constant;  $c$  = velocity of light;  $\Gamma$  = half-width at half height for the Raman transition;  $N$  = number density;  $\Delta$  = fractional population difference between initial and final state;  $\ell$  = interaction length;  $\frac{d\sigma}{d\Omega}$  = Raman scattering cross section; and  $I_1 I_2$  are intensities at  $\nu_1$  and  $\nu_2$ .

A recent very beautiful experiment in Raman gain spectroscopy at high resolution has been carried out by Owyong, Patterson and McDowell [14]. The resolution of the  $\nu_1$  band of methane (at pressures down to 20 torr) has been obtained using a multipass cell and two cw lasers. The resolution was 25 Mhz or approximately  $0.001 \text{ cm}^{-1}$ . This is quite an outstanding piece of research and one with considerable implications for future high resolution spectroscopy.

One of the processes which may be observed when both  $\nu_1$  and  $\nu_2$  are intense lasers focused into the sample is illustrated in figure 1(c). This is Coherent Anti-Stokes Raman Spectroscopy or, colloquially, CARS. The corresponding Stokes process is shown diagrammatically in figure 1(d) (CSRS). In all the cases where thin straight lines are shown, the



lines refer to coherent beams induced by the incident laser light. For these processes resonance enhancement occurs when  $|\nu_1 - \nu_2|$  is equal to a Raman active transition frequency. For a sample with an isolated relatively narrow Raman transition frequency with tightly focused beams the CARS power, assuming perfect phase matching, is given by

$$P_3 = \frac{3^2}{h^2 \pi^2 n_3 n_1^2 n_2 c^2} \cdot \frac{N^2}{\nu_2^6} \cdot \frac{\Delta^2}{\Gamma^2} \cdot \frac{d\sigma}{d\Omega}^2 P_1^2 P_2^2 \ell^2 \quad (7)$$

The attractions of coherent Raman spectroscopy are: (a) the possibility of very high resolution spectroscopy (note that the Doppler broadening is proportional to  $|\nu_1 - \nu_2|$ ); (b) the ease of nanosecond spectroscopy (using a wide band laser coupled with a narrow band laser and a monochromator which define the resolution); (c) the ability to obtain spatial resolution in the sample (CARS, CSRS); (d) the excellent discrimination against sample luminescence; and (e) the capability of excellent collection of the highly collimated signal. Note, also, that the selection rules [15] for CARS are identical to those for Raman spectroscopy (under non-resonant conditions) and that for linearly polarized incident beams, the polarization of  $\nu_3$  follows that of  $\nu_2$ . For polarized bands  $\rho_p$ , this lies between 0 and 9/16, while for depolarized bands,  $\rho_p$  is 9/16. Clearly  $I_{\perp}$  refers to  $\nu_1(x) \nu_2(y) \nu_3(y)$  where  $z$  is the propagation direction and the letters in brackets denote the polarization. Similarly  $I_{||}$  refers to  $\nu_1(x) \nu_2(x) \nu_3(x)$ .

For the average chemist (and his sample), the following drawbacks should be recognized: (a) difficulties in using high power narrow band width lasers; (b) the fact that signals from optical components are inevitably collected for a colinear beam geometry, since (non-colinear beams for gases lead to substantial signal losses because of phase matching criteria unless complicated geometries such as BOXCARS [16] are used (compare this with the spontaneous Raman effect where the collection geometry is optimized at the beam waist); (c) the problem of cleaning up the tunable source from the associated collimated super radiance at the signal frequency; (d) the separation of the wanted weak signal from an intense colinear source, notably at low frequency shifts and; (e) the complex and interdependent band profiles in the case of CSRS and CARS, including the problem of non-resonant background.

## 4.2 Results

In our experiments, we use a Nd/YAG laser (JK Lasers) in the unstable resonator configuration, frequency doubled to 532 nm. The output is about 3-4 MW peak power in a 10 ns pulse with a 25 Hz repetition rate. The tunable dye laser is either (i) a Chromatix CMX4 flash lamp pumped laser which (operating on Rhodamine 6G) gives an output power of up to 10 kW peak in a 2- $\mu$ s pulse again at a repetition rate of 25 Hz, or (ii) an in-house frequency doubled Nd/YAG pumped dye laser with up to 20 percent conversion efficiency from the 532 nm pump. The detector involves a box car with a 100 ns gate together with a double monochromator acting as a high quality filter. Spectra are run continuously with a recorder time constant of the order of 3s. Figure 2 shows a typical spectrum which can be routinely obtained with this equipment [17]. The principal problems arising at low frequency shifts

are: (a) dye fluorescence in a collimated beam (due to super radiance); (b) resonant CARS signals from the glass; and (c) the difficulty of separating the weak signal beam from the intense colinear incident laser beams. However the potential of CARS spectroscopy at low frequency shifts is demonstrated by the resolution of the  $60\text{ cm}^{-1}$  band in the pure rotational spectrum of air (fig. 3) [18].

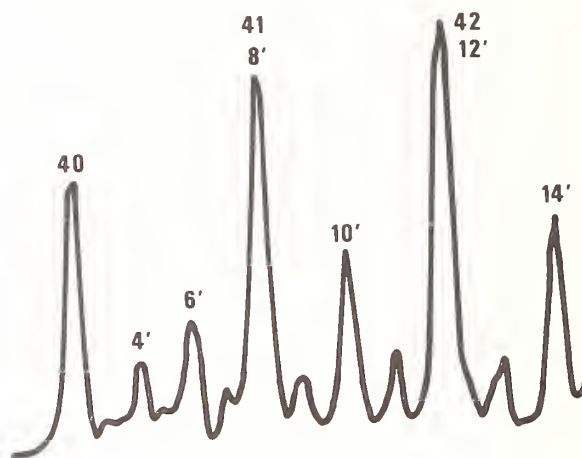


Figure 2. Portion of the first hot-band of nitrogen (820 °C) shown overlapping the fundamental (resolution  $\sim 0.15\text{ cm}^{-1}$ ). Primed numbers refer to the hot-band. The intensity scale is not correct as this is not a ratioed spectrum.



Figure 3. Resolution of the  $60\text{ cm}^{-1}$  band of air.

### 4.3 Discussion

In our experience, CARS (CSRS) spectroscopy in the region 1,000 to 3,200  $\text{cm}^{-1}$  is routine with the equipment described. Down to 600  $\text{cm}^{-1}$  spectra can be obtained without too much trouble if care is taken to avoid signals from the optical components. One solution to this problem is to beam expand during passage of the combined beams through thick glass components, such as lenses, and to use cell windows which either have no first order Raman spectrum or are very thin. Below 600  $\text{cm}^{-1}$ , CARS experiments are not easy, but under suitable conditions as we have shown, high quality spectra can be obtained. The problem for heated gases is increased by the  $\Delta^2/\Gamma^2$  function in the intensity.

The chief contender with coherent Raman spectroscopy for high resolution studies is infrared laser diode spectroscopy which is limited commercially to a low frequency limit of about 385  $\text{cm}^{-1}$ , but should increase in ease of handling as instrument design improves. Clearly, where selection rules prohibit infrared studies, coherent Raman spectroscopy is important. It will also be important for high resolution spectroscopy in the frequency region below 385  $\text{cm}^{-1}$  and, ideally, for pure rotational spectroscopy. However, except under resonance conditions [19], it is unlikely to be usable even in cooled molecular beams (e.g. by adiabatic expansion) of high temperature molecules.

For the high temperature chemist, coherent Raman spectroscopy provides the possibility of studying directly the molecular species in heated gases. CARS (CSRS) and to a lesser extent Raman gain (and loss) spectroscopy also allow for spatially resolved measurements within the sample. Although CARS is at the moment the preferred technique, CSRS is equally applicable and it must be noted that Raman gain (and loss) spectroscopy does not suffer from the problem of band distortion. It is also important to note that in a Raman spectrum the most intense bands are normally the totally symmetric vibrations and the spectra observed are essentially the line like Q-branches which do not suffer as much as the rotational (OPRS) wings from broadening at high temperature.

### 5. Future Prospects

In conclusion, it appears to us that for studying molecular geometry a rotational analysis of an infrared band (obtained using diode laser spectroscopy) or an electronic band (using a high resolution dye laser and fluorescence techniques) in a cooled molecular beam is the experiment of the future. Isentropic expansion of the compound mixed with a high pressure (say 1 atmosphere) of helium through a nozzle of about 0.01 mm diameter can be used to obtain rotational temperatures to a few K and vibrational temperatures of tens of K [20]. The sensitivity of the fluorescence experiments (say  $10^{-8}$  Torr) makes them particularly attractive for use in such dilute beams. In essence, these experiments refer to "gas phase matrix isolation spectra"<sup>11</sup>.

<sup>11</sup>Editor's note: the method described by Bonnell and Hastie elsewhere in this volume should be particularly useful in this regard.

## References

- [1] See for example, Beattie, I. R. and Horder, J. R., *J. Chem. Soc. (A)*, 2655 (1969).
- [2] Beattie, I. R., Blayden, H. E., Hall, S. M., Jenny, S. N., and Ogden, J. S., *J. Chem. Soc. (Dalton)*, 666 (1976), and references therein.
- [3] Lesiecki, M. L. and Nibler, J. W., *J. Chem. Phys.* 64, 871 (1976), and references therein.
- [3a] See for example Kashiwabara, K., Konaka, S., and Kimura, M., *Bull. Chem. Soc. Japan* 46, 410 (1973); Bauer, S. H. and Andreassen, A. L., *J. Phys. Chem.* 76, 3099 (1972); Kuchitsu, K., *Molecular Structure and Vibrations*, ed., Cyvin, S. J., Elsevier, Amsterdam, 1972; Hildebrandt, R. L. and Bonham, R. A., *Ann. Rev. Phys. Chem.* 22, 279 (1971); Morino, Y., Kuchitsu, K. and Murata, Y., *Acta Cryst.* 18, 549 (1965); Robiette, A. G., *Molecular Structure by Diffraction Methods*, Volume 1, Specialist Periodical Report (Chemical Society, London, 1973); Oberhammer, H., *Molecular Structure by Diffraction Methods*, Volume 4, Specialist Periodical Reports (Chemical Society, London, 1976).
- [4] See, for example, Büchler, A., Stauffer, J. L., Klemperer, W., and Wharton, L., *J. Chem. Phys.* 39, 2299 (1963); Kaiser, E. W., Falconer, W. E., and Klemperer, W., *J. Chem. Phys.* 56, 5392 (1972).
- [5] Mills, I. M., Watson, J. K. G., and Smith, W. L., *Mol. Phys.* 16, 329 (1969).
- [6] Büchler, A., Stauffer, J. S., and Klemperer, W., *J. Chem. Phys.* 46, 605 (1967).
- [7] Dyke, J., personal communication; see also, Egde, R. E. and Orchard, A. F., *J. Chem. Soc. (Faraday II)*, 74, 485 (1978).
- [8] Beattie, I. R., Price, D. D., and Ogden, J. S., unpublished work.
- [9] Jenny, S. N. and Ogden, J. S., personal communication.
- [10] Atkins, R. M. and Gingerich, K. A., *Chem. Phys. Letters*, 53, 347 (1978).
- [11] Jenny, S. N. and Price, D. D., unpublished work.
- [12] Vasile, M. J., Stevie, F. A., and Falconer, W. E., *Int. J. Mass. Spect. Ion Phys.* 17, 195 (1975).
- [13] Grimley, R. T., Wagner, L. C., and Castle, P. M., *J. Phys. Chem.* 79, 302 (1975).
- [14] Owyong, Patterson, C. W., and McDowell, R. S., personal communication.
- [15] Yuratch, M. A. and Hanna, D. C., *Mol. Phys.* 33, 671 (1977).
- [16] Eckbreth, A. C., *Appl. Phys. Lett.* 32, 421 (1978).
- [17] Beattie, I. R., Black, J. D., and Gilson, T. R., unpublished observations.
- [18] Beattie, I. R., Greenhalgh, D. A., and Gilson, T. R., *Nature*, in press.
- [19] For an interesting paper, see Hal, B. A., Schnepf, O. O., and Taran, J. P. E., *Optics Comm.* 24, 77 (1978).
- [20] See for example, Mariella, R. P., Neoh, S. K., Herschbach, D. R., and Klemperer, W., *J. Chem. Phys.* 67, 2981 (1977).

## Discussion

Comment (Chabay): I just wanted to clarify one thing; that is, when you said that you increased the laser frequency that really is only useful in terms of what is happening if you know where the absorption bands are. As you could be increasing the frequency if you are above the absorption band and you may not see, in fact, the high temperature species.

It is a function of the fact that you are more efficiently absorbing the power in that region and it depends exactly where you are in terms of the chromophore.

Response (Beattie): That is right.





## RAMAN SPECTROSCOPY IN HIGH TEMPERATURE CHEMISTRY

Michael C. Drake<sup>1</sup>

National Bureau of Standards

Washington, D.C. 20234

and

Gerd M. Rosenblatt

Department of Chemistry

The Pennsylvania State University

University Park, PA 16802

Raman spectroscopy (largely because of advances in laser and detector technology) is assuming a rapidly expanding role in many areas of research. This paper reviews the contribution of Raman spectroscopy in high temperature chemistry including molecular spectroscopy on static systems and gas diagnostic measurements on reactive systems. An important aspect of high temperature chemistry has been the identification and study of the new, and often unusual, gaseous molecules which form at high temperatures. Particularly important is the investigation of vibrational-rotational energy levels and electronic states which determine thermodynamic properties and describe chemical bonding. Some advantages and disadvantages of high temperature Raman spectroscopy for molecular studies on static systems are compared: (1) Raman vs infrared, (2) gas-phase vs condensed in matrices, and (3) atmospheric pressure Raman vs low pressure techniques, including mass spectroscopy, matrix isolation, and molecular beams. Raman studies on molecular properties of gases, melts, and surfaces are presented with emphasis on work not covered in previous reviews of high temperature and matrix isolation Raman spectroscopy.

A related problem in high temperature chemistry has been measurement of temperature and molecular species concentrations in high pressure-high temperature reactive environments. Intensity theory for rotational and vibrational Raman scattering is discussed as a basis for Raman temperature and concentration measurements. Raman spectroscopy is then compared to physical probe techniques (thermocouples, mass spectrometry) and to other spectroscopic techniques (fluorescence, emission, and absorption). Experimental results from Raman scattering on flames, chemical vapor deposition systems, engine exhausts, and other reactive

---

<sup>1</sup>NRC Postdoctoral Associate.

systems are summarized. Also discussed are new techniques including coherent anti-Stokes Raman, Raman induced Kerr and stimulated Raman gain, and future directions (particularly multichannel detection and time-resolved measurements of fluctuations) for Raman spectroscopy on high temperature systems.

## 1. Introduction--Role of Raman Studies in High Temperature Chemistry

### 1.1 Historical background and reasons for renewed interest in Raman techniques

An important aspect of high temperature chemistry has been the identification and study of the new, and often unusual, gaseous<sup>2</sup> molecules which are formed when solid samples or solid containers are heated in vacuum, or in the presence of permanent gases or of other materials [1-3]<sup>3</sup>. As was first pointed out by Brewer [4] and is now well recognized, new and unusual vapor<sup>2</sup> species in saturated vapors usually become more abundant as the temperature increases. Investigations of molecular structures, vibrational-rotational energy levels, and electronic states of these high temperature molecules have been of particular interest since these molecular properties determine macroscopic thermodynamic properties and describe chemical bonding. Studies of metal halide vapors, for example, have led to more accurate thermodynamic functions for these molecules (useful in analysis of diverse applied problems) and to a better understanding of chemical bonding of ionic molecules in general.

A related problem in high temperature chemistry has been the measurement of temperature and molecular concentrations in high temperature reactive environments under "real world" conditions, that is, at near-atmospheric pressures [1]. Understanding complex industrial processes (e.g., combustion, chemical vapor decomposition, or magnetohydrodynamic power generation) requires not only knowledge of the thermodynamics of the system, but also of the chemical kinetics and fluid dynamics including turbulence. Description of complex systems in a form suitable for analysis of kinetics, modeling, and process optimization requires detailed spatially (and, in some cases, temporally) resolved measurements.

Although Raman spectroscopy was discovered fifty years ago and the first elevated-temperature Raman spectra of gaseous molecules were obtained more than forty-five years ago [5,6], the real application of Raman spectroscopy to high temperature problems--as to many other areas--did not come about until the development of powerful, commercial lasers. Closely following the availability of laser sources, the feasibility and potential of Raman spectroscopy for structural and vibrational studies of high temperature gaseous molecules was demonstrated, particularly by the extensive work of I.R. Beattie and coworker at Southampton [7-10]. Raman scattering as a probe for examining high temperature reactive environments, pioneered in the study of flames by Lapp and Penney at General Electric, came somewhat later [11,12]. Both of these areas have been spurred by developments in lasers (continuous and pulsed) and in sensitive photoelectric detectors, the same developments

---

<sup>2</sup>Editor's note: The terms gaseous (or gas) and vapor are used interchangeably throughout this chapter.

<sup>3</sup>Figures in brackets indicate the literature references at the end of this paper.

which have given rise to the overall renaissance of Raman spectroscopy. In addition to this technological impetus, Raman spectroscopy applied to high temperature chemistry has experienced rapid growth because it complements other, more traditional, high temperature experimental techniques--such as mass spectrometry and matrix isolation infrared spectroscopy for molecular studies, and physical probe and classical visible spectroscopic techniques in reactive environment measurements.

## 1.2 Raman spectroscopy as a molecular-structure tool

A wide variety of experimental techniques--including electronic spectroscopy, x-ray and uv photoelectron spectroscopy, electric-dipole molecular beam deflection, microwave spectroscopy, electron and electron paramagnetic resonance, fluorescence, chemiluminescence, and electron diffraction--have been applied to high temperature gases and many of these techniques have been discussed elsewhere in this volume. However, these methods are often difficult to carry out (or to analyze) on polyatomic molecules at elevated temperatures. The technique most widely used to determine vibrational frequencies and molecular symmetries of high temperature polyatomic gases has been matrix isolation infrared spectroscopy [13]. This is now being supplemented by an increasing number of matrix Raman studies and studies utilizing direct, high temperature, gas-phase Raman spectroscopy.

Direct gas-phase Raman spectroscopy differs from matrix-isolation infrared spectroscopy in three ways, all of which may be utilized to extract information of value to high-temperature chemistry: (i) Raman vs infrared, (ii) gas-phase vs condensed in matrix, and (iii) near-atmospheric pressures vs low pressures.

(i) The complementary nature of infrared and Raman vibrational selection rules, exemplified by the mutual exclusion rule for molecules with a center of symmetry, is well known. This shows up in relative intensities as well as in selection rules so that an "ionic" vibration is strong in the infrared and weak or absent in the Raman, while a polarizable covalent vibration, such as the stretch of a metal-metal bond, is intense in the Raman and weak or absent in the infrared. Two of the major goals of vibrational spectroscopy are to elucidate molecular structure and to provide the information required to calculate thermodynamic properties by the methods of statistical mechanics. With many, probably most, molecules these goals can be attained only when both infrared and Raman spectra have been determined. Raman and infrared experiments also differ in the ease with which a broad range of frequencies can be scanned (it is easy to look at pure rotational transitions in the Raman effect) and in the role of fluorescence [14] (which can be a major problem in Raman work but is sometimes useful). Polarization measurements in Raman spectroscopy are an extremely useful way to help assign vibrational fundamentals. Correct assignments of vibrations in polyatomic molecules are required both to obtain molecular structures and, since they determine vibrational degeneracy, for thermodynamic purposes.

Another problem in high temperature chemistry is the determination of the energies of low-lying electronic states which contribute to the thermodynamic properties and, at least in simple molecules, help one understand bonding and stability. The difference in selection rules for Raman and electric dipole optical transitions makes Raman a potentially useful tool



for observing optically forbidden transitions involving low-lying electronic states. Such utility has not yet been demonstrated however.

(ii) The complementarity--for high temperature chemistry--of gas phase Raman spectroscopy and of matrix-isolation infrared also involves the comparison between direct high-temperature observations and the matrix-isolation technique. Low-temperature matrix spectra yield narrow bands which allow the use of isotopes to help in the assignments. However, the positions of the bands are shifted somewhat, by interaction with the matrix, from the energy differences which describe the isolated gaseous molecule. In contrast, direct high-temperature studies yield broad bands which reflect the many vibrational-rotational energy levels populated at high temperature. (These bands can be resolved for many diatomics and a few polyatomics.) In favorable cases, comparison of matrix and direct high-temperature spectra may yield information on anharmonicity, hot bands, and matrix shifts. Another difference between matrix and gas-phase spectra involves the interpretation of intensities. It is usually difficult to use relative intensities from matrix spectra to obtain quantitative information about the relative concentrations of the originating species in the gas phase (whether equilibrium or dynamic reaction) which was sampled. In addition to matrix perturbations and "site" effects, chemical reactions can occur during deposition or subsequent warmup. These reactions can be very valuable in forming new molecules for spectroscopic study [15], but they do not always make it easy to determine the relative stabilities of the new species. Sampling particular excited vibrational or electronic states is essentially impossible with matrix isolation, as is spatial sampling of a reacting gas mixture.

(iii) The third difference between high temperature Raman spectroscopy and matrix-isolation (or mass spectrometric) experiments lies in the pressure regime sampled. Knudsen effusion matrix isolation and mass spectrometry are essentially molecular beam techniques, most readily applied to sampling gases in the pressure range between  $10^{-2}$  and  $10^{-7}$  Torr. Raman spectroscopy, on the other hand, is most directly suited to looking at gases at pressures on the order of atmospheres ( $10^{-2}$  - 10 atm). This change to a higher pressure regime can be advantageous in structural studies in two ways.

(a) In gas-solid and gas-liquid equilibrium systems, by Brewer's rule [4] the concentrations of "novel," high-temperature, gaseous molecules usually increase as the temperature and saturation pressure increase [16]. For systems forming normal liquids, such as Na (cf. fig. 1), where the intermolecular bonds are primarily van der Waals, this increase is continuous all the way to the critical point [17]. However, in ionic systems which have relatively large enthalpies of fusion, dimer to monomer ratios may pass through a maximum. For a typical ionic system, such as KCl (cf. fig. 1), the maximum occurs at the melting point. This is because the enthalpy of vaporization of the dimer increases by twice the enthalpy of fusion upon melting whereas that of the monomer increases by the enthalpy of fusion. Saturated systems with partial ionic bonding, such as TlCl (cf. fig. 1), can show intermediate behavior, reaching maximal dimer to monomer ratios at temperatures near the boiling point [18]. In contrast, in ionic or covalent systems which form stable dimeric vapor compounds, the partial pressure of the monomer increases more rapidly relative to that of the dimer above the melting point than below it. In such systems monomer and dimer vapor



pressure curves may cross at temperatures below the boiling point. An example is LiI (cf. fig. 1) in which the monomer is the "high temperature" species. Thus, although the relative concentrations of novel high temperature gaseous species may or may not increase continuously with temperature for systems of technological interest, change of the experimental conditions from Knudsen effusion to direct observation, with a corresponding increase of about six orders of magnitude in pressure, may make it possible to study molecules not seen under molecular-beam conditions. (This is a potential result. No examples are yet known.)

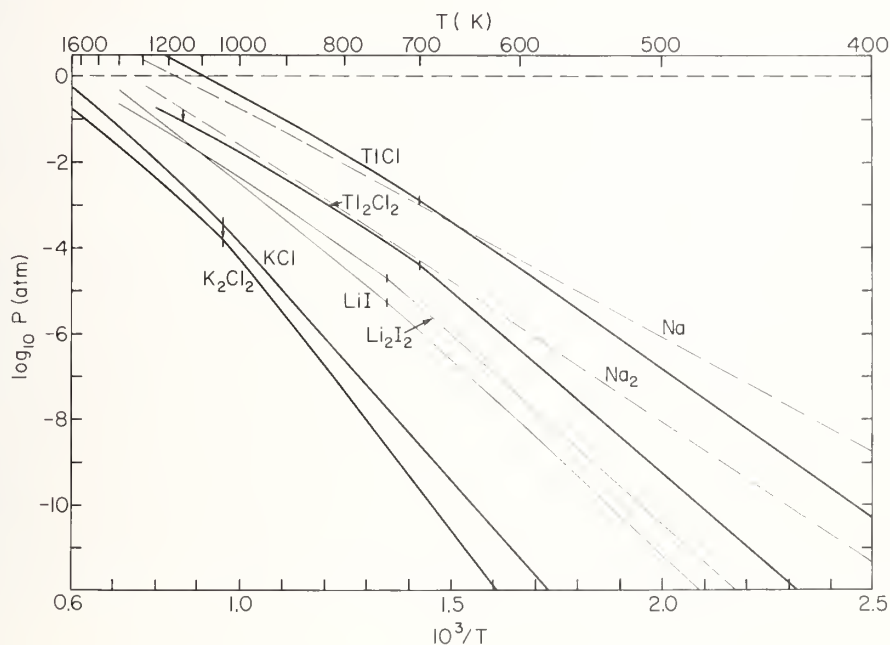


Figure 1. Equilibrium partial pressures of monomer and dimer molecules for Na, LiI, KCl, and TlCl. The vertical dashes indicate the melting point and the vertical arrows indicate the temperature at which the dimer to monomer ratio reaches a maximum.

(b) For systems in which the "high temperature molecules" [16] are dissociated fragments, it is easy to produce and superheat unsaturated vapors in closed cells, as in the studies on  $\text{GaCl}_3$  [8,19]. This makes possible the study of gas phase equilibria over a wide range of temperature and pressure (e.g.,  $\text{M}_2\text{X}_6 = 2\text{MX}_3$ ).

Raman spectroscopy is also suitable for studies of high temperature melts, solutions (particularly aqueous solutions in which infrared measurements are difficult), solids, and solid surfaces.

### 1.3 Gas diagnostic studies in reactive systems

The need for nonintrusive, nonperturbing diagnostic methods to measure temperature and molecular species concentrations with high spatial and/or temporal resolution in high

temperature reactive environments is well recognized [20]. Although techniques employing physical probes (i.e., thermocouples or sampling probes for mass spectrometry, gas chromatography or ionization detectors) or established spectroscopic methods (emission or absorption spectroscopy or spectral line reversal) have been valuable in high temperature studies for a long time [21-23]; each of these methods has its difficulties, as well as its advantages. Thus, they usually may be usefully supplemented--if not supplanted--by truly nonperturbing techniques which make use of laser radiation [20,23-26]. For example, comparisons with Raman results can help one assess the degree to which physical and thermal perturbation is a problem with a physical probe, be it a mass-spectrometer sampling nozzle or a thermocouple.

Laser techniques suitable for diagnostics of high temperature flows discussed in this volume include vibrational and rotational Raman scattering [27-30], nonlinear optical processes such as coherent anti-Stokes Raman, stimulated Raman, the Raman induced Kerr effect, inverse Raman and Raman induced gain [31,32], Rayleigh scattering [33], laser induced fluorescence [32-36], two line fluorescence [37], laser absorption [38,39], and the opto-galvanic effect [40]. Of these techniques, Raman, particularly vibrational Raman, scattering appears at this time to have the greatest applicability for temperature and major species concentration measurements in a wide range of laboratory and applied high temperature situations.

The advantages of Raman scattering include:

1. Sensitivity to almost any molecule, including homonuclear diatomics.
2. Selectivity in identifying and evaluating each molecular species independently.
3. Nonperturbing character. (There is only weak coupling between the flame species and the laser light because of the nonresonant nature of the Raman process. However, adsorption or laser-induced electrical breakdown can occur, particularly with pulsed lasers.)
4. Three dimensional spatial resolution ( $<1 \text{ mm}^3$ ).
5. Ability to measure relative populations of energy levels. For equilibrium systems, this is a temperature measurement.
6. Ability to measure relative molecular densities.
7. Well-established intensity theory which permits accurate temperature and density measurements.
8. The potential for rapid time resolution (limited by laser pulse width) to measure rapid fluctuations in density or temperature.

The disadvantages of Raman scattering result from the weakness of the Raman effect and include:

1. Interference by other sources of visible radiation, including other scattering processes involving the same incident laser radiation, can make Raman measurements difficult or impossible.
2. Limited sensitivity restricts studies to major species.
3. Relatively complex and expensive apparatus is required.

For example, vibrational Raman spectroscopy has become an established method for temperature and concentration measurements in laboratory scale nonsooty flames [25,26]. Recent work [41,42] has shown the value of rotational Raman scattering in such applications as well.

However, for analysis of external combustion exhausts or sooty, highly luminous flames, all Raman techniques are limited by the greatly increased background which arises from light scattering from particulates, black-body emission, fluorescence from particulates, and chemiluminescence [25,31,43]. Lock-in amplifiers or dual channel photon counters will shift the baseline to zero but will not reduce the fluctuations in the background which are proportional to the square root of the total number of photons incident upon the photomultiplier tube [44]. Pulsed lasers and gated detection, in either conventional Raman or CARS, can greatly reduce interference from black-body emission and chemiluminescence, but not interference from particulate light scattering [25,31,43]. For these reasons, it has been concluded, for example [45], that Raman measurements will have limited, if any, utility in the diagnosis of gas streams in a magnetohydrodynamic combustor. Thus, insofar as possible, anticipated intensities from Raman scattering and from potential sources of interference should be analyzed before Raman measurements are undertaken in a specific high-temperature environment.

This present paper attempts to access the current value and near term potential of Raman scattering as a tool for characterization of high temperature vapors and gases. Section 2 discusses measurements of molecular properties. Section 3 describes applications of Raman scattering to analysis of reacting systems. In Section 4, we briefly discuss the potential high temperature utility of a promising new laser technique, coherent anti-Stokes Raman spectroscopy.

## 2. Static Systems: Molecular Properties

### 2.1 Vapors

Numerous reviews have been published on Raman scattering from high temperature vapors [46-52], and from species condensed in low temperature, inert gas matrices [53-58]. Also see other discussions in this volume [59-63]. A list illustrating the wide range of vapor molecules for which Raman spectra are available is given in table 1. Most of these studies are described or referred to in the reviews cited. In this paper we shall focus on the information of importance to high temperature chemistry which Raman spectroscopy can provide, as illustrated by recent studies of vapors.

A major part of the work on Raman studies of vapors has been devoted to obtaining vibrational spectra of molecules of current high-temperature interest, particularly halides and oxides, using what has become, at least temporarily, the conventional way to make the measurements--sealed quartz cells surrounded by a resistance heated furnace, cw gas laser excitation (usually the 488 or 514.5 nm line of an  $\text{Ar}^+$  laser), double monochromator, lock-in detection of a modulated signal or photon counting [19,44,46,48] (see fig. 2). An important consideration in furnace design is minimizing the background thermal glow seen by the spectrometer. An example of a furnace used in Raman studies of high temperature vapors is shown in figure 3. The quartz cell with fused Brewster angle windows (see fig. 3) permits operation inside the laser cavity [44] or in external multipassing arrangements [18] which can increase signal intensities. The values of Raman active vibrational frequencies directly measured from Raman spectra combined with the results of matrix isolation studies can permit

inferences of molecular shape using group theory selection rules, frequency correlations, or force constant trends. With a complete vibrational assignment (usually requiring both infrared and Raman measurements) thermodynamic functions can be calculated. The availability of accurate thermodynamic functions affects reaction enthalpies as well as entropies, via the third-law method for evaluating enthalpies of reaction from equilibrium measurements. Raman spectroscopy is also useful for following gas phase equilibria. As an illustration, compare spectra shown in figure 4a and 4b. The marked spectral differences with changes in temperature reflect changes in the molecular species present; predominantly  $\text{Ga}_2\text{Cl}_6$  with small amounts of  $\text{GaCl}_3$  at low temperature (fig. 4a) and predominantly  $\text{GaCl}_3$  at 620 °C (fig. 4b). Gas phase equilibria measurements at high pressure may serve as a useful check on extrapolations of Knudsen measurements or as a measure of the stability of species present only under high pressure-high temperature conditions.

Table 1. Raman Studies of High Temperature Vapors<sup>a</sup>

	HIGH TEMPERATURE	MATRIX ISOLATION
ELEMENTS	$\text{P}_4, \text{As}_4, \text{As}_4\text{P}_{4-x}, \text{S}_2\text{-S}_8, \text{Rb}_2$	$\text{S}_2, \text{S}_3, \text{Ag}_2, \text{Ag}_3, \text{Sn}_2, \text{Br}_3, \text{Br}_4$
MONOHALIDES	$\text{InX}, \text{TlCl}$	$\text{TlX}, \text{Tl}_2\text{X}_2$
DIHALIDES	$\text{BeX}_2, \text{GeX}_2, \text{SnX}_2, \text{PbX}_2, \text{ZnX}_2,$ $\text{NF}_2, \text{HgX}_2, \text{TeX}_2, \text{SF}_2, \text{SCl}_2, \text{S}_2\text{Cl}_2$ $\text{CuCl}_2, \text{Cu}_2\text{Cl}_4$	$\text{MgX}_2, \text{SnX}_2, \text{PbX}_2, \text{PCl}_2, (\text{GeF}_2)_n$ $\text{MF}_2 (\text{M}=\text{alkali or inert gas}),$ $\text{MCl}_2 (\text{M}=\text{inert gas}).$ $\text{MX}_2, \text{MXY} (\text{M}=\text{Zn, Cd, Hg})$
TRIHALIDES	$\text{PX}_3, \text{AsX}_3, \text{SbX}_3, \text{BiX}_3, \text{Al}_2\text{X}_6,$ $\text{AlX}_3, \text{Ga}_2\text{X}_6, \text{GaX}_3, \text{In}_2\text{X}_6,$ $\text{InX}_3, \text{FeCl}_3, \text{Fe}_2\text{Cl}_6$	$\text{PrX}_3, \text{SiX}_3, \text{AlCl}_3, \text{FeCl}_3$
TETRAHALIDES	$\text{TiX}_4, \text{SnX}_4, \text{SeX}_4, \text{TeX}_4,$ $\text{ZrX}_4, \text{HfX}_4, \text{GeI}_4$	
PENTAHALIDES	$\text{PX}_5, \text{AsX}_5, \text{SbX}_5, \text{NbX}_5, \text{TaX}_5,$ $\text{MoX}_5, \text{IX}_5$	
HEXAHALIDES	$\text{SX}_6, \text{SeX}_6, \text{TeX}_6, \text{MoX}_6, \text{UX}_6,$ $\text{WF}_6, \text{TeX}_6, \text{XeX}_6$	$\text{SF}_6, \text{XeF}_6, \text{UF}_6$
OXIDES	$\text{P}_4\text{O}_6, \text{As}_4\text{O}_6, \text{Sb}_4\text{O}_6, \text{P}_4\text{O}_{10},$ $\text{OsO}_4, \text{Re}_2\text{O}_7, \text{SO}_3$	$\text{S}_2\text{O}, \text{SO}_3, \text{SeO}_2, (\text{SeO}_2)_2, \text{OsO}_4,$ $\text{MO}_2, \text{MO}_3, \text{MO}_4 (\text{M}=\text{alkali})$
OXYHALIDES	$\text{POCl}_3, \text{POF}_3, \text{VOF}_3, \text{VOCl}_3,$ $\text{FCIO}_3, \text{NbOCl}_3, \text{MoO}_2\text{Cl}_2,$ $\text{WOCl}_4, \text{PSCl}_3$	$\text{OF}_2, \text{Cl}_2\text{O}, \text{XeO}_3\text{F}_2, \text{OsO}_3\text{F}_2$
MIXED METAL HALIDES	$\text{CuAl}_2\text{Cl}_8, \text{PdAl}_2\text{Cl}_8, \text{PdAl}_2\text{Br}_8,$ $\text{CuGa}_2\text{Cl}_8, \text{CuIn}_2\text{Cl}_8, \text{CuAlCl}_5,$ $\text{InAlBr}_4, \text{InAlCl}_4$	

<sup>a</sup>Notation:  $x = 1-3$ ,  $X = \text{halogen group (usually Cl or F)}$



Information obtainable from Raman spectra of vapors is illustrated by the following examples from recently published studies. Questions concerning geometries (planar or pyramidal) and vibrational assignments in the Group III A trihalide molecules appear resolved by recent matrix Raman studies [64] and matrix infrared results [65] on  $\text{AlCl}_3$  and high temperature Raman measurements from  $\text{GaCl}_3$  and  $\text{GaI}_3$  [19]. The conclusion that all trihalides of aluminum and gallium are planar is in agreement with electron diffraction, *ab initio* molecular orbital calculations on  $\text{AlCl}_3$  [64,65], and geometry trends based upon the Rittner polarizability model [66]. A complex of  $\text{AlCl}_3$ , perhaps with  $\text{N}_2$ , was the probable source of the band attributed to  $\nu_1$  of  $\text{AlCl}_3$  in earlier matrix isolation work which had led to the postulate of a pyramidal  $\text{AlCl}_3$  equilibrium geometry [65]. Symmetric-stretching vibrational-frequency trends [19] and metal-trihalide geometry trends based upon a polarizability model [66] are suggestive of planar geometries for all other Group III A trihalide molecules, as well.

The Raman spectra of  $\text{GaBr}_3$  and  $\text{GaI}_3$  [19] illustrate the well-known dangers of attempting to ascertain molecular symmetry simply by counting the number of Raman or ir spectral peaks. Both of these molecules yield four gas-phase Raman peaks, two of which are polarized, numbers which taken by themselves might suggest pyramidal  $C_{3v}$  symmetry. However, in both cases, an assignment more consistent with other data is that the second polarized peak is an overtone or combination band in accidental degeneracy (Fermi resonance) with the symmetric  $\nu_1$  mode. It is likely that continuing investigation of the vibrational spectra of polyatomic high-temperature molecules containing heavy atoms will reveal many additional examples of Fermi resonance interactions.

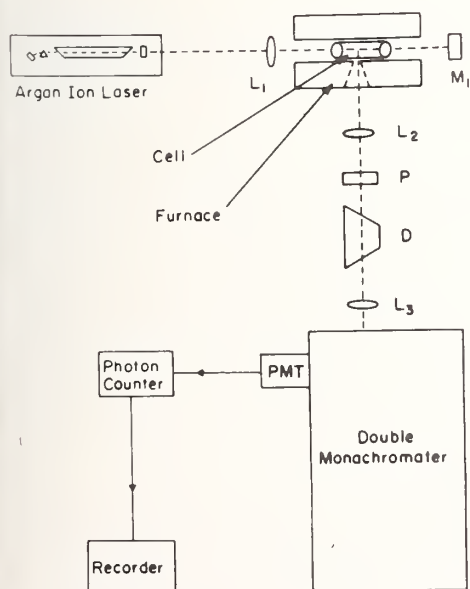


Figure 2. Laser Raman apparatus for furnace studies of polyatomic vapors. Lens  $L_1$  focuses the laser beam into the sample and mirror  $M_1$  reflects and refocuses the laser light back into the sample to increase the useful laser power. Light scattered at right angles is collected by lens  $L_2$ , analyzed by polarization analyzer  $P$ , rotated by  $90^\circ$  by dove prism  $D$ , and refocused by lens  $L_3$  into the entrance slit of a double monochromator. The output of a thermoelectrically cooled photomultiplier tube is processed with photon counting electronics.



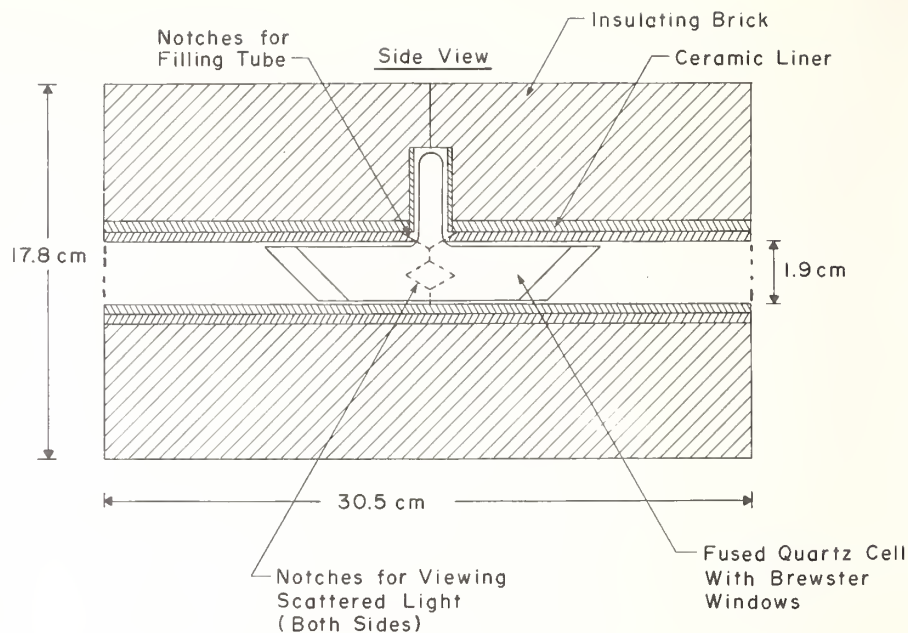


Figure 3. Furnace and cell for Raman studies of high temperature vapors. A viewport for scattered radiation is perpendicular to the main furnace axis. An opening in the furnace opposite the viewport minimizes the amount of thermal glow from the furnace that is seen by the spectrometer. The sample is contained in sealed quartz cells with Brewster angle windows.

The difficulties of arriving at a proper vibrational assignment for high temperature molecules may be further illustrated by recent matrix Raman results for  $\text{FeCl}_3$ . Givan and Loewenschuss [67] observe four Raman bands which they interpret to indicate  $C_{3v}$  pyramidal geometry for  $\text{FeCl}_3$ . However, the assignment of  $\nu_2$  ( $a_1$ ) at  $68.7 \text{ cm}^{-1}$  is quite different from the value expected from frequency trends in pyramidal Group V trihalides or planar Group III trihalides, trends which suggest a value of  $140 \pm 20 \text{ cm}^{-1}$ . Also, a pyramidal geometry seems inconsistent with matrix electron-spin-resonance studies which found the analogous  $\text{FeF}_3$  species to be planar [68], *ab initio* molecular orbital calculations which predict  $\text{FeF}_3$  to be planar [69], and bonding trends in other metal trihalides [66]. Thus, either  $\text{FeCl}_3$  is an exception to a number of periodic-table correlations or the assignment of  $\nu_2$  and of  $C_{3v}$  symmetry are in error.

A somewhat different kind of question about the molecular structure and thermodynamics of high temperature gaseous halides arose with respect to the dimeric thallous monohalides. A combination of infrared and Raman spectra [70] from matrix isolated  $\text{Tl}_2\text{F}_2$  and  $\text{Tl}_2\text{Cl}_2$  show that these molecules have planar, rhombic structures rather than linear geometries previously proposed from mass spectrometric, photoelectron, and matrix isolation infrared studies. A concurrent independent attempt to observe scattering from gaseous  $\text{Tl}_2\text{Cl}_2$  by direct high temperature Raman spectroscopy [71] failed. Only vibrational and rotational scattering from monomeric  $\text{TlCl}$  is seen in the direct Raman spectrum and no scattering from  $\text{Tl}_2\text{Cl}_2$  is observed, as shown in figure 5.

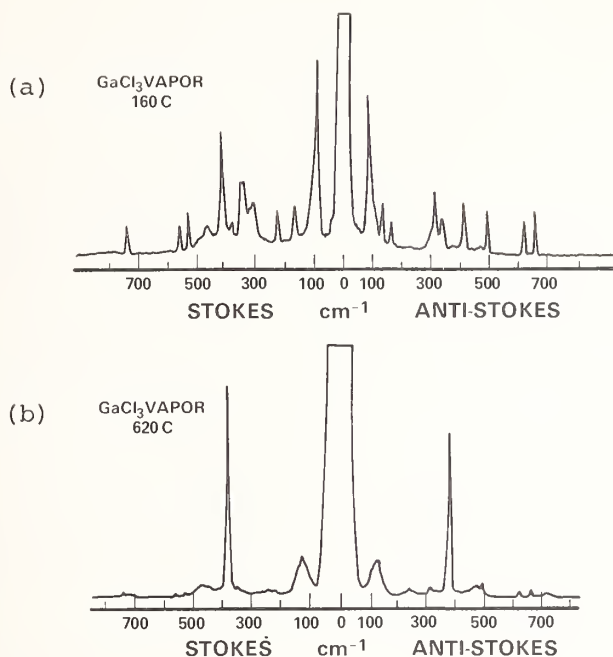


Figure 4. (a) Raman spectrum of saturated vapor over GaCl<sub>3</sub> at 160 °C. Predominately Ga<sub>2</sub>Cl<sub>6</sub>(g) with small amount of GaCl<sub>3</sub>(g), 0.4 atm total pressure. Excitation 4.2 W at 488 nm, polarizer parallel, 7  $\text{cm}^{-1}$  resolution, 3 s time constant, 0.5  $\text{cm}^{-1}/\text{s}$  scan speed. (b) Raman spectrum of GaCl<sub>3</sub>(g) at 620 °C. Predominately GaCl<sub>3</sub>(g) in unsaturated vapor at 1.1 atm pressure. Excitation 4.8 W at 488 nm, polarizer parallel, 7  $\text{cm}^{-1}$  resolution, 3 s time constant, 0.5  $\text{cm}^{-1}/\text{s}$  scan speed.

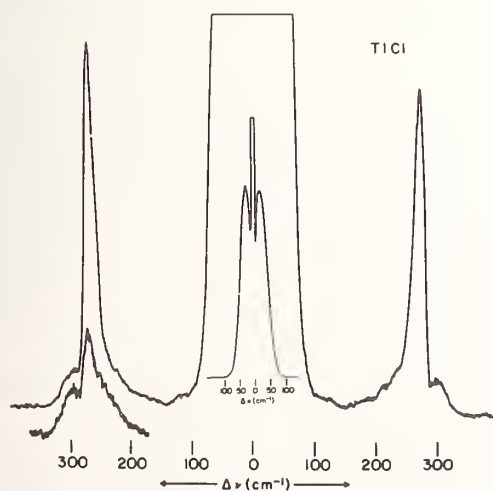


Figure 5. Vibrational and rotational Raman scattering from TlCl (g). Vibrational Raman: saturated vapor at 840 °C, 4.0 W at 488 nm, 2.25  $\text{cm}^{-1}$  resolution, 0.5  $\text{cm}^{-1}/\text{s}$  scan speed, 3 s time constant, polarizer parallel. Insert at  $\Delta = 200-300 \text{ cm}^{-1}$ : polarizer perpendicular, sensitivity 2X that of top curve, baseline shifted. Insert at  $\Delta = \pm 100 \text{ cm}^{-1}$ : rotational Raman scattering of saturated vapor at 920 °C, 5.6 W at 488 nm, polarizer parallel.

Failure to observe  $\text{Tl}_2\text{Cl}_2$  suggested inconsistencies in the thermodynamic data for  $\text{Tl}_2\text{Cl}_2$ . The inconsistencies arose, in large part, from the same errors in the entropy of  $\text{Tl}_2\text{Cl}_2$  which had led to the proposal of a linear structure and had motivated the Raman experiments. Combining thermodynamic functions [18] based upon the vibrational assignments of Lesiecki and Nibler [70] with new mass spectrometric measurements and re-analysis of earlier vapor pressure measurements leads to more consistent thermodynamic data [18]. These data, as represented in figure 1, indicate that the percentage of  $\text{Tl}_2\text{Cl}_2$  in the saturated vapor peaks at a dimer to monomer ratio of only 0.05 at 1150 K. This is about one-fifth of the ratio estimated from the earlier data and explains the inability to observe  $\text{Tl}_2\text{Cl}_2$  in the high temperature Raman experiments.

Turning to other recent studies of gaseous halides, linear geometries for the magnesium dihalides have been confirmed by a combination of matrix Raman and matrix infrared spectra [72]. Prior to this work, the question of whether  $\text{MgF}_2$  was linear or bent had been a subject of contention. Observation of the Raman spectrum also enabled determination of the  $\nu_1$  symmetric stretching frequencies, needed to compute thermodynamic functions. Irregularities in stretching-force-constant trends among the cadmium and mercury dihalides have led to the postulate that  $\text{HgBrI}$ ,  $\text{CdBrI}$ , and possibly other mixed dihalides are bent [73]. It would be interesting to test this by further experimental work.

There have also been a number of recent high-temperature Raman studies on the geometries and vibrational frequencies of mixed metal halide vapors, because of the potential technological importance of the volatile compounds formed and because of the interest in chemical bonding in these molecules [63,74].

The above paragraphs illustrate the way in which the observed frequencies of Raman-active vibrations have been utilized to address questions concerning the symmetry and thermodynamic properties of high temperature gaseous molecules. The major tools used for Raman frequency assignments have been comparison with ir, comparison with potentially similar molecules, polarization ratios, and when sufficient data are available, force constant calculations. Often the relative intensities, bandwidths, and band contours of Raman transitions have been qualitatively interpreted to provide additional clues to fundamental frequency assignments. For example, totally symmetric stretching frequencies generally give rise to the most narrow and intense Raman lines.

In addition to their utility in making frequency assignments, Raman intensities and depolarization ratios can be used to determine properties such as Coriolis constants, mean square vibrational amplitudes, and polarizability derivatives [75]. One anticipates that Raman intensity measurements will prove increasingly useful for such purposes. The temperature dependence of Raman band contours, particularly at high temperatures, is also useful for determinations of concentration from Raman intensities.

Clark [76,77] has made quantitative use of Raman band contours and band intensities for doubly degenerate fundamentals of high temperature spherical top molecules to obtain approximate values of Coriolis constants for molecules such as  $\text{MF}_6$  ( $\text{M} = \text{S, Se, Te, Mo or U}$ ),  $\text{P}_4$ ,  $\text{As}_2\text{O}_5$ ,  $\text{M}(\text{CH}_3)_4$  where  $\text{M} = \text{C, Si, Ge, Sn, or Pb}$  and  $\text{MX}_3$  where  $\text{M} = \text{P, As or Sb}$  and  $\text{X} = \text{halogen}$ . These measurements also allowed resolution of a discrepancy in the reported  $\nu_3$  fundamental of  $\text{P}_4$  [76] where, because of the overlap of  $\nu_3$  and  $\nu_4$  and the extensive OP and RS rotational sidebands at 570 K, the apparent maximum in the Raman profile is shifted  $10\text{--}15\text{ cm}^{-1}$  from

the  $\nu_3$  vibrational fundamental. Relative Raman intensities have allowed measurement of bond polarizability derivatives [78,79] and estimates of the degree of covalent character of MX chemical bonds in Group IV tetrahalides [80]. The pre-resonance or resonance enhancement of Raman intensities, as the laser exciting frequency approaches an allowed electronic transition of the molecule, has also been investigated for Group IV (C, Si, Ge, Sn, Ti) tetrahalides [81-83]. The stretching fundamentals exhibit pre-resonance while the bending fundamentals do not. This may have implications concerning the geometry of the excited state.

Another application of high temperature techniques involves the determination of the energies of low-lying electronic states. Although such measurements have not yet been made for high temperature gaseous molecules, electronic Raman transitions have been observed in  $O_2$  [84,85], NO [86] and in solids [87]. An example of one kind of low lying electronic state of high temperature interest is the  $0 \rightarrow 1$  triplet splitting accompanying the transition from Hund's case a or b to case c in heavy diatomic molecules. This splitting, for example, is  $12.9 \pm 2 \text{ cm}^{-1}$  for  $Se_2$  [88] and  $679 \text{ cm}^{-1}$  for TeO [98]. Although such splittings have not yet been measured by Raman techniques for high temperature molecules, the transitions are active in the Raman effect as exemplified by the  $O_2$  spectrum (shown in fig. 6) where the splitting of the lowest rotational states due to this spin-rotation interaction is readily observed and measured [82].

The foregoing has illustrated the utility of high temperature Raman spectra with little discussion of the problems--which can be overwhelming. Although there remain innumerable high-temperature gaseous molecules for which Raman spectra would be valuable, low vapor pressures, container interactions, electronic absorptions at the wavelength of the excitation line, fluorescence from impurities (especially with halides), and other experimental problems prevent accession of many desirable spectra. Present experimental capabilities appear restricted to samples in quartz cells which have vapor pressures above 10 Torr at temperatures below 1250 K. (This is for vibrational Raman spectra excited by commercially available argon ion lasers). These limitations arise primarily from signal-to-noise limitations set by the intensity of the Raman scattered radiation compared to the high-temperature background glow in the same wavelength region. This background radiation increases essentially exponentially with temperature (Wien law region). High temperature devitrification of quartz, the usual cell material, also limits Raman studies to  $T < 1300 \text{ K}$ . In order to push back these temperature and pressure limitations, and to overcome some of the other experimental difficulties alluded to above, five methods appear promising.

(1) Pulsed lasers and gated detection offer a potential theoretical signal-to-noise enhancement of more than an order of magnitude over cw laser sources.

(2) Coherent anti-Stokes Raman spectroscopy (CARS) appears to offer advantages over conventional Raman spectroscopy of gases at very high temperatures where many vibrational-rotational levels are populated and the background radiation is intense. The particular characteristics of CARS which make it attractive for high temperature molecular studies are discussed in the final section of this paper.

(3) Radio frequency heated heat pipe cells circumvent high temperature window problems and these cells appear to be well suited for Raman or CARS investigations. (For example, Raman studies of  $Rb_2$  [90] or Tl [91] vapors contained in a heat pipe cell).



- (4) Use of nozzle jets at temperatures above the melting point of quartz [48,59].
- (5) Expanded use of matrix isolation Raman techniques.

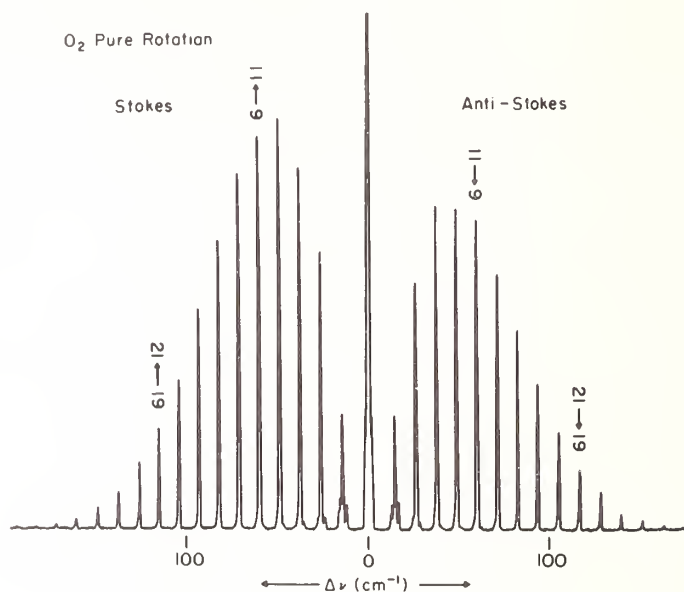


Figure 6. Rotational Raman scattering from  $O_2$  at room temperature, 1 atm pressure, 16 W at 488 nm,  $0.6\text{ cm}^{-1}$  resolution, 3 s time constant,  $0.1\text{ cm}^{-1}/\text{s}$  scan speed. Labels above the peaks are the rotational quantum numbers of the initial and final levels. Side peaks on the Rayleigh line and the first and second rotational lines are fine structure caused by interaction of electron spin with molecular rotation for the  $^3\Sigma_g^-$  ground state of  $O_2$ .

## 2.2 Melts

Raman spectroscopy, of course, can be applied to solids, melts, and solutions as well as to vapors. This makes Raman a valuable tool for studying the changes in molecular composition and/or structure with accompanying changes of state [49]. Of particular interest in high temperature chemistry is the molecular composition of melts. The early studies on molten mercuric, gallium, cadmium, and zinc dihalides were reviewed by Clark in 1973 [49]. More recently, Devlin [92] has reviewed Raman and infrared studies of ionic melts and compared them to ionic vapors and glasses. Raman spectra have been most useful in establishing the presence of and characterizing the vibrational frequencies and shapes of molecular ions in ionic melts. For example, the melts of alkali halides with the halides  $MgX_2$ ,  $GaX_3$ ,  $BeF_2$ ,  $YX_2$ , or  $ZnX_2$  give Raman spectra dominated by  $MgX_4^{-2}$ ,  $GaX_4^{-2}$ ,  $BeF_4^{-2}$  and  $Be_2F_7^{-3}$ ,  $YX_6^{-3}$ , and  $ZnX_6^{-2}$ , respectively. One of the more extensively studied system has been  $MF-AlF_3$  melts



similar to those used in commercial aluminum production). Raman spectra of alkali fluoride-aluminum trifluoride melts at temperatures to 1015 °C using a graphite cell [93] indicate a more complicated composition involving equilibrium between  $\text{AlF}_4^-$  and  $\text{AlF}_6^{3-}$  ions [94]. Quantitative analysis of the Raman intensity ratios of the  $\nu_1$  bands of  $\text{AlF}_4^-$  and  $\text{AlF}_6^{3-}$  as a function of the composition of the melt permits calculation of the stoichiometric dissociation constant  $K = X(\text{AlF}_4^-) \cdot X(\text{F}^-)^2 / X(\text{AlF}_6^{3-})$  for these melts. Solutions of  $\text{Al}_2\text{O}_3$  in molten cryolite ( $\text{Na}_3\text{AlF}_6$ ) have also been recently studied by Raman spectroscopy [95]. Equilibria among eight, seven and five-coordinate zirconium or thorium species in molten fluoride was also inferred from frequency shifts in Raman spectra of alkali fluoride-( $\text{ZrF}_4$  or  $\text{ThF}_4$ ) melts with varying mole percent concentration of  $\text{ZrF}_4$  or  $\text{ThF}_4$ . Although less studied than halide melts, Raman scattering from oxyanion melts (nitrates, chlorates, perchlorates, carbonates, sulfates, tungstates, and molybdates) have also been reported [92].

### 2.3 Solids and surfaces

There is an extensive literature on Raman scattering from solids which will not be discussed here. Examples of modern work can be found in references [96], [97], and [98]. In addition to studies of solids themselves, Raman studies of adsorbed species on surfaces and of changes in solid materials as a result of ion bombardment or high energy radiation have been obtained and will be reviewed because of their relevance to technological uses of modern high temperature materials. The study of surfaces is of obvious importance in heterogeneous catalysis and corrosion, and Raman scattering from surfaces and adsorbed layers is a rapidly growing field. Recent reviews [99,100] point out the two major advantages of Raman scattering compared to ir for vibrational studies of adsorbed species on oxide surfaces.

(1) Most oxides used as substrates absorb infrared radiation strongly below  $\sim 1000 \text{ cm}^{-1}$  so that ir studies of adsorbed species become difficult. In contrast, most oxides, since they are highly ionic, have weak Raman spectra which means that the background scatter due to the substrate is not large.

(2) Solid substrates do not have to be transparent and commercial catalyst pellets can be used without special preparation.

These advantages have been demonstrated for a variety of high surface area oxide substrates with both organic and inorganic physisorbed species [101-105]. Recent examples include  $\text{Mo}(\text{CO})_6$  adsorbed on vycor [102], pyridine on a supported nickel oxide surface [102], and  $\text{CCl}_4$  adsorbed on silica [104]. Reasonable sensitivities have been obtained (i.e., 4 percent of a monolayer for Raman scattering from  $\text{CCl}_4$  adsorbed on high surface area silica  $700 \text{ m}^2/\text{g}$ )).

Morrow [104] reported observation of vibrational Raman scattering from  $\text{SiOCH}_3$  formed by dissociative chemisorption of methanol on a silica surface. Comparisons of the Raman and ir spectra in this study show that under favorable conditions Raman spectra of chemisorbed species can be obtained with signal-to-noise ratios comparable to those in ir spectra.

Raman scattering from  $N_2$  and  $O_2$  adsorbed on molecular sieves [105], scattering from commercial catalysts used in the hydrosulfurization of petroleum products and coal [106], and scattering from thin films (1000 Å thick) on metal surfaces [107] indicate the wide range of current applications.

Experimental difficulties encountered in Raman studies of surface adsorbed species arise from the relative weak signals due to the inherent weakness of the Raman effect, background fluorescence mainly from organic materials (i.e., grease) on the surface, and sample heating which necessitates using low (<100 mW) laser powers. Some of these difficulties have been circumvented by rotating the samples to minimize heating, the use of pulsed lasers and gated detection to discriminate against fluorescence [108] and the use of resonance Raman effects to increase signal intensities markedly [109-111,185]. For example with a rotating sample cell resonance Raman spectra from only ~0.1 surface layer coverage of  $I_2$  on silica gel have been reported [109]. Of potential use in high temperature Raman studies of localized portions of surfaces is the Raman microprobe--capable of studying micrometer-size particles [112,113].

Raman spectroscopy has also been used recently to monitor material changes as a result of ion bombardment and high energy irradiation. In one investigation [114] changes in surfaces amorphization as a result of incident ion flux, and subsequent amorphous to crystalline changes upon annealing were monitored by observing changes in Raman bandwidths. In other examples, the formation of a metastable  $O_2$  species in  $\gamma$ -irradiated  $NaClO_3$  [115] and of hydride and hydroxide formation in hydrogen impregnated silica irradiated with gamma rays [116] were studied by Raman scattering.

### 3. Flames and Other Reactive Systems: Populations and Concentrations

Section 2 of this paper has been concerned with the use of measured wave-number shift in Raman spectra to determine molecular properties. Another important use of Raman scattering from high temperature vapors is the measurement of temperatures and concentrations in adverse high temperature chemical environments [20,23-26]. Examples, along with references to research from a number of currently active research groups appear, in table 2. These measurements rely upon the analysis of relative intensities from rotational and vibrational-rotational Raman transitions in diatomic and simple polyatomic molecules. In this section, we first describe some of the principles and pitfalls of Raman intensity measurements and then illustrate their utility by quoting examples of a few recent applications.

#### 3.1 Theoretical basis: Raman intensities

Although Raman intensity theory is well established [117], careful application is required to use Raman scattering properly as a diagnostic tool. A major reason for this is that the measured intensity of scattered light depends upon a number of different kinds of parameters, all of which have to be assessed, measured, calculated or controlled for accurate temperature or concentration measurements. The measured intensity depends upon:

Table 2. Spontaneous Raman diagnostic studies on high temperature gases.

<u>Systems</u>	<u>References</u>
Flames	11, 12, 20, 24-27, 41, 42 119, 123-133, 136, 137, 139, 141
Turbine, rocket and engine exhausts	28, 138, 144-147
Combustion chambers	133, 149
MHD exhausts	149
Chemical vapor deposition	29, 30, 35, 155, 156
Shock tubes	148
Atmospheric studies and pollution	151-154
Electric discharges	131, 157-160
Arc lamps	163-165
Gas-surface energy transfer	166, 167

(1) The experimental arrangement. This includes the wavelength and intensity of the incident light, the spatial and temporal stability of the volume sampled, the collection geometry and optics, the response of the detection system, etc. Usually, some effort is required to know these quantities or to hold them constant.

(2) The sum total of processes, that is, quantum-state to quantum-state transitions, which contribute to the detected signal. Sorting out these processes may take a number of forms: (a) corrections for background and noise; (b) correction for interference from molecules or processes (e.g., fluorescence) other than that of interest; (c) corrections for transitions other than those one is trying to measure, such as transitions which arise from accidental degeneracies or unresolved hot bands, or which occur in excited electronic or vibrational states; (d) summation of the state-to-state intensity contributions which contribute to the intensity between two degenerate energy levels.

(3) The theoretical relative intensity of each state-to-state process. This depends upon the type of process (e.g., Q-branch vibrational-rotational Raman scattering), the molecule undergoing the transition, the number density of these molecules, the quantum states involved, and the fraction of the molecules in these quantum states (i.e., the temperature in an equilibrium system).

With these factors qualitatively in mind, the intensity of the light scattered in most light scattering processes may be given by an equation of the form

$$I_s^v = I_{o^v o} \cdot N_m(i) \cdot \sigma_m^i \cdot \Omega \cdot \ell. \quad (1)$$

where the subscript m denotes properties which depend upon the molecule being investigated. In this equation:

$I_s = I \cdot R(\nu) \cdot \eta$  is the intensity (photons  $\text{cm}^{-3} \text{s}^{-1}$ ) [118] of the radiation scattered at frequency  $\nu$ .

$I_s$  is obtained from measured intensity  $I$  corrected for contributions  $\eta$  from processes (e.g., transitions in excited states) other than the process of interest and for the calibrated relative spectral response  $R(\nu)$  of the spectrometer and detection system.

$I_o$  is the incident laser intensity (photons  $\text{cm}^{-3} \text{s}^{-1}$ ) at frequency  $\nu_o$ .

$N_m(i)$  is the number density of scatterers of species  $m$  in the initial energy level  $i$  (molecules/ $\text{cm}^3$ ).

$\sigma'_m = (d\sigma/d\Omega)_m$  is the differential cross section for the scatterer  $m$  ( $\text{cm}^2/\text{steradian}$ ).

$\Omega$  is the solid angle over which the scattered light is collected (steradians).

$l$  is the length of the sample over which the scattered light is collected.

Typical cross section values for a number of light scattering processes are listed in table 3, taken from Lapp and Hartley [119], with the addition of electronic Raman cross sections reported by Vriens and Adriannsz [120]. Although the cross sections for Raman scattering are small, the advantages of Raman techniques (see Section 1.3) for measurement species concentrations and temperatures are substantial.

Table 3. Differential cross sections for 488.0 nm incident light

Process	Scatterer	$\sigma(\text{cm}^2/\text{steradian})$
Mie	0.1 $\mu\text{m}$ - 10 $\mu\text{m}$ diameter particles	$10^{-13} - 10^{-7}{}^{a,b}$
Fluorescence	Atoms	$10^{-16} - 10^{-13}{}^b$
Fluorescence	Molecules	$10^{-22} - 10^{-19}{}^b$
Rayleigh	$\text{N}_2$	$9 \times 10^{-28}{}^b$
Electronic Raman	Atoms, Al, Ga, In	$9 \times 10^{-27}{}^c$
Rotational Raman	$\text{N}_2(J=6 \rightarrow 8)$	$5.4 \times 10^{-30}{}^b$
Vibrational Raman Q branch	$\text{N}_2(Q \text{ branch})$	$6.8 \times 10^{-31}{}^b$

<sup>a</sup>Averaged over directions of scattering.

<sup>b</sup>M. Lapp and D. Hartley, Comb. Sci. Tech. 13, 199 (1976).

<sup>c</sup>L. Vriens and M. Adriannsz, J. Appl. Phys. 46, 3146 (1975).



### 3.1.1 Rotational Raman

For rotational Raman scattering the differential cross section for a transition between energy levels specified by rotational quantum numbers  $J_i$  and  $J_f$  can be expressed as [41,42,121].

$$\sigma'_m(J_i, J_f) = C \cdot \nu^4 \cdot C'_m(\text{rot}) \cdot S'(J_i, J_f) \cdot f_m(J_i, J_f) / (2J_i + 1) \quad (2)$$

where:

$C$  is a collection of physical constants.

$C'_m(\text{rot})$  is the square of the molecular polarizability anisotropy for molecular species  $m$ . For diatomic and linear molecules

$$C'_m(\text{rot}) = (\alpha_{zz} - \alpha_{xx})^2.$$

$S'(J_i, J_f) = S'(J_f, J_i)$  is the Raman line strength for a rigid rotator, harmonic oscillator and depends only upon  $J_i$  and  $J_f$ . For pure rotational Stokes and for S-branch transitions,

$$S'(J_i, J_i+2) = 3(J_i+1)(J_i+2)/[2(2J_i+3)].$$

$$\text{For pure rotational anti-Stokes and for O-branch transitions, } S'(J_i, J_i-2) = 3(J_i-1)J_i/[2(2J_i-1)].$$

$f_m(J_i, J_f)$  is a correction to the rigid rotator, harmonic oscillator line intensities which arises from centrifugal distortion.

Division by  $2J_i+1$  corrects for the fact that intensities fundamentally depend upon the population of the initial energy state not of the initial energy level [122]. This is an important point for fundamental understanding of the relative intensities of different rotational lines and of the basis for temperature determinations from rotational line intensities. It is most clearly illustrated by the following argument, due to Condon and Shortley [122].

The intensity of spontaneous emission or an induced Raman transition between two states  $a$  and  $b$  of a given molecule or atom can be written in the form:

$$I(a, b) = C \nu^3 \cdot N(a) \cdot S(a, b). \quad (3)$$

(Compare combined eqs. (1) and (2) in the rigid-rotator harmonic-oscillator limit.) The constant  $C$  in eq. (3) differs from the constant  $C$  in eq. (2) and groups together physical constants, geometric factors, and molecule-dependent parameters which are independent of states  $a$  and  $b$ . The principle of microscopic reversibility requires that the probability of transition between two states  $a$  and  $b$  is the same in both directions, i.e., that the line strengths are symmetric in the initial and the final states

$$S(a, b) = S(b, a). \quad (4)$$



Equations (3) and (4) describe transitions between states or between nondegenerate energy levels. For degenerate energy levels A and B

$$S(A,B) = \sum_b \sum_a S(a,b) = \sum_a \sum_b S(a,b) = \sum_a \sum_b S(b,a) = S(B,A) \quad (5)$$

where the sums are over the states in each degenerate level. Thus line strengths between degenerate energy levels are symmetric in the initial and final levels. The intensity of a transition between two degenerate energy levels is given by the sum of the intensities of transitions between the states involved.

$$I(A,B) = \sum_b \sum_a I(a,b) = C \nu^3 \sum_b \sum_a [N(a) \cdot S(a,b)] \quad (6)$$

Since, for an equilibrium system, the population of each state in a degenerate energy level is the same, i.e.,  $N(a_1) = N(a_2) = N(a_3) \cdots = N(a)$ :

$$I(A,B) = C \nu^3 \cdot N(a) \cdot S(A,B) \quad (7)$$

and

$$I(B,A) = C \nu^3 \cdot N(b) \cdot S(B,A). \quad (8)$$

The population  $N(a)$  is the population of any given state of the degenerate initial energy level A. Equations (5), (7), and (8) show that, neglecting the  $\nu^3$  factor, the intensity of transition from A to B compared to that from B to A depends only upon the population of an individual state in the originating level,  $I(A,B)/I(B,A) = N(a)/N(b)$ . At temperatures high enough that  $N(a) \approx N(b)$ ,  $I(A,B) \approx I(B,A)$ , irrespective of the degeneracy of levels A and B; compare the Stokes and anti-Stokes intensities of the transitions near the laser line in figure 6.

Returning specifically to eq. (2) and rotational Raman scattering from diatomic molecules, the molecular number density in a given rotational energy level of molecular species is

$$N_m(J_i) = [(2J_i+1)N_m/Q_{r,m}]g_m(J_i)\exp[-F_{o,m}(J_i)c_2/T] \quad (9)$$

where  $N_m$  is the total number density,  $g_m(J_i)$  is a nuclear spin degeneracy factor,  $Q_{r,m} \approx T/(\sigma c_2 B_0)$  is the conventional rotational partition function (including the symmetry number  $\sigma$  but otherwise excluding nuclear spin),  $F_{o,m}(J_i)$  is the wave number of level  $J_i$  above  $J = 0$ , and  $c_2 = hc/k$  is the second radiation constant. For a heteronuclear molecule  $g_m = 1$ . For a homonuclear diatomic  $g_m(J_i) = (I+1)/(2I+1)$  in either the odd or even  $J$  rotational levels, depending upon electronic symmetry, and  $g_m(J_i) = I/(2I+1)$  in the other half of the rotational levels [42,121].

Thermodynamic temperatures can be computed from the measured relative intensities of rotational Raman transitions, for a given molecular precursor at a given temperature, using the relation:

$$-F_0 c_2 / T = \ln(I_s / f S^1 \nu^3 g) + \text{const.} \quad (10)$$

The symbols in eq. (10) are the same as those in eqs. (1), (2), and (9) except that the subscript  $m$  and the parenthetical  $J$ 's have been dropped.

Figure 7 shows the pure rotational Raman spectrum of  $N_2$  at room temperature (top) and the rotational Raman spectrum of  $N_2$  in a flame (bottom). The two-to-one intensity alternation in adjacent peaks arises from the nuclear degeneracy factor for  $N_2(I=1)$ . Figure 8 shows the application of eq. (10) to the calculation of a rotational temperature from the spectrum in figure 7. The temperature is determined from the slope obtained as a computer least-squares fit. Points calculated from both Stokes and anti-Stokes intensities are plotted on the same graph which can lower the temperature uncertainty and allow easy identification of non-Boltzmann rotational populations. For example, both points (one Stokes and one anti-Stokes) for a given initial rotational level would simultaneously deviate from the least-squares line if the population of that level was different from that given by a Boltzmann distribution. The  $N_2$  rotational temperatures determined for figure 7 from the slopes of figure 8 are  $301 \pm 5$  K and  $1583 \pm 15$  K where the uncertainties represent two standard deviations.

Rotational Raman measurements are useful for determining flame temperature profiles. For example, rotational Raman spectra obtained from two regions of a  $CH_4$  Bunsen flame in air are presented in figure 9 [42]. Scattering below the primary reaction zone (see fig. 9a) is predominantly from  $O_2$  and  $N_2$ . Methane, since it is a spherical top molecule, has no rotational Raman spectra (at least in a harmonic oscillator-rigid rotator approximation). Above the primary reaction zone of this flame scattering from  $N_2$  and  $CO_2$  is evident in figure 9b. Quantitative temperature measurements have been made from  $N_2$  rotational Raman intensities in both flame regions.

Rotational temperatures are most accurately determined--and most readily computed--at temperatures below 1000-2000 K. Above these temperatures the  $f$  correction for centrifugal distortion (eq. (2)) and the  $\eta$  correction for contributions from rotational transitions from vibrationally excited molecules can become quite appreciable. Both of these factors,  $f$  and  $\eta$ , correct for deviations from rigid-rotator behavior.

The intensity correction  $f$  for centrifugal distortion is negligible for transitions involving small values of  $J$  for all molecules except  $H_2$ . For example,  $f_{N_2}(10, 12) = 1.025$ . Because the vibration-rotation correction  $f$  varies as  $J^2$ , this correction lowers temperatures calculated from  $N_2$  rotational spectra about 1 percent and temperatures calculated from  $H_2$  spectra about 10 percent. This large correction for  $H_2$  and the fact that only a few rotational lines are intense enough to be measured causes temperatures from  $H_2$  rotational Raman measurements to be relatively inaccurate.

Rotational temperature measurements from  $N_2$  Raman spectra are considerably more precise than from  $H_2$  because many more lines are measured. However, at temperatures above  $\sim 1000$  K, the measured intensities have to be corrected ( $\eta$ ) for the fact that pure rotational Raman transitions occur in vibrationally excited molecules as well as ground vibrational-level molecules [42]. The correction is necessary because transitions involving given rotational levels in different vibrational levels, which essentially overlap at low  $J$ , became displaced

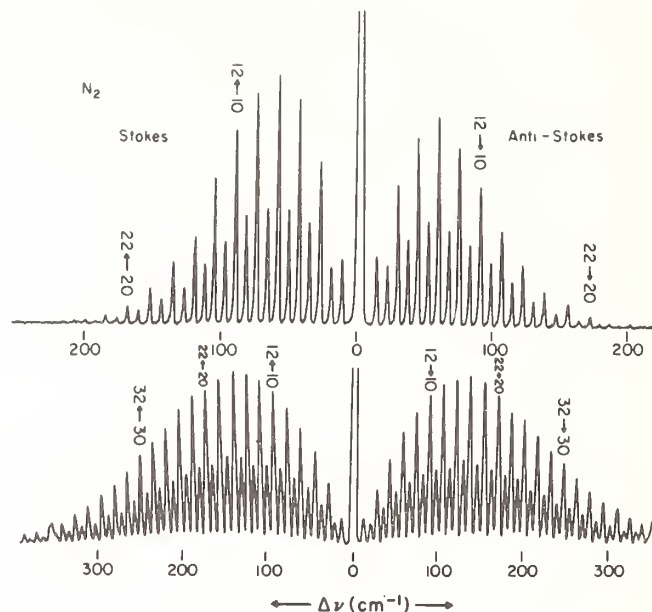


Figure 7. Rotational Raman spectra of  $N_2(g)$ . Top curve at room temperature, 1 atm, 15.8 W excitation at 488 nm,  $0.6 \text{ cm}^{-1}$  resolution,  $0.1 \text{ cm}^{-1}/\text{s}$  scan rate, 3 s time constant. Bottom curve in a cool region of a  $H_2$  diffusion flame, 1582 K, 14 W excitation at 488 nm,  $3 \text{ cm}^{-1}$  resolution,  $0.25 \text{ cm}^{-1}/\text{s}$  scan rate, 1 s time constant. Note that the two spectra have different wave-number shift scales.

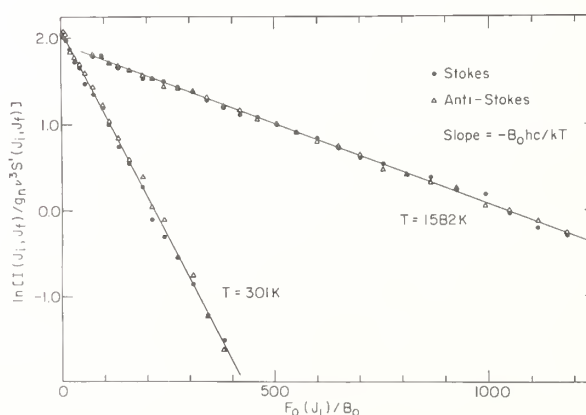
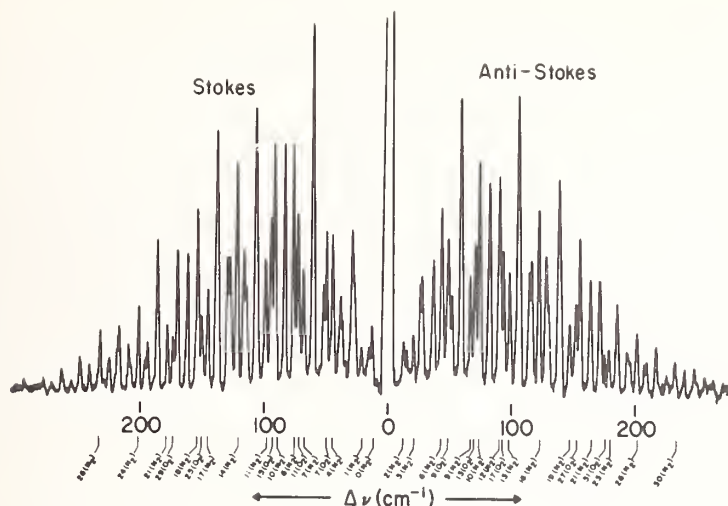


Figure 8.  $N_2$  rotational temperature determination plot for the spectra in figure 8.  $T_{\text{rot}}(N_2) = 301 \pm 5 \text{ K}$ ,  $T_{\text{rot}}(N_2) = 1582 \pm 13 \text{ K}$ . Uncertainty is two standard deviations calculated by a linear least-squares computer fit of the slopes.

(a)



(b)

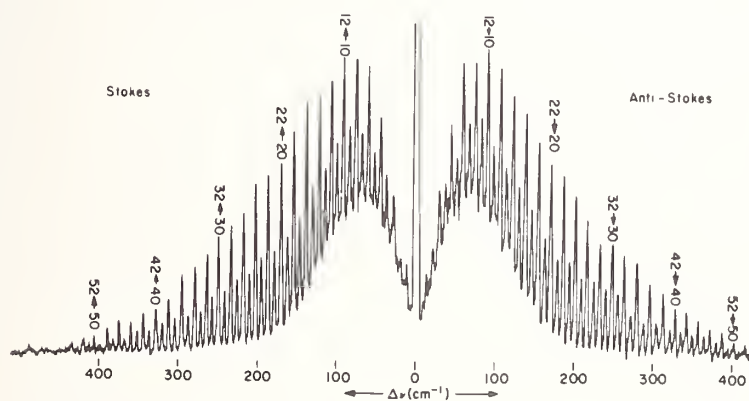


Figure 9 (a) Pure rotational Raman scattering from below the primary reaction of a Bunsen  $\text{CH}_4$ -air flame. Predominant species present are  $\text{N}_2$ ,  $\text{O}_2$ , and  $\text{CH}_4$ . Peaks are labeled with the rotational quantum number of the initial energy level and the chemical species involved in the transition. Excitation 10 W at 488 nm,  $1 \text{ cm}^{-1}$  resolution,  $0.25 \text{ cm}^{-1}$  scan speed, 3 s time constant.

(b) Rotational Raman scattering from about the primary reaction zone of the Bunsen  $\text{CH}_4$  flame. Predominant species are  $\text{N}_2$ ,  $\text{CO}_2$  and  $\text{H}_2\text{O}$ . 17 W at 488 nm,  $1.7 \text{ cm}^{-1}$  resolution,  $0.25 \text{ cm}^{-1}/\text{s}$  scan speed, 3 s time constant.

at high  $J$ . See figure 10. The displacement  $\delta\nu$  may be determined from literature equations for rotational term values and is given approximately by

$$\delta\nu = 4 (J_{\text{lower}} + \frac{3}{2}) \alpha_e \nu \quad (11)$$

where  $\alpha_e$  is the rotation-vibration interaction constant; thus, rotational transitions in excited vibrational levels contribute more to the measured intensity of low  $J$  peaks than of high  $J$  peaks. (See ref. [27] in this volume.) However, at high temperatures, there is a small, partially compensating, contribution to the intensity of high  $J$  peaks from transitions involving neighboring  $J$  levels in excited vibrational states. The overall correction for intensity contributions from vibrationally excited molecules raises computed rotational temperatures over calculations which neglect it. The increase becomes significant at high temperatures: 8 percent for  $N_2$  at 2000 K, with a triangular slit function having fwhm =  $2.6 \text{ cm}^{-1}$ . The correction depends upon both the temperature (vibrational population) and the spectrometer resolution (slit function) and so introduces additional complexities and possible uncertainties into rotational temperature calculations above 2000 K. The correction is not necessary for  $H_2$  as  $\alpha_e$  for  $H_2$  is large enough that rotational transitions in different vibrational levels are readily resolved, even at low  $J$ . For  $N_2$  and  $O_2$ , the  $\eta$  and  $f$  corrections essentially exactly cancel (within  $1^\circ$ ) at temperatures below 1000 K at typical slit widths of  $2\text{-}3 \text{ cm}^{-1}$ .

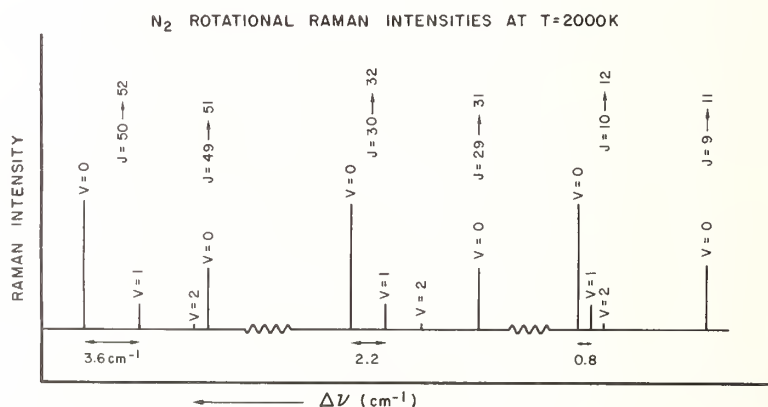


Figure 10. Calculated pure rotational Raman scattering from ground and vibrationally excited  $N_2$  molecules at 2000 K. The intensities of  $v=0$  transitions from  $J_i=10, 30$  and  $50$  have been normalized. The splitting  $\delta\nu$  of  $v=1$  compared to  $v=0$  transitions increases with  $J$ .



### 3.1.2 Vibrational Raman

Vibrational Raman scattering from diatomic molecules is dominated by Q( $\Delta J=0$ ) branch transitions, although weaker O( $\Delta J=-2$ ) and S( $\Delta J=+2$ ) side branches do occur. An example of a Stokes vibrational Raman spectrum from  $N_2$  in a premixed  $CH_4$ -air flame is given in figure 11. Scattering originating in vibrational levels up to  $v=3$  are clearly evident. With the exception of hydrogen-containing molecules, the high resolution required to resolve individual rotational lines in Raman Q-branches has not been feasible in high-temperature reactive environments. Because of this, differential vibrational Raman cross sections, measured from the intensity ratios of unresolved Q branches, are more accessible experimentally than the line intensities summarized in an equation such as (2). It is these values which are measured and tabulated [25].

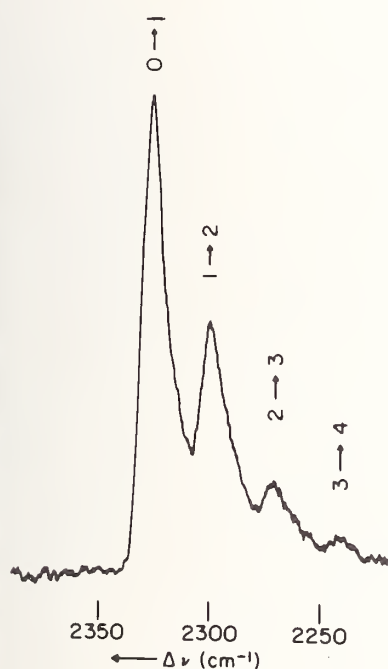


Figure 11. Stokes vibration Raman scattering from  $N_2$  in a  $CH_4$ -air flame. Labels indicate vibrational quantum numbers of initial and final states. Laser excitation is 17 W at 488 nm, 0.1  $cm^{-1}/s$  scan speed, 10 s time constant, polarizer parallel, 7  $cm^{-1}$  resolution.

The three approaches taken to obtain temperatures from the intensities of vibrational Raman bands are: (1) Stokes to anti-Stokes intensity ratios; (2) the Stokes or anti-Stokes band contour compared to theoretical predictions; or (3) relative intensity of Q-branch scattering from vibrationally excited molecules compared to that from ground vibrational-level molecules [26]. The last two methods require theoretical band contour calculations [26,123]. Most band contour calculations for  $N_2$  or  $O_2$  have included only the isotropic part [ $S' = \alpha_0(2J+1)$ ] of the Q branch-scattering.

A more exact calculation of  $N_2$  vibrational Raman profiles includes O and S branch transitions, the anisotropic part of the Q branch intensity in addition to the isotropic part and line strength corrections due to centrifugal distortion. For this calculation the value of

$\alpha_0$  in the Q branch line strength was determined to be 8.2 from the experimental ratio of intensities of the Q branch and the  $S_8$  rotation-vibration line in room temperature  $N_2$  gas ( $I(S_8)/I_Q = 8.0 \times 10^{-3}$  with a  $5 \text{ cm}^{-1}$  slit width and no polarization analyzer). The value of  $\alpha_0$  was varied in this band profile calculation until the calculated intensity ratio at 300 K equalled this experimental value. A comparison of this (more exact) profile with the usual  $N_2$  Q-branch profile at 2000 K is shown in figure 12. The baselines in the two calculations have been shifted for clarity. In the Q branch regions the two curves are essentially identical indicating that the neglect of O and S branches and the anisotropic parts of the Q branch does not introduce large systematic temperature errors in Raman temperature measurements based upon band intensities and shapes of  $N_2$  Q branches.

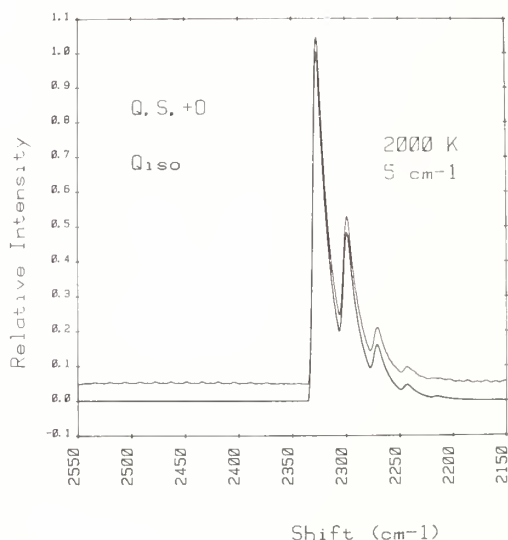


Figure 12. Band profile calculation of Stokes vibrational Raman scattering from  $N_2$  at 2000 K assuming a triangular spectrometer slit function with  $\text{fwhm} = 5.0 \text{ cm}^{-1}$ . Bottom curve includes isotropic part of  $Q(\Delta J=0)$  branch scattering only. Top curve is a more exact calculation including  $O(\Delta J=-2)$  and  $S(\Delta J=+2)$  branch transitions, the anisotropic part of the Q branch intensity in addition to the isotropic part, and line strength corrections due to centrifugal distortion. The baselines have been shifted vertically for clarity.

## 3.2 Flame diagnostics

As table 2 illustrates, the most extensive application of Raman intensity measurements as a diagnostic tool for reacting high-temperature systems has been to combustion. A number of comprehensive reviews describe Raman combustion studies, which range from studies of small laboratory flames to diagnosis of large combustors [24-26,119,123,124].

### 3.2.1 Time-averaged measurements

Most Raman studies of flames utilize very similar apparatus to that normally used for molecular Raman studies (cw argon ion laser, provision for laser multipassing, double monochromator, cooled photomultiplier detection, and photon counting electronics) [27]. This

system is particularly suited for time-averaged measurements of temperature and molecular density in flames with low levels of background luminosity or other sources of interference.

Analysis of Q-branch, Stokes vibrational Raman scattering has been used for temperature measurements in atmospheric pressure flames such as  $\text{H}_2$ -air [11,123,125,27,42], natural gas-air [12,126,42] and propane-air [127,42]. These and other vibrational Raman studies have also examined the concentrations of major, stable species ( $\text{N}_2$ ,  $\text{O}_2$ ,  $\text{H}_2$ ,  $\text{CO}_2$ ,  $\text{CO}$  and  $\text{H}_2\text{O}$ ) in hydrogen, acetylene, methane, and propane flames [20,25,26,119,123,124,128].

A good example of the current capability of cw argon ion laser Raman scattering is the measurement of  $\text{NO}$ ,  $\text{O}_2$  and  $\text{N}_2$  concentrations and temperatures (from  $\text{N}_2$  and  $\text{O}_2$  Stokes vibrational profiles) in a lean ammonia-oxygen flat flame [129].  $\text{NO}$  concentrations were measurable at levels of  $\sim 3 \times 10^{16}$  molecules/cc. Temperatures were measured with a precision (two standard deviations) of 38 K at 1600 K. A comparison of vibrational Raman temperatures from  $\text{O}_2$  and  $\text{N}_2$  with radiation corrected thermocouple temperature measurements in methane-air flat flames showed agreement within 2 percent. Ammonia-oxygen flames, because of laser-induced background interference, showed less satisfactory agreement ( $\sim 8$  percent) [130]. Further comparisons of temperatures determined from Raman scattering to thermocouple measurements in engine exhausts [28] or to  $\text{NaD}$  line and  $\text{OH}$  absorption in flames [27] are described elsewhere in this volume.

Although not nearly as pervasive as  $\text{N}_2$  or  $\text{O}_2$  vibrational Raman spectroscopy, rotational Raman scattering from  $\text{N}_2$ ,  $\text{O}_2$ , and  $\text{H}_2$  has been used for temperature measurements in  $\text{H}_2$ -air,  $\text{H}_2$ - $\text{O}_2$ ,  $\text{CH}_4$ -air, and propane-air flames [41,42,127,27]. For  $\text{H}_2$  or  $\text{CH}_4$  flames [42], temperatures based upon rotational Raman scattering from  $\text{N}_2$  have lower statistical uncertainties (1-4 percent) than those based upon vibrational Raman scattering (3-9 percent). Comparison of rotational and vibrational Raman scattering from  $\text{N}_2$  with similar apparatus suggests that rotational Raman yields considerably more accurate temperature measurements at temperatures below  $\sim 1500$  K, the advantage increasing as the temperature decreases. However, at temperatures above 2000 K, where interference from vibrationally excited molecules ( $\eta$ ) and corrections for molecular non-rigidity ( $f$ ) become important, vibrational Raman may be more reliable. Pure rotational scattering from  $\text{H}_2$  appears to be a promising method to measure  $\text{H}_2$  temperatures. However, the few  $\text{H}_2$  rotational temperature measurements reported appear to have relatively large uncertainties, perhaps because few lines are measured and a very wide wave-number range must be scanned [41,42]. Concentration measurements, particularly of polyatomic molecules, are much easier with vibrational than rotational Raman scattering with conventional spectrometers although the use of interferometers may make rotational measurements of polyatomic species possible and increase the sensitivity of rotational Raman scattering measurements [131].

Pulsed lasers with appropriate gated detection have also been employed for Raman flame studies. Examples include use of a cavity dumped argon ion laser with 70 W peak power, 1MHz repetition rate [132]; a 1kW, 3kHz frequency doubled Nd:YAG [128]; and 150 MW, 0.1 Hz Ruby laser [124]. As noted by Eckbreth, Bonczyk and Verdick [25], the intensity of Raman signals from a continuous 1W laser will be essentially identical to a pulsed laser of 1J/pulse at 1Hz repetition rate. However, the background luminosity interference in a pulsed laser system

can be reduced by orders of magnitude with a detection system synchronously gated to the laser pulse. Analysis of background luminosity [25,133] shows that continuous lasers are not suitable for luminous systems like model combustors but that high powered, pulsed lasers may be suitable, albeit at relatively low signal/noise ratios. The most serious problem appears to be laser-modulated particulate incandescence in sooty combustion environments [25,43,133].

### 3.2.2 Fluctuation measurements

In addition to time-averaged measurements on steady flames, there is a need for measurements of temperature and concentration fluctuations in turbulent combustion environments, particularly since nearly all technologically important combustion processes are turbulent. Temperature fluctuations are important in turbulent combustion modeling [119], in nitric oxide formation [134,135], and in hot corrosion of combustors and engines. Raman measurements of fluctuations are also important because time-averaged measurements of temperature density in turbulent flame systems can be in error because temperature is not a linear function of the Raman signal. The size of the errors depend upon the magnitude and correlation of the fluctuations in the flame [123,136].

Pulsed lasers of sufficient energy to give statistically significant Raman intensities in a single laser pulse can be used to make instantaneous ( $<1\mu$  s) temperature and species concentration measurements in flames [124,137]. The accumulation of a large number of data points ( $>100$ ) allows the determination of histograms indicating probability distributions. Temperature fluctuations at several positions in a turbulent  $H_2$ -air flame have been measured [137] using a 1J/pulse flashlamp-pumped dye laser and a two-channel polychromator accepting  $N_2$  Stokes and anti-Stokes Raman signals, respectively. Temperatures to an accuracy of 5-6 percent ( $\pm 1$  standard deviation) are determined from the anti-Stokes to Stokes intensity ratios for each laser pulse. A similar two channel detection system (this time detecting two segments of the rotational Raman profile) allowed measurement of temperature fluctuations in rocket exhausts [138]. Band contour temperature measurements are possible with multichannel detectors [139]. Recently, a free running ruby laser providing a train of pulses a few hundred nanoseconds apart with the flame located within the laser cavity was found suitable for quasi-continuous (15  $\mu$ s time constant) measurements of density and temperature fluctuations in clean flames [140].

Fast Fourier analysis of Raman intensities with a continuous laser source can provide information on average concentrations and on the magnitude and frequency distribution of the concentration fluctuations in individual species about that average. Such information complements the histograms obtained from pulsed laser excitation. Fourier transform techniques have been applied to turbulent  $CH_4$  flames [141]. Closely related autocorrelation techniques have been applied to nonreacting  $CH_4$  jets [142,143].



### 3.3 Other high temperature systems

Table 2 illustrates the types of high-temperature systems, in addition to atmospheric flames, to which Raman techniques have been applied for diagnostic purposes. There have been a number of efforts--with varying degrees of success--to study technological combustion systems such as combustion chambers [133], internal-combustion engine exhausts [144,145], gas turbine and rocket exhausts [28,138,146,147], shock tubes [148], and MHD exhausts [149]. Despite interferences from laser-induced particle incandescence and fluorescence, pulsed spontaneous Raman scattering appears generally suited for analysis of combustion, particularly on well-controlled, small, atmospheric pressure flames although results have been obtained on low pressure (0.1 atm) flames and in combustion furnaces [150].

In somewhat related developments, Raman techniques have been applied to remote atmospheric measurements. Vibrational Raman has been used for analysis of ppm air pollutants [151,152] and rotational Raman backscattering for temperature measurements. (See reviews of R. L. Byer [153] and H. Inaba [154]).

Spatially resolved concentration and temperature profiles have been obtained in model, industrial, chemical vapor deposition flow reactors [155, 156], and are discussed in detail by others in this volume [29,30,35]. Both Stokes and anti-Stokes  $N_2$ -vibrational Raman intensities [155] and  $N_2$  rotational Raman [30] intensities have been used to determine temperature profiles. Concentration profiles based on vibrational Raman for major species and fluorescence for minor species (i.e.,  $SiCl_2$ ) [35] have also been reported.

Electric discharges of  $N_2$  produce vibrationally excited molecules, the populations of which have been measured by vibrational [157] and rotational Raman scattering [158,131]. The rotational Raman study used a Fabry-Perot interferometer. Similarly, vibrational Raman scattering from  $H_2$  and  $D_2$  low-pressure arcs [159] and rotational Raman scattering from vibrationally excited molecules in  $CO_2$  electric discharges [160] have been reported. Measurements using coherent anti-Stokes Raman scattering (CARS) (discussed in Section 4) have been made in discharges of  $D_2$  [161] and  $N_2$  [162]. The latter workers observed CARS signals from vibrationally excited  $N_2$  molecules up to  $v=7$  and report that the populations of the vibrational levels deviate markedly from a Boltzmann distribution.

High pressure metal-halide arcs, such as those used in commercial lighting, operate at a few atmospheres total pressure with central axis temperatures of 5000-6000 K and wall temperatures of 1000 K. An extremely interesting development has been the use of electronic Raman scattering from gaseous atoms to make spatially resolved concentration measurements in these highly reactive, luminous systems [163-165]. Vriens and Adriaansz measured the densities of ground state ( $^2P_{1/2}$ ) Al atoms in lamps containing  $AlI_3$ , Hg, and Ar by measuring the intensity of Stokes scattering from the transition  $^2P_{3/2} \leftarrow ^2P_{1/2}$ . The anti-Stokes intensity of the same transition,  $^2P_{3/2} \rightarrow ^2P_{1/2}$ , gave the density of Al ( $^2P_{3/2}$ ) metastables. Similar measurements were carried out for In in lamps containing In, NaI, TlI, and  $HgI_2$ . The absolute electronic Raman cross sections for Al, Ga, In, and Tl had been obtained previously, both experimentally and theoretically [120].

In rather different applications, also of potential interest in high temperature technology, the intensity of  $N_2$  anti-Stokes vibrational Q-branch scattering was used to measure



the population of vibrationally excited  $N_2$ . The technique was applied to the measurement of the efficiency of vibrational deactivation by wall collisions [166] and, earlier, to monitor the production of vibrationally excited  $N_2$  in the reaction  $N + NO \rightarrow N_2^* + O$  [167].

#### 4. New Techniques: Coherent Anti-Stokes Raman Spectroscopy

Coherent anti-Stokes Raman spectroscopy (CARS), a relatively new multiphoton spectroscopic technique finding increasing use in molecular spectroscopy, has been the subject of number of recent articles and reviews [168-175]. The application of CARS to high temperature systems, pioneered by Taran [176] has already been extensive [168,169,174], because CARS offers the potential of alleviating the two major difficulties of high temperature Raman spectroscopy--weak signals and the presence of interfering background.

In CARS, input photons at  $\nu_1$  and  $\nu_2$  from two independent laser sources interact through the third order, nonlinear molecular susceptibility to generate a collimated beam of photons at the anti-Stokes frequency  $\nu_3 = 2\nu_1 - \nu_2$ . This mixing process occurs at all input frequencies and angles because of nonresonant processes, but the intensity of the output  $\nu_3$  signal is greatly enhanced when: (1) the energy difference  $h\nu_1 - h\nu_2$  equals an energy level difference in the molecule which corresponds to a classical Raman transition, and (2) linear momentum is conserved in the process. For gaseous samples the conservation of linear momentum is satisfied when the input beams are collinear which will result in an output signal beam which is also collinear. The signal intensity  $I_3$  at  $\nu_3$  is given by

$$I_3 \propto |\chi^{(3)}|^2 (I_1)^2 I_2 \quad (12)$$

where  $\chi^{(3)}$  is the third order nonlinear susceptibility and  $I_1$  and  $I_2$  are the intensities of the incident laser beams at  $\nu_1$  and  $\nu_2$ , respectively. Since  $\chi^{(3)}$  varies linearly with the normal Raman differential cross section, CARS selection rules are the same as conventional Raman spectroscopy. Also, since  $\chi^{(3)}$  is proportional to the molecular number density  $N$ , the CARS signal intensity increases with the square of the molecular density. Thus,

$$I_3 \propto N^2 \sigma^2 I_1^2 I_2. \quad (13)$$

Because the conversion efficiency can be quite high, as much as 1 percent in favorable case, CARS is more sensitive than conventional Raman spectroscopy in some, but not all, applications [169,170,177].

One area in which CARS appears to have potential advantages is in the Raman spectroscopy of high-temperature gases. The anti-Stokes and collimated nature of the CARS beam discriminates against just those kinds of noise which plague Raman spectroscopy of gases at elevated temperatures [169,172]. The fact that the output beam at  $\nu_3$  is anti-Stokes discriminates against laser-induced fluorescence and background chemiluminescence. Also, the fact that the output is a collimated laser beam permits spatial filtering to discriminate against background radiation. It is somewhat difficult to compare the ultimate sensitivity and signal-to-noise advantages of classical Raman as opposed to CARS for high-temperature

gases, although there have been recent efforts in this direction [177]. This is because CARS intensities increase as the cube of laser power, but also depend upon the square of the molecular concentration, and thus fall off more rapidly as the concentration is decreased than do normal Raman intensities. The background nonresonant CARS intensity increases linearly with number density. Recent calculations [177] indicate that the improvement is, at best, only marginal for detectability of small concentrations of gases at room temperature, but that detectability of individual, vibrational-rotational levels at high temperature, or under other conditions where high resolution is appropriate, will be considerably enhanced with CARS since CARS sensitivity increases as the laser linewidth narrows [169].

The potentially enhanced sensitivity of CARS, and the ability to discriminate against background radiation, appear promising for vibrational spectroscopy of polyatomic gases at elevated temperatures although no applications of CARS to determination of new vibrational spectra of high-temperature vapors have been reported to date. Another advantage of CARS in high-temperature studies is that it is somewhat easier to sample a high-temperature gas with a colinear output beam than when one is looking at scattered light at right angles and has to collect that isotropically scattered radiation with high efficiency. Thus, CARS is more compatible with induction-heated heat-pipe cells, for example. Gas-phase CARS results, as of this writing, are limited to vibrational CARS from a few diatomic-- $\text{H}_2$ ,  $\text{D}_2$ ,  $\text{N}_2$ ,  $\text{O}_2$ ,  $\text{CO}$ --[168,169,178,179] and polyatomic-- $\text{CH}_4$  ( $\nu_1$  and  $\nu_2$ ), [169]  $\text{C}_2\text{H}_2$  ( $\nu_1$  and  $\nu_2$ ) [179,180] and  $\text{SF}_6$  ( $\nu_1$  and  $\nu_2$ ) [181]--molecules, and rotational ( $J=3\rightarrow 5$ ) CARS from  $\text{H}_2$  [182].

All these transitions have large Raman cross sections and  $\Delta\nu$  values greater than  $900\text{ cm}^{-1}$  (except for  $\text{SF}_6$  where  $\nu_1=775$  and  $\nu_2=644\text{ cm}^{-1}$ ). The  $\text{SF}_6$  study [172] indicates that low  $\Delta\nu$  transitions, of greatest interest to high temperature inorganic chemists, can be investigated with CARS although with addition problems [172] of 1) separating the signals from the incident laser beams (requiring at least double monochromators), 2) interferences from dye laser fluorescence and super-radiance at the signal frequency, 3) CARS from other gases in the laser beam, from optics, and from cell windows, and 4) the lower Raman cross sections for low frequency, degenerate vibrational modes. Thus, the advantages and disadvantages of CARS for vibrational spectroscopy of high-temperature polyatomic vapors still have to be determined experimentally. Of potential use in spatially separating signal from incident beams is a crossed triple-beam, phase matched technique called BOXCARS [25,31,168]. CARS signals from low pressure gases can be enhanced by 2 to 3 orders of magnitude by using hollow glass capillary waveguides as sample cells [183] which may be applicable to some investigations of high temperature vapors.

The potential of CARS for high temperature diagnostics appears more certain and is described elsewhere in this volume [31,32,59]. Initial studies indicate CARS techniques are applicable to a number of high temperature situations where high backgrounds preclude spontaneous Raman measurements [31,168]. Both time-averaged [31] and single pulse [31,168,175] temperature measurements have been experimentally demonstrated with CARS.

There are a number of other new coherent, multi-photon laser techniques with potential for high temperature problems [59,169,170] among them being the Raman-induced Kerr effect (RIKES) [171] and Raman induced gain [184]. However, it is probably still too early in the development of RIKES and other coherent 3- and 4-photon techniques to assess their value as tools for high temperature molecular structure or gas diagnostic investigations.

We wish to recognize the useful discussions and interest in this work shown by Dr. John W. Hastie, Dr. M. Lapp and Dr. Ilan Chabay. National Science Foundation support (CHE 77-04404) is also gratefully acknowledged by G. M. R.

#### References

- [1] Hastie, J. W., High Temperature Vapors: Science and Technology (Academic Press, New York, 1975).
- [2] Margrave, J. L., ed., The Characterization of High Temperature Vapors (John Wiley and Sons, New York, 1967).
- [3] Gole, J. L., *Ann. Rev. Phys. Chem.* 27, 525 (1976).
- [4] Brewer, L., in The Chemistry and Metallurgy of Miscellaneous Materials, L. L. Quill, ed., p. 261 (McGraw-Hill, New York, 1950).
- [5] Braune, H. and Engelbrecht, G., *Z. phys. Chem. (Leipzig)* B19, 303 (1932).
- [6] Venkateswaran, C. S., *Proc. Indian Acad. Sci., Sec. A* 2, 260 (1935); 4, 345 (1936).
- [7] Beattie, I. R. and Ozin, G. A., *Spex Speaker*, 14, 1 (1969).
- [8] Beattie, I. R. and Horder, J. R., *J. Chem. Soc. A* 1969, 2655.
- [9] Beattie, I. R. and Ozin, G. A., *J. Chem. Soc. A* 1969, 2615.
- [10] Beattie, I. R. and Ozin, G. A., *J. Chem. Soc. A* 1969, 1691.
- [11] Lapp, M., Goldman, L. M. and Penney, C. M., *Science*, 175, 1112 (1972).
- [12] Vear, C. J., Hendra, P. J., and McFarlane, J. J., *J. Chem. Soc., Chem. Commun.*, 381 (1972).
- [13] Hastie, J. W., Hauge, R. H., and Margrave, J. L., *Ann. Rev. Phys. Chem.* 21, 475 (1970).
- [14] Beattie, I. R. and Perry, R. O., *J. Chem. Soc. A* 1970, 2429.
- [15] Lesiecki, M. L. and Nibler, J. W., *J. Chem. Phys.* 64, 871 (1976).
- [16] Drowart, J. and Goldfinger, P., *Ann. Rev. Phys. Chem.* 13, 459 (1962).
- [17] Lewis, G. N., Randall, M., Pitzer, K. S., and Brewer, L., in Thermodynamics, pp. 536-53 (McGraw-Hill, New York, 1961).
- [18] Drapcho, D. L. and Rosenblatt, G. M. (1978), to be published.
- [19] Drake, M. C. and Rosenblatt, G. M., *J. Chem. Phys.* 65, 4067 (1976).
- [20] Hartley, D., Lapp, M., and Hardesty, D., *Physics Today*, 28, 36 (1975).
- [21] Gaydon, A. G. and Wolfhard, H. G., Flames: Their Structure, Radiation, and Temperature Third edition (Chapman and Hall, London, 1970).
- [22] Fristom, R. M., *Survey of Progress in Chem.* 3, 55 (1966).
- [23] Goulard, R., Combustion Measurements (Academic Press, New York, 1976).
- [24] Lapp, M. and Penney, C. M., eds., Laser Raman Gas Diagnostics (Plenum Press, New York, 1974).
- [25] Eckbreth, A. C., Bonczyk, P. A., and Verdick, J. F., *Appl. Spectrosc. Reviews*, 13, 15 (1977).
- [26] Lapp, M. and Penney, C. M. in Adv. in Infrared and Raman Spectrosc., R. J. H. Clark and R. E. Hester, eds., Vol. 3, chap. 6 (Heyden and Sons Ltd., London, 1977).

- [27] Drake, M. C., Grabner, L. H., and Hastie, J. W., this volume.
- [28] Roquemore, W. M., Yaney, P. P., and Hemmer, T., this volume.
- [29] Hillel, R., Bouix, J., and Michaelides, A., this volume.
- [30] Miller, G. H., Mulac, A. J., and Hargis, P. J., Jr., this volume.
- [31] Eckbreth, A. C., this volume.
- [32] McDonald, J. R., Baronavski, A. P., Pasternack, L., Lemont, S., and Harvey, A. B., this volume.
- [33] Chan, C. and Daily, J. W., this volume.
- [34] Self, S. A., this volume.
- [35] Sedgwick, T. O., this volume.
- [36] Mueller, III, C. H., Scholfield, K., and Steinberg, M., this volume.
- [37] Bradshaw, J., Bower, J., Weeks, S., Fujiwara, K., Omenetto, N., Haraguchi, H., and Winefordner, J. D., this volume.
- [38] Gardiner, W., Jr., this volume.
- [39] Anderson, W. R., Allen, J. E., Jr., Fansler, T. D., and Crosley, D. R., this volume.
- [40] Smyth, K. C., Schenck, P. K., Mallard, W. G., and Travis, J. C., this volume.
- [41] Drake, M. C., and Rosenblatt, G. M., *Chem. Phys. Lett.* 44, 313 (1976).
- [42] Drake, M. C. and Rosenblatt, G. M., *Combustion and Flame*, 33, 179 (1978).
- [43] Eckbreth, A., *J. Appl. Phys.* 48, 4473 (1977).
- [44] Brumbach, S. B. and Rosenblatt, G. M., *J. Chem. Phys.* 56, 3110 (1972).
- [45] Self, S. A. and Kruger, C. H., *J. Energy*, 1, 25 (1977).
- [46] Barraclough, C., Beattie, I. R., and Everett D., in *Vib. Spectra and Structure*, J. R. Durig, ed., Vol. 5, p. 1 (Elsevier, New York, 1976).
- [47] Beattie, I. R., *Chem. Soc. Review*, 4, 107 (1975).
- [48] Beattie, I. R., Brumbach, S. B., Everett, D., and Moss, R., *Faraday Sym. Chem. Soc.* 8, 107 (1974).
- [49] Clark, R. J. H., *Spex Speaker*, 18, 1 (1973).
- [50] Beattie, I. R., in *Essays in Structural Chemistry*, A. J. Downs, ed., p. 111 (Plenum Press, New York, 1971).
- [51] Ozin, G. A., *Progr. Inorganic Chem.* 14, 173 (1971).
- [52] Beattie, I. R. and Ozin, G. A., *Spex Speaker*, 14, 1 (1969).
- [53] Andrews, L., *Appl. Spectros. Reviews*, 11, 125 (1976).
- [54] Moskovits, M. and Ozin, G. A., in *Vibrational Spectra and Structure*, J. Durig, ed., Vol. 4, p. 187 (Elsevier, New York, 1975).
- [55] Andrews, L., in *Vibrational Spectra and Structure*, J. Durig, ed., Vol. 4, p. 1 (Elsevier, New York, 1975).
- [56] Chadwick, B. M., *Molecular Spectroscopy*, R. F. Barrow, D. A. Long and D. J. Millen, eds., Vol. 3, p. 281 (The Chemical Society, London, 1974).
- [57] Nibler, J. W., *Adv. Raman Spectr.* 1, 70 (1972).
- [58] Ozin, G. A., *Spex Speaker*, 16, 1 (1971).
- [59] Beattie, I. R., this volume.
- [60] Ogden, J. S., this volume.



- [61] Hauge, R. H. and Margrave, J. L., this volume.
- [62] Froben, F. W., this volume.
- [63] Papatheodorou, G. N., this volume.
- [64] Beattie, I. R., Blayden, H. E., and Ogden, J. S., J. Chem. Phys. 64, 909 (1976).
- [65] Shirk, J. S., and Shirk, A. E., J. Chem. Phys. 64, 910 (1976).
- [66] Drake, M. C., and Rosenblatt, G. M., Proc. of the Symp. on High Temperature Metal Halide Chemistry, D. L. Hildenbrand and D. D. Cubicciotti, eds., p. 234 (Electrochem. Soc., Princeton, 1977).
- [67] Givan, A., and Loewenschuss, A., J. Raman Spectrosc. 6, 89 (1977).
- [68] DeVore, T. C., VanZee, R. J., and Weltner, Jr., W., Proc. of the Symp. High Temperature Metal Halide Chemistry, D. L. Hildenbrand and D. D. Cubicciotti, eds., p. 187 (Electrochem. Soc., Princeton, 1977).
- [69] Yates, J. H. and Pitzer, R. M., J. Chem. Phys. 70, 4049 (1979).
- [70] Lesiecki, M. L. and Nibler, J. W., J. Chem. Phys. 63, 3452 (1975).
- [71] Drake, M. C., Dissertation, The Pennsylvania State University, 1977; University Microfilms, Ann Arbor, MI.
- [72] Lesiecki, M. L. and Nibler, J. W., J. Chem. Phys. 62, 871 (1976).
- [73] Givan, A. and Loewenschuss, A., J. Chem. Phys. 65, 1851 (1976); 68, 2228 (1978).
- [74] Schafer, H., this volume.
- [75] Muller, A. and Mohan, N., J. Chem. Phys. 67, 1918 (1977).
- [76] Bosworth, Y. M., Clark, R. J. H., and Rippon, D. M., J. Mol. Spectros. 46, 240 (1973).
- [77] Clark, R. J. H., and Rippon, D. M., J. Mol. Spectros. 52, 58 (1974).
- [78] Clark, R. J. H., and Rippon, D. M., J. Chem. Soc., Faraday Trans 2, 69, 1496 (1973).
- [79] Clark, R. J. H., Hunter, B. K., and Rippon, D. M., Inorganic Chem. 11, 1439 (1972).
- [80] Clark, R. J. H. and Willis, C. J., J. Chem. Soc. A 1971, 838.
- [81] Clark, R. J. H. and Mitchell, P. D., J. Chem. Soc., Faraday Trans. 2 71, 515 (1975).
- [82] Clark, R. J. H. and Mitchell, P. D., J. Mol. Spectrosc. 51, 458 (1974).
- [83] Clark, R. J. H. and Mitchell, P. D., J. Amer. Chem. Soc. 95, 8300 (1973).
- [84] Renschler, D. L., Hunt, J. L., McCubbin, Jr., T. K., and Polo, S. R. S., J. Mol. Spectrosc. 31, 173 (1969).
- [85] Loete, M. and Berger, H., J. Mol. Spectrosc. 68, 317 (1977).
- [86] Rasetti, F., Phys. Rev. 34, 367 (1929).
- [87] Koningstein, J. A. and Mortensen, O. S., in The Raman Effect, A. Anderson, ed., Vol. 2, p. 519 (Marcell Dekker, New York, 1973).
- [88] Guedard, G. and Lehmann, J. C., J. Phys. B. 9, 2113 (1976).
- [89] Barrow, R. F. and Hitchings, M. R., J. Phys. B 5, L132 (1972).
- [90] Baierl, P. and Kiefer, W., Appl. Spectrosc. 32, 240 (1978).
- [91] Flusberg, A., Weingarten, R. A. and Hartman, S. R., Phys. Rev. Lett. 43A, 433 (1973).
- [92] Devlin, J. P., in Advances in Infrared and Raman Spectroscopy, R. J. H. Clark and H. E. Hester, eds., p. 153 (Heyden, New York, 1976).
- [93] Gilbert, B., Mamantov, G., and Begun, G. M., Appl. Spectrosc. 29, 276 (1975).
- [94] Gilbert, B., Mamantov, G., and Begun, G. M., J. Chem. Phys. 62, 950 (1975).



- [95] Gilbert, B., Mamantov, G., and Begun, G. M., *Inorg. Nucl. Chem. Lett.* 12, 415 (1976).
- [96] Balkanski, M., Leite, R. C. C., and Porto, S. P. S., eds., Light Scattering in Solids, 3rd Intl. Conf., Companis, Brazil (Flammarion, Paris, 1976).
- [97] Cardona, M., ed., Light Scattering in Solids, Topics in Applied Physics, Vol. 8, (Springer Verlag, New York, 1975).
- [98] Scott, J. F., in Vibrational Spectra and Structure, J. R. Durig, ed., Vol. 5, p. 67 (Elsevier, New York, 1976).
- [99] Eggerton, T. A. and Cardin, A. H., *Catal. Rev.* 11, 71 (1975).
- [100] P. J. Hendra, *Spex Speaker*, 14, 1 (1975).
- [101] Jeziorowski, H. and Knozinger, H., *Chem. Phys. Lett.* 43, 37 (1976).
- [102] Adams, D. M., Gardner, I. R., and Parkyns, N. D., *J. Catalysis*, 45, 145 (1976).
- [103] Howe, M. L., Watters, K. L., and Greenler, R. G., *J. Phys. Chem.* 80, 382 (1976).
- [104] Morrow, B. A., *J. Phys. Chem.* 81, 2663 (1977).
- [105] Saperstein, D. S. and Rein, A. J., *J. Phys. Chem.* 81, 2134 (1977).
- [106] Brown, F. R., Makovsky, L. E., and Rhee, K. H., *J. Catalysis*, 50, 162 (1977), 50, 385 (1977).
- [107] Menetrier, M., Dupeyrat, R., Levy, Y., and Imbert, G., *Opt. Comm.* 21, 162 (1977).
- [108] Yaney, P., *J. Raman Spectrosc.* 5, 219 (1976).
- [109] Nagasao, T. and Yamada, H., *J. Raman Spectrosc.* 3, 153 (1975).
- [110] Nakanaga, T. and Takenaka, T., *J. Phys. Chem.* 81, 645 (1977).
- [111] Takenaka, T., *Chem. Phys. Lett.* 55, 515 (1978).
- [112] Rosasco, G. J., and Etz, E. S., *Research/Development*, 28, 20 (1977).
- [113] Bridoux, M. and Delhay, M., in Adv. Infrared and Raman Spectroscopy, R. J. H. Clark and R. E. Hester, eds., p. 140 (Heyden, New York, 1976).
- [114] Gruen, D. M., Varma, R., and Wright, R. B., *J. Chem. Phys.* 64, 5000 (1976).
- [115] Bates, J. B. and Stidhan, H. D., *J. Chem. Phys.* 65, 3901 (1976).
- [116] Hartwig, C. M., *J. Chem. Phys.* 66, 227 (1977).
- [117] Weber, A. in The Raman Effect, A. Anderson, ed., Vol. 2, p. 543 (Marcel Dekker, New York, 1973).
- [118] Intensities in this paper are expressed in photons  $\text{cm}^{-3} \text{s}^{-1}$  rather than in the more familiar units of power density because this is the form in which intensities are directly measured using photon counting electronics.
- [119] Lapp, M. and Hartley, D., *Comb. Sci. and Tech.* 13, 199 (1976).
- [120] Vriens, L. and Adriannsz, M., *J. Appl. Phys.* 46, 3146 (1975).
- [121] Herzberg, G., Molecular Spectra and Molecular Structure, Vol. 1, Spectra of Diatomic Molecules (Van Nostrand, Princeton, 1950).
- [122] Condon, E. U. and Shortley, G. H., The Theory of Atomic Spectra, p. 98 (Cambridge Univ. Press, Cambridge, 1935).
- [123] Setchell, R. E., in Exp. Diagnostics in Gas Phase Combustion Systems, B. T. Zinn, ed., Progress in Astro. and Aero. Series, Vol. 53 (1977).
- [124] Lederman, S., *Progress Energy Combust. Sci.* 3, 1 (1977).

- [125] Lapp, M., in Laser Raman Gas Diagnostics, M. Lapp and C. M. Penney, eds., p. 107 (Plenum Press, New York, 1974).
- [126] Beardmore, L., Edwards, H. G. M., Long, D. A., and Tan, T. K., in Lasers in Chemistry M. A. West, ed., p. 79 (Elsevier, New York, 1977).
- [127] Stricker, W., Comb. Flame, 27, 133 (1976).
- [128] Stephenson, D. A. and Aiman, W. R., Comb. Flame, 31, 85 (1978).
- [129] Setchell, R. E. and Miller, J. A., Sandia Report SAND 77-8726 (Dec. 1977).
- [130] Schoenung, S. M. and Mitchell, R. E., Sandia Report SAND 77-8722 (Oct. 1977).
- [131] Barrett, J. J., Optical Engineering, 16, 85 (1977).
- [132] Mulac, A. J., Flower, W. L., Hill, R. A., Aeschliman, D. P., Sandia Report SAND 77-20 (June 1977).
- [133] Eckbreth, A. C., in Experimental Diagnostics in Gas Phase Comb. Systems, B. T. Zinn, ed., Vol. 53 in Progress in Astro. and Aero. Series, p. 517 (American Inst. of Aero. and Astro., New York, 1977).
- [134] Jones, W. P., Comb. Sci. and Tech. 10, 93 (1975).
- [135] Gouldin, F. C., Comb. Sci. and Tech. 9, 17 (1974).
- [136] Eckbreth, A. E., Comb. Flame, 31, 231 (1978).
- [137] Lapp, M., 6th Intl. Conf. Raman Spectrosc., Bangalore, India (Sept. 1978).
- [138] Williams, W. D., Powell, H. M., McGuire, R. L., Price, L. L., Jones, J. H., Weaver, D. P., and Lewis, J. W. L., in Turbulent Combustion, L. A. Kennedy, ed., Vol. 58 in Progress in Astro. and Aero., p. 273 (American Institute of Aero. and Astro., New York, 1977).
- [139] Black, P. C. and Chang, R. K., AIAA J. 16, 295 (1978).
- [140] Pealat, M., Bailly, R., and Taran, J. P. E., Opt. Commun. 22, 91 (1977).
- [141] Chabay, I., Rosasco, G. J., and Kashiwagi, T., Proc. 6th Int. Conf. Raman Spectrosc., Bangalore, India (Sept. 1978).
- [142] Birch, A. D., Brown, D. R., Dobson, M. G., and Thomas, J. R., J. Phys. D., Appl. Phys. 8, L 167 (1975).
- [143] Birch, A. D., Brown, D. R., Dobson, M. G., and Thomas, J. R., 16th Intl. Symp. Comb. Inst., Leeds, England (Sept. 1978).
- [144] Setchell, R. E. and Aeschliman, D. P., Appl. Spect. 31, 520 (1977).
- [145] Stricker, W. and Meinel, H., Comb. Flame, 29, 95 (1977).
- [146] Leonard, D. A. and Rubins, P. M., Amer. Soc. Mech. Engineers, ASME 75-GT-82 (1975).
- [147] Bailly, R., Pealat, M., and Taran, J. P. E., Opt. Comm. 17, 68 (1976).
- [148] Boiarski, A. A., Naval Surface Weapons Center Tech. Report NSWC/WOL/TR 75-53 (1975).
- [149] Boiarski, A. A. and Barnes, R. H., J. Energy, 1, 263 (1977).
- [150] Boiarski, A. A. and Barnes, R. H., and Kircher, J. F., Comb. Flame, 32, 111 (1978).
- [151] Hirschfeld, T., Schildkraut, E. R., Tannenbaum, T., and Tannenbaum, D., Appl. Phys. Lett. 22, 38 (1972).
- [152] Rosen, H., Robrish, R., and Chamberlain, O., Appl. Opt. 14, 2703 (1975).
- [153] Byer, R. L., Opt. and Quantum Electronics, 7, 147 (1975).

- [154] Inaba, H., in Topics in Applied Physics Vol. 14, Laser Monitoring of the Atmosphere, E. D. Hinkley, ed. (Springer-Verlag, Berlin, 1976).
- [155] Smith, J. E., Jr. and Sedgwick, T. O., Thin Solid Films, 40, 1 (1977).
- [156] Bouix, J. and Hillel, R., J. Less Common Metals, 47, 67 (1976).
- [157] Nelson, L. Y., Saunders, A. W., Jr., Harvey, A. B. and Weely, G. O., J. Chem. Phys. 55, 5127 (1971).
- [158] Barrett, J. J. and Harvey, A. B., J. Opt. Soc. Amer. 65, 392 (1975).
- [159] Shirley, J. A. and Hall, R. J., J. Chem. Phys. 67, 2419 (1977).
- [160] Barrett, J. J. and Weber, A., J. Opt. Soc. Amer. 60, 70 (1970).
- [161] Nibler, J. W., McDonald, J. R., and Harvey, A. B., Opt. Commun. 18, 271 (1976).
- [162] Shaub, W. M., Nibler, J. W., and Harvey, A. B., J. Chem. Phys. 67, 1883 (1977).
- [163] Adriaansz, M. and Vriens, L., Philips Res. Rpts., in press.
- [164] Vriens, L. and Adriaansz, M., Opt. Commun. 18, 187 (1976).
- [165] Vriens, L. and Adriaansz, M., J. Appl. Phys. 45, 4422 (1974).
- [166] Black, G., Wise, H., Schechter, S., and Sharpless, R. L., J. Chem. Phys. 60, 3526 (1974).
- [167] Black, G., Sharpless, R. L., and Slinger, T. G., J. Chem. Phys. 58, 4792 (1973).
- [168] Eckbreth, A. C., Bonczyk, P. A., and Shirley, J. A., Environmental Protection Agency Report EPA600/7-78-104 (June 1978).
- [169] Nibler, J. W., Shaub, W. M., McDonald, J. R., and Harvey, A. B., in Vibrational Spectra and Structure, J. R. Durig, ed., Vol. 6, p. 173 (Elsevier, Amsterdam, 1977).
- [170] Tolles, W. M., Nibler, J. W., McDonald, J. R., and Harvey, A. B., Appl. Spectros. 31, 253 (1977).
- [171] Levenson, M. D., Physics Today, p. 44 (May 1977).
- [172] Beattie, I. R., Black, J. D., Gilson, T. R., Greenhalgh, D., Hanna, D., and Laycock, L., in Lasers in Chemistry, M. A. West, ed., p. 7 (Elsevier, Amsterdam, 1977).
- [173] Harvey, A. B., McDonald, J. R., and Tolles, W. M., in Progress in Analytical Chemistry, Vol. 8, p. 211 (Plenum Press, New York, 1976).
- [174] Moya, F., Druet, S., Pealat, M., and Taran, J. P. E., in Experimental Diagnostics in Gas Phase Combustion Systems, B. T. Zinn, ed., Vol. 53 in Progress in Astro. and Aero. Series (American Inst. of Aero. and Astro., New York, 1977).
- [175] Roh, W., Schreiber, P. W., and Taran, J. P. E., Appl. Phys. Lett. 29, 174 (1976).
- [176] Regnier, P. R. and Taran, J. P. E., Appl. Phys. Lett. 27, 240 (1973).
- [177] Tolles, W. M. and Turner, R. D., Appl. Spectrosc. 31, 96 (1977).
- [178] Krynetsky, B. B., Kulevsky, L. A., Mishin, V. A., Prokhorov, A. M., Savel'ev, A. D., and Smirnov, V. V., Opt. Comm. 21, 225 (1977).
- [179] Nitsch, W. and Kiefer, W., Opt. Comm. 23, 240 (1977).
- [180] Fabelinsky, V. I., Krynetsky, B. B., Kulevsky, L. A., Mishin, V. A., Prokhorov, A. M., Savel'ev, A. D., and Smirnov, V. V., Opt. Comm. 20, 389 (1977).
- [181] Black, J. D., Gilson, T. R., Greenhalgh, D. A., and Laycock, L. C., Laser Focus, 84 (March 1978).
- [182] Barrett, J. J., Appl. Phys. Lett. 29, 722 (1976).

- [183] Miles, R. B., Laufer, G., and Bjorklund, G. C., Appl. Phys. Lett. 30, 417 (1977).  
[184] Owyong, A., Optics Letters, 2, 1978.  
[185] Van Duyne, R. P., J. Phys. (Paris) Colloq. 5, 239 (1977).

## RESONANCE RAMAN SPECTRA OF METAL HALIDE VAPOR COMPLEXES<sup>1</sup>

G. N. Papatheodorou  
Chemical Engineering Division  
Argonne National Laboratory  
Argonne, IL 60439

Resonance Raman spectra of complex vapor phase compounds formed by reacting "acidic" gases ( $A_2X_6 = Al_2Cl_6, Al_2Br_6, In_2Cl_6$ ) with metal halides have been measured. Spectra obtained from equilibrium vapor mixtures of  $A_2X_6$  over solid  $MX_2 (= PdCl_2, PdBr_2, CuCl_2, CoBr_2, TiCl_2, FeCl_2, NiCl_2, PtCl_2)$  were a superposition of the  $A_2X_6-AX_3$  bands and, in few cases, of new resonance-enhanced polarized bands due to  $MA_2X_8$  and/or  $MAX_5$  complexes. At temperatures above 800 K, characteristic bands due to  $MX_2(g)$  ( $M = Fe, Co, Ni, Cu, Zn$ ) and  $M_2X_4(g)$  ( $M = Cu$ ) were observed. The predominant features of the  $PdAl_2Cl_8, CuAl_2Cl_8$ , and  $PdAl_2Br_8$  spectra were three high-intensity, polarized bands which were attributed to the vibrational modes of the complex coupled to the electronic state of the central atom. The spectra of  $CuAlCl_5(g), CuInCl_5(g)$ , and  $Cu_2Cl_4(g)$  species showed resonance enhancement of selective fundamentals which were attributed to vibrational modes of trigonally coordinated Cu(II). Resonance Raman spectra of  $U_2Cl_{10}(g)$  and  $UCl_5 \cdot AlCl_3(g)$  were characterized by the presence of a strong band attributed to the  $U-Cl_t$  stretching frequency. Raman band intensity measurements were carried out for the iron(III) chloride vapors and for the vapor complexes of  $CuAl_2Cl_8, CuInCl_5$ , and  $UCl_5 \cdot AlCl_3$  using different laser powers and frequencies. The measurements suggested increasing spectroscopic temperatures and decomposition of the vapor complexes. The data are discussed in terms of the distribution of vibrational modes and the structure of the vapor species.

<sup>1</sup>Work performed under the auspices of the Division of Basic Energy Sciences of the U.S. Department of Energy.



## 1. Introduction

Reactions of "acidic" halide vapors (e.g.,  $\text{Al}_2\text{Cl}_6$ ,  $\text{In}_2\text{Cl}_6$ ,  $\text{Fe}_2\text{Cl}_6$ ) with solid metal halides have been widely investigated by various research groups [1-6]<sup>2</sup>. Spectrophotometric [2-5], mass spectrometric [1], and transpiration techniques [1,3,6] have been used to obtain thermodynamic information on these complexes. When the solid is a divalent metal halide, the predominant gaseous complex species is  $\text{MA}_2\text{X}_8$  [7-12], formed according to the reaction:



It has also been found that the acidic gas dimer-monomer equilibrium



plays an important role in the stability of these complexes [5,13,14,15]. Thus, at high temperatures and/or low pressures, equilibrium (2) shifts to the right and lower molecular weight complexes are formed:



The absorption spectra of some of these complexes are ligand-field sensitive, and thus yield information about the structure of these types of gaseous molecules. The electronic absorption spectra of  $\text{PdAl}_2\text{Cl}_8$  [7] and  $\text{PtAl}_2\text{Cl}_8$  [8] were found to be compatible with square planar coordination of the "central" M(II) ion, whereas for  $\text{CoAl}_2\text{Cl}_8$  [3,9] and  $\text{CoGa}_2\text{Cl}_8$  [2], the Co atoms were considered to be octahedrally and/or tetrahedrally coordinated. The electronic absorption spectra of  $\text{CrAl}_2\text{Cl}_8$  [11] were interpreted to mean that the transition metal was in distorted octahedral chloride coordination. However, the structural information obtained by absorption spectroscopy is not conclusive. At elevated temperatures, the bands are broad and their frequencies and/or intensities change drastically with increasing temperature; thus a direct comparison of the spectrum of the gas with known spectra of the solid or solution states is not always possible, and the results are ambiguous.

The present investigation was designed to characterize the structural properties of vapor complexes by means of Raman spectroscopy. Raman spectroscopy has been used successfully in the past to investigate the structures of single-component gases at high temperatures [16]. For the study of complex vapors, however, difficulties arise because, according to eqs. (1) and (3), the complexes exist only in equilibrium with the monomeric and dimeric acidic vapor. For the equilibrium gas mixture of reactions 1 and 3,  $\text{AX}_3(\text{g})$  and  $\text{A}_2\text{X}_6(\text{g})$  are the major components and in most cases, the vapor complexes of interest are minor components with partial pressures at least ten times less than those of the carrier gas. Thus, the

---

<sup>2</sup>Figures in brackets indicate the literature references at the end of this paper.

aman spectra are expected to be dominated by the bands due to the acidic halide, whereas the bands due to the small amounts of complex will be difficult to recognize. However, the electronic absorption spectra of most of these  $M^{+2}$  ions show bands near the region of the  $Ar^{+}$  and  $Kr^{+}$  laser lines; thus it might be possible to enhance the Raman band intensities of the complexes by using resonance Raman techniques [17].

The results reported in this paper are concerned with the resonance Raman spectra of vapor complexes of aluminum halides (mainly chloride) with transition-metal dihalides. Spectra of vapors in the system  $M-In-Cl$  ( $M = Fe, Co, Ni, Cu, Zn$ ) have been also investigated. At elevated temperatures, the vapor mixture formed according to reaction 2 and/or 3 also contains vapors of  $MX_2(s)$ , which in most cases yield resonance Raman and/or strong fluorescence spectra. Thus, it was necessary to investigate the spectra of the transition-metal chloride vapors in order to distinguish their vibrational frequencies from those of the vapor complexes. In addition, the resonance Raman spectra of both uranium pentachloride ( $U_2Cl_{10}$ ) vapors and of the  $UCl_5 \cdot AlCl_3$  vapor complex have been obtained and reported. Finally, the effects of laser power and frequency on the stability of vapor complexes and of iron trichloride vapors have been investigated.

## 2. Experimental Procedures

High purity "acidic" salts ( $Al_2Cl_6$ ,  $Al_2Br_6$ ,  $In_2Cl_6$ ) were prepared from the corresponding Cerac/Pure, Inc. reagent by repeated slow sublimations in fused silica tubes under vacuum. The palladium(II) halides were purchased from Mathey Bishop, Inc. Other anhydrous transition-metal chlorides were prepared by dehydrating  $MX_2 \cdot xH_2O$  (Baker A.R) in vacuum and/or in gaseous  $HCl$  atmosphere at elevated temperatures. A final purification of the metal halide salts was made by vapor-transporting them according to reactions 1 and 3 with the use of the corresponding "acidic" vapor halide. The  $UCl_5$  was synthesized from  $UO_2$ , aluminum chloride, and  $Cl_2$  at 300 °C according to the reaction:



The  $UCl_5(s)$  was further purified by vapor complex transport across a temperature gradient [18] in the presence of excess  $Al_2Cl_6$ .

Raman spectra were excited using either a Coherent Radiation argon or krypton ion laser, or a Coherent Radiation dye laser pumped by a 15 watt Control Laser Corporation argon laser. The scattered light was analyzed at 90° with a Spex 1400 or a Jobin-Yvon HG-2S double monochromator, and PAR(SSR) photon counting electronics or PAR chopper and lock-in amplifier electronics. Figure 1 shows the optics of the laser Raman system designed for use at high temperatures. To obtain the high-temperature gaseous spectra, a nichrome-wire dual-winding water-cooled optical furnace was constructed. The furnace was equipped with a chromel alumel thermocouple for monitoring the temperature and had an effective collection aperture of f 1.0. The furnace temperature gradients could be adjusted so that the window openings were always 5 to 10 °C hotter than the remaining part of the furnace. These

temperature gradients permitted studies of vapors in equilibrium with a solid and kept the solid away from the optical paths. A schematic of the furnace is shown in figure 2.

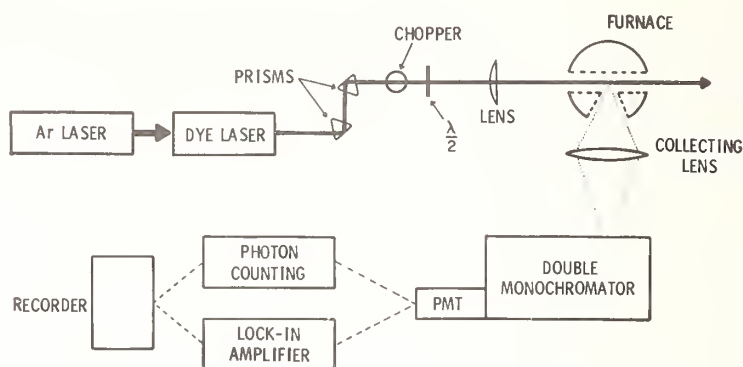


Figure 1. Instrumentation for high temperature Raman spectroscopy. The distance between the furnace and entrance slit is  $\sim 50$  cm.

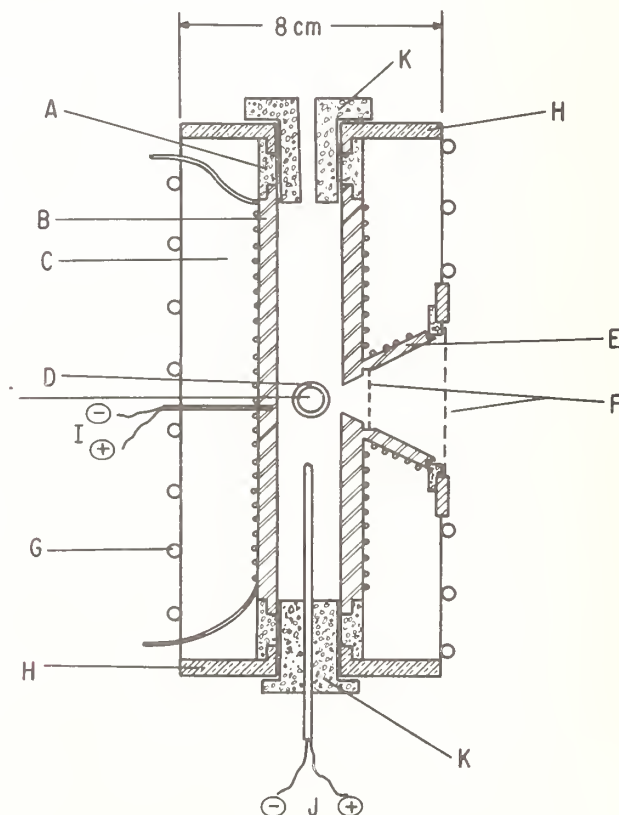


Figure 2. Optical furnace: (A) lavite rings, (B) main inconel heater, (C) bubble alumina insulation, (D) inconel tube opening, (E) inconel conical opening, (F) fused silica windows, (G) water cooling, (H) brass supports, (I) controlling thermocouple, (J) measuring thermocouple, and (K) lavite plugs.

The optical cells containing salt vapors with pressures less than 5 atm were made of fused silica tubing (20 mm OD, 18 mm ID and 2.5 to 5 cm long). For vapors having pressures above 5 atm, tubing of 3-mm wall thickness was used. Prew weighed amounts of the chemicals were transferred into a dry and degassed cell of known volume  $V$ . The cell was sealed under vacuum and attached to a fused silica manipulation rod. The "ideal gas" pressure  $P_0$  of undissociated  $A_2X_6$  at temperature  $T$  was calculated from the equation  $P_0 = nRT/V$ , where  $n$  is the number of moles of  $A_2X_6$  added to the Raman cell and  $R$  is the gas constant.

To prepare samples with no excess of  $MX_2(s)$ , a modified cell having a side tube was used. A chunk of  $MX_2(s)$  was placed into the side tube and equilibrated with the  $A_2X_6$  at a temperature  $\sim 50^\circ$  above the sublimation point of the acidic halide. The cell was then quickly cooled to solidify the gases present away from the solid. Finally, the remaining excess  $MX_2(s)$  was removed from the cell by sealing off the side tube. For each system studied, several (3-8) different cells were made.

Two polarization configurations were used to record the Raman spectra; one was designated as  $\perp, \perp$ , the other as  $\parallel, \perp$ . Thus,  $I_{\perp, \perp}$  is the Raman intensity measured with both the incident radiation and scattered radiation polarized perpendicularly to the scattering plane, whereas  $I_{\parallel, \perp}$  is the Raman intensity measured with the incident radiation polarized in the scattering plane and the scattered radiation analyzed perpendicular to the scattering plane.

The optical cells were placed inside the mechanically stable metal core of the furnace and were always in a fixed position relative to the collecting lens and/or entrance slit. A cell was first introduced in the optical furnace and the intensity of the scattered light was "maximized" by positioning the focusing and collecting lenses with two x, y, z micro-positioners. After obtaining the spectra, the cell could be removed and cooled to room temperature and then re-introduced into the optical furnace, yielding always, with no further micropositioner adjustments, the same Raman intensity. Thus, by using the same laser power, the Raman intensities were reproduced to within less than 5 percent and the relative Raman intensities of gases at different temperatures and pressures could be obtained within the same error [19].

### 3. Complexes of Aluminum Transition Metal Halides

Table 1 shows the various aluminum halide- $MX_2$  systems investigated by Raman spectroscopy. Only three out of nine systems gave bands attributable to the vapor complexes. The spectra of all other systems were dominated by the Raman bands of the "acidic" gas present in the cell.

Table 1. Aluminum halide-transition metal(II) halide vapors investigated by Raman spectroscopy

System	Predominant vapor complex	Reference for absorption spectra	Observed Raman bands
Ti-Al-Cl	$\text{TiAl}_3\text{Cl}_{11}$ [20]	20	Acidic vapor bands only.
Fe-Al-Cl	$\text{FeAl}_2\text{Cl}_8$ [6]	21	>>
Co-Al-Cl	$\text{CoAl}_2\text{Cl}_8$ [6,9]	9	>>
Co-Al-Br	$\text{CoAl}_2\text{Br}_8$ [5]	5	>>
Cu-Al-Cl	$\text{CuAl}_2\text{Cl}_8$ [22]	22,23	Bands due to $\text{CuAl}_2\text{Cl}_8$ , $\text{CuAlCl}_5$ and $\text{Al}_2\text{Cl}_6\text{-AlCl}_3$ .
Ni-Al-Cl	$\text{NiAl}_2\text{Cl}_8$ [6]	7	Acidic vapor bands only.
Pd-Al-Cl	$\text{PdAl}_2\text{Cl}_8$ [7]	7	Bands due to $\text{PdAl}_2\text{Cl}_8$ and $\text{Al}_2\text{Cl}_6\text{-AlCl}_3$ .
Pd-Al-Br	$\text{PdAl}_2\text{Br}_8$ [15]	15,24	Bands due to $\text{PdAl}_2\text{Br}_8$ and $\text{Al}_2\text{Br}_6\text{-AlBr}_3$ .
Pt-Al-Cl	$\text{PtAl}_2\text{Cl}_8$ [8]	8	Acidic vapor bands only.

The electronic absorption spectra of these vapor complexes showed ligand field bands which, in most cases, overlapped with the frequency region of the lasers used. Examples of such spectra are shown in figure 3 for the  $\text{nd}^8$  transition-metal complexes. The frequency region of the laser lines used is indicated by the vertical lines. In the presence of a high concentration of complex, the laser beam(s) was strongly absorbed giving very weak signals. Therefore, it was necessary to adjust the temperature and the "acidic" gas pressure by trial and error to find the optimum partial pressure of the complex which would allow the beam to go through the vapors and at the same time give rise to Raman signals. Cells with and without an excess of  $\text{MX}_2(\text{s})$  were examined at pressures of  $\text{A}_2\text{X}_6$  from  $\sim 0.1$  to 28 atm. It was found that best cells for achieving a high signal-to-noise ratio and a high ratio of vapor complex-to-"acidic" gas signals were those with no excess  $\text{MX}_2(\text{s})$ , having low partial pressures (less than 0.1 atm) of complex.



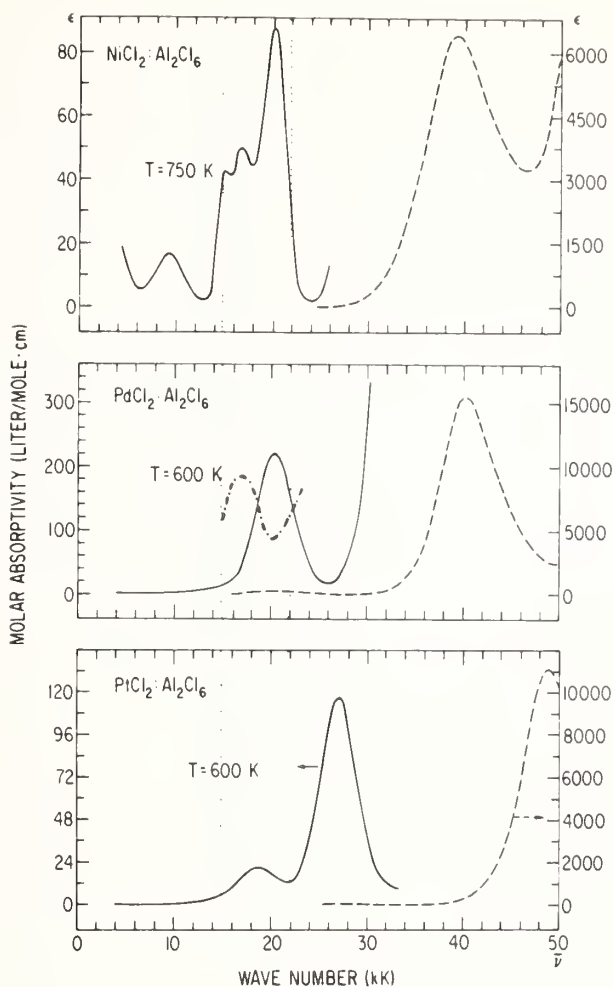


Figure 3. Electronic absorption spectra of  $nd^8$  vapor complexes  $NiAl_2Cl_8$  [7];  $PdAl_2Cl_8$  [7];  $PtAl_2Cl_8$  [8,21]. Vertical lines define the 647.1 to 457.9 nm region of laser frequencies. ...., calculated excitation profile from Raman intensities as a function of laser frequency ( $1 \text{ kK} = 1000 \text{ cm}^{-1}$ ).

### 3.1 Palladium complexes: $PdAl_2Cl_8$ ; $PdAl_2Br_8$ .

Figures 4 and 5 show representative Raman spectra of  $PdAl_2Cl_8-Al_2Cl_6-AlCl_3$  and of the  $PdAl_2Br_8-Al_2Br_6-AlBr_3$  gas mixtures excited with the 647.1 and 488.0 nm laser lines from a cell with  $P_{\text{complex}} \sim 0.3$  and  $\sim 0.10$  atm, respectively. Comparison with the spectra of pure aluminum halide vapors [15] reveals that some new bands are superimposed on the  $Al_2X_6-AlX_3$  modes. These new bands are attributed to  $PdAl_2X_8$  and are listed in table 2. The three strong polarized bands I, II, III, marked as a, c, and d on figures 4 and 5, were present in all spectra taken with different excitation lines at different temperatures and pressures. The intensities of bands a, c, and d measured from spectra excited with the "red" laser lines are similar in magnitude to those of  $Al_2X_6(g)$  polarized fundamentals. The pressure ratio of  $Al_2X_6$  to  $PdAl_2X_8$ , however, is  $\sim 10/1$ ; thus, it seems that the bands due to the complex exhibit preresonance enhancement.

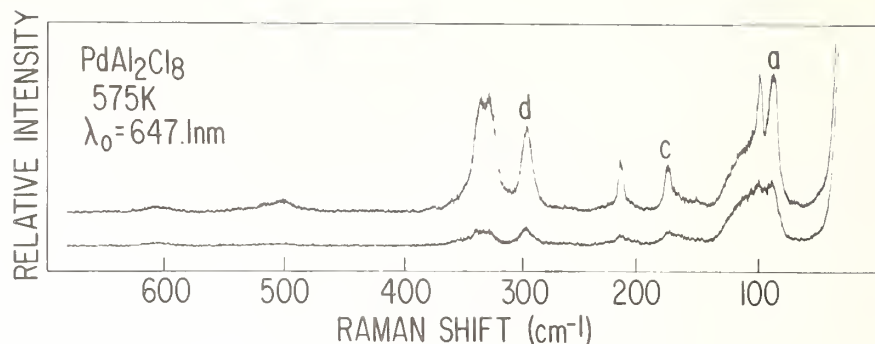


Figure 4. Raman spectrum of gaseous  $\text{PdAl}_2\text{Cl}_8\text{-Al}_2\text{Cl}_6$  mixture.  $P_{\text{Al}_2\text{Cl}_6} \sim 1 \text{ atm}$ ; excess of  $\text{PdCl}_2(\text{s})$ ,  $\lambda_0 = 647.1 \text{ nm}$ ; laser power 900 mW; spectral slit width,  $\sim 6 \text{ cm}^{-1}$ ; scan speed, 0.22 nm/min; time constant, 3 s; polarization: upper spectrum  $\perp, \perp$ ; lower spectrum  $\parallel, \perp$ ; a, c, d are the bands attributed to the gaseous complex.

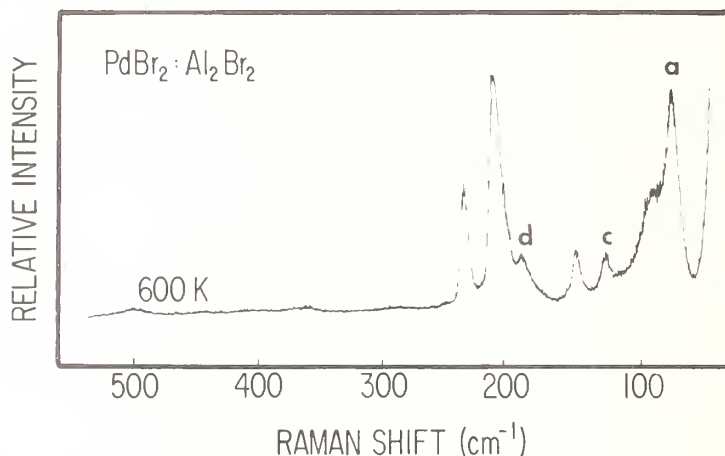


Figure 5. Raman spectrum of  $\text{PdAl}_2\text{Br}_8\text{-Al}_2\text{Br}_6\text{-AlBr}_3$  vapor mixture.  $P_{\text{Al}_2\text{Br}_6} \sim 1 \text{ atm}$ , no  $\text{PdBr}_2$  excess;  $\lambda_0 = 488.0 \text{ nm}$ ; laser power 1W; spectral slit width,  $\sim 6 \text{ cm}^{-1}$ ; scan speed 4 nm/min; time constant, 0.6 s; polarization  $\perp, \perp$ .

Table 2. Resonance Raman bands attributed to gaseous  $\text{MA}_2\text{X}_8$  molecules (frequency in  $\text{cm}^{-1}$ ).

Band	$\text{PdAl}_2\text{Cl}_8$	$\text{PdAl}_2\text{Br}_6$	$\text{CuAl}_2\text{Cl}_6$	Assignment
I	84.5	59	84.5	ring def.
II	176	114	174.5	$\delta_{\text{MX}_2\text{b}}$
III	298	180	281	$\text{M-X}_b$

At constant values of  $T$  and  $P_{Al_2X_6}$ , the intensities of bands a, c, and d, relative to the intensities of the  $Al_2X_6$  bands were found to vary with the frequency of the excitation line. This is shown quantitatively in figure 3, for the  $PdAl_2Cl_8(g)$  species where the relative intensities of band d to the  $218\text{ cm}^{-1}$  band of  $Al_2Cl_6$ , are plotted vs the laser excitation frequencies. Excitation profiles calculated for bands a and c were similar to the excitation profile of band d, but had larger experimental uncertainty.

This phenomenon is analogous to that observed for the  $\nu_1(A_{1g})$  mode of square planar  $MX_4^{-2}$  and octahedral  $MX_6^{-4}$  complexes [25-27]. Stein, et al. [26] have shown how de-enhancement of the symmetric stretch intensity arises in these complexes from interference between weak scattering from Laporte-forbidden electronic states and strong preresonance scattering from higher energy allowed charge-transfer states. A theoretical description of the same effect has been also given by Zgierski [28].

Assuming that two electronic states  $|s\rangle$  and  $|e\rangle$  are well separated, then the transition moments from the ground state  $|g\rangle$  to these states are

$$\langle g | \vec{M} | s \rangle = \vec{M}_{gs} \quad (5)$$

$$\langle g | \vec{M} | e \rangle = \vec{M}_{ge} \quad (6)$$

For an electronically allowed transition, both transition moments are different from zero, and the preresonance Raman intensity of a fundamental with Raman shift  $\nu_f$  is proportional to the A and/or B terms of Albrecht's theory [17].

$$I_s(\nu_f) \sim A_s \sim (\nu_o - \nu_f)^4 \left[ \frac{(\nu_s^2 - \nu_o^2)}{(\nu_s^2 - \nu_f^2)} \right]^2 \quad (7)$$

$$I_{se}(\nu_f) \sim B_{es} (\nu_o - \nu_f)^4 \left[ \frac{(\nu_s \nu_e + \nu_o^2)}{(\nu_s^2 - \nu_o^2)(\nu_e^2 - \nu_o^2)} \right]^2 \quad (8)$$

Apart from the frequency-dependent part, the A terms involve vibrational interaction with the  $|s\rangle$  (or  $|e\rangle$ ) state by way of Franck-Condon overlap integrals, and only totally symmetric vibrations are resonance enhanced. The B terms, on the other hand, involve Herzberg-Teller vibronic mixing of the two excited electronic states  $|s\rangle$  and  $|e\rangle$ , and all vibrational modes having any symmetry, which is contained in the direct product of the representations of the two electronic states, are resonance-enhanced.

If states  $|g\rangle$  and  $|s\rangle$  are of different parity, then the transition moment  $\vec{M}_{gs} = 0$  (Laporte forbidden) and the Raman intensities of totally symmetric modes do not show resonance enhancement, using the  $A_s$  term. It has been shown [14-20], however, that the Raman intensity of totally symmetric modes can be derived from preresonance enhancement using both the  $B_{es}$  term and the  $A_e$  term of the electronically allowed higher energy state  $|e\rangle$ . The Raman excitation profile is then proportional to

$$I(\nu_f) \sim \frac{1}{(\nu_e - \nu_0 - i\Gamma_e)^2} + R^0 \frac{1}{(\nu_e - \nu_0 - i\Gamma_e)(\nu_s - \nu_0 - i\Gamma_e)} \quad (9)$$

where  $R^0$  is the ratio of the  $I_{es}$  to  $I_e$  Raman intensities. As the laser frequency,  $\nu_0$ , is swept through the frequency of the forbidden state,  $\nu_s$ , the second term of the above equation changes sign and the Raman intensity of a totally symmetric fundamental is de-enhanced.

Presumably, the three polarized modes of  $\text{PdAl}_2\text{X}_8$  are coupled to the ligand field and charge-transfer electronic states of  $\text{Pd(II)}$  exhibiting the de-enhancement of the resonance Raman intensity described by eq. (9).

The frequency of band d is far below a  $\text{Pd-X}_t$  (terminal) frequency and lies below the  $\nu_2$  fundamental of  $\text{Al}_2\text{X}_6(\text{g})$  which describes a bridged  $\nu_{\text{Al-X}_b}$  mode. Thus, it is reasonable to assume that the Pd atom in the  $\text{PdAl}_2\text{X}_8$  is attached only to X-bridged halide atoms. Figure 6 shows three different molecular structures with the central ion bound to four or six X atoms. The number of polarized Raman bands,  $A_1$ , expected from these molecules are: Molecule a, 4; Molecule b, 5; Molecule c, 5.

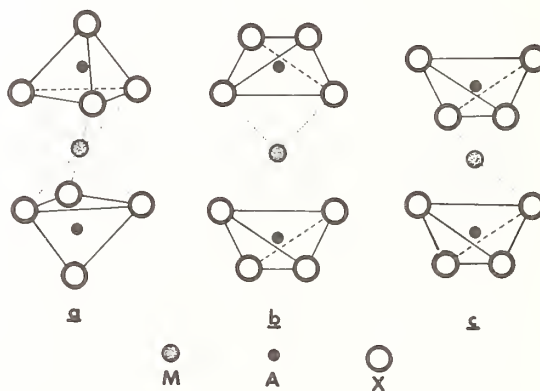


Figure 6. Molecular models for  $\text{MA}_2\text{X}_8$  vapors with M as central atom. Symmetries: a =  $D_{3h}$ ; b =  $D_{2h}$ ; c =  $D_{2d}$ .

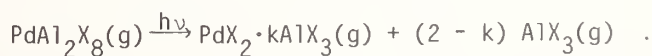
The electronic states of Pd(II) in these molecules are affected both by the geometric arrangement of the X atoms and, to some extent, by the neighboring Al(III) atoms [29]. Thus, the three  $A_1$  (resonance Raman) modes of  $\text{PdAl}_2\text{X}_8$  probably arise from the structural geometry of Pd(II) that includes the Al(III) atoms. There are three  $A_1$  species arising from these central atom geometries. These species are likely to show resonance enhancement due to coupling with the electronic states of the central atom. Thus, the polarized modes can be specified as follows:

$$\begin{aligned}\Gamma_{\text{mol. a}} &= A_{1g} (R) + 3 A_{1g} (R, rR) \\ \Gamma_{\text{mol. b}} &= 2 A_{1g} (R) + 3 A_1 (R, rR) \\ \Gamma_{\text{mol. c}} &= 2 A_{1g} (R) + 3 A_{1g} (R, rR)\end{aligned}\quad (10)$$

where  $rR$  and  $R$  indicate resonance Raman and Raman activity, respectively. Evidently, no distinction between molecules a, b, and c can be made, on the basis of these  $A_1(R, rR)$  modes alone. However, from previous studies [25,26,17], it appears that the de-enhancement of the symmetric fundamentals in the region of the  $d \rightarrow d$  electronic bands is a characteristic of "centrosymmetric complexes." Excitation of non-centrosymmetric tetrahedral  $\text{CoCl}_4^{-2}$  and  $\text{CoBr}_4^{-2}$  complexes within the  ${}^4A_2 \rightarrow {}^4T(P)$  absorption band gives rise to resonance enhancement of the Co-X stretching fundamental [30]. This is probably due to the fact that, in centrosymmetric complexes, the  $d \rightarrow d$  transitions are strictly Laporte-forbidden, whereas for non-centrosymmetric complexes, the ligand field transitions are partially allowed by d-p mixing and thus the  $\vec{M}_{gs}$  in eq. (5) does not vanish. These considerations and the observed minimum in the excitation profile of  $\text{PdAl}_2\text{X}_8$  suggest that the central Pd(II) atom possesses a center of symmetry in this molecule. Thus, structure c and/or strongly distorted structures a or b are excluded.

A distinction between the two structures, a and b can be made from the proximity of the d band of  $\text{PdAl}_2\text{X}_8(g)$  to the  $\nu_1$  ( $A_{1g}$ ) mode of square planar  $\text{PdX}_4^{-2}$  in  $\text{K}_2\text{PdX}_4$  [31]. Thus, structure b, having the Pd(II) in a square planar arrangement is the most probable one. The assignment of the three strong polarized modes observed in the spectra is given in the last column of table 2.

The intensities of bands a, c, and d, relative to the aluminum halide bands, were found to change with the power of the excitation line. Doubling the 488.0 nm line power from 450 to 300 nW increased the  $\nu_1$  intensity of the  $\text{AlX}_3$  monomer relative to the vapor complex and  $\text{Al}_2\text{X}_6(g)$  peaks. It is thus possible that the absorption of the laser line by the  $d \rightarrow d$  band gives rise to an increasing spectroscopic temperature and/or to a partial photodissociation of the complex:





Such a scheme alters the measurements of the relative intensities of the complex, and corrections should be made for the calculation of the excitation profile. However, due to the large intensity changes of the  $\text{PdAl}_2\text{X}_8$  bands observed as the excitation line is changed from 647.1 to 488.0 to 457.9 nm, these corrections are not large enough to alter the minimum in the excitation profile (fig. 3).

### 3.2 Copper complexes: $\text{CuAl}_2\text{Cl}_8$ , $\text{CuAlCl}_5$

The temperature dependence of the electronic absorption spectra of the Cu-Al-Cl system has been measured [23]. At lower temperatures, the spectra of the "yellow" gaseous complex(es) are characterized by a d-d band of low molar absorptivity ( $\sim 80$  liter/mol $\cdot$ cm) at 11.7 kK and three charge-transfer bands at 30.5, 38 (shoulder band), and 47.5 kK. In the temperature range from 445 to  $\sim 575$  K, the molar absorptivity of the d-d band is independent of temperature. At temperatures above 575 K, the molar absorptivity at 11.7 kK decreases with increasing temperature, a new band arises at 20 kK, and the color of the gaseous complex(es) changes from "yellow" to "red." All laser lines used to obtain the Raman spectra lie between the Cu(II) d-d band and the Cu-Cl charge transfer band. At high temperatures, the  $\text{Ar}^+$  laser lines were superimposed on the  $\sim 20$  kK "red" species band.

Figure 7 shows the Raman spectra obtained at 575 K, with different excitation lines, from a cell containing  $\sim 0.3$  atm of aluminum chloride and  $\sim 0.05$  atm of copper gaseous complex. The predominant features of the spectra obtained with the red 647.1 nm line are the  $\text{Al}_2\text{Cl}_6$  bands and four weak bands, namely, a ( $84.5\text{ cm}^{-1}$ ), c ( $175\text{ cm}^{-1}$ ), d ( $281\text{ cm}^{-1}$ ), and f ( $448\text{ cm}^{-1}$ ), whose intensities were found to increase with increasing temperature and frequency of the excitation line.

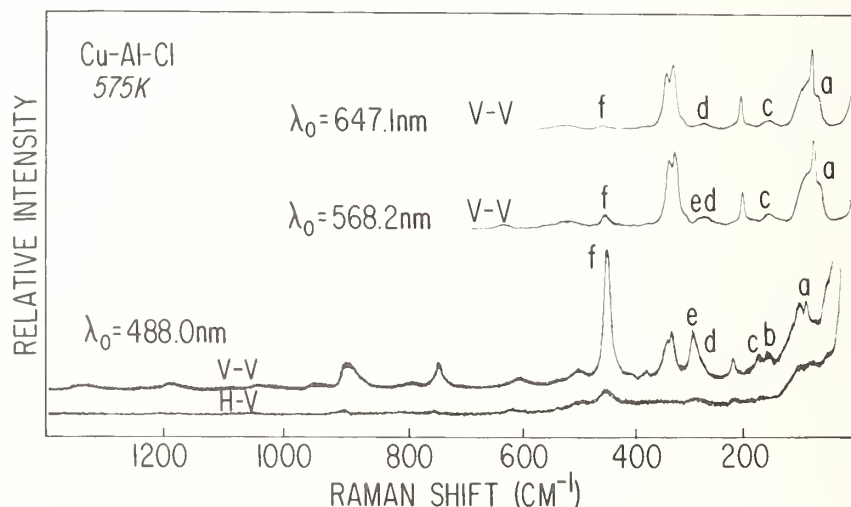


Figure 7. Raman spectra of Cu-Al-Cl vapor complexes.  $P_{\text{Al}_2\text{Cl}_6} \sim 0.3$  atm; furnace temperature,  $\sim 575$  K; spectral slit width,  $\sim 7\text{ cm}^{-1}$ ; polarization: V-V is  $\perp, \perp$  and H-V is  $\parallel, \perp$ . Note that the spectra were obtained using a double monochromator linear in wavelength and that the abscissa should be used only for approximating the band positions.

As the laser lines change from red to blue, the intensities of the a, c, and d bands increase relative to the intensities of the  $\text{Al}_2\text{Cl}_6$  bands, but not as fast as the intensity of band f. A new strong band (e) appears at  $291\text{ cm}^{-1}$ , and its intensity increases proportionately to the intensity of band f. Furthermore, a series of combination and overtone bands appears in the spectra excited with the  $\text{Ar}^+$  laser lines. Most of these bands can be accounted for in terms of overtones and combinations of the e and f bands. No combinations or overtones including a, c, and d bands are present in the spectra.

Further variations of the intensities of the Raman spectra result from changing either the power (intensity) of the excitation line at constant temperature or the furnace temperature at constant excitation line. Experiments designed to measure the effect of aluminum chloride pressure show that the intensities of band e and f decrease markedly with decreasing aluminum chloride pressure. These changes for the f band are shown in figure 8. The intensity of band e was also diminished in the high pressure cell with band d having the predominant intensity in the  $270\text{ to }300\text{ cm}^{-1}$  region. Bands a and c could be also recognized in the high pressure cell and their intensities slightly increased with increasing aluminum chloride pressure.

All observations are best interpreted to indicate that the Raman spectra can be accounted for in terms of two gaseous copper species. The bands a, c, and d, exhibiting preresonance Raman enhancement of their intensities, are attributed to the  $\text{CuAl}_2\text{Cl}_8$  gaseous molecule, which presumably has a structure similar to a, b, or c as presented in figure 6. The high intensity bands, e and f, and their combinations and overtones are attributed to the resonance-enhanced Raman bands of a "new" species.

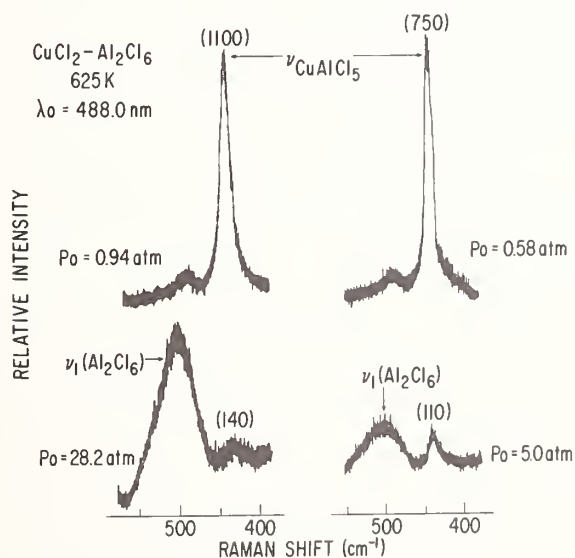


Figure 8. Effect of aluminum chloride pressure on Raman intensity of the  $448\text{ cm}^{-1}$  band. Furnace temperature,  $625\text{ K}$ ; power,  $500\text{ mW}$ ; spectral slit width,  $\sim 8\text{ cm}^{-1}$ . Numbers in parentheses indicate the intensity in counts/sec.

At this point, it should be noted that the temperature dependence of the absorption spectra [23] is indicative of a two-species equilibrium, in which the band at 11.7 kK is mainly associated with the "yellow" species and the band at 20 kK is associated with the high-temperature "red" species. It thus appears that the increasing intensity of the e and f Raman bands is related to the presence and increasing intensity of the 20 kK electronic transition and that the "new" species arises from a decomposition of the  $\text{CuAl}_2\text{Cl}_8$  molecule. A possible decomposition scheme, analogous to that found [14] for the  $\text{CoIn}_2\text{Cl}_8$  and  $\text{PdIn}_2\text{Cl}_8$  complexes, is as follows:



Choosing a possible structure (fig. 6) for the  $\text{CuAl}_2\text{Cl}_8$  molecule is difficult. Similarities between the  $\text{Cu-Cl}_b$  frequency and frequencies of other copper chlorides of known structure cannot be used in the selection since the Cu(II) exhibits strong Jahn-Teller distortions and all its halide compounds have strongly distorted octahedral or tetrahedral coordinations.

Based on the electronic absorption spectra, Satakshuto [22] proposed a distorted octahedral coordination for the Cu(II) in  $\text{CuAl}_2\text{Cl}_8$  and a structure similar to a in figure 6. The observed  $\nu_{\text{Cu-Cl}_b}$  frequency ( $281 \text{ cm}^{-1}$ ) for the gaseous complex lies below the  $297 \text{ cm}^{-1}$  value for  $\text{CuCl}_4^{2-}$  in distorted tetrahedral coordination [32] and is in support of a distorted structure a. On the other hand, the ring deformation ( $\sim 84 \text{ cm}^{-1}$ ) and angle bending ( $\sim 175 \text{ cm}^{-1}$ ) modes are the same for both the  $\text{PdAl}_2\text{Cl}_8$  and  $\text{CuAl}_2\text{Cl}_8$  complexes (table 2) and thus a square planar structure (structure b) is also acceptable.

The structure of the  $\text{CuAlCl}_5$  species is shown in figure 9. It is noteworthy that the 448 and  $291 \text{ cm}^{-1}$  bands are, respectively, very close to the Cu-Cl and Cu-Cl frequencies of trigonally coordinated copper (table 3 and Section 4).

Table 3. Resonance Raman bands attributed to gaseous  $\text{CuAlCl}_5$  and  $\text{Cu}_2\text{Cl}_4$  molecules (frequency in  $\text{cm}^{-1}$ )

Band	$\text{CuAlCl}_5$	$\text{CuInCl}_5$	$\text{Cu}_2\text{Cl}_4$	Assignment
I	291	300	314	$\text{Cu-Cl}_b$
II	448	442	442	$\text{Cu-Cl}_t$

### 3.3 Cobalt complexes: $\text{CoAl}_2\text{Cl}_8$ , $\text{CoAl}_2\text{Br}_8$

Cells having a variety of concentrations of the vapor complexes and with pressures of  $\text{Al}_2\text{X}_6(\text{g})$  up to 28 atm have been investigated. Both right angle and backscattering techniques have been used with all available laser lines. The scattered light, however, shows

only the presence of the  $\text{Al}_2\text{X}_6$ - $\text{AlX}_3$  bands and no bands due to the complexes. The relative concentrations of  $\text{CoAl}_2\text{X}_8(\text{g})$  and  $\text{Al}_2\text{X}_6(\text{g})$  were similar to those in the Cu-Al-Cl and Pd-Al-X systems, but no resonance enhancement of the cobalt complex fundamentals was observed.

The charge transfer bands of the  $\text{CoAl}_2\text{X}_8$  complexes are at higher energies [5,9] than those of the Cu or Pd complexes and do not overlap with the d→d bands. The laser lines used to excite the spectra cover part of the d→d bands but are far away from the CT band. Presumably, neither preresonance enhancement, eq. (7), nor destructive interference effects, eq. (9), can occur for these vapors.

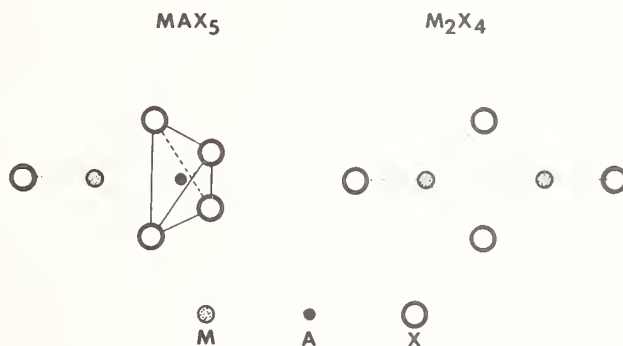


Figure 9. Molecular models for  $\text{MAX}_5$  and  $\text{M}_2\text{X}_4$  vapors.

As noted above, however, non-centrosymmetric  $\text{CoX}_4^{-2}$  shows resonance enhancement of its Raman fundamentals by involving the d-p mixing of the ligand field transitions [30]. It is thus possible that the absence of vapor complex bands from the Co-Al-X spectra arises from a near centrosymmetric coordination of Co in the  $\text{CoAl}_2\text{X}_8$  complex. This conclusion is tentative and questionable since other factors (e.g., laser decomposition of complex; see Section 4) might also prevent detection of vapor complex bands.

### 3.4 Complexes with Ti, Fe, Ni, and Pt

As in the case of the  $\text{CoAl}_2\text{X}_8(\text{g})$ , no Raman signals were obtained for the  $\text{MAl}_2\text{Cl}_8$  ( $\text{M} = \text{Ti, Fe, Ni, Pt}$ ) complexes, although many cells have been thoroughly investigated at different temperatures, pressures, and laser excitation lines. It has been demonstrated by spectrophotometric [8,20] and transpiration [6] techniques that these complexes have lower partial pressures than those for the Pd, Cu, and Co complexes. Thus, it is possible that the very small amounts of complexes present in the cells and/or their high energy CT bands (e.g., the ~48 kK band for  $\text{NiAl}_2\text{Cl}_8$ ; fig. 3) may account for very weak Raman signals which are completely obscured by the  $\text{Al}_2\text{Cl}_8$  bands.

#### 4. Complexes of Indium-Transition Metal Chlorides

Recent spectrophotometric [13,14] and mass spectrometric [33] studies have shown that the predominant vapor species of the indium complexes are formed according to reaction 3. In the present section, our attempts to obtain the Raman spectra of M-In-Cl (M = Fe, Co, Ni, Cu, Zn) vapor complexes are reported. For these studies, temperatures near or above the sublimation point of indium chloride are required; at these temperatures, the vapors from the  $MCl_2$  solids interfere with the spectra of the other vapor components. Thus, in order to distinguish the complex Raman active bands from those of the other gases, a detailed knowledge of both the  $In_2Cl_6$ - $InCl_3$  and the  $MCl_2$  vapor spectra are required. The temperature and pressure dependence of the indium chloride vapor spectra have been obtained and part of the results have been reported elsewhere [21]. The spectra obtained for the  $MCl_2$  (M = Fe, Co, Ni, Cu, Zn) vapors are outlined briefly here.

##### 4.1 $ZnCl_2$ , $FeCl_2$

Raman spectra of these vapors were obtained in the temperature range from 900 to 1150 K. Each spectrum was characterized by a single, strong polarized band. Figure 10 shows characteristic spectra for the zinc chloride vapors. The spectra for iron(II) chloride were similar, but were superimposed on a broad fluorescence background. The frequencies measured from the spectra are listed in table 4 and are assigned to stretching modes of linear triatomic molecules.

##### 4.2 $CuCl_2$

The temperature dependence of copper(II) chloride vapor spectra, obtained from a cell containing no excess of  $CuCl_2(s)$ , is shown in figure 11. Spectra were also measured using different excitation lines, different laser intensities and from cells containing  $\sim 1$  atm of  $Cl_2(g)$ . The resonance Raman character of the spectra is evident from the strong scattering signals observed from presumably a minor vapor component, the variation of the relative Raman intensities with excitation frequency, and the progression of combination-overtones. Three bands (table 4) and their combinations and overtones were found to increase in intensity with increasing temperature. Three other bands, at 314, 422, and  $545\text{ cm}^{-1}$ , decrease in intensity with increasing temperature.

The observed changes are best interpreted in terms of a dimer-monomer equilibrium:



The three bands listed in table 4 were assigned to the  $\nu_1(A_1)$ ,  $\nu_2(A_1)$  and  $\nu_3(B_1)$  fundamentals of a bent  $C_{2v}$  triatomic molecule. These frequencies are in agreement with the general trends observed for other metal chloride or fluoride triatomic molecules. A strong band at  $250\text{ cm}^{-1}$  is assigned to a difference band  $\nu_1 - \nu_2$ . Bands with frequencies above  $600\text{ cm}^{-1}$  were combinations of overtones of the three  $CuCl_2(g)$  fundamentals.



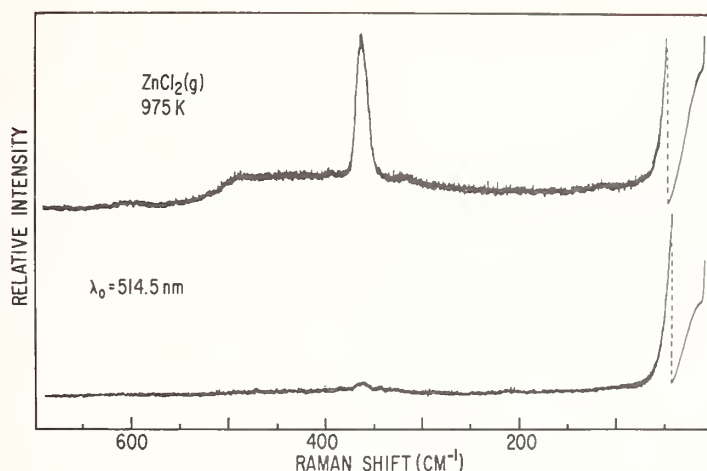


Figure 10. Raman spectra of vapors over liquid  $\text{ZnCl}_2$ . Spectral slit width;  $\sim 4 \text{ cm}^{-1}$ ; power, 6 W; scan speed,  $20 \text{ cm}^{-1}/\text{min}$ ; time constant, 0.5 s; polarization: upper spectrum  $\perp, \perp$ , lower spectrum  $\parallel, \perp$ .

As indicated in table 3, the fundamentals observed for the  $\text{Cu}_2\text{Cl}_4(\text{g})$  are assigned to the  $\text{Cu-Cl}_t$  and  $\text{Cu-Cl}_b$  modes of the copper in a trigonal configuration having one terminal chloride and two bridged ones (fig. 9).

Table 4. Observed frequencies ( $\text{cm}^{-1}$ ) of  $\text{MX}_2$  vapors at elevated temperatures.

	$\text{FeCl}_2$	$\text{CoCl}_2$	$\text{NiCl}_2$	$\text{CuCl}_2$	$\text{ZnCl}_2$
Temperature					
K	1100	1100	900	800	975
1	350 p	359	362	370 p	362 p
2		$177(2\nu_2)^a$	$170(2\nu_2)^a$	130 p	
3				503 dp	
Molecular Symmetry	$D_{\infty h}$	$D_{\infty h}$	$D_{\infty h}$	$C_{2v}(?)$	$D_{\infty h}$

<sup>a</sup>Tentative assignment.

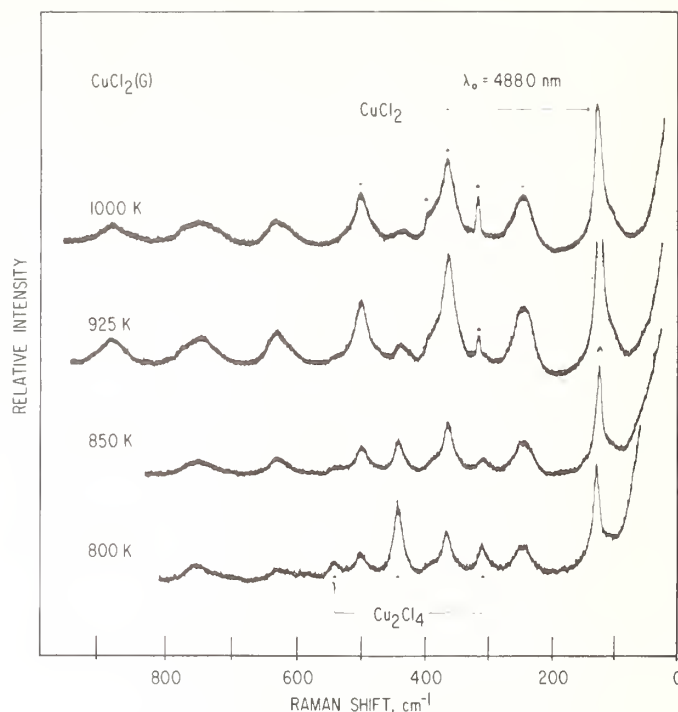


Figure 11. Temperature dependence of copper chloride spectra. No  $\text{CuCl}_2(\text{s})$  excess; spectral slit width,  $\sim 7.5 \text{ cm}^{-1}$ ; power, 740 mW; polarization  $\perp, \perp$ , scan speed, 2.2 A/min; time constant, 1.5 s; \* = fluorescence bands.

#### 4.3 $\text{NiCl}_2$ , $\text{CoCl}_2$

High temperature (resonance) fluorescence spectra were observed from these vapors. Figure 12 illustrates the  $\text{NiCl}_2(\text{g})$  spectrum from cells containing no excess of solid at 900 K. Increasing the temperature did not alter the relative intensities of the bands. The complicated nature of the spectrum, showing many overlapping bands, will not be discussed in detail. However, it should be noted that the intense bands observed for  $\text{NiCl}_2$  at wave numbers below  $19,500 \text{ cm}^{-1}$  were multiplets and/or combinations of two basic frequencies at  $362$  and  $170 \text{ cm}^{-1}$ . The  $\text{CoCl}_2$  spectra were also characterized by two basic frequencies, of  $359$  and  $177 \text{ cm}^{-1}$ .

A possible assignment of the  $362 \text{ cm}^{-1}$  ( $\text{NiCl}_2$ ) and  $359 \text{ cm}^{-1}$  ( $\text{CoCl}_2$ ) frequencies is the  $\nu_1$  symmetric stretch for the triatomic molecules. The proximity of these values to the  $\nu_1$  value of  $\text{ZnCl}_2(\text{g})$ ,  $\text{FeCl}_2(\text{g})$  and  $\text{CuCl}_2(\text{g})$  (table 4), and the previously measured  $\nu_1$  value for  $\text{NiCl}_2$  ( $340\text{--}370 \text{ cm}^{-1}$ ) [34,35] are in support of such assignment. The  $170 \text{ cm}^{-1}$  ( $\text{NiCl}_2$ ) and  $177 \text{ cm}^{-1}$  ( $\text{CoCl}_2$ ) frequencies may arise from the  $\nu_2$  mode, but the values are much higher than the frequencies observed by low temperature IR matrix isolation techniques [36] ( $85$  and  $95 \text{ cm}^{-1}$ , respectively). It is possible, however, that these bands arise from the Raman active first overtone of the  $\nu_2(\text{A}_2)$  mode of a linear triatomic molecule. Thus, the assignments given table 4 for  $\text{NiCl}_2$  and  $\text{CoCl}_2$  is in agreement with the IR data, but it should be considered tentative.

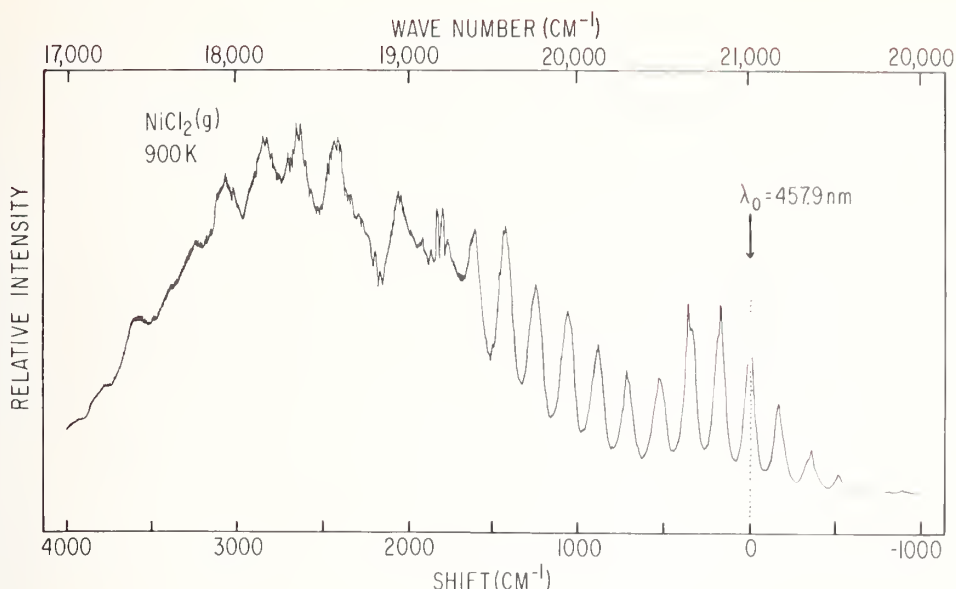
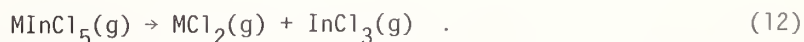


Figure 12. Nickel chloride vapor spectrum excited with 457.9 nm laser line. Spectral slit width,  $\sim 4.5 \text{ cm}^{-1}$ ; power, 250 nW; scan speed,  $500 \text{ cm}^{-1}/\text{min}$ ; time constant, 0.2 s.

For the investigation of the M-In-Cl complexes, a series of Raman cells having various partial pressures of the complex and various  $\text{In}_2\text{Cl}_6$ - $\text{InCl}_3$  pressures have been made. From all the systems studied ( $M = \text{Fe}, \text{Co}, \text{Ni}, \text{Cu}, \text{Zn}$ ), only the Cu-In-Cl vapors gave rise to resonance Raman signals which could be attributed to vapor complexes. Spectra obtained from Zn-In-Cl and Fe-In-Cl consisted of a superposition of the indium chloride fundamentals and the symmetric stretch of the  $\text{MCl}_2$  triatomic molecule. At temperatures above 1000 K, the Co-In-Cl and Ni-In-Cl spectra were obscured by the fluorescence spectra of  $\text{NiCl}_2(\text{g})$  and  $\text{CoCl}_2(\text{g})$ , respectively. At lower temperatures, where the  $\text{MCl}_2$  pressures were very low, only the characteristic indium chloride frequencies were observed. Measurements of the relative Raman intensities have shown that more  $\text{InCl}_3(\text{g})$  monomer was present in the cells containing the complex than in the cells having only indium chloride. The amounts of indium chloride added in both types of cells were calculated to create equal indium chloride pressures. Furthermore, it was found that the amount of  $\text{InCl}_3(\text{g})$  in the cells containing the complex increased with increasing laser power and laser frequency. These observations may imply that the laser beam either increased the spectroscopic temperature in the M-In-Cl cells and shifted the monomer-dimer equilibrium, or resulted to a photodissociation of the  $\text{MInCl}_5$  complex:



Both schemes increase the amounts of  $\text{InCl}_3(\text{g})$  and are similar to the dissociation schemes discussed in the last section of this paper. It appears that the lack of obtaining

spectra from the M-In-Cl complexes ( $M \neq \text{Cu}$ ) is mainly due to their low stability and to complications arising from the presence of strong  $\text{MCl}_2(\text{g})$  and indium chloride bands in the spectra which obscure the vapor complex bands.

#### 4.4 $\text{CuInCl}_5$

Figure 13 shows the Raman spectra obtained from a Cu-In-Cl cell containing no  $\text{CuCl}_2(\text{s})$  excess. The spectra are characterized by bands due to the  $\text{InCl}_3\text{-In}_2\text{Cl}_6$  modes and by two strong bands at  $442$  and  $300\text{ cm}^{-1}$  and their overtones and combinations which are attributed to the vapor complex modes. In table 3, the frequencies of the observed fundamentals are compared to those of  $\text{CuAlCl}_5$ , and an assignment based on a trigonally coordinated copper is given. Thermodynamic considerations [37] have suggested a  $\text{CuInCl}_5$  stoichiometry for the vapor complex, and the data in table 3 can be best interpreted to support a structure similar to that proposed in figure 9. Measurements of spectra obtained from the same cell have shown that the intensities of the copper complex, relative to those of indium chloride, increase with increasing frequency of laser excitation. These changes and the appearance of strong combinations and overtones are characteristics of the resonance Raman nature of the spectra. The other distinct bands seen in the spectra were attributed to the  $\text{In}_2\text{Cl}_6\text{-InCl}_3$  gas fundamentals. It is noteworthy however that the  $\text{InCl}_3(\text{g})$  bands  $\nu_1(\text{InCl}_3) = 350\text{ cm}^{-1}$  and  $\nu_4(\text{InCl}_3) = 95\text{ cm}^{-1}$  are the dominant bands indicating that the monomer is the major component. Spectra of pure indium chloride vapors obtained at similar pressures and temperature show intense  $\text{In}_2\text{Cl}_6(\text{g})$  dimer bands [21].

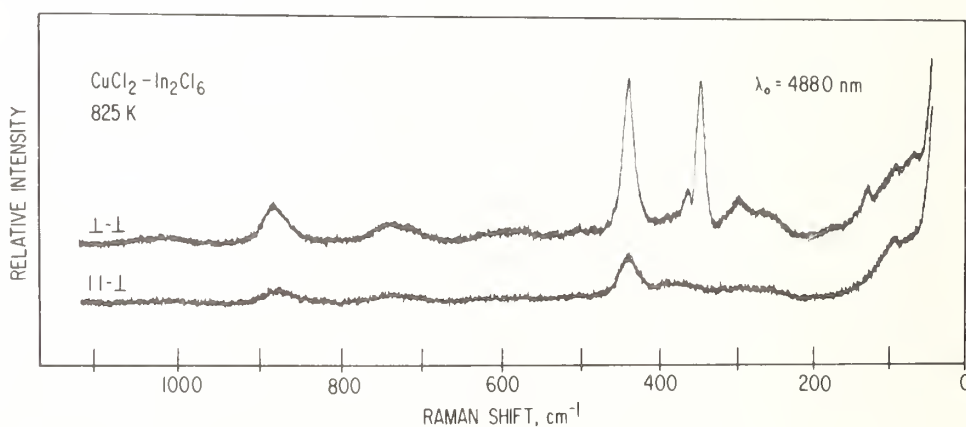


Figure 13. Spectra of Cu-In-Cl vapors. Spectral slit width,  $\sim 7.5\text{ cm}^{-1}$ ; power, 750 mW; polarizations  $\perp$ ,  $\perp$  and  $\parallel$ ,  $\parallel$ ; scan speed, 6  $\text{\AA}/\text{min}$ ; time constant, 1 s.

The temperature dependence of the Cu-In-Cl spectra (no  $\text{CuCl}_2$  excess) is shown in figure 14. The spectra are dominated by the  $\text{InCl}_3(\text{g})$  fundamentals and by the  $\text{CuInCl}_5$  bands. The relative intensities of the  $\nu_1(\text{InCl}_3)$  and  $\nu_{\text{Cu-Cl}_t}(\text{CuInCl}_5)$  change dramatically with increasing temperature and new bands arise at higher temperatures. The changes can be easily recognized by comparison with the  $\text{CuCl}_2(\text{g})$  spectra (fig. 11). It appears that the 970 K

spectrum is mainly a superposition of the  $\text{InCl}_3(\text{g})$  and  $\text{CuCl}_2(\text{g})$  spectra and that the dissociation reaction 12 can account for the large temperature-dependent features observed in figure 14. It must be emphasized, however, that the decomposition may be induced by the laser beam and/or by the increasing furnace temperature.

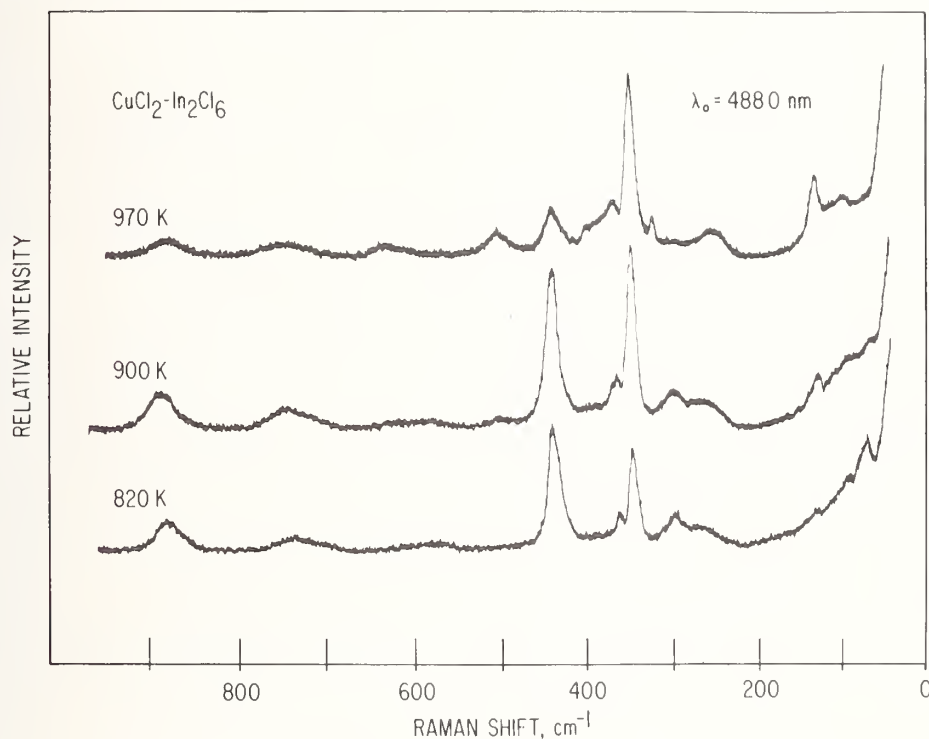
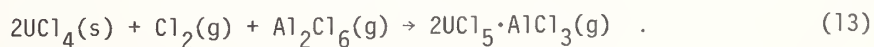


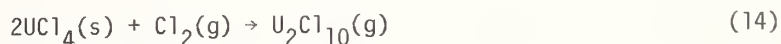
Figure 14. Temperature dependence of the Cu-In-Cl spectra. No  $\text{CuCl}_2(\text{s})$  excess; spectral slit width,  $\sim 7.5 \text{ cm}^{-1}$ ; power, 750 mW; polarization  $\perp, \parallel$ ; scan speed, 6 Å/min; time constants, 0.5 to 1.2 s; \* = fluorescence bands.

##### 5. Uranium(V)-Aluminum Chloride Vapors

Spectrophotometric [38] and mass spectrometric [39] studies have shown that  $\text{UCl}_4$  reacts in the presence of chlorine with aluminum chloride to form a volatile vapor complex:



In the absence of aluminum chloride, the chlorination of  $\text{UCl}_4$  yields a rather volatile  $\text{UCl}_5$  dimer:



whose stability decreases with increasing temperature [38,39]. The present section is concerned with the Raman spectra of vapors formed according to reactions 13 and 14. Raman cells were made using either  $\text{UCl}_4(\text{g})$  and  $\text{Cl}_2(\text{g})$  or  $\text{U}_2\text{Cl}_{10}(\text{s})$ . In early experiments, it was



found that the laser lines from  $\sim 640.0$  to  $457.9$  nm were strongly absorbed by both the  $\text{U}_2\text{Cl}_{10}(\text{g})$  and  $\text{UCl}_5 \cdot \text{AlCl}_3(\text{g})$  vapors, which in this energy region possess strong CT bands [38]. It was also found that the use of high-power laser lines at temperatures above  $\sim 520$  K reversed reactions 13 and 14 yielding solid  $\text{UCl}_4$ , which was deposited on the cell wall and consequently blocked the passage of the beam. It was possible, however, to obtain Raman spectra of both uranium gases from cells having low partial pressures and no solid present.

For investigating  $\text{U}_2\text{Cl}_{10}(\text{g})$ , it was necessary to introduce  $\sim 2$  atm of  $\text{Cl}_2$  into a cell containing small amounts of  $\text{UCl}_4$  or  $\text{U}_2\text{Cl}_{10}$  solids and to use furnace temperatures less than  $500$  K. The cells for the  $\text{UCl}_5 \cdot \text{AlCl}_3$  studies were made from  $\text{U}_2\text{Cl}_{10}$  and  $\text{Al}_2\text{Cl}_6$ , without or with  $\text{Cl}_2$  present; measurements could be made up to  $720$  K. It appeared that the formation of  $\text{UCl}_5 \cdot \text{AlCl}_3$  not only enhanced the  $\text{U}_2\text{Cl}_{10}(\text{s})$  volatility, but also raised the stability of the pentavalent state in the complex relative to that in pure  $\text{U}_2\text{Cl}_{10}(\text{g})$ .

The Raman spectra of the  $\text{U}_2\text{Cl}_{10}\text{-Cl}_2$  vapors are presented in figure 15. Superimposed on the pure rotational and vibrational-rotational contours of  $\text{Cl}_2$  is a strong polarized band at  $354.5\text{ cm}^{-1}$  and its overtone, both of which are attributed to  $\text{U}_2\text{Cl}_{10}(\text{g})$ . No other bands were observed, although recently reported spectra of  $\text{U}_2\text{Cl}_{10}$  in dichloromethane show, apart from an  $A_g$  mode at  $367\text{ cm}^{-1}$ , two other polarized bands at  $324$  and  $130\text{ cm}^{-1}$ . The structure of  $\text{U}_2\text{Cl}_{10}$  (fig. 16) is presumed to be two octahedra sharing an edge. The point group of the molecule is  $D_{2h}$  and six polarized,  $A_g$ , Raman active modes are expected. From the thermodynamics of reaction 14, the partial pressure of  $\text{U}_2\text{Cl}_{10}$  in the Raman cell is estimated to  $\sim 0.001$  atm. This low partial pressure may explain the absence of other (weaker) Raman bands from the spectra and suggests that the intensities of the observed mode and overtone are enhanced by resonance conditions. The  $354.5\text{ cm}^{-1}$  frequency is close to the stretching frequency observed in the solid ( $365\text{ cm}^{-1}$ ) and lies between the  $A_{1g}$  modes of  $\text{UCl}_6$  ( $\sim 370\text{ cm}^{-1}$ ) and  $\text{UCl}_6$  ( $\sim 340\text{ cm}^{-1}$ ). The observed band is thus assigned to the  $\text{U-Cl}_t$  stretching of the  $\text{U}_2\text{Cl}_{10}$  molecule.

The upper part of figure 15 presents the spectra obtained from a  $\text{U(V)-Al-Cl}$  cell in which the partial pressure of the vapor complex was  $\sim 0.003$  atm (at  $500$  K). At temperatures above  $480$  K, no solid phases could be visually detected in the cell. Superimposed on the aluminum chloride bands is one sharp band at  $362\text{ cm}^{-1}$  which is presumably due to  $\text{UCl}_5 \cdot \text{AlCl}_3(\text{g})$ . A weak peak at  $\sim 560\text{ cm}^{-1}$  is due to small amounts of  $\text{Cl}_2$  which probably resulted from partial decomposition of  $\text{U}_2\text{Cl}_{10}$  during the cell preparation.

Repeated measurements of  $\text{UCl}_5 \cdot \text{AlCl}_3$  have established a band frequency of  $362 \pm 1\text{ cm}^{-1}$ , a value that is  $\sim 7\text{ cm}^{-1}$  higher than the  $354.5\text{ cm}^{-1}$  band observed for  $\text{U}_2\text{Cl}_{10}(\text{g})$ . Adapting the molecular structure shown in figure 16, the new band is assigned to the  $\text{U-Cl}_t$  stretching frequency. The  $7\text{ cm}^{-1}$  difference between the  $\text{UCl}_5 \cdot \text{AlCl}_3$  and  $\text{U}_2\text{Cl}_{10}$  bands is probably due to the higher polarizing power of the aluminum as counter cation in the complex, relative to that of uranium as counter cation in the dimer. There are 24 vibrational modes for the

$\text{UCl}_5 \cdot \text{AlCl}_3$  molecule and their distribution for a  $C_{2v}$  point symmetry is

$$\Gamma = 9A_1 + 3A_2 + 6B_1 + 6B_2$$

All modes are Raman active but, as in the case of  $\text{U}_2\text{Cl}_{10}(\text{g})$ , only one strong resonance Raman band is observed in the spectrum.

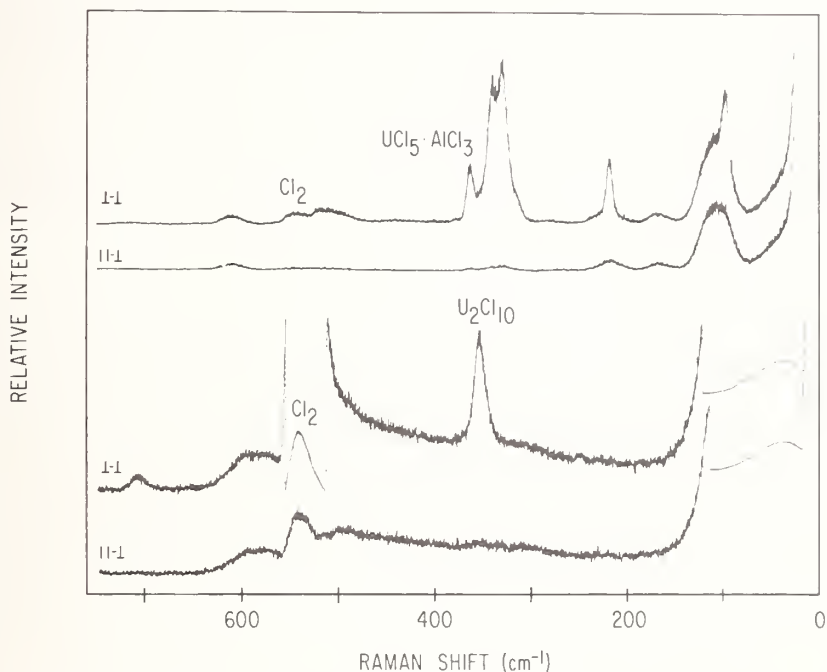


Figure 15. Raman spectra of  $\text{U}_2\text{Cl}_{10}(\text{g})$  and  $\text{UCl}_5 \cdot \text{AlCl}_3(\text{g})$  in the presence of  $\text{Cl}_2(\text{g})$  at 500 K excited with the 514.5 nm line.  $\text{U}_2\text{Cl}_{10}(\text{g})$ : spectral slit width, 7.5  $\text{cm}^{-1}$ ; power, 6 W; scan speed, 10  $\text{cm}^{-1}/\text{min}$ ; time constant, 1 s.  $\text{UCl}_5 \cdot \text{AlCl}_3(\text{g})$ : spectral slit width, 6  $\text{cm}^{-1}$ ; power, 2 W; scan speed, 20  $\text{cm}^{-1}/\text{min}$ ; time constant, 0.25 s.

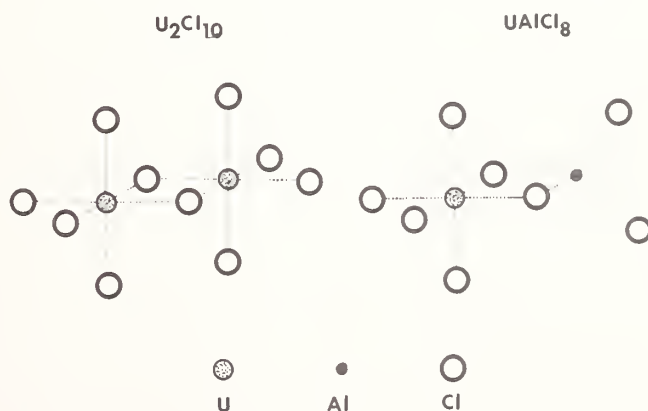


Figure 16. Molecular models for  $\text{U}_2\text{Cl}_{10}$  and  $\text{UCl}_5 \cdot \text{AlCl}_3$  vapors.

Changes in frequency of the excitation line produced changes in intensity of the  $362\text{ cm}^{-1}$  band relative to the aluminum chloride bands. On changing the excitation frequency from 457.9 to 501.7 nm, the  $\text{UCl}_5\cdot\text{AlCl}_3$  intensity increased relative to that of  $\text{Al}_2\text{Cl}_6$  (see fig. 17). However, further changes toward the blue lines resulted in decreasing intensities. This behavior suggests an excitation profile for the  $362\text{ cm}^{-1}$  band with a maximum near 500 nm. The absorption spectra of the complex [38] show that a strong CT band starts at  $\sim 700\text{ nm}$  but, due to the high molar absorptivity, the maximum of the band(s) has not been seen. Without taking into account any resonance Raman interference phenomena [28], the maximum of an electronically allowed transition is expected to coincide approximately with that of the excitation profile. Thus, it is possible that the maximum of the vapor complex CT band is also near 500 nm. However, interference between two or more electronic states and/or increasing decomposition of the complex with increasing laser frequency (see section below) may also cause the trend illustrated in figure 17.

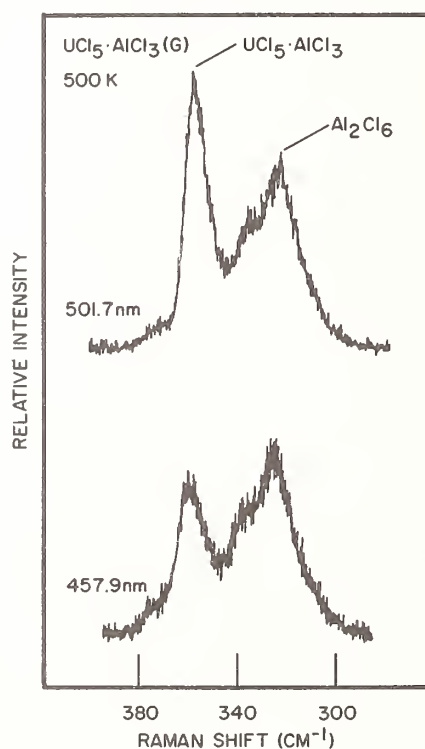


Figure 17. Dependence of the U(V)-Al-Cl spectra on excitation line. Intensity, 1 watt; spectra slit width,  $6\text{ cm}^{-1}$ ; temperature, 500 K. The 5017 Å scan was at  $10\text{ cm}^{-1}/\text{min}$ ; time constant of 1 s. The 4579 Å scan was at  $2\text{ cm}^{-1}/\text{min}$ ; time constant of 3 s.

## 6. Laser-Induced Dissociation of Vapors

It is apparent from the above sections that the feasibility of obtaining spectra from vapors possessing absorption bands in the laser line region, depends on the stability of the molecule at the furnace temperature and on the power and frequency of the excitation line.

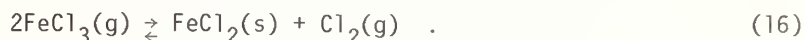
Following is a more detailed examination of the laser line effect on "colored" vapors at elevated temperature. Data on both the dimer-monomer iron(III) chloride and on vapor complexes are presented and discussed.

### 6.1 Iron(III) chloride

Vapor pressure studies [40] have shown that the vaporization of iron(III) chloride yields the monomer-dimer equilibrium:



Increasing the temperature results in partial decomposition and the formation of Fe(II):



The vapors formed according to eq. (15) are brown-yellow and the tail of their CT bands extends and covers the laser frequencies.

For obtaining Raman spectra from these vapors, iron trichloride cells with and without excess  $\text{Cl}_2$  were used. At temperatures below 620 K, the laser beam was quickly blocked by the formation of  $\text{FeCl}_2(\text{s})$  at the focusing point of entrance into the cell. Rotation of the cell temporarily solved the problem, but after 5-10 min, a "line" of solid  $\text{FeCl}_2$  was formed along the periphery of the cell where the beam was focused. With excess  $\text{Cl}_2(\text{g})$  ( $\sim 1$  atm) present in the cell and at temperatures near or above 650 K, it was possible to reverse reaction (16), evaporate the  $\text{FeCl}_2(\text{s})$ , unblock the beam, and obtain spectra from the iron(III) chlorides at pressures  $\sim 0.02$  atm. Figure 18 shows representative spectra of the  $\text{FeCl}_3$ - $\text{Fe}_2\text{Cl}_6$  vapor system measured with different excitation lines. Apart from the  $\text{Cl}_2$  rotational and vibrational-rotational band contours, the spectra contain a series of bands whose intensities change with excitation line. The three predominant bands are at 420, 370, and  $305\text{ cm}^{-1}$ . In accordance with the recent matrix isolation IR and Raman studies [41], the 420 and  $305\text{ cm}^{-1}$  bands are assigned to the  $\nu_1$  and  $\nu_2$  modes of  $\text{Fe}_2\text{Cl}_6(\text{g})$ , while the  $370\text{ cm}^{-1}$  bands correspond to the  $\nu_1$  mode of  $\text{FeCl}_3(\text{g})$ . Assignments of the remaining weak bands will be the subject of a future publication [42]. From the point of view of the present work, it is important to note that the dimer-monomer intensity ratio decreases with increasing laser frequency. The 595.0 nm spectrum is dominated by the  $\text{Fe}_2\text{Cl}_6(\text{g})$  modes, while the 457.9 nm spectrum is mainly due to  $\text{FeCl}_3(\text{g})$ . A comparison of the spectra (fig. 18) with spectra of pure  $\text{Cl}_2$  ( $\sim 1$  atm) obtained in separate cells under the same conditions, permitted measurements of the intensities of the  $\nu_1$  modes ( $\text{FeCl}_3$  and  $\text{Fe}_2\text{Cl}_6$ ) relative to each other and to those of  $\text{Cl}_2$  at  $\sim 540\text{ cm}^{-1}$ . It was found that increasing the laser frequency decreases the amount of dimer in favor of the monomer. It must be emphasized that the monomer CT bands lie at higher energies than the dimer CT bands and thus, on going from the red to the blue lines, the (pre) resonance intensities of  $\text{Fe}_2\text{Cl}_6$  bands should increase faster than those of  $\text{FeCl}_3$ . The opposite effect is observed in figure 18.

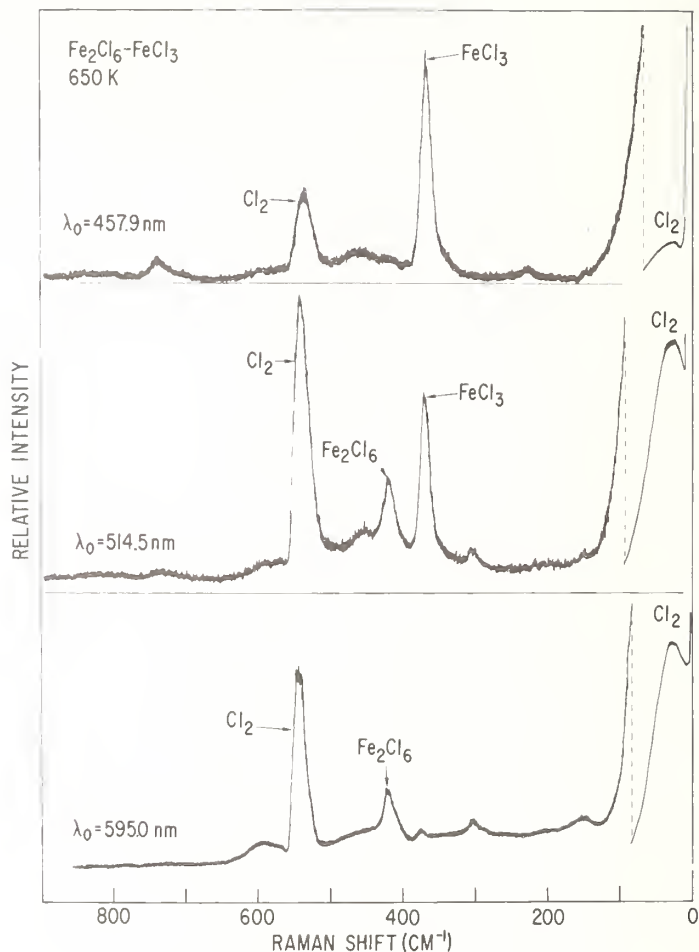


Figure 18. Raman spectra of  $\text{Fe}_2\text{Cl}_6\text{-FeCl}_3\text{-Cl}_2$  vapors. Polarization  $\perp; \perp$ .  
 $\lambda_0 = 595.0$  nm: slit width,  $\sim 7$   $\text{cm}^{-1}$ ; time constant, 1 s; power, 70 nW;  
 scan speed, 20  $\text{cm}^{-1}/\text{min}$ .  $\lambda_0 = 514.5$  nm: slit width, 7.5  $\text{cm}^{-1}$ ; time constant,  
 0.8 s; power, 1 W; scan speed, 20  $\text{cm}^{-1}/\text{min}$ .  $\lambda_0 = 457.9$  nm: slit width,  
 7.5  $\text{cm}^{-1}$ ; time constant, 0.5 s; power, 1 W; scan speed, 20  $\text{cm}^{-1}/\text{min}$ .

The effect of laser power on the spectra also leads to increasing  $\text{FeCl}_3$  intensities. This is depicted in figure 19 for the 514.5 nm line at powers of 1 and 5 W. Thus, it appears that both the laser power and frequency effects lead to higher spectroscopic temperature, thereby shifting reaction (15) to the right. Since the furnace temperature remains constant during the measurements, the spectra obtained represent a nonequilibrium situation along the passing laser beam.



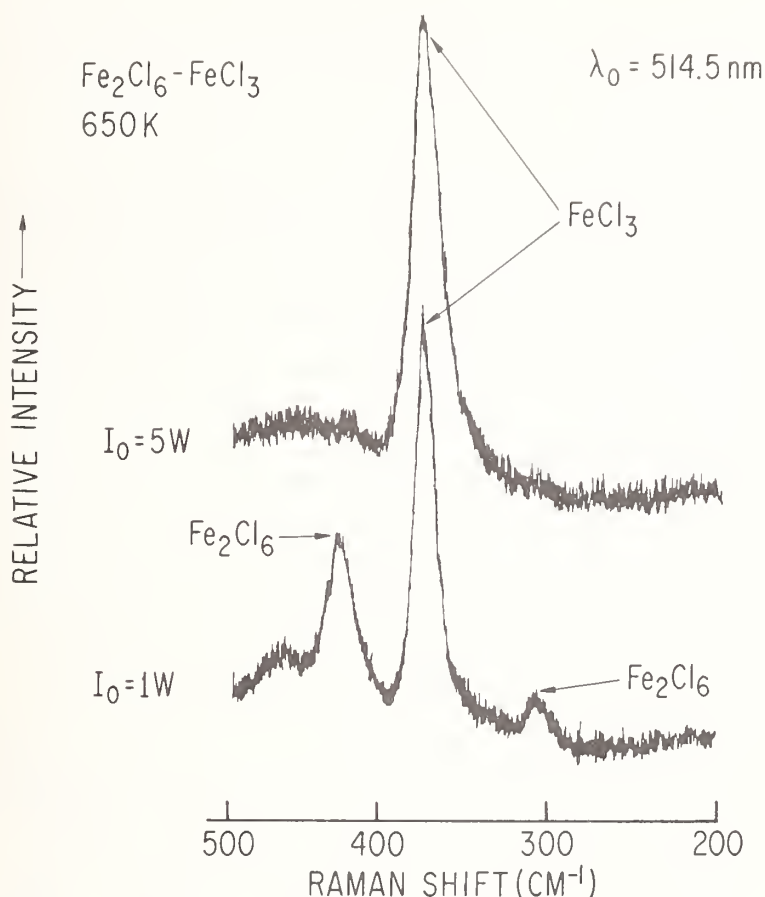
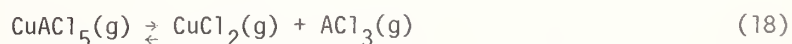
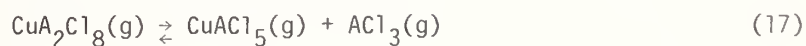


Figure 19. Effect of the intensity of excitation line on the Raman spectra of the  $\text{Fe}_2\text{Cl}_6\text{-FeCl}_3$  vapors. Polarization  $\parallel, \perp$ ; slit width,  $\sim 7.5 \text{ cm}^{-1}$ ; time constant, 0.25 s; scan speed,  $20 \text{ cm}^{-1}/\text{min}$ .

## 6.2 Copper(II) chloride complexes

The studies of the Cu-Al-Cl and Cu-In-Cl vapors (Sections 3 and 4) indicate that an increase in temperature dissociates the complexes according to the schemes:



where A = Al or In. Reaction 17 characterizes the aluminum complex while reaction 18 occurs for the indium complexes. Figures 20 and 21 illustrate the laser power dependence of the Cu-Al-Cl and Cu-In-Cl systems, respectively, at constant furnace temperature. The intensities of  $\text{CuAl}_2\text{Cl}_8$  and  $\text{Al}_2\text{Cl}_6$  bands diminish at higher laser power (fig. 20), while the

$\text{CuAlCl}_5$  and  $\text{AlCl}_3$  intensities increase. This behavior supports dissociation scheme 17. For the Cu-In-Cl vapors (fig. 21), the relative intensities of  $\text{InCl}_3(\nu_1)$  to  $\text{Cu-In-Cl}_5(\nu_{\text{Cu-Cl}})$  show that at higher laser power the  $\text{CuInCl}_5$  decreases in favor of  $\text{InCl}_3$  and thus supports scheme 18. In separate experiments, it was found that the monomer-dimer relative intensities of the colorless aluminum and indium chlorides were independent of the laser power and frequency.

These effects observed show that, at constant furnace temperature, the Raman intensities of the carrier gas cannot be used as internal standard of the cell for calculating the (pre) resonance excitation profiles of the complex bands. Furthermore, since the overlap of laser line and absorption band changes with temperature (e.g., broadening of absorption band), then studies of the relative Raman intensities at different temperatures cannot be used for estimating the thermodynamics of vapor reactions (e.g., reactions 17 and 18).

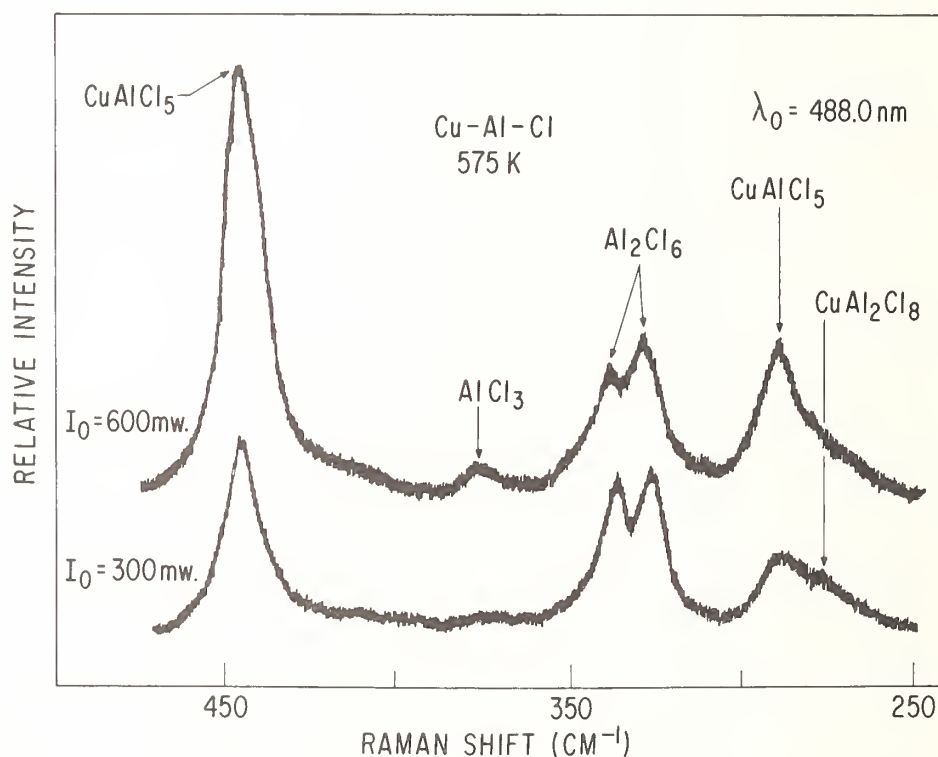


Figure 20. Effect of the intensity of excitation line on the Raman spectra of the Cu-Al-Cl gaseous complexes.  $P_{\text{Al}_2\text{Cl}_6}$ ,  $\sim 0.3$  atm; spectral slit width,  $\sim 8$   $\text{cm}^{-1}$ ; polarization  $\perp, \perp$ .

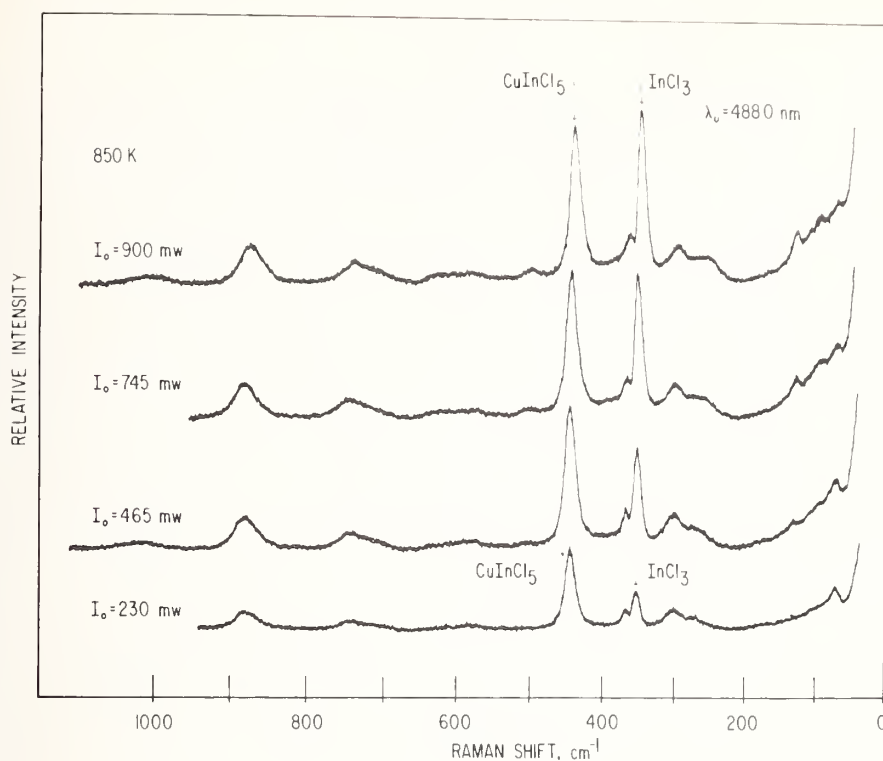


Figure 21. Dependence of the Cu-In-Cl spectra on laser line intensity. Polarization  $\perp, \parallel$ ; slit width,  $7.5 \text{ cm}^{-1}$ ; time constants, 1 to 1.25 s; scan speed,  $6 \text{ \AA/min}$ .

### 6.3 Uranium(V) chloride complex

The effect of the laser power of the  $\text{UCl}_5 \cdot \text{AlCl}_3$  spectra has been examined and typical results are presented in figure 22. Increasing laser power enhances the  $\nu_1(\text{AlCl}_3)$  band intensity and gives rise to a shoulder band at the lower frequency region of the  $362 \text{ cm}^{-1}$  band. This indicates a decomposition of the complex according to the scheme:



The rising shoulder band is attributed to the  $354 \text{ cm}^{-1}$  band of  $\text{U}_2\text{Cl}_{10}(\text{g})$ .

It has been suggested [43] that the vapor complexes of the actinides and lanthanides may have potential uses for laser isotope separations and/or construction of high power vapor lasers. The data presented here show that decomposition schemes similar to reactions 17, 18, and 19 play an important role (probably negative) for developing these applications.

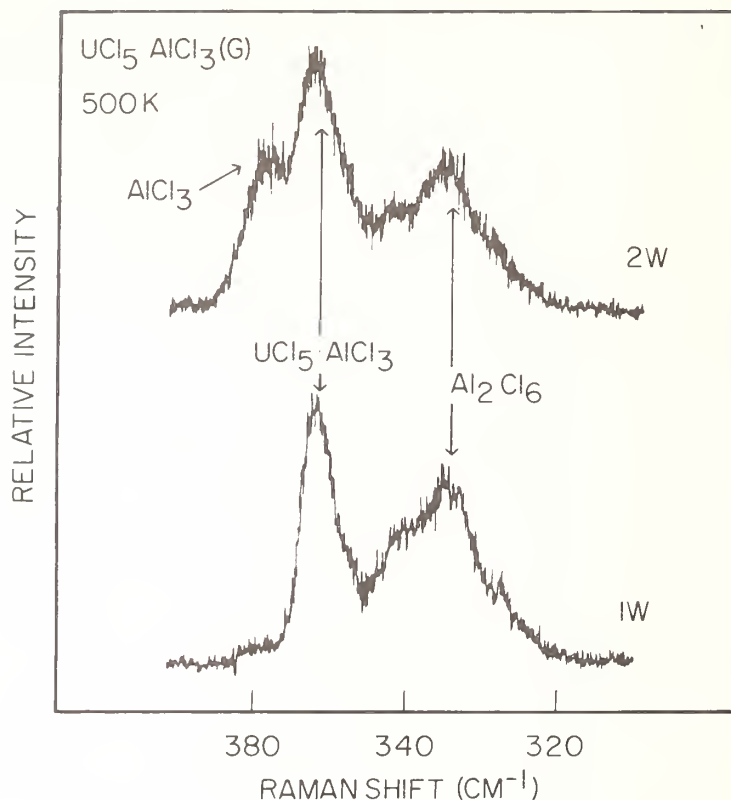


Figure 22. Dependence of the U(V)-Al-Cl spectra on laser line intensity. Excitation line 4880 nm; scan speed,  $10 \text{ cm}^{-1}/\text{min}$ ; time constant, 1 s; slit width,  $6 \text{ cm}^{-1}$ .

## 7. Conclusions

From the data and discussions presented above, the following conclusive remarks can be made.

- Resonance Raman spectroscopy can be used to study vibrational frequencies of some "colored" vapor complexes which exist as a minor component in an equilibrium vapor mixture. On the basis of the measured frequencies and Raman selection rules, the structure of the vapor can be characterized.
- The appearance of a resonance Raman signal depends on both the position of the charge transfer band and the thermodynamic stability of the complex. It also depends on the relative concentrations of the vapors present and on the laser power and frequency used.
- Increasing the frequency of the excitation line results in a variation in the resonance Raman intensities and a partial dissociation of the complex. Dissociation also occurs with increasing laser power.
- As a consequence of the laser-induced dissociation, the relative Raman intensities (i.e., complex vs. carrier-gas intensities) depend on the frequency and laser power and represent nonequilibrium situation. Hence, estimations of excitation profiles and calculations of gas phase thermodynamic quantities based on the assumption of equilibrium conditions will be grossly in error.

## References

- [1] Schäfer, H., *Angew. Chem. Int. Ed.* **15**, 713 (1976). A review article.
- [2] Anundskås, A. and Øye, H. A., *Acta Chem. Scand. Ser A*, **30**, 193 (1976).
- [3] Emmenegger, F. P., *Inorg. Chem.* **16**, 343 (1977).
- [4] Gregory, N. W., *J. Phys. Chem.* **81**, 1857 (1977).
- [5] Papatheodorou, G. N. and Kucera, G. H., *Inorg. Chem.* **16**, 1006 (1977).
- [6] Dewing, E. W., *Metall. Trans.* **1**, 2169 (1970).
- [7] Papatheodorou, G. N., *J. Phys. Chem.* **77**, 472 (1973).
- [8] Papatheodorou, G. N., *Inorg. Chem.* **12**, 1899 (1973).
- [9] Papatheodorou, G. N., *Allgem. Chem.* **411**, 153 (1975).
- [10] Anna, A. Dell and Emmenegger, T. P., *Helv. Chim. Acta*, **48**, 1145 (1975).
- [11] Von, Meinhart and Schaefer, H., *Z. Anorg. Allgen. Chem.* **408**, 37 (1974).
- [12] Anundskås, A., Mahyoub, A. E., and Øye, H. A., *Acta Chem. Scand.* **A30**, 193 (1976).
- [13] Dienstbach, F. and Emmenegger, F. P., *Helv. Chim. Acta*, **58**, 1145 (1976).
- [14] Kucera, G. H. and Papatheodorou, G. N., to be published (see Abstracts of Papers. American Chemical Society, 174th Meeting; August 28-September 2, 1977).
- [15] Capote, M. A., Kucera, G. H., and Papatheodorou, G. N., in *High Temperature Metal Halide Chemistry*, D. Cubicciotti and D. D. Hildenbrand, eds., **78-1** (1978), p. 367.
- [16] Beattie, I. R. and Horder, J., *J. Chem. Soc. (A)* 2655, (1969).
- [17] Johnson, B. B. and Peticolas, W. L., *Ann. Rev. Phys. Chem.* **27**, 465 (1976).
- [18] Papatheodorou, G. N. and Kucera, G. H., *Inorg. Chem.* (submitted).
- [19] Papatheodorou, G. N., *J. Chem. Phys.* **66**, 2893 (1977).
- [20] Sorlie, M. and Øye, H. A., *Inorg. Chem.* (in press).
- [21] Papatheodorou, G. N., unpublished results.
- [22] Sutakshuto, S., Copper(II) chloride gas complexation with acid halides, Thesis No. 31, Institute of Inorganic Chemistry, University of Trondheim (1976).
- [23] Papatheodorou, G. N. and Capote, M. A., *J. Chem. Phys.* **69**, xxx (1978), in press.
- [24] Capote, M. A. and Papatheodorou, G. N., *Inorg. Chem.* **17** xxx (1978), in press.
- [25] Bosworth, Y. M. and Clark, R. J. H., *Inorg. Chem.* **14**, 170 (1975).
- [26] Stein, P., Miskowski, V., Woodruff, W. H., Griffen, J. P., Werner, K. G., Gaber, B. P., and Spiro, T. G., *J. Chem. Phys.* **64**, 2159 (1976).
- [27] Clark, R. J. H. and Truble, W. R., *Inorg. Chem.* **15**, 1030 (1976).
- [28] Zgierski, M. Z., *J. Raman Spectrosc.* **6**, 53 (1977).
- [29] The effect of nearest-neighbor cations ( $\text{Li}^+$ ,  $\text{K}^+$ ,  $\text{Cs}^+$ ,  $\text{Al}^{+3}$ ) on the electronic states of  $\text{PtCl}_4^{-2}$  has been investigated and showed that energy shifts of  $\sim 2$  to  $3$  kK occur in the excited states  $^1\text{A}_{2g}$  and  $^1\text{E}_g$  of Pt(II) by substituting low field ions (i.e.,  $\text{Cs}^+$ ) with high field ions (i.e.,  $\text{Li}^+$ ). See, e.g., Papatheodorou, G. N. and Smith, G. P., *J. Inorg. Nucl. Chem.* **35**, 799 (1973), and reference [8].
- [30] Chottard, G. and Bolard, J., *Chem. Phys. Let.* **33**, 309 (1975).
- [31] Rush, R. M., Martin, D. S., and LeGrand, R. G., *Inorg. Chem.* **14**, 2543 (1975).
- [32] Avery, J. J., Burbridge, C. D., and Goodgame, D. L., *Spectrochim. Acta*, **24A**, 1721 (1968).



- [33] Schläpfer, C. W. and Rohrbasser, C., *Inorg. Chem.* 17, 1623 (1978).
- [34] Leroi, G. E., Jones, T. C., Hougen, J. T., and Klemperer, W., *J. Chem. Phys.* 36, 2879 (1962).
- [35] Gruen, D. M., Clifton, J. R., and DeKock, C. W., *J. Chem. Phys.* 48, 1394 (1968).
- [36] Ferraro, J. R., Low Frequency Vibrations of Inorganic and Coordination Compounds (Plenum Press, New York, 1971), p. 140.
- [37] Dienstbach, F. and Emmenegger, F. P., *Z. Anorg. Allg. Chem.* 436, 127 (1977).
- [38] Gruen, D. M. and McBeth, R. L., *Inorg. Chem.* 8, 2625 (1969).
- [39] Hildenbrand, D. L. and Cubicciotti, D. D., Stanford Research Institute Report, UCRL-13657 (1975).
- [40] Shieh, C. F. and Gregory, N. W., *J. Phys. Chem.* 79, 828 (1975), and references therein.
- [41] Loewenschuss, A. and Givan, A., *Ber. Bunsenges. Phys. Chem.* 82, 74 (1978).
- [42] Papatheodorou, G. N., to be submitted for publication.
- [43] Jacobs, R. R. and Krupke, W. F., in Lawrence Livermore Laboratory report, UCRL-50021-75 (1976), p. 529.

## INFRARED SPECTRAL MEASUREMENTS OF SPECIES IN A HIGH TEMPERATURE FLOW TUBE

Michael E. Gersh and Charles E. Kolb  
Center for Chemical and Environmental Physics  
Aerodyne Research, Inc.  
Bedford, MA 01730

A new type of apparatus has been constructed in which quantitative measurements of the infrared spectral characteristics of gas phase species at elevated temperatures can be performed. In the past, such measurements have been performed using either burners, shock tubes or heated cells to produce and/or maintain the species at high temperatures. For high temperature species, these approaches have an inherent uncertainty due to the fact that the number density of the absorbing species may not be measured concurrently with the spectroscopic measurements. In order to circumvent this problem, the present experimental program employs a different approach. The species of interest are introduced into, or are created by reaction in, a high temperature flow tube. Downstream of the reaction region the flow passes through a spectroscopic analysis region which consists of a multi-pass White cell mounted perpendicular to the flow direction. This cell is used to measure the absorption of infrared radiation by the species in the flow tube. The key feature of the analysis region is that the flow tube gas is aerodynamically confined in order to eliminate recirculation of the gases in the White cell, without having to resort to high temperature windows and their attendant problems. Finally, the gas in the flow reactor is sampled by a molecular beam mass spectrometer in order to determine the number density of absorber species present in the spectroscopic analysis region.

The design features of the apparatus will be discussed. In addition, the results of measurements of the absorption coefficients of the  $\text{BF}_3 \nu_3$  fundamental band at 1454 wavenumbers over the temperature range of 300 - 1500 K will be described and compared with existing room temperature measurements.

## 1. Introduction

The radiative properties of gaseous metal oxides and metal halides can play an important role in characterizing the performance of such high temperature devices as rocket engines, chemical lasers, planetary reentry vehicles and advanced coal combustors. Knowledge of these properties is also necessary for the study of laser blowoff from metal or ceramic surfaces and possibly for the understanding of corrosion in high temperature devices such as gas turbines, gun barrels and arc sources.

A great deal of qualitative spectral information about molecular metal halide and metal oxide species has been obtained from studies involving high temperature flames, arcs or shock tubes. However, such devices are often difficult to adapt to quantitative studies of transition f-numbers or integrated band intensities. This is particularly true for infrared vibrational/rotational bands where small transition probabilities and high levels of background radiation often combine to make quantitative studies difficult. In addition, most quantitative spectral studies performed in flame, arc or shock tube systems are inherently dynamic, and it is difficult to guarantee that the assumed equilibrium distributions are not kinetically inhibited. This problem is present even when, as is seldom the case, sufficiently accurate and detailed thermochemical data is available to correctly calculate the equilibrium state of the experimental system.

Qualitative spectral data for high temperature species may also be obtained by matrix isolation techniques, but here again the limitations of specifying the densities of radiatively active species usually precludes infrared band strength determinations while the matrix environment will not allow determination of high temperature band shapes.

High temperature fast flow systems, particularly when coupled with diagnostic devices such as a molecular beam sampled mass spectrometer, offer the possibility of introducing or producing known densities of infrared active species at predetermined and uniform temperatures. Such devices have been exploited to study the chemical kinetics of metal oxide and metal halide systems for a number of years [1-3]<sup>1</sup>. The purpose of this paper is to present a high temperature flow apparatus designed for detailed quantitative studies of the infrared bands of gaseous metal oxides and metal halides.

A detailed discussion of the apparatus, including a detailed flow simulation analysis of the optical measurement region, is presented in the following section. Section 3 contains a comparison of the room temperature and high temperature spectra of the 1454 wavenumber  $\nu_3$  band of  $\text{BF}_3$ , and Section 4 briefly discusses sources for transient high temperature metal oxide and metal halide species to be used in future experiments.

## 2. Apparatus Design

A conceptual diagram of the experimental apparatus is shown in figure 1. The species of interest are produced by reaction in, or introduced into, a variable temperature flow

---

<sup>1</sup>Figures in brackets indicate the literature references at the end of this paper.

reactor. Then, the flow is passed through an analysis region in which a multi-pass absorption cell (White cell) [4] is mounted perpendicular to the flow direction. Finally, a portion of the flow is sampled by a molecular beam mass spectrometer before being exhausted to a large mechanical vacuum pump. Since the number density of the absorbing species is measured in situ by the mass spectrometer, one can obtain absolute values for the absorption coefficients without assuming that the reactive species in the flow tube have achieved local thermodynamic equilibrium.

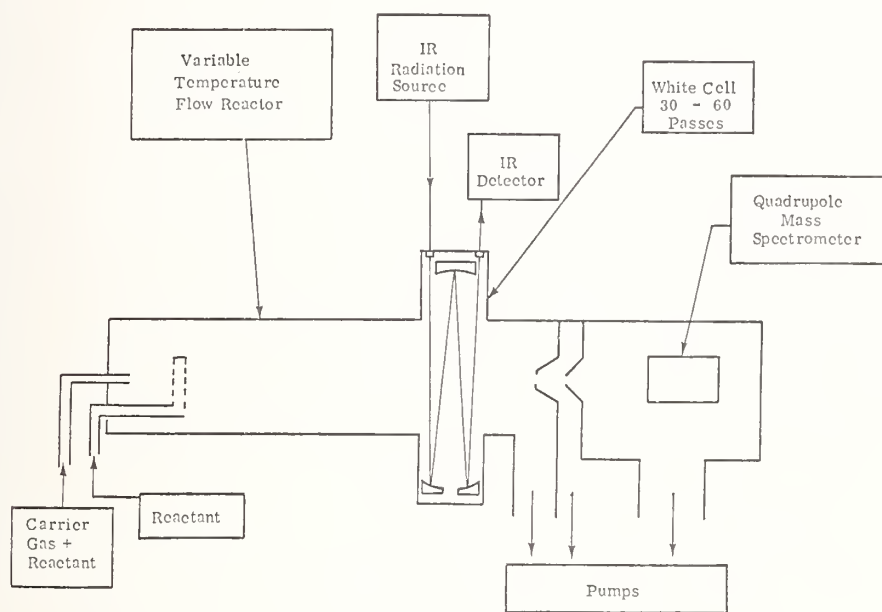


Figure 1. Conceptual diagram of flow reactor/infrared spectrometer.

## 2.1 Flow reactor design

The detailed design of the variable temperature flow reactor is shown in figure 2. The outer vacuum jacket is constructed of steel and is water-cooled, as are the aluminum end plate assemblies. The water cooling protects temperature-sensitive components and ensures stability of the White cell dimensions. The "rear" end plate holds the alumina flow tube, as well as power, gas, and thermocouple feedthroughs. The "front" flange is designed for mounting to the quadrupole mass spectrometer or to a blank flange for tests and for experiments for which mass spectrometer sampling is not required. In the analysis region, eight four-inch flanges are placed around the circumference of the vacuum jacket. Four of these ports are connected by alumina tubes to the main flow tube and provide for optical analysis of the hot flowing gas. This optical analysis can consist of absorption or emission measurements using the White cell or fluorescence measurements using two ports at right angles to each other. One of the remaining four ports is presently connected to

a Kinney Vacuum KMBD 1602 mechanical vacuum pump with an effective pumping speed of approximately 1000 cfm. The other three ports are presently unused.

The main elements of the thermal design include the heating elements and the surrounding layer of refractory insulation. The refractory insulation is composed of a self-supporting "spool" of rigid alumina fiber insulation (Zircar Products, Inc.), upon which is wound several layers of Zircar alumina fiber blanket insulation, followed by additional layers of Carborundum Company alumina-silica blanket insulation. The insulation assembly has an inside diameter of 6 inches (15 cm) and is designed to withstand continuous operating temperatures in excess of 1800 K. The commercially-available Kanthal A-1 heating elements that are currently being used have a design temperature rating of 1500 K and a power capability of over 6 kW (Thermcraft, Inc. type RH). The heaters are supplied with power by Love Controls Corporation solid-state temperature controllers and power supply units. The fully assembled flow reactor achieves a temperature of 1500 K with a power consumption of less than 3 kW. Thus, the thermal design of the flow reactor is adequate for the performance of experiments at 1500 K. Finally, it should be noted that the flow reactor could be operated at a temperature of 1800 K if one replaced the Kanthal heating elements with platinum-rhodium heater wire wound around the central alumina flow tube. This would also require a small change in the power supply circuit.

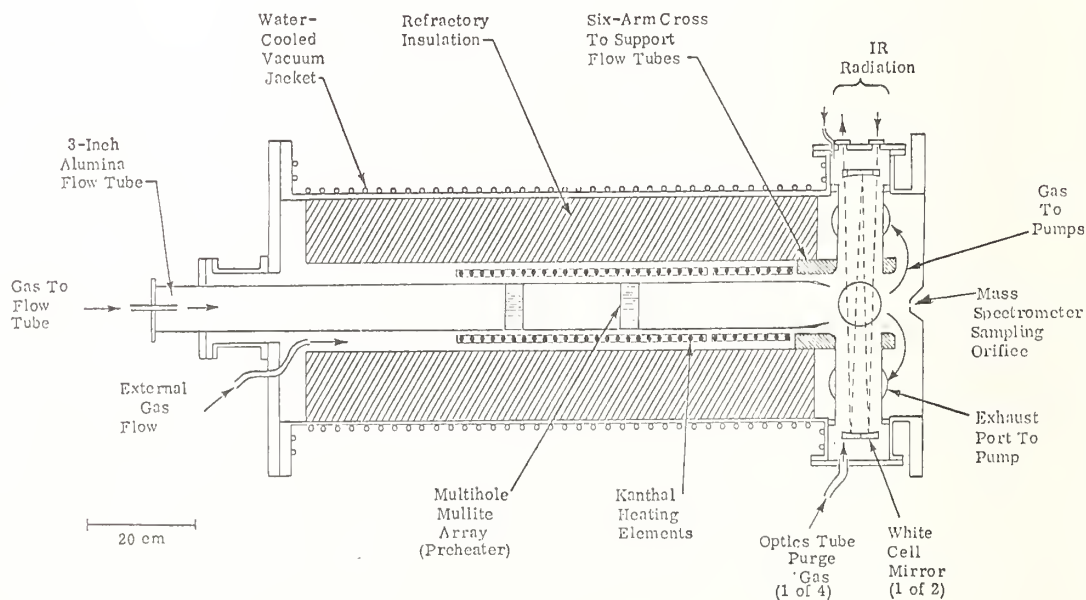


Figure 2. Cross-sectional view of heated flow reactor.



The design of the gas flow system within the variable temperature flow reactor is fairly complicated due to the constraints imposed by the necessity of making infrared absorption measurements in the analysis region. Figure 2 shows the configuration used in measurements on  $\text{BF}_3$ . The main flow inside the 2-7/8 inch (7.3 cm) inside diameter 99.8 percent alumina flow tube (McDanel Refractory Porcelain Company) contains argon carrier gas and  $\text{BF}_3$ . This gas is heated as it passes through two preheaters which are 1 inch (2.5 cm) thick mullite "honeycomb" hole arrays having 1/16 inch (1.6 mm) round holes and a 67 percent frontal open area (General Refractories Company). The heated gas then passes through an isothermal region of the flow tube and a subsonic nozzle before entering the spectroscopic analysis region. A second, external flow of Ar passes around the outside of the main, core flow. In addition, small flows of Ar are added to each of the four optics tubes as a purge gas in order to keep the optics clean. The six flows of gas meet in the center of the analysis region in a section of the flow system that is made from Cotronics Corporation 960 machinable alumina ceramic. This six-arm cross piece supports the main flow tube and the four optics tubes. However, its main purpose is to provide an environment in which the flow from the main tube will be well-behaved as it traverses the White cell, impinges on the mass spectrometer sampling orifice, and is exhausted by the mechanical pump. Thus, the design of this element of the flow system is particularly important to the success of the experimental program, and a separate experimental study, described below, was undertaken in order to ensure that the proposed design would adequately control the gas flow in the analysis region.

## 2.2 Flow simulation study

A crucial element of the apparatus design is the configuration of the flow system in the spectroscopic analysis region of the variable temperature flow tube. In order for one to be able to perform quantitative absorption (or emission) measurements on the flow tube gases, three criteria must be satisfied: (1) the geometry of the absorbing gas flow must be well defined in the region where it traverses the White cell; (2) the flow in this region must be stable; and (3) the temperature of the absorbing gas flow must be well defined (and, preferably, the gas should be isothermal). To satisfy these criteria, the absorbing flow should ideally be confined in a cylindrical geometry and be located in a stable position, without any recirculation of absorbing gas into the optics tubes (i.e., the flow should behave as if it were confined by a cylindrical tube). For an ambient temperature flow tube with single-pass optics, one could simply place optical windows on the flow tube; however, the present experiment requires high absorbing gas temperatures and a multi-pass absorption cell (for additional sensitivity). This necessitates the use of a wall-less confinement of the absorbing gases as they pass through the analysis region. This can only be accomplished by fluid mechanical confinement of the absorbing gas flow.

The analysis region design shown in figure 3 was considered to be most promising. Here, the main, absorbing gas flow and the outer, co-axial "shield" gas flow are both

passed through subsonic nozzles, after which they join and pass through the analysis region. The area ratio of the main flow nozzle to the shield flow nozzle is 2:1, and the corresponding flow rates are also designed to be in a 2:1 ratio so that the velocities of the two flows will be the same when they meet downstream of the nozzles. In addition, it was estimated that the flow of purge gas into the optics tubes should equal approximately 10 percent of the main flow and should be evenly divided between the four optics tubes.

This flow geometry is considerably more complicated than that used previously for flow reactors [1,5], and the design criteria for the confinement of the absorbing gas flow are quite strict. Thus, it was concluded that this crucial element of the flow system design should be tested in a flow simulation experiment before the fabrication of the six-arm cross out of machinable alumina ceramic. This would obviate the need for a major system redesign if the initial design proved to be inadequate and would establish the approximate range of operating flow conditions over which the flow confinement of the absorbing gas would be effective.

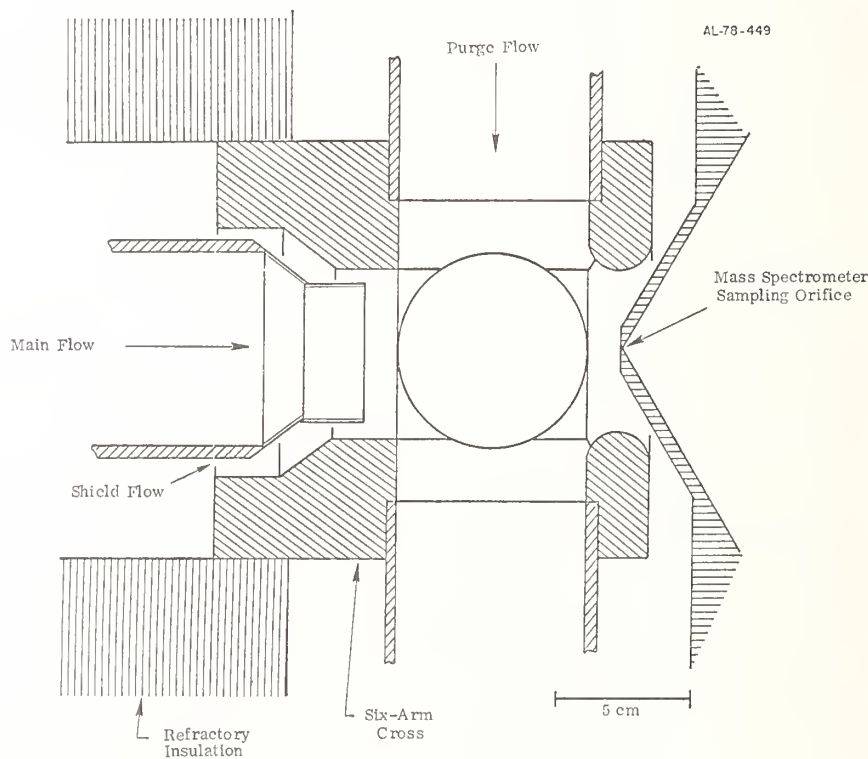


Figure 3. Cross-sectional view of analysis region.

The flow simulation experiment was set up in the following manner: a half scale model of the flow system was fabricated out of plastic (polymethyl methacrylate) with flowmeters monitoring the main flow, the shield flow, and the four purge flows. The gas flow was

simulated by using a water flow with the same Reynolds number, which is a standard technique in fluid mechanics and is valid for subsonic, incompressible flows [6]. The flow pattern is determined by injection of Fluorescein dye into any one of the water flows with observation of the bright fluorescence induced by illumination with a halogen lamp.

The required water flow velocity (and, therefore, flow rate) is obtained from the flow velocity of Ar that is to be simulated by equating the Reynolds numbers of the flows:

$$Re = n u d / w = n' u' d' / w' \quad . \quad (1)$$

where  $n$  is the density,  $u$  is the flow velocity,  $d$  is the tube diameter,  $w$  is the viscosity, and the prime refers to the conditions for water. Then, we let  $d' = 1/2 d$  and  $n = n(0) P$ , where  $n(0) = 2.35 \times 10^{**(-6)} \text{ g/cm}^{**3}/\text{Torr}$  and  $P$  is the Ar pressure in Torr. Also,  $n' = 1 \text{ g/cm}^{**3}$ ,  $w = 2.2 \times 10^{**(-4)} \text{ poise}$ , and  $w' = 1.0 \times 10^{**(-2)} \text{ poise}$  (at 20 C). This leads to the expression:

$$u' = 2.1 \times 10^{**(-4)} P u \quad . \quad (2)$$

Thus, for a given velocity  $u$  of Ar at 20 C and at a pressure  $P$ , we are able to obtain the water velocity  $u'$  that is required for the simulation. Of course, if one wanted to simulate Ar flows at other temperatures, one would then have to substitute the appropriate values of  $n$  and  $w$ .

When the flow simulation experiments were performed, a number of interesting results were observed. The major result is that with a Reynolds number for the main flow that is greater than approximately 100, and for the flow rate ratios given above (main: shield: purge = 10:5:1), the main flow appears to be stable and cylindrical in form as it passes through the analysis region. (From a practical point of view, it would probably be wise to operate the flow reactor at  $Re$  greater than 200.) Under these stable flow conditions, no recirculation pattern of the main flow water was observed in the "optics tubes." However, when dye was added to the water of the shield flow, a strong recirculation pattern of shield flow water was observed in the optics tubes, and this phenomenon persisted even at the highest main flow Reynolds number (560) used in the experiments. Thus, it may be concluded that a simpler flow configuration without a shield flow would not satisfy the analysis region design criteria since there would be recirculation of absorbing gas in the optics tubes. The present design is successful because only the non-absorbing shield gas recirculates in the optics tubes, while the main flow of the absorbing gas is confined by the shield flow to a cylindrical region in the center of the analysis region. In addition, since the shield gas is at the same temperature as the main flow, the column of absorbing gas should be essentially isothermal.

Finally, it is interesting to examine the practical consequences of the flow limits of the present apparatus. If we assume a minimum Reynolds number of 200 and a carrier gas of room temperature Ar, we obtain the minimum flow velocity  $u$  at a pressure  $P$  from equation (1).

This yields

$$[uP]_{\min} = 2560 \text{ Torr-cm/s} \quad . \quad (3)$$

For example, the minimum room temperature Ar flow velocity at 10 Torr would be approximately 2.6 m/s. Conversely, the maximum flow velocity (within the limits imposed by the pumping system) is determined by the Reynolds number above which the flow becomes turbulent. Since the transition region from laminar to turbulent flow occurs at a Reynolds number of between 2,000 and 10,000 [7], we may choose a value of 2,000 as a safe upper limit. This yields the relation

$$[uP]_{\max} = 25,600 \text{ Torr-cm/s} \quad . \quad (4)$$

Thus, it should be possible to operate the variable temperature flow reactor over its projected operating range of 1 - 760 Torr and 1 - 70 m/s flow velocity (limited by speed of pump). If necessitated by the experiments, these operating ranges could be extended, subject to the constraints of equations (3) and (4).

### 2.3 Optical system design

The design of the present external optical system for the infrared absorption measurements is shown in figure 4. This double beam optical system has been designed for low spectral resolution measurements. The infrared radiation source is a Perkin-Elmer Corporation "Opberman Source" which is used in their current infrared spectrometers. The radiation impinges on a mirror-bladed, 50 percent duty cycle chopping wheel (Valtec Corporation) which alternately allows it to pass into the White cell or reflects it, thereby bypassing the White cell. In figure 4, M2, M3, M4, M7 and M8 are flat mirrors; M1 and M9 are spherical mirrors; and M5 and M6 are off-axis paraboloid mirrors. The beam splitter is made of uncoated zinc selenide, the monochromator is a Spex Minimate, and the detector is a Santa Barbara Research Corporation HgCdTe photoconductive detector, in front of which is placed an order-sorting (long-wavelength pass) filter in order to avoid interference from higher order diffraction in the monochromator. Since the optical system consists of reflective optics (except for the zinc selenide beam splitter), it is achromatic, and it can be aligned with the use of a helium-neon laser.

The only other major subsystem, now being designed, is the interface between the variable temperature flow tube and the molecular beam mass spectrometer. This interface will allow quantitative determinations of species number densities, even when the species are chemically produced within the flow reactor. Examples of chemical sources for "transient" high temperature species are briefly described in Section 4.



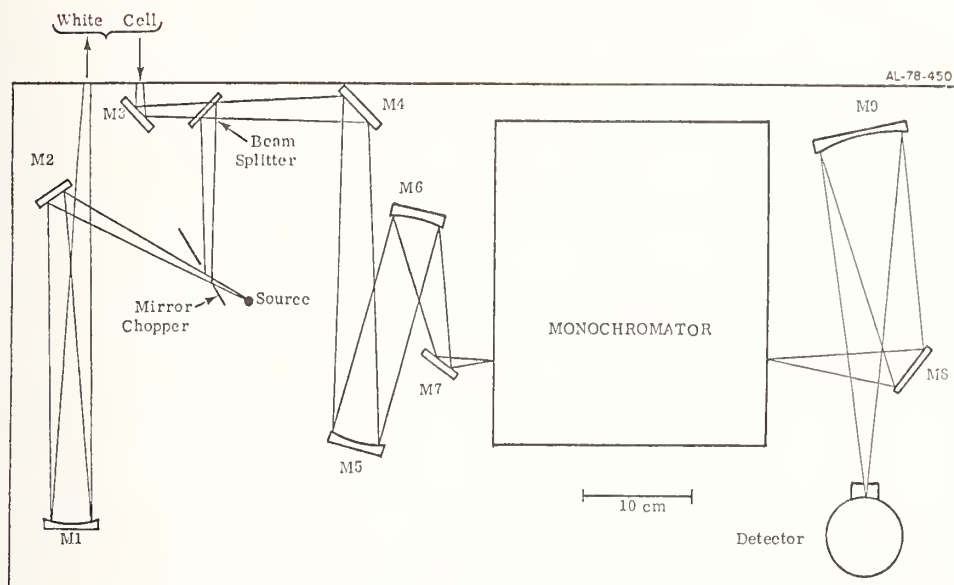


Figure 4. View of external optics.

### 3. $\text{BF}_3$ Absorption Measurements

The preliminary experiments performed with this apparatus were measurements of the spectral absorption coefficients of  $\text{BF}_3$ . These measurements are intended to serve two purposes. They provide the first high temperature measurements of the absorption coefficients of  $\text{BF}_3$ , and they provide the information necessary for the calibration of the apparatus and the assessment of its performance.

Figures 5 through 7 present the preliminary measurements of the spectral absorption coefficients of  $\text{BF}_3$  at 300 K, 1000 K, and 1500 K, respectively. In all of these figures the data are represented by the dots, and the lines drawn through the data points are "eyeball" fits to the data. In general, the scatter of the data points represent the uncertainty in the data. These uncertainties do not represent the ultimate limitations of the apparatus; refinements of the data acquisition and analysis procedures may be expected to reduce this scatter by more than an order of magnitude.

In general, the data are acquired and analyzed in the following manner. At a given wavelength the double beam optical system is used to measure the difference in signal ( $I_0 - I$ ) due to the presence of  $\text{BF}_3$  in the gas flow. Then, the intensity of the single beam passing through the gas flow  $I_0$  is measured in the absence of  $\text{BF}_3$ . The ratio of these measurements is related to the spectral absorption coefficient  $k$  by equation (5).



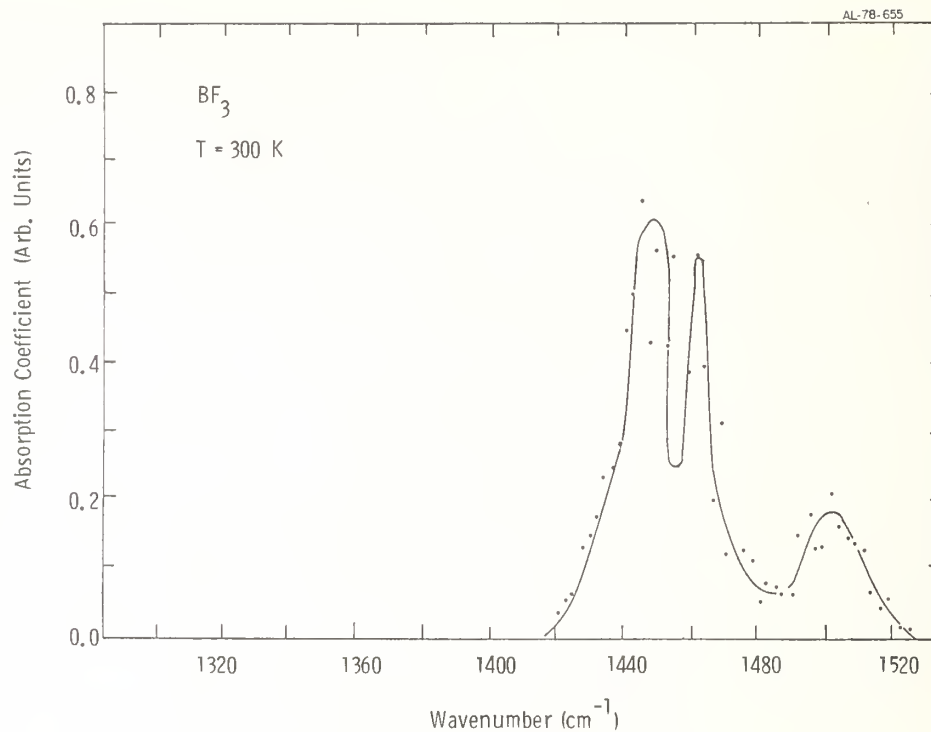


Figure 5.  $\text{BF}_3$  spectral absorption coefficients at 300 K.

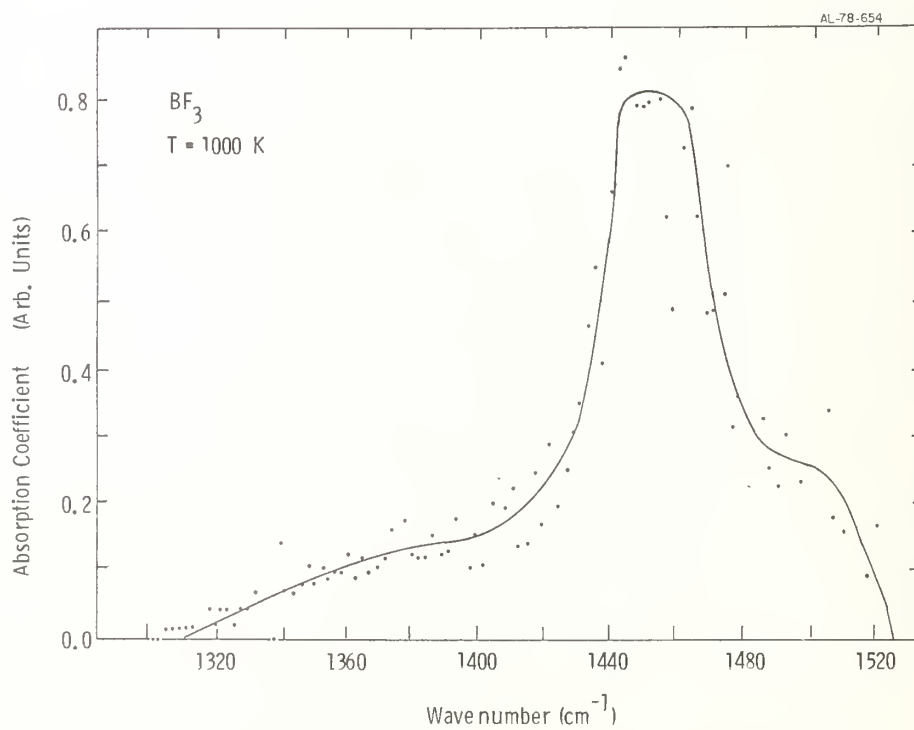


Figure 6.  $\text{BF}_3$  spectral absorption coefficients at 1000 K.

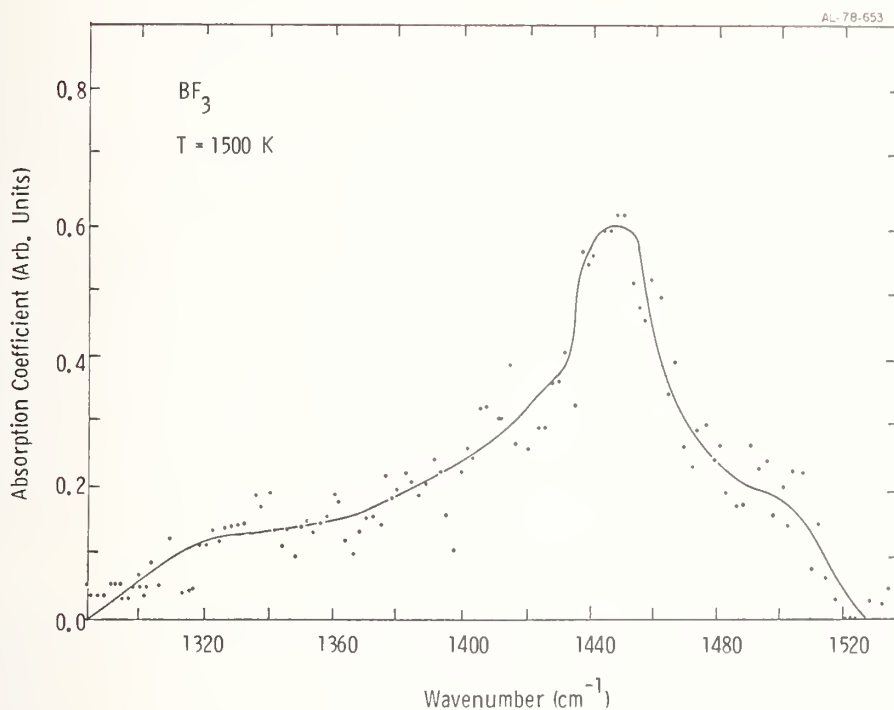


Figure 7.  $\text{BF}_3$  spectral absorption coefficients at 1500 K.

$$(I_0 - I)/I_0 = 1 - \exp(-k\ell) \quad (5)$$

where  $k$  has the units  $1/\text{cm}/\text{amagat}$  and  $\ell$  is the optical depth which is related to the physical absorption path length  $\ell'$  by

$$\ell = \ell' (P/760) (273/T) \quad (6)$$

In this equation  $P$  is the partial pressure of  $\text{BF}_3$ , and  $T$  is the temperature of the flowing gas. Thus, if  $\ell'$ ,  $P$  and  $T$  are known, one can use the data to calculate the spectral absorption coefficient  $k$ .

Since the physical path length is difficult to calculate a priori for the multiple passes through the (possibly) nonuniform cylinder of flowing gases; it is preferable to calibrate the physical path length for the flowing gases and number of White cell passes chosen by measuring the absorption coefficients of a gas such as  $\text{BF}_3$  with a known band strength [8]. Then, these measured absorption coefficients can be used to determine the unknown path length  $\ell'$ . This has not yet been done for the preliminary measurements reported in this paper. Thus, the measured absorption coefficients in figures 5 through 7 are presented in "arbitrary units."

The measurements were performed under the following conditions. The Reynolds number of the main flow was approximatedly 600. The total pressure in the analysis region (Ar plus  $\text{BF}_3$ ) was approximately 10 Torr. The spectral scans covered the region from 6 to 8 microns, and the monochromator was operated with a resolution of 0.04 microns. (The wavelength scale was calibrated by comparing a water vapor absorption spectrum with the absorption peaks measured by Oetjen, et al. [9].) The flow tube was operated at temperatures of 300 K, 1000 K and 1500 K. Finally, the  $\text{BF}_3$  was obtained from Matheson and had a stated purity of 99.5 percent.

The 300 K spectrum presented in figure 5 has the same general appearance as those measured near room temperature by other investigators [10,11]. (The dip near the center of the 1505 wavenumber boron-10 isotopic band was not resolved due to the scatter in the data.) The 1000 K and 1500 K spectra presented in figures 6 and 7 show the expected broadening with increasing temperature. In addition, in the 1000 K spectrum a hot band appears at wavelengths longer than the 1454 wavenumber fundamental, and its relative intensity increases as the temperature is raised to 1500 K. This band probably includes (and may be dominated by) absorption by the  $(\nu_1 + \nu_4)$  combination band at 1361 wavenumbers.

As was noted above, more work will be required in order to further reduce these data to obtain absolute values for the absorption coefficients. In order to do this it will be necessary to separate the fundamental band (of known integrated band strength) from the long wavelength hot band (whose temperature dependent band strength can then be measured). This can be done by developing a band model for the fundamental band and using it to separate the contributions of the fundamental band and the long wavelength hot band.

### 3.1 Assessment of apparatus performance

In addition to the direct absorption coefficient measurements described above, these preliminary experiments with  $\text{BF}_3$  provide several observations which verify the proper performance of the apparatus. For example, when one monitors the  $\text{BF}_3$  absorption at a fixed wavelength as a function of time, the observation can be made that the absorption signal is constant with time, with fluctuations of less than 3 percent over a period of five minutes. This indicates that the flow geometry of the hot gases in the analysis region is stable.

In addition, the 1000 K and 1500 K spectra do not exhibit absorptions due to cold  $\text{BF}_3$ , and thus, it is unlikely that there is any significant amount of recirculation of gases (containing  $\text{BF}_3$ ) from the main flow into the side arms of the optics tubes. This verifies (for the Reynolds number of these flows) the results of the flow simulation study described above.

Finally, the data indicate that the hot gases in the flow tube do not significantly defocus the infrared beam in the White cell as the temperature is increased from 300 K to 1500 K. If such a "thermal lensing" effect had been present, it might have reduced the I<sub>0</sub> signal, thereby decreasing the measurement sensitivity of the apparatus.

#### 4. In situ Sources for Metal Oxide and Metal Halide Species

The spectroscopic data presented in the previous section involved a metal halide species ( $\text{BF}_3$ ) which has a high room temperature vapor pressure and can be introduced into the flow system as a pure species. However, the apparatus described in Section 2 is designed to allow the in situ production of infrared active high temperature species which then can be quantified by mass spectrometric analysis as their infrared properties are measured.

The metal oxide or metal halide species of interest for further studies include both free radical molecular fragments and closed shell molecular species which are thermochemically unstable at lower temperatures. Since the infrared absorption system described in Section 2 is sensitive enough to measure the absorption due to 1 to 100 microns of an infrared active species with a moderately strong band strength, several in situ generating techniques appear capable of producing the necessary species densities. A few of the techniques which will be utilized in future studies are presented in this section.

##### 4.1 Discharge flow techniques

Microwave and radio frequency discharges have been widely utilized to provide free radical atomic and molecular species for both spectroscopic and kinetic investigations in flowing systems. The most widely used system is the Evenson type microwave cavity which operates at 2450 MHz. By varying the power coupled to the gas flow and the concentration of molecules subject to dissociation, a great deal of control can be achieved in producing the needed levels of specific molecular fragments. As shown in figure 1, the apparatus will be equipped with access tubes so that discharge-produced species may be introduced into the high temperature flow.

As an example of this technique, BF has been prepared for both microwave [12] and ultraviolet resonance fluorescence [13] studies by discharging  $\text{BF}_3$  in argon or helium. An extension of this technique involves simultaneous discharge of two or more molecular species. For example,  $\text{BO}_2$  has been prepared by codischarging  $\text{BCl}_3$  and  $\text{O}_2$  [14].

##### 4.2 Gas phase chemical titration techniques

In certain cases it may be possible to create the desired high temperature species by carefully reacting stoichiometric amounts of discharge-created free radicals with a volatile metal-containing molecule. For instance, it may prove possible to create controlled amounts of  $\text{BOCl}$  by titrating stoichiometric flows of  $\text{BCl}_3$  with discharge-produced atomic oxygen. The flow system will be equipped with injection systems so that reactions of this type can be performed in the high temperature flow.

##### 4.3 Gas/condensed phase reactions

The only practical way to create many metal oxide or metal halide species of interest may be the heterogeneous reaction, at high temperature, between a solid or molten condensed

phase reactant and a vaporized species. This technique often requires specialized crucible, wick or boat systems for containing the molten condensed phase systems while maintaining good contact with the gas phase reactant.

Examples of the successful utilization of this technique include the production of BOF by reacting  $\text{BF}_3$  with molten  $\text{B}_2\text{O}_3$  [15] and the production of  $\text{HBO}_2$  by reacting water vapor with molten  $\text{B}_2\text{O}_3$  [16,17].

---

This work was supported by the Air Force Office of Scientific Research under Contract No. F49620-77-C-0075. The authors would like to thank M. Camac and L. Bernstein for valuable technical discussions, J. Kerrebrock and A. Epstein for assistance in the design and analysis of the flow simulation tests and R. Brown for technical assistance in the construction and operation of the apparatus.

#### References

- [1] Fontijn, A., Kurzius, S. C., Houghton, J. J., and Emerson, J. A., Tubular fast flow reactor for high temperature gas kinetic studies, *Rev. Sci. Instr.* 43, 726 (1972).
- [2] Fontijn, A., Felder, W., and Houghton, J. J., Homogeneous and heterogeneous kinetics of the atomic  $\text{Al}/\text{O}_2$  reaction in the 1000-1700 K range, 15th Symposium on Combustion, p.775, Tokyo, Japan (1974).
- [3] Fontijn, A., Elementary combustion reaction kinetics measurement over large temperature ranges. The HTFFR technique, AIAA Paper, 76-131 (1976).
- [4] Edwards, T. H., Multiple-traverse absorption cell design, *J. Opt. Soc. Am.* 51, 98 (1961).
- [5] Ferguson, E. E., Fehsenfeld, F. C., and Schmeltekopf, A. L., Flowing afterglow measurements of ion-neutral reactions, *Adv. At. Mol. Phys.* 5, 1 (1969).
- [6] Kerrebrock, J., Massachusetts Institute of Technology, Private Communication (1977).
- [7] Kreith, F., Principles of Heat Transfer, Intl. Textbook Co., Scranton, Pennsylvania (1963).
- [8] McKean, D. C., Infrared absorption intensities and band moments in  $\text{BF}_3$  and related molecules, *J. Chem. Phys.* 24, 1002 (1956).
- [9] Oetjen, R. A., Kao, C., and Randall, H. M., The infra-red prism spectrograph as a precision instrument, *Rev. Sci. Instr.* 13, 515 (1942).
- [10] Dreska, S. N. and Rao, K. N., nu-3 of boron trifluoride, *J. Mol. Spectry.* 18, 404 (1965).
- [11] Levin, I. W. and Abramowitz, S., Force fields of the boron trihalides, *J. Chem. Phys.* 43, 4213 (1965).
- [12] Lovas, F. J. and Johnson, D. R., Microwave spectrum of  $\text{BF}$ , *J. Chem. Phys.* 55, 41 (1971).
- [13] Moeller, M. B. and Silvers, S. J., Fluorescence spectra of  $\text{PN}$  and  $\text{BF}$ , *Chem. Phys. Lett.* 19, 78 (1973).
- [14] Russell, D. K., Kroll, M., Dows, D. A., and Beaudet, R. A., The laser excited fluorescence spectra of  $\text{BO}_2$ , *Chem. Phys. Lett.* 20, 153 (1973).



- [15] Farber, M. and Blauer, J., The heat of formation and entropy of B<sub>2</sub>O<sub>3</sub>, Trans. Faraday Soc. 58, 2090 (1962).
- [16] Meschi, D. J., Chupka, W. A., and Berkowitz, J., Heterogeneous reactions studied by mass spectrometry. I. reaction of B<sub>2</sub>O<sub>3</sub>(s) with H<sub>2</sub>O(g), J. Chem. Phys. 33, 530 (1960).
- [17] White, D. , Mann, D. E., Walsh, P. N., and Sommer, A., Infrared emission spectrum of gaseous HBO<sub>2</sub>, J. Chem. Phys. 32, 488 (1960).

### Discussion

Question (Cater): I just wondered what variables are in the Reynolds numbers that permit you to model a high temperature gaseous flow by water?

Response (Gersh): Or for that matter, one would ask a low temperature gaseous flow. Well, the Reynolds number is the diameter times the flow velocity times the density divided by the viscosity. Why is this technique like we use it? I don't know, our fluid mechanics experts say they do it all the time, that it is a standard technique to determine what will happen at low temperatures or high temperatures. It works for subsonic incompressible flow.

(Editor's note): A question concerning path length in the cell was raised.

Response (Gersh): Okay, the physical path length of the flow as it comes out of the subsonic nozzle is approximately five centimeters and we can easily get sixty passes in our White cell.

We could get more passes, but in practice you don't gain after a certain point, because your reflective losses at the mirrors reduce your signal intensity and, in practice, you don't gain more sensitivity by going to an arbitrarily high number of passes. Basically, you optimize in the region of about 30 to 60 passes.

Moderator (Lovas): If I understood your diagram of the apparatus correctly, it appeared that your bypass gas flowed over the heating elements. Is that right?

Response (Gersh): Yes, what you want to do is keep the shield flow to the same temperature as the flow in the main gas. It is analogous to using a shield flame on a burner. This keeps you from mixing a hot main flow with a cold outer flow and therefore giving you an indeterminate temperature profile. It is an attempt to give you an isothermal temperature profile for the absorbing species.

Question (Lovas): Could that not cause some problems with chemical reaction in that region?

Response (Gersh): Oh, this is just argon in the outer flow. The absorbing species are only in the main flow.



## ROTATIONAL SPECTROSCOPY OF HIGH TEMPERATURE MOLECULES

T. Törring  
Freie Universität Berlin  
Berlin, Germany  
and

E. Tiemann  
Technische Universität  
Hannover, Germany

### 1. Introduction

In 1971, a review article "Microwave Spectroscopy of High Temperature Gases" was published by Lovas and Lide [1]<sup>1</sup>. Since then, considerable progress has been made in experimental techniques. A new modulation technique has increased the sensitivity of spectrometers in the mm-wavelength range and has made possible the use of heated absorption cells in the temperature range between 1000 and 2000 °C. In addition to direct evaporation, many high temperature reactions have been exploited for an effective production of high temperature molecules, including double oven techniques and nonequilibrium gas phase reactions. As a result, new classes of molecules can now be investigated; e.g., highly refractory compounds and unstable high temperature radicals.

The combination of microwaves and tunable lasers in double resonance experiments (MODR) is a field of growing interest. So this technique has been included in a separate section.

The intention of this article is to point out the main lines of the development by selected examples. No attempt was made to discuss spectroscopic results for special molecules or to provide a complete reference list for all published work.

### 2. Microwave spectroscopy<sup>2</sup>

Microwave spectroscopy is the most important source of precise information on rotational spectra of molecules. Interatomic distances and bond angles, constants of vibration-rotation interaction and centrifugal effects, quadrupole coupling constants, electric dipole moments, rotational magnetic moments, and other molecular properties have been obtained for hundreds of molecules which have a sufficient vapor pressure of 0.01 to 0.1 mm

---

<sup>1</sup>Figures in brackets indicate the literature references at the end of this paper.

<sup>2</sup>Prepared by T. Törring.

Hg at room temperature. For a detailed treatment, the reader is referred to the book of Gordy and Cook [2].

The basic construction of a mw-spectrometer consists of a tunable monochromatic source of mw-power, an absorption cell, and a detector with its associated amplifying system. Since absorption coefficients are small in most cases, a modulation technique in combination with narrow band amplification or signal averaging must be used for optimum performance. Although the set-up is basically very simple, many problems arise when the method is applied to molecules which are present only at elevated temperatures in measurable amounts under equilibrium conditions. In addition to technical difficulties, these problems are related to the great reduction of line strength which is to be expected in high temperature work.

At room temperature, absorption cells of 10 m length or even longer may be used and lines with a peak absorption coefficient of  $10^{-10} \text{ cm}^{-1}$  can be detected under favorable conditions. Lines with an absorption coefficient of  $10^{-9} \text{ cm}^{-1}$  can be found even if one has to search over an extended frequency range. At high temperatures, much smaller cells must be used for a number of technical reasons. Typical cell lengths are 100 cm or 20 cm for temperatures up to 1000 °C or 2000 °C, respectively. If the molecules are produced by a gas phase reaction in a free space cell, the effective absorption length is also of the order of 20 cm. Thus, absorption coefficients of about  $10^{-8}$  to  $10^{-7} \text{ cm}^{-1}$  are necessary in searching for spectra of high temperature molecules. In addition, spectral intensities decrease rapidly as the gas temperature is raised. For diatomic molecules in a  $^1\Sigma$ -ground state, the peak absorption coefficient for rotational transitions is given approximately by

$$\alpha = 1.5 \cdot 10^{-9} f_v i_c \mu_{v_0}^2 / T^3 \Delta v, \quad (1)$$

neglecting the temperature dependence of the line width parameter  $\Delta v$ . Symbols in this expression have the following meanings:

$\nu_0$  = peak frequency of the absorption line (in MHz);

$\mu$  = electric dipole moment (in Debye units);

$T$  = temperature (in K);

$\Delta v$  = line width parameter (in MHz/mm Hg);

$f_v$  = fraction of molecules in the vibrational state of quantum number  $v$ ; and

$i_c$  = fractional isotopic abundance.

It is assumed in this formula that there are no other species present in the absorption cell contributing to the line width. Hyperfine structure has also been neglected. Thus, the actual absorption coefficient will be smaller in most cases. Equation (1) demonstrates the strong dependence of line intensities on temperature. Typically, the absorption coefficient for molecules in the ground vibrational state goes down by a factor of approximately 150 if the temperature is raised from room temperature to 1000 °C, the exact factor depends on the vibrational frequency of the molecule. For polyatomic molecules, the situation is even worse since the additional vibrational degrees of freedom reduce  $f_v$ . Moreover, absorption coefficients for symmetric and asymmetric tops are much smaller even at room temperature due to the larger number of states and smaller transition matrix

elements for most transitions. Sensitivity is therefore a crucial problem in the application of mw-spectroscopy to high temperature species. The concentration of molecules under investigation should be at least 1 percent of total pressure in a heated absorption cell even for  $^1\Sigma$ -state diatomic molecules. Thus, spectrometers of high sensitivity and effective production processes for the molecules, are both of vital importance for successful work.

## 2.1 Spectrometer techniques

To obtain a spectrometer sensitivity as discussed in a later section, a fractional change of mw-power due to the gas absorption of  $10^{-7}$  to  $10^{-6}$  must be detected. This requires a modulation of the molecular absorptions in order to suppress background fluctuations. Stark-effect modulation is the most widely used technique in mw-spectroscopy. A static electric field is applied to the gas sample which is switched on and off periodically. The necessity of a well isolated Stark-electrode inside the hot cell adds considerable complications to the construction. The problems have been solved for temperatures up to 1000 °C. The various designs have been reviewed in [1]. It seems impossible, however, to extend the technique to much higher temperatures, mainly because electrons are emitted from the hot cell walls which cause gas discharges.

All molecules investigated with high temperature mw-spectroscopy so far exhibit a quadratic Stark-effect. The electric field strength required for complete modulation then increases roughly with the third power of the rotational quantum number. For technical reasons, application of Stark-effect modulation is therefore restricted to relatively low J-transitions. With the exception of a few very light molecules, this means a restriction to frequencies below 50 GHz. Since absorption coefficients increase with  $\nu_0^3$ --see eq. (1)--a modulation technique for higher frequencies is highly desirable.

Source modulation is a simple technique which can be generally applied. Unfortunately, suppression of background fluctuations is insufficient unless very low mw-power is used. This results in a reduction of sensitivity by a factor of 10 to 100. If only low power levels are available, simple video-detection in combination with signal averaging can give the same results. Both techniques have been successfully used in the mm- and sub-mm-range where the large absorption coefficients compensate the reduced sensitivity. It should be pointed out that these spectrometers are of optimum performance when the low power available from crystal harmonic generators is used as the source of mm-radiation. However, since backward wave oscillators are now commercially available which give 20-100 milliwatts of power at 300 GHz, considerable improvements are possible.

In 1973, a new modulation scheme was introduced by Törring [3]. This technique makes use of the fact that the absorption of the gaseous sample is proportional to the incident mw-power only when the rate of induced transitions is small compared to the relaxation rate. For higher power levels, saturation sets in and the absorption becomes nonlinear. This nonlinear response can be used to separate the signals resulting from gas absorptions from background fluctuations. It has been shown that the sensitivity of "saturation-effect



modulation" is comparable to Stark-effect modulation. Although the lines are saturated, detection of the nonlinear effects results in a somewhat reduced line width. There is no restriction with respect to the rotational state of the transition, and no disturbances occur from charged particles in the cell. Very sensitive spectrometers can be built in the mm-wavelength range if the mw-source can deliver a power of at least a few milliwatts and transition matrix elements are larger than 1 Debye. Since no Stark-electrode is necessary, construction of absorption cells become very simple. The remaining problem is to find materials which have satisfactory mw-transmission properties and which are also chemically inert to the substance under study. Rectangular shaped cells made of molybdenum or tantalum have been built for temperatures up to 2000 °C. Cylindrical cells made of tungsten have also been used. In both constructions, the cell was directly heated by a current of a few hundred amperes. The temperature range between 1000 and 2000 °C is very important not only for the evaporation of highly refractory compounds but even more for many high temperature reactions. Saturation-effect modulation has proved its usefulness in many applications. All high temperature open shell molecules studied so far have been measured with this method [4-8].

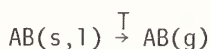
Molecular beam electric resonance at mw-frequencies can give the same sort of information as mw-spectroscopy. Activities with respect to high temperature molecules have been scarce during the last years. One important result was the investigation of the rf-spectrum of the LiO radical by Freund, et al. [9]. The development of tunable lasers has opened up new aspects for the application of beam techniques. The state selection by inhomogeneous fields in a MBER-spectrometer can be replaced by optical pumping. MW- or rf-transitions can be detected by monitoring the fluorescence of the optically pumped beam after passing the transition region. Rf-transitions of the Na<sub>2</sub>-molecule have been studied in this way by Rosner, et al. [10].

Cooling down the rotational and vibrational states in a supersonic nozzle beam gives an enormous gain of line intensities in molecular beam experiments. It seems not possible to produce a nozzle beam directly from high temperature molecules. In addition to technical difficulties, the material consumption would be intolerably high. However, the high pressure necessary to form the supersonic beam may be produced by an inert buffer gas with only a small fraction of high temperature molecules "seeded" into the beam [11,12]. Recently, direct mw-transitions have been observed for the first time by passing an argon nozzle beam containing approximately 1 percent of CsCl-molecules through a cavity [13]. The estimated rotational temperature of CsCl in this experiment was about 50 K. A line width of 5 kHz resulted from the time of flight through the cavity. It was thus possible to resolve the quadrupole hyperfine structure in the  $J = 1 \rightarrow 2$  transition. For other molecules, additional state selection by optical pumping seems feasible. This would actually be a MASER for high temperature molecules with a sensitivity 50 to 100 times larger than the present experiment.

## 2.2 Production of high temperature molecules.

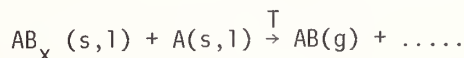
The molecules under investigation must be present in the absorption cell at a total pressure of 0.01 to 0.1 mm Hg. At lower pressures, the sensitivity decreases proportionally with pressure; higher pressures lead to line broadening with a fixed peak absorption coefficient given by eq. (1). Unfortunately, the usual modulation techniques become insufficient for broad lines. Therefore, the total vapor pressure is rather critical.

Most of the work up till now has been done by direct evaporation



at temperatures below 1000 °C. If decomposition and formation of polymers can be neglected, direct evaporation will give the highest possible concentration of molecules AB in the gas phase. In these favorable cases, the experimentally observed line intensities are in agreement with theoretical calculations. Since better absorption cells for the temperature range up to 2000 °C are now available, improved observations of the previously known spectra of BaO [14] and BaS [15] have been made. In this experiment, BaO was evaporated in a molybdenum cell at a temperature of 1450 °C. The observed signal to noise ratio of about 500 at a frequency of 75 GHz indicates that decomposition and reaction with the cell are still negligible. For BaS, evaporation is a much less efficient process for the production of the gaseous molecule. At a temperature of about 1700 °C, only a signal to noise ratio of about 35 was obtained under similar conditions. Attempts to produce gaseous SrO, CaO, and MgO in sufficient concentrations have failed so far, although molecular beam experiments [16] indicate that at least SrO should have a sufficient vapor pressure at temperatures below 2000 °C. Mass spectroscopic investigations have shown that the failure may be due to a reduction of these substances by oil from the diffusion pumps which is cracked at the hot oven. There is no doubt that clean vacuum conditions are very important at these extremely high temperatures.

High temperature reactions become more and more important for the production of unstable species. The first reactions which have been used in mw-spectroscopy were of the type

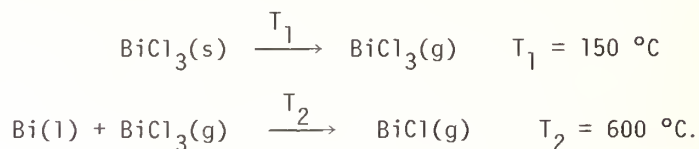


One very favorable example is the production of GeO [17]



where GeO is by far the most dominant species in the vapor. Many reactions of this type have been used to obtain optical absorption spectra, but unfortunately, only a few of them can be used directly for mw-spectroscopy. In most cases, the total pressure at the temperature required for the reaction is much higher than 0.1 mm Hg.

Kuijpers, et al. have shown a way out of these difficulties by using the so-called double-oven technique for the production of the  $^3\Sigma$ -state bismuth halides [4-7].

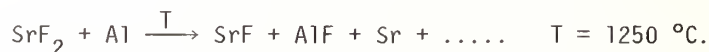
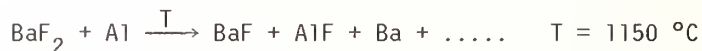


$\text{BiCl}_3$  is evaporated in a separate oven at a temperature  $T_1$ . The gaseous  $\text{BiCl}_3$  then flows through a quartz tube into the hot region of temperature  $T_2$  where it reacts with the liquid Bi to give  $\text{BiCl}$ . The other bismuth halides have been produced in the same manner. The efficiency of this production was very good giving a concentration of the monohalides in the absorption cell near to 100 percent. This was the first and most encouraging example for the application of high temperature mw-spectroscopy to open shell molecules. There is no doubt that the double-oven technique will prove very useful in many future experiments.

If the metal A is the most volatile partner in the reduction reaction, the pressure requirements can often be fulfilled by using another reducing agent C:



The reaction is more complicated and seems less favorable since generally there will be more gaseous reaction products so that the obtainable concentration of the desired molecule AB is reduced. On the other hand, if the spectrum of the molecule BC is known already, these lines may be used to monitor the reaction and to find the optimum temperature. Very recently, we succeeded in obtaining the spectra of the  $^2\Sigma$ -state radicals BaF and SrF [8] by using the reactions



The reaction works much better for BaF than for SrF, the latter giving a signal to noise ratio of only 5 at the present state of the experiment. It should be mentioned that the spectrum of SrF had been detected earlier by the MODR technique with a comparable signal to noise ratio (see Section 3.3). The line width was 15-20 MHz compared to 400 kHz in the present experiment.

There is some doubt if BaF and SrF were produced under equilibrium conditions. When Al-powder was mixed with  $\text{BaF}_2$  or  $\text{SrF}_2$ , no lines were observed and large quantities of Ba or Sr condensed at the cold ends of the absorption cell. Lines were found only when the cell walls were coated with Al and the difluorides evaporated into the cell from a separate

sample boat. There was no temperature gradient between the cell and the boat. The ratio between the reacting surface of the liquid Al and the openings through which the vapor can leave the cell can only be roughly estimated but is not much larger than 10. So nonequilibrium processes seem feasible. Similar results have been obtained both with tantalum and molybdenum cells. It thus seems unlikely that an alloy of Al with the oven material played an important role in the reaction.

Nonequilibrium processes may have played an important role also in the production of the copper halides from the elements. Evaporation of all copper halides except the fluorides results mainly in polymeric species. So the monohalides were produced in a stream of halogen gas over solid copper in a hot cell [18], e.g.,



Reactions between the elements have also been used to produce the highly refractory earth alkaline oxides. Since the oxides will stick on the metal surface the metal has to be evaporated first and carried away from the surface by a stream of inert buffer gas. The reaction then takes place in the gas phase definitely far from equilibrium conditions in a cold cell



This type of production has been used first in laser fluorescence measurements and MODR work (see Section 3.3). Recently, it was shown by Hocking, et al. [19] that the concentrations obtained in this way are high enough for direct mw-absorption measurements. Using a reaction with  $\text{N}_2\text{O}$ , they were also able to observe spectra of  $\text{SrO}$  and  $\text{CaO}$  which could not as yet be obtained by heating the solid oxide. There are two distinct advantages of this method. First, since the reaction takes place in a stream of buffer gas in a cold free space cell, no complications can occur from reactions with hot cell walls. Second, the molecules are produced at relatively low temperatures. Vibrational temperatures near  $250 \text{ }^\circ\text{C}$  have been observed and the rotational temperature will be even lower. From eq. (1), it can be seen that this implicates a considerable increase of the absorption coefficient so that much smaller concentrations are necessary compared to a hot cell. Similar reactions have been used in MODR experiments to produce  $\text{CaCl}$  and  $\text{SrF}$  using  $\text{Cl}_2$  or  $\text{SF}_6$  as oxidants.

The gas phase reactions discussed so far are all exothermic and run at low temperatures. Applications may be further extended by using reactions in a gas discharge. A very interesting mw-spectrometer has been designed by Woods [20] to study intermediate species directly in the plasma of a dc glow discharge. Although only spectra of gaseous species like the CN-radical and a number of gaseous molecular ions have been reported so far, it is quite obvious that the apparatus can also be used for the investigation of high temperature species.



### 2.3 Summary and future aspects

The development of recent years has clearly demonstrated that mw-spectroscopy of high temperature species is not restricted to relatively stable  $^1\Sigma$ -state diatomic molecules. The large variety of possible production schemes promises steady progress in the future. However, it is often a time-consuming enterprise to find optimum conditions or just one reaction of sufficient efficiency. Equilibrium reactions can, in principle, be calculated if reliable thermodynamic data are available. Mass spectrometric investigation can be of great help in this respect. Absolute partial pressures for all partners of a reaction are needed. Often this information is tedious or even impossible to extract from the published data. The accuracy of such predictions is moreover hard to estimate for a non-specialist.

Gas phase reactions in a flow system offer the opportunity of being free from the limitations of equilibrium thermodynamics. The large variety of high temperature species produced in this way and observed by chemiluminescence studies indicates that these reactions will be of increasing importance in future microwave spectroscopic work.

High resolution spectroscopy of diatomic free radicals which are gaseous at room temperature has attracted the activity of many research groups during the past decade. About 20 free radicals have been investigated by the methods of gas-phase EPR, MBER, or microwave absorption. All these species are relatively light molecules e.g., OH, SH, SF, NS, and NO. The coupling between the angular momenta in these light molecules is near to or intermediate between Hund's case, (a) and (b). High temperature spectroscopy offers the opportunity of studying heavier molecules where the effects of spin-orbit interaction become more and more important. The spectra of the bismuth halides give an example of strong Hund's case (c) coupling. A systematic study of other molecules can give precise information on the effects of spin-orbit coupling in the intermediate region. There is a good chance to obtain spectra for some of the transition metal compounds. New ground states which have never been observed in high resolution work may then be studied. Some high temperature molecules are known to be constituents of the atmospheres of cool stars. MW-spectroscopy may provide the spectroscopic data which are necessary to start a search for them with a radiotelescope. Further efforts in the field are therefore highly justified despite the experimental difficulties. On the whole, prospects for future work on high temperature diatomics look more promising than a few years ago and continuous progress may be expected.

Development in the spectroscopy of polyatomic high temperature species is more difficult to predict. Only little progress has been made during recent years. Effects of large amplitude internal motions have been studied in the spectra of the alkali hydroxides, most extensively for KOH [21,22]. The spectrum of KCN has been found [23], but an interpretation is not yet possible. *Ab initio* calculations made for LiNC [24] give a strong indication that the  $K^+$ -ion may move more or less freely around the  $(CN)^-$ -complex. In any case, the bond is extremely floppy and internal motions of very large amplitude are excited at the evaporation temperature of KCN. The spectrum can therefore not be described by the usual formulas which are based on the assumption of small amplitude normal vibrations. The



spectrum consists of many very weak lines of comparable strength so that it is impossible to distinguish between different states of internal excitation from intensity ratios. Cooling down the molecule in a nozzle beam seems to be a promising way to simplify the spectrum and to determine the structure of the molecule in its ground vibrational state. The present data are not consistent with a linear structure.

The problems with KCN seem to be characteristic for the investigation of polyatomic species at high temperatures. A break-through can be expected only if the methods to study high temperature species in a cool environment are further developed.

### 3. Microwave Optical Double Resonance<sup>3</sup>

In microwave-optical double resonance experiments, one observes an electronic transition in connection with a pure rotational transition in the microwave region. To obtain an observable double resonance signal, normally at least one transition must be saturated. Thus, in molecular spectroscopy, optical double resonance could be used in a wider range of applications only since the advent of high power tunable dye lasers.

From such experiments, one gains spectroscopic data of the molecule in its ground and in that excited state which was pumped. These are the typical molecular parameters, as in conventional microwave spectroscopy, and include hyperfine coupling and electric dipole moments.

The resonance volume for the transitions is determined by the overlap of the laser beam with the microwave radiation field. Therefore, this area is very small and can be chosen far away from any surfaces of the vacuum chamber. The molecular reaction is not disturbed by wall effects, and, in principal, by changing the place of the resonance volume, a spatial resolution can be obtained for the molecular distribution in specific molecular states. Detected by optical quanta, molecular species become observable with their pure rotational spectra which could not be measured before because of the severe problems in producing these molecules in typical microwave cells. In this respect, double resonance can be used as an analytical tool which will give the molecular and isotopic species together. As an example, the pure rotational spectra of CaCl and SrF [25] were first observed in an optical double resonance experiment. Another example of a high temperature species is BaO [26] as well as two triatomic molecules, NO<sub>2</sub> [27] and NH<sub>2</sub> [28], which have been studied in their ground and electronic excited state by double resonance. Similar to the optical double resonance, infrared-microwave double resonance has been applied to molecular studies. But there are no examples in the literature of high temperature studies with this method, so we will not go into any detail on this subject. A recent review can be found by Shimoda [29].

#### 3.1 Methods of detection

To describe the double resonance experiment, we use a three level system, where two levels are close together (MW-quantum) and the third has a much larger electronic energy

---

<sup>3</sup>Prepared by E. Tiemann.

separation in comparison to the other two levels. The electronic transition  $3 \leftarrow 2$  and the microwave transition  $2 \leftarrow 1$  are coupled by the common level 2 to give the double resonance effect (fig. 1). We give two different level schemes, the first case (fig. 1a) where the two levels with the low energy separation are below the third level and both show thermal distribution of their population and the second case (fig. 1b) with the opposite, where levels 1 and 2 have no population when the laser light is off. The double resonance can in principal be detected in both light channels.

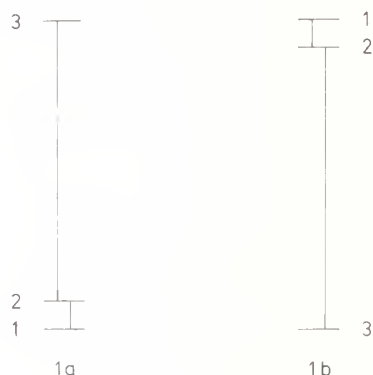


Figure 1. Principle level schemes for microwave optical double resonance.

To observe a change of microwave absorption (fig. 1a), it is necessary to reach the weak optical pumping limit with respect to the relaxation time between levels 1 and 2. The laser beam must be expanded to an area of more than  $1 \text{ mm}^2$  to get enough particles for the microwave absorption. Both conditions can hardly be satisfied with a conventional dye laser, but this method is very often used in infrared double resonance. Similar arguments hold for figure 1b and microwave detection.

Therefore, in most cases a change of fluorescence intensity due to resonance radiation of the microwave field was used to detect the double resonance.

For ground state microwave double resonance (fig. 1a), the total fluorescence will change by an amount equal to the relative population difference of levels 1 and 2 if the microwave transition is saturated and the optical transition shows a linear power dependence. For diatomics, this difference is typically of the order of  $10^{-2}$  to  $10^{-3}$ .

However, in the case of optical detection, the laser beam can be focused into the resonance volume and from there the fluorescence light onto the multiplier tube. Thus, the strong optical pumping limit can be reached with dye laser powers of 50 mW and this will give a change of fluorescence light up to 10 percent, if the microwave transition is saturated. For ground state microwave double resonance, the fluorescence light will only change in intensity but not in its spectral distribution. Therefore, there is no advantage to using a monochromator in the detection channel. However, the insertion of a cut-off filter to reduce the stray light from the fluorescence cell is advisable.

The case of figure 1b must be discussed differently since a second rotational level in the excited state will be populated by the saturating microwave radiation which gives

rise to a change in the spectral distribution of the fluorescence light. In the weak optical pumping limit, this is the only change. Using a monochromator with high resolving power (typical  $3 \cdot 10^4$ ) it is possible to get a double resonance signal without any background from the normal fluorescence. The optical pumping limit and the microwave saturation is here determined mainly by the natural lifetime of the excited state which results in higher power requirements of both radiation sources (compare Section 3.2).

The third possibility to detect double resonance is the use of changes in the polarization of the fluorescence light. The optical pumping with polarized laser light will produce an overall polarization of the molecular gas. The rotational transition induced by the microwave field changes this polarization because of the dependence of the averaged dipole moment on the rotational quantum number  $J$ . Thus, the fluorescence light will have a different polarization. The application of this method was demonstrated on low  $J$ -transitions in BaO [26].

The published experimental work on microwave double resonance has so far used rate equations for the description of observations. This is adequate if one is only interested in spectroscopic data and simple power or molecular density considerations. But, studying the different relaxation times which are involved in the double resonance effect, and the related lines shapes of the signal, one should use the density matrix formalism which is given in some detail for all detection methods by Takami [30].

### 3.2 Light sources for double resonance

Let us first look at the requirements for the laser to observe double resonance. The resonance chamber is a gas cell; thus, the transition shows Doppler broadening. At room temperature, this will give a linewidth of 500 to 1000 MHz for optical pumping. Therefore, the long-term stability of the laser need only to be several hundred MHz. But the spectral width of the laser should be similar to the level width of the molecular state given by relaxation time or natural lifetime in order to get a good spectral power density for the pumping. This leads to a typical spectral width of the laser of a few MHz, which is obtainable with commercial dye lasers.

If one compares the induced processes to the spontaneous processes of a specific optical transition, normally 10 mW of laser power focussed into the fluorescence cell would be enough for effective pumping. But in molecules, the fluorescence very often shows long vibrational progressions where a single fluorescence doublet can be stronger than the fluorescence on the pumping wavelength itself. This is explained by the Frank-Condon principle and can reduce the lifetime of the pumped level by more than an order of magnitude and leads to requirements of much higher pumping power to reach the strong optical pumping limit. A typical value is 100 mW or more.

A few remarks on the microwave sources will be given here. When using waveguide systems for the fluorescence cells, the saturation power is the same as for conventional microwave spectroscopy for ground state double resonance because pressure broadening is the main influence. But, for rotational transitions in the excited state, the natural lifetime

determines the microwave power which is necessary for saturation. This can lead to remarkable power levels of more than 1 W and microwave cavities should be used to obtain the high electric field strength. In these cases, the linewidth of the rotational transition increases very much compared to the typical width in ordinary microwave spectroscopy.

In the case of free space cells, studying the "undisturbed" vapor, the radiation is coupled by microwave horns which require higher power to obtain the same power density as in the waveguide. In conclusion, microwave oscillators for double resonance experiments should deliver typically at least 100 mW up to 1 W of power, much higher than in pure microwave spectroscopy.

### 3.3 Spectroscopic results

Double resonance experiments on high temperature species were performed on BaO [26], CaCl, and SrF [25]. These molecules were produced by chemical reaction of the metal vapor in an Ar carrier and an oxidant was added above the outlet of the oven. Very recently, this procedure was successfully applied to conventional microwave spectroscopy for the observations of SrO and CaO (compare Section 2.2). As oxidants, the elements like  $O_2$  or  $Cl_2$  have been used in most cases; for fluorides,  $SF_6$  is reacted with the metal. These reactions are exothermic and sometimes give bright chemiluminescence which can be used to optimize the reaction conditions.

BaO was detected in the ground state  $X^1\Sigma^+$  and the excited state  $A^1\Sigma^+$ . The rotational spectrum in  $A^1\Sigma^+$  shows some perturbations, which can be attributed to an interaction of other electronic states. With an analysis of the perturbation, the location of excited states which are not observed in the optical spectra is possible. For the  $A^1\Sigma^+$ ,  $v' = 7$  state, Stark-effect measurements [31] were successful, which yield a dipole moment of  $|\mu_7| = 2.20(11)D$  which is remarkably smaller than in the ground state  $|\mu_0| = 7.954(3)D$  [32]. This is explained in reference [31] as a change of an ionic bond in X to a covalent bond in A.

For CaCl and SrF, the double resonance experiment was the first observation of a pure rotational spectrum in a  $^2\Sigma^+$  state. The measurements were done only in the ground state and yield precise values of the rotational constant  $B_v$  and the spin-rotation-coupling constant  $\gamma_v$ . These constants could be applied to confirm the assignment of the laser excitation spectra of these molecules [33], and new molecular parameters were derived in the state  $B^2\Sigma^+$ .

In double resonance experiments, the observed linewidth (about 10 MHz) has been much broader than one would expect from the Doppler effect. No real explanation is given in the papers. It seems that the power dependence of the double resonance signals has not been studied in detail experimentally. Further work should be done so as to obtain the full resolving power of microwave optical double resonance.

Other molecules studied with this method recently are the triatomics  $NO_2$  [27] and  $NH_2$  [28], where the latter is produced by gas discharge in water with anhydrous hydrazine. Both spectra are doublet systems with magnetic hyperfine structure. The observations were



done in the ground and excited electronic state and several molecular parameters could be derived. These high resolution spectroscopic studies have greatly increased our knowledge of triatomic species with a free electron spin and allow one to choose the right effective hamiltonian which describes the intramolecular interactions.

### 3.4 Future aspects

The application of microwave-optical double resonance has been limited so far to the wavelength region of the very efficient Rhodamine 6G dye which allows output powers up to 100 mW in single mode operation. The development of tunable cw-dye lasers is still progressing rapidly; lasers operating in the blue region with high spectral purity are now available and deliver output powers of about 20 mW which should be sufficient to study other molecules with the double resonance method. Thus, its application to new high temperature species is expected to expand in the near future.

When pumping a specific rotational level in an excited molecular state, one can expect that this energy will be transferred by collisions to other rotational levels. Then, the microwave transition will take place from a level different to the excited one. Therefore, the level 2 in figure 1b which was common for both transitions is replaced by two rotational levels which are linked together by collisions (four level scheme). This effect which is called collision-induced transitions is more often observed in the infrared double resonance but very recently by optical resonance in the molecule  $\text{NH}_2$  [34]. From such experiments, one obtains data to check collision models for excited state molecules. Studies of collision induced transitions in the optical region are therefore an important tool to examine transfer of electronic energy in a gaseous system.

Finally, we should mention an experiment closely related to the double resonance method, the optical pumping method. A laser radiation field pumps an atom or a molecule in a magnetic field so as to produce a nuclear spin polarized particle by comparison to the overall polarization. Applying a second radiation field in the rf-region, a nuclear magnetic resonance (NMR) can be induced which is detected as a change of the light absorption. In addition to the spectroscopic data which was derived from such experiments, it was demonstrated in the vapor mixture of alkali atoms and dimers that a collision-induced process was occurring in the system [35]. After building up the nuclear spin polarization in the atom by optical pumping, the polarization is transferred to the molecule in an atom-molecule exchange collision, and can be detected by NMR. With this method, atom-molecule exchange rates and thermal dissociation could be studied in  $\text{Cs/Cs}_2$  and  $\text{Na/Na}_2$  [37] systems.

The above successful experiments show that detailed spectroscopic work which combines laser radiation and mw-radiation can yield much information about the processes in high temperature vapors.



## References

- [1] Lovas, F. J. and Lide, Jr., D. R., in Advances in High Temperature Chemistry, Vol. 3, 177-212 (1971).
- [2] Gordy, W. and Cook, R. L., Microwave molecular spectra, in Chemical Applications of Spectroscopy, Part II, Vol. IX (Wiley, New York, 1970).
- [3] Törring, T., J. Mol. Spectr. 48, 148 (1973).
- [4] Kuijpers, P., Törring, T., and Dymanus, A., Chem. Phys. 12, 309 (1976).
- [5] Chem. Phys. 18, 401 (1976).
- [6] Kuijpers, P. and Dymanus, A., Chem. Phys. Lett. 39, 217 (1976).
- [7] Chem. Phys. 24, 97 (1977).
- [8] Ryzlewicz, C. and Törring, T., to be published.
- [9] Freund, S. M., Hebert, E., Mariella, Jr., R. P., and Klemperer, W., J. Chem. Phys. 56, 1467 (1972).
- [10] Rosner, S. D., Holt, J. A., and Gaily, T. D., Phys. Rev. Lett. 35, 785 (1975).
- [11] Gordon, R. J., Lee, Y. T., and Hershbach, D. R., J. Chem. Phys. 54, 2393 (1971).
- [12] Malthan, H. and Toennies, J. P., in Proceedings of 9th International Symposium on Rarefied Gas Dynamics (1974).
- [13] Witek, H., Hoeft, J., and Törring, T., to be published.
- [14] Tiemann, E., Bojaschewski, M., Sauter-Servaes, Ch., and Törring, T., Z. Naturforsch. 29a, 1692 (1974).
- [15] Tiemann, E., Ryzlewicz, C., and Törring, T., Z. Naturforsch. 31a, 128 (1976).
- [16] Kaufmann, M., Wharton, L., and Klemperer, W., J. Chem. Phys. 43, 943 (1965).
- [17] Törring, T., Z. Naturforsch. 21a, 287 (1966).
- [18] Manson, E. L., deLucia, F. C., and Gordy, W., J. Chem. Phys. 62, 1040 (1975).
- [19] Hocking, W. H., Pearson, E. F., Cresswell, R. A., and Winnewisser, G., J. Chem. Phys. 68, 1128 (1978).
- [20] Woods, R. C., Rev. Sci. Instrum. 44, 274 and 282 (1973).
- [21] Kuijpers, P., Törring, T., and Dymanus, A., Z. Naturforsch. 30a, 1256 (1975).
- [22] Pearson, E. F., Winnewisser, B. P., and Trueblood, M. B., Z. Naturforsch. 31a, 1259 (1976).
- [23] Kuijpers, P., Törring, T., and Dymanus, A., Chem. Phys. Lett. 42, 423 (1976).
- [24] Clementi, E., Kistenmacher, H., and Popkie, H., J. Chem. Phys. 58, 2460 (1973).
- [25] Domaille, P. J., Steimle, T. C., and Harris, D. O., J. Mol. Spectr. 68, 149 (1977); 66, 503 (1977).
- [26] Field, R. W., English, A. D., Tanaka, T., Harris, D. O., and Jennings, D. A., J. Chem. Phys. 59, 2191 (1973).
- [27] Tanaka, T., Field, R. W., and Harris, D. O., J. Chem. Phys. 61, 3401 (1974);  
Tanaka, T., English, A. D., Field, R. W., Jennings, D. A., and Harris, D. O., J. Chem. Phys. 59, 5217 (1973); Tanaka, T. and Harris, D. O., J. Mol. Spectr. 59, 413 (1976).
- [28] Hills, G. W., Cook, J. M., Curl, Jr., R. F., and Tittel, F. K., J. Chem. Phys. 65, 823 (1976).

- [29] Shimoda, K., Double-resonance spectroscopy of molecules by means of lasers, in Topics in Applied Physics, Vol. 2, H. Walther, ed. (Berlin, 1976).
- [30] Takami, M., Jap. J. Appl. Phys. 15, 1063 (1976); 15, 1889 (1976); 17, 125 (1978).
- [31] Wormsbecher, R. F., Lane, S. L., and Harris, D. O., J. Chem. Phys. 66, 2745 (1977).
- [32] Lovas, F. J. and Tiemann, E., J. Phys. Chem. Ref. Data, 3, 609 (1974).
- [33] Domaille, P. J., Steimle, T. C., Wong, N. B., and Harris, D. O., J. Mol. Spectr. 65, 354 (1977); Steimle, T. C., Domaille, P. J., and Harris, D. O., J. Mol. Spectr. 68, 134 (1977).
- [34] Hills, G. W. and Curl, Jr., R. F., J. Chem. Phys. 66, 1507 (1977).
- [35] For example: König, F. and Weber, H. G., Chem. Phys. Lett. 44, 293 (1976), and literature cited therein.
- [36] Glas, H.-J. and Weber, H. G., Z. Phys. A284, 253 (1978).
- [37] Huber, R., Thesis, University Heidelberg (1978).

### Discussion

Comment (Froben): The production of  $2\Sigma^-$  ground state molecules could be enhanced using Sc instead of Al as mentioned in the paper. The line width of 300 to 400 kHz is an indication that the free spin is located very much on the metal atom.

The CsCl seeded beam experiment has been done not only using Ar, but also with He, Ne and Kr. The experimental line width changed as predicted by the different mass number.

To monitor the evaporation process VUV absorption can be used. That was shown recently by Tischer, Tarring and Froben using synchrotron radiation at Bonn University in collaboration with the Imperial College London. Systems used as a test for this method were SiO,  $P_3N_5$  and  $MgF_2 + Al$ . The VUV spectra show new band systems and allow one to determine the species produced. In the  $MgF_2 + Al$  reaction no MgF was formed, only AlF and Mg.



## MODERN HIGH-TEMPERATURE ELECTRON DIFFRACTION

V. P. Spiridonov and E. Z. Zasorin  
Department of Chemistry  
Moscow State University  
Moscow 117234 USSR

Work in the area of high-temperature electron diffraction by gases which has been carried out mainly at Moscow University in the period from 1967 is summarized. The topic to be considered covers the developments in (1) the determination of molecular potential functions and vibrational frequencies from diffraction information, (2) the apparatus for high-temperature studies, and (3) the experimental methods. A survey is also given of the structural results obtained.

### 1. Introduction

During the decade from 1967<sup>1</sup> structural investigations of high-temperature vapors by electron diffraction has been an active area of research. Since that time many new aspects of this particular diffraction technology have developed. The improved instrumentation and experimental methods for high-temperature studies have made it possible to measure diffraction intensities with appreciably greater accuracy. This, combined with more sophisticated computational and theoretical approaches, has led to an increased reliability and precision in structural data at high temperatures. Generally, the total uncertainty in principal internuclear distance measurements has been reduced to 0.003-0.008 Å as compared with 0.01-0.03 Å obtained in the pioneer days [1]<sup>2</sup>. Solutions have been provided to problems that earlier seemed insoluble. Notable among these are (1) the refinement of closely-spaced internuclear distances, (2) structural determinations under conditions of complex vapor composition, (3) the development of a low-pressure technique--allowing one to reduce the temperature-drop effect and to use conditions closer to those of mass spectrometry.

---

<sup>1</sup>Previous work in this area is summarized in chapter 12 of the book "The Characterization of High-Temperature Vapors" edited by J. L. Margrave in 1967 [1].

<sup>2</sup>Figures in brackets indicate the literature references at the end of this chapter.

Recently, in addition to these fairly sophisticated studies, there have appeared examples where high-temperature electron diffraction has been used to establish molecular structures free from harmonic vibrational effects and to provide accurate information on force fields and vibrational frequencies of molecules. Thus modern electron diffraction is developing as a valuable complement to vibrational spectroscopy for high-temperature vapors.

The present period of high-temperature electron diffraction is also characterized by a broader scope of molecular forms under study. As the technique improves, more complex molecules are becoming amenable to study. Among them are the polymeric oxides, mixed halides and salts of oxyacids.

The geography of high-temperature electron diffraction studies has broadened considerably since 1967. Earlier, these studies were concentrated mainly at Moscow University [1]. Currently, the results in this area are being regularly reported from (1) the Institute of High Temperatures of the Academy of Sciences of USSR, (2) the All-Union Research Institute of Metrological Service (Moscow, USSR), (3) the Institute of Chemical Technology (Ivanovo, USSR), (4) the Belorussian Institute of Technology (Minsk, USSR), (5) the Central Research Institute of Chemistry, Hungarian Academy of Sciences (Budapest, Hungary). Some studies are also being carried out in Japan.

Several review papers have appeared in recent years [2,3]. The review presented below covers mainly the results obtained during the last decade at the Laboratory of Electron Diffraction of Moscow State University.

## 2. New Gas-Phase Electron Diffraction Procedures for Determination of Molecular Force Fields and Vibrational Frequencies

The fundamentals of the theory for interpreting the electron diffraction patterns in fact remain similar no matter what temperatures are used. Therefore, any modifications and improvements in the general theory of electron diffraction can be readily adapted for high temperature use.

### 2.1 Some limitations of the conventional scheme of analysis

Conventional theory of modern electron diffraction analysis has been in routine use for over two decades [4-9]. According to this theory the refinement of the structural parameters is based upon comparisons of the experimental molecular intensities and radial distributions with the corresponding theoretical counterparts calculated for various molecular models. To do this many sophisticated programs have been developed for high-speed computers. The least squares technique is widely employed to produce optimal values of molecular parameters. These parameters are [10]:

(1) The thermally averaged internuclear distances  $r_a$  or  $r_g$ . The  $r_g$  distance is an effective parameter equal to the center of gravity position of the  $P(r)$  probability distribution function. Similarly, the  $r_a$  parameter is associated with the center of gravity of the  $P(r)/r$  function.



(2) The thermally averaged mean square amplitudes of vibration characterizing internal motion in molecules.

(3) The often neglected asymmetry parameters related to the anharmonicity of the molecular vibrations.

This scheme of structure analysis by electron diffraction has been remarkably successful for establishing numerous molecular structures including high-temperature ones [1]. However, obvious disadvantages of the  $r_a$  and  $r_g$  distance representations are the following [10]:

(1) Various vibrational effects, depending on a temperature, and particularly at high temperatures and when low frequencies of vibration are present.

(2) The failure of the  $r_a$  and  $r_g$  parameters for a nonbonded atom pair, coupled with those for corresponding bonded atom pairs, to rigorously obey the relationships resulting from the symmetry type of the equilibrium geometry (Bastiansen-Morino shrinkage effect [11]).

Thus an experimental molecular structure determination in terms of thermally averaged distance characteristics may sometimes result in appreciable uncertainty. Naturally, this situation deteriorates further at high temperatures where many excited vibrational levels can be appreciably populated. To partly deal with these disadvantages, harmonic vibrational corrections in the  $r_a$  or  $r_g$  distances are introduced [10], yielding the so-called  $r_\alpha$  structure, free from harmonic vibrational effects and consequently more geometrically consistent. But such a procedure requires knowledge of at least an approximate harmonic force field.

Thermally averaged mean amplitudes of vibration, measured by electron diffraction, are often applied to augment spectroscopic data in the characterization of force fields for polyatomic molecules [12]. For the same purpose the Bastiansen-Morino shrinkage effect [11] can be complementarily used, provided the symmetry type of the equilibrium geometry of the molecule is attainable from other sources [12]. However, it is well known that the number of constants associated with a general force field usually exceeds the number of measured amplitudes and shrinkages.

## 2.2 New intensity equation

The first attempt to devise a new approach for electron diffraction analysis has been made for diatomic molecules [13]. For these systems the Dunham-type vibrational anharmonic potential has been related to experimental intensities through a density matrix. This allows one to directly parametrize the intensity function in terms of the potential parameters  $r_e$ ,  $\omega_e$ ,  $k_3$  and  $k_4$ . From the results obtained for iodine, it was concluded that up-to-date electron diffraction looks promising as a valuable source of important spectroscopic information on molecules.

With this in mind considerable interest has been expressed recently in the production of molecular potential functions and vibrational frequencies from diffraction information for polyatomic systems [14]. To accomplish this, the effects of internal motion of atom-pairs in polyatomic systems upon the scattering of electrons were re-examined in the

harmonic approximation. As a result, new equations were derived for probability distribution and intensity functions.

The  $P(r)/r$  function for an arbitrary atom pair has been shown to be

$$P(r)/r = (2\pi\langle\Delta z^2\rangle)^{-1/2} \left[ 1 + \sum_{i=0}^3 \alpha_i (r - r_e^h)^i \right] \times \exp [-(r - r_e^h)^2 / 2\langle\Delta z^2\rangle] \quad (1)$$

where

$$\alpha_0 = -\frac{1}{(r_e^h)^2} \left[ \frac{u}{2} - \frac{v}{2\langle\Delta z^2\rangle} \right],$$

$$\alpha_1 = -\frac{1}{r_e^h} \left[ 1 - \frac{u}{2\langle\Delta z^2\rangle} + \frac{3}{2} \frac{v}{\langle\Delta z^2\rangle} \right],$$

$$\alpha_2 = \frac{1}{(r_e^h)^2} \left[ 1 - \frac{v}{2\langle\Delta z^2\rangle} \right],$$

$$\alpha_3 = \frac{1}{r_e^h} \frac{v}{\langle\Delta z^2\rangle^2},$$

$$u = \langle\Delta x^2\rangle + \langle\Delta y^2\rangle,$$

$$v = \langle\Delta x\Delta z\rangle^2 + \langle\Delta y\Delta z\rangle^2,$$

$\langle\Delta z^2\rangle$  is the parallel and  $\langle\Delta x^2\rangle$  and  $\langle\Delta y^2\rangle$  are the perpendicular mean square amplitudes of vibration, respectively,  $\langle\Delta x\Delta z\rangle$  and  $\langle\Delta y\Delta z\rangle$  are the mean cross-products,  $r_e^h$  is the equilibrium internuclear distance in the harmonic approximation. For simplicity,  $\langle\Delta z^2\rangle$  is often referred to as the amplitude of vibration.

The generalized amplitudes of vibration appearing in eq. (1) were first introduced in the theory of electron diffraction by Moripo and Hirota [15] and have never been used in structure analysis heretofore.

The corresponding total reduced molecular intensity function, including contributions from all atom pairs, was obtained as

$$sM(s) = \sum_{i,j}^N \frac{g_{ij}(s)}{r_{e,ij}^h} \exp \left[ -s^2 \frac{\langle\Delta_{ij}^2\rangle}{2} \right] \times \left[ L_{ij}(s) \sin(s r_{e,ij}^h) + N_{ij}(s) \cos(s r_{e,ij}^h) \right] \quad (2)$$

where

$$L_{ij}(s) = 1 + \frac{\langle \Delta z_{ij}^2 \rangle}{(r_{e,ij}^h)^2} - \frac{u_{ij}}{2(r_{e,ij}^h)^2} - \frac{s^2}{(r_{e,ij}^h)^2} \left[ \langle \Delta z_{ij}^2 \rangle - \frac{v_{ij}}{2} \right], \quad (3)$$

$$N_{ij}(s) = \frac{-s}{r_e^h} \left[ \langle \Delta z_{ij}^2 \rangle - \frac{u_{ij}}{2} + s^2 \frac{v_{ij}}{2} \right], \quad (4)$$

$g_{ij}(s)$  is the scattering function for the  $ij$  atom pair and  $s$  is the standard scattering variable.

If the following approximations are further introduced  $L_{ij}(s) \sim 1$  and  $N_{ij}(s) \sim 0$  for all values of the scattering variables eq. (2) reduces to a more common form

$$sM(s) = \sum_{i,j}^N \frac{g_{ij}(s)}{r_{e,ij}^h} \exp \left[ -s^2 \frac{(l_{a,ij}^h)^2}{2} \right] \times \sin \left[ s (r_{a,ij}^h - k_{ij}^h \cdot s^2) \right], \quad (5)$$

where

$$r_{a,ij}^h = r_{e,ij}^h - \frac{\langle \Delta z_{ij}^2 \rangle}{r_{e,ij}^h} + \frac{u_{ij}}{2 r_{e,ij}^h}, \quad (6)$$

$$(l_{a,ij}^h)^2 = \frac{\langle \Delta z_{ij}^2 \rangle}{(r_{e,ij}^h)^2} \left[ (r_{e,ij}^h)^2 + \langle \Delta z_{ij}^2 \rangle + u_{ij} - \frac{v_{ij}}{\langle \Delta z_{ij}^2 \rangle} \right], \quad (7)$$

$$k_{ij}^h = \frac{v_{ij}}{2 r_{e,ij}^h} \left[ 1 - \frac{2 \langle \Delta z_{ij}^2 \rangle}{(r_{e,ij}^h)^2} + \frac{u_{ij}}{2 (r_{e,ij}^h)^2} \right]. \quad (8)$$

It follows from the comparison of  $r_a^h$  defined in eq. (6) with the expression specifying the more common  $r_a$  parameter [10]

$$r_a = r_\alpha - \frac{\langle \Delta z^2 \rangle}{r_a} + \frac{u}{2 r_a}, \quad (9)$$

that the  $r_e^h$  parameter numerically should be close to the  $r_\alpha$  parameter of conventional theory [10]. Such a numerical correlation holds, however, only provided the approximations  $L_{ij}(s) \sim 1$  and  $N_{ij}(s) \sim 0$  in eq. (2) are valid at all values of the scattering variable  $s$ .

The harmonic phase shift in eq. (5) provides a distinction between the theory of ref. [14] and the more conventional one [4-10]. As a consequence, the constant  $k_{ij}^h$  (8) differs from that of the conventional theory.

The advantage of the new intensity eqs. (2) and (5) over that commonly used in structure analysis by electron diffraction is as follows. The  $r_{e,ij}^h$ ,  $\langle \Delta z_{ij}^2 \rangle$  and additional  $u_{ij}$  and  $v_{ij}$  perpendicular motion parameters are entered in eqs. (2) and (5) in a way which allows them to be separately obtained from the experimental data at a single temperature. This opens the way to direct determination of a molecular structure free from harmonic vibrational effects and extends the vibrational facilities of the method.

It is to be noted, however, that the new parameters  $u_{ij}$  and  $v_{ij}$  are weak as compared with the more common mean square parallel amplitude of vibration  $\langle \Delta z_{ij}^2 \rangle$ . For this reason, the accuracy demanded of the experimental data to yield reliable estimates of these parameters must be high. It is clear that such an application requires careful attention to delicate experimental details. However, many sources of possible errors encountered in experimental methods at high temperatures have been eliminated or minimized by steady improvements in the instrumentation. From this, it seems reasonable to expect that measurements of this kind would be justified in the high-temperature area. Some experimental evidence supporting this statement shall be presented below in Section 4.

### 2.3 New data analysis procedure

This Section focuses on a new procedure of analysis for determining molecular structures, potential functions and vibrational frequencies from diffraction information developed in ref. [14].

The main peculiarities of this procedure may be summarized as follows:

- (1) The more geometrically consistent  $r_e^h$  distances, free from harmonic vibrational effects, can be directly determined from the experiment. Thus the spectroscopic harmonic distance correction, providing  $r_\alpha$  parameters of conventional analysis from measured  $r_a$  or  $r_g$  distances, can be avoided. This is particularly important at high-temperatures where vibrational effects are significant.
- (2) For each atom pair additional perpendicular motion parameters are used in the analysis. This extends the facility of electron diffraction in evaluating force fields and vibrational frequencies beyond that of the more common procedure of analysis.
- (3) The intensity function is directly parametrized on harmonic force constants having more fundamental physical significance. The frequencies of vibration are obtained simultaneously, the assignment of them being performed without difficulty. Since lower frequencies of vibration affect the molecular intensities more strongly than the higher ones the former would be estimated more accurately. Fortunately, unlike spectroscopy the selection rules play no role in electron diffraction analysis. Since perpendicular motion parameters are dependent on the molecular symmetry [11] an assumption is to be made in the analysis on the symmetry type of the equilibrium geometry of the molecule to be studied.

(4) A study of the molecule at two or several temperatures provides additional equations for force field and vibrational frequency evaluations. In this regard, the super-heating technique of high-temperature electron diffraction developed earlier [16] may prove to be extremely profitable. In principle, with this procedure, the problem of general force field electron diffraction evaluation can be completely solved for some simple molecules (see  $\text{AsBr}_3$  below).

(5) The spectroscopic information on vibrational frequencies can be naturally included in the analysis thereby providing greater facility for force field evaluations. To do this, a more general expression for the deviations-squared is used

$$Q^2 = Q^2(\text{ED}) - WQ^2(\text{SP}), \quad (10)$$

where  $Q^2(\text{ED})$  and  $Q^2(\text{SP})$  are the electron diffraction and spectroscopic parts, respectively. Such a procedure allows one to combine use of electron diffraction and spectroscopic methods. It appears most effective in supplying useful information on force fields of polyatomic systems, particularly when spectroscopic frequencies for various isotopic species are observed and included in the analysis. This combined technique can also be regarded as complementing spectroscopy and should be extremely helpful when some of the vibrational frequencies are not available from spectra or seem improperly assigned or unreliably determined.

It should be pointed out that some further modifications and improvements in the procedure for analysis of electron diffraction data have been developed in ref. [14]. The improved procedure considerably reduces the amount of vibrational complexity for any molecule. For this reason it can be handled without recourse to ingenious mathematical procedures. Making due regard for anharmonic effects in a selected normal mode, this procedure would be particularly useful for handling high-temperature species that undergo large amplitude motion with relatively low frequencies of vibration. We do not consider here the details of this novel procedure since the computer program for handling it is presently under test in our laboratory and no experimental data have yet been treated in this manner.

Now a natural question arises as to how accurate are the electron diffraction evaluations of force constants and vibrational frequencies. The best answer would be provided by practical implementation of the method for these purposes and by comparing the results with those of spectroscopic methods.

## 2.4 Determination of force fields and vibrational frequencies

The potentiality of the new procedure for electron diffraction analysis was tested with the molecules  $\text{BF}_3$  and  $\text{AsBr}_3$ , for which reliable spectroscopic data are available. A similar treatment was then carried out for the  $\text{HgI}_2$  (410 K),  $\text{SnCl}_2$  (608 K) and  $\text{AlCl}_3$  (1150 K) molecules which can be regarded as near the being 'true' high-temperature species.



### 2.4.1 BF<sub>3</sub>

The experimental electron diffraction data for the planar BF<sub>3</sub> molecule taken from ref. [17] were treated [14] in two ways. First, a simplified version of the above procedure was applied for the purpose of comparing the experimental generalized amplitudes of vibration with those calculated from independent spectroscopic information. The results of the least squares analysis are presented in table 1 together with the corresponding values from the spectroscopic calculations of Cyvin [11]. For the second stage, the general force field of BF<sub>3</sub> was generated by the joint processing of electron diffraction [17] and spectroscopic data for two isotopic species (see table 2). The force constants for the symmetry coordinate system thus obtained are listed in table 3.

Table 1. Electron diffraction and spectroscopic measurements of generalized amplitudes of vibration (Å units).

Parameter	Electron diffraction data alone [14]	Spectroscopic calculations of Cyvin [11]	Electron diffraction and spectroscopic joint analysis [14]
$r_e^h$ (B-F)	1.311	$1.311_1(1_2)^a$	1.3111(8)
$\langle \Delta z_{BF}^2 \rangle^{1/2}$	0.0434	0.0425	0.0426 <sup>b</sup>
$\langle \Delta z_{FF}^2 \rangle^{1/2}$	0.0561	0.0562	0.0554 <sup>b</sup>
$u_{BF}$	0.0054	0.0062	0.0061 <sup>b</sup>
$u_{FF}$	0.0027	0.0020	0.0021 <sup>b</sup>

<sup>a</sup>The  $r_\alpha^0$  parameter from Kuchitsu and Konaka [17]. The  $r_a$  parameter is  $1.311_9 \pm 0.008$  Å and the  $r_g$  parameter is  $1.313_3 \pm 0.001_0$  [17].

<sup>b</sup>Calculated from the force constants determined by joint analysis of electron diffraction and spectroscopic data (see table 3).

Table 2. Spectroscopic frequencies of vibration (cm<sup>-1</sup>) for BF<sub>3</sub> and AlCl<sub>3</sub>.

Molecule	$\omega_1$	$\omega_2$	$\omega_e$	$\omega_4$	Ref.
<sup>10</sup> BF <sub>3</sub>	888	719.28	1505.25	481.13	[18-21]
<sup>11</sup> BF <sub>3</sub>	888	691.22	1453.72	479.36	[18-21]
AlCl <sub>3</sub>	393.5	183	618.8	151	[22,23]

Table 3. Structural and force field<sup>a</sup> parameters for BF<sub>3</sub> and AlCl<sub>3</sub> as obtained by joint use of electron diffraction and spectroscopic methods.

Molecule	$r_e^h, \text{\AA}$	$F_{11}$	$F_{22}$	$F_{33}$	$F_{34}$	$F_{44}$	Ref.
BF <sub>3</sub>	1.3111(18) <sup>b</sup>	8.884(6) <sup>c</sup>	0.288(4) <sup>c</sup>	7.05(3) <sup>c</sup>	-0.503(12) <sup>c</sup>	0.499(4) <sup>c</sup>	[14]
		8.82	0.288	6.52	-0.31	0.515	[25]
AlCl <sub>3</sub>	2.052 <sup>d</sup>	3.19	0.047	2.78	-0.089	0.095	[14]

<sup>a</sup>Force constants (mdyn/ $\text{\AA}$ ) for symmetry coordinate system.

<sup>b</sup>The B-F bond distance. The uncertainty is estimated as  $3\sigma$ .

<sup>c</sup>The standard deviation.

<sup>d</sup>The Al-Cl bond distance. The  $r_{\alpha_o}$  (Al-Cl) estimated from  $r_a$  (Al-Cl) using spectroscopic distance correction is 2.050(4)  $\text{\AA}$  (see table 12).

The main conclusions to be drawn from these data are as follows:

- (1) The  $r_e^h$  parameter for the B-F bond distance, directly determined from the experiment, is numerically equal to the  $r_{\alpha}$  parameter calculated [17] from conventional thermally averaged parameters using a spectroscopic harmonic distance correction.
- (2) The generalized amplitudes of vibration determined from the experimental data by the new procedure of analysis are in good agreement with those calculated from spectroscopic data. Hence, the precision now attainable by the electron diffraction technique can be regarded as sufficient to justify measurement of the perpendicular motion constants.
- (3) The force field of BF<sub>3</sub> generated by combined use of electron diffraction and spectroscopic methods is in agreement with the best available literature data (see, for example [24]).

#### 2.4.2 AsBr<sub>3</sub>

The pyramidal molecule AsBr<sub>3</sub> yielded another remarkable test [14] for the electron diffraction analysis procedure. The experimental intensities for AsBr<sub>3</sub> collected at two temperatures 373 and 466 K were taken from ref. [25]. The two data sets were treated simultaneously, as suggested above, to yield additional independent equations for general force field evaluation by electron diffraction alone. The structural and force field parameters of AsBr<sub>3</sub> thus obtained, along with the frequencies of vibration, are presented in tables 4 and 5, respectively. For comparison table 4 also lists the structural parameters of this molecule determined in ref. [25] by the conventional scheme of analysis and those from microwave measurements [26]. Table 5 also contains the force constants obtained in ref. [25] on the basis of more common amplitudes of vibration using supplementary spectroscopic information on the vibrational frequencies.

Table 4. Structural parameters (in Å and degrees) for AsBr<sub>3</sub>.

Parameter	Temperature, K		Ref.
	373	466	
$r_a(\text{As-Br})$	2.3244	2.3276	[25]
$r_\alpha(\text{As-Br})$	2.3206	2.3227	[25]
$r_z(\text{As-Br})^a$		2.324	[26]
$r_e^h(\text{As-Br})$		2.323	[14]
$\angle_\alpha \text{ BrAsBr}$	99.69	99.66	[25]
$\angle_z \text{ BrAsBr}^a$		99.8(0.2)	[26]
$\angle_e^h \text{ BrAsBr}$		99.8	[14]

<sup>a</sup>Microwave measurement.Table 5. Force field<sup>a</sup> and frequencies of vibration (cm<sup>-1</sup>) of AsBr<sub>3</sub>.

$f_r$	$f_{rr}$	$f_{r\alpha}$	$f_{r\alpha}^i$	$f_\alpha$	$f_{\alpha\alpha}$	Ref.
2.151(110)	0.325(90)	0.172(60)	0.200(80)	0.159(9)	0.022(8)	[25]
2.164	0.340	0.105	0.167	0.166	0.025	[14]

Method	$\omega_1$	$\omega_2$	$\omega_3$	$\omega_4$	Ref.
Spectr. <sup>b</sup>	289.7(4.0) <sup>c</sup>	125.4(2.0) <sup>c</sup>	284.0(8.0) <sup>c</sup>	92.5(1.5) <sup>c</sup>	[27]
Electr. diff.	285.9	124.9	293.6	94.1	[14]

<sup>a</sup>Force constants (mdyn/Å) for internal coordinate system.<sup>b</sup>Raman spectrum in the gaseous phase.<sup>c</sup>The uncertainty estimated in ref. [25].

From tables 4 and 5 one should note the following:

(1) The  $r_e^h$  parameter for the As-Br bond distance, directly determined from experiment, is numerically close to the  $r_\alpha$  distances for the two temperatures as calculated [25] from the  $r_a$  distances using spectroscopic distance corrections. The same is true for the angle parameters  $\angle_e^h \text{ BrAsBr}^3$  and  $\angle_\alpha \text{ BrAsBr}^3$ . It is remarkable that the  $r_e^h$  parameter is also close to the  $r_z$  microwave value.

<sup>3</sup>The designations  $\angle_e^h$  and  $\angle_\alpha$  mean that  $r_e^h$  and  $r_\alpha$  distances were used in the angle definitions, respectively.

(2) The force field of the  $\text{AsBr}_3$  molecule, independently determined from the diffraction data at two temperatures, is in good agreement with that estimated [25] from conventional amplitudes of vibration using supplementary spectroscopic information. The frequencies of vibration estimated from electron diffraction data alone are remarkably close to the Raman spectroscopic values.

These experimental results suggest the following conclusions:

(1) Electron diffraction is able to directly provide molecular structures free from harmonic vibrational effects. Hence, spectroscopic distance corrections can be avoided in structure analysis.

(2) Electron diffraction can be regarded as an excellent vibrational tool supplementing vibrational spectroscopy. The temperature variation technique of electron diffraction is able to provide general force fields of simple polyatomic systems with remarkably high accuracy. Both these new developments of modern electron diffraction may prove extremely useful when spectroscopic methods encounter difficulties in producing reliable values of vibrational frequencies for gaseous species. This is particularly important for high-temperature species where electron diffraction is easier to handle than optical spectroscopy.

Finally, the uncertainty limit in the electron diffraction evaluation of vibrational frequencies seems to be about  $10 \text{ cm}^{-1}$ , or less, provided delicate experimental details are scrupulously adhered to. Anyway, for some important situations this limit presumably would not exceed the matrix shift of the frequencies often observed in matrix isolation spectroscopic studies of high-temperature vapors.

#### 2.4.3 $\text{AlCl}_3$

For the monomeric  $\text{AlCl}_3$  molecule, the general force field cannot be derived from the four available fundamental frequencies since five constants are required for the symmetry coordinate system. Therefore, the supplementary use of electron diffraction data is crucial to obtainment of a general force field in this instance. The general force field of the  $\text{AlCl}_3$  molecule has been estimated by joint use of electron diffraction [28] and spectroscopic (see table 2) data [14]. In the analysis the equilibrium geometry of this molecule was assumed to be planar (see below), and the spectroscopic frequencies used are those presented in table 2. The results of the analysis in terms of the  $r_e^h$  (Al-Cl) bond distance and force constants are listed in table 3.

#### 2.4.4 $\text{HgI}_2$

The new analysis procedure was also applied to the linear  $\text{HgI}_2$  molecule [29] with the view to refinement of the bending  $\omega_2$  frequency for which the spectroscopic data, in the range of  $33\text{--}63 \text{ cm}^{-1}$ , are inconsistent [29].

Using the electron diffraction data alone resulted in the structural and force field parameters listed in table 6. Note (see table 6) that the value of  $\omega_2$  obtained by electron diffraction is in very good agreement with the infrared value of  $51 \text{ cm}^{-1}$  [30].

Table 6. Internuclear distance ( $\text{\AA}$ ), force constants ( $\text{mdyn/\AA}$ ) and vibrational frequencies ( $\text{cm}^{-1}$ ) of  $\text{HgI}_2$  as determined by electron diffraction in ref. [29].

Parameter	Electr. diff. alone	Joint electr. diff. and spectr. analysis
$r_e^h (\text{Hg-I})^a$	2.553	$2.554 \pm 0.003^b$
$f_r$	1.819	$1.838 \pm 0.005^c$
$f_{rr}$	-0.005	$-0.017 \pm 0.001^c$
$f_\alpha$	0.039	$0.0429 \pm 0.001^c$
$\omega_1$	156	156
$\omega_2$	49	51
$\omega_3$	235	237
$f_{21}^d$	-	0.0429
$f_{41}^e$	-	0.06688
$f_{61}^e$	-	0.001484

<sup>a</sup>The centrifugal distortion correction estimated by the classical expression is taken into account.

<sup>b</sup>The total uncertainty estimated at  $3 \sigma_{LS}$ .

<sup>c</sup>The standard deviation.

<sup>d</sup>The harmonic force constant for the new bending coordinate  $l = (\Delta x_{\text{HgI}}^2 + \Delta y_{\text{HgI}}^2)^{1/2}$ . Approximately  $f_{21} = f_\alpha$ . The  $\alpha$  is the angle displacement coordinate.

<sup>e</sup>The anharmonic force constants for the bending vibration.

The anharmonic approximation for the bending vibration has also been considered in ref. [29]. As a result, the anharmonic force constants for this vibration were estimated by electron diffraction (see table 6) leading to the evaluation of the bending vibration energy spectrum  $\Delta G_{v+1/2}$  ( $v = 0-5$ ) (for details ref. [29] should be consulted).



## 2.4.5 $\text{SnCl}_2$

It was hoped that application of the new analysis procedure to the bent  $\text{SnCl}_2$  molecule [31] would resolve discrepancies between various spectroscopic measurements of vibrational frequencies (see table 7).

Table 7. Vibrational frequencies ( $\text{cm}^{-1}$ ) of  $\text{SnCl}_2$  as determined by spectroscopy.

$\omega_1$	$\omega_2$	$\omega_3$	Type of spectrum <sup>a</sup>	Ref.
353	-	322	R, Ar matrix	[32]
341	124	320	R, $\text{N}_2$ matrix	[32]
354.8 } 352.3 }	- -	334.6 } 330.7 }	ir, Ar matrix	[33]
352	120	-	R, gas	[34]
350	120	-	CL, gas	[35]
220	120	275(278)	R, solution	[36]
398	102	406	Estimated values	[37]
-	120	-	E	[38]
355	122	-	E	[39]
377	207	-	E	[40]

<sup>a</sup>R-Raman, ir - infrared, CL - chemiluminescence, E - electronic.

The general force field of a bent  $\text{AB}_2$ -type molecule has four constants. Hence, they cannot all be obtained using conventional electron diffraction analysis for two measured amplitudes of vibration. Spectroscopic analysis suffers from a similar difficulty since only three fundamental frequencies of vibration are available from a spectrum. By contrast, there are five generalized amplitudes of vibration [11] only four of them being actually independent, however. Therefore, the new procedure for analysis allows the harmonic vibrational problem of this molecule to be completely solved by electron diffraction alone.

The results, based on electron diffraction data alone, are presented in column 2 of table 8. Comparison with the spectroscopic data listed in table 7 shows that the  $\omega_1$  and  $\omega_2$  electron diffraction frequencies are in good agreement with most reliable spectroscopic values. However, the  $\omega_3$  frequency is in fact not consistent with any of the spectroscopic values although it appears to be close to the estimated  $\omega_3 = 406 \text{ cm}^{-1}$  value reported in ref. [37]. For this reason, in the joint treatment only two spectroscopic frequencies  $\omega_1 = 352 \text{ cm}^{-1}$  and  $\omega_2 = 120 \text{ cm}^{-1}$  were included. The refined structural and force field

parameters thus obtained are presented in column 3 of table 8 along with the corresponding frequencies of vibration and Coriolis coupling constants  $\xi_{12}$  and  $\xi_{23}$ . Subsequent insertion in the analysis of the  $\omega_3 = 330 \text{ cm}^{-1}$  spectroscopic value led to an increase in the agreement factor by 1.1 percent.

Table 8. Structural and vibrational parameters<sup>f</sup> of  $\text{SnCl}_2$  [31].

Parameter	Electron diffr. alone	Joint electron diffr. and spectr. analysis
$r_e^h (\text{Sn-Cl}), \text{\AA}$	2.340 <sup>a</sup>	$2.340^a \pm 0.004^b$
$\angle \text{ClSnCl}^\circ$	98.6	$99.3 \pm 1.7^b$
$f_r, \text{mdyn/\AA}^\circ$	2.24	$2.22 \pm 0.06^c$
$f_{rr}, \text{mdyn/\AA}^\circ$	-0.21	$-0.23 \pm 0.02^c$
$f_{r\alpha}, \text{mdyn/\AA}^\circ$	-0.10	$-0.08 \pm 0.02^c$
$f_\alpha, \text{mdyn/\AA}^\circ$	0.14	$0.13 \pm 0.01^c$
$\omega_1, \text{cm}^{-1}$	362	356
$\omega_2, \text{cm}^{-1}$	121	121
$\omega_3, \text{cm}^{-1}$	397	398
$\xi_{12}^d$	-	0.348
$\xi_{23}^d$	-	0.938

<sup>a</sup>The centrifugal distortion correction is taken into account.

<sup>b</sup>The uncertainty is  $3 \sigma_{LS}$ .

<sup>c</sup>The standard deviation.

<sup>d</sup>Coriolis coupling coefficients calculated by equations cited in ref. [11].

<sup>e</sup>Angles in degrees.

<sup>f</sup>Force constants in  $\text{mdyn/\AA}^\circ$ , frequencies in  $\text{cm}^{-1}$ .

There is insufficient evidence at the present time to unambiguously resolve the discrepancy between the electron diffraction and spectroscopic values of  $\omega_3$ . A suggestion may be advanced that dimeric forms existing in the vapor at temperatures up to 850 K [41] might affect the electron diffraction evaluation of the  $\omega_3$  frequency. For this reason it seems evident that the  $\omega_3$  frequency of  $\text{SnCl}_2$  should be further refined by the electron diffraction technique but at conditions where dimeric species scattering can be safely ignored.

We conclude this section stating that the new procedure for electron diffraction analysis [14], combined with modern instrumentation, has considerably enhanced the facility for determination of molecular structures and potential functions from diffraction information. Many interesting problems with high-temperature vapors can now be resolved using the modern electron diffraction method.

### 3. Instrumentation and Experimental Methods

#### 3.1 Developments in apparatus

In recent years, several new high-temperature electron diffraction systems have been installed [42-44]. Modified electron diffraction instruments using high-temperature gas inlet systems are also in operation at the Institute of Chemical Technology at Ivanovo (USSR) and the Belorussian Institute of Technology at Minsk (USSR). The old instrument of Moscow University described earlier [1] has since been modified considerably to meet modern standards. The original low-power, and insufficiently stabilized, high-voltage supply has been replaced by that of the modern commercial EG-100 apparatus. The electron-optical system, the plate box, the sector assembly, the high-temperature evaporator and other key components have all been upgraded. This instrument still continues its everyday action.

In the USSR, the basic instrument for electron diffraction studies is the series-produced EG apparatus. This apparatus is a general purpose machine for studying solids, films, liquids and gases [45]. However, the commercial version is not adequately suited for gas-phase studies and particularly for those at high temperatures. For this reason, most systems incorporating this instrument, including the one at Moscow University, have been considerably modified except for the high-voltage supply [44]. To accomplish this, modifications have been made in the plate box and the sector assembly device. In addition, several new components have been developed. These include: (1) special evaporators with radiation heating for use up to 2000 °C, (2) a centering device for directing the electron beam into the center of the sector, (3) an optical device for camera geometry measurements, (4) special copper rings (coated with a graphite layer) used for trapping stray electrons thereby reducing extraneous background; these rings also reduce the light radiation from heated components, and (5) a control device for checking the perpendicularity of the electron beam with respect to the plane of the photographic plate. A more detailed description of some of these components is given below.

The plate box, charged with 12 plates of size 9x12 cm, is located in the photographic chamber (see fig. 1). A rod (1) shifts the plate box (2) into operating position under the sector blade (3). A trigger (5) holds down the photographic plates and releases one when the plate box is in fixed exposure position. A fluorescent screen (6) is placed at the bottom of the photographic chamber for visual control of the beam position relative to the center of the sector. Perfect alignment is considered to be achieved when the electron beam passes through the hole in the center of the 0.1 mm diameter sector and strikes the fluorescent screen. The quality of the beam alignment can be checked visually through a viewing window (7) or a system of prisms (8).

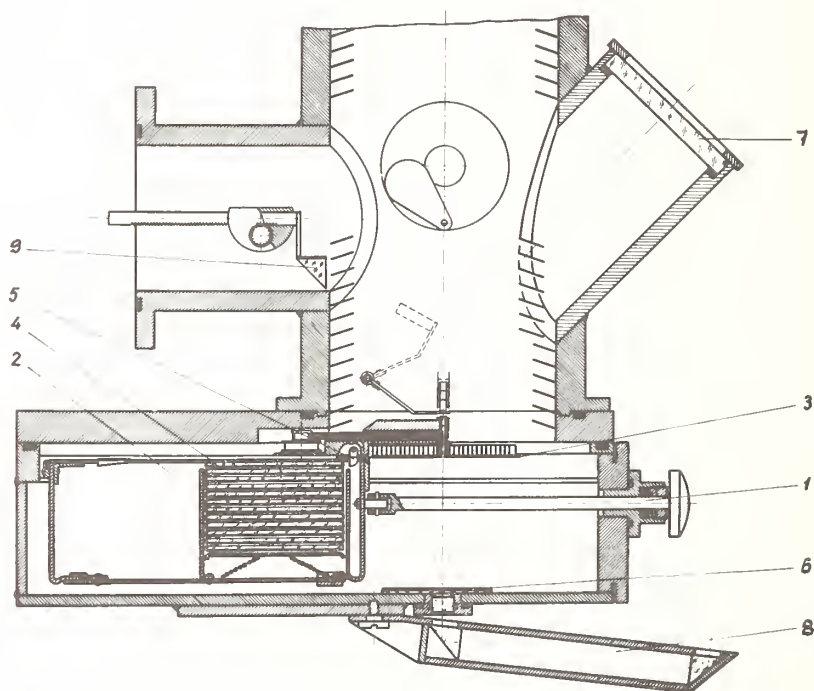


Figure 1. Schematic drawing of the lower part of the diffraction chamber: (1) rod for control of the plate box; (2) plate box; (3) sector; (4) cassette for photographic plates; (5) trigger; (6) fluorescent screen; (7) viewing window; (8) system of prisms; (9) prism with fluorescent screen.

To control the evaporator adjustment relative to the electron beam an additional prism-shaped fluorescent screen (9) covered by light-proofed material is inserted. The same screen (9) allows the diffraction picture to be viewed visually even at high temperatures. Before film exposure this screen is removed.

A center-driven sector assembly with sector blades made of bronze or duraluminium of 0.3 mm thickness is shown in figure 2. The maximum radius of the sector having  $r^3$  or

$(r^2 + r^4)/2$  shape is 70 mm. The beam stop (1) mounted on the support (4) is used primarily for absorbing the main electron beam. It can be simultaneously applied as a Faraday cage for measuring the electron beam current. The special beam traps (2) coated with a thin graphite layer are used for reducing the reflection of electrons striking the sector surfaces. The sector-to-photographic plate distance is in the range of 1.5-2.0 mm. The sector system rotates with a constant speed of 150 rev/min. The motion is transmitted by a rubber band (3). An arrangement is provided which guarantees a balanced weight distribution, and thus allows sector rotation that is practically free of disturbing vibrations.

The nozzle-to-plate distances of the apparatus are: 19, 48 and 74 cm. The nozzle position during the experiment is carefully controlled by a traveling microscope. The fixed position of the latter is periodically calibrated against special needles of standard length. The total limit of uncertainty in the nozzle-to-plate distance measurement does not exceed 0.02 mm.

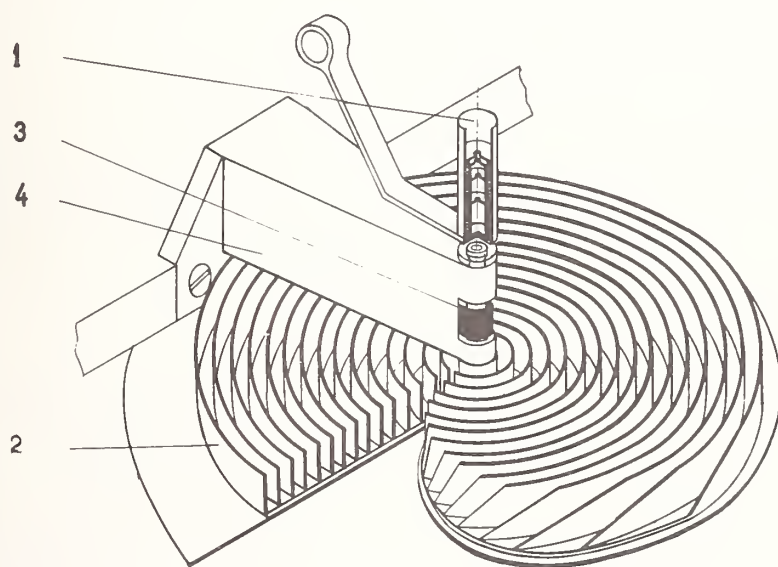


Figure 2. Sector device: (1) beam stop; (2) beam traps; (3) rubber band; (4) support.

### 3.2 High-temperature evaporators

For the obtainment of high temperatures, special evaporators were developed for the original work [1]. Two different methods of heating were applied, *viz.* heating by electron bombardment and radiation heating. The first type of evaporator used radiation heating and the consequent presence of a strong magnetic field seriously perturbed the primary electron beam. For this reason, at Moscow University [1,46] and other laboratories



(see, for example [43]), recent emphasis has been on the development of less perturbing electron bombardment heating methods. With such a system we have been able to obtain extremely high temperatures up to 2500 °C [47]. However, there are certain inherent disadvantages which make it somewhat inexpedient for general experimental use. These are:

- (1) The background produced by scattered and reflected electrons emitted from the cathode of the gas inlet system interferes with the diffracted electrons and lowers the quality of the photographic plates.
- (2) Light radiating from the heated cathodes of the evaporator provides an extra source of fogging on the photographic plates.
- (3) Electric discharges often arise in the system during the experiment and lead to an uncontrollable local superheating of the cell.

All of the above problems can be eliminated using a radiation heating system which has recently been designed and constructed by Ivanov [48]. An evaporator of this type, which can be heated up to 2000 °C, is shown in figure 3. The heating arrangement (fig. 4) is placed in the upper part of the cell. It consists of a flat spiral (3) made of tungsten wire of 0.3 mm diameter. The heating compartment is closed with a cover (4) to avoid extensive heat loss. The sample container (2) forms the lower part of the evaporator system. A small aperture at the top of the sample container protects the vapor canal (5) from being blocked by melted sample. Since the heating system is above the diffraction center the incoming electron beam is deflected only very slightly by the magnetic field of the heating spiral. This deflection can easily be compensated for by realinement of the electron beam.

Different styles of this radiation heater have been developed, according to the desired high temperature. For experiments up to 800 °C the cell of figure 5(a) with a container volume of 1 cm<sup>3</sup> is used. The cell 5(b) made of molybdenum and having a container volume of 0.2 cm<sup>3</sup> is suitable for temperatures up to 2000 °C. The power consumption is still below 1 kw. With the cell 5(c) the sample vapor can be superheated. The sample is placed in the lower chamber which is heated by conduction. The vapor streams through a vertical canal into the upper chamber where it is superheated by the radiator. The degree of superheating is regulated by varying the length and diameter of the vertical canal. For studies involving chemically aggressive substances the inner part of the sample container can be protected by a platinum insert (fig. 5(d)). The cell 5(e) having two sample containers and nozzles can be used for studying two different samples simultaneously one of them being the reference. This arrangement may also be useful for studying chemical reactions where the two canals are merged. A cell with merging vapor beams to increase the vapor density at the diffraction point is shown in figure 5(f).

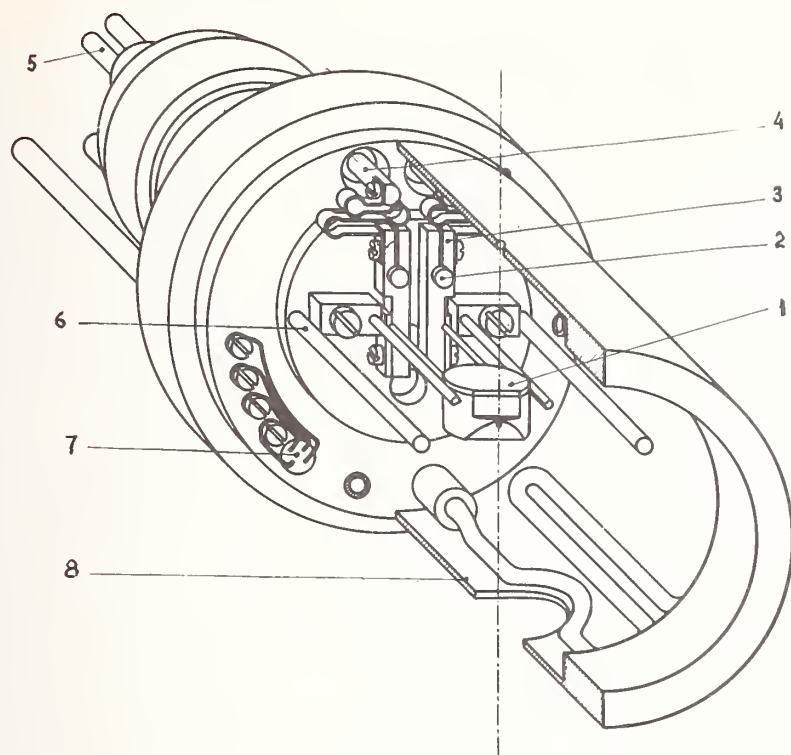


Figure 3. High-temperature inlet system: (1) cell; (2) insulator; (3) current-carrying plate; (4) current supply; (5) water cooling tube; (6) support for heat shield; (7) connections for thermocouples; (8) radiation shield.

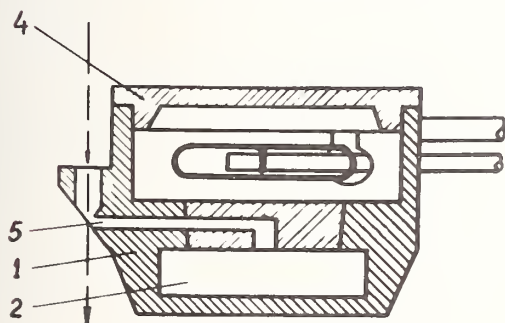
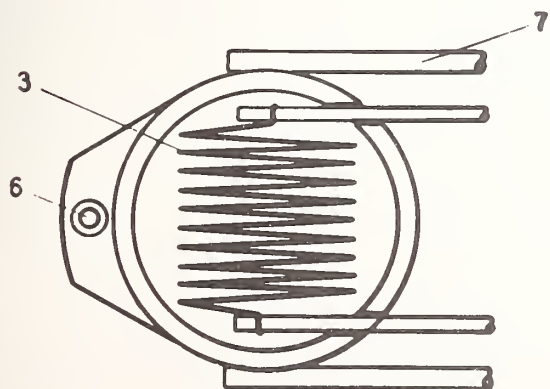


Figure 4. High-temperature cell:  
(1) body; (2) sample compartment;  
(3) tungsten spiral; (4) cover;  
(5) nozzle; (6) aperture;  
(7) support for cell.



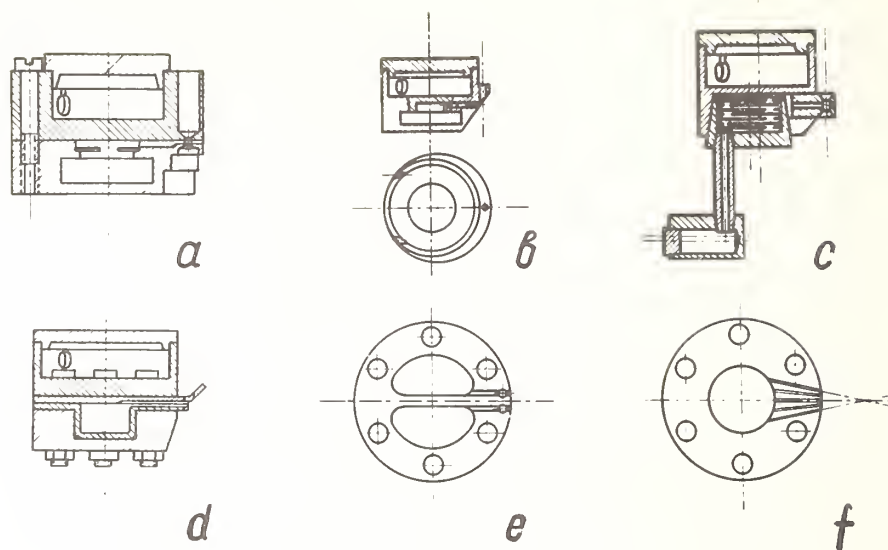


Figure 5. Various cell types (see the text).

For studies below 800-900 °C the various types of cells considered above do not generate much light radiation. Besides, the evaporator is surrounded by heat and radiation shields as shown in figure 3. By contrast, at higher temperatures special care has to be taken to protect the photographic plates from light exposure. In this case the photographic plates are covered with a thin layer of Indian ink which has to be carefully removed after exposure. The plates are then developed in the usual way. Protection of the photographic emulsion with thin aluminum foil pasted to the plates has been recommended recently [49].

The system temperature is measured by thermocouples welded to the body of the cell close to the nozzle. These thermocouples are calibrated against the melting points of several pure metals (Sn, Zn, Al, Cu). Temperature measurement uncertainty is estimated to be 20-30°.

A careful study of the errors resulting from the high-temperature technique indicated a total systematic uncertainty in internuclear distance measurements in the range of 0.12-0.17 percent.

The overall efficiency of the reconstructed EG-100 commercial apparatus has been checked against the reference vapor species  $I_2$  and  $CsCl$ .

### 3.3 The low-pressure technique

In modern electron diffraction equipment electron beams of 0.1-0.2 mm diameter are routinely in use, the beam current being in the range of 0.01-0.7 mA. The nozzle diameters are 0.1-0.5 mm and the beam vapor pressures vary in the interval of 1-10 mm Hg (sometimes

higher) causing viscous flow and cooling of the beam. The extra heating required experimentally limits the study of low-volatility substances since:

- (1) The condition of thermodynamical equilibrium between the solid and vapor phase can be violated due to rapid sample depletion and the failure to achieve uniform sample temperatures. This may cause an error in diffraction pattern assignment if the vapor phase composition is complex.
- (2) The vapor phase composition under these conditions may differ substantially from that of mass spectrometry since measurements by the latter technique are generally carried out at considerably lower vapor temperatures and pressures.
- (3) Additional uncertainty in vapor phase composition may result from the temperature-drop effect (resulting from adiabatic expansion under viscous flow).
- (4) Many substances may be thermally unstable at the temperatures needed for the diffraction experiment.
- (5) The population of excited rotational and vibrational levels is increased causing undesirable extra damping of the electron diffraction picture.
- (6) Sample utilization is inefficient since only a part of the vapor beam represents the scattering volume.
- (7) It is not possible to study molecular or ionic beams of low intensity.

These problems cannot be solved by a simple lowering of the temperature since in that case the extraneous scattering from the ambient gas in the diffraction chamber would be the largest part of the diffraction pattern. This is why it is generally not possible to obtain high-quality diffraction patterns in conventional apparatus at vapor pressures of 1 mm Hg or lower and long exposure times.

Bauer and Kimura [50] in 1961 developed a low-pressure electron diffraction technique. In their arrangement, the parallel electron beam passes along a slit-shaped nozzle (0.5 x 10 mm) which is parallel to the electron-optical axis of the apparatus. The shape of the nozzle makes it possible to increase the number of molecules crossing the electron beam which is important at low vapor pressures. The electrons scattered along the nozzle are focused by a two-lens system on the plane of the detector. However, this interesting arrangement was not brought into routine use.

Recently, a low-pressure technique of gas-phase electron diffraction has been developed at Moscow University [51]. No considerable reconstruction of the apparatus was necessary.

It is well known that the scattered intensity is directly proportional to the product of the number of the molecules in the scattering volume and the number of electrons passing through this volume (see, for example [52]). Approximate calculations show that at ordinary conditions of an electron diffraction experiment, the scattering volume contains  $10^{10}$ - $10^{12}$  molecules and the number of electrons passing through this volume is  $10^{10}$ - $10^{13}$  electrons per sec. This optimal ratio can be maintained at a vapor pressure reduced to  $10^{-2}$  mm Hg, provided the scattering volume is simultaneously increased. This can be done by changing the electron beam shape in the region of scattering and by an increase of the beam current.

In the method developed at Moscow University [51] cells with slit-shaped (0.1 x 2 mm) nozzles are used (see fig. 6). The cell is heated by radiation to a temperature where the



sample vapor pressure is  $10^{-1}$ - $10^{-2}$  mm Hg. These experimental conditions approximate molecular flow. In the devised arrangement, the cone-shaped convergent electron beam direction is perpendicular to the plane of the vapor beam (see fig. 6a). The electron beam diameter in the scattering region is about 2 mm. This beam is focused on the photographic plate. The total beam current is enhanced up to 15-20  $\mu$ A. The necessary parameters of the electron beam are obtained by installation of a special diaphragm having a diameter of 2.0-2.5 mm in the electron-optical system of the diffraction instrument. This technique has been adapted to routine use with the EG-100 system.

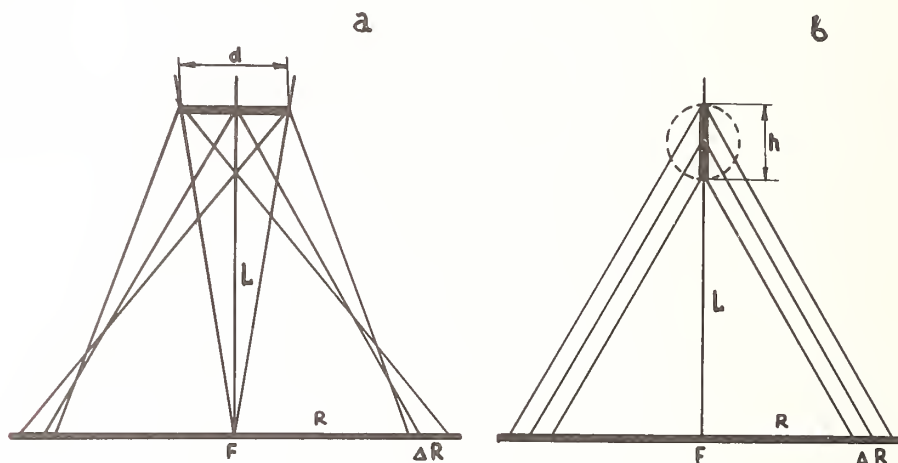


Figure 6. Geometrical relations for electron scattering: (a) low-pressure technique; (b) conventional technique.

It is seen from figure 6a that the use of a cone-shaped electron beam may cause the diffraction rings to be widened. It can be shown that the widening  $\Delta R$  of the diffraction ring having radius  $R$  is

$$\Delta R = \frac{d R^2 (4 L^2 + d^2)}{4 L^4 - d^2 R^2} \approx \frac{R^2}{L^2} d \quad (11)$$

where  $d$  is the electron beam diameter in the scattering region and  $L$  is the distance between the scattering region and photographic plate. However, eq. (11) does not take into account the widening caused by the height  $h$  of the vapor beam in the scattering region. This widening can be shown to be [see fig. 6(b)]



$$\Delta R = \frac{R}{L} k . \quad (12)$$

Hence, the total widening can be estimated to be

$$\Delta R_{\text{tot}} \approx \frac{R^2}{L^2} d + \frac{R}{L} h . \quad (13)$$

Estimates for 40 and 80 kV electrons and ring radii of 40 and 60 mm, respectively, showed that the relative widenings are 0.05-0.07 percent for  $L = 48$  cm and 0.25-0.35 percent for  $L = 19$  cm. Comparison of these widenings with those of a conventional parallel-beam technique shows that they are of the same order of magnitude for  $L > 40$  cm. It is worth mentioning that the widening under discussion may influence only the determination of vibrational parameters of the molecule.

The low-pressure technique has been checked against gaseous CsCl taken as the reference. The results presented in table 9 indicate that data obtained by the low-pressure electron diffraction technique are in good agreement with those of spectroscopy particularly for amplitudes of vibration.

Table 9. Experimental conditions and structural parameters of CsCl as obtained by conventional and low-pressure techniques of electron diffraction.<sup>a</sup>

Conditions o. parameters	Conventional technique	Low-pressure technique
Nozzle shape	cylinder	slit
Nozzle dimension	0.5 mm	0.1 x 2.0 mm
Nozzle temp., °C	740	570
Vapor pressure, mm Hg	1	0.01
Electron beam shape	parallel	cone
Electron beam diameter, mm	0.3	2.0
Electron beam current, $\mu\text{A}$	0.75	18.0
$r_g$ (Cs-Cl), Å ED	2.953(8)	2.942(9)
SP	2.952	2.943
$l$ (Cs-Cl), Å ED	0.128(8)	0.124(8)
SP	0.137	0.125

<sup>a</sup>ED - electron diffraction values.

SP - values calculated from spectroscopic data.

## 4. Results

This section focuses upon the results of gas-phase structural determinations of halides, oxides, complex halides and salts of oxyacids which have been obtained during the period from 1967 at Moscow University, sometimes in cooperation with other laboratories.

### 4.1. Halides

#### 4.1.1 Monohalides

Experimental data of previous electron diffraction studies on the structures of dimers for the halides of group 1 elements were consistent with a planar ring model [53]. However, in the case of  $\text{Li}_2\text{F}_2$  only the Li-F bond distance was determined and with a value of  $1.68 \pm 0.02$  Å. Reinvestigation of the lithium fluoride vapor by electron diffraction [54] has been carried out in cooperation with the Ivanovo group. The nozzle temperature was  $1360 \pm 50$  K. In the structure analysis the complex composition of the vapor has been considered since mass-spectrometric data [55,56] indicated the presence of dimeric as well as monomeric and trimeric species. The molecular parameters of monomeric LiF were assumed on the basis of spectroscopic data [57] and kept constant in the structure analysis. The structures of the dimer and the trimer were assumed to be cyclic and composed of alternating metal and fluorine atoms. The Li-F bond distances in the dimer and the trimer were taken to be equal. Since the scattering power of Li atoms is small, electron diffraction failed to measure the Li-Li distance both in the dimer and trimer species. However, other structural parameters of  $\text{Li}_2\text{F}_2$  obtained in ref. [54] can be regarded as consistent with a planar rhombic model resulting from the absence of a permanent electric dipole moment [58].

Structural parameters for  $\text{Li}_2\text{F}_2$  and the vapor phase composition, as determined by electron diffraction [54], are presented in table 10. It is worth noting that the vapor phase composition is consistent with mass spectrometric determinations [55,56]. The discrepancy between the  $r(\text{Li-F})$  value found in ref. [54] and that of an earlier electron diffraction study [53] can be accounted for by disregard of the complex vapor phase composition in the early work.

By analogy, the related  $\text{Tl}_2\text{F}_2$  molecules prevailing over solid thallium(I) fluoride [59] can be expected to have a similar rhombic structure. However, the results of thermodynamic studies [60,61], of infrared [62] and photoelectron spectra [63] were interpreted as favoring a linear geometry of the type F-Tl-Tl-F. A slow electron scattering study [64] showed that the instantaneous dipole moment of the  $\text{Tl}_2\text{F}_2$  molecule is several Debye units. This fact was associated with the distortions of a linear geometry. However, a molecular beam of  $\text{Tl}_2\text{F}_2$  is not deflected in an inhomogeneous electric field [65] thus indicating high molecular symmetry.

Electron diffraction patterns of  $\text{Tl}_2\text{F}_2$  [66] were obtained at a temperature of 700 K. The structure analysis unambiguously indicated an alternating metal-fluorine cyclic structure similar to that of the lithium halides. The effective configuration of the molecule was found to be slightly non-planar (see table 10). However, the uncertainty in

the F...F distance determination is rather large. Thus the data obtained can be regarded only as consistent with a planar rhombic structure. It should be pointed out that this electron diffraction result stimulated new investigations of the infrared and Raman spectra of  $\text{Tl}_2\text{F}_2$  and  $\text{Tl}_2\text{Cl}_2$  [67] and reinvestigation of the photoelectron spectrum of  $\text{Tl}_2\text{F}_2$  [68]. These studies unambiguously assigned a rhombic geometry to both molecules.

Table 10. Structural parameters of  $\text{Li}_2\text{F}_2$  and  $\text{Tl}_2\text{F}_2$ .<sup>a</sup>

Parameter	Molecule	
	$\text{Li}_2\text{F}_2$	$\text{Tl}_2\text{F}_2$
$r_g$ (M-F)	1.746(15)	2.305(14)
$l$ (M-F)	0.102(11)	0.109(10)
$r_g$ (M-M)	2.11 <sup>b</sup>	3.674(10)
$l$ (M-M)	0.18 <sup>b</sup>	0.140(6)
$r_g$ (F-F)	2.765(20)	2.64(14)
$l$ (F-F)	0.21(2)	0.18 <sup>b</sup>
$\angle_g$ FMF <sup>c</sup>	104.7(2,3)	69.6(4.7)
$\angle_g$ MFM	-	105.7(1.3)
$\alpha$ (MF) %	30 + 15	48 ± 8
	- 30	
$\alpha(\text{M}_e\text{F}_3)$ %	10 ± 5	-

<sup>a</sup>The internuclear distances and amplitudes of vibration in Å units. Parenthesized values are total uncertainties.

<sup>b</sup>Assumed.

<sup>c</sup>Angles in degrees.

#### 4.1.2 Dihalides

Among the dihalides, the studies of gaseous  $\text{SnCl}_2$  [69] and  $\text{PbCl}_2$  [70] molecules are noteworthy. The study of  $\text{PbCl}_2$  has been carried out at Moscow University and the Budapest laboratory independently. It was decided to reinvestigate the structures of these molecules in the hope of obtaining a more accurate valence angle which was not available from previous studies [71,72]. Moreover, the electron diffraction data for the  $\text{SnCl}_2$  molecule were treated by a new analysis procedure (see above).

The  $\text{SnCl}_2$  study was carried out at a temperature of  $683 \pm 5$  K and that of  $\text{PbCl}_2$  at 963 K (Moscow) and 853 K (Budapest). The structural results are presented in table 11.

These new electron diffraction studies allowed not only measurement of the valence angle but also refinement of the metal-halogen bond distances. Furthermore, spectroscopic calculations of harmonic distance corrections have made it possible to obtain the  $r_\alpha$

structure, free from harmonic vibrational effects. The  $\delta_\alpha$  ClMeCl angle parameters are:  $\text{SnCl}_2$ ,  $100^\circ$ ;  $\text{PbCl}_2$ ,  $98.7$  and  $98.0^\circ$  from two independent investigations.

Table 11. Structural parameters of  $\text{SnCl}_2$  and  $\text{PbCl}_2$ .<sup>a</sup>

Parameter	$\text{SnCl}_2$	$\text{PbCl}_2$	
		Budapest	Moscow
$r_a$ (M-Cl)	2.346(7)	2.443(5)	2.440(5)
$r_\alpha$ (M-Cl)	2.342	-	-
$r_a$ (Cl-Cl)	3.565(31)	3.645(21)	3.640(35)
$l$ (M-Cl)	0.059(6)	0.102	0.080(6)
$l$ (Cl-Cl)	0.221(27)	0.223(20)	0.199(27)
$\delta_a$ ClMeCl <sup>b</sup>	99(1)	98.3(1.0)	97.0(1.4)
$\delta_\alpha$ ClMeCl <sup>b</sup>	100	98.7 <sup>c</sup>	98.0 <sup>c</sup>

<sup>a</sup>The internuclear distances and amplitudes of vibration in Å units. Parenthesized values are total uncertainties.

<sup>b</sup>Angles in degrees.

<sup>c</sup>These values may be compared with a value of  $96 \pm 3^\circ$  obtained by the matrix isolation isotope shift method [Hastie, J. W., Hauge, R. H., and Margrave, J. L., High Temp. Sci. 3, 56 (1971)].

#### 4.1.3 Trihalides

Among the trihalides, the electron diffraction reinvestigation of monomeric  $\text{AlCl}_3$  [28] is of special interest since the structure of this molecule has been the subject of controversy in recent years.

It is well known that the dimeric form  $\text{Al}_2\text{Cl}_6$  is produced by vaporization of aluminum trichloride [73]. For this reason the pioneering electron diffraction investigation [74] was carried out using the double effusion cell technique [16]. The structural data obtained in the original study [74] led to the conclusion that the effective configuration of the  $\text{AlCl}_3$  molecule was flat pyramidal. However, the obtained ClAlCl angle of  $118.0 \pm 1.5^\circ$ , allowing for the possibility of shrinkage, has been taken to indicate a planar equilibrium geometry. Taking this geometry assignment, the authors of ref. [75] using electron diffraction measurements of amplitudes and shrinkage were able to estimate the out-of-plane and symmetric stretching frequencies of  $\text{AlCl}_3$  not available from the literature at that time. These estimates were not supported later on by spectroscopy, however.

Subsequently, from infrared data [76,77] different assignments were made relative to the molecular geometry of  $\text{AlCl}_3$ . Thus in ref. [77] on the basis of selection rules it was

concluded that the  $\text{AlCl}_3$  molecule was pyramidal. The authors supplemented their study with a normal coordinate analysis suggesting a  $\text{ClAlCl}$  angle near  $112^\circ$ . More recent spectroscopic studies [22,23] have yielded a complete and unambiguous set of vibrational frequencies for  $\text{AlCl}_3$  and a planar equilibrium geometry. This assignment has been supported by a new up-to-date electron diffraction study of the  $\text{AlCl}_3$  molecule [28]. The structural results obtained are presented in table 12. The  $r_\alpha$  parameters calculated from electron diffraction data using spectroscopic frequencies from [22,23] unambiguously indicate the equilibrium geometry of this molecule to be planar.

Table 12. Structural parameters of  $\text{AlCl}_3$ .<sup>a</sup>

Parameter	Ref. [74]		Ref. [28]	
	Al-Cl	Cl-Cl	Al-Cl	Cl-Cl
$r_g$	2.06(1)	3.53(1)	2.068(4)	3.571(9)
$r_\alpha$	-	-	2.050(4)	3.567(9)
$l_{\text{exp}}$	0.060(5)	0.180(10)	0.074(4)	0.187(6)
$l_{\text{calc}}$	0.065	0.152	0.077	0.185
$\angle_g \text{ClAlCl}^b$	118.0(1.5)		119.38(0.64)	
$\angle_\alpha \text{ClAlCl}^b$	-		120.90(0.64)	

<sup>a</sup>The internuclear distances and amplitudes of vibration in Å units. Parenthesized values are total uncertainties.

<sup>b</sup>Angles in degrees.

In recent years a series of electron diffraction investigations of the molecular structures of rare-earth trihalides has been carried out (for a summary see [78]). These studies were performed mainly at the Ivanovo Institute of Chemical Technology in cooperation with the Moscow University group.

The first investigations of rare-earth trihalides by electron diffraction were carried out about 20 years ago [79,80]. However, the structural data on the  $\text{LaX}_3$  and  $\text{NdX}_3$  molecules (X is F, Cl, Br, and I) and  $\text{ScF}_3$  did not contribute much to the discussion of the rare-earth halide structures since the molecular geometry in these early studies cannot be considered to be unambiguously established. Also, no conclusive evidence on the structures of these molecules has been gained from numerous subsequent spectroscopic studies [81-86]. Thus in infrared spectra of the trifluorides of La, Ce, Nd, Eu, Gd, Tb, Ho, Yb and Lu, isolated in solid argon matrices [81,82], four absorption bands have been observed. On the basis of selection rules, the pyramidal geometry was indicated for all



the molecules studied.<sup>4</sup> In other studies [83,84], infrared spectra of the trifluorides of La, Ce, Pr, Nd, Sm and Eu, isolated in solid argon, krypton and nitrogen matrices, suggested, by contrast, that these molecules be assigned a planar configuration.

Electric deflection studies on molecular beams of the lanthanide trifluorides have been carried out [87]. Substantial refocussing, indicative of a pyramidal geometry, has been observed for ScF<sub>3</sub>, LaF<sub>3</sub>, GdF<sub>3</sub> and LuF<sub>3</sub>. Weaker refocussing was present for other molecules barely above the noise level thus indicating the molecules to be planar or slightly pyramidal. Therefore, a firm conclusion for rare-earth trihalide structures was not possible from these studies.

A summary of the results of recently started systematic up-to-date electron diffraction studies [88-93] on the molecular structures of some rare-earth trihalides is presented in table 13.

Table 13. Structural parameters of rare-earth trihalides.<sup>a</sup>

Molecule	Temp. K	$r_g(M-X)$	$r_g(X-X)$	$l(M-X)$	$l(X-X)$	$\sum_g X-M-X^b$	Ref.
ScF <sub>3</sub>	1600(100)	1.926(5)	3.158(37)	0.078(6)	0.224(34)	110.0(2.5)	[89]
LaCl <sub>3</sub>	1250(50)	2.590(6)	4.309(44)	0.084(8)	0.338(75)	112.5(2.5)	[78]
PrCl <sub>3</sub>	1250(50)	2.553(6)	4.204(71)	0.085(5)	0.389(65)	110.8(2.5)	[92]
GdCl <sub>3</sub>	1325(25)	2.489(6)	4.150(43)	0.084(5)	0.312(42)	113.0(1.5)	[91]
TbCl <sub>3</sub>	1250(50)	2.478(5)	4.070(48)	0.091(5)	0.339(45)	110.5(1.7)	[91]
HoCl <sub>3</sub>	1200(50)	2.459(6)	4.058(38)	0.092(5)	0.321(39)	111.2(2.0)	[92]
LuCl <sub>3</sub>	1250(50)	2.417(6)	3.996(37)	0.086(5)	0.287(38)	111.5(2.0)	[89]
LaBr <sub>3</sub>	1300(100)	2.741(5)	4.634(43)	0.116(4)	0.416(39)	115.5(2.0)	[90]
GdBr <sub>3</sub>	1150(100)	2.640(6)	4.425(50)	0.098(4)	0.394(45)	113.8(2.5)	[88]
LuBr <sub>3</sub>	1100(100)	2.561(6)	4.308(33)	0.089(3)	0.333(31)	114.5(1.8)	[88]
PrI <sub>3</sub>	1050(30)	2.904(6)	4.835(57)	0.113(4)	0.448(45)	112.7(2.2)	[93]
NdI <sub>3</sub>	1070(30)	2.881(5)	4.772(48)	0.100(4)	0.397(35)	111.8(1.8)	[93]
GdI <sub>3</sub>	1060(30)	2.841(5)	4.596(57)	0.100(4)	0.416(40)	108.0(2.0)	[93]
LuI <sub>3</sub>	1015(30)	2.771(6)	4.660(51)	0.106(6)	0.339(30)	114.5(2.1)	[93]

<sup>a</sup>The internuclear distances and amplitudes of vibration in Å units. Parenthesized values are total uncertainties.

<sup>b</sup>Angles in degrees.

<sup>4</sup>Editor's note: This interpretation also gave the most consistent agreement between statistical and experimental entropies [82].

The effective configuration of all the molecules studied was found to be pyramidal with a central atom valence angle varying in the narrow range of  $110-115^\circ$  for different molecules. However, no conclusive evidence can be provided at this time on the symmetry type of the equilibrium geometry since no spectroscopic data are available on most of the molecules studied. In a few cases when frequencies of vibration are determined or estimated ( $\text{ScF}_3$ ,  $\text{LaCl}_3$ ,  $\text{GdCl}_3$ ,  $\text{LuCl}_3$  and  $\text{PrI}_3$ ) the comparison of calculated and observed shrinkages indicates a pyramidal equilibrium configuration. However, this inference based on spectroscopic calculations in the harmonic approximation could not be considered as fully unambiguous. Namely, anharmonicity in the angle bending vibration may seriously affect the angle parameter determination. Particularly, for molecules with relatively low frequencies of bending vibration (such seems to be the case for many rare-earth halides) the barrier separating two equivalent potential minima at pyramidal configurations may be rather low resulting in a large amplitude of motion. Ignorance of this effect in spectroscopic calculations of equilibrium angle parameters can cause uncertainty in electron diffraction data interpretation. Furthermore, for some molecules the influence of low-lying electronic states causing vibronic interactions should be considered. These states are expected to exist in some of the rare-earth halides [94]. Thus the rare-earth trihalides structural problem at this time calls for further experimental and theoretical study.

#### 4.1.4 Tetrahalides

Results of structural investigations of some  $T_d$ -symmetry tetrahalides are presented in table 14. These studies were carried out mainly in cooperation with the Ivanovo electron diffraction group. In addition to structural parameters, for most of the molecules listed in table 14 the force fields and Coriolis coupling constants were estimated using supplementary spectroscopic information. It is to be noted that for the  $\text{CeF}_4$  and  $\text{UF}_4$  molecules the  $r_g(\text{X}...\text{X})$  distances listed in table 14 are obtained assuming the  $T_d$ -symmetry for the equilibrium geometry. However, slightly distorted configurations of  $C_{3v}$  or  $C_{2v}$  symmetries seem somewhat preferable. Regrettably, for these molecules very little supplemental experimental evidence is available to make a more conclusive inference on the departure of structure from the  $T_d$ -symmetry type.

The  $\text{VBr}_4$  molecule data merit some discussion. It was found for this molecule [97] that any departure from the  $T_d$ -symmetry model results in poorer agreement with experiment. This finding has been interpreted as an indication of absence of any static distortions of the molecule which are predicted by the Jahn-Teller theorem [98]. Since  $\text{VBr}_4$  is considered to be in a doubly degenerate ground electronic state in a tetrahedral configuration [99] the electron diffraction data obtained [98] were rationalized in terms of the dynamic Jahn-Teller effect. The experimental estimates of vibronic parameters are: the first-order vibronic interactions constant  $^0a_E^0 = 1.36 \pm 0.07$ , the Jahn-Teller stabilization energy  $E_{JT} = 62 \pm 5 \text{ cm}^{-1}$  and the dynamic distortion parameter  $\rho_0 = 0.183 \pm 0.007 \text{ \AA}$ .

Table 14. Structural parameters of some tetrahalides.<sup>a</sup>

Molecule	Temp. K	$r_g(\text{M-X})$	$r_g(\text{X-X})$	$l(\text{M-X})$	$l(\text{X-X})$	Ref.
TiF <sub>4</sub>	475(15)	1.754(3)	2.859(11)	0.044(2)	0.129(7)	[78]
ZrF <sub>4</sub>	975(50)	1.902(4)	3.100(22)	0.059(3)	0.178(13)	[78]
HfF <sub>4</sub>	1025(50)	1.909(5)	3.140(34)	0.059(3)	0.187(23)	[78]
CeF <sub>4</sub>	1180(50)	2.040(10)	3.280(50)	0.088(12)	0.288(50)	[96]
UF <sub>4</sub>	1300(50)	2.068(5)	3.362(35)	0.067(3)	0.259(33)	[96]
TiBr <sub>4</sub>	300(5)	2.339(5)	3.812(10)	0.043(5)	0.134(6)	[95]
ZrBr <sub>4</sub>	470(15)	2.465(4)	4.012(13)	0.062(3)	0.192(12)	[95]
HfBr <sub>4</sub>	470(15)	2.450(4)	3.981(10)	0.054(3)	0.177(10)	[95]
TiI <sub>4</sub>	400(15)	2.546(4)	4.138(8)	0.052(6)	0.169(8)	[95]
ZrI <sub>4</sub>	490(20)	2.660(10)	4.351(24)	0.060(6)	0.215(20)	[95]
HfI <sub>4</sub>	540	2.662(8)	4.346(13)	0.072(3)	0.212(14)	[95]
VBr <sub>4</sub>	660(5)	2.276(4) <sup>b</sup>	-	0.081(4)	0.211(11)	[97]

<sup>a</sup>The internuclear distances and amplitudes of vibration in Å units. <sup>°</sup> Parenthesized values are total uncertainties.

<sup>b</sup> $r_\alpha$  - value.

#### 4.1.5 Pentachlorides

The molecular structures, vibrational assignments, and barriers to pseudorotation of gaseous niobium pentachloride and tantalum pentachloride were determined from electron diffraction data [100]. This study has been carried out jointly by the Moscow and Oslo University groups. It has been found that the pentachlorides of niobium and tantalum have trigonal bipyramidal structures ( $D_{3h}$ -symmetry) with thermally average axial bonds,  $r_\alpha$ , longer than the equatorial ones by 0.097(9) and 0.142(5) Å, respectively. The equatorial bonds are  $r(\text{Nb-Cl}) = 2.241(4)$  and  $r(\text{Ta-Cl}) = 2.227(3)$  Å. Calculated amplitudes of vibration for the  $e'$ -type of bending frequencies assigned as  $\nu_6$  (equatorial in-plane bend) <  $\nu_7$  (axial-equatorial bend) agree significantly better with the experimental vibrational amplitudes than do amplitudes for the opposite assignment. Assuming an analytical quartic-harmonic potential for the pseudorotational motion of the molecules, barriers to pseudorotation of 1.5(0.7) and 1.2(0.6) kcal mol<sup>-1</sup> are estimated from the electron diffraction data for NbCl<sub>5</sub> and TaCl<sub>5</sub>, respectively.

## 4.2 Oxides

In recent years the attention of the Moscow University group has been directed towards structural studies of  $\text{Al}_2\text{O}_3$ ,  $\text{NbO}_2$ ,  $\text{B}_2\text{O}_3$  and molecular species above the heated molybdenum, chromium, and tungsten oxides.

In the studies of  $\text{Al}_2\text{O}_3$  [101] ( $T = 2300\text{--}2400\text{ K}$ ) and  $\text{NbO}_2$  [47] ( $T = 2700\text{ K}$ ) the modified evaporator with electron bombardment heating [46] similar to that described earlier [1] has been used.

### 4.2.1 $\text{Al}_2\text{O}_3$ and $\text{NbO}_2$

Molybdenum and tungsten were the materials used in the fabrication of the cells for  $\text{Al}_2\text{O}_3$  and  $\text{NbO}_2$ , respectively. In the study of  $\text{Al}_2\text{O}_3$ ,  $\text{Al}_2\text{O}_3$  was taken as the source of vapor since it is known to be vaporized as  $\text{Al}_2\text{O}_3$  [102]. The structural results indicating a bent geometry for both oxides are shown in table 15.

Table 15. Structural parameters<sup>a</sup> of  $\text{Al}_2\text{O}_3$  [101] and  $\text{NbO}_2$  [47].

Parameter	$\text{Al}_2\text{O}_3$	$\text{NbO}_2$
$r_g(\text{M-O})$	1.73(1)	1.729(9)
$r_g(\text{M-M})$	3.26(3)	-
$r_g(\text{O-O})$	-	2.637(33)
$l(\text{M-O})$	0.11(1)	0.080(9)
$l(\text{M-M})$	0.23(2)	-
$l(\text{O-O})$	-	0.163(50)
$\angle_g \text{ Al-O-Al}^b$	141(5)	-
$\angle_g \text{ O-Nb-O}^b$	-	100(4)

<sup>a</sup>The internuclear distances and amplitudes of vibration in Å units. Parenthesized values are total uncertainties.

<sup>b</sup>Angles in degrees.



#### 4.2.2 B<sub>2</sub>O<sub>3</sub>

The molecular structure of B<sub>2</sub>O<sub>3</sub> has been the subject of several electron diffraction investigations. In the original work [103] a V-shaped structure having two linear BO<sub>2</sub>-fragments was regarded as the most probable. It was assumed that in the BO<sub>2</sub>-fragments the two boron-oxygen bond distances differ, being 1.36(2) and 1.20(3) Å. A tentative value of 95° was ascribed to the central oxygen valence angle. As the experimental methods of high-temperature electron diffraction have considerably improved since that time, several attempts were subsequently made to refine the structural data on the B<sub>2</sub>O<sub>3</sub> molecule.

Based on the analysis of the radial distribution curve it was concluded [104,105] that the difference between the two boron-oxygen bond distances does not exceed 0.1 Å. A value of 132±5° was obtained for the central oxygen atom valence angle [105].

The present authors carried out a new electron diffraction investigation on the molecular structure of B<sub>2</sub>O<sub>3</sub> using up-to-date experimental instrumentation and data treatments. The electron diffraction patterns of B<sub>2</sub>O<sub>3</sub> were made using the low-pressure technique described above at a temperature of 1620±20 K which was only slightly higher than that of the mass spectrometric experiment [106]. The sample was degassed carefully in the vacuum at a temperature of about 1300 K before the electron diffraction experiment was started. In the structure analysis the V-, W-, and T-shaped models of B<sub>2</sub>O<sub>3</sub> were tested against the experimental data. Special attention was devoted to consideration of the difference of the two boron-oxygen bond distances. The structural results are presented in table 16 where they are paralleled with those obtained earlier [105]. It has been concluded again that the V-shaped model is the most probable one. The difference in two boron-oxygen bond distances was found to be in the range of 0.1 Å. Thus the estimate of this difference in previous studies [104,105] has been supported. However, in the new study the amplitudes of vibration for principal distances have been refined considerably. Moreover, the effective configuration of the BO<sub>2</sub>-fragments has been found to be slightly bent in terms of the  $r_g$ -representation of internuclear distances. This finding can be attributed to the Bastiansen-Morino shrinkage effect [11].

#### 4.2.3 Oxides of Cr, Mo, and W

The studies of chromium, molybdenum and tungsten oxides provide examples where high-temperature electron diffraction is being used under conditions of complex vapor phase composition. The prevailing species above the solid trioxides of chromium, molybdenum and tungsten are the trimers and the tetramers (the vapor phase composition data above these systems are summarized in [107]).

Molybdenum trioxide vapor has been studied earlier by electron diffraction [108]. The data were interpreted under the assumption that the vapor consisted of cyclic trimeric species with alternating molybdenum and oxygen atoms forming a six-membered ring (see fig. 7). Based on the structure analysis it was concluded that the MoO<sub>4</sub>-fragments were distorted tetrahedra. The total symmetry of the molecule was found to be D<sub>3h</sub>, i.e., the six-membered ring was considered to be planar.



Table 16. Structural parameters of  $B_2O_3$ .<sup>a</sup>  
( $O_1 - B_2 - O_3 - B_4 - O_5$ )

Parameter	Data [105]	Present authors
$r_g(B_2-O_1)$	1.26(10) <sup>b</sup>	1.219(7)
$r_g(B_2-O_3)$		1.323(8)
$r_g(O_1-O_3)$	2.53(1)	2.525(5)
$r_g(B_2-O_5)$	3.52(2)	3.555(73)
$l(B_2-O_1)$	0.11(1) <sup>b</sup>	0.047(9)
$l(B_2-O_3)$		0.053(11)
$l(O_1-O_3)$	0.11(1)	0.071(3)
$l(B_2-O_5)$	0.14(2)	0.237(34)
$\sum_g B-O-B^c$	132(6)	137.5(6.3)

<sup>a</sup>The internuclear distances and amplitudes of vibration in Å units. Parenthesized values are total uncertainties.

<sup>b</sup>The average value for  $B_2-O_1$  and  $B_2-O_3$  distances.

<sup>c</sup>Angles in degrees.

Determination of the molecular structure for monomeric  $MoO_3$  has been attempted [51]. However, it was not possible to select conditions where  $MoO_3$  species prevail in the vapor phase. Only for the vapor over solid  $MoO_2$  [109] does the partial pressure of  $MoO_3$  exceed that of all other components. According to the mass spectrometric analysis [110,111] the vapor over solid  $MoO_2$  contains several species other than  $MoO_3$ , namely  $MoO_2$ ,  $Mo_2O_6$ , and  $Mo_3O_9$ . However, at temperatures of 1700-1770 K the partial pressures of  $MoO_3$  and  $Mo_2O_6$  are comparable whereas other components exist in smaller amounts.

The electron diffraction patterns of the  $MoO_2$  vapor [51] were recorded at a temperature of about 1870 K using the low-pressure technique. The temperature of the experiment was somewhat higher than that of mass spectrometric studies [110,111]. Therefore, the structure analysis was carried out under the assumption that the vapor consisted of a

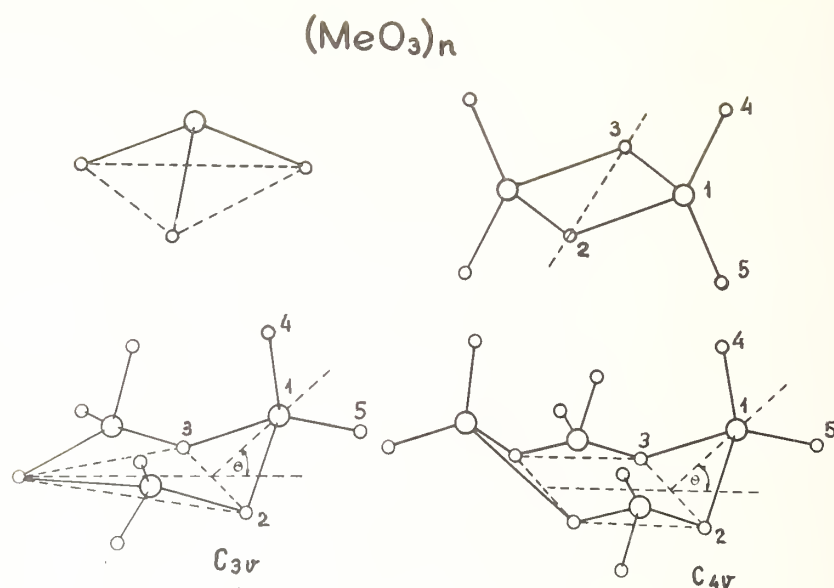


Figure 7. Structural models of  $(\text{MeO}_3)_n$  molecules.

mixture of  $\text{MoO}_3$  and  $\text{Mo}_2\text{O}_6$  species with the vapor phase composition being a variable parameter. Moreover, it has been assumed that the  $\text{Mo}_2\text{O}_6$  structure is similar to that of dimeric aluminum, gallium and iron halides (see fig. 7) and that the molybdenum-oxygen bond distance in the monomer is equal to the external molybdenum-oxygen bond distance in the dimer. It has been found that the monomer-dimer ratio in the electron diffraction experimental conditions is 1:1. The effective configuration of the  $\text{MoO}_3$  molecule is found to be slightly pyramidal whereas the  $\text{MoO}_4$ -fragment in the  $\text{Mo}_2\text{O}_6$  molecule is a considerably distorted tetrahedron. Thus an estimate of  $61.5^\circ$  for the  $\text{OMoO}$  angle in the  $\text{MoO}_3$  molecule made in ref. [112] on the basis of spectroscopic data seems to be unreliable. However, a rather large uncertainty in the electron diffraction evaluation of this angle makes it difficult at this time to yield a realistic estimate of the deviation of the equilibrium geometry of this molecule from planarity. The structural results obtained in ref. [51] are presented in table 17 where a comparison is also made with the structure of the related  $\text{Mo}_3\text{O}_9$  molecule [108].

The studies of chromium and tungsten trioxides have been carried out with the view to determining the structural parameters of trimeric and tetrameric components of the vapor which are the prevailing species over solid  $\text{CrO}_3$ ,  $\text{WO}_3$ , and  $\text{WO}_2$  [113-118]. In a previous electron diffraction study of tungsten trioxide vapor [119], carried out at a temperature of  $1400^\circ\text{C}$ , the main features of the  $\text{W}_3\text{O}_9$  molecular structure were established. The experimental data were best approximated by a geometry containing a six-membered non-planar ring skeleton with alternating tungsten and oxygen atoms. The mean tungsten-oxygen

Table 17. Structural parameters of  $(\text{MoO}_3)_n$ .

Parameter	$\text{MoO}_3$ [51]	$\text{Mo}_2\text{O}_6$ [51]	$\text{Mo}_3\text{O}_9$ [108]
$r_g(\text{Mo}_1-\text{O}_4)$ , Å	1.711(8)	1.711(8)	1.67(1)
$r_g(\text{Mo}_1-\text{O}_2)$ , Å	-	1.892(25)	1.89(1)
$\angle \text{O}_5-\text{Mo}-\text{O}_4^a$	112.(8)	120	106(2)
$\angle \text{O}_2-\text{Mo}-\text{O}_3^a$	-	85	107(2)

<sup>a</sup>Angles in degrees.

bond distance was found to be  $1.77 \pm 0.02$  Å. A series of models containing various combinations of bridging and terminal W-O bond distances were tested. However, the individual values of these distances were not determined whereas it was possible to ascertain that the bridging bond is longer than the terminal one.

An electron diffraction study of chromium and tungsten oxide vapors carried out recently at Moscow University [51] used as samples the solids  $\text{CrO}_3$  and  $\text{WO}_2$ . The latter was chosen for the reason that the vapor over solid  $\text{WO}_2$  has a simpler composition than that over solid  $\text{WO}_3$  [116]. The temperatures of the experiments were 550-570 K ( $\text{CrO}_3$ ) and 2070-2170 K ( $\text{WO}_2$ ). It has been assumed in the structure analysis that the vapors over these systems consist of the trimeric and tetrameric species having the molecular structures presented in figure 7. The molecular models considered contained planar and non-planar ring skeletons. A model for the tetramer having  $S_4$  symmetry has also been tested. The structure analysis was carried out under the assumption that the  $\text{MeO}_4$ -fragments in the trimer and tetramer are similar.

The large range of scattering angles obtained in the experiment ( $s_{\text{max}} = 26.4$  and  $36.2$  Å<sup>-1</sup> for chromium and tungsten oxides, respectively) allowed us to reliably establish the difference between the bridging and terminal Me-O bond distances and the corresponding amplitudes of vibration. The structural parameters for trimeric and tetrameric molecules of chromium and tungsten trioxides are presented in table 18. It is to be pointed out that for tungsten trioxide an approximately similar agreement was obtained for a trimeric model alone and for a mixture of trimeric and tetrameric models with the ratio given in table 18. However, since according to the independent information the vapor over solid  $\text{WO}_2$  consists of a mixture of both components (see above), preference should be placed on the models obtained under an assumption of a complex vapor phase composition. The trimer-tetramer ratio, estimated by electron diffraction (see table 18), actually does

not fully comply with the mass spectrometric determination [118] due to the slight difference of temperature in both experiments.

It is worth mentioning that the deviation of the OMeO angles in the  $\text{MeO}_4$ -fragments from regular tetrahedral values decreases under transition from chromium to tungsten derivatives.

Table 18. Structural parameters of chromium and tungsten trioxides [51].

Parameter	$(\text{CrO}_3)_n$		$(\text{WO}_3)_n$		
	$(\text{CrO}_3)_3$	$(\text{CrO}_3)_4$	$(\text{WO}_3)_3$	$(\text{WO}_3)_3$	$(\text{WO}_4)_4$
Vapor comp. %	30	70	100	80	20
$r_a(\text{Me}_1-\text{O}_4)$ , Å	1.580(5)	1.589(5)	1.704(5)	1.703(5)	1.703(5)
$r_a(\text{Me}_1-\text{O}_2)$ , Å	1.775(7)	1.775(7)	1.901(3)	1.899(3)	1.899(3)
$\angle \text{O}_5-\text{Me}-\text{O}_4^a$	132.6(2.2)	132.6(2.2)	109.0(2.7)	112.4(4.2)	112.4(4.2)
$\angle \text{O}_2-\text{Me}-\text{O}_3^a$	97.2(3.5)	97.2(3.5)	108.0(1.0)	110.2(1.2)	110.2(1.2)
$\angle \text{Me}-\text{O}-\text{Me}^a$	110.0(3.7)	128.3(1.0)	127.8(0.3)	128.0(0.5)	128.8(3.2)
$\theta$	39.2	38.7	14.2	9.6	37.3

<sup>a</sup>Angles in degrees.

#### 4.3 Mixed halides and salts of oxyacids

Several mixed halides having the general formula  $\text{M}_n\text{Me}_m\text{X}_{n+m}$  and salts of oxyacids have been studied in the vapor phase at Moscow University and the Institute of High Temperatures at Moscow. Some characteristic features were established which are common for both classes of compounds. Since most of these results are described in review papers [120-122] and in the book [123] only a short survey will be given below.

It has been found in electron diffraction studies of gaseous alkali metal metaborates [104,124-126] that the scattering of electrons by these molecules is associated mainly with a linear symmetric fragment,  $\text{BO}_2$ . A small contribution to total scattering from the alkali metal makes it difficult to fix its position in the molecule. A similar problem occurred in electron diffraction structural studies of sulfates of cesium [127,128], potassium [127] and monovalent thallium [128], of potassium chromate [127], of cesium molybdate and tungstate [128] and of thallium nitrate [129,130]. It has been found that

by using a conventional interpretational scheme of analysis, an agreement between theoretical and experimental intensities can be provided by a single model having anomalously large amplitudes of vibration associated with metal-oxygen bond distances (0.15-0.25 Å). The  $XO_4$  units in the salts of  $Me_2XO_4$  type ( $X = S, Cr, Mo, W$ ;  $Me = K, Cs, Tl$ ) were found to be tetrahedral within the experimental uncertainty.

Similarly, the  $NO_3$  group in the thallium nitrate was found to be a regular triangle with the N atom in the center. The results obtained for  $TlNO_3$  were interpreted in terms of a dynamic structure of the molecule in the vapor phase. The experimental data were best approximated by a composition of three models with relative abundancies of 18 ( $C_s$ ), 71 ( $C_{2v}$ ) and 11 percent ( $C_{3v}$ ). In the quoted series of studies, the possible uncertainty in central atom valence angles was estimated to be  $\pm 5^\circ$  and the possible difference in central group bond lengths was evaluated as not exceeding 0.1 Å.

To summarize, the most characteristic features of the molecular structures of the salts of oxyacids are a relatively high symmetry of acid groups and large mobility of the metal atom. Such rather unusual structural peculiarity has been confirmed by spectroscopic data. Thus, in infrared spectra of the metaborates of several metals [131-133], the frequency of vibration associated with the motion of the metal relative to the  $BO_2^-$  fragment was not observed. The frequencies of vibration in the range of 690-1940  $cm^{-1}$  were assigned to the  $BO_2$ -fragment and practically did not depend on the alkali atom attached. Similar results, indicating a small dependence of vibrational frequencies of  $NO_3$  and  $SO_4$  groups on the nature of the alkali atom, are reported in infrared studies of nitrates in the matrix [134] and in the gaseous phase [135] and those of sulfates of monovalent elements [136,137].

Practically the same structural features were observed in electron diffraction studies of mixed halides:  $NaAlF_4$  [138],  $KAlCl_4$  [139],  $KYCl_4$  [140] and  $TlInCl_4$  [141]. The  $MeX_4^-$  fragments in these molecules were found to be tetrahedral within the uncertainties quoted. The error in the angle determination was estimated to be  $\pm 5^\circ$  whereas the possible difference in central atom bond distances was found not to exceed 0.1 Å. However, in a more recent electron diffraction investigation of the vapor phase molecular structure of  $KAlF_4$  [142] a distorted tetrahedral coordination is found for the  $AlF_4$ -fragment. In a most probable geometry, the alkali (or Tl) atoms are located on axes which are perpendicular to the edges of a  $MeS_4$ -tetrahedron. Again, the abnormally large amplitudes of vibration are found for bonds associated with the alkali (or Tl) atoms. For example,  $l(Tl-Cl) = 0.19$  Å for  $TlInCl_4$  [141].

Finally, the electron diffraction study of the vapor phase molecular structure of  $MBeF_3$  ( $M = Li, Na$ ) [143] should be mentioned. It has been found that within the uncertainties of the experiment the  $BeF_3$ -fragment geometry is a regular triangle with the Be atom in the center and the alkali atom, in the most probable configuration, is situated on the perpendicular to one of the edges of the triangle.

To summarize, the presently available structural information on the salts of oxyacids and the mixed halides point up the considerable mobility of the alkali atoms and the relative rigidity of the remainder of the molecule. Apparently, in extreme cases of low



energy barriers and high temperatures, the outer atoms can migrate fairly freely around central units. This peculiarity indicates a dynamic configuration rather than a static one for the molecules under consideration.

A concluding remark seems pertinent here. The experimental and interpretational difficulties associated with the application of electron diffraction at high temperatures have already been mentioned. These difficulties are particularly great with the salts of oxyacids and mixed halides. In fact, high-temperature electron diffraction has not yet dealt with the problem of large amplitude motion in the molecules under consideration since no adequate interpretational theoretical model has been devised. For these reasons it seems desirable to repeat certain investigations with the improved instrumentation and experimental methods now available in high-temperature electron diffraction. Repeated studies may be aimed at gaining more insight into the nature of the potential governing the large amplitude motion and into other details of structural peculiarities (for example, the extent of a central structural unit distortion). To do this an adequate theoretical model should be devised for experimental data interpretation. Nevertheless, the general conclusion made on the large mobility of outer atoms and on the relative rigidity of the remainder of the molecule seems unambiguous.

Closely related to the problem under discussion are the results of several theoretical ab initio and semi-empirical calculations. In refs. [144,145] the electronic energy of the LiNC molecule was considered as a function of the Li atom position relative to the remainder of the molecule. The energy contours for the Li atom motion show that no substantial barrier exists for the LiCN and LiNC molecular configurations. Thermal excitation of about 0.3 eV is sufficient for the Li atom to move fairly freely around the NC-fragment.

Practically similar results are obtained in ab initio calculations of the  $\text{LiBO}_2$  [146],  $\text{LiNO}_3$  [147],  $\text{LiBH}_4$  [148,149] and  $\text{NaBH}_4$  [150] molecules. Semi-empirical calculations of the  $\text{TlNO}_3$  molecule [151] and the simple electrostatic calculations of the  $\text{CsNO}_3$  and  $\text{TlReO}_4$  molecules [152,153] are also relevant to the problem. It may be concluded that the theoretical approaches mentioned generally confirm the electron diffraction finding of a dynamic character for the molecular structure of some salts of oxyacids and mixed halides.

A dynamic geometry for molecules poses some problems in structural chemistry. In the first place this concerns the classical description of the geometrical arrangement of atoms in molecules and of the molecular symmetry. Such a description is based not on the physically fixed positions of the nuclei of the molecule but rather on experimentally unavailable positions of the minima on the multidimensional potential energy surface. The totality of these positions forms a geometrical arrangement of a certain symmetry. By contrast, if the nuclei of the molecule are subjected to large amplitude motion, the potential minima positions fail to adequately represent the molecular geometry. Such being the case, the molecular structure cannot be described by a time-independent geometrical arrangement in fixed nuclear positions and by the corresponding symmetry point group. If large amplitude motion occurs, only the nuclear probability distribution function resulting from the experiment or from theoretical calculations is able to provide an

adequate description of the molecular structure. With the help of this function it is possible to calculate the probability of any nuclear arrangement. In this regard ref. [154] is worth mention, where an attempt is made to devise a general description of a total potential energy surface.

The next problem worth considering is that of chemical bonding in molecules with large amplitude motion. The specific peculiarity of a chemical bond of the outer atom in the molecules considered is its distributed character in space since this bond cannot be considered as localized between two atoms. Rather, the outer atom belongs to the remainder of the molecule on the whole. The authors of ref. [145] referred to this bond as the polytopic one to stress its spatially distributed nature. This may be an indication of its ionic character, similar to that in ionic crystals. Another peculiarity of such chemical bonding deserves attention. Both the bond lengths and the vibrational amplitudes indicate that the disturbing effect of the outer atom on the remainder of the molecule is relatively small. However, on the basis of thermodynamic reasoning [155,156], this bond cannot be considered to be energetically weak and the corresponding molecules thermally unstable.

## 5. Concluding Remarks

The present survey shows that the instrumentation, experimental methods and interpretational procedures of high-temperature electron diffraction are steadily advancing. It is to be expected that the new procedure of analysis devised recently will prove extremely profitable for determining molecular structures, potential functions and vibrational frequencies from diffraction information. Combined with the refined facilities of modern high-temperature installations, it will yield solutions to many problems posed by high-temperature vapors. Thus the present experimental and theoretical status of high-temperature electron diffraction in fact is a starting point for new more imaginative and sophisticated approaches to the structural characterization of high-temperature vapors.

---

The authors wish to express their gratitude to Dr. J. W. Hastie from NBS for his kind suggestion and inspiration to contribute to this volume on the Characterization of High-Temperature Vapors and Gases. They also acknowledge the encouragement and steady support of Prof. Lev Gurvich from the Moscow Institute of High Temperatures.

## References

- [1] Akishin, P. A., Rambidi, N. G., and Spiridonov, V. P., in The Characterization of High-Temperature Vapors, J. L. Margrave, ed., chap. 12 (J. Wiley, N.Y., 1967).
- [2] Hilderbrandt, R., in Molecular Structure by Diffraction Methods, Vol. 3, G. A. Sim and L. E. Sutton, eds., Part I, chap. 2 (The Chemical Society, London, 1975).

- [3] Oberhammer, H., in Molecular Structure by Diffraction Methods, Vol. 4, G. A. Sim and L. E. Sutton, eds., Part I, chap. 2 (The Chemical Society, London, 1976).
- [4] Karle, J. and Karle, I. L., J. Chem. Phys. 18, 957 (1950).
- [5] Bartell, L. S., J. Chem. Phys. 23, 1219 (1955).
- [6] Kuchitsu, K., Bull. Chem. Soc. Japan, 40, 498 (1967).
- [7] Kuchitsu, K. and Bartell, L. S., J. Chem. Phys. 35, 1945 (1961).
- [8] Ukaji, T. and Kuchitsu, K., Bull. Chem. Soc. Japan, 39, 2153 (1966).
- [9] Kuchitsu, K., Bull. Chem. Soc. Japan, 40, 505 (1967).
- [10] Kuchitsu, K. and Cyvin, S. J., in Molecular Structure and Vibrations, S. J. Cyvin, sci. ed., chap. 12 (Elsevier, Amsterdam, 1972).
- [11] Cyvin, S. J., Molecular Vibrations and Mean Square Amplitudes (Elsevier, Amsterdam, 1968).
- [12] Spiridonov, V. P., Modern electron diffraction and some problems of molecular structures, a review paper in Sovremennyye Problemy Fisicheskoy Khimii (Modern Problems of Physical Chemistry), Vol. 9, pp. 226-286 (1976) (in Russian).
- [13] Spiridonov, V. P., Gershikov, A. G., and Butayev, B. S., J. Mol. Struct., in press.
- [14] Spiridonov, V. P., Gershikov, A. G., Zasorin, E. Z., and Butayev, B. S., in Diffraction Studies on Non-Crystalline Substances, I. Hargittai and W. J. Orville-Thomas, eds. (Akademia Kiadó, Budapest and Elsevier, Amsterdam), in press.
- [15] Morino, Y. and Hirota, E., J. Chem. Phys. 23, 737 (1955).
- [16] Rambidi, N. G. and Zasorin, E. Z., Teplofiz. Vys. Temp. 2, 705 (1964).
- [17] Kuchitsu, K. and Konaka, S., J. Chem. Phys. 45, 4342 (1966).
- [18] Lindeman, L. P. and Wilson, M. K., J. Chem. Phys. 24, 242 (1956).
- [19] Ginn, S. G., Kenney, J. K., and Overend, J., J. Chem. Phys. 48, 1571 (1968).
- [20] Duncan, J. L., J. Mol. Spectry. 22, 247 (1967).
- [21] Levin, I. W. and Abramowitz, S., Chem. Phys. Lett. 9, 247 (1971).
- [22] Beattie, I. R., Blayden, H. E., and Ogden, J. S., J. Chem. Phys. 64, 909 (1976).
- [23] Shirk, J. S. and Shirk, A. E., J. Chem. Phys. 64, 910 (1976).
- [24] Duncan, J. L., J. Mol. Spectry. 13, 338 (1964).
- [25] Samdal, S., Barnhart, D. M., and Hedberg, K., J. Mol. Struct. 35, 67 (1976).
- [26] Robiette, A. G., J. Mol. Struct. 35, 81 (1976).
- [27] Clark, R. J. H. and Rippon, D. M., J. Mol. Spectry. 52, 58 (1974).
- [28] Zasorin, E. Z., Popenko, N. I., Spiridonov, V. P., and Ivanov, A. A., Inorg. Chim. Acta, in press.
- [29] Spiridonov, V. P., Gershikov, A. G., and Butayev, B. S., J. Mol. Struct., in press.
- [30] Mal'tsev, A. A., Selivanov, G. K., Yampol'sky, V. I., and Zavalishin, N. I., Nat. Phys. Sci. 231, 151 (1971).
- [31] Spiridonov, V. P., Gershikov, A. G., Zasorin, E. Z., and Butayev, B. S., to be published.
- [32] Ozin, G. A. and Voet, A. V., J. Chem. Phys. 56, 4768 (1972).
- [33] Andrews, L. and Frederick, D. L., J. Amer. Chem. Soc. 92, 775 (1970).
- [34] Beattie, I. R. and Perry, R. O., J. Chem. Soc. A, 2429 (1970).
- [35] Haegeli, D. and Palmer, H. B., J. Mol. Spectry. 21, 325 (1966).

- [36] Delwaulle, M.-L. and Francois, M. F., C. R. Acad. Sci. (Paris) 211, 65 (1940).
- [37] Brewer, L., Somayajulu, G. R., and Brackett, E., Chem. Rev. 63 (1963).
- [38] Hastie, J. W., Hauge, R. H., and Margrave, J. L., J. Mol. Spectr. 29, 152 (1969).
- [39] Asundi, R. K., Karim, M. S., and Samuel, R., Proc. Phys. Soc. (London), 50, 581 (1938).
- [40] Deschamps, P. and Paunitier, G., J. Chim. Phys. 61, 1547 (1964).
- [41] Karpenko, N. V. and Novikov, G. I., Vest. Leningrad. Univ. 22, 72 (1967).
- [42] Hargittai, I., Hernadi, J., and Kolonits, M., Prib. Tekh. Eksp., 239 (1972).
- [43] Rambidi, N. G., Ezhov, Yu. S., Leontjev, K. L., Grajis, E. I., Kurkov, A. A., Horkov, N. A., Uljanova, E. L., Mikhailov, Yu. S., Ostapenko, R. G., Komarov, S. A., and Ugarov, V. V., Special Report of Institute of High Temperatures, USSR Academy of Sciences (Feb. 1974).
- [44] Ivanov, A. A., Spiridonov, V. P., Demidov, A. V., and Zasorin, E. Z., Prib. Tekh. Eksp., N 2, 270 (1974).
- [45] Kushnir, Yu. M., Alekseyev, N. V., and Levkin, N. P., Prib. Tekh. Eksp., 5 (1967).
- [46] Ivanov, A. A., Spiridonov, V. P., Erokhin, E. V., and Levitskii, V. A., Zh. Fiz. Khim. 12, 3030 (1973).
- [47] Erokhin, E. V., Prihod'ko, A. Ya., Spiridonov, V. P., and Kiseley, Yu. M., to be published.
- [48] Ivanov, A. A., Prib. Tekh. Eksp., N 2, 237 (1974).
- [49] Kakumoto, K., Ino, T., Kodera, S., and Kakinoki, J., J. Appl. Cryst. 10, 100 (1977).
- [50] Bauer, S. H. and Kimura, K., International Conference on Magnetism and Crystallography, Kyoto, Japan (1961).
- [51] Ivanov, A. A., Candidate Thesis, Moscow State University, Moscow (1976).
- [52] Bartell, L. S., in Physical Methods in Chemistry, 4th edition, Vol. 1, A. Weissberger and B. W. Rossiter (Interscience, N.Y., 1972).
- [53] Akishin, P. A. and Rambidi, N. G., Zh. Neorg. Khim. 5, 23 (1960).
- [54] Solomonik, V. G., Girichev, G. V., Krasnov, K. S. and Zosorin, E. Z., Izv. Vuz. SSSR, Khim. Khim. Tekhnol. 19, 280 (1976).
- [55] Chao, J., Thermochim. Acta, 1, 71 (1971).
- [56] Alikhanyan, A. S., Shol'ts, V. B., and Sidorov, L. N., Vestn. Mosk. Univer., Khim. N 6, 639 (1972).
- [57] Pearson, E. F. and Gordy, W., Phys. Rev. 177, 52 (1969).
- [58] Büchler, A., Stauffer, J. L., and Klemperer, W., J. Amer. Chem. Soc. 86, 4544 (1964).
- [59] Cubicciotti, D., High Temp. Sci. 2, 65 (1970).
- [60] Keneshea, F. J. and Cubicciotti, D., J. Phys. Chem. 69, 3910 (1965).
- [61] Keneshea, F. J. and Cubicciotti, D., J. Phys. Chem. 71, 1958 (1967).
- [62] Brom, J. M. and Franzen, H. F., J. Chem. Phys. 54, 2874 (1971).
- [63] Dehmer, J. L., Berkowitz, J., and Cusach, L. S., J. Chem. Phys. 58, 5681 (1973).
- [64] Fickes, M. G., Slater, R. C., Becker, W. G., and Stern, R. C., Chem. Phys. Letters, 24, 105 (1974).



- [65] Muentert, J. S., Chem. Phys. Letters, 26, 97 (1974).
- [66] Solomonik, V. G., Zasorin, E. Z., Girichev, G. V., and Krasnov, K. S., Izv. Vuz. SSSR, Khim. Khim. Tekhnol. 17, 136 (1974).
- [67] Lesiecki, M. L. and Nibbler, J. W., J. Chem. Phys. 63, 3452 (1975).
- [68] Streets, D. G. and Berkowitz, J., Chem. Phys. Letters, 38, 475 (1976).
- [69] Ischenko, A. A., Ivashkevich, L. S., Zasorin, E. Z., Spiridonov, V. P., and Ivanov, A. A., Sixth Austin Symposium on Gas Phase Molecular Structure. Abstracts, Austin, p. 89 (1976).
- [70] Hargittai, I., Tremmel, J., Vajda, E., Ischenko, A. A., Ivanov, A. A., Ivashkevich, L. S., and Spiridonov, V. P., J. Mol. Struct. 42, 147 (1977).
- [71] Lister, H. W. and Sutton, L. E., Trans. Farad. Soc. 37, 406 (1941).
- [72] Akishin, P. A., Spiridonov, V. P., and Khodchenkov, A. N., Zh. Fiz. Khim. 32, 1679 (1958).
- [73] Viola, J. T., Seegmiller, D. W., Fanning, Jr., A. A., and King, L. A., J. Chem. Eng. Data, 22, 367 (1977).
- [74] Zasorin, E. Z. and Rambidi, N. G., Zh. Strukt. Khim. 8, 391 (1967).
- [75] Zasorin, E. Z. and Rambidi, N. G., Zh. Strukt. Khim. 8, 591 (1967).
- [76] Beattie, I. R. and Horder, J. R., J. Chem. Soc. A, 2655 (1969).
- [77] Lesiecki, M. L. and Shirk, J. S., J. Chem. Phys. 56, 4171 (1972).
- [78] Krasnov, K. S., Girichev, G. V., Giricheva, N. I., Petrov, V. M., Danilova, T. G., Zasorin, E. Z., and Popenko, N. I., Seventh Austin Symposium on Gas Phase Molecular Structure, Abstracts, Austin, p. 89 (1978).
- [79] Akishin, P. A., Naumov, V. A., and Tatevskii, V. M., Vestn. Mosk. Univer., Khim. 229 (1959).
- [80] Naumov, V. A. and Akishin, P. A., Zh. Strukt. Khim. 2, 3 (1961).
- [81] Hauge, R. H., Hastie, J. W., and Margrave, J. L., J. Less-Common Metals, 23, 359 (1971).
- [82] Hastie, J. W., Hauge, R. H., and Margrave, J. L., J. Less-Common Metals, 39, 309 (1975).
- [83] Wesley, R. D. and DeKock, C. W., J. Chem. Phys. 55, 3866 (1971).
- [84] Lesiecki, M. L., Nibbler, J. W., and DeKock, C. W., J. Chem. Phys. 57, 1352 (1972).
- [85] Perov, P. A., Nedjak, S. V., and Mal'tsev, A. A., Vestn. Mosk. Univer. Khim. 16, 281 (1975).
- [86] Wells, Jr., J. C., Gruben, J. B., and Lewis, M., Chem. Phys. 24, 391 (1977).
- [87] Kaiser, E. W., Falconer, W. E., and Klemperer, W., J. Chem. Phys. 56, 5392 (1972).
- [88] Giricheva, N. I., Zasorin, E. Z., Girichev, G. V., Krasnov, K. S., and Spiridonov, V. P., Izv. Vuz. SSSR, Khim. Khim. Tekhnol. 17, 616, 762 (1974).
- [89] Giricheva, N. I., Zasorin, E. Z., Girichev, G. V., Krasnov, K. S., and Spiridonov, V. P., Zh. Strukt. Khim. 17, 797 (1976).
- [90] Giricheva, N. I., Zasorin, E. Z., Girichev, G. V., Krasnov, K. S., and Spiridonov, V. P., Izv. Vuz. SSSR, Khim. Khim. Tekhnol. 20, 284 (1977).
- [91] Danilova, T. G., Girichev, G. V., Giricheva, N. I., Krasnov, K. S., and Zasorin, E. Z., Izv. Vuz. SSSR, Khim. Khim. Tekhnol. 20, 1069, 1233 (1977).



- [92] Girichev, G. V., Danilova, T. G., Giricheva, N. I., Krasnov, K. S., Petrov, V. M., Utkin, A. I., and Zasorin, E. Z., *Izv. Vuz. SSSR, Khim. Khim. Tekhnol.* 21, 627 (1978).
- [93] Popenko, N. I., Zasorin, E. Z., Spiridonov, V. P., and Ivanov, A. A., *Inorg. Chim. Acta Letters* (in press).
- [94] Sviridov, D. T., Sviridova, R. K., and Smirnov, Yu. F., *Opticheskie spektry ionov perekhodnykh metallov v kristallakh* (Optical spectra of rare-earth metal ions in crystals), Nauka, M., 1976 (in Russian).
- [95] Girichev, G. V., Zasorin, E. Z., Giricheva, N. I., Krasnov, K. C., and Spiridonov, V. P., *Zh. Strukt. Khim.* 18, 42 (1977).
- [96] Petrov, V. M., Girichev, G. V., Giricheva, N. I., Krasnov, K. S., and Zasorin, E. Z., Fifth All-Union Symposium on Chemistry of Inorganic Fluorides, Abstracts, Nauka, M., p. 230 (1978).
- [97] Ivashkevich, L. S., Ischenko, A. A., Spiridonov, V. P., and Romanov, G. V., *J. Mol. Struct.* (in press).
- [98] Jahn, H. A. and Teller, E., *Proc. Roy. Soc.* 161, 220 (1937).
- [99] Trauax, D. R., Greer, J. A., and Ziegler, T., *Theoret. Chim. Acta*, 33, 299 (1974).
- [100] Ischenko, A. A., Strand, T. G., Demidov, A. V., and Spiridonov, V. P., *J. Mol. Struct.* 43, 227 (1978).
- [101] Ivanov, A. A., Tolmachev, S. M., Ezhov, Yu. S., Spiridonov, V. P., and Rambidi, N. G., *Zh. Strukt. Khim.* 14, 917 (1973).
- [102] Drowart, J., De Maria, G., Burns, R. P., and Inghram, M. G., *J. Chem. Phys.* 32, 1366 (1960).
- [103] Akishin, P. A. and Spiridonov, V. P., *Doklady Akad. Nauk SSSR*, 131, 557 (1960).
- [104] Ezhov, Yu. S., Tolmachev, S. M., Spiridonov, V. P., and Rambidi, N. G., *Teplofiz. Vys. Temp.* 6, 68 (1968).
- [105] Ezhov, Yu. S., Tolmachev, S. M., and Rambidi, N. G., *Zh. Strukt. Khim.* 11, 527 (1970).
- [106] Inghram, M. G., Porter, R. F., and Chupka, W. A., *J. Chem. Phys.* 25, 498 (1956).
- [107] Kasenas, E. K. and Chizhikov, D. M., *Davlenie i Sostav Para nad Okislamy Khimicheskikh Elementov* (The Pressure and Vapor Phase Composition Above Oxides of Chemical Elements) Nauka, M. (1976) (in Russian).
- [108] Egorova, N. M. and Rambidi, N. G., in Molecular Structure and Vibrations, S. Gyvin, sci. ed., chap. 13 (Elsevier, Amsterdam, 1972).
- [109] Blackburn, P. E., Hoch, M., and Johnston, H. L., *J. Phys. Chem.* 62, 769 (1958).
- [110] Burns, R. P., DeMaria, G., Drowart, J., and Grimley, R. T., *J. Chem. Phys.* 32, 1363 (1960).
- [111] Chizhikov, D. M., Kasenas, E. K., and Ermilova, I. O., *Zh. Fis. Khim.* 50, 1454 (1976).
- [112] Hemett, Jr., W. D., Newton, J. H., and Weltner, Jr., W., *J. Phys. Chem.* 79, 2640 (1975).

- [113] Schäfer, H. and Rinke, K., Z. Naturforsch. 20, 702 (1965).
- [114] McDonald, T. D. and Margrave, J. L., J. Inorg. Nucl. Chem. 30, 665 (1968).
- [115] Berkowitz, J., Chupka, W. A., and Inghram, M. G., J. Chem. Phys. 27, 85 (1957).
- [116] Ackerman, R. J. and Raugh, E. G., J. Phys. Chem. 67, 2596 (1963).
- [117] Kasenas, E. K. and Tsvetkov, Yu. V., Zh. Fis. Khim. 41, 3112 (1967).
- [118] Chizhikov, D. M., Kasenas, E. K., and Ermilova, I. O., Zh. Fis. Khim. 50, 3130 (1976).
- [119] Hargittai, I., Hargittai, M., Spiridonov, V. P., and Erokhin, E. V., J. Mol. Struct. 8, 31 (1971).
- [120] Spiridonov, V. P., Kémiai Közlemények, 37, 399 (1972).
- [121] Sidorov, L. N. and Zasorin, E. Z., Izv. Vuz., SSSR, Khim. Khim. Tekhnol. 18, 3 (1975).
- [122] Spiridonov, V. P., Ischenko, A. A., and Zasorin, E. Z., Usp. Khim. 48, 101 (1978).
- [123] Hargittai, M. and Hargittai, I., The molecular geometries of coordination compounds in the vapor phase, Akadémiai Kiadó, Budapest (1977).
- [124] Ezhov, Yu. S., Tolmachev, S. M., and Rambidi, N. G., Zh. Strukt. Khim. 13, 972 (1972).
- [125] Ezhov, Yu. S. and Komarov, S. A., Zh. Strukt. Khim. 16, 662 (1975).
- [126] Komarov, S. A. and Ezhov, Yu. S., Zh. Strukt. Khim. 16, 899 (1975).
- [127] Spiridonov, V. P. and Lutoshkin, B. I., Vestn. Mosk. Univers., Khim. N 5, 509 (1970).
- [128] Ugarov, V. V., Ezhov, Yu. S., and Rambidi, N. G., J. Mol. Struct. 25, 357 (1975).
- [129] Ischenko, A. A., Spiridonov, V. P., and Zasorin, E. Z., Zh. Strukt. Khim. 15, 300 (1974).
- [130] Ischenko, A. A., Spiridonov, V. P., and Zasorin, E. Z., Izv. Vuz. SSSR, Khim. Khim. Tekhnol. 17, 138 (1974).
- [131] Büchler, A. and Marram, E. P., J. Chem. Phys. 39, 292 (1963).
- [132] Seshadri, K. S., Nimon, L. A., and White, D., J. Mol. Spectry. 30, 128 (1969).
- [133] Shapovalov, A. M., Shevel'kov, V. F., and Mal'tsev, A. A., Zh. Strukt. Khim. 14, 560 (1973).
- [134] Smith, D., James, D. W., and Devlin, J. P., J. Chem. Phys. 64, 4437 (1971).
- [135] Shapovalov, A. M., Shevel'kov, V. F., and Mal'tsev, A. A., Vestn. Mosk. Univer., Khim. N 1, 151 (1973).
- [136] Belyayeva, A. N., Dvorkin, M. I., and Scherba, L. D., Optika Spectr. 34, 585 (1971).
- [137] Belyayeva, A. N., Dvorkin, M. I., and Scherba, L. D., *ibid*, 38, 308 (1975).
- [138] Spiridonov, V. P. and Erokhin, E. V., Zh. Neorg. Khim. 14, 636 (1969).
- [139] Spiridonov, V. P., Erokhin, E. V., and Lutoshkin, B. I., Vestn. Mosk. Univer., Khim. N 3, 296 (1971).
- [140] Spiridonov, V. P., Bresgin, Yu. A., and Shakhparonov, M. I., Zh. Strukt. Khim. 12, 1080 (1971).
- [141] Spiridonov, V. P., Bresgin, Yu. A., and Shakhparonov, M. I., *ibid*, 13, 320 (1972).
- [142] Vajda, E., Hargittai, I., and Tremmel, J., Inorgan. Chim. Acta, 25, L143 (1977).

- [143] Spiridonov, V. P., Erokhin, E. V., and Bresgin, Yu. A., Zh. Strukt. Khim. 13, 321 (1972).
- [144] Bak, B., Clementi, E., and Kortzeborn, R. N., J. Chem. Phys. 52, 764 (1970).
- [145] Clementi, E., Kistenmacher, H., and Popkie, H., J. Chem. Phys. 58, 2460 (1973).
- [146] Dementiev, A. and Kracht, D., Chem. Phys. Lett. 35, 243 (1975).
- [147] Almlöf, J. and Ischenko, A. A., Chem. Phys., in press.
- [148] Boldyrev, A. I., Charkin, O. P., Rambidi, N. G., and Avdeev, V. I., Chem. Phys. Lett. 44, 20 (1976).
- [149] Boldyrev, A. I., Charkin, O. P., Rambidi, N. G., and Avdeev, V. I., Zh. Strukt. Khim. 18, 16 (1977).
- [150] Boldyrev, A. I., Charkin, O. P., Rambidi, N. G., and Avdeev, V. I., Zh. Strukt. Khim. 19, 203 (1978).
- [151] Ischenko, A. A., Budnikov, S. S., Spiridonov, V. P., and Bersuker, I. B., Theor. Eksp. Khim. 11, 740 (1975).
- [152] Rambidi, N. G., J. Mol. Struct. 20, 77 (1975).
- [153] Rambidi, N. G., ibid, 20, 89 (1975).
- [154] Liehr, A. D., J. Phys. Chem. 67, 471 (1963).
- [155] Cubicciotti, D., High Temp. Sci. 2, 131 (1970).
- [156] Sidorov, L. N., Koordinat. Khim 3, 1128 (1977).



## PHOTOIONIZATION MASS SPECTROMETRY AND PHOTOELECTRON SPECTROSCOPY OF HIGH TEMPERATURE VAPORS

J. Berkowitz  
Argonne National Laboratory  
Argonne, IL 60439

### 1. Introduction

Seven years ago, I had occasion to publish a review paper with the same title as the present one. At that time, a fair amount of information was available on high temperature species from photoionization mass spectrometry (PIMS), but corresponding work by photoelectron spectroscopy (PES) was in its infancy. A point made in that article concerned the determination of dissociation energies. Earlier electron impact determinations of dissociative ionization thresholds had been shown to be inaccurate in a number of instances, and equilibrium methods (e.g. Knudsen cell mass spectrometry) had supplanted them. With the much greater precision available in photon impact mass spectrometry, it was felt that dissociative ionization threshold methods could, in favorable circumstances, provide higher accuracy than the equilibrium methods.

In the intervening years, high temperature PES has grown to adolescence. (See reference 2 for a review as of ca. 1975.) The two techniques (PES and PIMS) are complementary. In PES, one directs a monochromatic beam of electromagnetic radiation ( $h\nu$ ) on a target gas. If  $h\nu$  is greater than one or more ionization potentials (IP) of the target gas, photoelectrons will be generated. By measuring the kinetic energies (KE) of these photoelectrons in a suitable electron energy analyzer, one can infer the various ionization energies of the target gas from conservation of energy, i.e.

$$h\nu = (IP)_n + (KE)_n.$$

These ionization potentials correspond to different states of the molecular ion, which can often be related to binding energies of specific molecular orbitals in the neutral molecule via Koopmans' theorem [3]<sup>1</sup>. The shape and breadth of the photoelectron bands can tell us something about the nature of these molecular orbitals, i.e. their bonding, anti-bonding or non-bonding character. In the earliest publications [4] on high temperature PES, it was found that concepts of bonding and non-bonding orbitals commonly invoked to

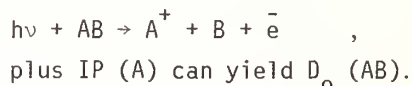
---

<sup>1</sup>Figures in brackets indicate the literature references at the end of this paper.



describe covalent bonding must be revised when ionic bonding is primarily responsible for molecule formation. This subject has been amply treated elsewhere [2,4] and we shall not dwell upon it at the moment.

In PIMS, we mass analyze the ions produced in the photoionization process. For such a study, one requires a source of continuum radiation and a vacuum ultraviolet monochromator to select the wavelength of light in successive increments. The onset of ionization producing the parent molecular ion can generally be identified with the adiabatic first ionization potential, a value which can also be obtained from PES. The threshold for fragment ion production can be related to the bond energy ( $D_0$ ) if one knows the first ionization potential of the fragment, i.e.



However, although impact methods (electron, ion, photon) have generally employed such an approach, it presupposes that states of the molecular ion are being formed in the relevant energy range, and this situation need not always exist. If there is a gap in the sequence of ionic states just in the threshold region for fragmentation, then one may in principle only obtain an upper limit for the bond energy. A notorious example [5] of this behavior is the threshold for formation of  $NO^+$  from  $N_2O$ . It is rather surprising that more pathological cases have not come to light, and that the fragmentation thresholds have generally given accurate bond energies. Weak autoionization processes have been suspected to occur, helping to fill in the region between ionic states. However, it may be instructive to examine juxtaposed PES and PIMS data from a number of high temperature molecular species in order to obtain some detailed information concerning the mechanism of formation of fragment ions.

## 2. PES and PIMS of Selected High Temperature Species

### 2.1 Covalent bonding - the $S_2$ molecule

Let us begin our comparative study of PES and PIMS by an investigation of the covalently bound molecule  $S_2$ . In figure 1 we display a photoelectron spectrum of this molecule [6] obtained with 21.2 eV incident radiation. The band at lowest ionization energy (ca. 9.5 eV) corresponds to removal of an electron from the uppermost occupied orbital,  $\pi_g$ , which is an anti-bonding orbital. Consequently, the ground state of  $S_2^+$  can be shown to be more strongly bound than the ground state of  $S_2$ . A doublet with vibrational fine structure superposed can be identified in the region ~11.5-13 eV. The next uppermost occupied orbital in  $S_2$  is  $\pi_u$ , and removal of an electron from this orbital results in both  $^4\Pi_u$  and  $^2\Pi_u$  ionic states. The  $\pi_u$  orbital is a bonding one, and hence  $S_2^+$  produced in these states should be less bound than  $S_2$  (ground state). The breadth of these bands ( $^4\Pi_u$  and  $^2\Pi_u$ ) is another indication that an electron has been removed from a bonding orbital. In PIMS, the formation of these ionic states, and the autoionizing Rydberg states converging upon the excited states, can be ob-

served at the  $S_2^+$  parent ion position. In this brief talk, however, we shall focus on the fragmentation process and not pursue the detailed mechanisms for formation of parent ions.

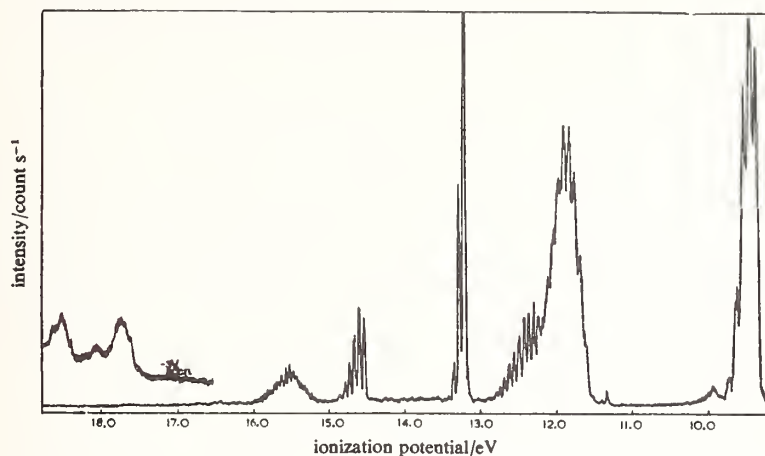


Figure 1. The photoelectron spectrum of  $S_2$ , obtained with 21.2 eV incident photon energy (from Dyke, et al. ref. 6).

Fragmentation to produce  $S^+ + S$  can first be observed in the neighborhood of the next set of bands, which are presented in expanded scale in figure 2. These bands are designated  $4\Sigma_g^-$  (ca. 13.2 eV) and  $2\Sigma_g^-$  (ca. 14.5 eV), and are formed when an electron is removed from a  $\sigma_g$  orbital, which is a bonding orbital.

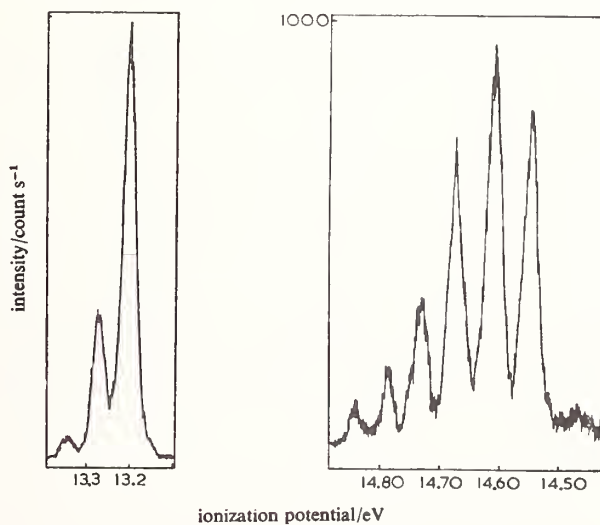


Figure 2. Expanded version of the photoelectron spectrum of  $S_2$ , in the energy region corresponding to the threshold for dissociative photoionization (from Dyke, et al. ref. 6).

The yield of  $S^+$  from photodissociative ionization of  $S_2$ , as obtained by PIMS, is shown in figure 3, taken from reference 7. A threshold can be seen at ca. 14.7 eV, which is well

within the band envelope of the  $2\Sigma_g^-$  ionic state. Hence, we can in this instance feel confident that states of the molecular ion exist in the vicinity of the fragmentation threshold. We note parenthetically that in the related  $O_2$  molecule, photodissociative ionization commences in the corresponding  $4\Sigma_g^-$  state, but receives enhancement at higher energy from the  $2\Sigma_g^-$  state.

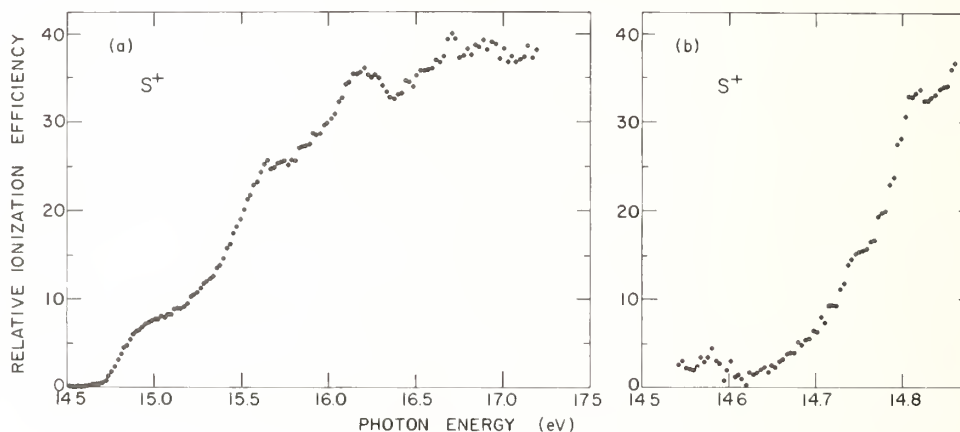


Figure 3. Direct measurement of dissociative photoionization in  $S_2$  in the threshold region.

The bumps and plateaus in the  $S^+$  curve of figure 3 have been interpreted as onsets for higher energy asymptotes, i.e. processes leaving either the S or  $S^+$  in excited states. A glance at figure 4 [6] provides an overview of the process. The Franck-Condon region spanned upon excitation from ground state  $S_2$  does not encompass sufficiently high vibrational levels of  $4\Sigma_g^-$  to permit dissociation from this state. Dissociation becomes energetically possible in the region of the  $2\Sigma_g^-$  state, but this state is bound, according to PES. Hence, it must be predissociated by repulsive states whose asymptotes correspond to the lowest levels at the right side of the figure.

The dissociative ionization processes in  $Se_2$  and  $Te_2$  appear [7,8] to be similar to that in  $S_2$  in that fragmentation seems to begin somewhere near the adiabatic onset of the  $2\Sigma_g^-$  band. However, small configuration interaction peaks appear in the photoelectron spectra [8] and tend to obscure the state(s) involved at the fragmentation threshold.

In summary, dissociative ionization in  $S_2$  proceeds by removal of an electron from a nominally bonding orbital. The ionic state formed is a bound one, in zeroth order, but is predissociated by repulsive states, giving rise to the structure in the fragment ion curve.

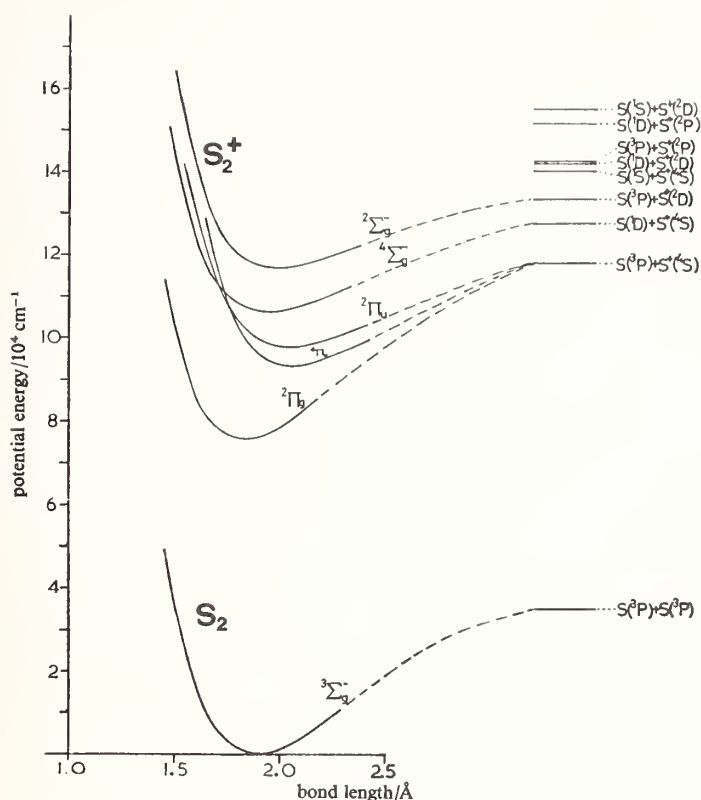


Figure 4. Potential energy curves of  $S_2$  and various  $S_2^+$  states relevant to the photoelectron spectrum and to the dissociative photoionization threshold (from Dyke, et al. ref. 6).

## 2.2 Intermediate ionic bonding - the Group III monohalides

Let us now turn to the Group III monohalides, which provide an example of ionic bonding. Our experimental studies have encompassed the thallium and indium halides, whereas ab initio Hartree-Fock calculations have been performed on boron, aluminum and gallium halides. However, in a homologous isoelectronic series one generally observes the same pattern of orbital energies, and hence it is possible to present a composite picture by making use of the best features of experiment and theory.

We shall not repeat here the details of the analysis leading to the assignment of bands in the photoelectron spectrum. The interested reader can find them elsewhere [4,9]. Instead, we shall proceed directly to the conclusions, and rationalize the experimental results by deduction. In figure 5, relevant potential energy curves of  $\text{AlCl}$  and  $\text{AlCl}^+$  calculated by M. Attermeyer, G. Das and A. C. Wahl, and presented in reference 9, are displayed. Note that the ionic ground state  $^2\Sigma$  has a shorter equilibrium internuclear distance than the neutral ground state (indicating removal of an electron from an antibonding orbital) whereas the excited  $^2\Pi$  state is repulsive (indicating removal of an electron from a bonding orbital).

Analysis of the molecular orbitals involved reveals that an ionic bonding structure ( $\text{Al}^+ \text{Cl}^-$ ) is appropriate. The uppermost occupied orbital is largely metallic "s." Removal of an electron from this orbital produces an  $\text{Al}^{++} \text{Cl}^-$  structure, which is bound more tightly by coulombic interaction than is the neutral ground state. The next deeper molecular orbital is largely chlorine 3p. Electron ejection from this orbital generates an entity  $\text{Al}^+ - \text{Cl}^0$ , which is very weakly bound at large internuclear distances, and is repulsive at shorter distances. Hence, paradoxically, removal of an electron from the electron deficient end of a molecule requires less energy than electron ejection from the end with an excess of electronic charge.

From figure 5, we would conclude that dissociative ionization should occur via direct transition to the repulsive  $^2\Pi$  state, whereas the  $^2\Sigma$  state has a sufficient well depth to sustain the parent molecular ion.

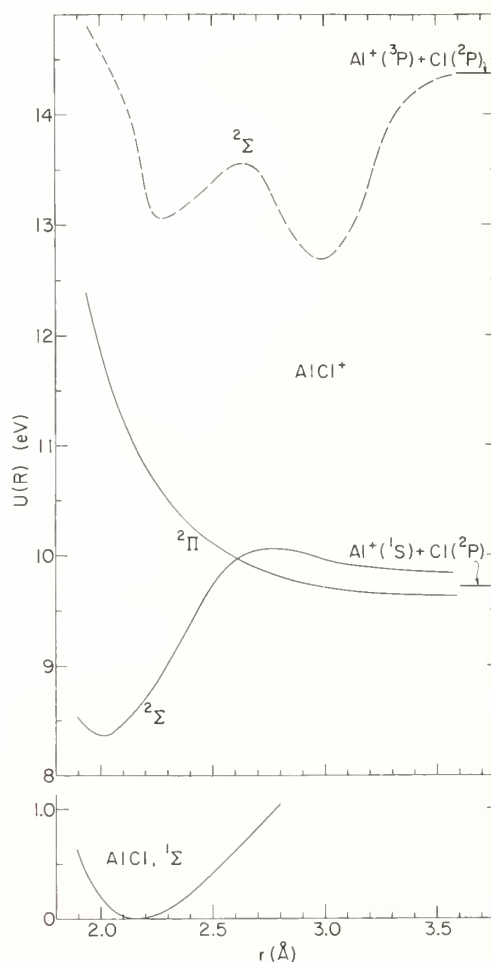


Figure 5. Calculated potential energy curves for  $\text{AlCl}$  and  $\text{AlCl}^+$  relevant to photoelectron spectroscopy and to the dissociative ionization process (from Attermeyer, Das and Wahl, presented in reference 9).



We have no direct measure of parent and fragment ion intensity of  $\text{AlCl}$  from photoionization mass spectrometry to test this hypothesis. However, a combination of the aforementioned calculations and PES experiments reveals that the separation between  $^2\Sigma$  and  $^2\Pi$  decreases in the sequence  $\text{AlCl} - \text{GaCl} - \text{InCl} - \text{TlCl}$ .

The photoelectron spectra of  $\text{InCl}$  and  $\text{TlCl}$  are shown in figure 6. We can see the narrowing of the gap between the relatively sharp peak corresponding to the ionic ground state ( $^2\Sigma$ ) and the broad peak ( $^2\Pi$ ), characteristic of electron removal from a bonding orbital. In the  $\text{TlCl}$  case, the adiabatic ionization energies of  $^2\Sigma$  and  $^2\Pi$  are not even distinctly resolved. The PIMS of  $\text{TlCl}^+$  and  $\text{Tl}^+$  from  $\text{TlCl}$  (taken from ref. 10) are presented in figures 7 and 8. (The semilogarithmic display clearly shows the influence of hot bands in the vibrational Boltzmann distribution at threshold). The adiabatic first ionization potential for  $\text{TlCl}$  is given as  $9.70 \pm 0.03$  eV in both PES and PIMS measurements (figs. 6 and 7). In addition, figure 8 yields  $9.92_5 \pm 0.02$  eV for the onset of  $\text{Tl}^+$ , the photodissociative ionization threshold. Comparing figures 6 and 8, we can plausibly conclude that  $^2\Pi$  of  $\text{TlCl}^+$  is the source of  $\text{Tl}^+$ , has an adiabatic ionization potential of 9.92 eV and is completely dissociated. It will be interesting to note the  $\text{M}^+$  and  $\text{MX}^+$  ionization potentials for  $\text{InCl}$ ,  $\text{GaCl}$  and  $\text{AlCl}$ , when data become available, to see if the separation in threshold energies parallels the gap between  $^2\Sigma$  and  $^2\Pi$  states.

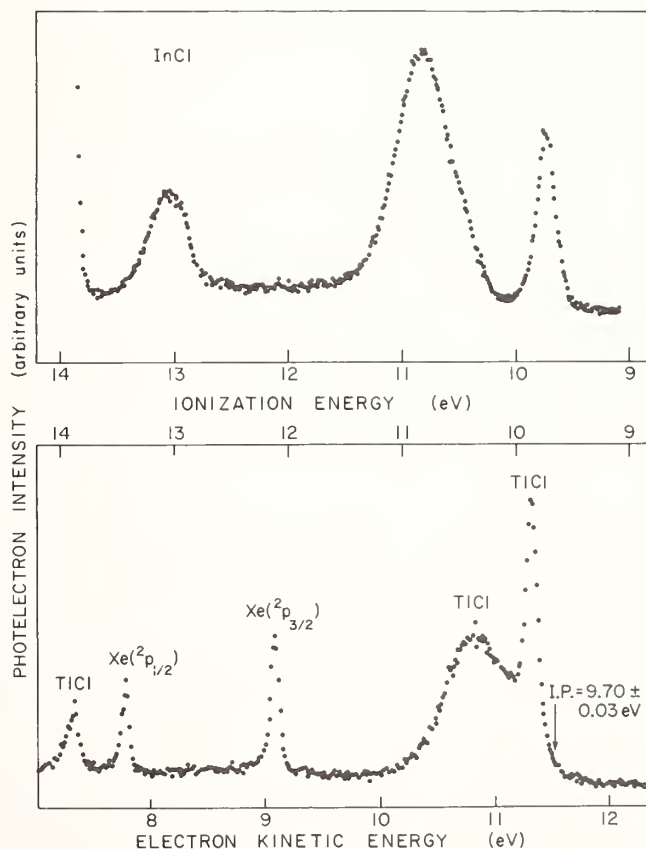


Figure 6. The photoelectron spectra of  $\text{InCl}$  and  $\text{TlCl}$ , obtained with 21.2 eV incident photon energy (from Berkowitz, ref. 2).

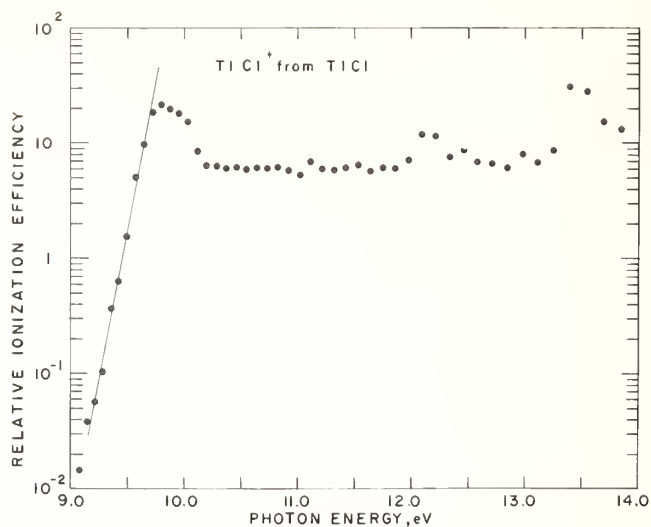


Figure 7. Relative ionization yield of parent ion ( $\text{TlCl}^+$ ) plotted in semilogarithmic coordinates to emphasize the exponential Boltzmann tail near threshold (from reference 10).

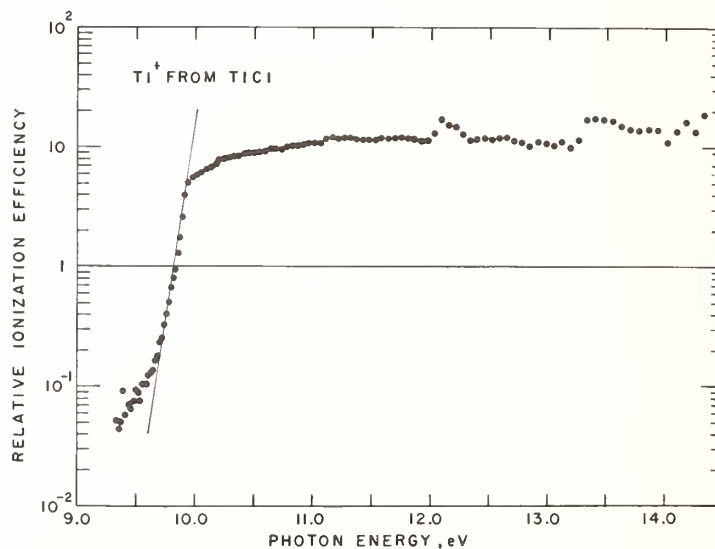


Figure 8. Relative ionization yield of fragment ion ( $\text{Tl}^+$ ) from  $\text{TlCl}_2$ , on a semilog scale (from reference 10).

### 2.3 Elucidation of molecular structure by PES - the case of $\text{Tl}_2\text{F}_2$

While on the subject of thallium halides, I should like to briefly digress from the main theme of this paper to discuss another application of PES to the characterization of high



## 2.4 Ionic bonding - the alkali halides

The alkali halides have been extensively studied, both from a calculational and experimental standpoint. The interested reader is referred to two recent reviews [2,13] covering different aspects of the problem. For the task at hand we present an abbreviated discussion, beginning with elementary considerations.

Alkali atoms have a single  $s$  electron outside a closed shell, and halogen atoms lack a  $p$  electron to complete a sub-shell. For these ionically bound molecules, a considerable degree of charge transfer occurs, giving rise to positive and negative ions which are almost spherically symmetric, but which polarize one another. The most loosely bound electron will clearly come from an orbital associated primarily with the negative ion, since ejection of an electron from the vicinity of the positive ion moiety is closely related to the ionization potential of the positive ion, or to the second ionization potential of the atom. This higher ionization potential is beyond the range of the 21.2 eV incident radiation for all alkalis except cesium. Hence, for our present purposes we can focus our attention on the orbital energies of a halogen negative ion in the field of a positive ion.

This field increases the first ionization potential of the negative ion from its field-free value (the electron affinity of the atom) by approximately  $e^2/r_e$  (where  $r_e$  is the equilibrium internuclear distance in the alkali halide molecule). In addition, the cylindrical electrostatic field splits the spherically symmetric  $p^6$  system into  $\pi$  and  $\sigma$  molecular orbitals. The magnitude of this splitting is related to the degree of ionicity of the molecule. The most ionic of the alkali halides (e.g. CsF, KF) maintain nearly spherical symmetry for the  $p^6$  orbital system of the halogen negative ion, or (equivalently) have very small  $\pi$ - $\sigma$  separation, whereas the least ionic ones (e.g. LiI, LiCl) involve substantial polarization of the negative ion charge cloud and significant  $\pi$ - $\sigma$  splitting. This behavior is illustrated for the cases of KF and LiCl in figures 10 and 11, based on Hartree-Fock calculations by M. Attermyer and A. C. Wahl, and taken from reference 14. The  $^2\Pi$  and  $^2\Sigma$  curves of  $KF^+$  (fig. 10) are very similar, the  $^2\Pi$  showing a very slight tendency toward binding, whereas the  $^2\Pi$   $LiCl^+$  (fig. 11) displays an appreciable well depth. Hence, we anticipate that bound  $^2\Pi$  ground states of these alkali halide ions can be associated with stable molecular ions, and these bound states are most likely when the  $\pi$ - $\sigma$  separations are large. The related  $^2\Sigma$  states can be expected to be repulsive, and yield only  $M^+$  fragment ions. Consequently, the most ionic alkali halides should have  $^2\Pi$  ionic ground states with almost no binding, and hence produce parent molecular ions either weakly or not at all, whereas the least ionic ones should generate a substantial fraction of parent molecular ions. The available data from both PIMS and electron impact mass spectrometry bear this out (see table VI of ref. 14). CsF has no detectable parent ion, and in KF it is extremely weak, whereas in LiCl the parent to fragment ratio is 3.39. A more detailed discussion must include the effect of spin-orbit splitting on the  $p^6$  system of the halogen negative ion, and is included in reference 14.

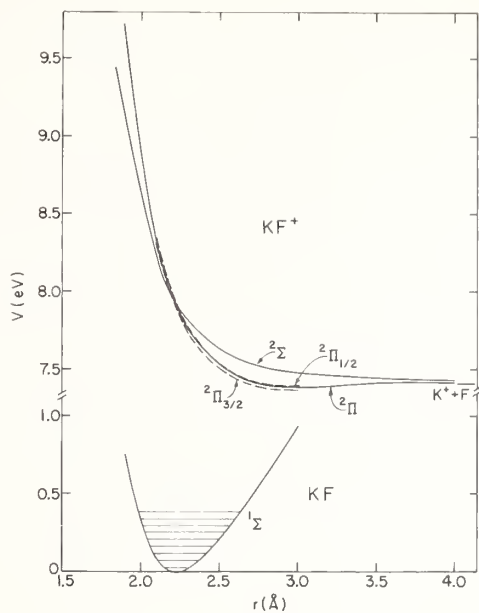


Figure 10. Calculated potential energy curves of KF and  $\text{KF}^+$ , obtained by Attermyer and Wahl, and presented in reference 14.

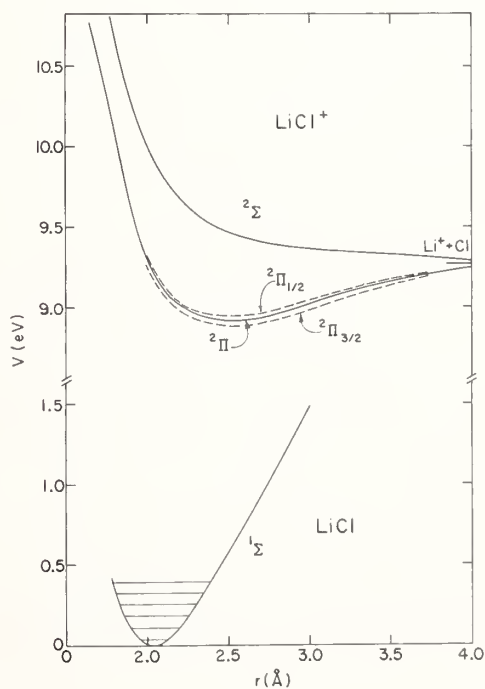


Figure 11. Calculated potential energy curves of LiCl and  $\text{LiCl}^+$ , obtained by Attermyer and Wahl and presented in reference 14.



I should like to conclude this presentation with a discussion of recent (as yet unpublished) work, which I hope will summarize past efforts and point the way for future work. Some time ago, Dr. D. G. Streets and I obtained the photoelectron spectra of a number of transition metal dihalides,  $MX_2$  ( $M = Mn, Fe, Co, Ni$ ;  $X = Cl, Br$ ). These are in some cases known, in others thought to be linear symmetric molecules. The usual method of interpreting such spectra is to obtain good calculations of the orbital energy sequence, and relate them to photoelectron peaks by making use of Koopmans' theorem [3]. For the transition metal dihalides, high quality Hartree-Fock calculations are very difficult to come by. They require much computational effort and are quite expensive. Semi-empirical methods such as CNDO and extended Hückel calculations are either not parametrized for the transition elements or are unreliable. The multiple scattering  $X_\alpha$  method shows great promise as a tool for filling this computational gap. We prevailed upon Dr. A. Garritz (National University of Mexico, Mexico City), who had been involved with such calculations on transition elements, to attempt calculations on our transition metal halide molecules. The initial results were discouraging. The experimental results displayed distinct features and trends which could not be distinguished in the calculations. These initial calculations were performed at the spin-restricted level. Subsequently, Dr. Garritz repeated these calculations with spin-polarized wave functions. In these calculations, the spin up electrons experience a different self-consistent field than the spin down electrons. As a consequence, the binding energy of a given orbital splits into two binding energies (the convention is to refer to them as having majority and minority spin) and hence should result in two peaks in the photoelectron spectrum. The magnitude of this splitting can be quite large (ca. 5 eV for  $MnCl_2$ ).

The new calculations explain the features and trends in the experimental data quite well. They therefore present as with a caveat for future investigations involving high temperature molecules containing transition, rare earth or actinide elements. Restricted Hartree-Fock or semi-empirical calculations are not likely to be adequate for the interpretation of photoelectron spectra in such systems.

We have seen how the interplay of theory and experiment in this field can provide us with a deeper knowledge of the geometric and electronic structure, and the nature of chemical bonding in high temperature systems. Fragmentation patterns in high temperature mass spectra can thereby be rationalized. For future work in this field, I believe we shall have to become more familiar with calculations involving spin-splitting, and perhaps relativistic effects.

#### References

- [1] Berkowitz, J., Adv. in High Temp. Chem. 3, 123 (1971).
- [2] Berkowitz, J. in Electron Spectroscopy-Theory, Applications and Techniques, 1, 355, et. seq., C. R. Brundle and A. D. Baker, eds. (Academic Press, London, 1977).

- [3] Koopmans, T., *Physica* 1, 104 (1934).
- [4] Berkowitz, J., *J. Chem. Phys.* 56, 2766 (1972).
- [5] Berkowitz, J. and Eland, J. H. D., *J. Chem. Phys.* 67, 2740 (1977).
- [6] Dyke, J. M., Golob, L., Jonathan, N., and Morris, A., *J. Chem. Soc. Far. Trans. II*, 71, 1026 (1975).
- [7] Berkowitz, J. and Chupka, W. A., *J. Chem. Phys.* 50, 4245 (1969).
- [8] Streets, D. G. and Berkowitz, J., *J. Electr. Spectr.* 9, 269 (1976).
- [9] Berkowitz, J. and Dehmer, J. L., *J. Chem. Phys.* 57, 3194 (1972).
- [10] Berkowitz, J. and Walter, T. A., *J. Chem. Phys.* 49, 1184 (1968).
- [11] Streets, D. G. and Berkowitz, J., *Chem. Phys. Lett.* 38, 475 (1976).
- [12] Solomonik, V. G., Zasorin, E. Z., Girichev, G. V., and Krasnov, K. S., *Izv. Vysshikh Uchebn. Zavedenii Khim. i Khim. Tekhnol.* 17, 136 (1974).
- [13] Berkowitz, J., in *Alkali Halide Vapors: Structure, Spectra and Reaction Dynamics*, Davidovits and McFadden, eds. (Academic Press, New York, 1979 or 1978).
- [14] Berkowitz, J., Dehmer, J. L., and Walker, T. E. H., *J. Chem. Phys.* 59, 3645 (1973).

#### Discussion

Question (Hastie): I would like to have some statement about what your most significant limitations are experimentally right now, such as the temperature at which you can make these photo-electron measurements, that sort of thing?

Response (Berkowitz): Yes, the apparatus that I showed for the photo-electron part was one that I have been using for the last seven or eight years and in the past several months I have started to break in a different apparatus.

The earlier apparatus had limitations of about 1000 degrees and, in fact, other laboratories that were doing this kind of work, also seemed to reach that kind of limitation and it doesn't have anything to do with being able to attain high temperatures, but rather the interaction between the attainment of high temperatures and the detection apparatus.

I think that the new apparatus that I have which tries to separate in space the manufacture of the molecular beam and its detection will be able to go considerably higher.

Also from something that has been published and I would like to talk further about with people here, the people at Southampton have an apparatus which is apparently capable of going to much higher temperature with the photo-electron spectroscopy experiments.

For photo-ionization, I think the problem is less difficult than it is for photo-electron spectroscopy. The instrumentation is a little bit more sophisticated, but we have it and it is just a matter of doing it.

I think that although the limitations have been around 1000 degrees, I see no reason why they shouldn't be 2000 degrees in the coming year.



## THE PHOTOELECTRON SPECTROSCOPIC CHARACTERIZATION OF VAPORS OVER HEATED INORGANIC SOLIDS

R. Allen Bowling, Thomas W. Lassiter, David O. Vick, and George K. Schweitzer

Department of Chemistry  
The University of Tennessee  
Knoxville, TN 37916

### 1. Introduction

Most inorganic compounds, particularly the ionic ones, are solids at room temperature. Some of them, when they are heated to produce vapors, maintain their atom-ratio integrities in the gaseous species. Of these, a sizable percentage yield the monomeric vapor species as the predominant constituent of the gaseous phase. It is chiefly this category of compounds that will be treated in the present paper, namely, those solid inorganic compounds which when heated produce vapors which are predominantly monomers having the same atom ratios as the solid substances.

A number of investigational methods have been applied to these vapor species.

- (1) Classical vapor measurements of various sorts (residue and sublimate analyses, static and flow methods, vapor density studies, effusion investigations, momentum and velocity determinations, DTA-TGA measurements) have been employed. These studies often indicate whether volatilization is congruent, sometimes give individual species vapor pressures, and sometimes identify the involved species; but for the most part, they have been supplanted by other techniques.
- (2) Chief among the techniques which have proved useful for measurements of high-temperature vapor concentrations and pressures is mass spectrometry. The approach has the potential to detect all species, is specific for each component, is highly sensitive, and can be employed over wide temperature ranges. Some difficulties can be encountered in relating the detected ions to their neutral precursors, but several techniques are available for overcoming most of these.
- (3) Electron diffraction measurements have proved useful in determinations of the interatomic distances in many gaseous species. However, there is a built-in difficulty associated with the interpretation of the data. Geometric models are assumed, calculations are made on the models, and the experimental radial distribution curves are matched. It is not always certain that the match is the only possible one or the best one.

- (4) Microwave spectroscopy has been applied to a number of simpler vapor species. These investigations lead to accurate internuclear distance values. However, as compounds become more complex and as the vapor temperature increases, the spectra tend to become so complicated that interpretation is problematic.
- (5) Infrared and Raman spectroscopies have also been employed in studies of these vapors. Thermal excitation brings complications to the investigations, but many force constants, bond lengths, and bond angles have been obtained.
- (6) Beam studies using electrostatic and magnetic deflection have yielded further information. The major data obtained from these investigations have been dipole moments.
- (7) Finally, the technique of matrix isolation has made possible a considerable amount of indirect information on the vapor species. The high-temperature vapors are isolated in appropriately-selected matrices and are then examined using various spectroscopies, the major one having been infrared. Caution must be exercised in extending the data from the matrix-isolated molecules to the free molecules.

Somewhat more recently than the above techniques, photoelectron spectroscopy (PES) has been applied to the vapors over solid inorganic compounds. This approach has the potential of providing data on vapors which are not available by any of the above methods, namely, electronic and bonding information expressed in molecular orbital (MO) terms. This technique and its application constitute the focus of this paper.

## 2. The Photoelectron Spectroscopic Technique

In a typical photoelectron spectroscopic investigation, a vapor is exposed to a beam of monoenergetic HeI photons ( $21.22 \pm 0.005$  eV). The electrons ejected in the photoelectron process are then subjected to electron spectroscopy in an electrostatic analyzer. The data usually emerge as a plot of electron intensity against kinetic energy, which is ordinarily translated into a plot of electron intensity (I) against ionization energy (in eV) by the subtraction of the electron kinetic energies from the energy of the impinging photons. The experimental apparatus must provide a proper pressure of vapor (at least  $10^{-2}$  to  $10^{-3}$  Torr) in a sample exposure chamber, a sufficiently-intense beam of photons, annulment of the magnetic fields (to below  $10^{-4}$  gauss), a high vacuum atmosphere in the spectrometer ( $10^{-5}$  Torr or better), an electron multiplying detector, and a recording system (digital or analog). Other photon sources may be used instead of the HeI one (the chief variation being the use of  $\text{AlK}\alpha$  or  $\text{MgK}\alpha$  x-rays of energies  $1486.6 \pm 0.5$  and  $1253.6 \pm 0.4$  eV), a wide variety of electrostatic as well as several magnetic spectrometers may be employed, several means of annulling the magnetic fields are available, two or three good options for electron detection are applicable, and a wide variety of recording systems can be used. The resolution of lines in an electron spectrum obtained from such an instrument depends on several factors including the linewidth of the impinging photons, the analyzer design, the analyzer aberrations, the thermal motion of the target



molecules, the constancy of the pressure, and the lifetime of the excited state. The best resolutions so far obtained are of the order of 7-9 meV with the HeI photon source and about 0.2 eV with a grating-monochromatized AlK $\alpha$  photon source.

Although Williamson irradiated K vapor with photons from a Hg arc (predominantly 4.89 eV) and subjected the emitted electrons to spectroscopy in 1928, and Lawrence and Chaffee irradiated K vapor with photons from a Co spark (monochromatized at  $5.2 \pm 0.5$  eV) and performed spectroscopy on the electrons in 1930, these experiments were followed by over 30 years inactivity. When the value of the HeI photon source was recognized, the field was reopened and work with high-temperature vapors was reinstituted in 1969.

### 3. High-Temperature Photoelectron Spectroscopy

To do photoelectron spectroscopy of vapors of the type being discussed here, it is necessary to equip the sample exposure chamber with a device which can be heated to temperatures necessary for the volatilizations. Among those capable of temperatures above 700 °C, ovens adjacent to, remote from, and directly within the sample regions have been used. Heating techniques have included wire-wound resistance heating, laser-beam irradiation, and electron bombardment.

Special difficulties are often involved in high-temperature measurements, the major ones in this case being: (a) interference of the magnetic and electrical fields of the heating devices with electron energy analysis, (b) deposition of target molecules on cooler surfaces giving rise to local and uneven surface charging which tends to broaden and shift spectral bands, (c) sample decomposition and reactions with the oven, inlet, probe, sample chamber, and spectrometer materials, (d) desorption of substances from inlet, probe, sample chamber, and spectrometer surfaces, (e) non-equilibrium volatilization in which nonreproducible mixtures of species occur, (f) uneven volatilization which results in pressure fluctuations producing band-intensity and band-position variations, and (g) vibrational hot-banding of the parent molecules.

Many modifications in instrumentation have been made in order to ameliorate or eliminate one or more of the above-mentioned problems, and varying degrees of success have been had. Problem (a) has been addressed through use of bifilar winding, shielding, and phase-sensitive detection. Problem (b) has been dealt with by directing the sample beam away from the spectrometer slit and by using cooled wells and probes for collection of the sample vapor. The troubles which arise over (c), sample decomposition and reaction, must be treated individually according to the specific properties of each high-temperature vapor species. Care must be exercised in using the available high-temperature data since some of it is subject to considerable error. The (d) desorption problem can often be handled by the techniques of baking, employing cooled probes and wells, and introducing a substance which reacts with the adsorbed contaminant and removes it as a gaseous material. The difficulty designated (e) has been eased by the use of double ovens, and (f) can be taken care of by careful design of oven geometry and heating facilities. Problem (g) has

not been addressed as yet, but could possibly be approached by use of molecular beams so disposed as to permit vibrational relaxation.

#### 4. Treatment of Photoelectron Spectroscopic Data

As mentioned before, photoelectron spectroscopic data are generally expressed as a plot of electron intensity against ionization energy. In the simplest case, a spectrum will consist of a series of bands, each band corresponding to the ionization of a single electron from one of the molecular-orbital energy levels of the target molecule. A band may contain fine structure due to the production of an ion in vibrationally and/or rotationally excited states. Further, bands may be split by Jahn-Teller and spin-orbit effects. The data derived from photoelectron spectra thus consist of the positions, intensities, splittings, and fine structures of the bands.

At the first level of approximation, the positions of the bands give the single-electron MO binding energies of the involved electrons of the neutral molecule as defined by the Hartree-Fock-Roothan theoretical approach. This oversimplification involves treating the electrons in the product ion as if they were frozen in precisely the same energy configuration as they were in the parent molecule. In spite of the obvious shortcomings of this viewpoint, the approximation has an amazingly small number of exceptions at the semi-quantitative level. The intensities, splittings, and fine structures of the bands act not only as aids in identifying the MO origins of the bands, but often give data applicable to the vibrational, rotational, and geometrical properties of the molecule and/or the product ion. Other assists in assigning MO origins to peaks in the photoelectron spectra include data from optical spectroscopy, symmetry considerations, substituent effects, relative band intensities, angular distributions, and photoelectron spectral data and interpretations on related molecules.

The importance of a knowledge of the electronic structure of a molecule expressed in terms of the MO model cannot be overemphasized. This powerful theoretical conceptuality has the potential to explain practically every physical and chemical property of any given molecule. In practice, the approach is living up to its potential as its successes continue to mount up especially in the areas of molecular structure, spectra, properties, and reactions.

#### 5. Atomic Vapors

Photoelectron spectroscopic investigations have been carried out on a number of mono-atomic vapors whose production requires heating of the solids. These are listed in table 1. All reference numbers with an X affixed indicate the use of x-ray photons; those without an X were research efforts using an ultraviolet source (usually HeI, sometimes HeII, a few with ArI). Figure 1 is a generalized representation of the type of spectrum that is usually seen. As the figure shows, the spectral display consists of several

Table 1. Atoms investigated by high-temperature PES.

K(1,5,13)	Zn(2,6,15,16X,17,83X)	Pb(4X,8X,11,18X,84X)
Rb(13)	Cd(2,6,15,16X,17,19,83X)	Bi(4X,8X,14)
Cs(13)	Hg(6,7,17,18X)	Eu(3X)
Mg(83X)		Yb(3X)
Ca(15)		
Sr(15,83X)		
Ba(9,10,15)		

sharp lines, most of them arising from ionization of the groundstate neutral atom to the ground and various excited states of the monovalent cation. Sometimes inelastic loss peaks in the neutral atom and Auger lines also appear. The most valuable data for interpreting the spectra are optical spectroscopic values. For example, the HeI photoelectron spectrum at atomic K (275 °C) arising from the 21.22 eV photons shows major lines at 4.34, 5.96, 7.01, and 7.57 eV, the first being far the most intense [13]<sup>1</sup>. The 4.34 eV line is assignable to the ionization of K(4s<sup>1</sup>) to K<sup>+</sup>, while the 5.96 and 7.01 eV lines are inelastic loss peaks arising from the excitation of neutral K to the <sup>2</sup>P(4p<sup>1</sup>) and <sup>2</sup>D(3d<sup>1</sup>) states. The line at 7.57 eV involves excitation of two neutral K atoms to the <sup>2</sup>P(4p<sup>1</sup>) state by an electron from the K(4s<sup>1</sup>) ionization. Some other lines are present due to ionization by other HeI photon lines. The spectra of Rb and Cs are similar, with the latter showing the results of spin-orbit splitting in inelastic loss peaks in the 6p level (<sup>2</sup>P<sub>1/2</sub>, <sup>2</sup>P<sub>3/2</sub>) of the neutral atom.

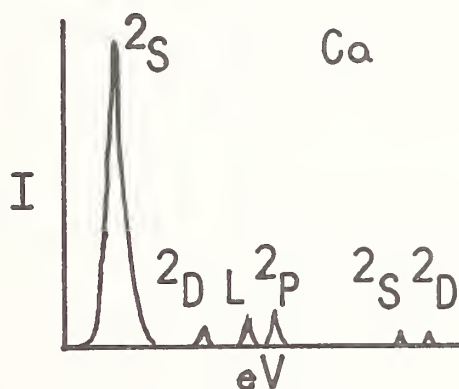


Figure 1. Representative PES spectrum of an atomic vapor.

<sup>1</sup>Figures in brackets indicate literature references at the end of this paper.

The HeI spectrum of atomic  $\text{Ca}(4s^2)$  at 740 °C shows peaks at 6.11, 7.82, 8.24, 12.60, and 13.16 eV corresponding to the  $^2S(4s^1)$ ,  $^2D(3d^1)$ ,  $^2P(4p^1)$ ,  $^2S(5s^1)$ , and  $^2D(4d^1)$  final states of  $\text{Ca}^+$  [15]. Another peak at 9.04 eV can be identified as an inelastic loss peak which arises from the excitation of neutral Ca to the  $^1P_1(4s^1 4p^1)$  state by electrons from the  $\text{Ca}(4s^2)$ -to- $^2S(4s^1)$  transition. The  $^2S(4s^1)$  peak is the most intense followed by the moderately weak  $^2P(4p^1)$  line, with the others being quite weak. The spectra of Sr and Ba are very similar.

The major lines in the  $\text{Zn}(3d^{10} 4s^2)$  spectrum (at 380 °C) appear at 9.39, 15.40, 15.51, 17.17, and 17.50 eV [15], these being identified as arising from the production of the following states of the  $\text{Zn}^+$  ion:  $^2S(3d^{10} 4s^1)$ ,  $^2P_{1/2}(3d^{10} 4p^1)$ ,  $^2P_{3/2}(3d^{10} 4p^1)$ ,  $^2D_{5/2}(3d^9 4s^2)$ ,  $^2D_{3/2}(3d^9 4s^2)$  [15]. The  $^2D$  peaks are the most intense, then the  $^2S$  peak, then the quite weak  $^2P$  peaks. A weak peak at 15.19 eV has its origin in the inelastic loss process to produce Zn in the  $^1P_1(3d^{10} 4s^1 4p^1)$  state. The spectra of Cd and Hg are similar.

Lead vapor produced at 715 °C was subjected to photoelectron spectroscopic study yielding major peaks at 7.42, 9.16, 14.59, 15.61, 15.97, 16.06, 16.57, and 18.35 eV [11]. These were assigned origins relating to the following  $\text{Pb}^+$  states:  $^2P_{1/2}(6s^2 6p^1)$ ,  $^2P_{3/2}(6s^2 6p^1)$ ,  $^4P_{1/2}(6s^1 6p^2)$ ,  $^4P_{3/2}(6s^1 6p^2)$ ,  $^2D_{5/2}(6s^2 6d^1)$ ,  $^2D_{3/2}(6s^2 6d^1)$ ,  $^4P_{5/2}(6s^1 6p^2)$ ,  $^2P_{1/2}(6s^1 6p^2)$ . The line of greatest intensity is the 7.42 eV line with the others being at least ten times weaker. The spectrum of  $\text{Bi}(6s^2 6p^3)$  at 750 °C [14] displayed four main peaks at 7.29, 8.94, 9.40, and 16.73 eV corresponding to  $^3P_0(6s^2 6p^2)$ ,  $^2P_1(6s^2 6p^2)$ ,  $^3P_2(6s^2 6p^2)$ , and  $^5S_2(6s^1 6p^3)$  states of  $\text{Bi}^+$  and three weaker peaks at 11.50, 17.12, and 17.47 eV corresponding to  $^1D_2(6s^2 6p^2)$ ,  $^3D_{2-1}(6s^2 6p^1 6d^1)$ , and  $^3F_{2-3}(6s^2 6p^1 6d^1)$  states of  $\text{Bi}^+$ .

## 6. Homonuclear Molecules

The heating of some chemical elements results in vapor species which contain more than one atom. Molecules of this sort which have been studied with photoelectron spectroscopy are listed in table 2. Again the suffix X on a reference number indicates that x-ray photons were employed in the study, where as unadorned reference numbers signify investigations using ultraviolet photons. Figure 2 is an idealized representation of a HeI photoelectron spectrum of a homonuclear diatomic molecule with the MO origins indicated above the peaks. Vibrational fine structure is depicted in this representation but will be omitted in succeeding figures. Vibrational structure may or may not appear in photoelectron spectral bands depending upon the nature of the original and final states and the



resolution of the instrument. The HeI photoelectron spectrum of  $P_2$  shows no  $\pi_g$  band since this level is unoccupied, a  $\pi_u$  band at 10.62 eV with considerable vibrational structure, a sharp  $\sigma_g$  band at 10.81 eV, and a weak  $\sigma_u$  band at 15.52 eV [25,29,33]. The structure of  $Bi_2$  is similar with spin-orbit split  $\pi_u$  peaks at 7.53 and 8.94 eV showing unresolved vibrational structure, a sharp  $\sigma_g$  peak at 9.30 eV, and a weak band with a peak at 14.87 eV possibly arising from the  $\sigma_u$  MO [14].

Table 2. Molecules of a single element investigated by high-temperature PES.

$P_2$ (25, 29, 33)	$S_2$ (2, 3, 13)
$P_4$ (26, 27, 28, 31X)	$S_8$ (20, 23, 32X)
$As_4$ (26)	$Se_2$ (24, 30)
$Sb_4$ (26)	$Te_2$ (21, 24, 30)
$Bi_2$ (8X, 14)	

The HeI photoelectron spectrum of  $S_2$  shows peaks at 9.41, 11.82, 12.33, 13.20, 14.62, 15.58, 17.70, 18.10, and 18.66 eV [22]. A complex splitting pattern is to be expected in the bands beneath the outermost band in this molecule since there are two unpaired electrons in the outermost MO( $\pi_g$ ). The peak at 9.41 eV has been assigned to the  $\pi_g$  MO, those at 11.82, 12.33, 15.58, and 18.66 to the  $\pi_u$  MO (ionic states  $^4\Pi$ ,  $^2\Pi(1)$ ,  $^2\Pi(3)$ ,  $^2\Pi(4)$ , with  $^2\Pi(2)$  undetected), those at 13.20 and 14.62 eV to the  $\sigma_g$  MO (ionic states  $^4\Sigma_g^-$  and  $^2\Sigma_g^-$ ), and those at 17.70 and 18.10 eV to the  $\sigma_u$  MO (ionic states  $^4\Sigma_u^-$  and  $^2\Sigma_u^-$ ). The spectra of  $Se_2$  and  $Te_2$  are similar except that the  $\pi_g$  band has been spin-orbit split and the bands at higher ionization energies are bunched together so much that analysis is very difficult [24]. When one compares the spectra of the series  $S_2$  to  $Se_2$  to  $Te_2$ , the bands mentioned under the  $S_2$  discussion become more closely spaced as the molecular weight rises.

Figure 3 is an idealized presentation of a HeI spectrum of a tetrahedral  $X_4$  molecule. In the  $P_4$  spectrum [28], the components at 9.5 and 9.9 eV are assigned to electron removal from the 2e orbital, those at 10.4 and 10.6 eV to the  $6t_2$  orbital, that at 11.9 eV to the  $5a_1$  orbital, and those at 15.2 and 16.3 eV to the  $5t_2$  orbital. The splits in the 2e,  $6t_2$ , and  $5t_2$  bands are Jahn-Teller in origin. The spectra of  $As_4$  and  $Sb_4$ , even though no detailed analysis of the bands has been published, are very similar to that of  $P_4$  [26]. As is often the case, the spectral bands span a smaller range of energies as one goes from  $P_4$  to  $As_4$  to  $Sb_4$ .



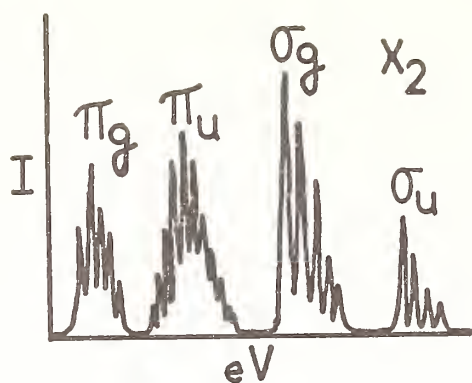


Figure 2. Representative PES spectrum of a homonuclear diatomic molecular vapor.

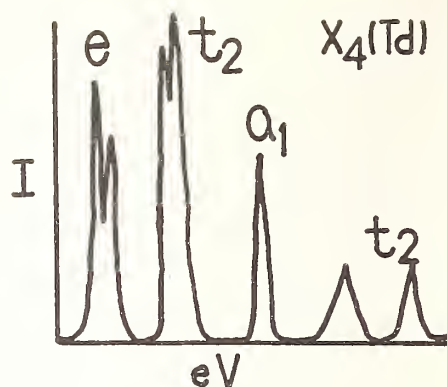


Figure 3. Representative PES spectrum of a homonuclear tetratomic molecular vapor.

## 7. Binary Molecules

Table 3 lists the binary compound vapor species which have been investigated by high-temperature photoelectron spectroscopy. As before, the presence of a suffix X on a reference indicates use of an x-ray photon source, and absence signifies use of an ultra-violet photon source. Figure 4 is a generalized representation of the HeI photoelectron spectrum of a high-temperature MX vapor. In the NaCl spectrum band peaks are seen at 9.3 and 9.8 eV, these being assigned origins from the  $\pi$  and  $\sigma$  MO levels [47,54]. In other alkali metal halides, the  $\pi$  and  $\sigma$  bands become more closely spaced as the atomic weight of the cation increases and the atomic weight of the anion decreases. In addition, as the atomic weight of the anion increases, spin-orbit splitting of the  $\pi$  band occurs. The net result in many of the K, Rb, and Cs halides is that the  $\sigma$  band and the  $\pi$  band(s) show considerable overlap. In TlCl, there is more covalent character, with the  $\pi$  and  $\sigma$  bands being spaced considerably (10.4, 13.9 eV) and a band originating from the Tl6s<sup>2</sup> electrons appearing at 9.9 eV [36]. The spectra of TlBr and TlI are similar but with spin-orbit split  $\pi$  bands and smaller spacing between the Tl6s<sup>2</sup> and the  $\pi$  band peaks. The situation is analogous for the indium halides [39]. The HeI photoelectron spectrum of SnTe vapor shows peaks at 8.6 and 8.9 eV (assigned to  $\pi_{3/2}$  and  $\pi_{1/2}$ ) and at 9.4 eV (assigned to  $\sigma$ ) [65]. The spectra of GeS, GeSe, SnS, and PbTe are similar except that no spin-orbit split of the  $\pi$  band can be seen in GeS [65]. The spectrum of TeO resembles that of Te<sub>2</sub>, this being reasonable since they are both open-shell configurations and are valence-level isoelectronic [63]. The spectrum of SiO shows three peaks, one at 11.6 eV( $\sigma$ ), another at 12.2 eV( $\pi$ ), and a third at a larger value ( $\sigma$ ) [67]. The spectrum of PN shows bands with peaks at approximately 11.9 eV( $\sigma$ ), 12.5 eV( $\pi$ ), 15.8 eV( $\sigma$ ), and 16.7 eV( $\sigma$ ) [67, 68].

The spectrum shown in figure 5 is an idealized high-temperature HeI spectrum of the vapor of a linear MX<sub>2</sub> molecule. For ZnCl<sub>2</sub> vapor, four bands appear with peaks at 11.7, 12.3, 13.0, and 14.0 eV corresponding to MO origins of  $\pi_g$ ,  $\pi_u$ ,  $\sigma_u$ , and  $\sigma_g$  [41]. The spectra of ZnBr<sub>2</sub> and ZnI<sub>2</sub> are similar except that spin-orbit splits are seen in the  $\pi$  bands. Analogous observations are made on the cadmium and mercury(II) halides [35,41,48].

Table 3. Binary molecules investigated by high-temperature PES.

NaCl (47,54)	MgCl <sub>2</sub> (69)	AlCl <sub>3</sub> (46)
NaBr (47,54)	MgI <sub>2</sub> (69)	AlBr <sub>3</sub> (46)
NaI (47,54)	CaCl <sub>2</sub> (69)	AlI <sub>3</sub> (46)
KCl (40,47,54,64)	CaI <sub>2</sub> (69)	GaCl <sub>3</sub> (46,53)
KBr (40,47,54,64)	SrCl <sub>2</sub> (69)	GaBr <sub>3</sub> (46,53)
KI (40,47,54,56,64)	SrI <sub>2</sub> (69)	GaI <sub>3</sub> (46,53,58)
RbCl (47,54,64)	BaCl <sub>2</sub> (69)	InCl <sub>2</sub> (53)
RbBr (47,54,64)	BaI <sub>2</sub> (69)	InBr <sub>3</sub> (53)
RbI (47,54,64)	ZnCl <sub>2</sub> (41,43,48,51,55)	InI <sub>3</sub> (53)
CsF (47,50,52)	ZnBr <sub>2</sub> (41,43,48,51,55)	SbCl <sub>3</sub> (60)
CsCl (45,47,49,50,52,54,64)	ZnI <sub>2</sub> (41,43,48,51,55)	SbBr <sub>3</sub> (60)
CsBr (47,49,50,52,54,64)	CdCl <sub>2</sub> (41,43,48,51)	SbI <sub>3</sub> (60)
CsI (47,49,50,52,54,56,64)	CdBr <sub>2</sub> (41,43,48,51)	P <sub>4</sub> S <sub>3</sub> (71,75X)
AgCl (62,72)	CdI <sub>2</sub> (41,43,48,51)	As <sub>4</sub> S <sub>3</sub> (71)
AgBr (62,72)	HgCl <sub>2</sub> (35,48,51,66)	P <sub>4</sub> Se <sub>3</sub> (71)
AgI (62,72)	HgBr <sub>2</sub> (35,48,51,56)	As <sub>4</sub> O <sub>6</sub> (71)
TlF (34,36,42,59,61)	HgI <sub>2</sub> (35,48,51)	
TlCl (34,36,37,56,61)	CrCl <sub>2</sub> (72)	
TlBr (34,36,37,38,61)	CrBr <sub>2</sub> (72)	
TlI (36,37,38,61)	MnCl <sub>2</sub> (72)	
InCl (39)	MnBr <sub>2</sub> (72)	
InBr (39)	FeCl <sub>2</sub> (72)	
InI (39)	FeBr <sub>2</sub> (72)	
SiO (67,73)	CoCl <sub>2</sub> (72)	
TeO (63)	CoBr <sub>2</sub> (72)	
GeS (65)	NiCl <sub>2</sub> (72)	
SnS (65)	NiBr <sub>2</sub> (72)	
GeSe (65)	PbCl <sub>2</sub> (37,70)	
SnTe (65)	PbBr <sub>2</sub> (37,56,70)	
PbTe (65)	PbI <sub>2</sub> (37,70)	
PN (57,68,73)	SnCl <sub>2</sub> (56)	
	SnBr <sub>2</sub> (56)	
	SiF <sub>2</sub> (44)	
	SeO <sub>2</sub> (74)	

The spectrum of CaCl<sub>2</sub> vapor shows a very broad band ranging from 8.8 to 11.6 eV which probably includes all four of the basic bands [69]. The spectra of the other alkaline earth chlorides and bromides are similar [69].

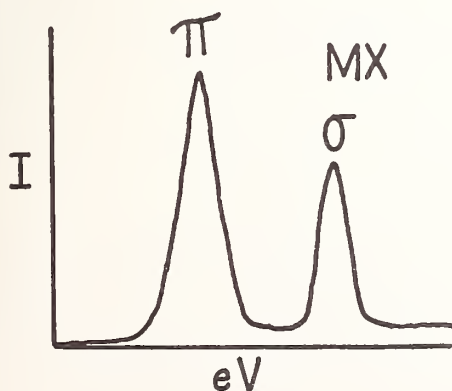


Figure 4. Representative PES spectrum of a binary MX molecular vapor.

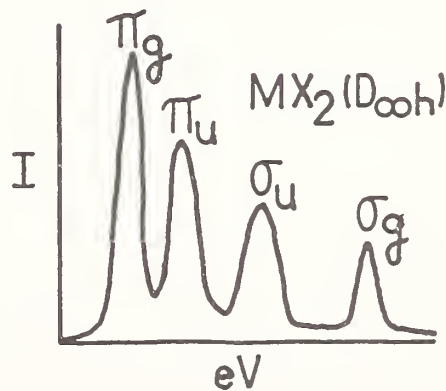


Figure 5. Representative PES spectrum of a linear MX<sub>2</sub> molecular vapor.

A typical HeI spectrum of a high-temperature vapor of a bent  $\text{MX}_2$  molecule is displayed as figure 6. A specific example of such a molecule is afforded by  $\text{PbBr}_2$  whose spectrum shows band peaks at 9.8 eV( $a_1$ ), 10.3 eV( $b_2$ ), 10.9 eV( $a_2$ ), 11.1 eV( $a_1$  and  $b_1$ ), 11.6 eV( $b_2$ ), and 16.3 eV( $a_1$ ) [56,70]. The spectra of  $\text{PbCl}_2$ ,  $\text{PbI}_2$ ,  $\text{SnCl}_2$ , and  $\text{SnBr}_2$  resemble the  $\text{PbBr}_2$  spectrum quite closely [56,70]. In the spectrum of  $\text{SiF}_2$ , peaks at 11.1 eV( $a_1$ ), 15.6 eV( $a_2$  and  $b_2$ ), and 17.1 eV( $a_1$  and  $b_1$ ) are seen [44]. For gas-phase  $\text{SeO}_2$ , the spectral peaks and their identifications are as follows: 11.76 eV( $a_1$ ), 12.18 eV( $a_2$  and  $b_2$ ), 14.56 eV( $b_2$ ), 14.95 eV( $a_1$  and  $b_1$ ), and 19.90 eV( $a_1$ ) [74].

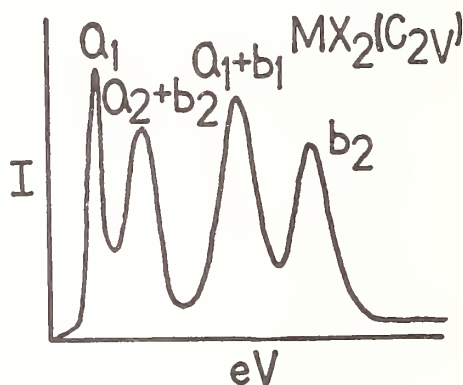


Figure 6. Representative PES spectrum of a bent  $\text{MX}_2$  molecular vapor.

A HeI spectrum of the type that would be expected for a planar  $\text{MX}_3$  compound is presented as figure 7. The experimental values observed for  $\text{AlCl}_3$  vapor are 12.01 eV( $a_2'$ ), 12.47 eV( $e'$ ), 12.73 eV( $e''$ ), 13.33 eV( $a_2''$ ), 14.04 eV( $e'$ ), and 15.97 eV( $a_1'$ ) [46]. The spectra of  $\text{AlBr}_3$  and  $\text{AlI}_3$  show about the same pattern except that the innermost  $e'$  band is split in  $\text{AlBr}_3$  and both  $e'$  bands as well as the  $e''$  band are split in  $\text{AlI}_3$  [46]. The situation in the gallium halides is about the same [46,53], whereas in the indium halides only  $e'$  splitting in  $\text{InBr}_3$  and  $\text{InI}_3$  has been identified [53].

Figure 8 is an idealized representation of the expected spectrum of a pyramidal  $\text{MX}_3$  compound. Experimental values for  $\text{SbCl}_3$  are 10.73 eV( $a_1$ ), 11.50 eV( $a_2$ ), 11.62 eV( $e$ ), 12.28 eV( $e$ ), 13.20 eV( $a_1$ ), and 13.98 eV( $e$ ). The data for  $\text{SbBr}_3$  and  $\text{SbI}_3$  are similar except that the bands are more closely spaced; the outermost  $e$  bands are split in  $\text{SbBr}_3$ , and all  $e$  bands are split in  $\text{SbI}_3$  [60].

## 8. Ternary Molecular Species

Table 4 is a compilation of the ternary compound monomeric vapor species which have been studied by high-temperature photoelectron spectroscopic procedures. All listed compounds were investigated using HeI photons. Figure 9 is the spectrum of a typical alkali metal cyanide. The values for KCN are 8.8 eV( $\sigma$  and  $\pi$ ) and 10.3 eV( $\sigma$ ), the MO assignments being predicted upon a linear  $\text{CN}^-$  ion with only minimal perturbation by the cation [81]. The other alkali metal cyanides are quite similar except the Cs 5p electron bands appear at the higher binding energies in the CsCN spectrum.  $\text{CsBO}_2$  is a representative alkali

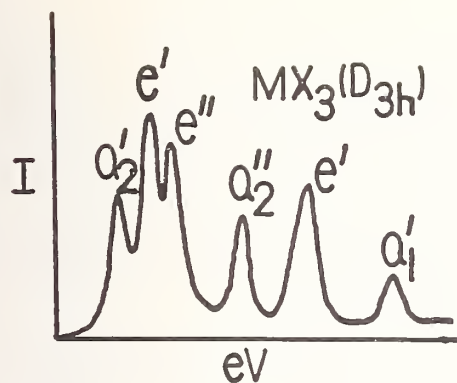


Figure 7. Representative PES spectrum of a planar  $\text{MX}_3$  molecular vapor.

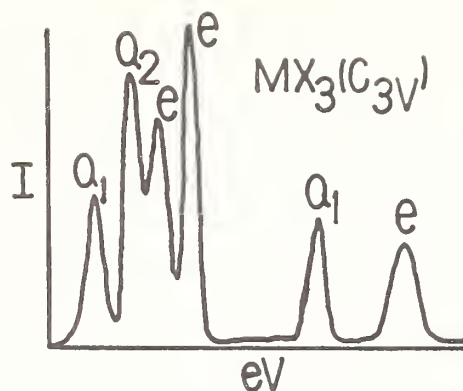


Figure 8. Representative PES spectrum of a pyramidal  $\text{MX}_3$  molecular vapor.

metal metaborate with values of 8.9, 11.3, 11.6, and 12.9 eV corresponding to  $\pi_g$ ,  $\pi_u$ ,  $\sigma_u$ , and  $\sigma_g$  MO involvements [82]. Again, the anion is assumed to be only slightly perturbed by the cation so that a linear  $\text{BO}_2^-$  can be taken as the basis of symmetry considerations leading to the MO assignments. The other alkali metaborates are similar with Cs 5p bands showing up in the  $\text{CsBO}_2$  spectrum and a Tl 6s band appearing in the spectrum of  $\text{TlBO}_2$ .

Table 4. Ternary compounds investigated by high-temperature PES.

NaOH (82)	NaPO <sub>3</sub> (80)
KOH (82)	KPO <sub>3</sub> (80)
RbOH (82)	RbPO <sub>3</sub> (80)
CsOH (82)	CsPO <sub>3</sub> (80)
NaCN (81)	CsClO <sub>4</sub> (82)
KCN (71)	NaReO <sub>4</sub> (78)
RbCN (81)	KReO <sub>4</sub> (78)
CsCN (81)	RbReO <sub>4</sub> (78)
Hg(CN) <sub>2</sub> (76)	CsReO <sub>4</sub> (78)
NaBO <sub>2</sub> (82)	TlReO <sub>4</sub> (77)
KBO <sub>2</sub> (82)	NaAlF <sub>4</sub> (82)
RbBO <sub>2</sub> (82)	KAlF <sub>4</sub> (82)
CsBO <sub>2</sub> (82)	RbAlF <sub>4</sub> (82)
TlBO <sub>2</sub> (77)	CsAlF <sub>4</sub> (82)
KNO <sub>3</sub> (79)	Tl <sub>2</sub> SO <sub>4</sub> (77)
RbNO <sub>3</sub> (79)	
CsNO <sub>3</sub> (79)	
TlNO <sub>3</sub> (77)	

Figure 10 depicts a generalized alkali metal nitrate spectrum. The peak values for  $\text{RbNO}_3$  are 8.9, 9.9, 10.6, 15.9, and 16.6 eV, these corresponding to electron expulsions from the  $a_2'$ ,  $e''$ ,  $e'$ ,  $e'$ , and  $a_2''$  MO levels (assuming a planar triangular  $\text{NO}_3^-$  with only slight perturbation by the cation) [79]. The other alkali metal nitrate spectra resemble that of  $\text{RbNO}_3$  very closely, as does the spectrum of  $\text{TlNO}_3$ , but with an added peak due to the Tl 6s electron level [77,79]. The spectra for the alkali metaphosphates are quite similar to those of the nitrates except the bands are more closely spaced [80].

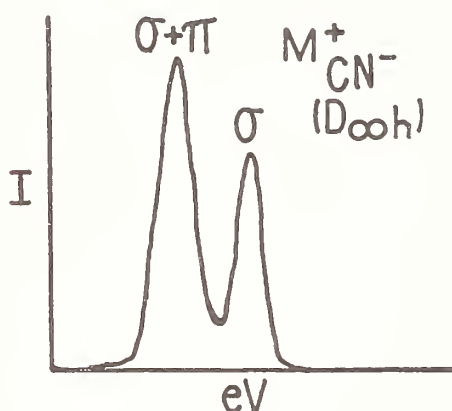


Figure 9. Representative PES spectrum of a typical alkali metal cyanide vapor.

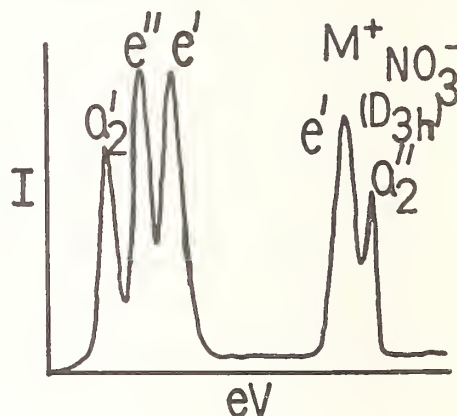


Figure 10. Representative PES spectrum of a typical alkali metal nitrate vapor.

The remainder of the compounds listed in table 4 have anions which are essentially tetrahedral. A typical HeI photoelectron spectrum for these is depicted in figure 11, the assumption being made that the anion is unperturbed by the cation so that it essentially retains its tetrahedral symmetry. The data on the perchlorate, sulfate, the perrhenates, and the tetrafluoraluminates fit this depiction very well [82,78,77]. However, in the case of the perrhenates, theoretical considerations lead to the ordering of the levels as  $t_1 t_2 a_1 t_2 e$  rather than  $t_1 t_2 e t_2 a_1$ . In the cases of the Cs compounds, Cs 5p bands are seen and for the Tl compounds, a Tl 6s band can be observed.

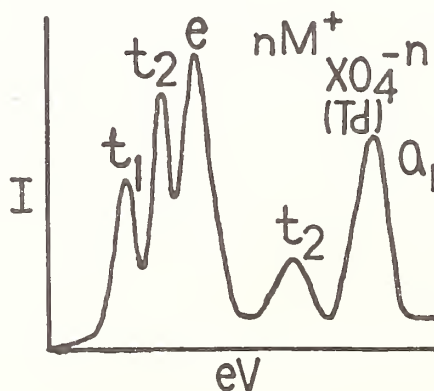


Figure 11. Representative PES spectrum of a tetrahedral anion molecular vapor.



## 9. Polytopic Bonding

Several investigators in recent years have proposed the idea of polytopic bonding to describe a number of monomeric gaseous ionic compounds made up of a simple cation and a complex anion [85]. Such vapors might include  $\text{MOH}$ ,  $\text{MCN}$ ,  $\text{MNO}_3$ ,  $\text{M}_2\text{SO}_4$ ,  $\text{M}_2\text{WO}_4$ ,  $\text{M}_2\text{MoO}_4$ ,  $\text{MReO}_4$ ,  $\text{MA}\ell\text{F}_4$ , and  $\text{MBO}_2$  where M is an alkali metal or univalent thallium. The idea of polytopicity was prompted by theoretical calculations and by observations which have been noted in electron diffraction, IR spectral, and microwave studies. The data in many cases point to the possibility that classical fixed-nuclei models for these vapor monomers at high temperatures are not entirely adequate, and that a model in which the cation makes large-amplitude motions with respect to the complex anion might fit better. Alternately, a model in which the cation relates equally to all of the ligands of the complex anion may be employed.

Experimental electron diffraction data (on  $\text{MBO}_2$ ,  $\text{MNO}_3$ ,  $\text{MReO}_4$ ,  $\text{M}_2\text{SO}_4$ ,  $\text{Na}_2\text{CrO}_4$ ,  $\text{Cs}_2\text{MoO}_4$ ,  $\text{Cs}_2\text{WO}_4$ ,  $\text{NaAlF}_4$ ,  $\text{KAlCl}_4$ ,  $\text{TlInCl}_4$ ) have been interpreted to indicate that the complex anion shows high symmetry with all bond angles and bond distances being essentially equal, and that the geometry of the complex anion is not greatly altered by the cation [86]. The root-mean-square amplitudes of the vibrations involving the cation are extraordinarily high, 0.20 Å and above, as compared to those only involving the anion atoms, in the range 0.03-0.07 Å; and the lengths of the bonds involving the cations are usually long as compared to such bonds in simple compounds. As the vapor temperature is increased, less usable structural information can be obtained from the diffraction patterns, especially information regarding the cation, and in a number of cases features characteristic of an associated cation seem to be missing.

These observations have been taken to indicate that the high-temperature vapors consist of a relatively rigid and symmetrical complex anion only moderately perturbed by the cation which shows considerable freedom of motion relative to the anion. This freedom of motion is assignable to population of higher vibrational levels of the molecules, the levels being those associated with the weakly-bonded cation, and thus being those requiring small amounts of excitation energy. It has been proposed that the cation motions might be represented as large displacements occurring on the surface of an imaginary sphere (or other appropriate surface of high symmetry) circumscribed about the complex anion. With sufficient excitation, the molecule could be viewed as having a dynamic configuration in which the cation is seen as belonging to all anion ligands with equal probability.

Several of these gaseous complex anion compounds have also been studied by infrared spectroscopy ( $\text{MOH}$ ,  $\text{NaCN}$ ,  $\text{KCN}$ ,  $\text{MBO}_2$ ,  $\text{CsNO}_2$ ,  $\text{CsNO}_3$ ,  $\text{MReO}_4$ ,  $\text{LiAlF}_4$ ,  $\text{NaAlF}_4$ ) [87]. Some usable data have been obtained, even though the investigations have been beset by numerous experimental difficulties largely due to thermal excitation. It has been observed that the vibrational frequencies of the complex anion are independent of the cation or nearly independent of the cation in the vapor species, and that the cation-involved frequencies (especially the bending frequencies) tend to be quite low (ca 120  $\text{cm}^{-1}$  and below), and in some cases

spectral lines associated with these frequencies seem to be missing. Several of the investigators have interpreted these observations to indicate that no single simple description of the cation-to-anion bonding in these compounds is completely satisfactory. They imply that a dynamic model might work better to explain the data. This approach fits well with the views expressed by the electron diffraction workers. In addition, infrared investigations have been carried out on matrix-isolated vapors ( $\text{MOH}$ ,  $\text{MCN}$ ,  $\text{MBO}_2$ ,  $\text{MNO}_3$ ,  $\text{MC}_2\text{O}_3$ ,  $\text{MC}_2\text{O}_4$ ,  $\text{K}_2\text{SO}_4$ ,  $\text{Rb}_2\text{SO}_4$ ,  $\text{MAlF}_4$ ) [88]. These studies show that the cation involved frequencies are quite low, an observation in accord with the vapor infrared studies.

The only gaseous compound of this type which has been investigated by microwave spectroscopy is  $\text{KCN}$  [89]. Because the compound is a ternary one and the temperature required for volatilization is relatively high, the spectrum tends to be so complicated that interpretation is difficult. This complication may be assignable to population of numerous excited rotational and vibrational levels which results in a large number of lines and a consequent reduction of individual line intensities. The overall behavior seems compatible with the idea of polytopicity, as the author notes. Similarly, little work has been done on these compounds with vapor Raman spectroscopy. The available spectra (on  $\text{InAlF}_4$  and  $\text{InAlCl}_4$ ) [90] do not show sufficient resolution to permit a decision regarding the symmetry of the complex anion. There is a possibility that results may be more conclusive with this method and investigations are now being attempted by this research group.

In addition to these experimental observations, a number of relevant theoretical calculations have been carried out. Initially, Bak, Clementi, and Kortzeborn [91] produced a detailed set of quantum-mechanical calculations which showed that only a marginal energy difference of about 0.4 eV exists between  $\text{LiNC}$  and  $\text{LiCN}$ . Clementi, Kistenmacher, and Popkie [92] followed this by mapping the energy surface for various positions of the  $\text{Li}^+$  ion around the  $\text{CN}^-$  anion. They found that the lowest energy path from  $\text{Li-NC}$  to  $\text{Li-CN}$  will permit the  $\text{Li}^+$  to "orbit" the  $\text{CN}^-$  upon excitation of about 0.3-0.4 eV. They stated that the situation is one for which no traditional preferred structural formula can be written. Other ways of interpreting their conclusions are to say that the  $\text{Li-N-C}$  bending vibrations change, in the limit, to an orbiting of the  $\text{Li}^+$  around the  $\text{CN}^-$ , or to say that the  $\text{Li}^+$  has an equal probability of being at any position on the energy surface about the  $\text{CN}^-$ .

Rambidi [85,93] followed these calculations with computations on  $\text{LiNC}$  assuming a relatively simple electrostatic model. He arrived at results very similar to those of Clementi, *et al.* [92]. Going on to treat  $\text{CsNO}_3$ ,  $\text{TlReO}_4$ , and  $\text{NaAlF}_4$  by the same model, he found that in each case there was a wide range of computational parameters for which the interaction energy varied only slightly for motion of the cation on an approximately spherical surface (or other appropriate surface of high symmetry) circumscribed about the complex anion. That is, only small variations in interaction energy result from large displacements of the cation relative to the anion.

Demetjev and Kracht [94] have conducted a quantum-mechanical SCF analysis of the  $\text{LiBO}_2$  vapor monomer. The results are quite similar to those for  $\text{LiNC}$ , with large amplitudes of vibration of the  $\text{Li}^+$  and a small force constant for this vibration. The investigators, therefore, believe that the molecule should be considered to be polytopic. Rambidi [94]

had previously made calculations of the root-mean-square vibrational amplitudes of the  $\text{MBO}_2$  monomer (with  $\text{M}=\text{Li}$ ,  $\text{Na}$ , and  $\text{Rb}$ ) for various temperatures. Comparisons of values for various atom pairs at 0 K and 1500 K are quite interesting. For example, the root-mean-square amplitude of the  $\text{Na-O}$  (stretching vibration) is 0.057 Å at 0 K and 0.129 Å at 1500 K, while for the  $\text{B=O}$  (stretching vibration) the values are 0.035 Å at 0 K and 0.042 Å at 1500 K. The 1500 K/0 K ratio is 2.26 for  $\text{Na-O}$  as compared to only 1.20 for  $\text{B=O}$ . Similar values were obtained for  $\text{LiBO}_2$  and  $\text{RbBO}_2$ , as well as for other pertinent compounds such as  $\text{MCN}$ ,  $\text{MNO}_3$ ,  $\text{MCrO}_3$ , and  $\text{M}_2\text{SO}_4$ . The results of such computations can be taken as an indication that these compounds constitute dynamic systems in which the alkali metal cations which are weakly bonded to a relatively rigid complex anion exhibit large displacements due to excitations involving low-frequency M-O (or M-appropriate ligand) vibrations.

Other views have also been expressed in explanation of these findings. One investigator has suggested quantum-mechanical tunneling with penetration of the walls of the energy wells. Still another way of interpreting the non-rigidity, as stated previously, has been to assume that the cation belongs to all anion ligands with equal probability. However, in any case, the excitation energy required for mobilizing the cation is largely supplied by the thermal energy employed to volatilize the compound.

In an effort to ascertain whether the technique of PES might be applicable to decisions on the geometries of ternary compound vapor monomers, a series of theoretical calculations have been made. For example, using both semi-empirical and *ab initio* SCF-procedures, molecular orbital energy calculations have been conducted for  $\text{Cs}^+\text{NO}_3^-$  in  $\text{C}_s$ ,  $\text{C}_{2v}$ , and  $\text{C}_{3v}$  configurations and for the  $\text{D}_{3h}\text{NO}_3^-$  ion. As the symmetry is reduced for  $\text{D}_{3h}$  to  $\text{C}_{3v}$  to  $\text{C}_{2v}$  to  $\text{C}_s$  splits in the bands have been followed. In almost all instances, the splitting is of the order of 0.1-0.2 eV. Similar results have been obtained on numerous other compounds. When one observes the band breadths in the experimental spectra, they are usually considerably more than 0.2 eV. Indications are, therefore, that PES investigations using presently available techniques will probably not be able to permit one to select among the various geometric possibilities. Further, it is not now possible to be sure, but indications are that higher resolution experiments might not be of any more assistance. It is difficult to tell the difference between band broadening produced by perturbation of the symmetry of the initial molecule and band broadening produced by the Jahn-Teller effect upon photoionization. That is, the band broadening produced by the effect of a localized  $\text{Cs}^+$  upon a  $\text{D}_{3h}\text{NO}_3^-$  (reducing the symmetry from  $\text{D}_{3h}$  to  $\text{C}_{2v}$ ) is difficult to distinguish from the band broadening produced by the Jahn-Teller effect upon ionization of a minimally perturbed or isotropically perturbed  $\text{D}_{3h}\text{NO}_3^-$ .

## 10. Conclusion

The photoelectron spectroscopic investigation of vapors produced by heating inorganic ionic solids has advanced rapidly during the past few years and has been extended to a wide variety of compounds. The major results have been the measurement of the MO structures of the vapor molecules. The importance of this elucidation of the electronic structures of



these species cannot be overestimated since practically all properties of the molecules can be related to the MO formalism. Experiments on other compounds are proceeding as improvements in the technique are made. Higher resolution work is being done permitting better study of fine structures, and higher temperature investigations are being carried out permitting data on many more substances to be obtained.

---

The authors wish to express their gratitude to the National Science Foundation for Grant CHE-76-23502 under which this work was performed. Appreciation is also expressed to John D. Allen, Jr. (for instrumentation), John E. Bloor, L. Chopin Cusachs, Frederick A. Grimm, Ronald E. Sherrod (for theoretical calculations), Gary W. Boggess, Timothy D. Goodman, Carol B. Hammer, Robert B. MacNaughton, and Andrew C. McMurtrie (for experimental investigations). We also wish to thank Anne M. Smalley for explanation of the Bench-Geronimo-Rose Phenomenon.

#### References

- [1] Williamson, R. C., Proc. Natl. Acad. Sci. 14, 796 (1928).
- [2] Harrison, H., J. Chem. Phys. 52, 901 (1970).
- [3] Fadley, C. S. and Shirley, D. A., Phys. Rev. A2, 1109 (1970).
- [4] Khodeyev, Y. S., et al., Uppsala Univ. Inst. Phys. Rpt. UUIP-802 (1972).
- [5] Lawrence, E. O. and Chaffee, M. A., Phys. Rev. 36, 1099 (1930); 37, 1233 (1931).
- [6] Walker, T. E. H., Berkowitz, J., Dehmer, J. L., and Waber, J. T., Phys. Rev. Lett. 31, 678 (1973).
- [7] Frost, D. C., McDowell, C. A., and Vroom, D. A., Chem. Phys. Lett. 1, 93 (1967).
- [8] Khodeyev, Y. S., Siegbahn, H., Hamrin, K., and Siegbahn, K., Chem. Phys. Lett. 19, 16 (1973).
- [9] Brehm, B. and Höfler, K., Intl. J. Mass Spectr. 17, 371 (1975).
- [10] Hotop, H. and Mahr, D., J. Phys. B8, L301 (1975).
- [11] Suzer, S., Banna, M. S., and Shirley, D. A., J. Chem. Phys. 63, 3473 (1975).
- [12] Krause, M. O., in NATO Advanced Institute Series B: Physics, F. Wiulleumier, ed. (Plenum Press, New York, 1976).
- [13] Williams, T. A. and Potts, A. W., J. Electr. Spectr. 8, 331 (1976).
- [14] Suzer, S., Lee, S. T., and Shirley, D. A., J. Chem. Phys. 65, 412 (1976).
- [15] Suzer, S., Lee, S. T., and Shirley, D. A., Phys. Rev. A13, 1842 (1976).
- [16] Banna, M. S., Frost, D. C., McDowell, C. A., and Wallbank, B., J. Chem. Phys. 68, 696 (1978).
- [17] Hush, N. S. and Suzer, S., Chem. Phys. Lett. 46, 411 (1977).
- [18] Siegbahn, K., J. Electr. Spectr. 5, 4 (1974).
- [19] Suzer, S. and Shirley, D. A., J. Chem. Phys. 41, 2481 (1974).

- [20] Boschi, R. and Schmidt, W., *Inorg. Nucl. Chem. Lett.* 9, 643 (1973).
- [21] Berkowitz, J., *J. Chem. Phys.* 62, 4075 (1975).
- [22] Dyke, J. M., Golob, L., Jonathan, N., and Morris, A., *J. Chem. Soc. Far. Trans. II* 71, 1026 (1975).
- [23] Richardson, N. V. and Weinberger, P., *J. Electr. Spectr.* 6, 109 (1975).
- [24] Streets, D. G. and Berkowitz, J., *J. Electr. Spectr.* 9, 269 (1976).
- [25] Bulgin, D. K., Dyke, J. M., and Morris, A., *J. Chem. Soc. Far. Trans. II* 72, 2225 (1976).
- [26] Berkowitz, J., in *Vacuum Ultraviolet Radiation Physics*, E.-E. Koch, R. Haensil, and C. Kunz, eds., p. 107 (Pergamon/Vieneg, New York, 1974).
- [27] Evans, S., Joachim, P. J., Orchard, A. F., and Turner, D. W., *Intl. J. Mass Spectr.* 9, 41 (1972).
- [28] Brundle, C. R., Kuebler, N. A., Robin, M. B., and Basch, H., *Inorg. Chem.* 11, 20 (1972).
- [29] Chong, D. P. and Takahata, Y., *J. Electr. Spectr.* 10, 137 (1977).
- [30] Lee, S. T., Suzer, S., and Shirley, D. A., *Chem. Phys. Lett.* 41, 25 (1976).
- [31] Banna, M. S., Frost, D. C., McDowell, C. A., and Wallbank, B., *J. Chem. Phys.* 66, 3509 (1977).
- [32] Banna, M. S., Frost, D. C., McDowell, C. A., and Wallbank, B., *Chem. Phys. Lett.* 43, 428 (1976).
- [33] Potts, A. W., Glenn, K. G., and Price, W. C., *Disc. Faraday Soc.* 54, 66 (1972).
- [34] Berkowitz, J. and Walter, T. A., *J. Chem. Phys.* 49, 1184 (1968).
- [35] Eland, J. H. D., *Intl. J. Mass Spectr.* 4, 37 (1970).
- [36] Berkowitz, J., *J. Chem. Phys.* 56, 2766 (1972).
- [37] Berkowitz, J., in *Electron Spectroscopy*, D. A. Shirley, ed., p. 391 (Elsevier, New York, 1972).
- [38] Evans, S., *Far. Disc.* 54, 143 (1972).
- [39] Berkowitz, J. and Dehmer, J. L., *J. Chem. Phys.* 57, 3194 (1972).
- [40] Allen, J. D., Jr., Boggess, G. W., Goodman, T. D., Wachtel, A. S., and Schweitzer, Geo. K., *J. Electr. Spectr.* 2, 289 (1973).
- [41] Boggess, G. W., Allen, J. D., Jr., and Schweitzer, Geo. K., *J. Electr. Spectr.* 2, 467 (1973).
- [42] Dehmer, J. L., Berkowitz, J., and Cusachs, L. C., *J. Chem. Phys.* 58, 5681 (1973).
- [43] Cocksey, B. G., Eland, J. H. D., and Danby, C. J., *J. Chem. Soc. Far. Trans. II* 69, 1558 (1973).
- [44] Fehlner, T. P. and Turner, D. W., *Inorg. Chem.* 13, 754 (1974).
- [45] Akopyan, M. E. and Timoshenko, M. M., *Prib. Tech. Eksp.*, 164 (1974).
- [46] Lappert, M. F., Pedley, J. B., Sharp, G. J., and Westwood, N. P. C., *J. Electr. Spectr.* 3, 237 (1974).
- [47] Goodman, T. D., Allen, J. D., Jr., Cusachs, J. C., and Schweitzer, Geo. K., *J. Electr. Spectr.* 3, 289 (1974).
- [48] Cusachs, L. C., Grimm, F. A., and Schweitzer, Geo. K., *J. Electr. Spectr.* 3, 229 (1974).



- [49] Berkowitz, J., Dehmer, J. L., and Walker, T. E. H., J. Electr. Spectr. 3, 323 (1974).
- [50] Timoshenko, M. M. and Akopyan, M. E., Khim. Vys. Energ. 8, 211 (1974).
- [51] Berkowitz, J., J. Chem. Phys. 61, 407 (1974).
- [52] Berkowitz, J., Dehmer, J. L., and Walker, T. E. H., J. Chem. Phys. 59, 3645 (1973).
- [53] Dehmer, J. L., Berkowitz, J., Cusachs, L. C., and Aldrich, H. S., J. Chem. Phys. 61, 594 (1974).
- [54] Potts, A. W., Williams, T. A., and Price, W. C., Proc. Roy. Soc. London, A341, 147 (1974).
- [55] Orchard, A. F. and Richardson, N. V., J. Electr. Spectr. 6, 61 (1975).
- [56] Evans, S. and Orchard, A. F., J. Electr. Spectr. 6, 207 (1975).
- [57] Wu, M. and Fehlner, T. P., Chem. Phys. Lett. 36, 114 (1975).
- [58] Wittel, K. and Manne, R., J. Chem. Phys. 63, 1322 (1975).
- [59] Streets, D. G. and Berkowitz, J., Chem. Phys. Lett. 38, 475 (1976).
- [60] Nicholson, D. G. and Rademacher, P., Acta Chem. Scand. A28, 1136 (1974).
- [61] Williams, D. R., Poole, R. T., Jenkins, J. G., Liesegang, J., and Lecky, R. C. G., J. Electr. Spectr. 9, 11 (1976).
- [62] Voubacho, P. S. and Saltsburg, H., J. Electr. Spectr. 8, 359 (1976).
- [63] Potts, A. W. and Williams, T. A., Chem. Phys. Lett. 42, 550 (1976).
- [64] Potts, A. W. and Williams, T. A., J. Chem. Soc. Far. Trans. II 72, 1892 (1976).
- [65] Wu, M. and Fehlner, T. P., J. Am. Chem. Soc. 98, 7578 (1976).
- [66] Egde11, R. G., Orchard, A. F., Lloyd, D. R., and Richardson, N. V., J. Electr. Spectr. 12, 415 (1977).
- [67] Bulgin, D., Dyke, J., Goodfellow, F., Jonathan, N., Lee, E., and Morris, A., J. Electr. Spectr. 12, 67 (1977).
- [68] Bulgin, D. K., Dyke, J. M., and Morris, A., J. Chem. Soc. Far. Trans. II 73, 983 (1977).
- [69] Hammer, C. A., Allen, J. D., Jr., Cusachs, L. C., and Schweitzer, Geo. K., J. Electr. Spectr. 13, 149 (1978).
- [70] Berkowitz, J., in Electron Spectroscopy: Theory, Techniques, and Applications, Vol. 1., C. R. Brundle and A. D. Baker, eds., pp. 414-420 (Academic Press, New York, 1977).
- [71] Cannington, P. H. and Whitfield, H. J., J. Electr. Spectr. 10, 35 (1977).
- [72] MacNaughton, R. B. and Schweitzer, Geo. K., to be published.
- [73] Chong, D. P. and Takahata, Y., J. Electr. Spectr. 10, 137 (1977).
- [74] Potts, A. W., J. Electr. Spectr. 11, 157 (1977).
- [75] Banna, M. S., Frost, D. C., McDowell, C. A., and Wallbank, B., J. Chem. Phys. 66, 3509 (1977).
- [76] Burroughs, P., Evans, S., Hamnett, A., Orchard, A. F., and Richardson, N. V., J. Chem. Soc. Chem. Comm., 921 (1974).
- [77] Schweitzer, Geo. K., McMurtrie, A. C., Allen, J. D., Jr., Cusachs, L. C., Vick, D. O., and Finkelstein, G., J. Electr. Spectr. 10, 155 (1977).
- [78] Vick, D. O., Woodley, D. G., Bloor, J. E., Allen, J. D., Jr., Mui, T. C., and Schweitzer, Geo. K., J. Electr. Spectr. 13, 247 (1978).
- [79] Bowling, R. A., Sherrod, R. E., Bloor, J. E., Allen, J. D., Jr., and Schweitzer, Geo. K., Inorg. Chem. (1978), to be published.

- [80] Bowling, R. A. and Schweitzer, Geo. K., to be published.
- [81] Bowling, R. A. and Schweitzer, Geo. K., to be published.
- [82] Lassiter, T. W. and Schweitzer, Geo. K., to be published.
- [83] Melhorn, W., Brenckman, B., and Hansman, D., *Phys. Scripta*, 16, 177 (1977).
- [84] Reiter, A., Dipl.-thesis, Univ. of Freiburg, 1977.
- [85] Rambidi, N. G., *J. Mol. Struct.* 28, 77, 89 (1975).
- [86] (a) Articles by Rambidi, N. G., Spiridonov, V. P., and their coworkers in *Russ. J. Struct. Chem.* 2, 63, 209 (1961); 3, 267 (1962); 5, 164 (1964); 11, 731 (1970); 12, 185, 990 (1971); 13, 3, 293, 295, 320, 910 (1972); 14, 317, 499 (1973); 15, 300, 591 (1974); 16, 611 (1975); *Mosc. Univ. Bull.* 25, 1 (1970); 26, 24 (1971). (b) Ugarov, V. I., Ezhov, Y. S., and Rambidi, N. G., *J. Mol. Struct.* 25, 357 (1975). (c) Rambidi, N. G., *J. Mol. Struct.* 28, 77 (1975). (d) Hargittai, M., and Hargittai, I., *The Molecular Geometries of Coordination Compounds in the Vapour Phase*, pp. 15-37, 128-154 (Elsevier, New York, 1977).
- [87] (a) Buchler, A. and Marram, E. P., *J. Chem. Phys.* 39, 292 (1963); (b) McCorry, L. D., et al., *J. Phys. Chem.* 67, 1086 (1963); (c) Spoliti, M. and Stafford, F. E., *Inorg. Chim. Acta*, 2, 301 (1968); (d) Leroi, G. E. and Klemperer, W., *J. Chem. Phys.* 35, 774 (1961); (e) Spinar, L. H., *Spectrochim. Acta*, 12, 244 (1958).
- [88] (a) Ismail, Z. K., et al., *J. Chem. Phys.* 57, 5137 (1972), *J. Mol. Spectr.* 45, 304 (1973). (b) Smyrl, N. and Devlin, J. P., *J. Phys. Chem.* 77, 3067 (1973); *J. Chem. Phys.* 60, 2540 (1974). (c) Snelson, A., et al., *J. Phys. Chem.* 75, 2609 (1971). (d) Smith, D., et al., *J. Chem. Phys.* 54, 4437 (1971). (e) Ritzhaupt, G. and Devlin, J. P., *J. Chem. Phys.* 62, 1982 (1975). (f) Hovdan, H., et al., preprint on  $\text{MA}_2\text{F}_4$  in Ar matrix (1977). (g) Seshadri, K. S., et al., *J. Mol. Spectr.* 30, 128 (1969). (h) Acquista, N. and Abramowitz, S., *J. Chem. Phys.*, 51, 2911 (1969). (i) Ritzhaupt, G. and Devlin, J. P., *Inorg. Chem.* 16, 486 (1977); *J. Phys. Chem.* 79, 2265 (1975).
- [89] (a) Pearson, E. F. and Trueblood, M. B., *Astrophys. J.* 179, L145 (1973); (b) Matsamura, C. and Lide, D. R., Jr., *J. Chem. Phys.* 50, 71 (1969); (c) Lide, D. R., Jr. and Matsamura, C., *J. Chem. Phys.* 50, 3080 (1969); (d) Kuczowski, R. L., Lide, D. R., Jr., and Krisher, L. C., *J. Chem. Phys.* 44, 3131 (1966); (e) Lide, D. R., Jr. and Kuczowski, R. L., *J. Chem. Phys.* 46, 4768 (1967); (f) Kuijpers, P., Torring, T., and Dymanus, A., *Chem. Phys. Lett.* 42, 423 (1976).
- [90] Radloff, P. L. and Papatheodorou, G. N., in *Proceedings of the Symposium on High Temperature Metal Halide Chemistry* (The Electrochemical Society, Electrothermics and Metallurgy Division, Atlanta, October 9-14, 1977), paper 394. [They also ran  $\text{InInX}_4$ , but the  $\text{InInX}_4$  monomer may not predominate in the vapor.]
- [91] Bak, B., Clementi, E., and Kortzeborn, R. N., *J. Chem. Phys.* 52, 746 (1970).
- [92] Clementi, E., Kistenmacher, H., and Popkie, H., *J. Chem. Phys.* 58, 2460 (1973).
- [93] Lunichev, V. N. and Rambidi, N. G., *J. Struct. Chem.* 18, 298, 300 (1977).
- [94] Dementjev, A. and Kracht, D., *Chem. Phys. Lett.* 35, 243 (1975).
- [95] Rambidi, N., *J. Struct. Chem.* 5, 165 (1964).

Question (Weltner): Is there any evidence for the "Spiridinoff (i.e., polytopical bonding) effect"? That is, the idea that in order to account for the thermodynamic third law values of molecules with large complex anions, that the "Spiridinoff effect" had to be invoked but this idea has been disputed. Can you comment on this?

Response (Bowling): Well, the big thing we see is that on going from lithium to cesium nitrate there is very little difference in the spectra obtained. So, that it is almost independent of the cation and it is associated with the anion. It causes maybe a shift of the spectral band, but the intensity and splittings remain relatively constant.

Comment (Berkowitz): My understanding is that the Spiridinoff effect was based on Spiridinoff's experiments by electron defraction and that he was getting large vibrational amplitudes in the electron diffraction study for these kinds of systems. And, therefore, he was invoking this large free displacement of the metal ions around the negative anion. I think that is the source of the Spiridinoff argument or one of the sources.

If I could just ask a question. The spectra you showed are primarily like hand drawn replicas of things?

Response (Bowling): I just did this to give you an idea of what the spectra looked like. Those are not the actual spectra obtained.

Question (Berkowitz): Isn't it much harder often to see the kind of details that you have shown for some of these more complex species?

Response (Bowling): Oh, yes, in some cases, the noise is tremendous. I would say you might get 100 counts per second, signal. The background might be up around 300 to 400 counts, so that sometimes it is difficult with some of the molecules. Another thing that I failed to mention, we have also made studies of the alkali- meta-phosphates,  $\text{NaPO}_3$  and through  $\text{CsPO}_3$  and the spectrum obtained was very similar to that for the nitrates except that the bands were compressed slightly and there was some overlapping of bands.

AB INITIO MOLECULAR ORBITAL STUDIES OF SOME HIGH TEMPERATURE METAL HALIDE COMPLEXES<sup>1</sup>

L. A. Curtiss  
Chemical Engineering Division  
Argonne National Laboratory  
Argonne, IL 60439

The use of ab initio molecular orbital calculations to aid in the characterization, i.e., structures and energies, of metal halide complexes present in high temperature salt vapors has been investigated. Standard LCAO-SCF methods were used and calculations were carried out using the minimal STO-3G basis set. The complexes included in this study were  $\text{Al}_2\text{F}_6$ ,  $\text{Al}_2\text{Cl}_6$ ,  $\text{AlF}_3\cdot\text{NH}_3$ ,  $\text{AlCl}_3\cdot\text{NH}_3$ , and  $\text{AlF}_3\cdot\text{N}_2$ . The  $\text{Al}_2\text{X}_6$  complexes are found to have  $\text{D}_{2h}$  symmetry in agreement with most experimental results. A planar form was found to be considerably higher in energy. The  $\text{AlX}_3\cdot\text{NH}_3$  complexes are found to have  $\text{C}_{3v}$  symmetry with a small barrier to rotation about the Al-N axis. The  $\text{AlF}_3\cdot\text{N}_2$  complex is found to be weakly bound together with a binding energy of -8.2 kcal/mole at the STO-3G level.

## 1. Introduction

There has been considerable interest in the complexes formed in the high temperature vapors (300-500 °C) of metal halide compounds having low volatility [1-3].<sup>2,3</sup> Vapor density, molecular beam, and mass spectrometric methods have been among the techniques used to help identify the polymeric species present in the high temperature vapors. Information on the structures of these complexes has been obtained using electron diffraction with help from Raman, infrared, and microwave spectroscopy. Still, there are many unanswered questions concerning the nature of the complexes.

<sup>1</sup>Work performed under the auspices of the Material Science Office of the Division of Basic Energy Science of the Department of Energy.

<sup>2</sup>Figures in brackets indicate the literature references at the end of this paper.

<sup>3</sup>Editor's note: see also chapters in this volume by Papatheodorou and by Schäfer and the book "High Temperature Vapors Science and Technology," J. W. Hastie, Academic Press (1975).



In order to develop other means of investigating these questions, we have undertaken a study of the use of ab initio molecular orbital theory as an aid in the characterization of metal halide complexes present in high temperature molten salt vapors. The complexes considered in this study are: (a) the aluminum halide dimers,  $\text{Al}_2\text{F}_6$  and  $\text{Al}_2\text{Cl}_6$ ; (b) the complexes between an aluminum halide molecule and ammonia,  $\text{AlF}_3 \cdot \text{NH}_3$  and  $\text{AlCl}_3 \cdot \text{NH}_3$ ; and (c) the complex between aluminum trifluoride and nitrogen,  $\text{AlF}_3 \cdot \text{N}_2$ . The structures and energies of these complexes are determined using a minimal basis set. In addition, force constants and electron distributions of several of these complexes are calculated.

Theoretical calculations on these complexes may help to answer questions raised by some of the experimental results, such as whether  $\text{Al}_2\text{Cl}_6$  is distorted from  $D_{2h}$  symmetry by rotation about a torsion axis as suggested by a recent electron diffraction study and whether  $\text{AlCl}_3 \cdot \text{NH}_3$  is eclipsed or staggered. Also, these calculations can give information on such things as the structure of the planar form of  $\text{Al}_2\text{Cl}_6$  and on the strength of the bond between  $\text{AlF}_3$  and  $\text{N}_2$ .

## 2. Computational Methods

In the following study, standard molecular orbital methods [4,5] are employed. The type of calculation carried out here is ab initio in the sense that it does not use any experimental information (except for the values of fundamental constants). Ab initio theories are generally divided into single determinant methods which use a single molecular orbital configuration and more complicated configuration interaction methods in which the wave function is written as the sum of several determinants.

In all the calculations carried out here, a spin restricted single determinant method for closed shell molecules (singlets) has been used. In this method, pairs of electrons are assigned to spatial molecular orbitals,  $\psi_i$ , which are, in turn, approximated as linear combinations of a set of basis functions  $\phi_u$ ,

$$\psi_i = \sum_u c_{ui} \phi_u \quad (1)$$

The coefficients  $c_{ui}$  are then chosen by a variational procedure in which the total energy of the molecule is minimized.

There are various different types of basis sets that are used in ab initio single determinant methods. The simplest is the minimal which consists of just enough atomic-orbital type functions to describe the ground state of the corresponding atom (1s for hydrogen; 1s, 2s,  $2p_x$ ,  $2p_y$ ,  $2p_z$  for fluorine). Improvements can be made on the minimal basis set by adding more s and p functions. These are generally called extended basis sets. Also these basis sets can be augmented by the addition of d or polarization functions. In all the calculations reported in this paper, the minimal STO-3G basis set [5] has been used. The STO-3G basis set uses a set of Slater type functions that are replaced by a least-squares-fitted combination of three Gaussian functions.



In a study of molecules containing second row atoms, Collins, et al. [6] noted that although the STO-3G basis is small and lacks  $d$  functions, it does quite well in determining the geometries of molecules containing aluminum atoms. The optimized STO-3G geometries for  $AlF_3$  and  $AlCl_3$  in table 1 are in very good agreement with the observed geometries. Hence, it is reasonable to expect that the STO-3G basis should do well for the structures of the complexes considered in this paper:  $Al_2F_6$ ,  $Al_2Cl_6$ ,  $AlF_3 \cdot NH_3$ ,  $AlCl_3 \cdot NH_3$ , and  $AlF_3 \cdot N_2$ .

Table 1. STO-3G optimized geometries<sup>a</sup> for  $AlF_3$  and  $AlCl_3$   
(experimental values in parentheses).

	$r(Al-X), \overset{\circ}{A}$	$X-Al-X, \text{degrees}$	Energy, a.u. <sup>d</sup>
$AlF_3^b$	1.60 (1.63 $\pm$ 0.01)	120 (120)	- 533.24983
$AlCl_3^c$	2.05 (2.06 $\pm$ 0.01)	120 (118 $\pm$ 1.5)	-1603.02719

<sup>a</sup> $C_{3v}$  symmetry assumed.

<sup>b</sup>Theory: reference [6] (note that the optimized bondlength is incorrectly reported as 1.56  $\overset{\circ}{A}$  in this reference). Experiment: reference [8].

<sup>c</sup>Theory: this work. Experiment: E. Z. Zasorin and N. G. Rambidi, Zh. Strukt. Khim, 8, 391 (1967).

<sup>d</sup>1 a.u. = 627.5 kcal/mole.

The structures of these complexes can be described in terms of a set of geometrical parameters which are discussed in the next section. In the geometry optimization procedure used here, these parameters are optimized with respect to the total energy. The resulting bondlengths and bond angles are believed to have computational uncertainties of  $\pm 0.01 \overset{\circ}{A}$  and  $\pm 1^\circ$ , respectively.

### 3. Results and Discussion

#### 3.1 $Al_2F_6$ and $Al_2Cl_6$

For  $Al_2F_6$  and  $Al_2Cl_6$ , we have considered the two structures illustrated in figure 1. Structure I is formed when two tetrahedra share a common edge. The aluminum atoms are located at the center of the tetrahedron and the halide atoms are at the apexes of the tetrahedra. Structure II is similar to I except that it is completely planar.

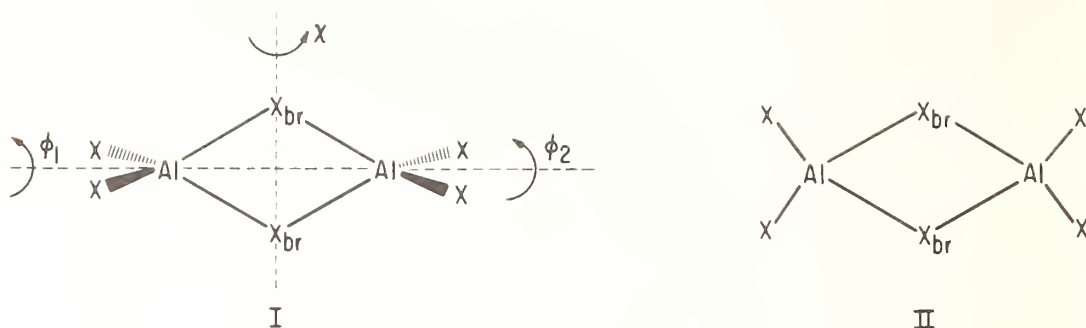


Figure 1.  $\text{Al}_2\text{X}_6$  structures with  $\text{X} = \text{F}$  or  $\text{Cl}$ .

In the geometry optimization of  $\text{Al}_2\text{Cl}_6$  (structure I)  $D_{2h}$  symmetry was imposed and the two tetrahedra were allowed to distort with the exception that the terminal  $\text{Al-Cl}$  bond-lengths were kept fixed at the ST0-3G optimized value for  $\text{AlCl}_3$  of 2.05 Å. This should be a good approximation since, as is shown later, the terminal  $\text{Al-F}$  bondlengths in  $\text{Al}_2\text{F}_6$  do not change significantly upon optimization. The parameters optimized are listed in table 2 along with the resulting values. The bridged  $\text{Al-Cl}$  bondlengths (2.24 Å) in  $\text{Al}_2\text{Cl}_6$  lengthen by 0.19 Å over their value in the monomer. The terminal  $\text{ClAlCl}$  bond angles increase only slightly from  $120.0^\circ$  in the monomer to  $122.8$  in the dimer, while the bridged  $\text{ClAlCl}$  angle decreases to  $94.7^\circ$ .

The  $D_{2h}$  symmetry of structure I was tested by rotating the terminal  $\text{AlCl}_2$  groups about axes ( $\phi_1$  and  $\phi_2$  in fig. 1) containing the bisectors of the terminal  $\text{ClAlCl}$  angles and the two aluminum atoms. Rotation of the two  $\text{AlCl}_2$  groups by  $5^\circ$  in the same direction ( $+\phi_1$ ,  $+\phi_2$ ) and in opposite directions ( $+\phi_1$ ,  $-\phi_2$ ) both led to increases in energy. Hence, the  $D_{2h}$  symmetry of structure I appears to be a definite minimum in the energy surface.

The geometry optimization of the planar structure of  $\text{Al}_2\text{Cl}_6$  (II) led to the results given in table 2. The energy of structure II is 84.2 kcal/mol above that of structure I, indicating considerable unfavorable interaction between the terminal chlorines and the bridged chlorines in the planar configuration. This is also indicated by the decrease in the terminal  $\text{ClAlCl}$  bond angle from  $120.0^\circ$  in monomer to  $103.3$  in the dimer.

Experimentally, the structure of  $\text{Al}_2\text{Cl}_6$  has been studied using electron diffraction by Palmer and Elliot [7] in 1938 and by Akishin, Rambidi, and Zasorin [8] in 1959. Both groups concluded that it has  $D_{2h}$  symmetry corresponding to structure I in figure 1 and the geometries that they determined are in good agreement with the ST0-3G results (see table 2). The electron diffraction results for  $\text{Al}_2\text{Cl}_6$  indicate that the bridge  $\text{Al-Cl}$  distances increase by 0.15-0.18 Å compared to the ST0-3G prediction of 0.19 Å. Both theory and experiment indicate that the terminal  $\text{ClAlCl}$  bond angle in the complex changes very little from the  $\text{ClAlCl}$  angle of  $120^\circ$  in the monomer. The experimental results indicate that the bridge  $\text{ClAlCl}$  angle in the complex decreases considerably from what it is in the monomer to a value of  $80-87^\circ$ . The ST0-3G calculation gives an angle of  $94.7^\circ$ .

Table 2. STO-3G optimized geometries<sup>a</sup> for Al<sub>2</sub>F<sub>6</sub> and Al<sub>2</sub>Cl<sub>6</sub>  
(experimental results<sup>b,c</sup> in parentheses).

Structure <sup>d</sup>	Parameter <sup>d</sup>	Al <sub>2</sub> F <sub>6</sub>	Al <sub>2</sub> Cl <sub>6</sub>
I	r(Al-X)	1.60 (1.63, 1.63) <sup>b</sup>	2.05 <sup>e</sup> (2.06, 2.04) <sup>c</sup>
	r(Al-X <sub>br</sub> )	1.72 (1.80, 1.80)	2.24 (2.21, 2.24)
	∠XAlX	124.6° (120°, 116°)	122.8° (118°, 122°)
	∠X <sub>br</sub> AlX <sub>br</sub>	80.0° ( 90°, 98°)	94.7° ( 80°, 87°)
II	r(Al-X)	1.61	2.05 <sup>e</sup>
	r(Al-X <sub>br</sub> )	1.75	2.31
	∠XAlX	104.2°	103.3°
	∠X <sub>br</sub> AlX <sub>br</sub>	73.0°	75.5°

<sup>a</sup>The parameters r(Al-X<sub>br</sub>) and ∠X<sub>br</sub>AlX<sub>br</sub> are given for comparison with experiment. The parameters actually optimized were r(X<sub>br</sub>-X<sub>br</sub>) and r(Al-Al). Bondlengths are in Å.

<sup>b</sup>For Al<sub>2</sub>F<sub>6</sub>, the experimental geometries were estimated from the geometries of AlF<sub>3</sub>, AlCl<sub>3</sub>, and Al<sub>2</sub>Cl<sub>6</sub>. The first set of values is from reference [10] and the second set is from reference [11].

<sup>c</sup>For Al<sub>2</sub>Cl<sub>6</sub>, the first set of values is from reference [7] and the second set is from reference [8].

<sup>d</sup>Illustrated in figure 1.

<sup>e</sup>Not optimized.

Some experimental results [1] have indicated that there may be some distortion of the D<sub>2h</sub> symmetry of Al<sub>2</sub>Cl<sub>6</sub> by a rotation of one of the AlCl<sub>2</sub> groups about an axis (χ in fig. 1) passing through the two bridged chlorines. To check out this possibility, we carried out a STO-3G calculation on structure I with one of the AlCl<sub>2</sub> groups rotated by 5° about the χ axis and found that the energy increased. This seems to indicate that the equilibrium structure of Al<sub>2</sub>Cl<sub>6</sub> does not have a tendency to distort from its D<sub>2h</sub> symmetry.

An estimate of the rigidity of twisting about the χ axis in comparison to the other motions may be made by calculating the second derivatives of the Al<sub>2</sub>Cl<sub>6</sub> energy with respect to coordinates corresponding to these motions. These derivatives may be approximated by changing each angle by ± 5° and using the formula

$$\partial^2 \epsilon / \partial \chi^2 = [\epsilon(\chi + \Delta) + \epsilon(\chi - \Delta) - 2\epsilon(\chi)] / \Delta^2 \quad (2)$$

where  $x$  is the coordinate,  $\Delta$  is the size of the variation in the coordinate, and  $\varepsilon$  is the energy. For  $\chi$ ,  $\phi$ , and  $\theta = \angle \text{ClAlCl}$ , the following results (with energy in atomic units and angles in radians) are obtained:

$$\partial^2 \varepsilon / \partial \chi^2 = 0.03228$$

$$\partial^2 \varepsilon / \partial \phi_1^2 = 0.16770$$

$$\partial^2 \varepsilon / \partial \theta^2 = 0.15744 .$$

They indicate that the  $\chi$  coordinate corresponds to a loose motion when compared to the  $\theta$  and  $\phi$  coordinates which are more rigid.

Turning now to the  $\text{Al}_2\text{F}_6$  complex, the geometry of structure I (fig. 1) was optimized in a similar manner as for structure I of  $\text{Al}_2\text{Cl}_6$ , except that the Al-F bond lengths were included in the optimization procedure. The parameters optimized and their resulting values are given in table 2. The  $D_{2h}$  symmetry of this structure was tested in the same manner as in the case of  $\text{Al}_2\text{Cl}_6$  by twisting the terminal FAlF groups about the Al-Al axis ( $\phi_1$  and  $\phi_2$ ) and about the  $\text{F}_{\text{br}}-\text{F}_{\text{br}}$  axis ( $\chi$ ). The results indicated that  $D_{2h}$  symmetry was again preferred.

The planar  $\text{Al}_2\text{F}_6$  structure (II in fig. 1) was also optimized in a similar manner to the  $\text{Al}_2\text{Cl}_6$  structure. The results are given in table 2. The energy is again considerably higher (69.6 kcal/mol) than structure I. In other work [9], structures were considered for  $\text{Al}_2\text{F}_6$  complexes in which the bridge was composed of 0, 1, and 3 fluorines. All of these structures were also found to be less stable than structure I.

The  $\text{Al}_2\text{F}_6$  geometry has not been measured experimentally, but has been estimated [10,11] by comparing the geometries of  $\text{AlF}_3$ ,  $\text{AlCl}_3$ , and  $\text{Al}_2\text{Cl}_6$  (see table 2). The only major discrepancy between the ST0-3G and the estimated geometries is for the bridge FAlF angle. The ST0-3G results indicate that this angle in  $\text{Al}_2\text{F}_6$  is  $80.0^\circ$ , a decrease from  $94.7^\circ$  in  $\text{Al}_2\text{Cl}_6$ . In contrast, the estimate for this angle in  $\text{Al}_2\text{F}_6$  is  $90-98^\circ$ , an increase from  $80-87^\circ$  in  $\text{Al}_2\text{Cl}_6$ . Since fluorine has a smaller van der Waals radius than chlorine, it would be expected that the fluorines should be closer together in the bridge. Hence, the ST0-3G prediction for the bridge angle in  $\text{Al}_2\text{F}_6$  is probably more reasonable than the estimated value.

Table 3 gives complexation energies for  $\text{Al}_2\text{F}_6$  and  $\text{Al}_2\text{Cl}_6$  (i.e., the difference between the energy of the complex and the energy of two monomers). The  $\text{AlF}_3$  dimer (structure I) has a complexation energy of -112.9 kcal/mol. Correction [12] for differences in vibrational, rotational, and translational energies between the complex and two  $\text{AlF}_3$  molecules gives an enthalpy of complexation of -109.9 kcal/mol. The  $\text{AlCl}_3$  dimer (structure I) has a complexation energy of -46.7 kcal/mol and an enthalpy of complex formation of -45.1. Experimentally [10], the enthalpies of complex formation have been measured to be -49.0 kcal/mol for  $\text{Al}_2\text{F}_6$  and -30.2 kcal/mol for  $\text{Al}_2\text{Cl}_6$ . Hence, the ST0-3G basis set overestimates by a considerable amount the interaction energy of these complexes. A larger basis set is probably necessary to obtain reasonable complexation energies [9]. However, the ST0-3G basis appears to do adequately when it comes to the geometries of these complexes.

Table 3. ST0-3G energies

Complex	Energy, a.u. <sup>a</sup>	Complexation Energy, a.u.
Al <sub>2</sub> F <sub>6</sub> (I)	-1066.67961	-112.9
Al <sub>2</sub> F <sub>6</sub> (II)	-1066.56863	- 43.3
Al <sub>2</sub> Cl <sub>6</sub> (I)	-3206.12874	- 46.7
Al <sub>2</sub> Cl <sub>6</sub> (II)	-3205.99466	+ 37.5
AlF <sub>3</sub> ·NH <sub>3</sub>	- 588.77159	- 41.6
AlCl <sub>3</sub> ·NH <sub>3</sub>	-1658.58159	- 62.1
AlF <sub>3</sub> ·N <sub>2</sub>	- 640.76356	- 8.2

<sup>a</sup>1 a.u. = 627.5 kcal/mol .

### 3.2 AlF<sub>3</sub>·NH<sub>3</sub> and AlCl<sub>3</sub>·NH<sub>3</sub>

We initially considered ethane-like structures with C<sub>3v</sub> symmetry for AlF<sub>3</sub>·NH<sub>3</sub> and AlCl<sub>3</sub>·NH<sub>3</sub> as illustrated in figure 2. ST0-3G optimized geometries for AlF<sub>3</sub> (table 1), AlCl<sub>3</sub> (table 1), and NH<sub>3</sub> [13] (r(N-H) = 1.033 Å, ∠HNH = 104.2°, E = -55.45542 a.u.) were used as initial guesses for the structures. The geometry and rotational conformation of each complex was determined.

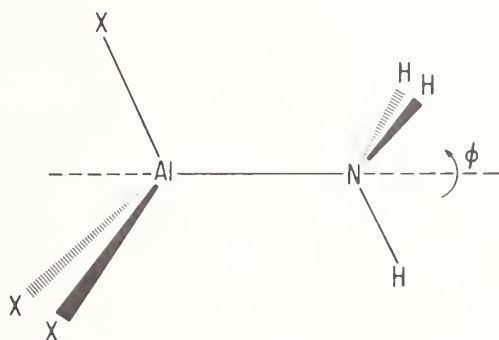


Figure 2. Structure of AlX<sub>3</sub>·NH<sub>3</sub> (in the figure  $\phi = 180^\circ$ ).

Both staggered and eclipsed forms of AlF<sub>3</sub>·NH<sub>3</sub> were optimized. The geometry of the eclipsed form is listed in table 4. The optimized Al-N bondlength is 1.99 Å, while the optimized values of the Al-F and N-H bondlengths in the complex remain nearly the same as in the monomers. The optimized geometry of the staggered form is nearly the same as the eclipsed form and is only 0.33 kcal/mol higher in energy. Hence, the barrier to rotation about the Al-N axis is very small.



Table 4. ST0-3G optimized geometries<sup>a</sup> for  $\text{AlF}_3 \cdot \text{NH}_3$  and  $\text{AlCl}_3 \cdot \text{NH}_3$  (experimental results<sup>b</sup> in parentheses).

Geometrical Parameter <sup>c</sup>	$\text{AlF}_3 \cdot \text{NH}_3$	$\text{AlCl}_3 \cdot \text{NH}_3$
$r(\text{Al-N})$	1.99	1.94 (1.996)
$r(\text{Al-X})$	1.62	2.05 <sup>d</sup> (2.10)
$r(\text{N-H})$	1.03	1.03 <sup>d</sup>
$\angle \text{XAlN}$	100.1°	101.2° (101.0°)
$\angle \text{HNA1}$	112.2°	112.4°
$\phi$	0.0°	180.0°

<sup>a</sup> $\text{AlF}_3 \cdot \text{NH}_3$  is eclipsed and  $\text{AlCl}_3 \cdot \text{NH}_3$  is staggered. Bondlengths in Å.

<sup>b</sup>Reference [14].

<sup>c</sup>Defined in figure 2.

<sup>d</sup>Held fixed at the monomer values.

The possibility that the  $\text{AlF}_3 \cdot \text{NH}_3$  complex does not have  $C_{3v}$  symmetry was investigated by relaxing its symmetry to  $C_s$ , i.e., a plane of symmetry passing through the Al-N axis, one of the hydrogens, and one of the fluorines. It was found that any changes in the geometry away from  $C_{3v}$  symmetry led to a higher energy. Hence, the minimum energy structure for  $\text{AlF}_3 \cdot \text{NH}_3$  appears to have  $C_{3v}$  symmetry.

In the case of the  $\text{AlCl}_3 \cdot \text{NH}_3$  complex, the same parameters as for the  $\text{AlF}_3 \cdot \text{NH}_3$  complex were optimized with the exception that the Al-F and N-H bondlengths were held fixed. This should be a good approximation since they do not change significantly upon optimization for  $\text{AlF}_3 \cdot \text{NH}_3$ . Both staggered and eclipsed forms were optimized. In contrast to  $\text{AlF}_3 \cdot \text{NH}_3$ , the staggered rotational conformation is lower in energy than the eclipsed form. Again, the difference in energy between the two forms is very small (0.13 kcal/mol). The resulting geometry for the staggered conformation is given in table 4.

The ST0-3G results for  $\text{AlCl}_3 \cdot \text{NH}_3$  are in very good agreement with the electron diffraction study of Hargittai, et al. [14] as indicated in table 4. The theoretical results for the similar complex,  $\text{AlF}_3 \cdot \text{NH}_3$ , indicate that the assumption of  $C_{3v}$  symmetry in the interpretation of the experimental results is valid. The ST0-3G results also indicate that there is almost free rotation about the Al-N axis. This may be due to the fact that the interaction between the chlorines and the hydrogens is quite small.

The energies for  $\text{AlF}_3 \cdot \text{NH}_3$  and  $\text{AlCl}_3 \cdot \text{NH}_3$  are given in table 3. The  $\text{AlF}_3 \cdot \text{NH}_3$  complex has a binding energy of -41.3 kcal/mol and that of the  $\text{AlCl}_3 \cdot \text{NH}_3$  is -62.1 kcal/mol. Correction for differences in vibrational, rotational, and translational energies between the complex and the  $\text{AlX}_3$  and  $\text{NH}_3$  molecules is difficult to calculate because many of the vibrational frequencies of the complex have not been reported. However, the correction should be small ( $\sim 2\text{-}4$  kcal/mol) as it was for  $\text{Al}_2\text{F}_6$  and  $\text{Al}_2\text{Cl}_6$ . Experimentally [15], the enthalpy of

complex formation of  $\text{AlCl}_3 \cdot \text{NH}_3$  has been measured to be  $-39.9 \text{ kcal/mol}$ . Again, as in the case of the  $\text{AlCl}_3$  dimer, the STO-3G basis set overestimates the interaction energy by a considerable amount. However, it does find that  $\text{AlCl}_3 \cdot \text{NH}_3$  is more strongly bound together than  $\text{Al}_2\text{Cl}_6$  in agreement with the experimental results.

It is interesting to compare the strengths of the various complexes considered so far. In the case of the  $\text{Al}_2\text{X}_6$  complexes, the largest binding energy occurs when  $\text{X} = \text{F}$ ; whereas, in the case of the  $\text{AlX}_3 \cdot \text{NH}_3$  complexes, the largest binding energy occurs when  $\text{X} = \text{Cl}$ . One explanation for this result can be found in the STO-3G Mulliken population analysis [16] in table 5. The aluminum atom has more of a positive charge on it in  $\text{AlCl}_3$  than in  $\text{AlF}_3$ . Hence, on the basis of a simple electrostatic interaction picture, the  $\text{AlCl}_3 \cdot \text{NH}_3$  complex is indeed expected to have a more negative binding energy than  $\text{AlF}_3 \cdot \text{NH}_3$ . On the other hand,  $\text{Al}_2\text{F}_6$  has a more negative binding energy than  $\text{Al}_2\text{Cl}_6$  because there is probably more repulsion between the two bridged chlorines than between the two bridged fluorines due to the fact that the chlorines are larger in size and have more negative charge than the fluorines.

### 3.3 $\text{AlF}_3 \cdot \text{N}_2$

The possibility that complexes may be formed between  $\text{AlCl}_3$  and nonpolar gases such as argon and nitrogen is quite intriguing, but no evidence for complexes of that type has yet been found [17]. To investigate this possibility, we carried out calculations on the complex between  $\text{AlF}_3$  and  $\text{N}_2$ . The structure considered is illustrated in figure 3. STO-3G optimized geometries for  $\text{AlF}_3$  (table 1) and  $\text{N}_2$  [13] [ $r(\text{N}-\text{N}) = 1.134 \text{ \AA}$ ,  $E = -107.50065 \text{ a.u.}$ ] were used as initial guesses for the structure.

Table 5. Atomic populations of  $\text{AlF}_3$ ,  $\text{AlCl}_3$ ,  $\text{AlF}_3 \cdot \text{NH}_3$ , and  $\text{AlCl}_3 \cdot \text{NH}_3$ .

	$\text{AlX}_3$		$\text{AlX}_3 \cdot \text{NH}_3$			
	Al	X	Al	X <sup>a</sup>	N	H <sup>a</sup>
X=F	11.825	9.392	11.838	9.449	7.494	0.773
X=Cl	11.730	17.423	11.731	17.510	7.503	0.746

<sup>a</sup>The population of all three atoms in each group are equivalent to the accuracy shown.

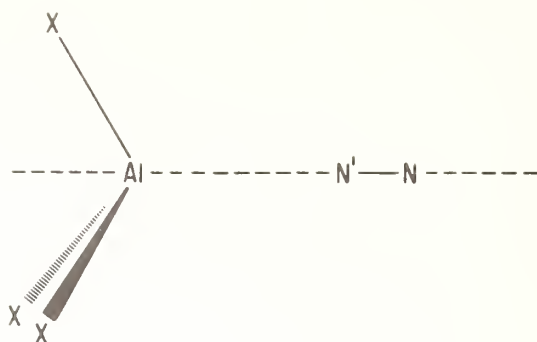


Figure 3. Structure of  $\text{AlX}_3 \cdot \text{N}_2$

Optimization of the geometry of  $\text{AlF}_3 \cdot \text{N}_2$  indicates that  $\text{N}_2$  lies on the  $C_3$  axis of the  $\text{AlF}_3$  molecule and is pointed towards the aluminum. The resulting geometry is

$$\begin{array}{ll} r(\text{Al}-\text{N}') = 2.942 \text{ \AA} & \angle \text{FAlN}' = 94.5^\circ \\ r(\text{Al}-\text{F}) = 1.605 \text{ \AA} & \angle \text{AlN}'\text{N} = 180.0^\circ \\ r(\text{N}'-\text{N}) = 1.136 \text{ \AA} & \end{array}$$

The  $\text{AlF}_3$  becomes pyramidal in the complex. The N-N bondlength increases slightly by 0.002 Å in the complex. A complex in which the  $\text{N}_2$  molecule was situated perpendicular to the  $C_3$  axis was also investigated. It was found to be considerably higher in energy than the complex in which  $\text{N}_2$  coincided with the  $C_3$  axis.

The binding energy of the  $\text{AlF}_3 \cdot \text{N}_2$  complex is -8.2 kcal/mol which is on the order of the binding energy of some hydrogen bonded complexes [18], but considerably smaller than that of most alkali halide complexes. Hence, since most hydrogen bonded complexes are difficult to "see" with such techniques as electron diffraction or infrared spectroscopy, the  $\text{AlF}_3 \cdot \text{N}_2$  complex probably would also be difficult to detect with such techniques. This would also apply to complexes of the other aluminum halides with  $\text{N}_2$ , such as  $\text{AlCl}_3 \cdot \text{N}_2$ .

#### 4. Conclusions

The following conclusions from this theoretical study of high temperature salt vapor species can be drawn:

1. Theoretical calculations can provide useful information concerning the structures and energies of metal halide complexes and may be helpful in the future as an aid in their characterization.
2. Both  $\text{Al}_2\text{F}_6$  and  $\text{Al}_2\text{Cl}_6$  are found to have  $D_{2h}$  bridged structures. The energies of both are overestimated by the ST0-3G basis, while the ST0-3G optimized geometries are in good agreement with experimental and estimated geometries.
3. The ST0-3G basis set results indicate that the experimental assumption of  $C_{3v}$  symmetry for complexes of the type  $\text{AlX}_3 \cdot \text{NH}_3$  is valid. The barrier to rotation about the Al-N axis is found to be very small.

4. The  $\text{AlF}_3 \cdot \text{N}_2$  complex is found to have a binding energy of  $-8.2 \text{ kcal/mol}$ . This is on the order of the typical hydrogen bonded complex and not nearly as strong as the other metal halide complexes considered in this study.

---

The author wishes to thank Dr. Milton Blander and Dr. George Papatheodorou for helpful discussions.

### References

- [1] Hargittai, M. and Hargittai, I., The Molecular Geometries of Coordination Compounds in the Vapour Phase (Elsevier Scientific Publishing Company, N.Y., 1977).
- [2] Bauer, S. H. and Porter, R. F., Molten Salt Chemistry, M. Blander, ed. (Interscience, N.Y., 1964).
- [3] Schäfer, H., Angew. Chem. Int. Ed., England, **15**, 713 (1976).
- [4] Schaeffer, H., The Electronic Structure of Atoms and Molecules (Addison-Wesley Publishing Company, Reading, Mass., 1972).
- [5] Hehre, W. J., Stewart, R. F., and Pople, J. A., J. Chem. Phys. **51**, 2657 (1969).
- [6] Collins, J. B., Schleyer, P. v. R., Binkley, J. S., and Pople, J. A., J. Chem. Phys. **64**, 5142 (1976).
- [7] Palmer, K. J. and Elliot, N., J. Amer. Chem. Soc. **60**, 1852 (1938).
- [8] Akishin, P. A., Rambidi, N. G., and Zasorin, E. Z., Kristallografiya, **4**, 186 (1959); Eng. Trans., p. 167.
- [9] Curtiss, L. A., to be published.
- [10] JANAF Thermochemical Tables, D. R. Stull and H. Prophet, Project Directors, 2nd Ed., NSRDS-NBS-37 (1971).
- [11] Snelson, A., J. Phys. Chem. **71**, 3202 (1967).
- [12] For details on this procedure, see Curtiss, L. A., J. Chem. Phys. **67**, 1144 (1977). The vibrational frequencies for  $\text{AlF}_3$ ,  $\text{Al}_2\text{F}_6$ ,  $\text{AlCl}_3$ , and  $\text{Al}_2\text{Cl}_6$  were taken from reference [10].
- [13] Lathan, W. A., Curtiss, L. A., Hehre, W. J., Lisle, J. B., and Pople, J. A., Progress in Physical Organic Chemistry, Vol. 11, A. Streitwieser and R. S. Taft, eds. (Wiley, N.Y., 1974) p. 175.
- [14] Hargittai, M., Hargittai, I., Spiridonov, V. P., Pelissier, M., and Labarre, J. F., J. Molec. Struct. **24**, 27 (1975); Hargittai, M., Hargittai, I., and Spiridonov, V. P., J. Chem. Soc. Chem. Comm., 750 (1973).
- [15] Laughlin, W. C. and Gregory, N. W., J. Chem. Eng. Data, **20**, 137 (1975).
- [16] Mulliken, R. S., J. Chem. Phys. **23**, 1833 (1955).
- [17] Lesiecki, M. L. and Shirk, J. S., J. Chem. Phys., **56**, 4171 (1972); Companion, A. L., J. Chem. Phys. **57**, 1807 (1972).
- [18] Pimentel, G. C. and McClellan, A. L., The Hydrogen Bond (W. H. Freeman and Co., San Francisco, Calif., 1960).

## Discussion

Question (Dewing): If there is, indeed, only eight kilo-calories difference between the two forms of  $\text{LiAlF}_4$ , at the temperatures where this stuff exists, namely around 1000 Centigrade, there should be significant quantities of both of them which presumably would complicate spectra quite considerably. Do you know of any experimental evidence that this happens?

Response (Curtiss): No, I don't know of any case where it has been experimentally determined.

Question (Dewing): The second question: if there is really eight kilo-calories free energy of formation for an aluminum fluoride-nitrogen complex this implies that aluminum fluoride would be substantially more volatile in nitrogen than it is in argon. This again is a fact that I have certainly never come across, but it should be relatively easy to check experimentally. To put it a slightly different way, it means that if you did determine the vapor pressure of aluminum fluoride by transpiration experiments in nitrogen, you would get a different answer compared to doing, say, an absolute sublimation pressure or something like that.

As I say, with eight kilo-calories, that should be just about big enough to see that difference. So an experimental check would be possible.

Response (Curtiss): Right.



# SYMPOSIUM PARTICIPANTS

V. O. Altemose  
Corning Glass Works  
Sullivan Park  
Corning, NY 14830

Robert M. Atkins  
Yale University  
Mason Lab. 9 Hillhouse Ave.  
New Haven, CT 06520

Giovanni Balducci  
University of Rome  
Istituto di Chimica Fisica  
Rome, Italy 00100

Eugene John Barber  
Union Carbide Corp. - Nuclear Div.  
P.O. Box P  
Oak Ridge, TN 37763

Ezra Bar-Ziv  
Israel Atomic Energy Commission  
Nuclear Research Center-Negev  
P.O. Box 9001  
Beer-Sheva, Israel

Leslie E. Bauman  
Mississippi State Univ.  
P.O. Box 5167  
Mississippi State, MS 39762

I. R. Beattie  
Univ. of Southampton  
Dept. of Chemistry  
Southampton SO9 5NH  
United Kingdom

James H. Bechtel  
General Motors Research Lab.  
Physics Dept.  
Warren, MI 48090

Robert G. Behrens  
Los Alamos Scientific Laboratory  
P.O. Box 1663  
Los Alamos, NM 87545

Joseph Berkowitz  
Argonne National Laboratory  
Physics Division  
9700 S. Cass Ave.  
Argonne, IL 60439

Richard Beyer  
Aberdeen Proving Ground  
Aberdeen, MD 21005

Paul Blackburn  
Chemical Engineering Division  
Argonne National Laboratory  
Argonne, IL 60439

Milton Blander  
Argonne National Laboratory  
9700 S. Cass Ave.  
Argonne, IL 60439

John Blanks  
Alcoa Aluminum Company of America  
Alcoa Technical Center  
Alcoa, PA 15069

Mary Blech  
General Electric  
Nela Park  
Cleveland, OH 44112

David Bonnell  
National Bureau of Standards  
Center for Materials Science  
Washington, DC 20234

Jean Bouix  
University of Lyons  
43 boulevard du 11 novembre 1918  
69621 Villeurbanne, France

James N. Bower  
University of Florida  
5 Leigh Hall  
Gainesville, FL 32601

Allen Bowling  
Univ. of Tennessee  
Dept. of Chemistry  
Knoxville, TN 37916

John Bradshaw  
University of Florida  
109 Leigh Hall  
Gainesville, FL 32611

Leo Brewer  
Univ. of California  
Dept. of Chemistry  
Berkeley, CA 94720

E. David Cater  
University of Iowa  
Dept. of Chemistry  
Iowa City, IA 52242

I. Chabay  
National Bureau of Standards  
Bldg. 222, Rm. A121  
Washington, DC 20234

Calvin Chan  
Univ. of California - Berkeley  
Dept. of Mechanical Engineering  
Berkeley, CA 94720

Malcolm W. Chase  
The Dow Chemical Company  
Thermal Research, 1707 Bldg.  
Midland, MI 48640

Christian Chatillon  
LTPCM/ENSEEG  
A324, Physics  
Washington, DC 20234

Jack H. Colwell  
National Bureau of Standards  
A324, Physics  
Washington, DC 20234

Alan Covington  
NASA - Ames Research Center  
Mail Stop 234-1  
Moffett Field, CA 94035

Tom Coyle  
National Bureau of Standards  
Center for Materials Science  
Washington, DC 20234

John Creighton  
Lawrence Livermore Laboratory  
P.O. Box 808 (L-35)  
Livermore, CA 94550

David R. Crosley  
Ballistic Research Laboratory  
Aberdeen Proving Ground  
Aberdeen, MD 21005

Larry A. Curtiss  
Chemical Engineering Div.  
Argonne National Laboratory  
Argonne, IL 60439

John W. Daily  
University of California  
Mechanical Engineering  
6163 Etcheverry Hall  
Berkeley, CA 94720

Mark A. DeWilde  
U.S. Army Ballistic Research Labs  
Aberdeen Proving Grounds  
Aberdeen Proving Grounds, MD 21030

Ernest W. Dewing  
Aluminum Co. of Canada  
Research Centre  
Kingston, Ontario  
Canada K7L 4Z4

Ray Dils  
National Bureau of Standards  
Center for Mechanical Engineering  
and Process Technology  
Washington, DC 20234

J. R. Downey  
Dow Chemical USA  
1707 Building  
Midland, MI 48640

Michael C. Drake  
National Bureau of Standards  
Bldg. 223, Rm. A329  
Washington, DC 20234

Alan C. Eckbreth  
United Technologies Res. Ctr.  
Silver Land  
East Hartford, CT 06108

Thomas L. Eddy  
West Virginia Univ.  
Dept. Mech. Engr. & Mechanics  
Morgantown, WV 26506

Jimmie G. Edwards  
Univ. of Toledo  
Dept. of Chemistry  
Toledo, OH 43606

John R. Ferron  
Dept. of Chem. Eng.  
Univ. of Rochester  
Rochester, NY 14627

A. Fontijn  
Aerochem Research Lab. Inc.  
P.O. Box 12  
Princeton, NJ 14627

R. M. Fristrom  
Applied Physics Laboratory  
Johns Hopkins University  
8621 Georgia Ave.  
Silver Spring, MD 20910

F. W. Froben  
Freie Universitat Berlin  
FB20, WE2, Boltzmannstrasse 20  
1000 Berlin 33, Germany

David J. Frurip  
Argonne National Laboratory  
Bldg. 205  
Argonne, IL 60439

Richard G. Gann  
National Bureau of Standards  
Center for Fire Research  
Washington, DC 20234

W. C. Gardiner  
Univ. of Texas  
WEL103W  
Austin, TX 78712

Michael Gersh  
Aerodyne Research, Inc.  
Crosby Dr.  
Bedford, MA 01730

Paul W. Gilles  
Univ. of Kansas  
Dept. of Chemistry  
Lawrence, KS 66045

Karl Gingerich  
Texas A & M Univ.  
Dept. of Chem.  
College Station, TX 77843

James L. Gole  
Georgia Inst. of Technology  
Chemistry Dept.  
Atlanta, GA 30332

William R. M. Graham  
Dept. of Physics  
Texas Christian Univ.  
P.O. Box 29160A  
Ft. Worth, TX 76129

Frank T. Greene  
Midwest Research Inst.  
425 Volken Blvd.  
Kansas City, MO 64410

Robert T. Grimley  
Purdue University  
Dept. of Chemistry  
W. Lafayette, IN 47907

Earl A. Gulbransen  
Dept. of Metallurgical and  
Materials Engineering  
Univ. of Pittsburgh  
Pittsburgh, PA 15261

L. Haas  
National Bureau of Standards  
Washington, DC 20234

Jeffrey C. Halle  
Naval Research Lab.  
Code 6130 - Chemistry Div.  
Washington, DC 20375

D. R. Hardesty  
Combustion Research Div.  
Sandia Laboratories  
Livermore, CA 94550

John Hastie  
National Bureau of Standards  
Center for Materials Science  
Washington, DC 20234

R. H. Hauge  
Rice University  
Dept. of Chemistry  
Houston, TX 77001

D. L. Hildenbrand  
SRI International  
Menlo Park, CA 94025

James C. Hindman  
Argonne National Laboratory  
8700 So. Cass Ave.  
Argonne, IL 60439

C. Hirayama  
Westinghouse Research &  
Development Center  
1310 Beulah Road  
Pittsburgh, PA 15235

John A. Holy  
Monsanto Research Corp.  
P.O. Box 32, A-158  
Miamisburg, OH 45542

William Horton  
National Bureau of Standards  
Center for Materials Science  
Washington, DC 20234

Chen-Chao Hsu  
Argonne National Laboratory  
D-205, 9700 S. Cass Ave.  
Argonne, IL 60439

L. W. Hunter  
Applied Physics Laboratory  
Johns Hopkins Rd.  
Laurel, MD 20810

Marilyn E. Jacox  
National Bureau of Standards  
Molecular Spectroscopy Div.  
Washington, DC 20234

Larry Jeffers  
Babcock Wilcox Co.  
1562 Beeson St.  
Alliance, OH 44601

Jack G. Kay  
Drexel Univ.  
32nd & Chestnut Streets  
Philadelphia, PA 19104

Werner Klotzbucher  
Univ. of Toronto  
Erindale College  
3359 Mississauga Rd.  
Mississauga, Ont. L5L 1C6

Lon B. Knight, Jr.  
Furman Univ.  
Chemistry Dept.  
Greenville, SC 29613

F. Kohl  
NASA Lewis Research Ctr.  
21000 Brookpark Road  
Cleveland, OH 44135

Charles Kolb  
Aerodyne Research, Inc.  
Crosby Drive  
Bedford, MA 01730

Mitsuo Koshi  
University of Tokyo  
Hongo, Bunkyo-ku, Tokyo  
Japan 113

Ralph Krause  
National Bureau of Standards  
Center for Materials Science  
Washington, DC 20234

Steven C. Lamey  
U.S. Dept. of Energy  
Morgantown Energy Tech. Ctr.  
P.O. Box 880  
Morgantown, WV 26505

Kenneth C. Lapworth  
National Physical Laboratory (U.K.)  
Teddington, England TW11 9LJ

Thomas W. Lassiter  
Dept. of Chemistry  
Univ. of Tennessee  
Knoxville, TN 37916

L. Leibowitz  
Argonne National Laboratory  
9700 S. Cass Avenue  
Argonne, IL 60439

Young F. Lee  
Union Carbide Corp.  
Metals Division  
4625 Royal Ave.  
Niagara Falls, NY 14302

D. R. Lide, Jr.  
National Bureau of Standards  
Office of Standard Reference Data  
Washington, DC 20234

M. C. Lin  
Naval Research Laboratory  
Code 6110  
Washington, DC 20375

Sing-Shong Lin  
Army Mat. & Mech. Research Ctr.  
Arsenal St.  
Watertown, MA 02172

Kenneth A. Lincoln  
NASA - Ames Research Ctr.  
Mail Stop 234-1  
Moffett Field, CA 94035

Frank Lovas  
National Bureau of Standards  
Center for Thermodynamics and  
Molecular Science  
Washington, DC 20234

Kenneth McCulloh  
National Bureau of Standards  
Center for Thermodynamics &  
Molecular Science  
Washington, DC 20234

J. R. McDonald  
Naval Research Laboratory  
Chemistry Division  
Washington, DC 20375

Michael E. McIlwain  
Argonne National Laboratory  
9700 So. Cass Ave.  
Argonne, IL 60439

Julius L. Mack  
Dept. of Chemistry  
Univ. of D.C.  
1331 H. St. NW  
Washington, DC 20005

G. Mallard  
National Bureau of Standards  
Washington, DC 20234

Thomas B. Malloy, Jr.  
Mississippi State Univ.  
P.O. Box 5167  
Mississippi State, MS 39762

Joseph F. Masi  
AFOSR/NA  
Bldg. 410, Bolling AFB  
Washington, DC 20332

Lynn A. Melton  
The Univ. of Texas at Dallas  
Chemistry Department, Box 688  
Richardson, TX 75080

Federico Miller  
Laredo Junior College  
West End Washington St.  
Laredo, TX 78040

Glenn H. Miller  
Sandia Laboratories  
Division 5216  
P.O. Box 5800  
Albuquerque, NM 87185

William Miller  
Aero Chem Research Labs  
P.O. Box 12  
Princeton, NJ 08540

Thomas A. Milne  
Solar Energy Research Inst.  
1536 Cole Blvd.  
Golden, CO 80401

J. W. Mitchell  
Bell Laboratories  
MH 10239 Bell Labs  
Murray Hill, NJ 07974

Barbara A. Mueller  
Los Alamos Scientific  
Laboratory MS-348  
P.O. Box 1663  
Los Alamos, NM 87645

Clifford E. Myers  
Dept. of Chemistry  
State Univ. of New York  
at Binghamton  
Binghamton, NY 13901

Stephen Nicolosi  
Brookhaven National Laboratory  
Upton, NJ 11973

J. S. Ogden  
Univ. of Southampton  
Dept. of Chemistry  
Southampton SO9 5NH  
United Kingdom

Roland W. Ohse  
Commission of the European  
Communities  
7500 Karlsruhe 1, postfach 2266  
Federal Republic of Germany

George N. Papatheodorou  
Argonne National Laboratory  
CEN-205  
Argonne, IL 60439

Ernest Plante  
National Bureau of Standards  
Center for Materials Science  
Washington, DC 20234

John W. Reed  
Monsanto Research Corporation  
P.O. Box 32, A-158  
Miamisburg, OH 45342

James J. Reuther  
Fuel Science Section  
The Pennsylvania State Univ.  
316 Steidle Bldg.  
University Park, PA 16802

Gary H. Rinehart  
Los Alamos Scientific Lab.  
P.O. Box 1663  
Los Alamos, NM 87545

Bruce Rising  
Penn State University  
316 Steidle Bldg.  
University Park, PA 16802

W. M. Roquemore  
Air Force Aero Propulsion Lab.  
Wright-Patterson AFB, OH 45433

Gerd M. Rosenblatt  
The Pennsylvania State Univ.  
Dept. of Chemistry, 152 Davey Lab.  
University Park, PA 16802

Daniel E. Rosner  
Yale University 319 ML  
New Haven, CT 06520



Paul Roth  
Univ. of Duisburg  
Kommandautenstr.60, 41 Duisburg 1  
Duisburg, Germany

D. Sanders  
National Bureau of Standards  
Bldg. 223, Rm. B328  
Washington, DC 20234

T. Sasamoto  
Mass. Inst. Tech.  
MIT, Ceramic Div.  
Rm. 13-4057  
Cambridge, MA 02139

Peter K. Schenck  
National Bureau of Standards  
Rm. A329, Bldg. 223  
Washington, DC 20234

Tom Sedgwick  
IBM Research  
P.O. Box 218  
Yorktown Hts., NY 10598

Sidney A. Self  
Stanford University  
Dept. of Mechanical Engineering  
Stanford, CA 94305

Walter M. Shaub  
2027 Winged Foot Court  
Reston, VA 22091

Richard R. Smardzewski  
Naval Research Laboratory  
Code 6130  
Washington, DC 20375

Richard D. Smith  
Battelle-Northwest  
Bldg. 329 - 300 Area  
Richland, WA 99352

John E. Spencer  
General Electric Co.  
Nela Park  
Cleveland, OH 44112

David R. Squire  
U.S. Army Research Office  
P.O. Box 12211  
Research Triangle Park, NC 27709

Carl A. Stearns  
NASA - Lewis Res. Ctr.  
21000 Brookpark Road  
Cleveland, OH 44135

Martin Steinberg  
Quantum Institute  
Univ. of California  
Santa Barbara, CA 93106

Kurt H. Stern  
Naval Research Laboratory  
Code 6130  
455 Overlook Ave.  
Washington, DC 20375

David Stevenson  
Stanford Univ.  
Dept. of Materials Science  
Stanford, CA 94305

Gerald W. Stewart  
U.S. Dept. of Energy, Morgantown  
Energy Technology Center  
P.O. Box 880  
Morgantown, WV 26505

Charter D. Stinespring  
U.S. Dept. of Energy  
Morgantown Energy Technology Ctr.  
P.O. Box 880  
Morgantown, WV 26505

E. K. Storms  
Los Alamos Scientific Lab.  
Los Alamos, NM

David Tevault  
Naval Research Lab.  
Code 6130  
Washington, DC 20375

Stephen S. C. Tong  
Corning Glass Works  
Sullivan Park  
Corning, NY 14830

W. Tsang  
National Bureau of Standards  
Washington, DC 20234

John Vitko, Jr.  
Sandia Laboratories  
Div 8342  
Livermore, CA 94550

Harue Wada  
University of Michigan  
4227 East Engineering, Dept.  
Mats. and Met. Engineering  
Ann Arbor, MI 48109

Donald Wagman  
National Bureau of Standards  
Center for Thermodynamics &  
Molecular Science  
Washington, DC 20234

B. Webb  
Propellants, Explosives and Rocket  
Motor Establishment  
Westcott, Aylesbury  
Buckinghamshire, England

William Weltner, Jr.  
Univ. of Florida  
Dept. of Chemistry  
Gainesville, FL 32611

Jack Wenzel  
National Bureau of Standards  
Bldg. 223  
Washington, DC 20234

Dale E. Work  
GTE Sylvania  
100 Endicott St.  
Danvers, MA 01923

Joda Wormhoudt  
Aerodyne Research Inc.  
Crosby Drive  
Bedford, MA 01730

Perry P. Yaney  
Dept. of Physics  
Univ. of Dayton, 300 College Park  
Dayton, OH 45469

L. N. Yannopoulos  
Westinghouse Res. & Dev. Center  
Churchill Boro  
Pittsburgh, PA 15235

Robert J. Zollweg  
Westinghouse R & D Center  
1310 Beulah Road  
Pittsburgh, PA 15235



# AUTHOR INDEX

Allen, Jr., J. E. . . . .	1153	Gilles, Paul W. . . . .	231
Allibert, M. . . . .	181	Gingerich, Karl A. . . . .	289
Anderson, W. R. . . . .	1153	Grabner, L. H. . . . .	1105
Arbach, G. U. . . . .	885	Gransden, S. E. . . . .	557
Babelot, J. F. . . . .	83	Greene, Frank T. . . . .	431
Baronavski, A. P. . . . .	817	Greehalch, D. A. . . . .	597
Beachey, Jacob E. . . . .	431	Grimley, Robert T. . . . .	211
Beattie, I. R. . . . .	597	Gruen, D. M. . . . .	1517
Behrens, Robert G. . . . .	125	Grunfelder, C. . . . .	1071
Berkowitz, J. . . . .	757	Gulbransen, E. A. . . . .	1639
Blander, M. . . . .	1597,1707	Hall, R. J. . . . .	943
Bonnell, David W. . . . .	357	Haller, W. K. . . . .	111
Bouix, J. . . . .	899	Haraguchi, H. . . . .	1079
Bower, J. . . . .	1079	Hardesty, D. R. . . . .	1407
Bowling, R. A. . . . .	771	Hargis, Jr., P. J. . . . .	1135
Bradshaw, J. . . . .	1079	Harvey, A. B. . . . .	817
Brostow, W. . . . .	1619	Hastie, John W. . . . .	357,1105
Cater, E. David . . . . .	3237	Hauge, R. H. . . . .	495,557
Cercignani, L. . . . .	83	Hildenbrand, D. L. . . . .	171
Chan, C. . . . .	847	Hillel, R. . . . .	899
Chase, M. W. . . . .	1581	Hirayama, C. . . . .	1539
Chatillon, C. . . . .	181	Hoshall, C. H. . . . .	1071
Chatwani, A. U. . . . .	1373	Hsu, C. C. . . . .	1683
Chidsey, I. L. . . . .	1181	Hunter, L. W. . . . .	1071
Creighton, J. R. . . . .	1223	Inomata, T. . . . .	1327
Crosley, D. R. . . . .	1153,1171,1181	Ip, P. . . . .	1161
Curtiss, L. A. . . . .	791	Jacox, Marilyn E. . . . .	529
Daily, J. W. . . . .	847	Jensen, D. E. . . . .	1195
Davidson, Ernest R. . . . .	545	Johnson, C. E. . . . .	1683
De La Mora, J. . . . .	1451	Just, T. H. . . . .	1339
DeWilde, M. A. . . . .	1171	Kauffman, J. W. . . . .	557
Dils, R. R. . . . .	1027	Kerr, D. L. . . . .	1373
Downey, J. R. . . . .	1581	Kinsman, P. R. . . . .	83
Drake, Michael C. . . . .	609,1105	Klotzbucher, Werner, E. . . . .	567
Dun, Haiping . . . . .	411	Knight, L. B. . . . .	545
Eckbreth, A. C. . . . .	943	Kobayashi, Michio . . . . .	283
Edwards, Jimmie G. . . . .	67	Kolb, C. E. . . . .	457,679
Fansler, T. B. . . . .	1153	Kohl, Fred J. . . . .	303,1451
Ferron, J. R. . . . .	1373	Korobeinichev, O. P. . . . .	479
Feugier, A. . . . .	1315	Lamont, S. . . . .	817
Follansbee, P. S. . . . .	1027	Larzilliere, Michael . . . . .	529
Fontijn, A. . . . .	1359	Lassiter, T. W. . . . .	771
Forsman, James. A. . . . .	211	Lide, Jr., D. R. . . . .	1571
Fries, James E. . . . .	237	Lin, C. Y. . . . .	1539
Fristrom, R. M. . . . .	1071	Lin, M. C. . . . .	1249,1551
Froben, F. W. . . . .	523	Long, K. A. . . . .	83
Fruvip, D. J. . . . .	1597	Lund, C. M. . . . .	1223
Fryburg, George C. . . . .	303,1451	Machaelides, A. . . . .	899
Fujiwara, K. . . . .	1079	Magill, J. . . . .	83
Gardiner, Jr., W. C. . . . .	835	Mallard, W. G. . . . .	865
Gersh, M. E. . . . .	679	Margrave, J. L. . . . .	495,557
Gevantman, L. N. . . . .	157	Martin, R. L. . . . .	545

Mattes, Brenton L. . . . . 411  
 McDonald, J. R. . . . . 817  
 Meier, G. H. . . . . 1639  
  
 Melton, L. A. . . . . 153  
 Miller, Federico . . . . . 39  
 Miller, G. H. . . . . 1135  
 Miller, Robert A. . . . . 303  
 Miller, W. J. . . . . 443  
 Milne, Thomas A. . . . . 431  
 Moriwaki, T. . . . . 1327  
 Mulac, A. J. . . . . 1135  
 Mueller, B. A. . . . . 143,237  
 Mueller, Barbara H. . . . . 237  
 Muller, III, C. H. . . . . 855  
  
 Ogden, J. S. . . . . 511  
 Ohse, R. W. . . . . 83  
 Okazaki, S. . . . . 1327  
 Omenetto, N. . . . . 1079  
 Orlovskii, V. P. . . . . 1497  
 Øye, H. A. . . . . 1517  
 Ozin, Geoffrey A. . . . . 567  
  
 Papatheodorou, G. N. . . . . 647  
 Pasternack, L. . . . . 817  
 Pattoret, A. . . . . 181  
 Plante, E. R. . . . . 265  
 Pohl, J. W. . . . . 1407  
 Pratt, D. T. . . . . 1265  
  
 Reuther, J. J. . . . . 1281  
 Rinehart, Gary H. . . . . 125  
 Roquemore, W. M. . . . . 973  
 Rosenblatt, Gerd M. . . . . 609  
 Rosner, D. E. . . . . 1451  
 Roth, P. . . . . 1339  
  
 Sanders, D. M. . . . . 111  
 Santoro, G. . . . . 1451  
 Sasamoto, Tadashi . . . . . 283  
 Sata, Toshiyuki . . . . . 283  
 Schafer, H. . . . . 1507  
 Schenck, P. K. . . . . 865  
 Schofield, K. . . . . 855  
 Schweitzer, G. K. . . . . 771  
 Scotti, A. . . . . 83  
 Sedgwich, T. O. . . . . 885  
 Self, S. A. . . . . 915  
 Seshadri, K. . . . . 1451  
 Shaub, W. M. . . . . 1249  
 Shelton, Robert I. . . . . 231  
 Smyth, K. C. . . . . 865  
 Spiridonov, V. P. . . . . 711  
 Stearns, Carl A. . . . . 303,1451  
 Steinberg, M. . . . . 855  
 Stevenson, David A. . . . . 411  
 Storms, E. K. . . . . 143  
 Strauss, H. L. . . . . 1611  
 Suzuki, M. . . . . 1327  
 Syverud, A. N. . . . . 1581

Taylor, J. E. . . . . 1353  
 Tereshenko, A. G. . . . . 479  
 Tevault, D. . . . . 1551  
 Tiemann, E. . . . . 695  
 Torring, T. . . . . 695  
 Travis, J. C. . . . . 865  
  
 Vick, D. O. . . . . 771  
  
 Weeks, S. . . . . 1079  
 Weltner, Jr., William . . . . . 587  
 White, Jr., H. J. . . . . 1571  
 Winefordner, J. D. . . . . 1079  
 Wormhoudt, J. C. . . . . 457  
  
 Yaney, P. O. . . . . 973  
  
 Zasorin, E. Z. . . . . 711  
 Zollweg, R. J. . . . . 1477



U.S. DEPT. OF COMM. BIBLIOGRAPHIC DATA SHEET	1. PUBLICATION OR REPORT NO.  NBS SP 561 Vo. 1	2. Gov't. Accession No.	3. Recipient's Accession No.
4. TITLE AND SUBTITLE CHARACTERIZATION OF HIGH TEMPERATURE VAPORS AND GASES		5. Publication Date September 1979	
		6. Performing Organization Code	
7. AUTHOR(S) Edited by John W. Hastie		8. Performing Organ. Report No.	
9. PERFORMING ORGANIZATION NAME AND ADDRESS  NATIONAL BUREAU OF STANDARDS DEPARTMENT OF COMMERCE WASHINGTON, DC 20234		10. Project/Task/Work Unit No.	
		11. Contract/Grant No.	
2. SPONSORING ORGANIZATION NAME AND COMPLETE ADDRESS (Street, City, State, ZIP)  Same as above		13. Type of Report & Period Covered  N/A	
		14. Sponsoring Agency Code	
5. SUPPLEMENTARY NOTES Library of Congress Number 79-600152  <input type="checkbox"/> Document describes a computer program; SF-185, FIPS Software Summary, is attached.			
6. ABSTRACT (A 200-word or less factual summary of most significant information. If document includes a significant bibliography or literature survey, mention it here.)  This book is based on the proceedings of the 10th Materials Research Symposium, held at the National Bureau of Standards, Gaithersburg, Maryland, September 18-22, 1978. The symposium was sponsored by the National Measurement Laboratory (formerly Institute for Materials Research). Modern technology increasingly requires materials and processes to function at high temperatures--a condition where the vapor, gaseous or plasma phase becomes significant. Characterization of such atmospheres, or components thereof, is a challenging problem requiring adaptation of existing and development of new experimental and theoretical techniques. The aim of the symposium was to assess the state-of-the-art and future directions and characterization methods for high temperature vapors including, where appropriate, gases and, to a lesser extent, plasmas. In order to prevent, as far as possible, serious omissions of important new or improved techniques, a number of papers not delivered at the Symposium were solicited for inclusion in this publication. A total of eighty-six papers (invited and contributed) or chapters representing nine countries are contained in these volumes. The discussion, which followed most of the delivered papers, is also included.			
7. KEY WORDS (six to twelve entries; alphabetical order; capitalize only the first letter of the first key word unless a proper name; separated by semicolons) Combustion; equilibrium; high temperature; isolation; lasers; mass spectrometry; matrix; modeling; vapors			
18. AVAILABILITY  <input checked="" type="checkbox"/> Unlimited  <input type="checkbox"/> For Official Distribution. Do Not Release to NTIS  <input checked="" type="checkbox"/> Order From Sup. of Doc., U.S. Government Printing Office, Washington, DC 20402, SD Stock No. SN003-003-02124-5  <input type="checkbox"/> Order From National Technical Information Service (NTIS), Springfield, VA, 22161		19. SECURITY CLASS (THIS REPORT)  UNCLASSIFIED  20. SECURITY CLASS (THIS PAGE)  UNCLASSIFIED	21. NO. OF PRINTED PAGES  800  22. Price  \$20.00 SET

There's  
a new  
look  
to...

# DIMENSIONS

... the monthly magazine of the National Bureau of Standards. Still featured are special articles of general interest on current topics such as consumer product safety and building technology. In addition, new sections are designed to ... PROVIDE SCIENTISTS with illustrated discussions of recent technical developments and work in progress ... INFORM INDUSTRIAL MANAGERS of technology transfer activities in Federal and private labs. ... DESCRIBE TO MANUFACTURERS advances in the field of voluntary and mandatory standards. The new DIMENSIONS/NBS also carries complete listings of upcoming conferences to be held at NBS and reports on all the latest NBS publications, with information on how to order. Finally, each issue carries a page of News Briefs, aimed at keeping scientist and consumer alike up to date on major developments at the Nation's physical sciences and measurement laboratory.

(please detach here)

## SUBSCRIPTION ORDER FORM

Enter my Subscription To DIMENSIONS/NBS at \$11.00. Add \$2.75 for foreign mailing. No additional postage is required for mailing within the United States or its possessions. Domestic remittances should be made either by postal money order, express money order, or check. Foreign remittances should be made either by international money order, draft on an American bank, or by UNESCO coupons.

Send Subscription to:

NAME-FIRST, LAST																							
COMPANY NAME OR ADDITIONAL ADDRESS LINE																							
STREET ADDRESS																							
CITY												STATE				ZIP CODE							

PLEASE PRINT

- ☐ Remittance Enclosed  
(Make checks payable to Superintendent of Documents)
- ☐ Charge to my Deposit Account No.

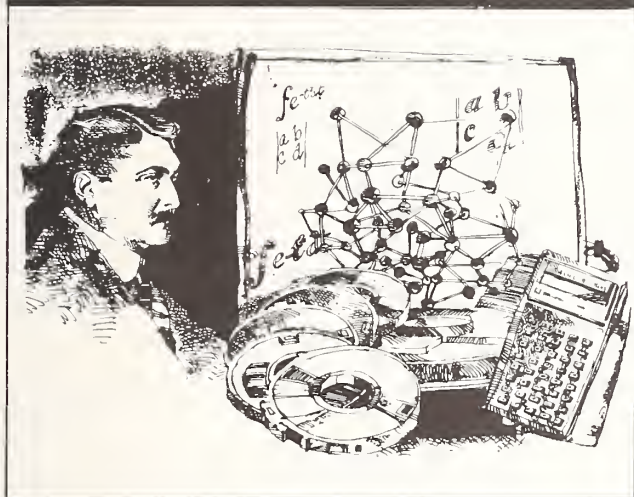
MAIL ORDER FORM TO:  
Superintendent of Documents  
Government Printing Office  
Washington, D.C. 20402

# JOURNAL OF RESEARCH

of the National Bureau of Standards



U.S. DEPARTMENT OF COMMERCE



## Subscribe now— The new National Bureau of Standards Journal

The expanded Journal of Research of the National Bureau of Standards reports NBS research and development in those disciplines of the physical and engineering sciences in which the Bureau is active. These include physics, chemistry, engineering, mathematics, and computer sciences. Papers cover a broad range of subjects, with major emphasis on measurement methodology, and the basic technology underlying standardization. Also included from time to time are survey articles on topics closely related to the Bureau's technical and scientific programs. As a special service to subscribers each issue contains complete citations to all recent NBS publications in NBS and non-NBS media. Issued six times a year. Annual subscriptions: domestic \$17.00; foreign \$21.25. Single copy, \$3.00 domestic; \$3.75 foreign.

- Note: The Journal was formerly published in two sections: Section A "Physics and Chemistry" and Section B "Mathematical Sciences."

NBS Board of Editors  
Churchill Eisenhart,  
Executive Editor (Mathematics)  
John W. Cooper (Physics)  
Donald D. Wagman (Chemistry)  
Andrew J. Fowell (Engineering)  
Joseph O. Harrison (Computer Science)  
Howard J. M. Hanley (Boulder Labs.)

### Subscription Order Form

Enter my subscription to NBS Journal of Research at \$17.00. Add \$4.25 for foreign mailing. No additional postage is required for mailing within the United States or its possessions. (SJRA—File Code 2N)

Send Subscription to:

Name-First, Last		
Company Name or Additional Address Line		
Street Address		
City	State	Zip Code
(or) COUNTRY		

PLEASE PRINT

### Credit Card Orders Only

Total charges \$ \_\_\_\_\_ Fill in the boxes below.

Credit Card No.	Master Charge Interbank No.	Expiration Date Month/Year

☐ Remittance Enclosed. Domestic: Check or money order. Foreign: International money order, draft on an American or Canadian Bank, or by UNESCO coupons, Made payable to the Superintendent of Documents.

☐ Charge to my Deposit Account No. \_\_\_\_\_

MAIL ORDER FORM TO:  
Superintendent of Documents  
Government Printing Office  
Washington, D. C. 20402

JOU  
of t  
and  
engi  
inclu  
com  
with  
the  
clud  
relat  
a sp  
citat  
NBS  
dom  
\$3.7  
Not  
Sect  
mat  
DIM  
This  
engi  
consc  
with  
high  
pro  
abab  
form  
gran  
of n  
insti  
A

Mon  
atur  
and  
Han  
trial  
tion  
and  
Spec  
spon  
pub  
posc  
App  
uals  
cher  
and  
Nati  
relat  
mat  
eval  
ordi  
Stan

The  
aggr  
Cry  
tu  
ti  
Liq  
Ann



# NBS TECHNICAL PUBLICATIONS

## PERIODICALS

**JOURNAL OF RESEARCH**—The Journal of Research of the National Bureau of Standards reports NBS research and development in those disciplines of the physical and engineering sciences in which the Bureau is active. These include physics, chemistry, engineering, mathematics, and computer sciences. Papers cover a broad range of subjects, with major emphasis on measurement methodology, and the basic technology underlying standardization. Also included from time to time are survey articles on topics closely related to the Bureau's technical and scientific programs. As a special service to subscribers each issue contains complete citations to all recent NBS publications in NBS and non-NBS media. Issued six times a year. Annual subscription: domestic \$17.00; foreign \$21.25. Single copy, \$3.00 domestic; \$3.75 foreign.

Note: The Journal was formerly published in two sections: Section A "Physics and Chemistry" and Section B "Mathematical Sciences."

### DIMENSIONS/NBS

This monthly magazine is published to inform scientists, engineers, businessmen, industry, teachers, students, and consumers of the latest advances in science and technology, with primary emphasis on the work at NBS. The magazine highlights and reviews such issues as energy research, fire protection, building technology, metric conversion, pollution abatement, health and safety, and consumer product performance. In addition, it reports the results of Bureau programs in measurement standards and techniques, properties of matter and materials, engineering standards and services, instrumentation, and automatic data processing.

Annual subscription: Domestic, \$11.00; Foreign \$13.75

## NONPERIODICALS

**Monographs**—Major contributions to the technical literature on various subjects related to the Bureau's scientific and technical activities.

**Handbooks**—Recommended codes of engineering and industrial practice (including safety codes) developed in cooperation with interested industries, professional organizations, and regulatory bodies.

**Special Publications**—Include proceedings of conferences sponsored by NBS, NBS annual reports, and other special publications appropriate to this grouping such as wall charts, pocket cards, and bibliographies.

**Applied Mathematics Series**—Mathematical tables, manuals, and studies of special interest to physicists, engineers, chemists, biologists, mathematicians, computer programmers, and others engaged in scientific and technical work.

**National Standard Reference Data Series**—Provides quantitative data on the physical and chemical properties of materials, compiled from the world's literature and critically evaluated. Developed under a world-wide program coordinated by NBS. Program under authority of National Standard Data Act (Public Law 90-396).

NOTE: At present the principal publication outlet for these data is the Journal of Physical and Chemical Reference Data (JPCRD) published quarterly for NBS by the American Chemical Society (ACS) and the American Institute of Physics (AIP). Subscriptions, reprints, and supplements available from ACS, 1155 Sixteenth St. N.W., Wash., D.C. 20056.

**Building Science Series**—Disseminates technical information developed at the Bureau on building materials, components, systems, and whole structures. The series presents research results, test methods, and performance criteria related to the structural and environmental functions and the durability and safety characteristics of building elements and systems.

**Technical Notes**—Studies or reports which are complete in themselves but restrictive in their treatment of a subject. Analogous to monographs but not so comprehensive in scope or definitive in treatment of the subject area. Often serve as a vehicle for final reports of work performed at NBS under the sponsorship of other government agencies.

**Voluntary Product Standards**—Developed under procedures published by the Department of Commerce in Part 10, Title 15, of the Code of Federal Regulations. The purpose of the standards is to establish nationally recognized requirements for products, and to provide all concerned interests with a basis for common understanding of the characteristics of the products. NBS administers this program as a supplement to the activities of the private sector standardizing organizations.

**Consumer Information Series**—Practical information, based on NBS research and experience, covering areas of interest to the consumer. Easily understandable language and illustrations provide useful background knowledge for shopping in today's technological marketplace.

Order above NBS publications from: Superintendent of Documents, Government Printing Office, Washington, D.C. 20402.

Order following NBS publications—NBSIR's and FIPS from the National Technical Information Services, Springfield, Va. 22161.

**Federal Information Processing Standards Publications (FIPS PUB)**—Publications in this series collectively constitute the Federal Information Processing Standards Register. Register serves as the official source of information in the Federal Government regarding standards issued by NBS pursuant to the Federal Property and Administrative Services Act of 1949 as amended, Public Law 89-306 (79 Stat. 1127), and as implemented by Executive Order 11717 (38 FR 12315, dated May 11, 1973) and Part 6 of Title 15 CFR (Code of Federal Regulations).

**NBS Interagency Reports (NBSIR)**—A special series of interim or final reports on work performed by NBS for outside sponsors (both government and non-government). In general, initial distribution is handled by the sponsor; public distribution is by the National Technical Information Services (Springfield, Va. 22161) in paper copy or microfiche form.

## BIBLIOGRAPHIC SUBSCRIPTION SERVICES

The following current-awareness and literature-survey bibliographies are issued periodically by the Bureau:

**Cryogenic Data Center Current Awareness Service.** A literature survey issued biweekly. Annual subscription: Domestic, \$25.00; Foreign, \$30.00.

**Liquefied Natural Gas.** A literature survey issued quarterly. Annual subscription: \$20.00.

**Superconducting Devices and Materials.** A literature survey issued quarterly. Annual subscription: \$30.00. Send subscription orders and remittances for the preceding bibliographic services to National Bureau of Standards, Cryogenic Data Center (736.00) Boulder, Colorado 80303.



**U.S. DEPARTMENT OF COMMERCE**  
**National Bureau of Standards**  
Washington, D.C. 20234

OFFICIAL BUSINESS

Penalty for Private Use, \$300

POSTAGE AND FEES PAID  
U.S. DEPARTMENT OF COMMERCE  
COM-215



SPECIAL FOURTH-CLASS RATE  
BOOK

---

















